frontiers | Research Topics

Geological disasters in deep engineering mechanism, warning and risk mitigation

Edited by
Guang-Liang Feng, Fengqiang Gong, Chi Zhang and Shibing Huang

Published in
Frontiers in Earth Science



FRONTIERS EBOOK COPYRIGHT STATEMENT

The copyright in the text of individual articles in this ebook is the property of their respective authors or their respective institutions or funders. The copyright in graphics and images within each article may be subject to copyright of other parties. In both cases this is subject to a license granted to Frontiers.

The compilation of articles constituting this ebook is the property of Frontiers.

Each article within this ebook, and the ebook itself, are published under the most recent version of the Creative Commons CC-BY licence. The version current at the date of publication of this ebook is CC-BY 4.0. If the CC-BY licence is updated, the licence granted by Frontiers is automatically updated to the new version.

When exercising any right under the CC-BY licence, Frontiers must be attributed as the original publisher of the article or ebook, as applicable.

Authors have the responsibility of ensuring that any graphics or other materials which are the property of others may be included in the CC-BY licence, but this should be checked before relying on the CC-BY licence to reproduce those materials. Any copyright notices relating to those materials must be complied with.

Copyright and source acknowledgement notices may not be removed and must be displayed in any copy, derivative work or partial copy which includes the elements in question.

All copyright, and all rights therein, are protected by national and international copyright laws. The above represents a summary only. For further information please read Frontiers' Conditions for Website Use and Copyright Statement, and the applicable CC-BY licence.

ISSN 1664-8714
ISBN 978-2-8325-2507-4
DOI 10.3389/978-2-8325-2507-4

About Frontiers

Frontiers is more than just an open access publisher of scholarly articles: it is a pioneering approach to the world of academia, radically improving the way scholarly research is managed. The grand vision of Frontiers is a world where all people have an equal opportunity to seek, share and generate knowledge. Frontiers provides immediate and permanent online open access to all its publications, but this alone is not enough to realize our grand goals.

Frontiers journal series

The Frontiers journal series is a multi-tier and interdisciplinary set of open-access, online journals, promising a paradigm shift from the current review, selection and dissemination processes in academic publishing. All Frontiers journals are driven by researchers for researchers; therefore, they constitute a service to the scholarly community. At the same time, the *Frontiers journal series* operates on a revolutionary invention, the tiered publishing system, initially addressing specific communities of scholars, and gradually climbing up to broader public understanding, thus serving the interests of the lay society, too.

Dedication to quality

Each Frontiers article is a landmark of the highest quality, thanks to genuinely collaborative interactions between authors and review editors, who include some of the world's best academicians. Research must be certified by peers before entering a stream of knowledge that may eventually reach the public - and shape society; therefore, Frontiers only applies the most rigorous and unbiased reviews. Frontiers revolutionizes research publishing by freely delivering the most outstanding research, evaluated with no bias from both the academic and social point of view. By applying the most advanced information technologies, Frontiers is catapulting scholarly publishing into a new generation.

What are Frontiers Research Topics?

Frontiers Research Topics are very popular trademarks of the *Frontiers journals series*: they are collections of at least ten articles, all centered on a particular subject. With their unique mix of varied contributions from Original Research to Review Articles, Frontiers Research Topics unify the most influential researchers, the latest key findings and historical advances in a hot research area.

Find out more on how to host your own Frontiers Research Topic or contribute to one as an author by contacting the Frontiers editorial office: frontiersin.org/about/contact

Geological disasters in deep engineering mechanism, warning and risk mitigation

Topic editors

Guang-Liang Feng — Institute of Rock and Soil Mechanics, Chinese Academy of Sciences (CAS), China

Fengqiang Gong — Southeast University, China

Chi Zhang — University of Vienna, Austria

Shibing Huang — Wuhan University of Science and Technology, China

Citation

Feng, G.-L., Gong, F., Zhang, C., Huang, S., eds. (2023). *Geological disasters in deep engineering mechanism, warning and risk mitigation*. Lausanne: Frontiers Media SA. doi: 10.3389/978-2-8325-2507-4

Table of contents

07 Editorial: Geological disasters in deep engineering: mechanism, warning and risk mitigation
Guang-Liang Feng

10 A Gray Wolf Optimization-Based Improved Probabilistic Neural Network Algorithm for Surrounding Rock Squeezing Classification in Tunnel Engineering
Xing Huang, Xin Yin, Bin Liu, Ziwei Ding, Chaofan Zhang, Boyu Jing and Xiaosheng Guo

19 Prediction Method of TBM Tunneling Parameters Based on PSO-Bi-LSTM Model
Qinglong Zhang, Yanwen Zhu, Rui Ma, Canxun Du, Sanlin Du, Kun Shao and Qingbin Li

35 Centrifugal Test and Instability Model Analysis of Excavation Surface Stability of a Shield Tunnel in a Clay Layer
Haoshuang Niu, Xiaolin Weng, Jibo Hu and Lele Hou

46 Influence Evaluation of Sensor Coordinate Error on Microseismic Source Location
Tao Li, Bing-Rui Chen, Qing Wang, Xin-Hao Zhu, Xu Wang and Ming-Xing Xie

55 Force-Chain-Based Analysis of Factors Influencing Pressure Arch Around Tunnel Under Earthquake
Sun Changxin, Zhang Yumin, Guan Lei, Zhang Liye and Peng Jiafeng

66 Determination Method of Excavation Damage Zone Based on Surrounding Rock Damage-Fracture Ratio in Underground Engineering
Haosen Guo, Jiaqi Tong, Qiancheng Sun, Xu Yang, Wenjun Luo and Yang Yu

75 Micropore Structure and Fractal Characteristics of Clays Due to Freeze-Thaw and Compression Based on Mercury Intrusion Porosimetry
Shengfu Wang, Liang Lv, Kaixi Xue, Dongjie Zhang, Mingdong Li, Dongwei Li and Chang Yuan

86 Influence of the Xianshuihe Fault Zone on *In-Situ* Stress Field of a Deep Tunnel and its Engineering Effect
Dong Yuan, Lanbin Zhang, Xiaoling Liu, Tao Feng, Guangze Zhang, Zhengxuan Xu, Zhewei Wang, Xiaojuan Yi, Zhiheng Lin, Yang Ren, Ru Zhang and Li Ren

98 Ground Surface Deformation in the Hanging Wall of the Jinshandian Underground Iron Mine in China
Tianlong Wang, Congxin Chen, Kaizong Xia, Chuqiang Zhang, Yue Wang and Xuanting Liu

114 Energy Evolution Characteristics of Rock Under Different Confining Conditions
Bi-Wen Zhang, Kai Fang, Chen Wang, Tong-Bin Zhao and Xiu-Feng Zhang

124 Study on Safety Management Assessment of Coal Mine Roofs Based on the DEMATEL-ANP Method
Lei Li and Youpeng Ouyang

135 Experimental Research and Instrument Design of Seepage Measurement in Rock and Soil Based on Heat Transfer
Xiushan Wu, Jiamin Cui, Renyuan Tong and Qing Li

144 Stability Analysis on the Steeply-Inclined Small-Angle Layered Surrounding Rock Masses at the Upstream High Sidewall of a Large-Span Cavern
Chong-Lin Jian, Ding-Ping Xu, Yang-Yi Zhou, Dong-Fang Chen, Shao-Wu Zhou, Lian-Xing Hu, Chong Wu and Sen-Lin Jiang

158 Analysis of the Mechanism of Ground Fissures in the Nairobi–Malaba Railway Rift Valley Area in Kenya
Bing Hao, Zhenghua Zhou, Yuandong Li, Xiaojun Li, Xujin Liu, Yi Han and Liguo Jin

171 Study on the Mechanism of Weakening Thick and Hard Roof by Deep-Hole Blasting in Deep Coal Mines
Chen Zhang, Junpeng Zou, Xiufeng Zhang, Chao Wang and Yu-Yong Jiao

182 A New Classification Method of Mine Goaf Ground Activation Considering High-Speed Railway Influence
Lian-wei Ren, Peng-fei He, You-Feng Zou, Zhi-Lin Dun, Zheng-sheng Zou and Shu-ren Wang

195 Study on Failure Difference of Hard Rock Based on a Comparison Between the Conventional Triaxial Test and True Triaxial Test
Guoqiang Zheng, Yonghui Tang, Yan Zhang, Yaohui Gao, Guoqiang Zhu, Meiben Gao, Junqian Ren, Kezhu Chen and Jicheng Sun

205 Microsimulation Study on Energy Release and Rock Block Ejection Force of Granite under Different Unloading Conditions
Xin-Yuan Wang, Yan-Chun Yin, Ming-Lu Xing, Dong-Dong Zhang, Yang Chen and En-Chao Wang

216 Experimental Analysis on Mechanical Characteristics of Foundation Soil in Rift Valley Area of Kenya Nairobi-Malaba Railway
Bing Hao, Zhenghua Zhou, Yuandong Li, Xiaojun Li and Liguo Jin

231 A Comparative Study of Six Hybrid Prediction Models for Uniaxial Compressive Strength of Rock Based on Swarm Intelligence Optimization Algorithms
Yu Lei, Shengtao Zhou, Xuedong Luo, Shuaishuai Niu and Nan Jiang

245 The Calculation of Inelastic Zone Width of Coal Pillar in Highwall Mining With Backfill
Juyu Jiang, Ye Lu, Lanzhu Cao, Dong Wang, Laigui Wang, Xinping Han, Huiwen Yang and Zhengzhao Jia

263 An Effective Denoising Method Based on Cumulative Distribution Function Thresholding and its Application in the Microseismic Signal of a Metal Mine With High Sampling Rate (6 kHz)
Da Zhang, Zhiyi Zeng, Yaqian Shi, Ying Chang, Rui Dai, Hu Ji and Peng Han

276 Triggering and Relationship Between Mine Earthquake Activities and Stress of Earth Tides During Deep Mining
Yuezheng Zhang, Hongguang Ji and Haoyuan Wu

286 Numerical Method for the Deformation Calculation of the Shallow Buried Tunnel Caused by the Excavation of Overlying Soil Based on Soil Rebounding Characteristics
Jian Li, Shichang Li, Yu Zhang, Shanxiong Chen, Fei Yu, Zhangjun Dai and Chaoxiong Li

303 Developing an evaluation model based on unascertained measurement for evaluation of tunnel squeezing
Cong Wei, Shuangli Zhu, Chao Chen and Jian Zhou

315 Workspace analysis and motion control strategy of robotic mine anchor drilling truck manipulator based on the WOA-FOPID algorithm
Zhang Jun, Wang Yiliang, Che Liming, Wang Ning, Bai Yuepin and Wang Chaofan

334 *In situ* stress measurement method of deep borehole based on multi-array ultrasonic scanning technology
Jinchao Wang, Chuanying Wang, Junfeng Huang, Zengqiang Han, Wenhao Zeng and Yiteng Wang

347 Deformation and Failure Characteristics of Loading and Unloading Rock Based on Volume Crack Strain
Xiaohui Liu, Yu Zheng, Jinyun Guo, Qijun Hao and Yang Xue

359 Frequency spectrum and energy refinement characteristics of blasting vibration signals in raw water pipeline tunnel excavation
Liang Zhang, Sheng Zhang, Tonghua Ling and Zongwei Deng

374 Study on anti-collision behavior of new precast concrete curb components in a highway tunnel
Changjun Li, Junpeng Zou, Wenbin He, Xianying Ding, Guoping Zheng, Yizhou Zhuang and Man Wang

383 Mechanical characteristics analysis of horizontal lifting of subsea pipeline with different burial depths
Dapeng Zhang, Bowen Zhao and Keqiang Zhu

395 Analytical solution of mechanical response in cold region tunnels under transversely isotropic freeze–thaw circle induced by unidirectional freeze–thaw damage
Zhitao Lv, Mingchao Wu, Faming Huang and Yi Cai

409 Settlement analysis of the giant open caisson during the construction of the Changtai Yangtze River Bridge
Mingwei Guo, Xuechao Dong and Zhi Yang

424 Study on critical slowdown characteristics and early warning model of damage evolution of sandstone under freeze–thaw cycles
Jiaxu Jin, Xinlei Zhang, Xiaoli Liu, Yahao Li and Shaohua Li

438 Analysis of geothermal potential in Hangjiahu area based on remote sensing and geographic information system
Linxia Xu, Wenyuan Wu, Junfeng Qian, Shujia Huang, Bin Xie, Tangao Hu, Xiayi Lang, Bowen He and Chenghao Hu

453 Evaluation of urban resilience level and analysis of obstacle factors: A case study of Hunan Province, China
Na Chen, Hongxia Guo and Hui Xiang

464 Research on prevention and control methods of land subsidence induced by groundwater overexploitation based on three-dimensional fluid solid coupling model—a case study of Guangrao County
Peijie Yang, Yulong Dong, Yongwei Zhang, Guangwei Wu and Yue Yao

484 Effects of deflection angle on the mechanical properties of constant-resistance, energy-absorbing, and anti-scouring bolts
Zhi Tang, Hao Wu, Jinguo Lv and Dezhi Chang

frontiers | Frontiers in Earth Science

TYPE Editorial
PUBLISHED 09 May 2023
DOI 10.3389/feart.2023.1193086

Check for updates

OPEN ACCESS

EDITED AND REVIEWED BY
Manoj Khandelwal,
Federation University Australia, Australia

*CORRESPONDENCE
Guang-Liang Feng,
glfeng@whrsm.ac.cn

RECEIVED 24 March 2023
ACCEPTED 20 April 2023
PUBLISHED 09 May 2023

CITATION
Feng G-L (2023), Editorial: Geological disasters in deep engineering: mechanism, warning and risk mitigation. *Front. Earth Sci.* 11:1193086. doi: 10.3389/feart.2023.1193086

COPYRIGHT
© 2023 Feng. This is an open-access article distributed under the terms of the Creative Commons Attribution License (CC BY). The use, distribution or reproduction in other forums is permitted, provided the original author(s) and the copyright owner(s) are credited and that the original publication in this journal is cited, in accordance with accepted academic practice. No use, distribution or reproduction is permitted which does not comply with these terms.

Editorial: Geological disasters in deep engineering: mechanism, warning and risk mitigation

Guang-Liang Feng[1,2]*

[1]State Key Laboratory of Geomechanics and Geotechnical Engineering, Institute of Rock and Soil Mechanics, Chinese Academy of Sciences, Wuhan, China, [2]School of Engineering Science, University of Chinese Academy of Sciences, Beijing, China

KEYWORDS

geological disasters, deep engineering, mechanism, warning, risk mitigation, rockburst

Editorial on the Research Topic
Geological disasters in deep engineering: mechanism, warning and risk mitigation

Introduction

With the increasing demand for infrastructure construction as the global economy progresses, the need for exploration and utilization of deep underground space becomes more crucial. Various deep underground projects are planned, are under construction, and have been built to encounter great construction challenges due to the complex geo-environment such as strong tectonic movement, fragile geo-environment and complex thermo-hydro-mechanical-chemical conditions. These deep engineering projects could be endangered by different kinds of geological disasters, such as intense rockburst, large deformation, strong water inrush, and large-scale collapse, which might result in massive loss of life and economic damage during the construction of deep underground projects.

Efforts are being called for strengthening science and technology innovation and cooperation in geological disaster mitigation and sustainable development during the construction of deep engineering projects. To mitigate the risk of geological disaster in deep engineering under the complicate geo-environment, the mechanism of the formation and evolution of geological disasters in deep engineering needs to be understood. The testing, monitoring, simulation, risk assessment and early warning methods for geological disaster in deep engineering are also needed urgently. New theories, methods and techniques related to the mechanism, warning and risk mitigation of geological disasters in deep engineering will be extremely helpful for the construction safety of deep engineering.

Progress in the Research Topic

In order to attract scholars' attention to geological disasters in deep engineering, the current Research Topic "Geological disasters in deep engineering: mechanism, warning and risk mitigation" was organized. This Research Topic has an overarching focus on new theories, methods and techniques that have been developed to reveal the mechanism and to

warn and mitigate the risk of geological disasters in deep engineering. There are 38 papers in this Research Topic with 210 authors. According to the main content of these papers and the Research Topic, I summarized and divided the papers into three parts and 10 papers were selected to show as an example.

Formation and evolution of geological disasters in deep engineering and their mechanism

Recognition of the characteristics, laws, and mechanisms of geological disasters in deep engineering is the basis for reasonable evaluation, warning, and control of them. Yuan et al. studied the influence of the Xianshuihe fault zone on *in-situ* stress field of a deep tunnel under construction in southwestern China and its engineering effect. Zhang et al. investigated the spatial and temporal distribution of mining-induced seismicity before and after multiple deep-hole blasting and simulated the stress and displacement in hard rock based on the engineering background of a panel of Dongtan deep coal mine. Zhang et al. studied the triggering and relationship between mine earthquake activities and stress of Earth tides during deep mining based on the Yanbei coal mine in China. Wang et al. elucidated the mechanism underpinning the surface deformation of the hanging wall in the eastern part of the Jinshandian iron mine based on surface deformation data collected over a period of 13 years. Zheng et al. studied the failure difference of hard rock based on a comparison between the conventional triaxial test and true triaxial test.

Testing and monitoring technologies for geological disaster in deep engineering

In order to study and reveal the formation mechanism of geological hazards in deep engineering and provide a warning, a series of monitoring and analysis techniques have been developed and optimized, such as microseismic monitoring technology, stress measurement technology, et al. Li et al. studied the influence of the microseismic sensor coordinate error on the microseismic source location and a calculation method for the microseismic sensor coordinate error threshold was proposed and used in Beiminghe iron mine in Hebei Province in China. Zhang et al. proposed an effective denoising method based on cumulative distribution function thresholding and applied it in a metal mine. Wang et al. proposed a deep borehole *in-situ* stress measurement method based on multi-array ultrasonic scanning technology based on the wall collapse in deep borehole.

Risk assessment and warning methods for geological disaster in deep engineering

Risk assessment and warning methods for geological hazards in deep engineering are the basis for specifying prevention strategies and adopting reasonable prevention measures, as well as the prerequisite for avoiding risks and ensuring the smooth implementation of deep engineering. Guo et al. proposed a method that takes into account the *in-situ* stress, rock mass integrity, span length, and depth of highly damaged zone to determine the excavation damage zone in underground engineering. Wei et al. developed a hybrid model based on information entropy and unascertained measurement incorporating four membership functions to evaluate the tunnel squeezing, which is able to enrich the available risk evaluation methods for deep underground excavation projects.

Development trend

Research on evolution mechanism, warning, and risk mitigation of disasters in deep engineering in different fields, such as water conservancy and hydropower, transportation, national defense, and deep basic physics laboratories, is a major topic in engineering construction and operation. The failure characteristics of rockmass in deep engineering are significantly different from those in shallow engineering, posing a huge challenge to the research on rock mechanical properties and disaster mechanism recognition, warning and analysis theory, and risk mitigation. There are various types of disasters in deep engineering, such as rockburst, deformation, water intrusion, collapse, et al. A rockburst is defined as damage to an excavation that occurs in a sudden or violent manner and is associated with a seismic event. The author of this Editorial is mainly engaged in research on the mechanism, monitoring, warning, and control of rockburst in deep engineering. Here, several suggestions on rockburst for future research are given as an example.

Considerable progress has been made in the study of rockburst development process. It includes the characteristics, types, induced effects of construction methods, mechanisms, testing and observation monitoring methods, as well as the theory and technology of rockburst warning and risk mitigation.

Observation, monitoring and mechanism of rockburst in deep engineering

Currently, a systematic indoor and on-site comprehensive observation and monitoring technology for rockburst in deep engineering has been established. The mechanism of rockburst development in deep engineering was revealed to a certain extent. A deeper understanding of the mechanism of immediate rockburst was obtained. However, the monitoring technology and mechanism of time-delay rockburst and intermittent rockburst in deep engineering still need further research.

Warning of rockburst in deep engineering

The author of this Editorial has conducted a large amount of research on the warning of immediate rockburst in deep engineering and proposed a real-time quantitative warning method for rockburst in deep tunnel. Rockburst warning has been changed from

qualitative to quantitative through the method. The method has been tested and applied in a large number of deep engineering projects. However, there is still a lack of effective warning methods for time-delay, intermittent, and fault slip rockbursts.

Risk mitigation of rockburst in deep engineering

The prevention and control of rockburst in deep engineering has changed from passive to active. And for intense and extremely intense rockbursts, the prevention and control method has risen from empirical to a scientific method. The future direction of efforts is to research new and efficient stress release technologies, energy absorption support systems, and more engineering practices.

Rockburst case database and artificial intelligence

The development process of rockbursts in deep engineering is a complex process. A large rockburst case database has been established. Using artificial intelligence methods, such as big data and deep learning, to conduct deep learning on rockburst databases and establish a fully intelligent system is a direction that needs urgent efforts. The rockburst mechanism and risk in different deep engineering projects are different with each other. Taking specific engineering examples to conduct rockburst research and enrich the mechanism understanding, warning, and risk mitigation technologies of rockburst in deep engineering are also the future development directions.

Author contributions

The idea of and concept of this Research Topic came from discussion amongst the guest editors. G-LF organized and wrote the manuscript. The author contributed to the submitted version of the article.

Acknowledgments

I thank the various authors for submitting their work to this Research Topic and the reviewers who agreed to review individual contributions.

Conflict of interest

The author declare that the research was conducted in the absence of any commercial or financial relationships that could be construed as a potential conflict of interest.

Publisher's note

All claims expressed in this article are solely those of the authors and do not necessarily represent those of their affiliated organizations, or those of the publisher, the editors and the reviewers. Any product that may be evaluated in this article, or claim that may be made by its manufacturer, is not guaranteed or endorsed by the publisher.

frontiers in Earth Science

ORIGINAL RESEARCH
published: 28 February 2022
doi: 10.3389/feart.2022.857463

A Gray Wolf Optimization-Based Improved Probabilistic Neural Network Algorithm for Surrounding Rock Squeezing Classification in Tunnel Engineering

Xing Huang[1], Xin Yin[2], Bin Liu[1], Ziwei Ding[3], Chaofan Zhang[3], Boyu Jing[3] and Xiaosheng Guo[4]*

[1]State Key Laboratory of Geomechanics and Geotechnical Engineering, Institute of Rock and Soil Mechanics, Chinese Academy of Sciences, Wuhan, China, [2]The Key Laboratory of Geotechnical and Structural Engineering Safety of Hubei Province, School of Civil Engineering, Wuhan University, Wuhan, China, [3]College of Energy Engineering, Xi'an University of Science and Technology, Xi'an, China, [4]Shaanxi Zhengtong Coal Industry Co., Ltd., Xianyang, China

OPEN ACCESS

Edited by:
Shibing Huang, Wuhan University of Science and Technology, China

Reviewed by:
Sen Wen, Henan University, China
Pengfei Wang, Taiyuan University of Technology, China

***Correspondence:**
Xin Yin
yinxin0506@126.com

Specialty section:
This article was submitted to Geohazards and Georisks, a section of the journal Frontiers in Earth Science

Received: *18 January 2022*
Accepted: *10 February 2022*
Published: *28 February 2022*

Citation:
Huang X, Yin X, Liu B, Ding Z, Zhang C, Jing B and Guo X (2022) A Gray Wolf Optimization-Based Improved Probabilistic Neural Network Algorithm for Surrounding Rock Squeezing Classification in Tunnel Engineering. Front. Earth Sci. 10:857463. doi: 10.3389/feart.2022.857463

Surrounding rock squeezing deformation is a common and prominent hazard in tunnel engineering projects, which often induces the shield jamming disaster during the TBM tunneling process. Based on the 139 groups of historical squeezing deformation cases, this study developed a hybrid PCA-IWGO-PNN model for squeezing classification. According to the influencing factors and characteristics of squeezing deformation, the strength-stress ratio, tunnel burial depth, tunnel equivalent diameter, rock mass quality index, and support stiffness were selected to establish the prediction index system of squeezing level. Because the probabilistic neural network (PNN) requires that the input variables are independent, principal component analysis (PCA) was used to preprocess the original data to eliminate the correlation between prediction indexes and achieve dimensionality reduction. The spread coefficient was the critical hyper-parameter in the PNN, and the improved gray wolf optimization (IGWO) algorithm was used to realize its efficient automatic optimization. Then, the PNN model was applied to engineering practice. Only 1 of 20 test samples was misjudged, achieving the 95% prediction accuracy. Finally, the comparison analysis with the artificial neural network (ANN) model, support vector machine (SVM) model, and random forest (RF) model was conducted. Among them, the PNN model achieved the highest prediction accuracy, followed by the artificial neural network (85%), RF (85%), and SVM (80%). In addition, the PNN model had the fastest running speed, which only consumed 5.6350 s, while the running time of ANN, SVM, and RF was 8.8340, 6.2290, and 6.9260 s, respectively. The hybrid PCA-IWGO-PNN model developed in this research provides an effective method for surrounding rock squeezing classification, and it has superiorities in both prediction accuracy and running speed.

Keywords: tunnel engineering, surrounding rock squeezing deformation, squeezing classification, probabilistic neural network, improved gray wolf optimization

1 INTRODUCTION

In recent years, limited by the shallow resources, underground space development and tunnel engineering construction have ushered in a peak period (Zhu et al., 2019). TBM (tunnel boring machine) is widely used in deep-buried and ultra-long tunnels because of high excavation efficiency, low construction cost, and minor environmental disturbance (Liu et al., 2016). However, most of these tunnels are located in areas with high seismic intensity, complex surface topography, and harsh geological conditions. These tunnels' safe and efficient construction faces enormous challenges, especially when TBM traverses the deep-buried, high-stress, weak, and broken stratum. Due to the narrow overcut gap between the TBM shield and surrounding rock, shield jamming disaster will be caused when the squeezing deformation of surrounding rock exceeds the overcut gap (Hasanpour et al., 2014). The handling of TBM jamming accidents not only seriously delays the construction schedule and threatens the safety of equipment and workers, but also causes huge economic losses and social impacts. Therefore, carrying out the study on the advancing prediction of surrounding rock squeezing levels is essential for TBM jamming disaster prevention and control.

Early studies primarily focused on empirical criteria, such as Singh B (Singh et al., 1992), Jimenez R (Jimenez and Recio, 2011) and Farhadian H (Farhadian and Nikvar-Hassani, 2020) proposed empirical criteria based on tunnel burial depth and rock quality index, and Jethwa J L (Jethwa, 1981), Aydan (Aydan et al., 1996), and Barla G (Barla, 1995) put forward empirical criteria based on tunnel burial depth, rock specific gravity, and uniaxial compressive strength. However, squeezing level prediction is a complex nonlinear problem, and it is difficult for empirical criteria to consider this nonlinear relationship between influencing factors and squeezing. With the deepening of researches, some soft science methods based on artificial intelligence have been introduced to solve nonlinear problems (Liu et al., 2020; Yin et al., 2021a; Zhang et al., 2020a; Zhang et al., 2021b; Yin et al., 2021b; Ge et al., 2021; Zhang et al., 2021a; Yin et al., 2022; Ge et al., 2022; Zhang and Phoon, 2022). Zhang J et al. (Zhang et al., 2020b) proposed a BP neural network method for predicting the squeezing level. Feng X and Jimenez R (Feng and Jimenez, 2015) adopted the strength-stress ratio, tunnel burial depth, tunnel diameter, rock quality index, and support stiffness as predictive indicators and established a Bayesian network (BN) model to predict the squeezing level. Sousa et al. (Sousa and Einstein, 2011) proposed a Bayesian network (BN)-based perception model of harsh geological conditions in front of the tunnel face with TBM tunneling data. R. Hasanpour et al. (Hasanpour et al., 2020a) applied the artificial neural network (ANN) and Bayesian network (BN) to TBM tunneling risk assessment under adverse geological conditions, such as the large squeezing deformation. Sun Y et al. (Sun et al., 2018) proposed a multi-class support vector machine (SVM) method based on tunnel burial depth, tunnel diameter, rock quality index, and support stiffness to evaluate the squeezing level. Chen Y et al. (Chen et al., 2020) developed a novel probabilistic multi-classification prediction framework for the squeezing level. The above prediction methods reveal the laws of squeezing occurrence from different aspects, which enriches the theory of squeezing deformation prediction. However, due to many factors influencing squeezing deformation, its inoculation mechanism is still unclear. It is necessary to make full use of the evaluation index information, explore the intrinsic relationship between the evaluation index characteristics and squeezing level, and combine multiple prediction techniques to conduct the squeezing level prediction, achieving a higher accuracy. Therefore, this study developed a novel multi-algorithm fusion prediction model based on PCA-IGWO-PNN for the squeezing level.

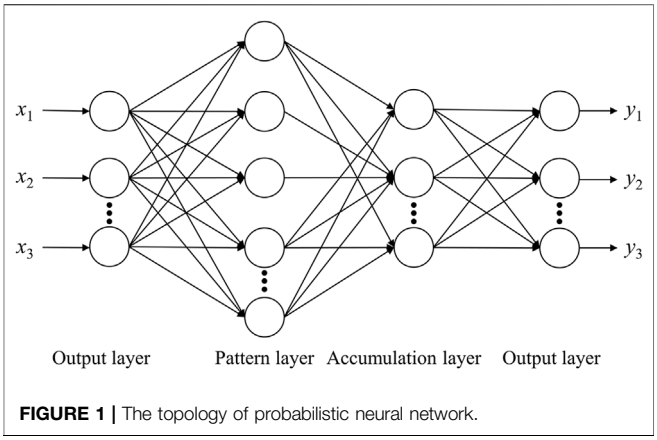


FIGURE 1 | The topology of probabilistic neural network.

Probabilistic neural network (PNN) has the advantages of simple structure, easy training, fast convergence speed, and robust fault tolerance, etc. It can use a linear learning algorithm to realize the function of a nonlinear learning algorithm, and it has been widely applied to pattern classification problems such as fault diagnosis (Zhang et al., 2021c). When the activation function of the PNN adopts the Gaussian function, the evaluation index need to be uncorrelated and identically distributed. In fact, there is a certain correlation between most of the evaluation indexes of squeezing levels and it is necessary to eliminate the correlation between them before applying PNN.

Common methods to eliminate the correlation between variables include limiting the number of variables, separating overlapping elements, modifying indicator weights, principal component analysis, and factor analysis, etc. Considering that there are multiple evaluation indexes selected in this research, the principal component analysis method (PCA) is used to preprocess the evaluation indexes of squeezing levels. In addition to eliminating the correlation between the indexes, it can also achieve dimensionality reduction and improve the training and prediction speed of the PNN. Finally, this study established a hybrid squeezing level prediction model based on the PCA and PNN, and the hyper-parameter of PNN was automatically tuned by the improved gray wolf optimization (IGWO) algorithm.

2 METHODOLOGY

2.1 Probabilistic Neural Network

Probabilistic neural network (PNN) is based on the radial basis neural network, using activation functions derived from statistical

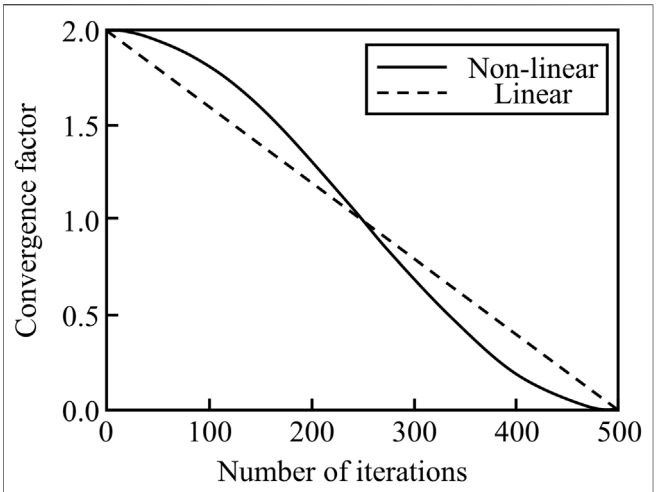


FIGURE 2 | Convergence factor decreasing strategy.

methods to replace sigmoid activation functions. The decision boundary realized by PNN approaches the Bayesian optimal decision surface, which is an organic fusion of radial basis network, Bayesian decision theory, and non-parametric probabilistic density function estimation (Sanal Kumar and Bhavani, 2019). The PNN network is composed of input, pattern, accumulation, and output layers (Dukov et al., 2019), and the network topology is shown in **Figure 1**.

The input layer receives training samples and the number of neurons is equal to the length of the input vector.

The pattern layer is used to calculate the matching relationship between the input vector and each pattern and returns a scalar value. The number of neurons in this layer is the same as the number of input training samples. The vector x is input to the pattern layer, then the output relationship of the j-th neuron of the i-th type pattern in the pattern layer is:

$$\phi_{ij} = 1 \Big/ \left[(2\pi)^{0.5} \sigma^{d} \right] \exp^{\left[-(x-x_{ij})(x-x_{ij})^{T} / \sigma^{2} \right]} \tag{1}$$

where: d is the dimension of the metric space, σ is the spread coefficient, x_{ij} is the j-th center of the i-th sample, and ϕ_{ij} is the output value of the j-th neuron of the i-th pattern in the pattern layer.

The main function of the accumulation layer is a linear summation and then weighted average. The number of neurons in this layer is the same as the total number of patterns.

The output layer is composed of competing neurons. The number of neurons is the same as the total number of patterns and each neuron corresponds to a pattern. The output of the neuron with the maximum posterior probability density is 1 and the others are 0.

2.2 Improved Gray Wolf Optimization

Gray wolf optimization algorithm is an intelligent algorithm based on the social behavior of wolves. Its basic idea is to search and locate prey for wolves with three leadership levels: α, β, and γ according to hierarchical social characteristics, and guide ω wolf to track and capture prey. The implementation steps of the gray wolf optimization algorithm are described in (Mirjalili et al., 2014a). The gray wolf optimization algorithm has fast optimization speed and high accuracy, but it still has the shortcoming of being easy to fall into the local optimum. Therefore, this paper proposes two strategies to improve the algorithm.

2.2.1 Non-Linear Decreasing Strategy of Convergence Factor

The performance of traditional gray wolf optimization algorithm is affected by the convergence factor a. The linear decreasing strategy of a cannot meet the balance of global and local search. Therefore, this paper proposes a cosine-based non-linear decreasing strategy (**Eq. 2**). This strategy is shown in **Figure 2**. As a gradually decreases, the ergodicity increases in the early stage and the local search can be emphasized later to balance the algorithm's global and local search capabilities.

$$a = \cos\left(\frac{\pi t}{n}\right) + 1 \tag{2}$$

Where: t is the current iteration number; n is the maximum iteration number.

2.2.2 Dynamic Weighting Strategy Based on Euclidean Distance

In the traditional gray wolf optimization algorithm, the guidance of α wolf, β wolf, and γ wolf to ω wolf is the same, which violates the unique social hierarchical characteristics of the algorithm. So, a dynamic weighting strategy based on Euclidean distance is proposed to handle this problem (Mirjalili et al., 2014b).

This strategy mainly calculates the learning ability of ω wolf against α wolf, β wolf, and γ wolf in the iterative process, and then finds the updated position of ω wolf under the guidance of α wolf, β wolf, and γ wolf, which can be expressed as:

$$\omega_1 = \frac{|X_1|}{|X_1| + |X_2| + |X_3|} \tag{3}$$

$$\omega_2 = \frac{|X_2|}{|X_1| + |X_2| + |X_3|} \tag{4}$$

$$\omega_3 = \frac{|X_3|}{|X_1| + |X_2| + |X_3|} \tag{5}$$

$$X(t+1) = \frac{\omega_1 X_1 + \omega_2 X_2 + \omega_3 X_3}{3} \tag{6}$$

2.3 Principal Component Analysis

When a correlation exists between input variables, it will increase the information redundancy, and then increase the running time of the model (Yin et al., 2021c). To eliminate the correlation, dimensionality reduction provides a practical way, such as principal component analysis (PCA) (Schimit and Pereira, 2018).

The detailed procedure of PCA is introduced as follows:

1) Establish the raw data matrix $X = (x_{ij})_{m \times n}$, in which m is the number of samples and n is the number of input variables;
2) Standardize the raw data matrix using;

$$x_{ij}^{*} = \frac{x_{ij} - mean_j}{std_j} \tag{7}$$

where: $mean_j$ and std_j are separately the mean and the standard deviation of the j-th input variable.

3) Calculate the correlation coefficient matrix $R = (r_{yz})_{n\times n}$ based on the standardized raw data matrix, in which r_{yz} represents the Pearson correlation coefficient between the y-th and z-th input variables;

$$r_{yz} = \frac{\sum(y_i - \bar{y})\sum(z_i - \bar{z})}{\sqrt{\sum(y_i - \bar{y})^2}\sqrt{\sum(z_i - \bar{z})^2}} \tag{8}$$

where: r_{yz} is Pearson correlation coefficient between input variables Y and Z; $\bar{y}$ and $\bar{z}$ are separately the mean of Y and Z.

4) Calculate the eigenvalues $\{\beta_1, \beta_2, \ldots, \beta_n\}$ and eigenvectors $\{\nu_1, \nu_2, \ldots, \nu_n\}$ of the correlation coefficient matrix;
5) Obtain the data matrix after dimensionality reduction using

$$\tilde{X} = X^{*} * V \tag{9}$$

where: $V = (\nu_1, \nu_2, \ldots, \nu_k)$ is the transform matrix, composed of the first k eigenvectors; X^{*} is the standardized raw data matrix.

The ratio (η) of the information contained in the dimensionality-reduced data to that contained in the raw data is calculated by **Eq. 10**. The criterion for determining k is that η is greater than 90%.

$$\eta = \frac{\beta_1 + \beta_2 + \ldots + \beta_k}{\beta_1 + \beta_2 + \ldots + \beta_n} \tag{10}$$

3 PCA-IGWO-PNN PREDICTION MODEL FOR SQUEEZING LEVELS

The model's framework is: (1) Collect squeezing cases according to the selected indicators; (2) In order to eliminate the dimension and magnitude order differences between indicators, standardize the original data; (3) Use principal component analysis (PCA) to preprocess the data for eliminating the correlation between indicators and reducing data dimensionality; (4) Set the IGWO parameters such as the number of wolves, the maximum number of iterations, etc.; (5) Initialize the location of the wolf pack, utilize α wolf, β wolf and γ wolf to guide ω wolf, and select **Eq. 11** as the fitness function; (6) Input the training and validation sets into the PNN and introduce the IGWO algorithm for iterative search to obtain the optimal spread coefficient σ of the PNN; (7) Bring the test set into the trained PNN and output the prediction results of the squeezing level; (8) Compare the prediction results of the PCA-IGWO-PNN with the actual situations and the prediction results of other models.

$$fitness = \frac{1}{Accuracy} \tag{11}$$

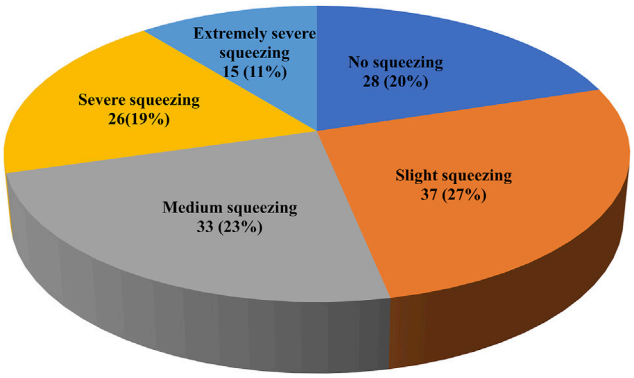


FIGURE 3 | Proportion of different squeezing levels in the database.

where: *Accuracy* is the model's prediction accuracy on the validation set.

4 DATABASE DESCRIPTION

A total of 139 squeezing cases were collected from (Jiao et al., 2021), including China, Nepal, India, and so on (**Supplementary Appendix SA**). In the 139 cases, no squeezing (Ⅰ) accounted for 20% (28 cases), slight squeezing (Ⅱ) accounted for 27% (37 cases), medium squeezing (Ⅲ) accounted for 23% (33 cases), severe squeezing (Ⅳ) accounted for 19% (26 cases), and extremely severe squeezing (Ⅴ) accounted for 11% (15 cases) (**Figure 3**). The determination of squeezing levels was based on the relative strain (ε), namely no squeezing with $\varepsilon < 1\%$, slight squeezing with $1\% \leq \varepsilon \leq 2.5\%$, medium squeezing with $2.5\% < \varepsilon \leq 5\%$, severe squeezing with $5\% < \varepsilon \leq 10\%$, and extremely severe squeezing with $\varepsilon > 10\%$ (Jiao et al., 2021). The relative strain (ε) is defined as .

$$\varepsilon = \mu / D \tag{12}$$

where: μ is tunnel convergence deformation; D is tunnel diameter.

The occurrence of squeezing is closely related to geological structure, ground stress, rock mass conditions, and excavation disturbances (Hasanpour et al., 2020b; Xu et al., 2021). The selection of squeezing prediction indicators should meet: (1) they are easy to obtain; (2) they have strong representativeness; (3) they can reflect the characteristics of the squeezing from different aspects. In the early empirical methods, the tunnel depth (H), rock mass quality index (BQ), and strength-stress ratio (SSR) are the most widely used indicators. In addition, support stiffness (K) plays a vital role in controlling the surrounding rock deformation (Dwivedi et al., 2013) and the scale effect of tunnels, namely tunnel equivalent diameter (D_0), should be taken into account (Goel et al., 1995). Therefore, five indicators [i.e., H, (BQ), SSR, K, and D_0] are finally selected as the prediction variables of squeezing levels. **Table 1** gives the acquisition methods of five prediction variables and **Table 2** shows the basic statistical description of five prediction variables.

TABLE 1 | The acquisition methods of five prediction variables.

Prediction variable	Full name	Acquisition method
SSR	Strength-stress ratio	$SSR = \sigma_{cm}/\gamma H$
H	Tunnel burial depth	Determined by geological survey
[*BQ*]	Rock mass quality index	$[BQ] = 63.029\ln(Q) + 327.5$
D_0	Tunnel equivalent diameter	$D_0 = \sqrt{4A/\pi}$
K	Support stiffness	$K = K_c + K_{sb} + K_b$

A, *tunnel cross-section area;* K_c, *shotcrete lining stiffness;* K_{sb}, *steel arch stiffness;* $K_$, *anchor stiffness;* σ_{cm}, *uniaxial compressive strength of rock mass;* γ, *rock specific gravity;* Q, *rock quality index.*

TABLE 2 | The basic statistical description of five prediction variables.

Statistical index	*SSR*	*H*/m	[*BQ*]	D_0/m	*K*/MPa
Minimum	0.01	45.10	70.00	4.00	2.98
Maximum	1.55	1,110.00	441.00	14.00	1979.56
Mean	0.3204	361.3856	216.0791	9.7495	1,110.3576
SD	0.27551	214.77502	72.58499	2.92968	482.01800
Skewness	1.704	0.882	0.675	–0.371	–0.522
Kurtosis	3.720	0.445	1.165	–0.946	–0.045

TABLE 3 | Correlation coefficients among the original prediction variables.

Prediction variables	*SSR*	*H*	[*BQ*]	D_0	*K*
SSR	1	–0.1974	0.6709	0.1043	–0.1541
H	–0.1974	1	0.163	0.1377	–0.2891
(*BQ*)	0.6709	0.163	1.0000	0.2518	–0.2461
D_0	0.1043	0.1377	0.2518	1	–0.0206
K	–0.1541	–0.2891	–0.2461	–0.0206	1

TABLE 4 | Calculation results of PCA.

Principal component	Eigenvalue	Contribution rate (%)	Cumulative contribution rate (%)
1	1.8650	37.30	37.30
2	1.2920	25.84	63.14
3	0.9791	19.58	82.72
4	0.6259	12.52	95.24
5	0.2380	4.76	100

5 DATABASE PREPROCESSING WITH PCA

Table 3 shows the correlation coefficients among five prediction variables. It can be seen that the correlation coefficient between *SSR* and (*BQ*) is over 0.5, indicating that there is a relatively obvious correlation. These redundant information will reduce the operating efficiency of the model, so it is necessary to use principal component analysis to eliminate the correlation between the variables. To avoid the influence of variable dimensions on the dimensionality reduction process, we first use the Z-score method to standardize the original data (**Eq. 7**). **Supplementary Appendix SB** demonstrates the standardized data.

Table 4 shows the variance contribution rate of each principal component and their cumulative contribution rate. Referring to **Table 4**, the cumulative contribution rate of the first four principal components reaches 95.24%, indicating that the first four principal components contain 95.24% of the original information, which meets the requirement of principal component selection. Therefore, this paper selects these four principal components as the new prediction variables to replace the five original ones. By analyzing the correlation, it can be found that the new prediction variables (y_1, y_2, y_3, and y_4) are totally independent of each other and the correlation coefficients are all 0 (**Table 5**). **Table 6** gives the principal component coefficient matrix, from which the relationship between the new prediction variables and the original ones can be expressed as **Eq. 13**. **Supplementary Appendix SB** shows the data after dimensionality reduction.

$$\begin{cases} y_1 = -0.5742x_1^* - 0.1573x_2^* - 0.6604x_3^* - 0.2949x_4^* + 0.3498x_5^* \\ y_2 = 0.4443x_1^* - 0.7573x_2^* + 0.0957x_3^* - 0.1473x_4^* + 0.4452x_5^* \\ y_3 = -0.1441x_1^* + 0.0496x_2^* + 0.0039x_3^* + 0.8478x_4^* + 0.5080x_5^* \\ y_4 = -0.0736x_1^* - 0.5455x_2^* - 0.3318x_3^* + 0.4091x_4^* - 0.6477x_5^* \end{cases} \tag{13}$$

where: x_1^*, x_2^*, x_3^*, x_4^*, and x_5^* separately refer to the standardized data of *SSR*, *H*, [*BQ*], D_0, and *K*.

TABLE 5 | Correlation coefficients among the new prediction variables.

Prediction variables	y_1	y_2	y_3	y_4
y_1	1.0000	0.0000	0.0000	0.0000
y_2	0.0000	1.0000	0.0000	0.0000
y_3	0.0000	0.0000	1.0000	0.0000
y_4	0.0000	0.0000	0.0000	1.0000

TABLE 6 | The coefficient matrix of principal components.

Prediction variables	Principal component			
	y_1	y_2	y_3	y_4
SSR	−0.5742	0.4443	−0.1441	−0.0736
H	−0.1573	−0.7573	0.0496	−0.5455
[*BQ*]	−0.6604	0.0957	0.0039	−0.3318
D_0	−0.2949	−0.1473	0.8478	0.4091
K	0.3498	0.4452	0.5080	−0.6477

TABLE 7 | The number of samples with varying squeezing levels in the training, validation, test sets.

Object	The number of samples				
	I	II	III	IV	V
Training set	20	27	23	18	11
Validation set	4	5	5	4	2
Test set	4	5	5	4	2

6 MODEL CONSTRUCTION AND APPLICATION

The database after dimensionality reduction is split into three parts by the stratified sampling: the training set (99 samples), the validation set (20 samples), and the test set (20 samples) (**Table 7**). The training set is used to train the model, the validation set is used to calculate the fitness function and optimize the model hyper-parameter, and the test set is used to evaluate the model performance in engineering practice.

6.1 Hyper-Parameter Optimization With IGWO

The spread coefficient plays a vital role in the prediction performance of PNN. If the value of the spread coefficient is too small, it is easy to cause the network to overfit; if the value of the spread coefficient is too large, the details cannot be wholly distinguished and the network is close to a linear classifier. This study adopts an improved gray wolf optimization algorithm to optimize the spread coefficient automatically.

The prediction variables (y_1, y_2, y_3, and y_4) after dimensionality reduction constitute the input vector of PNN. Moreover, there are 99 sets of training samples and five squeezing levels. Therefore, the number of neurons in the input layer, pattern layer, accumulation layer, and output layer of the PNN are 4, 99, 5, and 5, respectively. In order to select the optimal spread coefficient, 99 sets of training samples are firstly input to train PNN, and then 20 sets of validation samples are input to calculate the fitness function under different spread coefficients.

The optimization range of the spread coefficient is set to (0, 10). The wolf pack size in the improved gray wolf optimization algorithm is set to 30, and the maximum number of iterations is 400. **Figure 4** shows the evolution curve of the fitness function with the number of iterations. In the first 20 iterations, the fitness function dropped sharply. Between 20 and 140 iterations, the fitness function was stable, but then there was a decline. The fitness function did not truly converge until 150 iterations. The optimization result of the 400th iteration is used as the optimal spread coefficient. At this time, the spread coefficient is taken as 1.58 and the corresponding fitness function is 1.11.

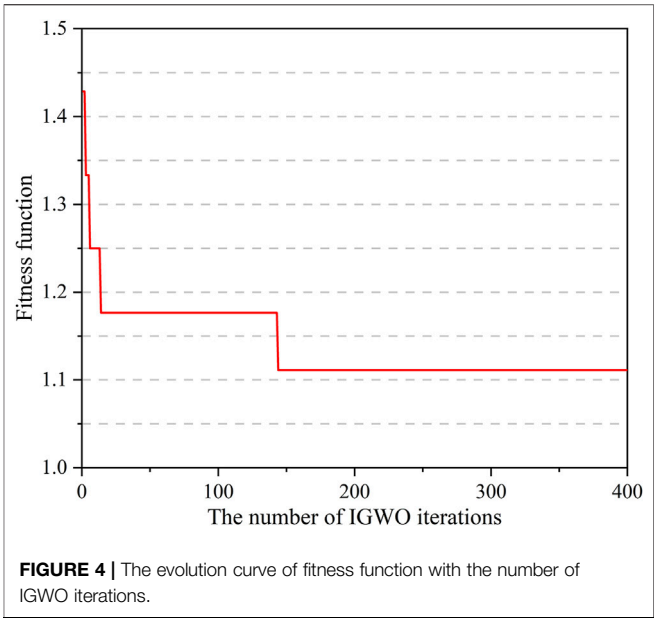


FIGURE 4 | The evolution curve of fitness function with the number of IGWO iterations.

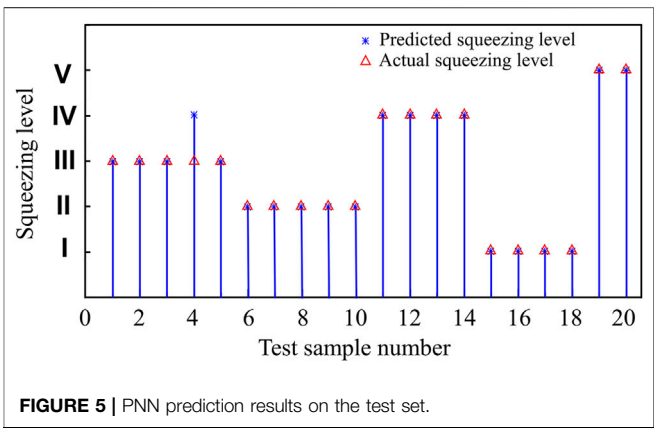


FIGURE 5 | PNN prediction results on the test set.

6.2 Prediction Performance Evaluation

The optimized PNN model is applied to the test set, and the prediction results of 20 sets of test samples are shown in **Figure 5**. Only one of the 20 test samples was misjudged by the PNN, reaching a prediction accuracy of 95%. For this misjudged test sample, its actual squeezing level is medium squeezing, but it is predicted to be a severe squeezing. From the perspective of engineering safety, this phenomenon is acceptable, because it is more advantageous for the predicted level to be higher than the actual level in comparison with the predicted level to be lower than the actual level. In particular, in two types of catastrophic accidents, namely severe squeezing and extremely severe squeezing, the PNN showed 100% prediction accuracy.

TABLE 8 | Comparison analysis of different prediction models.

Number	Posterior probability density of PNN					PNN results	ANN results	SVM	RF results	Actual level
	I	II	III	IV	V					
1	0.0163	0.2563	**0.5830**	0.1324	0.0119	3	3	3	3	3
2	0.0171	0.2761	**0.5370**	0.1563	0.0134	3	3	4	3	3
3	0.0168	0.2643	**0.5611**	0.1451	0.0127	3	3	4	3	3
4	0.0022	0.0037	0.4536	**0.5404**	0.0001	4	3	3	2	3
5	0.0038	0.3601	**0.6301**	0.0058	0.0003	3	3	3	2	3
6	0.0146	**0.5088**	0.4749	0.0015	0.0001	2	3	2	2	2
7	0.0000	**0.9999**	0.0001	0.0000	0.0000	2	2	2	2	2
8	0.0000	**0.9999**	0.0001	0.0000	0.0000	2	2	2	2	2
9	0.0000	**1.0000**	0.0000	0.0000	0.0000	2	2	2	2	2
10	0.0000	**1.0000**	0.0000	0.0000	0.0000	2	2	2	2	2
11	0.1020	0.1267	0.1688	**0.4720**	0.1305	4	4	4	4	4
12	0.0044	0.0086	0.3457	**0.3644**	0.2770	4	4	5	4	4
13	0.0005	0.0489	0.2393	**0.7098**	0.0015	4	4	4	4	4
14	0.0799	0.1722	0.3271	**0.3425**	0.0783	4	3	3	4	4
15	**0.8423**	0.0512	0.0384	0.0346	0.0336	1	1	1	1	1
16	**0.9021**	0.0762	0.0137	0.0045	0.0035	1	1	1	1	1
17	**0.9439**	0.0384	0.0079	0.0051	0.0048	1	1	1	1	1
18	**0.8688**	0.1255	0.0035	0.0012	0.0010	1	1	1	1	1
19	0.0061	0.0064	0.0243	0.0445	**0.9187**	5	4	5	4	5
20	0.0243	0.0245	0.0318	0.0409	**0.8786**	5	5	5	5	5

The maximum posterior probability density of PNN, for each test sample is bold; the misjudged test sample is highlighted in red.

TABLE 9 | Performance evaluation of different prediction models.

Model	Prediction accuracy (%)	Running time (s)
PNN	95	5.6350
ANN	85	8.8340
SVM	80	6.2290
RF	85	6.9260

To further illustrate the superiority of the PNN model, its prediction results are compared with that of the artificial neural network (ANN), support vector machine (SVM), and random forest (RF) (**Table 8**). Among the above four models, the PNN has the highest prediction accuracy with 95%, followed by the ANN (85%), RF (85%), and SVM (80%). In addition, the running times of the four models are separately 5.6350s (PNN), 8.8340s (ANN), 6.2290s (SVM), and 6.9260s (RF). It can be seen that the PNN consumes the shortest running time, achieving the fastest running speed. In terms of both prediction accuracy and running speed, the PNN built in this paper has certain advantages (**Table 9**).

7 CONCLUSION

Surrounding rock squeezing deformation is a common risk source, which can induce shield jamming disasters in TBM-excavated tunnels. To accurately predict the squeezing levels, this study proposed a hybrid model of PCA-IGWO-PNN. The main conclusions are as follows.

1) The strength-stress ratio, tunnel burial depth, tunnel equivalent diameter, rock mass quality index and support stiffness constitute the evaluation index system for the squeezing level prediction. Considering the index independence requirement of PNN, the PCA is used to preprocess the original data to eliminate the correlations and achieve dimensionality reduction. After that, four independent principal components, which are linearly combined by the original evaluation indexes, are used as the comprehensive evaluation indexes of squeezing levels.
2) The spread coefficient has a significant influence on the PNN performance, and the IGWO optimization results indicate that when the spread coefficient is taken as 1.58, the fitness function converges to the global minimum (1.11). Among the 20 test samples, the built PNN model with the optimal spread coefficient only misjudges 1, achieving the prediction accuracy of 95% in engineering application.
3) Comparison results with the ANN model, SVM model, and RF model show that the PNN model has the highest prediction accuracy, followed by ANN (85%), RF (85%), and SVM (80%). In addition, the PNN model runs fastest in the above four models, only consuming 5.6350s, while the ANN, SVM, and RF separately consume 8.8340, 6.2290, and 6.9260 s. From the aspects of the prediction accuracy and running speed, the PNN model proposed in this paper is the most superior and feasible, which provides an effective method for surrounding rock squeezing classification.

DATA AVAILABILITY STATEMENT

The original contributions presented in the study are included in the article/**Supplementary Material**, further inquiries can be directed to the corresponding author.

AUTHOR CONTRIBUTIONS

All authors listed have made a substantial, direct, and intellectual contribution to the work and approved it for publication.

FUNDING

This work was financially supported by the National Natural Science Foundation of China (Grant Nos. 52074258, 51874232), and the Natural Science Basic Research Program of Shaanxi Province (Shaanxi Coal and Chemical Industry Group Co., Ltd. Joint Fund Project, Grant No. 2021JLM-06), and Key Research and Development Project of Hubei Province (Grant Nos. 2020BCB073, 2021BCA133). Their support is gratefully acknowledged.

SUPPLEMENTARY MATERIAL

The Supplementary Material for this article can be found online at: https://www.frontiersin.org/articles/10.3389/feart.2022.857463/full#supplementary-material

REFERENCES

Aydan, A. T., Akagi, T., and Kawamoto, T. (1996). The Squeezing Potential of Rock Around Tunnels: Theory and Prediction with Examples Taken from Japan. *Rock Mech. Rock Engng* 29, 125–143. doi:10.1007/bf01032650

Barla, G. (1995). Squeezing Rocks in Tunnels. *ISRM News J.* 2, 44–49.

Chen, Y., Li, T., Zeng, P., Ma, J., Patelli, E., and Edwards, B. (2020). Dynamic and Probabilistic Multi-Class Prediction of Tunnel Squeezing Intensity. *Rock Mech. Rock Eng.* 53, 3521–3542. doi:10.1007/s00603-020-02138-8

Dukov, N. T., Ganchev, T. D., and Vrahatis, M. N. (2019). Evaluation of PNN Pattern-Layer Activation Function Approximations in Different Training Setups[J]. *Int. J. Speech Tech.* 22, 1039–1049. doi:10.1007/s10772-019-09640-7

Dwivedi, R. D., Singh, M., Viladkar, M. N., and Goel, R. K. (2013). Prediction of Tunnel Deformation in Squeezing Grounds. *Eng. Geology.* 161, 55–64. doi:10.1016/j.enggeo.2013.04.005

Farhadian, H., and Nikvar-Hassani, A. (2020). Development of a New Empirical Method for Tunnel Squeezing Classification (TSC). *Q. J. Eng. Geology. Hydrogeology* 53, 655–660. doi:10.1144/qjegh2019-108

Feng, X., and Jimenez, R. (2015). Predicting Tunnel Squeezing with Incomplete Data Using Bayesian Networks. *Eng. Geology.* 195, 214–224. doi:10.1016/j.enggeo.2015.06.017

Ge, Y., Cao, B., and Tang, H. (2022). Rock Discontinuities Identification from 3D Point Clouds Using Artificial Neural Network. *Rock Mech. Rock Eng.* doi:10.1007/s00603-021-02748-w

Ge, Y., Xie, Z., Tang, H., Du, B., and Cao, B. (2021). Determination of the Shear Failure Areas of Rock Joints Using a Laser Scanning Technique and Artificial Intelligence Algorithms. *Eng. Geology.* 293, 106320. doi:10.1016/j.enggeo.2021.106320

Goel, R. K., Jethwa, J. L., and Paithankar, A. G. (1995). Tunnelling through the Young Himalayas-A Case History of the Maneri-Uttarkashi Power Tunnel [J]. *Eng. Geology.* 39 (1), 31–44. doi:10.1016/0013-7952(94)00002-j

Hasanpour, R., Rostami, J., Schmitt, J., ilmaz, O., and Sohrabian, B. (2020b). Prediction of TBM Jamming Risk in Squeezing Grounds Using Bayesian and Artificial Neural Networks[J]. *J. Rock Mech. Geotechnical Eng.* 12 (01), 21–31. doi:10.1016/j.jrmge.2019.04.006

Hasanpour, R., Rostami, J., Schmitt, J., Ozcelik, Y., and Sohrabian, B. (2020a). Prediction of TBM Jamming Risk in Squeezing Grounds Using Bayesian and Artificial Neural Networks. *J. Rock Mech. Geotechnical Eng.* 12, 21–31. doi:10.1016/j.jrmge.2019.04.006

Hasanpour, R., Rostami, J., and Ünver, B. (2014). 3D Finite Difference Model for Simulation of Double Shield TBM Tunneling in Squeezing Grounds. *Tunnelling Underground Space Tech.* 40, 109–126. doi:10.1016/j.tust.2013.09.012

Jethwa, J. L. (1981). *Evaluation of Rock Pressures in Tunnels through Squeezing Ground in Lower Himalayas*. Roorkee: University of Roorkee.

Jiao, Y. Y., Ou, G., Wang, H., Zhang, G. H., Zou, J. P., Tan, F., et al. (2021). Prediction of Tunnel Squeezing Based on Evidence Theory [J]. *J. Appl. Basic Eng. Sci.* 29 (05), 1156–1170.doi:10.1155/2018/4543984

Jimenez, R., and Recio, D. (2011). A Linear Classifier for Probabilistic Prediction of Squeezing Conditions in Himalayan Tunnels. *Eng. Geology.* 121, 101–109. doi:10.1016/j.enggeo.2011.05.006

Liu, Q., Huang, X., Gong, Q., Du, L., Pan, Y., and Liu, J. (2016). Application and Development of Hard Rock TBM and its prospect in China. *Tunnelling Underground Space Tech.* 57, 33–46. doi:10.1016/j.tust.2016.01.034

Liu, Q., Wang, X., Huang, X., and Yin, X. (2020). Prediction Model of Rock Mass Class Using Classification and Regression Tree Integrated AdaBoost Algorithm Based on TBM Driving Data. *Tunnelling Underground Space Tech.* 106, 103595. doi:10.1016/j.tust.2020.103595

Mirjalili, S., Mirjalili, S. M., and Lewis, A. (2014a). Grey Wolf Optimizer. *Adv. Eng. Softw.* 69 (3), 46–61. doi:10.1016/j.advengsoft.2013.12.007

Mirjalili, S., Mirjalili, S. M., and Lewis, A. (2014b). Gray Wolf Optimizer. *Adv. Eng. Softw.* 69, 46–61. doi:10.1016/j.advengsoft.2013.12.007

Sanal Kumar, K. P., and Bhavani, R. (2019). Human Activity Recognition in Egocentric Video Using PNN, SVM, kNN, and SVM+kNN Classifiers[J]. *Cluster Comput.* 22, 3–4. doi:10.1007/s10586-017-1131-x

Schimit, P. H. T., and Pereira, F. H. (2018). Disease Spreading in Complex Networks: A Numerical Study with Principal Component Analysis. *Expert Syst. Appl.* 97, 41–50. doi:10.1016/j.eswa.2017.12.021

Singh, B., Jethwa, J. L., Dube, A. K., and Singh, B. (1992). Correlation between Observed Support Pressure and Rock Mass Quality. *Tunnelling Underground Space Tech.* 7, 59–74. doi:10.1016/0886-7798(92)90114-w

Sousa, R. L., and Einstein, H. H. (2011). Risk Analysis during Tunnel Construction Using Bayesian Networks: Porto Metro Case Study. *Tunnelling Underground Space Tech. incorporating Trenchless Tech. Res.* 27 (1), 86–100. doi:10.1016/j.tust.2011.07.003

Sun, Y., Feng, X., and Yang, L. (2018). Predicting Tunnel Squeezing Using Multiclass Support Vector Machines. *Adv. Civil Eng.* 2018, 1–12. doi:10.1155/2018/4543984

Xu, Z. H., Wang, W. Y., Lin, P., Nie, L. C., Wu, J., and Li, Z. M. (2021). Hard-rock TBM Jamming Subject to Adverse Geological Conditions: Influencing Factor, hazard Model and a Case Study of Gaoligongshan Tunnel. *Tunneling Underground Space Tech.* 108, 103683.doi:10.1016/j.tust.2020.103683

Yin, X., Liu, Q., Pan, Y., Huang, X., Wu, J., and Wang, X. (2021c). Strength of Stacking Technique of Ensemble Learning in Rockburst Prediction with Imbalanced Data: Comparison of Eight Single and Ensemble Models. *Nat. Resour. Res* 80, 1795–1815 doi:10.1007/s11053-020-09787-0

Yin, X., Liu, Q., Huang, X., and Pan, Y. (2022). Perception Model of Surrounding Rock Geological Conditions Based on TBM Operational Big Data and Combined Unsupervised-Supervised Learning. *Tunnelling Underground Space Tech.* 120, 104285. doi:10.1016/j.tust.2021.104285

Yin, X., Liu, Q., Huang, X., and Pan, Y. (2021b). Real-time Prediction of Rockburst Intensity Using an Integrated CNN-Adam-BO Algorithm Based on Microseismic Data and its Engineering Application. *Tunnelling Underground Space Tech.* 117, 104133. doi:10.1016/j.tust.2021.104133

Yin, X., Liu, Q., and Pan, Y. (2021a). A Novel Tree-Based Algorithm for Real-Time Prediction of Rockburst Risk Using Field Microseismic Monitoring. *Environ. Earth Sci.* 80, 1–19. doi:10.1007/s12665-021-09802-4

Zhang, J., Li, D., and Wang, Y. (2020a). Predicting Tunnel Squeezing Using a Hybrid Classifier Ensemble with Incomplete Data. *Bull. Eng. Geol. Environ.* 79, 3245–3256. doi:10.1007/s10064-020-01747-5

Zhang, W. G., and Phoon, K. K. (2022). Editorial for Advances and Applications of Deep Learning and Soft Computing in Geotechnical Underground Engineering. *J. Rock Mech. Geotech. Eng* doi:10.1016/j.jrmge.2022.01.001

Zhang, W., Li, H., Li, Y., Liu, H., Chen, Y., and Ding, X. (2021a). Application of Deep Learning Algorithms in Geotechnical Engineering: a Short

Critical Review. *Artif. Intell. Rev.* 54, 5633–5673. doi:10.1007/s10462-021-09967-1

Zhang, W., Wu, C., Zhong, H., Li, Y., and Wang, L. (2021b). Prediction of Undrained Shear Strength Using Extreme Gradient Boosting and Random forest Based on Bayesian Optimization. *Geosci. Front.* 12, 469–477. doi:10.1016/j.gsf.2020.03.007

Zhang, W., Zhang, R., Wu, C., Goh, A. T. C., Lacasse, S., Liu, Z., et al. (2020a). State-of-the-art Review of Soft Computing Applications in Underground Excavations. *Geosci. Front.* 11, 1095–1106. doi:10.1016/j.gsf.2019.12.003

Zhang, Y., Guo, J., Zhou, Q., and Wang, S. (2021c). Research on Damage Identification of hull Girder Based on Probabilistic Neural Network (PNN). *Ocean Eng.* 238, 15. doi:10.1016/j.oceaneng.2021.109737

Zhu, H., Yan, J., and Liang, W. (2019). Challenges and Development Prospects of Ultra-long and Ultra-deep Mountain Tunnels. *Engineering* 5, 384–392. doi:10.1016/j.eng.2019.04.009

Conflict of Interest: Author XS was employed by Shaanxi Zhengtong Coal Industry Co., Ltd.

The remaining authors declare that the research was conducted in the absence of any commercial or financial relationships that could be construed as a potential conflict of interest.

Publisher's Note: All claims expressed in this article are solely those of the authors and do not necessarily represent those of their affiliated organizations, or those of the publisher, the editors, and the reviewers. Any product that may be evaluated in this article, or claim that may be made by its manufacturer, is not guaranteed or endorsed by the publisher.

Copyright © 2022 Huang, Yin, Liu, Ding, Zhang, Jing and Guo. This is an open-access article distributed under the terms of the Creative Commons Attribution License (CC BY). The use, distribution or reproduction in other forums is permitted, provided the original author(s) and the copyright owner(s) are credited and that the original publication in this journal is cited, in accordance with accepted academic practice. No use, distribution or reproduction is permitted which does not comply with these terms.

frontiers in Earth Science

ORIGINAL RESEARCH
published: 09 March 2022
doi: 10.3389/feart.2022.854807

Prediction Method of TBM Tunneling Parameters Based on PSO-Bi-LSTM Model

Qinglong Zhang[1,2], *Yanwen Zhu*[1], *Rui Ma*[2], *Canxun Du*[3], *Sanlin Du*[3], *Kun Shao*[3] *and Qingbin Li*[2]*

[1]Department of Civil Engineering, School of Civil and Resource Engineering, University of Science and Technology Beijing, Beijing, China, [2]State Key Laboratory of Hydroscience and Engineering, Tsinghua University, Beijing, China, [3]HUANENG Tibet Hydropower Safety Engineering Technology Research Center, Chengdu, China

With the wide application of full-face rock tunnel boring machine (TBM) in tunnel construction, the self-adaptive adjustment of TBM tunneling parameters is of great significance for the safety and efficiency of TBM tunnelling. Aiming at the shortcomings of the current TBM data mining capability and optimization methods of tunneling parameters, this paper proposes a prediction method of TBM tunneling parameters based on particle swarm optimization-bi-directional long short-term memory (PSO-Bi-LSTM) model, which selects the complete tunneling cycle data to predict the TBM tunneling parameters, and uses a number of numerical methods such as binary state discriminant function and 3σ criterion to preprocess the operation data of TBM3 bid section of Songhua River water conveyance project. By comparing with the Bi-LSTM model and evaluating the prediction effect under different surrounding rock levels, the applicability and prediction performance of the model to different strata are verified. The results show that the prediction accuracy of the model is proportional to the surrounding rock grade. Compared with the Bi-LSTM, the overall prediction effect of the proposed PSO-Bi-LSTM model is better, which can assist the intelligent construction of TBM with similar geological conditions.

Keywords: tunnel engineering, TBM, PSO-Bi-LSTM, tunneling parameter prediction, intelligent construction

OPEN ACCESS

Edited by:
Guang-Liang Feng,
Institute of Rock and Soil Mechanics (CAS), China

Reviewed by:
Yaxun Xiao,
Institute of Rock and Soil Mechanics (CAS), China
Mingyang Liu,
Tianjin Research Institute of Water Transport Engineering, China
Zaizhan An,
China Academy of Railway Sciences, China

***Correspondence:**
Qingbin Li
qingbinli@tsinghua.edu.cn

Specialty section:
This article was submitted to Geohazards and Georisks, a section of the journal Frontiers in Earth Science

Received: *14 January 2022*
Accepted: *27 January 2022*
Published: *09 March 2022*

Citation:
Zhang Q, Zhu Y, Ma R, Du C, Du S, Shao K and Li Q (2022) Prediction Method of TBM Tunneling Parameters Based on PSO-Bi-LSTM Model. Front. Earth Sci. 10:854807. doi: 10.3389/feart.2022.854807

INTRODUCTION

With the large-scale development of infrastructure construction and the continuous application of new technologies in China, large-scale engineering equipment integrating soil cutting, tunnel support and other functions, namely tunnel boring machine (TBM), has become the first choice for various medium and long-distance tunnel construction due to its remarkable advantages such as high efficiency, safety, and economy (Gao et al., 2019; Hou and Liu, 2021). However, due to the variability of TBM tunneling parameters and the complexity of geological conditions (Feng et al., 2015; Feng et al., 2022; Yang et al., 2022), it is difficult to quantitatively analyze the interaction law between TBM and rock. Tunneling often relies on human experience to adjust repeatedly, and the real-time matching is poor, and it cannot adapt to the complex geological environment (Zhang et al., 2018a; Afradi et al., 2021). Therefore, accurate and effective real-time prediction of TBM tunneling parameters has become an urgent problem to be solved in the field of tunnel engineering.

In recent years, scholars have proposed a series of prediction models around the prediction of TBM tunneling parameters, including theoretical prediction models (Evans, 1965; Zhou et al., 2016),

empirical prediction models (Barton, 2000; Gertsch et al., 2007), and prediction models based on machine learning methods (Sun et al., 2018; Zhang et al., 2021a). Based on indentation test or full-scale laboratory cutting test, the theoretical prediction model quantifies the equilibrium force equation required for cutting force. For example, the CSM model proposed by the Colorado School of Mines (Rostami, 1997) summarizes rock breaking laws and calculates TBM tunneling parameters based on the results of full-scale laboratory cutting tests on plenty of rock samples. This type of model considers limited engineering factors and has certain limitations. For improving the applicability of the theoretical model, Yagiz (Yagiz, 2006) improved the CSM model and introduced the research on the brittleness and discontinuity of rock mass. Zhang et al. (Zhang et al., 2013) established a theoretical load prediction model for shield tunneling machines with Earth pressure balance considering the influence of soil-rock interlayer foundation. Zhou and Zhai (Zhou and Zhai, 2018) extended the theoretical cutter head torque model to mixed surface grinding. In addition to the above theoretical prediction models, different scholars have conducted multi-angle explorations on the prediction of TBM tunneling parameters based on empirical learning methods and have made certain research progress. Krause (Krause, 1976) proposed a widely used empirical formula for TBM load prediction. Xue et al. (Jing et al., 2019) studied the rock crushing process based on experiments. Entacher et al. (Entacher et al., 2014) proposed a rock crushing test method for cutting experiments and used an empirical method to estimate the load in the light of the test results. In addition, with the continuous improvement of test equipment, multi-factor prediction models represented by the Norwegian Institute of Technology (NTNU) model (Sun et al., 2018) have been widely used. Although the above models have achieved abundant research results, they still have different degrees of limitations in the prediction process. Based on the existing engineering experience and through regression analysis, the empirical prediction model establishes the empirical relationship between the TBM tunneling parameters and rock mass parameters, but it only has a good prediction effect on specific strata, and the factors considered in the prediction process are limited. It has great limitations and poor universality under different geological conditions. The theoretical prediction model is mainly based on the summary of test results and mechanical theoretical analysis and cannot sensitively capture the small changes of TBM load, which is quite different from the actual TBM tunneling construction.

With the rapid development of artificial intelligence technology and the continuous improvement of various detection technologies (Zhang et al., 2020a; Zhang et al., 2021b), to make up for the shortcomings of the above traditional prediction models, many scholars have proposed a series of new intelligent prediction models for TBM tunneling parameters based on machine learning algorithms. Wen et al. (Wen et al., 2009) established a predication model based on Monte Carlo-BP neural network and ranked the importance of parameters to improve the prediction accuracy of TBM tunneling speed. Mahdevari et al. (Mahdevari et al., 2014) and Tao et al. (Tao et al., 2015) applied support vector regression (SVR) and random forest to predict the penetration rate of TBM in hard rock conditions, respectively. Xiong et al. (Xiong et al., 2017) established a BP neural network model through MATLAB based on the surrounding rock and machine performance parameters to predict the penetration of TBM. Compared with other optimization algorithms, particle swarm optimization (PSO) has the several advantages, that is, fewer parameters need to be adjusted, the algorithm implementation is simpler, the efficiency is higher, the robustness is better, and it is easy to converge. Therefore, Hou et al. (Hou et al., 2020) improved the standard particle swarm optimization (PSO) algorithm and proposed a TBM prediction model based on the improved PSO to optimize the BP neural network. In addition, Hou et al. (Hou et al., 2019) proposed an exponential adjustment inertia weight immune particle swarm optimization to enhance the accuracy and reliability regarding the selection of shield tunneling parameter values. The application of machine learning algorithm effectively improves the prediction accuracy of TBM tunneling parameter. However, due to the timeliness of TBM parameters, the machine learning algorithm fails to consider the time variation characteristics of various parameters, which greatly increases the difficulty of feature extraction and analysis in the prediction process. Therefore, the further development of more robust and effective algorithms is still an urgent problem to be solved.

As a new field, deep learning (Zhang et al., 2021c) has the advantages of efficient learning, transferability and strong adaptability compared with traditional machine learning algorithms. Due to advanced optimization techniques and powerful GPU computing power, deep learning models have been successfully applied in practical engineering fields such as speech recognition (Zhang et al., 2018b), image processing (Graves et al., 2009), and machine translation (Tan et al., 2018). Recurrent neural network (RNN) (Jin et al., 2018) is a special network structure in neural network for processing time series data, which is widely used in sequence related fields such as language model (Zhao and Dong, 2018), part-of-speech tagging (Si et al., 2018). The long-short term memory (LSTM) network (Vlachas et al., 2018; Liu et al., 2019; Zhang et al., 2020b; Wang et al., 2021) improves the unit structure of the traditional recurrent neural network and effectively solves the long-term dependency problems such as gradient disappearance in the RNN network. However, LSTM network is a one-way sequence structure, which cannot use the subsequent time information to calculate the output, and the data processing process is cumbersome. To solve this problem, this paper improves the propagation mode of LSTM neural network, introduces a bidirectional learning strategy, optimizes the model by PSO, and puts forward a prediction method of TBM tunneling parameters based on PSO-Bi-LSTM model.

Taking the data set based on the TBM3 bid section of Songhua River water conveyance project as the research object, 9,350 tunneling cycles are randomly selected as the model training set in the light of the ratio of 17:1 by data mining method. Different from the traditional prediction method that uses the data of the ascending segment to predict the parameters of the

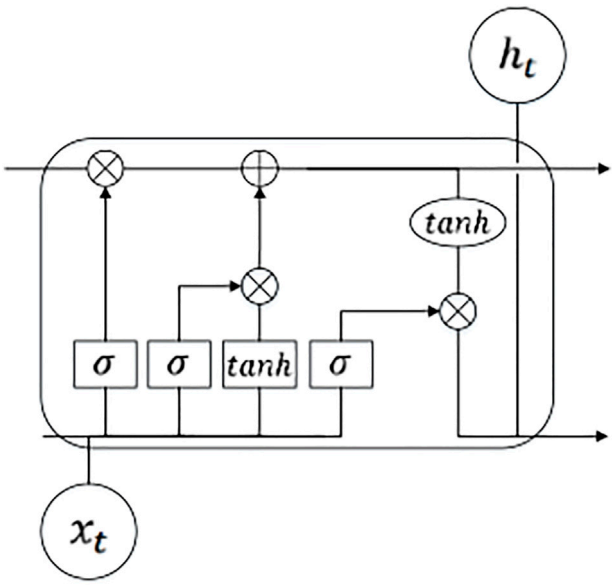


FIGURE 1 | LSTM structure diagram (Gao et al., 2019).

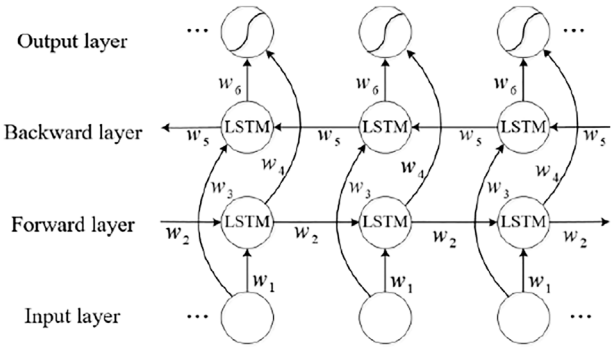


FIGURE 2 | Bi-LSTM network structure diagram.

stable segment, this paper selects the data of the complete tunneling cycle to predict the TBM tunneling parameters. Using Pearson correlation analysis, this paper extracts the 21 key parameters with the highest correlation with the predicted parameters from the 199-dimensional tunneling parameters of the complete tunneling cycle as the model input features. Meanwhile, the Adam optimizer is used to train Bi-LSTM, and the mean square error (MSE) is used as the loss function of the model. By comparing with the current relevant algorithms and analyzing the prediction effect under different surrounding rock grades, the prediction performance of the PSO-Bi-LSTM model and its applicability under different surrounding rock grades are verified, to provide a more feasible intelligent decision-making method of tunneling parameters for TBM-assisted intelligent construction.

BI-LSTM MODEL OPTIMIZED BY PSO

Unidirectional LSTM

RNN is a special kind of network structure used to process sequence data. Different from the traditional neural network model, the RNN network has a high-dimensional hidden nonlinear internal structure, which can memorize the information of the previous moment and apply it to the current output vector. Theoretically, the RNN network can process sequence data of any length. But in practice, the information that the RNN network can store is limited, and there may be varying degrees of information forgetting during long-distance data transmission, and the input of the hidden layer has a significant impact on the output of the network. The influence decays as the network loop continues to recurse, making it difficult to deal with long-term dependencies such as vanishing gradients.

To solve this problem, related scholars introduced a gating mechanism upon the RNN network to form a LSTM network. Compared with the RNN network, LSTM adds three control gates, namely input gate, output gate, and forget gate. The unit structure of LSTM is shown in **Figure 1**, which is mainly composed of one memory unit and three gating units. Through the gated unit structure, the memory unit can effectively filter the historical information. The output vector of the hidden layer at the previous moment and the information at the current moment are combined into the input vector at the current moment, and then be stored, forgotten and output adaptively through the LSTM unit.

Bi-LSTM

LSTM network can effectively deal with long-term dependence problems such as gradient disappearance in variable-length sequences, but TBM tunneling parameters are time-dependent, and the data change law is not only related to past information, but also considers the impact of future information on the model prediction performance. For changing the limitation that the traditional LSTM network only draws conclusions from past information, some scholars have improved the propagation method of the LSTM network and proposed a Bi-LSTM network.

Bi-LSTM network is composed of forward LSTM and backward LSTM. Compared with traditional LSTM network, Bi-LSTM network can better adapt to sequence data with strong round-trip correlation and effectively capture the dynamic characteristics of TBM tunneling parameters. **Figure 2** shows the Bi-LSTM network structure, which adds a backpropagation layer upon LSTM. The forward training sequence and the backward training sequence are two independent LSTM structures. The two structures are symmetrical, and the information transmission directions are opposite. The forward training sequence calculates the current moment information forward, and the backward training sequence calculates the same sequence backwards. Bi-LSTM predicts all input vectors based on the timing of the input features, the hidden layer integrates the past and future

information and outputs to the output layer, and finally integrates the forward and reverse information to output the prediction result.

$$h_t = f(w_1 x_t + w_2 h_{t-1}) \tag{1}$$

$$h_t^{'} = f\left(w_3 x_t + w_5 h_{t+1}^{'}\right) \tag{2}$$

$$y_t = g\left(w_4 h_t + w_6 h_t^{'}\right) \tag{3}$$

where, h_t is the current state of the forward hidden layer; $h_t^{'}$ is the current state of the reverse hidden layer; x_t is the input value of the input layer at the current moment; y_t is the output value of the output layer at the current moment; w_1、 w_2、 w_3、 w_4、 w_5、 w_6 are the corresponding weight matrices of information propagating along the time series respectively.

Particle Swarm Optimization

PSO is a population-based computational method for intelligent bionic evolution, first proposed by American professors Eberhart and Kennedy in 1995. The concept of PSO originates from the research on the predation behavior of birds and realizes the intelligence of problem solving through cooperation and information sharing among individuals in the group. Compared with optimization algorithms such as genetic algorithm and ant colony algorithm, PSO has a relatively simple structure, fewer adjustment parameters, and has the advantage of fast convergence.

PSO uses the velocity-position iterative search method to determine the global optimal solution when solving the optimization problem. First, some particles are randomly initialized in the solution space. Each particle can be regarded as a search individual in the search space. The current velocity and position of the particle correspond to a candidate set of the optimization problem and are dynamically adjusted in accordance with the fitness function. The point where the fitness function is optimal is recorded as the current individual extreme value, also known as the local optimal solution. The local optimal solution is shared with other particles in the particle swarm, and the optimal individual extreme value is obtained by comparative analysis as the current global optimal solution of the whole particle swarm. The particle speed and position adjust the update state in the light of the two optimal solutions in the optimization process, and finally find the optimal parameters. According to the principle of the PSO above, the state update equation of the particle at time t+1 is as follows:

$$v(t+1) = \omega v_t + c_1 r_1 (P_t - x_t) + c_2 r_2 (G_t - x_t) \tag{4}$$

$$x(t+1) = x_t + v(t+1) \tag{5}$$

where, v is the particle swarm velocity; ω is the inertia weight (non-negative), the larger the value of ω, the stronger the global optimization ability and the weaker the local optimization; x is the particle swarm position; r_1, r_2 are a random function in the range [0, 1]; c_1, c_2 are the learning factor; P_t is the local optimal solution; G_t is the global optimal solution.

Bi-LSTM Model Optimized by PSO

The basic idea of constructing the PSO-Bi-LSTM model is to use the PSO to optimize the bias and weights of the Bi-LSTM neural network, thereby improving its convergence speed and prediction accuracy. Compared with some deterministic algorithms, the PSO, as an uncertain algorithm of bionic optimization, has self-organization, robustness, and essential parallelism. Each particle cooperates with each other to better adapt to the environment, ensuring the effectiveness and practicability of the algorithm under different conditions and environments. **Figure 3** is the specific algorithm flow of PSO.

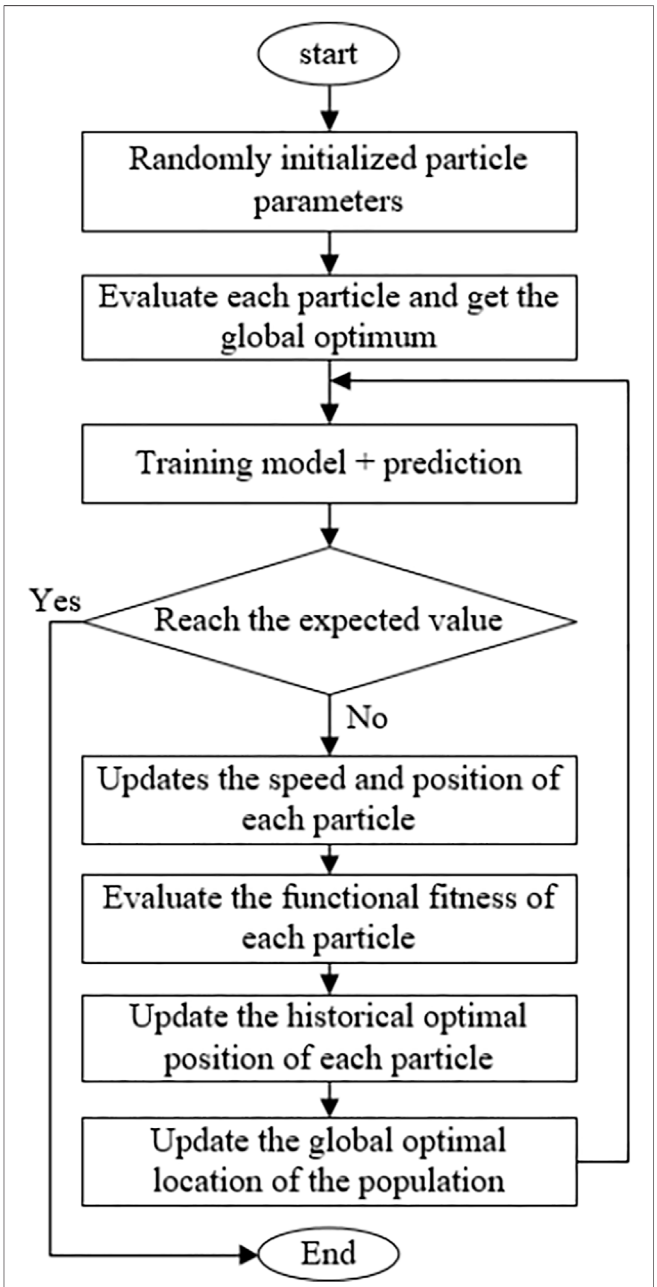


FIGURE 3 | Flow chart of PSO algorithm.

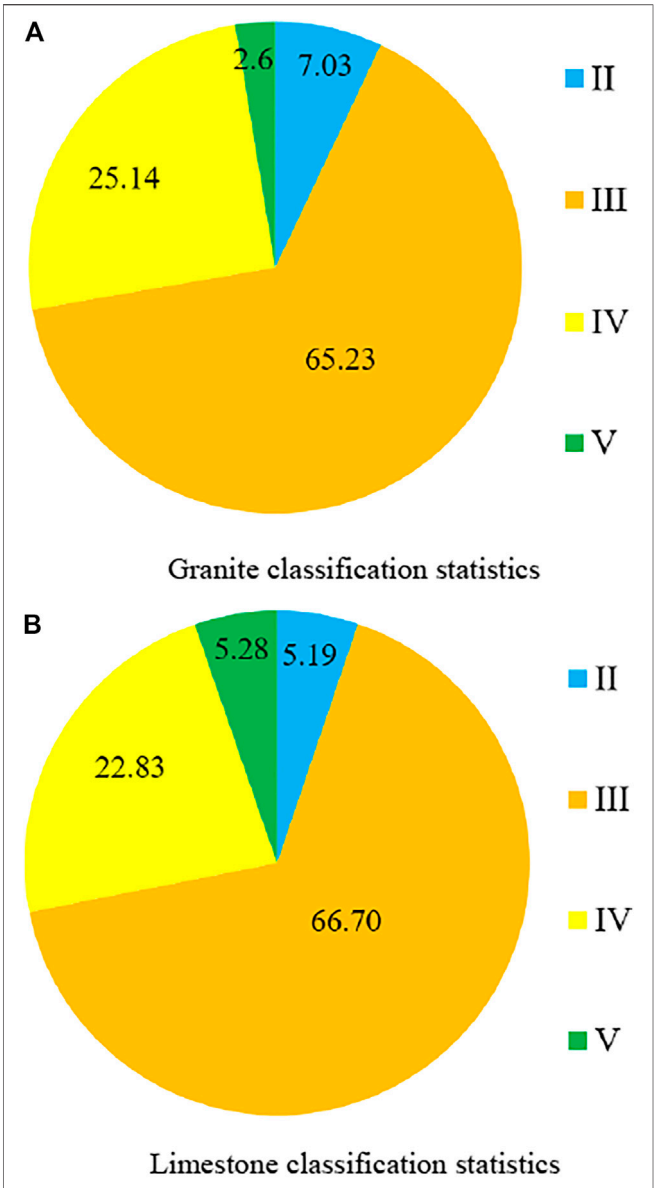


FIGURE 4 | Statistics on geological conditions of TBM construction section. **(A)** Granite classification statistics; **(B)** Limestone classification statistics.

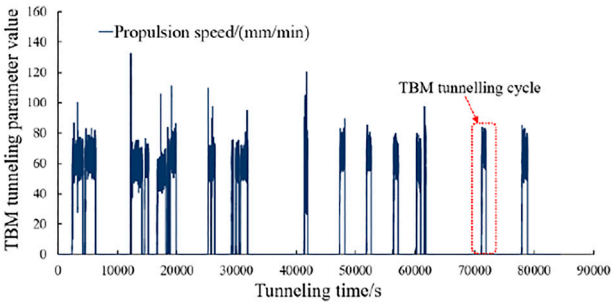


FIGURE 5 | Variation curve of TBM tunneling parameters in 1 day.

The specific steps of PSO to optimize Bi-LSTM are as follows:

1) The method of constructing binary state discriminant function is used to preprocess the original data of TBM tunneling, and the data and outliers of the stop section are eliminated to obtain valid data samples.
2) Normalize the input data, import the PSO-Bi-LSTM model, determine the particle swarm search space, initialize the particle swarm parameters, set the optimization function, parameter dimension, number of iterations, and upper and lower limits of the parameters to be optimized.
3) Calculate the fitness value of each particle, update the particle based on the fitness function, and determine the local optimal solution; and compare the local optimal solution of each particle to obtain the current global optimal solution.
4) Determine the velocity and position of the particle at the current moment in the light of **Eqs 4**, **5**.
5) Train the model and judge whether the predicted value reaches the expected value or reaches the maximum number of iterations. If the conditions are met, end the model training, and output the optimization result; otherwise, after recording the historical information, continue to execute the Bi-LSTM algorithm to train the model until it reaches the expectation.
6) In accordance with the optimized parameters of PSO, a PSO-Bi-LSTM model is constructed to predict the TBM tunneling parameters, and an appropriate evaluation function is selected to evaluate the prediction effect.

PROJECT OVERVIEW AND DATA PROCESSING

Project Overview

The Songhua River water conveyance project in Jilin Province has a total length of 263.01 km and a water diversion tunnel of 133.98 km. It is a large-scale cross-regional water diversion project with the largest scale, the longest water transmission line, and the most difficult construction in Jilin Province. The total length of the TBM3 bid section is 22,955 m, and the construction projects are mainly water diversion tunnels, shaft excavation, support, and drainage work. Among them, the tunnel excavation section with a total length of 20,198 m and a maximum buried depth of 260 m is mainly constructed by TBM and supplemented by the drilling and blasting method, and its engineering geological conditions are shown in **Figure 4**. The lithology of the stratum involved in this section is mainly granite and limestone, and the surrounding rock grades II to V are distributed. The groundwater is divided into five grades in the light of the degree of humidity. The distribution ratio of the granite area to the limestone area is 1:1.58; the proportions of grades II to V of the surrounding rocks in the granite area are 7.03, 65.23, 25.14 and 2.60% respectively; the proportions of grades II to V of the surrounding rocks in the limestone area are 5.19, 66.70, 22.83 and 5.28% respectively.

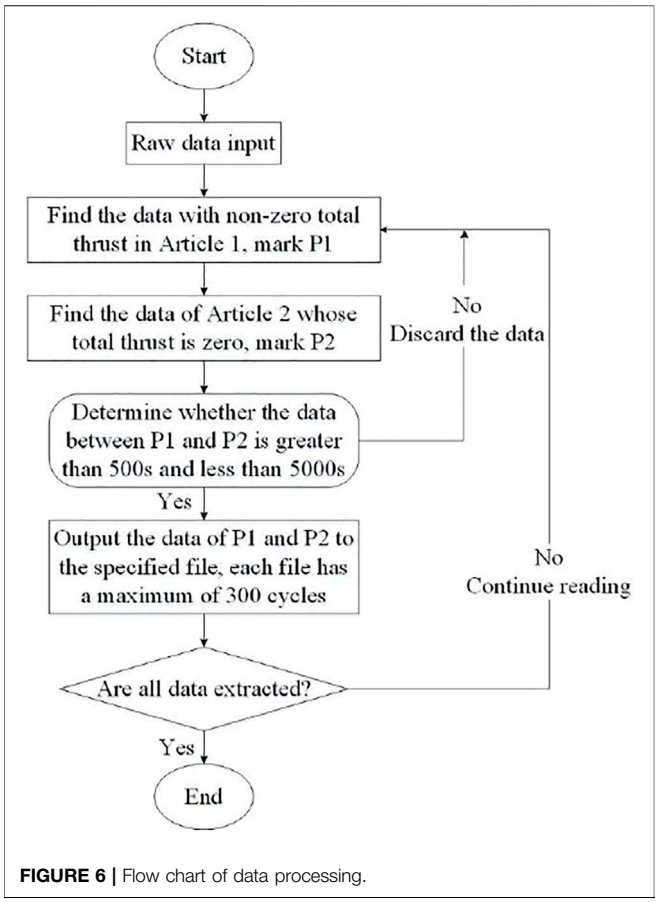


FIGURE 6 | Flow chart of data processing.

The data of the TBM3 bit section is taken as the research object. The data collection frequency is 1 Hz, and an average of 86,400 data are collected every day. Each data includes 199-dimensional TBM tunneling parameters such as the propulsion speed, total thrust, cutter head torque and cutter head power. As shown in **Figure 5**, the TBM tunneling process is composed of several tunneling cycles. Generally, the cylinder stroke is used as one tunneling cycle, with about 10–20 tunneling cycles per day. The tunneling data of a complete tunneling cycle is selected to predict the tunneling parameters of the stable segment of the next tunneling cycle, thereby judging the tunneling state of TBM.

Data Preprocessing

Figure 5 shows that the TBM tunneling parameter-time variation in a certain day. The adjacent tunneling cycles are divided by the shutdown state. The shutdown data (that is, the data with the TBM tunneling parameter value of 0) belongs to useless data for the machine learning algorithm. For eliminating the influence of the shutdown state data, the binary state discriminant function is constructed to preprocess the original working data and extract the effective tunneling data of each tunneling cycle from the record file. The formula for judging whether the TBM tunneling parameter value is the data of the shutdown section is as follows:

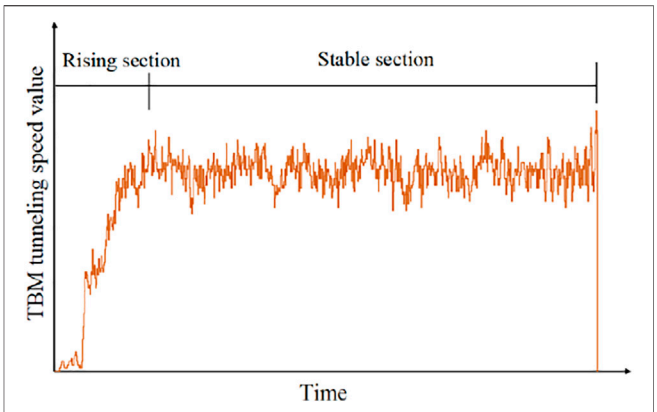


FIGURE 7 | A certain complete tunneling cycle during TBM construction.

$$I = f(N)f(T)f(F)f(V) \tag{6}$$

$$f(x) = \begin{cases} 1, & x \neq 0 \\ 0, & x = 0 \end{cases} \tag{7}$$

where, I is the binary state discriminant function; N is the propulsion speed; F is total thrust; T is cutter head torque; V is cutter head power. When the binary state discriminant function I = 0, it means that this segment of data is the shutdown segment data; when I = 1, it means that this segment of data is the TBM normal running state data.

Due to the influence of equipment factors, construction environment and construction experience of operators, there are abnormal working conditions in the collected data samples, which affect the prediction accuracy of the model. Therefore, the 3 σ criterion is used to identify and remove outliers. The data processing flow is shown in **Figure 6**.

The original data is read row by row, and the input data is marked and judged based on total thrust. The first total thrust (non-zero value) data is marked as P1; then continue to read the next data, and the second total thrust (zero value) data is marked as P2. Subsequently, it is necessary to determine whether the data between P1 and P2 is within the range of 500 s to 5,000 s. If not, discard the data; if it is, output the data of P1 and P2 to the corresponding file. According to the above method, all data are sequentially extracted, and the data preprocessing process ends. Based on data preprocessing, a total of 9,900 groups of valid tunneling cycles were extracted, 9,350 groups of tunneling cycles were randomly selected as the model training set, and the remaining 550 groups of tunneling cycles were used as the model test set.

Tunneling Cycle Extraction

In accordance with the data preprocessing results, the working state of the TBM at each moment is determined, and valid data samples are extracted, wherein each group of continuous tunneling sequences corresponds to a complete tunneling cycle, and the data between adjacent tunneling cycles

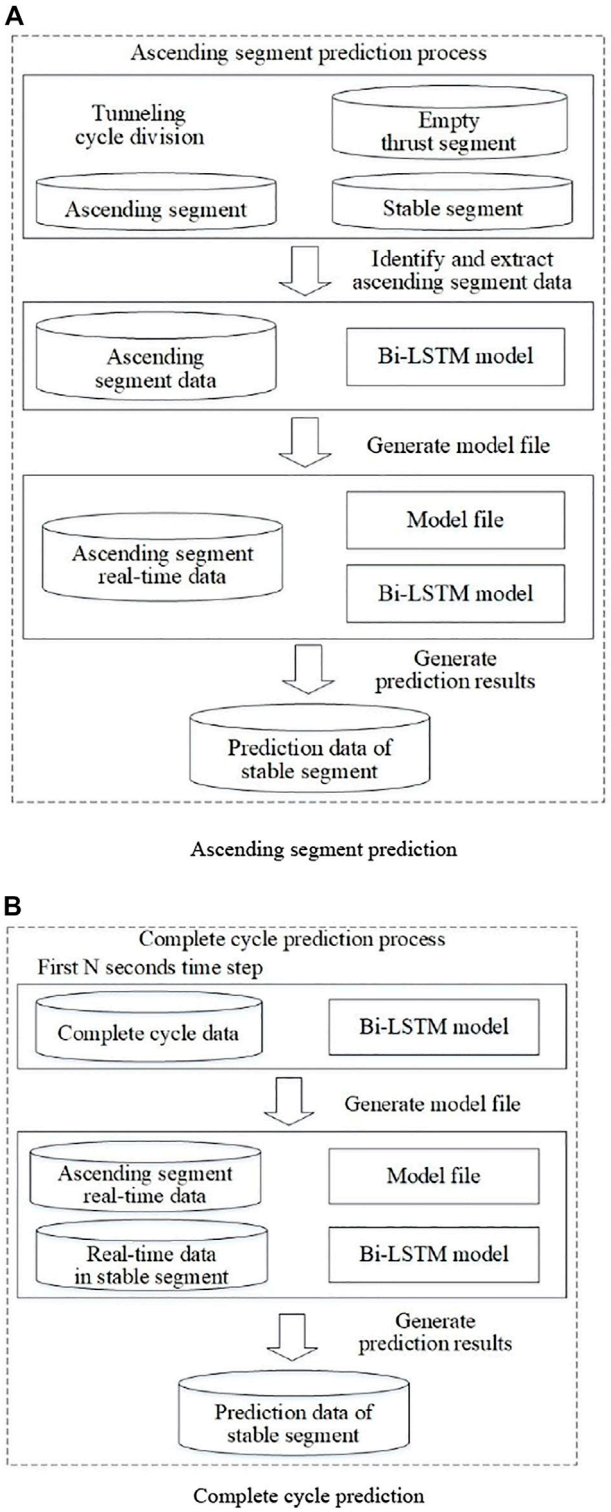


FIGURE 8 | Comparison of the prediction processing flow between the ascending segment and the complete cycle. **(A)** Ascending segment prediction (Hou et al., 2020); **(B)** complete cycle prediction.

corresponds to a set of stop data. As shown in **Figure 7**, the TBM tunneling process can generally be divided into an ascending segment and a stable segment.

In the existing TBM tunneling parameter prediction research, several scholars such as Hou et al. (Hou et al., 2020) and Zhou et al. (Zhou et al., 2020) usually analyze and predict the parameters of the stable segment based on the data of the ascending segment, which helps the driver to judge the tunneling state and optimize the adjustment of parameters to a certain extent. However, the method of predicting TBM tunneling parameters by using the ascending segment data requires a lot of time to identify and extract data. The accuracy of the ascending segment identification directly affects the model prediction performance. Therefore, how to avoid the extraction of invalid features of the ascending segment is still an urgent problem to be solved. Secondly, the duration of the ascending segment is short, and the amount of data contained is limited, which cannot completely and accurately display the law of rock-machine interaction. In addition, the stable segment occupies most time of the total tunneling section. For the geological conditions that may be different from the ascending segment, when only the rock-machine interaction law of the ascending section is used to reflect the working state of the TBM stable segment, there will be large error. Therefore, this paper uses the data of the complete tunneling period to train the prediction model, which can effectively reduce the complexity and difficulty of the huge data processing generated during the TBM tunneling process, greatly improve the data preprocessing efficiency, and more accurately display the rock-machine interaction. It can provide a higher-quality intelligent decision-making method for TBM tunneling construction (**Figure 8**).

PREDICTION MODEL BASED ON PSO-BI-LSTM

Feature Selection

The construction conditions of TBM tunneling are often complex, and the data generated during the working process of the equipment contains 199- dimensional parameters. However, when predicting TBM tunneling parameters, the selection of characteristic variables is not the better. On the one hand, too many parameters will cause the model dimension to be too high and the calculation will be slow; on the other hand, some parameters are not highly correlated with the prediction parameters, and too many selections will reduce the model prediction accuracy. Therefore, it is necessary to perform feature selection on the 199-dimensional tunneling parameters in the TBM operating data, with the aim of assisting the optimization and adjustment of the TBM tunneling parameters.

There are many factors affecting the prediction of TBM tunneling parameters, but most of the parameters that characterize the law of rock-machine interaction are greatly influenced by human factors and have poor correlation with rock-machine interaction, so they cannot be directly used for model prediction and analysis. Therefore, this paper only selects the propulsion speed, total thrust, cutter head torque and cutter

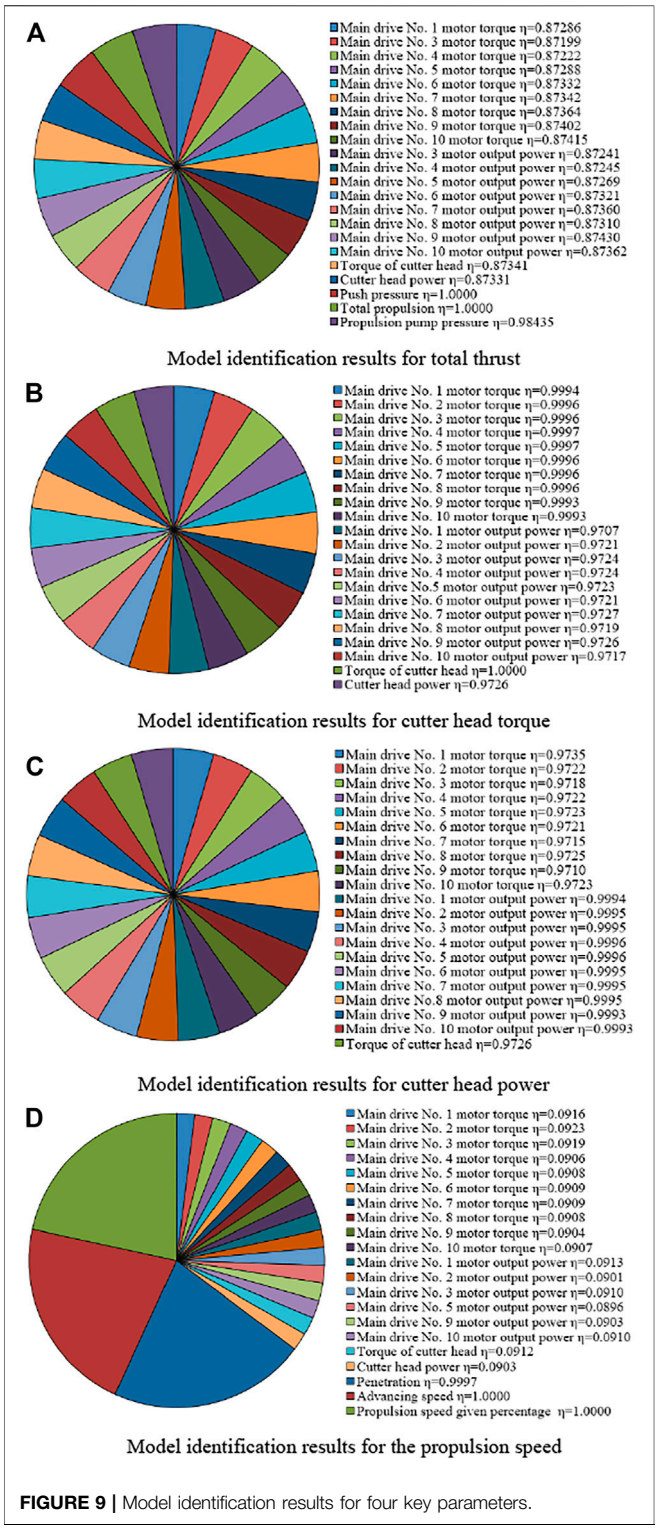


FIGURE 9 | Model identification results for four key parameters.

head power of the TBM tunneling stable segment as the output characteristics of the model.

The selection of input features is of great significance to the parameter optimization of the model and the efficiency of intelligent decision-making. Based on the complexity of the model, the accuracy of prediction and the comprehensive consideration of previous studies, this paper uses Pearson correlation analysis to identify the 199-dimensional TBM tunneling parameters, eliminates irrelevant parameter variables, and selects key model parameters as model inputs. The formula for calculating the Pearson correlation coefficient is as follows:

1) Calculate the average of the data:

$$E(X) = \sum_i p_i x_i \tag{8}$$

2) Calculate the variance of the data:

$$Var(X) = \frac{1}{n}\sum_1^n (x_i - \mu)^2 \tag{9}$$

3) Compute data covariance:

$$cov(X, Y) = E(X \cdot Y) - \mu\nu \tag{10}$$

4) Calculate data correlation:

$$\eta = \frac{cov(X, Y)}{\sqrt{Var(X)Var(Y)}} \tag{11}$$

where, μ is the mean of the data sample X; ν is the mean of the data sample Y; x_i is the input parameter; p_i is the frequency of occurrence of the input parameter; the larger the absolute value of η, the stronger the correlation; the closer η is to 0, the weaker the correlation.

Based on the Pearson correlation analysis results, the PSO-Bi-LSTM model constructed in this paper selects the 21 key parameters with the highest correlation with the predicted parameters in the complete tunneling cycle data as the input features of the model, to realize the prediction and analysis of the four key parameter indicators in the TBM stable segment. The 21-dimensional input feature identification results corresponding to the four prediction parameters of the model divided according to the size of the correlation coefficient of each parameter are shown in **Figure 9**.

To solve the problems of low prediction efficiency and slow convergence speed caused by the dimensional difference between the tunneling parameters, this paper normalizes the input data of the model, and the formula is as follows:

$$x' = \frac{x - x_{\min}}{x_{\max} - x_{\min}} \tag{12}$$

where, $x^{'}$ is the normalized input parameter; x is the actual input value; $x_{\min}$ is the minimum value of the input parameter; $x_{\max}$ is the maximum value of the input parameter.

Model Establishment

Figure 10 shows the TBM tunneling parameter prediction model based on the PSO-Bi-LSTM. Before using the PSO to optimize, the Bi-LSTM model structure needs to be determined first.

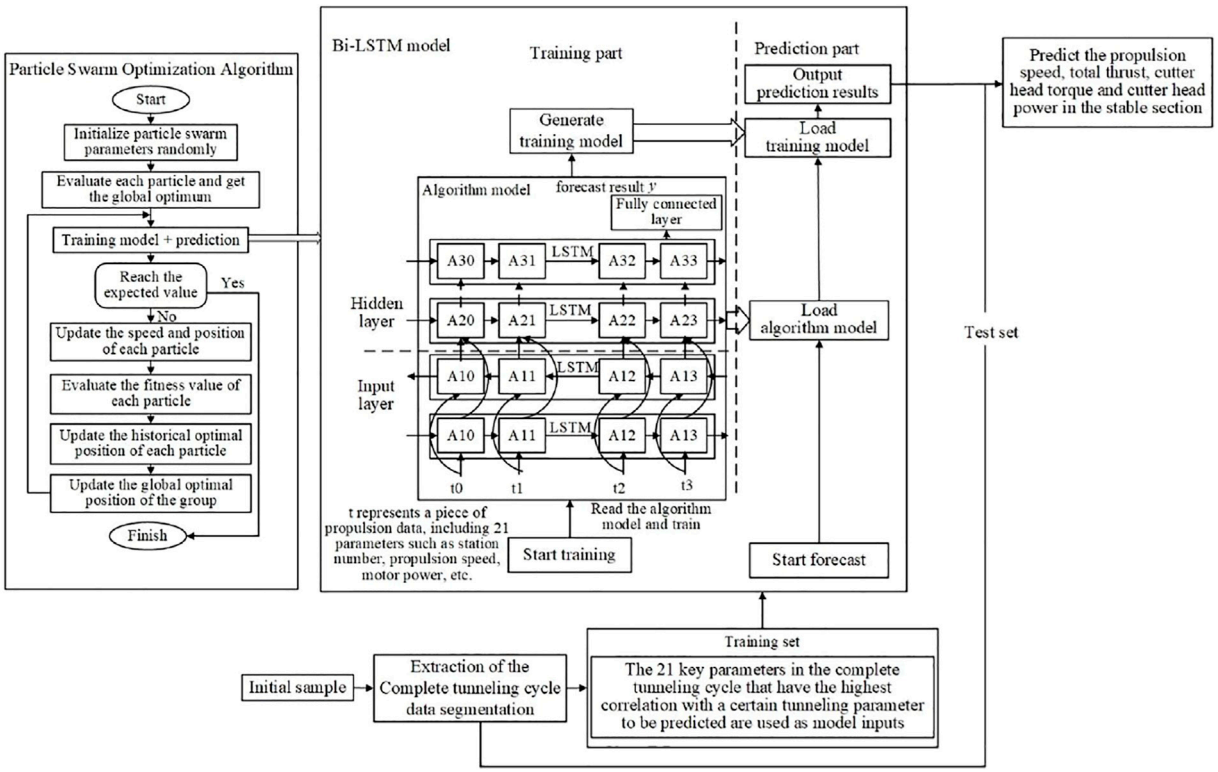


FIGURE 10 | Prediction model of TBM tunneling parameters based on PSO-Bi-LSTM.

Compared with the unidirectional LSTM, a back-propagation layer is added. Each layer of this structure contains two parallel layers, which control the forward and backward outputs respectively, and can utilize the contextual information in the meanwhile.

After data preprocessing, the original data is divided into training set and test set in a ratio of 17:1. The 21 key parameters with the highest correlation with a certain tunneling parameter to be predicted in the complete tunneling cycle extracted from the training set are input into the Bi-LSTM. The Bi-LSTM is optimized by PSO, and the global optimal solution obtained by iterative optimization is input into the Bi-LSTM.

Model Training and Evaluation

To verify the generalization ability of the model, this paper adopts the goodness of fit R^2 and the mean absolute percentage error (MAPE) as the performance indicators for evaluating the intelligent prediction model.

$$MAPE = \frac{1}{n}\sum_{i=1}^{n}\frac{\left|y_i^* - y_i\right|}{y_i} \tag{13}$$

$$R^2 = 1 - \sqrt{\frac{\sum_{i-1}^{n}\left(y_i - y_i^*\right)^2}{\sum_{i=1}^{n} y_i^2}} \tag{14}$$

where, y_i^* is the predicted value of the model; y_i is the true value; i is the sample number; n is the total number of samples in the test set.

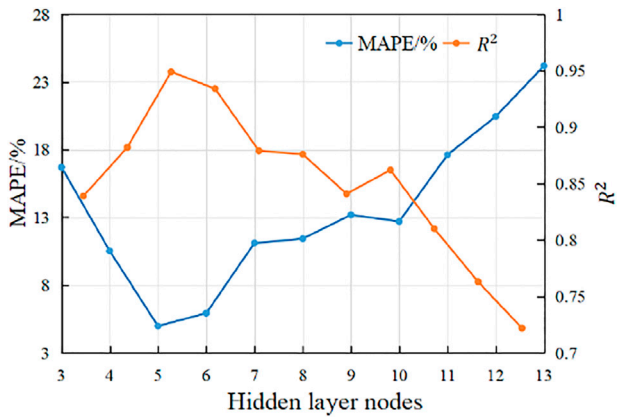


FIGURE 11 | Prediction results of the propulsion speed under different number of hidden layer nodes.

The preprocessed data set is divided into training set and test set proportionally, in which the data of the training set is continuously used to iteratively optimize the model and update the model parameters; the test set is used to test the performance of the model and verify the generalization ability of the model. To improve the accuracy of the training model, this paper uses the Adam optimizer to update and optimize the network, and the loss function is the MSE function. The

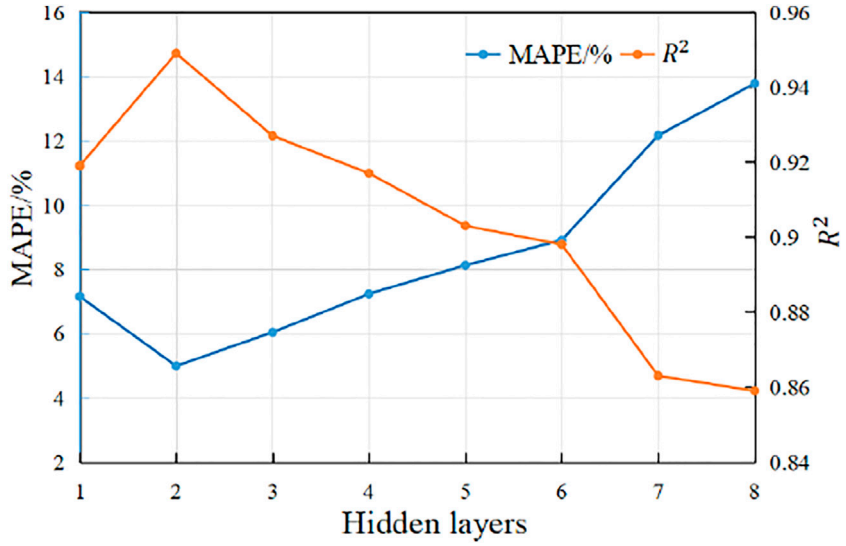


FIGURE 12 | Prediction results of the propulsion speed with different number of hidden layers.

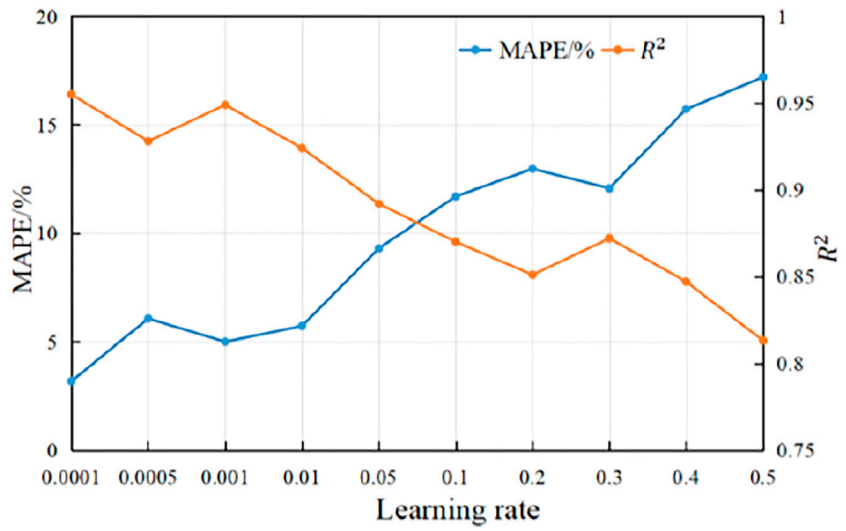


FIGURE 13 | Predicted results of the propulsion speed at different learning rates.

number of hidden layer nodes and layers will be discussed in *Model Parameter Analysis*. A fully connected layer is added after the hidden layer, and the learned distributed feature representation is mapped to the sample label space, so that the output feature dimension is represented as one dimension, which speeds up the model calculation efficiency. Considering the prevention of the model from overfitting, each layer of unit is regularized, and the dropout probability is set to 0.3. The maximum number of iterations is set to 50. When the number of iterations reaches the requirement or the average loss value no longer decreases with the iterations, the training is stopped.

Model Parameter Analysis

Before using PSO to optimize Bi-LSTM, the network structure of Bi-LSTM needs to be determined. Parameters such as the number of hidden layer nodes, the number of hidden layers, and the training learning rate α of the Bi-LSTM network need to be adjusted many times, so it is difficult to effectively judge the optimal state of the model. To improve the prediction accuracy, this paper takes the propulsion speed as an example to discuss the hyperparameters and determines the optimal parameters of the model through two indicators, namely the MAPE and the goodness of fit R^2.

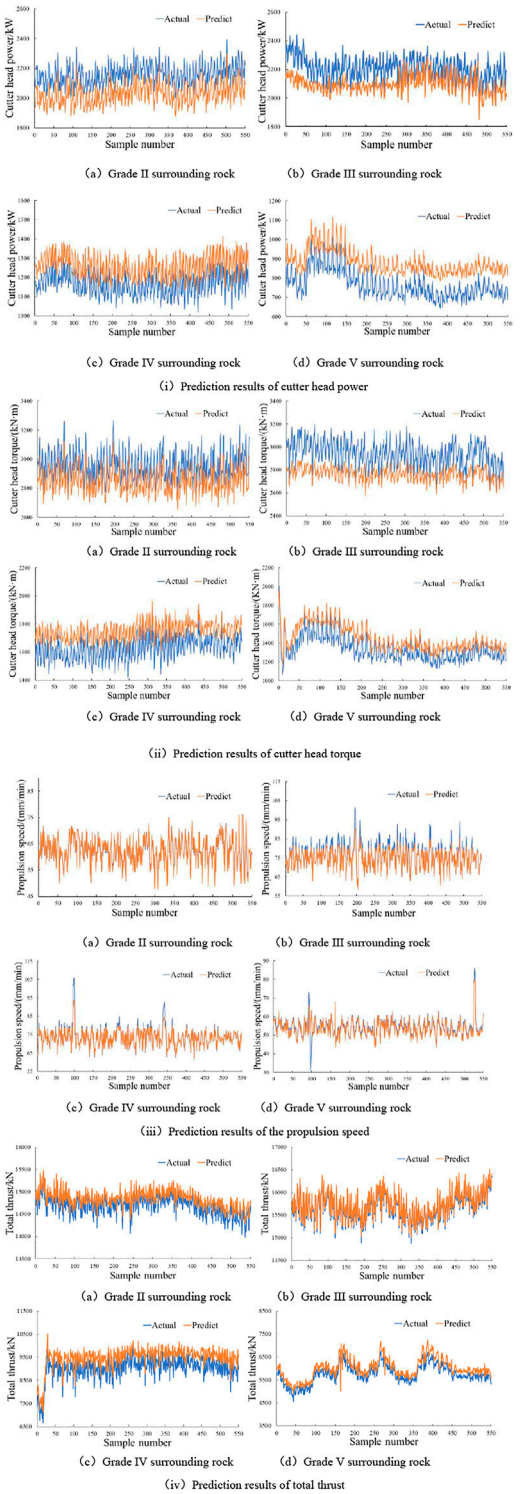


FIGURE 14 | Prediction results of the PSO-Bi-LSTM model under different surrounding rock grades.

1) Discussion on number of hidden layer nodes in Bi-LSTM network

In the Bi-LSTM neural network, the selection of the number of hidden layer nodes is extremely important, which not only has a great impact on the performance of the neural network model, but also is the direct cause of overfitting. However, the theory of determining the optimal number of hidden layer nodes in neural networks is not yet mature. Research shows that the number of hidden layer nodes is not only related to the number of input/output layer nodes, but also depends on the complexity of the problem to be solved and the characteristics of the sample. If the number of nodes is too large, it is prone to over-fitting, which reduces the generalization ability of the model; if the number of nodes is too small, the model cannot fully learn the characteristics of time series data and reduces the performance of the model. To solve the above problems, scholars have proposed a variety of discrimination methods to determine the number of hidden layer units based on many experimental studies (Liu et al., 2012; Han et al., 2020; Zheng et al., 2020). In this study, the empirical formula is used to determine the value range of the number of hidden layer units:

$$N_{hid} = (N_{in} + N_{out})^{\frac{1}{2}} + a \tag{15}$$

where, N_{in} is the number of nodes in the input layer; N_{hid} is the number of hidden layer nodes; N_{out} is the number of output layer nodes; a is a constant, $1 \le a \le 10$.

To prevent the model from overfitting and reduce the complexity of the model, the maximum number of iterations of the model in this section is 50, and the number of particle swarm populations is 30; other parameters such as the number of hidden layers is set to two according to experience, the learning rate is set to 0.001, and the value range of the number of the hidden layer is 3–13. **Figure 11** shows the prediction of the propulsion speed with different numbers of hidden layer units based on lots of training samples. As the number of hidden layer units increases, the mean absolute percent error first decreases and then increases, and the goodness of fit first increases and then decreases. Too many or too few hidden layer nodes will reduce the prediction performance of the model. To sum up, when the number of nodes is 5, the prediction effect is optimal, so the number of hidden layer nodes in this model is set to 5.

2) Discussion on hidden layers of Bi-LSTM network

For the sake of exploring the optimal network structure, the number of layers of the model is further analyzed and studied. Theoretically, the prediction performance of the model is proportional to the number of hidden layers, but the time cost of model training increases gradually with the increase of the number of layers, the convergence effect and efficiency drop sharply, and the model often falls into the dilemma of local optimal solution, which leads to training long-term dependency problems such as information loss and gradient disappearance in the process.

Taking the propulsion speed as an example, the number of hidden layer nodes is set to 5, the maximum number of iterations is 50, the number of particle swarm populations is 30, the range of layers is set to 1~8 based on experience, and the learning rate is 0.001.

TABLE 1 | Statistics of evaluation indicators of four tunneling parameters under different surrounding rock grades.

Surrounding rock classification	Evaluation indicators	Cutter head power P	Cutter head torque T	Propulsion speed *v*	Total thrust F
Grade II	R^2	0.938	0.962	0.994	0.989
	MAPE/%	6.195	3.723	0.473	1.009
Grade III	R^2	0.944	0.937	0.974	0.996
	MAPE/%	5.087	5.965	1.151	0.352
Grade IV	R^2	0.918	0.925	0.981	0.948
	MAPE/%	8.167	7.539	0.509	5.161
Grade V	R^2	0.849	0.909	0.951	0.953
	MAPE/%	15.357	8.651	2.352	4.381

As shown in **Figure 12**, when the number of hidden layers of Bi-LSTM is 2, the model accuracy is higher than that of single layer. However, the increase of the number of layers did not improve the prediction performance of the model. On the contrary, it fell into the problem of unable to find the global optimal solution, which greatly increased the risk of overfitting. Therefore, the number of hidden layers in this paper is selected as 2.

3) Discussion on learning rate α for Bi-LSTM network training

After the Bi-LSTM neural network structure is determined, the training learning rate of the model needs to be discussed. As an important hyperparameter in deep learning, the learning rate determines whether the objective function can converge to the local minimum and the convergence efficiency. If the learning rate is set too small, the convergence process is very slow, and even the algorithm does not converge; if the learning rate is set too large, the algorithm is prone to oscillation or divergence, resulting in gradient explosion (Shen et al., 2020). Therefore, the maximum number of iterations of the established model is 50, the number of particle swarm populations is 30, the number of hidden layer nodes is set to 5, the number of layers is set to 2, and the learning rate is set to 0.0001, 0.0005, 0.001, 0.01, 0.05, 0.1, 0.2, 0.3, 0.4, 0.5 according to experience, respectively.

Taking the propulsion speed as an example, **Figure 13** shows the prediction results of the model under different learning rates. When the learning rate is 0.001, the prediction result of the model is the most stable, the MAPE is relatively low compared to other cases, and the goodness of fit is relatively high, so this paper selects the model learning rate of 0.001.

In summary, the final structural parameters of the model are determined through experimental research: the number of hidden layers is 2, the number of nodes is 5, and the learning rate is 0.001.

MODEL APPLICATION AND COMPARISON

Application of PSO-Bi-LSTM Model Under Different Surrounding Rock Grades

In the actual tunneling process, the interaction between the TBM and the surrounding rock produces a complex rock-machine relationship. How to realize the real-time perception of the current rock mass information and ensure that the current TBM tunneling state matches the complex and changeable rock mass conditions is still a hot issue in TBM construction. This section studies the prediction performance of PSO-Bi-LSTM model under different surrounding rock grades based on the construction database of TBM3 bid section of Songhua River water conveyance project in Jilin Province. The 21-dimensional parameters with the highest correlation with the predicted parameters in the complete tunneling cycle are selected as the input features of the model to realize the prediction and analysis of the four key parameters (total thrust, the propulsion speed, cutter head torque and cutter head power) in the stable segment of the TBM tunneling; and the goodness of fit R^2 and the MAPE are used as evaluation indicators to judge the validity of the model prediction.

The data samples in this paper are collected from a certain construction section of the TBM3 bid section. Based on the data preprocessing, a total of 9,900 valid tunneling cycles are extracted, and 9,350 tunneling cycles are randomly selected as the model training set, and the remaining data are used as the model test set. It is used to verify the applicability of the trained model to different surrounding rock levels. Among them, the surrounding rock grades are mainly distributed in grades II to V, among which grade III surrounding rock accounts for the largest proportion in this tunneling section, and there are relatively few grades II and V surrounding rock.

Figure 14 shows the prediction results of the PSO-Bi-LSTM model under different surrounding rock levels. It can be seen from the analysis of the figure that the predicted result and the measured value of each tunneling parameter have a high degree of fitting, and there is a large deviation only in individual samples. In addition, the prediction agreement between the propulsion speed and total thrust is the highest under the conditions of different surrounding rock grades; the prediction agreement between cutter head power and cutter head torque is relatively low.

Table 1 shows the statistical analysis results of the evaluation indicators of the four key tunneling parameters under different surrounding rock grades. From the analysis of the goodness of fit and error of the prediction results, the PSO-Bi-LSTM model has high prediction accuracy. The higher the goodness of fit R^2 of the TBM tunneling parameters, the lower the MAPE, and the better the prediction effect of the model. Comparing the goodness of fit, the average values of the goodness of fit of the cutter head power,

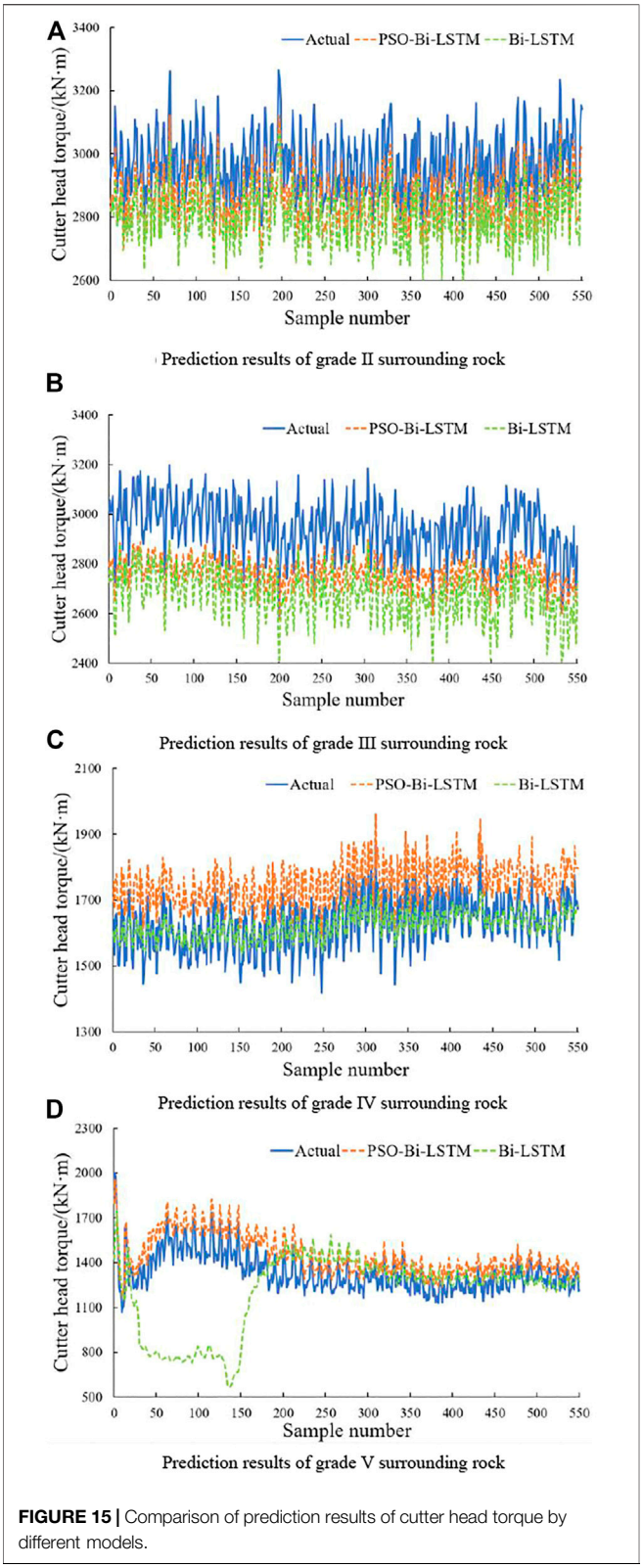


FIGURE 15 | Comparison of prediction results of cutter head torque by different models.

cutter head torque, the propulsion speed and total thrust are 0.912, 0.933, 0.975 and 0.972, respectively, and the goodness of fit of all reached above 0.91. This shows that the PSO-Bi-LSTM model has excellent prediction effect for each parameter. The prediction accuracy of total thrust in surrounding rocks at all levels is relatively high, and the fluctuation of the goodness of fit of its samples is much lower than that of other parameters, and the goodness of fit of other parameters fluctuates greatly under different surrounding rock grades.

TABLE 2 | Comparison of evaluation indicators for prediction results of different models.

Model	Surrounding rock classification	R^2	MAPE/%
PSO-Bi-LSTM	Grade II	0.962	3.723
	Grade III	0.937	5.965
	Grade IV	0.925	7.539
	Grade V	0.909	8.651
Bi-LSTM	Grade II	0.932	5.332
	Grade III	0.909	9.078
	Grade IV	0.852	15.138
	Grade V	0.828	19.172

In consideration of the influence of different surrounding rock grades on the prediction effect of the model, it can be found that the average values of R^2 of the tunneling parameters of grade II surrounding rock, grade III surrounding rock, and grade IV surrounding rock are 0.971, 0.962, 0.943, and 0.916, respectively. This shows that the PSO-Bi-LSTM model has a good fitting effect and can sensitively reflect the interaction information between the surrounding rock at all levels and the TBM. By comparing the goodness of fit under different surrounding rock grades, it is found that the higher the surrounding rock grade, the better the stability. Similarly, among the four types of surrounding rock grades, the MAPE of each tunneling parameter of grade V surrounding rock is also relatively high, reaching 7.685%. The average MAPE of the other three types of surrounding rocks is not much different, and they are 2.850, 3.139 and 5.344% respectively according to the grades from high to low. This shows that the stability of low-grade surrounding rock is relatively poor, and the rock-mechanism relationship is greatly affected by human factors, so the prediction accuracy is lower than that of high-grade surrounding rock. In addition, the fitting fluctuations of the parameters of the low-grade surrounding rock are relatively large, and it is difficult for the model to learn its variation law. Meanwhile, compared with high-grade surrounding rock, the problem of the number of samples of low-grade surrounding rock may cause larger accidental errors, which is also one of the reasons for the decline of model accuracy.

Comparison With the Prediction Effect of the Bi-LSTM Model

The same set of data was selected to quantitatively analyze the prediction performance of the Bi-LSTM model under different surrounding rock levels. Since total thrust is less affected by external factors, and the propulsion speed and cutter head torque are greatly affected by external rock mass information factors and have high sensitivity to the rock-machine relationship, this

section takes cutter head torque as the research object and predict and analyze different surrounding rock grades in turn, and the prediction result is shown in **Figure 15**.

Figure 15 shows that the fluctuation of the prediction result curve of the Bi-LSTM model for cutter head torque under all levels of surrounding rock is significantly larger than that of the PSO-Bi-LSTM model. Combining with **Table 2**, among the grade II, III, IV and V surrounding rocks, the MAPE of the Bi-LSTM model is 1.938, 3.765, 1.890, and 3.408%, respectively, which is much larger than that of the PSO-Bi-LSTM model. On the one hand, it shows that the prediction accuracy of the traditional Bi-LSTM model is relatively poor; on the other hand, the Bi-LSTM model optimized by PSO can almost accurately predict the change law of tunneling parameters under different surrounding rock levels. This shows that the PSO-Bi-LSTM model has higher prediction accuracy and faster convergence speed for time sample series and can more effectively predict TBM tunneling parameters.

Given all of that, compared with the Bi-LSTM, the prediction model based on PSO-Bi-LSTM has better prediction performance and generalization ability. It can assist the safe and efficient tunneling of TBM under different stratum conditions and provide certain guidance for the optimization and adjustment of parameters.

CONCLUSION

To make the model better match the characteristics of TBM construction data under different surrounding rock levels, this paper uses PSO to optimize the Bi-LSTM model and establishes the PSO-Bi-LSTM model. This paper takes the construction data set of the TBM3 bid section of Songhua River water conveyance project as the research object and uses plenty of data processing methods such as constructing a binary state function and 3σ criterion to correct the original data. Different from the traditional ascending segment data to predict the parameter values of the stable segment, this paper selects the 21-dimensional tunneling parameters with the highest correlation with the predicted parameters in the complete tunneling cycle as the model input features to realize the accurate prediction of the four key tunneling parameters in the TBM stable segment. The discussion of model hyperparameters is completed by experimental analysis. The prediction results of the model under different surrounding rock levels are evaluated, and the influence of different formation conditions on the prediction accuracy of the model is studied, and the Bi-LSTM model are compared. The conclusions and results obtained are as follows:

1) An intelligent prediction model of TBM tunneling parameters based on PSO-Bi-LSTM is proposed. The prediction analysis was carried out for the formation sections under different surrounding rock grades, and the time series prediction method of the tunneling parameters was given by the PSO-Bi-LSTM model. The average R^2 of each parameter is above 0.910, and the highest is 0.996. The prediction results can provide certain guidance for the safe and efficient tunneling construction of TBM.
2) Different from the existing methods that use the data of the ascending segment to predict the tunneling parameters of the stable segment, this paper selects the data of the complete tunneling cycle to predict the tunneling parameters of the stable segment. The amount of data contained is rich, which can improve the quality of intelligent decision-making during TBM construction.
3) The higher the surrounding rock grade, the smaller the prediction error and the higher the prediction accuracy of the PSO-Bi-LSTM model. The fluctuations of the prediction results on the propulsion speed and total thrust are smaller in surrounding rocks at all levels, and the prediction performance is relatively stable.
4) Compared with the Bi-LSTM, the intelligent prediction method proposed in this paper has stronger prediction performance for different surrounding rock grades and different prediction parameters. This method can effectively assist the optimization and adjustment of tunneling parameters during TBM construction and can provide a more effective intelligent decision-making method for TBM-assisted intelligent construction.

DATA AVAILABILITY STATEMENT

The original contributions presented in the study are included in the article/Supplementary Material, further inquiries can be directed to the corresponding author.

AUTHOR CONTRIBUTIONS

All authors listed have made a substantial, direct, and intellectual contribution to the work and approved it for publication.

FUNDING

Fundamental Research Funds for the Central Universities (Project No: FRF-TP-20-043A1), Open Research Fund Program of State Key Laboratory of Hydroscience and Engineering (Project No: sklhse-2021-C-04), and Science and Technology Project of Huaneng Group Headquarters (Project No: HNKJ19-H15) are gratefully acknowledged. The data are from the National Program on Key Basic Research Project (973 Program) (Grant No. 2015CB058100).

REFERENCES

Afradi, A., Ebrahimabadi, A., and Hallajian, T. (2021). Prediction of TBM Penetration Rate Using Fuzzy Logic, Particle Swarm Optimization and Harmony Search Algorithm. *Geotechnical Geol. Eng.*, 1–24. doi:10.1007/s10706-021-01982-x

Barton, N. R. (2000). *TBM Tunnelling in Jointed and Faulted Rock*. Balkema,Rotterdam: CRC Press, 3–38.

Entacher, M., Lorenz, S., and Galler, R. (2014). Tunnel boring Machine Performance Prediction with Scaled Rock Cutting Tests. *Int. J. Rock Mech. Mining Sci.* 70, 450–459. doi:10.1016/j.ijrmms.2014.04.021

Evans, I. (1965). The Force Required to Cut Coal with blunt Wedges. *Int. J. Rock Mech. Mining Sci. Geomechanics Abstr.* 2 (01), 1–12. doi:10.1016/0148-9062(65)90018-5

Feng, G. L., Chen, B. R., Xiao, Y. X., Jiang, Q., Li, P. X., Zheng, H., et al. (2022). Microseismic Characteristics of Rockburst Development in Deep TBM Tunnels with Alternating Soft–Hard Strata and Application to Rockburst Warning: A Case Study of the Neelum–Jhelum Hydropower Project. *Tunnelling Underground Space Techn.* 122, 104398. doi:10.1016/j.tust.2022.104398

Feng, G. L., Feng, X. T., Chen, B. R., Xiao, Y. X., and Yu, Y. (2015). A Microseismic Method for Dynamic Warning of Rockburst Development Processes in Tunnels. *Rock Mech. Rock Eng.* 48 (05), 2061–2076. doi:10.1007/s00603-014-0689-3

Gao, X., Shi, M., Song, X., Zhang, C., and Zhang, H. (2019). Recurrent Neural Networks for Real-Time Prediction of TBM Operating Parameters. *Automation in Construction* 15, 130–140. doi:10.1016/j.autcon.2018.11.013

Gertsch, R., Gertsch, L., and Rostami, J. (2007). Disc Cutting Tests in Colorado Red Granite: Implications for TBM Performance Prediction. *Int. J. Rock Mech. Mining Sci.* 44 (02), 238–246. doi:10.1016/j.ijrmms.2006.07.007

Graves, A., Liwicki, M., Fernández, S., Bertolami, R., Bunke, H., and Schmidhuber, J. (2009). A Novel Connectionist System for Unconstrained Handwriting Recognition. *IEEE Trans. Pattern Anal. Mach Intell.* 31 (05), 855–868. doi:10.1109/TPAMI.2008.137

Han, Y., Ding, N., Geng, Z., Wang, Z., and Chu, C. (2020). An Optimized Long Short-Term Memory Network Based Fault Diagnosis Model for Chemical Processes. *J. Process Control.* 92, 161–168. doi:10.1016/j.jprocont.2020.06.005

Hou, G. Y., Xu, Z. D., Liu, X., and Jin, C. (2019). Improved Particle Swarm Optimization for Selection of Shield Tunneling Parameter Values. *CMES-Computer Model. Eng. Sci.* 118 (02), 317–337. doi:10.31614/cmes.2019.04693

Hou, S. K., and Liu, Y. R. (2021). Numerical Simulations of Double-Shield TBM Tunneling for Analyzing Shield Jamming Control Factors. *J. Tsinghua Univ. (Science Technology)* 61 (08), 809–817. doi:10.16511/j.cnki.qhdxxb.2021.26.013

Hou, S. K., Liu, Y. R., and Zhang, K. (2020). TBM Tunneling Parameter Prediction Based on IPSO-BP Hybrid Model. *Chin. J. Rock Mech. Eng.* 39 (08), 1648–1657. doi:10.13722/j.cnki.jrme.2019.1084

Jin, L., Li, S., and Hu, B. (2018). RNN Models for Dynamic Matrix Inversion: A Control-Theoretical Perspective[J]. *IEEE Trans. Ind. Inform.* 14 (01), 189–199. doi:10.1109/tii.2017.2717079

Jing, X., Xia, Y. M., Ji, Z. Y., and Zhou, X. W. (2019). Soft Rock Cutting Mechanics Model of TBM Cutter and Experimental Research. *ICIRA Intell. Robotics Appl.* 5928, 383–391. doi:10.1007/978-3-642-10817-4_38

Krause, H. (1976). *Geologische Erfahrungen beim Einsatz von Tunnelvortriebs maschinen in Baden-Württemberg*. Vienna: Springer. doi:10.1007/978-3-7091-8452-3_3

Liu, Y., Zhong, P. A., Zhang, M. R., Kong, Y., and Xu, B. (2012). Application Effect Evaluation of Empirical Formula of Hidden Layer Node Number in Reservoir Operation Rule Extraction. *Water Resour. Power* 30 (11), 42–44.

Liu, Z. B., Li, L., Fang, X. L., Qi, W. B., Shen, J. M., Zhou, H. Y., et al. (2021). Hard-rock Tunnel Lithology Prediction with TBM Construction Big Data Using a Global-Attention-Mechanism-Based LSTM Network. *Automation in Construction* 15, 130–140. doi:10.1016/j.autcon.2021.103647

Mahdevari, S., Shahriar, K., Yagiz, S., and Akbarpour Shirazi, M. (2014). A Support Vector Regression Model for Predicting Tunnel boring Machine Penetration Rates. *Int. J. Rock Mech. Mining Sci.* 72, 214–229. doi:10.1016/j.ijrmms.2014.09.012

Rostami, J. (1997). "Development of a Force Estimation Model for Rock Fragmentation with Disc Cutters through Theoretical Modeling and Physical Measurement of Crushed Zone Pressure," (Golden: Colorado School of Mines). Ph.D. Thesis.

Shen, H. J., Luo, Y., Zhao, Z. C., and Wang, H. J. (2020). Prediction of Summer Precipitation in China Based on LSTM Network. *Clim. Change Res.* 16 (03), 263–275. doi:10.11896/j.issn.1002-137X.2018.04.009

Si, N. W., Wang, H. J., Li, W., Shan, Y. D., and Xie, P. C. (2018). Chinese Part of Speech Tagging Model Based on Attention Long Short- Term Memory Network. *Comp. Sci.* 45 (004), 66–70. doi:10.11896/j.issn.1002-137X.2018.04.009

Sun, W., Shi, M., Zhang, C., Zhao, J., and Song, X. (2018). Dynamic Load Prediction of Tunnel boring Machine (TBM) Based on Heterogeneous *In-Situ* Data. *Automation in Construction* 92 (05), 23–34. doi:10.1016/j.autcon.2018.03.030

Tan, Y. M., Wang, M. W., and Li, M. X. (2018). Automatic post Editing of Neural Network Translation Based on Translation Quality Estimation. *Acta Scientiarum Naturalium Universitatis Pekinensis* 54 (02), 255–261. doi:10.13209/j.0479-8023.2017.153

Tao, H., Wang, J., and Zhang, L. (2015). "Prediction of Hard Rock TBM Penetration Rate Using Random Forests," in 27th Chinese Control and Decision Conference (CCDC), Qingdao, China, 23-25 May 2015 (IEEE).

Vlachas, P. R., Byeon, W., Wan, Z. Y., Sapsis, T. P., and Koumoutsakos, P. (2018). Data-driven Forecasting of High-Dimensional Chaotic Systems with Long Short-Term Memory Networks. *Proc. R. Soc. A.* 474 (2213), 20170844. doi:10.1098/rspa.2017.0844

Wang, R. H., Li, D. Q., Chen, E. J., and Liu, Y. (2021). Dynamic Prediction of Mechanized Shield Tunneling Performance. *Automation in Construction* 132, 1–14. doi:10.1016/j.autcon.2021.103958

Wen, S., Zhao, Y. X., and Yang, S. Q. (2009). TBM Tunneling Speed Prediction Based on Monte Carlo BP Neural Network. *Rock Soil Mech.* 30 (10), 3127–3132. doi:10.3969/j.issn.1000-7598.2009.10.040

Xiong, F., Hu, Z. P., Ren, X., and Zhang, P. (2017). Application of BP Neural Network Based on MATLAB in Predicting TBM Tunneling Speed. *Mod. Tunnel Techn.* 54 (05), 101–107. doi:10.13807/j.cnki.mtt.2017.05.014

Yagiz, S. (2006). A Model for the Prediction of Tunnel boring Machine Performance. *Proc. 10th IAEG Congress*, 1–10.

Yang, Y., Feng, G. L., Xu, C. J., Chen, B. R., Geng, D. X., and Zhu, B. T. (2022). Quantitative Threshold of Energy Fractal Dimension for Immediate Rock-Burst Warning in Deep Tunnel: a Case Study. *Lithosphere*, 1699273.

Zhang, N., Li, J. B., Jing, L. J., Li, P. Y., and Xu, S. T. (2018). Study and Application of Intelligent Control System of TBM Tunneling Parameters. *Tunnel Construction* 38 (10), 1734–1740. doi:10.3973/j.issn.2096-4498.2018.10.019

Zhang, P., Wu, H. N., Chen, R. P., Dai, T., Meng, F. Y., and Wang, H. B. (2020). A Critical Evaluation of Machine Learning and Deep Learning in Shield-Ground Interaction Prediction. *Automation in Construction* 106, 1–14. doi:10.1016/j.tust.2020.103593

Zhang, Q., Huang, T., Huang, G. Y., Cai, Z. X., and Kang, Y. L. (2013). Theoretical Model for Loads Prediction on Shield Tunneling Machine with Consideration of Soil-Rock Interbedded Ground. *Sci. China Technol. Sci.* 56 (09), 2259–2267. doi:10.1007/s11431-013-5302-6

Zhang, Q. L., An, Z. Z., Liu, T. Y., Zhang, Z. S., and Huangfu, Z. H. (2020). Intelligent Control Theory of Earth-Rock Dam Compaction. *J. Hydroelectric Eng.* 39 (07), 34–40. doi:10.11660/slfdxb.20200704

Zhang, Q. L., Ma, R., Hu, Y., An, Z. Z., Yin, T., and Li, Q. B. (2021). Intelligent Control Theory of thermal Stress in Mass concrete Structures. *J. Hydroelectric Eng.* 40 (05), 11–21. doi:10.11660/slfdxb.20210502

Zhang, Y., Zhang, P. Y., and Yan, Y. H. (2018). Far Field Speech Recognition Based on Attention LSTM and Multitasking Learning. *J. Tsinghua Univ. (Science Technology)* 58 (03), 249–253. doi:10.16511/j.cnki.qhdxxb.2018.25.016

Zhang, Y., Zhang, Y. B., and Chen, L. (2021). Optical Surface Impurity Detection Based on Deep Learning. *Acta Physica Sinica* 70 (16), 353–361. doi:10.7498/aps.70.20210403

Zhang, Z. M., Li, X. Y., and Ji, J. (2021). TBM Tunneling Parameter Prediction Model Based on LS-SVM. *J. Hohai Univ. (Natural Sciences)* 49 (04), 373–379. doi:10.3876/j.issn.1000-1980.2021.04.012

Zhao, S. F., and Dong, X. Y. (2018). Speech Recognition Based on Improved LSTM Deep Neural Network. *J. Zhengzhou Univ. (Engineering Science)* 39 (05), 63–67. doi:10.13705/j.issn.1671-6833.2018.02.004

Zheng, C., Deng, J. J., Hong, Z. X., and Wang, G. H. (2020). Prediction Model of Suspension Density in the Dense Medium Separation System Based on. *LSTM. Process.* 8 (08), 976. doi:10.3390/pr8080976

Zhou, S. Y., Kang, Y. L., Su, C. X., and Zhang, Q. (2016). Study on Prediction Model of TBM Driving Total Thrust Based on Mechanical Analysis. *J. Mech. Eng.* 52 (020), 76–82. doi:10.3901/jme.2016.20.076

Zhou, X. X., Gong, Q. M., Yin, L. J., Xu, H. Y., and Ban, C. (2020). Prediction of Tunneling Parameters in TBM Stable Section Based on BLSTM-AM Model. *Chin. J. Rock Mech. Eng.* 39 (S2), 3505–3515. doi:10.13722/j.cnki.jrme.2019.1158

Zhou, X.-P., and Zhai, S.-F. (2018). Estimation of the Cutterhead Torque for Earth Pressure Balance TBM under Mixed-Face Conditions. *Tunnelling Underground Space Techn.* 74, 217–229. doi:10.1016/j.tust.2018.01.025

Conflict of Interest: CD, SD, and KS were employed by the HUANENG company.

The remaining authors declare that the research was conducted in the absence of any commercial or financial relationships that could be construed as a potential conflict of interest.

Publisher's Note: All claims expressed in this article are solely those of the authors and do not necessarily represent those of their affiliated organizations, or those of the publisher, the editors and the reviewers. Any product that may be evaluated in this article, or claim that may be made by its manufacturer, is not guaranteed or endorsed by the publisher.

Copyright © 2022 Zhang, Zhu, Ma, Du, Du, Shao and Li. This is an open-access article distributed under the terms of the Creative Commons Attribution License (CC BY). The use, distribution or reproduction in other forums is permitted, provided the original author(s) and the copyright owner(s) are credited and that the original publication in this journal is cited, in accordance with accepted academic practice. No use, distribution or reproduction is permitted which does not comply with these terms.

frontiers in Earth Science

ORIGINAL RESEARCH
published: 23 March 2022
doi: 10.3389/feart.2022.850505

Centrifugal Test and Instability Model Analysis of Excavation Surface Stability of a Shield Tunnel in a Clay Layer

Haoshuang Niu, Xiaolin Weng, Jibo Hu and Lele Hou*

Key Laboratory for Special Area Highway Engineering of Ministry of Education, Chang'an University, Xi'an, China

In order to study the variation law of support pressure and instability mode of excavation face under different soil parameters, a complete set of centrifugal model seepage test device is independently developed. The results of centrifugal tests with different *C/D* (where *C* is the overburden thickness of the tunnel and *D* is the tunnel diameter), internal friction angles, and heights of water head show that with the increase of the retreating displacement *S* of the excavation surface, the support pressure *P* of the excavation surface can be divided into three stages: rapid decline ($S < 1.5D\%$), slow rebound after reaching the limit support pressure P_{lim} ($1.5D\% \le S \le 3D\%$), and gradually reaching the stable value ($3D\% < S$). With the increase of *C/D*, the limit support pressure on the excavation face gradually increases and tends to be stable. For different soil properties, when $C/D > 1.5$, the limit support pressure on the excavation face tends to be stable. With the increase of internal friction angle, the limit support pressure decreases gradually, and its influence on support pressure can be ignored when $\varphi > 40^{\circ}$. With the increase of height of water head H_w, the limit support pressure increases linearly. By establishing a numerical analysis model and analyzing the instability modes of soil under different *C/D*, internal friction angles, and cohesion, the instability mode of soil in front of the excavation face can have a great correlation with *C/D* of the soil and internal friction angle, while the influence of cohesion is minimal. With the increase of *C/D*, the soil changes from overall failure to local failure, the change of *C/D* mainly affects the height of soil arching effect and the width of the wedge below, while the internal friction angle mainly affects the width of the wedge and the instability angle of soil.

Keywords: tunnel, stability, centrifugal test, numerical simulation, limit support pressure

OPEN ACCESS

Edited by:
Guang-Liang Feng,
Institute of Rock and Soil Mechanics (CAS), China

Reviewed by:
Songhe Wang,
Xi'an University of Technology, China
Wenyuan Ren,
Northwest A&F University, China
Lisi Niu,
Henan Polytechnic University, China
Zhiyong Shi,
Southeast University, China

****Correspondence:***
Xiaolin Weng
wengxl2000@126.com

Specialty section:
This article was submitted to Geohazards and Georisks, a section of the journal Frontiers in Earth Science

Received: *07 January 2022*
Accepted: *14 February 2022*
Published: *23 March 2022*

Citation:
Niu H, Weng X, Hu J and Hou L (2022) Centrifugal Test and Instability Model Analysis of Excavation Surface Stability of a Shield Tunnel in a Clay Layer. Front. Earth Sci. 10:850505. doi: 10.3389/feart.2022.850505

INTRODUCTION

How to reasonably develop and utilize underground space has become an important step in the process of modern urbanization. In recent years, with the gradual increase of urban population and the increasing shortage of land resources, traffic congestion has become a major problem perplexing urban development. With the rapid development of urban rail transit, tunnel shield construction with high safety, fast construction speed, and less condition constraints has been widely used. However, if the setting of support pressure acting on the tunnel surface is unreasonable, it may cause soil collapse or uplift (Feng et al., 2015; Han et al., 2020; Feng et al., 2022). Therefore, calculating the

support pressure required by a shield tunnel is very important to maintain the stability of tunnel working face. In order to obtain more accurate critical support pressure, the influencing factors and failure area must be determined at the same time.

Many scholars have conducted a series of theoretical and experimental studies on the stability of excavation face through different research methods (Zhang and Sun, 2018; Li et al., 2019; Liu et al., 2021; Yu et al., 2022). Horn (1961) first used the limit equilibrium method to construct the collapse form in front of the tunnel excavation surface, which is composed of a wedge and a simple warehouse on its upper part. This model provides a research basis for the subsequent limit equilibrium method to calculate the support pressure of the excavation surface. Broere (2001) applied it to multi-layer soil for analysis, and the calculation results are close to the actual project. Jancsecz and Steiner (1994) improved a new limit equilibrium model based on horn. The top of the model is composed of prisms. The soil arching effect in the soil is studied, and the relationship between the coefficient of soil lateral pressure and internal friction angle, tunnel buried depth ratio, and wedge angle is established. The calculation results are expressed by the three-dimensional earth pressure index. Anagnostou and Kovári (1996) established a wedge model to analyze the stability of tunnel excavation surface in a homogeneous soil layer. The results show that the limit support pressure of the excavation surface in dry sand layer is related to the buried depth of tunnel vault, tunnel diameter, internal friction angle of soil, cohesion of soil, and other factors, but there is no regular analysis on each influencing factor. Based on the upper bound theorem of limit analysis, Mollon et al. (2011) and others studied the stability of shield excavation face in heterogeneous sandy soil by constructing the failure mode of two-dimensional rotating multi block set. It is found that the results of limit support pressure and failure mode of the excavation surface obtained by this method are close to those obtained by finite difference numerical analysis. Liu et al. (2012) established the upper bound solution of stability limit and effective support pressure of shield excavation face in a saturated sandy soil layer under steady-state seepage. The research shows that under steady-state seepage, the shield buried depth and surface overload have little influence on the limit support pressure, and the seepage and shield diameter have a significant influence on the limit support pressure. Yang et al. (2010) and others analyzed the stability of the excavation surface of two-dimensional shallow tunnel by using the upper bound method, which assumed that the failure mode of the excavation surface was composed of a group of rigid blocks. The results show that the cohesion and friction angle of soil are positively correlated with the stability of the excavation surface. However, when the internal friction angle and cohesion of soil are small, the influence of tunnel buried depth on the stability of the excavation surface is obvious. In the numerical simulation and model test, Vermeer et al. (2002) used finite element analysis to simulate the stability of the excavation surface, and explored the effects of soil gravity, cohesion, and surface overload on the limit support pressure. Zhu et al. (2005) used FLAC 3D to model and analyze the relationship between support pressure and tunnel face soil deformation, and obtained their relationship curve. Oblozinsky and Kuwano (2006) studied the influence law of tunnel buried depth on the failure mode of the excavation surface and minimum support pressure in a sandy soil layer, and obtained the influence law between them. However, due to its single consideration factor, it has not been applied in engineering practice. Meguid et al. (2008) pointed out the advantages of centrifugal model test in the stability simulation of the excavation surface by summarizing the previous test results. Lv et al. (2019) studied the failure process of extreme instability of the excavation surface under different buried depths through model tests, and improved the traditional wedge model into a wide wedge model. Li et al. (2011) revealed the dissipation process of soil arch and the instability form of the excavation surface through a large-scale model test and combined with the stress state of the soil in front of the excavation surface.

Because the stress level of soil determines its own mechanical characteristics, while the stress level of the 1 g model test is small, and the test results still have a certain gap with the actual project (Taylor, 2005), it has become a reliable means to explore the support pressure of excavation face by using a geotechnical centrifuge. Through a series of centrifugal model tests and comparative analysis of numerical simulation, this paper studies the change and instability mode of excavation face support pressure under different buried depths, internal friction angles, cohesions, and head differences; reveals the response law of different cohesive soils in the process of instability; and provides a theoretical basis for the study of excavation face support pressure in shield tunnel construction.

CENTRIFUGAL MODEL TEST

Test Preparation

According to the three basic laws of similarity theorem and the results of the model test (Weng et al., 2019), the similarity ratio can be deduced through equation analysis to meet the similarity relationship. The soil is regarded as a homogeneous, continuous, and isotropic material, and only the self-weight stress is considered. The relationship is as follows.

From three governing equations, such as **Eqs. 1–6**:

$$\left(\sigma_{ij}, j\right)_m + \frac{C_\gamma C_L}{C_\sigma}\gamma_m = 0 \tag{1}$$

$$\left(\varepsilon_{ij.j}\right)_m = \frac{C_m}{C_L C_\varepsilon}\frac{1}{2}\left[\left(u_{i,j}\right)_m + \left(u_{j,i}\right)_m\right]\left(i, j = x_m, y_m, z_m\right) \tag{2}$$

$$\{d\sigma\}_m = \frac{C_D C\varepsilon}{C_\sigma}\left[D_{ep}\right]_m\{d\varepsilon\}_m \tag{3}$$

When conducting the model test, if the three governing equations of prototype and model are the same, the stress–strain relationship between prototype and model can fully meet the following conditions:

$$\frac{C_\gamma C_L}{C_\sigma} = 1 \tag{4}$$

TABLE 1 | Similarity constants of commonly used physical quantities in centrifugal test (scale 1: *N*, *C* = prototype parameter/model parameter).

Physical quantity name	Symbol	Dimension	Similar constant value
Centrifugal acceleration	g	LT^{-2}	1/N
Length	l	L	N
Displacement	δ	L	N
Quality	m	M	N^3
Density	ρ	ML^{-3}	1
Strength	F	MLT^{-2}	N^2
Stress, pressure	σ	$ML\text{-}1T^{-2}$	1
Soil pressure	P	—	N
Strain	ε	—	1
Time	T	T	N^2
Moisture content	ω	—	1

$$\frac{C_u}{C_L C_\varepsilon} = 1 \tag{5}$$

$$\frac{C_D C\varepsilon}{C_\sigma} = 1 \tag{6}$$

According to **Eqs. 4–6**, in the centrifugal model experiment, if the geometric similarity ratio is N, the corresponding centrifugal acceleration is $Ng, C_\gamma = N, C_L = \frac{1}{N}, C_u = \frac{1}{N}$; derivation can be obtained $C_\sigma = C\varepsilon = C_D = 1$. As shown in **Table 1**, the common similarity constants for the centrifugal test are shown in **Table 1**.

Test Device

The test was carried out on a TLJ-3 centrifuge, a large geotechnical centrifuge of Chang'an University, with a maximum capacity of 60 gt, a rotation radius of 2 m, and a maximum centrifugal acceleration of 200 *g* (Weng et al., 2019), as shown in **Figure 1**.

Figure 2 shows the centrifugal test device for tunnel face stability of the shield tunnel under different working conditions. The whole set of device consists of a model box, a lower water storage tank, a tunnel model (permeable tunnel face, steel shield shell), a cushion block, a high water level control hole, stress acquisition element FBG (fiber Bragg grating), a displacement stepping device, a loading dowel bar, etc.; the size of the model box is 700 mm × 400 mm × 500 mm. The front of the model box is high-strength transparent glass, through which it is easy to observe the characteristics of the tunnel face after instability. The other three sides and the bottom plate are high-strength steel plates. The shield model is mainly composed of shield shell, permeable excavation glass panel, FBG element, and stepper device to control displacement. Water level control is also an important part of the device. The water pump in the bottom water storage tank is used to pump water into the model box, the water level is kept unchanged through the water level control hole, and the overflow water flows back into the water tank to realize the displacement change of the shield excavation surface, which can be realized through the motor unit and the force transfer loading rod (Niu et al., 2020). When the centrifuge works, FBG can transmit the data of support pressure on the shield excavation surface to the external computer host by wireless transmission. Due to the symmetry of the tunnel, to reasonably observe the deformation and displacement, half of the tunnel model is made, that is, the shield shell with cross section of "D", and the inner diameter of the shield shell is 100 mm. Because the test content of this paper mainly monitors the stress law and instability mode of the tunnel surface, the influence of materials on the tunnel structure and stress is ignored.

Test Scheme and Steps

A series of comparative test conditions are set according to the influence of different soil parameters and working conditions. The main factors considered are shown in **Table 2**, where *C* is the overburden thickness of the tunnel, H_w is the height of water head at the center of the excavation surface, and *D* is the tunnel diameter. The internal friction angle is adjusted by mixing

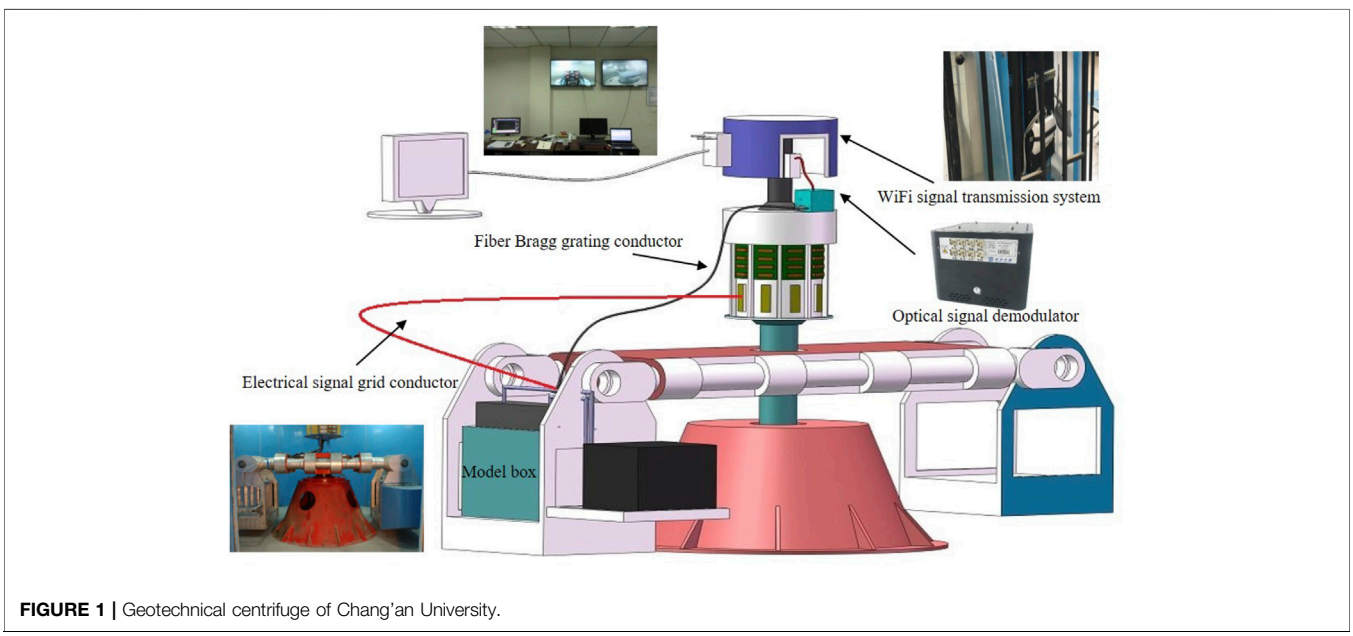


FIGURE 1 | Geotechnical centrifuge of Chang'an University.

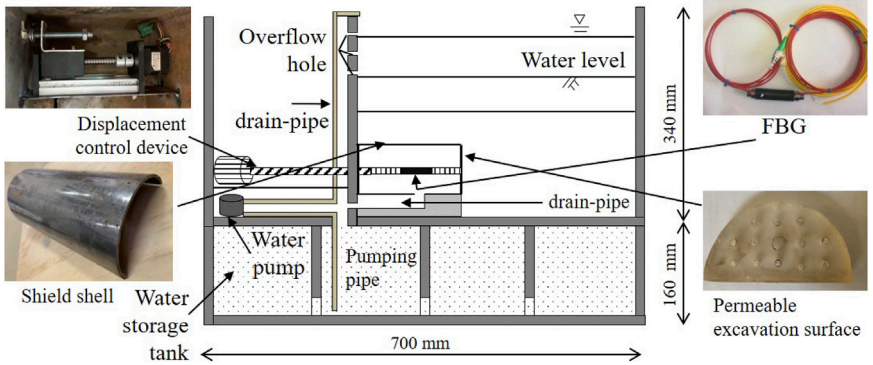


FIGURE 2 | Centrifugal test model box for stability of shield tunnel excavation face.

local clay with different proportions of river sand, which is measured by direct shear test. Combined with the power tunnel of Guangzhou trunk line, the tunnel diameter is 5 m, the scale of the model is 100 mm, and the centrifugal acceleration is designed as 50 *g*. In the instability mode analysis, $C/D = 1$ remains unchanged. In the whole test, the displacement control device is programmed to control the retreat of the permeable excavation surface of the shield model. The instability of the soil in front of the model is used to simulate the instability and failure of the soil in front of the shield excavation surface under seepage conditions. The support pressure on the excavation surface is measured by FBG, and the variation law and instability mechanism of each soil layer parameter on the support pressure under different working conditions are analyzed.

1) Put the prepared model box into the centrifuge test boom as a whole, and turn on the water pump to inject water into the box to the water level required for the test condition, that is, to reach the overflow hole (this process is not required for water free test).
2) Start the centrifuge, set the acceleration from 0 to 50 *g*, and stabilize for 30 min; this process keeps the position of the excavation surface unchanged, mainly to make the soil closer to the nature of the undisturbed soil.
3) After the support pressure remains stable, the displacement control device gradually retreats to the excavation surface at a certain rate, and the data are collected through the fiber Bragg grating system.
4) At the end of the centrifugal test, the acceleration gradually decreased from 50 *g* to 0. In the whole process, the displacement control was programmed by the stepper control system, and the support pressure of the excavation surface was monitored in real time by the FBG on the loading rod.

TABLE 2 | Conditions of centrifuge model tests.

Test variables		
C/D	***φ*(°)**	***H_w/D***
0.5, 1, 1.5, 2	25, 28, 32	0, 1, 1.5, 2

Experimental Treatment

In order to prevent soil particles from flowing into the tunnel under high acceleration and seepage, Vaseline is applied between the excavation surface and the shield tunnel wall to fill the gap. At the same time, the contact between the shield tunnel and plexiglass plate and support is bonded with glass glue to prevent water, but although this measure can prevent soil particles from entering the tunnel. On the other hand, it causes the tunnel to retreat and produce certain friction during the test, which cannot be ignored. Especially for the high-sensitivity element FBG (Fiber Bragg Grating), it affects the accuracy of the support pressure data on the excavation surface (Niu et al., 2020). Using the method proposed by Idinger et al. (2011), the model box is idled without soil and water, and the centrifugal conditions are consistent with the test conditions, Under the condition of 50 *g*, the average value of the retreating friction of the excavation surface can be obtained by this calibration method. It should be pointed out that the retreating friction of the excavation surface in this test is significantly less than the test results of Chen et al. (2015). The main reason is that the excavation surface here is made of high-strength glass and the filling material is Vaseline, which has a lubricating effect.

FBG writes the grating on the optical fiber with ultraviolet light, which can directly measure the support pressure on the excavation surface through the conversion formula, and has the characteristics of high sensitivity and strong adaptability (Taylor, 2005).

INSTABILITY MODE ANALYSIS

Support Pressure Change Process

The variation law of the support pressure on the excavation surface of the core test tunnel is shown in **Figure 3**. The whole evolution process can be divided into three stages: the first stage is when the displacement is small ($S < 1.5D\%$), the support pressure

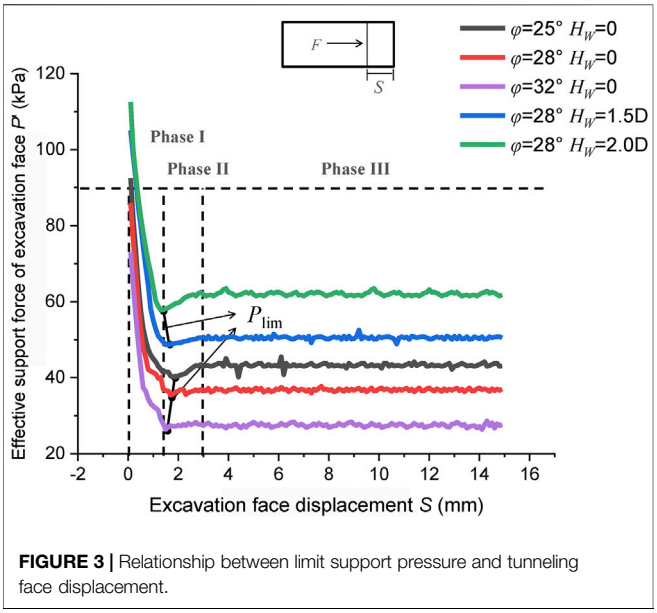


FIGURE 3 | Relationship between limit support pressure and tunneling face displacement.

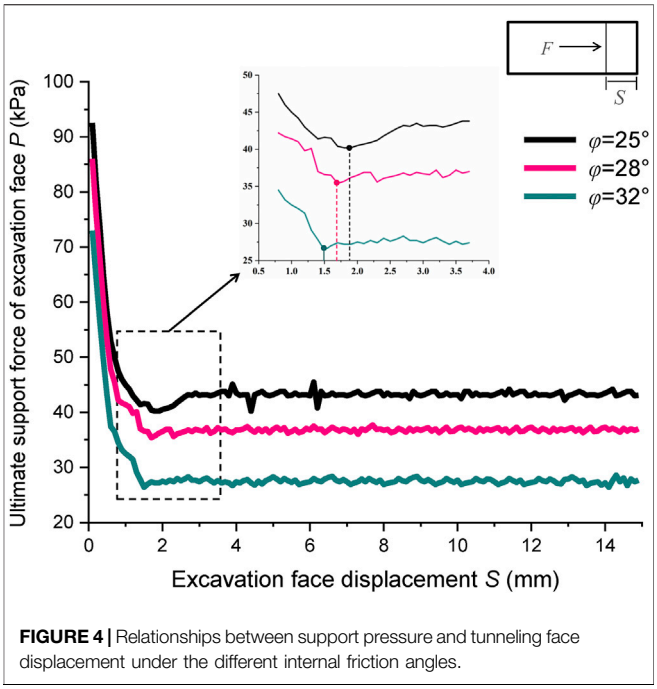


FIGURE 4 | Relationships between support pressure and tunneling face displacement under the different internal friction angles.

decreases rapidly with the increase of the displacement of the excavation surface, and the slope of the drawn line gradually decreases. The main reason is that with the retreat of the excavation surface, some collapsed soil mass is re-balanced under the action of surrounding forces. No more sliding with the soil below. The second stage is that the displacement of the excavation surface is between 1.5*D*% and 3*D*%. In this stage, with the increase of the retreat displacement of the tunnel excavation surface, the support pressure of the excavation surface reaches the limit state, and then the support pressure of the excavation surface rises slowly, which is in a circular arc shape in the graph. It can be seen from **Figure 3** that the displacement points of soil mass with different internal friction angles reach the limit state and are also different at $\varphi = 25^{\circ}$, the displacement of the excavation surface is $S = 1.9D\%$, and the soil reaches the limit bearing state. Similarly, when at $\varphi = 28^{\circ}$ and 32°, the displacement of the excavation surface reaches the limit bearing state at 1.7*D*% and 1.5*D*%, respectively. The analysis shows that the fluidity of sandy soil is better than that of clay. When the proportion of sandy soil increases, the cohesion of soil decreases gradually. When the excavation surface retreats, the "reaction" time of soil deformation becomes longer. However, under seepage conditions, such as $H_w = 1.5D$ and $2D$, under the action of seepage force, the soil flow speed will be accelerated and the soil deformation time will be shortened. The greater the water level difference under the same conditions, the shorter the time to reach the limit point. The main reason for the rebound of support pressure is the increase of retreat displacement, which makes the deformation of soil above the collapse lag after reaching the limit state. At the same time, it can be seen that different soil bodies also have different rebound times at $\varphi = 25^{\circ}$; the longest time is about 7 min, at $\varphi = 32^{\circ}$, and the shortest time is about 3 min. Therefore, seepage does not play a major role in the rebound time of support pressure. In the third stage, when the displacement of the excavation surface is greater than 3*D*%, the support pressure of the excavation surface gradually tends to a stable value with the increase of displacement. In this stage, it can be judged that the soil has been unstable.

Change of Support Pressure on Excavation Face of Dry Soil

Figure 4 shows the soil support pressure displacement relationship curve with different internal friction angles. Under the same buried depth ratio $C/D = 1$, the increase of the internal friction angle of the tunnel significantly reduces the support pressure on the excavation surface. The limit support pressures of the three kinds of soil are 40.2, 35.4, and 26.1 kPa, respectively. The instability modes of different soils are also different. With the increase of the displacement of the excavation surface, the soil mass in front of it deforms, and the soil particles above this part of the soil mass loosen along the vertical direction, which directly leads to the rapid reduction of the vertical earth pressure of the soil mass, while the horizontal earth pressure increases rapidly, which shows that the horizontal soil mass is more dense. At this time, the soil arching effect plays a role and initially forms a soil arching. The introduced lateral pressure coefficient K = horizontal earth pressure/vertical earth pressure. When $K > 1$, that is, the horizontal earth pressure is greater than the vertical earth pressure, the stress direction of soil changes, resulting in the rotation of the principal stress axis. As the excavation surface continues to retreat, the K value in the upper area in front of the tunnel gradually increases to the maximum value. At this time, the soil arching effect plays an extreme value, and the minimum value of the support pressure on the excavation surface is obtained. P_{min} is the limit support pressure obtained from the test, that is, the lowest point of the

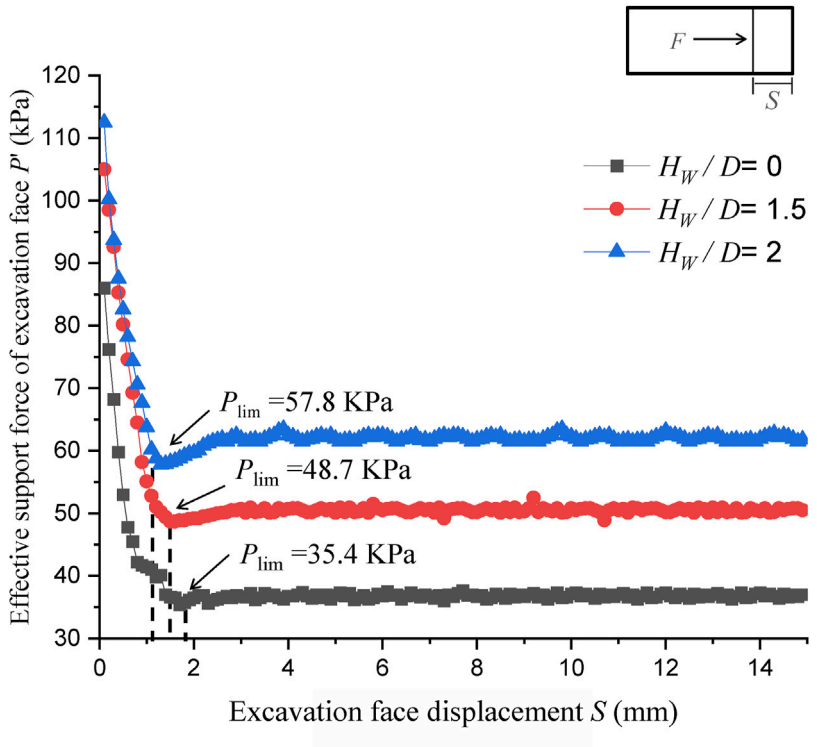


FIGURE 5 | Relationships between limit support pressure and tunneling face displacement under the different head pressures.

curve in **Figure 3**. There is a local shear failure area in front of the excavation surface, but at this time, the soil is in a limit equilibrium state. When the excavation surface continues to retreat, the *K* value gradually decreases from the peak value, and the local shear failure area develops into a shear sliding area. The sliding surface initially forms and extends upward, resulting in the failure of the original soil arch; the soil above the soil arch collapses and finally forms local instability failure. At this time, the support pressure of the excavation surface gradually increases, that is, the rebound in the second stage mentioned above. The soil arch continues to move upward, iterates over the new soil arch, and finally plays a bearing role. Due to different soil properties, when the horizontal earth pressure and vertical earth pressure reach equilibrium, the new soil arch is sufficient to bear the load of the upper loose soil, and the soil arch completes the whole extension process and finally ends in the local instability state.

The continuous soil arch iteration makes the soil near the surface loose and the surface has small settlement. Currently, the loose soil is particularly sensitive. When the excavation surface continues to retreat, the loose soil will collapse with the soil arch iteration, resulting in large settlement of the surface, and overall instability and failure of the soil. In this process, the soil arching effect plays a role from bottom to top along the top of the tunnel, and destroys with the expansion of the unstable sliding surface, then produces loose soil areas, circulates in turn, and finally develops to the surface. The soil arching effect gradually fails, and the support pressure of the excavation surface tends to a stable value, that is, the third stage mentioned above. The surface settlement is similar to funnels and chimneys, which is mainly related to soil quality, *C*/*D*, and hydrological conditions.

Variation of Support Pressure on Excavation Face of Saturated Soil

It can be seen from the curve of limit support pressure displacement under different head pressures in **Figure 5** that when H_w = 1.5*D*, the limit effective support pressure P'_{lim} = 48.7 kPa, which is 37.6% higher than that under dry conditions. When H_w = 2*D*, the limit effective support pressure P'_{lim} = 57.8 kPa, which is 63.3% higher than that under dry condition and 18.7% higher than that under H_w = 1.5*D* condition. The data fitting shows that the limit effective support pressure increases linearly with the increase of head pressure.

When the overall instability failure of the soil occurs, the surface presents a chimney shape. Under the action of seepage force, the deformation of the soil is accelerated, resulting in the expansion of the width and a larger volume of the collapse body, extending from the bottom to the surface, which intensifies the iteration speed and failure strength of the soil arch. In the theoretical calculation and numerical simulation, for the convenience of calculation, the seepage coefficient is often regarded as isotropic. In the comparison of the test results in this paper, it can be seen that the seepage force of the soil in the collapse area along the tunnel is significantly greater than

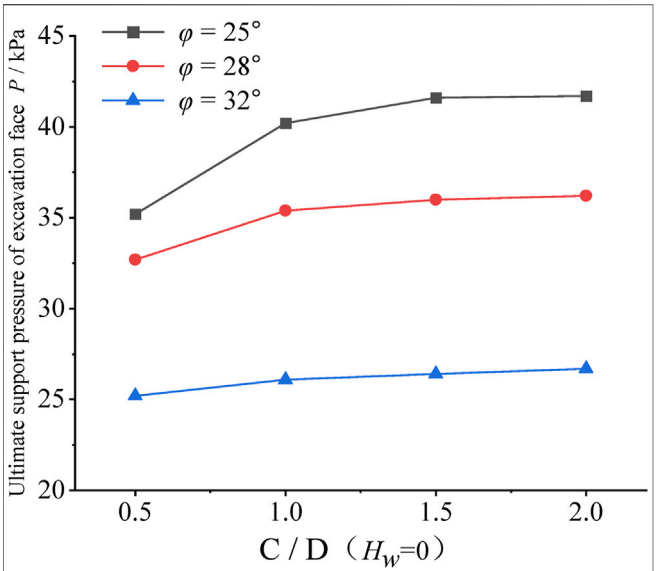


FIGURE 6 | Relationship between limit support pressure and ratio of tunnel *C/D*.

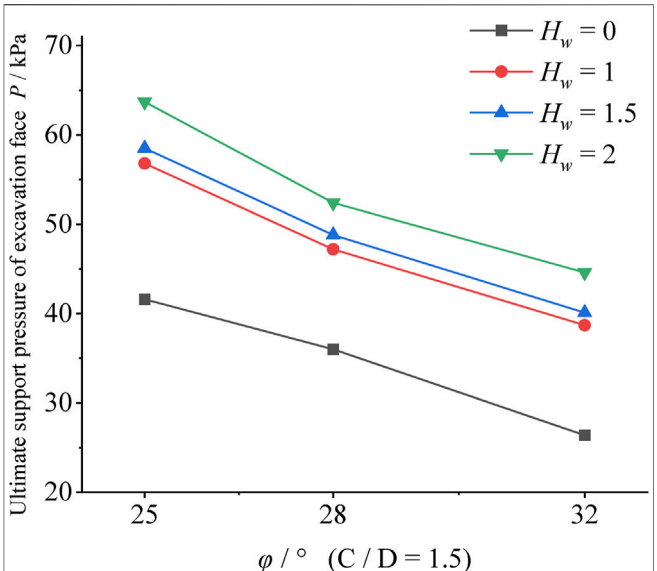


FIGURE 7 | Relationship between limit support pressure and internal friction angle of tunnel.

that outside the failure surface, and the seepage force near the tunnel surface is significantly greater than that far away from the tunnel surface. It is not difficult to see that if the excavation surface continues to retreat, under the action of seepage force, the soil particles with original force balance will be carried to the lower part, making the chimney shape wider and wider, and finally leading to the tunnel filled with soil. This is also the key to increase the support pressure of the excavation surface in time to prevent the further development of collapse and prevent water and mud gushing in the process of shield instability.

FACTOR INFLUENCE ANALYSIS

Influence of *C/D* on Limit Support Pressure of Tunnel

The variation law of tunnel limit support pressure with *C/D* is shown in **Figure 6**. It can be seen that with the increase of *C/D*, the limit support pressure gradually decreases and tends to a stable value φ = 28°, increased by 7.6%, 1.7%, and 0.6%, respectively, with the increase of *C/D*. When *C/D* = 2, the limit support pressure is stable at 41.7, 36.2, and 26.7 kPa. From φ = 32° to φ = 25°C at *C/D* = 0.5, the limit support pressure is reduced by 28.4%. When *C/D* = 0.5, because it is a shallow buried tunnel, overall instability will occur. At this time, *P* is 35.2 kPa. With the increase of *C/D*, when *C/D* = 1, the buried depth increases, the soil arching effect is further developed, and local instability will occur. At this time, *P* is equal to 40.2 kPa with an increase of 14.2%, which is shown in the figure, where the first half of the curve is steep. When φ is 28°, the slope of the first half section decreases compared with that at 25°, which is mainly due to the more effective role played by the soil arching effect with the increase of internal friction angle. Similarly, when φ is 32°, the limit support pressure is hardly affected by *C/D*, and only increases by 3.5%. When *C/D* > 1.5, the buried depth has little effect on the limit support pressure of the tunnel. It can be seen that the soil with larger internal friction angle is more likely to produce a soil arching effect, which plays a more effective role. In the construction of a shallow buried tunnel, attention should be paid to the soil with a smaller internal friction angle.

Influence of Internal Friction Angle on Limit Support Pressure of Tunnel

It has been known from the section ***Influence of C/D on Limit Support Pressure of Tunnel*** that when *C/D* > 1.5, *P* will tend to be stable, so this group selects *C/D* = 1.5 for the test. The variation law of tunnel limit support pressure with internal friction angle is shown in **Figure 7**. It can be seen that with the increase of internal friction angle, the limit support pressure decreases linearly. Due to the limited test conditions, the test with larger internal friction angle is not continued. However, it can be seen from literature (Du and Han, 2010; Idinger et al., 2011), when internal friction angle φ is more than 40°, that *P* gradually tends to a stable value with the continuous increase of φ. Taking H_w = 1.5 as an example, with the increase of internal friction angle, it decreases by 16.6% and 17.9%, respectively. At the same head height, with the increase of H_w, φ = 28° more than φ = 25°. The limit support pressure is reduced by 15.5%, 16.9%, 20.3%, and 21.6%. It can be seen from the comparison that in the case of no water, with the increase of internal friction angle, the reduction rate of limit support pressure is slow, and when the height of water head increases continuously, it will accelerate the reduction of limit support pressure. The main reason is that under the action of seepage force, the formation of soil arch effect is accelerated, its iterative development is terminated, and smaller limit support pressure is obtained. With the increase of head height, there is no significant increase between H_w = 1 and H_w = 1.5. The main

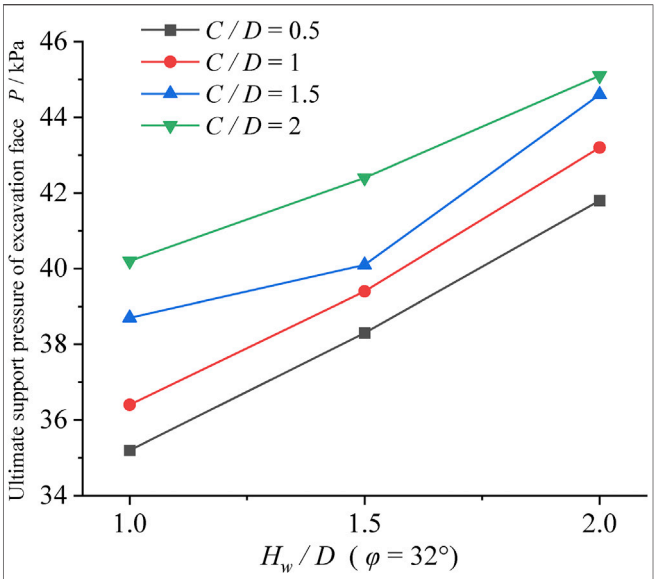


FIGURE 8 | Relationship between limit support pressure and height of water head of tunnel.

reason is that during the centrifugal test, because the head water level is lower than the soil layer height, the overflow of the centrifuge is blocked by soil particles at high acceleration, resulting in the actual head height being greater than the control the height of water head and no head increment of 0.5 H_w. It can be seen that in the construction of high water level or shallow buried tunnel, the value of soil limit support pressure with a low internal friction angle should be more conservative.

Influence of Height of Water Head on Limit Support Pressure of Tunnel

It can be seen from *Influence of Internal Friction Angle on Limit Support Pressure of Tunnel* that with the increase of internal friction angle, the limit support pressure gradually tends to a stable value. That is, the larger value of φ is, the smaller the influence on the support pressure of the excavation face is, so $\varphi = 32^{\circ}$ is selected. This group of tests shall be carried out for 32° soil. It can be seen from **Figure 8** that with the increase of H_w, the limit support pressure increases linearly, and there is a sudden change when $C/D = 1$ and $H_w = 1.5$. The reason is the same as that in *Influence of Internal Friction Angle on Limit Support Pressure of Tunnel*. The overflow is blocked by soil particles, which also provides improvement ideas for researchers who conduct subsequent centrifugal tests. When $H_w = 1$, with the increase of C/D, the limit support pressure increases by 3.4%, 6.3%, and 3.8%, respectively. When $H_w = 1.5$, it increases by 2.9%, 1.8%, and 5.7%, respectively. When $H_w = 2$, it increases by 3.3%, 3.2%, and 1.2%, respectively. It can be seen that under the condition of height of water head, with the increase of C/D, the increase of limit support pressure caused by H_w also gradually decreases, which is consistent with the fact that the increase of C/D obtained in *Influence of C/D on Limit Support Pressure of Tunnel* to a certain extent is no longer the main factor affecting limit support pressure. At the same time, with the continuous increase of H_w, the limit support pressure of the tunnel under different buried depths increases linearly. It can be obtained from Yu et al. (2020). Due to the influence of tunnel diameter, with the continuous increase of H_w, the seepage force on the tunnel excavation surface will not increase linearly, but gradually flatten. Due to the complex test conditions, the influence of tunnel diameter on the limit support pressure is not considered in the test, but this influencing factor cannot be ignored.

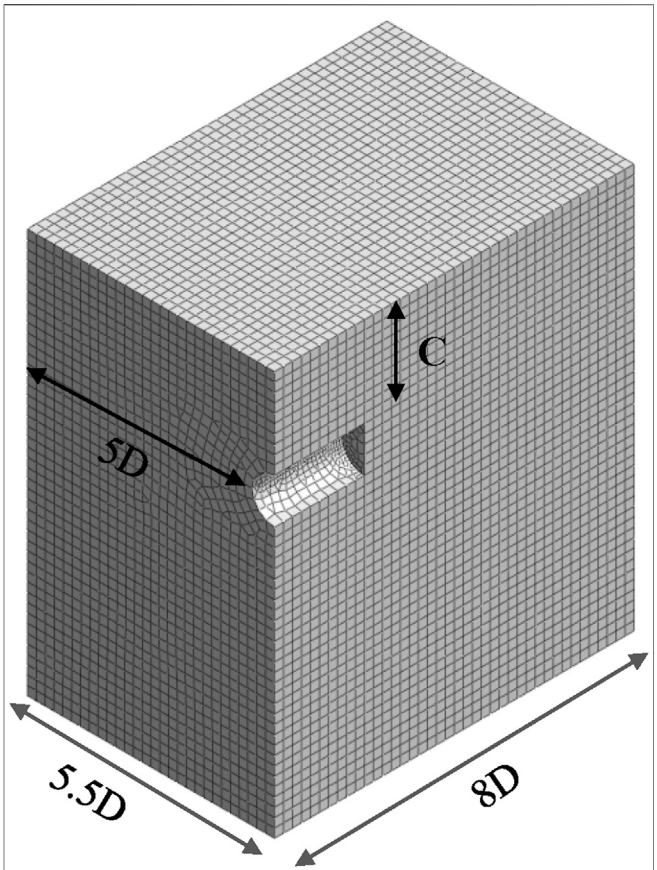


FIGURE 9 | Numerical analysis model.

NUMERICAL ANALYSIS

Due to the limited test conditions and the need to invest more human and material resources, and the uncertain randomness of the data results, in order to better analyze the research of different factors on the instability mode of the tunnel excavation surface, this paper will carry out modeling and analysis in combination with the finite element software, considering the directness of the analysis and the symmetry of the data. Half of the circular tunnel cut longitudinally along the central axis is used as the analysis model (Li et al., 2018, Lu et al., 2016). As shown in **Figure 9**, the tunnel diameter is 10 m,

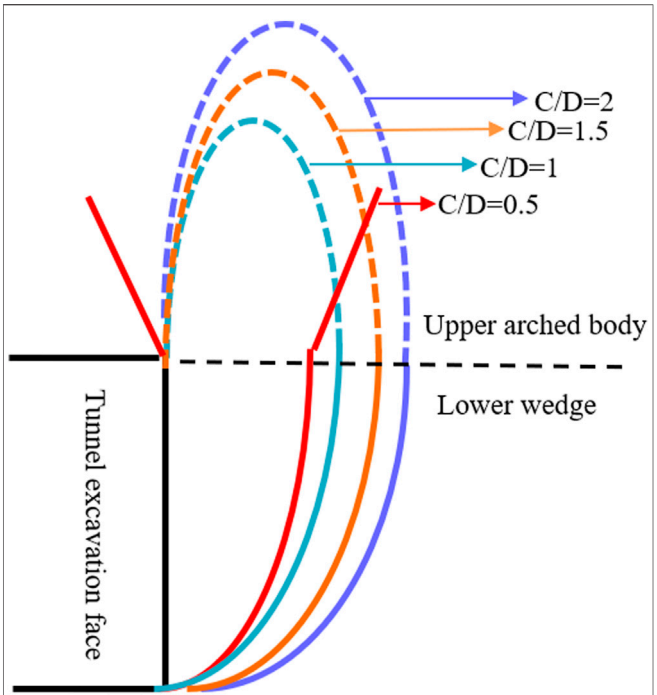


FIGURE 10 | Relationship between *C/D* and tunnel instability mode.

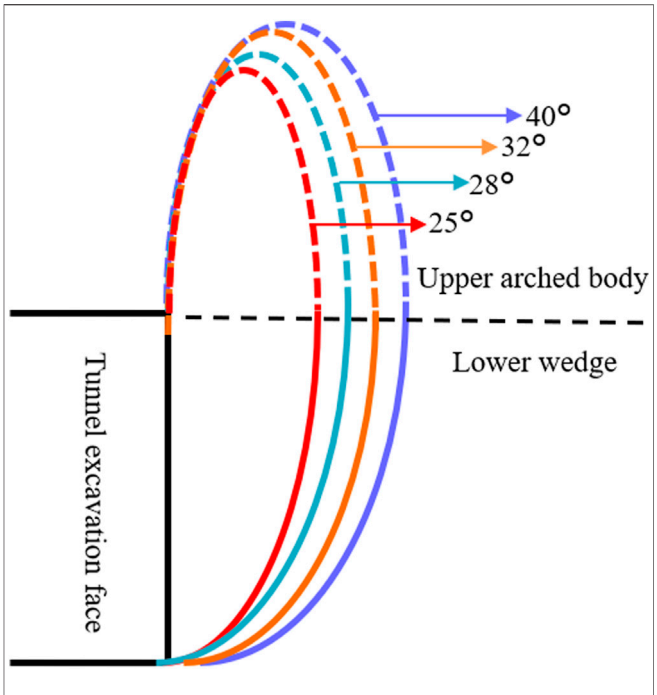


FIGURE 11 | Relationship between internal friction angle and tunnel instability mode.

and the length and width of the model are 80 m and 55 m, respectively. The model is large enough to avoid boundary effect, where *C* is the buried depth of the tunnel. The soil model adopts the M-C model, and the lining structure is represented by the shell element, with a thickness of 35 mm. Earth pressure monitoring points are set within the three-dimensional and two-dimensional range in front of the tunnel excavation surface to judge the tunnel instability contour. In the result analysis diagram, the black contour is the tunnel body, the color line is the instability contour drawing, and the contour line is fitted and linearized.

The boundary conditions of the model are as follows: only the top surface of the model can move freely. The normal direction of all vertical planes is fixed. The bottom surface of the model is also fixed. The surface between soil and lining is fixed.

Influence of *C/D* on Tunnel Instability Mode

The influence of *C*/*D* on the tunnel instability mode is shown in **Figure 10**. Similar to the previous centrifugal test results, the tunnel is prone to overall instability under shallow buried conditions, such as $C/D < 1$. When the red line *C*/*D* in the figure is 0.5, the overall instability occurs, and the instability range is expanded in a trumpet shape. With the continuous increase of *C*/*D*, the soil arch effect plays a role. It can be seen that the soil arch continues to develop above the soil, up to 1.2*D*, but its development speed continues to slow down. With the increase of *C*/*D*, the instability angle of the tunnel also gradually slows down, the width of the wedge below increases, and the height of the soil arch continues to increase. In other words, for the same soil layer, with the increase of *C*/*D*, the soil mass in front of the tunnel excavation face gradually changes from initial overall instability to local instability, and the height and width of soil arch continue to increase. When *C*/*D* increases to a certain extent, the soil arch effect will no longer extend and play a role, and *C*/*D* will no longer have an impact on the limit support pressure of the excavation face.

Internal Friction Angle φ Influence on Tunnel Instability Mode

The influence of the internal friction angle on the tunnel instability mode is shown in **Figure 11**. It can be seen from the figure that with the increase of the internal friction angle, the soil instability mode has not changed greatly, and the height of the soil arch is not greatly affected by the internal friction angle. With the increase of the internal friction angle, the height of the soil arch increases by 1/5*D*, while the width of the wedge below increases by 2/5*D*. For the collapse mode, the inclination angle of unstable soil decreases continuously and does not increase continuously with the increase of internal friction angle. With the increasing internal friction angle, the wedge will not continue to grow, but will tend to a stable instability state, which is similar to the conclusion obtained from the previous centrifugal test. For the soil layer with high internal friction angle, the increase of *C*/*D* has little effect on the support pressure of the excavation face. Instead, we should pay more attention to the expansion of the instability range in front of the excavation face, explore how to take effective measures to reduce the collapse volume of the soil in front, and pay more attention to the shallow tunnel with low internal friction angle.

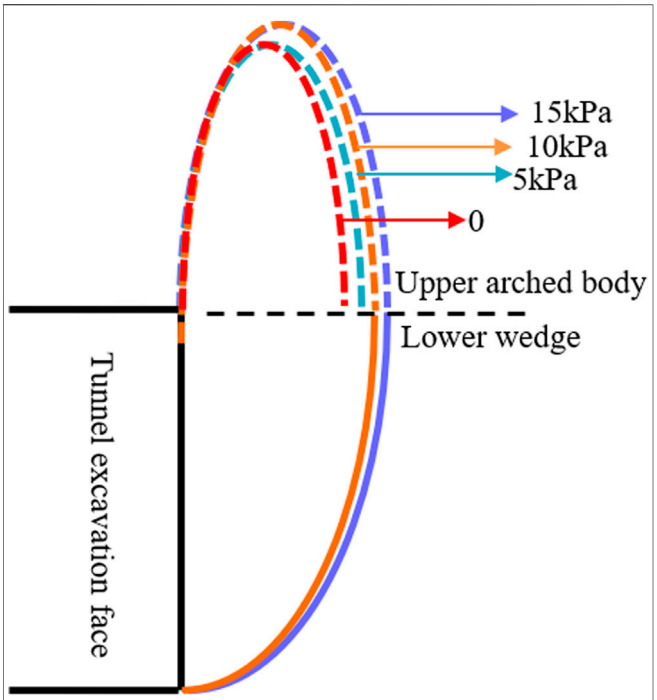


FIGURE 12 | Relationship between cohesion and instability mode of tunnel.

Influence of Cohesion c on Instability Mode of Tunnel

In the centrifugal test, it is difficult to take the cohesion as the variable, so the influence of soil cohesion on the tunnel instability mode is studied in the numerical simulation stage. The relationship between cohesion and tunnel instability mode is shown in **Figure 12**. It can be seen that the overall instability mode and contour of the tunnel have not changed substantially. With the increase of cohesion, the height of soil arch has hardly changed, with a maximum increase of 0.1–0.2*D*, and the width of wedge below has a slight increase. Similarly, the influence of cohesion on the support pressure of the excavation face is not the main factor, which is why most scholars do not take cohesion as the main research object when studying the influence on the support pressure of the excavation face.

CONCLUSION

Through the centrifugal model test and numerical modeling analysis of the instability of the excavation surface of the shield tunnel, comparing the support pressure and instability form of the lower excavation surface within different soil parameters, and analyzing its influence on the support pressure of the excavation surface and its effect on the instability mechanism, the following conclusions can be obtained:

1) The instability process of excavation face can be divided into three stages. In the first stage ($S < 1.5D\%$), P decreases rapidly with the increase of S. In the second stage ($1.5D\% \le S \le 3D\%$), with the increase of S, the support pressure of the excavation face reaches the limit state, namely, PLIM, and then P rises slowly, showing a circular arc in the graph. In the third stage ($3D\% < S$), as S continues to increase, P gradually approaches the stable value.
2) The C/D and internal friction angle are positively correlated with the ultimate support pressure of the excavation face. When $\varphi > 40^{\circ}$ or $C/D > 1.5$, the impact is small and can be ignored. With the increase of the height of water head, the limit support pressure increases linearly.
3) With the increase of C/D, the soil is in the gradual process from overall failure to local failure. The change of C/D mainly affects the height of soil arch and the width of wedge below, and the internal friction angle mainly affects the width of wedge and soil instability angle.

DATA AVAILABILITY STATEMENT

The original contributions presented in the study are included in the article/Supplementary Material, further inquiries can be directed to the corresponding author.

AUTHOR CONTRIBUTIONS

HN: Conceptualization, Data Curation, Validation, Investigation, Writing—original draft, and Writing—review and editing. XW: Research Conceptualization, Writing—review and editing, Resources, Supervision, and Funding acquisition. JH: Test help. LH: Data processing.

FUNDING

The authors would like to acknowledge the financial support of the National Natural Science Foundation of China (Grant No. U1934213).

REFERENCES

Anagnostou, G., and Kovári, K. (1996). Face Stability Conditions with Earth-Pressure-Balanced Shields. *Tunnelling Underground Space Technol.* 11 (2), 165–173. doi:10.1016/0886-7798(96)00017-x

Broere, W. (2001). *Tunnel Face Stability and New CPT Application*. Amsterdam: Delft University Press.

Chen, R. P., Yin, X. S., Tang, L. J., and Chen, Y. M. (2015). Limit Theoretical Study on Face Stability of Shield Tunnels. *Rock Soil Mech.* 36 (S1), 225–229. doi:10.3724/SP.J.1077.2011.00271

Du, Y. L., and Han, L. B. (2010). *Geotechnical Centrifugal Model Test Technology*. Beijing: China water resources and Hydro-power Press. (in Chinese).

Feng, G.-L., Chen, B.-R., Xiao, Y.-X., Jiang, Q., Li, P.-X., Zheng, H., et al. (2022). Microseismic Characteristics of Rockburst Development in Deep TBM Tunnels with Alternating Soft-Hard Strata and Application to

Rockburst Warning: A Case Study of the Neelum-Jhelum Hydropower Project. *Tunnelling Underground Space Technol.* 122, 104398. doi:10.1016/j.tust.2022.104398

Feng, G.-L., Feng, X.-T., Chen, B.-R., Xiao, Y.-X., and Yu, Y. (2015). A Microseismic Method for Dynamic Warning of Rockburst Development Processes in Tunnels. *Rock Mech. Rock Eng.* 48 (5), 2061–2076. doi:10.1007/s00603-014-0689-3

Han, Z., Li, D., Zhou, T., Zhu, Q., and Ranjith, P. G. (2020). Experimental Study of Stress Wave Propagation and Energy Characteristics across Rock Specimens Containing Cemented Mortar Joint with Various Thicknesses. *Int. J. Rock Mech. Mining Sci.* 131, 104352. doi:10.1016/j.ijrmms.2020.104352

Horn, N. (1961). "Horizontal Earth Pressure on the Vertical Surfaces of the Tunnel Tubes," in National Conference of the Hungarian Civil Engineering Industry, Budapest, November, 1961, 7–16.

Idinger, G., Aklik, P., and Wu, W. (2011). Centrifuge Model Test on the Face Stability of Shallow Tunnel. *Acta Geotech* 6 (2), 105–117. doi:10.1007/s11440-011-0139-2

Jancsecz, S., and Steiner, W. (1994). "Face Support for a Large Mix-Shield in Heterogeneous Ground Conditions," in Proceeding of the 7th International Symposium on Tunneling, Boston, MA, 531–550. doi:10.1007/978-1-4615-2646-9_32

Li, D., Han, Z., Sun, X., Zhou, T., and Li, X. (2019). Dynamic Mechanical Properties and Fracturing Behavior of marble Specimens Containing Single and Double Flaws in SHPB Tests. *Rock Mech. Rock Eng.* 52 (6), 1623–1643. doi:10.1007/s00603-018-1652-5

Li, J., Chen, R. P., and Kong, L. G. (2011). Model Test Study of the Failure Mechanism of Shallow Tunnels in Dry Sands. *China Civil Eng.* 4 (07), 142–148. (in Chinese). doi:10.1631/jzus.B1000185

Li, W., Zhang, C., and Zhang, X. (2018). Stability Analysis of the Tunnel Face in the Cohesive-Frictional Soils Considering the Arch Effect and Rotational Mechanism. *J. Chin. Inst. Eng.* 41 (8), 697–709. doi:10.1080/02533839.2018.1534615

Liu, G.-F., Jiang, Q., Feng, G.-L., Chen, D.-F., Chen, B.-R., and Zhao, Z.-N. (2021). Microseismicity-Based Method for the Dynamic Estimation of the Potential Rockburst Scale during Tunnel Excavation. *Bull. Eng. Geol. Environ.* 80 (5), 3605–3628. doi:10.1007/s10064-021-02173-x

Liu, W., Zhang, X. J., and Tang, X. W. (2012). Supporting Pressure for Earth Pressure Balance Tunnel Face Stability sandy Soil when Tunneling Is Implemented in Saturated. *J. Zhejiang Univ. (Engineering Science)* 46 (4), 664–704. doi:10.3785/j.issn.1008-973X.2012.04.014

Lu, X., Zhou, Y., Huang, M., and Li, F. (2016). Computation of the Minimum Limit Support Pressure for the Shield Tunnel Face Stability under Seepage Condition. *Int. J. Civ Eng.* 15, 849–863. doi:10.1007/s40999-016-0116-0

Lv, X. L., Zeng, S., Wang, Y. P., Ma, S. K., and Huang, M. S. (2019). Physical Model Tests on Stability of Shield Tunnel Face in Saturated Gravel Stratum. *Chin. J. Geotechnical Eng.* 41 (S2), 129–132. (in Chinese). doi:10.11779/CJGE2019S2033

Meguid, M. A., Saada, O., Nunes, M. A., and Mattar, J. (2008). Physical Modeling of Tunnels in Soft Ground: A Review. *Tunnelling Underground Space Technol.* 23 (2), 185–198. doi:10.1016/j.tust.2007.02.003

Mollon, G., Phoon, K. K., Dias, D., and Soubra, A.-H. (2011). Validation of a New 2D Failure Mechanism for the Stability Analysis of a Pressurized Tunnel Face in a Spatially Varying Sand. *J. Eng. Mech.* 137 (1), 8–21. doi:10.1061/(asce)em.1943-7889.0000196

Niu, H. S., Weng, X. L., Yu, H. F., and Hu, J. B. (2020). Centrifugal Test Study on Instability Mode of Shield Tunnel Excavation Facein Silty Sand Stratum under Seepage. *China Civil Eng.* 53 (S1), 99–104+118. (in Chinese). doi:10.15951/j.tmgcxb.2020.s1.017

Oblozinsky, P., and Kuwano, J. (2006). "Centrifuge Experiments on Stability of Tunnel Face in sandy Ground," in Proceedings of the 5th International Conference on Geotechnical Aspects of Underground Construction in Soft Ground, Amsterdam, Netherlands, June 15-17, 2006, 271–275.

Taylor, R. N. (2005). *Geotechnical Centrifuge Technology*. Amsterdam: Taylor & Francis.

Vermeer, P. A., Ruse, N., and Marcher, T. (2002). Tunnel Heading Stability in Drained Ground. *Felsbau* 20 (8), 8–18. Available at: https://www.researchgate.net/publication/228751251_Tunnel_Heading_Stability_in_Drained_Ground

Weng, X. L., Sun, Y. F., Yan, B. H., Niu, H. S., and Zhou, S. Q. (2019). Centrifuge Testing and Numerical Modeling of Tunnel Face Stability Considering Longitudinal Slope Angle and Steady State Seepage in Soft clay. *Tunn Undergr Sp Tech.* 101 (2), 103406. doi:10.1016/j.tust.2020.103406

Yang, F., Yang, J. S., and Zhao, L. H. (2010). Collapse Mechanism and Support Pressure for Shallow Tunnel Face. *Chin. J. Geotechnical Eng.* 32 (2), 279–281. (in Chinese). Available at: https://kns.cnki.net/kcms/detail/detail.aspx?FileName=YTGC201002023andDbName=CJFQ2010.

Yu, L., Zhang, D., Fang, Q., Cao, L., Zhang, Y., and Xu, T. (2020). Face Stability of Shallow Tunnelling in sandy Soil Considering Unsupported Length. *Tunnelling Underground Space Technol.* 102, 103445. doi:10.1016/j.tust.2020.103445

Yu, Y., Feng, G. L., Xu, C. J., Chen, B. H., Geng, D. X., and Zhu, B. T. (2022). Quantitative Threshold of Energy Fractal Dimension for Immediate Rock-Burst Warning in Deep Tunnel: A Case Study. *Lithosphere* 2022, 1699273. doi:10.2113/2021/1699273

Zhang, D. L., and Sun, Z. Y. (2018). Structural Stability of Complex Tunnel Surrounding Rock and its Control. *J. Hydroelectric Eng.* 37 (02), 1–11. (in Chinese). doi:10.11660/slfdxb.20180201

Zhu, W., Qin, J. S., and Lu, Y. H. (2005). Numerical Study on Face Movement and Collapse Around Shield Tunnels in Sand. *Chin. J. Geotechnical Eng.* 27 (8), 897–902. (in Chinese).

Conflict of Interest: The authors declare that the research was conducted in the absence of any commercial or financial relationships that could be construed as a potential conflict of interest.

Publisher's Note: All claims expressed in this article are solely those of the authors and do not necessarily represent those of their affiliated organizations, or those of the publisher, the editors and the reviewers. Any product that may be evaluated in this article, or claim that may be made by its manufacturer, is not guaranteed or endorsed by the publisher.

Copyright © 2022 Niu, Weng, Hu and Hou. This is an open-access article distributed under the terms of the Creative Commons Attribution License (CC BY). The use, distribution or reproduction in other forums is permitted, provided the original author(s) and the copyright owner(s) are credited and that the original publication in this journal is cited, in accordance with accepted academic practice. No use, distribution or reproduction is permitted which does not comply with these terms.

frontiers in Earth Science

ORIGINAL RESEARCH
published: 30 March 2022
doi: 10.3389/feart.2022.873986

Influence Evaluation of Sensor Coordinate Error on Microseismic Source Location

Tao Li[1,2], *Bing-Rui Chen*[1,2]*, *Qing Wang*[1,2]*, *Xin-Hao Zhu*[1,2], *Xu Wang*[1,2] and *Ming-Xing Xie*[3]

[1]State Key Laboratory of Geomechanics and Geotechnical Engineering, Institute of Rock and Soil Mechanics, Chinese Academy of Sciences, Wuhan, China, [2]University of Chinese Academy of Sciences, Beijing, China, [3]Beiminghe Iron Mine of Minmetals Hanxing Mining Co., Ltd., Handan, China

In microseismic (MS) source localization, it is usually assumed that the sensor coordinates are accurate. However, there are generally measurement errors for the sensor coordinates in practical engineering, which severely affect the location accuracy of the MS sources. Therefore, based on the least square linear inversion equation, the theoretical analysis shows that the location error is proportional to the sensor coordinate error. To reduce the systematic error of the MS source location, a calculation method for the sensor coordinate error threshold is proposed. First, the theoretical arrival time of each sensor is calculated. Then, the sensor coordinate error is added and combined with the original sensor coordinate for location. Finally, the sensor coordinate error threshold that makes the location results reach the source location accuracy is obtained. Furthermore, based on this method and assuming that the sensor coordinate error is in a normal distribution, a comprehensive evaluation index of the sensor coordinates is proposed to evaluate the influence of the sensor coordinates on the MS source location. The application results of the Beiminghe Iron Mine in Hebei Province show that the farther the source is from the sensor array, the smaller the sensor coordinate error threshold is. The sensor coordinate error threshold in the sensor array is larger than that outside the sensor array. The sensor coordinate error threshold decreases rapidly in the sensor array and slowly outside the sensor array. After removing sensor No. 201, which has the greatest influence on MS source location and has a large measurement error, the average location accuracy of blasting test events is improved by 25.74%. The research results have a certain guiding significance for the sensor coordinate measurement.

Keywords: microseismic, sensor coordinate error, monitoring area, sensor array center, threshold, comprehensive evaluation index

OPEN ACCESS

Edited by:
Shibing Huang,
Wuhan University of Science and Technology, China

Reviewed by:
Yi Duan,
CSIRO, Australia
Nan Li,
China University of Mining and Technology, China

***Correspondence:**
Bing-Rui Chen
brchen@whrsm.ac.cn
Qing Wang
wangqing202@mails.ucas.ac.cn

Specialty section:
This article was submitted to Geohazards and Georisks, a section of the journal Frontiers in Earth Science

Received: *11 February 2022*
Accepted: *11 March 2022*
Published: *30 March 2022*

Citation:
Li T, Chen B-R, Wang Q, Zhu X-H, Wang X and Xie M-X (2022) Influence Evaluation of Sensor Coordinate Error on Microseismic Source Location. Front. Earth Sci. 10:873986. doi: 10.3389/feart.2022.873986

INTRODUCTION

With the China's 13th Five-year Plan on Technology and Innovation strengthening the development and utilization of deep resources, there are an increasing number of deep-buried mines and tunnels, and rockburst disasters are becoming increasingly severe. To effectively avoid and prevent loss caused by deep engineering geological disasters, the microseismic (MS) monitoring technique plays a key role as a new rock mass microfracture monitoring technique. Multiple mature MS monitoring systems have emerged, such as the Institute of Mine Seismology (IMS) in Australia, Engineering Seismology Group (ESG) in Canada, and SinoSeism (SSS) MS monitoring system jointly developed

by the Institute of Rock and Soil Mechanics, Chinese Academy of Sciences, and Hubei Seaquake Technology Co., Ltd. (Chen et al., 2021). The MS monitoring techniques can obtain the MS information in the process of rock mass disaster preparation in real time and evaluate the region, probability, and scale of rock mass instability, providing the basis for early warning and prevention of rock mass risk. Currently, this approach has been widely used in many fields, such as mines, slopes, and tunnels (Leśniak and Isakow, 2009; Xu et al., 2010; Feng et al., 2015; Dai et al., 2016; Feng et al., 2022; Yu et al., 2022; Zhang et al., 2022). In the MS research, the MS source location directly affects the calculation of radiant energy, the analysis of the MS activity, and the early warning of the rockburst. Therefore, the accuracy of the MS source location is directly related to the analysis and prediction of rock engineering disasters.

Scholars worldwide have carried out much research work on the MS source location and have achieved very fruitful results. According to the principle of the MS source location, the key factors affecting the MS source location mainly include the location method, sensor array, first-arrival waveform pickup, and velocity model. In terms of the location method, location methods based on different arrival times are widely used, mainly including noniterative methods (Liu and Gao, 2012), iterative methods (Geiger, 1912; Li et al., 2014b), and swarm intelligence methods (Kennett and Sambridge, 1992; Chen et al., 2009). In terms of the sensor array, the field mainly has D-optimal design theory and C-optimal design theory (Kijko, 1977a; Kijko, 1977b), and layout optimization and evaluation methods of the MS sensor array based on D-optimal design theory (Gong et al., 2010) and the influence mechanism of the two-dimensional plane sensor array (Li et al., 2014a; Li, 2014) have been further proposed. In terms of first-arrival waveform pickup, there are many mature methods for P-wave and S-wave arrival time pickups, such as the correlation method (Bai and Kennett, 2000), energy ratio method (Saragiotis et al., 2002), and maximum amplitude method (Paige and Saunders, 1982; Cao and Greenhalgh, 1993; Boschetti et al., 1996). In terms of the velocity model, most scholars use the uniform velocity model, which simplifies the velocity of the regional rock mass and ignores the difference in rock mass characteristics. In addition, the uniform velocity model simplifies the calculation process and has strong stability. To adapt to the stratigraphic conditions, the layered velocity model (Crosson and Peters, 1974) and the anisotropic velocity model (Mooney et al., 1998) have been proposed and applied, greatly reducing the MS source location error.

In addition to the above factors affecting the MS source location, the sensor coordinates have measurement errors, which also will affect the MS source location. At present, research on the influence of sensor coordinate errors on localization mainly focuses on satellite navigation (Zhang et al., 2018), missile location (Yang and Ho, 2009; Wei et al., 2010; Sun and Ho, 2011), radar detection (Wang and Ho 2013), and communication systems (Rockah and Schultheiss, 1987; Kovavisaruch and Ho, 2005). Due to the concealment and mobility of the observation stations, research efforts are mainly aimed at the development of high-performance location methods with observation station coordinate errors. However, in the MS monitoring field, the influence of sensor coordinate errors on MS source location is rarely studied. In mine and tunnel engineering, the sensor is often installed in the borehole of the sidewall or the vault, which increases the difficulty of the sensor coordinates measurement. At the same time, the size effect of the sensor, the accuracy of the measurement equipment, and the improper operation of the measurement personnel also lead to large measurement errors in the sensor coordinates. When there is a measurement error in the sensor coordinates, the location accuracy of the MS source is significantly reduced. The sensors installed in different spatial positions have different effects on the MS source location. Therefore, to reduce the systematic error of the MS source location, it is indeed necessary to propose a corresponding sensor coordinate error threshold and quantitatively evaluate the influence of different sensors on the MS source location.

Therefore, the influence of the sensor coordinate error on the MS source location error is theoretically analyzed by the least square linear inversion equation, and the calculation method of the sensor coordinate error threshold is proposed. The influence of different sensors on the MS source location is comprehensively evaluated, which is applied in engineering. The research results have a certain guiding significance for installation and sensor coordinate measurement in actual engineering.

LEAST SQUARE LINEAR INVERSION EQUATION AND LOCATION ERROR ANALYSIS

Least Square Linear Inversion Equation

In the MS source localization, the objective function (Liu 2007) is

$$F(X) = \left(t_i - f_i(X)\right)^2 \tag{1}$$

$$f_i(X) = \sqrt{(x_i - x_0)^2 + \left(y_i - y_0\right)^2 + (z_i - z_0)^2} + t_0 \tag{2}$$

where t_i is the observed arrival time of the ith sensor and source parameters $X = \{x_0, y_0, z_0, t_0\}^T$; (x_0, y_0, z_0) are the MS source coordinates, and t_0 is the seismogenic time; (x_i, y_i, z_i) are the coordinates of the ith sensor, and $f_i(X)$ is the theoretical arrival time of the ith sensor.

The nonlinear function $f_i(X)$ is expanded by the Taylor series in the neighborhood of the initial solution X^0, and the terms above quadratic are omitted:

$$f_i(X) \approx f_i(X^0) + f_i^{'}(X^0)\delta X \tag{3}$$

where $\delta X = \{\delta x_0, \delta y_0, \delta z_0, \delta t_0\}^T$ is the source parameter correction.

We substitute **Equation 3** into **Equation 1**:

$$F(X) \approx \left(t_i - f_i(X^0) - f_i^{'}(X^0)\delta X\right)^2 \tag{4}$$

From the extreme value theory of multivariate function, we let $\partial F(X)/\partial \delta X = 0$:

$$\frac{\partial F(X)}{\partial \delta X} \approx - f_i^{'}(X^0)^T \left[t_i - f_i(X^0) - f_i^{'}(X^0)\delta X\right] = 0 \tag{5}$$

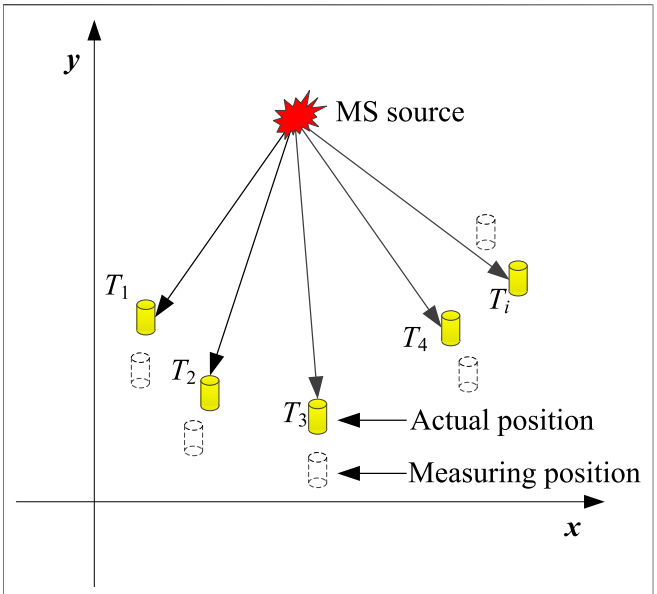


FIGURE 1 | Schematic diagram of the source location with sensor coordinate error.

We let $A = f_i^{'}(X^0)$, which is the partial derivative matrix, and $b = t_i - f_i(X^0)$, which is the data residual vector. Then, the linearized inversion equations in the sense of least squares are

$$A\delta X = b \tag{6}$$

where the coefficient matrix $A \in R^{n\times4}$, and $n \geq 4$. Solution vector $\delta X \in R^4$, and n is the number of triggering sensors.

The expression of coefficient matrix A is

$$A = \begin{pmatrix} \frac{\partial f_1(X)}{\partial x_0} & \frac{\partial f_1(X)}{\partial y_0} & \frac{\partial f_1(X)}{\partial z_0} & 1 \\ \vdots & \vdots & \vdots & \vdots \\ \frac{\partial f_n(X)}{\partial x_0} & \frac{\partial f_n(X)}{\partial y_0} & \frac{\partial f_n(X)}{\partial z_0} & 1 \end{pmatrix} \tag{7}$$

We let $X^{k+1} = X^k + \delta X$, which is the location solution of the MS source in the k+1-th iteration, and X^k is the kth iteration solution.

Location Error Analysis

After the MS monitoring system is arranged, the sensor coordinates need to be measured. During the measurement, the sensor coordinates inevitably have errors, as shown in **Figure 1** where T_i represents the ith sensor. The arrival time information is received by the sensor in the actual position. Therefore, when the sensor coordinates and the arrival time information do not match, systematic errors will arise.

The coordinate error of the sensor is mainly reflected in the coefficient matrix A. The error of the coefficient matrix A is δA, and the location error is $\Delta\delta X$. Then (Li et al., 2008),

$$(A + \delta A)(\delta X + \Delta\delta X) = b \tag{8}$$

We subtract **Equation 6** from **Equation 8**:

$$(A + \delta A)\Delta\delta X = -\delta A\delta X \tag{9}$$

$$\Delta\delta X = -\left(I + A^{-1}\delta A\right)^{-1}A^{-1}\delta A\delta X \tag{10}$$

The norm of **Equation 10** is obtained as follows:

$$\frac{\|\Delta\delta X\|}{\|\delta X\|} \leq \frac{\|A^{-1}\| \cdot \|\delta A\|}{1 - \|A^{-1}\| \cdot \|\delta A\|} = \frac{\|A^{-1}\| \cdot \|A\| \frac{\|\delta A\|}{\|A\|}}{1 - \|A^{-1}\| \cdot \|A\| \frac{\|\delta A\|}{\|A\|}} \tag{11}$$

Equation 11 shows that as the sensor coordinate error increases, the coefficient matrix error $\|\delta A\|$ increases, and the location error $\|\Delta\delta X\|$ increases accordingly. The condition number of the coefficient matrix $cond(A) = \|A^{-1}\| \cdot \|A\|$, which is related to the sensor array and the position of the MS source, reflects the sensitivity of the location solution to the original data. Therefore, the location error is proportional to the sensor coordinate error for the determined sensor array and source position. To control the systematic error of the MS source location in practical engineering, it is necessary to study the influence of the sensor coordinate error on the MS source location.

INFLUENCE EVALUATION OF THE SENSOR COORDINATE ERROR ON THE MICROSEISMIC SOURCE LOCATION

Sensor Array Center

For the sensor array arranged at the vertex of the regular geometry, the center of the array is the center of the regular geometry. For example, the center of the cube array is the center point of the cube, and the center of the spherical array is the center point of the sphere. However, the sensor arrangement in actual engineering is usually presented as an array in the form of irregular geometry, whose array center is often difficult to determine, so it is urgent to study the center position of the irregular sensor array.

Kijko (1977a), Kijko (1977b) proposed an objective function for evaluating the optimal layout of the sensor array based on the D-optimal design theory. After that, Gong et al. (2010) established the expression of the covariance matrix based on the D-optimal design theory after considering the influence of the P-wave velocity error and the P-wave arrival time error:

$$C_X(X) = \left(A^T W A\right)^{-1} \tag{12}$$

The diagonal elements in the diagonal matrix W can be expressed as:

$$W_{i,i} = \frac{1}{\left(\frac{\partial f_i(X)}{\partial v}\right)^2 \sigma_v^2 + \sigma_t^2} \tag{13}$$

where σ_v and σ_t are the variances of the P-wave velocity and P-wave arrival time, respectively, and v is the P-wave velocity.

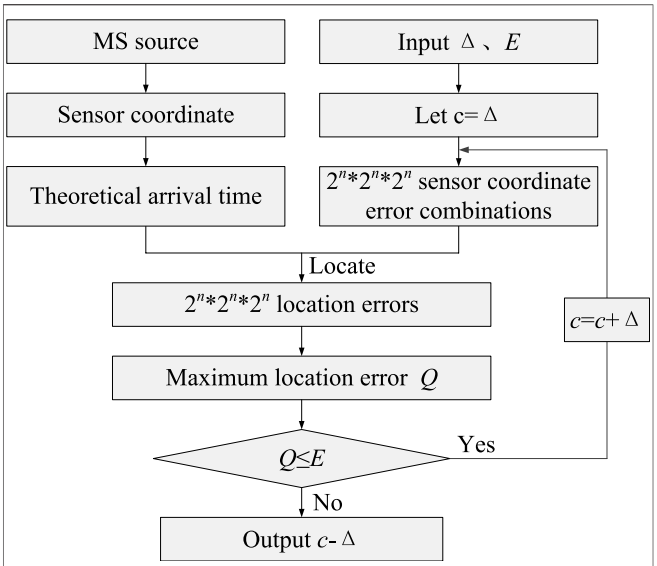


FIGURE 2 | Calculation method of the sensor coordinate error threshold.

The geometric significance of the covariance matrix $C_X(X)$ is described by the confidence ellipsoid, and the characteristic value of $C_X(X)$ is the length of the principal axis of the ellipsoid. According to the D-optimal design theory, the volume of the ellipsoid is proportional to the determinant of the covariance matrix $\det[C_X(X)]$. The smaller the volume of the ellipsoid is, the more concentrated the distribution of the source parameters and the more accurate the location results. Therefore, the center of the sensor array is defined as the position where the determinant $\det[C_X(X)]$ of the covariance matrix is minimal.

Sensor Coordinate Error Threshold

The larger the sensor coordinate error is, the larger the location error of the MS source. To reduce the systematic error of the MS source location and guide the measurement of sensor coordinates, it is necessary to propose the corresponding sensor coordinate error threshold under the MS source location accuracy required by the project. Therefore, a calculation method of the sensor coordinate error threshold is proposed for an MS source. The flow chart is shown in **Figure 2**, and the specific steps are as follows:

1) The coordinates of the sensor are given, and the sensor coordinate error c = Δ, and the step length is Δ. The MS source location error is E, and the number of sensors is n.
2) For an MS source in the monitoring area, the theoretical times of the sensor are calculated based on the sensor coordinates.
3) It is assumed that there are errors in the x, y, and z directions of the sensor coordinates, and the error value can be taken as c or $-c$. Therefore, the number of coordinate error combinations in the x, y, and z directions is 2^n, so the number of coordinate error combinations of the whole sensor array is $2^n \times 2^n \times 2^n$.
4) The coordinates of each sensor are added to the corresponding coordinate error, and localization is carried out in combination with the theoretical arrival time of the sensor. The $2^n \times 2^n \times 2^n$ location results are obtained, and the maximum value of the location error is obtained by comparison, which is set as Q.
5) When $Q \le E$, we let $c = c+\Delta$ and proceed to step 3). When $Q > E$, the calculation is stopped, and c-Δ is the sensor coordinate error threshold of the MS source.

Since the coordinate errors of each sensor are different, it is difficult to make the coordinate errors of all sensors equal to the sensor coordinate error threshold, so the calculated sensor coordinate error threshold is an upper limit value. The sensor coordinate error threshold solved is not less than the coordinate errors of all the sensor. Therefore, the sensor coordinate error threshold is a value with high safety factor.

In the above method, there are $2^n \times 2^n \times 2^n$ sensor coordinate error combinations for each increased step length Δ and corresponding $2^n \times 2^n \times 2^n$ location times. When the number of the sensors n is small, the calculation amount is small. However, as the number of sensors n increases, the calculation amount increases exponentially. Therefore, it is necessary to simplify steps 3) and 4) in the above method. The coordinate errors of the whole sensor array in the x, y, and z directions are calculated separately, and the coordinate errors of n sensors in the x, y, and z directions are all 2^n. Taking the sensor coordinate error in the x direction and no coordinate error in the y and z directions as an example, the sensor coordinate error combinations in the x direction are obtained when the location error is the largest, which is denoted as x_a. Similarly, the corresponding sensor coordinate error combinations in the y and z directions are y_b and z_c, respectively. The influence of the sensor coordinate errors in each direction on the MS source location can be superimposed. Therefore, for the whole sensor array, when the coordinate error combinations in the x, y, and z directions are x_a, y_b, and z_c, respectively, the calculated location error is the maximum value in the $2^n \times 2^n \times 2^n$ location results. Therefore, the number of localizations is simplified from $2^n \times 2^n \times 2^n$ to $3 \times 2^n+1$, and the amount of calculation is greatly reduced.

Comprehensive Evaluation Index

In the same monitoring area, each sensor has a different influence on the MS source location. Therefore, it is necessary to evaluate the influence degree of different sensors on the MS source location. For an MS source in the monitoring area, when calculating coordinate error threshold of the sensor based on calculation method of the sensor coordinate error threshold, it is assumed that one sensor in the array has a coordinate error in a normal distribution and the other sensors have no coordinate error. Accordingly, steps 3) and 4) in *Sensor Coordinate Error Threshold* subsection are modified as follow:

3) The sensor coordinate errors in the x, y, and z directions follow the same normal distribution, respectively, i.e., $x \sim N(\hat{x},c)$, $y \sim N(\hat{y},c)$, and $z \sim N(\hat{z},c)$. The sample number of normal distribution is set to N_m.
4) The coordinates of each sensor are added to the corresponding coordinate error, and localization is carried out in combination with the theoretical arrival time of the

TABLE 1 | Sensor coordinates.

Sensor Number	Coordinate/m			Sensor Type
	x	*y*	*z*	
101	1599.54	8771.51	−245.77	Mono-component
102	1688.85	8749.96	−226.38	Mono-component
103	1775.20	8690.28	−230.48	Mono-component
104	1818.63	8743.12	−227.06	Three-component
105	1912.76	8750.27	−244.76	Mono-component
106	1892.18	8699.04	−230.23	Mono-component
201	1956.15	8646.69	−235.43	Mono-component
202	1965.26	8737.80	−218.34	Mono-component
203	2075.01	8675.53	−229.89	Mono-component
204	2020.12	8567.80	−221.69	Mono-component
205	2057.23	8526.09	−231.02	Mono-component
206	2138.42	8693.26	−230.23	Three-component

sensor. The location error of N_m samples are obtained, and its average value is set as Q.

Similarly, the coordinate error thresholds of other sensors can also be obtained. Then, the normalization transformation is performed on the coordinate error thresholds of all sensors, and the formula is as follows:

$$x_i^* = \frac{x_{\max} - x_i}{x_{\max} - x_{\min}} \tag{14}$$

where x_i is the coordinate error threshold of the ith sensor and x_i^* is the normalization result of x_i, which is recorded as the evaluation index of the ith sensor. In addition, x_{max} and x_{min} are the maximum and minimum coordinate error thresholds of all sensors, respectively.

It is necessary to comprehensively evaluate the influence of the sensor coordinate error on the MS source location for the whole monitoring area Ω. Therefore, the monitoring area is meshed, where each grid point is taken as an MS source, and the number of MS sources is M. The evaluation indexes of all MS sources are comprehensively analyzed, and the comprehensive evaluation indexes of the *ith* sensor in the monitoring area Ω are as follows:

$$\overline{x_i^*} = \frac{\sum_{j=1}^{M} x_{ij}^*}{M} \tag{15}$$

where x_{ij}^* is the evaluation index of the *ith* sensor in the jth MS source and $\overline{x_i^*}$ is the comprehensive evaluation index of the *ith* sensor in the whole monitoring area.

The larger the comprehensive evaluation index $\overline{x_i^*}$ is, the greater the influence of the *ith* sensor coordinate error on the MS source location in the monitoring area.

FIELD APPLICATIONS

The workers of the Beiminghe Iron Mine in Hebei Province have found abnormal phenomena in the mining area many times since 2017, mainly located in the substation on the -122 m level and the excavation roadway at the -185 m level. It is preliminarily inferred that these phenomena are related to illegal mining. Therefore, to protect mineral resources and production safety, the mine has introduced a new generation of SinoSeism (SSS) MS monitoring systems jointly developed by the Institute of Rock and Soil Mechanics, Chinese Academy of Sciences, and Hubei Seaquake Technology Co., Ltd. Due to the limitation of site conditions, a total of 10 mono-component sensors and 2 three-component sensors are arranged at the roadways of the -230 m level. The sensor coordinates initially measured are shown in **Table 1**, and the plane diagram of the sensor layout is shown in **Figure 3**.

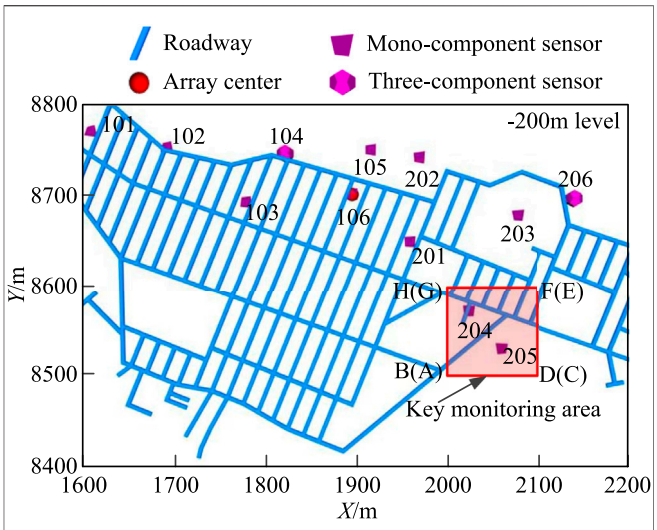


FIGURE 3 | lane diagram of the sensor layout and -200 m level in the mining area.

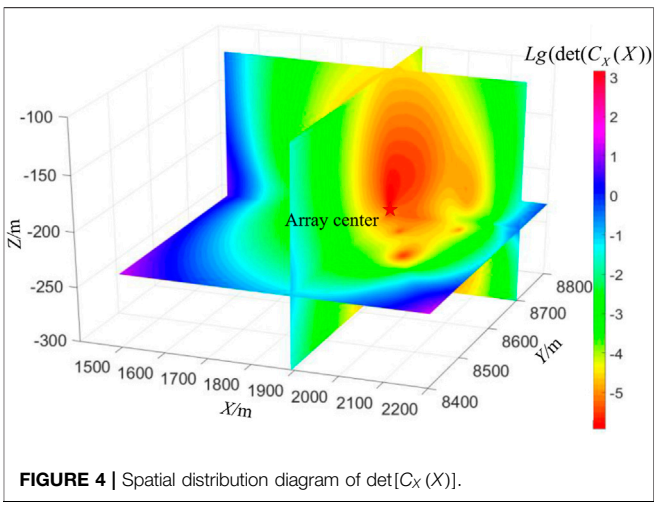


FIGURE 4 | Spatial distribution diagram of det[$C_X(X)$].

Sensor Array Center in the Mine

Based on the sensor coordinates of the initial measurement, the determinant of the covariance matrix is calculated by **Equation 12**, and its spatial distribution diagram is shown in **Figure 4**. The expected velocity of the P-wave is 5222 m/s, the variance in the velocity is 50 m/s, and the P-wave arrival time error is 0.005 s. **Figure 4** shows that there is a minimum determinant of the

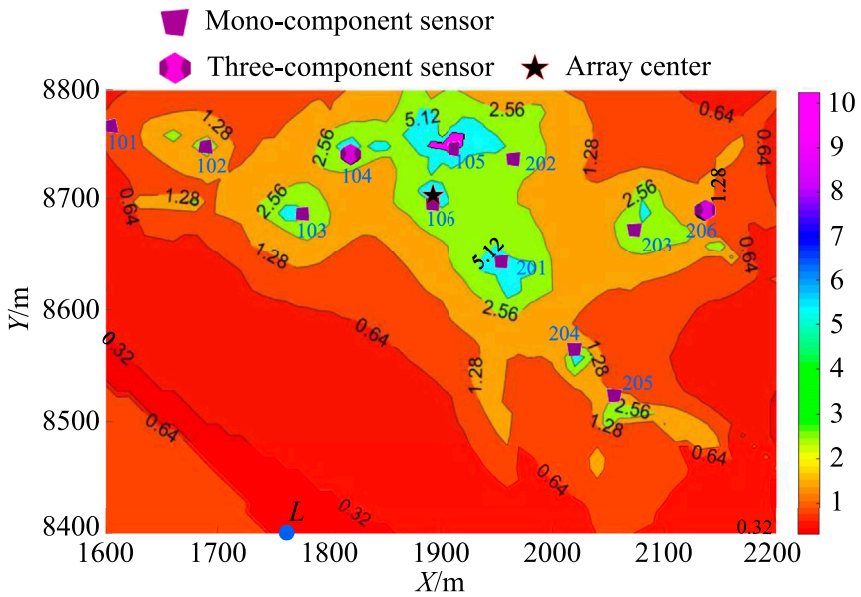


FIGURE 5 | Contour diagram of the sensor coordinate error threshold at the -200 m level.

covariance matrix in the space, which is the array center. The farther the MS source is from the center of the sensor array, the larger the determinant of the covariance matrix $\det[C_X(X)]$. To find the position of the sensor array center, the particle swarm optimization (PSO) algorithm is used to search for the minimum value of $\det[C_X(X)]$. The PSO algorithm parameters (Feng et al., 2017) are set to: the learning factor $c_1 = c_2 = 2$, inertial weight $w = 0.8$, population number N_{pop} = 4,000, flying times N_g = 5000, and fitness conditions $e = 1.0 \times 10^{-10}$. The range of coordinates is $x \in (1500, 2200)$, $y \in (8400, 8800)$, and $z \in (-250, -150)$; and the unit is m. It can be obtained by calculation that when $\det[C_X(X)]$ is the smallest, the coordinates of the array center are (1892.10, 8698.89, -232.82), and the unit is m.

Sensor Coordinate Error Threshold and Comprehensive Evaluation Index in the Monitoring Area

The coordinate range of the -200 m level in the Beiminghe Iron Mine is set to $x \in (1600, 2000)$, y $\in (8400, 8800)$, z = -200, and the unit is m. The plane diagram of the monitoring area at the -200 m level is shown in **Figure 3**. The monitoring area at the -200 m level meshes, and the grid spacing in the x and y directions is 5 m. The MS source location accuracy is set to 15 m, and the calculation method of the sensor coordinate error threshold is used to solve the sensor coordinate error threshold of the monitoring area. The contour diagram of the sensor coordinate error threshold at the -200 m level is shown in **Figure 5**. The farther the MS source is from the sensor array, the smaller the sensor coordinate error threshold. The sensor coordinate error threshold inside the array is larger than that outside the array, and the sensor coordinate error threshold decreases rapidly inside the array and slowly outside the array. The minimum value of the sensor coordinate error threshold within the -200 m level is 0.27 m, indicating that the measurement error of the sensor coordinates should not exceed 0.27 m when the MS source is in the -200 m level, and the corresponding coordinate is in the lower boundary point L (1760 m, 8400 m, -200 m). From the location relationship between the lower boundary point L and the sensor array center, it can be seen that the minimum sensor coordinate error threshold in the -200 m level is located on the boundary line farthest from the array center. Therefore, the minimum value of the sensor coordinate error threshold of the whole monitoring area can be quickly calculated through this law.

TABLE 2 | Vertex coordinates of the key monitoring area.

Vertex Number	Coordinate/m		
	x	*y*	*z*
A	2000	8500	−220
B	2000	8500	−180
C	2000	8500	−220
D	2000	8500	−180
E	2100	8600	−220
F	2100	8600	−180
G	2100	8600	−220
H	2100	8600	−180

To evaluate the influence of different sensors on the MS source location, the area near stope No. 7 is further selected as the key monitoring area. The plane diagram of the key monitoring area is shown in **Figure 3**, and the scope of the key monitoring area is shown in **Table 2**. The key monitoring area meshes, and the grid spacing in the x, y, and z directions is 5 m. The grid point is taken as the MS source and the sample number N_m of normal

TABLE 3 | Comprehensive evaluation index of each sensor.

Sensor Number	101	102	103	104	105	106
$\overline{x_i^*}$	0.27	0.42	0.26	0.06	0.63	0.28
Sensor number	201	202	203	204	205	206
$\overline{x_i^*}$	0.86	0.43	0.54	0.84	0.50	0.75

TABLE 4 | Blasting test location.

Event Number	Time	Coordinate/m		
		x	*y*	*z*
1	3 October 2018 22:29	2028.46	8574.56	−198
2	5 October 2018 22:39	2032.51	8573.11	−198
3	5 October 2018 22:49	2073.15	8579.18	−198
4	6 October 2018 14:29	2087.38	8566.32	−198
5	6 October 2018 22:24	2034.44	8572.42	−198

distribution is set to 500. Then, the comprehensive evaluation index of each sensor in the key monitoring area is calculated through **Equation 15**. The comprehensive evaluation index of each sensor is shown in **Table 3**.

Table 3 shows that in the key monitoring areas, the number of sensors whose coordinate error affects the MS source location from large to small is 201, 204, 206, 105, 203, 205, 202, 102, 106, 101, 103 and 104. Therefore, in sensor coordinates measurement, the sensor with a large comprehensive evaluation index should be focused on to improve the measurement accuracy of their sensor coordinates.

Comparison of the MS Location Results Before and After Remeasurement of Sensor Coordinates

According to the above calculation results, the coordinate errors of sensors 201, 204, 206, and 105, whose comprehensive evaluation index exceeds 0.6, have the greatest influence on the MS source location in key monitoring areas. Therefore, it is necessary to recheck the coordinate accuracy of the four sensors. The coordinate accuracy of sensors No. 204, 206, and 105 is within the sensor coordinate error threshold through remeasurement by the field staff. There is a fault fracture zone in the area near sensor No. 201, whose position and crushing degree are not detected in time, and hole collapse occurs in the borehole. Therefore, sensor No. 201 is not installed at the bottom of the borehole. Due to the permanent grouting installation, the coordinates of sensor No. 201 in **Table 1** inevitably have measurement errors and cannot be remeasured. When the blasting events occur in the key monitoring area, the measurement error of sensor No. 201 severely affects the location accuracy of the MS source. Therefore, when the number of trigger sensors meets the minimum number of sensors required by the location method, sensor No. 201 can be discarded to improve the location accuracy of the MS source.

Five blasting tests are carried out in the key monitoring area. The locations of the test points are shown in **Table 4**, and the arrival time information of each test events is shown in **Table 5**. Since the blasting test area is far from sensors 101 and 102, these two sensors do not receive the 5 blasting test signals. The number of triggering sensors in the five blasting tests exceeds 4, so sensor No. 201 with large measurement

TABLE 5 | Arrival time of the sensor for the blasting test event.

Sensor Number	Event No.1	Event No.2	Event No.3	Event No.4	Event No.5
101	—	—	—	—	—
102	—	—	—	—	—
103	6.75161	—	2.81036	3.68136	1.22361
104	6.75311	—	2.82411	3.68286	1.22586
105	6.74286	—	2.81211	3.66911	1.21736
106	6.73611	—	2.80836	3.66436	1.20836
201	6.72136	4.24761	2.77761	3.65011	1.19311
202	6.73161	4.25811	2.78786	3.65736	1.20336
203	6.71936	4.24486	2.77486	3.63936	1.19011
204	6.70336	4.22936	2.75961	3.63261	1.17486
205	6.71086	4.23561	2.76611	3.63261	1.18086
206	6.72886	4.25461	2.78436	3.64561	1.19936

TABLE 6 | Comparison of location results before and after sensor coordinate adjustment.

Test Events	Location Results before Sensor Coordinate Adjustment/m				Location Results after Sensor Coordinate Adjustment/m			
	x	*y*	*z*	D_{error}	*x*	*y*	*z*	D_{error}
1	2037.91	8574.23	−199.05	9.52	2037.17	8575.16	−201.67	9.47
2	2041.12	8575.41	−205.77	11.83	2036.84	8575.55	−201.26	5.94
3	2071.03	8562.03	−210.75	21.17	2045.50	8570.04	−198.78	17.09
4	2087.67	8572.98	−190.92	17.30	2085.13	8575.12	−198.02	9.08
5	2045.62	8569.90	−198.40	11.46	2045.50	8570.04	−198.78	11.33

D_{error}—*spatial error*.

errors should be discarded during localization. Based on the original sensor coordinates (as shown in **Table 1**), the location results of the five blasting test events are shown in **Table 6**. After removing sensor 201, the location results of the five blasting test events are shown in **Table 6**. After the sensor coordinates are remeasured, the location errors of the five blasting test events are reduced by 0.05 m, 5.89 m, 4.08 m, 8.22 m, and 0.13 m. The average location error is reduced by 3.67 m, and the location accuracy is improved by 25.74%.

The accuracy range of the sensor coordinates can be obtained based on the calculation method of the sensor coordinate error threshold to guide the on-site sensor coordinate measurement. The comprehensive evaluation index of sensor coordinates is used to evaluate the influence of different sensor coordinates on the MS source location and accurately identify the sensors that have a greater impact on the MS source location. Finally, sensors with large coordinate measurement errors are focused on to improve the location accuracy of the MS sources.

CONCLUSION

The influence of the sensor coordinate error on the MS source location is studied, and the following conclusions can be drawn:

1) The influence of the sensor coordinate error on the location error is theoretically analyzed, and it is concluded that the location error is proportional to the sensor coordinate error.
2) The sensor array center is obtained based on D-optimal design theory. A calculation method for the sensor coordinate error threshold is proposed to obtain the sensor coordinate error threshold of different MS sources.
3) A comprehensive evaluation index of the sensor is proposed to evaluate the influence of different sensors in the monitoring area on the MS source location. The larger the comprehensive evaluation index is, the greater the influence of the sensor coordinate error on the MS source location and the higher the required accuracy of the sensor coordinate.
4) The distribution of the sensor coordinate error threshold at the -200 m level shows that the farther the source is from the sensor array, the smaller the sensor coordinate error threshold. The sensor coordinate error threshold in the array is larger than that outside the array, and the sensor coordinate error threshold decreases rapidly in the array and slowly outside the array.
5) The application results in the key monitoring areas of the Beiminghe Iron Mine show that the average location accuracy of blasting test events is improved by 25.74% by remeasuring the coordinates of sensors whose comprehensive evaluation index exceeds 6 and discarding sensors with large measurement error.

DATA AVAILABILITY STATEMENT

The raw data supporting the conclusions of this article will be made available by the authors, without undue reservation.

AUTHOR CONTRIBUTIONS

TL: Conceptualization, Resources, Methodology, Writing-Original draft preparation. B-RC: Visualization, Writing—Review and Editing. QW: Visualization, Investigation. X-HZ: Supervision. XW and M-XX: Validation.

FUNDING

The authors are grateful for the financial support from the National Natural Science Foundation of China (Grant No. 42077263) and the China Railway Corporation Science and Technology Research and Development Project (Grant No. P2019G001).

ACKNOWLEDGMENTS

We would like to thank the staff at the Beiminghe Iron Mine of Minmetals Hanxing Mining Co., Ltd., in Hebei Province for their support and assistance in the field monitoring and data acquisition.

REFERENCES

Bai, C.-Y., and Kennett, B. L. N. (2000). Automatic Phase-Detection and Identification by Full Use of a Single Three-Component Broadband Seismogram. *Bull. Seismological Soc. America* 90 (1), 187–198. doi:10.1785/0119990070

Boschetti, F., Dentith, M. D., and List, R. D. (1996). A Fractal-Based Algorithm for Detecting First Arrivals on Seismic Traces. *Geophysics* 61 (4), 1095–1102. doi:10.1190/1.1444030

Cao, S., and Greenhalgh, S. (1993). Calculation of the Seismic First-Break Time Field and its ray Path Distribution Using a Minimum Traveltime Tree Algorithm. *Geophys. J. Int.* 114 (3), 593–600. doi:10.1111/j.1365-246x.1993.tb06989.x

Chen, B. R., Feng, X. T., Li, S. L., Yuan, J. P., and Xu, S. C. (2009). Microseism Source Location with Hierarchical Strategy Based on Particle Swarm Optimization. *Chin. J Rock Mech Eng* 28 (4), 740–749. doi:10.3321/j.issn:1000-6915.2009.04.012

Chen, B. R., Li, T., Zhu, X. H., Wei, F. B., Wang, X., and Xie, M. X. (2021). Microseismic Source Location Method Based on a Velocity Model Database and Statistical Analysis. *Arab J. Geosci.* 14 (19), 2017. doi:10.1007/s12517-021-08311-9

Crosson, R. S., and Peters, D. C. (1974). "Estimates of Miner Location Accuracy: Error Analysis in Seismic Location Procedures for Trapped Miners," in *Seismic Detection and Location of Isolated Miners*. Washington, D.C.: United States Department of the Interior - Bureau of Mines.

Dai, F., Li, B., Xu, N., Fan, Y., and Zhang, C. (2016). Deformation Forecasting and Stability Analysis of Large-Scale Underground Powerhouse Caverns from

Microseismic Monitoring. *Int. J. Rock Mech. Min Sci. [Internet]* 86, 269–281. doi:10.1016/j.ijrmms.2016.05.001

Feng, G.-L., Feng, X.-T., Chen, B.-R., Xiao, Y.-X., and Yu, Y. (2015). A Microseismic Method for Dynamic Warning of Rockburst Development Processes in Tunnels. *Rock Mech. Rock Eng.* 48 (5), 2061–2076. doi:10.1007/s00603-014-0689-3

Feng, G.-L., Feng, X.-T., Chen, B.-R., and Xiao, Y.-X. (2017). Performance and Feasibility Analysis of Two Microseismic Location Methods Used in Tunnel Engineering. *Tunnelling Underground Space Technol.* 63, 183–193. doi:10.1016/j.tust.2017.01.006

Feng, G.-L., Chen, B.-R., Xiao, Y.-X., Jiang, Q., Li, P.-X., Zheng, H., et al. (2022). Microseismic Characteristics of Rockburst Development in Deep TBM Tunnels with Alternating Soft-Hard Strata and Application to Rockburst Warning: A Case Study of the Neelum-Jhelum Hydropower Project. *Tunnelling Underground Space Technol.* 122, 104398. doi:10.1016/j.tust.2022.104398

Geiger, L. (1912). Probability Method for the Determination of Earthquake Epicenters from Arrival Time Only. *Bull. Saint Louis Univ.* 8, 60–71.

Gong, S. Y., Dou, L. M., Cao, A. Y., He, H., Du, T. T., and Jiang, H. (2010). Study on Optimal Configuration of Seismological Observation Network for Coal Mine. *Chin. J Geophys* 53 (2), 457–465. doi:10.3969/j.issn.0001-5733.2010.02.025

Kennett, B. L. N., and Sambridge, M. S. (1992). Earthquake Location-Genetic Algorithms for Teleseisms. *Phys. Earth Planet. Inter.* 75 (1–3), 103–110.

Kijko, A. (1977a). An Algorithm for the Optimum Distribution of a Regional Seismic Network-I. *Pure Appl. Geophys.* 115 (4), 999–1009. doi:10.1007/bf00881222

Kijko, A. (1977b). An Algorithm for the Optimum Distribution of a Regional Seismic Network - II. An Analysis of the Accuracy of Location of Local Earthquakes Depending on the Number of Seismic Stations. *Pure Appl. Geophys.* 115 (4), 1011–1021. doi:10.1007/bf00881223

Kovavisaruch, L., and Ho, K. C. (2005). "Modified Taylor-Series Method for Source and Receiver Localization Using TDOA Measurements with Erroneous Receiver Positions," in Proc - IEEE Int Symp Circuits Syst., Kobe, Japan, 25 July 2005, 1, 2295–2298

Leśniak, A., and Isakow, Z. (2009). Space-time Clustering of Seismic Events and hazard Assessment in the Zabrze-Bielszowice Coal Mine, Poland. *Int. J. Rock Mech. Min Sci.* 46 (5), 918–928. doi:10.1016/j.ijrmms.2008.12.003

Li, Q. Y., Wang, N. C., and Yi, D. Y. (2008). *Numerical Analysis*. 5th Edition. Beijing: Tsinghua University Press.

Li, N., Ge, M., and Wang, E. (2014a). Two Types of Multiple Solutions for Microseismic Source Location Based on Arrival-Time-Difference Approach. *Nat. Hazards* 73 (2), 829–847. doi:10.1007/s11069-014-1110-y

Li, N., Wang, E., Ge, M., and Sun, Z. (2014b). A Nonlinear Microseismic Source Location Method Based on Simplex Method and its Residual Analysis. *Arab J. Geosci.* 7 (11), 4477–4486. doi:10.1007/s12517-013-1121-0

Li, N. (2014). *Study on the Mechanism and Reliability of the Key Factors of Microseismic Source Location*. Xuzhou, China: China University of Mining and Technology.

Liu, J. L., and Gao, J. (2012). Hypocenter Location by Using Combined Method of Inglada and Geiger Algorithms. *J. Inst. Disaster Prev.* 14 (2), 54–59. doi:10.3969/j.issn.1673-8047.2012.02.010

Liu, H. F. (2007). *Linear and Non-linear Inversion Methods Research on Direct Current IP Measurements*. Changsha, China: Central South University.

Mooney, W. D., Laske, G., and Masters, T. G. (1998). Crust 5.1: A Global Crustal Model at 5°×5°. *J. Geophys. Res.* 103 (1), 727–747. doi:10.1029/97jb02122

Paige, C. C., and Saunders, M. A. (1982). Algorithm 583: LSQR: Sparse Linear Equations and Least Squares Problems. *ACM Trans. Math. Softw.* 8 (2), 195–209. doi:10.1145/355993.356000

Rockah, Y., and Schultheiss, P. (1987). Array Shape Calibration Using Sources in Unknown Locations--Part II: Near-Field Sources and Estimator Implementation. *IEEE Trans. Acoust. Speech, Signal. Process.* 35 (6), 724–735. doi:10.1109/tassp.1987.1165222

Saragiotis, C. D., Hadjileontiadis, L. J., and Panas, S. M. (2002). PAI-S/K: A Robust Automatic Seismic P Phase Arrival Identification Scheme. *IEEE Trans. Geosci. Remote Sensing* 40 (6), 1395–1404. doi:10.1109/tgrs.2002.800438

Sun, M., and Ho, K. C. (2011). An Asymptotically Efficient Estimator for TDOA and FDOA Positioning of Multiple Disjoint Sources in the Presence of Sensor Location Uncertainties. *IEEE Trans. Signal. Process.* 59 (7), 3434–3440. doi:10.1109/tsp.2011.2131135

Wang, Y., and Ho, K. C. (2013). TDOA Source Localization in the Presence of Synchronization Clock Bias and Sensor Position Errors. *IEEE Trans. Signal. Process.* 61 (18), 4532–4544. doi:10.1109/tsp.2013.2271750

Wei, H. W., Peng, R., Wan, Q., Chen, Z. X., and Ye, S. F. (2010). Multidimensional Scaling Analysis for Passive Moving Target Localization with TDOA and FDOA Measurements. *IEEE Trans. Signal. Process.* 58 (3 PART 2), 1677–1688. doi:10.1109/tsp.2009.2037666

Xu, N. W., Tang, C. A., Chun, S., Liang, Z. Z., Yang, J. Y., and Zou, Y. Y. (2010). Microseismic Monitoring System Establishment and its Engineering Applications to Left Bank Slope of Jinping I Hydropower Station. *Chin. J Rock Mech Eng* 29 (5), 915–925.

Yang, L., and Ho, K. C. (2009). An Approximately Efficient TDOA Localization Algorithm in Closed-Form for Locating Multiple Disjoint Sources with Erroneous Sensor Positions. *IEEE Trans. Signal. Process.* 57 (12), 4598–4615. doi:10.1109/tsp.2009.2027765

Yu, Y., Feng, G.-L., Xu, C.-J., Chen, B.-R., Geng, D.-X., and Zhu, B.-t. (2022). Quantitative Threshold of Energy Fractal Dimension for Immediate Rock Burst Warning in Deep Tunnel: A Case Study. *Lithosphere* 2021, 1699273. doi:10.2113/2022/1699273

Zhang, X. S., Cai, W., Yang, Z. Y., Wang, B., and Hou, Y. G. (2018). The Analysis Influence of Positioning Error on Global Navigation Short Baseline Satellite System Orientating. *Sci. Technol. Eng.* 18 (35), 157–161. doi:10.3969/j.issn.1671-1815.2018.35.026

Zhang, J. C., Wu, B. C., Wang, F., Shi, S. Z., Liu, J. J., Wang, M. X., et al. (2022). Experimental Research of Compound Monitoring on Multiple Temporary Blocking Refracturing for Long-Section Horizontal Wells. *Front. Earth Sci.* 9, 1–12. doi:10.3389/feart.2021.760390

Conflict of Interest: M-XX was employed by the Company Beiminghe Iron Mine of Minmetals Hanxing Mining Co., Ltd.

The remaining authors declare that the research was conducted in the absence of any commercial or financial relationships that could be construed as a potential conflict of interest.

Publisher's Note: All claims expressed in this article are solely those of the authors and do not necessarily represent those of their affiliated organizations, or those of the publisher, the editors and the reviewers. Any product that may be evaluated in this article, or claim that may be made by its manufacturer, is not guaranteed or endorsed by the publisher.

Copyright © 2022 Li, Chen, Wang, Zhu, Wang and Xie. This is an open-access article distributed under the terms of the Creative Commons Attribution License (CC BY). The use, distribution or reproduction in other forums is permitted, provided the original author(s) and the copyright owner(s) are credited and that the original publication in this journal is cited, in accordance with accepted academic practice. No use, distribution or reproduction is permitted which does not comply with these terms.

frontiers in Earth Science

ORIGINAL RESEARCH
published: 30 March 2022
doi: 10.3389/feart.2022.851285

Force-Chain-Based Analysis of Factors Influencing Pressure Arch Around Tunnel Under Earthquake

Sun Changxin, Zhang Yumin*, Guan Lei, Zhang Liye and Peng Jiafeng*

College of Geosciences and Engineering, North China University of Water Resources and Electric Power, Zhengzhou, China

The force chain method is a powerful tool to analyze the pressure arch of a tunnel, which has important influence on the seismic stability of tunnel structures. The force distribution around the tunnel before and after an earthquake was observed with numerical simulation and shaking table test, and then some parameters related to the pressure arch around the tunnel were analyzed. The discrete element method software PFC was used to numerically simulate the variation of shape and height of pressure arch with tunnel depth before and after an earthquake. The effect of tunnel depth, span, section shape, lining stiffness, seismic spectrum, and seismic amplitude on the shape and height of pressure arch was numerically simulated. The numerical results show that the tunnel depth, span, section shape, and seismic amplitude have great effect on the pressure arch shape, while the lining stiffness and seismic spectrum has little effect on the pressure arch shape. In addition, the shaking table tests were conducted to observe the pressure arch shape before and after an earthquake, and the experimental results were applied to verify the numerical simulation results.

Keywords: force chain, pressure arch, earthquake action, shaking table test, influential factors

OPEN ACCESS

Edited by:
Guang-Liang Feng,
Institute of Rock and Soil Mechanics (CAS), China

Reviewed by:
Li Liang Ying,
Lanzhou Jiaotong University, China
Qinglai Fan,
Ludong University, China
Shizhong Liu,
Taiyuan University of Science and Technology, China
Shuqian Duan,
Zhengzhou University, China

****Correspondence:***
Sun Changxin
schx80@sohu.com
Zhang Yumin
zhangyumin@ncwu.edu.cn

Specialty section:
This article was submitted to Geohazards and Georisks, a section of the journal Frontiers in Earth Science

Received: *09 January 2022*
Accepted: *18 February 2022*
Published: *30 March 2022*

Citation:
Changxin S, Yumin Z, Lei G, Liye Z and Jiafeng P (2022) Force-Chain-Based Analysis of Factors Influencing Pressure Arch Around Tunnel Under Earthquake. Front. Earth Sci. 10:851285. doi: 10.3389/feart.2022.851285

INTRODUCTION

A great number of tunnels are planned, are under construction, and have been built all over the world (Feng et al., 2015; Feng et al., 2022; Yu et al., 2022). For example, there are 20 tunnels that are greater than 15 km long and 12 potential focal regions along the under-construction Sichuan–Tibet Railway in China, and the seismic intensity is partly up to 0.3 g (Peng et al., 2020). Therefore, seismic tunnel disasters are increasingly observed, and, for example, 40 of 59 investigated tunnels suffered from the 2008 Wenchuan earthquake in China, among which 19 tunnels were seriously damaged (Zang, 2017). As a consequence, much attention is paid to the seismic stability of tunnel structures. The pressure arch, which exists widely in most tunnels, has a direct effect on the bearing capacity of tunnels.

Much achievement has been obtained in pressure arch research. In 1884, Roberst firstly provided the concept of "granary effect," namely, the "pressure arch effect," by observing the phenomenon in which the pressure at the granary bottom will be constant when the grain accumulation height is greater than a given value. Terzaghi testified the existence of pressure arch with the trap-door experiment (Terzaghi, 1936). Inst Min Eng (IME) considered that the pressure arch resulted from the stress redistribution and exists at every excavation cavern (IEM, 1936). Handy described the pressure arch with the path of minor principal stress which is approximately like a catenary (Handy, 1985). Tien analyzed the arching mechanism in terms of the micro-level by photo-elasticity modeling (Tien, 2001). Song Yuxiang numerically simulated the formation process of pressure arches in terms of

principal stress around tunnels and analyzed various factors influencing the pressure arch (Song et al., 2017). Zeng Xinping used numerical simulation to explore the formation mechanism of deeply buried tunnels and the distribution of vertical Earth pressure (Zeng, 2018). Shang Bin et al. numerically simulated the internal and external boundaries of pressure arches and provided the formula for the surrounding rock pressure with linear regression analysis (Shang et al., 2020). In addition, they considered that the surrounding rock pressures are basically affected by tunnel depth H, span B, internal friction angle φ, and rock unit weight γ.

The pressure arch is traditionally considered as a shield for the tunnel, and hence the evolution of the pressure arch under the earthquake may have great effect on the seismic stability of the tunnel. However, little attention has been paid to the research in the pressure arch under earthquakes.

After tunnel excavation, the initial stress field is disturbed, and the surrounding rock moves due to unbalanced force. When the new balance state is reached, the surrounding rock within a certain scope is in the unidirectional compression state, just like an arch, which is defined as the pressure arch. The formation and shape of the pressure arch is closely related to the microscopic motion of rock particles.

A force chain is defined as a line segment that supports a compressive force (Socolar et al., 2002), which is a powerful tool to analyze the microscopic displacement and motion of rock particles. The pressure arch may be considered to consist of one or more strong force chains, and thus the shape and stability of the pressure arch can be analyzed by the force chain method.

Many scholars have carried out in-depth research on the force chain. Dantu observed the tree-pattern structure of the force chain with photo-elasticity method (Dantu, 1957). Sanfratello et al. firstly obtained the structure of the force chain within a dense 3D granular assembly by observing the internal force chain structure with magnetic resonance elastography technique (Sanfratello et al., 2009). Oda observed the microstructure in shear band with micro-focus X-ray computed tomography and found that the local dilatation in a shear band is inevitably related to the extensive rotation of particles (Oda et al., 2004). Miao Tiande observed the contact force at the bottom of 3D ordered granular arrays jointly by the aluminum-plastic board and carbon paper techniques and found that all arrays have obvious arching effect and the force distribution depends largely on the crystal structure (Miao et al., 2007). Sun Qicheng numerically simulated the force chain pattern and stress distribution of 12,000 static sand grains by 2D discrete element method (DEM) based on strict contact theory and found that the friction coefficient of particles has great effect on the force chain behavior (Sun and Wang, 2008). Majmudar used PFC2D to analyze the tangential and normal grain-scale forces inside 2D photo-elastic disks subject to pure shear and isotropic compression (Majmudar and Behringer, 2005). Iwashita analyzed the force chain by slightly modified DEM and found that the applied stress is basically transferred by the force chain which is parallel to the principal stress, and the force chain varies with stress (Iwashita and Oda, 2000).

Therefore, it is feasible to study the shape and influential factors of a pressure arch with force chain due to its successful development.

NUMERICAL SIMULATION

The Particle Flow Code (PFC) was developed by Itasca Consulting Group, Inc., in America to analyze the mechanical properties and behavior of granular and solid materials in terms of a microscope, and PFC consists basically of variably sized rigid spherical particles. The conventional macroscopic constitutive relation and its corresponding parameters can be automatically determined in PFC, and only the geometric and mechanical parameters of rigid particles and their contact need be defined. The motion of each particle arising from the contact and body forces acting upon it is determined by Newton's second law, while the contact forces arising from the relative motion at each contact is updated by the force-displacement law. Thus, PFC may well simulate the mechanical behavior of inherently loose granular materials such as soil. In addition, PFC is especially suitable for the simulation of large deformation problems such as fracturing, and therefore it has been widely used in the tunnel and underground engineering.

The force chain pattern around the tunnel before and after an earthquake were numerically simulated by the DEM software of PFC and then was used to analyze the shape and influential factors of a pressure arch under an earthquake.

The microscopic parameters of soil and lining for numerical simulation were determined by adjusting them in a numerical triaxial model until the macroscopic behavior of the numerical model was almost identical to the experimental counterparts (Badakhshan et al., 2020; Chen et al., 2022; Wang and Zhao, 2022). Finally, the parameters were obtained, as listed in **Tables 1** and **2** (Chang-nü et al., 2021; Hu et al., 2021; Zhou et al., 2022).

The particles in PFC^{2D} are generally formed by generating non-overlapping sets of balls with the ball generate command or by distributing overlapping balls to match a specified size distribution with the ball distribute command. The two particle generation methods are greatly different from each other. In this paper, the particles were formed by the ball generate command which generates non-overlapping balls. This process stops when the number of attempts to place balls without overlap is achieved or when the target number of balls is created. By default, the ball positions and radii are drawn from uniform distributions throughout the model domain. Therefore, the set of balls is greatly affected by the state of the random-number generator. The optional range is applied to each ball upon generation, and, if the ball does not fall within the range, it is not added to the model and does not affect the stopping criteria.

Various contact models are provided in PFC^{2D}, and the linear parallel bond model, which has constant normal and shear stiffness at the contact point and permits some tension between the contact, was applied in this paper. According to the force-displacement law for the linear parallel bond model, the contact force and moment are updated by

TABLE 1 | Microscopic parameters of soil.

Min. Radius	Maximum radius	Normal contact stiffness Kn	Shear contact stiffness Ks
0.1	0.17	1e9	6.67e8
Tensile strength cb_tenf	Shear strength cb_shearf	Contact friction coefficient	Particle density
1e8	1e8	0.5	2,200

TABLE 2 | Microscopic parameters of tunnel lining.

Tensile strength cb_tenf	Shear strength cb_shearf	Normal contact stiffness Kn	Shear contact stiffness Ks	Lining density	Lining thickness
1e15	1e15	1e10	1e10	2,500	0.2

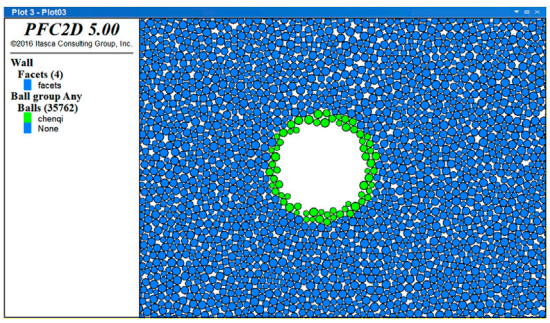


FIGURE 1 | 2D PFC model of tunnel.

$$F_c = F^l + F^d + \bar{F} \tag{1}$$

$$M_c = \bar{M} \tag{2}$$

where F_c is the contact force, F^l is the linear force, F^d is the dashpot force, $\bar{F}$ is the parallel-bond force, M_c is the contact moment, and $\bar{M}$ is the parallel-bond moment. The parallel-bond force is then resolved into a normal and shear force which are computed by

$$\bar{F}_n = \bar{F}_n + \bar{K}_n \bar{A} \Delta\delta_n \tag{3}$$

$$\bar{F}_t = \bar{F}_t - \bar{K}_t \bar{A} \Delta\delta_t \tag{4}$$

where $\bar{F}_n$ is the parallel-bond normal force, $\bar{K}_n$ is the normal stiffness, $\bar{A}$ is the contact area, $\Delta\delta_n$ is the relative normal-displacement increment, $\bar{F}_t$ is the parallel-bond shear force, $\bar{K}_t$ is the shear stiffness, and $\Delta\delta_t$ is the relative shear-displacement increment.

The balls were appropriately scaled up during model generation for the purpose of higher computation efficiency. A total of 35,762 particles were formed, and the established model is shown in **Figure 1**.

The pressure arch shapes before and after an earthquake were firstly simulated based on force chain pattern, and then the effects of tunnel depth, span, section shape, lining stiffness, seismic spectrum, and seismic amplitude on the pressure arch shape were analyzed.

Effect of Tunnel Depth

The magnitude of contact force between particles can be represented in terms of the thickness of force chain. The thicker the force chain, the larger the contact force, and vice versa (Chen-Peng, 2021; Deng et al., 2021; Wang et al., 2022). The force chain patterns of 15 and 25 m deep tunnels before and after an earthquake are shown in **Figures 2** and **3**, respectively.

Figure 2 shows that the force chain around a shallow tunnel before an earthquake is thick, with obvious pressure arch structure, indicating that the stress within the surrounding rock is large. In addition, the upper pressure arch is relatively weak in structure. When the shallow tunnel suffers from the horizontal earthquake, the force chain around the tunnel becomes thin, indicating that the stress within the surrounding rock decreases, and the lining deforms largely due to the increasing stress of lining structure. The results demonstrate that the pressure arch may be weakened to some extent when the tunnel is subject to seismic load.

Figure 3 shows that the pressure arch exists for deep tunnel before an earthquake, with strong structures at the left and right sides and weak structures above the tunnel. After the horizontal earthquake is applied, the force chain around the tunnel becomes thick, and the pressure arch expands and moves away from the tunnel, with little change in tunnel deformation. It is inferred that the seismic load may damage the original pressure arch around the deep tunnel and cause the surrounding rock to be denser. Thus, a new stronger pressure arch forms, with some change in shape and position.

Therefore, the tunnel depth has a large effect on the pressure arch under an earthquake. For a shallow tunnel, seismic load may totally or partly damage the original pressure arch, and no new pressure arch forms. For a deep tunnel, seismic load may change the shape and position of the original pressure arch, and a new stronger one forms. Because the vertical load applied on the tunnel depends largely on the height of the pressure arch above the tunnel, the heights of the pressure arch before and after an earthquake are listed in **Table 3**.

Effect of Tunnel Span

The force chain patterns of circular tunnels with diameters of 4, 8, and 12 m were numerically simulated under the same horizontal seismic acceleration, respectively, as shown in **Figure 4**.

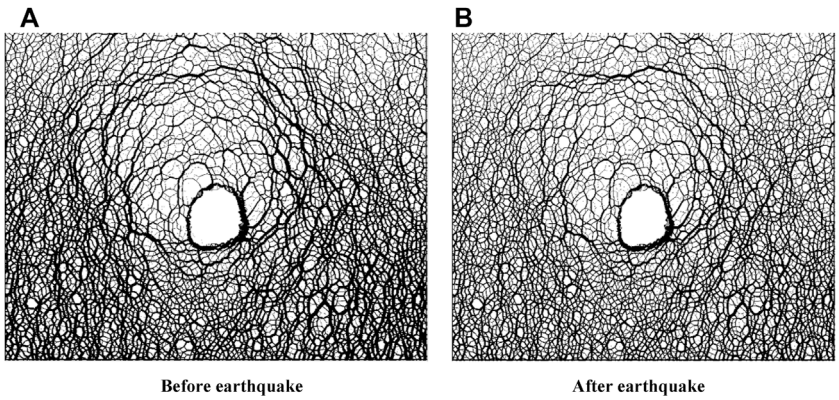


FIGURE 2 | Force chain pattern of 15 m deep tunnel. **(A)** Before earthquake. **(B)** After earthquake.

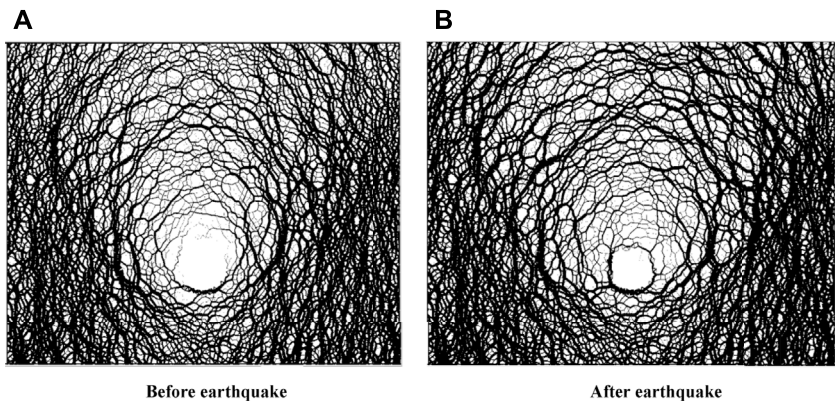


FIGURE 3 | Force chain pattern of 25 m deep tunnel. **(A)** Before earthquake. **(B)** After earthquake.

TABLE 3 | Factors influencing the height of pressure arch above tunnel.

Item factor	Value	Before earthquake	After earthquake	Increment	Increment rate	Value rate	Height rate before earthquake	Height rate after earthquake	Sensitivity before earthquake	Sensitivity after earthquake
Depth (m)	15	0.8	1	0.2	0.25					
	20	1.2	2.1	0.9	0.75	0.33	0.50	1.10	1.50	3.30
	25	1.5	3.3	1.8	1.20	0.25	0.25	0.57	1.00	2.29
Span (m)	4	2	2.1	0.1	0.05		0.33	−0.36		
	8	2.9	5.8	2.9	1.00	1.00	0.45	1.76	0.45	1.76
	12	3.3	9.1	5.8	1.76	0.50	0.14	0.57	0.28	1.14
Section shape	Circular	2.9	5.8	2.9	1.00		−0.12	−0.36		
	Rectangular	4.1	8.8	4.7	1.15		0.41	0.52		
Lining stiffness	1E+10	2.9	5.8	2.9	1.00		−0.29	−0.34		
(N/m)	5E+10	2	5.3	3.3	1.65	4.00	−0.31	−0.09	−0.08	−0.02
	1E+11	1.2	5.1	3.9	3.25	1.00	−0.40	−0.04	−0.40	−0.04
Seismic spectrum	El Centro	2.9	5.8	2.9	1.00		1.42	0.14		
	Kobe	2.9	5.3	2.4	0.83		0.00	−0.09		
	Wenchuan	2.9	5.1	2.2	0.76		0.00	−0.04		
Seismic	0.1	2.9	3.6	0.7	0.24		0.00	−0.29		
amplitude (g)	0.2	2.9	4.3	1.4	0.48	1.00	0.00	0.19	0.00	0.19
	0.3	2.9	5.8	2.9	1.00	0.50	0.00	0.35	0.00	0.70

Sensitivity here is defined as the ratio of height rate to value rate.

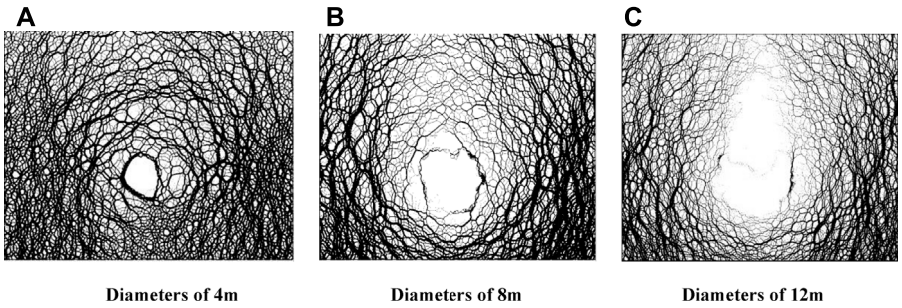


FIGURE 4 | Force chain patterns of circular tunnel with diameters of 4, 8, and 12 m after earthquake. **(A)** Diameters of 4 m. **(B)** Diameters of 8 m. **(C)** Diameters of 12 m.

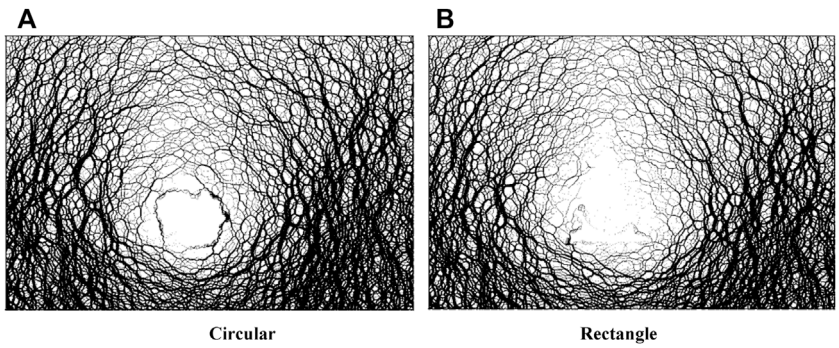


FIGURE 5 | Force chain patterns of circular and rectangular tunnels after earthquake. **(A)** Circular. **(B)** Rectangular.

Figure 4 shows that when the tunnel span is small, the force chain around the tunnel is thick and continuous, with small lining deformation, indicating that a complete pressure arch exists and the tunnel lining is stable. When the tunnel span is moderately large, the force chain above the tunnel is thin while those at the two sides are thick, with relatively large lining deformation, demonstrating that the pressure arch above the tunnel tends to fail and the left and right sides of lining are subject to large stress. When the tunnel span is large, the force chain above the tunnel disappears and those at the two sides become thin, with large lining deformation, which indicates that the pressure arch fails and the tunnel lining is not stable. Therefore, under the same horizontal seismic acceleration, the small-span tunnel may be stale. As the tunnel span increases, the pressure arch above the tunnel firstly fails, then the other pressure arch, and the seismic stability tends to decrease rapidly. The height of the pressure arch under various span conditions before and after an earthquake are listed in **Table 3**.

Effect of Section Shape

The force chain patterns of circular and rectangular tunnels with identical span and lining structure were numerically simulated under the same horizontal seismic acceleration, respectively, as shown in **Figure 5**.

Figure 5 shows that the force chain of a circular tunnel is thick and complete, indicating that the pressure arch is continuous and the lining is stable, while the force chain of a rectangular tunnel is thin above the tunnel and thick on the two sides of the tunnel, indicating that the upper force chain tends to fail and the lining may become unstable due to the large applied stress. Therefore, the circular tunnel has better seismic stability than the rectangular tunnel. The height of the pressure arch of circular and rectangular tunnels before and after an earthquake are listed in **Table 3**.

Effect of Lining Stiffness

The force chain patterns of circular tunnels with lining stiffness of $1e^{10}$, $5e^{10}$, and $10e^{10}$ N/m (the selected value is close to the actual project) were numerically simulated under the same horizontal seismic acceleration, respectively, as shown in **Figure 6**.

Figure 6 shows that, as the lining stiffness increases, the force chain of a circular tunnel changes a little, and the lining deformation decreases, indicating that the lining stiffness has little effect on the shape of the pressure arch. In addition, the increase in lining stiffness can reduce the lining deformation and improve the seismic stability of the tunnel. The height of the pressure arch of tunnels with various stiffness before and after an earthquake are listed in **Table 3**.

Effect of Seismic Spectrum

The El Centro earthquake, Kobe earthquake, and Wenchuan earthquake have different seismic spectra and were selected to numerically simulate force chain patterns of circular tunnels under the same horizontal seismic acceleration. Three seismic waves of various types are shown in the **Figure 7**.

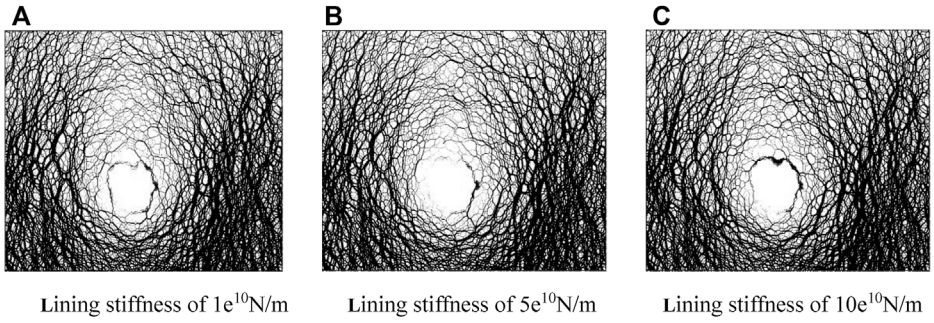


FIGURE 6 | Force chain patterns of circular tunnels with various lining stiffness after earthquake. **(A)** Lining stiffness of $1e^{10}$N/m. **(B)** Lining stiffness of $5e^{10}$N/m. **(C)** Lining stiffness of $10e^{10}$N/m.

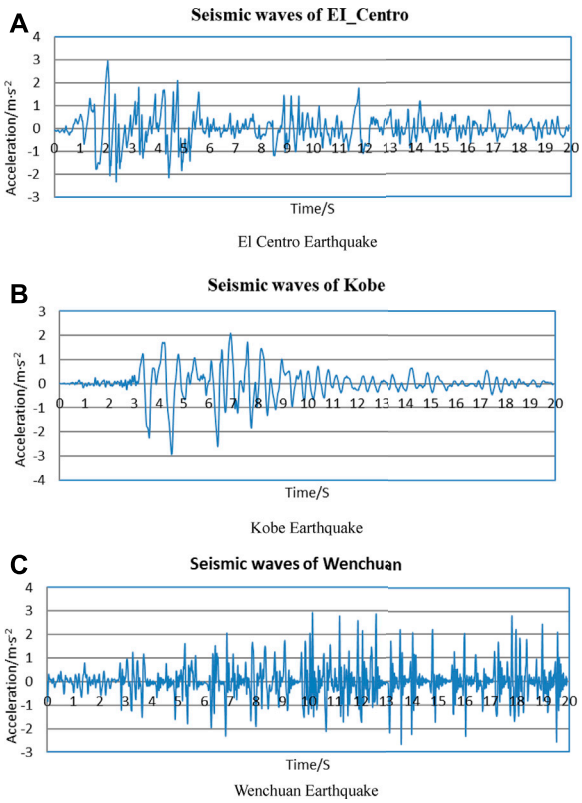


FIGURE 7 | Three seismic waves of various types. **(A)** El Centro earthquake. **(B)** Kobe earthquake. **(C)** Wenchuan earthquake.

The numerical results are shown in **Figure 8**.

Figure 8 shows that the force chain patterns are almost identical under three various earthquakes, indicating that the seismic spectrum has little effect on the pressure arch. The height of pressure arch of tunnels before and after earthquakes of various spectra are listed in **Table 3**.

Effect of Seismic Amplitude

The force chain patterns of circular tunnels with seismic amplitudes of 0.1, 0.2, and 0.3 g were numerically simulated under the El Centro earthquake, respectively, as shown in **Figure 9**.

Figure 9 shows that, as the seismic amplitude increases, the force chain around the tunnel becomes thick, especially on the two sides, and the lining deformation increases greatly due to the increasing stress, indicating that the lining structure may suffer great deformation or even failure under the large horizontal seismic amplitude. In addition, the pressure arch around the tunnel may become thick if the seismic amplitude increases. The height of the pressure arch of tunnels before and after the El Centro earthquake of various amplitudes are listed in **Table 3**.

Table 3 shows that the tunnel depth has the largest effect on the shape of the pressure arch; the span, section shape, seismic amplitude, and lining stiffness have moderate effect, and the seismic spectrum has little effect. The factor sensitivity after the earthquake is greater than that before the earthquake, and the reason is as follows: before the earthquake, it is a static problem, and after the earthquake, it is a wave dynamic problem. The six influencing factors have different mechanisms for static and dynamic effects, so their sensitivities are also different. In addition, only the values about the pressure arch above the tunnel are listed in **Table 3**, and the values about the pressure arch under and on the two sides of the tunnel differ from the values in **Table 3**.

SHAKING TABLE TEST

The shaking table test was conducted to verify the numerical results about the force chain and pressure arch around the tunnel under an earthquake.

The device for the test is the hydraulic ES-5 shaking table system, which was manufactured by the Suzhou Sushi Testing Instrument Co., Ltd, China, and consists mainly of the platform, power amplifier, sensors, and controller, with maximum acceleration of 40 m/s^2, maximum load of 1,500 kg, and rated excitation force of 50 kN. The model has a scale of 1:50, as shown in **Figure 10**.

The grid was notched on the glass window of a model box to observe the shape variation of the pressure arch, and some foam board was installed to reduce the boundary effect (Wen-guang et al., 2005). The lining materials are usually made of waterproof

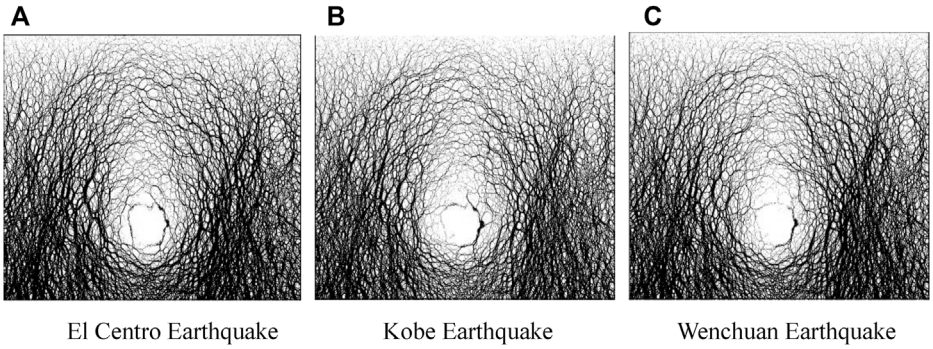


FIGURE 8 | Force chain patterns of circular tunnels under earthquake of various spectra. **(A)** El Centro earthquake. **(B)** Kobe earthquake. **(C)** Wenchuan earthquake.

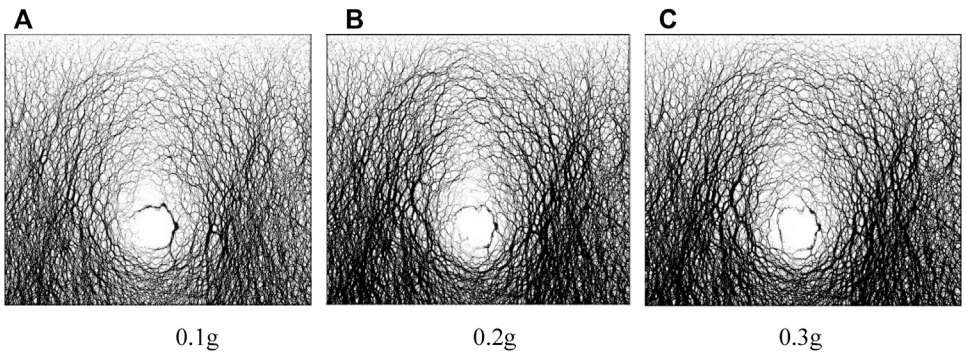


FIGURE 9 | Force chain patterns of circular tunnels under earthquake of various amplitudes. **(A)** 0.1 g. **(B)** 0.2 g. **(C)** 0.3 g.

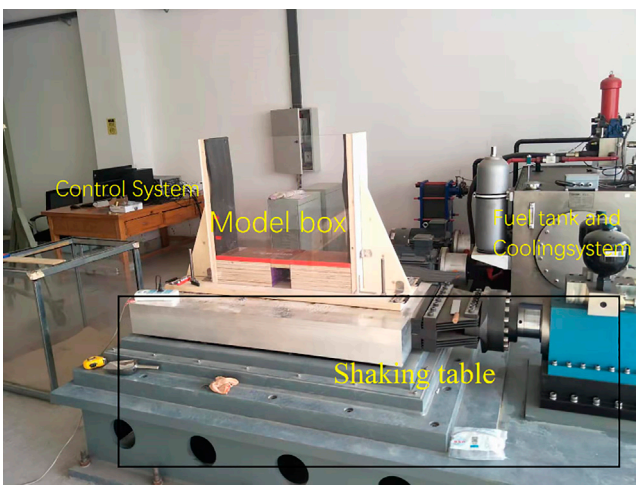


FIGURE 10 | Shaking table and model box.



FIGURE 11 | Shock absorption structure of molded polystyrene foam for shaking table test

sponge, latex, molded polystyrene foam, and rubber. The friction along the contact surface may be simulated by means of a thin layer of polystyrene foam on the inner lining surface. According the laboratory equipment conditions and testing requirements, an about 22.5 cm thick layer of molded polystyrene foam was chosen as the shock absorption structure on the inner lining surface, as shown in **Figure 11**.

TABLE 4 | Major mechanical parameters of original surrounding rock and mixture materials.

Class-V surrounding rock	Elastic modulus (MPa)	Poisson's ratio	Unit weight (KN/m³)	Cohesion (kPa)	Angle of internal friction (°)
Original	1,800	0.35	21	200	25°
Testing	60	0.35	7	1.03	25°

TABLE 5 | Mixture ratio of simulated Class-V surrounding rock.

Name	River sand	Sawdust	Water	Laundry liquid
Ratio (%)	41.3	49.6	4.1	5

The surrounding rock for the shaking table test was made by a mixture of river sand, laundry liquid, and sawdust. The river sand was selected as the aggregate because it not only matches well the general requirements of aggregate similarity but also has better simulation on the discreteness of the surrounding rock due to the great variability of its grain size. Additionally, the water content of the mixture was kept almost constant because the river sand has low moisture content, ensuring good stability in the physical and mechanical properties of the mixture. The sawdust was used to adjust the unit weight of the mixture and enhance the stabilization in the mixture properties because the sawdust can absorb much water and cementation material. The laundry liquid has low cementation and thus reduces the mixture strength to better simulate the mechanical behavior of surrounding rock. Furthermore, the three different materials did not react chemically with each other after mixing, so the physical and mechanical properties of the mixture was very stable. The major mechanical parameters of the original surrounding rock and the mixture materials are listed in **Table 4**.

The mixture ratio of the simulated Class-V surrounding rock for the shaking table test was finally determined by a series of trial tests, as listed in **Table 5**.

The tunnel excavation was simulated with a special device by the aeration and deflation of a balloon. This device is basically made with two layers of rubber acting as the tunnel and lining, respectively. The tunnel layer is divided into two parts, one over the tunnel axis and another beneath the tunnel axis. The upper part and arch support jointly form an arch area. Each aeration bag has one inlet and one outlet. The outside of the arch support is attached with several strain gauges or connected to a pressure gauge. When the aeration bag is fully aerated through the inlet, the arch-shaped bag and the lining can be tightly joined. When the air in the aeration bag is drained through the outlet, the stress change in the arch support can be measured by the strain gauges or pressure gauge. Thus, the tunnel excavation processes can be judged.

The fully aerated bag embedded in the soil is used to simulate the tunnel excavation. The pressure gauge connected to the aeration bag is used to simulate the stress release of tunnel excavation by releasing air to some extent and therefore the effect of excavation method on the formation and variation of the pressure arch and the seismic performance of the tunnel structure. To gain the goals above, the fully aerated bag is firstly embedded in the soil to simulate the tunnel conditions before excavation, and then some air is released with the pressure gauge to simulate the tunnel excavation. Thirdly, the outside bag is aerated to simulate the tunnel reinforcement by controlling the pressure gauge. Finally, various seismic waves are exerted on the model bottom. The formation of the pressure arch and the variation of soil particles before and after the earthquake were recorded with a camera. Thus, the shapes of the pressure arch can be compared with these photos and numerical results.

TABLE 6 | Seismic loading scheme for shaking table test.

No	Earthquake name	Direction	Peak acceleration (g)
1	El Centro earthquake	Along *x*-axis	0.05
2	El Centro earthquake	Along *x*-axis	0.1
3	El Centro earthquake	Along *x*-axis	0.2
4	El Centro earthquake	Along *x*-axis	0.3
5	Kobe earthquake	Along *x*-axis	0.05
6	Kobe earthquake	Along *x*-axis	0.1
7	Kobe earthquake	Along *x*-axis	0.2
8	Kobe earthquake	Along *x*-axis	0.3
9	Wenchuan earthquake	Along *x*-axis	0.05
10	Wenchuan earthquake	Along *x*-axis	0.1
11	Wenchuan earthquake	Along *x*-axis	0.2
12	Wenchuan earthquake	Along *x*-axis	0.3

In terms of tunnel depth, seismic spectrum, and seismic amplitude, a total of 12 testing situations were schemed for the shaking table test, as listed in **Table 6**.

According to the testing scheme in **Table 6**, the El Centro earthquake, Kobe earthquake, and Wenchuan earthquake were separately applied on the model in terms of the tunnel depth, seismic spectrum, and seismic amplitude. The experimental and numerical results are shown in **Figures 12–14** for comparative purposes.

Figures 12–14 show that the shape of the pressure arch by the shaking table test is basically identical to that by numerical simulation. When the tunnel is shallow, the failure plane extends to the ground surface, and thus no pressure arch is formed. The soil pressure around the tunnel decreases gradually with the tunnel depth, indicating that the pressure applied on the tunnel also decreases gradually with tunnel depth. In addition, the collapse degree of the pressure arch under the earthquake reduces obviously with the tunnel depth, which demonstrates that it is feasible to use the force chain to analyze the shape of the pressure arch.

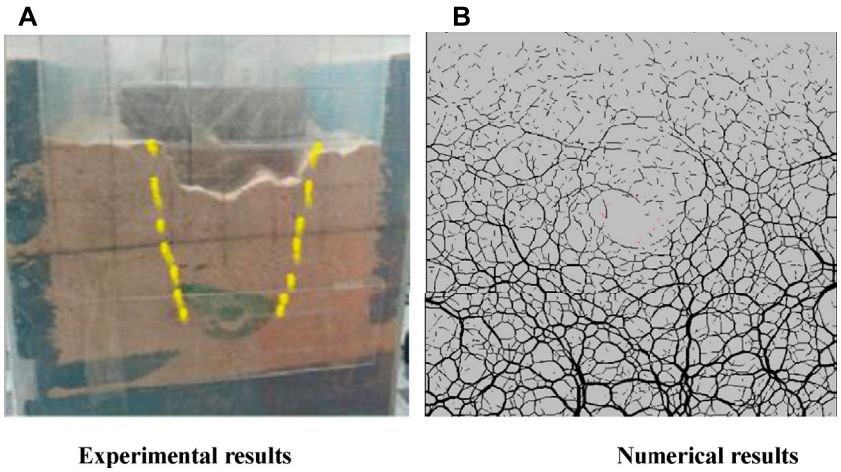


FIGURE 12 | Experimental and numerical results of 15 m deep tunnel after earthquake. **(A)** Experimental results. **(B)** Numerical results.

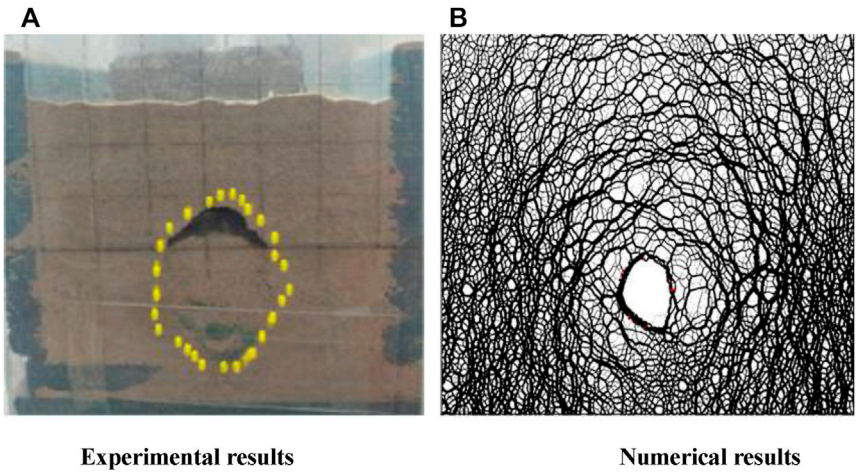


FIGURE 13 | Experimental and numerical results of 20 m deep tunnel after earthquake. **(A)** Experimental results. **(B)** Numerical results.

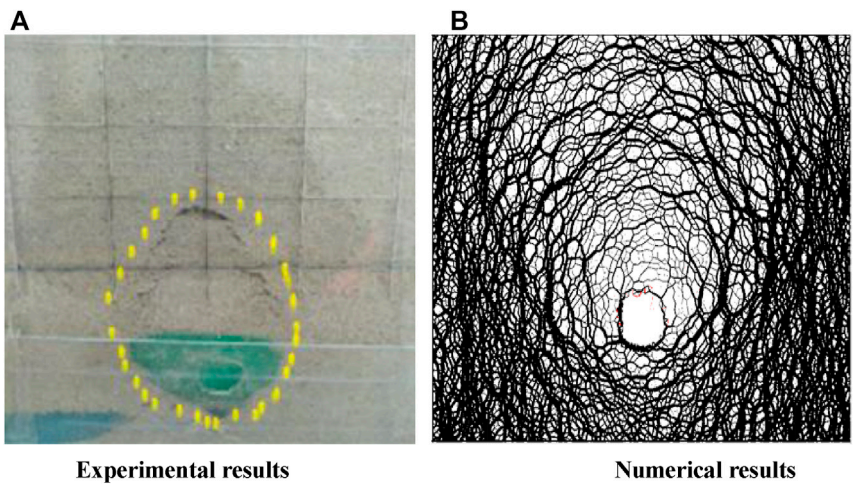


FIGURE 14 | Experimental and numerical results of 25 m deep tunnel after earthquake. **(A)** Experimental results. **(B)** Numerical results.

CONCLUSION

In this paper, the force chain was used to analyze the shape of the pressure arch around the tunnel before and after an earthquake, and the effect of some factors on the shape of the pressure arch was studied. In addition, the shaking table test was carried out to verify the numerical results. Some preliminary conclusions were obtained as follows:

1) The shape of the pressure arch can be well represented by some easily visible indexes such as the thickness, integrity, and density of the force chain. Thus, the force chain is a powerful tool for the study on pressure arches around a tunnel.
2) The area of the pressure arch decreases gradually with the tunnel depth, indicating that the smaller the area of the pressure arch, the less surrounding rock that the tunnel self-stabilization needs, the more stable the tunnel, and the better the seismic stability of the tunnel. When the tunnel depth reaches a given value, the tunnel depth has little effect on the seismic stability of the tunnel.
3) As the tunnel span increases, the area of the pressure arch increases, and the tunnel becomes less stable. Therefore, the larger the tunnel span, the less the seismic stability of the tunnel. The rectangular tunnel has a larger area of pressure arch than the circular tunnel, and thus it is less stable than the circular tunnel. The lining of a rectangular tunnel suffers from large deformation after an earthquake. The lining stiffness has little effect on the shape of the pressure arch. However, the lining stiffness has a direct effect on the seismic stability of the tunnel. The larger the lining stiffness, the better the seismic stability of the tunnel.
4) The seismic spectrum has little effect on the shape of the pressure arch because the tunnel has less self-vibration characteristics than the on-ground buildings. As the seismic amplitude decreases, the tunnel deformation and pressure arch height decrease gradually. Therefore, the smaller the seismic amplitude, the more stable the tunnel.
5) This paper mainly calculates and analyzes the change law of the pressure arch shape around the circular tunnel lining structure; it has similar conclusions under the conditions of other lining shapes (horseshoe and rectangle).

Generally, it is suitable to analyze the variation of pressure arch shape by means of the force chain. This paper is an attempt to study the pressure arch through the force chain, and the next step needs to be combined with theoretical methods to conduct in-depth research. Only the 2D numerical simulation was conducted in this paper, and the 3D visualization study on the force chain may be carried out by transparent soil model test in the next stage. The research results of this paper can be used for seismic calculation and design of tunnel and underground engineering.

DATA AVAILABILITY STATEMENT

The original contributions presented in the study are included in the article/supplementary material; further inquiries can be directed to the corresponding authors.

AUTHOR CONTRIBUTIONS

SC and ZY contributed to conception and design of the study. GL organized the database. ZL and PJ performed the statistical analysis. SC wrote the first draft of the manuscript. All authors contributed to manuscript revision and read and approved the submitted version.

FUNDING

This work was funded by the National Natural Science Foundation of China No:51408222.

REFERENCES

Badakhshan, E., Noorzad, A., Bouazza, A., Zameni, S., and King, L. (2020). A 3D-DEM Investigation of the Mechanism of Arching within Geosynthetic-Reinforced Piled Embankment. *Int. J. Sol. Structures* 187, 58–74. doi:10.1016/j.ijsolstr.2019.03.035

Chang-nü, Z., Xin, L., Fan, L., and Bin, Z. (2021). Experimental Study and Numerical Simulation Analysis on Influencing Factors of Vertical Pressure at the Bottom of Stored Grain[J]. *J. Henan Univ. Technology(Nat. Sci. Edition)* 42 (6), 96–104. doi:10.16433/j.1673-2383.2021.06.013

Chen, X-B., Zhao-Sheng, Y., Zhou, Y-Q., Zhang, J-S., and Qian, Y. (2022). Prediction Model of Desiccation Shrinkage Fracture Depth and Spacing of Argillaceous Cement in Red Mudstone. *Rock Soil Mech.* 43 (4), 1–11. doi:10.16285/j.rsm.2021.1084

Chen-Peng, S. (2021). Discrete Element Simulation of the Effects of Intergranular Rolling Resistance on the Sand Compression Characteristics[J]. *J. Water Resour. Architectural Eng.* 19 (06), 70–75. doi:10.3969/j.issn.1672-1144.2021.06.011

Dantu, P. (1957). "A Contribution to the Mechanical and Geometrical Study of Non-cohesive Masses[C]," in Proceedings of the 4th International Conference on Soil Mechanics and Foundations Engineering (London: Butterworths Scientific Publications), 144–148.

Deng, J., Liang, A., and Wang, S-N. (2021). Microcosmic Analysis on Loess at Different Intake Orientation Sections and Dynamic Triaxial Simulation by Particle Flow Code [J]. *J. Southeast Univ. (Natural Sci. Edition)* 51 (05), 833–840. doi:10.3969/j.issn.1001-0505.2021.05.015

Feng, G.-L., Chen, B.-R., Xiao, Y.-X., Jiang, Q., Li, P.-X., Zheng, H., et al. (2022). Microseismic Characteristics of Rockburst Development in Deep TBM Tunnels with Alternating Soft-Hard Strata and Application to Rockburst Warning: A Case Study of the Neelum-Jhelum Hydropower Project. *Tunnelling Underground Space Technol.* 122, 104398. doi:10.1016/j.tust.2022.104398

Feng, G.-L., Feng, X.-T., Chen, B.-R., Xiao, Y.-X., and Yu, Y. (2015). A Microseismic Method for Dynamic Warning of Rockburst Development Processes in Tunnels. *Rock Mech. Rock Eng.* 48 (5), 2061–2076. doi:10.1007/s00603-014-0689-3

Handy, R. L. (1985). The Arch in Soil Arching. *J. Geotechnical Eng.* 111 (3), 302–318. doi:10.1061/(asce)0733-9410(1985)111:3(302)

Hu, S-X., Xiao-guang, J., Guo-dong, S., Han-lin, L., and Zi-heng, N. (2021). Triaxial Test and PFC-FLAC Coupling Simulation Study on Material Parameters and Deformation Characteristics of Soil-Rock Mixture[J]. *Chin. J. Rock Mech. Eng.* 40 (Suppl. 2), 3344–3356. doi:10.13722/j.cnki.jrme.2021.0019

IEM (1936). Third Progress Report of Investigation into Causes of Falls and Accidents Due to Falls in Bord and Pillar Whole Workings-Roof-Fracture Control in Bords. *Trans. Inst. Min. Eng.* 90 (4), 241–242.

Iwashita, K., and Oda, M. (2000). Micro-Deformation Mechanism of Shear Banding Process Based on Modified Distinct Elementmethod [J]. *Powder Technol.* 109 (1), 192–205. doi:10.1016/s0032-5910(99)00236-3

Majmudar, T. S., and Behringer, R. P. (2005). Contact Force Measurements and Stress-Induced Anisotropy in Granular Materials. *Nature* 435 (23), 1079–1082. doi:10.1038/nature03805

Miao, T., Yi, C., Qi, Y., Qing-Song, M., and Yuan, L. (2007). Force Transmission in Three-Dimensional Hexagonal-Close-Packed Granular Arrays Submitted to a Point Load. *Acta Phys. Sin.* 56 (8), 4713–4721. doi:10.7498/aps.56.4713

Oda, M., Takemura, T., and Takahashi, M. (2004). Microstructure in Shear Band Observed by Microfocus X-ray Computed Tomography. *Géotechnique* 54 (8), 539–542. doi:10.1680/geot.2004.54.8.539

Peng, J., Cui, P., and Zhuang, J. (2020). Challenges to Engineering Geology of Sichuan-Tibet Railway. *Chin. J. Rock Mech. Eng.* 39 (12), 2377–2389. (in Chinese). doi:10.13722/j.cnki.jrme.2020.0446

Sanfratello, L., Fukushima, E., and Behringer, R. P. (2009). Using MR Elastography to Image the 3D Force Chain Structure of a Quasi-Static Granular Assembly. *Granular Matter* 11 (1), 1–6. doi:10.1007/s10035-008-0112-4

Shang, B., Jin, X., Ao, G., Chen, Q., and Qiu, Q. (2020). Calculation of Surrounding Rock Pressure of Undercut Subway Station Based on Multi-Factor Affecting Pressure Arch Theory. *Engineering* 12, 59–70. doi:10.4236/eng.2020.122006

Socolar, J. E. S., Schaeffer, D. G. D. G., and Claudin, P. (2002). Directed Force Chain Networks and Stress Response in Static Granular Materials. *Eur. Phys. J. E* 7, 353–370. doi:10.1140/epje/i2002-10011-7

Song, Y., Zhang, Y., and Liu, Y. (2017). Calculation of the Surrounding Rock Pressure Based on Pressure Arch Theory. *J. Disaster Prev. Reduction* 33 (2), 45–51. doi:10.13693/j.cnki.cn21-1573.2017.02.008

Sun, Q., and Wang, G. (2008). Force Distribution in Static Granular Matter in Two Dimensions. *Acta Physica Sinica* 57 (008), 4667–4674. doi:10.7498/aps.57.4667

Terzaghi, K. (1936). "Stress Distribution in Dry and in Saturated Sand above a Yielding Trap-Door," in Proceedings of 1st Conference of Soil Mechanics and Foundation Engineering, Boston, 307–316.

Tien, H-J. S. (2001). *The Arching Mechanism on the Micro Level Utilizing Photoelasticity Modeling*. United States: Massachusetts Lowell University.

Wang, Y-W., Liu, R., Sun, R-H., and Xu, Z-W. (2022). Correlation of Microscopic and Macroscopical of Granular Materials Based on Rolling Resistance Linear Contact Model. *Rock Soil Mech.* 43 (4), 1–13. doi:10.16285/j.rsm.2021.0918

Wang, Z-C., and Zhao, X-Y. (2022). Mesoscopic Study on Mechanical Properties of Metakaolin-Based Geopolymer Reinforced by Fine Sand[J]. *J. Dalian Jiaotong Univ.* 43 (1), 82–87. doi:10.13291/j.cnki.djdxac.2022.01.016

Wen-guang, L., Bei-shu, F., He, W-F., Hao, X., and Miyama, T. (2005). Study on Dynamic Response and Shaking Table Test of Isolated Structure with Isolation Bearing Arranged along Curved Surface[J]. *J. Building Structures* 435 (23), 1079–1082. doi:10.14006/j.jzjgxb.2020.0270

Yu, Y., Feng, G-L., Xu, C-J., Chen, B-R., Geng, D-X., and Zhu, B-T. (2022). Quantitative Threshold of Energy Fractal Dimension for Immediate Rock-Burst Warning in Deep Tunnel: a Case Study. *Lithosphere* 2021, 1699273. doi:10.2113/2021/1699273

Zang, W. (2017). Damage to Highway Tunnels Caused by the Wenchuan Earthquake. *Mod. Tunneling Technol.* 54 (2), 17–25. (in Chinese). doi:10.13807/j.cnki.mtt.2017.02.003

Zeng, X. (2018). Numerical Analysis of the Effects of Soil Arching and Earth Pressure Acting Modes in Metro Tunnels. *Shanxi Architecture* 44 (17), 186–187. (in Chinese). doi:10.13719/j.cnki.cn14-1279/tu.2018.17.098

Zhou, Y-Q., Qin, M., Xiao-yang, Z., Zhi-yuan, Z., Hao, L., and De-zhong, M. (2022). Experimental and Simulation Researchon the Influencing Factors of Particlevelocity[J]. *Phys. Eng.* 32 (1), 123–129. Available at: https://kns.cnki.net/kcms/detail/11.4483.o3.20211223.1723.006.html.

Conflict of Interest: The authors declare that the research was conducted in the absence of any commercial or financial relationships that could be construed as a potential conflict of interest.

Publisher's Note: All claims expressed in this article are solely those of the authors and do not necessarily represent those of their affiliated organizations or those of the publisher, the editors, and the reviewers. Any product that may be evaluated in this article, or claim that may be made by its manufacturer, is not guaranteed or endorsed by the publisher.

Copyright © 2022 Changxin, Yumin, Lei, Liye and Jiafeng. This is an open-access article distributed under the terms of the Creative Commons Attribution License (CC BY). The use, distribution or reproduction in other forums is permitted, provided the original author(s) and the copyright owner(s) are credited and that the original publication in this journal is cited, in accordance with accepted academic practice. No use, distribution or reproduction is permitted which does not comply with these terms.

frontiers | Frontiers in Earth Science

ORIGINAL RESEARCH
published: 07 April 2022
doi: 10.3389/feart.2022.836313

Determination Method of Excavation Damage Zone Based on Surrounding Rock Damage-Fracture Ratio in Underground Engineering

Haosen Guo[1,2], Jiaqi Tong[2], Qiancheng Sun[3,4], Xu Yang[4], Wenjun Luo[1,2] and Yang Yu[2]*

[1]Jiangxi Key Laboratory of Disaster Prevention-mitigation and Emergency Management, Nanchang, China, [2]School of Civil Engineering and Architecture, East China Jiaotong University, Nanchang, China, [3]National Field Observation and Research Station of Landslides in Three Gorges Reservoir Area of Yangtze River, Yichang, China, [4]College of Civil Engineering and Architecture, China Three Gorges University, Yichang, China

The depth of the excavation damage zone in the surrounding rock mass is an important parameter to determine the support design scheme, and is also of great reference significance to evaluate the stability of the surrounding rock. An acoustic test is the most commonly used method to obtain the depth of the excavation damage zone in surrounding rock. However, under high stress conditions, the surrounding rock is seriously broken and the internal structural planes are significantly developed, leading to the test error reaching meter-level. This paper, based on dimensional analysis, proposed the surrounding rock damage-fracture ratio R, which was defined as the depth of excavation damage zone to the depth of highly damaged zone, to characterize the relationship between the excavation damage zone and highly damaged zone. The established indicator considered the stress condition of the engineering zone, rock integrity, tunnel excavation span, and rock fracture zone depth and was verified with allowable error in engineering practice. The results show that the model can overcome the limitations of the acoustic wave testing method in surrounding rock testing of deep underground caverns, and the method of determining the depth of the surrounding rock damage zone based on the damage-fracture ratio R provides a practical and alternative method for determining the damage zone of surrounding rock excavation.

Keywords: damage-fracture ratio, excavation damage zone, highly damaged zone, underground engineering, surrounding rock

OPEN ACCESS

Edited by:
Shibing Huang,
Wuhan University of Science and Technology, China

Reviewed by:
Yi Luo,
Wuhan University of Technology, China
Yong Fan,
China Three Gorges University, China
Yangyi Zhou,
Northeastern University, China

****Correspondence:***
Qiancheng Sun
qc_sun@ctgu.edu.cn

Specialty section:
This article was submitted to Geohazards and Georisks, a section of the journal Frontiers in Earth Science

Received: *15 December 2021*
Accepted: *21 February 2022*
Published: *07 April 2022*

Citation:
Guo H, Tong J, Sun Q, Yang X, Luo W and Yu Y (2022) Determination Method of Excavation Damage Zone Based on Surrounding Rock Damage-Fracture Ratio in Underground Engineering. Front. Earth Sci. 10:836313. doi: 10.3389/feart.2022.836313

INTRODUCTION

In the early 1980s, a large number of verification and promotion work on the supporting theory of loose circle, based on the excavation damage zone (EDZ) in domestic mines, was carried out. Kelsall et al. (1984) put forward the importance of the excavation damage zone of the surrounding rock. The academic seminars, 1988 in Winnipeg, Canada, 1998 in Paris, and 2003 in Luxembourg, are based on the excavation damage zone (EDZ) and safe storage of the waste issues related to the theme, and greatly promoted the scholars in the research of the excavation damage zone (EDZ). Harrison, et al. (2000) hold the opinion that the damage in the surrounding rock can be divided into inevitable damage during excavation and extra damage caused by the excavation method. Zou and Xiao, (2010); Zhou and Qian, (2007), according to some engineering examples, put forward the theory of zonal disintegration in the excavation damage zone.

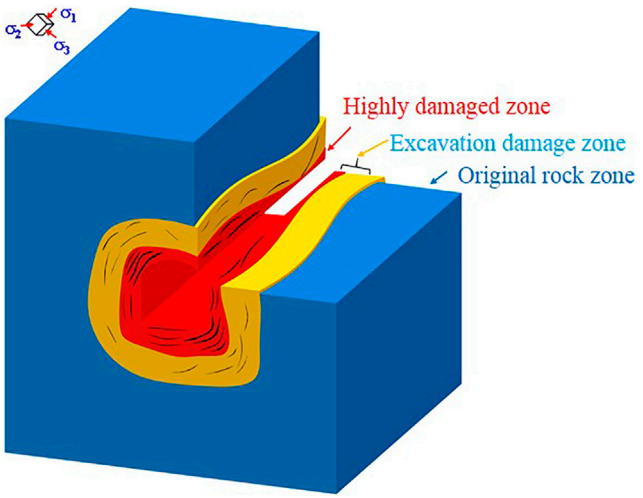


FIGURE 1 | Two major categories in surrounding rock.

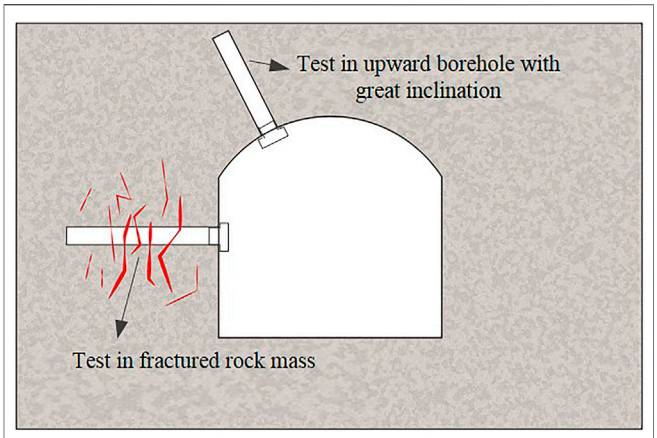


FIGURE 2 | Limitations of acoustic test in determining excavation damage zone.

Eberhardt and Diederichs, (2012) further distinguished the excavation damage from construction damage zone (CDZ)and stress-induced excavation damage zone, (EDZ_{SI}). Siren, et al. (2015) proposed the concept of excavation disturbed zone (EdZ), which is in essence the same as the excavation disturbed zone (EDZ) proposed by Malmgren, (2007). Yang et al. (2020) estimated the rock mass properties of the excavated damage area (EDZ) based on the generalized Hoek-Brown damage criteria. Fan et al. (2021) and Feng et al. (2022) also analyzed the influences of stress unloading path induced by blasting excavation and tunnel boring machine (TBM) excavation on the EDZ using theoretical calculation and numerical simulation. The study of rock burst is also involved in the energy change of the excavation damage zone (Fan et al., 2015; Feng et al., 2015; Yu et al., 2022).

In fact, whatever the causes of damage, construction personnel are more focused on the depth of rock damage in the surrounding rock, which is vital to determine the economic and reasonable supporting scheme. Therefore, the surrounding rock can be divided into two major categories: excavation damage zone and the original rock zone (**Figure 1**).

The original rock zone refers to the area not affected by excavation. The excavation damage zone (EDZ) is characterized by internal fissure expansion and the acoustic wave velocity falling; it is partially connected to isolated damage and is invisible, in which the observed interconnected macro-fractures are defined as the highly damaged zone (HDZ). Scholars have studied the influence of different factors on the damage of rock mass, such as the burial depth and the cross section shape (Pusch and Stanfors, 1992), surrounding rock support (Jing, 1999), the excavation blasting (Sato et al., 2000), stress field (Baechler et al., 2011), and the joint in rock mass (Sun et al., 2019).

There are two main ways to achieve the depth of excavation damage zone in the surrounding rock: theoretical calculation and field measurement method. Wu et al. (2009) established the quantitative relation of damage zone of the surrounding rock according to the unloading strain energy released in the process of the rock mass excavation. Zou and Xiao, (2010) nonlinearly fitted the damage depth considering the uniaxial strength and stress field. Also, Huang et al. (2016) derived the elastic-plastic theory for the damage zone of surrounding rock based on D—P criterion. However deep underground excavation engineering practice shows essential difference in the mechanical behavior of surrounding rock compared with shallow buried rock mass (Xie et al., 2015); the theoretical calculation method on the premise of simplified assumption of the surrounding rock is of inadequate applicability to deep underground engineering. Therefore, the evaluation of the actual measured data is accepted as the most intuitive and reasonable method to determine the excavation damage zone. The acoustic test method has the advantages of being simple to cost-effective to operate and is the most commonly used method in current engineering practice.

It is essential for construction safety to determine the depth of the excavation damaged zone (EDZ) and highly damaged zone (HDZ) in rock masses around a tunnel. Sun et al. (2021) found there is a certain relationship between the excavation damage zone and highly damaged zone for columnar jointed rock mass in Baihetan based on field test data.

In this paper, the *in situ* test data of the excavation damage zone from a deep buried engineering case was further analyzed. In combination with field excavation condition, *in-situ* stress testing, acoustic test, and test results of borehole camera, the dimensional analysis method is employed to generate an expression for surrounding rock damage-fracture ratio (R), which was defined as the depth of excavation damage zone to the depth of highly damaged zone. The method was verified as being reliable. Moreover, the idea behind the proposal of this evaluation method, and some relevant problems facing its application, were also discussed.

LIMITATIONS OF ACOUSTIC TEST IN DETERMINING EXCAVATION DAMAGE ZONE

Acoustic testing is to excite the ultrasonic wave to propagate in the rock mass medium, and the propagation speed of the wave

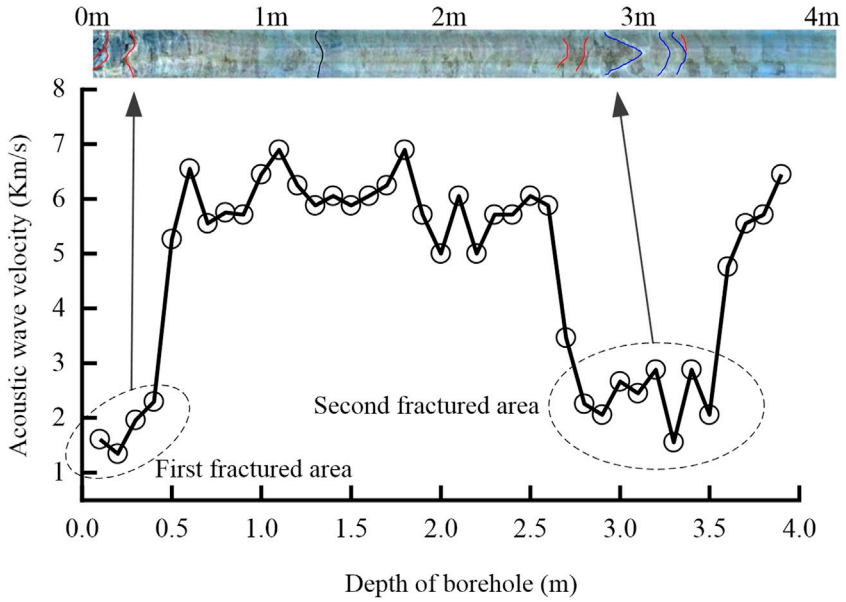


FIGURE 3 | Test in area with several fractured zone.

depends on the integrity of the rock mass. The wave velocity of intact rock mass is generally high, but it decreases relatively in the loose zone where the stress drops and the fracture expands. Therefore, there is an obvious change of wave velocity in rock mass with different damage degrees. In the highly damaged zone, there are visible cracks in the rock mass, which can be obtained by borehole television test. In the minor damaged zone, although there is no visible fissures, the propagation of sonic wave velocity in this area still drops significantly compared with that of the original rock mass. Moreover, there is obvious uncertainty in the excavation disturbed zone, part of which becomes the original rock zone as the elastic deformation recovers, while the other part of rock mass produces damage during stress dissipation (a crest in the curve due to stress adjustment) and becomes part of the excavation damaged zone (minor or highly damaged zone). The curve of wave velocity at different lengths of drilling from the surface of the surrounding rock can be obtained by using the propagation characteristics of ultrasonic wave, and then the EDZ depth of the surrounding rock can be inferred according to the variation curve (V-L curve) and relevant geological data.

The acoustic test method is restricted in the following conditions as shown in **Figure 2**. When sound waves spread in the fractured rock mass, the test result is significantly lower because of ultrasonic propagation in air. When the test is carried out in an upward borehole with great inclination, the coupling water creates instability, leading to the low acoustic wave velocity and inability to obtain valid test data. In addition, site construction, vehicles, and other drilling vibrations will also cause inaccuracy in acoustic test results. Thus, the applicability of the acoustic test method in deep underground engineering is limited, and errors caused by severe test conditions may exceed meter-level.

Digital borehole televiewers can intuitively reflect the drilling geological characteristics of surrounding rock from borehole, and more importantly, the test method has strong anti-interference immunity from the influence of environmental change. As shown in the engineering case, the position of crack initiation and expansion obtained from digital borehole televiewers corresponds with acoustic wave velocity descent (**Figure 3**), even in some visible fractures of rock mass, where the results of the acoustic test are unable to accurately determine the location of the crack (**Figure 4**).

EVALUATION METHOD OF ROCK MASS DAMAGE BASED ON SURROUNDING ROCK DAMAGE-FRACTURE RATIO

3.1 Definition and parameters of surrounding rock damage-fracture ratio

Testing practices in deep underground engineering show that there is local similarity in the depth of the excavation damage zone and highly damaged zone (Sun et al., 2021). Surrounding rock damage-fracture ratio (R) is defined as the depth of excavation damage zone to the depth of the highly damaged zone. That is,

$$R = \frac{H_{EDZ}}{H_{HDZ}} \tag{1}$$

Obviously, R is a dimensionless quantity and directly related to the excavation damage zone and highly damaged zone of the surrounding rock. Guo et al. (2017) put forward the rock mass integrity index (*RMIBT*) (by measuring the proportion of rock mass without macroscopic fissures in the

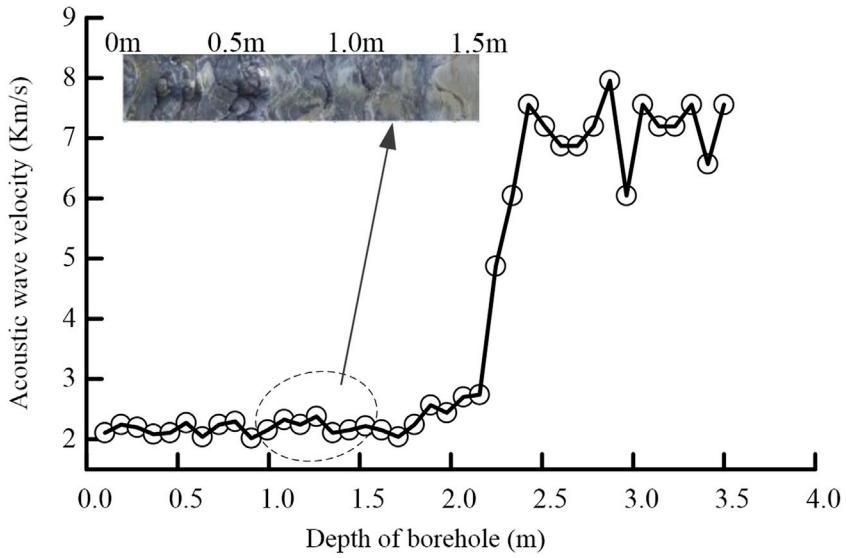


FIGURE 4 | Visible fracture of rock mass from digital borehole televiewers.

borehole wall) based on digital borehole televiewer; it can be used to characterize the relation of the rock mass integrity and damage or fracture state of rock mass. It was applied in multiple deep rock excavations and proved to be useful. In addition, the RMIBT can be used to dynamically assess the integrity of macroscopic rock masses and the evolution of fractures in the excavation damaged zone.

The most common damage zone theoretical model showed the damage area affected by the stress conditions in the deep surrounding rock mass (Martin et al., 1999). Richards and Bjorkman, (1978) emphasized the influence of excavation shape and size on the development of the surrounding rock damage. Given the test data, we considered the excavation span along the damaged direction without the effect of shape.

Mathematical Model for R

Dimensional analysis, which is often used in the mathematical model of complex engineering problems, is adopted to determine the mathematical expression of R affected by multiple factors.

It involves the principal stress difference of stress field σ_1-σ_3, the rock mass integrity index RMIBT, the excavation span along the damaged direction B, the depth of excavation damage zone $H_{EDZ,}$ and the highly damaged zone H_{HDZ}, then,

$$R = f\left(\sigma_1 - \sigma_3, RMIBT, H_{HDZ}, B, H_{EDZ}\right) \tag{2}$$

Dimensions for each control variable are:

$$[\sigma_1 - \sigma_3] = ML^{-1}T^2$$
$$[RMIBT] = M^0L^0T^0$$
$$[H_{HDZ}] = M^0L^1T^0$$
$$[B] = M^0L^1T^0$$
$$[H_{EDZ}] = M^0L^1T^0$$

K as the objective function of the dimensional matrix, and,

$$K = \begin{pmatrix} 1 & 0 & 0 & 0 & 0 & (M) \\ -1 & 0 & 1 & 1 & 1 & (L) \\ 2 & 0 & 0 & 0 & 0 & (T) \end{pmatrix}$$

Solving zero space for matrix K,

$$X = \begin{pmatrix} 0 & 0 & 0 \\ 1 & 0 & 0 \\ 0 & -1 & -1 \\ 0 & 1 & 0 \\ 0 & 0 & 1 \end{pmatrix} \tag{3}$$

Therefore, the dimensionless factors are $RMIBT$, BH_{HDZ}^{-1}, $H_{EDZ}H_{HDZ}^{-1}$. Solution of dimensional matrix zero space showed no correlation between R and the stress field of the surrounding rock. The equivalence relation of the objective function is,

$$R = g\left(RMIBT, BH_{HDZ}^{-1}, H_{EDZ}H_{HDZ}^{-1}\right) \tag{4}$$

Determination of the Parameters in R

With better integrity of the surrounding rock, the depth of the excavation damage zone (H_{EDZ}) and the highly damaged zone (H_{HDZ})can be obtained by acoustic test and digital borehole televiewers. The established model should meet the requirement that there is a very small difference between the calculated value and the measured value:

$$H_{EDZ}^{cal} - H_{EDZ}^{mea} \approx 0 \tag{5}$$

The test data were shown in **Table 1**; the appropriate relation and suitable parameters can be derived from the engineering practice.

TABLE 1 | Test data in Baihetan engineering practice.

NO.	Excavation damage zone(m)	Highly damaged zone(m)	RMIBT	B
1	0.9	0.72	0.48	9
2	1.23	0.88	0.4	9
3	1.65	1.16	0.42	9
4	1.89	1.26	0.4	9
5	1.68	1.15	0.4	9
6	1.26	0.92	0.49	9
7	0.99	0.76	0.68	9
8	2.13	1.5	0.55	9
9	1.81	1.27	0.6	9
10	1.09	0.82	0.5	9
11	2.37	1.6	0.55	9
12	2.8	1.88	0.55	9
13	2.61	1.8	0.57	9
14	2.38	1.6	0.6	9
15	2.71	1.85	0.53	9
16	3.7	2.19	0.3	9
17	4.61	2.92	0.61	9
18	3.47	2.37	0.7	9
19	4.55	2.74	0.4	9
20	3.45	2.35	0.73	9

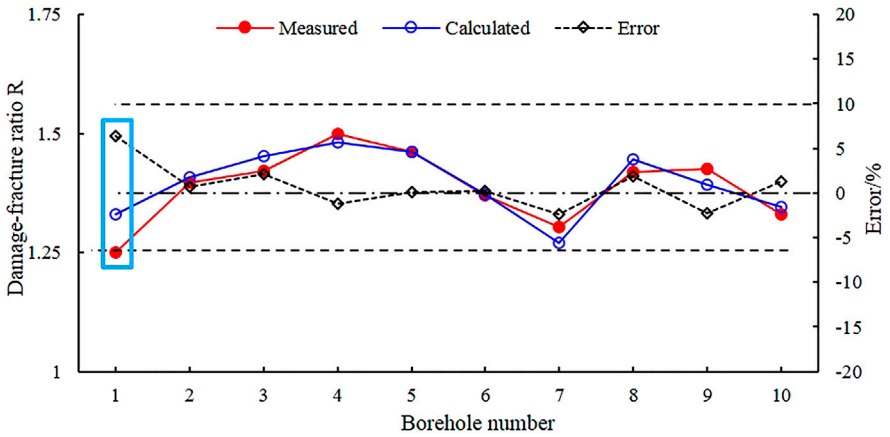


FIGURE 5 | Error analysis of the proposed method.

Using a hybrid explicit and implicit algorithm, the expression of R can be shown in the following form:

$$R = b_1 RMIBT^{b_2}\left(\frac{B}{H_{HDZ}}\right)^{b_3} \tag{6}$$

In which R is the surrounding rock damage-fracture ratio, H_{HDZ} is the depth of highly damaged zone, $RMIBT$ is the rock mass integrity index, and they can be determined by digital borehole televiewer. B is the excavation span along the damaged direction. According to the test data from the engineering practice, the parameters b_i are $b_1 = 1.7015$, $b_2 = -0.1532$, $b_3 = -0.1419$.

The Error Analysis

Comparing the measured R from different rock mass integrity conditions with the calculated value, the error analysis is shown in **Figure 5**. The error between measured data and calculated data is relatively small both in good or bad integrity conditions. However, in the area with low strength or with already released stress, the depth of excavation damage zone and highly damaged zone are close to each other, and the calculated EDZ is obtained from calculated R of greater safety reserves.

Compared with the acoustic test, the proposed method, considering the integrity of rock mass and excavation span of surrounding rock, is only dependent on the results of borehole camera which has strong anti-interference and applicability.

ENGINEERING PRACTICE

The test data were obtained from famous deep underground engineering. After evaluating the integrity of the surrounding

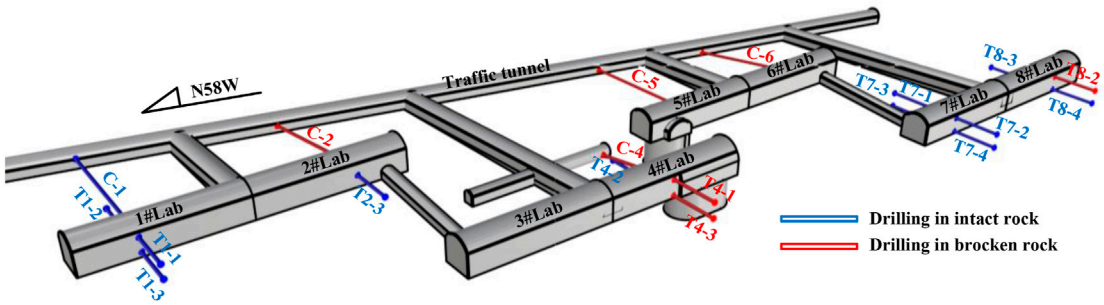


FIGURE 6 | Drilling arrangement in engineering case.

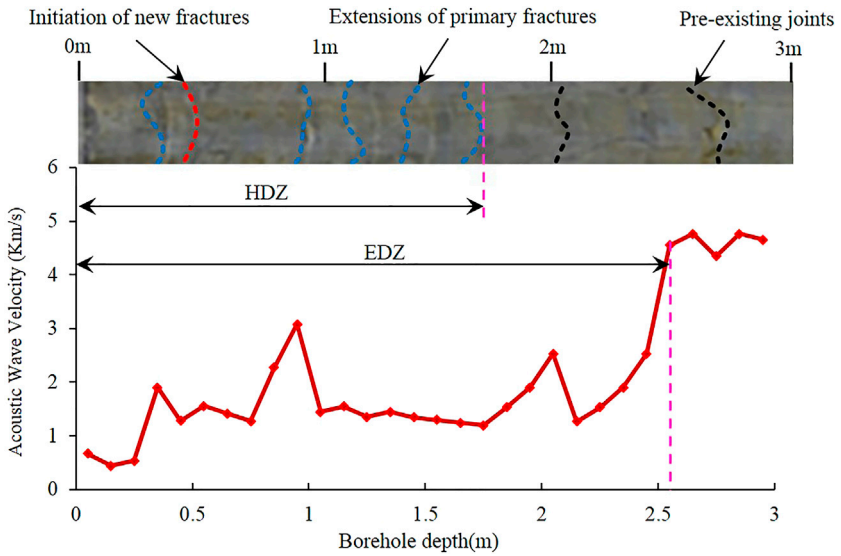


FIGURE 7 | Test result in borehole T4-2.

rock mass using the RMIBT method proposed by Guo et al. (2017), the surrounding rock masses were divided into intact rock (RMIBT≥0.5) and broken rock (RMIBT<0.5), as shown in **Figure 6**. Twenty randomly selected boreholes in the cavern with 14 m excavation spans were used as training samples to solve the coefficient in the model, and two boreholes, T4-2 and T7-4, were used as test samples to validate the calculation model.

The lithology of the surrounding rock mass in T4-2 is polychromatic marble. The observation results in **Figure 7** showed that the depth of the highly damaged zone is 1.8 m with an integrity index RMIBT 0.568. The acoustic test showed 2.6 m for the excavation damage zone, so the test surrounding rock damage-fracture ratio of the surrounding rock is 1.4, while the calculated damage-fracture ratio of the surrounding rock is 1.45.

The lithology of the surrounding rock mass in T7-4 is grey marble. The observation results in **Figure 8** showed that the depth of the highly damaged zone is 0.6 m with an integrity index RMIBT of 0.75. The acoustic test showed 1.2 m for the excavation damage zone, so the test damage-fracture ratio of the surrounding rock is 2.0 while the calculated ratio is 2.07, and there is little difference between the calculated value and the measured value.

The calculated values of the T4-2 and T7-4 are basically consistent with the acoustic test values, which indicates that the established model of the surrounding rock damage-fracture ratio R can be used to evaluate the depth of EDZ under different surrounding rock integrity conditions.

DISCUSSION

The applicability of this method has been verified to be good. It is worth noting that when the method is used independently, as several parameters involved in the calculation model are obtained from field tests, the values of the parameters are highly susceptible to affecting the accuracy of the calculation results, and in order to clearly understand the influence of these parameters on the calculated value, a parameter sensitivity analysis was

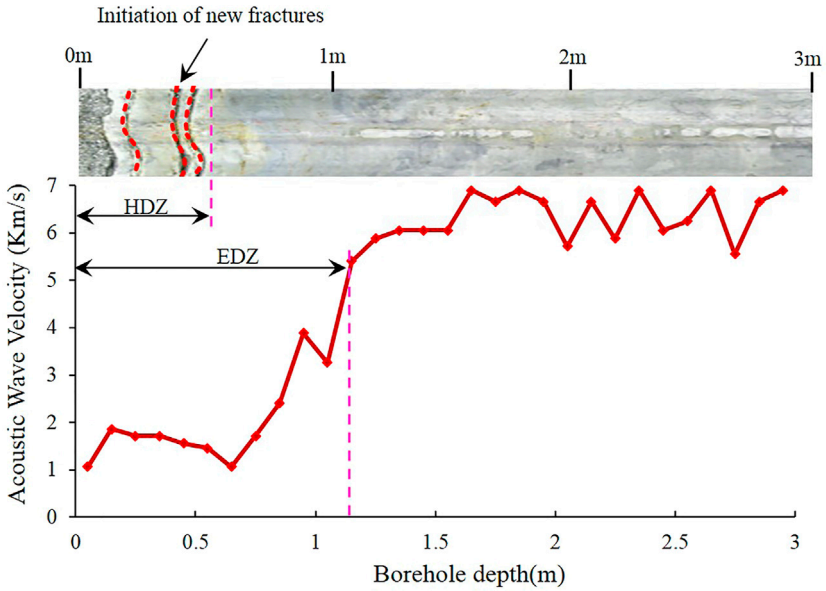


FIGURE 8 | Test result in borehole T7-4.

performed on the recommended surrounding rock damage-fracture ratio model.

Variance-based sensitivity analysis, often referred to as the Sobol method (Sobol, 2001), is a form of global sensitivity analysis that can handle nonlinear effects. The calculation results are relatively robust and reliable. It has been widely used in sensitivity analysis of large nonlinear models in environmental and economic fields. In this method, the total variance of the model can be decomposed into a combination of individual parameters and multiple parameter interactions.

$$D = \sum_i D_i + \sum_{i<j} D_{ij} + \cdots + D_{1,2,\cdots,n} \tag{3a}$$

Where D is the total variance of the model. D_i is the variance generated by parameter x_i. D_{ij} is the variance resulting from the interaction of parameter x_i and parameter x_j. $D_{1,2,\cdots,n}$ is the variance produced by the co-action of several parameters.

Normalizing the above equation, the sensitivity of the model to each parameter and the correlation of each parameter can be achieved.

$$1 = \sum_i \frac{D_i}{D} + \sum_{i<j} \frac{D_{ij}}{D} + \cdots + \frac{D_{1,2,\cdots n}}{D}$$

Then the Total-effect index of the model can be expressed as,

First-order index $S_i = \frac{D_i}{D}$

Total-effect index $S_{Ti} = 1 - \frac{D_{\sim i}}{D}$ Where, S_i is called the first-order sensitivity index or "main effect index". This is the contribution to the output variance of the main effect of x_i; therefore, it measures the effect of varying x_i alone. S_{Ti} is the total-effect index. This measures the contribution to the output variance of x_i including all variance caused by its interactions, of any order, with any other input variables. Higher values mean a greater impact for both indexes.

TABLE 2 | Results of the sensitivity analysis.

	First-order index S_i	Total-effect index S_{Ti}
RMIBT	0.0135	0.0137
B	0.2074	0.2091
H_{hdz}	0.7778	0.7786

$D_{\sim i}$ is the variance resulting from all parameters except x_i.

The global sensitivity analysis of the damage-fracture ratio R of the surrounding rock was carried out, and the sampling was carried out according to the range of the independent variables, and the sampling method was adopted by the Monte Carlo method. 40,000 sets of model parameters were randomly selected, and the calculation results tended to converge after the calculation. The results of the first-order index and total-effect index of the parameters are shown in **Table 2** below.

The results showed that the damage-fracture ratio R is more influenced by the depth of the highly damaged zone than the integrity of rock mass. And the total sensitivity of the parameters does not differ much from the first-order sensitivity, which indicates that the model is immune from the multiple parameter interactions.

In this model, several parameters were obtained from the engineering practice based on the available data. In fact, it is also feasible to select other characteristic parameters, such as principal stress ratio, strength stress ratio, and high-span ratio, to establish the model. However, it is not advisable to use more parameters, because too many parameters will make it difficult to determine the special solution of matrix zero space, thus introducing more influencing factors. On the other hand, more parameters may make the calculation results satisfactory at the expense of the applicability of the method in engineering. After all, construction

workers are not good at performing complex calculations and error analysis of the results.

CONCLUSION

An acoustic wave test is still a commonly used method to determine the excavation damage zone (EDZ) because of its low cost and easy implementation. However, the performance of the method is negatively affected by the drilling environment and the fracture of the rock mass.

This paper proposed a method that takes into account the *in-situ* stress, rock mass integrity, span length, and depth of highly damaged zone to overcome these effects for reliable determination of EDZ. First, surrounding rock damage-fracture ratio (R) is defined as the depth of the excavation damage zone to the depth of the highly damaged zone. Multiple factors were summarized from the existing research results of surrounding rock damage as the dominant influence. Then, the dimensional analysis method was employed to generate an implicit expression. To determine the impact of selected parameters on the results, the parameter sensitivity analysis was demonstrated. For better practicality, different deep engineering case data were verified in the proposed method. The results prove that the proposed method is remarkably successful in the determination of EDZ evaluation of deep buried engineering projects, and also has strong anti-noise capability due to the independence of the acoustic test.

DATA AVAILABILITY STATEMENT

The original contributions presented in the study are included in the article/Supplementary Material, further inquiries can be directed to the corresponding author.

AUTHOR CONTRIBUTIONS

Investigation, HG and JT; methodology, HG and QS, writing—original draft preparation, HG and QS; writing—review and editing, HG and QS; data curation, HG and WL. All authors have read and agreed to the published version of the manuscript.

FUNDING

This study was funded by the National Natural Science Foundation of China (Grant No. 51978265, 51909136), and the Open Research Fund of Key Laboratory of Geological Hazards on Three Gorges Reservoir Area (China Three Gorges University), Ministry of education, Grant number 2020KDZ03.

REFERENCES

Baechler, S., Lavanchy, J. M., Armand, G., and Cruchaudet, M. (2011). Characterisation of the Hydraulic Properties within the Edz Around Drifts at Level 490 M of the Meuse/haute-marne Url: a Methodology for Consistent Interpretation of Hydraulic Tests. *Phys. Chem. Earth Parts A/b/c* 36 (17-18), 1922–1931. doi:10.1016/j.pce.2011.10.005

Eberhardt, E., and Diederichs, M. (2012). *Review of Engineering Geology and Rock Engineering Aspects of the Construction of a KBS-3 Repository at the Forsmark Site—Initial Review Phase*. Stockholm: Swedish Radiation Safety Authority.

Fan, Y., Lu, W. B., Yan, P., Chen, M., and Zhang, Y. Z. (2015). Transient Characters of Energy Changes Induced by Blasting Excavation of Deep-Buried Tunnels. *Tunnelling Underground Space Tech.* 49, 9–17. doi:10.1016/j.tust.2015.04.003

Fan, Y., Zheng, J. W., Cui, X. Z., Leng, Z. D., Wang, F., and Lv, C. C. (2021). Damage Zones Induced by *In Situ* Stress Unloading during Excavation of Diversion Tunnels for the Jinping II Hydropower Project. *Bull. Eng. Geology. Environ.* 2021 (8), 1–27. doi:10.1007/s10064-021-02172-y

Feng, G.-L., Chen, B.-R., Xiao, Y.-X., Jiang, Q., Li, P.-X., Zheng, H., et al. (2022). Microseismic Characteristics of Rockburst Development in Deep TBM Tunnels with Alternating Soft-Hard Strata and Application to Rockburst Warning: A Case Study of the Neelum-Jhelum Hydropower Project. *Tunnelling Underground Space Tech.* 122, 104398. doi:10.1016/j.tust.2022.104398

Feng, G.-L., Feng, X.-T., Chen, B.-r., Xiao, Y.-X., and Yu, Y. (2015). A Microseismic Method for Dynamic Warning of Rockburst Development Processes in Tunnels. *Rock Mech. Rock Eng.* 48 (5), 2061–2076. doi:10.1007/s00603-014-0689-3

Guo, H.-S., Feng, X.-T., Li, S.-J., Yang, C.-X., and Yao, Z.-B. (2017). Evaluation of the Integrity of Deep Rock Masses Using Results of Digital Borehole Televiewers. *Rock Mech. Rock Eng.* 50 (6), 1371–1382. doi:10.1007/s00603-017-1173-7

Harrison, J., Hudson, J., and Popescu, M. (2002). Engineering Rock Mechanics: Part 2. Illustrative Worked Examples. *Appl. Mech. Rev.* 55 (2). doi:10.1115/1.1451166

Huang, F., Zhu, H. H., Li, Q. S., and Li, E-P. (2016). Field Detection and Theoretic Analysis of Loose circle of Rock Mass Surrounding Tunnel. *Rock Soil Mech.* 37, 145–150. doi:10.16285/j.rsm.2016.S1.019

Jing, H., WFu, G. B., and Guo, Z. (1999). Measurement and Analysis of Influential Factors of Broken Zone of Deep Roadways and Study on its Control Technique. *Chin. J. Rock Mech. Eng.* 18 (1), 70–74.

Kelsall, P. C., Case, J. B., and Chabannes, C. R. (1984). Evaluation of Excavation-Induced Changes in Rock Permeability. *Int. J. Rock Mech. Mining Sci. Geomechanics Abstr.* 21 (5), A177. doi:10.1016/0148-9062(84)91530-4

Malmgren, L., Saiang, D., Töyrä, J., and Bodare, A. (2007). The Excavation Disturbed Zone (EDZ) at Kiirunavaara Mine, Sweden-by Seismic Measurements. *J. Appl. Geophys.* 61, 1–15. doi:10.1016/j.jappgeo.2006.04.004

Martin, C. D., Kaiser, P. K., and McCreath, D. R. (1999). Hoek-Brown Parameters for Predicting the Depth of Brittle Failure Around Tunnels. *Can. Geotech. J.* 36 (1), 136–151. doi:10.1139/t98-072

Pusch, R., and Stanfors, R. (1992). The Zone of Disturbance Around Blasted Tunnels at Depth. *Int. J. Rock Mech. Mining Sci. Geomechanics Abstr.* 29 (5), 447–456. doi:10.1016/0148-9062(92)92629-q

Richards, R., Jr, and Bjorkman, G. S., Jr (1978). Optimum Shapes for Unlined Tunnels and Cavities. *Eng. Geology.* 12, 171–179. doi:10.1016/0013-7952(78)90010-8

Sato, T., Kikuchi, T., and Sugihara, K. (2000). *In-situ* Experiments on an Excavation Disturbed Zone Induced by Mechanical Excavation in Neogene Sedimentary Rock at Tono Mine, central Japan. *Eng. Geology.* 56, 97–108. doi:10.1016/s0013-7952(99)00136-2

Siren, T., Kantia, P., and Rinne, M. (2015). Considerations and Observations of Stress-Induced and Construction-Induced Excavation Damage Zone in Crystalline Rock. *Int. J. Rock Mech. Mining Sci.* 73, 165–174. doi:10.1016/j.ijrmms.2014.11.001

Sobol, I. M. (2001). Global Sensitivity Indices for Nonlinear Mathematical Models and Their Monte Carlo Estimates. *MATH. COMPUT. SIMULAT* 55 (1–3), 271–280. doi:10.1016/S0378-4754(00)00270-6

Sun, Q. C., Zheng, M. Z., Li, S. J., Guo, H-S., Cheng, Y., Pei, S-F., et al. (2019). Variation Characteristics and Determination of Tunnel Relaxation Depth of Columnar Jointed Rock Mass. *Rock Soil Mech.* 40 (2), 728–736. doi:10.16285/j.rsm.2017.1616

Sun, Q., Li, S., Guo, H., Zheng, M., and Yang, Z. (2021). *In Situ* test of Excavation Damaged Zone of Columnar Jointed Rock Masses under Different Borehole Conditions. *Bull. Eng. Geol. Environ.* 80 (4), 2991–3007. doi:10.1007/s10064-020-02100-6

Wu, F. Q., Liu, J. Y., Liu, T., Zhuang, H., and Yan, C. (2009). A Method for Assessment of Excavation Damaged Zone (EDZ) of a Rock Mass and its Application to a Dam Foundation Case. *Eng. Geology.* 104 (3), 254–262. doi:10.1016/j.enggeo.2008.11.005

Xie, H. P., Gao, F., and Ju, Y. (2015). Research and Development of Rock Mechanics in Deep Ground Engineering. *Chin. J. Rock Mech. Eng.* 34 (11), 2161–2178. doi:10.13722/j.cnki.jrme.2015.1369

Yang, J., Dai, J., Yao, C., Jiang, S., Zhou, C., and Jiang, Q. (2020). Estimation of Rock Mass Properties in Excavation Damage Zones of Rock Slopes Based on the Hoek-Brown Criterion and Acoustic Testing. *Int. J. Rock Mech. Mining Sci.* 126, 104192. doi:10.1016/j.ijrmms.2019.104192

Yu, Y., Feng, G.-l., Xu, C.-j., Chen, B.-r., Geng, D.-x., and Zhu, B.-t. (2022). Quantitative Threshold of Energy Fractal Dimension for Immediate Rock Burst Warning in Deep Tunnel: A Case Study. *Lithosphere* 2021, 1699273. doi:10.2113/2021/1699273

Zhou, X. P., and Qian, Q. H. (2007). Zonal Fracturing Mechanism in Deep Tunnel. *Chin. J. Rock Mech. Eng.* 26 (5), 877–885. doi:10.1016/S1872-2067(07)60020-5

Zou, H. Y., and Xiao, M. (2010). Study of Methodology for Assessment of Excavation Disturbed Zone of Underground Caverns. *Chin. J. Rock Mech. Eng.* (293), 513–519.

Conflict of Interest: The authors declare that the research was conducted in the absence of any commercial or financial relationships that could be construed as a potential conflict of interest.

The reviewer YF declared a shared affiliation the author XY, to the handling editor at the time of the review.

Publisher's Note: All claims expressed in this article are solely those of the authors and do not necessarily represent those of their affiliated organizations, or those of the publisher, the editors and the reviewers. Any product that may be evaluated in this article, or claim that may be made by its manufacturer, is not guaranteed or endorsed by the publisher.

Copyright © 2022 Guo, Tong, Sun, Yang, Luo, Yu. This is an open-access article distributed under the terms of the Creative Commons Attribution License (CC BY). The use, distribution or reproduction in other forums is permitted, provided the original author(s) and the copyright owner(s) are credited and that the original publication in this journal is cited, in accordance with accepted academic practice. No use, distribution or reproduction is permitted which does not comply with these terms.

frontiers | Frontiers in Earth Science

ORIGINAL RESEARCH
published: 08 April 2022
doi: 10.3389/feart.2022.851673

Micropore Structure and Fractal Characteristics of Clays Due to Freeze-Thaw and Compression Based on Mercury Intrusion Porosimetry

Shengfu Wang, Liang Lv, Kaixi Xue, Dongjie Zhang, Mingdong Li, Dongwei Li and Chang Yuan*

Department of Civil and Architecture Engineering, East China University of Technology, Nanchang, China

The artificial ground freezing method has been widely used in shield end reinforcement and connecting channel reinforcement of urban subway tunnel in water-rich soft soil. Accurate quantification of micropore change and redistribution due to freeze-thaw is important to understand frost heave and thaw settlement of soft soils including mucky clay and silty clay. This paper presents Mercury Intrusion Porosimetry (MIP) data for mucky clay and silty clay specimens before and after freeze-thaw and compression. MIP tests were conducted on the soil samples of undisturbed soil, frozen-thawed soil, compressed soil and compressed frozen-thawed soil. The pores of clays were divided into five groups according to the diameter, including 1) macro pore, 2) medium pore, 3) small pore, 4) micro pore, 5) ultramicro pore. Micro pores and ultramicro pores account for more than 80% of clays' total pore volume and pore surface area. The pore distribution characteristics of mucky clay and silty clay were studied, and the pore volume and pore surface area distributions' capacity dimension was estimated. The particle contact, pore changes of clays due to freeze-thaw and compression were analyzed quantitatively. Total pore volume and pore surface area of clays increased due to freeze-thaw, and decreased due to compression correspondingly. The distribution of clays' pore volume and pore surface area have statistical self similarity, and it is effective to quantify the microstructure changes of clays due to freeze-thaw and compression by estimating capacity dimension, which can provide a new way to reveal the internal micro-pore change of clays due to freeze-thaw and compression quantitatively.

Keywords: micro pore, mercury intrusion porosimetry, freeze-thaw, compression, clay

OPEN ACCESS

Edited by:
Shibing Huang,
Wuhan University of Science and Technology, China

Reviewed by:
Dongdong Ma,
Anhui University of Science and Technology, China
Yanjun Shen,
Xi'an University of Science and Technology, China

****Correspondence:***
Kaixi Xue
xkx1257@foxmail.com

Specialty section:
This article was submitted to Geohazards and Georisks, a section of the journal Frontiers in Earth Science

Received: *10 January 2022*
Accepted: *18 March 2022*
Published: *08 April 2022*

Citation:
Wang S, Lv L, Xue K, Zhang D, Li M, Li D and Yuan C (2022) Micropore Structure and Fractal Characteristics of Clays Due to Freeze-Thaw and Compression Based on Mercury Intrusion Porosimetry. Front. Earth Sci. 10:851673. doi: 10.3389/feart.2022.851673

1 INTRODUCTION

The artificial ground freezing method (AGF) has been widely adopted in urban subway construction in Ningbo, a coastal city in eastern China, which is located in a soft soil area that is rich in water (Wang et al., 2017; Wang et al., 2018; Fan et al., 2019). However, the AGF would cause frost heaves and thaw settlement in water rich areas (Yamamoto and Springman, 2014; Marwan et al., 2016). The key problem to be solved is to reduce the thaw settlement deformation caused by the AGF (Civan, 2000; Jin et al., 2010; Shen et al., 2018). For soft soil, due to its unique soil structure, the change in the microstructure before and after the freeze-thaw is the fundamental cause of macro thaw settlement deformation (Yamamuro and Wood, 2004; Cuisinier et al., 2011; Lieb-Lappen et al., 2017).

TABLE 1 | Soil index properties of the tested samples.

Engineering index	Value	
	Mucky clay	Silty clay
Water content, ω (%)	51	39
Natural bulk density, ρ (g/cm3)	1.67	1.82
Void ratio, e	1.43	1.08
Specific gravity, G_S	2.69	2.68
Liquid limit, LL (%)	43	44
Plastic limit, PL (%)	20	21
Plasticity index, PI	23	23

TABLE 2 | Test groups and samples.

Mucky clay	Silty clay	State of samples
M1	S1	Undisturbed samples
M2	S2	Compressed samples
M3	S3	Frozen-thawed samples
M4	S4	Compressed samples upon freezing-thawing

At present, the research methods for investigating soil microstructure mainly include mercury intrusion porosimetry (MIP), gas absorption operations (BET), energy dispersive spectroscopy, computed tomography (CT), and scanning electron microscopy (SEM) (Yamamuro and Wood, 2004; Grimstad et al., 2010; Cuisinier et al., 2011; Gu et al., 2013; Lopes, 2016; Lieb-Lappen et al., 2017). Among them, MIP has been widely used due to its large measurement range and good repeatability of measurement results (Romero and Simms, 2009; Lubelli et al., 2013; Lopes, 2016; Wang et al., 2016). Cui and Tang (2011) used MIP to study the evolution of the pore size distribution of natural structures in soft soil during compression, and proposed the concept of the pore structure damage potential, which is used to characterize the variation in the pore distribution with load. Tang and Yan (2015) revealed the micromechanism of the effect of freeze-thaw cycles on soil strength through mercury intrusion tests and scanning electron microscopy. In addition, the application of MIP in studies of soil microstructure has included the following aspects: 1) the variation law of the soil pores under different degrees of compression (Cudny and Vermeer, 2004; Liu and Zhang, 2014; Jarvis et al., 2017; Wang et al., 2020), 2) the consolidation and dynamic load conditions based on mercury intrusion tests (Dean et al., 1987; Jiang et al., 2014; Tang and Li, 2018) and SEM analyses (Kang et al., 2003; Cui and Jia, 2013), 3) the micropore characteristics and their changes with engineering properties such as compression deformation and seepage consolidation (Kawaragi et al., 2009; Le Runigo et al., 2009; Aldaood et al., 2014; Yi et al., 2015; Lei et al., 2019; Liu et al., 2020).

Fractal theory is a very popular, active new theory (Mandelbrot, 1967). The most basic characteristic of fractal theory is to describe and study objective things from the perspective of fractal dimension and mathematical methods, that is, to describe and study objective things using the mathematical tools of the fractal dimension (Mandelbrot, 1983; Avnir et al., 1985; Avnir, 1989; Moore and Donaldson, 1995; Zeng et al., 1996; Liu et al., 2011). It breaks away from the traditional barriers of one-dimensional line, two-dimensional surface, three-dimensional shapes, and even four-dimensional space-time. Its results are closer to the description of the real attributes and states of complex systems, and they are more in line with the diversity and complexity of objective things. Since Tyler (Tyler and Wheatcraft, 1992) introduced the use of fractal theory in the study of soil structures, many scholars have carried out fractal research on the quantity distribution, mass distribution, volume distribution, surface area, and contour line of particles in geotechnical media (Peyton et al., 1994; Zeng et al., 1996; Cai et al., 2010; Caruso et al., 2011; Zhang et al., 2015; Zhao et al., 2017; Wang and Guo, 2019), and many important achievements have been made in the study of the microstructure of non-freeze-thaw soils. However, research on the microstructure of frozen soils has mainly focused on the compression deformation of disturbed perennial and seasonal frozen soils, the shear damage, and the change in the soil properties under freeze-thaw cycles (Zhang and Zhang, 2006; Tang and Yan, 2015; Ding et al., 2019). Numerous qualitative studies have been carried out in combination with mercury intrusion tests, SEM image processing, and CT scanning technology (Chunhua et al., 2005; Bornert, 2010; Hamamoto et al., 2016; Ding et al., 2019). Because of the large number of micro parameters, it is difficult to establish a macroscopic quantitative expression based on the microstructural parameters that reflects the actual engineering problem.

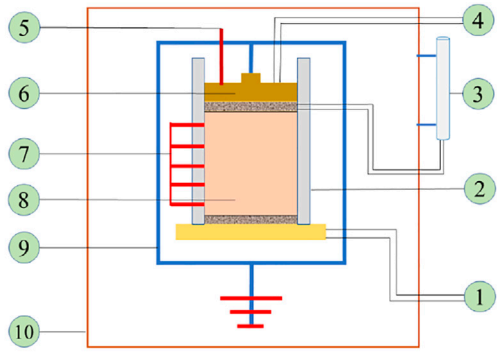
The structure of the disturbed soil has changed, and its microscopic particle state, interparticle contact state, and pore characteristics cannot fully reflect the structural characteristics of the undisturbed soil. Little research has been conducted on the micro-mechanism of undisturbed artificial frozen and thawed soils. Tang et al. (2011) (Zhou and Tang, 2015a; Zhou and Tang, 2015b; Tang and Yan, 2015; Jie and Tang, 2018; Tang and Li, 2018; Zhou and Tang, 2018) compared and analyzed the micromechanisms of the dynamic characteristics of frozen and thawed dark green silty clay by combining the microstructure scanning pictures of the soil before and after freezing. Taking the fourth layer of muddy clay in Shanghai as the research object, we studied the influence of the soil freezing temperature on the pore diameter, pore shape, directivity, porosity, and surface void ratio.

Many achievements have been made in the study of the microstructure of rocks and soils, while little research has been conducted on the micro-mechanism of the thawing settlement characteristics of undisturbed artificial frozen-thawed soils. Systematic research on the pore distribution and variation law of undisturbed soft soil, frozen-thawed soil, compressed undisturbed soil, and compressed thawed soil is still lacking. Therefore, through MIP tests and based on fractal geometry theory, quantitative and qualitative research was carried out. Therefore, it is necessary to study the pore distribution characteristics and the micro-mechanism of thaw settlement.

2 EXPERIMENTS

2.1 Soil Samples

Mucky clay and silty clay samples were obtained from 12 to 35 m below the ground surface using a thin-walled sampler (11 cm ID) and carefully transported to the laboratory from a site in Ningbo, China. **Table 1** presents the soils' index properties.



1-Cold plate, 2- Specimen tube, 3- Makeup water, 4- Loading device,

5- Displacement transducer, 6-Warm plate, 7-Temperature transducer,

8-Soil sample, 9- Loading rack, 10-Environmental chamber

FIGURE 1 | Schematic of the freeze-thaw simulation apparatus. 1-Cold plate, 2- Specimen tube, 3- Makeup water, 4- Loading device, 5-Displacement transducer, 6-Warm plate, 7-Temperature transducer, 8-Soil sample, 9- Loading rack, 10-Environmental chamber.

2.2 Apparatus for the Freeze-Thaw Simulation

Figure 1 shows a schematic of the apparatus designed to simulate the freeze-thaw process using the artificial ground freezing method (AGF). It consists of a temperature controlled environmental chamber, a specimen tube, top and bottom plates, a makeup water device, a loading device, and a temperature and vertical displacement monitoring system.

The main steps of the experiment are as follows: 1) The undisturbed soil sample was cut into a cylinder with a diameter of 79.8 mm and a height of 50 mm using a soil cutter. 2) The soil specimen was packed into a tube and wrapped with an insulation layer. Then, the tube was placed in the environmental chamber with a constant temperature. The top and bottom plates were connected to the cold liquid circulation pipeline, the displacement sensor was installed, and the temperature of the thermostat and the top and bottom plates was set to 1°C. The sample was held constant for 6 h, and the temperature and deformation were monitored. 3) When the initial temperature of the sample equally reached 1°C, the water supply pipeline was opened, the water level of the water supply device was adjusted, and the freeze-thaw test began. 4) The temperature of the bottom plate was adjusted to −10°C, and the sample was frozen from the bottom to the top. The temperature of the environmental chamber and the warm end was maintained at 1°C. The initial water level was recorded, and the water level, temperature, and deformation was recorded in real time. The frost heave test was completed when the height change of the sample was less than 0.02 mm in 2 h 5) After the frost heave test, the upper and lower cold plate supply and the water supply device were closed, and the temperature of the environment box was adjusted to 20°C to simulate the thawing of frozen soil in a natural environment. The temperature and deformation were recorded in real time. 6) Within 2 h, the height change value of the sample was less than 0.05 mm, and the test was complete. The components of the instrument were dismantled, the sample was removed, and the next test was carried out.

2.3 Consolidation Test

To study the compressibility of undisturbed and frozen-thawed soils, the maximum compressive load was set to 600 kPa based on the burial depth. The test was carried out according to Standard GB/T50123-2019 for the Geotechnical Test Method. Additional details can be found in references (Morgenstern and Smith, 1973; Chai et al., 2004; Cui and Jia, 2013; Zhang et al., 2016).

2.4 Mercury Intrusion Porosimetry

Mercury intrusion porosimetry (MIP) was used to observe the change of the soil's micropore after the freeze-thaw and compression. The MIP test was carried out using an Auto-pore 9,500 mercury porosimeter with a pore size range of 5–360,000 nm. The mercury injection test samples were prepared by the liquid nitrogen vacuum freeze-drying method, which had little effect on the microstructure of the soil samples. As shown in **Table 2**, the specimens were prepared under four different test conditions (undisturbed samples, compressed samples, frozen-thawed samples, compressed samples upon freezing-thawing) and were immersed in mercury. The mercury was gradually pressed into the pores of the specimens by applying pressure on the mercury. MIP is a common method used to study the pore size and distribution of solid materials such as rocks and soils. The testing process is divided into two stages: low pressure and high pressure. The pore size measurement capability ranges from several nanometers to several hundred microns. The experimental principle is that non-wetting liquids (such as mercury) will not flow into the pores of solid materials without external pressure. An assumption was made that cylindrical flow channels with a radius r exist in the soil, and the radius of the pores are intruded by mercury under an applied pressure, p. For a cylindrical pore, the Washburn Equation can be used to calculate the pore radius (Washburn, 1921).

$$p = -2\sigma \cos \alpha / r \tag{1}$$

where p is the applied external pressure (psia); σ is the surface tension coefficient of the mercury (N/m), taken as 0.484 N/m at normal temperatures; α is the infiltration angle of the mercury into the soil, taken as 130°; and r is the radius of a cylindrical pore (m).

3 RESULTS AND ANALYSIS

3.1 Freeze-Thaw Characteristics

The freeze-thaw properties and the physical properties of soft clay were obtained through freeze-thaw tests and are presented in **Table 3**.

3.2 Compression Characteristics

The *e-p* curves obtained from the compression tests on the mucky clay and silty clay samples before and after the freeze-thaw are

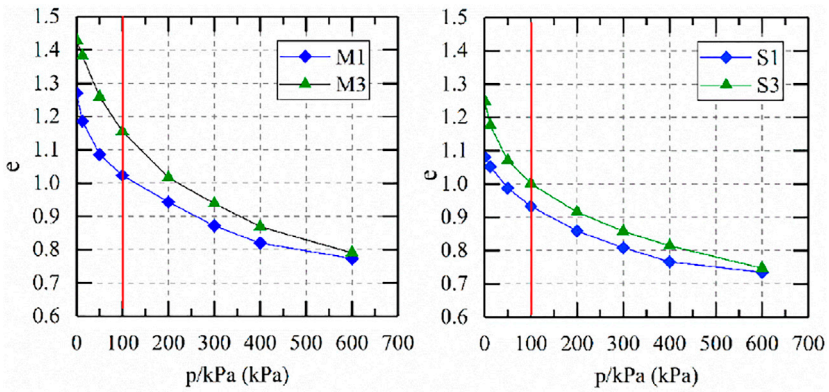


FIGURE 2 | e-p curves for the soil specimens before and after the freeze-thaw.

TABLE 3 | Freeze-thaw properties and physical properties of the specimens.

Freeze-thaw properties and physical properties	Mucky clay	Silty clay
Frost heaving ratio, (%)	13.64	16.54
Thaw settlement coefficient, (%)	15.85	17.91
Density of undisturbed soil, (g/cm^3)	1.67	1.82
Density of frozen-thawed soil, (g/cm^3)	1.72	1.76
Moisture content of undisturbed soil, (%)	51.39	39.23
Moisture content of frozen-thawed soil, (%)	48.21	37.57

shown in **Figure 2**. The overall curve can be divided into two stages by the red line in the figure: the rapid decrease in the void ratio and the slow decrease in the void ratio. During the process of clay compression, when the load is small, the compression mainly destroys the structure of the soil sample. The freeze-thaw action destroys the original skeleton structure of the soil and reorganizes it into a new structure. For the mucky clay and silty clay samples, the reduction in the void ratio of the soil after the freeze-thaw and compression was greater than that in the undisturbed soil. In addition, the compression coefficients of the mucky clay and silty clay samples after the freeze-thaw were reduced by nearly 20%, which indicates that the structure of the soft clay was disturbed by the freeze-thaw, and its compressibility was decreased.

3.3 Analysis of the Mercury Intrusion Porosimetry Test Results

According to the shear's pore size division theory (Shear et al., 1993) and the microstructure and pore size characteristics of clays in the Ningbo area, the pore size of clays can be divided into the following five categories according to the diameter (d): 1) macro pore ($d > 20$ μm), including intergranular pores and some intragranular pores; 2) medium pore (10 μm $< d <$ 20 μm), mainly intragranular pores; 3) small pore (2 μm $< d <$ 10 μm), including intragranular pores and some intergranular pores; 4) micro pore (0.1 μm $< d <$ 2 μm), mainly intergranular pores; and 5) ultramicro pore ($d <$ 0.1 μm), mainly intragranular pores.

3.3.1 Mercury Intrusion Characteristics of Clays

According to the principle of MIP, different mercury injection pressures correspond to different pore sizes. A complete mercury injection test includes two processes: mercury injection and mercury withdrawal.

Figures 3A,B show the cumulative mercury injection and mercury pressure curves of the mucky clay and silty clay, respectively. The mercury injection curves of the mucky clay and silty clay can be divided into three stages. The two soils exhibit the same trend: the first stage pressure was less than 100 psia, the second stage pressure was 100–10,000 psia, and the third stage pressure was greater than 10,000 psia until the set pressure value reached 300,000 psia. The overall curve shows that in the first stage, the mercury pressure was small, and the amount of mercury injection increased slowly. In the second stage, the mercury injection pressure increased continuously, and the cumulative mercury injection volume increased rapidly. In the third stage, the mercury pressure continued to increase to the set value, but the cumulative mercury intake growth was gentle at this stage. Only the first stage of the thawed silty soil stopped at 300 psia, and the increase rate in the second stage was higher than that in the other two stages, which is likely due to the heterogeneity of the soil samples.

In the mercury withdrawal stage of the mucky clay and silty clay samples, the curve was smooth. The mercury pressure decreased continuously in the mercury withdrawal stage, and the cumulative mercury injection volume did not return to 0. The mercury injection curve and the mercury withdrawal curves are not closed, which indicates that some mercury remained in the soil pores after the mercury withdrawal stage. The residual amount remaining in the pores is related to the pore characteristics of the soil samples. The larger the pore size and pore volume, the greater the residual mercury content.

3.3.2 Distribution of the Cumulative Pore Volume and Pore Surface Area

According to the cumulative distribution curve or differential curve of pore size corresponding to different pressures in mercury injection experiment, the cumulative pore volume or pore surface

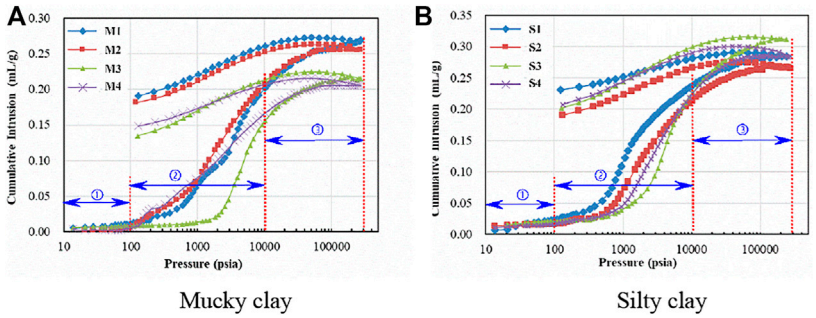


FIGURE 3 | The cumulative mercury intrusion amount of different pressures. **(A)** Mucky clay, **(B)** Silty clay.

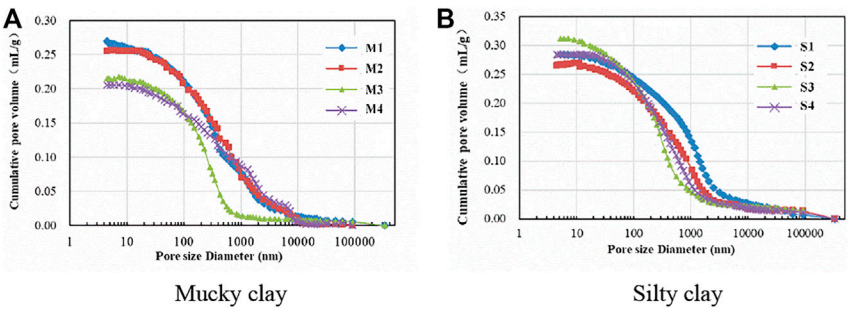


FIGURE 4 | The cumulative pore volume at different pore sizes. **(A)** Mucky clay, **(B)** Silty clay

area can be calculated. **Figure 4** shows the curves of the cumulative mercury injection versus pore size for the mucky clay and silty clay. As can be seen, the pore volumes of the silty undisturbed soil, compressed undisturbed soil, and compressed thawed soil are mainly distributed in the less than 6,000 nm pore diameter range, while the pore size of the frozen-thawed soil is mainly distributed in the less than 1,000 nm pore diameter range. The pore volumes of the clay undisturbed soil, compressed undisturbed soil, and compressed thawed soil are mainly distributed in the less than 6,000 nm pore diameter range, while that of the frozen-thawed soil is mainly distributed in the less than 2,000 nm pore diameter range. The results show that the pore size of soft soil decreases and the proportion of micropores increase. The curve for the mucky clay and silty clay thawed soils after compression plot above those of the frozen-thawed soils, which indicates that the compression improved the pore connectivity and decreased the pore volume of the large-diameter pores.

Figure 5 shows the curves of the cumulative pore surface area versus pore size for mucky clay and silty clay. The pore surface areas of the mucky clay and silty clay are mainly distributed in the pores with pore diameters of less than 1,000 nm.

3.3.3 Pore Distribution Characteristics of the Soil Samples After the Freeze-Thaw and Compression

The total pore volumes and the total pore surface areas of the mucky clay under different conditions are shown in **Figure 6A** and **Figure 7A**, respectively. After the freeze-thaw, the total pore volume and the pore surface area decreased. Total pore volume and pore surface area of the samples was shown in **Table.4**, compared with the undisturbed soil, the pore volume and pore surface area of the thawed mucky clay soil decreased by 20.49 and 8.03%, respectively. The pore volumes and surface areas of the soil samples were decreased by the compression. The pore volumes of the undisturbed soil and the frozen-thawed soil decreased by 5.47 and 5.73%, respectively, and their pore surface areas decreased by 2.45 and 7.66%, respectively. As the volume of the soil sample decreased after the freeze-thaw, it can be concluded that the soil particles are incompressible, so the pore volume inevitably decreased. With decreasing pore volume, the proportion of the pore volume accounted for by the small pores increased, so the pore surface area decreased. The freeze-thaw process transformed the pores larger than the mesopores into micropores and ultramicropores, decreasing pore sizes smaller, and it transformed the pores within some of the aggregates into pores between and within the particles. The pore surface area of the sludge was mainly distributed in the micropores. Although some of the pore volume accounted for by the pores larger than micropores, their pore surface area can be ignored. For mucky clay, the proportion of ultramicropores in pore surface area is high, up to about 70%. The remaining 30% of the pore surface area is almost microporous.

The total pore volumes and total pore surface area distributions of the silty clay under different conditions are shown in **Figures 6B**, **7B**, respectively. The pore volume and pore surface area of the silty clay increased after thawing, and the

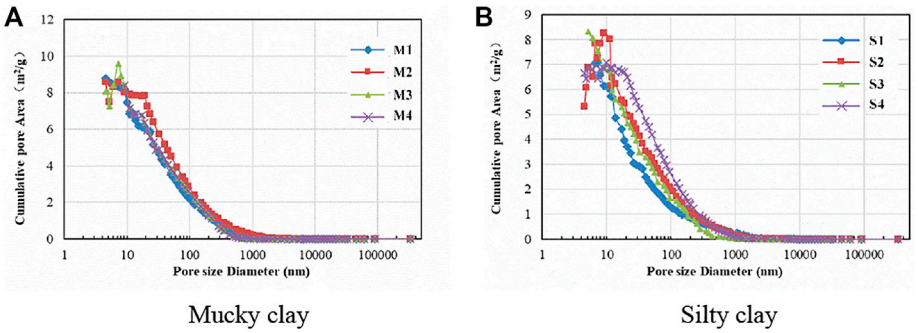


FIGURE 5 | The cumulative pore area at different pore sizes. **(A)** Mucky clay, **(B)** Silty clay.

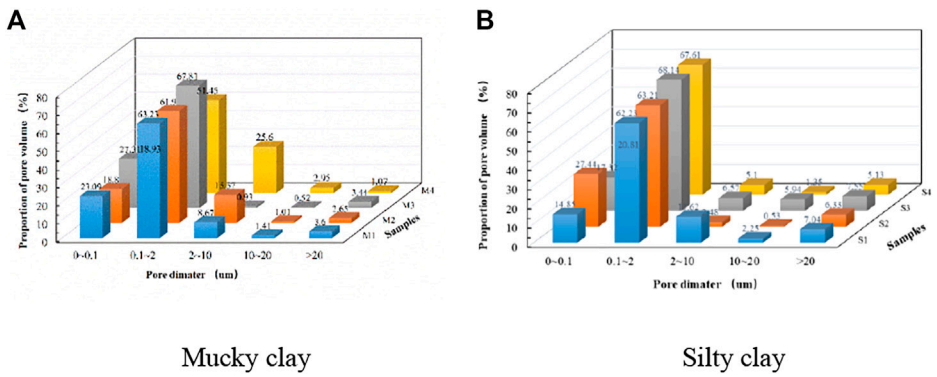


FIGURE 6 | The pore volume distribution. **(A)** Mucky clay, **(B)** Silty cla.

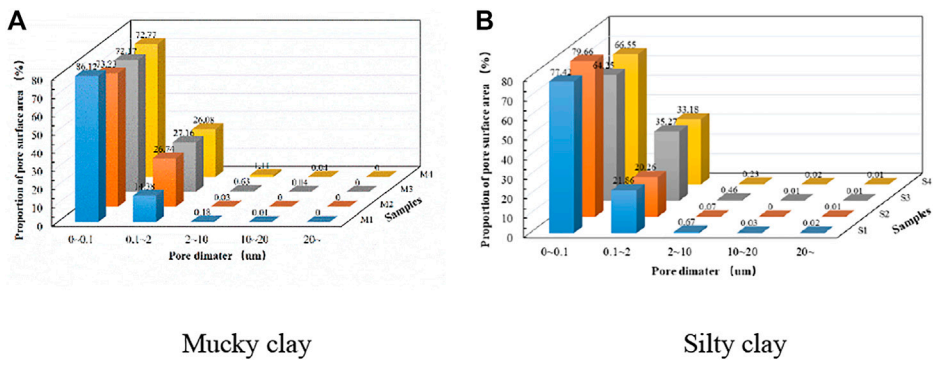


FIGURE 7 | The pore area distribution. **(A)** Mucky clay, **(B)** Silty clay.

pore ratio of the clay was increased by the freeze-thaw process. Compared with the undisturbed soil, the pore volume and pore surface area of the silty clay increased by 9.99 and 15.62% due to freeze-thaw, respectively. The pore volume of the undisturbed soil and the thawed soil decreased by 7.33 and 10.11%, respectively; and the pore surface area decreased by 32.43 and 22.47%, respectively due to compression (shown in **Table 4**). The freeze-thaw process transformed the pores larger than the micropores in the silty clay into micropores and ultramicropores, increasing the pore size, even if the pores within some of the aggregates were transformed into pores between and within the particles. The pore volume ratios of the micropores and ultramicropores increased after compression of the undisturbed and frozen-thawed soils, whereas the proportion of the micropores decreased, that is, the transformation of the small pores into micropores and

TABLE 4 | Total pore volume and pore surface area of the samples.

Samples	Total Pore Volume, (ml/g)	Total Pore Surface Area, (m^2/G)
M1	0.2698	8.7751
M2	0.2558	8.5649
M3	0.2145	8.0702
M4	0.2055	7.4956
S1	0.2841	7.0484
S2	0.2647	5.3223
S3	0.3125	8.1481
S4	0.2838	6.6531

ultramicropores. The pore surface area of the clay is mainly distributed in the ultramicropores and micropores, accounting for 99%. Compared with the micropores, the area distribution ratio of the ultramicropores is larger, about 80% for the undisturbed soil and the compressed undisturbed soil and about 70% for the frozen-thawed soil and the compressed thawed soil, which indicates that the freeze-thaw process decreased the surface area of the ultramicropores, creating pores larger than micropores.

4 FRACTAL QUANTITATIVE CHARACTERISTICS OF THE SOIL MICROPORES

4.1 Computation of the Capacity Dimension

Fractal features are usually expressed as the fractal dimension. The fractal dimension D is used to quantitatively describe the complexity and irregularity of the different fractal graphics. The larger the D value, the richer the details. In this paper, the fractal dimensions of the pore volume distribution and the pore surface area distribution were calculated using the capacity dimension method as follows:

$$D = -\lim_{\varepsilon \to \infty} \frac{\ln N(d)}{\ln(d)} \tag{2}$$

In the calculation, D was the particle size or pore diameter, ln D was taken as the abscissa, and lnN(d) was the logarithm of the pore volume lnv(d) or the logarithm of the pore surface area lnA(d), which was larger than the pore diameter, was taken as the ordinate. If there is a linear segment in the curve, the pore volume distribution and the pore surface area distribution has fractal characteristics. The negative slope value of the stable straight-line section was taken as the fractal dimension value of the pore volume distribution and the pore surface area distribution. The pore size, pore volume, and pore surface area were directly obtained from the mercury injection test.

The geometric meaning of the fractal dimension of the pore volume distribution and the pore surface area distribution are as follows: the larger the fractal dimension, the more uneven the distribution of the pore volume, and the larger the pore volume (or pore surface area), the smaller pore diameter. Based on the pore volume, the pore surface area of soft clay, and the linear correlation degree in a specific particle size range, the self-similar interval was determined. Finally, the pore diameter range was determined to be 0.4–3.5 μm for pore volume distribution, and 0.01–0.25 μm for the pore surface area distribution.

It was found that the pore volume distribution and the pore surface area distribution of the soil have fractal characteristics. Taking the calculation of the pore volume distribution fractal dimension of the mucky clay as an example, the pore volume of the mucky clay is mainly distributed in the less than 0.1–2 μm pore diameter range, but there are still a small number of pores in the 2–10 μm pore diameter range, so the upper limit of the pore size is 2.5 μm. By taking ln (d) as the abscissa and lnv (d) as the ordinate, the regression line was obtained, and the negative number of the slope of the straight line was taken as the fractal dimension. In a linear regression, when the number of test points is more than 10, the correlation coefficient is greater than 0.95, which indicates that the correlation is very good. When the lower limit of the aperture range was 0.05 μm, the linear regression correlation coefficient was less than 95%; and when the lower limit was 0.10 μm, the linear regression correlation coefficient was greater than 95%, which meets the requirements. Therefore, the lower limit is 0.1 μm, and the fractal dimension is 0.589. The larger the fractal dimension, the more uneven the distribution of the pore volume; and the smaller the pore diameter, the larger the pore volume.

4.2 Fractal Quantitative Characteristics of the Soil Pore Volume Distribution

According to the method described in the previous section, the pore volume of the silty soil under various states has fractal characteristics within the pore size range of 0.1–2.5 μm. The fractal dimension regression curve of the pore volume distribution of the silty soil for under different states is shown in **Figure 8A**.

As can be seen from **Figure 8A**, the fractal dimension of the pore volume distribution of the undisturbed soil is smaller than that of the frozen-thawed soil; that of the compressed undisturbed soil is slightly smaller than that of the undisturbed soil; and that of the compressed thawed soil is smaller than that of the frozen-thawed soil. The fractal dimension of the pore volume increases by 75.38% after the freeze-thaw, and the fractal dimensions of the pore volume distributions of the undisturbed soil and the frozen-thawed soil decreased by 15.95 and 66.11% due to compression, respectively. The fractal dimension of the pore volume distribution of the frozen-thawed soil is larger than that of the undisturbed soil, which indicates that the pore volume distribution in this pore size range is uneven due to the freeze-thaw action. The pore volume distribution of the smaller pore size is greater than that of the slightly larger pore size. The fractal dimension of the pore volume distribution decreases after compression, which indicates that the distribution of the pore volume in each pore size range is made more uniform by the compression. In particular, the distribution of the pore volume tends to be more uniform after compression. The fractal dimension of the pore volume

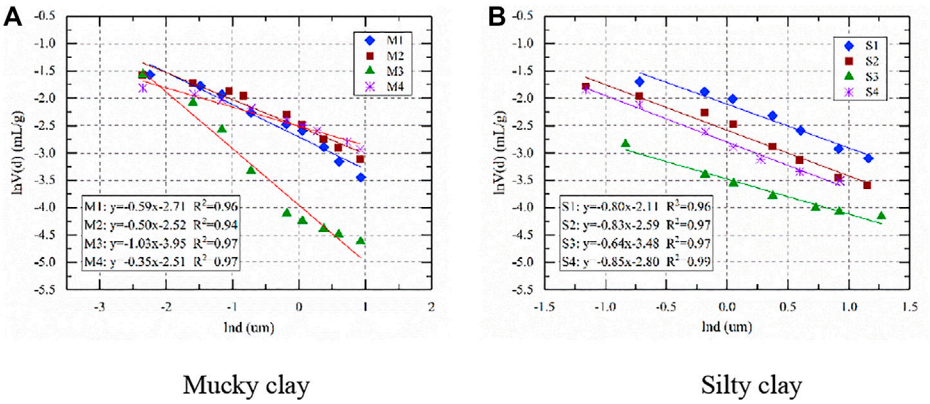


FIGURE 8 | Capacity dimension distribution curve of the soil pore volume. **(A)** Mucky clay, **(B)** Silty clay.

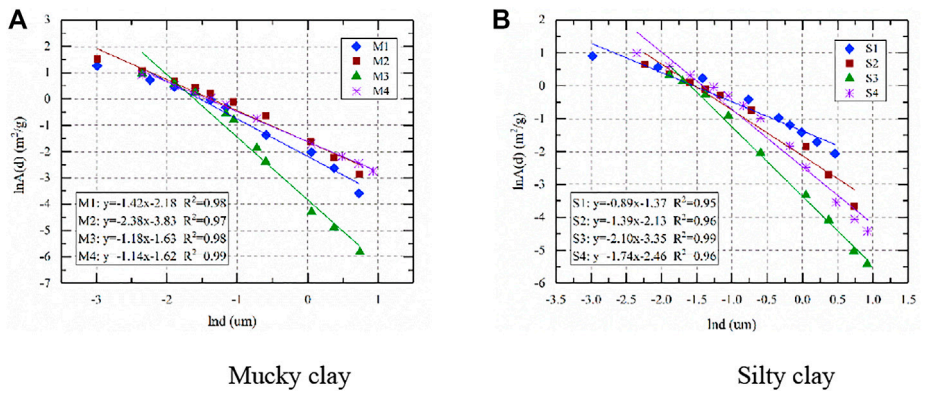


FIGURE 9 | Capacity dimension distribution curve of the soils' pore surface area. **(A)** Mucky clay, **(B)** Silty clay.

distribution is approximately positively correlated with the proportion of the pore volume in this range. The larger the proportion of the pore volume in this range, the larger the fractal dimension of the pore volume distribution.

The pore volume of the silty clay is mainly distributed in the less-than-0.1–2 μm pore size range, but there are still some pores in the 2–10 μm pore size range, so the upper limit of the pore size is 3.5 μm. Taking the undisturbed silty clay as an example, the correlation coefficient is only 88% when the lower limit is 0.1 μm, and the correlation coefficient is greater than 95% until the lower limit of 0.4 μm. The pore size range is 0.4–3.5 μm. The fractal dimension of the pore volume distribution of the silty clay is shown in **Figure 8B**.

Figure 8B shows that the pore volume integral dimensions of the thawed clay soil and the undisturbed soil are very similar, and the pore volume distribution fractal dimensions of the undisturbed soil and the frozen-thawed soil increase slightly after compression, but the increase is not very significant. The fractal dimension of the pore volume distribution of the silty clay decreased by 19.79%, and the fractal dimensions of the pore volume distributions of the undisturbed soil and the frozen-thawed soil decreased by 4.51 and 32.81%, respectively. The fractal dimension of the pore volume distribution of the frozen-thawed soil is smaller than that of the undisturbed soil, which indicates that the pore volume distribution of the clay within this pore size range is homogenized by the freeze-thaw action. The fractal dimension of the pore volume distribution is increased by compression, which indicates that the pore volume distribution of the clay is non-uniform in this pore size range due to compression. In particular, the pore size range tends to be more uneven after compression. The fractal dimension of the pore volume distribution is approximately positively correlated with the proportion of the pore volume in this range. The larger the proportion of the pore volume in this range, the larger the fractal dimension of the pore volume distribution.

4.3 Fractal Quantitative Characteristics of the Soils' Pore Surface Area

The pore surface areas of the mucky clay and silty clay soils are mainly distributed in the less-than-0.1 μm pore diameter range, and the proportion is greater than 60%. The method of

calculating the fractal dimension of the pore surface area distribution is the same as that for calculating the fractal dimension of the pore volume distribution. By taking ln(d) as the abscissa and the natural logarithm of the hole surface area lnA(d) as the ordinate, the regression of the straight line was obtained, and the negative value of the slope of the straight line was taken as the fractal dimension. It was found that there is a good linear relationship in the 0.01–0.25 μm range. The larger the fractal dimension, the more uneven the distribution of the pore surface area, that is, the smaller the pore diameter, the greater the pore surface area.

The numerical value of the fractal dimension of the pore surface area of the mucky clay soil does not vary significantly, and it has a certain regularity. As shown in **Figures 9A,B** after thawing, the fractal dimension of the pore surface area distribution increases slightly, and the fractal dimensions of the pore surface areas of the undisturbed soil and the frozen-thawed soil increase slightly. As shown in **Figure 9B**, the numerical value of the fractal dimension of the pore surface area of the silty clay soil does not vary significantly, and it has a certain regularity. The fractal dimension of the pore surface area distribution slightly increases after thawing, and it decreases slightly after the compression of the undisturbed soil and the frozen-thawed soil. The fractal dimension of the pore surface area distribution of the silty clay is 2.08% larger than that of the undisturbed soil, and the fractal dimensions of the pore surface area distributions of the undisturbed soil and the frozen-thawed soil decrease by 4.90 and 10.66%, respectively. The fractal dimension of the pore surface area distribution of the frozen-thawed soil is greater than that of the undisturbed soil, which indicates that the pore area distribution of the clay within this pore size range is non-uniform due to the freeze-thaw action. The fractal dimension of the pore surface area distribution increases after compression, which indicates that the pore surface area distribution of the clay is uniform in this pore size range. In particular, the pore size range of the frozen-thawed soil tends to be more uniform after compression.

5 LIMITATIONS AND ENGINEERING IMPLICATIONS

The soil skeleton structure is a function of the three-dimensional stress on the stratum, and in the natural state, it retains its inherent structural, shape. In this paper, to determine the change in the soil pores under freeze-thaw action and compression more accurately, original soil samples were tested. We ignored the influence of the disturbance on the soil pore structure caused by the sampling and the sample preparation processes. Furthermore, as the sample size of the MIP is small, to avoid the influence of the structural differences between the soil samples in different states, for all the states, mercury intrusion tests were run in triplicate and the three groups of parallel test data were averaged.

6 CONCLUSION

This study 1) presents micropores test data obtained from MIP tests conducted on undisturbed samples, compressed samples, frozen-thawed samples, and compressed samples upon freezing-thawing; 2) analyzes the quantitative changes in the micropores of mucky clay and silty clay after freeze-thaw and compression; and 3) establishes the quantitative relationship between the pore volume and pore surface area based on the fractal dimension. The following conclusions are drawn from the results of this study:

1) Freeze-thaw action and compression have different effects on the pore characteristics of mucky clay and silty clay. The results show that the pore volume and pore surface area of the mucky clay decreased by 20.49 and 8.03% due to freeze-thaw, respectively, which is in accordance with the law of the smaller pore ratio. The pore volume and pore surface area of the thawed silty clay soil increased by 9.99 and 15.62% due to freeze-thaw, respectively, which is in line with the law of the larger pore ratio. After compression, for the mucky clay, the pore volumes of the undisturbed and frozen-thawed soils decreased by 5.47 and 5.73%, respectively; and their pore surface areas decreased by 2.45 and 7.66%, respectively. For the silty clay, the pore volumes of the undisturbed clay and the frozen-thawed soil decreased by 7.33 and 10.11%, respectively, and their pore surface areas decreased by 32.43 and 22.47%, respectively.
2) Micro pores and ultramicro pores account for more than 80% of clays' total pore volume and pore surface area. The proportion of the micropores in the pore volume is about three times that of the ultramicropores. The pore surface area is also mainly distributed in the micropores and the ultramicropores, accounting for about 99% of the total pore surface area. The proportion of the micropores in the pore surface area is about four times that of the ultramicropores.
3) Both the pore volume distribution and the pore surface area distribution have fractal characteristics. The pore volume of the mucky clay has fractal characteristics in the 0.1–2.5 μm pore diameter range, the pore volume of the silty clay has fractal characteristics in the 0.4–3.5 μm pore diameter range, and the pore surface area has fractal characteristics in the 0.01–0.2 μm pore diameter range. The fractal dimension is positively correlated with the proportion of the pore volume and the pore surface area.
4) The fractal dimension of the pore volume distribution of soft soil is smaller than that of undisturbed soil, and it decreases after compression. The fractal dimension of the thawed clay soil is smaller than that of the undisturbed soil, and it increases after compression.
5) The fractal dimension of the pore surface area distribution of soft soil is similar to that of undisturbed soil, and it increases after compression. The fractal dimension of the thawed clay soil is larger than that of the undisturbed soil, and it decreases after compression.

DATA AVAILABILITY STATEMENT

The original contributions presented in the study are included in the article/Supplementary Material, further inquiries can be directed to the corresponding author.

AUTHOR CONTRIBUTIONS

All authors listed have made a substantial, direct, and intellectual contribution to the work and approved it for publication.

FUNDING

The work was supported by the National Natural Science Foundation of China (Nos. 42167024, 52168043, 42061011, 41977236, and 42107203), Natural Science Foundation of Jiangxi Province (Nos. 20202BABL214044, and 20192ACBL20002), and the Doctoral Scientific Research Foundation of East China University of Technology (No. DHBK2017121), Science and Technology Project Founded by the Education Department of Jiangxi Province (No. GJJ200701).

REFERENCES

Aldaood, A., Bouasker, M., and Al-Mukhtar, M. (2014). Impact of Freeze-Thaw Cycles on Mechanical Behaviour of Lime Stabilized Gypseous Soils. *Cold Regions Sci. Techn.* 99, 38–45. doi:10.1016/j.coldregions.2013.12.003

Avnir, D., Farin, D., and Pfeifer, P. (1985). Surface Geometric Irregularity of Particulate Materials: The Fractal Approach. *J. Colloid Interf. Sci.* 103 (1), 112–123. doi:10.1016/0021-9797(85)90082-7

Farin, D., and Avnir, D. (1989). *The Fractal approach to heterogeneous chemistry*. Hoboken, NY: John Wiley and Sons.

Bornert, M. (2010). X-ray Micro CT for Studying Strain Localization in clay Rocks under Triaxial Compression. *Adv. X-ray Tomography Geomaterials* 118, 35. doi:10.1002/9780470612187.ch2

Cai, J., Yu, B., Zou, M., and Mei, M. (2010). Fractal Analysis of Invasion Depth of Extraneous Fluids in Porous media. *Chem. Eng. Sci.* 65 (18), 5178–5186. doi:10.1016/j.ces.2010.06.013

Caruso, T., Barto, E. K., Siddiky, M. R. K., Smigelski, J., and Rillig, M. C. (2011). Are Power Laws that Estimate Fractal Dimension a Good Descriptor of Soil Structure and its Link to Soil Biological Properties? *Soil Biol. Biochem.* 43 (2), 359–366. doi:10.1016/j.soilbio.2010.11.001

Chai, J.-C., Miura, N., Zhu, H.-H., and Yudhbir (2004). Compression and Consolidation Characteristics of Structured Natural clay. *Can. Geotech. J.* 41 (6), 1250–1258. doi:10.1139/t04-056

Chunhua, X., Xueyan, X., and Xiaodong, S. (2005). Study on Residual Strain of Frozen Soil and CT Analysis under Cyclic Loading of Variable Amplitudes. *Yantu Lixue(rock Soil Mech.* 26 (4), 572–576. doi:10.1007/s11769-005-0030-x

Civan, F. (2000). Unfrozen Water in Freezing and Thawing Soils: Kinetics and Correlation. *J. Cold Reg. Eng.* 14 (3), 146–156. doi:10.1061/(asce)0887-381x(2000)14:3(146)

Cudny, M., and Vermeer, P. A. (2004). On the Modelling of Anisotropy and Destructuration of Soft Clays within the Multi-Laminate Framework. *Comput. Geotechnics* 31 (1), 1–22. doi:10.1016/j.compgeo.2003.12.001

Cui, Z., and Tang, Y. (2011). Microstructures of Different Soil Layers Caused by the High-Rise Building Group in Shanghai. *Environ. Earth Sci.* 63, 109–119. doi:10.1007/s12665-010-0673-5

Cui, Z.-D., and Jia, Y.-J. (2013). Analysis of Electron Microscope Images of Soil Pore Structure for the Study of Land Subsidence in Centrifuge Model Tests of High-Rise Building Groups. *Eng. Geology*. 164, 107–116. doi:10.1016/j.enggeo.2013.07.004

Cuisinier, O., Auriol, J.-C., Le Borgne, T., and Deneele, D. (2011). Microstructure and Hydraulic Conductivity of a Compacted Lime-Treated Soil. *Eng. Geology*. 123 (3), 187–193. doi:10.1016/j.enggeo.2011.07.010

Dean, T., Bell, J., and Baty, A. (1987). Soil Moisture Measurement by an Improved Capacitance Technique, Part I. Sensor Design and Performance. *J. Hydrol.* 93 (1), 67–78. doi:10.1016/0022-1694(87)90194-6

Ding, Z., Kong, B., Wei, X., Zhang, M., Xu, B., and Zhao, F. (2019). Laboratory Testing to Research the Micro-structure and Dynamic Characteristics of Frozen-Thawed Marine Soft Soil. *Jmse* 7 (4), 85. doi:10.3390/jmse7040085

Fan, W., Yang, P., and Yang, Z. (2019). Impact of Freeze-Thaw on the Physical Properties and Compressibility of Saturated clay. *Cold Regions Sci. Techn.* 168, 102873. doi:10.1016/j.coldregions.2019.102873

Grimstad, G., Degago, S. A., Nordal, S., and Karstunen, M. (2010). Modeling Creep and Rate Effects in Structured Anisotropic Soft Clays. *Acta Geotechnica* 5 (5), 69–81. doi:10.1007/s11440-010-0119-y

Gu, X., Huang, M., and Qian, J. (2013). DEM Investigation on the Evolution of Microstructure in Granular Soils under Shearing. *Granular Matter* 16 (1), 91–106. doi:10.1007/s10035-013-0467-z

Hamamoto, S., Moldrup, P., Kawamoto, K., Sakaki, T., Nishimura, T., and Komatsu, T. (2016). Pore Network Structure Linked by X-ray CT to Particle Characteristics and Transport Parameters. *Soils and Foundations* 56 (4), 676–690. doi:10.1016/j.sandf.2016.07.008

Jarvis, N., Larsbo, M., and Koestel, J. (2017). Connectivity and Percolation of Structural Pore Networks in a Cultivated silt Loam Soil Quantified by X-ray Tomography. *Geoderma* 287, 71–79. doi:10.1016/j.geoderma.2016.06.026

Jiang, M., Zhang, F., Hu, H., Cui, Y., and Peng, J. (2014). Structural Characterization of Natural Loess and Remolded Loess under Triaxial Tests. *Eng. Geology*. 181, 249–260. doi:10.1016/j.enggeo.2014.07.021

Jie, Z., and Tang, Y. (2018). Practical Model of Deformation Prediction in Soft clay after Artificial Ground Freezing under Subway Low-Level Cyclic Loading. *Tunnelling Underground Space Techn.* 76, 30–42. doi:10.1016/j.tust.2018.03.003

Jin, H., Hao, J., Chang, X., Zhang, J., Yu, Q. h., Qi, J., et al. (2010). Zonation and Assessment of Frozen-Ground Conditions for Engineering Geology along the China-Russia Crude Oil Pipeline Route from Mo'he to Daqing, Northeastern China. *Cold Regions Sci. Techn.* 64 (3), 213–225. doi:10.1016/j.coldregions.2009.12.003

Kang, M.-S., Watabe, Y., and Tsuchida, T. (2003). *Effect of Drying Process on the Evaluation of Microstructure of Clays Using Scanning Electron Microscope (SEM) and Mercury Intrusion Porosimetry (MIP), the Thirteenth International Offshore and Polar Engineering Conference*, Honolulu, Hawaii, May 25–30, 2003. International Society of Offshore and Polar Engineers.

Kawaragi, C., Yoneda, T., Sato, T., and Kaneko, K. (2009). Microstructure of Saturated Bentonites Characterized by X-ray CT Observations. *Eng. Geology*. 106 (1-2), 51–57. doi:10.1016/j.enggeo.2009.02.013

Le Runigo, B., Cuisinier, O., Cui, Y.-J., Ferber, V., and Deneele, D. (2009). Impact of Initial State on the Fabric and Permeability of a Lime-Treated silt under Long-Term Leaching. *Can. Geotech. J.* 46 (11), 1243–1257. doi:10.1139/t09-061

Lei, H., Song, Y., Qi, Z., Liu, J., and Liu, X. (2019). Accumulative Plastic Strain Behaviors and Microscopic Structural Characters of Artificially Freeze-Thaw Soft clay under Dynamic Cyclic Loading. *Cold Regions Sci. Techn.* 168, 102895. doi:10.1016/j.coldregions.2019.102895

Lieb-Lappen, R. M., Golden, E. J., and Obbard, R. W. (2017). Metrics for Interpreting the Microstructure of Sea Ice Using X-ray Micro-computed Tomography. *Cold Regions Sci. Techn.* 138, 24–35. doi:10.1016/j.coldregions.2017.03.001

Liu, J., Zha, F., Xu, L., Kang, B., Yang, C., Feng, Q., et al. (2020). Strength and Microstructure Characteristics of Cement-Soda Residue Solidified/stabilized Zinc Contaminated Soil Subjected to Freezing-Thawing Cycles. *Cold Regions Sci. Techn.* 172, 102992. doi:10.1016/j.coldregions.2020.102992

Liu, J., and Zhang, L. (2014). The Microstructure Characters of Saline Soil in Qarhan Salt Lake Area and its Behaviors of Mechanics and Compressive Strength. *Arab J. Sci. Eng.* 39 (12), 8649–8658. doi:10.1007/s13369-014-1410-2

Liu, X. H., Liu, J. H., and Wang, Y. (2011). *Fractal Characteristic Analysis of Rock Breakage Based on CT Images International Conference on Civil Engineering*

and Information Technology. Sham Shui Po: Int Industrial Electronic Center, 22–26.

Lopes, B. d. C. F. L. (2016). Microstructural-Based Approach to the Interpretation of Clays and Transitional Soils Behaviour. *Universidade de Brasília*.

Lubelli, B., de Winter, D. A. M., Post, J. A., van Hees, R. P. J., and Drury, M. R. (2013). Cryo-FIB-SEM and MIP Study of Porosity and Pore Size Distribution of Bentonite and Kaolin at Different Moisture Contents. *Appl. Clay Sci.* 80-81, 358–365. doi:10.1016/j.clay.2013.06.032

Mandelbrot, B. B. (1983). The Fractal Geometry of Nature*Am. J. of Phys.*. Macmillan 51, 286. doi:10.1119/1.13295

Mandelbrot, B. (1967). How Long Is the Coast of Britain? Statistical Self-Similarity and Fractional Dimension. *Science* 156 (3775), 636–638. doi:10.1126/science.156.3775.636

Marwan, A., Zhou, M.-M., Zaki Abdelrehim, M., and Meschke, G. (2016). Optimization of Artificial Ground Freezing in Tunneling in the Presence of Seepage Flow. *Comput. Geotechnics* 75, 112–125. doi:10.1016/j.compgeo.2016.01.004

Moore, C. A., and Donaldson, C. F. (1995). Quantifying Soil Microstructure Using Fractals. *Géotechnique* 45 (1), 105–116. doi:10.1680/geot.1995.45.1.105

Morgenstern, N. R., and Smith, L. B. (1973). Thaw-Consolidation Tests on Remoulded Clays. *Can. Geotech. J.* 10 (1), 25–40. doi:10.1139/t73-003

Peyton, R. L., Gantzer, C. J., Anderson, S. H., Haeffner, B. A., and Pfeifer, P. (1994). Fractal Dimension to Describe Soil Macropore Structure Using X ray Computed Tomography. *Water Resour. Res.* 30 (3), 691–700. doi:10.1029/93wr02343

Romero, E., and Simms, P. H. (2009). *Microstructure Investigation in Unsaturated Soils: A Review with Special Attention to Contribution of Mercury Intrusion Porosimetry and Environmental Scanning Electron Microscopy, Laboratory and Field Testing of Unsaturated Soils*. Springer, 93–115. doi:10.1007/978-1-4020-8819-3_8

Shear, D., Olsen, H., and Nelson, K. (1993). *Effectsof Desiccation on the Hydraulic Conductivity versus Void Ratio Relationship Fora Natural clay, Transportation Research Record*. Washington DC: National academy press, 1365–1370.

Shen, Y.-j., Wang, Y.-z., Zhao, X.-d., Yang, G.-s., Jia, H.-l., and Rong, T.-l. (2018). The Influence of Temperature and Moisture Content on sandstone thermal Conductivity from a Case Using the Artificial Ground Freezing(AGF) Method. *Cold Regions Sci. Techn.* 155, 149–160. doi:10.1016/j.coldregions.2018.08.004

Tang, Y.-q., and Yan, J.-j. (2015). Effect of Freeze-Thaw on Hydraulic Conductivity and Microstructure of Soft Soil in Shanghai Area. *Environ. Earth Sci.* 73 (11), 7679–7690. doi:10.1007/s12665-014-3934-x

Tang, Y.-q., Zhou, J., Hong, J., Yang, P., and Wang, J.-x. (2011). Quantitative Analysis of the Microstructure of Shanghai Muddy clay before and after Freezing. *Bull. Eng. Geol. Environ.* 71 (2), 309–316. doi:10.1007/s10064-011-0380-9

Tang, Y., and Li, J. (2018). Experimental Study on Dynamic Cumulative Axial-Strain Performance of Freezing-Thawing Saturated sandy silt. *Cold Regions Sci. Techn.* 155, 100–107. doi:10.1016/j.coldregions.2018.08.001

Tyler, S. W., and Wheatcraft, S. W. (1992). Fractal Scaling of Soil Particle-Size Distributions: Analysis and Limitations. *Soil Sci. Soc. America J.* 56 (2), 362–369. doi:10.2136/sssaj1992.03615995005600020005x

Wang, S.-l., Lv, Q.-f., Baaj, H., Li, X.-y., and Zhao, Y.-x. (2016). Volume Change Behaviour and Microstructure of Stabilized Loess under Cyclic Freeze-Thaw Conditions. *Can. J. Civ. Eng.* 43 (10), 865–874. doi:10.1139/cjce-2016-0052

Wang, S., and Guo, Z. (2019). Random Heterogeneous Microstructure Construction of Composites via Fractal Geometry. *Appl. Math. Mech.-Engl. Ed.* 40 (10), 1413–1428. doi:10.1007/s10483-019-2522-5

Wang, S., Yang, P., Dai, D., Xue, K., and Li, D. (2020). A Study on Micro-pore Characteristics of Clay Due to Freeze-Thaw and Compression by Mercury Intrusion Porosimetry. *Front. Earth Sci.* 7 (344). doi:10.3389/feart.2019.00344

Wang, S., Yang, P., and Yang, Z. (2018). Characterization of Freeze-Thaw Effects within clay by 3D X-ray Computed Tomography. *Cold Regions Sci. Techn.* 148, 13–21. doi:10.1016/j.coldregions.2018.01.001

Wang, S., Yang, Z., and Yang, P. (2017). Structural Change and Volumetric Shrinkage of clay Due to Freeze-Thaw by 3D X-ray Computed Tomography. *Cold Regions Sci. Techn.* 138, 108–116. doi:10.1016/j.coldregions.2017.03.007

Washburn, E. W. (1921). Note on a Method of Determining the Distribution of Pore Sizes in a Porous Material. *Proc. Natl. Acad. Sci. U.S.A.* 7 (4), 115–116. doi:10.1073/pnas.7.4.115

Yamamoto, Y., and Springman, S. M. (2014). Axial Compression Stress Path Tests on Artificial Frozen Soil Samples in a Triaxial Device at Temperatures Just below 0 °C. *Can. Geotech. J.* 51 (10), 1178–1195. doi:10.1139/cgj-2013-0257

Yamamuro, J. A., and Wood, F. M. (2004). Effect of Depositional Method on the Undrained Behavior and Microstructure of Sand with silt. *Soil Dyn. Earthquake Eng.* 24 (9-10), 751–760. doi:10.1016/j.soildyn.2004.06.004

Yi, Y., Gu, L., and Liu, S. (2015). Microstructural and Mechanical Properties of marine Soft clay Stabilized by Lime-Activated Ground Granulated Blastfurnace Slag. *Appl. Clay Sci.* 103, 71–76. doi:10.1016/j.clay.2014.11.005

Zeng, Y., Payton, R. L., Gantzer, C. J., and Anderson, S. H. (1996). Fractal Dimension and Lacunarity of Bulk Density Determined with X-ray Computed Tomography. *Soil Sci. Soc. Am. J.* 60 (6), 1718–1724. doi:10.2136/sssaj1996.03615995006000060016x

Zhang, H., Zhang, J., Zhang, Z., Chen, J., and You, Y. (2016). A Consolidation Model for Estimating the Settlement of Warm Permafrost. *Comput. Geotechnics* 76, 43–50. doi:10.1016/j.compgeo.2016.02.013

Zhang, Q., Yin, G., Fan, X., Wei, Z., Wang, W., and Nie, W. (2015). Loading Capacity and Deformation Characteristics of Tailings Based on a Fractal Geometrical Analysis of the Particle Microstructure. *Minerals* 5 (1), 86–103. doi:10.3390/min5010086

Zhang, S. G., and Zhang, X. D. (2006). "Dynamic Damage and Microscopic Analysis of Frozen Aeolian Soil in the West of Liaoning Province," in *Key Engineering Materials* (Switzerland: Trans Tech Publications, Ltd.) 324–325, 751–754. doi:10.4028/www.scientific.net/kem.324-325.751

Zhao, H., Zhang, H., Li, H., Wang, F., and Zhang, M. (2017). Formation and Fractal Characteristics of Main Fracture Surface of Red sandstone under Restrictive Shear Creep. *Int. J. Rock Mech. Mining Sci.* 98, 181–190. doi:10.1016/j.ijrmms.2017.07.011

Zhou, J., and Tang, Y. (2015a). Artificial Ground Freezing of Fully Saturated Mucky clay: Thawing Problem by Centrifuge Modeling. *Cold Regions Sci. Techn.* 117, 1–11. doi:10.1016/j.coldregions.2015.04.005

Zhou, J., and Tang, Y. (2015b). Centrifuge Experimental Study of Thaw Settlement Characteristics of Mucky clay after Artificial Ground Freezing. *Eng. Geology*. 190, 98–108. doi:10.1016/j.enggeo.2015.03.002

Zhou, J., and Tang, Y. (2018). Practical Model of Deformation Prediction in Soft clay after Artificial Ground Freezing under Subway Low-Level Cyclic Loading. *Tunnelling Underground Space Techn.* 76, 30–42. doi:10.1016/j.tust.2018.03.003

Conflict of Interest: The authors declare that the research was conducted in the absence of any commercial or financial relationships that could be construed as a potential conflict of interest.

Publisher's Note: All claims expressed in this article are solely those of the authors and do not necessarily represent those of their affiliated organizations, or those of the publisher, the editors and the reviewers. Any product that may be evaluated in this article, or claim that may be made by its manufacturer, is not guaranteed or endorsed by the publisher.

Copyright © 2022 Wang, Lv, Xue, Zhang, Li, Li and Yuan. This is an open-access article distributed under the terms of the Creative Commons Attribution License (CC BY). The use, distribution or reproduction in other forums is permitted, provided the original author(s) and the copyright owner(s) are credited and that the original publication in this journal is cited, in accordance with accepted academic practice. No use, distribution or reproduction is permitted which does not comply with these terms.

frontiers | Frontiers in Earth Science

ORIGINAL RESEARCH
published: 28 April 2022
doi: 10.3389/feart.2022.886876

Influence of the Xianshuihe Fault Zone on *In-Situ* Stress Field of a Deep Tunnel and its Engineering Effect

Dong Yuan[1,2,3], Lanbin Zhang[1,2], Xiaoling Liu[1,2]*, Tao Feng[3], Guangze Zhang[3], Zhengxuan Xu[3], Zhewei Wang[3], Xiaojuan Yi[3], Zhiheng Lin[3], Yang Ren[4], Ru Zhang[1,2] and Li Ren[1,2]*

[1]State Key Laboratory of Hydraulics and Mountain River Engineering, College of Water Resource and Hydropower, Sichuan University, Chengdu, China, [2]MOE Key Laboratory of Deep Earth Science and Engineering, Sichuan University, Chengdu, China, [3]China Railway Eryuan Engineering Group Company, Ltd., Chengdu, China, [4]State Key Lab Geohazard Prevent and Geoenvironm Pro, Chengdu University of Technology, Chengdu, China

OPEN ACCESS

Edited by:
Guang-Liang Feng,
Institute of Rock and Soil Mechanics (CAS), China

Reviewed by:
Shikuo Chen,
Southwest Jiaotong University, China
Changbao Guo,
Chinese Academy of Geologi-cal Sciences (CAGS), China

***Correspondence:**
Lanbin Zhang
2021223060011@stu.scu.edu.cn
Xiaoling Liu
Dazzling_Liu@163.com

Specialty section:
This article was submitted to Geohazards and Georisks, a section of the journal Frontiers in Earth Science

Received: 01 March 2022
Accepted: 06 April 2022
Published: 28 April 2022

Citation:
Yuan D, Zhang L, Liu X, Feng T, Zhang G, Xu Z, Wang Z, Yi X, Lin Z, Ren Y, Zhang R and Ren L (2022) Influence of the Xianshuihe Fault Zone on In-Situ Stress Field of a Deep Tunnel and its Engineering Effect. Front. Earth Sci. 10:886876. doi: 10.3389/feart.2022.886876

The *in-situ* stress distribution near a fault zone is affected by factors such as tectonic movement and rock mass property deterioration, and it often shows unique characteristics and further affects the mechanical response of the rock mass and the safety of underground engineering construction. The Xianshuihe fault zone is one of the most active fault zones in the world. To understand the impact of the Xianshuihe fault zone on a tunnel under construction in southwestern China, the *in-situ* stress measured near the tunnel site at different distances from the faults of the Xianshuihe fault zone is obtained. Furthermore, the characteristics of the *in-situ* stress at the tunnel site and its engineering influence effect are analyzed. The results indicate the following: 1) Around the Xianshuihe fault zone, the fault mainly affects the maximum horizontal principal stress and the minimum horizontal principal stress in the shallow strata, and the *in-situ* stress closer to the fault is more greatly affected. 2) In the shallow area near the Selaha-Kangding fault, the maximum horizontal principal stress, minimum horizontal principal stress and lateral pressure coefficient at a borehole increase with increasing distance from the fault. Greater than 600 m from the fault, the horizontal stress plays a dominant role. In the deeper strata, the maximum horizontal principal stress, the minimum horizontal principal stress and the lateral pressure coefficient exhibit no obvious change with distance from the fault. 3) According to the inversion of the *in-situ* stress field and the stress in the tunnel site, the *in-situ* stress in the tunnel barrel is affected by the depth and the fault. The *in-situ* stress is higher at greater depths. The *in-situ* stress is partially released at the fault so that the *in-situ* stress is relatively low, and the degree of stress decline at different faults is different. 4) Tunnel rockbursts tend to occur in surrounding rock sections with high stress, which are usually located in the middle of a rock mass between two faults. Large deformation mainly occurs in the fault and its influence zone.

Keywords: fault zone, *in-situ* stress, underground engineering, rockburst, large deformation

INTRODUCTION

Regarding underground engineering construction, the *in-situ* stress field environment affects the mechanical response of the surrounding rock during excavation, so it is necessary to investigate the *in-situ* stress characteristics of the surrounding rock (Lu et al., 2012; Ai et al., 2020). As the number of deeply buried long tunnels in complex and dangerous mountain areas increases, the difficulties tunnel construction faced, such as rockburst and large deformation, are becoming more prominent, which is closely related to the geological environment (Jia et al., 2020; Lin et al., 2017). For example, the tunnel of the Shiman expressway had serious deformation, which was related to the tectonic effect of the Yunxi-Yunxian fault zone in the crossing area (Luo et al., 2006). The geological structure of Pajares in the Cantabrian Mountains in northern Spain or the geomechanical anisotropy of the rock contact zone with its strength differences affected the high-speed railway tunnels in this area, resulting in significant deformation along some areas of four tunnels during excavation (Hijazo and de Vallejo, 2012). Gaoligong Mountain is located in the southern Hengduan Mountain near the collision suture zone between the Indian plate and Eurasian plate. Due to large topographic fluctuations, complex structures and strong activity, tunnel construction was facing many problems (Yu et al., 2017). The rock mass along a tunnel of the Iranian water conveyance system located in the contact zone between the Iranian plate and the Arabian plate intensified the problems related to tunnel excavation and compression due to strong joints and faults in the surrounding rock (Ajalloeian et al., 2017). The *in-situ* stress field will be disturbed when the tunnel crosses the fault zone. And the *in-situ* stress field is an important factor that determines the stress, displacement distribution and failure form of the surrounding rock encountered in underground engineering (Li et al., 2017; Zhang et al., 2019). Therefore, studying the influence of faults on the *in-situ* stress field is helpful to analyze the geological information and risk of tunnel rock mass instability, to ensure the safe design and construction of underground engineering.

Many scholars (Li and Miao, 2016; Guo et al., 2017; Cao et al., 2018; Zhao et al., 2019; Qiao, 2021; Zhang, 2021) have analyzed the characteristics of *in-situ* stress based on measured data or stress field inversion results, and some scholars (Zoback and Roller, 1979; Bell and Babcock, 1986; Stephansson and Angman, 1986; Martin, 1990; Aleksandrowski et al., 1992; Lei and Chen, 2011; Li et al., 2012; Ren et al., 2019; Pham et al., 2020; Yang, 2020) have studied the influence of fault zones on *in-situ* stress. Ren Huiliang et al. studied the influence of composite structures, including faults and folds, on the distribution patterns of the *in-situ* stress field (Ren et al., 2019). Yang Yalun investigated the influence of fault structure on the *in-situ* stress field by establishing a small-scale model of a fault area (Yang, 2020). Aleksandrowski et al. found that in a NE-trending normal fault, the stress orientation on one of the two sides of the fault was consistent with the regional stress orientation, while the maximum horizontal principal stress of the other plate was deflected by nearly 90°. Near a fault in Canada, the maximum deflection was measured to be more than 45° from the direction of a regional principal stress (Aleksandrowski et al., 1992). Lei Xianquan et al. applied the discontinuous contact model to study the impact of faults on crustal stress and concluded that the fault zone had a high shear stress, while the maximum horizontal principal stress in the nearby local area was weakened to a certain extent (Lei and Chen, 2011). Zoback found that the horizontal principal stress increases with increasing depth and increases gradually with increasing distance from the fault (Zoback and Roller, 1979). The maximum principal stress and shear stress near a fault are low. With the gradual increase in the distance between a measuring point and a fault, the two types of stress values increase significantly. Some scholars also found that the change in the maximum horizontal principal stress near a fault zone was not continuous. There have been many studies on the distribution characteristics of the *in-situ* stress field. However, because a fault is usually simplified into a homogeneous rock mass in simulation and *in-situ* stress data measured across faults are relatively scarce, the influence of a fault zone on the local *in-situ* stress is still not particularly clear (Chen, 2022). Therefore, it is of great significance to further study the influence of fault zones on the *in-situ* stress field.

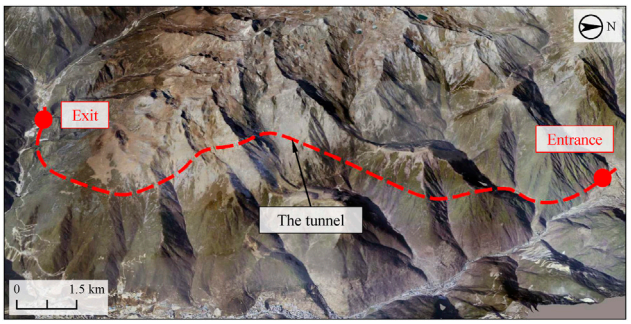


FIGURE 1 | Topographic map of the tunnel site.

Taking a tunnel in the Xianshuihe fault zone as the research object, this paper analyzes the influence of the Xianshuihe fault zone on the local *in-situ* stress field based on measured *in-situ* stress data. Combined with the three-dimensional inversion of the *in-situ* stress field, the distribution characteristics of the *in-situ* stress along the tunnel are studied. The prediction and analysis of tunnel rockburst and large deformation are carried out, which provides a reference for the design of engineering construction and safety plans.

GEOLOGICAL SETTING

Topography

The tunnel is located on the southwestern margin of the transition between the Sichuan Basin and the Tibetan Plateau. The Minjiang River, Dadu River and other river systems with severe cutting result in large topographic height differences and complex landforms. The surface elevation of the region is

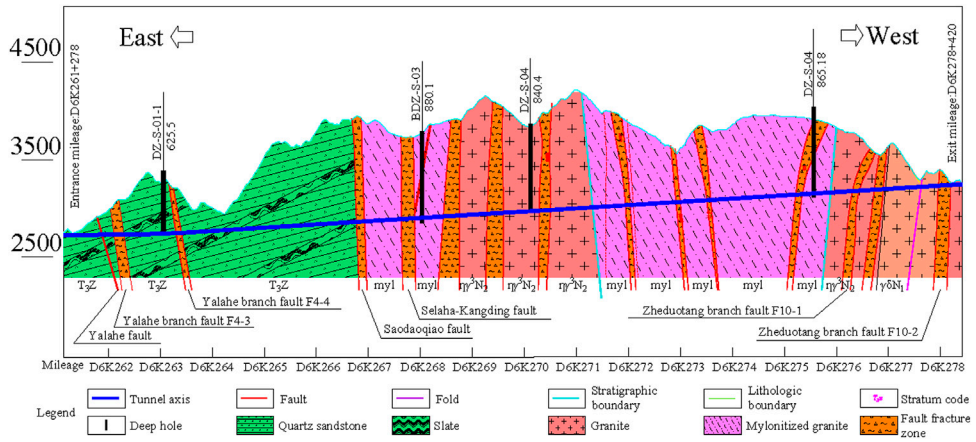


FIGURE 2 | Geological section of the tunnel site.

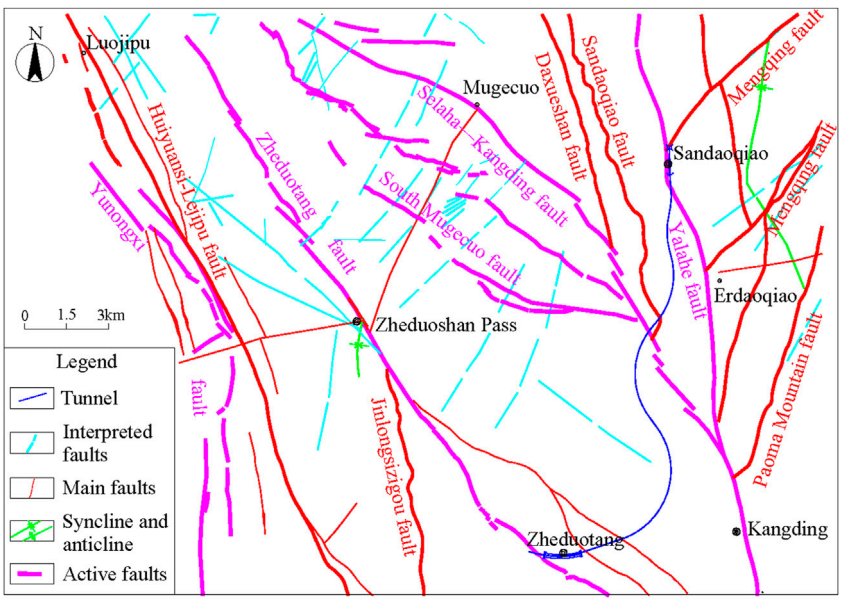


FIGURE 3 | Fault distribution map of the tunnel site.

2,715–4,225 m, and the exogenous forces are mainly glacial water erosion and freezing and thawing, accompanied by biological weathering. The tunnel site topography is a typical plateau landform as shown in **Figure 1**.

Formation Lithology

As shown in **Figure 2**, the strata exposed in the tunnel site mainly consist of Quaternary Holocene sediments: the colluvial layer is coarse breccia soil, gravel soil and block rock soil, the alluvial-diluvial layer is silty clay (breccia), fine pebble soil, pebble soil and drift rock soil, and the slope residual layer is silty clay (breccia), coarse (fine) breccia soil and gravel soil (breccia). The underlying bedrock is metamorphic quartz sandstone with slate of the Upper Triassic Zagunao Formation. The strata in this area also include granodiorite, fine-grained biotite monzogranite and mylonitized granite.

Geological Structure

The tunnel is located west of the junction between the Yangtze block and the Qiangtang-Sanjiang orogenic system, the Kang-Yunnan basement complex belt of the Yangtze block in the east, and the Yajiang remnant basin of the Qiangtang-Sanjiang orogenic system in the west. The tunnel site is located in the southeastern margin of the Songpan-Ganzi orogenic belt, where folds and faults are well developed and predominantly trend NNE, followed by NS and NNW. In terms of first-order structure, the tunnel site is located at the junction of the Sichuan-Yunnan

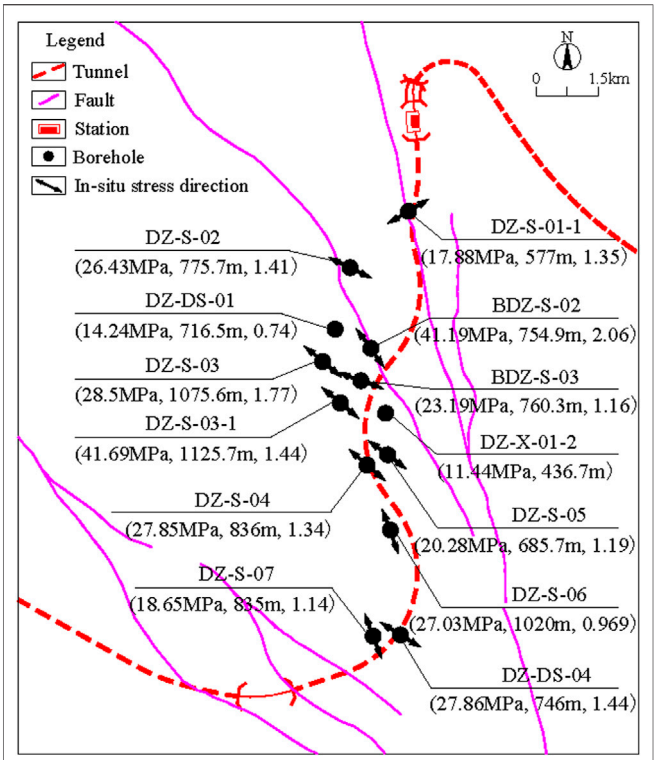


FIGURE 4 | The location sketch of boreholes.

syncline, Kang-Yunnan syncline and Longmenshan fold belt of the Songpan-Ganzi fold belt on the western margin of the Yangtze platform, adjacent to the Kang-Yunnan axis to the west, the Longmenshan structural belt to the north, the Western Sichuan platform depression of the Sichuan platform depression to the east, and the Liangshan depression fold bundle to the south. In terms of secondary structure, it is located in the Xianshuihe structural belt. The orientations of the structures near the tunnel site are mainly N20°~30°W, which is consistent with the strike of the Xianshuihe fault zone, as shown in **Figure 3**. The faults developed around the tunnel and were greatly influenced by the Yalahe fault and Selaha-Kangding fault. The Yalahe fault is near the entrance end of the tunnel, and the rocks at the entrance end of the tunnel have been seriously crushed. The rocks are obviously cataclastic, and joints have developed. The tunnel site is dominated by NW-trending faults, followed by NE-trending faults (interpreted faults).

IN-SITU STRESS MEASUREMENTS AND MAIN CHARACTERISTICS

The In-Situ Stress Testing Method

The hydraulic fracturing method, one of the recommended methods for determining rock stress issued by the ISRM Commission on Testing Methods in 1987, was used to measure the *in-situ* stress of deep holes near the tunnel. The test section of each borehole was determined according to the test requirements and the actual situation of the corresponding test hole, and the straddle packer system was used for the test. Water was injected into the test section through the drill pipe, and the water injection pressure was recorded through the wireless pressure sensor placed on the surface. The measured record curve was analyzed to obtain the characteristic pressure parameters and the minimum principal stress of the formation. Then, according to the corresponding theoretical formula, the magnitude of the maximum horizontal principal stress at the measuring point and the rock mechanical parameters such as the hydraulic fracturing tensile strength of the rock were calculated. The baseline orientation and fracturing crack orientation can be obtained through the impression tool and orientation tool, and the orientation of the maximum horizontal principal stress can be further calculated. Thirteen boreholes were tested for *in-situ* stress by the hydraulic fracturing method. Their positions are shown in **Figure 4**, and the measurements are shown in **Table 1**. Based on the measured data, the *in-situ* stress magnitude, maximum principal stress direction and lateral pressure coefficient of the tunnel section were analyzed.

The In-Situ Stress Value

Table 1 shows that the maximum horizontal principal stress (S_H) measured in the Xianshuihe fault zone ranges from 6.18 to 41.69 MPa, the minimum horizontal principal stress (S_h) ranges from 4.37 to 29.84 MPa, and the vertical stress (S_V) ranges from 7.41 to 35.85 MPa within the hole depth range of 279.5–1,353 m. According to the measured borehole stress data, a scatter diagram of the stress value and depth is shown in **Figure 5**. In general, the *in-situ* stress increases gradually with increasing depth. Through linear fitting, the formula of the principal stress gradient can be obtained:

$$\mathbf{S_H} = 0.0533\mathbf{H} - 14.6247 \quad (1)$$

$$\mathbf{S_h} = 0.0382\mathbf{H} - 10.2708 \quad (2)$$

where H represents the depth, m. The maximum and minimum horizontal principal stress gradients are approximately 5.33 MPa/100 m and 3.82 MPa/100 m, respectively, and the S_h gradient is less than 2.66 MPa/100 m of the vertical stress gradient.

Maximum Principal Stress Direction

Figure 6 shows the relationship between the principal stress directions and depth of the measured holes near this tunnel, and the dominant orientation of the maximum horizontal principal stress is NW. The direction of the maximum horizontal principal stress is mainly N40°W ~ N75°W, and the azimuth angle of the maximum horizontal principal stress becomes more concentrated in distribution with increasing burial depth. Faults in the tunnel site mainly strike NW, and the direction of the maximum horizontal principal stress is consistent with the strike of fault.

Lateral Pressure Coefficient

The lateral pressure coefficient k is used to study the distribution law of horizontal stress. The closer this value is to 1, the closer the stress state is to hydrostatic. The larger the value is, the more

TABLE 1 | Statistical table of *in-situ* stress and rock types in the tunnel site of the Xianshuihe fault zone.

Borehole number	Test depth range (m)	Maximum horizontal principal stress (MPa)	Minimum horizontal principal stress value (MPa)	Formation lithology	Direction of maximum horizontal principal stress
DZ-S-01-1	571.40–577.00	13.55–17.88	9.07–10.84	Sand slate	N59°E
DZ-S-02	775.00–1005.00	26.43–36.91	20.76–28.53	Granite	N56°W-N68°W
DZ-DS-01	642.50–716.50	11.85–14.24	10.33–11.19	Granite	Not measured
BDZ-S-02	594.6–754.9	23.94–41.19	17.35–28.55	Fault breccia	N24.3°W-N40.4°W
DZ-S-03	279.5-1353	12.17–26.24	6.8–18.71	Fault breccia	N30.5°W-N70.7°W
BDZ-S-03	645.6–760.3	18.6–23.19	12.95–15.56	Granite	N70°E
DZ-S-03-1	560.0–1125.0	19.99–41.69	15.08–29.84	Granite	N55°W-N63°W
DZ-S-05	380.0–685.0	10.99–20.28	8.94–15.98	Limestone	N53°W-N65°W
DZ-S-04	455.0–835.0	14.78–27.85	12.23–22.12	Limestone	N49°W-N57°W
DZ-S-06	550.5-1020	13.22–26.18	8.31–19.05	Fault breccia	N2.8°W-N39.7°W
DZ-DS-04	365.0–745.0	12.70–27.86	10.22–20.39	Limestone	N58°W-N69°W
DZ-S-07	294.5–835.0	8.91–18.65	5.85–13.49	Crushed rock	N20.7°W-N71.6°W
DZ-X-01-2	350–436.7	9.7–11.44	7.31–7.91	Mylonitic granite	N31°E-N70°E

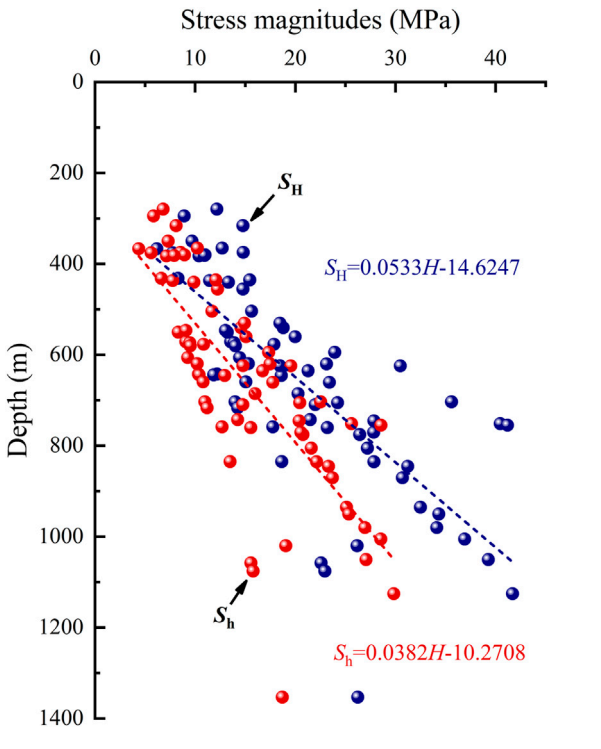


FIGURE 5 | Scatter diagram and fitting curves of |*in situ* stress.

dominant the horizontal tectonic force. The lateral pressure coefficient k is also expressed by the ratio of the average value of the two horizontal stresses to the vertical stress, and the calculation formula is as follows:

$$\mathbf{k} = \frac{(\mathbf{S_H} + \mathbf{S_h})}{(2\mathbf{S_V})} \quad (3)$$

According to **Formula (3)**, the lateral pressure coefficients of each measured hole are shown in **Table 2**. The lateral pressure coefficients range from 0.560 to 1.744. The lateral pressure coefficients of holes DZ-S-02, BDZ-S-02, DZ-S-03-1, DZ-S-05, DZ-S-04 and DZ-DS-S-04 are greater than 1, and the *in-situ* stress is $S_H > S_h > S_v$, indicating that horizontal tectonic activity is dominant in the vicinity of these holes. The lateral pressure coefficients of holes DZ-DS-01, BDZ-S-03, DZ-S-06, DZ-S-07 and DZ-X-01-2 are mainly less than 1, and the *in-situ* stress mainly shows $S_H > S_v > S_h$, indicating that the self-weight of the rock plays a dominant role in determining the stress state near these holes.

INFLUENCE OF THE FAULT ZONE ON THE STRESS DISTRIBUTION OF THE TUNNEL SITE

The Xianshuihe fault zone mainly experienced two periods of tectonic stress field activity (Xie et al., 1995). At present, the Xianshuihe horizontal fault zone is characterized by sinistral strike-slip movement, and its activity may affect the local *in-situ* stress field.

Influence Characteristics of the Fault Zone on the *In-Situ* Stress

To understand the influence of the Xianshuihe fault zone on the *in-situ* stress as a whole, the boreholes near a tunnel are divided into four categories according to the distance perpendicular to the nearest fault strike: 0–500 m, 500–1,000 m, 1,000–1,500 m and 1,500–2000 m. The relationships between the measured maximum horizontal principal stress, minimum horizontal principal stress, maximum principal stress direction and the burial depth and distance to the fault are shown in **Figures 7A,B,C**, respectively. As shown in **Figures 7A,B**, the maximum horizontal principal stress and the minimum horizontal principal stress linearly increase with increasing burial depth. Regardless of the distance from the fault, the rate of increase in the maximum horizontal principal stress with burial depth is greater than that in the minimum horizontal

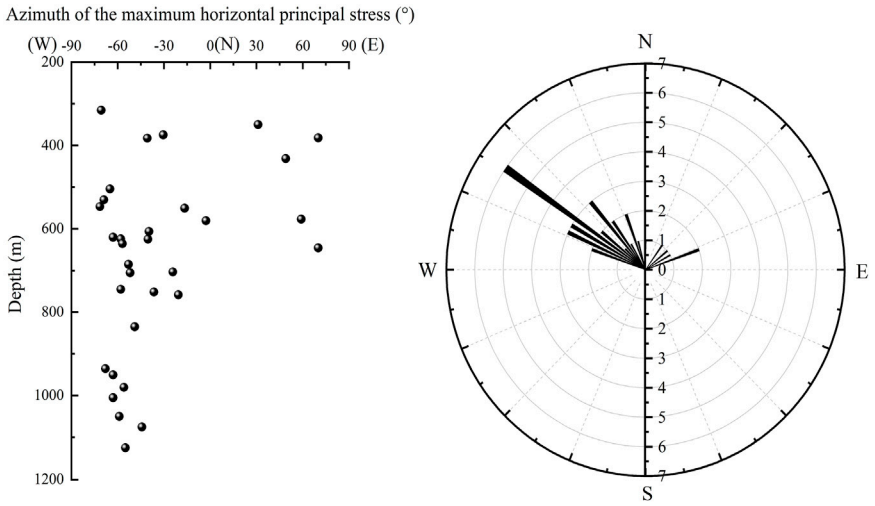


FIGURE 6 | Direction of the maximum horizontal principal stress.

TABLE 2 | Lateral pressure coefficients of different boreholes.

Hole	Lateral pressure coefficient	Lateral pressure coefficient
DZ-S-01-1	0.860~1.082	$S_H > S_v > S_h$, $S_H > S_h > S_v$
DZ-S-02	1.165~1.252	$S_H > S_h > S_v$
DZ-DS-01	0.646~0.664	$S_H > S_v > S_h$
BDZ-S-02	1.309~1.743	$S_H > S_h > S_v$
DZ-S-03	0.679~1.368	$S_H > S_v > S_h$, $S_H > S_h > S_v$
BDZ-S-03	0.918~0.988	$S_H > S_v > S_h$
DZ-S-03-1	1.199~1.241	$S_H > S_h > S_v$
DZ-S-05	1.008~1.042	$S_H > S_h > S_v$
DZ-S-04	1.141~1.218	$S_H > S_h > S_v$
DZ-S-06	0.737~0.836	$S_H > S_v > S_h$
DZ-DS-S-04	1.207~1.259	$S_H > S_h > S_v$
DZ-S-07	0.726~0.946	$S_H > S_v > S_h$
DZ-X-01-2	0.559~0.958	$S_H > S_v > S_h$

principal stress. In addition, when the burial depth is less than 600 m, the farther the borehole is from the fault, the greater the measured maximum horizontal principal stress and minimum horizontal principal stress. When the burial depth is greater than 600 m, the variations in the maximum horizontal principal stress and minimum horizontal principal stress with increasing distance to the fault are not consistent. Therefore, the fault has a significant differential impact on the *in-situ* stress of the shallow stratum. The fastest rates of increase in the maximum horizontal principal stress and minimum horizontal principal stress, which are 0.0910 MPa/m and 0.0534 MPa/m, respectively, are observed at the boreholes less than 500 m from the fault. When the distance from a borehole to the fault is greater than 500 m, the trend of the rate of increase in maximum horizontal principal stress with the distance from the borehole to the fault is not obvious, and the rate of increase in the minimum horizontal principal stress increases slightly with increasing distance from the fault. As shown in **Figure 7C**, when a borehole is less than 1,000 m from the fault, the direction of the maximum principal stress of the borehole is different from the dominant NW direction of the maximum principal stress in the area, instead showing a NE direction. The *in-situ* stress direction near the fault is complex and may be deflected under the influence of the fault.

To investigate the distribution characteristics of *in-situ* stress in the control area of a single fault in the Xianshuihe fault zone, the measured *in-situ* stress values of boreholes perpendicular to the strike of the Selaha-Kangding fault are selected for analysis. Because the factors affecting the *in-situ* stress are mainly the burial depth and fault, the horizontal principal stress of the same burial depth is selected for comparison between different boreholes to eliminate the influence of burial depth. Considering that there are some differences in the range of the measured sections of the boreholes, boreholes with the same depths are selected for analysis. According to the above analysis, the *in-situ* stress obeys different laws in deep and shallow strata. Therefore, for the borehole measured sections selected, burial depth ranges of less than 600 m and more than 600 m are selected for comparison (namely, burial depths of 450 and 750 m). Among them, boreholes DZ-X-01-2, BDZ-S-03, DZ-S-03, DZ-S-04 and DZ-S-05 are selected for the 450 m burial depth, and boreholes BDZ-S-02, DZ-S-02, DZ-DS-01, DZ-S-03-1 and DZ-S-06 are selected for the 750 m burial depth. The stress values of each burial depth are obtained based on the approximate linear relationship between the measured stress value and the burial depth. The relationships between the maximum horizontal principal stress, the minimum horizontal principal stress, the lateral pressure coefficient and the distance from the borehole to the fault are shown in **Figure 8**. As shown in **Figure 8A**, for the boreholes near the Selaha-Kangding fault, when the burial depth is 450 m, the overall maximum horizontal principal stress and minimum horizontal principal stress increase with increasing distance from the fault. The maximum horizontal principal stress and the minimum horizontal principal stress of the borehole

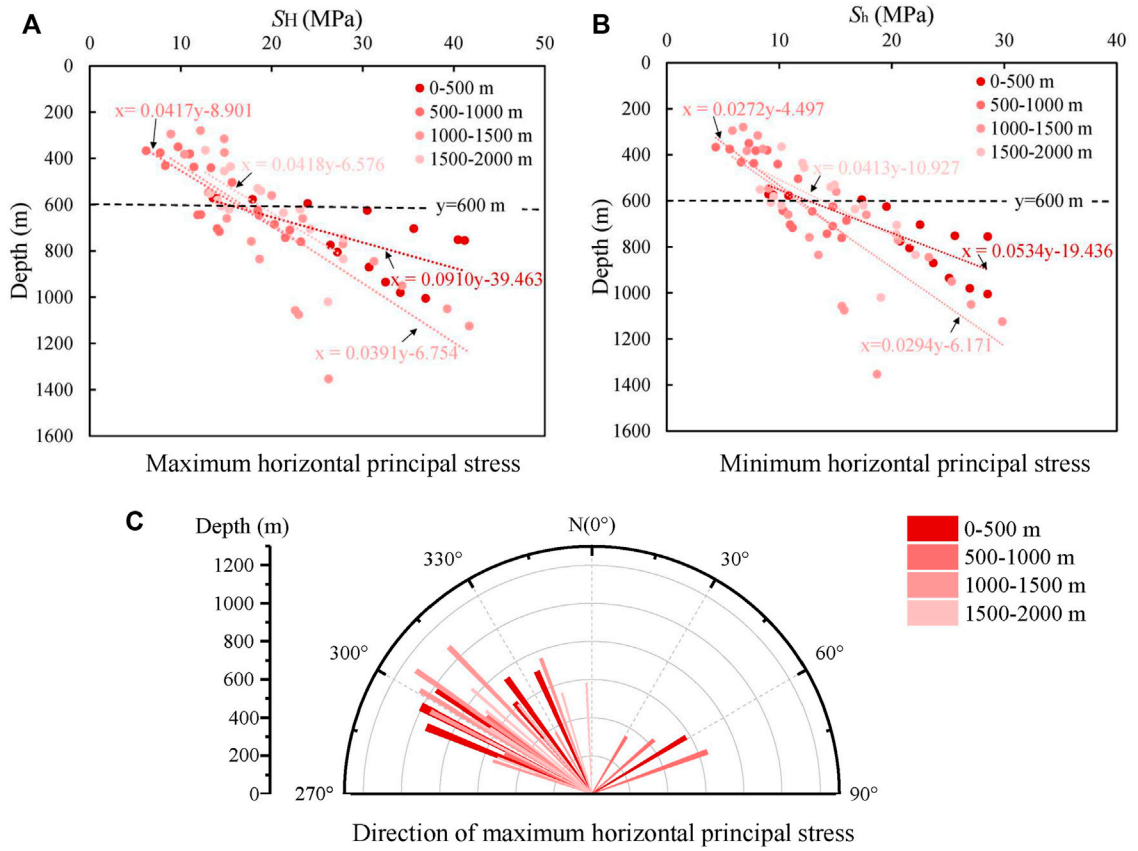


FIGURE 7 | In-situ stress at different spatial locations **(A)** Maximum horizontal principal stress **(B)** Minimum horizontal principal stress **(C)** Direction of maximum horizontal principal stress.

farthest from the fault increased by nearly 47 and 66%, respectively, compared with the maximum horizontal principal stress and the minimum horizontal principal stress of the borehole nearest to the fault. **Figure 8B** shows that when the borehole is close to the fault, k is less than 1, which means that the geostatic stress is dominant; however, when the fault distance is greater than 600 m, k is greater than 1, which means that the tectonic stress is dominant. This may be because in the shallow area, the tectonic influence is weakened due to the deterioration of rock mass properties near the fault, so the horizontal stress is reduced more. As shown in **Figures 8C,D**, when the burial depth is 750 m, the variation pattern of the maximum horizontal principal stress, minimum horizontal principal stress and lateral pressure coefficient with the distance from the borehole to the fault is not significant, which may be due to the greater influence of gravity of the rock mass in the deep area and the weakening of tectonic influence, so the change in horizontal stress is not obvious.

Distribution Characteristics of the *In-Situ* Stress at the Tunnel Barrel

To ensure the safety of tunnel construction, it is necessary to determine the *in-situ* stress distribution along the tunnel. Therefore, based on the inversion of the *in-situ* stress field at the tunnel site, the contour map of the maximum principal stress of the section where a tunnel is located and the line map of the maximum principal stress at the tunnel depth are extracted, as shown in **Figure 9**. It can be seen from this figure that the maximum horizontal principal stress of the tunnel is 3~44 MPa, and the *in-situ* stress of the entrance and exit of the tunnel is low, while the *in-situ* stress in the surrounding rock of the tunnel barrel is high. The maximum horizontal principal stress of the tunnel barrel is affected by the depth and fault. The maximum horizontal principal stress increases with increasing depth, while the *in-situ* stress release at the fault leads to a decrease in the *in-situ* stress, which corresponds to an area of lower *in-situ* stress at the fault on the contour map of the maximum horizontal principal stress. However, the *in-situ* stress increases away from the fault, and there is usually a maximum *in-situ* stress in the tunnel segment between two faults due to the dual influence of burial depth and fault. For example, the highest maximum horizontal principal stress between the Yalahe fault and the Sandaoqiao fault is 34 MPa, which is approximately three times the maximum horizontal principal stress at the Yalahe fault and the Sandaoqiao fault. The highest maximum horizontal principal stress between the Sandaoqiao fault and the Selaha-Kangding fault is approximately 28 MPa, which is approximately three times the maximum horizontal principal stress value at the Sandaoqiao fault and approximately twice the maximum horizontal principal stress

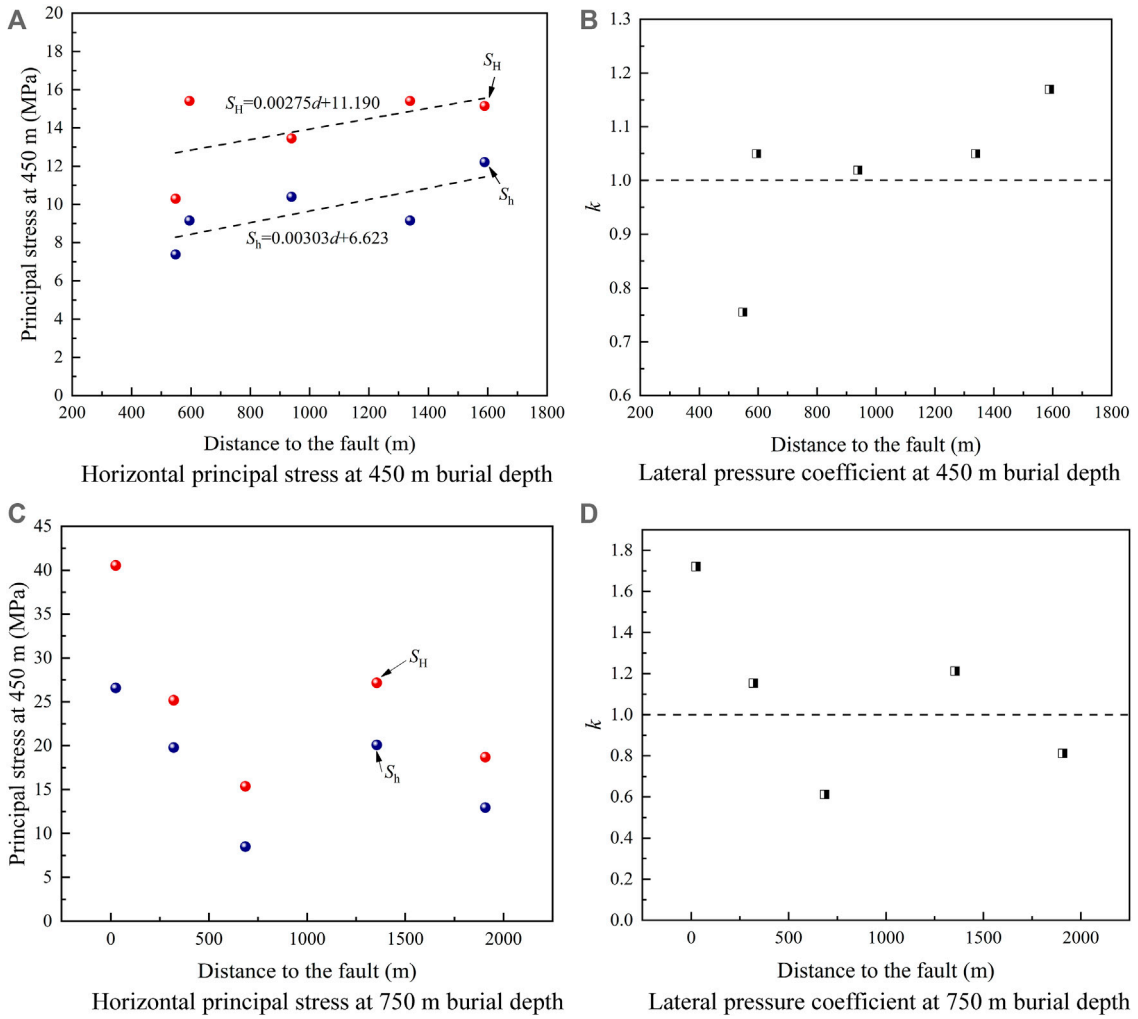


FIGURE 8 | The relationship between horizontal principal stress and lateral pressure coefficient of borehole and the distance to the fault (d represents the distance from borehole to fault) **(A)** Horizontal principal stress at 450 m burial depth **(B)** Lateral pressure coefficient at 450 m burial depth **(C)** Horizontal principal stress at 750 m burial depth **(D)** Lateral pressure coefficient at 750 m burial depth.

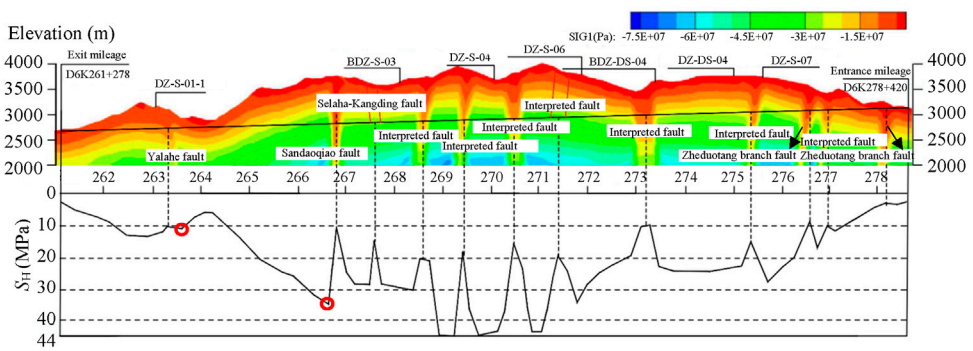


FIGURE 9 | The contour map and line chart of the maximum horizontal principal stress of a tunnel.

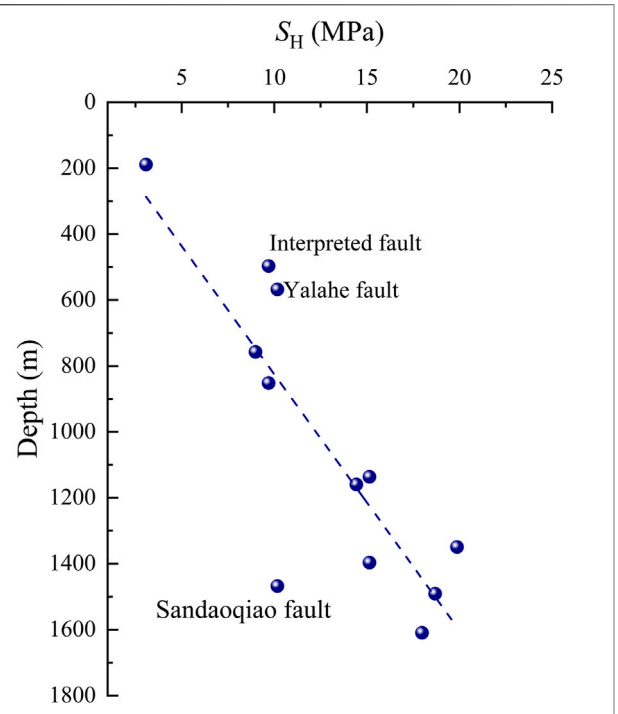


FIGURE 10 | Maximum horizontal principal stress and depth in the intersection area of fault and the tunnel barrel.

value at the Selaha-Kangding fault. From the variation in the maximum horizontal principal stress between the Sandaoqiao fault and the Selaha-Kangding fault, it is obvious that the variation in the maximum horizontal principal stress of the rock mass between the two faults is roughly the same as that of the burial depth of the tunnel barrel. This phenomenon indicates that the maximum horizontal principal stress of the middle segment is mainly controlled by depth. Moreover, there is stress concentration near the fault due to tectonic influence.

The relationship between the maximum horizontal principal stress in the intersection area of the tunnel barrel and fault and depth is shown in **Figure 10**. The maximum horizontal principal stress in the intersection area of the tunnel barrel and fault increases roughly with increasing depth, except at the Sandaoqiao fault, Yala River fault and the interpreted fault of mile D6K276 + 996. That is, the depth of the tunnel barrel section of one fault is less than that of the tunnel barrel section of another fault, but the *in-situ* stress value of the former may be greater than that of the latter. For example, the depth of the Sandaoqiao fault (1,467 m) is greater than that of the D6K270 + 565 fault (1,396 m), while the maximum horizontal principal stress value of the former (10 MPa) is less than that of the latter (15 MPa). This indicates that different faults have different effects on the *in-situ* stress.

ENGINEERING EFFECT ANALYSIS

On the whole, the formation of the fault zone reflects the considerable tectonic activity and high *in-situ* stress in this region, and the disturbance of tunnel excavation under high *in-situ* stress can easily induce underground engineering disasters such as rockburst and large deformation (Zhang et al., 2021). Many scholars have carried out relevant research (Aydan et al., 1993; Feng et al., 2015; Chen et al., 2020; Feng et al., 2022; Yu et al., 2022). In this section, the prediction of rockburst and large deformation in the tunnel site are carried out.

Rockburst Prediction at the Tunnel Site

The occurrence of rockburst is affected by many factors, so these factors should be comprehensively considered to establish their prediction criteria. In this paper, the strength-stress ratio method is used for prediction and combined with the results of the geological analysis method. The geological analysis method mainly aims at macroscale prediction, taking geological exploration data as the basis and similar engineering data as the analogy to make a simple macroscale prediction of the research object from the aspects of *in-situ* stress, lithology, hydrology, structural geology and so on. The strength-stress ratio rule is used to establish the quantitative index of rockburst prediction according to the *in-situ* stress and rock mass properties, which is calculated according to the following formula (National Railway Administration of the People Republic of China, 2016):

$$\mathbf{p} = \frac{\mathbf{R_c}}{\boldsymbol{\sigma}_{\mathbf{max}}} \tag{4}$$

where p is the rockburst classification index, and the relationship between its value and rockburst classification is shown in **Table 3**. R_c is the saturated uniaxial compressive strength of the rock mass; σ_{max} is the maximum *in-situ* stress. Although the occurrence of rockburst is caused by stress redistribution due to excavation, the stress redistribution is based on the initial stress of the rock mass. Therefore, the initial maximum horizontal principal stress of the surrounding rock is used in this paper to reflect the relative magnitude of stress redistribution after excavation.

The strength-stress ratio method and geological analysis method were used to analyze and predict a tunnel rockburst. Due to the complex strata, broken rock mass and severe weathering, the surrounding rock is mostly grade Ⅳ~Ⅴ, and only some parts of $\eta\gamma^3N_2$ are grade Ⅲ. First, it is preliminarily found that the surrounding rocks of grade Ⅳ and below do not have the conditions of rockburst, so rockburst is not considered, and only the possibility of rockburst occurring in the surrounding rocks of grade Ⅲ and above is considered, so the rockburst discrimination and prediction analysis is

TABLE 3 | Rockburst grade of hard rock section (National Railway Administration of the People Republic of China, 2016).

Rockburst grade	Strength-stress ratio of surrounding rock (R_c/σ_{max})
Light	4~7
Moderate	2~4
Severe	<2

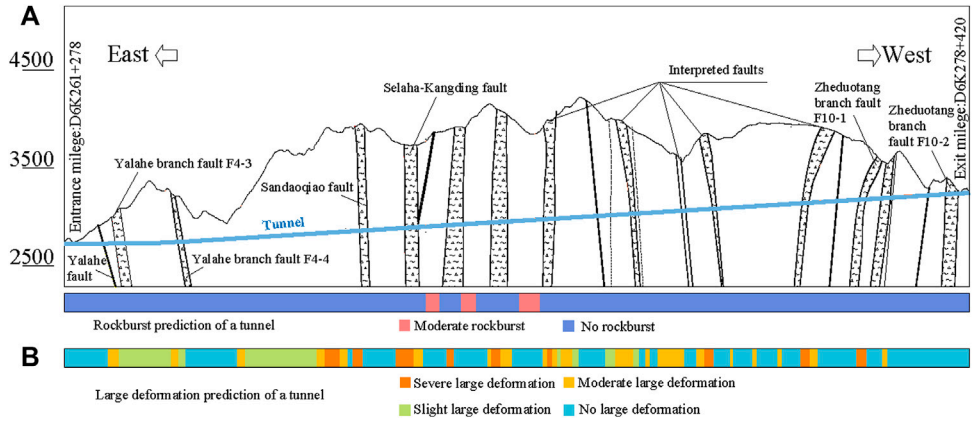


FIGURE 11 | Prediction results of underground engineering disasters **(A)** Rockburst prediction of a tunnel **(B)** Large deformation prediction of a tunnel.

TABLE 4 | Large deformation grade (National Railway Administration of the People Republic of China, 2016).

Deformation grade of soft rock with high in-situ stress	Strength-stress ratio of surrounding rock (R_b/σ_{max})	The deformation trend
I	0.25~0.5	Light
II	0.15~0.25	Moderate
III	<0.15	Severe

carried out only for the surrounding rocks of grade Ⅲ. According to the rock burst prediction results of a tunnel obtained by the strength stress ratio method and geological analysis method (as shown in **Figure 11A**), rockburst occurs mainly in grade III surrounding rock of $\eta\gamma^3N_2$, where the rock mass strength is higher, and the section is mainly in the middle of a rock mass between two adjacent faults, so the maximum principal stress value is relatively high (greater than 30 MPa). The tunnel is mainly subject to moderate rockburst, and the length of the tunnel with moderate rockburst is 980 m.

Prediction of Large Deformation at the Tunnel Site

The classification index for large deformation prediction of soft rock segments is calculated according to the strength-stress ratio **formula (5)**(National Railway Administration of the People Republic of China, 2016):

$$\mathbf{q} = \frac{\mathbf{R_b}}{\boldsymbol{\sigma}_{\mathbf{max}}} \tag{5}$$

where q is the large deformation classification index, and its value and corresponding large deformation classification are shown in **Table 4**. R_b is the strength of the surrounding rock mass; σ_{max} is the maximum *in-situ* stress.

According to the numerical results of the tunnel axis stress corresponding to the mileage section of the *in-situ* stress simulation and geological prospecting section division, the identification and division of the large deformation of the surrounding rock were carried out, and the prediction results of large deformation were obtained (as shown in **Figure 11B**). The results of large tunnel deformation include slight large deformation, moderate large deformation, and severe large deformation, and most of them occur in fault zones or affected areas of fault zones. Although the *in-situ* stress at the fault is relatively low, the rock strength here is also low, so large deformation easily occurs. In the statistical range, the length of the section with severe large deformation is 1900 m, accounting for 11% of the total length of the tunnel, and almost all of them occur at the fault. In these sections, the *in-situ* stress is higher than 12 MPa, mostly at the moderate stress level. Due to the low strength of the surrounding rock, the final strength-stress ratio is low. The moderately large deformation section is 3,170 m, accounting for 18.35% of the total length of the tunnel. Most of these sections are faults or fault-affected areas. There are two situations: one is that the *in-situ* stress value is equal to or even slightly lower than the *in-situ* stress value of the section with severe large deformation, and the strength of the surrounding rock is slightly higher than that of the section with severe large deformation; the other is that the *in-situ* stress value of the $\eta\gamma^3N_2$ stratum is very high (all greater than 40 MPa), and the strength of the surrounding rock is relatively high. In both cases, moderate deformation is more likely to occur. The section with slightly large deformation is 2,940 m, accounting for 17.02% of the total length of the tunnel. Most of these

sections are affected areas of fault zones or T_3z and myl strata. The *in-situ* stress level of this section is relatively low, mostly below 20 MPa, and the strength of the surrounding rock is relatively high.

CONCLUSION

The *in-situ* stress of a tunnel site in the Xianshuihe fault zone is analyzed, and the following conclusions are drawn:

1) Regarding the overall situation of the Xianshuihe fault zone, the fault mainly affects the maximum horizontal principal stress and the minimum horizontal principal stress in the shallow stratum. The *in-situ* stress near the fault is greatly affected, resulting in a deviation in the direction of the maximum principal stress from the direction of the regional dominant principal stress. In the shallow area near the Selaha-Kangding fault, the maximum horizontal principal stress, minimum horizontal principal stress and lateral pressure coefficient of the borehole increase with increasing distance from the fault. Farther than 600 m from the fault, the horizontal stress is greatest. In the deeper area, the maximum horizontal principal stress, the minimum horizontal principal stress and the lateral pressure coefficient exhibit no obvious change with increasing distance from the fault.
2) According to the inversion of the *in-situ* stress field in the studied tunnel site and the stress in the tunnel, the maximum principal stress in the axial direction of a tunnel is 3~44 MPa, the *in-situ* stress at the entrance and exit of the tunnel is low, and the *in-situ* stress at the tunnel barrel is high. The *in-situ* stress around the tunnel barrel is affected not only by the burial depth but also by the fault. The *in-situ* stress at greater burial depths is high, and the *in-situ* stress at the fault has been released to a certain extent. The *in-situ* stress is relatively low, and the degree of stress decline at different faults is different.
3) The rockburst prediction results for the tunnel are obtained by the comprehensive strength-stress ratio method and geological analysis method. The prediction results are as follows: the length of the moderate rockburst risk is 980 m, accounting for 5.67%, which tends to coincide with the rock section with high stress located in the middle of a rock mass between two faults. The large deformation grade of the tunnel is obtained by the strength-stress ratio method, which mainly indicates in slight large deformation, moderate large deformation, and severe large deformation mainly occurs in the fault and its influence zone. The length of slight large deformation is 2,940 m, accounting for 17.02%. The length of moderate large deformation is 3,170 m, accounting for 18.35%. The length of severe large deformation is 1900 m, accounting for 11%.

DATA AVAILABILITY STATEMENT

The original contributions presented in the study are included in the article/Supplementary Material, further inquiries can be directed to the corresponding authors.

AUTHOR CONTRIBUTIONS

DY mainly participated in the field work and formed the idea of the article. LZ and XL wrote the first draft of the manuscript. All authors contributed to manuscript revision, read, and approved the submitted version.

FUNDING

This study was funded by the research project of China Railway Eryuan Engineering Group Company, Ltd. (Grant Nos. KSNQ200002, KDNQ213043, KSNQ213010, and KDNQ201004).

REFERENCES

Ajalloeian, R., Moghaddam, B., and Azimian, A. (2017). Prediction of Rock Mass Squeezing of T4 Tunnel in Iran. *Geotech Geol. Eng.* 35 (2), 747–763. doi:10.1007/s10706-016-0139-y

Ai, T., Wu, S. Y., Zhang, R., Gao, M. Z., Zhou, J. E., Xie, J., et al. (2021). Changes in the Structure and Mechanical Properties of a Typical Coal Induced by Water Immersion. *Int. J. Rock Mech. Min.* 138. doi:10.1016/j.ijrmms.2020.104597

Aleksandrowski, P., Inderhaug, O. H., and Knapstad, B. (1992). "Tectonic Structures and Wellbore Breakout Orientation," in Proceedings of the 33rd United-States Symp on Rock Mechanics, Rotterdam, Netherlands, June 1992, 29–37.

Aydan, O., Akagi, T., and Kawamoto, T. (1993). The Squeezing Potential of Rocks Around Tunnels; Theory and Prediction. *Rock Mech. Rock Engng* 26 (2), 137–163. doi:10.1007/bf01023620

Bell, J. S., and Babcock, E. A. (1986). The Stress Regime of the Western Canadian Basin and Implications for Hydrocarbon Production. *Bull. Can. Pet. Geology.* 34 (3), 364–378.

Cao, P., Li, K., Li, C. J., and Zhang, L. D. (2018). Back-Calculation of Ground Stress Field and Rockburst Analysis for Wunvfeng Tunnel. *Mod. tunnelling Technol.* 55 (05), 45–52. doi:10.13807/j.cnki.mtt.2018.05.006

Chen, X. Q. (2022). Influence of Fault Fracture Zone on Initial *In-Situ* Stress Field in Tongmai Tunnel of the Sichuan-Tibet Railway. *Earth Sci.* [Epub ahead of print], 1–9. doi:10.3799/dqkx.2021.263

Chen, Z., He, C., Yang, W., Guo, W., Li, Z., and Xu, G. (2020). Impacts of Geological Conditions on Instability Causes and Mechanical Behavior of Large-Scale Tunnels: a Case Study from the Sichuan-Tibet Highway, China. *Bull. Eng. Geol. Environ.* 79 (7), 3667–3688. doi:10.1007/s10064-020-01796-w

Feng, G.-L., Chen, B.-R., Xiao, Y.-X., Jiang, Q., Li, P.-X., Zheng, H., et al. (2022). Microseismic Characteristics of Rockburst Development in Deep TBM Tunnels with Alternating Soft-Hard Strata and Application to Rockburst Warning: A Case Study of the Neelum-Jhelum Hydropower Project. *Tunnelling Underground Space Technol.* 122, 104398. doi:10.1016/j.tust.2022.104398

Feng, G.-L., Feng, X.-T., Chen, B.-r., Xiao, Y.-X., and Yu, Y. (2015). A Microseismic Method for Dynamic Warning of Rockburst Development Processes in Tunnels. *Rock Mech. Rock Eng.* 48 (5), 2061–2076. doi:10.1007/s00603-014-0689-3

Guo, C. B., Zhang, Y. S., Jiang, L. W., Shi, J. S., Meng, W., Du, Y. B., et al. (2017). Discussion on the Environmental and Engineering Geological Problems along the Sichuan-Tibet Railway and its Adjacent Area. *GEOSCIENCE* 31 (05), 877–889.

Hijazo, T., and González de Vallejo, L. I. (2012). *In-situ* Stress Amplification Due to Geological Factors in Tunnels: The Case of Pajares Tunnels, Spain. *Eng. Geology*. 137-138, 13–20. doi:10.1016/j.enggeo.2012.03.007

Jia, Z. Q., Xie, H. P., Zhang, R., Li, C. B., Wang, M., Gao, M. Z., et al. (2020). Acoustic Emission Characteristics and Damage Evolution of Coal at Different Depths Under Triaxial Compression. *Rock Mech. Rock Eng.* 53 (5), 2063–2076. doi:10.1007/s00603-019-02042-w

Lei, X. Q., and Chen, Y. P. (2011). Effects of Faults on Crustal Stress Using Discontinuous Model. *J. Cent. South Univ. (Science Technology)* 42 (08), 2379–2386.

Li, H., Xie, F. R., Wang, H. Z., Dong, Y. K., and Yu, J. J. (2012). Characteristics of *In-Situ* Stress Measurements Near the Fault and Fault Activity in Urumqi City. *Chin. J. Geophys.* 55 (11), 3690–3698. doi:10.6038/j.issn.0001-5733.2012.11.016

Li, K., Jiang, X. H., Wu, M. J., and Ding, H. (2017). Numerical Reversion of Tunnel Initial Stress Field in Fault Disturbed Zone. *China Civil Eng. J.* 50 (S2), 255–259. doi:10.15951/j.tmgcxb.2017.s2.040

Li, P., and Miao, S. J. (2016). Analysis of the Characteristics of *In-Situ* Stress Field and Fault Activity in the Coal Mining Area of China. *J. China Coal Soc.* 41 (S2), 319–329. doi:10.13225/j.cnki.jccs.2016.0303

Lin, D. M., Yuan, R. M., Shang, Y. J., Bao, W. X., Wang, K. Y., Zhang, Z. J., et al. (2017). Deformation and Failure of a Tunnel in the Restraining Bend of a Strike-Slip Fault Zone: An Example from Hengshan Mountain, Shanxi Province, China. *Bull. Eng. Geol. Environ.* 76 (1), 263–274. doi:10.1007/s10064-016-0850-1

Lu, W. B., Yang, J. H., Yan, P., Chen, M., Zhou, C. B., Luo, Y., et al. (2012). Dynamic Response of Rock Mass Induced by the Transient Release of in-situ Stress. *Int. J. Rock Mech. Min.* 53, 129–141. doi:10.1016/j.ijrmms.2012.05.001

Luo, X. D., Chen, J. P., Fan, J. H., and Zuo, C. Q. (2006). "Studying on Large Deformation Mechanism of Soft Rock Tunnel Fluenced by Yunxi-Yunxian Fault," in Proceedings of the 2nd International Conference on Environmental and Engineering Geophysics, Wuhan, P.R. China, June 4-9, 2006, 927–931.

Martin, C. D. (1990). Characterizing *In Situ* Stress Domains at the AECL Underground Research Laboratory. *Can. Geotech. J.* 27 (5), 631–646. doi:10.1139/t90-077

National Railway Administration of the People Republic of China (2016). *Code for Design of Railway Tunnel*. Beijing: China Railway Publishing House.

Pham, C., Chang, C., Jang, Y., Kutty, A., and Jeong, J. (2020). Effect of Faults and Rock Physical Properties on *In Situ* Stress within Highly Heterogeneous Carbonate Reservoirs. *J. Pet. Sci. Eng.* 185, 106601. doi:10.1016/j.petrol.2019.106601

Qiao, Z. B. (2021). Study on Rockburst Intensity Prediction Based on the Characteristics of *In-Situ* Stress Field in Deep Tunnel on Sichuan-Tibet Railway. *Railway Stand. Des.* 65 (02), 89–94+103. doi:10.13238/j.issn.1004-2954.202005120002

Ren, H. L., Duan, D., and Chen, S. S. (2019). Influence of Composite Structure on the Distribution Characteristics of Geostress. *Mining Res. Develop.* 39 (06), 58–62. doi:10.13827/j.cnki.kyyk.2019.06.012

Stephansson, O., and Angman, P. (1986). Hydraulic Fracturing Stress Measurements at Forsmark and Stidsvig, Sweden. *Bull. Geol. Soc. Finland* 58 (58), 307–333. doi:10.17741/bgsf/58.1.021

Xie, F. R., Zhu, J. Z., and Shu, S. B. (1995). Study of Different Stage Quaternary Tectonic Stress Field for the Xianshuihe Fault Zone. *Seismology Geology.* 17 (01), 35–43.

Yang, Y. L. (2020). Analysis of Geostress Field in the Gong Jue Tunnel of Sichuan-Tibet Railway Project and the Effect of Fractures. Master's thesis. Chengdu: Southwest Jiaotong University.

Yu, N., Hu, X. Y., Li, J., Zhao, N., Zhou, J., Cai, X. L., et al. (2017). Electrical Structure of the Longling Area in Western Yunnan and its Effect on Route Selection of the Dali-Ruili Railway. *Chin. J. Geophysics-Chinese Edition* 60 (6), 2442–2455. doi:10.6038/cjg20170632

Yu, Y., Feng, G.-l., Xu, C.-j., Chen, B.-r., Geng, D.-x., and Zhu, B.-t. (2022). Quantitative Threshold of Energy Fractal Dimension for Immediate Rock Burst Warning in Deep Tunnel: A Case Study. *Lithosphere* 2021, 1699273. doi:10.2113/2022/1699273

Zhang, M., Huang, J., Ju, N. P., Zhang, Y. L., and Zhang, G. Z. (2019). Inverse Analysis on *In-Situ* Stress Field of Super-long and Deep Buried Tunnel in Chuan-Zang Railway. *Chin. J. Underground Space Eng.* 15 (04), 1232–1238+1257.

Zhang, Y. X. (2021). Characteristics of Current *In-Situ* Stress Field about Sejila Mountain Traffic Corridor. *J. Eng. Geology*. 29 (02), 394–403. doi:10.13544/j.cnki.jeg.2021-0126

Zhang, A. L., Xie, H. P., Zhang, R., Ren, L., Zhou, J. F., Gao, M. Z., et al. (2021). Dynamic Failure Behavior of Jinping Marble Under Various Preloading Conditions Corresponding to Different Depths. *Int. J. Rock Mech. Min.* 148. doi:10.1016/j.ijrmms.2021.104959

Zhao, L., Zhang, Z. D., Li, L. M., Wang, P., Meng, J., and Tao, L. (2019). Study on Characteristics of Geostress Field in Qinling Water Conveyance Tunnel of Hanjiang to Weihe River Valley Water Diversion Project and its Inverse Analysis. *Water Resour. Hydropower Eng.* 50, 90–96.

Zoback, M. D., and Roller, J. C. (1979). Magnitude of Shear Stress on the San Andreas Fault: Implications of a Stress Measurement Profile at Shallow Depth. *Science* 206 (4417), 445–447. doi:10.1126/science.206.4417.445

Conflict of Interest: Author DY, TF, GZ, ZX, ZW, XY and ZL are employed by China Railway Eryuan Engineering Group Co., Ltd.

The remaining authors declare that the research was conducted in the absence of any commercial or financial relationships that could be construed as a potential conflict of interest.

Publisher's Note: All claims expressed in this article are solely those of the authors and do not necessarily represent those of their affiliated organizations, or those of the publisher, the editors and the reviewers. Any product that may be evaluated in this article, or claim that may be made by its manufacturer, is not guaranteed or endorsed by the publisher.

Copyright © 2022 Yuan, Zhang, Liu, Feng, Zhang, Xu, Wang, Yi, Lin, Ren, Zhang and Ren. This is an open-access article distributed under the terms of the Creative Commons Attribution License (CC BY). The use, distribution or reproduction in other forums is permitted, provided the original author(s) and the copyright owner(s) are credited and that the original publication in this journal is cited, in accordance with accepted academic practice. No use, distribution or reproduction is permitted which does not comply with these terms.

frontiers | Frontiers in Earth Science

ORIGINAL RESEARCH
published: 10 May 2022
doi: 10.3389/feart.2022.909466

Ground Surface Deformation in the Hanging Wall of the Jinshandian Underground Iron Mine in China

Tianlong Wang[1,2], *Congxin Chen*[1,2], *Kaizong Xia*[1,2]*, *Chuqiang Zhang*[3], *Yue Wang*[1,2] and *Xuanting Liu*[1,2]

[1]State Key Laboratory of Geomechanics and Geotechnical Engineering, Institute of Rock and Soil Mechanics, Chinese Academy of Sciences, Wuhan, China, [2]University of Chinese Academy of Sciences, Beijing, China, [3]School of Civil Engineering, Architecture and Environment, Hubei University of Technology, Wuhan, China

When sublevel caving is used in metal mines, the stress state in the rock mass that initially existed around the mined-out area will be destroyed. This will lead to the rock strata deforming and moving and also, potentially, to large-scale collapse and cracking of the ground surface. Such ground surface deformation can cause significant damage to buildings and other structures. Therefore, it is very important to study the mechanism responsible for this ground surface deformation so that methods can be devised to protect the mine's production facilities as well as the property and safety of nearby residents. In this study, the mechanism responsible for the surface deformation of the hanging wall in the eastern part of the Jinshandian iron mine was investigated by analyzing monitoring data collected *in situ* on the surface (from 2008 to 2020) and other related information (occurrence of surface cracking and collapse and geological conditions). The results show that the ground surface deformation can be divided into four stages (initial, creep, slow, and accelerating deformation stages). A flexural toppling failure model is proposed to account for the surface deformation. The model suggests that large-scale deformation of the ground surface at the hanging wall occurs due to the combined effect of *in situ* ground stress, occurrence of steep dip discontinuities and faults, the dips and strikes of the two parallel orebodies, and underground mining activity. Furthermore, the surface deformation can be divided into six regions corresponding to caved, rapidly-accelerating deformation, slowly-accelerating deformation, acceptable deformation, slight deformation, and no deformation zones. In the rapidly-accelerating deformation zone, the ratio of the horizontal to vertical displacement is greater than 1 and some major cracks can be found. Large-scale cracks begin to form when the horizontal velocity of the ground surface is greater than 1 mm/day.

Keywords: metal mine, underground mining, hanging wall, *in situ* monitoring data, discontinuities and faults, ground surface deformation

OPEN ACCESS

Edited by:
Shibing Huang,
Wuhan University of Science and Technology, China

Reviewed by:
Yingjie Xia,
Dalian University of Technology, China
Kun Du,
Central South University, China

***Correspondence:**
Kaizong Xia
kzxia@whrsm.ac.cn

Specialty section:
This article was submitted to Geohazards and Georisks, a section of the journal Frontiers in Earth Science

Received: *31 March 2022*
Accepted: *26 April 2022*
Published: *10 May 2022*

Citation:
Wang T, Chen C, Xia K, Zhang C, Wang Y and Liu X (2022) Ground Surface Deformation in the Hanging Wall of the Jinshandian Underground Iron Mine in China. Front. Earth Sci. 10:909466. doi: 10.3389/feart.2022.909466

1 INTRODUCTION

In China, the number of open-pit mines is decreasing and more metal mining is taking place deep underground. Sublevel caving is one of the most widely used mining methods employed in such mines. However, as the orebodies are mined out using this method, the rock strata begin to deform and this deformation gradually spreads to the surface. On reaching the surface, the deformation may cause a significant amount of damage to the buildings and structures erected there. Therefore, the

deformation not only affects the safety of the underground mining activity but also threatens the safety of the mine's production facilities and the nearby residents. The geological disasters (ground surface collapse and cracking) often occur in the mining area, because of the deep underground mining activities. What is worse, sometimes rockburst is found in deep underground (Feng et al., 2015; Feng et al., 2020). Consequently, it is imperative that the mechanism driving the surface deformation induced by underground mining is understood in great detail. Much research has been carried out on surface deformation using a variety of approaches including theoretical analysis, physical modeling experiments, numerical simulation, and *in situ* monitoring.

Hoek (1974) used a limit equilibrium approach to analyze the failure of the rock masses in the hanging wall. Lupo (1996a) has carried a lot of research on metal mines and suggested that the ground surface deformation can be divided into three zones: a caved zone, large-scale surface cracking zone, and a continuous surface subsidence zone. Lupo (1996b) also pointed out that shear failure is the dominant failure mechanism in the footwall, while a combination of shear and toppling failure occurs in the hanging wall. Lupo (1997) subsequently introduced an analytical model that combines a limit equilibrium approach for the hanging wall and footwall with a Coulomb-type surface-traction force to represent the caved rock. Svartsjaern (2019) used conceptual models to refine calibrated models detailing the damage development process and failure mechanisms acting. Physical modeling experiments have been used to predict the ranges of collapse pits and figure out the mechanism responsible for surface collapse (Wu et al., 2009; Wang et al., 2019). Also, many scholars have used numerical simulation to study metal mines/tunnels. For example, codes PHASE2 (Villegas and Nordlund, 2008a; Blachowski and Ellefmo, 2012), FLAC3D (Parmar et al., 2019), PFC2D (Villegas and Nordlund, 2008b; Svartsjaern and Saiang, 2017), UDEC (Pinheiro et al., 2015; Svartsjaern et al., 2016), 3DEC (Wang et al., 2012) and FEM/DEM-DFN (Vyazmensky, 2008) have been used to study break and limit angles, ground surface subsidence, caved rock zone deformation, and failure mechanisms in discontinuous rock masses. Finite-difference continuum damage mechanics approach was used to study roof caving (Eremin et al., 2020).

Many scholars have also studied surface deformation by directly monitoring it *in situ*. For example, time–displacement, time–inverse velocity, and time–velocity curves were generated and used to analyze the ground surface deformation at the Kiirunavaara mine in Sweden at different mining stages (Villegas and Nordlund, 2012). Xia et al. (2016a), Xia et al. (2016b), Xia et al. (2019b) extensively studied the ground deformation, movement, and collapse mechanism at the Chengchao iron mine in China based on deformation data monitored *in situ* and field investigations. Studies centered on the Jinchuan Nickel Mine in China found that the horizontal displacement of the underground roadway was larger than its vertical displacement and that the maximum cumulative vertical displacement at the hanging wall surface was smaller than that at the footwall. In the mining area, almost all of the plane displacement vectors were found to point towards the mined-out area. Moreover, three failure mechanisms were suggested to be involved: double-sided embedded-beam deformation, fault activation, and cantilever-articulated rock beam failure (Ma et al., 2012; Ma et al., 2013; Zhao et al., 2013; Ma et al., 2015; Ding et al., 2018; Lu et al., 2018). Xia Y. et al. (2018) have also used a combination of techniques (D-InSAR and GIS) to identify the scope of illegal underground mines. LiDAR mapping and geological penetration radar (GPR) were used to analyze roof damage (Evanek et al., 2021; Li et al., 2021).

According to the scholar's research, few of them study the mechanism of ground surface deformation, with consideration of geological condition (such as steeply dipping discontinuities and faults), especially the unique geological condition like Jinshandian Iron Mine. The geological conditions in the eastern part of the Jinshandian mine in China are complicated. There are discontinuities with steep dip angles, four faults distributed in the area with east–west strikes, and two orebodies that are essentially parallel. There are also a large number of buildings and structures on the surface in the hanging wall region. The surface first collapsed in 2008 near a private mining site (site no. 3) and a further surface collapse occurred in 2013. Since October 2016, the underground roadway has become damaged due to the ground pressure in the hanging wall which has also led to large-scale collapse and cracking, both underground and on the surface (Yang, 2019). The deformation of the surface has also resulted in buildings and other structures suffering from subsidence, becoming inclined and cracked. However, there is a lack of research on the characteristics of surface deformation and deformation mechanisms in metal mines with steeply dipping discontinuities and two parallel orebodies. In this study, the mechanism underpinning the surface deformation of the hanging wall is elucidated based on surface deformation data collected over a period of 13 years. The results can be used to help guide subsequent underground mining work and relocate residents on the surface in a safe and timely manner. The result can be a refence to the underground metal mines which have the similar engineering geology condition.

2 ENGINEERING GEOLOGY OF THE MINING SITE

The Jinshandian iron mine is located near Jinshandian town, which is 30 km southwest of Huangshi in Hubei province, China. The eastern area is taken to lie between exploratory lines nos. 25 and 43. Its east–west extension corresponds to nearly 1,000 m and its north–south extension is 990 m. Mining started at the –270 m level (altitude, the sea level is 0). There are two main orebodies present ('Fe I' and 'Fe II') that are separated by a 50–150 m thick rock wall.

2.1 Strata Lithology

The lithographic forms most widely distributed in the eastern part of the Jinshandian iron mine are hornstone, marble, magmatic (mainly diorite), orebody, and fault (**Figure 1**). The hornstone (labeled A in **Figure 2**) can be subdivided according to its distance from the orebody. Type A_1 hornstone (located far from the orebody) shows good quality, whereas type A_2 hornstone (close to the orebody) has poor quality. Marble is

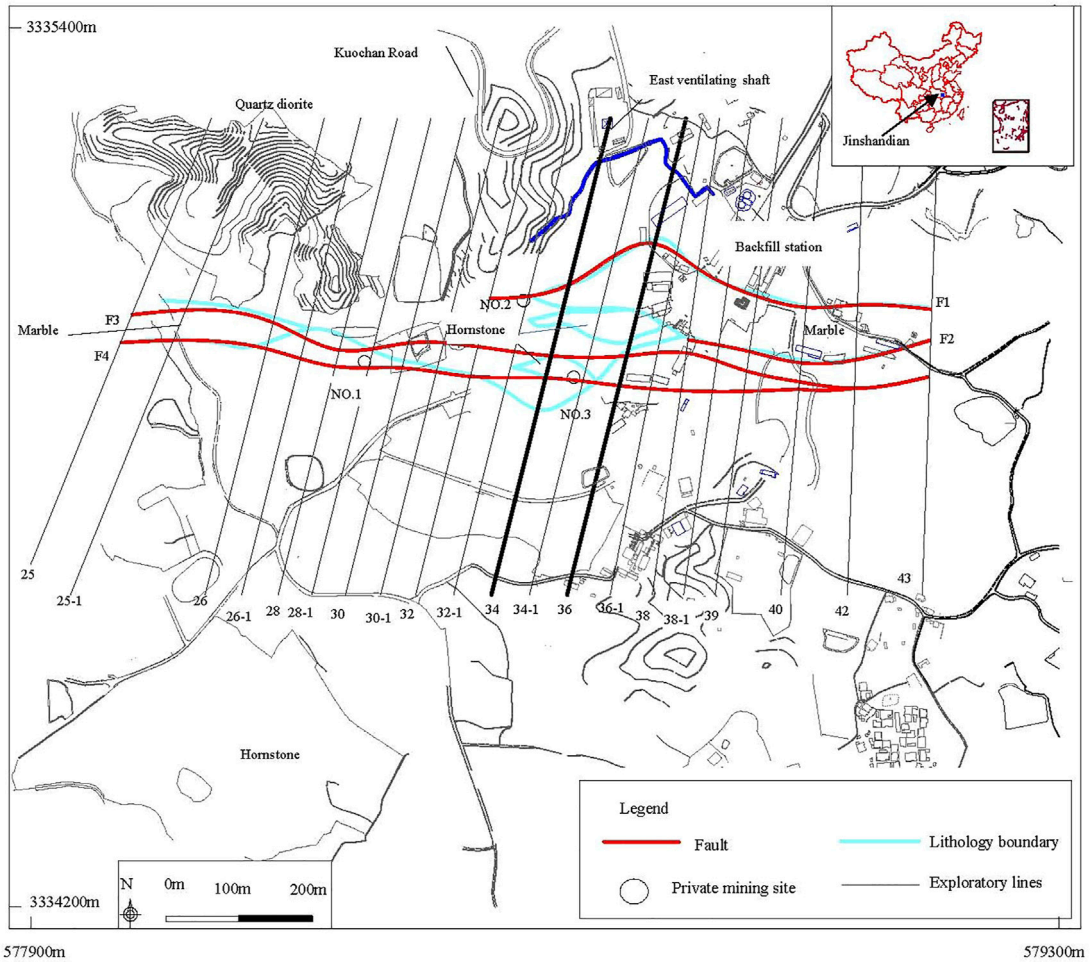


FIGURE 1 | Lithology, faults, and private mining sites in the study area.

labeled using the letter B, while the magmatic rocks are labeled C. The latter can also be subdivided into types C_1 (rocks that are far away from the orebody and have good quality) and C_2 (rocks that are close to the orebody and show poor quality). The orebodies (D) can also be divided into two types: D_1 (block structure; good condition) and D_2 (powdery structure; poor condition). In terms of rock mass quality, the lithography can be ranked from good to poor as follows: $C_1 > A_1 \geq C_2 > A_2 \geq B > D_1 > D_2$.

2.2 Discontinuities and Faults

2.2.1 Discontinuities

An *in situ* geological investigation was carried out on the ground surface and −340, −354, −368, −382, and −396 m levels in July 2018.

The discontinuities in the hanging wall were then classified. It can be seen that there are three main groups of dominating discontinuities in the hornstone (**Table 1**).

2.2.2 Faults

The mining area is crossed by four parallel fault zones with east–west strikes in plane projection. In addition, the upper parts of the faults tend to be steeper than their lower parts when viewed in cross-section along exploratory lines (as shown in **Figure 1**). Some specific observations can also be made:

1) Fault F1 extends eastwards from exploratory line 32. It is about 1,500 m in length and 15–35 m wide. It has a dip direction that ranges from 160° to 200° and a dip angle of 60°–75°.
2) Fault F2 extends eastwards from exploratory line 38 and its length is about 1,200 m. Its dip direction ranges from 180° to 190° and its dip angle is 55°–85°.
3) Fault F3 lies between exploratory lines 25 and 43 with a width that ranges from 15 to 35 m. It dips to the south and has a dip angle that ranges from 55° to 87°.
4) Fault F4 is roughly parallel to F3 and runs 25–150 m to the south of it. It also dips to the south. Its dip angle is in the range from 55° to 85° and its width is 10–35 m. F3 and F4 coalesce near exploratory line 42, forming a 100-m wide fault zone on the surface.

2.3 *In Situ* Ground Stress

The stress relief method, which is based on elastic mechanics theory, was used to measure the level of *in situ* ground stress. The

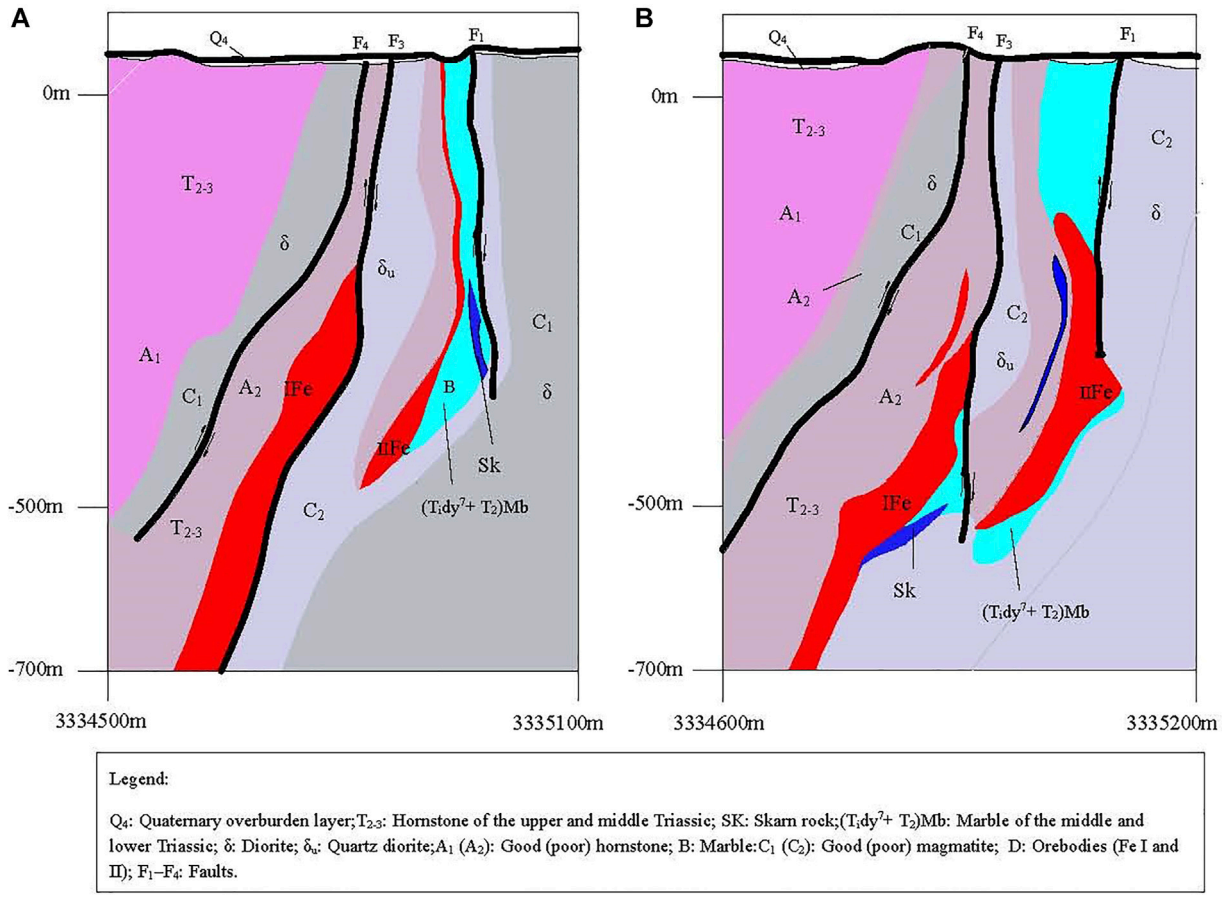


FIGURE 2 | Geological sections along exploratory lines 34 and 36. **(A)** Exploratory line 34. **(B)** Exploratory line 36.

TABLE 1 | Major discontinuities in the hanging wall.

No.	Dip direction	Strike	Dip angle (°)	Spacing (m)
1	217° (S 37° W)	S 53° E	70	/
2	106° (S 74° E)	S 14° W	78	/
3	181° (S 1° W)	S 89° E	66	0.30

rock mass is assumed to be an infinite elastic body. Any boreholes in the rock will thus be elastically deformed by the initial ground stress. Therefore, the stress state in the plane perpendicular to a borehole axis can be calculated by measuring the deformation (change in diameter) of the borehole during the stress relief process. Stress tests were carried out *in situ* in December 2019 in the −410 and −500 m levels. The results obtained are shown in **Table 2**.

2.4 Description of the Orebodies

2.4.1 Orebody Distribution

There are two main orebodies (Fe I and Fe II) in the eastern part of the Jinshandian iron mine that are parallel to each other. Between Fe I and Fe II, there is a rock wall composed of hornstone and quartz diorite with a thickness of 50–150 m. Fe I is 1,320 m long from east to west (stretching from exploratory line 23 to exploratory line 43). Fe II has a length of about 1,020 m (stretching from exploratory line 26 to exploratory line 43). Fe II lies to the north of Fe I and the two orebodies are imbricated when viewed in cross-section.

2.4.2 Mining Situation

In September 2005, the roof of the −270 m level began to cave. Orebody Fe I was mined from north to south, while orebody Fe II was mined from south to north. Due to relocation problems on the surface, mining work had to be suspended from early April 2009 to the end of February 2012. Mining resumed in early March 2012. Due to the COVID-19 pandemic, mining work had to be stopped on January 18, 2020; it subsequently resumed on March 21, 2020. See **Table 3**.

Mining work is now taking place in the −382 and −396 m levels. The partly situation with respect to mined-out areas is shown in **Figure 3**.

In addition, as parts of the orebodies were quite near the surface (some were even directly exposed on the surface), many private mining sites were set up. Among them, there are three main sites of interest (labeled site nos. 1, 2 and 3 in **Figure 1**). It is understood that the mining depth of these private mining sites is

TABLE 2 | *In situ* ground stress levels (December 2019). The principal stress is specified *via* three components: σ_H (maximum horizontal stress), σ_h (horizontal intermediate stress) and σ_v (minimum vertical stress). The angle θ is the angle between the horizontal principal stress and north direction.

No.	Lithology	Method	Depth underground (m)	Borehole depth (m)	Density (10^3 kg/m^3)	σ_H (MPa)	σ_h (MPa)	σ_v (MPa)	θ (°)
1	Hornstone	Stress relief	508.38	53.6	2.51	21.4	16.6	12.5	291.1
2	Diorite	Stress relief	575.67	33.3	2.66	21.9	20.4	15	30.5
3	Diorite	Stress relief	576.8	34.5	2.66	23.2	19.6	15.0	3.5

TABLE 3 | Mining situation.

Mining level (m)	Mining dates	
	Start	End
−270	Feb 2007	Apr 2009
−284	Dec 2007	Dec 2012
−298	Mar 2012, Fe I and Fe II	Sep 2013, Fe I and June 2014, Fe II
−312	Apr 2012, Fe II and December 2012, Fe I	Jun 2014, Fe I and November 2014, Fe II
−326	May 2014 Fe I and December 2014 Fe II	Aug 2015, Fe I and March 2016, Fe II
−340	Mar 2015, Fe I and Fe II	Mar 2016, Fe I and April 2017, Fe II
−354	Dec 2015, Fe I and February 2017, Fe II	Dec 2018, Fe I and April 2018, Fe II
−368	Feb 2017, Fe I and February 2018, Fe II	Oct 2019, Fe II and July 2020, Fe I
−382	Feb 2018, Fe I and August 2018, Fe II	Nov 2020, Fe II and Mining, Fe I
−396	Mar 2019, Fe I and June 2019, Fe II	Currently being mined

about −160 m and the amount of stoping ore involved is about 2 million tons. Much of the important information about the locations and shapes of the mined-out areas formed underground at these sites is unknown. However, the mining-out of these shallow orebodies was found to have a significant impact on the deformation of the surface, leading to collapse at several places near the private sites when the mining activity began.

3 NATURE OF THE GROUND SURFACE CRACKING AND COLLAPSE

3.1 Ground Surface Collapse

In April 2007, the ground surface collapsed at the no. 2 private mining site near exploratory line 36 (collapse pit no. I). The area affected measured ~250 m^2 and three nearby houses were cracked and deformed. In September 2008, a second collapse occurred near the no. 3 private site (in the courtyard of a food company) affecting an area of ~620 m^2 (collapse pit no. II). The evolution of the surface collapse and cracking processes in this region is shown in **Figure 3** and **Figure 4**.

In February and May 2013, the surfaces near collapse pits II and I collapsed again (respectively). Thereafter, the two collapsed areas continued to extend outwards in all directions. In November 2013, a new collapse pit with an area of ~300 m^2 appeared on the surface just south of collapse pit II which gradually merged into one collapse pit with pit no. II.

In April 2017, a collapse pit with a diameter about 6 m and depth of about 3 m appeared next to the railway between exploratory lines 38 and 38-1 (collapse pit no. III). This pit was funnel-shaped and left part of the railway hanging in the air. Due to the scale of the collapse, the railway became severely deformed and was demolished after it was found to be unusable.

In April 2018, a larger funnel-shaped collapse pit (diameter ~20 m) appeared between exploratory lines 34-1 and 36 (collapse pit no. IV). By June 2018, the collapse pit had expanded slightly and deepened, and there were also many cracks visible in the ground nearby.

In November 2018, another funnel-shaped collapse pit (collapse pit no. V) appeared 150 m west of collapse pit I between exploratory lines 30-1 and 32. The diameter of this pit was ~18 m and its depth was ~10 m.

In June 2019, a pit with a depth of ~5 m and diameter ~5 m (collapse pit no. VI) appeared to the east of collapse pit no. IV. In the same month, a large number of collapse pits formed to the east of collapse pit no. II. One particular collapse pit, referred to as a 'pit-in-pit', measured ~10 m (diameter) by ~7 m (depth).

By the beginning of 2007, the area of the ground affected by surface collapse and cracking had expanded in all directions as the mining activity proceeded. As a result, the buildings and structures on the surface had been seriously damaged. Aerial photographs of the mining area taken in 2020 (**Figure 3**) clearly show the pattern in the surface deformation and damage caused by the underground mining activity. The scope of the surface collapse was investigated *via in situ* field investigation, three-

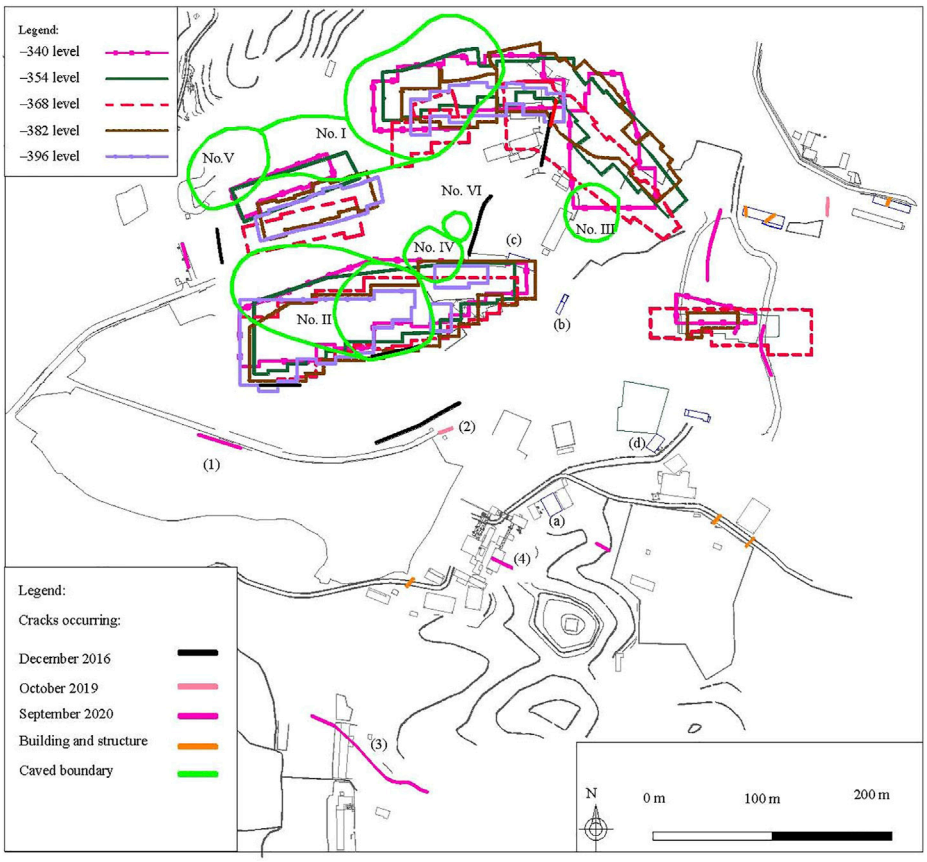


FIGURE 3 | Planar projection of the collapse pits and cracks.

dimensional (3D) laser scanning, and aerial photography, giving the results shown in **Figure 4**.

It can be seen that four of the collapse pits lie above orebody Fe I (nos. II–IV and VI). The current area of collapsed ground associated with these pits is ~15,800 m^2. The surface subsidence in the region was originally caused by the private mining sites which led to funnel-shaped collapse pits nos. I and II being formed near the nos. 2 and 3 private mines. As the underground mining commenced, the scope of the collapse continued to increase in extent. When the mining was suspended, the collapse of the pits continued to extend slowly due to the creep characteristics of the rock masses. Then, when the mining was restarted in March 2012, the collapsed area extended further still. After October 2016, the underground roadways in the hanging wall were destroyed by underground pressure (Yang, 2019) which led to large-scale deformation of the surface. From April 2017 to June 2019, the collapse of pits nos. III, IV, V, and VI occurred sequentially in that order. At present, the deformation of collapse pits nos. II, III, IV, and VI above orebody Fe I continues to increase. The rock mass of roof was fractured which influenced by F4 and F3 fault, and steeply dipping discontinuities. After the roof collapsed, chimney caving emerged above the mined-out area. In effect, by June 2019, the caving of the deep rock mass propagated to the ground surface forming a large-scale area of deformation above the mined-out area.

3.2 Cracking and Damage to the Ground Surface, Buildings, and Other Structures

An investigation of the surface cracking (from 2016 to 2020) and damage to buildings and structures (investigation made in December 2020) was made in the hanging wall (see **Figure 3** for details). Due to the effect of the underground mining, a large number of cracks had appeared on the surface. Before 2016, there were clearly more cracks in the footwall than the hanging wall. Xia et al. (2019a) explained this by suggesting that the footwall rock mass had undergone slipping–toppling failure. After October 2016, the cracks in the hanging wall had gradually increased.

The cracks around the collapse pits are essentially parallel to their boundaries and have the same strike as orebody Fe I. The cracks that are far away from the collapse pits are essentially parallel to the strikes of the discontinuities. For example, cracks (1), (3), and (4) are consistent with the first group of discontinuities in **Table 1** and crack (2) is consistent with the second group of discontinuities.

Due to the deformation and destruction of the ground surface in the hanging wall, the buildings and structures have become cracked and show signs of subsidence. The buildings close to the collapsed pits

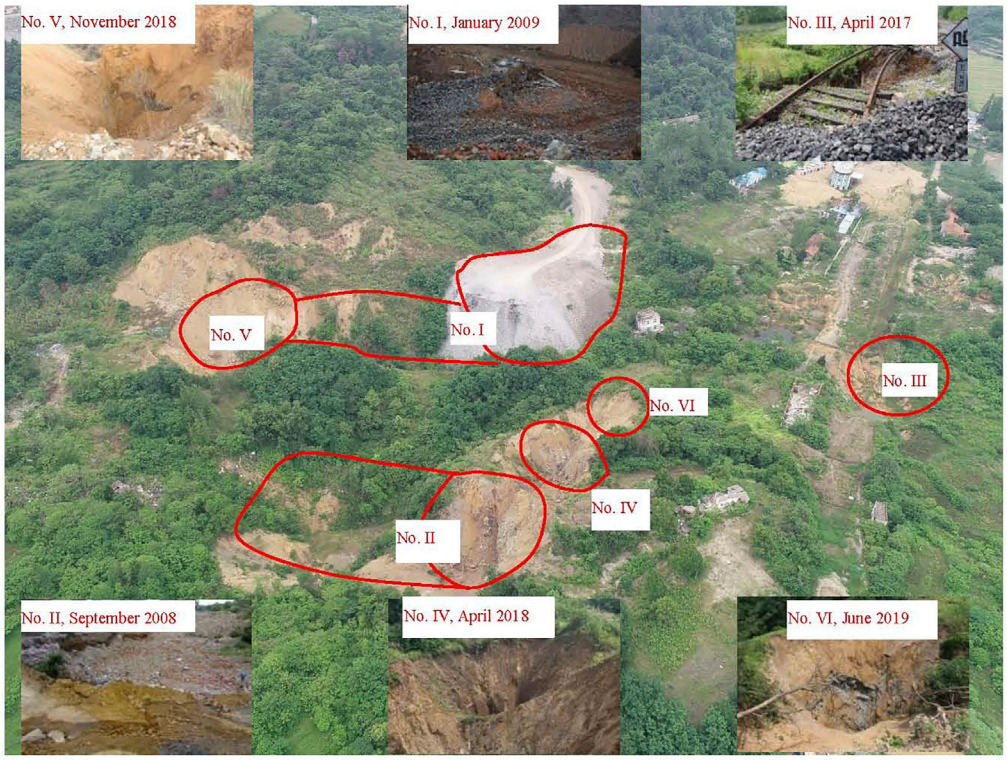


FIGURE 4 | Aerial photographs of the mined-out area (main image captured in May 2020).

have become strongly inclined and subsided and the displacement in the vertical direction is greater than that in the horizontal direction—for example, (b) and (c). A certain distance from the collapse pits, cracking and horizontal movement can be seen to occur in buildings that have good integrity [for example, the building (a) in the concrete frame structure]. Other buildings with poor integrity have also cracked but the dip direction of these cracks deviate from those of the collapse pit, as shown by the (d) in **Figure 3**.

Affected by the steeply dipping discontinuities, cracks around the collapse pits are essentially parallel to the boundaries of the pits, while the cracks far away from the pits are consistent with the strikes of the discontinuities.

4 NATURE OF THE GROUND SURFACE DEFORMATION

The horizontal and vertical deformation of the ground surface in the hanging wall region was studied based on the monitored GPS and level data. Some of the monitoring points used are shown in **Figure 5**.

4.1 Methods Used to Monitor the Deformation

A GPS technique was used to monitor the horizontal displacement. HiPer II and V receivers (manufactured by Topcon) and the Sheshan coordinate system were used. The radius of the ellipsoid used is 6,378,245 m, the reciprocal of curvature is 298.3, the central meridian is 114° E, and the offset value is 500,000 m. The 3D coordinates of the two reference points employed are G1 (3,335,533.049 m, 578,779.2745 m, 110.59958 m) and G2 (3,335,331.055 m, 579,266.8118 m, 47.42427 m). The position coordinates of the monitoring points can be calculated using the GPS receivers and two known reference points.

Two methods can be used to monitor the vertical displacement. One is based on GPS measurement. These measurements can be made simultaneously with the horizontal displacement measurements (using the same monitoring points). The other method involves level monitoring. In this work, Leica DNA03 digital levels were employed.

A number of monitoring points in the hanging wall were selected to determine the characteristics of the surface deformation (36 GPS and 18 level monitoring points). The monitoring data were then used to construct displacement–time and velocity–time curves. In addition, the data can be used to elucidate further deformation parameters at each monitoring point (cumulative horizontal and vertical displacements, ratio of horizontal to vertical displacement, and horizontal and vertical deformation velocities).

4.2 Surface Displacement–Time Curves

4.2.1 Horizontal Displacement

The horizontal displacement–time curves obtained at the various monitoring points present different deformation

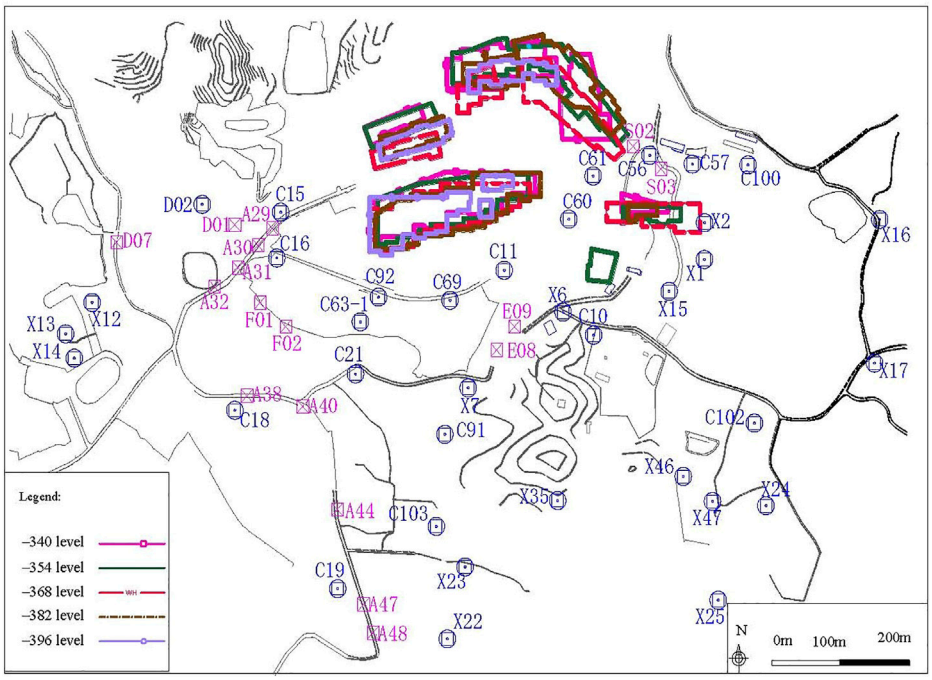


FIGURE 5 | Locations of some of the GPS (in blue) and level (in magenta) monitoring points used.

characteristics and can be divided into five types. The first type is generally found at points that lie close to the mined-out areas, e.g., points C10, C11, C15, C21, C56, C57, C60, C61, and C63-1. At these points, the displacement curves generally exhibited three inflection points which occurred around March 2009, February 2012, and October 2016 (**Figure 6**). At monitoring point C15, however, the third inflection point appeared to occur later, around October 2017. It shows that the deformation produced by the initial mining activity was quite small before March 2009. The surface deformation increased slowly thereafter due to the suspension of mining from April 2009 to February 2012. The deformation slowly increased from March 2012 onwards due to the resumption of the mining activity. Around October 2016, the deformation rate increased sharply. At point C15, however, the deformation increased only slowly after October 2017, and the cumulative horizontal displacement appeared to stabilize at around 63 cm now.

The second type of displacement curve has just two inflection points—March 2009 and February 2012—as found at points C16, C18, and C19 for example (see **Figure 6** for details). The third type of curve has just one inflection point which occurred around October 2016, e.g., points C69, C91, and C92. The fourth type of curve has no inflection points, the displacement generally increasing linearly in time, e.g., C100, C102, C103, D02, X1, X2, X6, X7, X15, X22, X23, and X35 (where the displacement of X1, X2, X6, X7, X15, and X35 appear to be larger and faster than the others). The fifth type of curve corresponds to data that undergoes small fluctuations, e.g., X12, X13, X14, X16, X17, X24, X25, X46, and X47.

In order to better understand the surface deformation data recorded at the monitoring points during different mining periods, the first type of deformation curve with three inflection points is divided into four stages: Period 1 (P1) from 2008/5/5 to 2009/3/23; Period 2 (P2) from 2009/3/23 to 2012/2/25; Period 3 (P3) from 2012/2/25 to 2016/10/18; and Period 4 (P4) from 2016/10/18 to 2020/12/22. These divisions are also used when considering other GPS and level monitoring points. The cumulative horizontal displacements (until December 2020) in the first three types of displacement curve lie in the ranges 62.96–479.5 cm, 13.89–22.72 cm, and 172.74–420.40 cm, respectively. Those in the last two types lie in the ranges 2.28–152.95 cm and 0.5–2.84 cm, respectively. The point that exhibited the largest horizontal displacement is C11 where the maximum displacement reaches 479.5 cm.

For a given monitoring point, the horizontal displacement gradually increased as the mining activity proceeded. Also, the deformation suffered over a given period of time gradually increases the closer the point is to the void boundary. Apart from the boundary points X14, X17, X24, and X25, the horizontal displacement vectors were measured at each GPS monitoring location points towards the mined-out areas. The main deformation seemed to occur after October 2016. For example, the horizontal deformation at C11 during P4 exceeded 450 cm, which is 19 times larger than the sum of P1, P2 and P3.

4.2.2 Vertical Displacement

The vertical displacement–time curves presented here are based on the level monitoring data recorded. Two types of curves are found (**Figure 7**). The first type features 4 inflection points

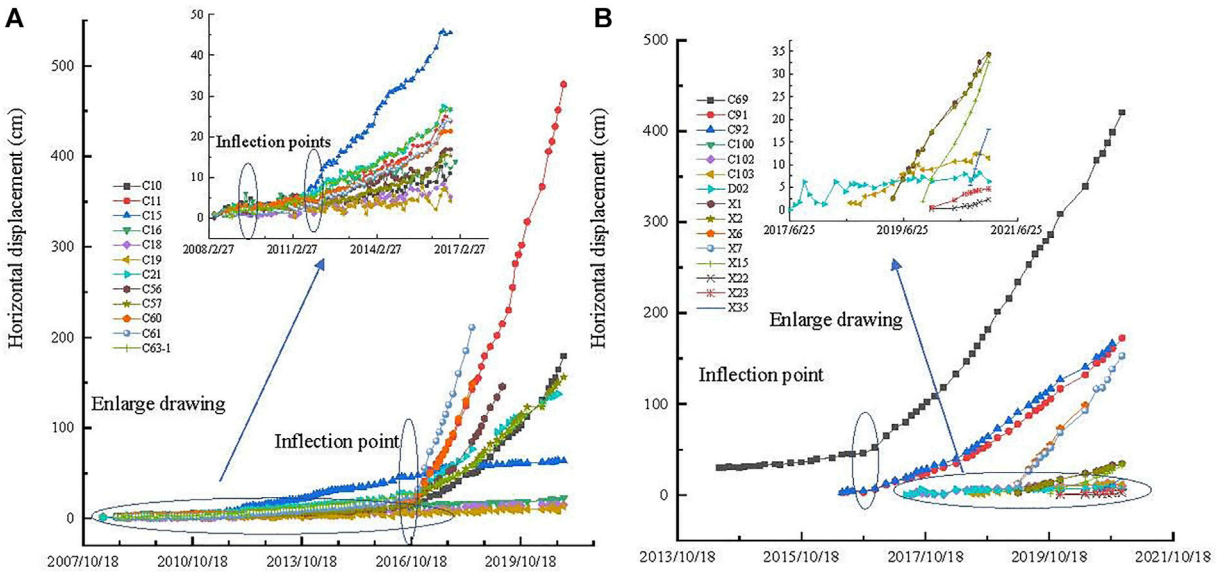


FIGURE 6 | Horizontal displacement–time curves **(A)** With two and three inflection points. **(B)** With one inflection point.

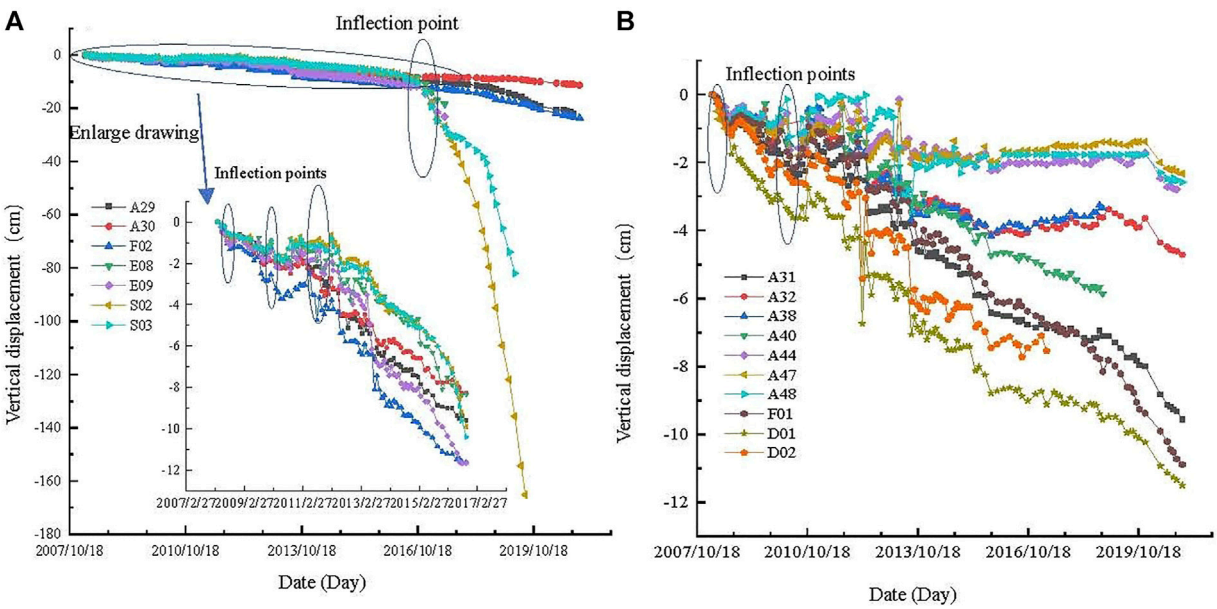


FIGURE 7 | Vertical displacement–time curves **(A)** With four inflection points. **(B)** With two inflection points.

(around September 2008, May 2010, February 2012, and October 2016) as found at points A29, A30, F02, E08, E09, S02, and S03. In September 2008, collapse pit no. II was formed. There was a lot of rain from March to May 2010 but the vertical displacement changed very little around June 2010. The vertical displacements of the monitoring points range from −11.32 to −165.22 cm (the largest displacement occurring at S02).

The data recorded at points A31, A32, A38, A40, A44, A47, A48, F01, D01, and D02, however, exhibit two inflection points (around September 2008 and May 2010) and the displacements (until December 2020) range from −1.47 to −11.5 cm.

As can be seen, some points (C10, C11, C56, C57, C60, C61, C63-1, C69, C91, C92, X6, and X7) experienced large vertical displacements (until December 2020) that range from −71.51 to −378.25 cm. Point C69 suffered the largest change (−315.74 cm) in P4, which is more than 5 times larger than P3. The vertical displacements (until December 2020) of points C15, C16, C18, C19, C21, C100, X1, X2, X13, X15, and X35 fall in the range

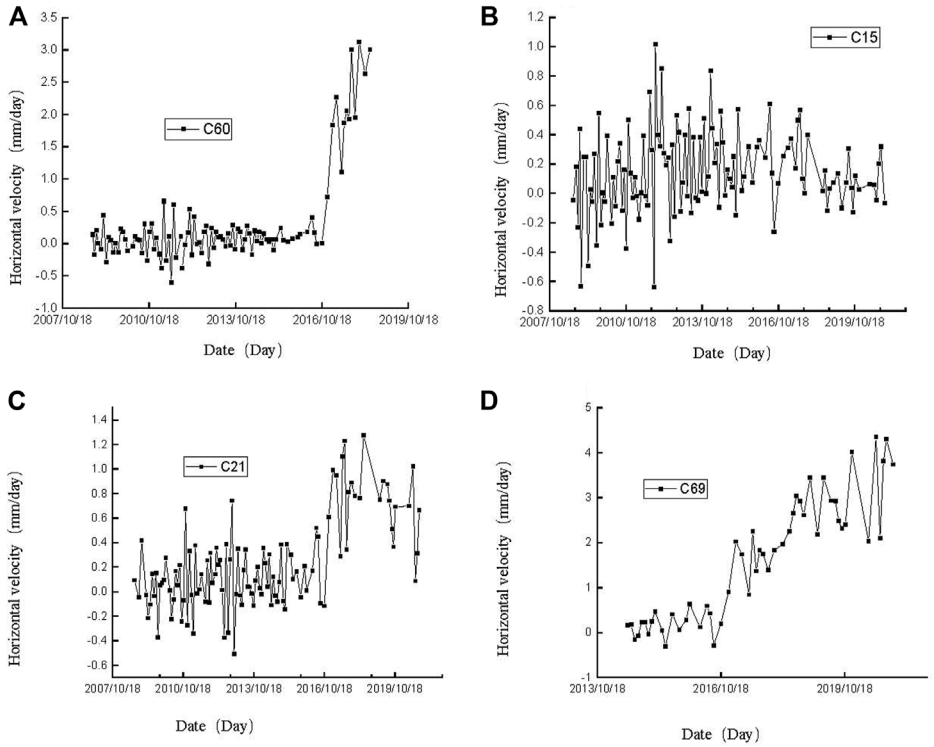


FIGURE 8 | Horizontal velocity–time curves **(A)** C60; **(B)** C15; **(C)** C21; **(D)** C69.

−11.84 to −45.76 cm. In contrast, the vertical displacements measured at C102, C103, D02, X12, X14, X16, X17, X22, X23, X24, X25, X46, and X47 are rather small (between −0.4 and −8.92 cm). For a given monitoring point, the vertical displacement tends to increase as the mining activity becomes deeper. In addition, the closer the monitoring point is to the mined-out areas, the greater the deformation suffered over a certain period of time.

4.3 Surface Displacement Velocity–Time Curves

The influence that the mining activity has on the ground surface is also reflected in the rate at which the deformation of the ground surface changes. Therefore, the data were used to construct horizontal and vertical velocity–time curves, as shown in **Figure 8** and **Figure 9**.

The horizontal velocity–time curves (constructed using the GPS monitoring data) illustrate the 6 kinds of horizontal velocity variation found in the area. The first type is exemplified by points such as C10, C11, C56, C57, C60, C61, and C63-1. Here, the horizontal velocity undergoes large fluctuations at first but the amplitudes of the fluctuations become smaller as times passes. After a while, the velocity increased rapidly in a linear manner (starting around October 2016). At C11, for example, the horizontal velocity had reached 9.5 mm/day by August 2019.

The second type of behavior was found at C15, C16, and C18. Here, the horizontal velocity fluctuated sharply at first but this fluctuation decreased in significance as time progresses. That is, the velocity–time curve constantly fluctuated but the amplitude of the fluctuation became relatively small after October 2016. The third type was observed at points such as C21. The curve fluctuated at first, then increased linearly around October 2016, and continued to fluctuate after April 2017.

The fourth type of horizontal velocity curve (e.g., C69, C91 and C92) fluctuates steadily at first and then more rapidly after October 2016. In the fifth type of curve (e.g., X1, X2, X6, X7, X15, X35, C100, C102, C103, D02, and D07) it was fairly linear. The behavior was established after October 2016 and fluctuated steadily at a certain velocity (although the velocities at points X6, X7, and X35 are higher than the others). The sixth type of curve involved constant fluctuation—C19 and other monitoring points were included in this type.

The horizontal velocities at points C10, C11, C56, C60, C61, C69, C91, C92, X6, X7, and X35 are all greater than 1 mm/day in the P4. In fact, the velocities in this interval fall in the range 1.10–3.07 mm/day. On the other hand, their velocities (except for X6, X7 and X35) in P3 lie in the range 0.05–0.54 mm/day. The velocities of points X1, X2, X15, C21, C57, and C63-1 range from 0.55 to 0.92 mm/day in the interval P4. The horizontal velocities at points C15, C16, C18, C19, D02, C100, C102, and C103 are all very small in P4 (ranging from 0.06 to 0.24 mm/day and increasing slowly). The horizontal velocities of the other monitoring points in P4 range from 0.02 to 0.21 mm/day. For the displacement-time curves with four stages, most of the horizontal velocities obey the following rule: P4 > P3 > P1 > P2.

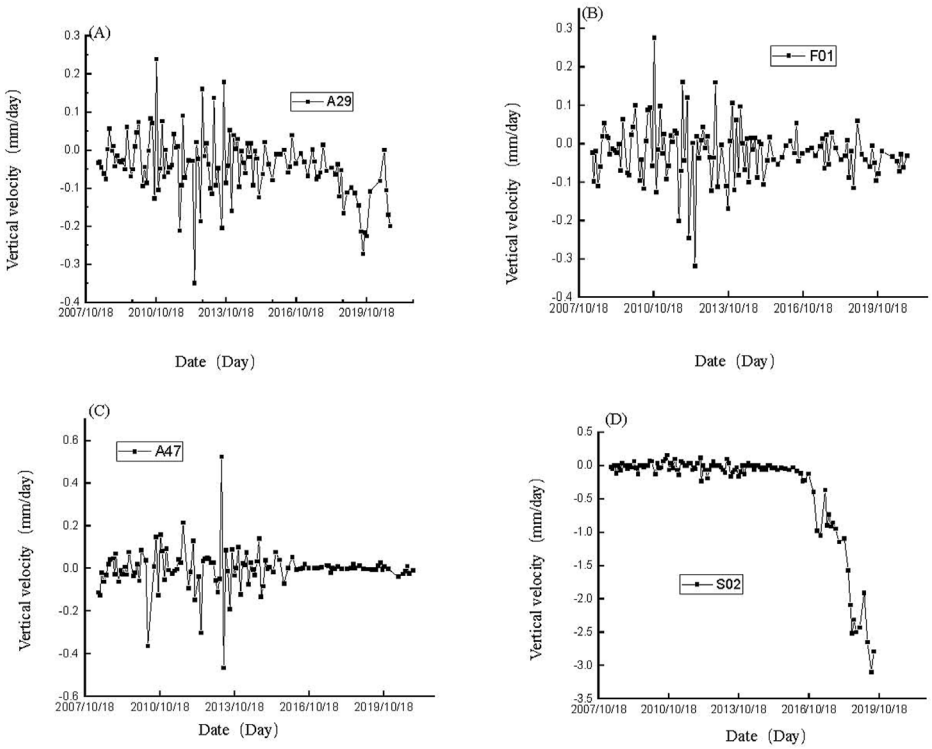


FIGURE 9 | Vertical velocity–time curves **(A)** A29; **(B)** F01; **(C)** A47; **(D)** S02.

Vertical velocity–time curves were also drawn using the level monitoring data. There were four kinds of types classified and summarized. At point A29, the vertical velocity fluctuates at first but an obvious change occurs around October 2016. Points A30, A31, A32, A38, A40, A44, F01, F02, D01, and D02 essentially appeared to be in a constant state of fluctuation. However, the amplitude of the fluctuations was large at first but then became smaller with a demarcation point around July 2014. Points A47 and A48 fluctuated at first and the amplitude of the fluctuation appeared to increase linearly. However, the velocity was basically zero after July 2014 implying that these points essentially stopped moving up/down. Points S02, S03, E08, and E09 had vertical velocities that fluctuated strongly at first and then showed an obvious inflection point around October 2016 after which the downward velocity increased sharply.

The vertical velocities of points C10, C11, C56, C57, C60, C61, C63-1, C69, C91, C92, X6, X7, and X35 are in the range −0.18 to −2.8 mm/day during the interval P4. Moreover, the velocity of point C61 in P4 is 26 times larger than that in P3. Apart from points X46 and X47, the other GPS monitoring points have velocities ranging from −0.02 to −0.33 mm/day. The vertical velocities of S02, S03, E08, and E09 during P4 are in the range from −0.3 to −1.53 mm/day. The velocities of the rest of the level monitoring points are between 0 and −0.06 mm/day.

The velocity–time curves all fluctuate to some degree. Such fluctuations were studied by Ma et al. (2007). When underground mining is carried out, strain energy accumulates in the rock strata. When this energy exceeds a certain critical threshold, the energy is released and the velocity of the rock mass will increase. As the stored energy is subsequently dissipated, the velocity of the rock mass will decrease.

The monitoring results presented here allow the following conclusions to be drawn. The horizontal displacement–time curves (from May 2008 to December 2020) that have three inflection points can be divided into four stages: P1, P2, P3, and P4. P1 corresponds to the initial deformation stage. In this stage, both the displacement and velocities are small with some fluctuation. The deformation is small and mainly caused by the private mining activity. P2 is the 'creep' deformation stage and is caused by the creeping movement of the rock. There is a small increase in deformation at this stage. Therefore, the displacement and velocity are again small but occur at a rate that is greater than that in the P1 stage. P3 is a slow deformation stage in which the deformation increases steadily at a certain rate. Finally, P4 is the accelerating deformation stage in which there is a significant increase in the rate of horizontal and vertical deformation. Almost all of the monitoring points that have four stages are such that their horizontal velocities show the same rule: P4 > P3 > P1 > P2.

Depend on the GPS monitoring points, the horizontal displacement velocity of C60, C61, C11, C92, are larger than 1 mm/day. At the meantime, many major cracks are found there, like crack (1) to crack (4). Especially C92, it was close to crack (1) which emerged on September 2020, and the horizontal displacement velocity of C92 was 1.43 mm/day. So did the crack (2) which was found on October 2019, and the

horizontal displacement velocity of GPS points C11 and C69 was 3.48 mm/day and 2.40 mm/day. Depend on the horizontal displacement velocity of GPS monitoring points close to major crack, we get the conclusion that major cracks on the surface will emerge when horizontal velocities exceed 1 mm/day.

4.4 Ratio of Horizontal to Vertical Displacement

Most of the monitoring points have horizontal to vertical displacement (H/V) ratios that increase the further the point is away from the void boundary. According to our statistical analysis, 26 of the 36 GPS monitoring points have H/V values that are greater than 1 until December 2020. This shows that the current surface deformation process is dominated by horizontal displacement.

According to the displacement–time curves, displacement velocity–time curves, and ratio of horizontal to vertical displacement, a conclusion can be got, that is the horizontal displacement plays an important role in ground surface deformation. This is mainly affected by *in situ* ground stress, and steeply dipping discontinuities. When the orebody is mined in the deep, the *in situ* ground stress is released which cause the rock column cut by steeply dipping discontinuities to topple. Disturbed by the rock mass F4 fault start to slip, the failure of F4 fault and rock mass gradually spreads to the surface in months.

5 DEFORMATION MECHANISM AND GROUND SURFACE ZONES

5.1 Ground Surface Deformation Mechanism

Many researchers have used physical models to study the mechanism responsible for the ground surface deformation in the Jinshandian iron mine region (Cai et al., 2006; Chen, 2006; Ren et al., 2010). Xia K. et al. (2018) pointed out that the majority of the deformation above the mined-out area was gradually spreading upwards from the deep regions to the surface. Yang (2019), based on the results of *in situ* field investigations, deformation and microseismic monitoring experiments, and theoretical analysis, managed to explain why ground pressure had been produced in the haulageway of the mining level after October 2016. Moreover, the work of Brady and Brown (2006) and Xia et al. (2016a), Xia et al. (2016b) showed that it was mainly toppling failure occurring in the metal mine. Also, Du et al. (2020a) and (2020b) did lots of study on rock failure depend on acoustic emission.

The discontinuities in the rock mass are steeply dipping in the eastern part of the Jinshandian mine. The first group of discontinuities cut the hanging wall of the rock mass into column-shaped blocks. In addition, the rock masses surrounding the mined-out area are of relatively poor quality. As the underground mining activity proceeds, the initial stress in the rock is released after the rock mass near the void is disturbed. This caused the forces acting on the opposite sides of the columnar rock masses to become unbalanced. When the tensile strength of a column is reached, it will be subjected to flexural toppling failure. Failure occurs on the side of the rock column near the void. As a result, a large amount of caved rock will be created that will fall into the void. As the mining activity moved to greater depths, the upper part of fault F4 slipped and caved, further damaging the rock columns. The scope of the caved rock masses is also extended (see **Figure 10** for details).

The deformation of the hanging wall can now be seen to be highly significant. The deformation is closely related to the dips and strikes of the orebodies in the mining area, the distributions of the discontinuities and faults, and the direction of the initial ground stress. The two orebodies are parallel to each other and have strikes in nearly east–west directions and dip towards the south. In addition, four faults are distributed around the orebodies with east–west strikes which means the quality of the rock masses around the orebodies is poor. The steeply dipping discontinuities play a crucial role in the surface deformation. Also, the initial ground stress is oriented in a nearly north–south direction. After the underground orebody is mined out, the initial stress is released and the rock mass and roof near the mined-out area are destroyed due to the *in situ* ground stress, pressure from the overlying rock masses, and the effect of gravity on them. When a large amount of orebody has been mined, the deformation in the deep rock strata gradually spreads to the surface. This, in turn, leads to subsidence and horizontal movement of the ground surface and hence damage and destruction of buildings and other structures thereon.

5.2 Ground Surface Zones

Lupo (1996a), Fu et al. (2015), Xia et al. (2020), and Pang et al. (2020) have carried out a great deal of research on surface deformation zones. In this paper, the surface deformation in the hanging wall is divided into six zones based on the results of our GPS and level monitoring data, the cracks observed in the Jinshandian surface and its state of collapse, and the results of other studies. Here, we refer to the zones as: (i) the caved zone (CZ), (ii) fast-accelerating deformation zone (FADZ), (iii) slowly-accelerating deformation zone (SADZ), (iv) acceptable deformation zone (ADZ), (v) slight deformation zone (SDZ), and (vi) no deformation zone (NDZ). The suggested boundaries of these zones are shown in **Figure 11**.

The CZ, which is located directly above the void, may contain a large amount of caved rock (which moved to the mined-out area under the action of its own gravity). After a certain amount of time, the deformation gradually spreads to the surface, causing the surface to collapse and crack. On the surface near the collapsed pit, there are a lot of large cracks and the soil layer is very soft. The CZ boundary (CZB) is based on the topographic map generated by 3D laser scanning and other observation methods (aerial drone photography, GPS and level monitoring, and field investigation). The CZB lies about 5 m away from the collapsed pit boundary (CPB) and a large number of tension cracks are visible on the surface which are quite deep and have strikes parallel to the CPB. Due to the large deformation encountered in the CZ, no monitoring points are set up inside it in the interest of safety. As found previously by Lupo (1997), the CZ is dominated by vertical deformation.

The columnar rock masses in the FADZ undergo flexural toppling (towards the void side) due to the subsidence and

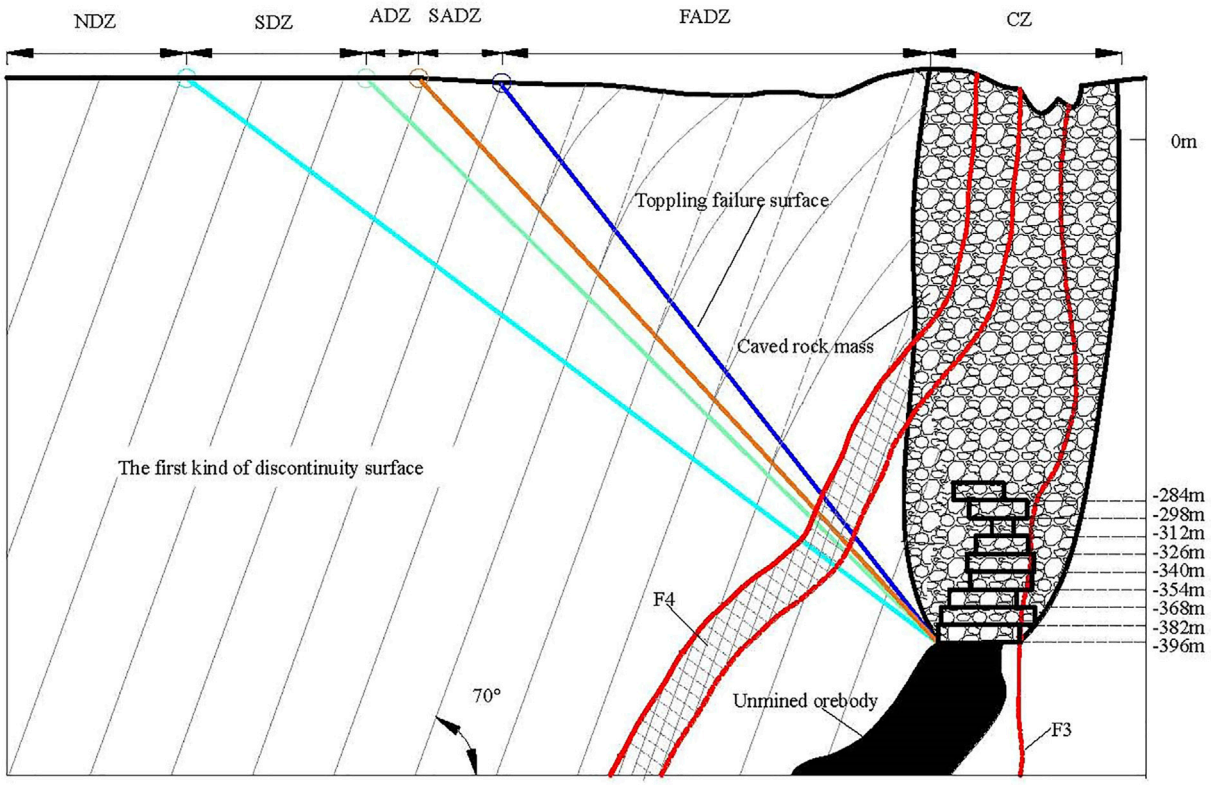


FIGURE 10 | Schematic diagram showing the deformation mechanism in the deep rock strata.

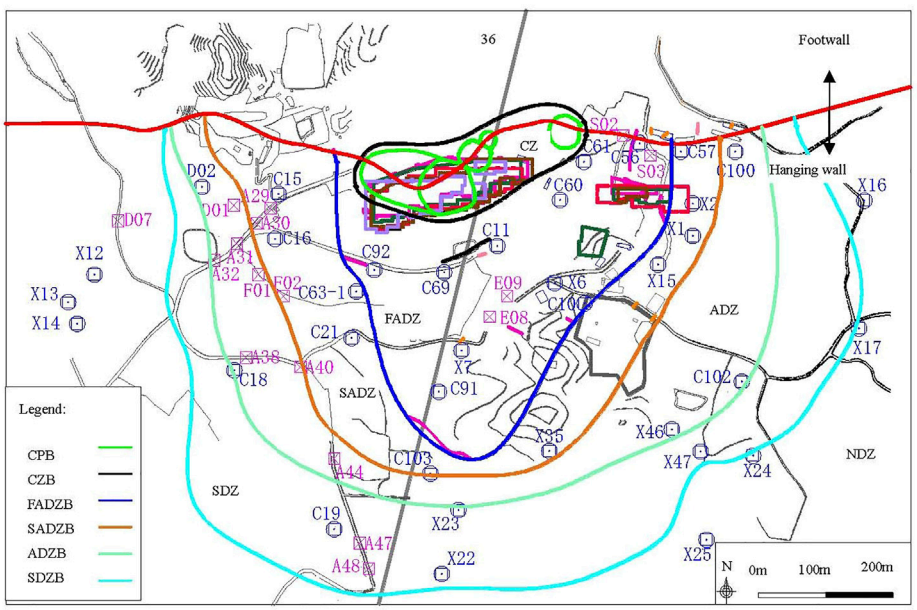


FIGURE 11 | The zones formed on the ground surface.

horizontal movement of the rock masses in the CZ. The numerous failing rock columns lead to the formation of a slip surface. The failed rock masses are relatively broken and will readily move to the mined-out area along the sliding surface along with the caved rock masses in the CZ. In the FADZ, the buildings are sinking heavily and the surface cracks are large. The monitoring points in this area exhibit obvious signs of accelerated deformation. At the same time, it can be seen that the H/V ratios of the GPS monitoring points in this area are all greater than 1 and their horizontal velocities are greater than 1 mm/day. The FADZ boundary (FADZB) is determined by the locations of the major cracks on the surface and the coordinates of the GPS monitoring points whose horizontal velocities exceed 1 mm/day.

In the SADZ, there are a few cracks on the ground surface and the deformation is mainly that caused by the flexural toppling failure of the rock masses. The SADZ boundary (SADZB) is drawn according to the horizontal displacement field derived from the GPS monitoring data. A critical strain value of 6 mm/m (0.006) is used to define the boundary based on Chinese specification (The Coal Industry Bureau of the People's Republic of China, 2017).

Pang et al. (2020) has carried out a lot of research on ADZs. In the ADZ, there is movement and deformation of the ground surface but cracks do not form. However, a few cracks can be found on the buildings and other structures. The rock mass below this zone is disturbed and the displacement–time curves of the monitoring points on the surface show a fluctuating and increasing trend. The ADZ boundary (ADZB) is drawn, based on the horizontal displacement field, using a critical strain value of 2 mm/m (0.002).

In the SDZ, there is only slight movement of the ground surface and the underground rock mass is subject to minimal disturbance. As a result, the deformations of the monitoring points in the zone fluctuate. Using the horizontal displacement field, the SDZ boundary (SDZB) is drawn with a 1 cm displacement boundary contour curve in consideration of measurement errors.

In the NDZ, the underground rock mass and the surface are not deformed at all. The monitoring points exhibit small fluctuations due to measurement errors.

The zones and zone boundaries outlined above change dynamically as the underground mining activity deepens.

6 CONCLUSION

Based on the monitoring data, some conclusions can be drawn as follows, the result in this paper can be a refence to the metal mines which have the similar engineering geology condition.

1) The cracks around the collapse pits are essentially parallel to the boundaries of the pits and the cracks far away from the pits are essentially consistent with the strikes of the discontinuities. The closer one is to the mined-out area, the more severe the damage observed in buildings and structures.
2) The horizontal displacement–time curves exhibit five types of behavior. Curves with three inflection points can be divided into four stages: initial deformation stage, creep deformation stage, slow deformation stage, and accelerating deformation stage. Currently, the horizontal to vertical displacement ratio is greater than 1, indicating that the horizontal displacement is playing the dominant role in the surface deformation.
3) The failure mechanism acting in the hanging wall is flexural toppling of rock column and slipping of F4 fault. The large deformation in the hanging wall is due to the combined effect of *in situ* horizontal ground stress, steeply dipping discontinuities and faults, the dip directions and strikes of two parallel orebodies, and the underground mining activity. The deformation in the deep rock strata gradually spreads to the surface which causes the crack and damage on the ground surface and buildings.
4) The surface deformation can be divided into six zones (CZ, FADZ, SADZ, ADZ, SDZ, and NDZ). The caved zone boundary extends 5 m beyond the collapse pit. The boundary of the fast-accelerating deformation zone is determined by the occurrence of major cracks and surface points with horizontal velocities >1 mm/day. The slowly-accelerating deformation zone, acceptable deformation zone, and slight deformation zone boundaries can be defined in a similar way (corresponding to horizontal deformations of 6 mm/m (0.006), 2 mm/m (0.002), and 1 cm displacement, respectively). Moreover, the data indicate that large-scale cracks will emerge when the horizontal velocity of the ground surface exceeds 1 mm/day.

DATA AVAILABILITY STATEMENT

The original contributions presented in the study are included in the article/Supplementary Material, further inquiries can be directed to the corresponding author.

AUTHOR CONTRIBUTIONS

TW: Conceptualization, Methodology, Investigation, Writing—original draft, Writing—review and editing. CC: Supervision, Conceptualization, Resources, Project administration. KX: Conceptualization, Investigation, Methodology, Writing—review and editing. CZ: Investigation, Methodology. YW: Investigation. XL: Investigation.

FUNDING

Financial support for this work was provided by the Young Scholar Fund of National Natural Science Foundation of China (Grant no. 42002292).

ACKNOWLEDGMENTS

We are very grateful for the Foundation's continuous support and also to our colleagues for their valuable help with this research.

REFERENCES

Blachowski, J., and Ellefmo, S. (2012). Numerical Modelling of Rock Mass Deformation in Sublevel Caving Mining System. *Acta Geodyn. Geomater.* 9 (3), 379–388. doi:10.3969/j.issn.1673-193X.2006.05.003

Brady, B. H. G., and Brown, E. T. (2006). *Rock Mechanics for Underground Mining*. Third ed. Berlin: Springer.

Cai, S. J., Chen, Q. Y., and Ming, S. X. (2006). Study on Subsidence Prediction of Underground Mining of Parallel Ore Bodies in Jinshandian Mine by Physical Modeling. *J. Saf. Sci. Technol.* 2 (5), 13–19. (in Chinese). doi:10.3969/j.issn.1673-193X.2006.05.003

Chen, Q. Y. (2006). Research on Strata Movement in Sub-Level Caving for Parallel Ore Bodies in Jinshandian Iron Ore Mine. Ph. D. Thesis. Beijing, China: University of Science and Technology Beijing.

Ding, K., Ma, F., Guo, J., Zhao, H., Lu, R., and Liu, F. (2018). Investigation of the Mechanism of Roof Caving in the Jinchuan Nickel Mine, China. *Rock Mech. Rock Eng.* 51 (4), 1215–1226. doi:10.1007/s00603-017-1374-0

Du, K., Yang, C., Su, R., Tao, M., and Wang, S. (2020a). Failure properties of cubic granite, marble, and sands sandstone specimens under true triaxial stress. *Int. J. Rock. Mech. Min. Sci.* 130, 104309. doi:10.1016/j.ijrmms.2020.104309

Du, K., Li, X., Tao, M., and Wang, S. (2020b). Experimental study on acoustic emission (AE) characteristics and crack classification during rock fracture in several basic lab tests. *Int. J. Rock. Mech. Min. Sci.* 133, 104411. doi:10.1016/j.ijrmms.2020.104411

Eremin, M., Esterhuizen, G., and Smolin, I. (2020). Numerical Simulation of Roof Cavings in Several Kuzbass Mines Using Finite-Difference Continuum Damage Mechanics Approach. *Int. J. Min. Sci. Technol.* 30, 157–166. doi:10.1016/j.ijmst.2020.01.006

Evanek, N., Slaker, B., Iannacchione, A., and Miller, T. (2021). LiDAR Mapping of Ground Damage in a Heading Re-orientation Case Study. *Int. J. Min. Sci. Technol.* 31, 67–74. doi:10.1016/j.ijmst.2020.12.018

Feng, G., Chen, B., Xiao, Y., Jiang, Q., Li, P., Zheng, H., et al. (2022). Microseismic characteristics of rockburst development in deep TBM tunnels with alternating soft-hard strata and application to rockburst warning: A case study of the Neelum-Jhelum hydropower project. *Tunn. Undergr. Sp. Tech.* 122, 104398. doi:10.1016/j.tust.2022.104398

Feng, G., Feng, X., Chen, B., Xiao, Y., and Yu, Y. (2015). A microseismic method for dynamic warning of rockburst development processes in tunnels. Rock Mechanics and Rock Engineering. *Int. J. Min. Sci. Technol.* 48(5), 2061–2076. doi:10.1007/s00603-014-0689-3

Fu, H., Chen, C. X., Xia, K. Z., and Deng, Y. Y. (2015). Analysis of Rock Deformation Caused by Underground Mining of Metal Mines. *Chin. J. Rock Mech. Eng.* 34 (9), 1859–1868. (in Chinese). doi:10.13722/j.cnki.jrme.2014.1303

Hoek, E. (1974). Progressive Caving Induced by Mining an Inclined Orebody. *Trans. Instn Min. Metall.* 83, A133–A139.

Li, Y., Ren, Y., Peng, S. S., Cheng, H., Wang, N., and Luo, J. (2021). Measurement of Overburden Failure Zones in Close-Multiple Coal Seams Mining. *Int. J. Min. Sci. Technol.* 31, 43–50. doi:10.1016/j.ijmst.2020.12.009

Lu, R., Ma, F. S., Guo, J., and Zhao, H. J. (2018). Analysis and Monitoring of Roadway Deformation Mechanisms in Nickel Mine, China. *Concurr. Comput. Pract. Exper* 31 (10), e4832. doi:10.1002/cpe.4832

Lupo, J. F. (1996b). Evaluation of Deformations Resulting from Mass Mining of an Inclined Orebody. Ph. D. Thesis. Golden, CO: Colorado School of Mines.

Lupo, J. F. (1996a). Large-Scale Surface Disturbances Resulting from Underground Mass Mining. *Int. J. Rock Mech. Min. Sci.* 35 (4), 399.

Lupo, J. F. (1997). Progressive Failure of Hanging Wall and Footwall Kiirunavaara Mine, Sweden. *Int. J. Rock Mech. Min. Sci.* 34 (3-4), 684. doi:10.1016/s1365-1609(97)00277-3

Ma, F.-S., Deng, Q.-H., Cunningham, D., Yuan, R.-M., and Zhao, H.-J. (2013). Vertical Shaft Collapse at the Jinchuan Nickel Mine, Gansu Province, China: Analysis of Contributing Factors and Causal Mechanisms. *Environ. Earth Sci.* 69 (1), 21–28. doi:10.1007/s12665-012-1930-6

Ma, F. S., Yuan, R. M., Deng, Q. H., Li, G. Q., Zhao, H. J., Ding, D. M., et al. (2007). GPS Monitoring of Ground Movement and Mechanism of Underground Mining Influence in Jinchuan Mine. *J. Eng. Geol.* 15 (S2), 84–97. (in Chinese).

Ma, F., Zhao, H., Yuan, R., and Guo, J. (2015). Ground Movement Resulting from Underground Backfill Mining in a Nickel Mine (Gansu Province, China). *Nat. Hazards* 77 (3), 1475–1490. doi:10.1007/s11069-014-1513-9

Ma, F., Zhao, H., Zhang, Y., Guo, J., Wei, A., Wu, Z., et al. (2012). GPS Monitoring and Analysis of Ground Movement and Deformation Induced by Transition from Open-Pit to Underground Mining. *J. Rock Mech. Geotechnical Eng.* 4 (1), 82–87. doi:10.3724/sp.j.1235.2012.00082

Pang, H. S., Chen, C. X., Xia, K. Z., and Zhang, C. Q. (2020). Study on the Methodology for Determining the Ground accepTABLE Deformation Limit in Sublevel Caving Mining Based on Monitoring Data. *Chin. J. Rock Mech. Eng.* 39 (4), 736–748. (in Chinese). doi:10.13722/j.cnki.jrme.2019.0966

Parmar, H., Bafghi, Y. A., and Najafi, M. (2019). Impact of Ground Surface Subsidence Due to Underground Mining on Surface Infrastructure: The Case of the Anomaly No. 12 Sechahun, Iran. *Environ. Earth Sci.* 78, 409. doi:10.1007/s12665-019-8424-8

Pinheiro, A. L., Lana, M. S., and Sobreira, F. G. (2015). Use of the Distinct Element Method to Study Flexural Toppling at the Pico Mine, Brazil. *Bull. Eng. Geol. Environ.* 74 (4), 1177–1186. doi:10.1007/s10064-014-0713-6

Ren, W., Guo, C., Peng, Z., and Wang, Y. (2010). Model Experimental Research on Deformation and Subsidence Characteristics of Ground and Wall Rock Due to Mining under Thick Overlying Terrane. *Int. J. Rock Mech. Min. Sci.* 47 (4), 614–624. doi:10.1016/j.ijrmms.2009.12.012

Svartsjaern, M. (2019). A Prognosis Methodology for Underground Infrastructure Damage in Sublevel Cave Mining. *Rock Mech. Rock Eng.* 52, 247–263. doi:10.1007/s00603-018-1464-7

Svartsjaern, M., and Saiang, D. (2017). Discrete Element Modelling of Footwall Rock Mass Damage Induced by Sub-Level Caving at the Kiirunavaara Mine. *Minerals* 7, 109. doi:10.3390/min7070109

Svartsjaern, M., Saiang, D., Nordlund, E., and Eitzenberger, A. (2016). Conceptual Numerical Modeling of Large-Scale Footwall Behavior at the Kiirunavaara Mine, and Implications for Deformation Monitoring. *Rock Mech. Rock Eng.* 49, 943–960. doi:10.1007/s00603-015-0750-x

The Coal Industry Bureau of the People's Republic of China (2017). *Regulations of Buildings, Water, Railway and Coal Pillar Set for Roadway and Coal Mining*. Beijing: Coal Industry Press. (in Chinese).

Villegas, T., and Nordlund, E. (2008a). "Numerical Analysis of the Hangingwall Failure at the Kiirunavaara Mine," in Proceedings of MassMin 2008, The 5th International Conference and Exhibition on Mass Mining, 9-11 June 2008. (Lulea, Sweden: Lulea University of Technology), 867–876.

Villegas, T., and Nordlund, E. (2008b). "Numerical Simulation of the Hangingwall Subsidence Using PFC2D," in Proceedings of MassMin 2008, The 5th International Conference and Exhibition on Mass Mining, 9-11 June 2008. (Lulea, Sweden: Lulea University of Technology), 907–916.

Villegas, T., and Nordlund, E. (2012). Time-Dependent Movements of the Hangingwall at the Kiirunavaara Mine. *Int. J. Min. Reclam. Environ.* 26 (2), 119–133. doi:10.1080/17480930.2011.552287

Vyazmensky, A. (2008). Numerical Modelling of Surface Subsidence Associated with Block Cave Mining Using a Finite Element/Discrete Element Approach. PhD thesis. Vancouver, Canada: Simon Fraser University.

Wang, F., Jiang, B., Chen, S., and Ren, M. (2019). Surface Collapse Control under Thick Unconsolidated Layers by Backfilling Strip Mining in Coal Mines. *Int. J. Rock Mech. Min. Sci.* 113, 268–277. doi:10.1016/j.ijrmms.2018.11.006

Wang, X., Kulatilake, P. H. S. W., and Song, W.-D. (2012). Stability Investigations Around a Mine Tunnel through Three-Dimensional Discontinuum and Continuum Stress Analyses. *Tunn. Undergr. Sp. Tech.* 32, 98–112. doi:10.1016/j.tust.2012.06.003

Wu, X., Jiang, X.-W., Chen, Y.-F., Tian, H., and Xu, N.-X. (2009). The Influences of Mining Subsidence on the Ecological Environment and Public Infrastructure: a Case Study at the Haolaigou Iron Ore Mine in Baotou, China. *Environ. Earth Sci.* 59 (4), 803–810. doi:10.1007/s12665-009-0076-7

Xia, K., Chen, C., Deng, Y., Xiao, G., Zheng, Y., Liu, X., et al. (2018). *In Situ* monitoring and Analysis of the Mining-Induced Deep Ground Movement in a Metal Mine. *Int. J. Rock Mech. Min. Sci.* 109, 32–51. doi:10.1016/j.ijrmms.2018.06.014

Xia, K., Chen, C., Fu, H., Pan, Y., and Deng, Y. (2016b). Mining-induced Ground Deformation in Tectonic Stress Metal Mines: A Case Study. *Eng. Geol.* 210, 212–230. doi:10.1016/j.enggeo.2016.06.018

Xia, K., Chen, C., Liu, X., Fu, H., Pan, Y., and Deng, Y. (2016a). Mining-Induced Ground Movement in Tectonic Stress Metal Mines: A Case Study. *Bull. Eng. Geol. Environ.* 75 (3), 1089–1115. doi:10.1007/s10064-016-0886-2

Xia, K., Chen, C., Lu, Z., Yang, K., Zheng, Y., Pang, H., et al. (2019a). Investigation of the Ground Movement Due to Underground Mining at the Jinshandian Iron Mine in China. *Environ. Earth Sci.* 78, 715. doi:10.1007/s12665-019-8753-7

Xia, K., Chen, C., Yang, K., Zhang, H., and Pang, H. (2020). A Case Study on the Characteristics of Footwall Ground Deformation and Movement and Their Mechanisms. *Nat. Hazards* 104, 1039–1077. doi:10.1007/s11069-020-04204-4

Xia, K., Chen, C., Zheng, Y., Zhang, H., Liu, X., Deng, Y., et al. (2019b). Engineering Geology and Ground Collapse Mechanism in the Chengchao Iron-Ore Mine in China. *Eng. Geol.* 249, 129–147. doi:10.1016/j.enggeo.2018.12.028

Xia, Y., Wang, Y., Du, S., Liu, X., and Zhou, H. (2018). Integration of D-InSAR and GIS Technology for Identifying Illegal Underground Mining in Yangquan District, Shanxi Province, China. *Environ. Earth Sci.* 77 (8), 319. doi:10.1007/s12665-018-7488-1

Yang, K. Y. (2019). Study on Ground Pressure Activity Law of a Metal Mine Adopted Non-pillar Sublevel Caving Method. Ph. D. Thesis. Wuhan: Institute of Rock and Soil Mechanics, Chinese Academy of Sciences.

Zhao, H., Ma, F., Zhang, Y., and Guo, J. (2013). Monitoring and Analysis of the Mining-Induced Ground Movement in the Longshou Mine, China. *Rock Mech. Rock Eng.* 46 (1), 207–211. doi:10.1007/s00603-012-0232-3

Conflict of Interest: The authors declare that the research was conducted in the absence of any commercial or financial relationships that could be construed as a potential conflict of interest.

Publisher's Note: All claims expressed in this article are solely those of the authors and do not necessarily represent those of their affiliated organizations, or those of the publisher, the editors and the reviewers. Any product that may be evaluated in this article, or claim that may be made by its manufacturer, is not guaranteed or endorsed by the publisher.

Copyright © 2022 Wang, Chen, Xia, Zhang, Wang and Liu. This is an open-access article distributed under the terms of the Creative Commons Attribution License (CC BY). The use, distribution or reproduction in other forums is permitted, provided the original author(s) and the copyright owner(s) are credited and that the original publication in this journal is cited, in accordance with accepted academic practice. No use, distribution or reproduction is permitted which does not comply with these terms.

frontiers | Frontiers in Earth Science

ORIGINAL RESEARCH
published: 26 May 2022
doi: 10.3389/feart.2022.886134

Energy Evolution Characteristics of Rock Under Different Confining Conditions

Bi-Wen Zhang[1], *Kai Fang*[1,2]*, *Chen Wang*[1], *Tong-Bin Zhao*[1,2] *and Xiu-Feng Zhang*[3]

[1]College of Energy and Mining Engineering, Shandong University of Science and Technology, Qingdao, China, [2]Mine Disaster Prevention and Control-Ministry of State Key Laboratory Breeding Base, Shandong University of Science and Technology, Qingdao, China, [3]Research Center for Rock Burst Control, Shandong Energy Group Co., Ltd., Jinan, China

Constant stiffness confining condition seems more reasonable than constant stress confining condition to simulate the actual confining stress environment of *in situ* rock which varies with the lateral strain. Compression tests of sandstone samples with two different confining conditions were conducted to study the energy evolution characteristics of rock under constant stress confining condition and constant stiffness confining condition. Except for the conventional triaxial compression tests, CFRP-confined rock samples were also used to simulate the constant stiffness confinement of the rock specimen in the laboratory. The stress–strain curve and failure mode of the samples under different confining conditions were compared. The influence of confining condition on the characteristics of rock energy evolution was investigated. The results show that the stress–strain curves under the confining conditions of constant stress and constant stiffness exhibited strain softening and strain hardening, respectively. Under constant stress confining condition, the specimen failed in the ductile mode while the specimen exhibited a sudden and brittle failure behavior under constant stiffness confining condition. The evolution trend of the elastic strain energy was greatly affected by the magnitude of confining stiffness. The elastic strain energy of the specimen under low stiffness confining condition decreased slightly after reaching its peak. As the confining stiffness increased, the elastic strain energy would not decrease but continued to increase until the failure of the specimen. The maximum elastic strain energy under the confining condition of the high confining stiffness is greater than that of constant stress. Considering the influence of confining stiffness on the storage and release of the strain energy, to obtain the true mechanical behavior of the rock mass under confining conditions, stiffness confining conditions should be taken into consideration in the laboratory.

Keywords: constant confining stress, constant confining stiffness, energy evolution, elastic strain energy, fracture mode

OPEN ACCESS

Edited by:
Guang-Liang Feng,
Institute of Rock and Soil Mechanics (CAS), China

Reviewed by:
Dongdong Xu,
Changjiang River Scientific Research Institute (CRSRI), China
Zhiyong Fu,
Liaoning Technical University, China

***Correspondence:**
Kai Fang
fk861018@163.com

Specialty section:
This article was submitted to Geohazards and Georisks, a section of the journal Frontiers in Earth Science

Received: *28 February 2022*
Accepted: *06 April 2022*
Published: *26 May 2022*

Citation:
Zhang B-W, Fang K, Wang C, Zhao T-B and Zhang X-F (2022) Energy Evolution Characteristics of Rock Under Different Confining Conditions. Front. Earth Sci. 10:886134. doi: 10.3389/feart.2022.886134

INTRODUCTION

In deep underground rock mass engineering, engineering activities can induce severe rock failure of the surrounding rock masses due to the release of strain energy stored in the rocks (Ma et al., 2020; Yu et al., 2022). The mechanical behavior of the rock mass is an important factor affecting the failure mechanism. Due to high confining stress *in situ*, the mechanical characteristics of deep rock are

significantly different from those of shallow rock (Xie H. P. et al., 2021). The mechanical behavior of rock under confining conditions is a critical topic concerned in engineering. In previous studies, scholars investigated rock under different lateral pressures to simulate the confining environment *in situ* (Li et al., 1999; Chen and Feng, 2006; Zhang and Zhao, 2014). Triaxial loading tests are the most common laboratory method and the mechanical behavior of rock under constant confining stress has been widely investigated by means of laboratory tests and numerical modeling (Fang et al., 2019; Liu et al., 2020; Xie H. et al., 2021). However, for the *in situ* rock, its constraints come from the surrounding rock mass, and the confining stresses are not fixed during the deformation and failure process. When the rock deforms outward, it will squeeze the surrounding rock mass, and the confining stress will increase accordingly. It means that the confining stress is dependent on the lateral strain of the rock. The confining condition can be regarded as a constant confining stiffness condition. For the laboratory test, a constant stiffness confining condition seems more reasonable than constant stress confining condition to simulate the actual confining environment.

The mechanical behavior of the rock is driven by the evolution and release of energy (Xie et al., 2009; Bagde and Petroš, 2009; Feng et al., 2022). Energy evolution can better describe the deformation and failure mechanisms of the rock (Wang and Cui, 2018; Jia et al., 2019; Zhang et al., 2021). Some researchers have carried out studies to analyze the energy evolution characteristics of the rock under various confining pressures (Peng et al., 2014; Zhang and Gao, 2015; Meng et al., 2022). Li et al. (2017) studied the characteristics of energy evolution and dissipation during hard rock during triaxial failure with different loading and unloading paths. Huang and Li (2014) studied the conversion characteristics of strain energy with conventional triaxial unloading tests at different unloading rates and initial confining pressures. The results show that the confining pressure has a significant influence on the energy evolution of rock. Increases in the confining pressures can improve cumulative strain energy density and effectively limit the energy dissipation and release due to fracture or failure of the rock. However, most of the research to date has focused on the mechanical behavior and energy evolution of rock under constant confining stress. Few studies have been conducted to explore the mechanism of the energy evolution of rock under constant confining stiffness. Tests on the concrete showed that axial stress–strain curves under constant confining stiffness were obviously different from those under constant confining stress (Dong et al., 2015). The stiffness of the loading system has also been proven to have an important impact on the energy release of the rock (Feng et al., 2014; Wang and Kaunda, 2019). Therefore, the influence of confining stiffness on the evolution and release of the rock strain energy is a critical issue that should be further clarified.

In this study, compression tests of sandstone samples with different confining conditions were conducted to study the energy evolution characteristics of rock under constant confining stiffness and constant confining stress. Except for the conventional triaxial compression tests, CFRP-confined rock samples were also used to simulate the constant confining stiffness of the rock in the laboratory. The stress–strain curve and failure mode of the samples under different confining conditions were compared. The influence of confining condition on the characteristics of rock energy evolution was investigated.

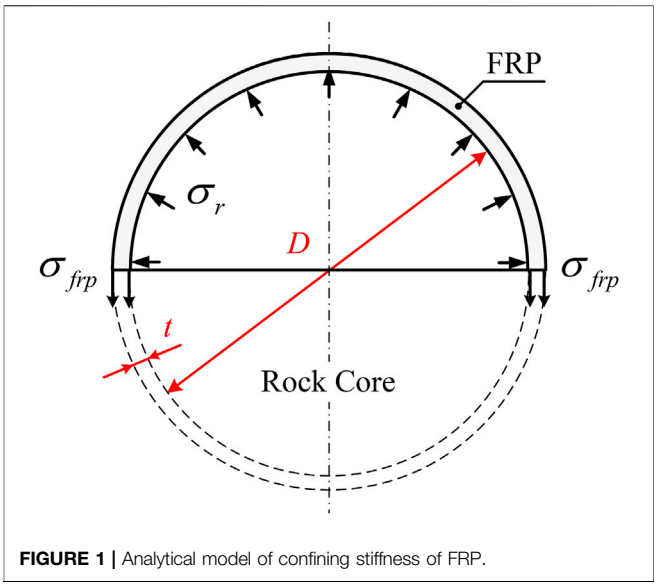


FIGURE 1 | Analytical model of confining stiffness of FRP.

STIFFNESS CONFINING CONDITION

In order to simulate the confining conditions with different constant stiffness, fiber-reinforced polymer (FRP) was used as the confining material to form the FRP jackets in the hoop direction of the specimen. FRP materials have high tensile strength and deformation modulus, and it has been widely used as confining materials for concrete structures to improve the performance of the concrete building (Lam and Teng, 2004; Jiang and Teng., 2007). Due to their ultra-high ductility and strength, FRP materials could provide a substantially constant confining stiffness for the test rock core (Dong et al., 2015). Different confining stiffness of rock samples can be achieved by overlapping FRP materials with different layers.

The following analytical model can be used to quantify the confining stiffness provided by FRP when the fibers of the FRP are wrapped in the hoop direction. As shown in **Figure 1**, considering the equilibrium condition in the in-plane direction of the rock core section, the confining stress in the rock core can be calculated as follows:

$$\sigma_r = \frac{2\sigma_{frp}t}{D}, \tag{1}$$

where σ_{frp} is the hoop stress in FRP; t is the thickness of FRP; and D is the diameter of the rock core.

Assuming that the FRP is linearly elastic until rupture, its stress–strain relation can be written as follows:

TABLE 1 | Calculated confining stiffness for different thicknesses of confining jacket.

Fiber type	Thickness t (mm)	E_{frp} (GPa)	k_{frp} (MPa)	ρ_s
CFRP	0.111	241	1070	0.18
CFRP	0.222	241	2140	0.37
CFRP	0.333	241	3210	0.55
CFRP	0.444	241	4280	0.74
CFRP	0.555	241	5350	0.92
CFRP	0.666	241	6420	1.10

$$\sigma_{frp} = \varepsilon_{frp} E_{frp}, \tag{2}$$

where ε_{frp} is the hoop strain in FRP and E_{frp} is the Young's modulus of FRP.

Considering the compatibility condition in the in-plane direction of the rock core section, the strain of the FRP is equal to the circumference strain of the rock core,

$$\varepsilon_r = \varepsilon_{frp}. \tag{3}$$

Substituting **Eq. 2** and **Eq. 3** into **Eq. 1**, an expression between the confining stress and the confining strain can be obtained as follows:

$$\sigma_r = \frac{2tE_{frp}}{D}\varepsilon_r. \tag{4}$$

The structural confining stiffness of the FRP jacket can be calculated as the ratio of confining stress to the confining strain. It can be evaluated as in the following equation:

$$k_{frp} = \frac{2tE_{frp}}{D}. \tag{5}$$

Based on **Eq.5**, the specific confining stiffness corresponding to different layers of the FRP jacket can be calculated. For the convenience of the following discussion, confining stiffness can be normalized by the elastic modulus of the rock core sample. A new parameter, confining stiffness ratio, can be introduced as in the following equations:

$$\rho_s = \frac{2E_{frp}t}{E_c D}, \tag{6}$$

where E_c is the Young's modulus of the rock sample.

It can be found that confining stiffness is directly proportional to the thickness of the FRP material. Different confining stiffness can be achieved conveniently by different layers of fiber jackets. Several types of FRP have been used in practice. In the present experimental work, 200 g class I carbon-fiber-reinforced polymer (CFRP) was selected as the confining material. It has the advantages of high tensile strength, lightweight, and small-fiber diameter. The carbon fiber sheets had a nominal thickness of 0.111 mm. Its elastic modulus is 241 GPa, and its tensile strength along the fiber direction is greater than 1600 MPa. The calculated confining stiffness for different thicknesses of confining jackets is listed in **Table 1**.

Considering that the rock *in situ* is confined by the surrounding rock mass, one layer of CFRP jacket can be regarded as a rock sleeve with a certain thickness. Assuming that the rock core was confined by the rock sleeve with a certain thickness, an equivalent thickness of the surrounding rock sleeve can be obtained based on the equal confining stiffness. The surrounding confining rock sleeve can be regarded as a thick-walled hollow cylinder. The elastic solution of the thick-walled hollow cylinder under uniform internal radial pressure can be used to obtain the relationship between the radial stress and the radial strain. According to the definition, the confining stiffness of the rock sleeve can be determined by the ratio of radial stress and radial strain as shown in **Eq. 8**. By equating the confining stiffness of **Eqs 5** and **8**, the equivalent thickness of the rock sleeve can be obtained. The calculated equivalent thickness of the rock sleeve for different numbers of CFRP layers is shown in **Figure 2**. It can be found that one layer of CFRP jacket is equivalent to a 5 mm rock sleeve in confining stiffness. When the thickness of the surrounding rock sleeve approaches infinity, the equivalent number of CFRP layers is 4.3. It means that 4.3 layers of CFRP jacket can be used to simulate the confining stiffness of surrounding rock *in situ*.

$$\begin{cases} \sigma_r = \dfrac{a^2 p}{b^2 - a^2}\left(1 - \dfrac{b^2}{r^2}\right) \\ \sigma_\theta = \dfrac{a^2 p}{b^2 - a^2}\left(1 + \dfrac{b^2}{r^2}\right) \\ \varepsilon_r = \dfrac{1 - \nu^2}{E}\left(\sigma_r - \dfrac{\nu}{1 - \nu}\sigma_\theta\right) \end{cases}, \tag{7}$$

$$k_c = \frac{E}{1 + \nu}\frac{b^2 - a^2}{(b^2 - (1 - 2\nu)a^2)}, \tag{8}$$

where a is the radius of the rock core, and b is the radius of the confining rock sleeve.

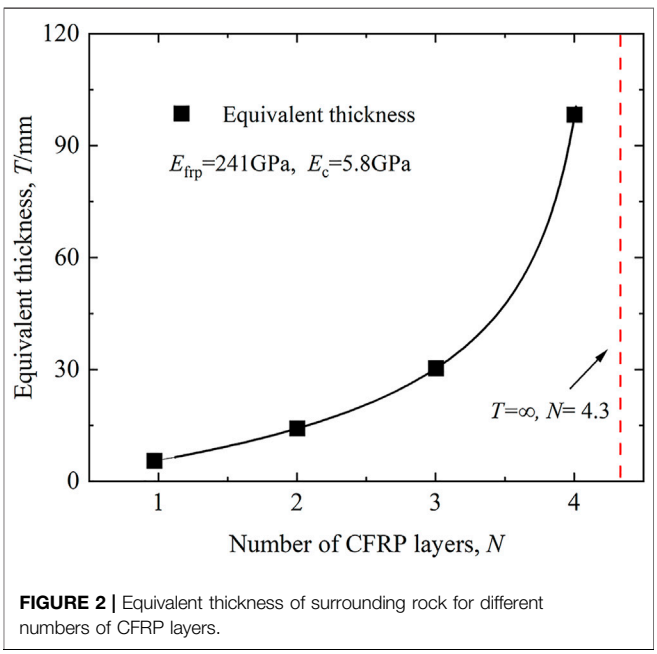


FIGURE 2 | Equivalent thickness of surrounding rock for different numbers of CFRP layers.

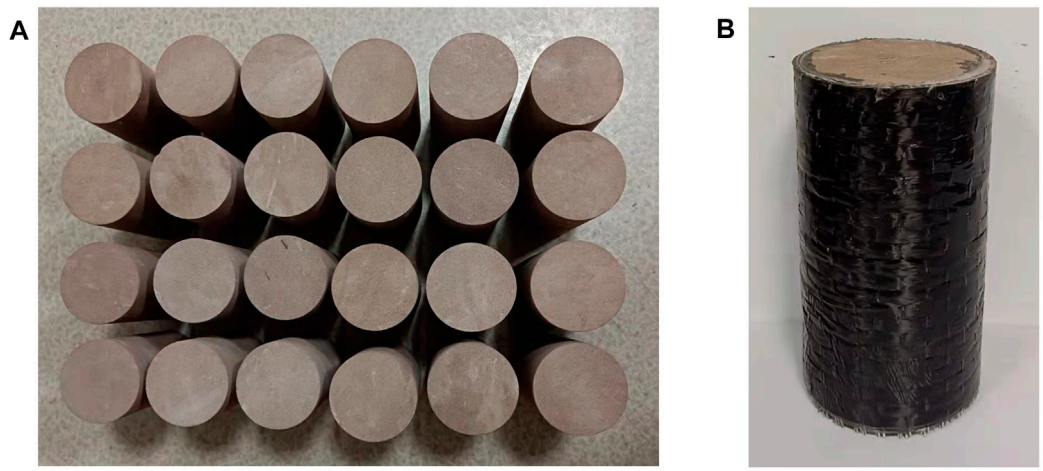


FIGURE 3 | Specimens for tests. **(A)** Cylindrical samples; **(B)** CFRP-confined rock specimens.

TABLE 2 | Two groups of specimens with different confining conditions.

Confining condition	σ_3 (MPa)	Specimen number	Confining condition	ρ_s	Specimen number
Constant confining pressure	0	S0-1,2,3	Constant confining stiffness	0.18	k1-1,2
	8	S8-1,2,3		0.37	k2-1,2
	16	S16-1,2,3		0.55	k3-1,2
	24	S24-1,2,3		0.74	k4-1,2
	32	S32-1,2,3		0.92	k5-1,2
				1.10	k6-1,2

SPECIMEN PREPARATION AND TESTING

A total of 27 specimens were prepared from a sandstone block in Jining of Shandong, China. Cylindrical specimens were drilled and prepared with a diameter of 50 mm and a height of 100 mm as shown in **Figure 3**. The specimens were divided into two groups to be tested under different confining conditions as listed in **Table 2**. The preparation of the CFRP-confined specimens followed a standard procedure, which has been described elsewhere (Jiang and Teng, 2007; Micelli and Modarelli, 2013).

The tests were carried out on the RLJW-2000 rock mechanics testing apparatus. The tests under constant confining stress and constant confining stiffness were conducted following the standard procedure of triaxial tests and uniaxial tests, respectively. The axial pressure was applied in a displacement-controlled way, and the loading rate was 0.005 mm/s. Both the axial and circumferential strains were recorded by the LVDT during the tests.

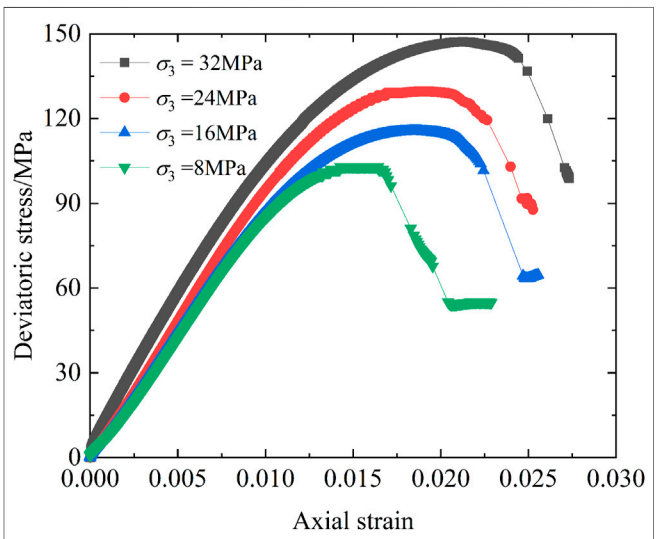


FIGURE 4 | Deviatoric stress axial strain curves under different confining pressures. Stress–strain relationship under constant confining stiffness tests.

TEST RESULTS

Stress-Strain Relationship Under Different Confining Conditions

The typical deviatoric stress–axial-strain curves of sandstone samples under different confining pressures are shown in **Figure 4**. It can be seen that both the peak deviatoric stress and corresponding peak strain increase as the confining pressure increases. When the confining pressure increases from 8 to 32 MPa, the peak deviatoric stress and peak strain increase by 43.15% and 36.75%, respectively.

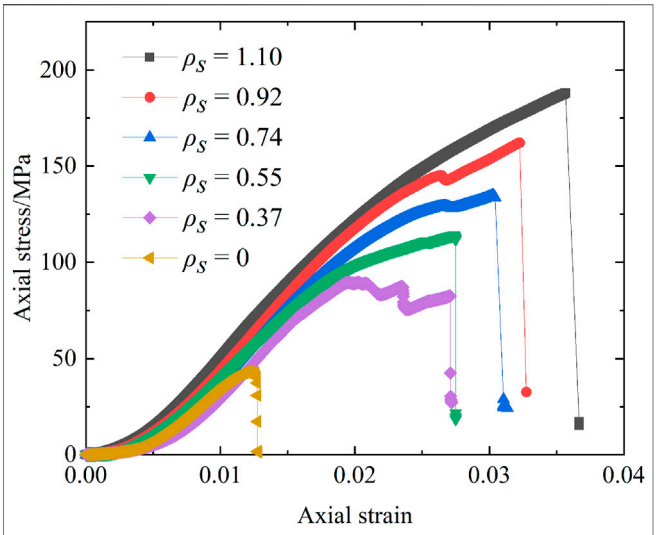


FIGURE 5 | Axial-stress–axial-strain curves under different confining stiffness ratios.

The typical axial stress–strain curves under different confining stiffness ratios are shown in **Figure 5**. It can be found that the curve shape under constant confining stiffness is not the same as that under constant confining stress. The stress–strain curve under constant confining stress exhibits strain softening. But the stress–strain curve under constant confining stiffness may not have a descending portion. For low confining stiffness, the stress–strain curve would first exhibit strain softening and then exhibit strain hardening. For high confining stiffness, the stress–strain curve would exhibit strain hardening only. The axial stress ascends to a certain turning point and then continues to ascend at a slower rate.

Furthermore, it can be seen from **Figure 5** that with the increase in confining stiffness ratio, the ultimate axial stress and ultimate axial strain increase. When the confining stiffness ratio increases from 0.37 to 1.10, the ultimate stress and strain increase by 127% and 33%, respectively.

Failure Mode Under Different Confining Conditions

The typical failure modes of the specimens under different confining conditions are shown in **Figure 6**. Different failure modes are exhibited for the specimen under constant confining stress and constant confining stiffness. As shown in **Figure 6A**, for the tests under constant confining stress (triaxial test), the failure mode of rock samples is basically the same even with

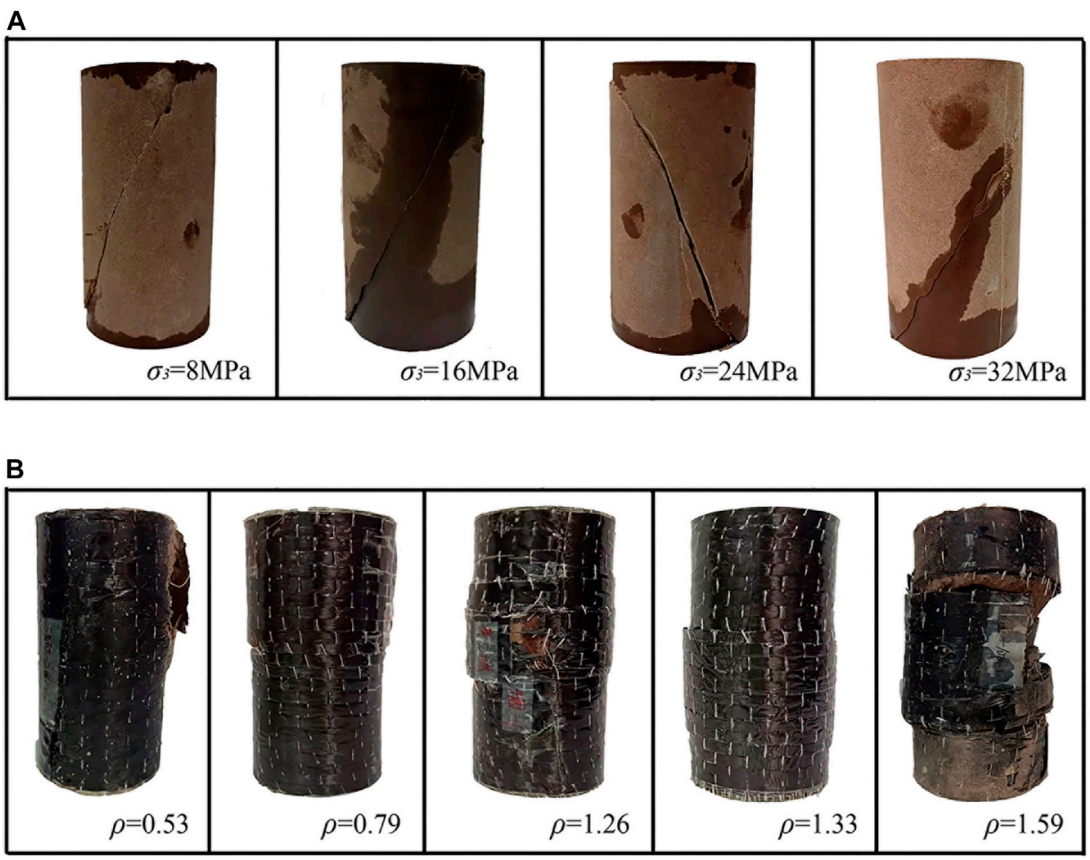


FIGURE 6 | Failure mode of the specimen under different confining conditions. **(A)** constant confining stress; **(B)** constant confining stiffness.

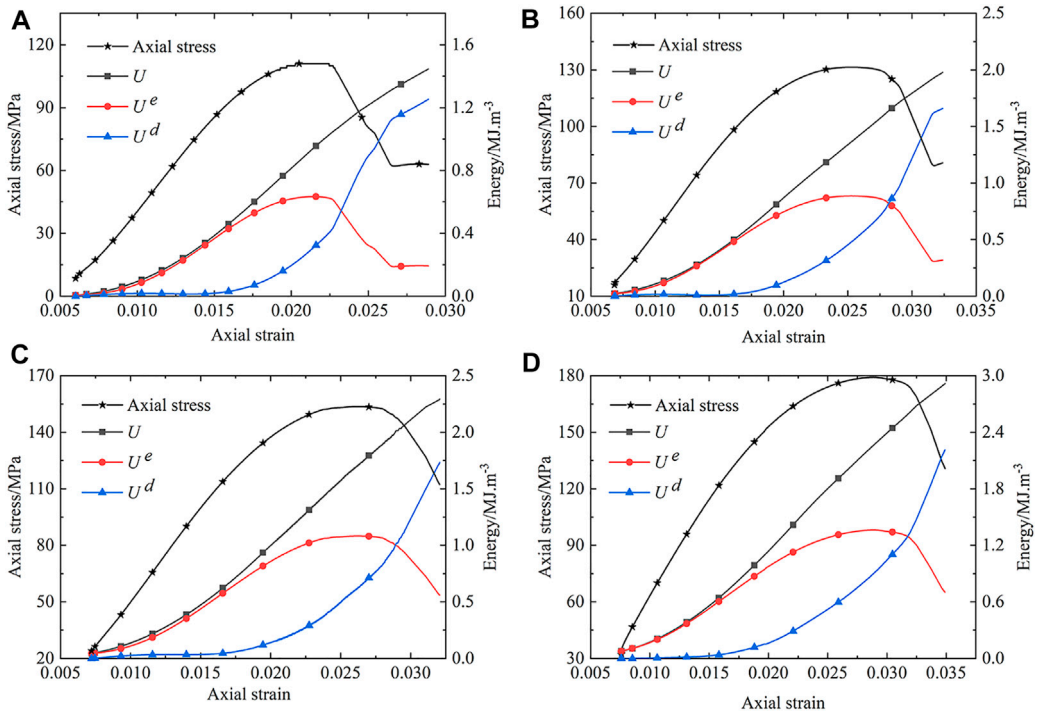


FIGURE 7 | Energy evolution curve of the specimen under different confining pressures. **(A)** Confining pressure = 8 MPa; **(B)** confining pressure = 16 MPa; **(C)** confining pressure = 24 MPa; **(D)** confining pressure = 32 MPa.

different confining pressures. The macroscopic shear fracture surface can be seen when the failure of the rock specimen occurs. However, for the specimen under constant confining stiffness, the failure mode appears more complex. Failure of CFRP-confined specimens occurred in a sudden and explosive way due to fiber rupture that reached their ultimate tensile strain. The rock specimens expanded outward and were severely damaged. For the specimen under low confining stiffness, the CFRP jacket broke in the upper section of the specimen accompanied by spalling of the broken rock. For the specimen under high confining stiffness, a cone-shape failure surface is generated in the mid-height region of the specimen. Both the stress–strain curve and the failure mode of the samples show a significant differentiation between the two confining conditions.

EVOLUTION OF STRAIN ENERGY

Calculation of Strain Energy

During the process of loading, the test machine does work on the specimen. Part of the energy is transformed from the mechanical energy of the test machine into the deformation energy of the rock, which is stored in the rock mass. And the other part is dissipated due to the plastic deformation and crack propagation in the specimen. Assuming that there was no heat exchange between the specimen and the environment during the loading, the total input energy generated by external force work can be written as follows:

$$U = U^e + U^d, \tag{9}$$

where U is the total strain energy, U^e is the elastic strain energy stored in the specimen, and U^d is the dissipated strain energy.

Under triaxial loading conditions, the total strain energy U and elastic strain energy U^e can be calculated as follows:

$$U = \int_0^{\varepsilon_1} \sigma_1 d\varepsilon_1 + \int_0^{\varepsilon_2} \sigma_2 d\varepsilon_2 + \int_0^{\varepsilon_3} \sigma_3 d\varepsilon_3, \tag{10}$$

$$U^e = \frac{1}{2}\sigma_1\varepsilon_{e1} + \frac{1}{2}\sigma_2\varepsilon_{e2} + \frac{1}{2}\sigma_3\varepsilon_{e3}. \tag{11}$$

The total energy absorbed by the rock sample can be obtained by the integral of the stress–strain curve. Considering that medium principal stress is equal to small principal stress for this test, then **Eq. 10** and **Eq. 11** can be written as follows:

$$\begin{cases} U = \sum_{i=1}^{n} \frac{1}{2}(\sigma_{1i} + \sigma_{1i-1})(\varepsilon_{1i} - \varepsilon_{1i-1}) + \sum_{i=1}^{n}(\sigma_{2i} + \sigma_{2i-1})(\varepsilon_{2i} - \varepsilon_{2i-1}) \\ U^e = \frac{1}{2}\sigma_1\varepsilon_{e1} + \sigma_3\varepsilon_{e3} \\ U^d = U - U^e. \end{cases} \tag{12}$$

The elastic strain can be obtained by the unloading elastic modulus and Poisson's ratio.

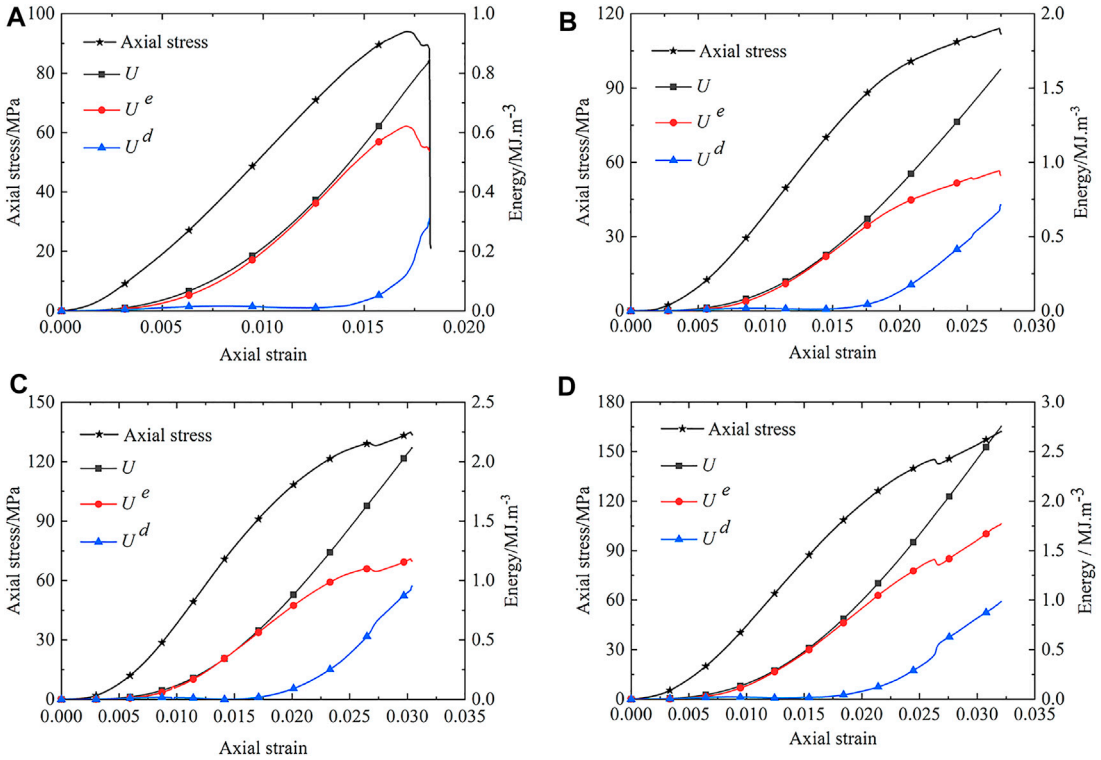


FIGURE 8 | Energy evolution curve of the specimen under different confining stiffness. **(A)** ρ_s = 0.37; **(B)** ρ_s = 0.55; **(C)** ρ_s = 0.74; **(D)** ρ_s = 0.92.

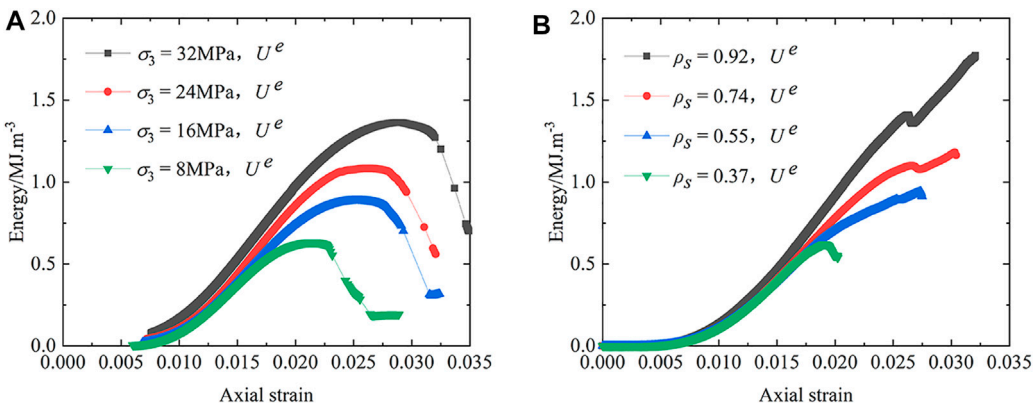


FIGURE 9 | Energy evolution curve of elastic energy under different confining conditions. **(A)** Constant confining stress; **(B)** constant confining stiffness.

$$\varepsilon_{ei} = \frac{1}{E_u}\left[\sigma_i - \nu_u\left(\sigma_j + \sigma_k\right)\right]. \tag{13}$$

Existing studies have shown that the unloading elastic modulus and Poisson's ratio were close to the initial value of uncracked rock (Yu et al., 2005; David et al., 2012). So the initial elastic modulus and Poisson's ratio were used for the calculation. For constant confining stiffness conditions, the confining pressure of the specimen can be calculated by **Eq. 4** based on the measured strain of FPR.

Evolution of Strain Energy Under Constant Confining Stress

Based on the above calculation method, the energy evolution curves of rock specimens under different confining pressures are given in **Figure 7**. It can be seen that the evolution curves of the specimen under different confining pressures exhibit great similarity. The total strain energy absorbed by the rock sample and the dissipated strain energy show a nonlinear increasing trend. The elastic strain energy presented a trend of first

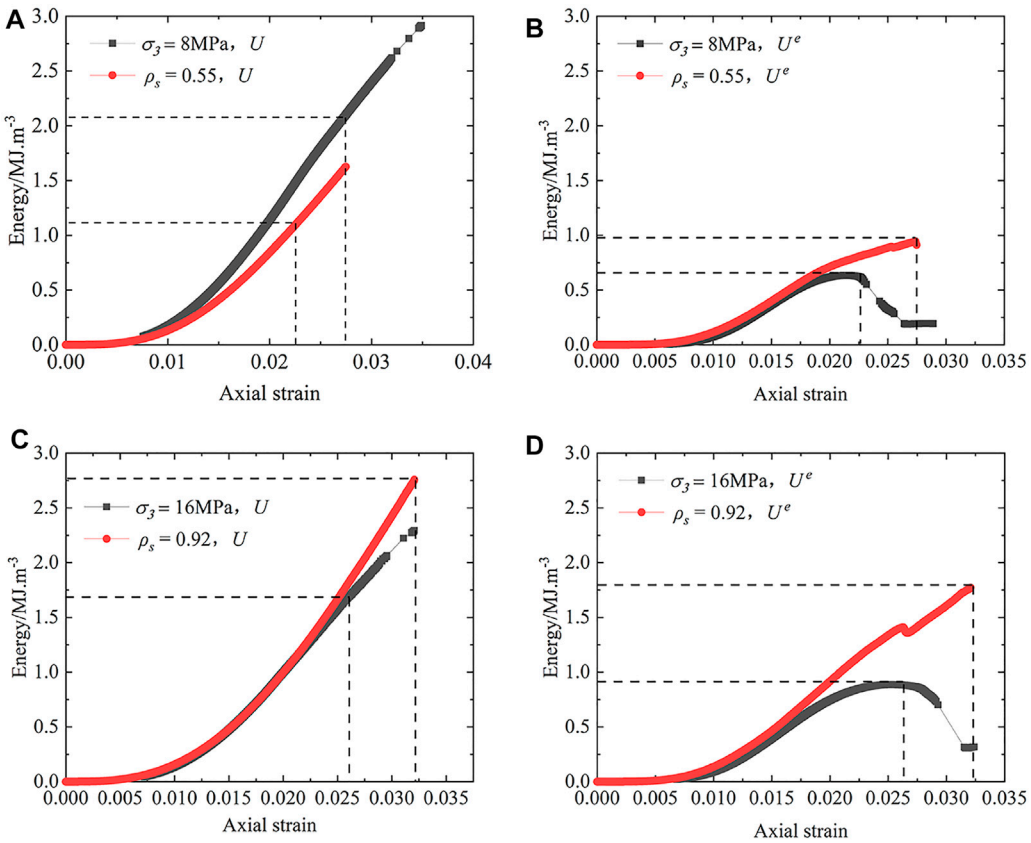


FIGURE 10 | Comparison of energy evolution curve between the two conditions under the same confining stress standard. **(A)** Total absorbed energy (8 MPa); **(B)** elastic energy (8 MPa); **(C)** total absorbed energy (16 MPa); **(D)** elastic energy (16 MPa).

increasing and then decreasing. The evolution process can be divided into several stages. In the initial stage, the total absorbed strain energy was mainly converted into elastic strain energy, and the dissipated strain energy was very low. With the crack initiation and plastic deformation, the dissipated strain energy begins to increase when the axial strain reaches about 0.015. Before the peak point, the dissipated strain energy is much smaller than the elastic strain energy. The elastic strain energy reaches its peak at the peak strength of the specimen and is then released quickly. In the post-peak stage, the dissipated strain energy increases rapidly until the failure of the specimen.

It can also be found that U, U^e, and U^d corresponding to the peak point are all increased with the increase in confining pressure. When the confining pressure is increased from 8 to 32 MPa, the total strain energy absorbed by the rock sample at failure increases by 102.7%. The elastic strain energy corresponding to the peak point increased by 104%. It means that the stored energy of the confined specimen before failure increases appreciably with the increase in confining pressure.

Evolution of Strain Energy Under Constant Confining Stiffness

The energy evolution curves of rock specimens under different confining stiffness ratios are given in **Figure 8**. It can be seen that different energy evolution characteristics are exhibited for the specimen under constant confining stiffness. The total strain energy U and the dissipated strain energy U^d show a nonlinear increasing trend, which is similar to the condition of constant confining stress. However, the evolution trend of the elastic strain energy is greatly affected by the magnitude of confining stiffness. When the confining stiffness is small, the elastic strain energy decreases gradually after reaching its peak. But the magnitude of the decrease is less than the condition of constant confining stress. As the confining stiffness increases, the elastic strain energy will not decrease but continue to increase until the failure of the specimen.

It can also be noted that U, U^e, and U^d are all increased with the increase in confining stiffness. When the confining stiffness ratio is increased from 0.37 to 0.92, the total strain energy absorbed by the rock sample and the elastic strain energy corresponding to the peak point increase by 104% and 127%, respectively.

COMPARISON UNDER DIFFERENT CONFINING CONDITIONS

It is well-known that the failure mode of the rock is to a large extent dependent on the release of the stored elastic strain energy. In order to analyze the difference between the two

conditions, the evolution curve of elastic strain energy under different confining conditions is compared in **Figure 9**. For the constant confining stress, there is a declining stage of elastic strain energy after reaching its peak. In this stage, the volume of the specimen expands gradually with the initiation, propagation, and coalescence of new cracks. The elastic strain energy decreases gradually with an axial strain increase. The failure process of the specimen exhibits ductile failure behavior. For the constant confining stiffness, the elastic strain energy continues to increase with the increase of axial strain until the sudden rupture of the CFRP jacket. At this stage, the confining stress increases with the increase of dilatational strain of the specimen because of the constant confining stiffness. And then the increased confining stress further limits the internal crack propagation of the specimen. A proportion of the absorbed energy is converted to the elastic energy of the CFRP jacket. When the strain of CFRP reaches the ultimate tensile strain, failure occurs in a sudden and explosive way, and the failure process of the specimen exhibits brittle failure behavior.

In order to compare the energy evolution characteristics between the two conditions under the same confining pressure standard, according to the measured hoop strain, the confining stress provided by the CFRP jacket can be calculated by using **Eq. 3** and **Eq. 4**. Considering that the confining stress of the CFRP jacket changes continually in the loading process, the maximum confining stress corresponding to the ultimate strain of the CFRP jacket before failure was selected to compare with the constant stress condition. Based on the measured ultimate strain of the CFRP jacket, the ultimate confining stresses are about 8 and 16 MPa for the specimen, with a confining stiffness ratio of 0.79 and 1.33, respectively. **Figure 10** shows the comparison of the total absorbed and elastic energy evolution curve between the two confining conditions. It can be found that the total absorbed energy of the specimen under the confining condition of constant stress is greater than that of constant stiffness when the confining stiffness is low. But for the high confining stiffness, an opposite conclusion can be observed. It indicated that confining stiffness conditions should be simulated reasonably in the laboratory to obtain the actual mechanical behavior of the rock *in situ*. In addition, it can be noted that the maximum elastic strain energy under the condition of constant stiffness is greater than that of constant stress by a factor of 1.4–2, corresponding to confining stress from 8 to 16 MPa. The confining stiffness of the rock has a significant effect on the storage and release of the energy. It is difficult to obtain the true mechanical behavior when only taking into consideration the confining stress conditions.

CONCLUSION

The stress–strain curve and failure mode of the samples are significantly influenced by the confining conditions. The stress–strain curves under the confining conditions of constant stress and constant stiffness exhibit strain softening and strain hardening, respectively. Under constant stress confining conditions, the specimen failed in the ductile mode with the generation of the macroscopic shear fracture surface. Under constant stiffness confining conditions, the specimen failed in a sudden and violent way, and the failure process exhibits brittle failure behavior.

The total absorbed strain energy, the dissipated strain energy, and elastic energy are all increased with the increase in confining stiffness. The evolution trend of the elastic strain energy is greatly affected by the magnitude of confining stiffness. When the confining stiffness is small, the elastic strain energy decreases slightly after reaching its peak. As the confining stiffness increases, the elastic strain energy will not decrease but continue to increase until the failure of the specimen.

Taking the ultimate confining stresses as a standard, the total absorbed energy of the specimen under the confining condition of constant stress is greater than that of constant stiffness when the confining stiffness is low. But for the high confining stiffness, an opposite conclusion can be observed. The maximum elastic strain energy under the condition of constant stiffness is greater than that of constant stress.

DATA AVAILABILITY STATEMENT

The raw data supporting the conclusions of this article will be made available by the authors, without undue reservation.

AUTHOR CONTRIBUTIONS

B-WZ and KF designed experiments; B-WZ and CW carried out experiments; B-WZ, T-BZ, X-FZ and KF analyzed experimental results; B-WZ and CW wrote the manuscript.

FUNDING

This work was supported by the Major Program of the Shandong Provincial Natural Science Foundation (No. ZR2019ZD13), the Shandong Province Natural Science Fund (No. ZR2019QEE015), China, and the Major Scientific and Technological Innovation Project of the Shandong Provincial Key Research Development Program (No. 2019SDZY02).

REFERENCES

Bagde, M. N., and Petroš, V. (2009). Fatigue and Dynamic Energy Behaviour of Rock Subjected to Cyclical Loading. *Int. J. Rock Mech. Mining Sci.* 46, 200–209. doi:10.1016/j.ijrmms.2008.05.002

Chen, J. T., and Feng, X. T. (2006). True Triaxial Experimental Study on Rock with High Geostress. *Chin. J. Rock Mech. Eng.* 25, 1537–1543. doi:10.3321/j.issn:1000-6915.2006.08.004

David, E. C., Brantut, N., Schubnel, A., and Zimmerman, R. W. (2012). Sliding Crack Model for Nonlinearity and Hysteresis in the Uniaxial Stress-Strain Curve of Rock. *Int. J. Rock Mech. Mining Sci.* 52, 9–17. doi:10.1016/j.ijrmms.2012.02.001

Dong, C. X., Kwan, A. K. H., and Ho, J. C. M. (2015). Effects of Confining Stiffness and Rupture Strain on Performance of FRP Confined concrete. *Eng. Structures* 97, 1–14. doi:10.1016/j.engstruct.2015.03.037

Fang, K., Zhao, T., Zhang, Y., Qiu, Y., and Zhou, J. (2019). Rock Cone Penetration Test under Lateral Confining Pressure. *Int. J. Rock Mech. Mining Sci.* 119, 149–155. doi:10.1016/j.ijrmms.2019.04.018

Feng, G.-L., Chen, B.-R., Xiao, Y.-X., Jiang, Q., Li, P.-X., Zheng, H., et al. (2022). Microseismic Characteristics of Rockburst Development in Deep TBM Tunnels with Alternating Soft-Hard Strata and Application to Rockburst Warning: A Case Study of the Neelum-Jhelum Hydropower Project. *Tunnelling Underground Space Techn.* 122, 104398. doi:10.1016/j.tust.2022.104398

Feng, G.-L., Feng, X.-T., Chen, B.-r., Xiao, Y.-X., and Yu, Y. (2014). A Microseismic Method for Dynamic Warning of Rockburst Development Processes in Tunnels. *Rock Mech. Rock Eng.* 48, 2061–2076. doi:10.1007/s00603-014-0689-3

Huang, D., and Li, Y. (2014). Conversion of Strain Energy in Triaxial Unloading Tests on Marble. *Int. J. Rock Mech. Mining Sci.* 66, 160–168. doi:10.1016/j.ijrmms.2013.12.001

Jia, Z., Li, C., Zhang, R., Wang, M., Gao, M., Zhang, Z., et al. (2019). Energy Evolution of Coal at Different Depths under Unloading Conditions. *Rock Mech. Rock Eng.* 52, 4637–4649. doi:10.1007/s00603-019-01856-y

Jiang, T., and Teng, J. G. (2007). Analysis-oriented Stress-Strain Models for FRP-Confined concrete. *Eng. Structures* 29, 2968–2986. doi:10.1016/j.engstruct.2007.01.010

Lam, L., and Teng, J. G. (2004). Ultimate Condition of Fiber Reinforced Polymer-Confined Concrete. *J. Compos. Constr.* 8, 539–548. doi:10.1061/(asce)1090-0268(2004)8:6(539)

Li, D., Sun, Z., Xie, T., Li, X., and Ranjith, P. G. (2017). Energy Evolution Characteristics of Hard Rock during Triaxial Failure with Different Loading and Unloading Paths. *Eng. Geology.* 228, 270–281. doi:10.1016/j.enggeo.2017.08.006

Li, H. B., Zhao, J., and Li, T. J. (1999). Triaxial Compression Tests on a Granite at Different Strain Rates and Confining Pressures. *Int. J. Rock Mech. Mining Sci.* 36, 1057–1063. doi:10.1016/s1365-1609(99)00120-3

Liu, X., Feng, X.-T., and Zhou, Y. (2020). Experimental Study of Mechanical Behavior of Gneiss Considering the Orientation of Schistosity under True Triaxial Compression. *Int. J. Geomechanics* 20. doi:10.1061/(asce)gm.1943-5622.0001838

Ma, C. C., Chen, K. Z., Li, T. B., Zeng, J., and Ma, J. J. (2020). Numerical Simulation of Stress-Structural Rockburst Based on GDEM Software. *Hazard. Control. Tunnelling Underground Eng.* 2 (3), 85–94.

Meng, Q.-b., Liu, J.-f., Huang, B.-x., Pu, H., Wu, J.-y., and Zhang, Z.-z. (2022). Effects of Confining Pressure and Temperature on the Energy Evolution of Rocks under Triaxial Cyclic Loading and Unloading Conditions. *Rock Mech. Rock Eng.* 55, 773–798. doi:10.1007/s00603-021-02690-x

Micelli, F., and Modarelli, R. (2013). Experimental and Analytical Study on Properties Affecting the Behaviour of FRP-Confined concrete. *Composites B: Eng.* 45, 1420–1431. doi:10.1016/j.compositesb.2012.09.055

Peng, R., Ju, Y., Wang, J. G., Xie, H., Gao, F., and Mao, L. (2014). Energy Dissipation and Release during Coal Failure under Conventional Triaxial Compression. *Rock Mech. Rock Eng.* 48, 509–526. doi:10.1007/s00603-014-0602-0

Wang, F., and Kaunda, R. (2019). Assessment of Rockburst hazard by Quantifying the Consequence with Plastic Strain Work and Released Energy in Numerical Models. *Int. J. Mining Sci. Techn.* 29, 93–97. doi:10.1016/j.ijmst.2018.11.023

Wang, Y., and Cui, F. (2018). Energy Evolution Mechanism in Process of Sandstone Failure and Energy Strength Criterion. *J. Appl. Geophys.* 154, 21–28. doi:10.1016/j.jappgeo.2018.04.025

Xie, H., Li, C., He, Z., Li, C., Lu, Y., Zhang, R., et al. (2021b). Experimental Study on Rock Mechanical Behavior Retaining the *In Situ* Geological Conditions at Different Depths. *Int. J. Rock Mech. Mining Sci.* 138, 104548. doi:10.1016/j.ijrmms.2020.104548

Xie, H., Li, L., Peng, R., and Ju, Y. (2009). Energy Analysis and Criteria for Structural Failure of Rocks. *J. Rock Mech. Geotechnical Eng.* 1, 11–20. doi:10.3724/sp.J.1235.2009.00011

Xie, H. P., Li, C. P., Gao, M. Z., Zhang, R., Gao, F., and Zhu, J. B. (2021a). Conceptualization and Preliminary Research on Deep *In Situ* Rock Mechanics. *Chin. J. Rock Mech. Eng.* 40 (02), 217–232. doi:10.13722/j.cnki.jrme.2020.0317

Yu, X. B., Xie, Q., Li, X. Y., Na, Y. K., and Song, Z. P. (2005). Cycle Loading Tests of Rock Samples under Direct Tension and Compression and Bi-modular Constitutive Model. *Chin. J. Geotechnical Eng.* 27, 988–993. doi:10.3321/j.issn:1000-4548.2005.09.003

Yu, Y., Feng, G.-l., Xu, C.-j., Chen, B.-r., Geng, D.-x., Zhu, B.-t., et al. (2022). Quantitative Threshold of Energy Fractal Dimension for Immediate Rock Burst Warning in Deep Tunnel: A Case Study. *Lithosphere* 2021, 1699273. doi:10.2113/2022/1699273

Zhang, L., Cong, Y., Meng, F., Wang, Z., Zhang, P., and Gao, S. (2021). Energy Evolution Analysis and Failure Criteria for Rock under Different Stress Paths. *Acta Geotech.* 16, 569–580. doi:10.1007/s11440-020-01028-1

Zhang, Q. B., and Zhao, J. (2014). A Review of Dynamic Experimental Techniques and Mechanical Behaviour of Rock Materials. *Rock Mech. Rock Eng.* 47, 1411–1478. doi:10.1007/s00603-013-0463-y

Zhang, Z. Z., and Gao, F (2015). Confining Pressure Effect on Rock Energy. *Chin. J. Rock Mech. Eng.* 34, 1–11. doi:10.13722/j.cnki.jrme.2015.01.001

Conflict of Interest: Author X-FZ was employed by the company Shandong Energy Group Co., Ltd.

The remaining authors declare that the research was conducted in the absence of any commercial or financial relationships that could be construed as a potential conflict of interest.

Publisher's Note: All claims expressed in this article are solely those of the authors and do not necessarily represent those of their affiliated organizations, or those of the publisher, the editors, and the reviewers. Any product that may be evaluated in this article, or claim that may be made by its manufacturer, is not guaranteed or endorsed by the publisher.

Copyright © 2022 Zhang, Fang, Wang, Zhao and Zhang. This is an open-access article distributed under the terms of the Creative Commons Attribution License (CC BY). The use, distribution or reproduction in other forums is permitted, provided the original author(s) and the copyright owner(s) are credited and that the original publication in this journal is cited, in accordance with accepted academic practice. No use, distribution or reproduction is permitted which does not comply with these terms.

frontiers | Frontiers in Earth Science

ORIGINAL RESEARCH
published: 31 May 2022
doi: 10.3389/feart.2022.891289

Study on Safety Management Assessment of Coal Mine Roofs Based on the DEMATEL-ANP Method

Lei Li[1,2]* *and Youpeng Ouyang*[1,2]

[1]College of Safety Science and Engineering, Xi'an University of Science and Technology, Xi'an, China, [2]Key Laboratory of Western Mine Exploration and Hazard Prevention, Ministry of Education, Xi'an, China

Coal mine roof accidents are one of the main single risks faced by coal miners. According to the statistical data of coal mine accidents in China, there were 40 roof accidents and 55 deaths in 2020 alone, accounting for 32.8 and 24.4% of the total, respectively. Therefore, we can see its danger. To realize the comprehensive scientific assessment of coal mine roof accidents, first, through the collation and analysis of relevant literature reviews and accident investigation reports, combined with the expert investigation method, an assessment index system of coal mine roof accidents is constructed. Then, based on the analysis of the characteristics of the influencing factors of coal mine roof accidents, the assessment model of coal mine roof accidents is established by using the DEMATEL-ANP method. Finally, the established assessment model is applied to a coal mine to verify the rationality of the model.

Keywords: roof accident, index system, DEMATEL method, ANP method, assessment model

OPEN ACCESS

Edited by:
Shibing Huang,
Wuhan University of Science and Technology, China

Reviewed by:
Ionut Cristi Nicu,
Norwegian Institute for Cultural Heritage Research, Norway
Hao-sen Guo,
East China Jiaotong University, China

***Correspondence:**
Lei Li
lilei_safety@xust.edu.cn

Specialty section:
This article was submitted to Geohazards and Georisks, a section of the journal Frontiers in Earth Science

Received: *07 March 2022*
Accepted: *19 April 2022*
Published: *31 May 2022*

Citation:
Li L and Ouyang Y (2022) Study on Safety Management Assessment of Coal Mine Roofs Based on the DEMATEL-ANP Method. Front. Earth Sci. 10:891289. doi: 10.3389/feart.2022.891289

1 INTRODUCTION

Roof accident is the type of coal mine accident with the largest number of occurrences and deaths. No matter what the scale of the coal mine is, there will be a certain degree of roof safety hazards in the mining process (Zhu et al., 2018; Xu et al., 2021; Zhang et al., 2021). However, because the occurrence of roof accidents is affected by many factors, it is difficult to prevent and control them, which seriously restricts the safe production of coal enterprises. Therefore, analyzing the causes of roof accidents and determining the influence degree of various factors to formulate effective prevention and control measures is still an important work content of the coal industry.

Roof fall refers to the sudden and violent collapse of the roadway roof, resulting in the collapse of roof rock. Roof fall is different from the rockburst disaster in deep engineering (Feng et al., 2015; Feng et al., 2022; Yu et al., 2022a; Yu et al., 2022b). However, it is also very dangerous and causes serious economic losses. Early studies were mostly considered from the perspective of geology and considered that weak and defective roofs, changes in stress conditions, and bedding plane faults and folds were the main reasons for roof collapse (Molinda, 2003; Phillipson, 2003; Düzgün, 2005). In recent years, with the deepening of research, the vibration, humidity in the air, coal pillar stability, and roof rock hanging length after the use of explosives have also been found to have an obvious correlation with roof falling (Yasidu et al., 2019; Liu et al., 2018). Because of the obvious differences in geological conditions in different regions, some scholars have carried out research on the causes of roof accidents under specific geological conditions. For example, Wang et al. (2018) analyzed a roof fall accident in the Huangyanhui coal mine in the Taihang Mountain area of Shanxi Province, China, and found that tectonic stress and fault sliding caused by mining activities are the driving forces of roof fall; Fei et al. (2020) found that under the condition of a thin bedrock and clay roof, the

movement of post-mining overburden is complex. The analysis of the causes of roof falls has laid a certain foundation for evaluating roof safety and putting forward control methods, and relevant research has also been carried out. Oraee et al. (2016) believed that the discontinuity of geological structures would lead to large-area roof collapse, and proposed a roof fall risk assessment method based on structural data and analysis of wedge geometry and stability in coal mines. Bai et al. (2021) took the roof separation and horizontal displacement as the key factors leading to roof falling and proposed that the horizontal displacement can be reduced by increasing the bolt pretension load. Xiong et al. (2021) combined the analytic hierarchy process and fuzzy comprehensive evaluation method and established the cloud model of roof fall risk evaluation by constructing a quantitative grade interval and calculating the weight of each index.

To sum up, the research on the causes of roof falls, roof evaluation, and control is very rich, and the relevant achievements have also played an important role in reducing roof accidents and realizing the scientific management of roofs. However, after further analysis, it is found that the existing research is mainly carried out from geological or closely related factors, and the occurrence of coal mine roof accidents is the result of the coupling of geological uncertainty, stress change, mining conditions, surrounding environments, and safety management (Shen et al., 2017; Tubis et al., 2020; Njock et al., 2021). There is a certain one-sidedness in analyzing only from the geological aspect, and in terms of safety management, because of China's unique coal enterprise management mode and national policies, a roof safety management evaluation method based on China's national conditions is needed.

The Decision Making Trial and Assessment Laboratory (DEMATEL) is a method to solve complex and difficult problems in the real world by using the graph theory and matrix tools. The Analytic Network Process (ANP) method is a decision-making method based on the Analytic Hierarchy Process (AHP), which is suitable for non-independent hierarchical structures. The combination of DEMATEL and ANP can effectively reduce the inconsistency and uncertainty caused by people's subjective judgment in the evaluation of roof safety management. Therefore, first, through literature sorting and the collection and analysis of roof accident investigation reports in China in the past 5 years, find out the influencing factors involved in the coal mine roof accident, classify the influencing factors through expert interviews, establish the coal mine roof safety management evaluation index system, and then use the DEMATEL-ANP to establish the coal mine roof safety management evaluation model for empirical applications.

2 ESTABLISHMENT OF THE EVALUATION INDEX SYSTEM OF COAL MINE ROOF SAFETY MANAGEMENT

2.1 Identification of the Influencing Factors of Coal Mine Roof Safety Management

Identifying the influencing factors of coal mine roof safety management is an important step in establishing the evaluation index system. To achieve this goal, the following databases were searched: *Elsevier Science Direct*, *CNKI*, *Google academic*, and *SpringerLink*. The combination of search terms used is roof accident or event and influencing factors, roof accident or event and evaluation, and DEMATEL-ANP. References cited in the article are also used as additional sources for our search.

In addition, to make the research conform to the actual situation of China's coal mine production and national supervision, the coal mine roof accident reports published in China in the past 5 years (2016–2021) were sorted and analyzed to determine the factors not mentioned in the literature. There are 96 accident reports in total, and each report is proposed by the official investigation team formed in accordance with the requirements of laws and regulations and includes the analysis of the influencing factors leading to the accident. Since the accident investigation report comes from different accident investigation teams, there may be inconsistencies in the description of the same influencing factor. Therefore, integrate the different descriptions of the same influencing factor. For example, the safety education and training work are not solid, the safety education and training are not effective, and the safety education and training are not in-depth unified into safety education and training. To sum up, through the literature review and sorting of accident investigation reports, representative evaluation indexes of coal mine roof accidents are obtained, as shown in **Table 1**.

2.2 Selection of Evaluation Indexes for Coal Mine Roof Safety Management

For the identified 26 evaluation indicators, five experts were invited to interview and classify the indicators, including three scholars who have long studied coal mine safety management and two managers engaged in coal mine safety management. During the interview, the experts defined the meaning of each index in detail and classified the index on the basis of fully understanding the connotation and value of the index. Finally, according to expert opinions, 26 coal mine roof accident evaluation indexes were established and divided into five dimensions: principal responsibility, site management, technical management, individual factors, and environmental change, as shown in Appendix 1.

2.3 Establishment of the Evaluation Index System of Coal Mine Roof Safety Management

To further determine the effectiveness of the selected indicators and the accuracy of classification, the expert investigation method is used to analyze the rationality of the evaluation indicators. When using the expert survey method, the number of members of the expert group is generally not less than 10, but not more than 20, because when the number is more than 20, it has little impact on the accuracy of the evaluation results (Lin, 2017). Therefore, a total of 15 questionnaires were distributed and recovered, with a questionnaire recovery rate of 100%.

TABLE 1 | Coal mine roof safety management assessment index.

Number	Index	Number	Index
1	Risk management	14	Break regulations to direct
2	Safety education and training	15	Break regulations to work
3	Leadership lead work groups system	16	Risk Identification ability
4	Safety investment	17	Self-mutual protection awareness
5	Legal mining	18	Working skill
6	Territorial supervision	19	Operation regulation
7	Supervision of the superior company	20	Technical measures
8	Responsibility system for safety in production	21	Roadway layout
9	Timber setting	22	Safety monitoring system
10	Arranging construction	23	Geologic structure
11	Knock ring and roof testing	24	Stress concentration
12	Organizing workers	25	Roof pressurized
13	Emergency disposal	26	Surrounding rock deformation

TABLE 2 | Results of expert survey indicators.

Dimension	Index	min	max	μ	δ	CV	S	R.
Principal responsibility	Risk management	5	5	5.00	0.00	0.00	100.0%	√
	Safety education and training	4	5	4.93	0.26	0.05	93.8%	√
	Leadership lead work groups system	4	5	4.20	0.41	0.10	100.0%	√
	Safety investment	5	5	5.00	0.00	0.00	93.8%	√
	Legal mining	4	5	4.87	0.35	0.07	100.0%	√
	Territorial supervision	4	5	4.20	0.41	0.10	93.8%	√
	Supervision of superior company	4	5	4.20	0.41	0.10	93.8%	√
	Responsibility system for safety in production	4	5	4.80	0.41	0.09	100.0%	√
Site management	Timber setting	4	5	4.87	0.35	0.07	93.8%	√
	Arranging construction	4	5	4.20	0.41	0.10	100.0%	√
	Knock ring and roof testing	4	5	4.87	0.35	0.07	93.8%	√
	Organizing workers	4	5	4.87	0.35	0.07	100.0%	√
	Emergency disposal	4	5	4.87	0.35	0.07	87.5%	√
Individual factors	Break regulations to direct	4	5	4.87	0.35	0.07	87.5%	√
	Break regulations to work	4	5	4.87	0.35	0.07	100.0%	√
	Risk Identification ability	4	5	4.87	0.35	0.07	100.0%	√
	Self-mutual protection awareness	4	5	4.87	0.35	0.07	100.0%	√
	Working skill	4	5	4.20	0.41	0.10	100.0%	√
Technology management	Operation regulation	4	5	4.93	0.26	0.05	100.0%	√
	Technical measures	4	5	4.93	0.23	0.05	100.0%	√
	Roadway layout	4	5	4.20	0.41	0.10	100.0%	√
	Safety monitoring system	4	5	4.20	0.41	0.10	87.5%	√
Environmental change	Geologic structure	5	5	5.00	0.00	0.00	100.0%	√
	Stress concentration	5	5	5.00	0.00	0.00	100.0%	√
	Roof pressurized	5	5	5.00	0.00	0.00	100.0%	√
	Surrounding rock deformation	5	5	5.00	0.00	0.00	100.0%	√

R stands for rationality.

Using a Likert scale to measure and count the importance of preselected indicators, they is divided into five levels: 1 indicates very unimportant, 2 indicates unimportant, 3 indicates average, 4 indicates important, and 5 indicates very important. The maximum and minimum values of each index score are counted and recorded as max and min, respectively. The mean value, standard deviation, and coefficient of variation of each index score are calculated and recorded as μ, δ, and CV, respectively. The index meeting $\mu \geq 3.5$ and $0.1 < CV < 0.2$ is regarded as meeting the important requirements. At the same time, according to Wang et al. (2019), 2 subscale is used to measure the rationality of index classification. Unreasonable classification is represented by 0, 1 represents reasonable classification, and S is the proportion of the number of experts with 1 score in the total number of replies. When S-7, it is considered that the classification of the index is reasonable, which is expressed by √ and vice versa × express. Through the statistics of the questionnaire results, the index score results are obtained, as shown in **Table 2**.

It can be seen from **Table 5** that the coefficient of variation of all indicators is less than 0.2, and the s value is greater than 80%, that is, the classification of all indicators is reasonable and does not need to be modified. To verify the rationality of expert

TABLE 3 | Expert synergy coefficient test.

Project	W value	P value
Expert estimation	0.621	***

*** *indicates P <0.001.*

TABLE 4 | Relationship strength metric table.

Point	Implication
4	Very high influence
3	High influence
2	Low influence
1	Very low influence
0	No impact

opinions, the Kendall W synergy coefficient is used for the consistency test, and its calculation formula is as follows:

$$W = \frac{12}{m^2(n^3 - n)} \sum_{i=1}^{n} \left(R_i - \frac{m(n+1)}{2} \right)^2, \quad (1)$$

where m is the number of experts, n is the number of indicators, and R_i is the sum of the ranks of the i th indicator. The value of W is between 0–1. The larger the value is, the more consistent the expert opinion is, and the evaluation result is reasonable; otherwise, it means that the expert opinion is random and the evaluation result is unreasonable. Through spss25 0, calculate the W synergy coefficient of expert opinions, as shown in **Table 3**.

It can be seen from **Table 4** that the synergy coefficient of expert scoring is 0.621, indicating that the consensus of expert group members is strong, and the significance level P value of the synergy coefficient is less than 0.001, indicating that the synergy coefficient is significant. Therefore, the evaluation results are consistent. To sum up, the coal mine roof accident evaluation system is shown in **Figure 1**.

3 CONSTRUCTION OF THE COAL MINE ROOF SAFETY MANAGEMENT EVALUATION MODEL

3.1 Applicability Analysis of DEMATEL-ANP

The evaluation indexes of coal mine roof accidents affect each other, and the weight of each index is different. Enterprise managers need to not only know the evaluation results but also to clarify the influence relationship between various indicators and identify key factors, to take targeted measures for control and treatment. Using traditional evaluation and analysis methods, it is difficult to determine the complex relationship between indicators in a real situation, and the DEMATEL-ANP rule solves this defect well (Dehdasht et al., 2017). The DEMATEL has the advantages of not relying on big data samples and simplifying the factor correlation analysis. It

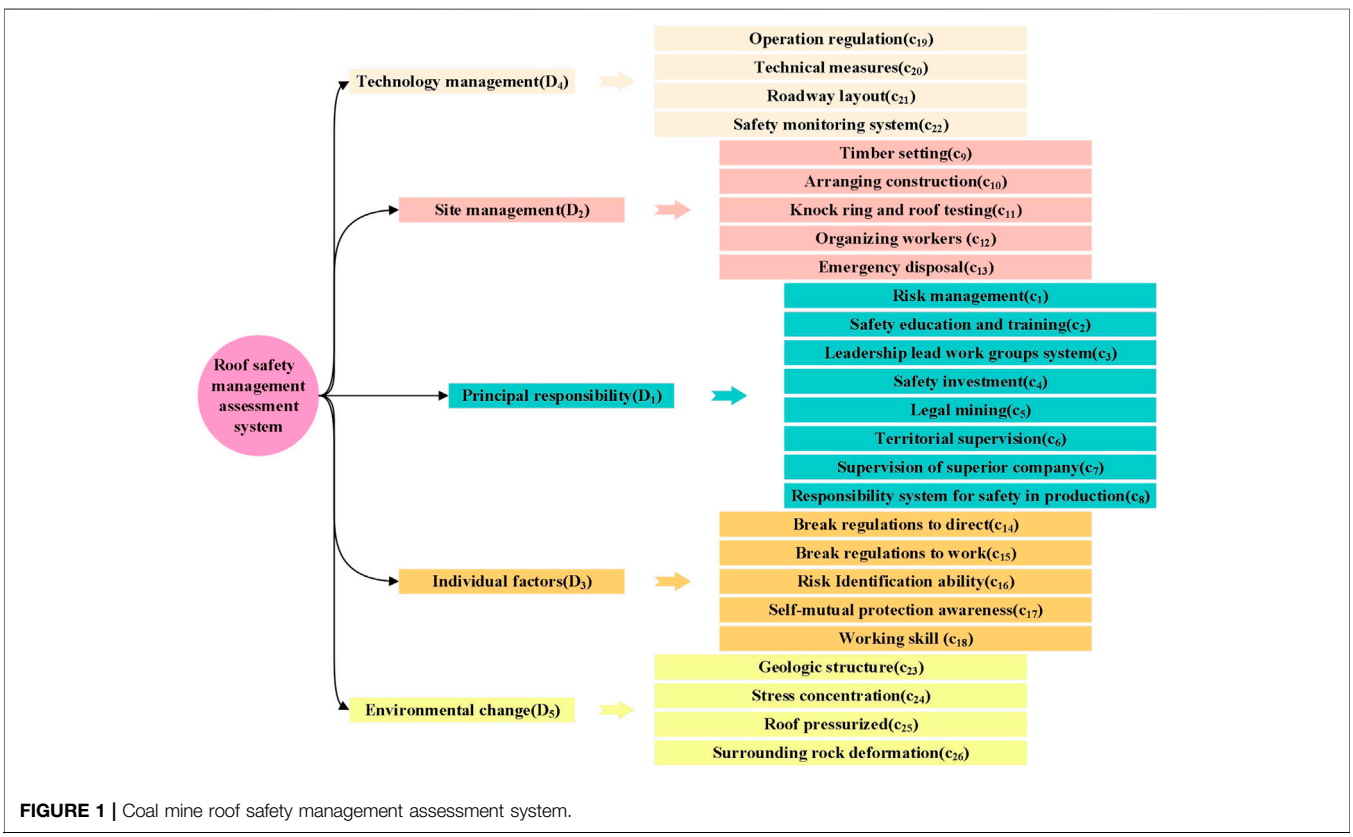


FIGURE 1 | Coal mine roof safety management assessment system.

can build a mapping structure with clear relationships between sub criteria for each criterion and establish a cause and effect diagram that can visualize the cause and effect relationship. In a network with relevant standards, the ANP can make the prediction more accurate through better priority calculation. At present, this method has been applied in many fields and received positive feedback (Chukwuma et al., 2021; Osintsev et al., 2021; Mubarik et al., 2021). Therefore, the application of the DEMATEL-ANP method for coal mine roof accident evaluation has the following applicability:

1) DEMATEL can clarify the relationship between evaluation indicators.

First, through the steps of determining the direct influence matrix, standardizing the direct influence matrix, and determining the comprehensive influence matrix, the influence diagram of coal mine roof accident evaluation indexes is drawn to intuitively show the interaction relationship between each index. Second, the ANP model of coal mine roof accidents is established by using the drawn influence relationship network diagram, to avoid the problem of being too subjective in determining the influence relationship of indicators. Finally, by calculating the influence intensity of the relationship between the indicators, the cause degree and centrality are determined. On this basis, the indicators are arranged according to the influence to identify the key factors affecting coal mine roof accidents and lay a foundation for formulating targeted control measures.

2) ANP determines the relative importance of the criterion layer and index layer of the index system.

After the DEMATEL identifies the relationship between coal mine roof accident indicators, the ANP can capture the interdependence between decision attributes to realize a more systematic analysis. First, compared with the AHP, which assumes that the relationship between indicators is independent, the ANP provides a more general decision-making model without assuming the independence between indicators at the same level and different levels. Second, by determining the index weight, enterprise managers can pay more balanced attention to the overall influence of various dimensions on roof accidents. Finally, when constructing the judgment matrix, the nine-level scaling method is used to assign the value, which greatly reduces the subjective influence caused by human reasons.

3.2 Evaluation Index Influence Relationship and Weight Establishment

3.2.1 Identifying the Impact Relationship Between Indicators

1) Determining the Direct Impact Matrix

To construct the network diagram of roof safety management evaluation, first, experts need to judge the influence relationship and degree of all indicators and form an influence relationship matrix. Among them, indicators S_i and S_j should be compared twice, which are the direct impacts of indicator S_i on $S_j$and the direct influence of index S_i on S_j. For the whole system, if there are n indicators, it needs to be compared $n(n-1)$ times. The index itself does not need to be compared, that is, the value on the diagonal of the matrix is usually represented by 0. The 5-point scale is adopted in the process of expert scoring, as shown in **Table 4**.

TABLE 5 | Direct impact matrix.

M	D_1	D_2	D_3	D_4	D_5
D_1	0	$m_{1,2}$	$m_{1,3}$	$m_{1,4}$	$m_{1,5}$
D_2	$m_{2,1}$	0	$m_{2,3}$	$m_{2,4}$	$m_{2,5}$
D_3	$m_{3,1}$	$m_{3,2}$	0	$m_{3,4}$	$m_{3,5}$
D_4	$m_{4,1}$	$m_{4,2}$	$m_{4,3}$	0	$m_{4,5}$
D_5	$m_{5,1}$	$m_{5,2}$	$m_{5,3}$	$m_{5,4}$	0

In actual decision-making, there will also be interactions between different dimensions and different indicators. It can be assumed that there is relationship between all indicators, but this assumption will lead to more complex problems. Therefore, this study assumes that the interaction relationship of 26 indicators is the same as that of five dimensions. The scoring results of each expert's influence relationship are expressed in the matrix $X^k = [x_{ij}^k]_{5\times5}$, where x_{ij}^k represents the influence degree of dimension B_i on B_j considered by the k expert, and k experts form the 5-order matrix X^1、X^2、X^3、X^4、X^5. Treat the evaluation matrix of k experts according to **the** following equation:

$$m_{ij} = \frac{1}{k}\sum_{k=1}^{k} x_{ij}^k, i, j = 1, 2, \ldots, 5. \tag{2}$$

The initial direct influence matrix $M = [m_{ij}]_{5\times5}$ is obtained. The direct influence matrix represents the influence relationship and degree between the performance evaluation dimensions obtained by the arithmetic averaging of the opinions of each expert, as shown in **Table 5**.

2) Normalized Direct Impact Matrix

The normalized influence matrix can be obtained by standardizing the direct influence matrix M with **Eqs (3)**, **(4)**, as shown in **Table 6**.

$$\lambda = \min\left(\frac{1}{\max_{1\le i\le n}\sum_{j=1}^{n} a_{ij}}, \frac{1}{\max_{1\le j\le n}\sum_{i=1}^{n} a_{ij}}\right), \tag{3}$$

$$N = \lambda \times M. \tag{4}$$

3) Determining the Comprehensive Impact Matrix

The comprehensive influence matrix T can be obtained by calculating the limit of the specification influence matrix N in **Equation (5)**, as shown in **Table 7**. The comprehensive impact matrix shows all the direct and indirect impact relationships between the dimensions of the index system.

TABLE 6 | Norm influence matrix.

N	D_1	D_2	D_3	D_4	D_5
D_1	0	$\lambda m_{1,2}$	$\lambda m_{1,3}$	$\lambda m_{1,4}$	$\lambda m_{1,5}$
D_2	$\lambda m_{2,1}$	0	$\lambda m_{2,3}$	$\lambda m_{2,4}$	$\lambda m_{2,5}$
D_3	$\lambda m_{3,1}$	$\lambda m_{3,2}$	0	$\lambda m_{3,4}$	$\lambda m_{3,5}$
D_4	$\lambda m_{4,1}$	$\lambda m_{4,2}$	$\lambda m_{4,3}$	0	$\lambda m_{4,5}$
D_5	$\lambda m_{5,1}$	$\lambda m_{5,2}$	$\lambda m_{5,3}$	$\lambda m_{5,4}$	0

TABLE 7 | Comprehensive influence matrix.

T	D_1	D_2	D_3	D_4	D_5
D_1	0	$t_{1,2}$	$t_{1,3}$	$t_{1,4}$	$t_{1,5}$
D_2	$t_{2,1}$	0	$t_{2,3}$	$t_{2,4}$	$t_{2,5}$
D_3	$t_{3,1}$	$t_{3,2}$	0	$t_{3,4}$	$t_{3,5}$
D_4	$t_{4,1}$	$t_{4,2}$	$t_{4,3}$	0	$t_{4,5}$
D_5	$t_{5,1}$	$t_{5,2}$	$t_{5,3}$	$t_{5,4}$	0

$$\mathrm{T} = \lim_{\mathrm{k}\to\infty}\left(\mathrm{N} + \mathrm{N}^2 + \cdots + \mathrm{N}^5\right) = \mathrm{N}\left(\mathrm{I} - \mathrm{N}\right)^{-1} = \left[\mathrm{t}_{\mathrm{ij}}\right]_{5\times5}, \quad (5)$$

where T is the comprehensive influence matrix; the influence matrix is normalized into N; I is the identity matrix; and $(I - N)^{-1}$ is the inverse matrix of $(I - N)$.

4) Calculating the Center Degree and Cause Degree of Each Index

The sum of the values of each row and column of the comprehensive influence matrix T is calculated through **Equations (6)**, **(7)** to represent the comprehensive influence value of the corresponding indicators of each row and column on all other indicators, that is, the influence degree and the affected degree, which are recorded as sets R and C, respectively.

$$\mathrm{R_i} = \sum_{j=1}^{5} t_{ij},\ (i = 1, 2, \cdots, 5), \quad (6)$$

$$\mathrm{C_i} = \sum_{j=1}^{5} t_{ij},\ \left(j = 1, 2, \cdots, 5\right). \quad (7)$$

Based on the calculation of centrality and cause degree, using **Equation (8)**, add the influence degree and affected degree of index i to obtain the centrality of the index, which is recorded as Z_i, indicating the position of the index in the evaluation index system and its role. Use **Equation 9** to subtract the influence degree and affected degree of index i to obtain the cause degree of this element, which is recorded as Y_i. If it is greater than 0, it indicates that this index has a great impact on other indexes, which is called cause element, otherwise, it is the result factor.

$$Z_i = R_i + C_i, \quad (8)$$

$$Y_i = R_i - C_i. \quad (9)$$

5) Drawing the Network Diagram

To more clearly describe the relationship between indicators, an impact relationship diagram with a threshold is established, which is used to deal with the impact value in the overall relationship comprehensive impact matrix T. The impact graph only describes the impact beyond the threshold, which simplifies the decision-maker's identification of important information. The drawing of the influence relation diagram can be used as the basis of the ANP analysis. The indexes have mutual influence, one-way influence, and no influence, which are represented by a two-way arrow, one-way arrow, and no arrow, respectively.

3.2.2 Determining the Index Weight

By determining the relationship between the criterion layers of the coal mine roof safety management evaluation index system, we can identify the criteria that have great influence or are easily affected. According to the DEMATEL analysis results, we can put forward scientific and reasonable improvement measures, but we should also clearly realize that the criteria closely related to other criteria are not necessarily the most important in the evaluation index system, and the weight of each index needs to be identified to determine the real key factors of roof safety management. Therefore, the ANP method is applied to further clarify the weight of each index.

1) Constructing the judgment matrix

According to the internal correlation of risk evaluation indexes in the DEMATEL model, the network hierarchy diagram of roof safety management evaluation is formed. For all indicators with a mutual influence relationship, the importance judgment is carried out by using the 1-9 scale method (**Table 8**), to construct the pairwise judgment matrix of the relative importance of indicators in a certain dimension with different indicators as the sub-criteria. Each group of judgment matrix is summarized to form the initial relative importance judgment matrix after checking the consistency through the consistency index CI and consistency ratio CR.

$$B_c = \begin{array}{c} \\ D_1 \\ \\ \\ \\ D_i \\ \\ \\ \\ D_5 \\ \\ \end{array} \begin{array}{c} \begin{array}{cccccccccc} & D_1 & & & & D_j & & & & D_5 \\ & c_{1,1} & \cdots & c_{1,m_1} & \cdots & c_{j,1} & \cdots & c_{j,m_j} & \cdots & c_{5,1} & \cdots & c_{5,m_5} \end{array} \\ \begin{array}{c} c_{1,1} \\ c_{1,2} \\ \vdots \\ c_{1,m_1} \\ c_{i,1} \\ c_{i,2} \\ \vdots \\ c_{i,m_i} \\ c_{5,1} \\ c_{5,1} \\ \vdots \\ c_{5,m_5} \end{array} \begin{bmatrix} B_c^{1,1} & \cdots & B_c^{1,j} & \cdots & B_c^{1,5} \\ \vdots & & \vdots & & \vdots \\ B_c^{i,1} & \cdots & B_c^{i,j} & \cdots & B_c^{i,5} \\ \vdots & & \vdots & & \vdots \\ B_c^{5,1} & \cdots & B_c^{5,j} & \cdots & B_c^{5,5} \end{bmatrix} \end{array} \quad (10)$$

2) Getting the unweighted super matrix

Each group of pairwise comparison matrices is standardized and transposed to obtain the eigenvalue vector W_{ij}. The matrix obtained by summarizing the eigenvalue vectors of all pairwise comparison matrices is the unweighted super matrix W, as shown in Equation (11). If the index in D_j and the index $c_{i,1}, c_{i,2}, \cdots\cdots, c_{i,m_i}$ in D_i are independent of each other, then $W_{i,j} = 0$. Each set of eigenvalue vectors of the unweighted super matrix represents the weight of each index in a certain dimension under a certain criterion. The unweighted super matrix can select the criteria of the judgment

TABLE 8 | Reference table for assignment.

Scores	Implication
1	Indicator *i* and indicator *j* are equally important
3	Indicator *i* is slightly more important than indicator *j*
5	Indicator *i* is significantly more important than indicator *j*
7	Indicator *i* is much more important than indicator *j*
9	Index *i* is more important than index *j* at the extreme
2, 4, 6, 8	Between two adjacent judgment levels

matrix and the element set of the judgment matrix. The correlation of all elements in all element sets will be quantitatively reflected in the way of this judgment matrix.

$$W = \begin{array}{c} \\ D_1 \\ \\ \\ \\ D_i \\ \\ \\ \\ D_5 \\ \\ \end{array} \begin{array}{c} \begin{array}{cccccccccc} & D_1 & & & & D_j & & & D_5 & \\ c_{1,1} & \cdots & c_{1,m_1} & \cdots & c_{j,1} & \cdots & c_{j,m_j} & \cdots & c_{5,1} & \cdots \quad c_{5,m_5} \end{array} \\ \begin{bmatrix} W_{1,1} & & \cdots & & W_{i,1} & & \cdots & & W_{5,1} \\ \vdots & & & & \vdots & & & & \vdots \\ W_{1,j} & & \cdots & & W_{i,j} & & \cdots & & W_{5,j} \\ \vdots & & & & \vdots & & & & \vdots \\ W_{1,5} & & \cdots & & W_{i,1} & & \cdots & & W_{5,5} \end{bmatrix} \end{array} \quad (11)$$

3) Getting the weighted super matrix

Although each of the unweighted hypermatrices is normalized, the overall unweighted hypermatrix is not normalized. Therefore, by multiplying the standardized importance judgment matrix of each dimension with the unweighted super matrix, the standardization of the super matrix is realized, that is, the weighted super matrix is obtained.

Taking the safety evaluation of coal mine roof construction as the criterion and dimension $D_j\,(j = 1, 2, 3, 4, 5)$ as the sub-criterion, the relative importance of the dimensions with an influence relationship with D_j is compared in pairs. After traversing all dimensions, the judgment matrix B_D of each dimension is obtained, as shown in the following equation:

$$B_D = \begin{bmatrix} b_D^{1,1} & \cdots & b_D^{1,j} & \cdots & b_D^{1,5} \\ \vdots & \cdot & \vdots & \cdot & \vdots \\ b_D^{i,1} & \cdots & b_D^{i,j} & \cdots & b_D^{i,5} \\ \vdots & \cdot & \vdots & \cdot & \vdots \\ b_D^{5,1} & \cdots & b_D^{5,j} & \cdots & b_D^{5,5} \end{bmatrix}. \quad (12)$$

The matrix B_D is standardized to obtain B_D^{α}, and the weighted super matrix W^{α} is obtained by multiplying B_D^{α} with the unweighted super matrix W. As shown in **Equation (13)**, the weighted super matrix constitutes the weight of the normalized coal mine roof safety management evaluation index, but the super matrix is unstable and needs further limit treatment.

$$W^{\alpha} = B_D^{\alpha} \times W = \begin{bmatrix} B_D^{\alpha_{1,1}} \times W_{1,1} & \cdots & B_D^{\alpha_{i,1}} \times W_{i,1} & \cdots & B_D^{\alpha_{5,1}} \times W_{5,1} \\ \vdots & \cdot & \vdots & \cdot & \vdots \\ B_D^{\alpha_{1,j}} \times W_{1,j} & \cdots & B_D^{\alpha_{i,j}} \times W_{i,j} & \cdots & B_D^{\alpha_{5,j}} \times W_{5,j} \\ \vdots & \cdot & \vdots & \cdot & \vdots \\ B_D^{\alpha_{1,5}} \times W_{1,5} & \cdots & B_D^{\alpha_{i,5}} \times W_{i,5} & \cdots & B_D^{\alpha_{5,5}} \times W_{5,5} \end{bmatrix}. \quad (13)$$

4) Calculating local and global weights

To reflect the dependency between elements, it is necessary to stabilize the weighted hypermatrix, that is, calculate the limit matrix of the matrix. Calculate the multiple power of the weighted hypermatrix, and note that the t power of W^{α} is $W^{\alpha t} = (W_{i,j}^{\alpha t})$. When W^{α} is in $t \to \infty$, the limit exists, that is, $W^{\infty} = \lim_{n \to \infty} W^{\alpha t}$.

5) Determining the comprehensive weight

When the column vectors are equal, the hypermatrix converges to stability to obtain the limit relative ranking of the indicators in each dimension, that is, the weight of each indicator. The weight determined by the DEMATEL-ANP considers the relative importance determined by the influence relationship between indicators, so it can better adapt to the characteristics of mutual influence among coal mine roof safety management evaluation indicators.

4 CASE ANALYSIS

4.1 Data Collection

Based on the established risk evaluation index system and the DEMATEL-ANP risk evaluation model, 12 of the 15 experts were organized to conduct a five-day field investigation in the SL coal mine during the construction of the index system, meeting the requirements of 8–15 experts for the DEMATEL method (Mavi and Standing, 2018). Then, according to the present situation of

TABLE 9 | Overview of the members of the group of experts.

Category	Research/professional experience		Proportion/%
	≤ 10 years	> 10 years	
Coal mine safety scholars	2	4	50
Coal mine safety management practitioners	1	3	33.3
Safety assessment organization practitioners	1	1	16.7

roof management in the coal mine, a questionnaire survey was carried out among experts. The details of the members of the expert group are shown in **Table 9**.

4.2 Establishment and Analysis of Influence Relationships Among Indicators

According to the data collected by the questionnaire, first calculate the arithmetic average value from **Equation 2** to form the initial direct influence matrix. Second, standardize the direct influence matrix according to **Eqs (3)**, **(4)** to form a standardized direct influence matrix. Finally, calculate the comprehensive influence matrix T according to **Equation (5)**, as shown in **Table 10**. After many expert discussions, it is agreed that the comprehensive impact matrix $t_{i,j} \leq 0.2$ indicates that D_i indicates that D_j has no impact relationship; 0.2–0.4 indicates that the influence of D_i on D_j is weak; 0.4–0.6 indicates that the influence of D_i on D_j is general; 0.6–0.8 indicates that D_i has a strong influence on D_j; and 0.8–1 indicates that the influence of D_i on D_j is very strong.

It can be seen from **Table 10** that each dimension of coal mine roof safety management evaluation has an impact on the five dimensions (including itself) and is also affected by the five dimensions (including itself). But the degree of mutual influence is different.

Based on the comprehensive influence matrix T, the influence degree R and affected degree C are calculated according to **Equations (6)**, **(7)**, and the centrality and cause degree of each dimension of coal mine roof accident evaluation are formed, as shown in **Table 11**. By analyzing the centrality and cause degree, we can identify the key factors affecting the safety management of coal mine roofs, and each key factor will form its own influence relationship network through the influence relationship.

Finally, according to the results of **Table 10** and **Table 11**, the network relationship model between each dimension is obtained, as shown in **Figure 2**. To show the strength of the influence relationship between different dimensions, **Figure 2** is distinguished by the color and thickness of the line. The drawing of this model can lay a foundation for the drawing of the network structure in the ANP analysis.

4.3 Calculation and Analysis of the Evaluation Index Weight

Based on the final influence matrix and network relationship model determined by the DEMATEL, the ANP network structure diagram of coal mine roof safety management evaluation is constructed by using super decisions software, as shown in **Figure 3**. A loop indicates that there is an interactive relationship within each dimension.

After determining the structural relationship of the ANP network, the 19-scale method (**Table 9**) is used to compare the relative importance of two risk factors to obtain the judgment matrix at the dimension level and the unweighted super matrix at the index level to further obtain the weighted super matrix and limit super matrix. Finally, the local and global weights of each dimension and each index are shown in **Table 12**. In the whole calculation process, the software will conduct a consistency inspection. The consistency ratio CR is a measure of consistency. When $CR < 0.1$, it shows strong consistency. In this study, CR is less than 0.1, which meets the research requirements.

TABLE 10 | Comprehensive impact matrix of dimensions.

T	D_1	D_2	D_3	D_4	D_5
D_1	0.517	0.886	0.842	0.460	0.585
D_2	0.704	0.688	0.866	0.501	0.675
D_3	0.676	0.845	0.628	0.539	0.583
D_4	0.636	0.813	0.773	0.289	0.598
D_5	0.644	0.841	0.782	0.499	0.463

TABLE 11 | Importance and causes of dimensions.

Dimension	R	C	R + C	R − C
Principal responsibility	3.291	3.178	6.469	0.113
Site management	3.435	4.073	7.508	−0.638
Individual factors	3.271	3.892	7.163	−0.621
Technology management	3.109	2.288	5.397	0.821
Environmental change	3.229	2.904	6.133	0.325

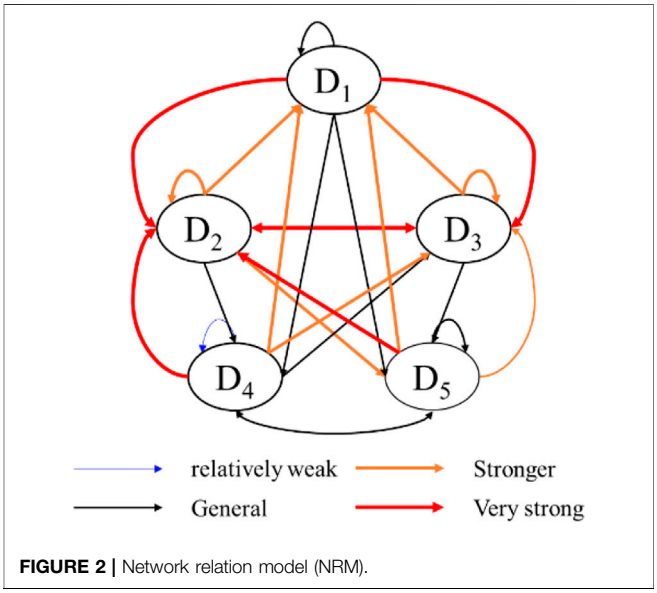


FIGURE 2 | Network relation model (NRM).

5 DISCUSSION

Through sorting out and analyzing the influencing factors of coal mine roof accidents, this study puts forward a coal mine roof safety management evaluation model based on the DEMATEL-ANP method. The model evaluates the overall risk of coal mine roof management by determining the main aspects and key factors. According to the analysis of literature reviews and

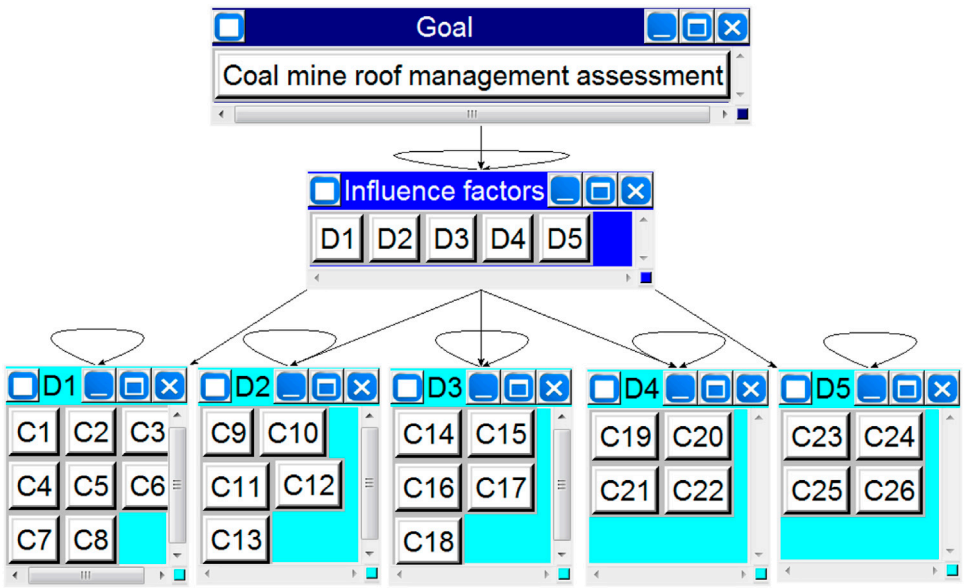


FIGURE 3 | ANP decision network model.

roof accident investigation reports and through expert interviews, 26 risk factors related to coal mine roof accidents in five categories are determined.

The DEMATEL can be used to determine the interdependence between influence dimensions and the results are shown in **Tables 10**, **11**. The centrality of site management (D_2) is the highest, which is 7.508, while the individual factor (D_3) is not different from it, which also reaches 7.163, followed by the principal responsibility (D_1), environmental change (D_5), and technology management (D_4). Because of the complex underground environment of coal mines, the site management involves the technology, individual, environment, and other aspects, which makes the underground site management closely related to other dimensions. Statistics show that the deviation of human behavior is the main cause of coal mine accidents (Chang, 2016), and people are very vulnerable to the influence of surrounding factors in the process of work, so the relationship between individual factors (D_3) and other dimensions is also very close. Although the centrality of principal responsibility (D_1), environmental change (D_5), and technology management (D_4) is slightly lower than that of the site management (D_2) and individual factors (D_3), because coal mine safety management is a systematic project, involving many factors and will have a certain impact on each other, the relationship between these three dimensions and other dimensions is also very close.

In terms of the cause degree, the order from large to small is the principal responsibility (D_1), environmental change (D_5), technology management (D_4), individual factors (D_3), and site management (D_2). The first three dimensions are positive, which

TABLE 12 | Weight of the roof safety management assessment index in coal mines.

Dimension	Dimension weight	Indicators	Local weight	Global weight
Principal responsibility	0.619	Risk management	0.284	0.176
		Safety education and training	0.038	0.023
		Leadership shift system	0.009	0.006
		Safety investment	0.277	0.172
		Legal mining	0.286	0.177
		Territorial supervision	0.003	0.002
		Supervision of superior company	0.003	0.002
		Responsibility system for safety in production	0.099	0.061
Site management	0.047	Timber setting	0.279	0.013
		Arranging construction	0.238	0.011
		Knock on top	0.185	0.009
		Work organization	0.194	0.009
		Emergency disposal	0.103	0.005
Individual factors	0.094	Violate commanding	0.171	0.016
		Work performed against regulation	0.156	0.015
		Risk Identification ability	0.238	0.022

means they have a strong impact on the other dimensions. The latter two dimensions are negative, indicating that they are easily affected by the other dimensions, which is also consistent with the aforementioned analysis. Taking the principal responsibility (D_1) as an example, the reason degree is as high as 0.821, which is related to China's national policy. China has attached great importance to safety production for a long time and has written the implementation of enterprise principal responsibility into the work safety law of the People's Republic of China, which has formed a consensus that China's government and enterprises attach great importance to the implementation of principal responsibility.

According to table 13, the order of the weight of the five dimensions is principal responsibility, technology management, site management, individual factors, and environmental impact. Among the 26 indicators, three indicators have relatively large weights, exceeding 0.1, including hidden danger investigation and treatment (0.165), safety investment (0.160), and legal mining (0.148), indicating that key attention should be paid to coal mine management. However, other influencing factors should not be ignored, such as the safety production responsibility system, operation procedures, and technical measures, which are more than 0.05, and can be used as the next level of concern. Other indicators are directly related to roof accidents, such as support setting, knocking on the top, construction arrangement, labor organization, and monitoring system, which also exceed 0.01, so the management should be strengthened. Although the weight of other factors is small, no more than 0.01, sometimes roof accidents will occur due to improper control. Therefore, these factors should be properly managed.

To sum up, the DEMATEL-ANP method can directly reflect the causal relationship between the influencing factors of coal mine roof safety management, and clarify the weight of each index. The determination of the influence relationship between factors can help coal mine managers accurately find out the root causes affecting coal mine roof safety management, and the determination of the index weight is conducive to coal mine managers quickly identifying the key factors affecting coal mine roof safety management. The combination of the two can effectively guide coal mine supervision and managers to improve the level of roof safety management.

6 CONCLUSION

Roof fall is one of the important dangers faced by workers during underground coal mining. To realize the comprehensive and scientific evaluation of roof safety management of coal enterprises, first, the evaluation index system of coal mine roof safety management is constructed by combining literature reviews, accident investigation report analyses, and expert interviews. The system includes five dimensions and 26 indexes. Second, to determine the relationship and action degree between the influencing factors of roof management, a coal mine roof safety management evaluation model is constructed based on the DEMATEL-ANP. The application of this method can effectively reduce the inconsistency in the judgment process and make the evaluation results more objective. Finally, the empirical application of the model shows that the influence degree of the dimensions on roof safety management from high to low is principal responsibility, technical management, individual factors, site management, and environmental impact, while in terms of specific indicators, it is proposed that hierarchical control should be given according to the degree of influence.

DATA AVAILABILITY STATEMENT

The original contributions presented in the study are included in the article/**Supplementary Material**, further inquiries can be directed to the corresponding author.

AUTHOR CONTRIBUTIONS

LL, resources, writing—original draft preparation, and validation; OY, writing—review and editing, and supervision. All authors have read and agreed to the published version of the manuscript.

FUNDING

This work was supported by grants from the National Natural Science Foundation of China (52074214), the Social Science Foundation of Shaanxi Province (2020M010), and Xi'an Science and Technology Program Project (21SFSF0010).

SUPPLEMENTARY MATERIAL

The Supplementary Material for this article can be found online at: https://www.frontiersin.org/articles/10.3389/feart.2022.891289/full#supplementary-material

REFERENCES

Bai, J., Feng, G., and Wang, X. (2021). Investigation on the Mechanism and Control Methods for Roof Collapse Caused by Cable Bolt Shear Rupture[J]. *Eng. Fail. Anal.* 130, 105724. doi:10.1016/j.engfailanal.2021.105724

Chang, F. (2016). Investigation on the Coal Mine Workers' Unsafe Behavior Management[J]. *Energy Energy Conservation* 1, 9–10. doi:10.16643/j.cnki.14-1360/td.2016.01.005

Chukwuma, E. C., Okonkwo, C. C., Ojediran, J. O., Anizoba, D. C., Ubah, J. I., and Nwachukwu, C. P. (2021). A GIS Based Flood Vulnerability Modelling of Anambra State Using an Integrated IVFRN-DEMATEL-ANP Model. *Heliyon* 7 (9), e08048. doi:10.1016/j.heliyon.2021.e08048

Dehdasht, G., Mohamad Zin, R., Ferwati, M., Mohammed Abdullahi, M. a., Keyvanfar, A., and McCaffer, R. (2017). DEMATEL-ANP Risk Assessment in Oil and Gas Construction Projects. *Sustainability* 9 (8), 1420. doi:10.3390/su9081420

Düzgün, H. S. B. (2005). Analysis of Roof Fall Hazards and Risk Assessment for Zonguldak Coal Basin Underground Mines[J]. *Int. J. Coal Geol.* 64 (1-2), 104–115. doi:10.1016/j.coal.2005.03.008

Fei, Y., Liu, S., Xu, Y., and Zhao, L. (2020). Failure Analysis of Thin Bedrock and Clay Roof in Underground Coal Mining: Case Study in Longdong Coal Mine. *Int. J. Geomech.* 20 (10), 04020187. doi:10.1061/(asce)gm.1943-5622.0001839

Feng, G. L, Bing-Rui, C., Ya-Xun, X., Jiang, Q., Li, P. X., and Zhang, W. (2022). Microseismic Characteristics of Rockburst Development in Deep TBM Tunnels with Alternating Soft–Hard Strata and Application to Rockburst Warning: A Case Study of the Neelum–Jhelum Hydropower Project[J]. *Tunn. Undergr. Space Technol.* 122, 104398. doi:10.1016/j.tust.2022.104398

Feng, G. L, Xia-Ting, F., Bing-Rui, C., and Yaxun, X. (2015). A Microseismic Method for Dynamic Warning of Rockburst Development Processes in Tunnels [J]. *Rock Mech. Rock Eng.* 48 (5), 2061–2076. doi:10.1007/s00603-014-0689-3

Kiani Mavi, R., and Standing, C. (2018). Critical Success Factors of Sustainable Project Management in Construction: A Fuzzy DEMATEL-ANP Approach. *J. Clean. Prod.* 194, 751–765. doi:10.1016/j.jclepro.2018.05.120

Lin, C. (2017). *Research on the Performance Assessment System of Policy-Based Financing Institutions in china[D]*. Shenyang: Liaoning University. (in Chinese).

Liu, C., Yang, Z., Gong, P., Wang, K., Zhang, X., Zhang, J., et al. (2018). Accident Analysis in Relation to Main Roof Structure when Longwall Face Advances toward a Roadway: a Case Study[J]. *Adv. Civ. Eng.*, 2018, 3810315. doi:10.1155/2018/3810315

Molinda, G. M. (2003). "Geologic Hazards and Roof Stability in Coal Mines[M]," in *US Department of Health and Human Services, Public Health Service, Centers for Disease Control and Prevention, National Institute for Occupational Safety and Health. Pittsburgh Res. Laboratory* (Washington, DC: NationalInstitute for Occupational Safety and Health).

Nilashi, M., Zakaria, R., Ibrahim, O., Majid, M. Z. A., Zin, R. M., and Farahmand, M. (2015). MCPCM: A DEMATEL-ANP-Based Multi-Criteria Decision-Making Approach to Evaluate the Critical Success Factors in Construction Projects. *Arab. J. Sci. Eng.* 40 (2), 343–361. doi:10.1007/s13369-014-1529-1

Njock, P. G. A., Shen, S.-L., Zhou, A., and Modoni, G. (2021). Artificial Neural Network Optimized by Differential Evolution for Predicting Diameters of Jet Grouted Columns. *J. Rock Mech. Geotechnical Eng.* 13 (6), 1500–1512. doi:10.1016/j.jrmge.2021.05.009

Oraee, K., Oraee, N., Goodarzi, A., and Khajehpour, P. (2016). Effect of Discontinuities Characteristics on Coal Mine Stability and Sustainability: A Rock Fall Prediction Approach. *Int. J. Min. Sci. Technol.* 26 (1), 65–70. doi:10.1016/j.ijmst.2015.11.012

Osintsev, N., Rakhmangulov, A., and Baginova, V. (2021). Evaluation of Logistic Flows in Green Supply Chains Based on the Combined Dematel-Anp Method. *FU Mech. Eng.* 19 (3), 473–498. doi:10.22190/fume210505061o

Phillipson, S. E. (2003). The Control of Coal Bed Decollement-Related Slickensides on Roof Falls in North American Late Paleozoic Coal Basins. *Int. J. coal Geol.* 53 (3), 181–195. doi:10.1016/s0166-5162(02)00196-9

Shen, S. L., Wang, Z. F., and Cheng, W. C. (2017). Estimation of Lateral Displacement Induced by Jet Grouting in Clayey Soils. *Géotechnique* 67 (7), 621–630. doi:10.1680/jgeot.16.p.159

Tubis, A., Werbińska-Wojciechowska, S., and Wroblewski, A. (2020). Risk Assessment Methods in Mining Industry-A Systematic Review. *Appl. Sci.* 10 (15), 5172. doi:10.3390/app10155172

Wang, H., Xue, S., Jiang, Y., and Deng, D. (2018). Field Investigation of a Roof Fall Accident and Large Roadway Deformation under Geologically Complex Conditions in an Underground Coal Mine[J]. *Rock Mech. Rock Eng.* 51 (17). doi:10.1007/s00603-018-1425-1

Wang, N., Ma, M., Wu, G., Liu, Y., Gong, Z., and Chen, X. (2019). Conflicts Concerning Construction Projects under the Challenge of Cleaner Production - Case Study on Government Funded Projects. *J. Clean. Prod.* 225, 664–674. doi:10.1016/j.jclepro.2019.03.315

Xiong, Y., Kong, D., Cheng, Z., Wu, G., and Zhang, Q. (2021). The Comprehensive Identification of Roof Risk in a Fully Mechanized Working Face Using the Cloud Model. *Mathematics* 9 (17), 2072. doi:10.3390/math9172072

Xu, G., Huang, Z., Fan, Z., Lu, Z., Zhang, Z., Xue, J., et al. (2021). Types, Monitoring and Prevention Technology System of Roof Disasters in Mining Face[J], *Coal Sci. Technol.*, 49 (02), 1–11. doi:10.13199/j.cnki.cst.2021.02.001

Yu, Y., Guang-Liang, F., Chang-Jie, X., Bing-Rui, C., and Bi-Tang, Z. (2022a). Quantitative Threshold of Energy Fractal Dimension for Immediate Rock-Burst Warning in Deep Tunnel: a Case Study[J]. *Lithosphere* 2022, 1699273. doi:10.2113/2022/1699273

Yu, Y., Zhao, D. C, Guang-Liang, F., Geng, D. X., and Guo, H. S. (2022b). Energy Evolution and Acoustic Emission Characteristics of Uniaxial Compression Failure of Anchored Layered Sandstone. *Front. Earth Sci.* 10, 841598. doi:10.3389/feart.2022.841598

Yasidu, U. M., Fujii, Y., Kodama, J., Fukuda, D., Maneya, G. J., Dandadzi, J., et al. (2019). Influences of Water Vapor on Roof Fall Accidents in Selected Underground Coal Mines in Malawi[J]. *Adv. Civ. Eng.*, 2019, 5350686. doi:10.1155/2019/5350686

Zhang, P., Niu, H., Zhu, H., and Li, F. (2021). Analysis of Coal Mine Safety Production Situation in China from 2019 to 2020[J], *Saf. Coal Mines*, 52 (11), 245–249. doi:10.13347/j.cnki.mkaq.2021.11.039

Zhu, L., Lv, W., Yang, P., et al. (2018). Statistical Analysis and Occurrence Laws of Coal Mine Accidents of China from 2007 to 2016[J], *Saf. Coal Mines*, 49 (07), 237–240. doi:10.13347/j.cnki.mkaq.2018.07.061

Conflict of Interest: The authors declare that the research was conducted in the absence of any commercial or financial relationships that could be construed as a potential conflict of interest.

Publisher's Note: All claims expressed in this article are solely those of the authors and do not necessarily represent those of their affiliated organizations, or those of the publisher, the editors, and the reviewers. Any product that may be evaluated in this article, or claim that may be made by its manufacturer, is not guaranteed or endorsed by the publisher.

Copyright © 2022 Li and Ouyang. This is an open-access article distributed under the terms of the Creative Commons Attribution License (CC BY). The use, distribution or reproduction in other forums is permitted, provided the original author(s) and the copyright owner(s) are credited and that the original publication in this journal is cited, in accordance with accepted academic practice. No use, distribution or reproduction is permitted which does not comply with these terms.

frontiers | Frontiers in Earth Science

ORIGINAL RESEARCH
published: 17 June 2022
doi: 10.3389/feart.2022.917561

Experimental Research and Instrument Design of Seepage Measurement in Rock and Soil Based on Heat Transfer

Xiushan Wu[1,2], *Jiamin Cui*[2], *Renyuan Tong*[3] *and Qing Li*[3]*

[1]Key Laboratory for Technology in Rural Water Management of Zhejiang Province, Hangzhou, China, [2]School of Electrical Engineering, Zhejiang University of Water Resources and Electric Power, Hangzhou, China, [3]College of Mechanical and Electrical Engineering, China Jiliang University, Hangzhou, China

Seepage in the underground rock and soil is one of the main causes of geological disasters. Precursor information for geological disasters is provided by accurately measuring the seepage flow in rock and soil, so as to provide disaster warnings in time. This article analyzes the principle of seepage measurement in rock and soil based on heat transfer, deduces the relationship between the flow rate and temperature of the fluid with a seepage sensor, designs and manufactures an entire seepage measurement sensor, and designs a seepage measurement circuit. Finally, a set of portable geotechnical seepage measuring instruments is designed. An experimental platform is designed to realize seepage flow and temperature change experiments with the seepage sensor, it is proved that the sensor can effectively measure the seepage flow for different experimental samples, the measurement range is 0.06–0.160 ml/s. Based on the measured characteristic temperature of the seepage sensor, the calculated seepage flow is obtained, the relative error between the calculated value and the measured value is within 3%.

Keywords: seepage measurement, heat transfer, small flow rate, online monitoring, geological monitoring

OPEN ACCESS

Edited by:
Fengqiang Gong,
Southeast University, China

Reviewed by:
Annan Jiang,
Dalian Maritime University, China
Luzhen Wang,
Yancheng Institute of Technology, China

***Correspondence:**
Qing Li
lq_cjlu@163.com

Specialty section:
This article was submitted to Geohazards and Georisks, a section of the journal Frontiers in Earth Science

Received: *11 April 2022*
Accepted: *31 May 2022*
Published: *17 June 2022*

Citation:
Wu X, Cui J, Tong R and Li Q (2022) Experimental Research and Instrument Design of Seepage Measurement in Rock and Soil Based on Heat Transfer. Front. Earth Sci. 10:917561. doi: 10.3389/feart.2022.917561

INTRODUCTION

China has a large land area and a complex geological environment. As changes in natural conditions and the intensity of human engineering activities increase, the number of geological disasters caused by seepage deformation and ground subsidence caused by seepage in rock and soil is increasing year by year. Seepage in rock and soil refers to the flow of water in the porous media of underground soil and rock. Seepage in rock and soil can cause the seepage deformation of rock and soil and causes ground settlement (Wang et al., 2018), which can cause geological disasters such as leakages of gates and dams, the collapse of dams, instability of foundation pit slopes, landslides, soil movement, underground equipment damage, and building collapse (Ghafoori et al., 2020). The areas prone to geological disasters in China account for about 65% of China's total land area. As of 2018, according to statistics, the country has nearly 230,000 hidden danger points of geological disasters, among which 25,000 are prone to super-large and large-scale geological disasters, which would seriously threaten the personal and economic safety of human beings.

Precursor information for the occurrence of geological disasters such as landslides and mudslides can be provided by measuring the seepage flow in rock and soil, so as to provide timely disaster

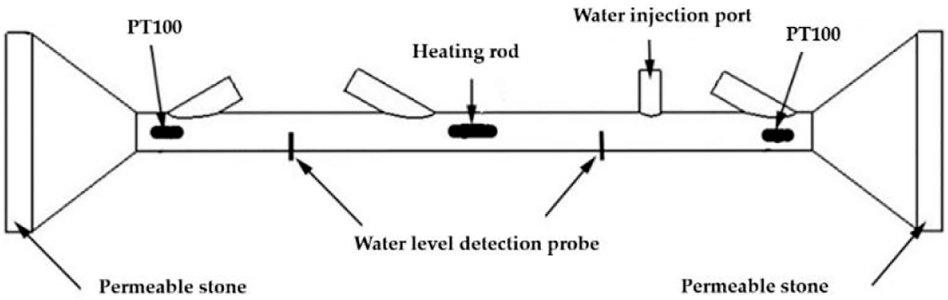


FIGURE 1 | Sensing structure of thermal seepage sensor.

warnings and to protect people's lives. The current research on seepage measurement in rock and soil mainly focuses on the rule of water movement in rock and soil and the distribution of the seepage field, so that the degree of seepage can be calculated through the thickness of the permeable foundation, the permeability coefficient, etc. (He et al., 2021). Then, the potential of geological damage occurring is determined, and reasonable anti-seepage measures are given to effectively control the impact of seepage in rock and soil on the surrounding environment. At present, the relatively mature way to achieve accurate measurements of seepage in rock and soil is to use pore water pressure gauges and piezometers to measure water pressure in order to characterize seepage in rock and soil. Commonly used methods include sonar detection (Leifer et al., 2011), optical fiber monitoring (Su et al., 2017; Chen et al., 2019; Fang et al., 2019), the resistivity method (Panthulu, 2001; Bolève et al., 2011; Dusabemariya et al., 2021), the ground penetrating radar method (Galagedara et al., 2003), the electromagnetic method (Rosenberry and Morin, 2004), etc. Seepage flow in rock and soil has the characteristics of a low velocity, small flow, and complex composition. In traditional seepage monitoring methods, a pipe for measuring the pressure and an osmometer use the pressure of pore water to obtain the seepage flow in rock and soil indirectly. Because rock and soil materials in nature are often mixtures, their compositions are also complex and uneven, and the accuracy of the measuring instruments used is often not high enough, which results in unsatisfactory measurement results; further, there is no sufficient basis for qualitative and quantitative analysis, so it is difficult to accurately obtain the true amount of seepage in rock and soil (Rosenberry et al., 2020). The ground penetrating radar method is susceptible to interference from external magnetic fields, and requires large, expensive instruments, and researchers with instrument operation experience and image analysis capabilities. The resistivity method is realized by arranging a large number of electrodes, which is characterized by low accuracy and construction difficulties. The deeper the rock and soil depths, the lower the accuracy. The sonar detection method is expensive and is currently only used in the measurement of seepage flows in deep foundation pits. The distributed optical fiber temperature measurement method can realize distributed measurement, but it also requires large and expensive instruments (Selker and Selker, 2014). Skinner and Lambert (Skinner and Lambert, 2009) proposed a novel seepage meter composed of single self-referencing thermistor with a constant heat power to measure groundwater flow velocities. The device was particularly sensitive to very slow fluid flows in the range 0.03–3 mm/s, groundwater flow velocities as low as 0.01 μm/s (0.9 mm/day) could be measured using this sensor under certain conditions. In the (Ballard, 1996), *In Situ* Permeable Flow Sensor used a thermal perturbation technique proposed to directly measure the direction and magnitude of the full three-dimensional groundwater flow velocity vector in unconsolidated, saturated, porous media. The technology is able to measure flow velocities in the range of 5×10^{-6} to 1×10^{-3} cm/s.

In this paper, theoretical analysis and experiments are closely combined, and a method for measuring seepage in rock and soil for heat transfer is proposed. Based on the self-designed thermal seepage sensor, the design of a portable rock and soil seepage measuring instrument was completed. The experiment proved the feasibility of using heat transfer to measure seepage in rock and soil, and the temperature characteristic values with regards to the relationship between temperature differences and seepage flow rates were obtained. The temperature difference method can directly measure seepage flows in rock and soil, and can determine the seepage direction; the sensor can be buried in underground rock and soil for long-term measurement.

PRINCIPLE OF SEEPAGE MEASUREMENT BASED ON HEAT TRANSFER

The designed thermal seepage sensor is based on the principle of convection heat transfer in order to measure the temperature difference between the two ends of the sensor, so as to obtain the seepage flow in rock and soil. Among them, the seepage flow value in rock and soil is obtained by determining the heat exchange between the built-in heating source of the sensor and the fluid in the thin tube of the sensor (Rakesh et al., 2020).

The seepage sensor in rock and soil developed in this paper is shown in **Figure 1**. In this structure, a PT100 platinum resistance temperature measuring probe with metal sleeve protection is placed at both ends of the thin tube, and a ceramic heating rod is placed in the middle of the thin tube. One of the PT100 platinum resistance temperature measurement probes measures the initial

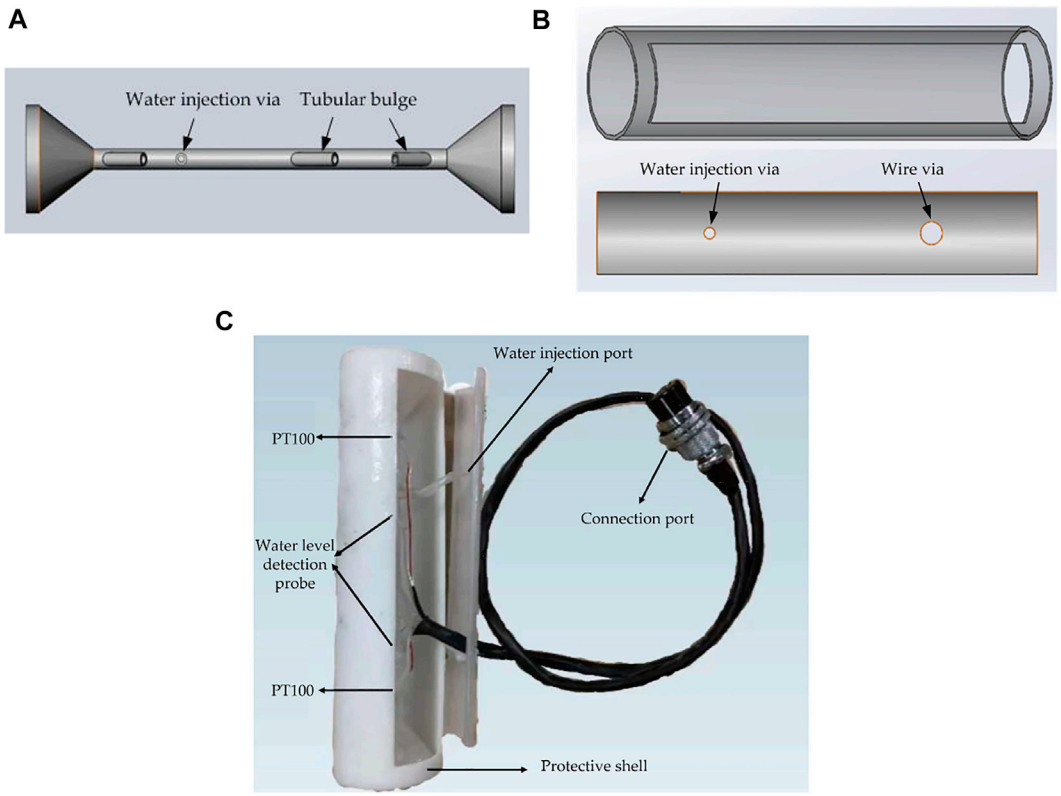


FIGURE 2 | Seepage sensor **(A)** the structure of the sensor; **(B)** Seepage meter protective shell and packaging cover; **(C)** Physical image of seepage meter sensor.

temperature of the inflow end of the seepage liquid, and the other probe measures the temperature of the fluid flowing through the other end of the thin tube after it is heated. There is a temperature difference between the two probes due to the action of the heating rod. When the fluid flows through the heating rod, the heat taken away is directly related to the flow rate of the fluid. When the heating power of the heating rod is constant, the larger the flow in the thin round tube of the sensor, the smaller the temperature difference measured by the two platinum resistance probes, and vice versa (Shen et al., 2015; Solder et al., 2016).

According to the heat transfer principle, the relationship between the heat Q taken away by the fluid per unit time, the temperature difference ΔT between the heating rod and the fluid, and the flow velocity v of the fluid can be expressed by the following formula:

$$\frac{Q}{\Delta T} = k_1 + k_2 (\rho v)^{k_3} \tag{1}$$

In the formula, ρ represents the density of the fluid; k_1, k_2, and k_3 are constants in the same fluid.

If the cross section of the thin round tube structure of the sensor is A, its mass flow rate is $q_m = \rho v A$. When measuring the seepage in rock and soil, the ceramic heating rod with the resistance of R_j is heated by the current of I_j to heat the fluid in the thin tube. After a period of time, it will reach an equilibrium state. At this time, the heat generated by the heating rod per unit time is the same as the heat carried away by the surrounding fluid by the heating rod, that is, $Q=I_j^2 R_j^2$, so there is a functional relationship between the mass flow q_m and $Q/\triangle T$, which can be expressed by the following formula (Munaf et al., 1993):

$$q_m = f\left[\frac{I_j^2 R_j^2}{\Delta T}\right] \tag{2}$$

From equation (Ghafoori et al., 2020), it can be concluded that the seepage flow can be obtained by measuring temperature difference ΔT of the fluid at both ends of the thin round tube through the sensor when the current I_j flowing through the heating rod is constant.

Temperature changes can affect the physical and chemical parameters of water and soil, thereby affecting the distribution of seepage fields in the soil. The parameters closely related to seepage field and temperature field in rock and soil include porosity, specific heat capacity, heat conduction, thermal conductivity, and other parameters. With the increase of temperature, the viscosity of water decreases and the permeability coefficient increases. Due to the small power of the heating rod in this paper, the effect of temperature change on the seepage was ignored in the experiments and measurements (Huang et al., 2021).

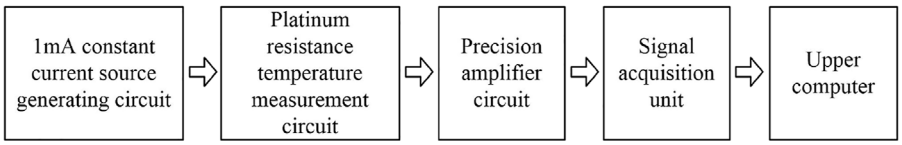


FIGURE 3 | Block diagram of the temperature measurement principle.

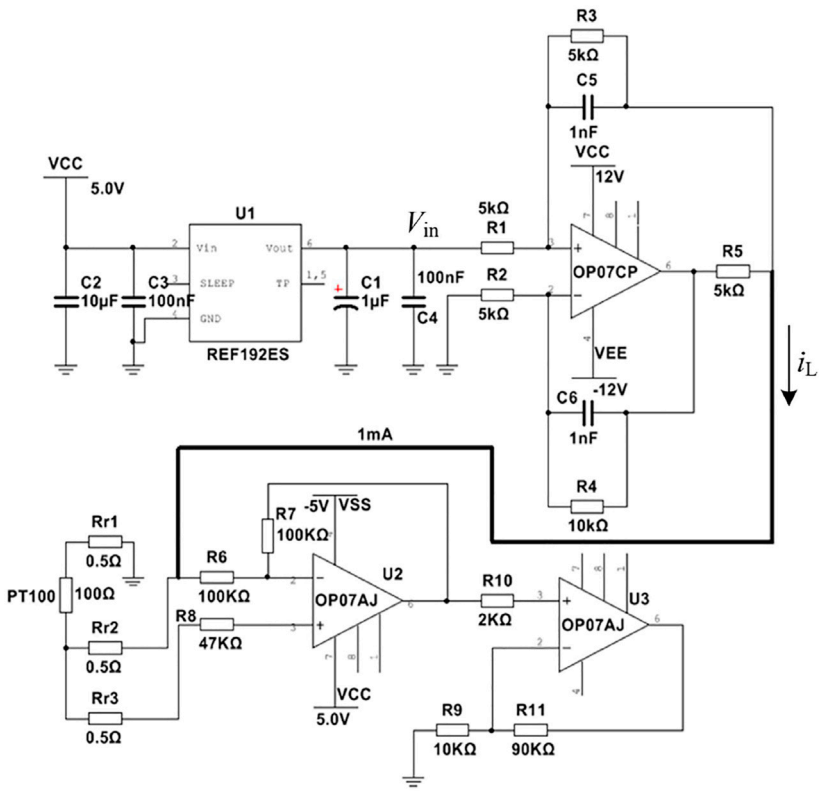


FIGURE 4 | The platinum resistance temperature measurement circuit.

SENSOR DESIGN

Structural Design of Thermal Seepage Sensor

The sensor structure shown in **Figure 1** mainly includes a water filtration structure made of permeable stone, a heating rod, and a PT100 temperature measurement instrument (Aranzabal et al., 2019). A funnel-shaped water collection device was designed at both ends of the sensor to increase the flow in the thin tube. When the seepage in rock and soil flows into the sensor from left to right or from right to left, it first passes through the upstream PT100 platinum resistance temperature sensor to collect the initial water temperature flowing into the thin tube, and then the seepage flows through the heating rod to be heated. The fluid then flows through the downstream PT100 platinum resistance temperature sensor. The temperature measured downstream is the water temperature after it is heated by the heating rod. At this time, if the heating power of the heating rod is kept constant, the greater the seepage flow rate in the thin round tube, the smaller the temperature difference measured by the upstream and downstream platinum resistance PT100 sensors, and vice versa.

At present, distributed optical fiber temperature measurement technology is commonly used in seepage flow measurement in rock and soil. The temperature sensitivity of Brillouin method based on distributed optical fiber temperature measurement technology in practical projects is about ±4°C, and which in the laboratory is generally less than ±2°C, Raman method can reach ±0.5°C. However, the temperature measurement accuracy of the platinum resistance PT100 sensors can reach ±0.1°C. The system

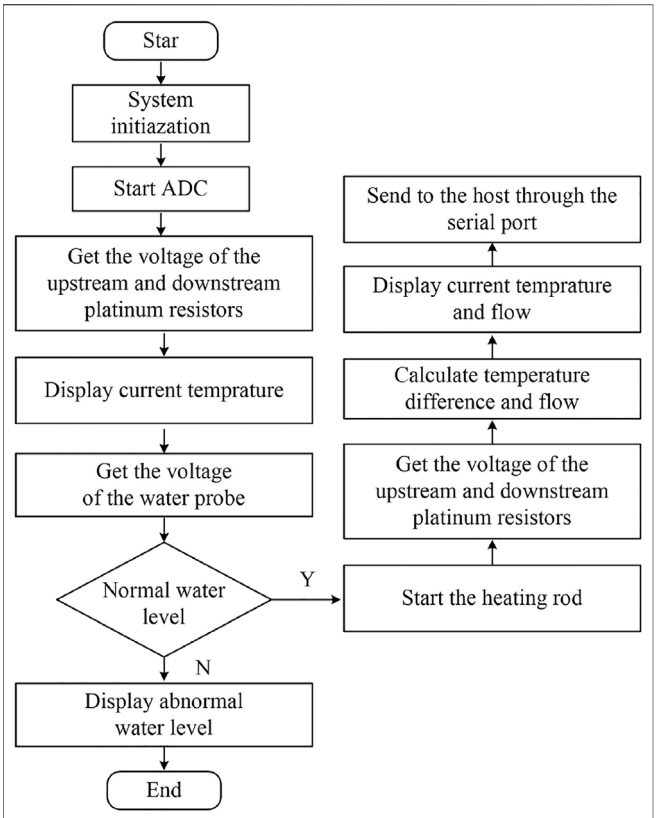


FIGURE 5 | System program flow chart.

experimental tests are all measured at room temperature, the influence of the ambient temperature on its measurement can be ignored since the temperature difference between the two PT100 is measured.

Because seepage flows in rock and soil are very small, the smaller the diameter of the thin tube, the better the effect. An alumina ceramic heating rod with many advantages was used in the design, the power of the heating rod is 5 W under the power supply voltage of 5 V. It has been proved by experiments that the liquid in the thin tube will not produce air bubbles under this power value, so that it has little influence on the measurement results.

Principle of Water Level Detection

In **Figure 1**, two thin probes were designed and inserted perpendicular to the inner wall of the thin tube of the fluid meter. If the thin tube is filled with water, the water resistance between the two probes is a fixed value; if the thin tube is not filled with water, the resistance between the two probes becomes larger. During the actual experimental measurements, when the thin tube was filled with water, the resistance between the two probes was about 70 kΩ. A 70 kΩ matching resistance was selected in series with the two ends of the water level detection probe, and power was applied to both ends to measure the voltage on the matching resistance. The water level in the capillary could be easily determined.

Selection of Permeable Materials

The rock—soil seepage measurement sensor based on heat transfer designed in this paper needs to be placed in the rock and soil for actual applied measurements. Because the fine particles present in seepage in rock and soil can easily block the sensor, the sensor needs permeable materials to filter the seepage. At present, the commonly used water-permeable materials include fibrous materials, activated carbon, diatomaceous earth, porous ceramics, etc. The sensor needs to be placed in the rock and soil when used, so the water-permeable material needs to have good mechanical properties and stable chemical properties. Compared with other water-permeable materials such as fibrous materials, activated carbon, etc., porous ceramic materials have many advantages; for example, they can be used in high temperature, high pressure, acid, alkali, and organic environments; their pore structures and porosity can be controlled; their service life is long. The product has

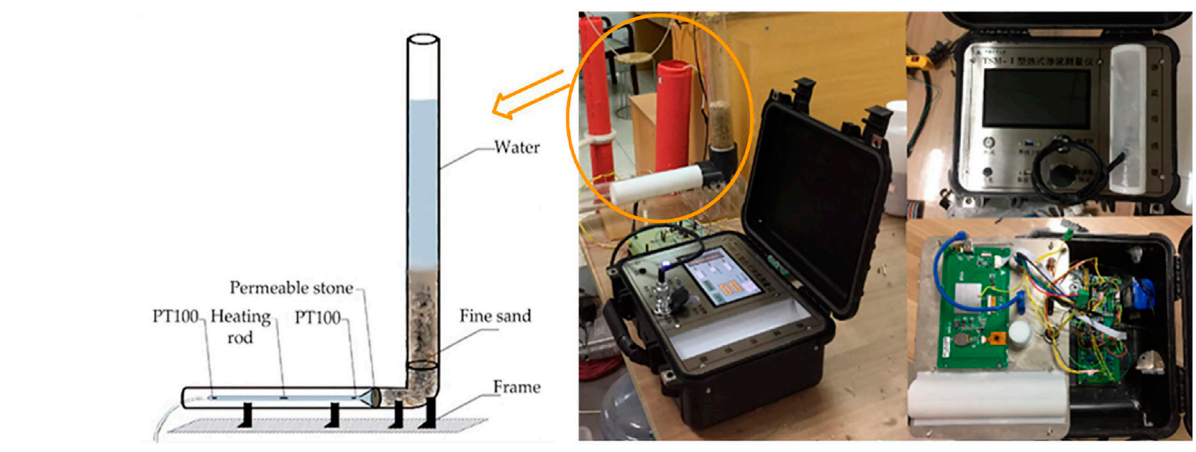


FIGURE 6 | The overall structure of the portable seepage meter.

TABLE 1 | Reference values of permeability coefficients of different diameter particles.

Formation lithology	Particle diameter (mm)	Permeability coefficient (m/d)
Clay	0.001–0.002	<0.005
Clay	0.002–0.005	0.1–0.5
Powder	0.005–0.075	0.5–1.0
Fine sand	0.075–0.25	1.0–5.0
Moderate sand	0.25–0.5	5.0–20
Coarse sand	0.5–2	20–50
Fine Gravel	2–3	50–100

good regeneration performance, so porous ceramic materials were used as the water-permeable material in this design.

Structural Design of Seepage Meter

Because the sensor, heating rod, and porous ceramics are placed on the seepage sensor, high mechanical strength, and strict waterproofing are required. After repeated experiments, the structure shown in **Figure 2A** and 3D printing were used to form one piece to achieve a precise size and good waterproof performance. 3D printing uses transparent resin raw materials, which were convenient for observing the position and seepage of the temperature probe and heating rod in the thin tube during the experiment. The diameters of the funnel on both sides are 40 cm, and the diameter of the thin tube in the middle is 6 cm. There are tubular protrusions on the thin tube. In order to place the sensor in them easily and to waterproof them, the cylindrical housing and back cover of the sensor were designed at the same time, and the measuring structure was also placed in it by 3D printing. Its appearance is shown in **Figure 2B**. A physical map of the seepage sensor is shown in **Figure 2C**.

The platinum resistance temperature probe, heating rod, and water level measurement probe were installed and wrapped with a heat-shrinkable tube. At the same time, they were filled with silica gel for waterproofing. In order to facilitate the observation of seepage, the structure of the sensor shell and the thin round tube funnel were made from translucent materials.

THERMAL SEEPAGE SENSOR SIGNAL ACQUISITION AND PROCESSING SYSTEM

Thermal Seepage Sensor Temperature Measurement Circuit Design

The principle of the temperature measurement is shown in **Figure 3**. The 1 mA constant current source generating circuit provides a constant current for the platinum resistance temperature measurement circuit. The temperature measurement circuit converts the resistance change in the platinum resistance into a voltage value change, which is then amplified by a precision amplifier circuit. The signal acquisition unit converts the collected temperature voltage value into a digital quantity and sends it to the microprocessor by A/D converter,

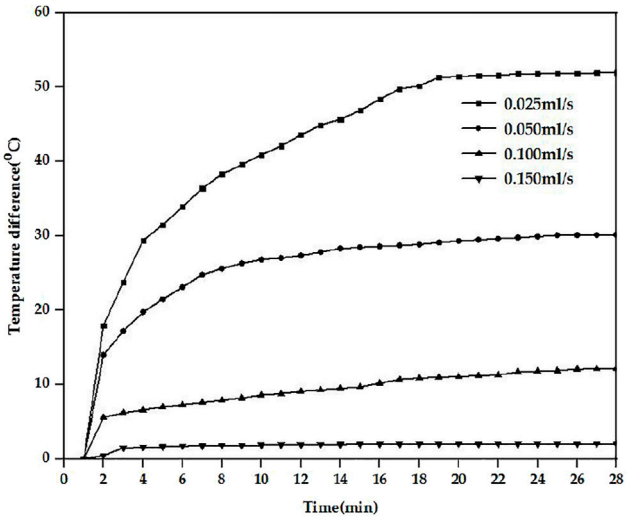


FIGURE 7 | The relationship between different flow rates and corresponding temperature differences.

and finally, the calculated temperature value is sent by the microprocessor through the serial port to the upper computer. The platinum resistance temperature measurement circuit is shown in **Figure 4**.

The REF192ES in **Figure 4** is a voltage reference chip used to generate a 2.5 V reference voltage. The 1 mA constant current source generation circuit uses the Howland operational amplifier current source structure. The constant current source circuit uses a low-noise and high-precision OP07CP operational amplifier, which uses a dual power supply. In this design, R_1=R_2=5 kΩ, R_3=R_5=5kΩ, R_4=10kΩ; in order to ensure the accuracy of the constant current source, the resistance selects a BWL-EE type resistor with an accuracy of 0.1% and a temperature drift of 5 ppm. The Howland operational amplifier current source structure can be obtained:

$$i_L = \frac{2}{R_1} V_{\text{in}} \tag{3}$$

Signal Acquisition Unit Design

The signal acquisition unit of the thermal seepage sensor is responsible for the acquisition of measurement process information and the transmission of data. Taking into account the needs of the measurement system, cost, power consumption, and other factors, it adopts STMicroelectronics' STM32F103 series 32-bit MCU STM32F103ZET6 chip and its internal with an ARM Cortex-M3 core, which can use registers and library files for programming and which is very simple and easy to transplant. The signal acquisition program mainly completes the functions of water level detection, voltage value detection at both ends of the platinum resistor, temperature calculation, heating rod on–off control, flow calculation, results display and data transmission. The system program flow chart is shown in **Figure 5**.

TABLE 2 | Measured temperature characteristics of seepage sensor under different seepage flows.

Seepage flow (mL/s)	Experiment start temperature (/°C)	Tt (/°C)	Heating time (min)
0.025	21.8	52.0	22
0.050	21.8	32.0	20
0.100	21.8	13.0	18
0.150	21.8	2.0	15

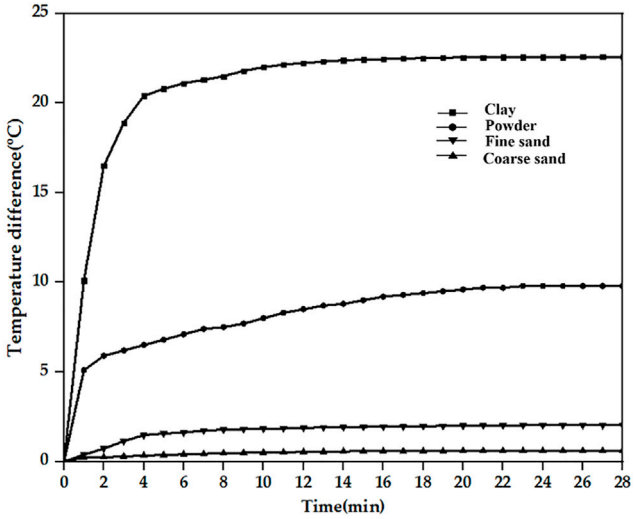


FIGURE 8 | Corresponding temperature difference curves of different diameter particles.

Portable Geotechnical Seepage Measuring Instrument

For the portable application of the instrument, the designed and implemented thermal seepage measuring instrument is shown in **Figure 6**. It uses a 10.2-inch portable instrument waterproof box. The power supply, measurement circuit and control circuit are all placed inside the box. The panel is designed with various function buttons, a touch screen and a sensor card slot. The realized portable thermal seepage measuring instrument is powerful, the VGUS graphical design interface is easy to use, the VGUS built-in virtual serial screen can be used to easily design the display interface, display controls, touch functions, etc., and it also has a curve control to display the data as a curve.

In order to obtain the real situation of seepage in rock and soil, and to simulate the conditions and environment of seepage in rock and soil more realistically, the experimental platform built shown in **Figure 6** was designed. It was connected by a transparent tube with a length of 110 cm and a diameter of 40 cm, an elbow with a DN40 caliber, and a transparent tube with a horizontal length of 50 cm and the diameter of the thin tube in the middle is 6 cm. The bottom plate adopted thick acrylic for counterweight. The schematic diagram of the experimental device in the circle is shown on the left in **Figure 6**. The horizontally placed transparent tube was the thin tube funnel part of the thermal percolation meter. Because the seepage direction was determined, the experimental device in the figure only used unidirectional water-permeable ceramics. The joints of the whole device were sealed and waterproofed with waterproof glue (Ma et al., 2014).

EXPERIMENTAL MEASUREMENT

Experiment on the Relationship Between Flow Rate and Temperature Change

Soil structures in different regions are different, and compositions of rock and soil are complex. Most rock and soil materials are composed of coarse sand or loose deposits with large particle diameters. According to Engineering Classification Standard of Soil (GB/T50145-2007), the particle groups of soil are divided according to diameter. The particle size and permeability coefficient reference values of various soils are shown in **Table 1**. The experiments were carried out using clay, powder, fine sand, moderate sand and coarse sand. The diameter of the clay was about 0.003 mm, and the permeability coefficient was 0.3 m/d, the diameter of powder was about 0.006 mm, and the permeability coefficient was 0.8 m/d, the water flow velocity in the experiment was about 4–5 drops/s; the diameter of fine sand particles was about 0.1 mm, and the permeability coefficient was 3 m/d, the flow

TABLE 3 | Temperature characteristics and seepage flow under different geotechnical conditions.

Geotechnical type	Particle samples diameter (mm)	Experiment start temperature (/°C)	Tt (°C)	Measured seepage flow (ml/s)	Calculated seepage flow (ml/s)	Relative error (%)
Clay	0.003	21.80	22.5	0.070	0.072	2.79
Powder	0.006	21.80	9.8	0.112	0.113	1.39
Fine sand	0.100	21.80	2.6	0.143	0.147	2.98
Coarse sand	1.000	21.80	0.6	0.158	0.159	0.61

rate is about 17–18 drops/s. In the above process, that each drop of water was about 0.05 ml based on calibration and repeated experiments (Abdullah et al., 2020).

The restrictor valve was used to adjust the flow rate of water to simulate the seepage flows of different rock and soil materials in the experiment. Therefore, a restrictor valve was installed at the water outlet end of the thin tube of the test device. By adjusting the restrictor valve, the flow rate of water droplets can be controlled per second: 1 drop, 2 drops, 4 drops per second, etc. After repeated experiments under the same conditions, the volume of each drop of water could be considered constant, so the volume of 100 drops of water flowing out of the infusion device measured by a graduated cylinder was about 5 ml, and the volume of each drop of water under the same experimental conditions was about 0.05 ml. **Figure 7** shows the temperature difference curves measured at different flow rates.

It can be seen from the **Figure 7** that under different flow rate conditions, the temperature differences changed the most from about 0–4 min, the temperature differences for the PT100 at both ends of the seepage meter continued to increase, and the temperature differences changed slowly after 4 min. When the seepage flow rate was 0.025 ml/s, the temperature difference tended to remain unchanged at about 52°C after 20 min. When the seepage flow rate was 0.05 ml/s, the temperature difference tended to remain unchanged at about 30°C after 20 min. When the seepage flow rate was 0.10 ml/s, the temperature difference stabilized after 20 min at 12°C. When the seepage flow rate was 0.15 ml/s, the temperature difference stabilized after 4 min at 2°C.

In the experiments, if the temperature difference change rate within 5 min was less than 0.1°C/min, the temperature could be called the characteristic value T_t of the sample. **Table 2** shows the data of the temperature characteristics and heating times under different flow rates for the silty sand, it can be determined that as the flow rate increased, T_t was decreased linearly, and the heating time became shorter. T_t and the seepage flow rate can be polynomially fitted to obtain the relational expression, where the ordinate y represents the temperature of the temperature difference of the value in degrees Celsius (°C), and the abscissa x represents the percolation flow rate in milliliters per second (ml/s), the goodness of fit of the curve is 0.988.

$$y = -27.81 \ln(x) - 50.67 \quad (4)$$

Seepage Measurement Experiment

To carry out the seepage measurement experiment conducted in this study, put equal volumes of clay, powder, fine sand, and coarse sand into a round pipe with a permeable ceramic backing, and measure its actual penetration according to the constant head permeability test. Add an equal volume of water, measure the temperature difference determined by the platinum resistance at the upstream and downstream ends of the thin round tube, and obtain the output characteristic curves of the clay, powder, fine sand and coarse sand shown in **Figure 8**.

It can be concluded from **Figure 8** that for the different rock soils used in the experiments, the temperature differences rose significantly in the first 4 min, and then increased slowly until they stabilized. After the system was powered on, the heating rod began to heat, and the temperature differences measured by the upstream and downstream PT100 platinum resistors increased rapidly, and after a period of time, the temperature differences increased slowly until they stabilized.

The characteristic temperature measured by the experiment is brought into the formula (Leifer et al., 2011), and the flow rate can be obtained, **Table 3** shows the data of temperature characteristics, the measured seepage flow and the calculated seepage flow under different geotechnical condition, the relative error is defined as the absolute value of the calculated seepage flow minus the measured value divided by the measured value, and which are all within 3%.

CONCLUSION

Based on the basic principles of heat transfer in seepage measurement, a thermal seepage sensor was proposed, and the fabrication has been completed. The following conclusions were drawn based on the theoretical analysis and experimental results.

(1) The structure of the sensor is composed of a thin tube in the middle and two funnels connected at both ends of the thin tube. The small end of the funnel is fixed to the end of the thin tube and communicates with the thin tube. The heating rod is controlled inside the thin tube, the two ends of the thin tube are equipped with temperature sensors, and the probe needle is arranged in the middle of the thin tube.

(2) An experimental platform for thermal seepage measurement was built, and experiments on flow velocity and temperature changes, seepage meter calibration experiments, and rock and soil seepage measurement experiments were carried out. The temperature characteristic values of the silty sand with seepage flow of 0.025 ml/s, 0.050 ml/s, 0.100 ml/s and 0.150 ml/s are obtained by experiments, and measured temperature characteristic values are 52.0, 30.0, 12.0 and 2.0°C, respectively. Formulas for the characteristic values of seepage flow and temperature are presented.

(3) Based on the same experimental method, the temperature characteristic values and seepage flow of clay, powder, fine sand, and coarse sand were measured. The seepage flow rate under different sample conditions were calculated based on the relationship formula between seepage flow rate and temperature characteristic, the errors between the experimental value and the calculated value are within 3%.

Our future work will focus on the study of the influence on the seepage flow rate under different heating power conditions is extreme for the same sample. Secondly, we will expand the types of experimental samples to obtain more abundant experimental data.

DATA AVAILABILITY STATEMENT

The original contributions presented in the study are included in the article/supplementary material, further inquiries can be directed to the corresponding author.

AUTHOR CONTRIBUTIONS

XW wrote the manuscript. JC and RT performed the experiments. QL proposed the idea and guided the experiments and writing.

FUNDING

The research was supported by The National Key Research and Development Program of China (2017YFC0804604), and open fund of Key Laboratory for Technology in Rural Water Management of Zhejiang Province.

REFERENCES

Abdullah, T. O., Ali, S. S., Al-Ansari, N. A., Knutsson, S., and Laue, J. (2020). Magnitude and Direction of Groundwater Seepage Velocity in Different Soil and Rock Materials. *Eng* 12, 242–253. doi:10.4236/eng.2020.124020

Aranzabal, N., Martos, J., Steger, H., Blum, P., and Soret, J. (2019). Temperature Measurements along a Vertical Borehole Heat Exchanger: a Method Comparison. *Renew. Energy* 143, 1247–1258. doi:10.1016/j.renene.2019.05.092

Bolève, A., Janod, F., Revil, A., Lafon, A., and Fry, J. J. (2011). Localization and Guantification of Leakages in Dams Using Time-lapse Self-potential Measurements Associated with Salt Tracer Injection. *J. Hydrol.* 403, 242–252. doi:10.1016/j.jhydrol.2011.04.008

Ballard, S. (1996). The *In Situ* Permeable Flow Sensor: A Ground-Water Flow Velocity Meter. *Groundwater* 34, 231–240. doi:10.1111/j.1745-6584.1996.tb01883.x

Chen, J., Xiong, F., Zheng, J., Ge, Q., and Cheng, F. (2019). Calibration Experiment for Seepage Monitoring Using Fiber Bragg Grating Hydrothermal Cycling Integration System. *Geotech. Test. J.* 42, 2017017. doi:10.1520/gtj20170179

Dusabemariya, C., Jiang, F., Qian, W., Faruwa, A. R., Bagaragaza, R., and Ali, M. (2021). Water Seepage Detection Using Resistivity Method Around a Pumped Storage Power Station in China. *J. Appl. Geophys.* 188, 104320. doi:10.1016/j.jappgeo.2021.104320

Fang, X., Xiong, F., and Chen, J. (2019). An Experimental Study on Fiber Bragg Grating-point Heat Source Integration System for Seepage Monitoring. *IEEE Sens. J.* 19, 12346. doi:10.1109/jsen.2019.2937155

Galagedara, L. W., Parkin, G. W., and Redman, J. D. (2003). An Analysis of the Ground-Penetrating Radar Direct Ground Wave Method for Soil Water Content Measurement. *Hydrol. Process.* 17, 3615–3628. doi:10.1002/hyp.1351

Ghafoori, Y., Maček, M., Vidmar, A., Říha, J., and Kryžanowski, A. (2020). Analysis of Seepage in a Laboratory Scaled Model Using Passive Optical Fiber Distributed Temperature Sensor. *Water* 12, 367. doi:10.3390/w12020367

He, F., Chen, J., and Xiong, F. (2021). Comparison of the Seepage Monitoring Results between Saturated and Unsaturated State Using Point Heat Source Method. *KSCE J. Civ. Eng.* 25, 4567. doi:10.1007/s12205-021-1635-z

Huang, Y.-H., Yang, S.-Q., and Teng, S.-Y. (2021). Temperature Dependence of the Permeability of Sandstone under Loading and Unloading Conditions of Confining Pressure. *Math. Geosci.* 53, 551–570. doi:10.1007/s11004-020-09860-7

Leifer, I., Luyendyk, B. P., and Culling, D. (2011). Active Multibeam Sonar-derived Bubble Plume Fluxes and Dynamics. *J. Acoust. Soc. Am.* 129, 2653. doi:10.1121/1.3588852

Ma, D., Miao, X. X., Jiang, G. H., Bai, H. B., and Chen, Z. Q. (2014). An Experimental Investigation of Permeability Measurement of Water Flow in Crushed Rocks. *Transp. Porous Med.* 105, 571–595. doi:10.1007/s11242-014-0385-5

Munaf, D., Wineman, A. S., Rajagopal, K. R., and Lee, D. W. (1993). A Boundary Value Problem in Groundwater Motion Analysis - Comparison of Predictions Based on Darcy's Law and the Continuum Theory of Mixtures. *Math. Models Methods Appl. Sci.* 03, 231–248. doi:10.1142/s0218202593000138

Panthulu, T. V., Krishnaiah, C., and Shirke, J. M. (2001). Detection of Seepage Paths in Earth Dams Using Self-Potential and Electrical Resistivity Methods. *Eng. Geol.* 59, 281–295. doi:10.1016/S0013-7952(00)00082-X

Rakesh, N. S., Ahmed, A., Joseph, J., Aouti, R. S., and Ananthasuresh, G. K. (2020). Analysis of Heat Paths in Dual-Probe-Heat-Pulse Soil-Moisture Sensors for Improved Performance. *Sens. Actuat. A-Phys.* 318, 112520. doi:10.1016/j.sna.2020.112520

Rosenberry, D. O., Duque, C., and Lee, D. R. (2020). History and Evolution of Seepage Meters for Quantifying Flow between Groundwater and Surface Water: Part 1 - Freshwater Settings. *Earth-Science Rev.* 204, 103167. doi:10.1016/j.earscirev.2020.103167

Rosenberry, D. O., and Morin, R. H. (2004). Use of an Electromagnetic Seepage Meter to Investigate Temporal Variability in Lake Seepage. *Groundwater* 42, 68–77. doi:10.1111/j.1745-6584.2004.tb02451.x

Selker, F., and Selker, J. S. (2014). Flume Testing of Underwater Seep Detection Using Temperature Sensing on or Just below the Surface of Sand or Gravel Sediments. *Water Resour. Res.* 50, 4530–4534. doi:10.1002/2014wr015257

Shen, X., Zhang, M., Zhang, J., and Yang, H. (2015). Development on Measuring Devicefor Seepage Coefficient of Super-size Coarse-Grained Soil. *J. Coast. Res.* 73, 375–379. doi:10.2112/si73-066.1

Skinner, A. J., and Lambert, M. F. (2009). Evaluation of a Warm-Thermistor Flow Sensor for Use in Automatic Seepage Meters. *IEEE Sensors J.* 9, 1058–1067. doi:10.1109/jsen.2009.2024056

Solder, J. E., Gilmore, T. E., Genereux, D. P., and Solomon, D. K. (2016). A Tube Seepage Meter for *In Situ* Measurement of Seepage Rate and Groundwater Sampling. *Groundwater* 54, 588–595. doi:10.1111/gwat.12388

Su, H., Tian, S., Kang, Y., Xie, W., and Chen, J. (2017). Monitoring Water Seepage Velocity in Dikes Using Distributed Optical Fiber Temperature Sensors. *Automation Constr.* 76, 71–84. doi:10.1016/j.autcon.2017.01.013

Wang, S., Liu, D., and Wang, Z. (2018). Feature Analysis and Control Method of Seepage Deformation of Rock and Soil in Port and Coast. *J. Coast. Res.* 83, 436–441. doi:10.2112/SI83-073.1

Conflict of Interest: The authors declare that the research was conducted in the absence of any commercial or financial relationships that could be construed as a potential conflict of interest.

Publisher's Note: All claims expressed in this article are solely those of the authors and do not necessarily represent those of their affiliated organizations, or those of the publisher, the editors and the reviewers. Any product that may be evaluated in this article, or claim that may be made by its manufacturer, is not guaranteed or endorsed by the publisher.

Copyright © 2022 Wu, Cui, Tong and Li. This is an open-access article distributed under the terms of the Creative Commons Attribution License (CC BY). The use, distribution or reproduction in other forums is permitted, provided the original author(s) and the copyright owner(s) are credited and that the original publication in this journal is cited, in accordance with accepted academic practice. No use, distribution or reproduction is permitted which does not comply with these terms.

frontiers | Frontiers in Earth Science

ORIGINAL RESEARCH
published: 17 June 2022
doi: 10.3389/feart.2022.937893

Stability Analysis on the Steeply-Inclined Small-Angle Layered Surrounding Rock Masses at the Upstream High Sidewall of a Large-Span Cavern

Chong-Lin Jian[1], Ding-Ping Xu[2], Yang-Yi Zhou[3], Dong-Fang Chen[4], Shao-Wu Zhou[5], Lian-Xing Hu[5], Chong Wu[6] and Sen-Lin Jiang[6]*

[1]China Three Gorges Construction Engineering Corporation, Chengdu, China, [2]State Key Laboratory of Geomechanics and Geotechnical Engineering, Institute of Rock and Soil Mechanics, Chinese Academy of Sciences, Wuhan, China, [3]Key Laboratory of Ministry of Education on Safe Mining of Deep Metal Mines, Northeastern University, Shenyang, China, [4]Hubei Province Key Laboratory Processing of Mineral Resources and Environment, Wuhan University of Technology, Wuhan, China, [5]China Three Gorges Corporation, Wuhan, China, [6]Sinohydro Bureau 6 Co. Ltd, Shenyang, China

OPEN ACCESS

Edited by:
Shibing Huang,
Wuhan University of Science and Technology, China

Reviewed by:
Ang Li,
Chang'an University, China
Gang Wang,
Shaoxing University, China
Qiang Zhang,
China University of Mining and Technology, China

***Correspondence:**
Ding-Ping Xu
dpxu@whrsm.ac.cn

Specialty section:
This article was submitted to Geohazards and Georisks, a section of the journal Frontiers in Earth Science

Received: *06 May 2022*
Accepted: *24 May 2022*
Published: *17 June 2022*

Citation:
Jian C-L, Xu D-P, Zhou Y-Y, Chen D-F, Zhou S-W, Hu L-X, Wu C and Jiang S-L (2022) Stability Analysis on the Steeply-Inclined Small-Angle Layered Surrounding Rock Masses at the Upstream High Sidewall of a Large-Span Cavern. Front. Earth Sci. 10:937893. doi: 10.3389/feart.2022.937893

The underground powerhouse of China's Wudongde hydropower station is one of the world's underground powerhouses with the largest span and height. Because the underground powerhouse is all located in steeply-inclined layered rock masses, and the bedding plane strike of the rock mass has a small angle with the axis of the main caverns, there is a serious risk of high sidewall instability. According to the basic principles of the structurally-controlled concept, the mechanical properties of bedding planes and other discontinuities are largely attributed to this problem. A thorough investigation was conducted into the Wudongde underground powerhouse throughout the excavation process to clarify the possible mechanisms behind these failures and to realize the dynamic adjustment of construction. First, the geological conditions and mechanical properties of the rock masses in the study area were introduced in detail. The stability of the right bank underground powerhouse's surrounding layered rock mass was then investigated using a discontinuum-based numerical method. Special attention was paid to the excavation-induced failure mechanisms of the steeply-inclined small-angle layered rock masses at the upstream high sidewall. The results show that the failure of steeply-inclined small-angle layered surrounding rock masses presents significant three-stage characteristics, i.e., 1) rock plate forms due to the unloading opening of the bedding plane; 2) rock plate cracks due to bending; and 3) rock plate buckles or slides due to crack penetration. Based on the understanding of the deformation and failure mechanisms of steeply-inclined small-angle layered rock masses, the excavation sequence needs to be optimized according to local geological conditions. In practice, it is vital to insist on the principles of excavation by thin layers and finish all the supports before the next-step excavation.

Keywords: steeply-inclined small-angle layered rock mass, large-span high-sidewall underground powerhouse, bedding plane, stability, discrete element method

INTRODUCTION

As part of one of China's largest multipurpose water conservation projects, a hydropower station is being constructed downstream of the Jinsha River at Wudongde town. The Wudongde hydropower station consists of three parts: an underground powerhouse, a dam, and a navigation facility. The underground powerhouse covers both sides of the river in the downstream direction. The Wudongde underground powerhouse has the main powerhouse (333 m long, 30.5–32.5 m wide, and 89.8 m high), a transformation chamber (270 m × 18.5 m × 35 m), and three surge shafts (53 m in diameter, 100 m in height) (**Figure 1**). The main powerhouse is the largest underground main powerhouse in the hydropower industry in terms of height and span. The large-span high-sidewall underground powerhouse is excavated in steeply-inclined layered rock masses, with the bedding plane strike of the rock mass having a small angle (less than 30°) with the main powerhouse's axis. Therefore, knowing the mechanical response of steeply-inclined small-angle layered rock masses under excavation unloading is crucial to the success of the Wudongde underground powerhouse construction.

The excavation-induced response of rock masses is considered a stability problem of surrounding rock masses in underground engineering. A large amount of excavation generally induces substantial disturbance to the surrounding rock mass, leading to different kinds of engineering geological problems. Under low-moderate geostress, structurally-controlled instabilities are the primary form (Fekete and Diederichs, 2013), while stress-related issues are often encountered in deep-buried caverns (Diederichs et al., 2004; Martin and Christiansson, 2009; Cai and Kaiser, 2014). The rock mass structure; however, is undoubtedly one of the most salient factors influencing the stability of a large underground powerhouse.

Bedding planes, like other structural plane systems, introduce significant anisotropy both in deformation pattern as well as strength (Fortsakis et al., 2012). The places with more displacements and failures are closely related to the spatial relationship between cavern axes and bedding plane strikes (Zhou Y.-Y. et al., 2016; Zhou YY. et al., 2016). For example, typical geomechanical issues of underground powerhouses excavated in steeply-inclined layered rock masses are primarily the excessive deformation of high straight sidewalls. Failure mechanisms of steeply-inclined small-angle layered surrounding rock masses, however, become more complicated than massive, almost isotropic rock masses due to the presence of bedding planes. Combined failure types, such as tensile fractures through rocks plus shearing along bedding planes, are more commonly observed. Therefore, the bedding plane-induced discontinuous and anisotropic nature (Singh, 1973; Amadei and Pan, 1992; Marinos and Hoek, 2000; Xiao and Wang, 2002; Zhang and Liu, 2002; ZhanG et al., 2004; Wu et al., 2006; Zhang, 2006; Peng et al., 2007; Zhu et al., 2009; Fan and Wang, 2011) is critical to analyzing the stability of layered surrounding rock masses. This also indicates that successful pertinent support for layered surrounding rock masses should be used as an improved means to eliminate the negative impact of steeply-inclined bedding planes. In such a case, it is an important issue to evaluate the stability of steeply-inclined layered surrounding rock masses with or without support during the construction of a large-span high-sidewall underground powerhouse within these rock masses.

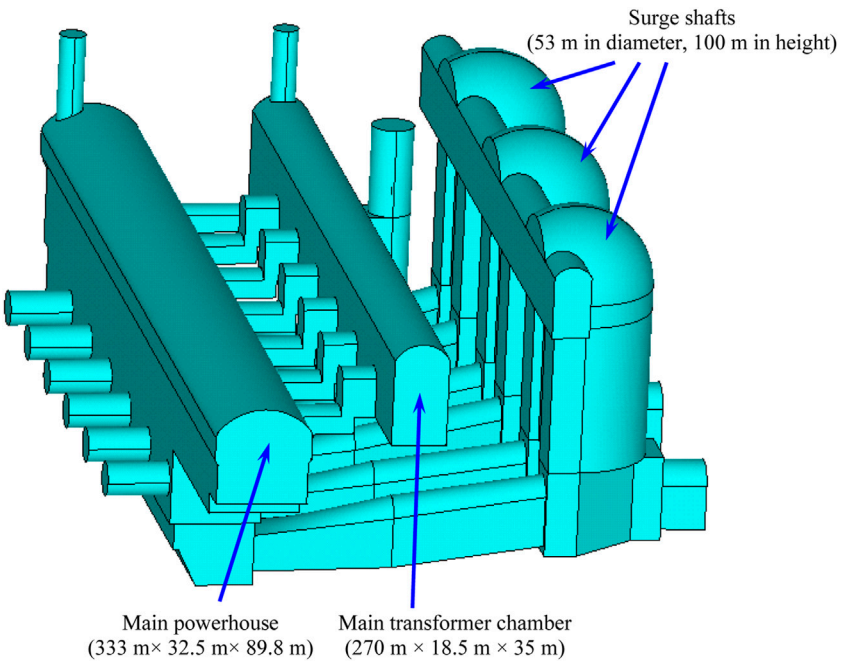


FIGURE 1 | Overview of the Wudongde underground powerhouse.

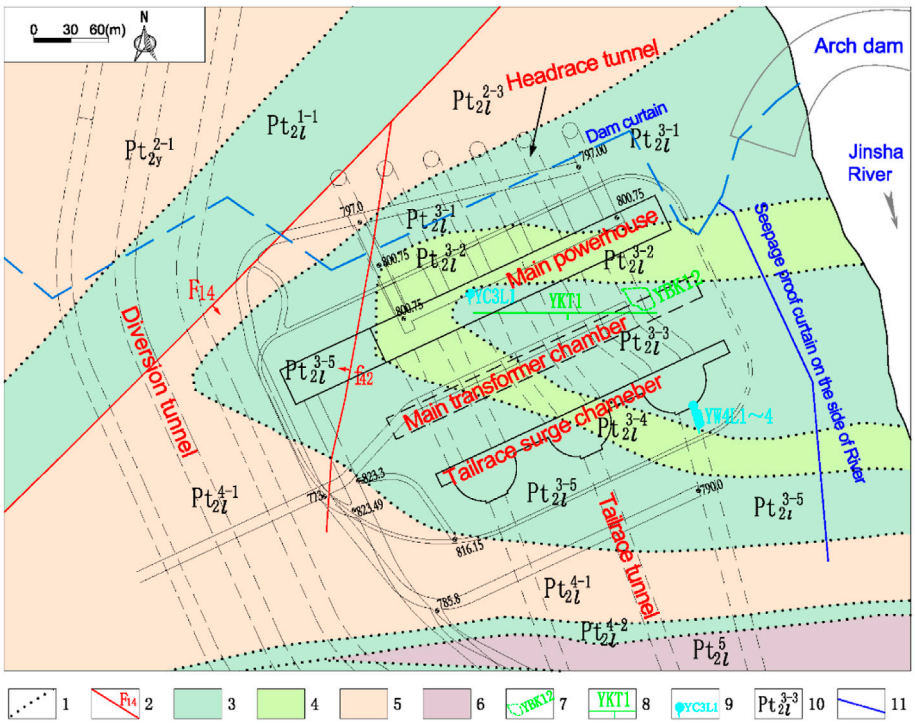


FIGURE 2 | Geological map of the underground powerhouse on the right bank at EL800 m (1) stratigraphic boundary, (2) fault, (3) moderate karst rock formation, (4) weak karst rock formation, (5) slight karst rock formation, (6) non-karst rock formation, (7) karst cave, (8) corrosion discontinuity, (9) spring, (10) strata code, (11) curtain.

In this paper, the stability of the steeply-inclined small-angle layered surrounding rock masses at the upstream high sidewall of the Wudongde right main powerhouse is investigated using the discrete element method (DEM). The study mainly focuses on the excavation-induced failure mechanisms of the steeply-inclined small-angle layered surrounding rock masses at the upstream high sidewall between the seven# and eight# generator sections. Some suggestions for optimizing the excavation scheme and supporting measures are proposed. It is hoped that this case study will be of practical significance to other large-scale excavations with similar geological conditions.

ENGINEERING BACKGROUND

Geological Setting

The geological map of the Wudongde underground powerhouse on the right bank at an elevation of 850 m is demonstrated in **Figure 2**. The whole underground powerhouse on the right bank is situated in steeply-dipping layered carbonate rock masses belonging to the meso-proterozoic eon (*Pt*), most of which are moderately thick (bed thickness of 30–50 cm) to the thick (bed thickness of 50–100 cm). Slight metamorphism has been experienced in these areas, leading to some low-level metamorphic rocks in specific strata. According to the differences between lithological and engineering properties, the whole geological formation can be divided into several subsections. Here the symbol Pt_{2l}^{x-y} is used to indicate one of these subsections, where 2L stands for the Luoxue formation, x means the xth member, and y means the yth submember. The surrounding rock mass of the underground powerhouse is mainly thick layered limestone and marble (Pt_{2l}^{3-1}), thickly layered dolostone and moderately thick limestone (Pt_{2l}^{3-2}), thick to moderately thick limestone (Pt_{2l}^{3-3}), thick dolostone (Pt_{2l}^{3-4}), and moderately thick limestone and marble (Pt_{2l}^{3-5}) (Niu et al.,



FIGURE 3 | f_{42} fault in the main powerhouse of the right bank.

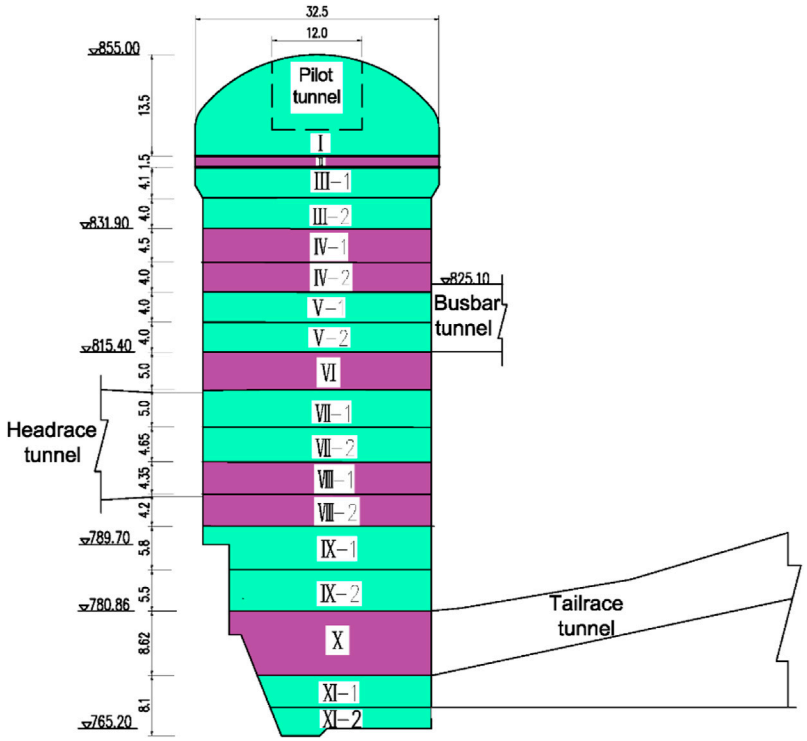


FIGURE 4 | Schematic view of the excavation sequence for the right bank powerhouse (Unit: m).

2011). The bedding plane strikes 260–280° and is inclined downstream with dip angles ranging from 75° to 85°.

There are no large-scale faults in the areas of underground powerhouse. Only five small-scale faults of several meters in length and several centimeters in width have been identified. There is a fold whose axial plane is also steeply dipping and oblique to cavern axes in the area of right underground powerhouse. The core stratum of the fold is made up of Pt_{2l}^{3-3}. The orientations of the two flanks are 164°∠75° and (15–26)°∠(76–88)°, respectively. One large-scale fracture and one small fault are identified in the powerhouse (**Figure 3**). Fractures are sparse on the whole, being primarily trended in the SN direction and inclined in the west with a medium dip angle. Surrounding rock masses are generally unweathered, with some small karst caves and dissolution fractures in local areas. The thickness of the overburden strata on the underground powerhouse of the right bank is 220–390 m, and the horizontal buried depth is 120–140 m. The measured *in situ* stress magnitudes of the maximum and minimum principal stresses are 4.1–9.4 MPa and 3.0–5.0 MPa, respectively. From the measured *in situ* stress magnitudes, it is reasonably judged that the underground powerhouse area is a low-stress zone.

Excavation, Support, and Monitoring Plan

The powerhouse on the right bank was constructed in January 2013 and is designed to be excavated in 11 layers (**Figure 4**). Systematic supports for the powerhouse are comprised of rock bolts, prestressed cables, shotcrete with wire mesh, etc. Detailed support parameters are summarized in **Table 1**. At the beginning of June 2015, the excavation of Layer V and systematic support were finished.

For the underground powerhouse, eight systematic monitoring cross-sections are chosen, including the central line of each generator as well as the main and auxiliary erection bays. The primary monitoring items are the displacements of surrounding rocks at different depths, stresses and forces in supports, and crane girders deformations. The pre-embedded multipoint extensometers are arranged around a typical monitoring cross-section in the roof, crane girder, and sidewalls on both sides. Rock bolt stress meters and anchor cable dynamometers are fixed to rock bolts or cables to record variations of stresses or forces, which are installed after excavation. The layout of the monitoring devices around a cross-section is shown in **Figure 5**.

CHARACTERISTICS OF LAYERED ROCK MASSES

The macroscopic behavior of a layered rock mass is generally determined by its components, that is, interlayered rocks and bedding planes. The mechanical behavior tests of layered or foliated rocks (Nasseri et al., 2003; Hakala et al., 2007; Cho et al., 2012) show that the directionality of deformation and strength are the most significant characteristics of these rocks. It is generally accepted that deformation perpendicular to the

TABLE 1 | Systematic support parameters for the main powerhouse.

	Range	Parameters
Rockbolts	Above EL789.7 m	Φ32 mm, L = 6 m/9 m@1.5 m × 1.5 m, fully grouted and installed alternately. In addition, 9 m rockbolt is pretensioned with T = 50 kN
	Below EL789.7 m	Φ28 mm, L = 6 m@1.5 m × 1.5 m, fully grouted
Prestressed anchor cables	Above reinforced concrete crane girder	L = 20–45 m@4.5 m × 4.5 m, T = 2000 kN
	Between reinforced concrete crane girder and EL789.7 m	L = 22–25 m@4.5 m × 4.5 m, T = 2000 kN
Shotcrete with wire mesh	All	Total thickness 15 cm, most of which is mixed with steel fibers

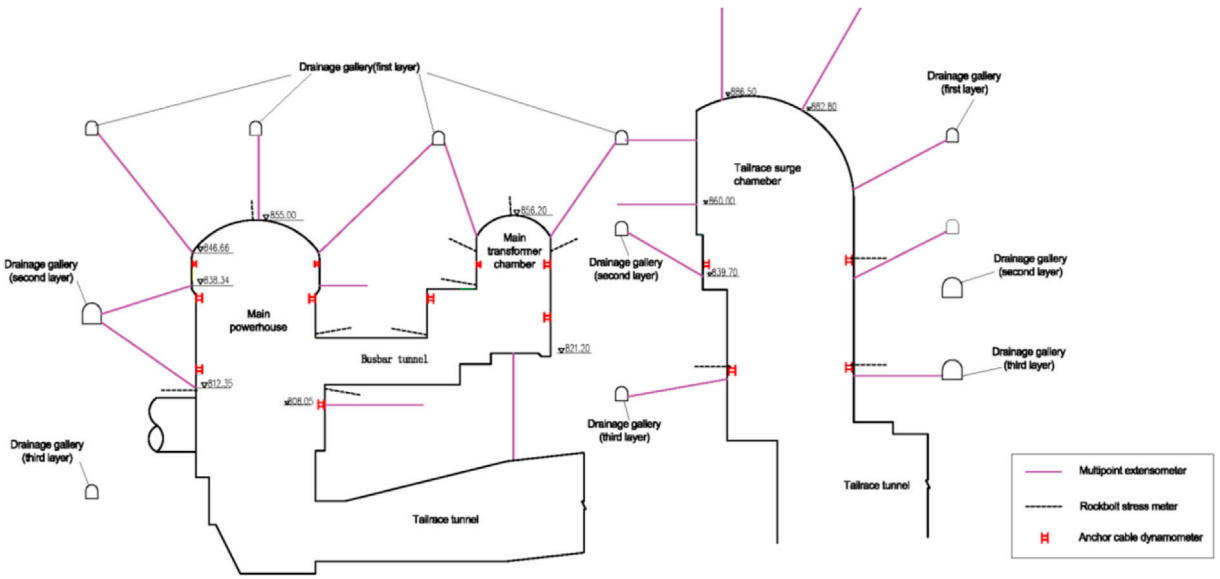


FIGURE 5 | Layout of the monitoring devices instrumented for one of the cross-sections of the underground powerhouse.

bedding plane is more pronounced than that parallel to the bedding plane. Therefore, greater deformation in the field is more likely to occur in the direction perpendicular to the bedding plane. In addition, normal joint stiffness is sensitive to changes in normal stress (Bandis et al., 1983) and decreases nonlinearly when unloaded. As a result, the bedding plane deformation can reach an acceleration phase gradually. When exposed to or experiencing environmental changes, various bedding planes, especially those with clay fill, may exhibit time-dependent behavior. Natural surface conditions of bedding planes typically exhibit mineral coatings and suffer from various degrees of weathering, which can significantly reduce bond strength compared with unweathered and cemented discontinuities. Based on these observations, it is reasonable to believe that layered rock mass provides the possibility of more deformation perpendicular to bedding and bedding plane opening when the surrounding constraints are suddenly reduced to a negligible level (Xu et al., 2017). Moreover, the spatial continuity of bedding planes provides another possibility that, once part of the bedding plane is kinematically admissible, it tends to move as a whole, resulting in an expansion of the fracture area. The last special feature of this rock mass that needs to be noted is that the plate shape of each layer makes it easier to bend than other massive or jointed rock masses (Zhou et al., 2017). Therefore, proper consideration of the distribution laws and mechanical properties of bedding planes in numerical simulations is the premise of reasonable analysis based on field geological analysis.

DISCONTINUUM ANALYSIS OF THE FAILURE MECHANISMS OF STEEPLY-INCLINED SMALL-ANGLE LAYERED SURROUNDING ROCK MASSES

Model and Parameters

In light of the anisotropic and discontinuous nature of layered rock masses, the excavation of the right bank powerhouse is simulated using the discrete element software 3DEC (Itasca Consulting Group and Inc, 2007). According to previous descriptions, the bedding plane strike of the steeply-inclined layered rock mass of the upstream sidewall between the seven[#]

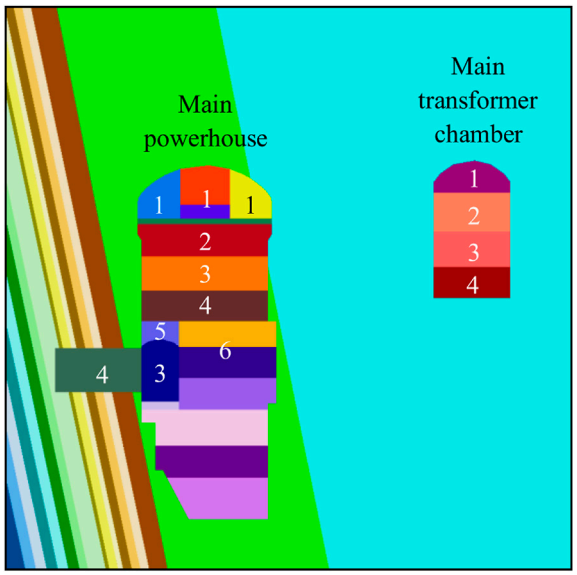


FIGURE 6 | Simulated excavation sequence for the main powerhouse and main transformer chamber.

and eight# generator sections has a small angle with the main powerhouse's axis. Furthermore, the bedding planes are inclined toward the interior of the powerhouse, which is unfavorable to the stability of the sidewalls after the excavation. Considering these conditions, all the rock mass of the seven# generator unit and part of the rock mass of the eight# generator unit are incorporated into the numerical model, and the stability of surrounding rock masses in these areas is particularly concerned in the simulation.

The numerical model includes the mountain, surrounding rock masses, and caverns (**Figure 6**). The total length of the model along the cavern axis is 82 m, and the maximum buried depth of the top arch of the main powerhouse is 286 m. To simulate the structure of steeply-inclined small-angle layered surrounding rock masses at the upstream sidewall, the rock masses are divided into layers with a thickness of 2 m. The angle between the bedding plane strike and the cavern axis is 14°, and the dip angle is 79°. There are 638,857 nodes and 257,041 elements in the model.

The *in situ* stress field is generated according to the investigation reports provided by relevant geological departments. Self-weight stress is applied as the maximum principal stress. The lateral pressure coefficients along and normal to the cavern axis are 0.8 and 0.6, respectively. The upper surface of the model is a free boundary, while normal constraints are applied to the rest of the surfaces. The internal unbalanced forces of rocks and bedding planes are calculated to equilibrium using the elastic constitutive model, and the equilibrium convergence value is 1×10^{-4}. The input parameters of the model are shown in **Table 2**.

TABLE 3 | Input parameters for the excavation simulation.

Intact rock		Bedding plane	
Density (kg/m^3)	2,740	Normal stiffness (GPa/m)	5.0
Bulk modulus (GPa)	8.4	Shear stiffness (GPa/m)	1.0
Shear modulus (GPa)	5.0	Cohesion (MPa)	0.1
Cohesion (MPa)	8.0	Friction angle (°)	35
Internal friction angle (°)	45	Dilation angle (°)	2
Dilation angle (°)	5	Residual cohesion (MPa)	0.05
Tensile strength (MPa)	1.0	Residual friction angle (°)	20
		Tensile strength (kPa)	1.0

In the numerical simulations, the Mohr–Coulomb strength criterion is used for rocks, and the Coulomb strength criterion with residual strengths is adopted for bedding planes. Mechanical parameters of rock masses provided by geological departments are employed as input parameters (**Table 3**). Cable elements are used to simulate the reinforcement effects of the pertinent supports (systematic rock bolts and anchor cables) on the steeply-inclined small-angle layered surrounding rock masses at the upstream sidewall under supported condition. The input parameters for the systematic support are demonstrated in **Table 4**.

Protocol

The simulation is performed under supported and non-supported conditions. After excavation, the system supports are applied to the upstream sidewall in the corresponding elevation ranges, and the excavation sequence is simulated by the actual excavation, as shown in **Figure 6**. The support forms are demonstrated in **Figure 7**. Because the tailrace surge chambers are far from the main powerhouse, their excavation influence on the stability of the surrounding rock masses of the main powerhouse can be negligible. Therefore, the numerical model does not include the excavations of the tailrace surge chambers. The equilibrium convergence value is 1×10^{-4}. The specific steps are shown as follows.

Step 1: Layers I of the main powerhouse and the main transformer chamber are excavated.
Step 2: Layers II and III of the main powerhouse and Layer II of the main transformer chamber are excavated, as well as the busbar tunnel and the outlet shaft.
Step 3: Layer IV of the main powerhouse, Layer III of the main transformer chamber, and the L3 tunnel are excavated.

TABLE 2 | Input parameters for generating the *in situ* stress field.

Intact rock			Bedding plane	
Density (kg/m^3)	Deformation modulus (GPa)	Poisson's ratio	Normal stiffness (GPa/m)	Shear stiffness (GPa/m)
2,740	20.0	0.26	10.0	2.0

TABLE 4 | Input parameters for systematic supports.

Systematic rockbolt		Anchor cable	
Length (m)	6, 9	Length (m)	22,23,25
Cross-sectional area ($\times10^{-4}$ m^2)	8.042	Cross-sectional area ($\times10^{-4}$ m^2)	19.6
Young's modulus (GPa)	200	Young's modulus (GPa)	200
Bond stiffness of grout ($\times10^{9}$ N/m^2)	0.5	Bond stiffness of grout ($\times10^{9}$ N/m^2)	1.0
Bond strength of grout ($\times10^{6}$ N/m)	2.38	Bond strength of grout ($\times10^{6}$ N/m)	8.3
Compressive yield strength ($\times10^{9}$ N)	1.0	Compressive yield strength ($\times10^{9}$ N)	1.0
Tensile yield strength ($\times10^{5}$ N)	1.33	Tensile yield strength ($\times10^{6}$ N)	1.6
Pre-tension force (kN)	50 (L = 9 m)	Pre-tension force (kN)	1800, 2,200

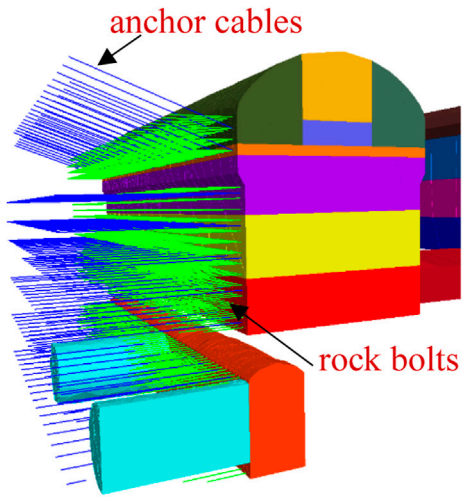


FIGURE 7 | Simulated systematic support for the main powerhouse.

Step 4: Layer V of the main powerhouse, Layer IV of the main transformer chamber, and the headrace tunnels are excavated.

Step 5: The top layer of the L3 tunnel of the main powerhouse is removed.

Step 6: Layers VI and VII of the main powerhouse are excavated.

L3 tunnel (9 m × 11–15 m) is pre-excavated in the lower part of the main powerhouse to excavate the headrace tunnel. After excavating Layer V, the thickness of the overburdened rocks on the top of the L3 tunnel is 2.7–7.6 m.

Results and Discussion

Under non-supported conditions, the deformation fields of surrounding rock masses and failure characteristics of bedding planes after Steps one to four are shown in **Figures 8**,**9**.

Based on the distribution characteristics of deformation of surrounding rock masses, after step 1, the largest deformation occurs in the central line of the top arch and the floor (**Figure 8**). The location of maximum deformation gradually transfers to the steeply-inclined bedding planes and occurs on the bedding planes of the upstream sidewall after Steps two to four as the bench excavation proceeds. After Step 4, the largest deformation reaches 32 mm.

As shown in **Figure 9**, the tensile failure mode of bedding planes near the excavation boundary is mainly the unloading and opening of bedding planes. Furthermore, tensile failure occurs in the intact rocks, producing tensile cracks. The failure mode of the bedding planes inside the surrounding rock masses is dominated by shear failure, and the maximum depth where shear failure takes place gradually increases with excavation. The failure of bedding planes extends to the interior of the surrounding rock masses, activating internal bedding planes, causing certain shear slip in the surrounding rock masses, and also increasing the slipping area of a single bedding plane. This indicates that the influence of steeply-inclined small-angle layered rock masses on the stability of the main powerhouse's upstream sidewall gradually increases with excavation.

Table 5 shows the maximum deformation of surrounding rock masses and their corresponding locations under supported and non-supported conditions. Compared with that under non-supported conditions, systematic support can reduce the maximum deformation of surrounding rock masses to some extent. In particular, when large deformations such as unloading openings and shear slip along bedding planes occur, the supports of systematic rock bolts can fully reinforce surface rocks, while anchor cables can inhibit the deformation of the interior bedding planes, as demonstrated in **Figure 10**. The main differences between rock bolts and anchor cables are their effective anchor length and loading capacity. Rock bolts are usually shorter than anchor cables, and have lower ultimate tensile strength and smaller pretension value. Therefore anchor cables can restrain failure of discontinuities deep inside rock mass, while rock bolts are mainly used to reinforce shallow rock mass.

Tables 6,**7** demonstrate the failure indices of rock masses after each step in sequential excavations under non-supported conditions. Shear failure hardly ever happens inside the rocks, and almost all failures are exhibited as tensile failure under low-stress conditions. By comparing failure indices of surrounding rock masses after each step under the two conditions, it is concluded that systematic supports are effective in restraining tensile failure, while the inhibition effects on shear failures are limited. The reason is that systematic supports can bear axial tension and provide partial shear-resisting capacity. However, software built-in cable element mainly considers the axial force characteristics of support but cannot take the shear-

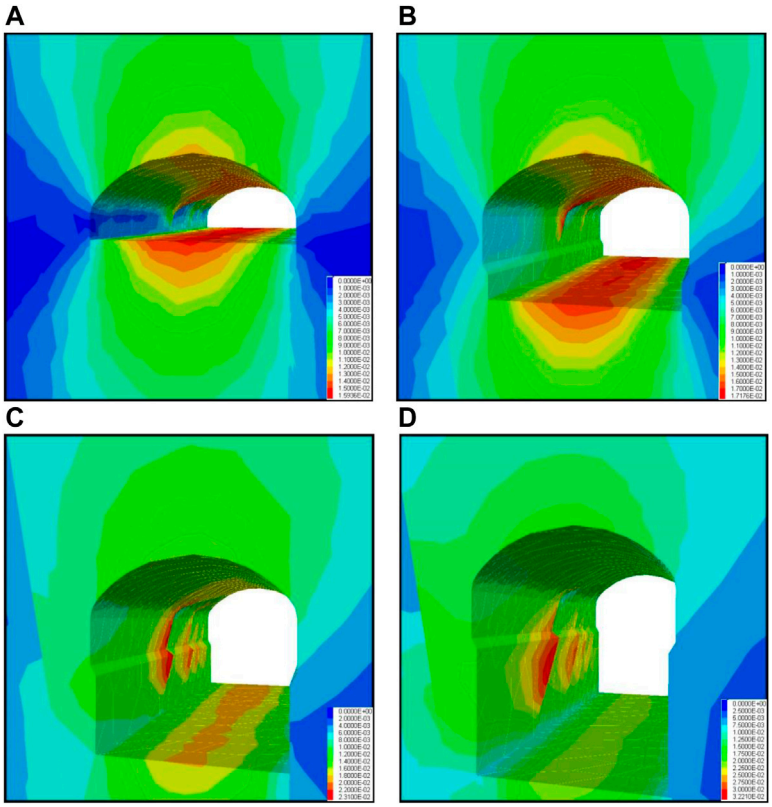


FIGURE 8 | Deformation distribution of surrounding rock masses at the upstream sidewall after sequential excavations under nonsupported conditions (Unit: m). **(A)** step 1, **(B)** step 2, **(C)** step 3, and **(D)** step 4.

resisting function into account. This explains the differences between numerical simulation and actual situations. For the sake of inhibiting their separation during construction, the rock bolts are designed to be approximately normal to the bedding planes. However, by theoretical and experimental results in the literature (Ge and Liu, 1988; Pellet and Egger, 1996), rock bolts strictly normal to the bedding planes cannot sufficiently play their roles in shear-resisting. Therefore, in actual situations, rock bolts, and cables are combined to inhibit the deformation and failure in the direction normal to bedding planes. Since systematic rock bolts are usually installed evenly around the tunnel, in different positions the angle between rock bolt and bedding plane must be different. In order to make full use of rock bolts and anchor cables in the case of sub-vertical bedding plane reinforcement, angles between bedding plane and these structural elements should be adjusted locally. More specifically, at the high sidewalls where bedding planes are more likely to separate or slip, the structural elements should form an optimized angle to the local bedding plane, depending on the predicted failure mode. If tensile failure is anticipated, reinforcements should be as perpendicular to bedding plane as possible, while for the slip failure case, an angle which can fully mobilize the shear resistance of rock bolts should be considered.

The influences of steeply-inclined small-angle layered surrounding rock masses on the upstream sidewall's stability are mainly reflected by the mechanical responses of original bedding planes in rock masses based on the numerical simulations. Either obvious deformation or failures on the surface and inside rock masses appear at bedding planes. Failed zones of bedding planes gradually increase with the sequential excavation. The characteristics of steeply-inclined small-angle layered surrounding rock masses are that, due to the unloading of normal stresses after excavation together with the anisotropy of rock mass deformation, the deformation of high sidewalls of the rock masses under this condition is more obvious than that of rock masses under other orientation conditions. This is particularly unacceptable for construction safety. Systematic support shows significant inhibiting effects on the separation and failure of bedding planes. However, to fully use the shear-resisting capacity of systematic supports, it is required to further investigate and optimize the layout of rock bolts and cables.

Figure 11 shows the schematic view of the failure mechanisms of the steeply-inclined small-angle layered surrounding rock masses in the right main powerhouse. As the profile of the main powerhouse is high and narrow, with a height of 90 m and a ratio of height to the span of close to three,

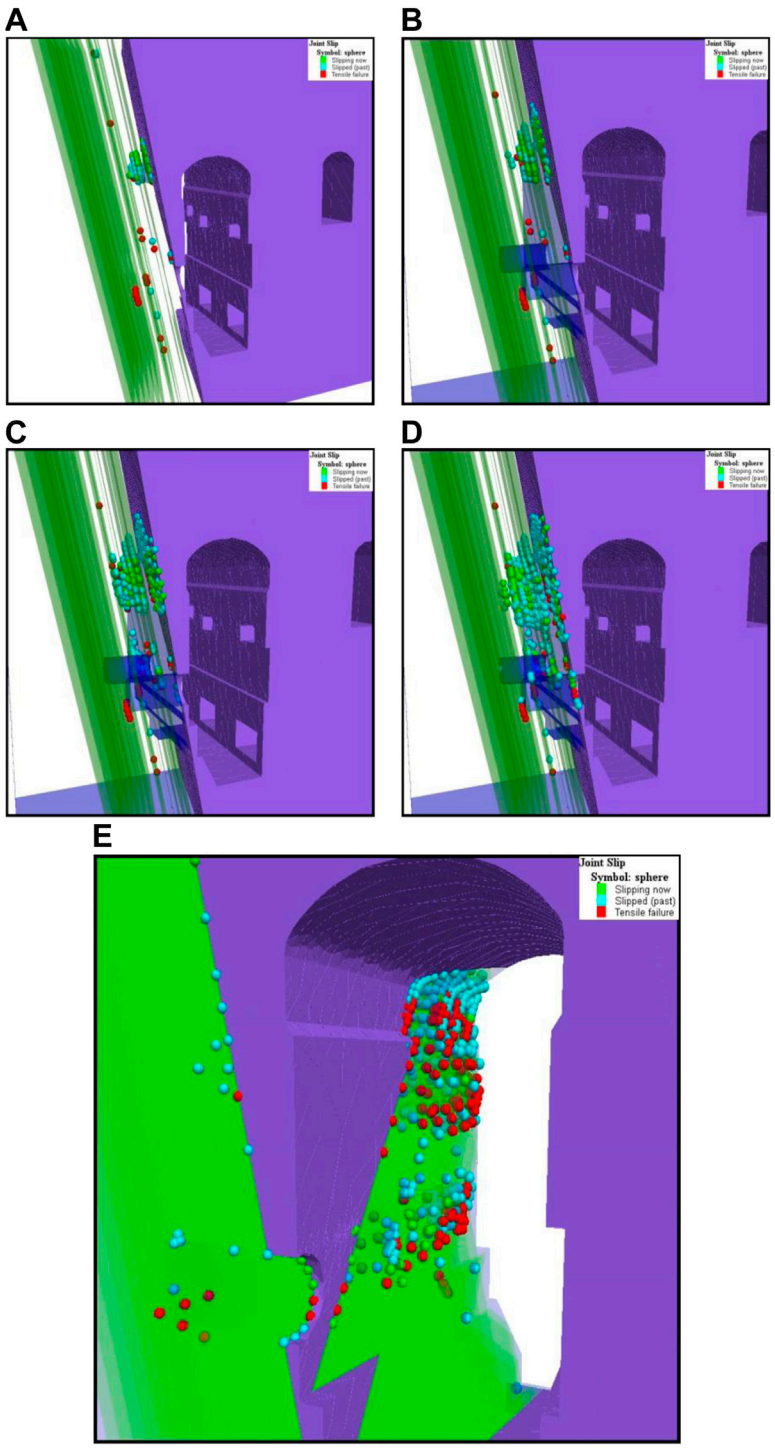


FIGURE 9 | Failure characteristics of surrounding rocks on upstream sidewall after sequential excavations under unsupported condition. **(A)** step 1, **(B)** step 2, **(C)** step 3, **(D)** step 4, **(E)** front view after step 4. Red ball-tensile failure, blue ball-shear failure in previous steps, green ball-current shear failure.

the unexcavated rock masses can provide sufficient support for both sidewalls, thus constraining the deformation of the sidewalls. Layered excavation gradually reduces the supporting effect of the remaining rock masses. The failure of steeply-inclined small-angle layered surrounding rock masses presents significant three-stage characteristics during these excavations. 1) Bedding planes open due to large-scale excavation unloading, which makes the steeply-inclined small-

TABLE 5 | Summary of the maximum deformation under supported and nonsupported conditions.

Step	Without supports (mm)	With supports (mm)
1	15.94 (top arch and floor)	15.96 (top arch and floor)
2	17.18 (upstream sidewall and floor)	16.56 (upstream sidewall and floor)
3	23.1 (upstream sidewall)	21.16 (upstream sidewall)
4	32.21 (upstream sidewall)	29.24 (upstream sidewall)

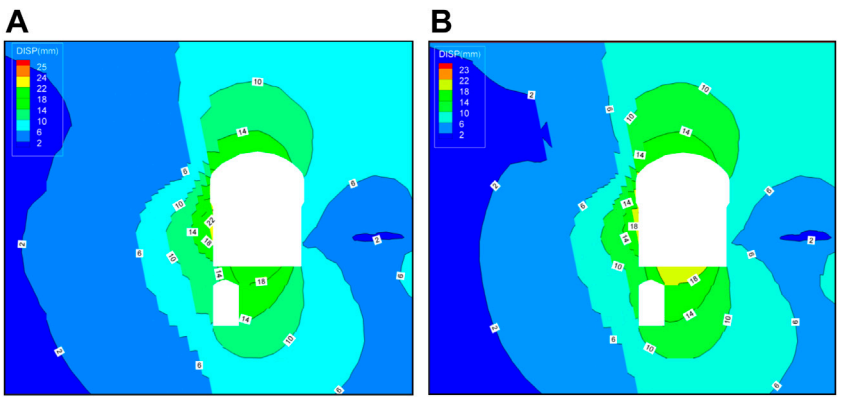


FIGURE 10 | Contour plot of the deformation distribution after step 4 excavation under the supported and unsupported conditions (Unit: mm). **(A)** non-supported condition, **(B)** systematic support condition.

TABLE 6 | Summary of the rock mass failure indices under nonsupported conditions.

Step	Failure volume of intact rocks (m^3)				Failure areas of bedding planes (m^2)		
	Current shear failure	Current tensile failure	Previous shear failure	Previous tensile failure	Current shear failure	Previous shear failure	Previous tensile failure
1	0	220	3	5,987	655	594	2064
2	1	58	6	3,765	829	1,447	1938
3	0	208	7	8,203	2,106	3,521	1887
4	0	896	13	13,561	3,142	7,158	2,291

TABLE 7 | Summary of the rock mass failure indices under supported conditions.

Step	Failure volume of intact rocks (m^3)				Failure areas of bedding plane (m^2)		
	Current shear failure	Current tensile failure	Previous shear failure	Previous tensile failure	Current shear failure	Previous shear failure	Previous tensile failure
1	2	145	3	5,978	667	578	2062
2	1	39	6	3,742	644	1,606	1923
3	0	217	6	7,786	708	4,673	1815
4	1	386	8	12,630	1819	7,822	1930

angle layered surrounding rock masses form a plate-type structure. 2) High tangential stress inside the sidewall induced by stress redistribution leads to the bending of rock plates with fixed ends, resulting in a large number of cracks. 3) Rock plates with cracks buckle or slide due to their insufficient bending strength under the longitudinal load at the plate ends.

REINFORCEMENT PRACTICE AND VALIDATION VERIFICATION

Based on the abovementioned deformation and failure mechanisms of the steeply-inclined small-angle layered surrounding rock masses of the main powerhouse, excavation

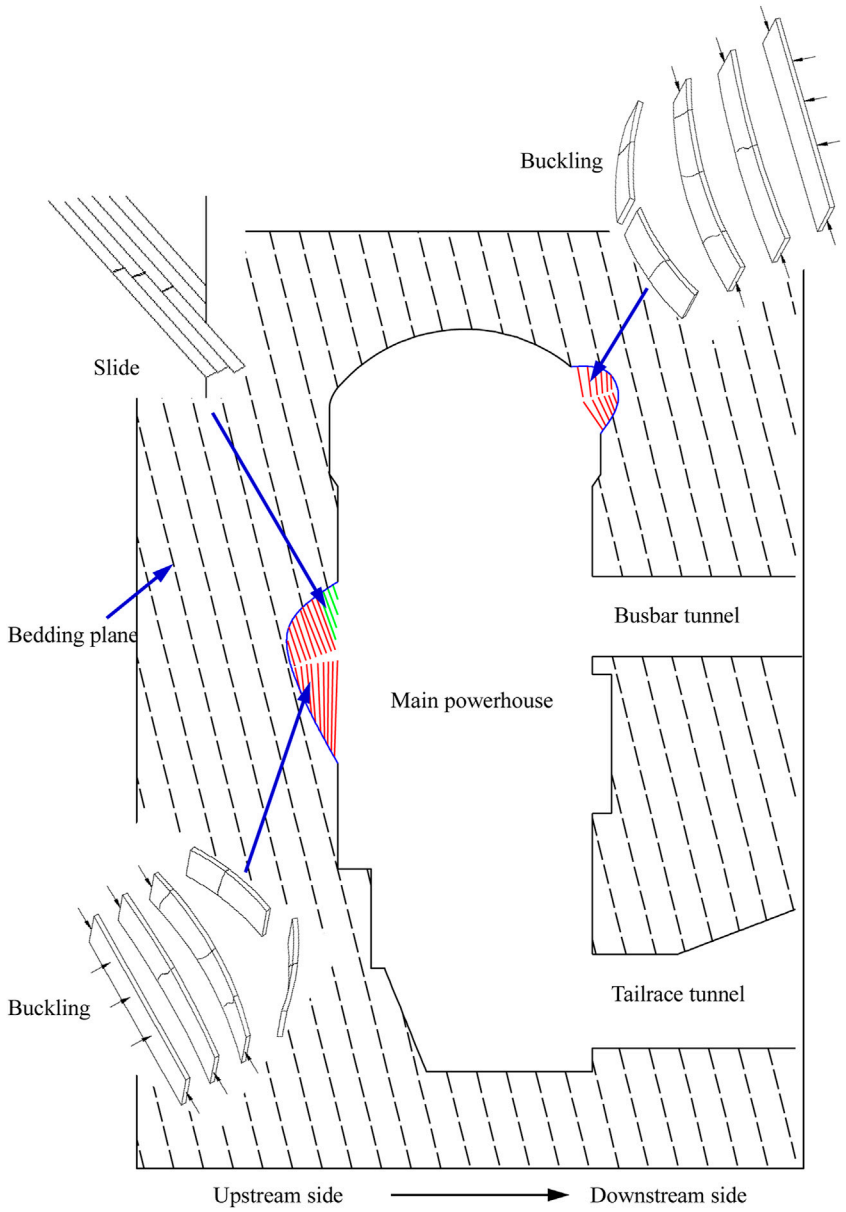


FIGURE 11 | Schematic view of the deformation and failure mechanisms of the steeply inclined small-angle layered rock mass in the right bank powerhouse.

and support measures were optimized for these rock masses to reinforce the overall stability of the high sidewalls.

Optimization of Excavation Method and Sequence

Firstly, the heights of excavated layers in corresponding cavern sections were strictly controlled. A large layer was generally excavated into two sublayers with a height of 4–5 m. In this way, stress inside the surrounding rock masses of sidewalls was slowly unloaded to avoid violent stress redistribution.

Secondly, each layer was excavated by the first middle groove and then protective layers. The middle groove and the protective layers were excavated through small gradient blasting and smooth blasting, respectively. Hereinafter, the unloading degree of surrounding rock masses of sidewalls for each blasting was further reduced, and the protective layers were able to provide certain lateral constraints for convergence deformation of sidewalls and decrease the damage of rock masses of sidewalls caused by blasting.

Finally, blasting parameters were optimized. The maximum explosive charge of each blasting was controlled by 20 kg. The row space and the diameter of blasting holes for excavating medium grooves were 3 m × 2.5 m and 90 mm, respectively. Moreover, the distance between perimeter holes, the diameter of cushion holes, the interval, and the diameter of blasting holes for excavating the

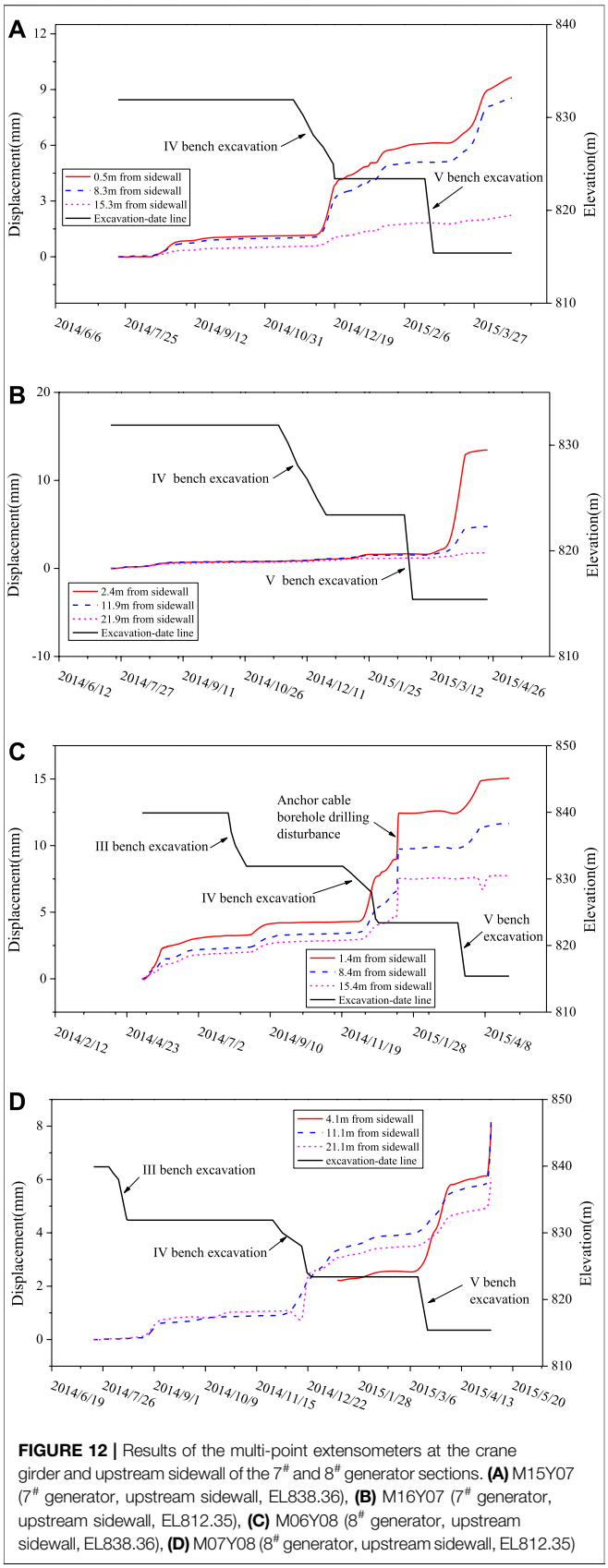


FIGURE 12 | Results of the multi-point extensometers at the crane girder and upstream sidewall of the 7# and 8# generator sections. **(A)** M15Y07 (7# generator, upstream sidewall, EL838.36), **(B)** M16Y07 (7# generator, upstream sidewall, EL812.35), **(C)** M06Y08 (8# generator, upstream sidewall, EL838.36), **(D)** M07Y08 (8# generator, upstream sidewall, EL812.35)

protective layers through smooth blasting was 50 cm, 120 cm, 180 cm, and 42 mm, respectively. Controlled blasting can not only effectively decrease the damage degree of intact rocks, but also reduce vibration disturbance to other excavated parts, especially positions with unstable blocks.

Optimization of Support Design

Support optimization includes optimizing support installation time and parameters. As for installation time, according to the deformation characteristics of hard rocks after excavation, supports needed to be finished on time. Random rock bolts and shotcrete with wire mesh were required to be finished as soon as possible to control the unloading and relaxation of surface rocks, and then systematic rock bolts and cables were installed after excavation. Random supports were performed next to the working face immediately after excavation, while systematic supports were generally performed after the working face within 15 m. After excavation, the support with anchor cables was required to be finished within 1 month. As to support parameters, the angles of rock bolts were adjusted by the orientation of rock strata. The aim is to provide certain normal constraints for bedding planes to inhibit opening. Prestressed rock bolts of 9 m long with 50 kN of pretension forces were utilized to substitute the original fully grouted rock bolts applied in regions with small angles between the strike of rock strata and the cavern axis, while row space between anchor cables was adjusted to 3 m × 4.5 m.

Implementation Effect Verification

By 1 May 2015, Layer V of the main powerhouse had been excavated. The monitoring data obtained by the multipoint extensometers in the upstream sidewall and rock crane girder in the section of 7# and 8# generator units is shown in **Figure 12**. After excavating Layer V, the accumulated deformations of the surrounding rock masses are within 20 mm. Similar to the monitoring results (Wei et al., 2010; Fan et al., 2011) of other underground powerhouses, the displacement-time curve exhibits a stepwise shape: the displacement of surrounding rock masses significantly increases in a short time and gradually stabilizes after excavating each layer. The plateau of the curves shows that the current deformation of the surrounding rock masses is convergent.

From the monitoring data, it can be seen that the displacement increments of surrounding rock masses induced by the excavation of each layer within the 7# and 8# generator units were generally within 5 mm. Compared with the accumulated deformations in other generator units whose strata do not form a small angle with the cavern axis, it can be found that the deformations in small-angle sections are usually larger. This indicates that the angle between the bedding plane strike and the main powerhouse's axis is one of the controlling factors affecting the displacement and stability of sidewalls. Both the accumulated displacement values and the characteristics of curves demonstrate that the adopted excavation and support measures show desirable effects on the deformation and failure of high sidewalls.

CONCLUSION

The failure mechanisms of steeply-inclined small-angle layered surrounding rock masses at the upstream high sidewall during excavation in this study were first investigated using DEM. After excavation, the optimized excavation schemes and supporting measures for the steeply-inclined small-angle layered surrounding rock masses were then proposed to reinforce the overall stability of the high sidewalls. The main conclusions can be drawn as follows:

1) While shear failure is the most significant failure mode in deep regions, the failure of bedding planes close to the excavation boundary is dominated by tensile failure. With the increase in the exposed height of sidewalls, the failure range and depth of bedding planes also increase.
2) The failure of steeply-inclined small-angle layered surrounding rock masses presents significant three-stage characteristics, that is, 1) rock plate forms due to the unloading opening of bedding plane; 2) rock plate cracks due to bending, and 3) rock plate buckles or slides due to crack penetration.
3) The stability of steeply-inclined small-angle layered surrounding rock masses is largely attributed to the mechanical properties of bedding planes. Therefore, the spatial distribution of the main bedding planes needs to be first explored when the underground caverns are planned to be constructed in layered rock masses. Using discontinue mechanics, the rock masses are better treated as a discontinuous medium. The construction processes should be optimized by local geological conditions. Furthermore, it is suggested to insist on the principles of excavation by thin layers and accomplish all the supports before the next-step excavation.

DATA AVAILABILITY STATEMENT

The original contributions presented in the study are included in the article/Supplementary Material, further inquiries can be directed to the corresponding author

AUTHOR CONTRIBUTIONS

C-LJ: Methodology, Writing- Original draft preparation. D-PX: Conceptualization, Methodology, Writing- Reviewing and Editing. Y-YZ: Discontinuum analysis. D-FC: Investigation. S-WZ: Data curation. L-XH: Investigation. CW: Data curation.

FUNDING

The authors gratefully acknowledge financial support from the National Natural Science Foundation of China (Nos. 52079027 and 51709043), the Open Research Fund of State Key Laboratory of Geomechanics and Geotechnical Engineering, Institute of Rock and Soil Mechanics, Chinese Academy of Sciences (NO. Z019007).

REFERENCES

Amadei, B., and Pan, E. (1992). Gravitational Stresses in Anisotropic Rock Masses with Inclined Strata. *Int. J. Rock Mech. Min. Sci. Geomechanics Abstr.* 29 (3), 225–236. doi:10.1016/0148-9062(92)93657-6

Bandis, S. C., Lumsden, A. C., and Barton, N. R. (1983). Fundamentals of Rock Joint Deformation. *Int. J. Rock Mech. Min. Sci. Geomechanics Abstr.* 20, 249–268. doi:10.1016/0148-9062(83)90595-8

Cai, M., and Kaiser, P. K. (2014). *In-situ* Rock Spalling Strength Near Excavation Boundaries. *Rock Mech. Rock Eng.* 47, 659–675. doi:10.1007/s00603-013-0437-0

Cho, J.-W., Kim, H., Jeon, S., and Min, K.-B. (2012). Deformation and Strength Anisotropy of Asan Gneiss, Boryeong Shale, and Yeoncheon Schist. *Int. J. Rock Mech. Min. Sci.* 50, 158–169. doi:10.1016/j.ijrmms.2011.12.004

Diederichs, M. S., Kaiser, P. K., and Eberhardt, E. (2004). Damage Initiation and Propagation in Hard Rock during Tunnelling and the Influence of Near-Face Stress Rotation. *Int. J. Rock Mech. Min. Sci.* 41, 785–812. doi:10.1016/j.ijrmms.2004.02.003

Fan, Q. X., Liu, Y. Y., and Wang, Y. F. (2011). Construction Monitoring Study of Large Underground Powerhouse Caverns of Xiangjiaba Hydropower Station. *Chin. J. Rock Mech. Eng.* 30 (4), 666–676.

Fan, Q. X., and Wang, Y. F. (2011). A Case Study of Rock Mass Engineering of Underground Powerhouse at Xiluodu Hydropower Station. *Chin. J. Rock Mech. Eng.* 30 (S1), 2986–2993.

Fekete, S., and Diederichs, M. (2013). Integration of Three-Dimensional Laser Scanning with Discontinuum Modelling for Stability Analysis of Tunnels in Blocky Rockmasses. *Int. J. Rock Mech. Min. Sci.* 57, 11–23. doi:10.1016/j.ijrmms.2012.08.003

Fortsakis, P., Nikas, K., Marinos, V., and Marinos, P. (2012). Anisotropic Behaviour of Stratified Rock Masses in Tunnelling. *Eng. Geol.* 141-142, 74–83. doi:10.1016/j.enggeo.2012.05.001

Ge, X. R., and Liu, J. W. (1988). Study on the Shear Resistance Behavior of Bolted Rock Joints. *Chin. J. Geotechnical Eng.* 10 (1), 8–19.

Hakala, M., Kuula, H., and Hudson, J. A. (2007). Estimating the Transversely Isotropic Elastic Intact Rock Properties for *In Situ* Stress Measurement Data Reduction: a Case Study of the Olkiluoto Mica Gneiss, Finland. *Int. J. Rock Mech. Min. Sci.* 44, 14–46. doi:10.1016/j.ijrmms.2006.04.003

Itasca Consulting Group, Inc (2007). *3DEC — Three-Dimensional Distinct Element Code*. Minneapolis: MN: Itasca Consulting Group, Inc. Ver. 4.1.

Marinos, P., and Hoek, E. (2000). "GSI: a Geologically Friendly Tool for Rock Mass Strength Estimation," in ISRM International Symposium. International Society for Rock Mechanics, Melbourne, Australia, November 19–24, 2000.

Martin, C. D., and Christiansson, R. (2009). Estimating the Potential for Spalling Around a Deep Nuclear Waste Repository in Crystalline Rock. *Int. J. Rock Mech. Min. Sci.* 46, 219–228. doi:10.1016/j.ijrmms.2008.03.001

Nasseri, M. H. B., Rao, K. S., and Ramamurthy, T. (2003). Anisotropic Strength and Deformational Behavior of Himalayan Schists. *Int. J. Rock Mech. Min. Sci.* 40, 3–23. doi:10.1016/s1365-1609(02)00103-x

Niu, X. Q., Shi, B. X., and Weng, Y. H. (2011). *Feasibility Study Report for Jinsha River Wudongde Hydropower Station*. Wuhan: Changjiang institute of survey, planning, design and research Co., Ltd.

Pellet, F., and Egger, P. (1996). Analytical Model for the Mechanical Behaviour of Bolted Rock Joints Subjected to Shearing. *Rock Mech. Rock Engng* 29 (2), 73–97. doi:10.1007/bf01079755

Peng, Q., Wang, D. K., Deng, J. H., Xie, H. P., Tang, R., and Gao, P. (2007). Analysis of Surrounding Rock Deformation Characteristics in Underground Powerhouse. *Chin. J. Rock Mech. Eng.* 26 (12), 2583–2587.

Singh, B. (1973). Continuum Characterization of Jointed Rock Masses. *Int. J. Rock Mech. Min. Sci. Geomechanics Abstr.* 10 (4), 311–335. Pergamon. doi:10.1016/0148-9062(73)90041-7

Wei, J. B., Deng, J. H., Wang, D. K., Cai, D. W., and Hu, J. Z. (2010). Characterization of Deformation and Failure for Rock Mass in Underground Powerhouse of Jinping I Hydropower Station. *Chin. J. Rock Mech. Eng.* 29 (6), 1198–1205.

Wu, A. Q., Ding, X. L., Chen, S. H., and Shi, G. H. (2006). Researches on Deformation and Failure Characteristics of an Underground Powerhouse with Complicated Geological Conditions by DDA Method. *Chin. J. Rock Mech. Eng.* 25 (1), 1–8.

Xiao, M., and Wang, Y. X. (2002). Stability Analysis on Underground Houses in the Rock Masses with Steep Obliquity. *Chin. J. Rock Mech. Eng.* 21 (B06), 2057–2060.

Xu, D.-P., Feng, X.-T., Chen, D.-F., Zhang, C.-Q., and Fan, Q.-X. (2017). Constitutive Representation and Damage Degree Index for the Layered Rock Mass Excavation Response in Underground Openings. *Tunn. Undergr. Space Technol.* 64, 133–145. doi:10.1016/j.tust.2017.01.016

Zhang, G. K. (2006). *Study on Equivalent Orthotropic Mechanical Parameters and Yield Criterion of Jointed Rock Mass and its Engineering Application*. Nanjing: Hohai University. Ph. D. Thesis.

ZhanG, Q. H., Wu, A. Q., and Shi, G. H. (2004). Application of Key Block Theory to Analysis of Rock Stability for Underground Plant in Baise Hydraulic Project. *Chin. J. Rock Mech. Eng.* 23 (15), 2609–2614.

Zhang, Y. J., and Liu, Y. P. (2002). 3D Elasto-Plastic FEM Analysis for Bolted Orthotropic Rockmass. *Chin. J. Rock Mech. Eng.* 21 (8), 1115–1119.

Zhou, Y. Y., Feng, X. T., Xu, D. P., Li, S. J., and Chen, D. F. (2016b). Experimental Study of the Shear Behavior of Carbonate Bedding Planes Cemented by Different Materials. *Chin. J. Rock Mech. Eng.* 35, 1161–1172.

Zhou, Y.-Y., Feng, X.-T., Xu, D.-P., and Fan, Q.-X. (2017). An Enhanced Equivalent Continuum Model for Layered Rock Mass Incorporating Bedding Structure and Stress Dependence. *Int. J. Rock Mech. Min. Sci.* 97, 75–98. doi:10.1016/j.ijrmms.2017.06.006

Zhou, Y.-Y., Feng, X.-T., Xu, D.-P., and Fan, Q.-X. (2016a). Experimental Investigation of the Mechanical Behavior of Bedded Rocks and its Implication for High Sidewall Caverns. *Rock Mech. Rock Eng.* 49, 3643–3669. doi:10.1007/s00603-016-1018-9

Zhu, D. J., Yang, L. D., and Cai, Y. C. (2009). Research on Anisotropic Characteristics and Size Effect of Columnar Jointed Rock Mass. *Chin. J. Rock Mech. Eng.* 28 (7), 1405–1414.

Conflict of Interest: Author C-LJ is employed by the company China Three Gorges Construction Engineering Corporation. Author L-XH and S-WZ are employed by the company China Three Gorges Corporation. Authors CW and S-LJ are employed by the company Sinohydro Bureau 6 Co. Ltd.

The remaining authors declare that the research was conducted in the absence of any commercial or financial relationships that could be construed as a potential conflict of interest.

Publisher's Note: All claims expressed in this article are solely those of the authors and do not necessarily represent those of their affiliated organizations, or those of the publisher, the editors and the reviewers. Any product that may be evaluated in this article, or claim that may be made by its manufacturer, is not guaranteed or endorsed by the publisher.

Copyright © 2022 Jian, Xu, Zhou, Chen, Zhou, Hu, Wu and Jiang. This is an open-access article distributed under the terms of the Creative Commons Attribution License (CC BY). The use, distribution or reproduction in other forums is permitted, provided the original author(s) and the copyright owner(s) are credited and that the original publication in this journal is cited, in accordance with accepted academic practice. No use, distribution or reproduction is permitted which does not comply with these terms.

frontiers | Frontiers in Earth Science

ORIGINAL RESEARCH
published: 20 June 2022
doi: 10.3389/feart.2022.916753

Analysis of the Mechanism of Ground Fissures in the Nairobi–Malaba Railway Rift Valley Area in Kenya

Bing Hao[1], Zhenghua Zhou[1], Yuandong Li[1], Xiaojun Li[2], Xujin Liu[1], Yi Han[1] and Liguo Jin[3]*

[1]College of Transportation Engineering, Nanjing Tech University, Nanjing, China, [2]Key Laboratory of Urban Security and Disaster Engineering of China Ministry of Education, Beijing University of Technology, Beijing, China, [3]Institute of Geophysics, China Earthquake Administration, Beijing, China

During the rainy season from March to May 2018, four ground fissures were generated in the rift valley area along the first phase of the Nairobi–Malaba Railway in Kenya, among which the ground fissures B3 highway, DK76, and DK77 were larger in scale, which seriously endangered the safety of the railway. According to the author's previous study, the ground fissure B3 highway belongs to a typical fault-type fissure, and the ground fissures DK76 and DK77 are qualitatively concluded to be generated under the groundwater erosion of collapsible soils. To quantitatively summarize the mechanism of ground fissures, DK76 and DK77, physical model tests on the overlying soil properties, compactness, the intersection angle between hidden cracks and the water flow direction, the height of confined water level, and the groundwater flow rate are conducted to analyze the effect of these factors on the formation and expansion of ground fissures. The test results show that the soil with strong collapsibility under the action of underground erosion produces fissures, collapses, and holes similar to those in the rift valley area along the first phase of the Nairobi–Malaba Railway in Kenya; the loose overburden is conducive to the occurrence of surface collapse; the collapse of the soil surface is the most severe when the underlaid cracks are parallel to the water flow direction; the higher confined water level and faster inflow rate will aggravate the collapse of the overlying soil layer.

Keywords: Rift Valley area, ground fissure, underground erosion, physical model test, collapsibility, compactness

OPEN ACCESS

Edited by:
Guang-Liang Feng,
Institute of Rock and Soil Mechanics (CAS), China

Reviewed by:
Weibing Gong,
University of California, Berkeley, United States
Weiyun Chen,
Sun Yat-sen University, China

****Correspondence:***
Xiaojun Li
lixiaojun@bjut.edu.cn

Specialty section:
This article was submitted to Geohazards and Georisks, a section of the journal Frontiers in Earth Science

Received: *10 April 2022*
Accepted: *09 May 2022*
Published: *20 June 2022*

Citation:
Hao B, Zhou Z, Li Y, Li X, Liu X, Han Y and Jin L (2022) Analysis of the Mechanism of Ground Fissures in the Nairobi–Malaba Railway Rift Valley Area in Kenya. Front. Earth Sci. 10:916753. doi: 10.3389/feart.2022.916753

1 INTRODUCTION

From March to May 2018, it was the rainy season in Kenya, and four ground fissures appeared successively in the Rift Valley along the Nairobi–Malaba Railway (hereinafter referred to as Nei-Ma railway). Among them, three larger ones are named ground fissure DK76, ground fissure DK77, and ground fissure B3 highway. The three ground fissures are arranged and spread from southwest to northeast, extending approximately vertically. The ground fissure B3 highway is distributed along the eastern boundary fault zone of the East African Rift Valley and consists of a series of nearly north–south strike normal faults, which belongs to a typical fault-type ground fissure. Compared to the ground fissure B3 highway, ground fissures DK76 and DK77 are small in scale, and there are a number of uneven ground settlements (as shown in **Figures 1A,B**) and local collapses along the fissures (**Figures 1C,D**). As can be seen from the figures, the vegetation covering the local uneven settlement and the collapsed cave is largely intact, and this geomorphic feature indicates that the

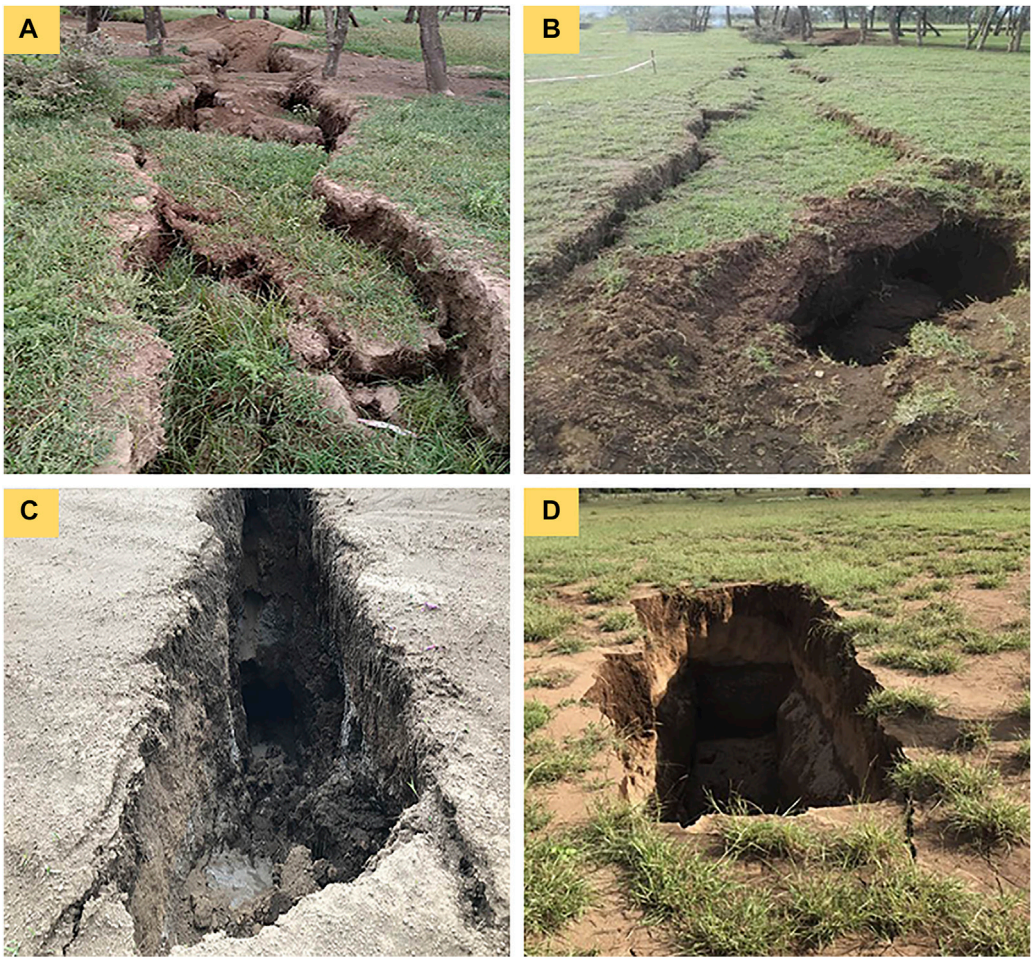


FIGURE 1 | Uneven settlement of the surface. **(A)** Surface uneven settlement with complete vegetation; **(B)** surface uneven settlement with holes; **(C)** collapsed hole; and **(D)** collapsed hole with the complete surrounding vegetation.

formation of ground fissures is due to the loss of bearing capacity of the underlying soil layer, rather than the scouring effect of rainwater on the surface soil.

Leonard (1929) started the first research on the mechanism of ground fissures, and then scholars usually divided them into structural and non-structural ground fissures for research. Structural ground fissures are mainly caused by crustal tectonic movement. In crustal tectonic movement, sudden seismic activity and tectonic creep activity occurring under the slow accumulation of tectonic stress over a large area may trigger ground fissures (Dobrev and Košťák, 2000; Wheeler, 2006; Bergemann et al., 2020; Mibei et al., 2021). The ground fissure B3 highway is characterized by such ground fissures. Non-structural ground fissures mainly include collapse-type ground fissures (Billi et al., 2016; Xu et al., 2016; Venturi et al., 2018), settlement-type ground fissures (Liu et al., 2015; Jin et al., 2016; Peng et al., 2018; Li et al., 2019), soil physical property ground fissures (Lu et al., 2019, 2021), and meteorological ground fissures (Gutie´rrez et al., 2014). It has been shown that many ground fissures are not of a single cause but are integrated causes of fissures dominated by one cause and influenced by other conditions (Wang et al., 2018; Yang et al., 2018; Valenta et al., 2021).

Therefore, when analyzing the conditions of formation of ground fissures, it is necessary to conduct targeted research in connection with specific phenomena. The primary condition controlling the activity of ground fissures is the degree of tectonic activity, followed by the degree of dynamical activity of disasters such as collapse and landslide as well as the conditions of hydrodynamic activity (Zhang et al., 2014; Peng et al., 2016; Bergemann et al., 2019; Jia et al., 2019; Nina et al., 2019; Wang et al., 2019).

2 ANALYSIS OF INFLUENCING FACTORS ON GROUND FISSURES DK76 AND DK77

Through physical and mechanical tests on the soils at the ground fissures DK76 and DK77, combined with the results of the exploratory trench, our team proposed the conclusion that

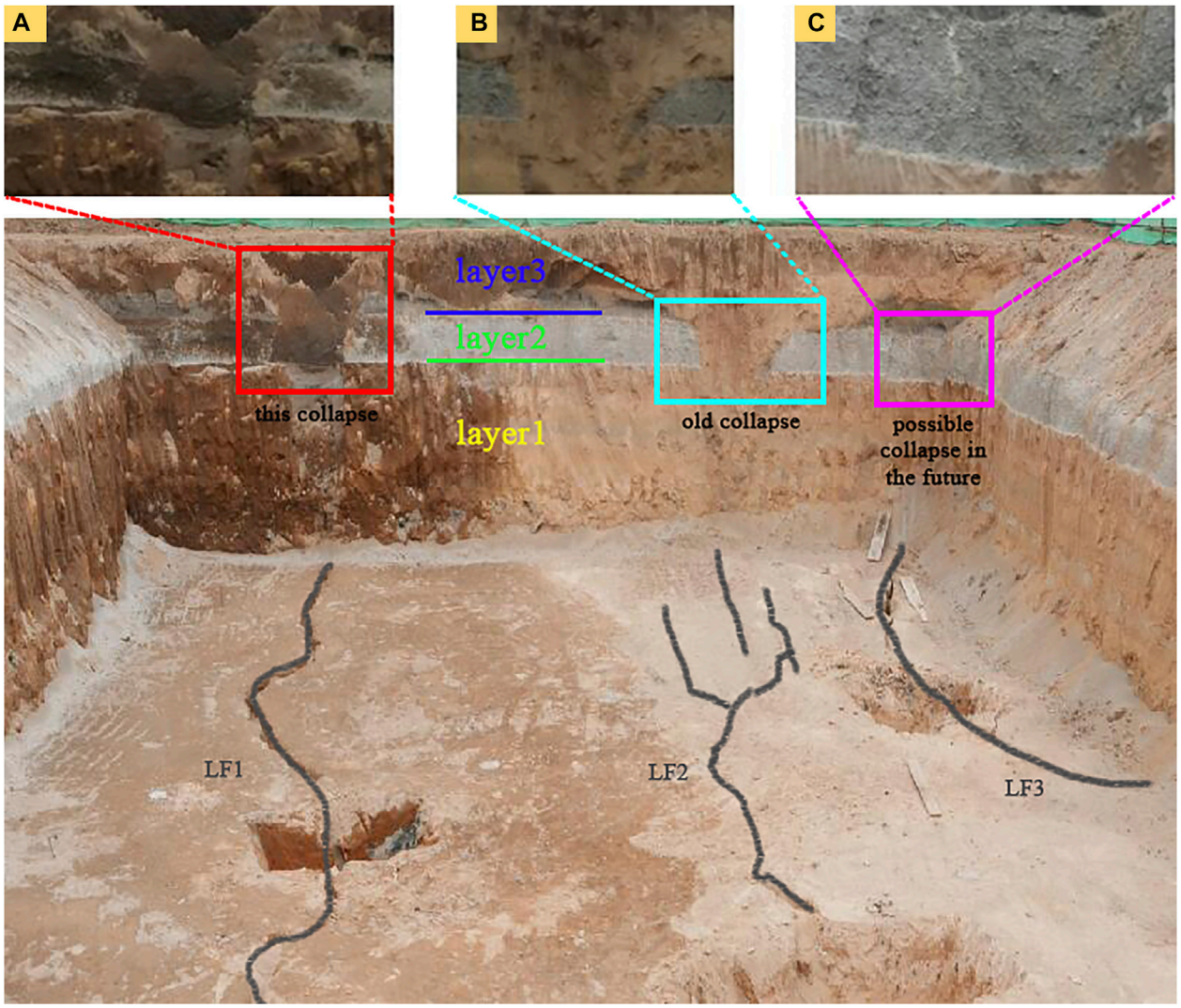


FIGURE 2 | Location relation of overlying soil collapse and bedrock cracks in exploratory trench nearby ground fissure DK76. **(A)** Location of "this collapse"; **(B)** position of "old collapse"; **(C)** position of "possible collapse in the future."

collapsible soils subjected to groundwater erosion is the mechanism of the ground fissures DK76 and DK77. First, during the geological tectonic activities, fractures and cracks form in the underlying bedrock, providing channels for groundwater intrusion into the overlying loose soil layer. During the dry season, the water level is low and the overlying soil layers are not affected by groundwater erosion, while in the rainy season, as the groundwater level rises, the groundwater flows along the bedrock cracks to the overlying soil layers, soaks the soils, destroying the cohesion of soils, stripping the soil particles, and subsequently leading to the continuous loss of soil-bearing capacity. As the water level drops, groundwater wrapped with stripped soil particles flows along the bedrock cracks to the lower part of the bedrock, causing the overlying soil layer to form a cavity at the bottom due to the loss of soil particles. With multiple cycles of groundwater fluctuations, the cavity at the bottom of the overlying soil layer gradually expands until the overlying soil layer loses its bearing capacity and collapses, manifesting as ground fissures and subsidence on the surface. Based on qualitative analysis, our research verified the rationality of the mechanism of ground fissures DK76 and DK77 by geotechnical and physical model tests (Hao et al., 2022).

From the previous mechanism analysis, it can be concluded that the main influencing factors for the formation and expansion of ground fissures DK76 and DK77 include: the influence of geological tectonic activities on the soil layer and the erosion of groundwater, *etc.* Geological tectonic activities, especially the tensional fault activities, will lead to the loosening of the overlying soil of the fault; the erosion action of groundwater is influenced by the confined water level, inflow rate, and outflow rate of groundwater and the intersection angle between hidden crack and the water flow direction.

On this basis, this study will analyze the effects of overlying soil collapsibility, compactness, confined water-level height,

groundwater flow rate, and other factors on the formation and expansion of ground fissures through further physical model tests.

In addition, it is found that there are three hidden cracks in the bedrock through the ground fissure DK76 field exploratory trench, named LF1, LF2, and LF3, respectively (**Figure 2**), and there are three layers of soil overburden on the bedrock, the bottom layer is brownish-yellow silty clay (layer 1), the middle layer is green–gray volcanic ash (layer 2), and the top layer is grayish-yellow silty clay (layer 3). LF1 with a width of about 5 cm and no filler runs through the entire trench from south to north, and at its south end, a local collapse can be clearly seen in the soil profile corresponding to the ground fissure DK76 (the location of "this collapse" is shown in **Figure 2A**). LF2 filled with soil is intermittently distributed throughout the exploratory trench from south to north, and there is no surface collapse along LF2, but there are historical traces of large-scale collapse of the overlying soil at the southern end of LF2 (**Figure 2B**), and the structure of the overlying soil layer has changed, with layer 1 and layer 2 disappearing and only layer 3 covering the bedrock. LF3, which is about 5 cm wide and without fill, extends in an arc from the southwest corner of the exploratory trench to the east, while the volcanic ash layer of the overlying soil layer at the southern end of LF3 is about 5 cm lower than the volcanic ash layer at both sides ("predict the possible collapse in the future" in **Figure 2C**). To sum up, the overlying soil layers corresponding to LF1 and LF3 expose different degrees of settlement, while the overlying soil layers above LF2 are not, which results from the difference in the structure of the overlying soils. As shown in **Figure 2**, the overlying soil structure of LF1–LF3 from bottom to top is layer 1, layer 2, and layer 3, respectively. However, the overlying soil layer of LF2 is layer 3. The test study by Hao et al. (2022) shows that soil layer 1 has strong collapsibility compared with soil layer 2 and soil layer 3. Thus, it can be concluded that the soil property of the soil layer above the bedrock cracks is one of the factors affecting the formation and expansion of ground fissures under underground erosion.

Based on the mechanism analysis of ground fissures, DK76 and DK77, in this study, physical model tests will be conducted on the effects of properties and compactness of the overlying soil layer, confined water level, inflow and outflow rates of groundwater, and the intersection angle between hidden cracks and the water flow direction, so as to reveal the formation mechanism and expansion feature of ground fissures DK76 and DK77.

3 PHYSICAL MODEL TEST ON THE GENETIC MECHANISM OF GROUND FISSURES IN KENYA

3.1 Physical Model Design Principles

In the physical model test design, it should be given full consideration to the hydraulic conditions, property, and compactness of the overlying soil, to analyze the influence of various factors on the formation and expansion of ground fissures.

3.2 Test Modeling

Based on the aforementioned principles of the test model design, the model is designed into two parts, that is, a tempered glass chamber and a glass fiber-reinforced plastic tank, as represented in **Figure 3**. The bottom plate of the tempered glass chamber is set with three penetration joints with a parallel spacing of 50 mm to simulate hidden bedrock cracks; the test soil layer is laid on them. The tempered glass chamber is 780 mm diameter and 1000 mm height, the cracks are 5 mm wide and 760 mm long, and the chamber is equipped with a cover plate, and a positioning camera point is arranged in the center of the cover plate. A glass fiber-reinforced plastic tank is divided into the horizontal tank and vertical tank. The horizontal tank size is 1300 mm*1000 mm*500 mm, paved with stones to simulate the effect of the connecting channel under the hidden cracks and effectively reduce the speed of water influx and outflow. The top plate of the horizontal tank is equipped with an 800 mm diameter hole for positioning and installing a reinforced glass chamber, which simulates the change of the angle between the hidden cracks and the groundwater flow direction by rotating the reinforced glass chamber. There are four drainage holes with a diameter of 50 mm in front of the horizontal tank to control the falling speed of the groundwater level. The vertical flume size is 1000 mm*300 mm*1000 mm, for controlling the height of the water head and the rising speed of the groundwater level.

It is not difficult to obtain that the ratio of crack length to width is 152, and the ratio of crack spacing to crack width is 10. This design can better reflect the striking effect of hidden cracks and eliminate the mutual influence between cracks. In addition, the height of the reinforced glass chamber is set at 1000 mm to place the HD camera on the cover plate, to photograph the whole process of the soil surface change during underground erosion.

3.3 Test Design and Results Analysis

According to the factors affecting the breeding and development of ground fissures DK76 and DK77 mentioned earlier, quantitative physical model tests are carried out on the soil properties and compactness of the overlying soil layer, the angle between water flow direction and hidden cracks, the height of confined water level, inflow and outflow rates, and other factors.

3.3.1 Comparison Test of Overlying Soil Properties

Due to the shortage of undisturbed soil in the Kenya Rift Valley area, the test requirements could not be met. Therefore, based on the corresponding physical and mechanical properties obtained from geotechnical tests on undisturbed soil in the Kenya rift zone (basic physical indexes of soils are listed in **Table 1**). The northwest loess is used to replace layer 1, the brownish-yellow silty clay with strong collapsibility; the non-cohesive sand is used to replace the cyan–gray volcanic ash of layer 2; the silty clay with cohesive force but low collapsibility is used to simulate the grayish-yellow silty clay of layer 3, to compare and analyze the influence of soil properties of the overlying soil layers. The comparison test setup is shown in **Table 2**, and the tests are compared in two aspects: the first aspect is to observe the development degree of ground fissures after a long period of underground erosion. The comparison test group with thinner



FIGURE 3 | Designed test model. **(A)**, **(B)** Hydrological condition control tank; **(C,D)** reinforced glass chamber of the simulated bedrock layer.

TABLE 1 | Basic physical indexes of three types of soils.

Types of soil	Dry density (g/cm^3)	Water content (%)	Specific gravity	Plastic limit (%)	Liquid limit (%)	Porosity
Sand	1.81	10.24	2.65	-	-	0.59
Silty clay	1.75	19.81	2.74	24.82	40.93	0.55
Loess	1.45	5.15	2.72	14.79	27.32	0.53

TABLE 2 | Test design of soil property comparison.

Case	Soil property	Thickness (cm)	Confined water level (cm)	Rate characteristics	Compactness (kg)	Crack layout
1	Sand	2	1	f–f	7.51	Parallel
2	Silty clay	2	1	f–f	7.51	Parallel
3	Loess	2	1	f–f	7.51	Parallel
4	Sand	5	3	s–s	15.02	Parallel
5	Silty clay	5	3	s–s	15.02	Parallel
6	Loess	5	3	s–s	15.02	Parallel

soil layer thickness and higher water flow rate is selected, which has a strong erosion effect, and the surface collapse can reach stability after a few times of water reserve and water discharge. The comparative analysis of the degree of collapse development can be carried out according to the collapse degree on the soil surface (Cases 1, 2, and 3). The second aspect is the collapsed form of the overlying soil layer in the process of erosion. The test group with a thicker soil layer and lower water rate, which has weaker erosion and slower development of bottom holes, was selected for the quantitative water reserve and discharge process,

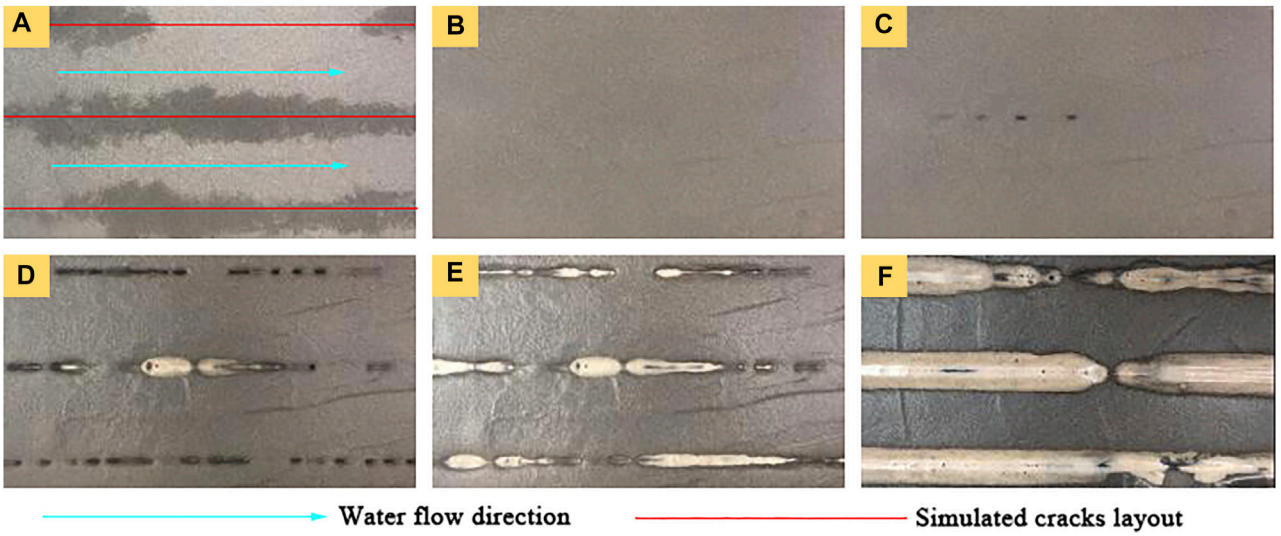


FIGURE 4 | Surface collapse process under sand erosion. **(A)** After the first water reserve–discharge cycle; **(B)** after three water reserve–discharge cycles; **(C)** after five water reserve–discharge cycles; **(D)** after seven water reserve–discharge cycles; **(E)** after ten water reserve–discharge cycles; and **(F)** after thirteen water reserve–discharge cycles.

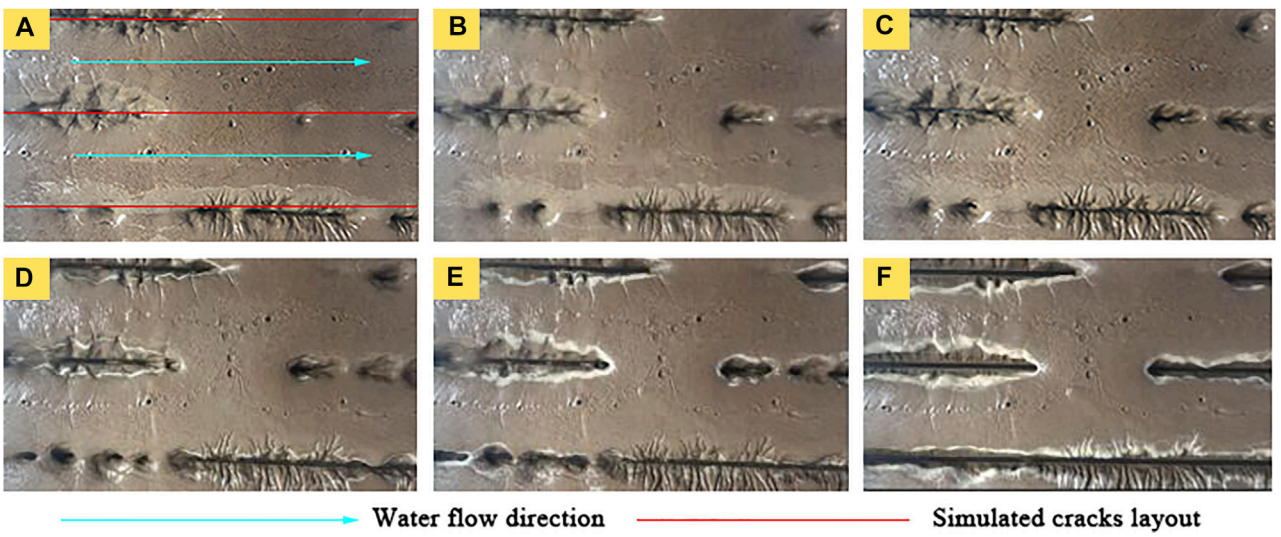


FIGURE 5 | Surface collapse process under loess erosion. **(A)** After the first water reserve–discharge cycle; **(B)** after three water reserve–discharge cycles; **(C)** after five water reserve–discharge cycles; **(D)** after seven water reserve–discharge cycles; **(E)** after ten water reserve–discharge cycles; **(F)** and after thirteen water reserve–discharge cycles.

and the collapsed form can be observed from the profile and comparatively analyzed (Cases 4, 5, and 6).

3.3.1.1 Comparative Analysis of Soil Collapse Degree in Different Overlying Soil Layers

The test result of Case 1 is shown in **Figure 4**. The soil layer directly above the hidden cracks quickly infiltrates and quickly spreads to the whole soil layer when the silt clay is under erosion (e.g., **Figures 4A,B**); after repeated water reserve and discharge cycles, the surface collapses, followed by the formation of penetrating holes (e.g., **Figures 4C,D**), and a certain length of voids extend along the crack direction (e.g., **Figures 4E,F**).

Under the action of erosion, the surface layer of non-collapsibility silt clay in Case 2 does not appear phenomenal, such as wetting belt, cracking, and collapse after exposing the same water reserve-drainage process as silt clay.

The test result of Case 3 is shown in **Figure 5**. Loess under the action of erosion, the surface fracture directly above the hidden cracks appears during a few times of water reserve and discharge cycle, and the surface soil is completely infiltrated (e.g., **Figures 5A,B**); after

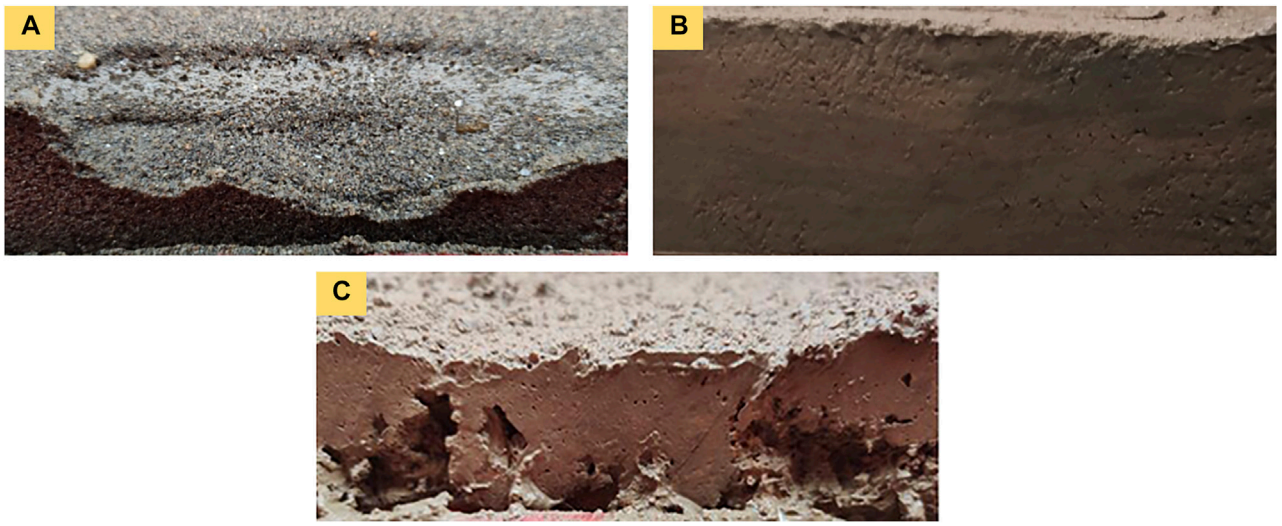


FIGURE 6 | Profile phenomena after the erosion of three types of soils. **(A)** Silt; **(B)** silty clay; and **(C)** loess.

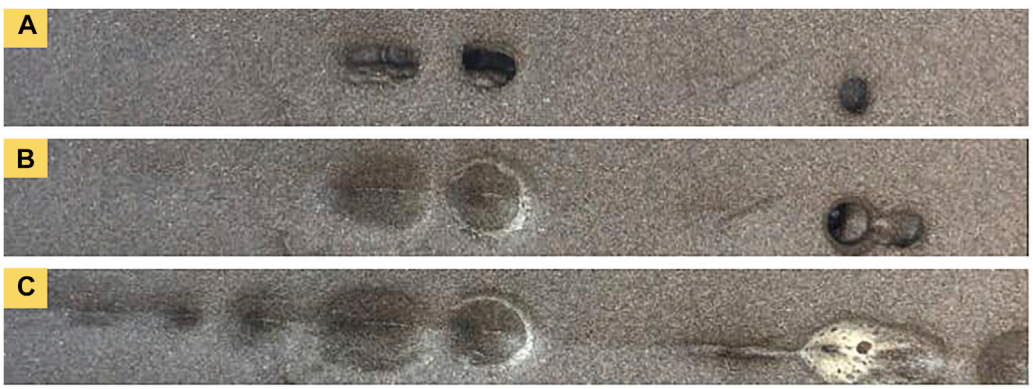


FIGURE 7 | Test phenomena of the sand surface under subsurface erosion. **(A)** After three water reserve–discharge cycles; **(B)** after five water reserve–discharge cycles; and **(C)** after ten water reserve–discharge cycles.

multiple water reserve–discharge cycles, the holes are further developed (e.g., **Figures 5C,D**), and intermittent penetration channels appear intermittently along the crack direction (e.g., **Figures 5E,F**).

Comparing the test results of three types of soils, it can be seen that under the strong erosion effect, the test group with silt clay and loess as the overlying soil layer has an obvious collapse phenomenon, while the test group with silty clay has no surface collapse. The test results show that when the overlying soil layer is cohesionless or strong collapsibility soil, the ground surface is prone to ground fissures and collapses under erosion.

3.3.1.2 Comparative Analysis of Soil Collapse Forms in Different Overlying Layers

The profile comparison of the three categories of soils under weak erosion is given in **Figure 6**. The profile of Case 4 is shown in **Figure 6A**, it is obvious that silt forms a slide when it collapses, which is because the slit clay has low structural strength. When the silt particles at the bottom along the bedrock cracks are carried away by erosion and the bottom soil along the bedrock cracks is gradually lost, the upper soil gradually loses bearing capacity and slips toward the bottom, eventually forming a funnel-type hole or a slope-type groove above the bedrock cracks. During the test, the cracks expand to the surface at first and then filled by the slip silt, as shown in **Figure 7**. In the silt clay test, some small penetrating holes to the surface first appear by water reserve and discharge (**Figure 7A**); further water reserve and discharge makes the holes become larger, but some of the holes are filled gradually by slip silt (**Figure 7B**); finally, all the holes become larger and are filled by slip silt (**Figure 7C**). It can be seen that the characteristics of silt clay exhibits are significantly different from those investigated in field ground fissures. **Figure 6B** shows the test profile of Case 5, where the soil layer is undisturbed, due to the weak erosion of the low collapsibility silty clay.

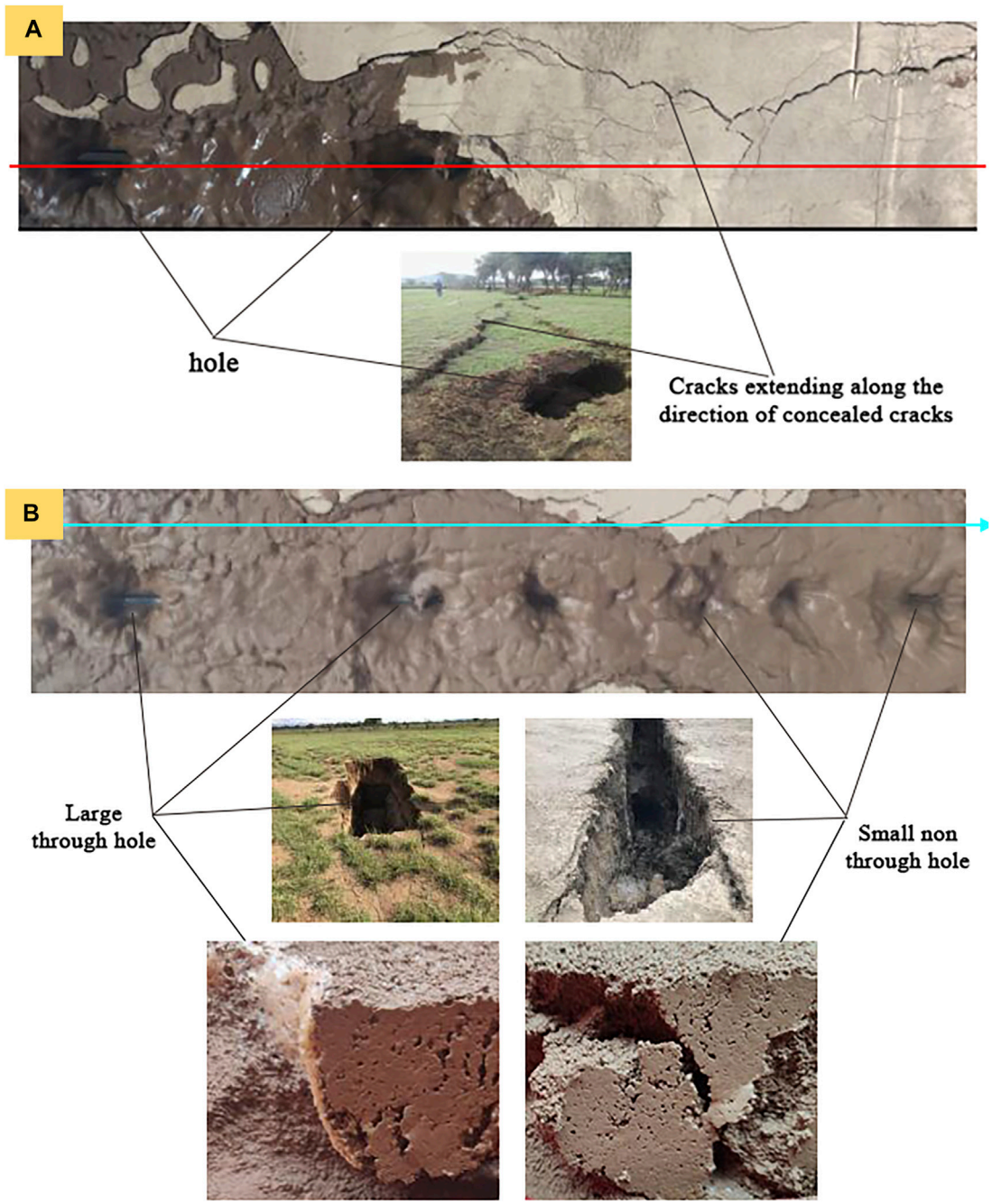


FIGURE 8 | Comparison between loess test results and ground fissures with holes. **(A)** After the first impoundment and drainage (red line is the direction of simulated hidden fissures); and **(B)** after five times of impoundment and drainage (the blue arrow is the flow direction of water).

The profile of Case 6 is shown in **Figure 6C**, the loess forms holes at the bottom of the soil layer under erosion, and its collapse pattern is different from that of the silt clay, which is due to the difference in cohesive force. By the continuous water reserve and discharge, the bottom soil particles along the bedrock cracks are taken away, the collapse holes are formed above the bedrock cracks, and due to the cohesive force, the soil on both sides of collapse holes does not slip. From the test results of loess under weak erosion, it can be seen that holes appear on the surface of loess and ground fissures appear along the direction of bedrock cracks, which is very similar to the phenomenon of uneven surface settlement accompanied by holes *in situ* (**Figure 8A**).

As can be observed from **Figure 8B**, when the underground erosion reaches a certain extent, two types of holes begin to appear in the loess surface layer, one is the larger penetration hole, occurring at the location close to the water inlet. From the

TABLE 3 | Test design of loess erosion.

Case	Soil property	Thickness (cm)	Confined water level (cm)	Rate characteristic	Compactness (kg)	Crack layout
7	Loess	5	3	f–f	23.07	Parallel
8	Loess	5	3	f–f	15.02	Vertical
9	Loess	2	1	s–s	7.51	Parallel
10	Loess	2	1	s–f	7.51	Parallel
11	Loess	2	1	f–s	7.51	Parallel
12	Loess	5	3	s–f	15.02	Parallel
13	Loess	5	3	f–s	15.02	Parallel
14	Loess	5	3	f–f	15.02	Parallel

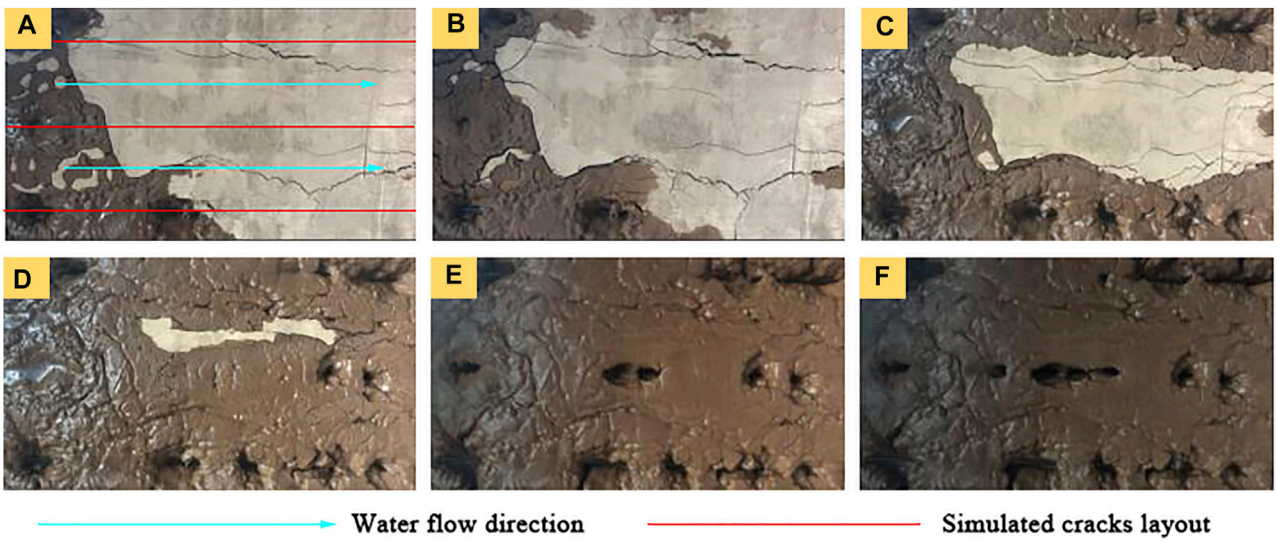


FIGURE 9 | Test results of 2-cm-thick soil layer and 1-cm confined water level. **(A)** After the first water reserve–discharge cycle, **(B)** after three water reserve–discharge cycles; **(C)** after five water reserve–discharge cycles; **(D)** after seven water reserve–discharge cycles; **(E)** after ten water reserve–discharge cycles; and **(F)** after thirteen water reserve–discharge cycles.

corresponding profile, it can be seen that the collapse is vertical subsidence, similar to the deeper, large holes found by field investigation, and the other is the smaller size non-penetration holes, occurring at a location close to the water outlet. The collapse also shows vertical subsidence with possible small channels through the bottom, similar to the smaller holes found in the field survey.

Comparison tests results show that soils without cohesion exhibit slope collapse under erosion action, while silty clay with cohesion but weak collapsibility does not collapse under erosion, and only soils with cohesion and strong collapsibility can have a similar phenomenon to that of the ground fissure in Kenya, which is consistent with the test results of Hao Bing's study that the brownish-yellow silty clay of layer 1 at the LF1 crack has strong collapsibility. It also explains the phenomenon that the collapse occurred after rainfall when the overlying layer of bedrock at LF2 was soil layer 1, while the collapse did not occur after rainfall when the overlying layer of bedrock was filled with layer 3, which has cohesive force but low collapsibility.

The subsequent tests will be conducted with loess as the overlying soil layer and analyzed the effects of soil compactness, simulated cracks and water flow direction angle, confined water-level height, and flow rate on the formation and development of ground fissures. The test design is listed in **Table 3**.

3.3.2 Comparison Test on the Compactness of the Overlying Soil Layer

The test results of Case 7 and Case 14 are used to compare and analyze the effect of overlying soil compactness on ground fissures' incubation and development. The test results of compacted soil show local wetting near the water inlet and clear cracks appear on the top surface of the soil, while the test results of loose soil show penetration holes on the soil surface and locally connected collapse along the direction of hidden cracks. This indicates that the compacted soil has stronger resistance to erosion compared with the loose soil, and the loose soil is more likely to form ground fissures and collapses

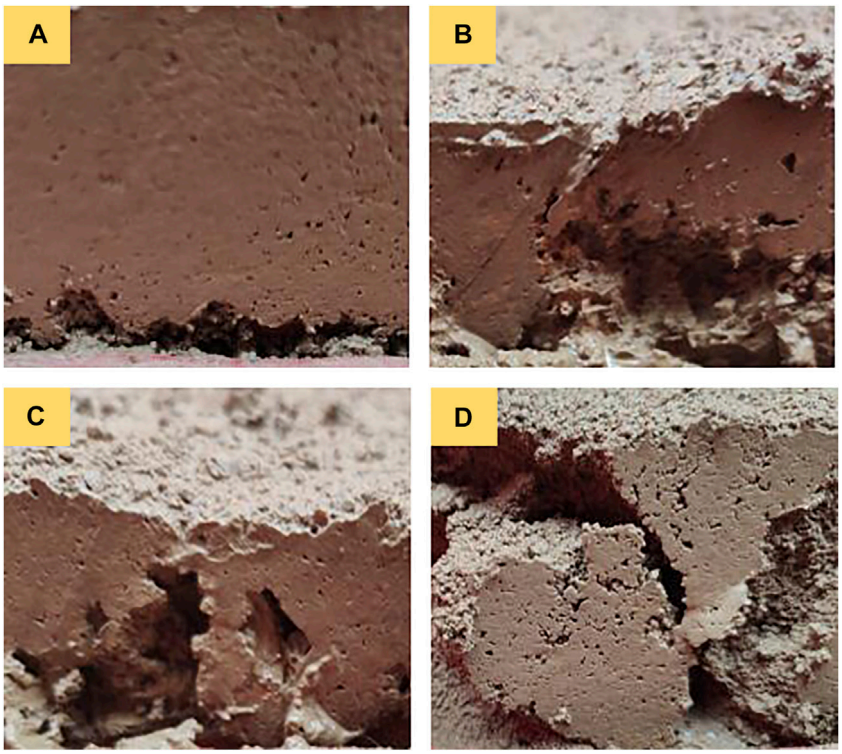


FIGURE 10 | Profile maps of the subsurface erosion test.

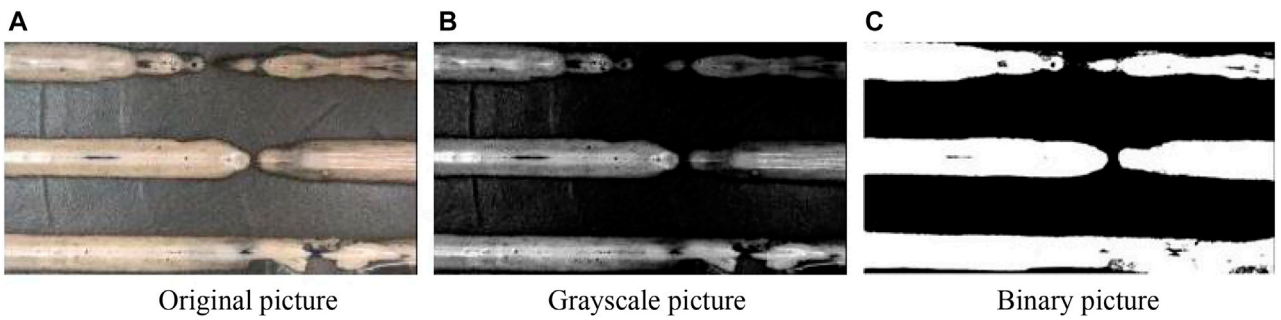


FIGURE 11 | Display of picture-processing results. **(A)** Original picture, **(B)** grayscale picture, and **(C)** binary picture.

under the erosion of groundwater. The characteristics of this test are similar to the field investigation results. Combined with the previous study, it suggests that lower compacted site soils are more likely to form ground fissures and collapses under erosion.

3.3.3 Comparison Test on the Included Angle Between Simulated Crack and Water Flow Direction

Based on the test results of Case 8 and Case 14, we compare and analyze the effect of the included angle between hidden cracks and water flow direction on the incubation and development of ground fissures. The tests with an angle of 0° present discontinuous penetration holes on the surface, while the tests with an included angle of 90° present wetting and ground fissures on the surface. The test phenomenon of 0° is consistent with the distribution characteristics of ground fissures and collapses along the hidden cracks in the field.

3.3.4 Comparative Test of Different Confined Water Levels and Water Flow Rates

Tests are designed for a 2-cm-thick soil layer with a 1-cm high confined water level, and a 5-cm-thick soil layer with a 3-cm high confined water level two group tests. Each test set shows slow water reserve–slow water discharge, fast water reserve–slow water discharge, slow water reserve–fast water discharge, and fast water reserve–fast water discharge in four comparison groups. The phenomenon of the test group with a 2-cm-thick soil layer

TABLE 4 | Proportion of the crack discrimination area in the binary image.

Test number	Soil property	Flow rate characteristic	Thickness-confined water level (cm)	Proportion of crack discrimination area (%)
9	Loess	s–s	2–1	23.42
10	Loess	s–f	2–1	24.86
11	Loess	f–s	2–1	28.89
3	Loess	f–f	2–1	32.52
6	Loess	s–s	5–3	15.67
12	Loess	s–f	5–3	16.42
13	Loess	f–s	5–3	19.87
14	Loess	f–f	5–3	23.19

and a 1-cm high confined water level is the collapse process shown in **Figure 7**, which is not repetitious here. The phenomenon of the test group with a 5-cm-thick soil layer and 3-cm high confined water level is shown in **Figure 9**. Loess under the action of erosion, the surface fracture directly above the hidden cracks appears during the first water reserve and discharge cycle, accompanied by holes, and the surface soil is not completely infiltrated (e.g., **Figures 9A,B**); after multiple water reserve–discharge cycles, the soil is gradually infiltrated, the holes are further developed (e.g., **Figures 9C,D**), and holes of different scales appear intermittently along the direction of cracks (e.g., **Figures 9E,F**).

To further explain the progress of ground fissure formation, the relative test profiles are drawn in **Figure 10**. It is seen that the collapse progress of collapsibility soil performs as follows: under the action of erosion, first the collapsibility soil layer is hollowed out and small holes are formed (**Figure 10A**); next, the holes gradually expand and interpenetrate (**Figure 10B**); then, the holes continue to expand upward to the surface and penetrate along bedrock cracks (**Figure 10C**) and eventually, forms collapse holes or gutters (**Figure 10D**).

There are two kinds of water reserve speed settings: slow water injection and fast water injection: slow water injection is carried out by a water pipe with a diameter of 30 mm; rapid water injection is to calculate the water injection amount in advance and quickly inject the required test water into the water injection tank. Discharge speed is set to two forms middle double-hole and four-hole discharge. Each test ends after 20 cycles of water reserve and discharge.

The test phenomena under different reserve–discharge combinations with the same collapse form are very close, and it is difficult to conduct a comparative analysis. Therefore, it is necessary to quantify the test results and quantitatively analyze the effects of water reserve and discharge rate on underground erosion. Quantitative analysis of test pictures requires data processing of images, and binarization of the pictures is a simple and effective method for data processing of images. The RGB images of the test results are grayed out according to the test situation to obtain grayed-out images that retain information about the collapse, and then the grayed-out images are binarized by selecting a threshold value to obtain binarized images with only black and white color points. The binary images are read and the proportion of white spots is determined, to determine the proportion of the crack area in the whole shooting area. The specific processing method is as follows: **Figure 11A** is the original RGB image, and the image is processed to obtain a grayscale image where the ground fissures and the uncollapsed soil can be clearly distinguished, as shown in **Figure 11B**; an appropriate threshold is selected to make the image become a binarized image while keeping the shape of the cracks on the soil surface as much as possible, as shown in **Figure 11C**, from which the number of white spots is calculated as 6,92,386, accounting for 36.61% of the total points, and the crack development degree is determined to be 36.61%.

According to the aforementioned image-processing method, the crack development degree determined after processing the test results is listed in **Table 4**. It can be concluded that the closer the confined water level is to the soil surface, the easier it is to breed and develop ground fissures. Under the conditions of fast reserve and fast discharge, the proportion of crack area discrimination is the largest, while under the conditions of slow reserve and slow discharge, the proportion of crack area discrimination is the smallest, which shows that fast reserve and fast discharge aggravate the occurrence of cracks. Under the condition of the same layer thickness and confined water level, the discrimination ratio of a crack area in fast reserve–slow discharge test is larger than that in slow reserve–fast discharge test, which indicates that fast reserve is more likely to cause ground cracks than fast discharge.

4 DISCUSSION

Combining the previously mentioned tests for a comprehensive analysis, the overlying soil layer above the bedrock has strong cohesion and collapsibility. The continuous expansion of rock cracks loosens the overlying soil layer near the bedrock cracks, and the included angle between hidden cracks and the groundwater flow direction is close to 0°—are important factors to produce ground fissures DK76 and DK77. The closer the confined water level is to the soil surface, the faster the groundwater flows into and out of the overlying soil layer and the more obvious the development of ground fissures is. Based on the earlier findings, the inference of the formation mechanism of ground fissures in the valley floor area of Nei-Ma Railway in Kenya proposed by previous research is supplemented as follows:

First, during the geological tectonic activity, the bedrock is subjected to tension and pressure to produce hidden cracks, forming a channel for the upward and downward flow of groundwater; the continuous expansion of bedrock cracks makes the overlying soil near it loose and susceptible to underground erosion and makes groundwater flow easily along

the direction of crack extension, providing tectonic conditions for the formation of ground fissures. During strong rainfall, the groundwater level in bedrock cracks rises continuously due to rainwater inflow, and groundwater flows upward through the hidden cracks, soaking the brownish-yellow silty clay layer with high cohesion and strong collapsibility, partially destroying its structure, and with the continuous erosion effect, the soil structure damage area increases and gradually spreads to the surface. After heavy rainfall, the groundwater level decreases due to seepage, and some soil particles flow out along bedrock cracks to lower cracks and cavities, forming small holes at the bottom of the overlying soil layer. Because of the high cohesive force of soil, there is still partial bearing capacity for the upper part of the soil layer, and the ground surface will not collapse immediately. During the strong rainfall season, the groundwater level keeps rising and falling, and the cavity at the bottom of the overlying soil layer gradually expands, leading to the gradual loss of its bearing capacity on the upper part of the soil layer. When the groundwater level is far from the surface of the soil layer and the flow rate is slow, it is easy to produce ground fissures, uneven settlement, and intermittent holes on the surface; when the groundwater level is close to the surface of the soil layer and the flow rate is fast, it is easy to trigger geological disasters such as surface collapses and gullies.

5 CONCLUSION

Based on the inference of the genesis mechanism of ground fissures DK76 and DK77 in the rift valley area of Kenya, through field investigation and combined with geological exploration data, this study concluded that the influencing factors of ground fissure incubation and development include the properties and compactness of the overlying soil on the bedrock, the included angle between the hidden cracks and the water flow direction, the height of confined water level, and the rate of groundwater flow. The main conclusions drawn from the item-by-item analysis in combination with the physical model tests are as follows:

1) The cohesive force and high collapsibility of the overlying soil layer on the bedrock are important factors for the generation of ground fissures DK76 and DK77. When the overlying soil layer has no cohesion, it is easy to form landslide collapse under the action of erosion; when the overlying soil layer has cohesion but low collapsibility, the surface is not easy to appear ground fissure or collapse; only when the overlying soil has cohesion and high collapsibility, it can produce geological phenomena similar to the field situation.
2) The small compactness of soil and the angle between hidden cracks and the direction of groundwater flow is close to 0° are important factors for the generation of ground fissures. Therefore, before the occurrence of a ground fissure, the continuous expansion of bedrock cracks loosens the overlying soil near the bedrock cracks, making it easy for groundwater to flow along the direction of crack extension, providing tectonic conditions for the formation of ground fissures.
3) The closer the confined water level is to the soil surface, the easier it is to breed and develop ground fissures; the faster the groundwater inflow and outflow rates are, the more remarkable the development of fissures is. When the groundwater level is far from the surface of the soil layer and the flow rate is slow, it is easy to produce ground fissures, uneven settlement, and intermittent holes on the surface; when the groundwater level is close to the surface of the soil layer and the flow rate is fast, it is easy to trigger geological disasters such as surface collapses and gullies.

DATA AVAILABILITY STATEMENT

The original contributions presented in the study are included in the article/Supplementary Material; further inquiries can be directed to the corresponding author.

AUTHOR CONTRIBUTIONS

All authors contributed to the study conception and design. XiL provided the background conditions for the research. ZZ contributed to the conception of the study and the materials needed for the experiments. YL and BH designed and completed a series of experimental works. YL, XuL, and YH processed and analyzed the results. YL wrote the first draft of the manuscript. BH enriched the manuscript and improved the quality of all the images. ZZ revised and embellished the language, and LJ revised the overall framework and format of the manuscript. All authors read and approved the final manuscript.

FUNDING

The authors would like to thank the financial support for the study presented in this article from the National Natural Science Foundation of China (Grant Nos. U1839202 and 41374049).

REFERENCES

Bergemann, C. A., Gnos, E., Berger, A., Janots, E., and Whitehouse, M. J. (2020). Dating Tectonic Activity in the Lepontine Dome and Rhone-Simplon Fault Regions through Hydrothermal monazite-(Ce). *Solid earth.* 11 (1), 199–222. doi:10.5194/se-11-199-2020

Bergemann, C. A., Gnos, E., and Whitehouse, M. J. (2019). Insights into the Tectonic History of the Western Alps through Dating of Fissure Monazite in the Mont Blanc and Aiguilles Rouges Massifs. *Tectonophysics* 750, 203–212. doi:10.1016/j.tecto.2018.11.013

Billi, A., De Filippis, L., Poncia, P. P., Sella, P., and Faccenna, C. (2016). Hidden Sinkholes and Karst Cavities in the Travertine Plateau of a Highly-Populated Geothermal Seismic Territory (Tivoli, Central Italy). *Geomorphology* 255, 63–80. doi:10.1016/j.geomorph.2015.12.011

Dobrev, N. D., and Košťák, B. (2000). Monitoring Tectonic Movements in the Simitli Graben, SW Bulgaria. *Eng. Geol.* 57 (3-4), 179–192. doi:10.1016/s0013-7952(00)00027-2

Gutie´rrez, F., Parise, M., De Waele, J., and Jourde, H. (2014). A Review on Natural and Human-Induced Geohazards and Impacts in Karst. *Earth Sci. Rev.* 138, 61–88.

Hao, B., Zhou, Z. H., Li, Y. D., Li, X. J., and Jin, L. G. (2022). Experimental Analysis on Mechanical Characteristics of Foundation Soil in Rift Valley Area of Kenya Nairobi-Malaba Railway. *Front. Earth Sci.* 2022, Under review. doi:10.3389/feart.2022.909102

Jia, Z., Lu, Q., Peng, J., Qiao, J., Wang, F., Wang, S., et al. (2019). Analysis and Comparison of Two Types of Ground Fissures in Dali County in the Weihe Basin, China. *Environ. Earth Sci.* 79 (1), 38. doi:10.1007/s12665-019-8783-1

Jin, W.-z., Luo, Z.-j., and Wu, X.-h. (2016). Sensitivity Analysis of Related Parameters in Simulation of Land Subsidence and Ground Fissures Caused by Groundwater Exploitation. *Bull. Eng. Geol. Environ.* 75 (3), 1143–1156. doi:10.1007/s10064-016-0897-z

Leonard, R. J. (1929). An Earth Fissure in Southern Arizona. *J. Geol.* 37, 765–774. doi:10.1086/623676

Li, M., Ge, D., Liu, B., Zhang, L., Wang, Y., Guo, X., et al. (2019). Research on Development Characteristics and Failure Mechanism of Land Subsidence and Ground Fissure in Xi'an, Monitored by Using Time-Series SAR Interferometry. *Geomatics, Nat. Hazards Risk* 10 (1), 699–718. doi:10.1080/19475705.2018.1542350

Liu, H., Deng, K., Lei, S., and Bian, Z. (2015). Mechanism of Formation of Sliding Ground Fissure in Loess Hilly Areas Caused by Underground Mining. *Int. J. Min. Sci. Technol.* 25 (4), 553–558. doi:10.1016/j.ijmst.2015.05.006

Liu, N., Feng, X., Huang, Q., Fan, W., Peng, J., Lu, Q., et al. (2019). Dynamic Characteristics of a Ground Fissure Site. *Eng. Geol.* 248, 220–229. doi:10.1016/j.enggeo.2018.12.003

Liu, Z., Lu, Q., Qiao, J., and Fan, W. (2021). *In Situ* water Immersion Research on the Formation Mechanism of Collapsible Earth Fissures. *Eng. Geol.* 280, 105936. doi:10.1016/j.enggeo.2020.105936

Lu, Q. Z., Qiao, J. W., Peng, J. B., Liu, Z. H., Liu, C., Tian, L. Y., et al. (2019). A Typical Earth Fissure Resulting from Loess Collapse on the Loess Plateau in the Weihe Basin. *China. Eng. Geol.* 259. doi:10.1016/j.enggeo.2019.105189

Mibei, G., Harðarson, B. S., Franzson, H., Bali, E., Geirsson, H., and Guðfinnsson, G. H. (2021). Eruptive History and Volcano-Tectonic Evolution of Paka Volcanic Complex in the Northern Kenya Rift: Insights into the Geothermal Heat Source. *J. Afr. Earth Sci.* 173, 103951. doi:10.1016/j.jafrearsci.2020.103951

Peng, J., Qu, W., Ren, J., Zhang, Q., and Wang, F. (2018). Geological Factors for the Formation of Xi'an Ground Fractures. *J. Earth Sci.* 29 (2), 468–478. doi:10.1007/s12583-018-0841-1

Peng, J., Xu, J., Ma, R., and Wang, F. (2016). Characteristics and Mechanism of the Longyao Ground Fissure on North China Plain, China. *Eng. Geol.* 214, 136–146. doi:10.1016/j.enggeo.2016.10.008

Valenta, J., Verner, K., Martínek, K., Hroch, T., Buriánek, D., Megerssa, L. A., et al. (2021). Ground Fissures within the Main Ethiopian Rift: Tectonic, Lithological and Piping Controls. *Earth Surf. Process. Landf.* 46 (15), 3158–3174. doi:10.1002/esp.5227

Venturi, S., Tassi, F., Vaselli, O., Vougioukalakis, G. E., Rashed, H., Kanellopoulos, C., et al. (2018). Active Hydrothermal Fluids Circulation Triggering Small-Scale Collapse Events: the Case of the 2001-2002 Fissure in the Lakki Plain (Nisyros Island, Aegean Sea, Greece). *Nat. Hazards* 93 (2), 601–626. doi:10.1007/s11069-018-3318-8

Wang, F. Y., Peng, J. B., Meng, Z. J., Qiao, J. W., Wen, H. G., Ma, P. H., et al. (2019). The Origin and Impact of the Shizhuang Ground Fissure, Yingxian Area, Datong Basin, China. *Eng. Geol.* 261. doi:10.1016/j.enggeo.2019.105283

Wang, Z.-F., Cheng, W.-C., and Wang, Y.-Q. (2018). Investigation into Geohazards during Urbanization Process of Xi'an, China. *Nat. Hazards* 92 (3), 1937–1953. doi:10.1007/s11069-018-3280-5

Wheeler, R. L. (2006). Quaternary Tectonic Faulting in the Eastern United States. *Eng. Geol.* 82 (3), 165–186. doi:10.1016/j.enggeo.2005.10.005

Xu, L., Li, S., Cao, X., Somerville, I. D., Suo, Y., Liu, X., et al. (2016). Holocene Intracontinental Deformation of the Northern North China Plain: Evidence of Tectonic Ground Fissures. *J. Asian Earth Sci.* 119 (1), 49–64. doi:10.1016/j.jseaes.2016.01.003

Yang, C., Lu, Z., Zhang, Q., Zhao, C., Peng, J., and Ji, L. (2018). Deformation at longyao ground fissure and its surroundings, north china plain, revealed by alos palsar ps-insar. *Int. J. Appl. Earth Observation Geoinformation* 67 (1), 1–9. doi:10.1016/j.jag.2017.12.010

Zhang, R., Jiang, Z., Zhou, H., Yang, C., and Xiao, S. (2014). Groundwater Outbursts from Faults above a Confined Aquifer in the Coal Mining. *Nat. Hazards* 71 (3), 1861–1872. doi:10.1007/s11069-013-0981-7

Conflict of Interest: The authors declare that the research was conducted in the absence of any commercial or financial relationships that could be construed as a potential conflict of interest.

Publisher's Note: All claims expressed in this article are solely those of the authors and do not necessarily represent those of their affiliated organizations, or those of the publisher, the editors, and the reviewers. Any product that may be evaluated in this article, or claim that may be made by its manufacturer, is not guaranteed or endorsed by the publisher.

Copyright © 2022 Hao, Zhou, Li, Li, Liu, Han and Jin. This is an open-access article distributed under the terms of the Creative Commons Attribution License (CC BY). The use, distribution or reproduction in other forums is permitted, provided the original author(s) and the copyright owner(s) are credited and that the original publication in this journal is cited, in accordance with accepted academic practice. No use, distribution or reproduction is permitted which does not comply with these terms.

frontiers | Frontiers in Earth Science

ORIGINAL RESEARCH
published: 22 June 2022
doi: 10.3389/feart.2022.933192

Study on the Mechanism of Weakening Thick and Hard Roof by Deep-Hole Blasting in Deep Coal Mines

Chen Zhang[1], *Junpeng Zou*[1]*, *Xiufeng Zhang*[2], *Chao Wang*[2] *and Yu-Yong Jiao*[1]*

[1]Faculty of Engineering, China University of Geosciences, Wuhan, China, [2]Shandong Energy Group Co., Ltd., Jinan, China

In the mining process of deep coal mines with a thick and hard roof, it is easy to form a large overhanging roof and accumulate a lot of strain energy. The sudden breaking of the suspended roof may induce seisms, which seriously threaten the safety of underground miners and equipment. To reveal the mechanism of weakening the thick and hard roof by blasting in deep mining, the four times deep-hole blasting in $63_{upper}06$ panel of Dongtan coal mine are considered. First, the temporal and spatial distribution of seismicity events monitored before and after blasting is investigated. Second, the process of deep-hole blasting is simulated using finite element and discrete element methods. After blasting, the small-energy mining-induced seismicities within 20 m of the roof suddenly increase and gradually transfer to the mined-out area and the front of the working face. Meanwhile, the high rock stratum is broken and a large amount of strain energy is released, which causes the range of fall zone enlarge a lot, and the stress in the roof is decreased obviously. With the increase in the number of deep-hole blasting, the pressure relief effect becomes more obvious, and the newly developed fracture is mainly located in the low strata. Microseismic monitoring results agree with the calculated results. Moreover, the rock caving steps are easily formed after deep-hole blasting, and the collapse is more sufficient. Furthermore, blasting cracks are most restrained in the vertical direction of the maximum principal stress. Moreover, the delayed blasting method is more conducive to the expansion and penetration of blasting cracks. Results show that the deep-hole blasting technology has a significant effect on weakening the roof of coal seam and preventing and controlling large-energy mining-induced seismicities.

Keywords: deep coal mining, deep-hole blasting, mining-induced seismicities, energy release, numerical simulation

OPEN ACCESS

Edited by:
Shibing Huang,
Wuhan University of Science and Technology, China

Reviewed by:
Chuangzhou Wu,
Zhejiang University, China
Yucong Pan,
Wuhan University, China

***Correspondence:**
Junpeng Zou
zoujunpeng@cug.edu.cn
Yu-Yong Jiao
yyjiao@cug.edu.cn

Specialty section:
This article was submitted to Geohazards and Georisks, a section of the journal Frontiers in Earth Science

Received: *30 April 2022*
Accepted: *12 May 2022*
Published: *22 June 2022*

Citation:
Zhang C, Zou J, Zhang X, Wang C and Jiao Y-Y (2022) Study on the Mechanism of Weakening Thick and Hard Roof by Deep-Hole Blasting in Deep Coal Mines. Front. Earth Sci. 10:933192. doi: 10.3389/feart.2022.933192

INTRODUCTION

Coal is an important fossil energy. With the decrease of shallow coal resources, coal mining gradually shifts to the deep. Due to the deep mining environment with high stress (He et al., 2015), the rock will have the characteristics of good integrity and high strength, and then thick and hard roofs will be formed at the top of the coal seam. Therefore, long cantilevers will be formed during mining, resulting in rock burst (Senfaute and Chambo, 1997), mine seismicities (Gibowicz and Lasocki, 2001), land subsidence (Zhang, et al., 2022), and other hazards. At present, the main methods to prevent and control these disasters include the hydraulic fracturing method (Huang

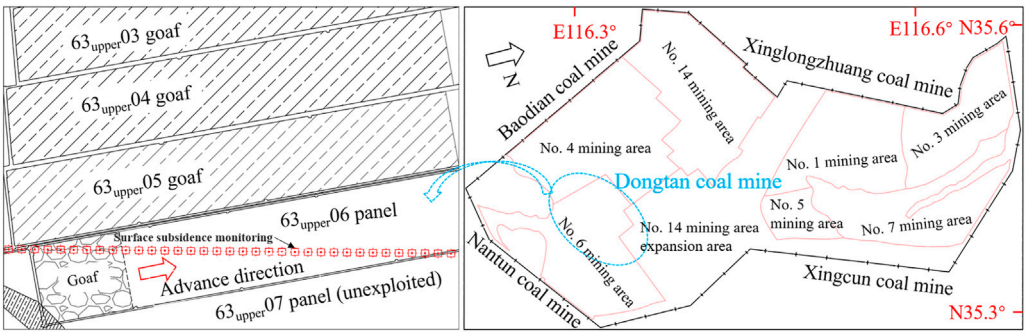


FIGURE 1 | Distribution of mining areas in Dongtan coal mine and panels in No. 6 mining area.

TABLE 1 | Main physical and mechanical parameters of the strata in No. 6 mining area.

Lithology	Elastic Modulus /GPa	Compressive Strength /MPa	Tensile Strength /MPa	Average Density /G/Cm^3	Poisson's	Cohesion /MPa	Friction Angle /°	Thickness /m
Soil	—	20	2.1	2.41	0.3	13.21	24	150
Sandstone	21.01	85.6	8.17	2.49	0.29	17.99	31	160
Mudstone	11.55	43.99	3.73	2.44	0.41	15.46	20	10
Sandstone	18.7	63.22	6.29	2.33	0.22	15.29	28	258
Mudstone	35.51	72.24	7.17	2.63	0.27	12.68	20	108
Sandstone	36.63	90.25	8.61	2.59	0.23	13.84	27	27
Siltstone	50.89	107	7.57	2.61	0.26	16.21	11	5.73
3_{upper} coal	—	—	—	—	—	—	—	5.39
Medium sandstone	50.9	105.6	5.9	2.56	0.33	14.32	18	10

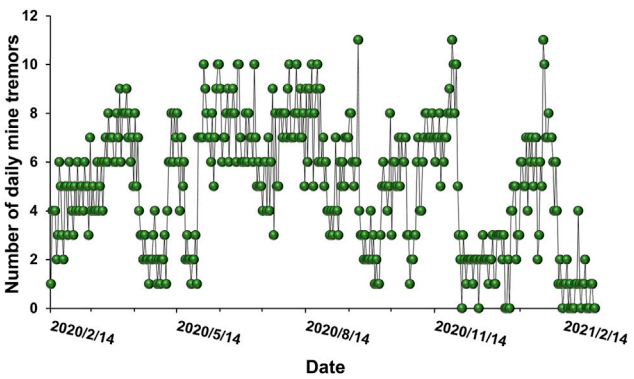


FIGURE 2 | Distribution of the mining-induced seismicities on the 63_{upper}06 panel before the treatment.

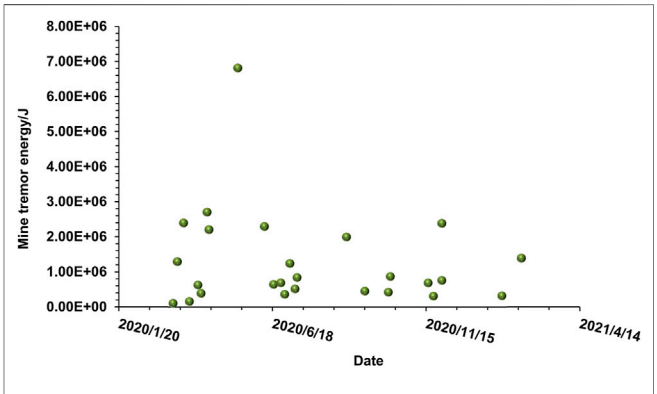


FIGURE 3 | Strong mining-related seismicities (>10^5 J).

et al., 2015), the deep-hole blasting method, and so on. The deep-hole blasting method is used to weaken the thick and hard roof in the sixth mining area of Dongtan Coal Mine in Yanzhou, Shandong Province, China, and a good governance effect was obtained. Thus, combined with the actual engineering background, this work studies the mechanism of deep-hole blasting to weaken the thick and hard roof to prevent mine seismicities disasters.

The weakening mechanism of rock blasting is still an ongoing topic. The generally accepted theory is that after rock blasting, the instantaneous reflection and tensile effect of explosive stress wave and the gas wedge effect of detonation gas increase the radius of the blast hole cavity, and generate a crushing zone and a fracture zone, thereby reducing the strength of rock (Kutter and Fairhurst, 1971; Xie et al., 2017) Due to the large horizontal ground stress in deep coal mining, the elastic stage, plastic strain stage, and damage softening stage of rock failure are different from those



FIGURE 4 | Schematic diagram of deep-hole blasting position.

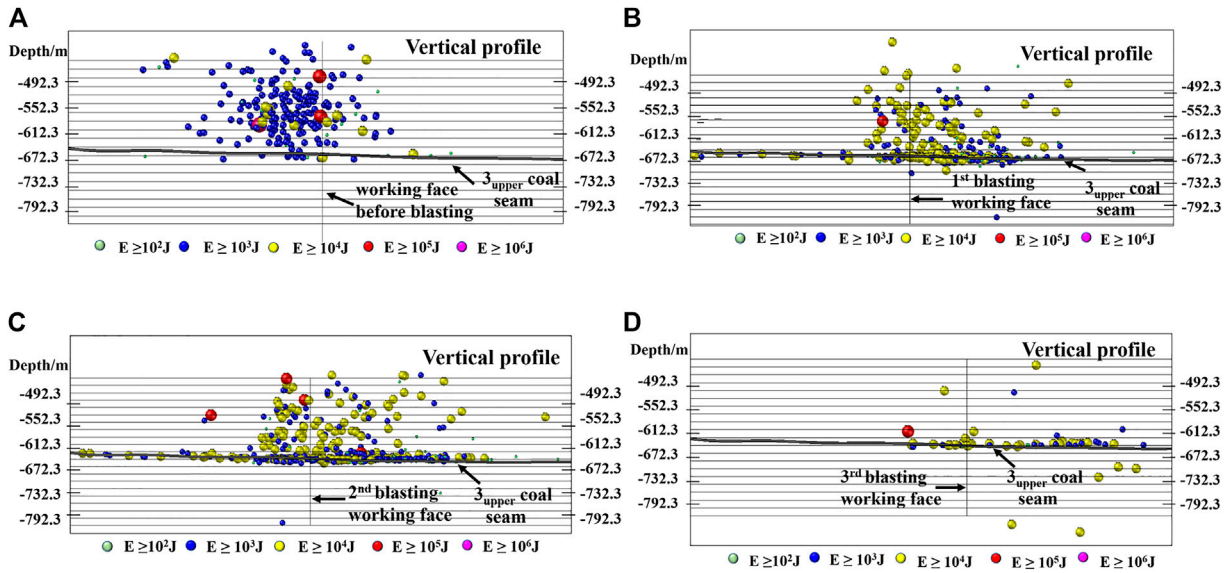


FIGURE 5 | Profile distribution of mining-induced seismicities before and after deep-hole blasting: **(A)** distribution of mining-induced seismicities before blasting, **(B)** distribution of mining-induced seismicities after the first blasting at 597 m, **(C)** distribution of mining-induced seismicities after the second blasting at 651 m, and **(D)** distribution of mining-induced seismicities after the third blasting at 712 m.

of shallow rock. Researchers proposed a failure surface equation for concrete under large strain, high strain rate, and high pressure (Holmquist et al., 1993). On this basis, the RHT constitutive model is proposed (Riedel, 2004), which provides the possibility for the damage calculation of rock after blasting in a deep high-stress environment. Meanwhile, deep-hole blasting is equivalent to a black box, and how the rock damage and cracks in the roof evolve in the high-stress environment cannot be directly observed. So, the method of numerical simulation has become an important research way. The RHT constitutive model is embedded into the finite element software AUTODYN, and the research on the parameter setting of the RHT constitutive model has made great progress in the study of rock blasting weakening. It systematically analyzes the rock breaking process in borehole blasting and puts forward the ' dynamic and static pressure ' breaking principle of rock borehole blasting (Century Dynamics Ltd., 2000). More numerical models of borehole blasting began to be simulated by AUTODYN software, such as rock breaking process of single-hole and double-hole blasting, borehole non-coupling charge blasting, etc. (Chun et al., 2009). With the development of finite element software, the RHT constitutive model is applied to the penetration experiment of LS-DYNA, and better damage and fracture evolution are obtained. It is found that the blasting effect of triangle hole arrangement is better than that of traditional straight hole arrangement (Zuo et al., 2019). For this reason, this study establishes a triangular hole model by the LS-DYNA finite element software based on the RHT constitutive model to explore the damage evolution law of rock under high confining pressure.

In terms of the mechanism of induced mine seismicities in coal mining with the thick and hard roof, the initial caving interval of roof collapse above the coal seam is large, and the rotation and subsidence of the suspended roof will produce higher lateral support pressure above the working face, which is the main source of strong activity of rock strata above the working face (Chen and Liu, 2018). According to the research, the mine seismicities are prone to occur at the first square. The mechanism of rock movement and instability in the coal mine is studied when there are multi-layer thick and hard rock layers above the coal seam. The analysis shows that the early mine seismicities occur frequently in the low rock layer and the released energy is small, in the form of rotating sliding. With the advancement of the working face, it gradually shifts to the

TABLE 2 | RHT constitutive model parameters.

Mid	Ro	Shear	Onempa	Epsf	b0	b1	t1
1	2.7	0.2417	0.0	2.0	1.68	1.68	0.8671
a	n	fc	fs*	ft*	q0	b	t2
1.6	0.6	0.00119	0.38	0.1	0.64	0.0105	0
e0c	e0t	ec	et	betac	betat	ptf	—
3E-11	3E-12	3E19	3E19	0.0106	0.0144	0.001	—
gc*	gt*	xi	d1	d2	epm	af	nf
gamma	a1	a2	a3	pe1	pco	np	alpha
0.0	0.8671	1.4567	0.8903	4E-4	0.06	4.0	1.1

TABLE 3 | Explosive material and its state equation parameters.

Density	Detonation Velocity	Cj Pressure	State Parameters of the JWL Equation					
/kg·m^{-3}	/m·s^{-1}	/GPa	*A*/ GPa	*B*/ GPa	R_1	R_2	ω	*E*/ GPa
1,200	4,950	6.125	52.4	0.768	4.2	1.1	0.34	8.5

high strata. Shear slip often occurs in high strata, which leads to large-energy mine seismicities. A large mine seismicity will be caused by the synergistic rupture of multi-layer hard rock (He et al., 2015; Jiao et al., 2021). After rock fracture, the contact behavior is controlled by the asperity when the working face is disturbed again by the external force. The researchers compared and analyzed the application effect of two roughness peak recognition and evaluation methods in the three-dimensional field (Tang et al., 2022), which provides a worthy reference method for conducting laboratory experiments to study the mechanism of mineral seismicities generated by the remotion of fractured rocks due to the transport of overlying rocks.

In terms of the mechanism of weakening the thick and hard roof by deep-hole blasting, the blasting pressure relief technology was first used in the mining of metal mines in South Africa and achieved a good pressure relief effect (Guest et al., 1995). The monitoring results of the working resistance of the hydraulic support show that the deep-hole blasting technology can effectively shorten the periodic weighting step and reduce the variation range of the stress redistribution of the weathered rock. The mechanism of weakening the thick and hard roof is mainly reflected in the two aspects of static load reduction and dynamic load response (Lu et al., 2021). In the study of blast hole parameters, it is found by numerical simulation that when the aperture is constant, with the increase of the hole depth, the stress time of the unit at the same position is gradually extended, and the cracks in the coal seam are easier to expand, that is, the deeper the borehole is, the better the effect of weakening the thick and hard roof is (Liu et al., 2012). Finally, there are some studies on the evaluation of the blasting effect. Using the microseismic monitoring method, it is found that the microseismic waveform information induced by pressure relief blasting can describe the release process of blasting stress and mining stress, so the blasting efficiency index to evaluate the pressure relief effect can be proposed to better guide the actual production (Kan et al., 2022).

The existing research has made many in-depth discussions on the prevention and control of rock burst and mine seismicities disasters by blasting weakening the thick and hard roof in terms of theoretical analysis. However, the numerical analysis of practical engineering is mainly based on the observation of micro-hole cracks, which is lack macroscopic simulation of the whole mining process. It is unable to intuitively observe the migration and stress change of the hard roof after blasting. Based on the engineering background of the $63_{upper}06$ mining panel of Dongtan deep coal mine, this study statistically analyzethe spatial and temporal distribution of mine seismicities before and after multiple blasting. Moreover, the stress change in the hard strata above the coal seam is also studied. Both results are used to reveal the mechanism of blasting weakening the thick and hard roof to prevent mine seismicities.

ENGINEERING BACKGROUND

Geological Conditions of the Mining Area

The $63_{upper}06$ panel is located in the No.6 mining area of the Dongtan coal mine (see **Figure 1**). The coal seam in this mining area is gently undulating, and the dip angle of the coal seam is 0°~14°, with an average of about 4°. The strata in the mining area generally have a large dip angle in the west, and gentle in the east. The main stratigraphic physical and mechanical parameters of the studied panel roof are listed in **Table 1**.

Mining-Induced Seismicities During Coal Seam Mining

A total of 1927 seisms occur in the 63upper06 panel of Dongtan coal mine from March 2020 to the first deep-hole blasting on March 9, 2021 (see **Figure 2**). Among them, there are 26 large seisms with the energy of 10^5 J and above, and the largest energy is 6.81×10^6 J (see **Figure 3**).

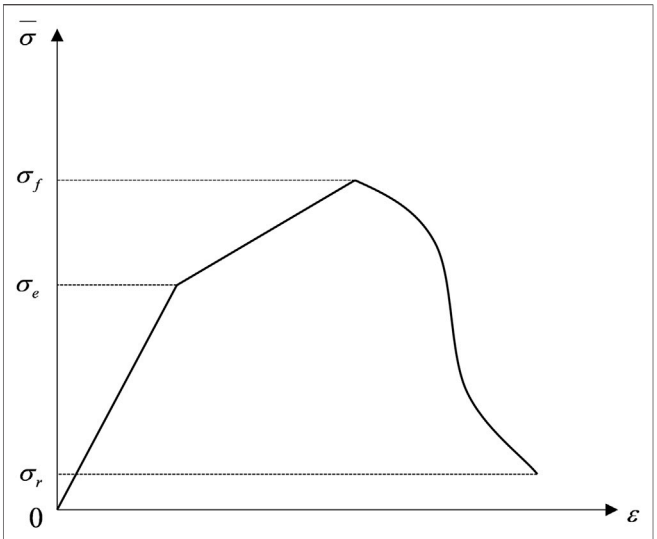


FIGURE 6 | RHT constitutive model.

Deep-Hole Blasting Scheme and Seismicities Monitoring

A total of four times deep-hole blasting are conducted at the 63upper06 panel in the Dongtan No.6 mining area. The first deep-hole blasting is carried out when the working face is advanced by 597 m, with a total of 12 holes arranged, each at a depth of 90 m, in a vertical direction, with a charge of 90 kg. When the working face is advanced 651 m, the second blasting is carried out, 17 holes are set and the sequence of detonation is adjusted. When the working face is advanced to 712 and 753 m, the 3rd and 4th blasting are implemented, and 16 holes are arranged with a depth of 90m, breaking the sandstone layer in the range of 50–90 m above the coal seam. The holes are inclined to the trackside with an inclination of 80°~90° (see **Figure 4**).

The profile locations of mine-induced seismicities before and after blasting are shown in **Figure 5**, and the following analysis can be derived from the figure:

Figure 5A shows that before blasting, the influence range of seismicity events is from 275 m in the goaf behind the working face to 80 m in front of the solid coal side. The seisms with large energy are mostly distributed in the range of 180–50 m in the goaf behind the working face, and the sections are 40 m, 60 m, and 140 m away from the coal seam roof on the profile, respectively.

Figure 5B shows that after the first blasting, the number of mining-induced seismicities in the 20 m range of coal seam roof and floor increased sharply, and the seisms are obviously transferred to the front of the working face. The influence range is from 116 m in the goaf behind the working face to 258 m in front of the solid coal side. The major mining-induced seismicities decrease and occur at 100 m in the goaf behind the working face and 80 m from the section to the coal seam roof on the profile. No mining-induced seismicities with energy greater than or equal to 10^6 J occur again.

Figure 5C shows that compared with the situation after the first blasting, the mining-induced seismicities and their energy increase significantly after the second blasting. The number of mining-induced seismicities continued to increase within the 20 m range of the roof and floor, a total of four major mining-induced seismicities occurred, and the magnitude of strong seisms energy is 10^5 J. The first major mine tremor occurs 63 m behind the working face and 200 m above the roof; the second occurs close to the working face, 157 m above the roof; the third large mine tremor occurs in the immediate roof of the coal seam and 140 m ahead of the working face; the fourth is 266 m behind the working face, 100 m above the coal seam. The influence range of mine earthquake after blasting is from 138 m behind the working face to 436 m in front of the solid coal side.

As shown in **Figure 5D**, after the third deep-hole blasting, the number of mining-induced seismicities decreases significantly, and the influence range is from 188 m behind the goaf to 470 m in front of the solid coal measurement. A major seism occurs 186 m behind the working face, 30 m above the coal seam.

According to the field monitoring data, the distribution of mining-induced seismicities before and after several deep-hole blastings can be concluded that after blasting, mining-induced seismicities may shift from the back of the working face to the front. The number of mining-induced seismicities within 20 m of the roof and floor of the coal seam increase significantly. Therefore, the average height of mine seismic events decreases, and the accumulated strain energy releases well. Compared with that before blasting, there has been a noticeable increase in the number of tremors with an energy of 10^4 J. However, the number of major mining-induced seismicities decreases, and those with energy that reaches 10^6 J basically disappear.

TABLE 4 | Air material and its state equation parameters.

Density /g·cm^{-3}	C_0	C_1	C_2	C_3	C_4	C_5	C_6	E/GPa
1.29e-5	0	0	0	0	0.4	0.4	0	0.025

NUMERICAL SIMULATION OF THE DEEP-HOLE BLASTING

Plane Strain Model of Deep-Hole Blasting

Different from the shallow coal seam, deep coal features higher *in situ* stresses. The different blasting methods also have a great influence on the evolution of rock damage cracks. The smaller the blasting hole spacing is, the more concentrated the effective stress action range generated by the blasting stress waves. Meanwhile, the energy decay rate will be slower, the rock crushing plastic zone and fracture zone will be extended to a larger extent, and the blasting effect will be better. Therefore, the triangular hole plane strain model with concentrated stress action is established, and it is simulated in the following three conditions:

I. Basic group model A. The rock mechanics parameters using $63_{upper}06$ panel high rock sandstone physical and mechanical parameters, no confining pressure, and five holes simultaneously detonated (see **Figures 7A,B**).

II. Control model B. Based on A, the X direction is applied with 20 MPa compressive stress, and the Z direction is applied with 5 MPa

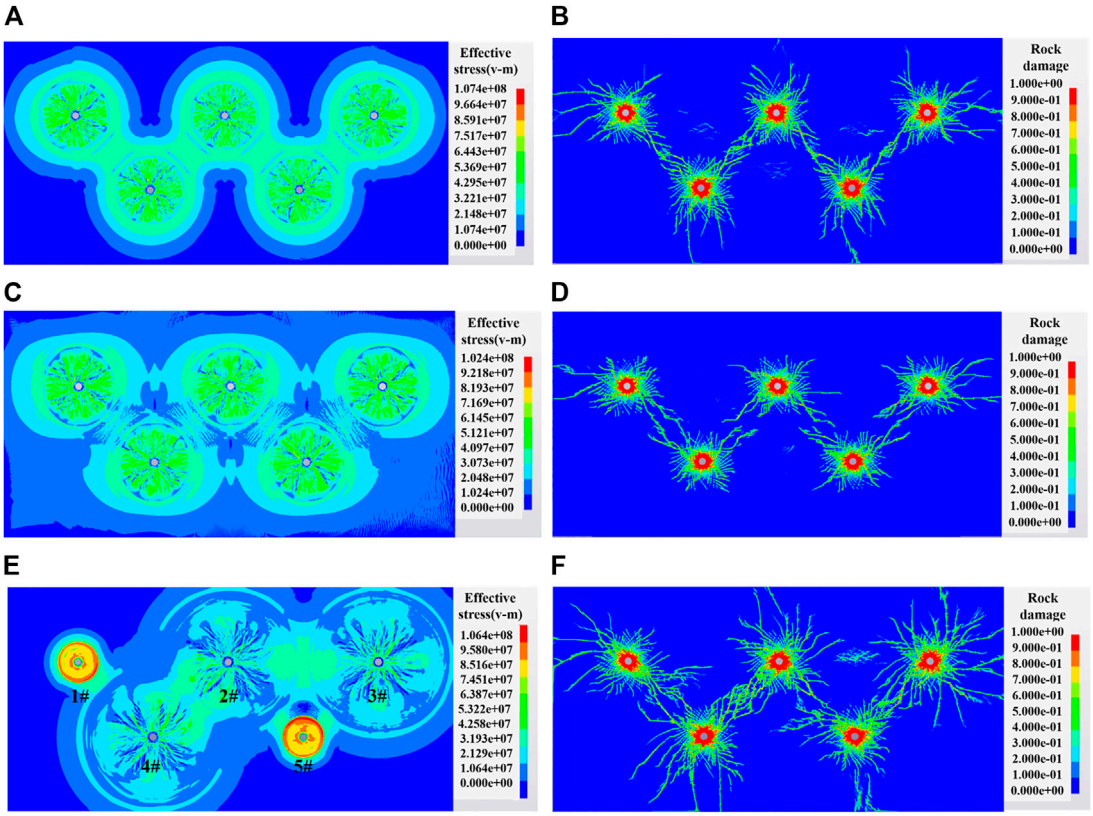


FIGURE 7 | Stress and damage nephogram of rock blasting: **(A)** stress wave expansion nephogram of model A, **(B)** final damage nephogram of model A, **(C)** stress wave expansion nephogram of model B, **(D)** final damage nephogram of model B, **(E)** stress wave expansion nephogram of model C, and **(F)** final damage nephogram of model D.

compressive stress. The impact of high *in situ* stresses on explosive crack growth could be investigated by comparing models A and B (see **Figures 7C,D**).

III. Control group model C. Model C is a case of delay blasting with two holes on the top left and bottom right with 1 ms delay initiation (see **Figures 7E,F**).

LS-DYNA finite element software is used to simulate the fluid-solid coupling of air and rock. The constitutive model of rock is the RHT model, and RHT constitutive equations are as **Eq. 1**, **Eqs 6**, **8**. The parameters are listed in **Table 2**. The curve of RHT can be divided into three stages: elastic stage (equivalent stress $\bar{\sigma} \le \sigma_e$), linear strengthening stage ($\sigma_e \le \bar{\sigma} \le \sigma_f$), and damage softening stage (see **Figure 6**). In the damage softening stage, the damage amount accumulates and leads to material softening. The yield stress decreases with the increase of damage amount, and finally decreases to residual stress σ_r. The failure stress σ_f, elastic limit stress σ_e, and residual stress σ_r are determined by the current pressure, deviatoric stress, and strain rate.

The failure stress σ_f is given as follows:

$$\sigma_f(p,\theta,\dot{\varepsilon}) = f_c \cdot \sigma^*_{TXC}(p_s) \cdot R_3(\theta) \cdot F_{rate}(\dot{\varepsilon}) \tag{1}$$

$$p_s = \frac{p}{F_{rate}(\dot{\varepsilon})} \tag{2}$$

The strain rate factor is given as follows:

$$F_{rate}(\dot{\varepsilon}) = \begin{cases} \left(\frac{\dot{\varepsilon}}{\dot{\varepsilon}^c_0}\right)^a & p \ge f_c/3 \\ \frac{p+f_t/3}{f_c/3+f_t/3}\left(\frac{\dot{\varepsilon}}{\dot{\varepsilon}^t_0}\right)^\delta + \frac{p-f_c/3}{-f_c/3-f_t/3}\left(\frac{\dot{\varepsilon}}{\dot{\varepsilon}^t_0}\right)^\delta & -f_t/3 < p < f_c/3 \\ \left(\frac{\dot{\varepsilon}}{\dot{\varepsilon}^t_0}\right)^\delta & p \le -f_t/3 \end{cases} \tag{3}$$

where f_c is single-axis compressive strength; f_t is uniaxial tensile stress; $F_{rate}(\dot{\varepsilon}) \ge 1$. $\dot{\varepsilon}^c_0 = 30 \times 10^{-6}\dot{\varepsilon}_0$. $\dot{\varepsilon}^t_0 = 3 \times 10^{-6}\dot{\varepsilon}_0$, $\dot{\varepsilon}^t_0 = 1.0s^{-1}$; a and δ are material parameters; σ^*_{TXC} is compressive equivalent stress strength of failure surface; and θ is Lode angle ($\theta \in [0, \pi/3]$).

$$R_3(\theta,Q) = \frac{2(1-Q^2)\cos\theta + (2Q-1)\sqrt{4(1-Q^2\cos^2\theta - 4Q + 5Q^2}}{4(1-Q^2)\cos^2\theta + (1-2Q)^2} \tag{4}$$

where Q is the ratio of the tensile and compressive strength.

Under quasi-static loading conditions, $\sigma^*_{TXC} = \sigma^*_{TXC}(p_s)$

$$\sigma^*_{TXC}(p_s) = \begin{cases} \frac{p_s}{-f_t/3}\frac{f_t}{f_cQ} + \frac{p_s+f_t/3}{f_t/3}\frac{f_s}{f_t/3}\frac{f_s}{f_cR^S_3} & -HTL \le p_s \le 0 \\ \frac{p_s-f_c/3}{f_c/3}\frac{f_s}{f_cR^S_3} + \frac{p_s}{f_c/3} & 0 < p_s \le f_c/3 \\ A(p^*_s - HTL^*)^n & p_s > f_c/3 \end{cases} \tag{5}$$

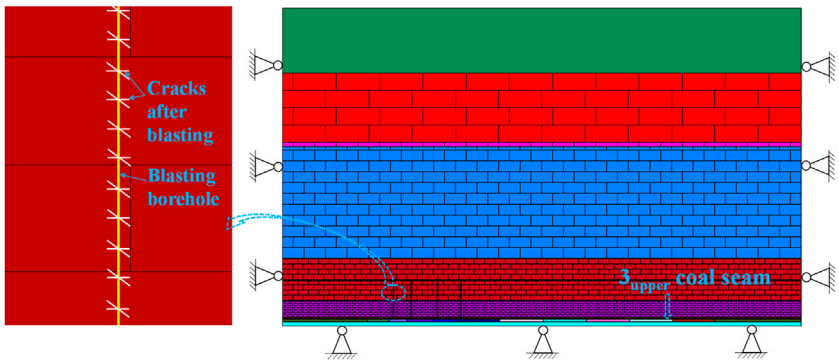


FIGURE 8 | Excavation and the blast hole model.

where A is failure surface parameters; n is failure surface index; and f_s is shear strength of pure shear.

When $\sigma^*_{TXC}(p_s)$ satisfies continuity at $p_s = f_c/3$, HTL^* can be obtained as follows:

$$HTL^* = 1/3 - (1/A)^{1/n}$$

The elastic limit stress σ_e is given as follows:

$$\sigma_e = f_c \cdot \sigma^*_{TXC}\left(p_{s,el}\right) \cdot R_3(\theta) \cdot F_{rate}(\dot{\varepsilon}) \cdot F_e \cdot F_c \tag{6}$$

$$F_e = \begin{cases} R_e & p_s \geq f_{c,el}/3 \\ \dfrac{p + f_{t,el}/3}{f_{c,el}/3 + f_{t,el}/3} R_c + \dfrac{p - f_{c,el}/3}{-f_{c,el}/3 - f_{t,el}/3} R_t & -f_{t,el}/3 < p < f_{c,el}/3 \\ R_t & p_s \leq -f_{t,el}/3 \end{cases} \tag{7}$$

where $f_{c,el} = f_c R_c$, $f_{t,el} = f_t R_t$, $p_{s,el} = \frac{p_s}{F_e}$; and Rc and Rt are material parameters.

The residual stress σ_r is given as follows:

$$\sigma_r = f_c B\left(p^*\right)^M \leq f_c S^f_{\max} \tag{8}$$

where B, M, and $S^f_{\max}$ are material parameters.

The equation of state parameters of the explosive and air are listed in **Table 3** and **Table 4**, equations of state for the explosive and air, as shown in **Eqs 5**, **6**. The model size is 12 m (length) × 6 m (height), the accuracy is 0.001 m, and the vertical and horizontal spacings between adjacent boreholes are 2 m.

The equation of the explosive state is given as follows:

$$P = A\left(1 - \frac{\omega}{R_1 V}\right)e^{-R_1 V} + B\left(1 - \frac{\omega}{R_2 V}\right)e^{-R_2 V} + \frac{\omega E_0}{V} \tag{9}$$

where P is the pressure of detonation products; V is relative volume; E_0 is the initial internal energy density; and A, B, R_1, R_2, ω are constants.

The equation of air state is given as follows:

$$P = C_0 + C_1\mu + C_2^2\mu^2 + C_3\mu^3 + \left(C_4 + C_5\mu + C_6\mu^2\right)E \tag{10}$$

where, C_1, C_2, C_3, C_4, C_5, and C_6 are coefficients of the state equation; E is unit initial internal energy of relative volume; and $\mu = \frac{1}{V} - 1$, V is relative volume.

Expansion Mechanism of Rock Damage Under Blasting

After the model A damage stops expanding, the radius of the smash district is 2–3 times of the aperture, the radius of the fracture zone is 11–17 times of the aperture, and the longest fracture radius is more than 2 m. After the damage of model B stops expanding, the radius of the smash district is 1–2 times of the aperture, the radius of the fracture zone is 10–13 times of the aperture, and the longest fracture is about 1.6 m. **Figure 7D** shows that the maximum principal stress has a great inhibitory effect on the crack propagation in the vertical direction. After the damage of model C stops expanding, the radius of the smash district is 2–3 times the pore diameter, the radius of the fracture zone is 11–20 times, and the longest fracture radius is 2.5 m. According to the crack propagation direction in the crack zones of No. 1 and No. 5 holes, the holes with cracks produced by blasting have an obvious orientation to the crack propagation of the unexploded holes, and the crack zone of the blast hole with delayed initiation becomes an ellipse with long axis pointing to the blast hole. The stress wave and detonation gas produced by delay initiation further activate the existing cracks, expand the crack area of the blast hole, and deepen the penetration of the blast hole spacing.

NUMERICAL SIMULATION OF MINING-INDUCED ROCK BROKEN AFTER BLASTING

Modeling and Numerical Simulation Methods

According to the engineering geological conditions and the expansion law of burst cracks under the deep high stress conditions as described earlier, a discrete element model of the whole process of mining on the $63_{upper}06$ panel is established by UDEC software. The size of the model is 1,200 m (length) × 735 m (height), which limits the displacement of each node on both sides of the model and at the bottom (see **Figure 8**). The block element of rock and

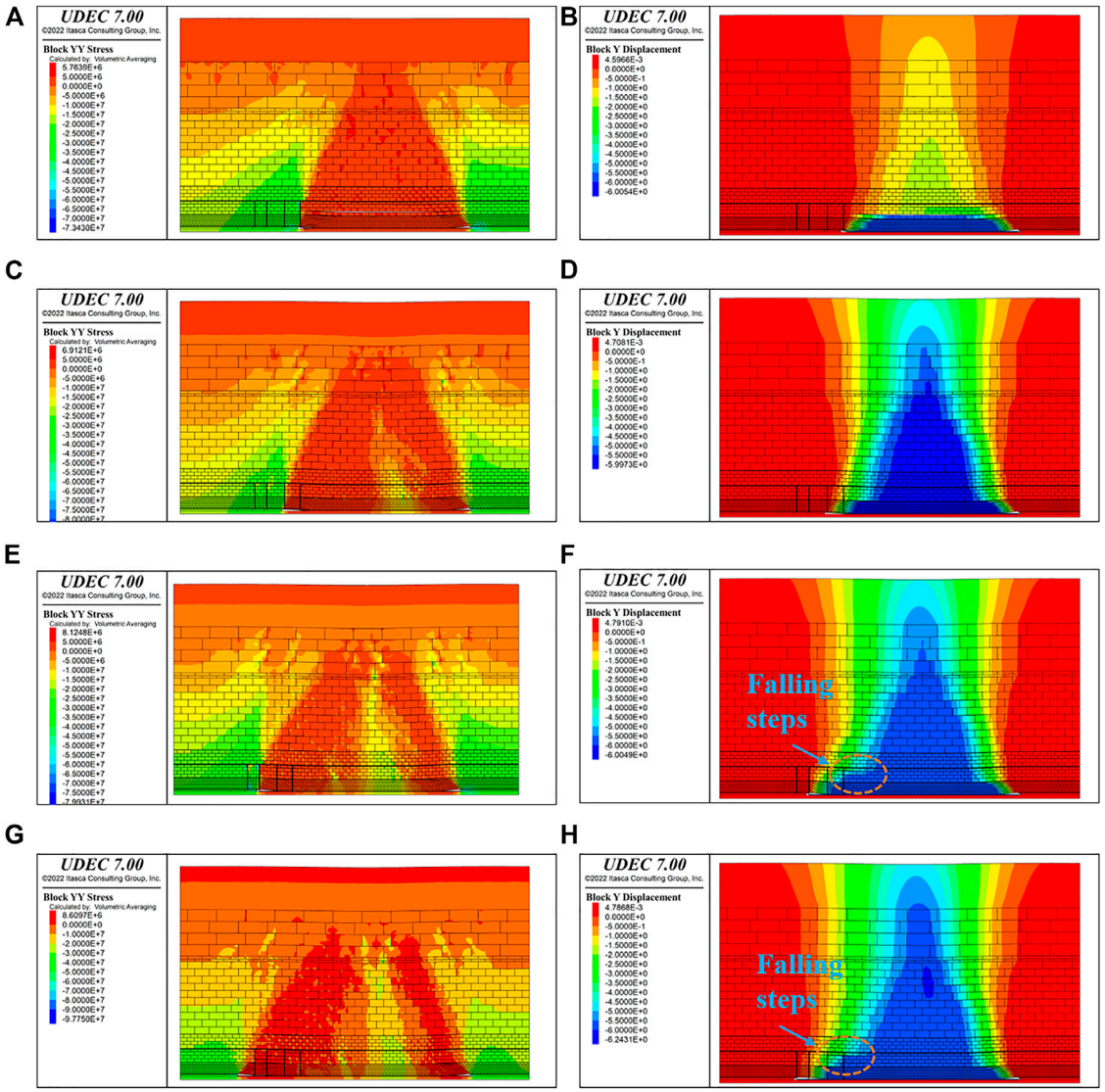


FIGURE 9 | Stress and displacement nephograms of deep-hole blasting (+ represents the tensile stress, - represents compressive stress): **(A)** the stress nephogram after the 1st blasting; **(B)** the displacement nephogram after the 1st blasting; **(C)** the stress nephogram after the 2nd blasting; **(D)** the displacement nephogram after the 2nd blasting; **(E)** the stress nephogram after the 3rd blasting; **(F)** the displacement nephogram after the 3rd blasting; **(G)** the stress nephogram after the 4th blasting; and **(H)** the displacement nephogram after the 4th blasting.

coal seam adopts the Mohr-Coulomb constitutive model, and the contact constitutive model of the elastic-plastic joint zone with Coulomb slip failure is adopted. The cracks after blasting are approximately simulated by horizontal and cross joints, with a length of 8–10 times the aperture. From right to left, 500 m of excavation is divided into five steps, and then four times deep-hole blasting is carried out. The blasting positions are all within the range of 10 m behind the working face. Finally, 50 m of excavation is continued to observe the subsequent stress distribution. The horizontal ground stress is applied to the model at 23 MPa. The physical and mechanical parameters in **Table 1** are used for the stratigraphic parameters.

Pressure Relief Mechanism of Blasting Weakening the Thick Hard Roof During Deep Coal Excavation

Figure 9 shows the displacement and stress changes in the vertical profile after four simulated roof breaking. When the working face is advanced 597 m, the first blasting is carried out (see **Figures 9A,B**). The following three blastings are conducted when the working face is advanced at 651 (**Figures 9C,D**), 712 (**Figures 9E,F**), and 753 m (**Figures 9G,H**), respectively.

After the first blasting, the suspended roof collapses rapidly. Within the range of 56 m above the coal seam and 80 m behind the working face, the roof weighting fracture and rotary

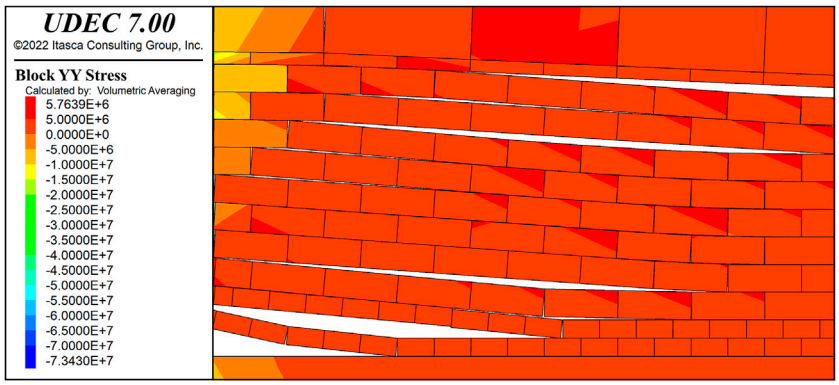


FIGURE 10 | Delamination and rotary instability failure.

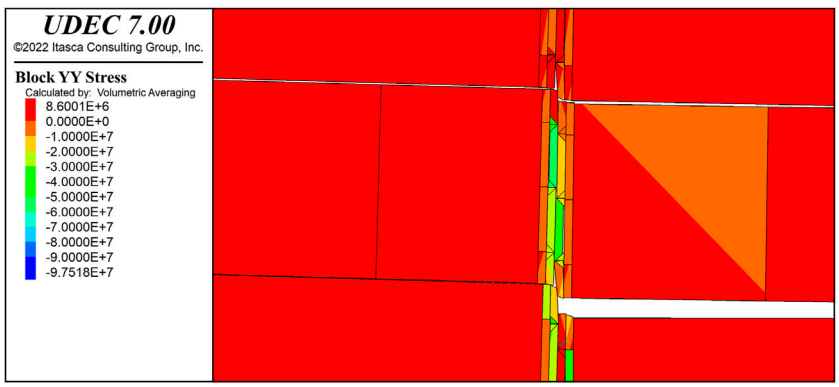


FIGURE 11 | Blasting borehole damage.

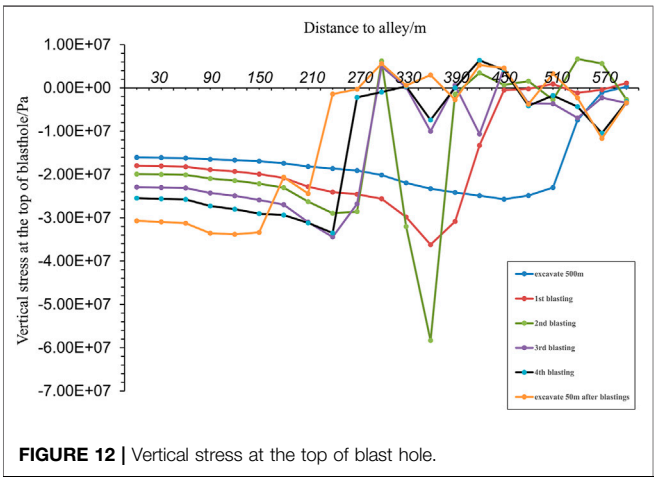


FIGURE 12 | Vertical stress at the top of blast hole.

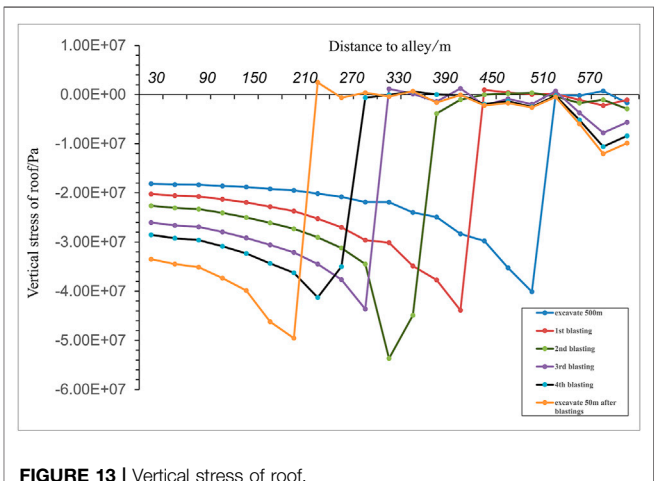


FIGURE 13 | Vertical stress of roof.

instability failure occur in the low strata, which is easy to produce high-frequency and low-energy mining-induced seismicities. The range of tensile stress zone after roof cutting is expanded, and the stress concentration zone is formed within the range of 73–86 m above the roof near the end of the blasting hole. It is prone to mining-induced seismicities. Combined with the spatial and temporal distribution range of mining-induced seismicities in the mining area after blasting and the location of major

mining-induced seismicities mentioned in Chapter 2, the results are close to the numerical simulation results, which verifies the feasibility of the model. Meanwhile, the suddenly forced roof caving causes the separation of the low rock layer from the upper mudstone layer and the separation of the mudstone layer, leaving a large space for the activity of the upper roof rock. (see **Figure 10**). The damage form of the blast hole is shown in **Figure 11**.

After the second blasting, the cantilever made up of a long hard roof is further weakened. The mudstone in the hard roof fully collapses and fills the separation space generated by the first deep-hole blasting. The rock's broken height rises rapidly and migrates violently, the stress changes sharply, and the accumulated energy released from the top cutting hole. The thick sandstone in the high layer above the working face suddenly bears great compressive stress, thus the extrusion shear failure occurs, as shown in **Figure 12**. On account of the energy accumulated in the high layer being much larger than that in the low layer, the possibility of major mining-induced seismicities increases. Combined with the field monitoring results, two large seisms with the energy of 10^5 J occur in the high layer above the working face after the second blasting. The simulation results are in accordance with the reality.

After the second blasting, the rock fully collapses and the space is filled. From **Figure 13**, the peak stress of the third and fourth blasting is significantly reduced, and lower than the peak stress of the working face without blasting. The peak compressive stress after blasting is in front of the working face and farther away from the working face. The newly emerged faults are mainly in the low layers, where the depth of mining-induced seismicities and their energy will be reduced. However, the frequency will be increased. Mining-induced seismicity events should be lower than the total number of events after either the first blasting or the second blasting.

From **Figure 9F** and **Figure 9H**, it can be concluded that the rock strata with top-cutting blasting are more likely to form step collapse. In this way, in the process of advancing the working face, the roof collapse rate will slow down, but the collapse will be more fully and gradually stable filling goaf behind the working face, which is conducive to safe production.

CONCLUSION

Based on the engineering background of the $63_{upper}06$ panel of Dongtan deep coal mine, we first investigate the spatial and temporal distribution of mining-induced seismicities before and after multiple deep-hole blastings, and then the stress and displacement in hard rock are simulated. Results reveal the mechanism of blasting weakening the thick and hard roof to prevent and control mining-induced seismicities. The main conclusions are as follows:

1) After deep-hole blasting, the mining-induced seismicities gradually transferred from the back of the working face to the solid coal side in front of the working face, with an increase in small mining-induced seismicities and an overall decrease in major seismicities. Small mining-induced seismicities are more concentrated within 20 m of the near field.
2) After deep-hole blasting, the crack propagation perpendicular to the direction of the maximum principal stress is inhibited. Delayed blasting could enlarge the range of the fractured zone and deepen the penetration between blasting holes.
3) The first deep-hole blasting may generate a large number of voids and abscission layers in the thick roof. After the second blasting, the rock mass breaks and collapses, with the stress changing rapidly, and cracks developing faster. After the stress released by the second deep-hole blasting, the peak stress decreases significantly after the third blasting, and the energy accumulated in the high strata reduces a lot. The mining-induced seismicities may be greatly diminished and mainly occur in the low layer.
4) Deep-hole blasting cuts off the upper roof, which is easier to form stepped collapse. The roof caving rate is reduced, making the roof collapse more fully as well.

In conclusion, the deep-hole blasting technology has a remarkable effect on weakening coal seam roofs and preventing and controlling large-energy mining-induced seismicities.

DATA AVAILABILITY STATEMENT

The original contributions presented in the study are included in the article/Supplementary Material, further inquiries can be directed to the corresponding authors.

AUTHOR CONTRIBUTIONS

XZ: investigation; CW: methodology; CZ: writing-original draft preparation; JZ and Y-YJ: writing-review and editing. All authors have read and agreed to the published version of the manuscript.

FUNDING

This work was supported by the China National Natural Science Foundation (Nos. 41731284, 41920104007, 42177152, and 41902293) and the Fundamental Research Funds for the Central Universities, China University of Geosciences (Wuhan) (Nos. 107-162301202609 and 107-162301212608).

REFERENCES

Century Dynamics Ltd. (2000). *AUTODYN: Theory Manual*. 4.3 edition. California: Concord.

Chen, B., and Liu, C. (2018). Analysis and Application on Controlling Thick Hard Roof Caving with Deep-Hole Position Presplitting Blasting. *Adv. Civ. Eng.* 2018 (1), 1–15. doi:10.1155/2018/9763137

Chun-rui, L., Li-jun, K., Qing-xing, Q., De-bing, M., Quan-ming, L., and Gang, X. (2009). The Numerical Analysis of Borehole Blasting and Application in Coal Mine Roof-Weaken. *Procedia Earth Planet. Sci.* 1 (1), 451–459. doi:10.1016/j.proeps.2009.09.072

Gibowicz, S. J., and Lasocki, S. (2001). Seismicity Induced by Mining: Ten Years Later. *Adv. Geophys.* 44, 39–181. doi:10.1016/S0065-2687(00)80007-2

Guest, A. R., Chitombo, G. P., and Grobler, H. P. (1995). Blast Optimization for Efficient Extraction of a Block Cave Undercut-Case Studies at De Beers Consolidated Mine Ltd., South Africa. *Proc. EXPLO* 95, 75–80.

He, H., Dou, L., Cao, A., and Fan, J. (2015). Mechanisms of Mining Seismicity under Large Scale Exploitation with Multikey Strata. *Shock Vib.* 2015 (8), 1–9. doi:10.1155/2015/313069

Holmquist, T. J., Johnson, G. R., and Cook, W. H. (1993). A Computational Constitutive Model for Concrete Subjected to Large Strains, High Strain Rates, and High Pressures. *Proc. 14thInternational Symposium Ballist.* 91 (22), 116–125. doi:10.1016/j.ijimpeng.2016.01.003

Hua, Z. S. (2019). Study on Rock Mechanics in Deep Mining Engineering. *Chin. J. Rock Mech. Eng.* 24 (16), 163449–163460. doi:10.1142/9789812772411_0003

Huang, B., Wang, Y., and Cao, S. (2015). Cavability Control by Hydraulic Fracturing for Top Coal Caving in Hard Thick Coal Seams. *Int. J. Rock Mech. Min. Sci.* 74, 45–57. doi:10.1016/j.ijrmms.2014.10.011

Jiao, Y.-Y., Wu, K., Zou, J., Zheng, F., Zhang, X., Wang, C., et al. (2021). On the Strong Earthquakes Induced by Deep Coal Mining under Thick Strata-A Case Study. *Geomech. Geophys. Geo-energ. Geo-resour.* 7 (7), 1. doi:10.1007/s40948-021-00301-1

Kan, J., Dou, L., Li, J., Li, X., Bai, J., and Wang, M. (2022). Characteristics of Microseismic Waveforms Induced by Underground Destress Blasting: Comparison with Those Induced by Ground Blasting and Coal Mining. *Front. Earth Sci.* 10, 797358. doi:10.3389/feart.2022.797358

Kutter, H. K., and Fairhurst, C. (1971). On the Fracture Process in Blasting. *Int. J. Rock Mech. Min. Sci. Geomechanics Abstr.* 8 (3), 181–202. doi:10.1016/0148-9062(71)90018-0

Liu, Z., Zhang, Y., Huang, Z., Gao, Y., and Zhang, Y. (2012). Numerical Simulating Research on Orifice Pre-splitting Blasting in Coal Seam. *Procedia Eng.* 45, 322–328. doi:10.1016/j.proeng.2012.08.165

Lu, A., Dou, L., Bai, J., Chai, Y., Zhou, K., Kan, J., et al. (2021). Mechanism of Hard-Roof Rock Burst Control by the Deep-Hole Blasting: Numerical Study Based on Particle Flow. *Shock Vib.* 2021 (5), 1–14. doi:10.1155/2021/9527956

Riedel, W. (2004). "Beton unter dynamischen Lasten: meso- und makromechanische Modelle und ihre Parameter," in *Institut für Kurzzeitdynamik, Ernst-Mach-Institut EMI*. Editor Fraunhofer (Freiburg/Brsg: Fraunhofer IRB Verlag). doi:10.1002/best.198500370

Senfaute, G., Chambon, C., Bigarré, P., Guise, Y., and Josien, J. P. (1997). Spatial Distribution of Mining Tremors and the Relationship to Rockburst Hazard. *Pure Appl. Geophys.* 150 (3-4), 451–459. doi:10.1007/s000240050087

Tang, Z. C., Wu, Z. L., and Zou, J. (2022). Appraisal of the Number of Asperity Peaks, Their Radii and Heights for Three-Dimensional Rock Fracture. *Int. J. rock Mech. Min. Sci.* 153, 105080–111609. doi:10.1016/j.ijrmms.2022.105080

Xie, L. X., Lu, W. B., Zhang, Q. B., Jiang, Q. H., Chen, M., and Zhao, J. (2017). Analysis of Damage Mechanisms and Optimization of Cut Blasting Design under High Iin-Ssitu Stresses. *Tunn. Undergr. Space Technol.* 66, 19–33. doi:10.1016/j.tust.2017.03.009

Zhang, Y., Du, C., Feng, G., Yuan, H., Deng, X., Zhang, R., et al. (2022). Study on the Law of Subsidence of Overburden Strata above the Longwall Gob. *Geofluids* 2022, 1–10. doi:10.1155/2022/6321031

Zuo, J., Li, Z., Zhao, S., Jiang, Y., Liu, H., and Yao, M. (2019). A Study of Fractal Deep-Hole Blasting and its Induced Stress Behavior of Hard Roof Strata in Bayangaole Coal Mine, China. *Adv. Civ. Eng.* 2019 (1), 1–14. doi:10.1155/2019/9504101

Conflict of Interest: XZ and CW were employed by the Company Shandong Energy Group Co., Ltd.

The remaining authors declare that the research was conducted in the absence of any commercial or financial relationships that could be construed as a potential conflict of interest.

Publisher's Note: All claims expressed in this article are solely those of the authors and do not necessarily represent those of their affiliated organizations, or those of the publisher, the editors, and the reviewers. Any product that may be evaluated in this article, or claim that may be made by its manufacturer, is not guaranteed or endorsed by the publisher.

Copyright © 2022 Zhang, Zou, Zhang, Wang and Jiao. This is an open-access article distributed under the terms of the Creative Commons Attribution License (CC BY). The use, distribution or reproduction in other forums is permitted, provided the original author(s) and the copyright owner(s) are credited and that the original publication in this journal is cited, in accordance with accepted academic practice. No use, distribution or reproduction is permitted which does not comply with these terms.

frontiers | Frontiers in Earth Science

ORIGINAL RESEARCH
published: 27 June 2022
doi: 10.3389/feart.2022.896459

A New Classification Method of Mine Goaf Ground Activation Considering High-Speed Railway Influence

Lian-wei Ren[1], Peng-fei He[1], You-Feng Zou[2], Zhi-Lin Dun[1], Zheng-sheng Zou[1] and Shu-ren Wang[1]*

[1]School of Civil Engineering, Henan Polytechnic University, Jiaozuo, China, [2]School of Surveying and Land Information Engineering, Henan Polytechnic University, Jiaozuo, China

With the rapid development of high-speed railways in China, it is inevitable that some of the lines will have to traverse through the mine goaf ground, and there is little research on whether the "activation" of the foundation of the mine goaf ground occurs under the influence of train loads. In order to provide a safe and reliable basis for the construction of high-speed railway in mine goaf ground, a new classification method of mine goaf ground activation is proposed considering the stability and railway influence. First, the stability evaluation system of the mine goaf site is established with 3 primary indexes and 12 secondary indexes. The 47 groups' data of the mine goaf ground site are collected as learning samples. Five machine learning methods including decision tree, discriminant analysis, support vector machine, and classifier ensemble are used to learn and test the data. The optimal algorithm is selected and the stability evaluation model is established to classify the stability of the mine goaf site. Second, influencing factors of railway are graded to establish an extension comprehensive evaluation model. Finally, based on the above two models, a new classification method of high-speed railway goaf ground activation considering the two factors and five sub-factors is proposed. Through the verification of two engineering examples, the prediction result of this method is "easily activation" and the need to treat the goaf area, and the actual construction is also taken to grouting treatment, proving that the method has certain guiding significance for the project.

Keywords: mine goaf ground, activation classification, high-speed railway, machine learning, extension theory

OPEN ACCESS

Edited by:
Shibing Huang,
Wuhan University of Science and Technology, China

Reviewed by:
Danqing Song,
Tsinghua University, China
Xiangxin Liu,
North China University of Science and Technology, China

****Correspondence:***
Peng-fei He
212008010028@home.hpu.edu.cn

Specialty section:
This article was submitted to Geohazards and Georisks, a section of the journal Frontiers in Earth Science

Received: *15 March 2022*
Accepted: *09 May 2022*
Published: *27 June 2022*

Citation:
Ren L-w, He P-f, Zou Y-F, Dun Z-L, Zou Z-s and Wang S-r (2022) A New Classification Method of Mine Goaf Ground Activation Considering High-Speed Railway Influence. Front. Earth Sci. 10:896459. doi: 10.3389/feart.2022.896459

1 INTRODUCTION

With the acceleration of China's railway network construction, construction conditions faced by railway engineering are becoming more and more demanding. Taking Shanxi Province as an example, due to its rich coal resources, after years of intensive mining, it has formed nearly 2300 km^2 of goaf areas, the size of which makes it inevitable that many planned high-speed railway lines will have to pass through these goaf areas (**Figure 1A**). When the high-speed railway passes through the mine goaf ground (**Figure 1B**), the influence of the train load may lead to the separation closure or the instability of the stable structure in the mine goaf ground (Du et al., 2020), which leads to the "activation" deformation of the foundation and the uneven settlement of the high-speed railway subgrade, thus affecting the safety of the train operation (Jiang and Wang, 2019).

Many scholars have conducted extensive research on the stability of underground spaces and disaster prevention (Liu et al., 2020, 2021). Helm et al. (2013) established 1,320 numerical simulation models to analyze the influence of shallow-buried room-and-pillar mine goaf ground on surface traffic

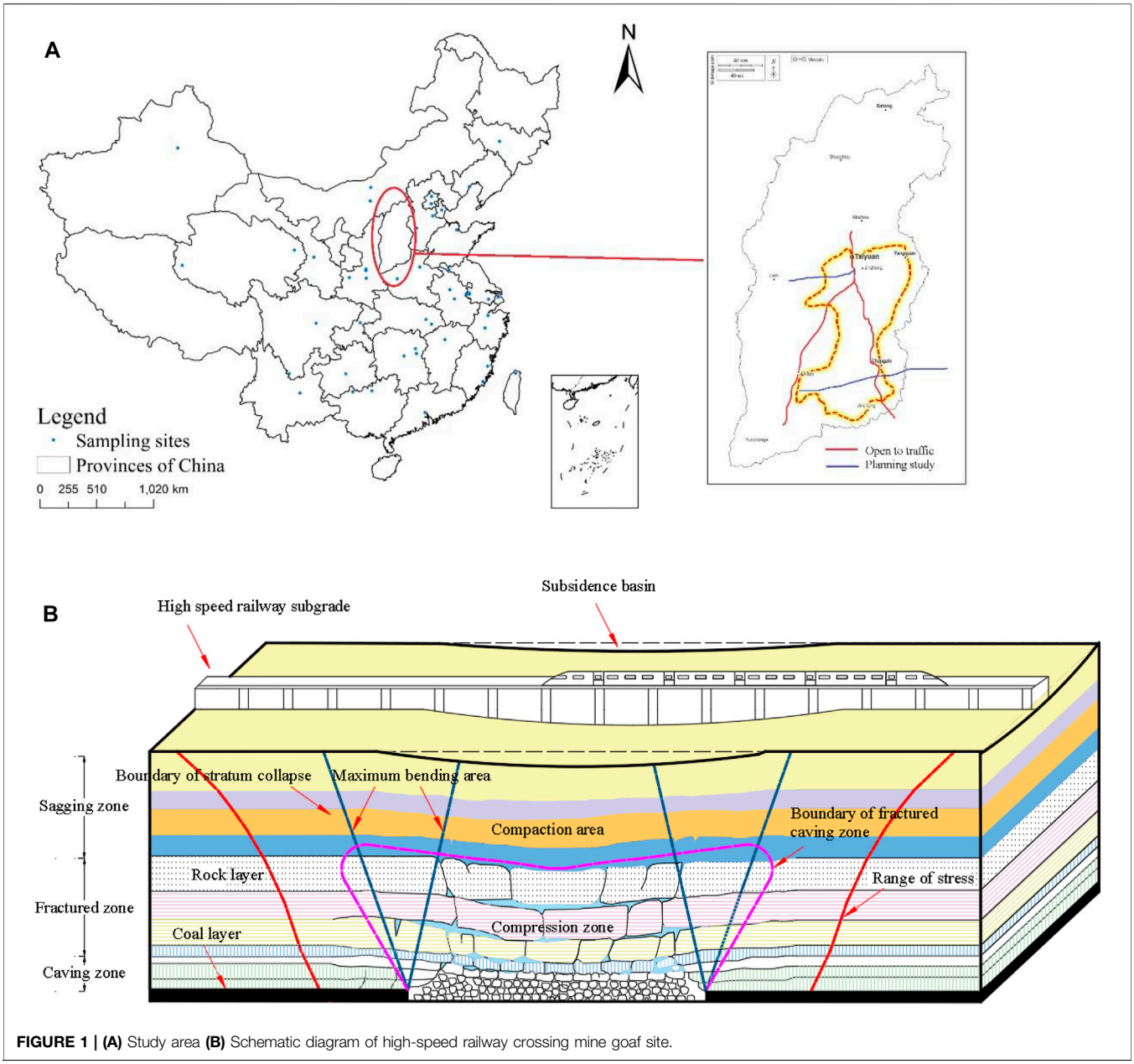


FIGURE 1 | (A) Study area **(B)** Schematic diagram of high-speed railway crossing mine goaf site.

facilities, and pointed out that seasonal water-level changes would have a great impact on the stability of overlying strata and surface in the mine goaf ground. Liu et al. (2018, 2019) monitored the rock burst of the tunnel using the acoustic emission technology and infrared monitoring equipment. Cui et al. (2014) and Bell et al. (2001) analyzed the collapse instability cases of shallow mining areas after partial mining, and revealed that the partial mining instability was caused by the decrease of residual coal pillar strength, which made the internal and external stress arches interrelated. Li et al. (2016) proposed a calculation method of release space based on the pore distribution characteristics of rock strata above mine goaf ground and applied it to engineering practice to prove the effectiveness of this method. Hu and Li (2012) selected four indicators as the risk identification factors of mine goaf ground stability and proposed a mine risk analysis method based on Bayesian discriminant analysis. Through the training of 40 samples, the model accuracy reached 0.025. Qin et al. (2019) proposed an improved tradabost algorithm and introduced the concept of dynamic factor to improve the generalization ability of the algorithm for different mine goaf ground samples. The algorithm can also maintain high accuracy with fewer samples. Guo et al. (2019), based on fuzzy theory, established the instability risk evaluation model of an expressway construction site in the mine goaf ground. The weight and membership degree were determined by the gray correlation method and the Delphi method. The reliability of the model was verified by subgrade settlement monitoring data.

Although there has been some research into the stability of the mine goaf ground and the effects of external loads on the

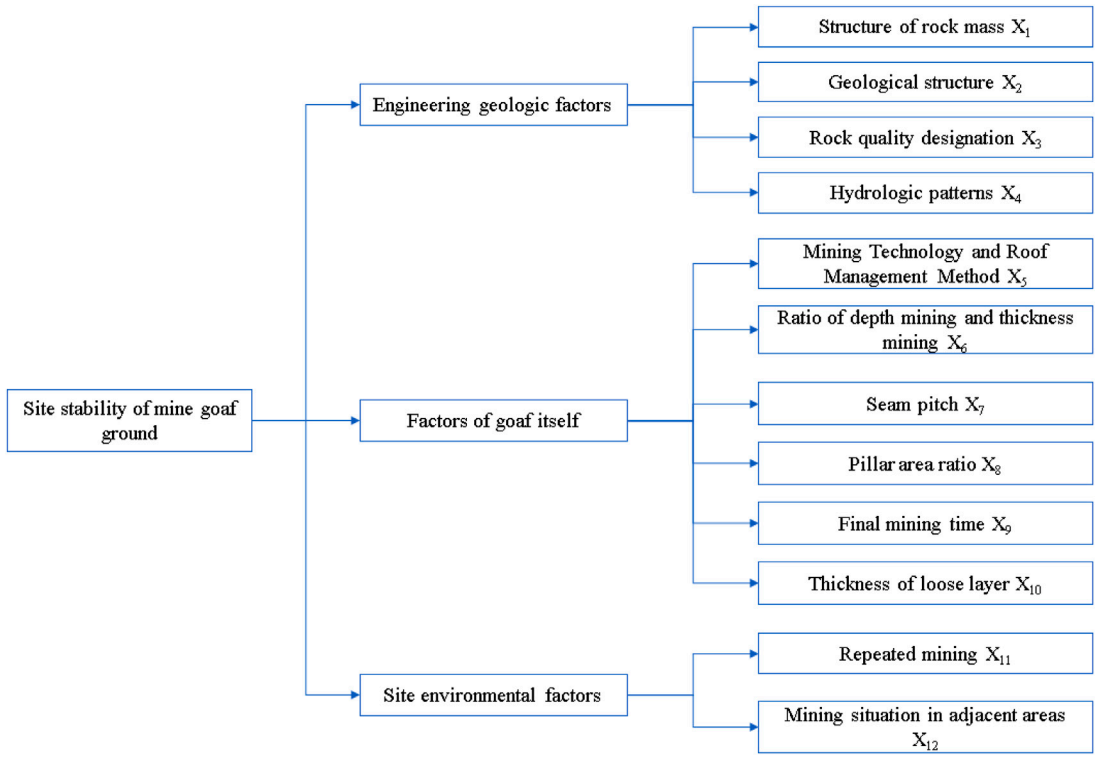


FIGURE 2 | Stability evaluation index system.

mine goaf ground, there has been less research into the "activation" of mine goaf ground of high-speed railway. The foundation problem of the mine goaf ground is an extremely complex problem, which is not only affected by mining technology, burial depth, and mining height but also by hydrogeology, spatial location distribution, and external load. In order to establish a reasonable evaluation system of high-speed railway mine goaf ground activation, first, collect a large number of mine goaf ground data, select the evaluation index of mine goaf ground stability, adopt the classification algorithm of machine learning to learn the samples, and complete the classification of stability grade so as to determine the stability grade of the mine goaf ground. Then, the information entropy-extension comprehensive evaluation model is established (Xie et al., 2021), and the mine goaf ground activation grade is obtained by combining the stability of the mine goaf ground and the influence of train load.

Compared with traditional evaluation methods, it not only solves the problem of subjective selection of weights in the comprehensive evaluation method but also solves the problem of difficult selection of parameters and complicated calculation in the mechanical analysis method.

2 STABILITY EVALUATION OF MINE GOAF GROUND

2.1 Evaluation Index System

The deformation of a mining site is an extremely complex process, and the most critical step in establishing a scientific index system for evaluating the stability of a mine goaf ground is to fully consider the impact of various factors on the mine goaf ground. Guo et al. (2019) and Zhao et al. (2021) established different evaluation index systems of mine goaf

TABLE 1 | Stability classification of the mine goaf ground.

Level	Hierarchical features
I	The caving zone and fault zone in mine goaf ground are dense and have little influence on engineering construction
II	The caving zone and fault zone of mine goaf ground are basically dense, which have little influence on engineering construction, and the residual deformation is small
III	The caving of mine goaf ground is insufficient and discontinuous deformation may occur, which has great influence on engineering construction
IV	The collapse of mine goaf ground is not sufficient, which is prone to discontinuous deformation and has great influence on engineering construction

TABLE 2 | Qualitative evaluation index rating and assignment.

Factor	I	II	III	IV
Assignment	1	2	3	4
Structure of rock mass	Complete block structure	Laminated structure	Crushing structure	Loose smut of wheat structure
Geological structure	No faults and folds	The fault depth is less than the thickness of the loose layer	Fault partial cutting	Fault runs through wall rock
Hydrologic patterns	There is no water around the wall rock	Water around the wall rock, less affected	Leaching occurs in rainy season and surrounding rock is affected by water	Long-term leaching, wall rock affected greatly
Repeated mining	No impact	Less impact	Greater impact	Great impact
Mining situation in adjacent areas	No other mine goaf grounds within the affected area	The area of mine goaf ground is small, the quantity is not much, and the mine goaf ground is concentrated	Large area, large quantity, and scattered distribution of mine goaf ground within the scope of influence	The mine goaf ground within the scope of influence is large, a large number, more concentrated, as the mine goaf ground group

ground stability. In this study, the above three evaluation index systems are comprehensively considered, and the evaluation index system of mine goaf ground stability is established as shown in **Figure 2**. Compared with other evaluation systems, the two factors of final mining time and loose layer thickness are added to the consideration. The final mining time is related to the residual deformation of the mine goaf ground, which plays a relatively important role in the construction of the mine goaf ground site, and the thickness of the loose layer also has a certain influence. Many scholars have found that the loose layer will form a loose arch structure under a certain thickness, and bear part of the external load.

2.2 Stability Classification

To be better combined with the analysis of train load, this study combined with the code for investigation of geotechnical engineering in the coal mine goaf (GB51044-2014, 2014) and

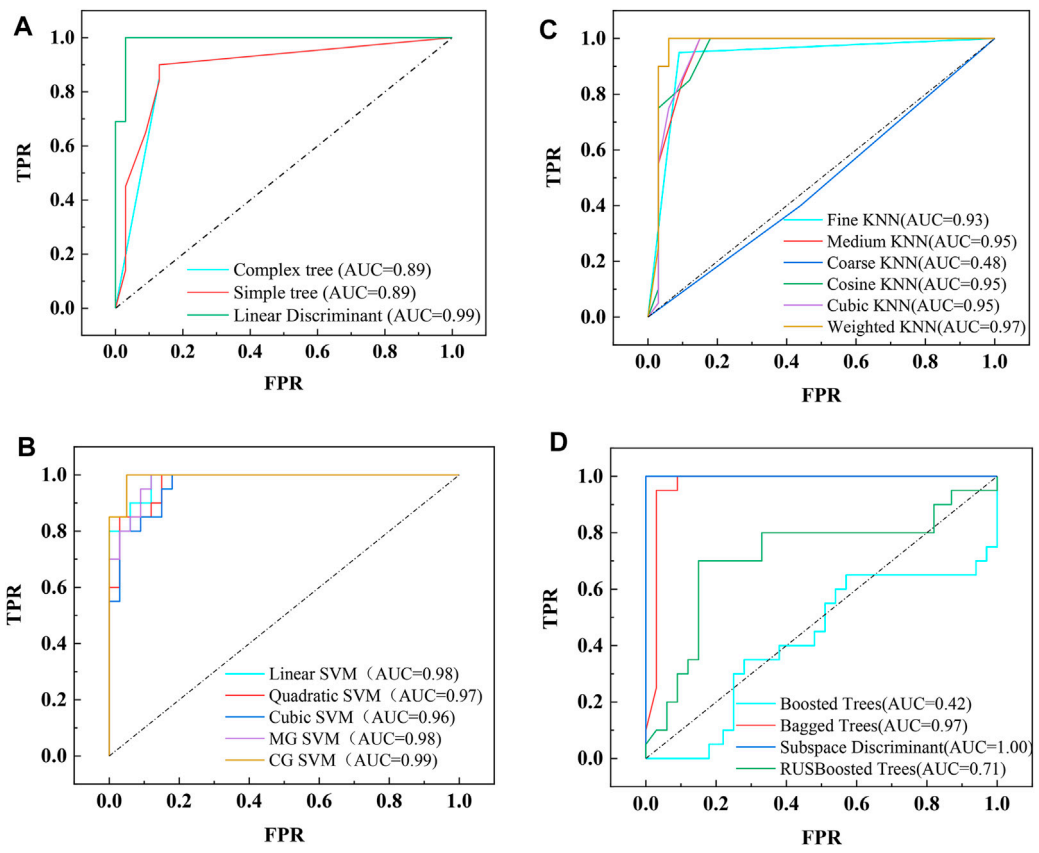


FIGURE 3 | Performance of AUC values of each model. **(A)** Decision tree and discriminant analysis, **(B)** support vector machine, **(C)** K-nearest neighbor, and **(D)** classifier ensemble.

TABLE 3 | Optimal model performance data for algorithms.

Algorithm	Model	Accuracy, %	AUC
Decision tree	Complex tree	86.5	0.96
	Medium tree	86.5	0.96
	Simple tree	86.5	0.96
Discriminant analysis	Linear discriminant	94.6	1.00
	Quadratic discriminant	Failed	Failed
SVM	Linear SVM	91.9	0.98
	Quadratic SVM	97.3	0.99
	Cubic SVM	94.6	0.98
	Medium Gaussian SVM	86.5	0.98
	Coarse Gaussian SVM	75.7	0.95
KNN	Fine KNN	89.2	0.96
	Medium KNN	78.4	0.94
	Coarse KNN	35.1	0.44
	Cosine KNN	70.3	0.95
	Cubic KNN	81.1	0.94
	Weighted KNN	86.5	0.98
Classifier ensemble	Boosted trees	32.4	0.53
	Bagged trees	86.5	1.00
	Subspace discriminant	97.3	1.00
	RUSBoosted trees	48.6	0.66

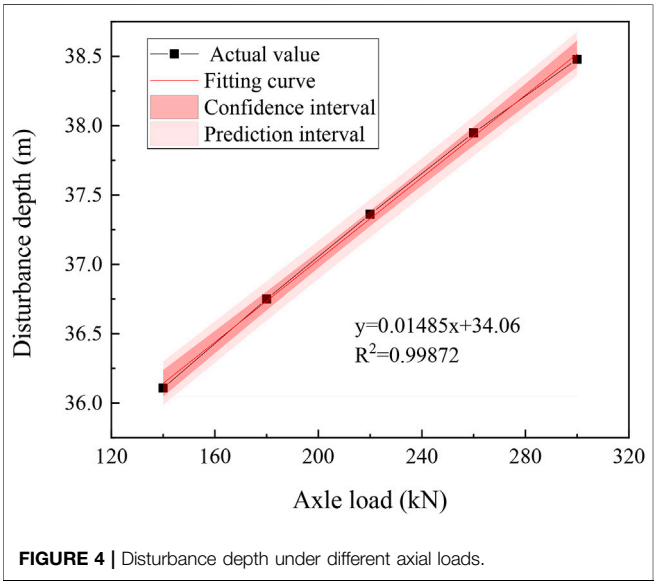


FIGURE 4 | Disturbance depth under different axial loads.

the research of some scholars (Gong et al., 2008; Song et al., 2020; Song D. et al., 2021; Song DQ. et al., 2021). The stability grade of the mine goaf ground is divided into four grades according to **Table 1**, and the qualitative index grade is divided and assigned according to **Table 2**.

2.3 Filtering Algorithms

Machine learning and deep learning are the hotspots of artificial intelligence research, and many related algorithms and theories have been applied in many geotechnical engineering (Cai et al., 2020, He et al., 2020; Lawal and Kwon, 2021; Tarawneh et al., 2018). In the era of big data, the ability of machine learning to mine effective information in the data has been greatly improved. In order to better evaluate the stability of the mine goaf ground and excavate the key factors, this study selects five machine learning methods, namely, decision tree, discriminant analysis, support vector machine, nearest neighbor classifier, and classifier ensemble, to process the data, and selects AUC value (area under curve) and accuracy as the criteria for the evaluation algorithm. AUC (Toh et al., 2008) is defined as the area under the ROC curve, which is usually used as the evaluation standard of the machine learning model. The abscissa of the ROC curve is the false positive rate and the ordinate is the true positive rate.

The index data of mine goaf ground site in reference and the evaluation grade of mine goaf ground site based on unascertained mathematics and actual working conditions are used (Gong et al., 2008).

This study selected five algorithms and twenty models for training. The accuracy and AUC of each model are shown in **Figure 3** and **Table 3**.

It can be seen from **Figure 3** and **Table 3** that the accuracy of Subspace Discriminant and Quadratic SVM models in the integrated classifier algorithm is the highest, but the AUC value of the former reaches 1.00, which belongs to the perfect classifier. Therefore, this algorithm model is used to evaluate and predict the stability of the mine goaf ground.

TABLE 4 | Classification of impact of axle weight.

Level	Axle weight interval
I	$p \leq 180$ kN
II	180 kN $< p \leq 220$ kN
III	220 kN $< p \leq 260$ kN
IV	260 kN $< p$

TABLE 5 | Classification of impact of railway speed.

Level	Speed interval
I	$v \leq 150$
II	$150 < v \leq 200$
III	$200 < v \leq 300$
IV	$300 < v$

3 CLASSIFICATION OF HIGH-SPEED RAILWAY INFLUENCE

The main problem faced by the construction of high-speed railway in the mine goaf ground is whether the project will cause the activation deformation of the mine goaf ground, and when the activation deformation occurs, whether the deformation will affect the train operation. The influence of railway engineering on the foundation of mine goaf ground generally has four aspects, namely, the train axle load (Shi and Hou, 2017), train speed (Bratov et al., 2014; Lamas-Lopez et al.,

TABLE 6 | Classification of orbital type impacts.

Level	Track type
I	Ballasted track, high subgrade or ballastless track, pile–slab composite subgrade
II	Ballastless track, high subgrade stiffness
III	Short roadbed with roadcut
IV	Ballastless track, short roadbed

2016), track type (Connolly et al., 2020) and the distance between the railway line and the surface center of the mine goaf ground. In this study, according to the relevant norms (GB 51044-2014, 2014), the impact of each factor is divided into four levels.

3.1 Train Axle Load

The axle loads of different types of trains are also different. The greater the axle load of the train, the greater the force on the foundation of the goaf, and the deeper the influence depth. When the influence depth of the force reaches the fault zone area, it will have a safety impact on the use of buildings on the foundation of the mine goaf ground. The influence of axle load is analyzed by FLAC3D software to simulate the disturbance depth of train load under different axle load conditions. As shown in **Figure 4**, the influence depth of train is linearly related to the change of axle load. At present, the range of axle load in China is between 140–300 kN, considering the full load and no-load running vehicles. The influence degree of this classification and the corresponding axle load range are shown in **Table 4**.

3.2 Railway Speed

Train speed is the most obvious and indigenous factor affecting the dynamic load inside the subgrade of high-speed trains, and the magnitude of the dynamic load inside the subgrade is an important factor to determine whether the foundation in the mine goaf ground activated deformation. Based on the field measurement data, Bian et al. (2014) found that when the vehicle speed was lower than 150 km/h or higher than 300 km/h, the dynamic stress of subgrade no longer changed with the speed. When the train speed was between 150 and 300 km/h, the dynamic stress of the subgrade changed linearly with the vehicle speed. The influence degree and speed range of this classification are shown in **Table 5**.

3.3 Track Type

The influence of track mainly lies in the selection of track type (Li et al., 2021) and the height of subgrade (Mosayebi et al., 2017). Li et al. (2018) proposed the attenuation formula of subgrade dynamic stress along depth as shown in **Eq. 1**:

$$\eta = 1 - \frac{z}{a + b \cdot z}, \tag{1}$$

where η is the attenuation coefficient; z is the subgrade depth; a and b are the fitting coefficients, ballastless track $a = 2.12$, $b = 1.18$; ballasted track $a = 0.64$, $b = 0.86$.

Since there are many types of orbital structures, four representative orbital structures are selected and divided into four grades according to **Table 6**.

3.4 Railway Line Location

Through the study, Qian et al. (1996) found that after the mine goaf ground was mined, a region similar to the masonry beam structure appeared at both ends of the mine goaf ground. The length of this region was approximately 8 times the periodic pressure step distance of the working face cycle, and the stability of the masonry beam structure was mainly determined by the key block (Cao and Zhou, 2015). According to this study, the mine goaf ground is horizontally divided into four regions. As shown in **Figure 5**, the risk is small when the region far from the mine goaf ground boundary is constructed. It is most dangerous to build in the key block area of a masonry

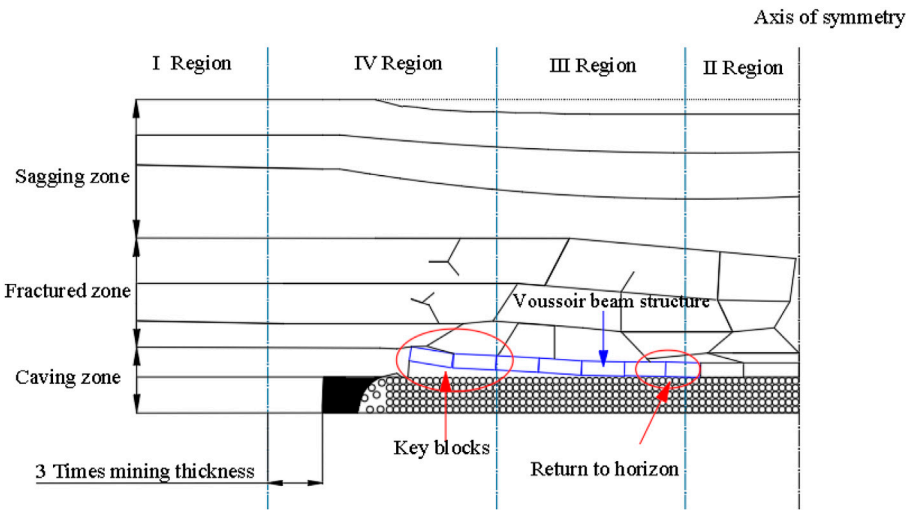


FIGURE 5 | Geographic division.

TABLE 7 | Classification of the influence of the railway main line location.

Level	Line location
I	$R_m+3H_m \le L$
II	$L \le R_m - R_b$
III	$R_m-R_b < L < R_m - R_k$
IV	$R_m - R_k < L < R_m+3H_m$

Notes: L in the table indicates the distance between the railway trunk line and the surface center of the mine goaf ground. R_m, H_m, R_b, and R_k represent the width radius of the mine goaf ground, the mining height of the mine goaf ground, the length of the masonry beam and the length of the key block, respectively.

beam, which may make the masonry beam structure unstable. In the construction of the non-key block area of the masonry beam structure, although there is cushion support, the risk is still large. When the central area of the mine goaf ground is constructed, most of the area has been compacted, there are no large cracks and separate layers, and the risk is small.

To study the different impacts of different distances between the railway trunk line and the surface center of the mine goaf ground, the influence degree is divided according to **Table 7**.

4 EXTENSION EVALUATION MODEL

Extension theory is a method proposed to solve complex problems by combining matter-element theory with extension set theory (Smarandache, 2012). The extension comprehensive evaluation model has been widely used in various fields.

In this article, the influence factors of mine goaf ground are simplified by the machine learning method, and the influence of the mine goaf ground is evaluated by the stability grade of the mine goaf ground site. The extension evaluation system of foundation activation for mine goaf ground of high-speed railway is constructed as shown in **Figure 6**. Referring to the specifications and research results, combined with the classification of the stability grade of the mine goaf ground and the train influence grade, the goaf foundation activation grade is divided into four grades (**Table 8**):

$$\begin{aligned} V &= [V_1, V_2, V_3, V_4] \\ &= [\text{Not activated, Not easily activated, Easily activated, Activated}]. \end{aligned} \tag{1a}$$

4.1 Identification of Classic and Joint Domains

Let

$$R_{0j} = \left(N_{0j}, C, V_{0j}\right) = \begin{bmatrix} N_{0j} & c_1 & V_{0j1} \\ & c_2 & V_{0j2} \\ & \cdots & \cdots \\ & c_n & V_{0jn} \end{bmatrix}, \tag{1b}$$

where N_{0j} represents level j, c_n represents each evaluation index of the model, and V_{0ji} represents the value range of each evaluation index at level j.

According to the division of **Tables 4**–**7**, the classical domain construction is carried out. Because the track type cannot be quantitatively assigned, this study takes (0, 2), (2, 4), (4, 6), and (6, 8) as characteristic value ranges. When the track type is I, II, III, and IV, then 1, 3, 5, and 7 are given as the evaluation values, and the mine goaf ground stability is also treated according to this method. The influence of the main line position is related to the factors of the mine goaf ground itself, which needs to be calculated according to the actual working conditions.

The classical domain matter elements of mine goaf ground influencing each level established in this study are

$$\begin{aligned} R_{01} &= [N_{01} \text{ Stability grade of mine goaf ground } (0,2)] \\ R_{02} &= [N_{02} \text{ Stability grade of mine goaf ground } (2,4)] \\ R_{03} &= [N_{03} \text{ Stability grade of mine goaf ground } (4,6)] \\ R_{04} &= [N_{04} \text{ Stability grade of mine goaf ground } (6,8)] \end{aligned}$$

The joint domain matter element is

$$R_D = [D \text{ Stability grade of mine goaf ground } (0,8)]$$

The classical domain matter elements of the train influencing each level are

$$R_{01} = \begin{bmatrix} N_{01} & \text{axle load} & (140, 180) \\ & \text{speed} & (120, 150) \\ & \text{track type} & (0, 2) \\ & \text{line location} & (R_m+3H_m, 1.5R_m) \end{bmatrix}, \tag{1c}$$

$$R_{02} = \begin{bmatrix} N_{02} & \text{axle load} & (180, 220) \\ & \text{speed} & (150, 200) \\ & \text{track type} & (2, 4) \\ & \text{line location} & (0, R_m-R_m) \end{bmatrix}, \tag{1d}$$

TABLE 8 | Activation grade classification table.

Activation grade	Classification description
V_1	The goaf ground is stable and can be constructed without engineering
V_2	The goaf ground is relatively stable and can be constructed after taking general engineering protection measures
V_3	The goaf ground is unstable and needs to be constructed after treatment
V_4	The goaf ground is very unstable, which needs comprehensive design of planning, structure, mined-out area treatment, and foundation treatment before construction

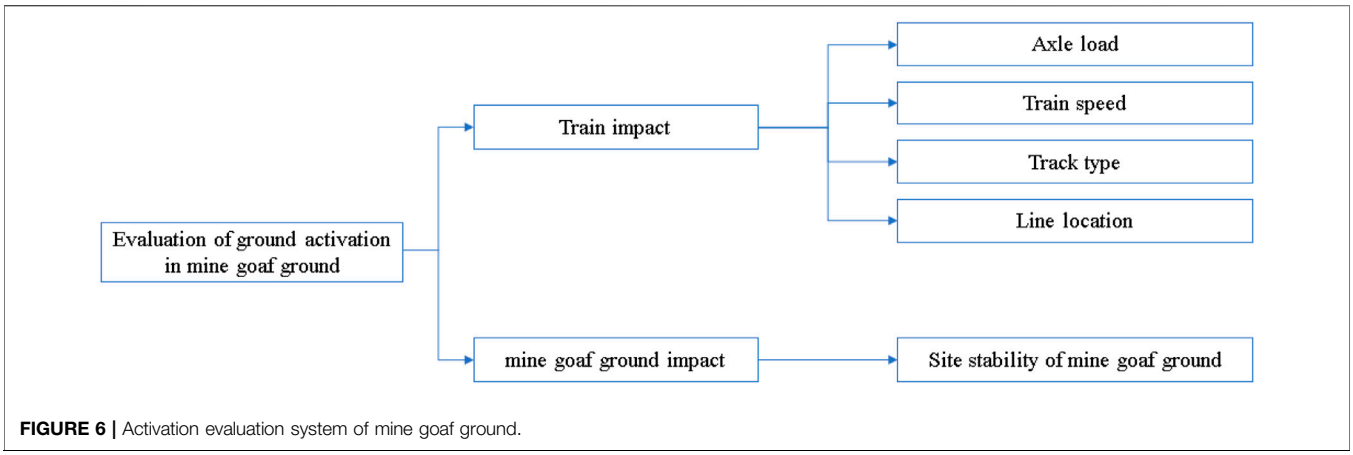


FIGURE 6 | Activation evaluation system of mine goaf ground.

$$R_{03} = \begin{bmatrix} \mathrm{N}_{03} & \text{axle load} & (220, 260) \\ & \text{speed} & (200, 300) \\ & \text{track type} & (4, 6) \\ & \text{line location} & (R_m - R_{b,}\ R_m - R_k) \end{bmatrix}, \quad (1e)$$

$$R_{04} = \begin{bmatrix} \mathrm{N}_{04} & \text{axle load} & (260, 300) \\ & \text{speed} & (300, 350) \\ & \text{track type} & (6, 8) \\ & \text{line location} & (R_m - R_k, R_m + 3H_m) \end{bmatrix}. \quad (1f)$$

The joint domain matter element is

$$R_{\mathrm{D}} = \begin{bmatrix} \mathrm{D} & \text{axle load} & (140, 300) \\ & \text{speed} & (120, 350) \\ & \text{track type} & (0, 8) \\ & \text{line location} & (0, 1.5R_m) \end{bmatrix}. \quad (1g)$$

4.2 Matter Element

The data of the evaluation object a_i are represented by matter elements, and the matter element R_i to be evaluated is obtained.

$$R_i = (p_i, C, V_i) = \begin{bmatrix} p_i & c_1 & v_{i1} \\ & c_2 & v_{i2} \\ & \cdots & \cdots \\ & c_n & v_{in} \end{bmatrix}, \quad (1h)$$

where p_i is the ith evaluation object and v_{ij} is the value of p_i with respect to characteristic index c_j.

4.3 Index Weight

Evaluation of x requires I_1, I_2, ..., I_m, m indicators, x_j is the measured value of x on I_j. For x_{ij}, there are p evaluation grades c_1, c_2, . . . , c_n, and let $\mu_{jk} = \mu\ (x_j \in c_k)$ denote the degree to which x_j belongs to the kth evaluation class c_k.

$$0 \le \mu\left(x_{ij} \in c_k\right) \le 1 \qquad (k = 1, 2, ..., p), \quad (2)$$

$$\mu\left(x_{ij} \in \bigcup_{l=1}^{p} c_l\right) = 1 \qquad (j = 1, 2, ..., m), \quad (3)$$

$$\mu\left(x_{ij} \in \bigcup_{l=1}^{k} c_l\right) = \sum_{l=1}^{k} \mu\left(x_{ij} \in c_l\right) \qquad (k = 1, 2, ...p) \quad (4)$$

satisfies that μ of **Eqs 2–4** is an unascertained measure, and the matrix

$$\begin{bmatrix} \mu_{11} & \cdots & \mu_{1p} \\ \vdots & \ddots & \vdots \\ \mu_{m1} & \cdots & \mu_{mp} \end{bmatrix} \quad (4a)$$

is called a single index measure evaluation matrix.

According to the influence degree division of 3.1–3.4 subsections, the single index measure function diagram of each factor can be obtained. As shown in **Figure 7**, the single index measure evaluation matrix of the instance can be obtained by substituting the instance data.

After getting the single index measurement matrix, it is necessary to determine the weight of each index. To make w_j a weight of x_j, w_j needs to satisfy two conditions:

① $0 \le w_j \le 1$
② $w_1 + w_2 + \ldots + w_m = 1$.

At this time, the information entropy theory is used to calculate the weight, and the calculation steps are shown in **Eqs 5**, **6**.

$$v_j = 1 + \frac{1}{\lg p} \sum_{i=1}^{p} \mu_{ji} \lg \mu_{ji} \quad (5)$$

$$w_j = v_j \Big/ \sum_{i=1}^{m} v_i \quad (6)$$

The determination of the index weight coefficient in the first layer of the extension system considers the value of other scholars in the evaluation system of goaf foundation stability. It is known that the weight of building load or traffic load is mostly between 0.116 (Zhang, 2009) and 0.232 (Wang, 2016). In this study, 0.2 and 0.8 are selected as the weight coefficients of train load and goaf stability, respectively.

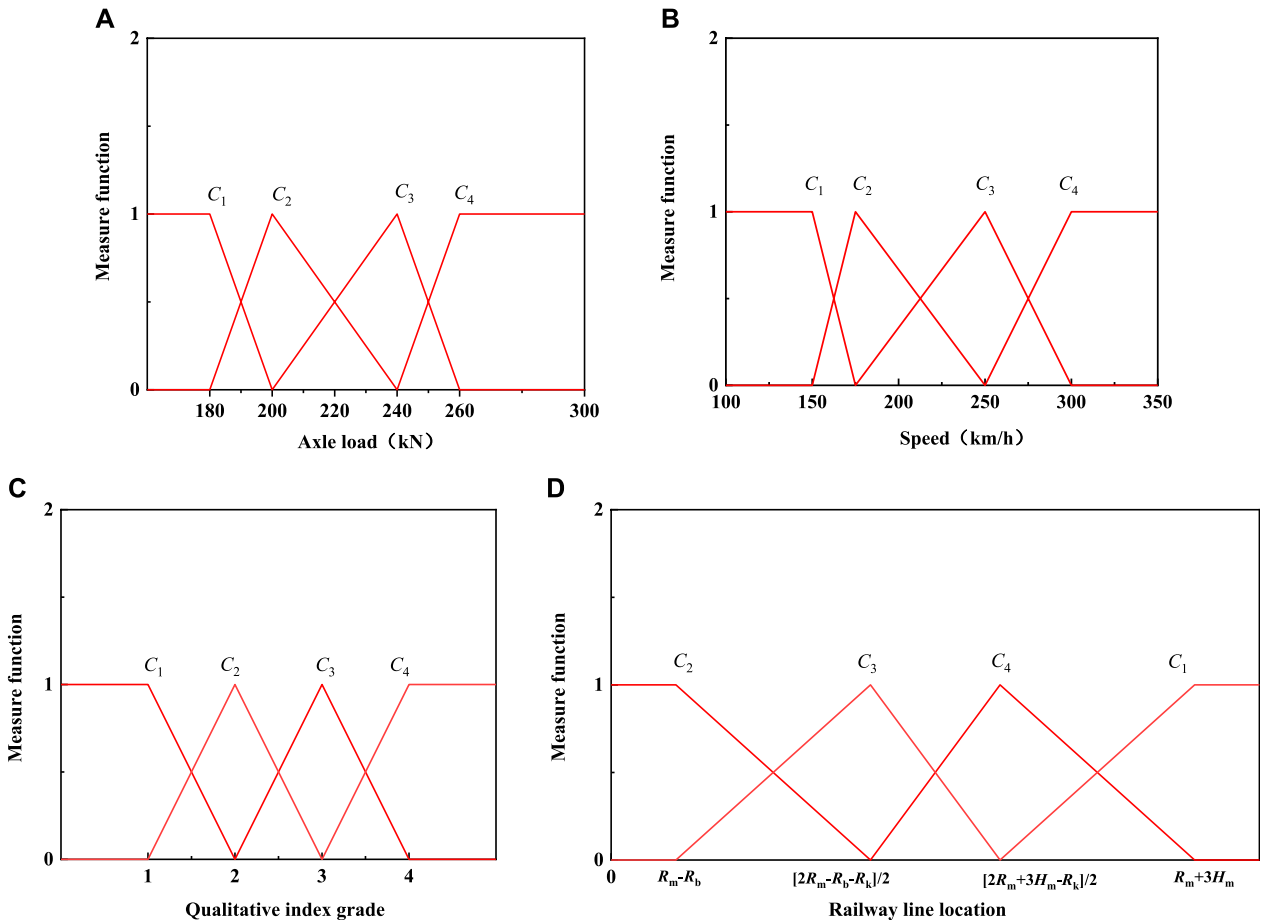


FIGURE 7 | Uncertainty measurement function of different factors: **(A)** axle load, **(B)** train speed, **(C)** qualitative index grade, and **(D)** railway line location.

4.4 Correlation Function

The calculation formula of the distance between point and interval is

$$\rho\left(v_{ki}, V_{0ji}\right) = \left|v_{ki} - \frac{a_{0ji} + b_{0ji}}{2}\right| - \frac{1}{2}\left(b_{0ji} - a_{0ji}\right). \tag{7}$$

When $v_{ki} \notin V_{0ji}$, the correlation function is

$$K_j\left(v_{ki}\right) = \frac{\rho\left(v_{ki}, V_{0ji}\right)}{\rho\left(v_{ki}, V_{0Pi}\right) - \rho\left(v_{ki}, V_{0ji}\right)}. \tag{8}$$

When $v_{ki} \in V_{0ji}$, the correlation function is

$$K_j\left(v_{ki}\right) = -\frac{\rho\left(v_{ki}, V_{0ji}\right)}{\left|b_{0ji} - a_{0ji}\right|}. \tag{9}$$

4.5 Correlation Degree

To facilitate analysis and comparison, the correlation degree is standardized by **Eq. 10**.

$$K_j^{'}\left(v_{ki}\right) = \frac{K_j\left(v_{ki}\right)}{\max\limits_{1 \le i \le m}\left|K_j\left(v_{ki}\right)\right|} \tag{10}$$

4.6 Activation Classification

The weight coefficient of each eigenvalue and the normalized correlation degree are calculated according to **Eq. 11**, and the comprehensive correlation degree of the evaluation object is obtained.

$$K_j\left(\rho_k\right) = \sum_{i=1}^{n} w_i K_j\left(v_{ki}\right) \tag{11}$$

If

$$K_k\left(\rho\right) = \max_{k \in (1,2\ldots,m)} K_j\left(\rho_i\right), \tag{12}$$

then the activation level of evaluation object p is k.

5 CASE STUDY

5.1 Case 1

Case 1 selects a section of the Tai-Jiao high-speed railway crossing the mine goaf ground site project to verify the established classification method of mine goaf ground activation. The length, width, and mining thickness of the mine goaf ground under the section of Tai-Jiao higher railway are about 110 m, 18, and 1.8 m, respectively. The overall buried depth of the mine goaf ground is 56 m. The wall rock is flooded for a long time, the rock mass structure is relatively loose, and the joint fissures are developed. There is an adjacent mine goaf ground near the section. The dip angle of the ore layer is 12°, the area ratio of the ore pillar is 15%, the stop mining time is 20 a, and the thickness of the loose layer is 15 m. The axle load of a high-speed railway is 17 t, and the designed speed is 250 km/h. The low subgrade of the ballasted track is used in the track, and the railway line is about 20 m away from the center of the mine goaf ground.

5.1.1 Stability Evaluation

According to the comparison test of the machine learning algorithm model, the subspace discriminant algorithm model is selected as the classifier for evaluating the stability of mine goaf ground. The input matrix of the engineering example to be verified is compiled in Matlab. According to the engineering situation, the input matrix is

$$X_1 = [3\ 3\ 48\ 4\ 4\ 2\ 2\ 36\ 10\ 15\ 18\ 18]. \tag{13}$$

The input matrix is imported into the ensemble classification learner, and the stability evaluation level of the mine goaf ground is grade III.

5.1.2 Activation Evaluation of Mine Goaf Ground

5.1.2.1 Extension Evaluation of Mine Goaf Ground Stability

The matter element to be evaluated is

$$R_1 = [p_1 \text{ Stability grade of mine goaf ground } 5].$$

The correlation matrix K_1 is obtained by calculating with **Eqs 7–9**.

$$K_1 = [-0.5\ \ -0.25\ 0.5\ \ -0.25] \tag{14}$$

According to **Eq. 10**, correlation matrix $K_1^{'}$ is obtained.

$$K_1[-1\ \ -0.5\ 1\ \ -0.5] \tag{15}$$

According to **Eq. 11**, the comprehensive correlation degree is calculated, and matrix K_{p1} is obtained. Since this evaluation layer has only one index, the weight coefficient is 1.

$$K_{p1} = w_1 \cdot K'_1 = [-1\ \ -0.5\ 1\ \ -0.5] \tag{16}$$

5.1.2.2 Extension Evaluation of Train Impact

According to the general situation of the project, the matter element to be evaluated of Tai-Jiao high-speed railway is

$$R_2 = \begin{bmatrix} p_2 & \text{axle load} & 170 \\ & \text{speed} & 250 \\ & \text{track type} & 5 \\ & \text{line location} & 20 \end{bmatrix}. \tag{17}$$

The correlation matrix K_2 is obtained by calculating with **Eqs 7–9**.

$$K_2 = \begin{bmatrix} 0.25 & -0.25 & -0.625 & -0.75 \\ -0.5 & -0.333 & 0.5 & -0.333 \\ -0.5 & -0.25 & 0.5 & -0.25 \\ -0.2 & 0.167 & -0.556 & -0.667 \end{bmatrix} \tag{18}$$

According to **Eq. 10**, correlation matrix $K_2^{'}$ is obtained.

$$K_2 = \begin{bmatrix} 0.333 & -0.333 & -0.833 & -1 \\ -1 & -0.666 & 1 & -0.666 \\ -1 & -0.5 & 1 & -0.5 \\ -0.3 & 0.250 & -0.834 & -1 \end{bmatrix} \tag{19}$$

Through the measure function of **Figure 6**, the single index evaluation measure matrix of train influencing factors is determined:

$$\begin{bmatrix} 1 & 0 & 0 & 0 \\ 0 & 0 & 1 & 0 \\ 0 & 0 & 1 & 0 \\ 0 & 0.67 & 0.33 & 0 \end{bmatrix}. \tag{20}$$

It can be seen from **Eqs 5**, **6** that

$$v_1 = 1, v_2 = 1, v_3 = 1, v_4 = 0.542, \tag{21}$$

$$(w_1, w_2, w_3, w_4) = (0.282, 0.282, 0.282, 0.154). \tag{22}$$

According to **Eq. 11**, comprehensive correlation matrix K_{p1} of the Tai-Jiao high-speed railway is calculated as follows:

$$K_{p2} = (w_1, w_2, w_3, w_4) \cdot K_2 = [-0.516\ \ -0.384\ 0.201\ \ -0.765]. \tag{23}$$

5.1.2.3 Extensible Pre-Evaluation of Ground Activation Grade in Mine Goaf Ground

According to **Eq. 11**, the comprehensive evaluation of the first level of Tai-Jiao high-speed railway is as follows:

$$\begin{aligned} \mathrm{K} = w \times K_{p2} &= (0.8\ 0.2)\begin{bmatrix} -1 & -0.5 & 1 & -0.5 \\ -0.516 & -0.384 & 0.201 & -0.765 \end{bmatrix} \\ &= [-0.903\ -0.477\ 0.840\ -0.553]. \end{aligned} \tag{24}$$

According to **Eq. 12**, the activation grade of mine goaf ground in the Tai-Jiao high railway section is "Easily activated." In practical engineering, through a large number of exploration and tests in the early stage, the grouting treatment of goaf is decided. At present, the operation condition of this section is well, which proves that the method in this article has a certain reference value.

5.2 Case 2

In the second engineering case, a section of the Nan-Qin railway crossing the mine goaf ground along the coast of Guangxi is selected. The buried depth of the mine goaf ground under the Nan-Qin railway is 142 m, and the mining thickness is 5 m. The

buried rock structure is loose, and the mine goaf ground is rich in water and high in water pressure. The dip angle of the coal seam is 20°, and the area ratio of the pillar is 15%. The stop mining time is 10 a, and the thickness of the loose layer is 10 m.

The axle load of the railway is 20 t, and the designed speed is 250 km/h. The low subgrade of the ballasted track is used in the track, and the Nan-Qin line is about 70 m according to the center of mine goaf ground.

5.2.1 Site Stability Evaluation

The input matrix of Nan-Qin railway is

$$X_2 = [4\ 3\ 35\ 4\ 3\ 4\ 2\ 28.4\ 20\ 15\ 10\ 10]. \tag{25}$$

The input matrix is imported into the ensemble classification learner, and the stability evaluation level of the mine goaf ground is grade III.

5.2.2 Activation Evaluation of Mine Goaf Ground

5.2.2.1 Extension Evaluation of Mine Goaf Ground Stability

According to the evaluation results of machine learning, the evaluation results of two engineering examples are the same, and the extension evaluation results should be the same. So, the correlation matrix is the same as that of instance one.

$$K_{p1} = w_1 \cdot K_1 = [-1\ \ -0.5\ 1\ \ -0.5] \tag{26}$$

5.2.2.2 Extension Evaluation of Train Impact

According to the general situation of the project, the matter element to be evaluated of Nan-Qin high-speed railway is

$$R_2 = \begin{bmatrix} p_2 & \text{axle load} & 200 \\ & \text{speed} & 250 \\ & \text{track type} & 5 \\ & \text{line location} & 70 \end{bmatrix}. \tag{27}$$

Correlation matrix K_2 is obtained by calculating with **Eqs 7–9**.

$$K_2 = \begin{bmatrix} -0.25 & 0.5 & -0.25 & -0.5 \\ -0.5 & -0.333 & 0.5 & -0.333 \\ -0.5 & -0.25 & 0.5 & -0.25 \\ -0.167 & 0.292 & -0.327 & -0.407 \end{bmatrix} \tag{28}$$

According to **Eq. 10**, correlation matrix $K_2^{'}$ is obtained.

$$K_2^{'} = \begin{bmatrix} -0.5 & 1 & -0.5 & -1 \\ -1 & -0.666 & 1 & -0.666 \\ -1 & -0.5 & 1 & -0.5 \\ -0.41 & 0.717 & -0.803 & -1 \end{bmatrix} \tag{29}$$

Through the measure function of **Figure 6**, the single index evaluation measure matrix of the train influencing factors is determined:

$$\begin{bmatrix} 0 & 1 & 0 & 0 \\ 0 & 0 & 1 & 0 \\ 0 & 0 & 1 & 0 \\ 0 & 0.417 & 0.583 & 0 \end{bmatrix}. \tag{30}$$

It can be seen from **Eqs 5**, **6** that

$$\nu_1 = 1, \nu_2 = 1, \nu_3 = 1, \nu_4 = 0.51, \tag{31}$$

$$(w_1, w_2, w_3, w_4) = (0.285, 0.285, 0.285, 0.145). \tag{32}$$

According to **Eq. 11**, comprehensive correlation matrix K_{p1} of Tai-Jiao high-speed railway is calculated as follows:

$$K_{p2} = (w_1, w_2, w_3, w_4) \cdot K_2^{'}[-0.772\ 0.057\ 0.311\ \ -0.762]. \tag{33}$$

5.2.2.3 Extensible Pre-Evaluation of Ground Activation Grade in Mine Goaf Ground

According to **Eq. 11**, the comprehensive evaluation of the first level of Nan-Qin high-speed railway is as follows:

$$K = A \times K_{p1} = (0.8\ 0.2)\begin{bmatrix} -1 & -0.5 & 1 & -0.5 \\ -0.772 & 0.057 & 0.311 & -0.762 \end{bmatrix} = [-0.954\ -0.387\ 0.862\ -0.552]. \tag{34}$$

According to **Eq. 12**, the activation grade of the mine goaf ground in the Nan-Qin high railway section is "Easily activated." In the engineering construction, through the investigation of the site and the verification of the geological data, the constructor adopted the grouting method to reinforce the goaf. In the years of train operation, there was no activation deformation in the site, which proved that the research method in this article was effective.

6 CONCLUSION

Coal is the main energy in China, and the main coal base formed a large area of mine goaf ground due to high strength mining; at the same time, with the rapid layout of China's high-speed railway network, some lines will inevitably cross the mine goaf ground, and whether the mine goaf ground is activated under the influence of the train load is an important research direction. Considering the stability of the mine goaf ground and the influence of train, a new classification method of ground activation in the mine goaf ground is proposed. The main conclusions are as follows:

1) The evaluation of the mine goaf ground activation is divided into the evaluation of the stability level of the mine goaf ground and the evaluation of the train impact level, and the overall evaluation is completed by combining the two evaluation results through the extension theory and the unascertained measure theory, which greatly simplifies the evaluation process of the activation level of the mine goaf ground.
2) Through numerical simulation, theoretical derivation, and reference to other scholars' research, the factors influencing the construction of high-speed railways at mined sites are categorized into four main categories: axle weight, vehicle speed, trunk line location, and roadbed structure, and their influence levels are classified and described qualitatively and quantitatively.

3) The field engineering examples of the mine goaf grounds passed by the Tai-Jiao high-speed railway and the Nan-Qin high-speed railway are selected to verify the model established in this article. The analysis results of engineering examples show that the model established in this article is suitable for the ground activity analysis and discrimination of high-speed railway mine goaf ground.

DATA AVAILABILITY STATEMENT

The raw data supporting the conclusion of this article will be made available by the authors, without undue reservation.

AUTHOR CONTRIBUTIONS

L-wR is responsible for the investigation and data sorting of the cases, P-fH is responsible for the selection of machine learning algorithms and the writing of articles, Y-FZ is responsible for the work related to extension theory, Z-LD is responsible for the establishment of unascertained measure function, Z-sZ and S-rW are responsible for reviewing the quality, format, and logic of the article.

FUNDING

This work was supported by the National Natural Science Foundation of China (No. U1810203).

REFERENCES

Bell, F. G., Bullock, S. E. T., Halbich, T. F. J., and Lindsay, P. (2001). Environmental Impacts Associated with an Abandoned Mine in the Withbank Coalfield, South Africa. *Int. J. Coal Geol.* 45 (2-3), 195–216. doi:10.1016/s0166-5162(00)00033-1

Bian, X., Jiang, H., Cheng, C., Chen, Y., Chen, R., and Jiang, J. (2014). Full-scale Model Testing on a Ballastless High-Speed Railway under Simulated Train Moving Loads. *Soil Dyn. Earthq. Eng.* 66, 368–384. doi:10.1016/j.soildyn.2014.08.003

Bratov, V., Petrov, Y., Semenov, B., and Darienko, I. (2014). Modelling the High-Speed Train Induced Dynamic Response of Railway Embankment. *Mater. Phys. Mech.* 22 (1), 69.

Cao, Z., and Zhou, Y. (2015). Research on Coal Pillar Width in Roadway Driving along Goaf Based on the Stability of Key Block. *Comput. Mater. Continua* 48 (2), 77. doi:10.3970/cmc.2015.048.077

Connolly, D. P., Dong, K., Alves Costa, P., Soares, P., and Woodward, P. K. (2020). High Speed Railway Ground Dynamics: a Multi-Model Analysis. *Int. J. Rail Transp.* 8 (4), 324–346. doi:10.1080/23248378.2020.1712267

Cui, X., Gao, Y., and Yuan, D. (2014). Sudden Surface Collapse Disasters Caused by Shallow Partial Mining in Datong Coalfield, China. *Nat. Hazards* 74 (2), 911–929. doi:10.1007/s11069-014-1221-5

Du, H., Song, D., Chen, Z., and Guo, Z. (2020). Experimental Study of the Influence of Structural Planes on the Mechanical Properties of Sandstone Specimens under Cyclic Dynamic Disturbance. *Energy Sci. Eng.* 8, 4043–4063. doi:10.1002/ese3.794

Gong, F., Li, X., Dong, L., and Liu, X. (2008). Underground Goaf Risk Evaluation Based on Uncertainty Mensurement Theory. *Chin. J. Rock Mech. Eng.* (02), 323. doi:10.3321/j.issn:1000-6915.2008.02.014

Guo, Q., Li, Y., Meng, X., Guo, G., and Lv, X. (2019). Instability Risk Assessment of Expressway Construction Site above an Abandoned Goaf: a Case Study in China. *Environ. Earth Sci.* 78 (20), 8599. doi:10.1007/s12665-019-8599-z

He, X., Xu, H., Sabetamal, H., and Sheng, D. (2020). Machine Learning Aided Stochastic Reliability Analysis of Spatially Variable Slopes. *Comput. Geotechnics* 126, 103711. doi:10.1016/j.compgeo.2020.103711

Helm, P. R., Davie, C. T., and Glendinning, S. (2013). Numerical Modelling of Shallow Abandoned Mine Working Subsidence Affecting Transport Infrastructure. *Eng. Geol.* 154, 6–19. doi:10.1016/j.enggeo.2012.12.003

Hu, Y.-x., and Li, X.-b. (2012). Bayes Discriminant Analysis Method to Identify Risky of Complicated Goaf in Mines and its Application. *Trans. Nonferrous Metals Soc. China* 22 (2), 425–431. doi:10.1016/s1003-6326(11)61194-1

Jiang, S., and Wang, Y. (2019). Long-Term Ground Settlements over Mined-Out Region Induced by Railway Construction and Operation. *Sustainability* 11 (3), 30875. doi:10.3390/su11030875

Lamas-Lopez, F., Cui, Y.-J., Calon, N., Costa D'Aguiar, S., Peixoto De Oliveira, M., and Zhang, T. (2016). Track-bed Mechanical Behaviour under the Impact of Train at Different Speeds. *Soils Found.* 56 (4), 627–639. doi:10.1016/j.sandf.2016.07.004

Lawal, A. I., and Kwon, S. (2021). Application of Artificial Intelligence to Rock Mechanics: An Overview. *J. Rock Mech. Geotechnical Eng.* 13 (1), 248–266. doi:10.1016/j.jrmge.2020.05.010

Li, L., Wu, K., and Zhou, D. (2016). Evaluation Theory and Application of Foundation Stability of New Buildings over an Old Goaf Using Longwall Mining Technology. *Environ. Earth Sci.* 75 (9), 5574. doi:10.1007/s12665-016-5574-9

Li, S., Ling, X., Tian, S., Ye, Y., Tang, L., Cai, D., et al. (2021). *In-situ* Test and Analysis of Subgrade Vibration with Ballasted Track in Deep Seasonally Frozen Regions. *Transp. Geotech.* 31, 100658. doi:10.1016/j.trgeo.2021.100658

Li, W., Bian, X., Duan, X., Tutumluer, E., and Erol (2018). Full-Scale Model Testing on Ballasted High-Speed Railway: Dynamic Responses and Accumulated Settlements. *Transp. Res. Rec.* 2672 (10), 125–135. doi:10.1177/0361198118784379

Liu, X., Liang, Z., Zhang, Y., Liang, P., and Tian, B. (2018). Experimental Study on the Monitoring of Rockburst in Tunnels under Dry and Saturated Conditions Using AE and Infrared Monitoring. *Tunn. Undergr. Space Technol.* 82 (12), 517–528. doi:10.1016/j.tust.2018.08.011

Liu, X., Wu, L., Zhang, Y., Liang, Z., Yao, X., and Liang, P. (2019). Frequency Properties of Acoustic Emissions from the Dry and Saturated Rock. *Environ. Earth Sci.* 78 (3), 67. doi:10.1007/s12665-019-8058-x

Liu, X., Wu, L., Zhang, Y., and Mao, W. (2021). Localized Enhancement of Infrared Radiation Temperature of Rock Compressively Sheared to Fracturing Sliding: Features and Significance. *Front. Earth Sci.* 9, 756369. doi:10.3389/feart.2021.756369

Liu, X., Wu, L., Zhang, Y., Wang, S., Yao, X., and Wu, X. (2020). The Characteristics of Crack Existence and Development during Rock Shear Fracturing Evolution. *Bull. Eng. Geol. Environ.* 80 (2), 1671–1682. doi:10.1007/s10064-020-01997-3

Mosayebi, S.-A., Zakeri, J.-A., and Esmaeili, M. (2017). Vehicle/track Dynamic Interaction Considering Developed Railway Substructure Models. *Struct. Eng. Mech.* 61 (6), 775–784. doi:10.12989/sem.2017.61.6.775

Qian, M., Miu, X., and Xu, J. (1996). Theoretical Study of Key Stratum in Ground Control. *J. China Coal Soc.* 21 (03), 2–7.

Qin, Y., Luo, Z., Wang, J., Ma, S., and Feng, C. (2019). Evaluation of Goaf Stability Based on Transfer Learning Theory of Artificial Intelligence. *Ieee Access* 7, 96912–96925. doi:10.1109/access.2019.2929533

Shi, J., and Hou, D. (2017). Failure Analysis for Railroad Embankment under Heavy Haul Wagon Loads. *Mechanika* 23 (2), 197–203. doi:10.5755/j01.mech.23.2.13911

Smarandache, F. (2012). Generalizations of the Distance and Dependent Function in Extenics to 2D, 3D, and N - D. *Prog. Phys.* 3, 54. doi:10.1136/ard.2003.014274

Song, D., Liu, X., Huang, J., and Zhang, J. (2020). Energy-based Analysis of Seismic Failure Mechanism of a Rock Slope with Discontinuities Using Hilbert-Huang Transform and Marginal Spectrum in the Time-Frequency Domain. *Landslides* 18, 105–123. doi:10.1007/s10346-020-01491-7

Song, D., Liu, X., Li, B., Zhang, J., and Volcan, J. (2021a). Assessing the Influence of a Rapid Water Drawdown on the Seismic Response Characteristics of a

Reservoir Rock Slope Using Time-Frequency Analysis. *Acta Geotech.* 16, 1281–1302. doi:10.1007/s11440-020-01094-5

Song, D. Q., Liu, X., and Huang, J. (2021b). Seismic Cumulative Failure Effects on a Reservoir Bank Slope with a Complex Geological Structure Considering Plastic Deformation Characteristics Using Shaking Table Tests. *Eng. Geol.* 286 (3). 106085. doi:10.1016/j.enggeo.2021.106085

Tarawneh, B., Nusairat, J., and Hakam, Y. (2018). Load Testing and Settlement of Shallow Foundation on Desert Sands. *Proc. Institution Civ. Eng. - Geotechnical Eng.* 171 (1), 52–63. doi:10.1680/jgeen.16.00109

The Professional Standards Compilation Group of People's Republic of China (2014). *Code for Investigation of Geotechnical Engineering in the Coal Mine Goaf (GB 51044-2014)* Beijing: China Planning Press.

Toh, K.-A., Kim, J., and Lee, S. (2008). Maximizing Area under ROC Curve for Biometric Scores Fusion. *Pattern Recognit.* 41 (11), 3373–3392. doi:10.1016/j.patcog.2008.04.002

Wang, J. (2016). *Activation Law and Stability Evaluation of Goaf under Railway Load: Qingdao*. China: Qingdao University of technology, 86.

Xie, X., Shi, S., Bu, L., Li, L., Sun, K., and Liu, H. (2021). Dynamic Optimization Risk Assessment Model and Control Measures for Tunnel Collapse and its Engineering Application. *Himal. Geol.* 42 (1), 117.

Zhang, J. (2009). Fuzzy Comprehensive Evaluation Method of the Foundation Stability of New-Buildings above Worked-Out Area. *J. Univ. Sci. Technol. Beijing* 31 (11), 1368–1372. doi:10.13374/j.issn1001-053x.2009.11.026

Zhao, B., Zhao, Y., and Wang, J. (2021). New Stability Forecasting Model for Goaf Slope Based on the AHP-TOPSIS Theory. *Arabian J. Geosci.* 14 (1), 6292. doi:10.1007/s12517-020-06292-9

Conflict of Interest: The authors declare that the research was conducted in the absence of any commercial or financial relationships that could be construed as a potential conflict of interest.

Publisher's Note: All claims expressed in this article are solely those of the authors and do not necessarily represent those of their affiliated organizations, or those of the publisher, the editors, and the reviewers. Any product that may be evaluated in this article, or claim that may be made by its manufacturer, is not guaranteed or endorsed by the publisher.

Copyright © 2022 Ren, He, Zou, Dun, Zou and Wang. This is an open-access article distributed under the terms of the Creative Commons Attribution License (CC BY). The use, distribution or reproduction in other forums is permitted, provided the original author(s) and the copyright owner(s) are credited and that the original publication in this journal is cited, in accordance with accepted academic practice. No use, distribution or reproduction is permitted which does not comply with these terms.

frontiers | Frontiers in Earth Science

ORIGINAL RESEARCH
published: 28 June 2022
doi: 10.3389/feart.2022.923611

Study on Failure Difference of Hard Rock Based on a Comparison Between the Conventional Triaxial Test and True Triaxial Test

Guoqiang Zheng[1], Yonghui Tang[2], Yan Zhang[3]*, Yaohui Gao[4], Guoqiang Zhu[5], Meiben Gao[6,7], Junqian Ren[8], Kezhu Chen[1] and Jicheng Sun[2]*

[1]Sichuan Communication Surveying and Design Institute Co., Ltd, Chengdu, China, [2]Sichuan Transportation Construction Group Co., Ltd, Chengdu, China, [3]State Key Laboratory of Geohazard Prevention and Environment Protection, Chengdu University of Technology, Chengdu, China, [4]PowerChina Huadong Engineering Corporation Limited, Hangzhou, China, [5]Badong National Observation and Research Station of Geohazards, China University of Geosciences, Wuhan, China, [6]School of Emergency Science, Xihua University, Chengdu, China, [7]Key Laboratory of Geohazard Prevention of Hilly Mountains, Ministry of Natural Resources, Fuzhou, China, [8]Sichuan Highway Planning, Survey, Design and Research Institute Ltd, Chengdu, China

OPEN ACCESS

Edited by:
Guang-Liang Feng, Institute of Rock and Soil Mechanics (CAS), China

Reviewed by:
Chang'An Qin, Beijing University of Civil Engineering and Architecture, China
Zhongyuan Xu, Southwest Jiaotong University, China

***Correspondence:**
Yonghui Tang
790279442@qq.com
Yan Zhang
zhangyan2020@cdut.edu.cn
zhylr1988@126.com

Specialty section:
This article was submitted to Geohazards and Georisks, a section of the journal Frontiers in Earth Science

Received: *19 April 2022*
Accepted: *18 May 2022*
Published: *28 June 2022*

Citation:
Zheng G, Tang Y, Zhang Y, Gao Y, Zhu G, Gao M, Ren J, Chen K and Sun J (2022) Study on Failure Difference of Hard Rock Based on a Comparison Between the Conventional Triaxial Test and True Triaxial Test. Front. Earth Sci. 10:923611. doi: 10.3389/feart.2022.923611

The study on the failure difference of deep hard rock based on the comparison between conventional and true triaxial tests can help us better understand the fracture processes and failure characteristics of the deep rock mass. Therefore, this article carries out a comparative analysis of the failure of hard rock under conventional and true triaxial stress states. Within the scope of this study, it is found that the brittle–ductile transformation properties can be intuitively reflected in the rock stress–strain curve and failure mode. The brittle–ductile transition point of rock can also be determined by the difference between peak and residual strengths. The rock failure strength increases with the increase of σ_2, the peak strain decreases with the increase of σ_2, the stress drop of the post-peak curve becomes more obvious with the increase of σ_2, and the rock tends toward Class II brittle failure after the peak with the increase of σ_2. When σ_3 is relatively high, the rock fracture angle increases with the increase of σ_2 with obvious regularity. Compared with conventional triaxial stress conditions, the differential stress-induced anisotropy failure is the biggest difference in rock fracture characteristics between true and conventional triaxial stress states. This study can supply useful references to the study of failure properties of hard rock under complex stress states.

Keywords: failure, deep hard rock, conventional triaxial, true triaxial, mechanical properties

INTRODUCTION

The continuous demand for resources makes human activities continue to expand to "deep space, deep sea, deep earth." Among them, due to the complexity of the earth's internal system and the uniqueness of the geological medium, the research of "deep earth" is in a "black box" state. The difficulty of scientific research on "deep earth" is no less than that of "deep space and deep sea." The excavation depth of underground works in international and domestic industries such as transportation, water conservation, hydropower, mineral resource development, oil and gas reservoir development, geological storage, and military protection engineering is still increasing (Martin and Chandler 1994; Malan 2002; Hajiabdolmajid and Kaiser 2003; Diederichs 2007; Zhao



FIGURE 1 | Rockburst disasters occurred at Paoma mountain No. 1 tunnel.

et al., 2014; Zhuang et al., 2017; Bai et al., 2019; Feng et al., 2022). For example, the deepest oil well in the world is drilled by the Orlan platform of Chaivo oilfield, and its depth has reached 15,000 m. At present, there are more than 120 metal mines with a mining depth of more than 1,000 m in the world, and the mining depth of the Mponeng gold mine in South Africa is as deep as 4,350 m (Zhang 2020). Besides, there are many underground projects with a depth of more than kilometers in China. For example, the diversion tunnel in Jinping II hydropower station has a maximum buried depth of 2,525 m. The Jinping underground laboratory in China built on this diversion tunnel is also the laboratory with the largest rock coverage depth in the world with a buried depth of 2,400 m (Feng et al., 2018; Zhang 2020).

Different from shallow-rock mechanical engineering, in the deep tunnel construction process, it is inevitable to face the challenges of high ground stress, complex geological conditions, strong excavation unloading, and mechanical and blasting disturbance (Wang et al., 2004; Qiu et al., 2012; Feng et al., 2015; Gao et al., 2018; Feng et al., 2019; Do et al., 2020). Generally, the surrounding rock of the cavern is mostly high-strength hard rock. For example, the maximum ground stress of Jinping I Hydropower Station is 40 MPa, and the surrounding rock is mainly marble. The uniaxial compressive strength is 50–80 MPa (Gong et al., 2010). The Paoma mountain No. 1 tunnel is located in the northeast of Kangding City. The maximum buried depth of the Paoma mountain No. 1 tunnel is 1,250 m, more than 85% of the whole tunnel section is hard granite, and the saturated uniaxial compressive strength is 48.82–49.74 MPa.

Generally, there is a high possibility of stress-induced failure in deep buried hard rock tunnels, such as cracking, wall splitting, and rockburst, which will seriously threaten the lives of workers and the safety of construction equipment and will also affect the construction cycle and the final completion of the tunnel, resulting in huge economic losses. As shown in **Figure 1**, rockburst disasters occurred at different locations during the construction of the Paoma mountain No. 1 tunnel.

The site selection of deep underground engineering, such as deeply buried tunnels and underground powerhouses of hydropower stations, tends to be the hard rock area with relatively complete lithology, so as to ensure the stability of

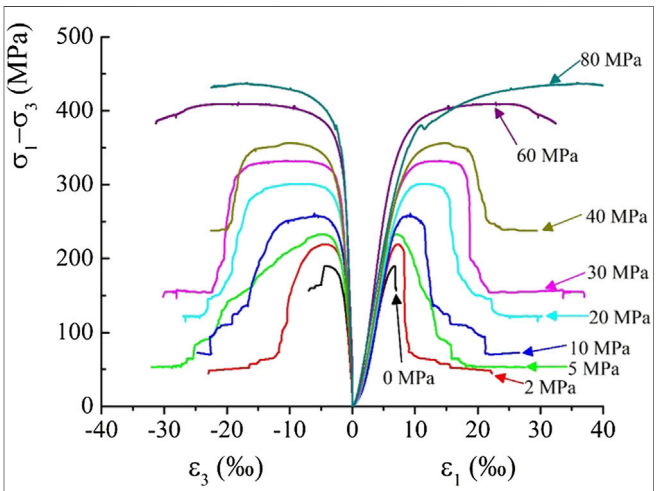


FIGURE 2 | Stress–strain curves of the tested samples under conventional triaxial compression state (revised form Gao 2020).

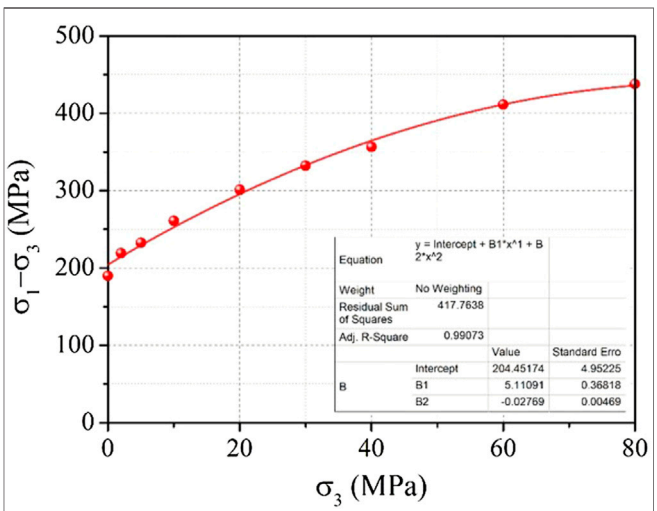


FIGURE 3 | Peak strength of the tested samples under conventional triaxial compression state.

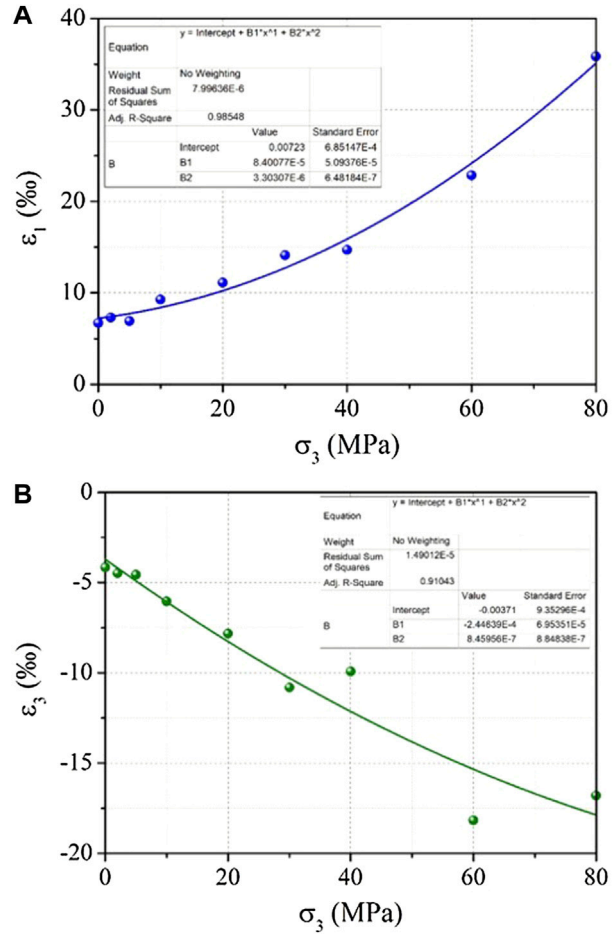


FIGURE 4 | Strain characteristics of the tested samples under conventional triaxial compression state.

deep engineering. Many scholars have carried out a great number of in-depth studies on the mechanical characteristics of deep buried hard rock and its influence from many angles such as theory, experiment, and numerical calculation. In this study, the mechanical properties and failure differences of hard rock based on a comparison between conventional and true triaxial tests are analyzed. The research of this article is helpful to deeply understand the fracture and failure characteristics of deep hard rock mass and can provide a useful reference for disaster prevention and reduction of deep rock mass engineering.

FAILURE ANALYSIS OF MARBLE SAMPLE BASED ON CONVENTIONAL TRIAXIAL TEST

Figure 2 and **Figure 3** are the stress–strain curve and failure–strength diagrams of a group of Jinping marble samples in a conventional triaxial compression test (Gao 2020). **Figure 4** shows the corresponding peak axial and radial strains (ε_1 and ε_3) diagram in **Figure 2** and **Figure 3**.

It can be found from the **Figures 2–4** that when confining pressure is 0 MPa, 2 MPa, 5 MPa, 10 MPa, 20 MPa, 30 MPa, 40 MPa, 60 MPa, and 80 MPa, respectively, the corresponding peak strength is 190 MPa, 219 MPa, 233 MPa, 261 MPa, 301 MPa, 332 MPa, 356 MPa, 411 MPa, and 438 MPa, respectively, the corresponding peak ε_1 is 0.0067, 0.0073, 0.0069, 0.0111, 0.0141, 0.0147, 0.0229, and 0.0359, respectively, and the corresponding peak ε_3 is −0.0042, −0.0045, −0.0046, −0.0061, −0.0078, −0.0108, −0.0099, −0.0182, and −0.0168, respectively. It could be concluded that peak strength increases with the increasing confining pressure, the ε_1 and ε_3 also increase with the increasing confining pressure, but the difference is that the ε_1 is the compression deformation and ε_3 is the expansion deformation. The variations of peak strength, axial strain ε_1, and radial strain ε_3 with confining pressure are shown in formula as below:

$$(\sigma_1 - \sigma_3)_{\text{peak}} = -0.0277\sigma_3^2 + 5.11\sigma_3 + 204.45\,(R^2 = 0.99) \quad (1)$$

$$\varepsilon_1 = 3.30 \times 10^{-6}\sigma_3^2 + 8.40 \times 10^{-5}\sigma_3 + 0.0072\,(R^2 = 0.99) \quad (2)$$

$$\varepsilon_3 = 8.46 \times 10^{-7}\sigma_3^2 - 2.45 \times 10^{-4}\sigma_3 - 0.0037\,(R^2 = 0.91) \quad (3)$$

As shown in **Figure 2** and **Figure 5**, the brittle–ductile transformation properties of rock could be reflected in the sample stress–strain curve and failure mode (Lajtai 1974; Tarasov and Potvin 2013; Ai et al., 2016; Tarasov and Stacey 2017; Kanaya and Hirth 2018; Ning et al., 2018; Zhao et al., 2018; Gao 2020). When confining pressure is small (confining pressure is less than 10 MPa), there is no platform section at the peak section of stress–strain curve for the marble sample, and the stress-drop phenomenon after the peak is obvious. The rock failure surface shows splitting failure characteristics, and the failure surface is basically parallel to the maximum principal stress direction (axial direction), indicating that the rock brittleness under this stress condition is obvious.

With increasing confining pressure, the rock ductile deformation increases, that is, the rock peak platform section on the stress–strain curve is gradually significant, the stress drop after the peak decreases, and the failure of the sample gradually transitions from complete splitting to single shear plane, indicating that the brittleness of the rock decreases and the ductility increases. After the confining pressure reaches 60 MPa, the ductile deformation characteristics of the sample are particularly obvious, the post-peak stress-drop phenomenon of the sample basically disappears, and the failure of the sample is obviously bulking in the middle; when the confining pressure reaches 80 MPa, there is no macro fracture surface, and only weak bulking exists in the middle of the sample. Therefore, it can be considered that the confining pressure of 60 MPa is the brittle–ductile transformation point of marble samples.

In addition, the brittle–ductile transition point of rock can also be determined by the difference between peak and residual strength. With increasing confining pressure, the difference between peak and residual strength gradually decreases. Even in an ideal ductile state, the difference is 0, that is, the rock peak strength is equal to residual strength.

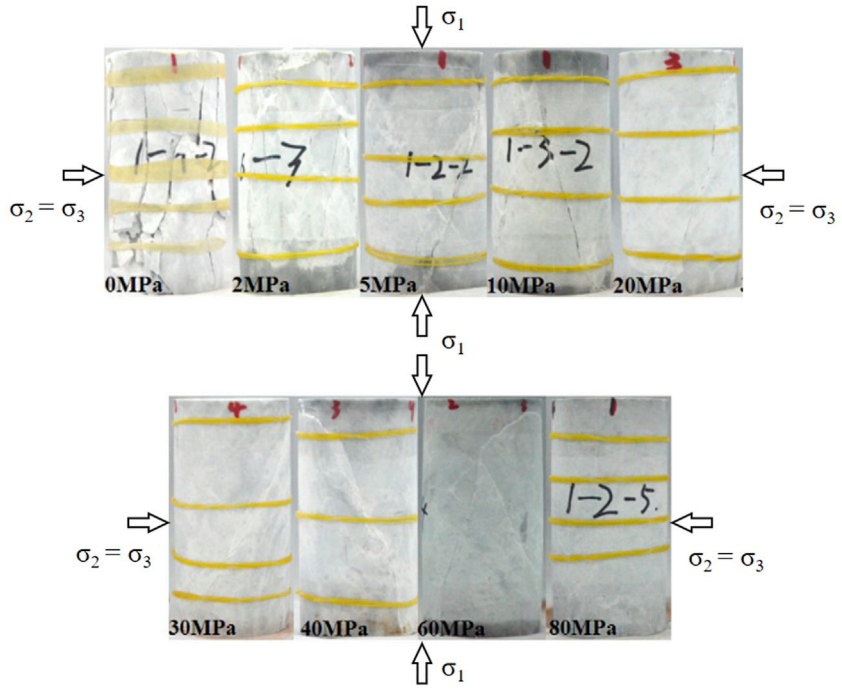


FIGURE 5 | Failure modes of the tested samples under conventional triaxial compression state (revised form Gao 2020).

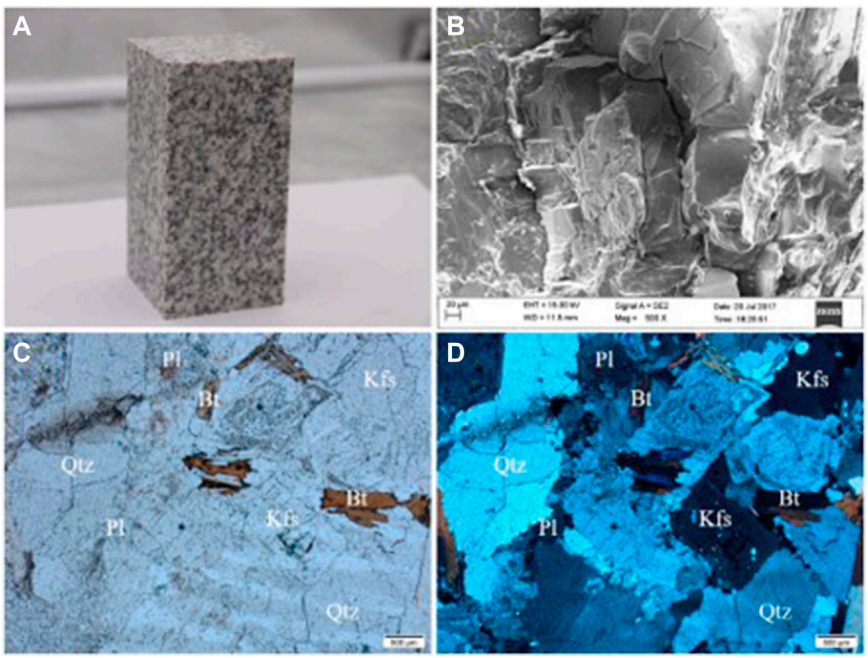


FIGURE 6 | Schematic diagram of granite samples used in the true triaxial experiment. **(A)** Sample physical drawing, **(B)** sample SEM image, **(C)** plane polarized light micrograph of sample, and **(D)** crossed polars micrograph of sample (quartz = Qtz, K-feldspar = Kfs, plagioclase = Pl, biotite = Bt).

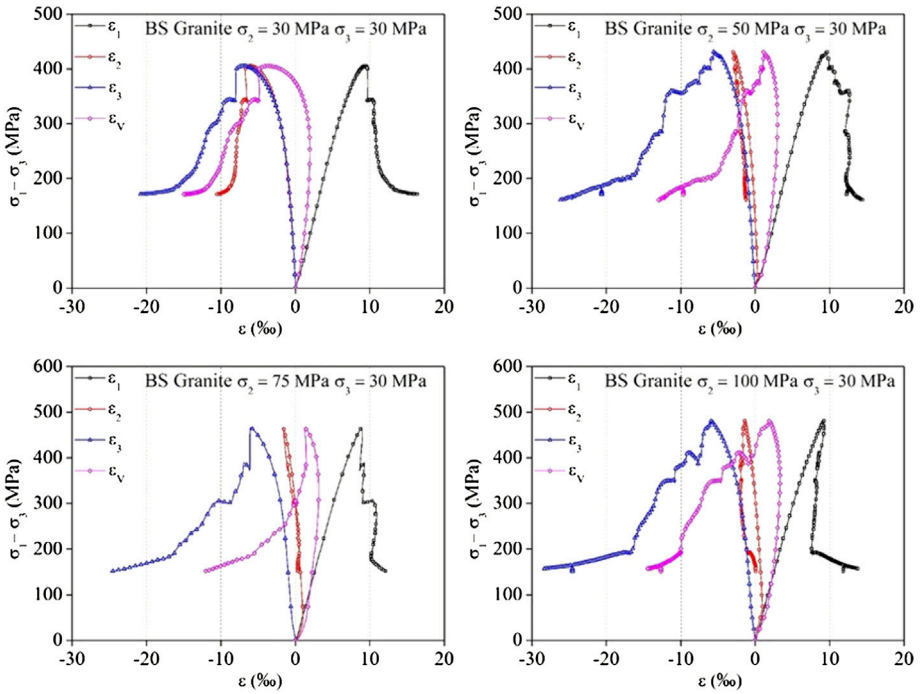


FIGURE 7 | Stress–strain curves of granite samples adopted in the true triaxial experiment (revised form Zhang 2020).

FAILURE ANALYSIS OF GRANITE SAMPLE BASED ON TRUE TRIAXIAL TEST

Figure 6 shows the granite sample used in the true triaxial test (Zhang 2020). The rock thin-section micrograph obtained shows the microstructure and mineral composition of the granite. It can be seen from **Figure 6** that the granite is a medium-grain coarse-grain structure with strong isotropy in structure and mineral composition. The density of the granite is 2.61 g/cm^3, and the tested granite has the characteristics of high density, dense lithology, and high rock strength. The tested granite is mainly composed of about 40% plagioclase, 33% quartz, 17% potassium feldspar, and 10% other materials.

To simulate the stress path of rock mass failure in deep underground engineering, the typical stress path (Zhang et al., 2019) finally adopted in this study is shown as follows: (a) Hydrostatic loading stage: loading simultaneously in three principal stress directions ($\sigma_1 = \sigma_2 = \sigma_3$) at a loading rate of 0.5 MPa/s to the minimum principal stress level. (b) Intermediate principal stress loading stage: keeping σ_3 unchanged and loading σ_1 and σ_2 simultaneously ($\sigma_1 = \sigma_2$) at a loading rate of 0.5 MPa/s to set the σ_2 level. (c) Maximum principal stress loading stage: keeping σ_2 and σ_3 unchanged and loading σ_1 at loading rate of 0.5 MPa/s. When σ_1 reached the crack damage stress of the sample, the control mode was changed from stress control to strain control ε_1 with the rate of 0.015 mm/min.

Figure 7 and **Figure 8** show the variation of stress–strain relationship and strength characteristic of granite with different σ_2 under true triaxial compression stress state (Zhang 2020). It can be found from **Figure 7** and **Figure 8** that within the scope of this study, when σ_3 is 30 MP and σ_2 is 30 MPa, 50 MPa, 75 MPa, and 100 MPa, respectively, the peak failure strength σ_{1peak} of granite shows an increasing rule with increasing of σ_2. Meanwhile, for the stress–strain curve shape, the rock tends toward Class II failure with the increase of σ_2, and the post-peak stress drop of the curve is more obvious, indicating that the increase of σ_2 makes the rock failure more prone to brittle failure. In addition, with the increase of σ_2, the degree of differentiation of the σ_1–ε_2 curve and

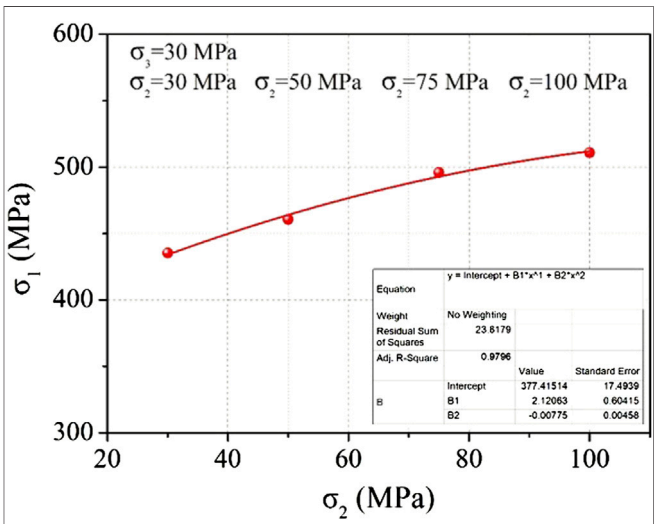


FIGURE 8 | Peak strength of granite samples adopted in the true triaxial experiment.

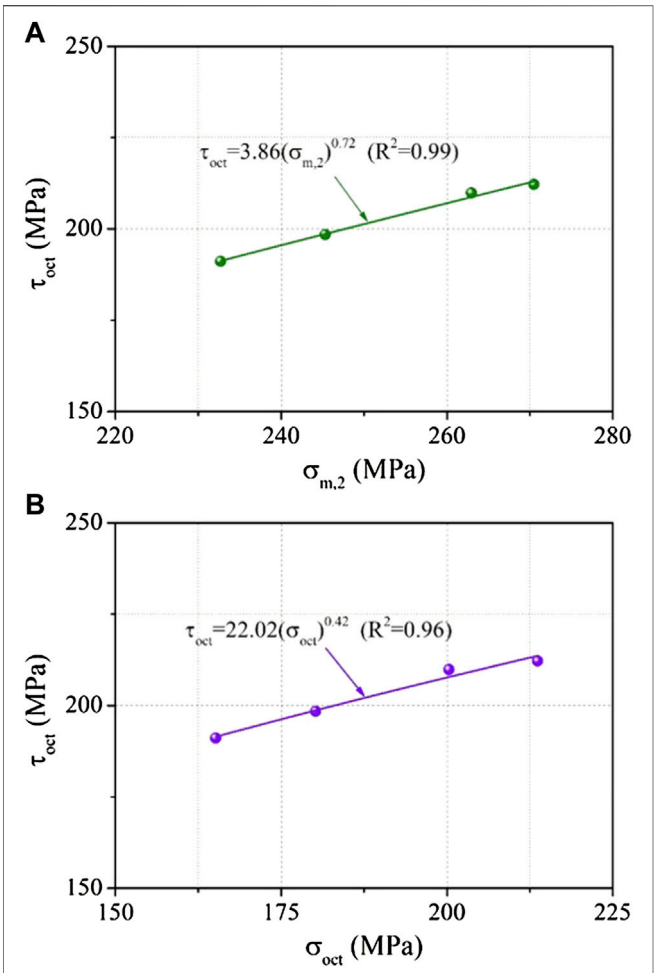


FIGURE 9 | True triaxial compression strength for tested granite in terms of **(A)** τ_{oct} versus σ_{oct} and **(B)** τ_{oct} versus $\sigma_{m,2}$.

the σ_1–ε_3 curve of rock is increasing, which indicates that under true triaxial stress conditions, the differential stress makes the deformation of rock appear anisotropic, and the greater the differential stress between σ_2 and σ_3, the more obvious the deformation anisotropy of ε_2 and ε_3.

Nadaia used octahedral shear stress τ_{oct} and octahedral normal stress σ_{oct} to describe rock materials' three-dimensional failure strength criterion, namely, $\tau_{oct} = f(\sigma_{oct})$ (Nadaia 1950). Subsequently, based on a large number of tests and the analysis of the true triaxial compression failure mode of hard rock, Mogi revised the three-dimensional failure strength criterion proposed by Nadaia and replaced σ_{oct} with $\sigma_{m,2}$ (Mogi 1971). The obtained three-dimensional failure strength criterion is shown as follows:

$$\tau_{oct} = 1/3\left[(\sigma_1 - \sigma_2)^2 + (\sigma_2 - \sigma_3)^2 + (\sigma_3 - \sigma_1)^2\right]^{1/2} \quad (4)$$

$$\sigma_{oct} = (\sigma_1 + \sigma_2 + \sigma_3)/3 \quad (5)$$

$$\sigma_{m,2} = (\sigma_1 + \sigma_3)/2 \quad (6)$$

The peak strength characteristics of granite under true triaxial stress conditions obtained in this article are shown in **Figure 8**.

Using the aforementioned two three-dimensional failure strength criteria, the strength data obtained in **Figure 8** are fitted by power law form. The relationship between τ_{oct} and σ_{oct} in Nadaia's domain (**Figure 9A**) and between τ_{oct} and $\sigma_{m,2}$ in the Mogi domain (**Figure 9B**) are obtained. The following formulas are obtained:

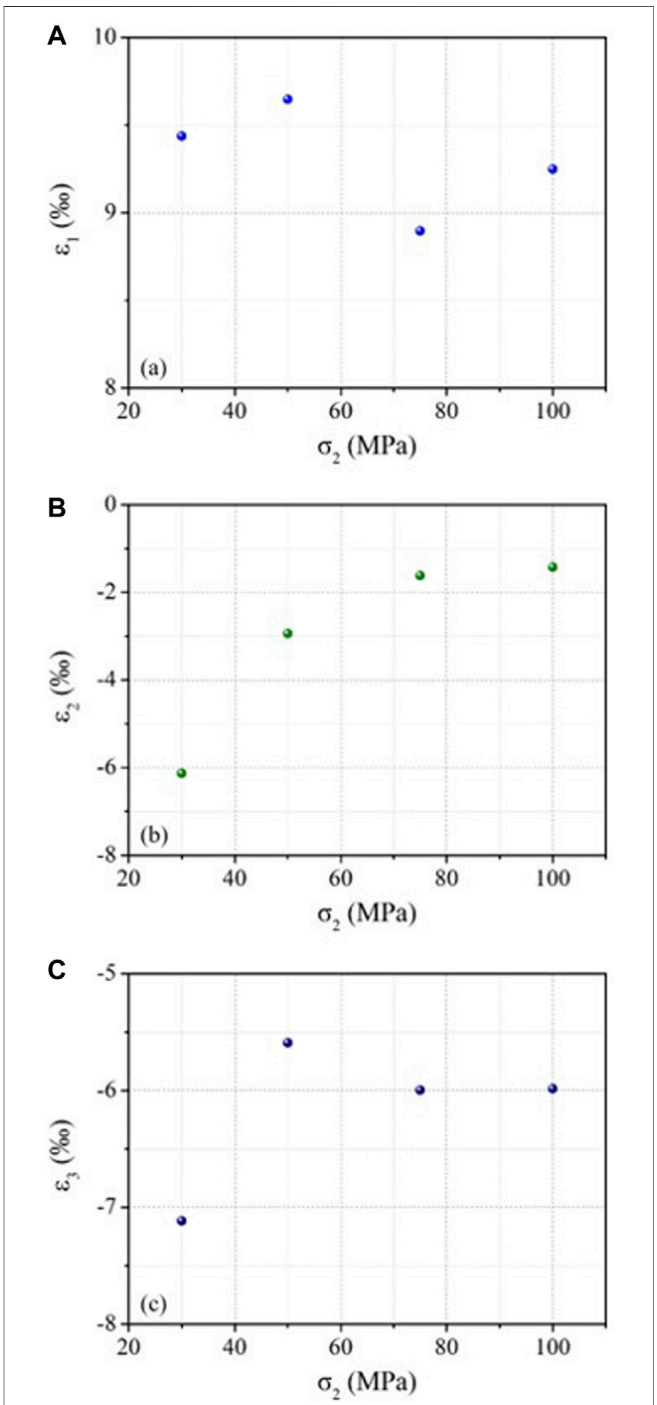


FIGURE 10 | Strain characteristics of granite samples adopted in the true triaxial experiment. **(A)** ε_1 versus σ_2, **(B)** ε_2 versus σ_2, and **(C)** ε_3 versus σ_2.

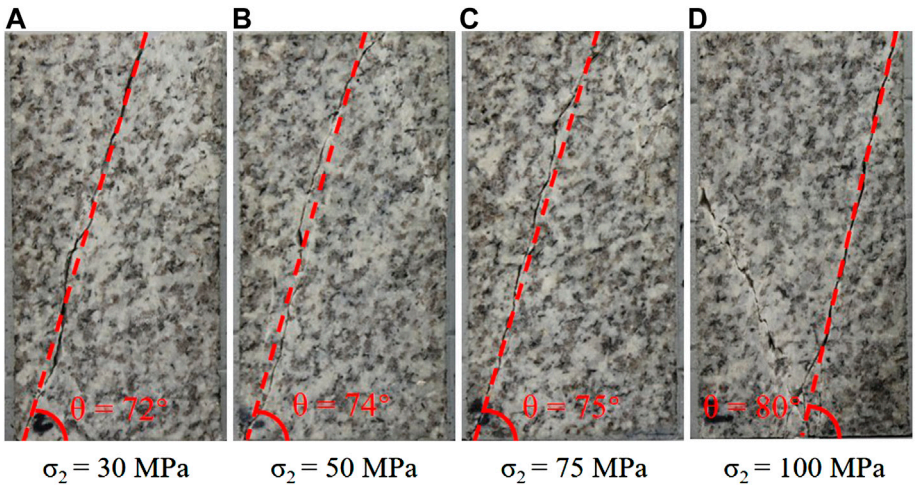


FIGURE 11 | Fracture angle and failure mode of granite samples adopted in the true triaxial experiment (revised form Zhang 2020).

$$\tau_{oct} = 3.86\left(\sigma_{m,2}\right)^{0.72}\left(R^2 = 0.99\right) \quad (7)$$

$$\tau_{oct} = 22.02\left(\sigma_{oct}\right)^{0.42}\left(R^2 = 0.96\right) \quad (8)$$

It can be found from **Figure 9** that τ_{oct} monotonically increases with increasing σ_{oct} or $\sigma_{m,2}$, and the fitting goodness of the modified strength criterion proposed by Mogi is $R^2 = 0.99$, which is better than that proposed by Nadai ($R^2 = 0.96$).

Figure 10 shows the variation of principal strain ε_1, ε_2, and ε_3 of granite samples with intermediate principal stress σ_2. Within the research scope of this article, it can be seen from **Figure 10** that when σ_3 is 30 MP and σ_2 is 30 MPa, 50 MPa, 75 MPa, and 100 MPa, respectively, the principal strain ε_2 increases with increasing σ_2, and its variation law is good (**Figure 10B**), while the variation law of principal strain ε_1 and ε_3 with intermediate principal stress σ_2 is not obvious (**Figures 10A,C**).

Figure 11 shows the variation of failure mode and fracture angle of granite under true triaxial compression with σ_2 (Zhang 2020). In practical tests, the macroscopic main crack morphology perpendicular to the σ_2 sample surface is not a straight line, but an irregular broken line, which makes it difficult to determine the fracture angle (θ). In this article, the fracture angle (θ) is determined by the angle between the overall direction of a macroscopic main crack and the σ_3 loading direction. It can be seen from **Figure 11** that within the scope of this study, when σ_3 = 30 MPa and when σ_3 is 30 MPa, 50 MPa, 75 MPa, and 100 MPa, the fracture angles of granite are 72°, 74°, 75°, and 80°, respectively. It can be found that the fracture angle of granite increases with the increase of σ_2 and the regularity is obvious.

DISCUSSION

Figure 12 shows the comparison of the failure of the sandstone samples under conventional triaxial ($\sigma_2 = \sigma_3$) and true triaxial ($\sigma_2 > \sigma_3$) stress conditions. The first pictures in **Figure 12A** and **Figure 12B** are the actual failure situations of the samples, the second pictures are the computed tomography (CT) scan results corresponding to the first picture, and the third pictures are CT scan of the I-I cross-section of the samples corresponding to the second picture (Lu et al., 2018).

It can be clearly concluded from **Figure 12A** that the sample failure under the condition of conventional triaxial stress ($\sigma_2 = \sigma_3$) is random, and its crack presents irregular propagation and evolution. This is due to the fact that the σ_2 is equal to σ_3 so the cracks of the sample randomly propagate and evolve on the σ_2-σ_3 plane. The failure of the sample under true triaxial stress ($\sigma_2 > \sigma_3$) is different, and it can be clearly found from **Figure 12B** that the sample main crack growth is obviously parallel to the σ_2 action direction and perpendicular to the σ_3 action direction. It can be concluded that under the condition of true triaxial stress ($\sigma_2 > \sigma_3$), the cracks of the sample cannot propagate randomly, but they have a certain directional arrangement and distribution characteristics.

Obviously, compared with the uniaxial and conventional triaxial stress conditions ($\sigma_2 = \sigma_3$) (Ingraham et al., 2013; Frash et al., 2014; Li et al., 2015; Ma and Haimson 2016; Meng et al., 2016; Shi et al., 2017; Yu et al., 2022), this is due to the particular point that σ_2 is greater than σ_3 under true triaxial stress conditions (σ2 > σ3), and the anisotropic fracture characteristics of sample under true triaxial stress conditions ($\sigma_2 > \sigma_3$) are different from the failure anisotropy of the layered rock mass due to the layered structure, which is caused by the difference of stress, also called the differential stress-induced anisotropy under true triaxial stress ($\sigma_2 > \sigma_3$) condition. This differential stress-induced anisotropy failure characteristic is the biggest difference between the fracture characteristics of samples under true triaxial stress conditions ($\sigma_2 > \sigma_3$) and those under conventional triaxial stress conditions ($\sigma_2 = \sigma_3$), this also makes a series of hard rock failure and disaster problems under deep true triaxial stress ($\sigma_2 > \sigma_3$) very complex.

For the differential stress-induced anisotropy failure of the rock, Feng et al. (2019) have made a systematic quantitative study on it. They used the following **Eqn. 9** as an index to quantitatively

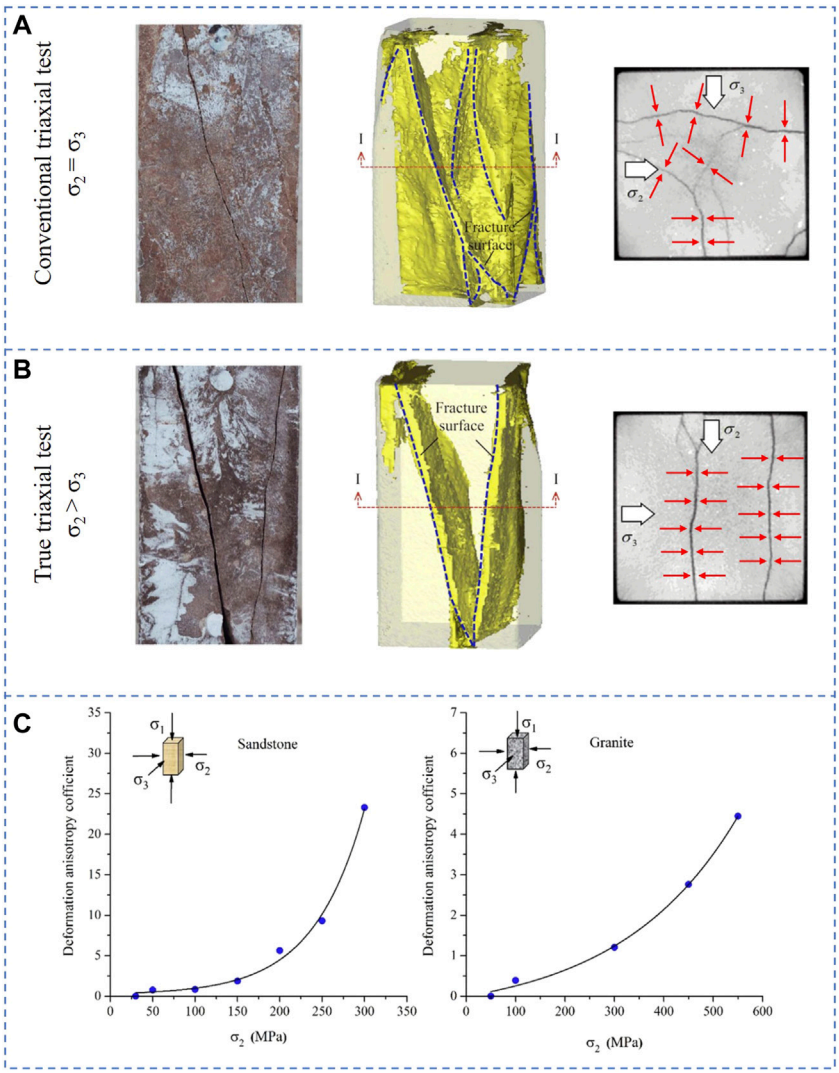


FIGURE 12 | Failure difference of hard rock based on comparison between the conventional triaxial test and true triaxial test (revised form Lu et al., 2018 and Feng et al., 2019). **(A)** Conventional triaxial stress state, **(B)** true triaxial stress state, and **(C)** differential stress-induced anisotropy failure analysis.

study the differential stress-induced anisotropy failure of the rock:

$$A = \frac{K_{12} - K_{13}}{K_{13}} \tag{9}$$

where K_{12} and K_{13} are the deformation moduli of the stress–strain curve corresponding to σ_2 and σ_3.

It can be found from the definition of **Eqn. 9** that when the differential stress of σ_2 and σ_3 is larger, the value of A in **Eqn. 9** is larger, indicating that the anisotropic failure of rock induced by differential stress is more obvious. **Figure 12C** shows the variation of differential stress-induced anisotropy failure index of sandstone and granite with intermediate principal stress σ_2. It can also be found that when the intermediate principal stress σ_2 is larger, the anisotropy index A is larger, which indicates that the anisotropic failure of rock is more obvious.

It should be noted that this differential stress-induced anisotropy failure of the rock is essentially different from the initial anisotropic failure of layered rock. Layered rock is a typical complex geological body, which widely exists in the engineering surrounding rock. The layered rock is distributed with a group of dominant primary bedding structural planes (bedding planes), and usually has a relatively determined occurrence and good spatial continuity, which makes the mechanical properties of layered hard rocks differ greatly in the direction parallel to and perpendicular to the bedding plane, showing significant initial anisotropy and heterogeneity.

Under deep complex geological conditions, engineering excavation and other activities lead to stress transfer and stress concentration of surrounding rock, which not only enhances the intermediate principal stress effect in surrounding rocks but also makes the phenomenon of true triaxial high stress and high-stress difference of deep hard rock remarkable. The typical stress

characteristics in the deep rock make the energy storage and release threshold of rock mass increase, and the energy release intensity increases, leading to the deep rock mass becoming a high-energy environmental field. Under the condition of true triaxial stress, the process and mechanism of energy storage, distribution, driving, and release in the failure process of layered rock will be more complex. Deep-layered hard rock shows the characteristics of complex stress, prone to a variety of disaster phenomena and complex disaster causing mechanisms. The failure and instability of deep-layered hard rock are significantly greater than those of shallow rock engineering in terms of type, quantity, frequency, scale, and strength.

When the layered rock mass is in the deep true triaxial stress state, its failure problem becomes very complex. Under the coupling action of true triaxial stress and layered rock dip angle, the layered hard rock has obvious mixed anisotropy. This complex mixed action between differential stress-induced anisotropy failure and initial anisotropy failure of the rock makes the mechanical properties, fracture mechanism, and energy evolution process of deep layered hard rock very complex. Therefore, the research on the true triaxial mechanical properties of deep layered hard rock is a very important research topic that needs to be further explored.

CONCLUSION

In this article, the conventional triaxial test and true triaxial test of hard rock are carried out respectively to explore the influence and mechanism of stress state on the failure characteristics of hard rock. The following conclusions within the research scope have been obtained:

1) Brittle–ductile transformation properties of rock can be reflected from the stress–strain curve and failure mode. With increasing confining pressure, the ductile deformation of the sample increases, the peak platform section of the sample stress–strain curve is gradually significant, the post-peak stress drop decreases, and the failure of the sample gradually transitions from complete splitting to a single shear plane.
2) The brittle–ductile transition point of rock can also be determined by the difference between peak and residual strength. With increasing confining pressure, the difference between peak, and residual strength gradually decreases.
3) Within the scope of this study, the rock failure strength under true triaxial stress conditions increases with increasing σ_2, the peak strain decreases with the increase of σ_2, the stress drop of the post-peak curve becomes more obvious with the increase of σ_2, and the rock tends to Class II brittle failure after the peak with the increase of σ_2.
4) When σ_3 is relatively high, most rock samples have only one macroscopic main crack under true triaxial stress condition, and the fracture angle of granite samples increases with the increase of σ_2 with obvious regularity.
5) Compared with the conventional triaxial stress, due to the stress difference of rock under true triaxial stress (σ_2 is greater than σ_3), the differential stress-induced anisotropy failure is the biggest difference between the fracture characteristics of rock under true triaxial stress and the conventional triaxial stress state.

DATA AVAILABILITY STATEMENT

The raw data supporting the conclusions of this article will be made available by the authors, without undue reservation.

AUTHOR CONTRIBUTIONS

All authors listed have made a substantial, direct, and intellectual contribution to the work and approved it for publication.

FUNDING

This study is supported by the National Natural Science Foundation of China (Grant No. 42107211) and China Postdoctoral Science Foundation (Grant No. 2021M691000). This study is also supported by the Opening Foundation of Key Laboratory of Geohazard Prevention of Hilly Mountains, Ministry of Natural Resources (Fujian Key Laboratory of Geohazard Prevention) (Grant No. FJKLGH 2022K005).

ACKNOWLEDGMENTS

The authors sincerely acknowledge the research support from Key Laboratory of Ministry of Education on Safe Mining of Deep Metal Mines, Northeastern University.

REFERENCES

Ai, C., Zhang, J., Li, Y.-w., Zeng, J., Yang, X.-l., and Wang, J.-g. (2016). Estimation Criteria for Rock Brittleness Based on Energy Analysis during the Rupturing Process. *Rock Mech. Rock Eng.* 49 (12), 4681–4698. doi:10.1007/s00603-016-1078-x

Bai, Q., Tibbo, M., Nasseri, M. H. B., and Young, R. P. (2019). True Triaxial Experimental Investigation of Rock Response Around the Mine-By Tunnel under an *In Situ* 3D Stress Path. *Rock Mech. Rock Eng.* 52 (10), 3971–3986. doi:10.1007/s00603-019-01824-6

Diederichs, M. S. (2007). The 2003 Canadian Geotechnical Colloquium: Mechanistic Interpretation and Practical Application of Damage and Spalling Prediction Criteria for Deep Tunnelling. *Can. Geotech. J.* 44 (9), 1082–1116. doi:10.1139/t07-033

Do, D.-P., Tran, N.-T., Mai, V.-T., Hoxha, D., and Vu, M.-N. (2020). Time-dependent Reliability Analysis of Deep Tunnel in the Viscoelastic Burger Rock with Sequential Installation of Liners. *Rock Mech. Rock Eng.* 53, 1259–1285. doi:10.1007/s00603-019-01975-6

Feng, G.-L., Chen, B.-R., Xiao, Y.-X., Jiang, Q., Li, P.-X., Zheng, H., et al. (2022). Microseismic Characteristics of Rockburst Development in Deep TBM Tunnels with Alternating Soft-Hard Strata and Application to Rockburst Warning: A

Case Study of the Neelum-Jhelum Hydropower Project. *Tunn. Undergr. Space Technol.* 122, 104398. doi:10.1016/j.tust.2022.104398

Feng, G.-L., Feng, X.-T., Chen, B.-r., Xiao, Y.-X., and Yu, Y. (2015). A Microseismic Method for Dynamic Warning of Rockburst Development Processes in Tunnels. *Rock Mech. Rock Eng.* 48 (5), 2061–2076. doi:10.1007/s00603-014-0689-3

Feng, X.-T., Kong, R., Zhang, X., and Yang, C. (2019). Experimental Study of Failure Differences in Hard Rock under True Triaxial Compression. *Rock Mech. Rock Eng.* 52, 2109–2122. doi:10.1007/s00603-018-1700-1

Feng, X.-T., Xu, H., Qiu, S.-L., Li, S.-J., Yang, C.-X., Guo, H.-S., et al. (2018). *In Situ* observation of Rock Spalling in the Deep Tunnels of the China Jinping Underground Laboratory (2400 M Depth). *Rock Mech. Rock Eng.* 51, 1193–1213. doi:10.1007/s00603-017-1387-8

Frash, L. P., Gutierrez, M., and Hampton, J. (2014). True-triaxial Apparatus for Simulation of Hydraulically Fractured Multi-Borehole Hot Dry Rock Reservoirs. *Int. J. Rock Mech. Min. Sci.* 70 (9), 496–506. doi:10.1016/j.ijrmms.2014.05.017

Gao, Y.-H., Feng, X.-T., Zhang, X.-W., Feng, G.-L., Jiang, Q., and Qiu, S.-L. (2018). Characteristic Stress Levels and Brittle Fracturing of Hard Rocks Subjected to True Triaxial Compression with Low Minimum Principal Stress. *Rock Mech. Rock Eng.* 51 (12), 3681–3697. doi:10.1007/s00603-018-1548-4

Gao, Y. H. (2020). *Study on Failure Mechanism of Deep-Buried Marble Tunnel with Calcium-Cemented Stiff Discontinuity*. Wuhan: Institute of Rock and Soil Mechanics, Chinese Academy of Sciences.

Gong, M., Qi, S., and Liu, J. (2010). Engineering Geological Problems Related to High Geo-Stresses at the Jinping I Hydropower Station, Southwest China. *Bull. Eng. Geol. Environ.* 69 (3), 373–380. doi:10.1007/s10064-010-0267-1

Hajiabdolmajid, V., and Kaiser, P. (2003). Brittleness of Rock and Stability Assessment in Hard Rock Tunneling. *Tunn. Undergr. Space Technol.* 18 (1), 35–48. doi:10.1016/s0886-7798(02)00100-1

Ingraham, M. D., Issen, K. A., and Holcomb, D. J. (2013). Response of Castlegate Sandstone to True Triaxial States of Stress. *J. Geophys. Res. Solid Earth* 118 (2), 536–552. doi:10.1002/jgrb.50084

Kanaya, T., and Hirth, G. (2018). Brittle to Semibrittle Transition in Quartz Sandstone: Energetics. *J. Geophys. Res. Solid Earth* 123, 84–106. doi:10.1002/2017jb014682

Lajtai, E. Z. (1974). Brittle Fracture in Compression. *Int. J. Fract.* 10 (4), 525–536. doi:10.1007/bf00155255

Li, X., Du, K., and Li, D. (2015). True Triaxial Strength and Failure Modes of Cubic Rock Specimens with Unloading the Minor Principal Stress. *Rock Mech. Rock Eng.* 48 (6), 2185–2196. doi:10.1007/s00603-014-0701-y

Lu, Y., Li, W., Wang, L., Li, Z., Meng, X., Wang, B., et al. (2018). Damage Evolution and Failure Behavior of Sandstone under True Triaxial Compression. *Geotech. Test. J.* 42 (3), 20170295. doi:10.1520/gtj20170295

Ma, X., and Haimson, B. C. (2016). Failure Characteristics of Two Porous Sandstones Subjected to True Triaxial Stresses. *J. Geophys. Res. Solid Earth* 121 (9), 6477–6498. doi:10.1002/2016jb012979

Malan, D. F. (2002). Manuel Rocha Medal Recipient Simulating the Time-dependent Behaviour of Excavations in Hard Rock. *Rock Mech. Rock Eng.* 35 (4), 225–254. doi:10.1007/s00603-002-0026-0

Martin, C. D., and Chandler, N. A. (1994). The progressive fracture of Lac du Bonnet granite. *Int. J. Rock Mech. Min. Sci. Geomechanics Abstr.* 31 (6), 643–659. doi:10.1016/0148-9062(94)90005-1

Meng, Q., Zhang, M., Han, L., Pu, H., and Nie, T. (2016). Effects of Acoustic Emission and Energy Evolution of Rock Specimens under the Uniaxial Cyclic Loading and Unloading Compression. *Rock Mech. Rock Eng.* 49, 3873–3886. doi:10.1007/s00603-016-1077-y

Mogi, K. (1971). Fracture and Flow of Rocks under High Triaxial Compression. *J. Geophys. Res.* 76, 1255–1269. doi:10.1029/jb076i005p01255

Nadai, A. (1950). *Theory of Flow and Fracture of Solids II[M]*. New York: McGraw-Hill, 94–108.

Ning, J., Wang, J., Jiang, J., Hu, S., Jiang, L., and Liu, X. (2018). Estimation of Crack Initiation and Propagation Thresholds of Confined Brittle Coal Specimens Based on Energy Dissipation Theory. *Rock Mech. Rock Eng.* 51, 119–134. doi:10.1007/s00603-017-1317-9

Qiu, S. L., Feng, X. T., Zhang, C. Q., and Yang, J. B. (2012). Experimental Research on Mechanical Properties of Deep Marble under Different Initial Damage Levels and Unloading Paths[J]. *Chin. J. Rock Mech. Eng.* 31 (8), 1686–1697. doi:10.3969/j.issn.1000-6915.2012.08.024

Shi, L., Li, X., Bing, B., Wang, A., Zeng, Z., and He, H. (2017). A Mogi-type True Triaxial Testing Apparatus for Rocks with Two Moveable Frames in Horizontal Layout for Providing Orthogonal Loads. *Geotech. Test. J.* 40 (4), 20160242. doi:10.1520/gtj20160242

Tarasov, B. G., and Stacey, T. R. (2017). Features of the Energy Balance and Fragmentation Mechanisms at Spontaneous Failure of Class I and Class II Rocks. *Rock Mech. Rock Eng.* 50 (10), 2563–2584. doi:10.1007/s00603-017-1251-x

Tarasov, B., and Potvin, Y. (2013). Universal Criteria for Rock Brittleness Estimation under Triaxial Compression. *Int. J. Rock Mech. Min. Sci.* 59, 57–69. doi:10.1016/j.ijrmms.2012.12.011

Wang, S. H., Liu, J. X., Tang, C. A., Li, L. C., and Zhao, X. D. (2004). Stability Analysis of a Large-Span and Deep Tunnel. *Int. J. Rock Mech. Min. Sci.* 41 (3), 870–875. doi:10.1016/j.ijrmms.2004.03.150

Yu, Y., Zhao, D.-C., Feng, G.-L., Geng, D.-X., and Guo, H.-S. (2022). Energy Evolution and Acoustic Emission Characteristics of Uniaxial Compression Failure of Anchored Layered Sandstone. *Front. Earth Sci.* 10, 841598. doi:10.3389/feart.2022.841598

Zhang, Y. (2020). *Energy Evolution Mechanism of Failure Process of Deep Hard Rock and Discrimination of Typical Hazard Types of Deep Tunnel*. Shengyang: Northeastern University.

Zhang, Y., Feng, X.-T., Yang, C., Zhang, X., Sharifzadeh, M., and Wang, Z. (2019). Fracturing Evolution Analysis of Beishan Granite under True Triaxial Compression Based on Acoustic Emission and Strain Energy. *Int. J. Rock Mech. Min. Sci.* 117, 150–161. doi:10.1016/j.ijrmms.2019.03.029

Zhao, J., Feng, X.-T., Zhang, X.-W., Zhang, Y., Zhou, Y.-Y., and Yang, C.-X. (2018). Brittle-ductile Transition and Failure Mechanism of Jinping Marble under True Triaxial Compression. *Eng. Geol.* 232, 160–170. doi:10.1016/j.enggeo.2017.11.008

Zhao, X. G., Wang, J., Cai, M., Cheng, C., Ma, L. K., Su, R., et al. (2014). Influence of Unloading Rate on the Strainburst Characteristics of Beishan Granite under True-Triaxial Unloading Conditions. *Rock Mech. Rock Eng.* 47 (2), 467–483. doi:10.1007/s00603-013-0443-2

Zhuang, D. Y., Tang, C. A., Liang, Z. Z., Ma, K., Wang, S. Y., and Liang, J. Z. (2017). Effects of Excavation Unloading on the Energy-Release Patterns and Stability of Underground Water-Sealed Oil Storage Caverns. *Tunn. Undergr. Space Technol.* 61, 122–133. doi:10.1016/j.tust.2016.09.011

Conflict of Interest: Authors GZ and KC were employed by the Sichuan Communication Surveying & Design Institute Co., Ltd. Authors YT and JS were employed by the Sichuan Transportation Construction Group CO., LTD. Author YG is employed by the PowerChina Huadong Engineering Corporation Limited. Author JR is employed by the Sichuan Highway Planning, Survey, Design and Research Institute Ltd.

The remaining authors declare that the research was conducted in the absence of any commercial or financial relationships that could be construed as a potential conflict of interest.

Publisher's Note: All claims expressed in this article are solely those of the authors and do not necessarily represent those of their affiliated organizations, or those of the publisher, the editors, and the reviewers. Any product that may be evaluated in this article, or claim that may be made by its manufacturer, is not guaranteed or endorsed by the publisher.

Copyright © 2022 Zheng, Tang, Zhang, Gao, Zhu, Gao, Ren, Chen and Sun. This is an open-access article distributed under the terms of the Creative Commons Attribution License (CC BY). The use, distribution or reproduction in other forums is permitted, provided the original author(s) and the copyright owner(s) are credited and that the original publication in this journal is cited, in accordance with accepted academic practice. No use, distribution or reproduction is permitted which does not comply with these terms.

frontiers | Frontiers in Earth Science

ORIGINAL RESEARCH
published: 29 June 2022
doi: 10.3389/feart.2022.909371

Microsimulation Study on Energy Release and Rock Block Ejection Force of Granite under Different Unloading Conditions

Xin-Yuan Wang[1], Yan-Chun Yin[1], Ming-Lu Xing[1], Dong-Dong Zhang[2], Yang Chen[2] and En-Chao Wang[3]*

[1]College of Energy and Mining Engineering, Shandong University of Science and Technology, Qingdao, China, [2]Shandong Energy Group Co., Ltd., Jinan Shandong, China, [3]Jining Energy Bureau, Jining Shandong, China

OPEN ACCESS

Edited by:
Fengqiang Gong,
Southeast University, China

Reviewed by:
Xiaoping Zhou,
Chongqing University, China
Yong Fan,
China Three Gorges University, China

***Correspondence:**
Yan-Chun Yin
yycrsd@163.com

Specialty section:
This article was submitted to Geohazards and Georisks, a section of the journal Frontiers in Earth Science

Received: *31 March 2022*
Accepted: *05 May 2022*
Published: *29 June 2022*

Citation:
Wang X-Y, Yin Y-C, Xing M-L, Zhang D-D, Chen Y and Wang E-C (2022) Microsimulation Study on Energy Release and Rock Block Ejection Force of Granite under Different Unloading Conditions. Front. Earth Sci. 10:909371. doi: 10.3389/feart.2022.909371

Rock burst is one typical dynamic disaster caused by excavation in deep underground engineering. High-stress unloading test is a common research method for rock bursts. Due to the limitation of laboratory test conditions, it is difficult to monitor the energy release and dissipation information during rock bursts in the unloading test. But the study of energy evolution law is more helpful to reveal the essential characteristics of rock burst. Therefore, the energy evolution process and ejection failure characteristics of granite after unloading were analyzed through the unloading simulation test in this paper, and the influence of unloading velocity, lateral stress, and axial stress were researched. The microstructure numerical model of the granite was established by using digital image processing technology and PFC2D software, aiming to match the real granite. The energy evolution process of unloading granite can be divided into three stages, namely the whole energy rapid release stage, sidewall energy slow-release stage, and rock block ejection stage. The area near the unloading sidewall is the main energy release and rock block ejection area. In the whole energy rapid release stage, the energy release velocity and dissipation velocity show similar law, i.e., a positive power function correlation with unloading velocity, a negative power function correlation with lateral stress, and a positive linear function correlation with axial stress. In the rock block ejection stage, with increasing the unloading velocity and axial stress, the rock block ejection force increases as a power function, while it decreases with increasing lateral stress. This research is an important supplement to the laboratory unloading test. It has theoretical guiding significance for rock burst hazard assessment during excavation in deep underground engineering.

Keywords: rock burst, microsimulation, energy evolution, energy release law, rock block ejection characteristics

INTRODUCTION

Rock burst is a common dynamic disaster in the deep hydraulic tunnel, traffic tunnels, and another underground rock engineering. With the expansion of the scale and depth of underground engineering construction, the frequency and intensity of rock burst disasters increase (Li et al., 2008; Feng et al., 2012; Zhao et al., 2018; Yin et al., 2019; Guo et al., 2019). Rock burst disaster has become a research focus in the field of deep rock engineering.

Rock burst mechanism and key disaster-causing factors identifications are the premise and foundation for prevention and control of rock burst. Many experts and scholars have carried out a lot of research work on rock burst mechanisms from the aspects of external stress load, mechanical properties of the rock, and dynamic load (Zhao et al., 2015; Xiao et al., 2016). He et al. (2012; 2018) divided the rock burst into two categories, namely, strain rock burst and impact-induced rock burst, and obtained their criteria. In order to understand the mechanism of rock burst and simulate the conditions of rock burst, Jiang et al. (2010) proposed a new energy index, namely local energy release rate, which can better evaluate the rock burst phenomenon in deep underground excavation. Li (2020) researched the principle of rock support to control rock bursts, and explained the energy source and conversion during rock burst in the conceptual model. Li et al. (2014) studied the influence of rock excavation unloading in the deep tunnel, and analyzed the influence of stress path and other factors on rock excavation unloading. Excavation unloading is an important cause of rock burst (Wu et al., 2009). True triaxial unloading test is often used to simulate rock burst process. For example, He et al. (2009) carried out one-side dynamic unloading test under true triaxial condition, analyzed the spectrum of full-wave acoustic emission data, obtained the frequency-amplitude relationship of acoustic emission signal in rock burst stage, and summarized the dynamic damage process and characteristics of rock under test conditions. Li et al. (2014) carried out true triaxial rock burst tests at different unloading velocities, and studied the damage evolution law of rock burst. Si and Gong (2020) carried out triaxial compression and biaxial compression tests under the same confining stress, and the effects of three-dimensional stress state and unloading velocity on rock burst mechanism was studied. Zhai et al. (2020) researched on rock burst process by using high-speed camera, acoustic emission system, and scanning electron microscope. Existing studies provide a lot of research basis for revealing rock burst mechanisms.

Rock burst is a dynamic failure phenomenon driven by energy. Studying the energy evolution law in the process of rock burst is more helpful to reveal the essential characteristics of rock burst (Wang et al., 2012). However, limited to the laboratory test conditions, the energy evolution process is less studied in the true triaxial unloading test, and more attention is paid to the study of disaster-causing stress conditions, acoustic emission characteristics, rock block fractal dimension, and ejection velocity, et al. Compared with laboratory tests, numerical simulation is an effective method to study rock burst energy (Sun et al., 2007). Therefore, this studytakes the granite which is commonly used in rock burst tests as the research object. Based on the micronumerical model of the granite, the energy evolution law and rock block ejection failure characteristics of granite during unloading were researched. The influences of unloading velocity and stress level on rock burst were studied.

MICROSIMULATION UNLOADING TEST OF GRANITE

Microstructure Characterization of Granite

Rock is a typical heterogeneous material, and its heterogeneity mainly includes two aspects. One is the heterogeneity of microparameters, and the other is the heterogeneity of minerals distribution. The weibull function is often used to characterize the heterogeneity of microparameters for rock materials with relatively homogeneous mineral structures, such as the sandstone. For the granite, its minerals distribution is very obvious, and the color difference between different minerals is also relatively large. Therefore, the microscopic structure is often extracted and characterized according to the color difference of rock minerals to establish the heterogeneous model for the granite (Chen et al., 2003; Chen et al., 2004; Zhu et al., 2008; Tan et al., 2016; Meng et al., 2018). The digital image processing technology is an effective method to obtain the microstructure of the rock. Its basic principle is to re-segment the digital image of rock into some groups according to the color of different minerals. The granite used in this simulation test (as shown in **Figure 1A**) is composed of black mica, transparent quartz (appearing gray), and white feldspar. The key to the characterization of the microstructure is to obtain the color segmentation thresholds among the three minerals. In this paper, the Otsu multi-thresholds segmentation method is used to obtain the segmentation thresholds of granite microstructures. The thresholds (t_1, t_2) that satisfy the maximum gray variance S^2 among the minerals are taken as the optimal segmentation thresholds, and the formula is:

$$S^2(t_1, t_2) = \text{argmax} \sum N_i (u_i - u)^2, \tag{1}$$

where u is the whole gray value of the granite image, N_i and u_i are the number and average gray value of pixels of the three different minerals, respectively.

The microstructure characterization image of the granite with a size of 100 × 100 mm obtained by the Otsu multi-thresholds segmentation method was shown in **Figure 1B**. The distribution and shapes of the three minerals in the characterization image are highly consistent with the real granite image.

Building of Microstructure Numerical Model

There are many numerical methods to simulate rocks' mechanical properties and behavior. The finite element method (FEM) and fast Lagrangian analysis of continue (FLAC) are continuum analysis methods. They can simulate

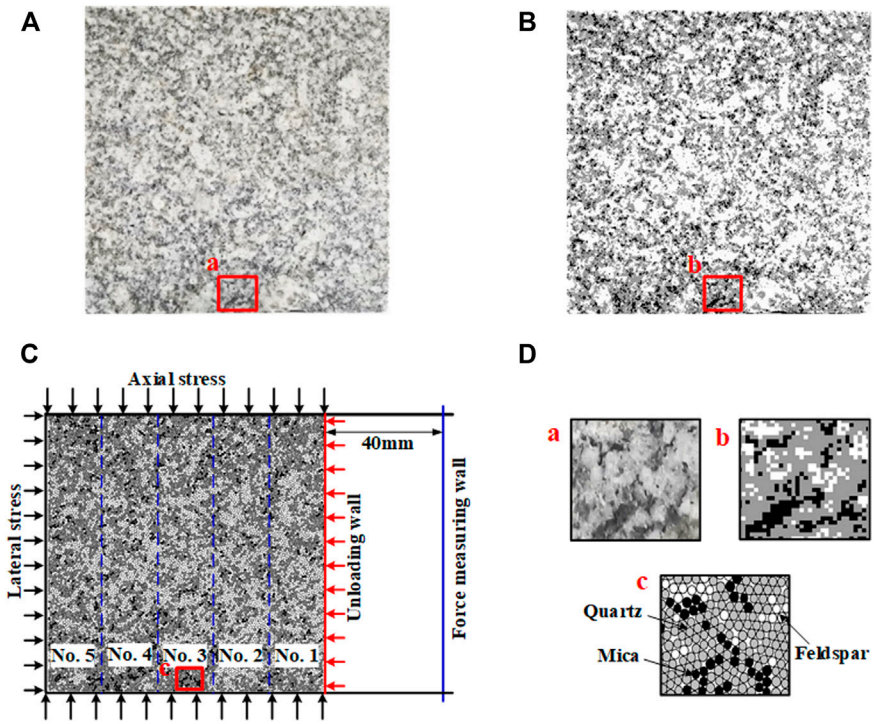


FIGURE 1 | Image of the granite. **(A)** True digital image; **(B)** characterization image; **(C)** layout of model grouping and ejection force monitoring; **(D)** local image comparison.

the yield, plastic flow, softening, and large deformation of materials, especially in the field of elastic-plastic analysis, large deformation analysis, and simulation of the construction process. Peridynamics (PD) (Wang et al., 2016; Wang et al. 2017; Wang et al., 2018), field enriched finite element method (Zhou et al., 2021), and general particle dynamics (GPD) (Zhou et al., 2015; Bi et al., 2016) can simulate the initiation, propagation, and coalescence of microcracks as well as formation of macro-scale cracks. Particle flow code (PFC) (Potyondy and Cundall, 2014) is one discrete element method, and it can simulate rock macro mechanical behavior by analyzing the movement and interaction of particles. It is not limited by the amount of deformation and is convenient to deal with the problem of the discontinuous medium. These numerical methods above are very helpful for studying rock fractures.

In this simulation, not only the energy evolution law in the process of rock fracture was studied, but also the rock block ejection characteristics after rock burst. Compared with other numerical methods, PFC can intuitively obtain the rock block motion behavior of rock failure (Yoon, 2007). Therefore, this paper used PFC^{2D} to build the microstructure model of granite and study the mechanical behavior during unloading. In the modeling process, firstly one granite specimen model with a size of 100 × 100 mm was generated by using PFC. In order to reduce the size effect (Zhao et al., 2012), the radius of the particles was set to 0.4–0.5 mm, and the average ratio of specimen size to particle radius was 220. Then, the coordinates and gray information of each pixel in the characterization image were imported into PFC through the FISH function. According to the gray information of pixels, the color codes of particles with the closest coordinates were assigned respectively (Zhang et al., 2019). The microstructure numerical model of the granite specimen as shown in **Figure 1C**. The black particles are mica, the gray particles are quartz, and the white ones are feldspar, as shown in **Figure 1D**. The three mineral particles were assigned with corresponding material parameters respectively, and the parameters of the cementation surface between minerals were set according to the parameters of low strength minerals. A parallel bond model was chosen to simulate the mechanical properties of rock materials. In the parallel bond model, the microparameters including the friction coefficient μ, contact stiffness k_n and k_s, parallel bonded stiffness $\bar{k}^n$ and $\bar{k}^s$, parallel bonded strength σ_n and σ_s, and parallel bonded radius λ. Based on the work by Potyondy and Cundall. (2004), the microparameters can be determined by the following formulas:

$$k_n = 2E_c, \tag{2}$$

$$\bar{k}_n = \frac{\bar{E}_c}{2\bar{r}}, \tag{3}$$

where E_c and $\bar{E}_c$ are Young's modulus of the particles and bond respectively; $\bar{r}$ is average radius of two contact particles. In general, k_n/k_s and $\bar{k}_n/\bar{k}_s$ can be set to 2.5, λ is 1, μ is 0.5. E_c and $\bar{E}_c$ are proportional to the macro Young's modulus of the rock. σ_n and σ_s are proportional to the macro strength.

TABLE 1 | Microstructure model parameters of granite minerals (Zhang et al., 2019).

Mineral	ρ/Kg·m^{-3}	k_n/GPa	k_s/GPa	$\bar{k}^n$/GPa	$\bar{k}^s$/GPa	σ_n/MPa	σ_s/MPa	λ
Mica	2,800	20	8	40	16	115	115	1
Feldspar	2,700	28	11.2	56	22.4	130	130	1
Quartz	2,650	36	14.4	72	28.8	175	175	1

TABLE 2 | Unloading simulation schemes of the granite.

No.	Unloading Velocity, v_o/Mm/s	Lateral Stress, σ_3/MPa	Axial Stress, σ_1/MPa
1	0.05、0.1、0.2、0.5	30	160
2	0.1	10、20、30、40	160
3	0.1	30	160、170、180、190、200

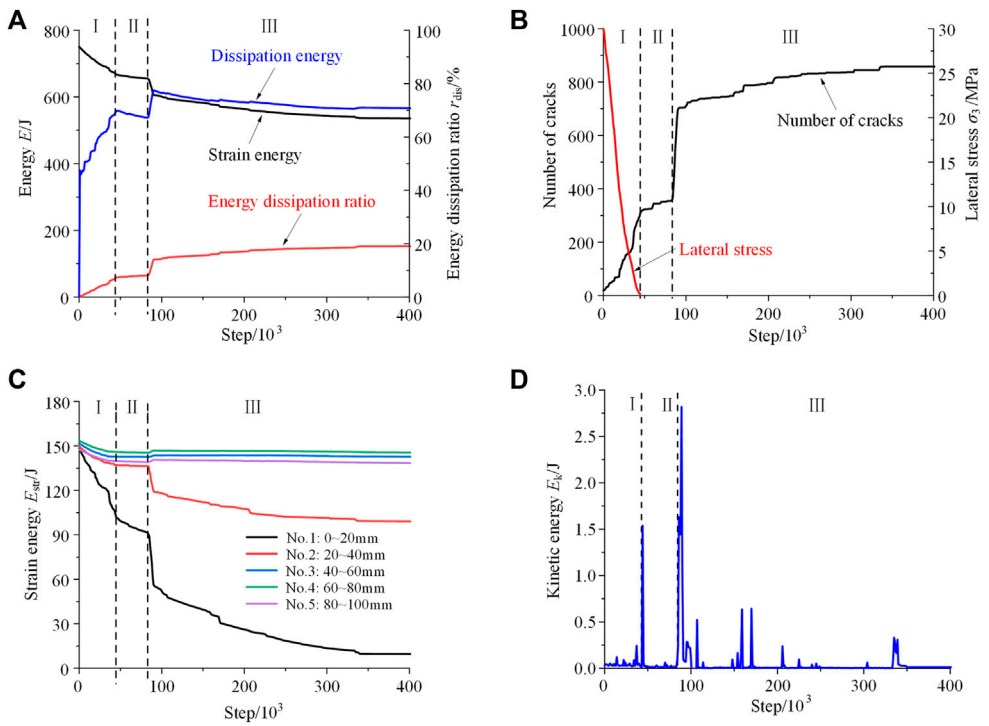


FIGURE 2 | Energy release process of unloading granite. **(A)** Energy of the whole specimen; **(B)** crack and lateral stress; **(C)** energy released in different groups; **(D)** kinetic energy.

Using **Eqs 2**, **3**, the microparameters of the model can be estimated, but there are often some errors. Therefore, a trial-and-error method should be used to calibrate the suitable microscopic parameters (Peng et al., 2018). In the paper, the microstructure model parameters of the granite were selected from Zhang et al. (2019), as shown in **Table 1**.

Simulation Scheme

In thisarticle, numerical simulation test was carried out based on true triaxial loading and single-side unloading laboratory test of granite. In the loading stage, the axial stress and lateral stress were applied to the granite specimen by the loading wall. When the stress was loading to the predetermined value, the displacement of the upper and the left wall was fixed, avoiding unreasonable loading displacement of the wall under stress constraint, which is different from the laboratory test. In the unloading stage, the right wall was applied with a certain velocity to unload the lateral stress. The simulation variables are unloading velocity, lateral stress, and axial stress, respectively. The specific schemes were shown in **Table 2**.

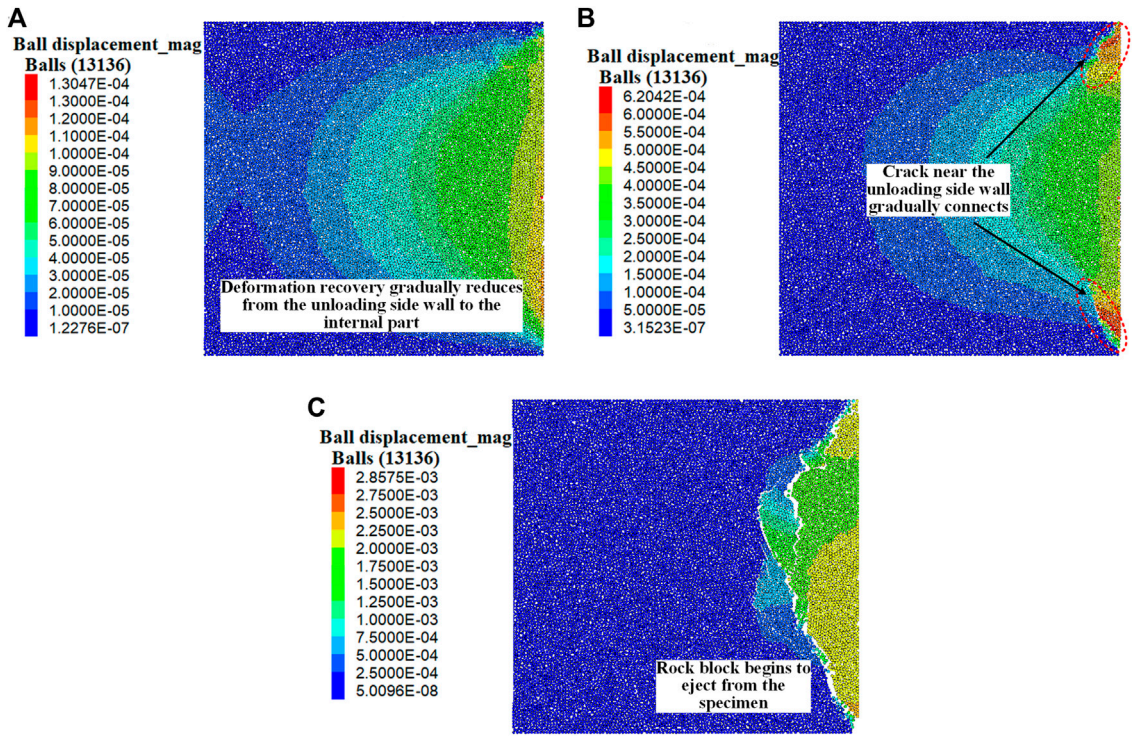


FIGURE 3 | Displacement field of the specimen at step. **(A)** 1e4; **(B)** 6e4; **(C)** 2e5.

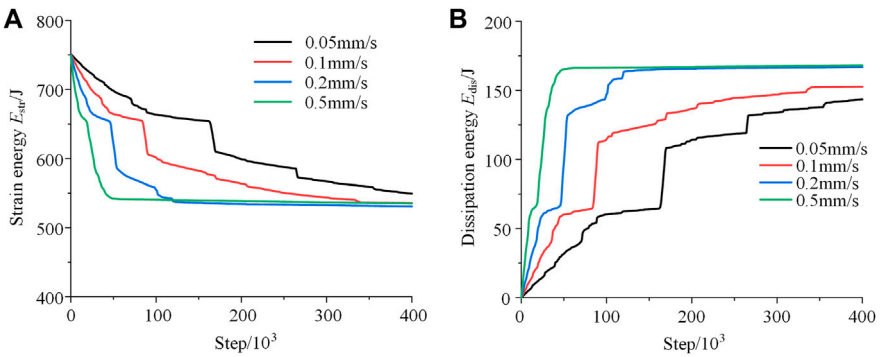


FIGURE 4 | (A) Energy release and **(B)** energy dissipation process of granite under different unloading velocities.

Energy Calculation and Monitoring Schemes

In PFC^{2D}, the work done by the external load on the granite specimen is the input energy, which can be calculated by the load and displacement of the loading wall, as follows:

$$E_{tot} = \sum F_{\varepsilon} \Delta U_{\varepsilon}, \tag{4}$$

where E_{tot} is the input energy, F_{ε} is the load of the loading wall, and ΔU_{ε} is the displacement increment of the loading wall.

The input energy of granite under external load is divided into two parts, namely, strain energy and dissipation energy. The strain energy includes two parts, one is the contact strain energy between particles, and the other is the parallel bond strain energy. The calculation formula of strain energy is as follows:

$$E_{str} = E_{str}^{c} + E_{str}^{pb}, \tag{5}$$

where

$$E_{str}^{pb} = \frac{1}{2} \sum_{i \in N_{pb}} \left(\frac{\left|\bar{F}_i^n\right|^2}{A_i \bar{k}_i^n} + \frac{\left|\bar{F}_i^s\right|^2}{A_i \bar{k}_i^s} + \frac{\left|\bar{M}_i\right|^2}{I_i \bar{k}_i^n} \right), \tag{6}$$

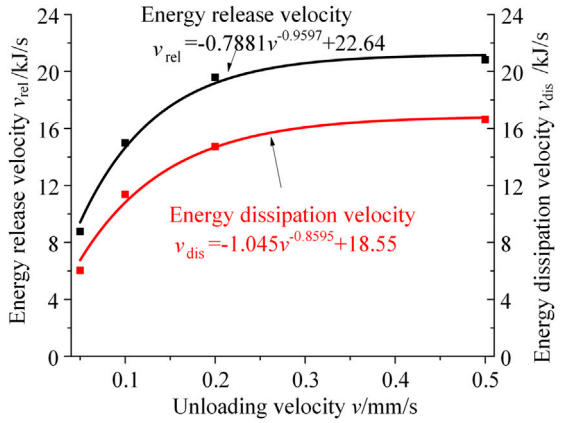


FIGURE 5 | Relationship between unloading velocity, energy release velocity, and energy dissipation velocity.

$$E_{str}^{c} = \frac{1}{2}\sum_{i\in N_c}\left(\frac{\left|F_i^n\right|^2}{k_i^n} + \frac{\left|F_i^s\right|^2}{k_i^s}\right), \tag{7}$$

where E_{str} is the strain energy, E_{str}^{c} and E_{str}^{pb} are the contact strain energy and the parallel bond strain energy, respectively. F_i^n and F_i^s are the normal force and tangential force at the contact point i of particles, respectively. $\bar{F}_i^n$、 $\bar{F}_i^s$、 $\bar{M}_i$ is the normal force, tangential force, and bending moment respectively at the i parallel bond. A_i is the parallel bond interface area, and I_i is the moment of inertia. N_c and N_{pb} are the number of particle contact and the number of parallel bonds, respectively.

The calculation formula of dissipation energy E_{dis} is:

$$E_{dis} = E_{tot} - E_{str}. \tag{8}$$

In the simulation process, in addition to monitoring the energy and crack of the model, the model was divided into five groups, and the energy data in different groups of the model were monitored too. Each group was 20 mm wide, and group No.1 was close to the unloading wall, as shown in **Figure 1C**.

The rock burst area and rock block ejection force are also important indicators for evaluating the rock burst intensity. A force measuring wall was arranged at 40 mm far away from the unloading wall to monitor the rock block ejection force.

In order to clearly and reasonably describe the process of energy release, the parameters need to be defined as follows:

v_{rel} energy release velocity—equals the ratio of released strain energy to time; vdi_s energy dissipation velocity—equals the ratio of dissipation energy to time

r_{dis} energy dissipation ratio—equals the ratio of dissipation energy to released strain energy;

F rock block ejection force—represents rock block ejection force on the force measuring wall;

A rock burst area—represents the size of the rock burst pit.

ENERGY RELEASE LAW OF UNLOADING GRANITE

Energy Release Process and Stage Division

Taking the test results of the granite with lateral stress of 30MPa, axial stress of 160 MPa, and unloading velocity of 0.1 mm/s as an example, the energy and stress evolution curves after unloading were shown in **Figure 2**. According to the energy release and dissipation law of the whole granite and each group, the energy release process can be divided into three stages: I- whole energy rapid release stage, II- side wall energy slow-release stage, and rock block ejection stage.

1) Step I: whole energy rapid release stage. During the initial unloading stage, with decreasing lateral stress, the lateral deformation of the specimen is beginning to recover, and part of the strain energy accumulated in the specimen is released in the form of elastic energy, as shown in **Figures 2A,B**. The deformation recovery of the specimen gradually reduces from the unloading sidewall to the internal part (**Figure 3A**), and the corresponding released energy is also gradually reduced, as shown in **Figure 2C**. According to the Mohr-Coulomb criterion, when the lateral stress decreases, the ultimate bearing strength of the specimen decreases. During unloading, the crack gradually generates, and part of strain energy is released in the form of dissipation energy.

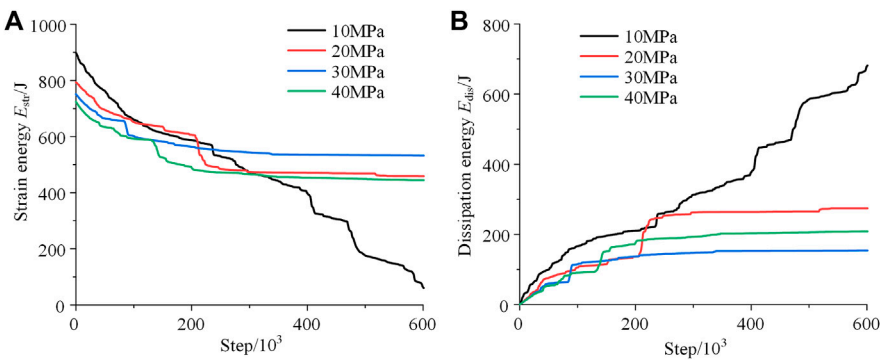


FIGURE 6 | (A) Energy release and **(B)** energy dissipation process of granite under different lateral stress.

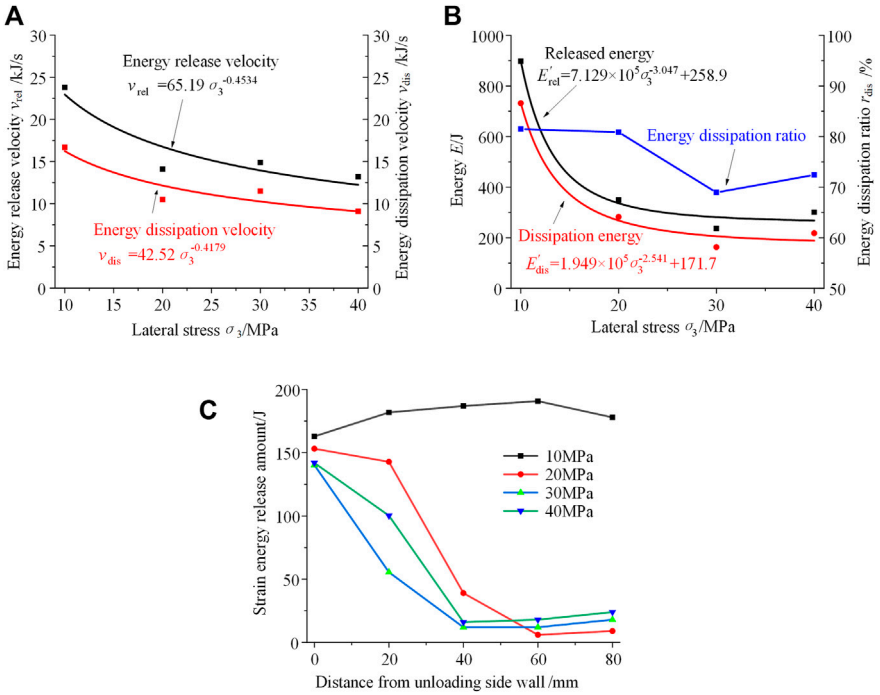


FIGURE 7 | (A) Velocity and **(B)** amount of energy release and energy dissipation, and **(C)** energy released amount in different groups of granite under different lateral stress.

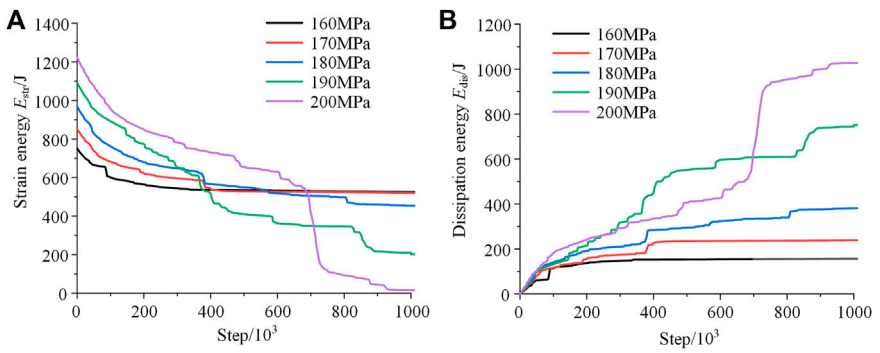


FIGURE 8 | (A) Energy release and **(B)** energy dissipation process of granite under different axial stress.

With increasing crack number, the energy dissipation ratio increases gradually. Because cracks are mainly generated near the unloading sidewall of the granite, the energy release in this region is more obvious.

2) Step II: sidewall energy slow-release stage. After the lateral stress is reduced to zero and the lateral deformation of the specimen is recovered, the crack near the unloading side wall gradually connects, as shown in **Figure 3B**. Only the strain energy near the side wall still keeps releasing, and the energy release velocity is slower than that in Step I. The energy dissipation ratio gradually reduces due to the decrease of crack generating velocity.
3) Step III: rock block ejection stage. After the crack near the side wall coalesced into the fracture zone, the rock block begins to eject from the specimen, and part of the strain energy is released in the form of kinetic energy, as shown in **Figure 2D** and **Figure 3C**. After the ejection of large size blocks, the bearing capacity of the specimen decreases sharply, and the fracture zone expands rapidly. A large number of small size blocks generate and eject in a short time. After rock blocks eject, there appears a triangular rock burst pit, which is similar to the engineering field example in Li (2020). The size of the rock burst pit equals the rock burst area.

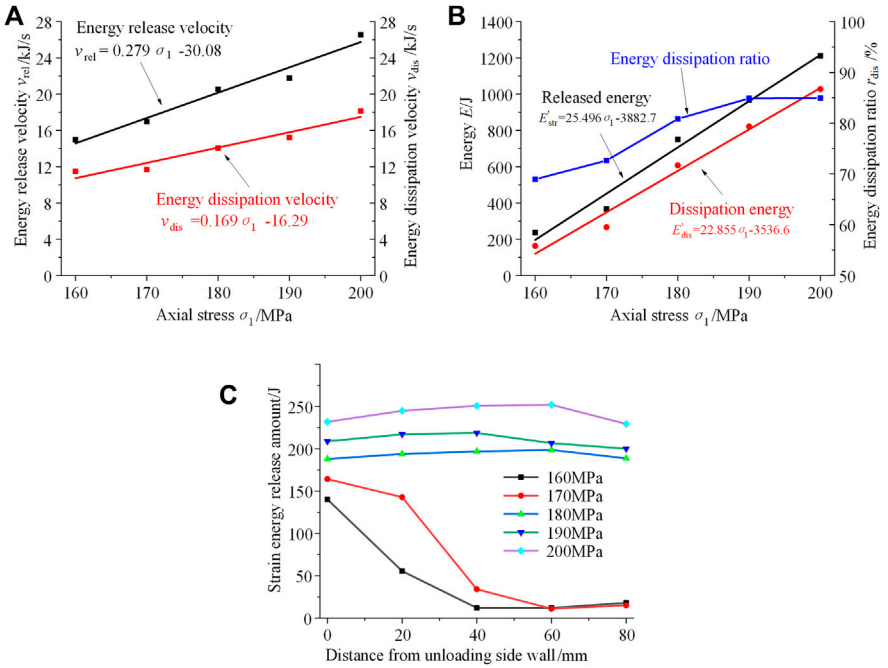


FIGURE 9 | (A) Velocity and **(B)** amount of energy release and energy dissipation, and **(C)** energy released amount in different groups of granite under different axial stress.

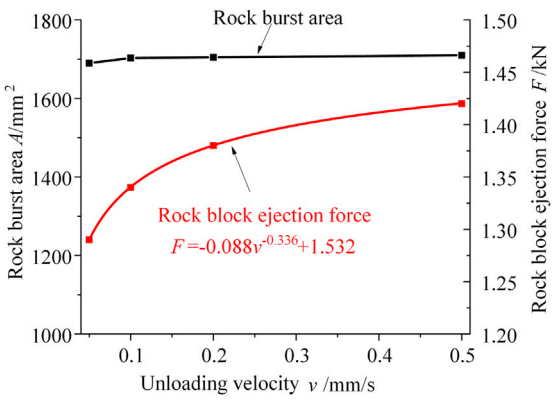


FIGURE 10 | Relationship among the rock burst area, rock block ejection force, and unloading velocity.

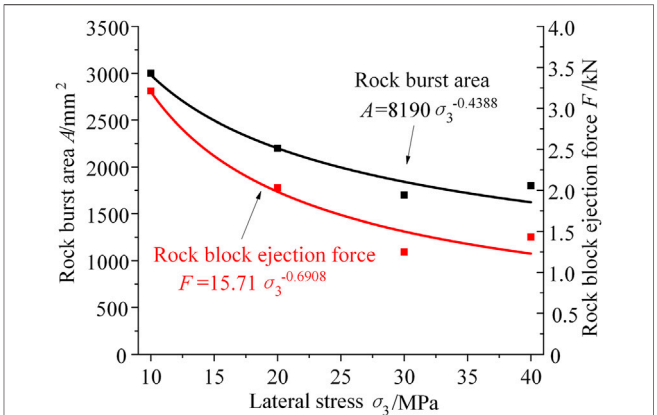


FIGURE 11 | Relationship among the rock burst area, rock block ejection force, and lateral stress.

Influence of Unloading Velocity on Energy Release

With the same lateral stress and axial stress, the energy evolution curves of granite under different unloading velocities were shown in **Figure 4**. With increasing unloading velocity, the duration time of energy release is significantly shortened, while the total energy release amount changes little. The farther away from the sidewall, the smaller the strain energy released. Both the energy dissipation ratio and total amount increase with increasing unloading velocity. In the whole energy rapid release stage, the strain energy release velocity and dissipation velocity increase with the unloading velocity in a power function relationship, as shown in **Figure 5**.

Influence of Lateral Stress on Energy Release

The energy evolution curves of granite under different lateral stress were shown in **Figure 6**. Under the same axial stress, with increasing lateral stress, the accumulated strain energy in granite before unloading decreases. This is because when the axial stress does positive work on the specimen, the lateral stress does negative work. The greater the lateral stress is, the greater the

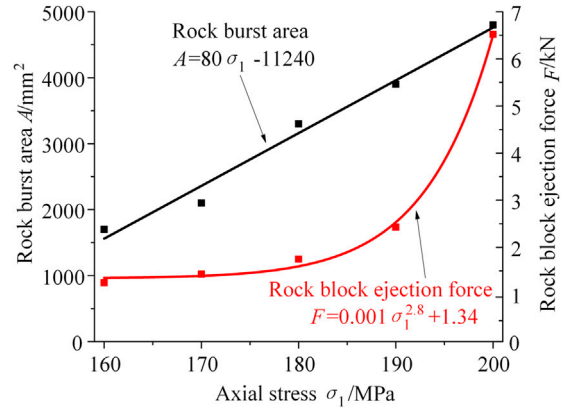


FIGURE 12 | Relationship among the rock burst area, rock block ejection force, and axial stress.

negative work is done, which causes smaller accumulated strain energy. The result is consistent with that of Huang and Li (2014).

When the lateral stress is 10 MPa, the energy is continuous released at a high velocity, and the specimen fractures whole in a short time after unloading. When the lateral stress exceeds 20 MPa, the three-stage characteristics of energy release of granite are relatively obvious. With the increase of lateral stress, the total amount and velocity of energy release and energy dissipation decrease gradually, which all show a power function relationship with lateral stress, as shown in **Figures 7A,B**. Also, the main area of energy release gradually decreases when the lateral stress increases. When the lateral stress is 30 MPa or 40 MPa, the energy release body is only within the area of 40 mm from the side wall, as shown in **Figure 7C**.

Influence of Axial Stress on Energy Release

The energy evolution curves of granite under different axial stress were shown in **Figure 8**. With the increase of axial stress, the total energy accumulated in the granite increases gradually before unloading and the duration of energy release after unloading increases too. The energy release velocity and dissipation velocity are linearly correlated with the axial stress, as shown in **Figure 9A**. After rock burst, the total amount of energy release and energy dissipation, and the energy dissipation ratio increase with the increase of axial stress, as shown in **Figure 9B**. Under low axial stress, such as 160 and 170 MPa, the main energy release area locates at the 40 mm range from the side wall. When the axial stress exceeds 180 MPa, the whole body is the main energy release area, as shown in **Figure 9C**.

ROCK BLOCK EJECTION CHARACTERISTICS

Influence of Unloading Velocity

The unloading velocity has little effect on the rock burst area. However, due to the rapid release of energy at high unloading velocity, more energy is released in the form of kinetic energy, and the rock block ejection force is significantly increased, which shows one power function relationship with the unloading velocity, as shown in **Figure 10**.

Influence of Lateral Stress

Rock burst forms and rock block ejection force of the granites under different lateral stress were shown in **Figure 11**. When the lateral stress is 10 MPa, the rock burst area is about 3,000 mm^2, and the rock block ejection force is about 3.21 kN. With increasing lateral stress, rock burst area, and rock block ejection force decrease, which shows one exponential function with lateral stress. When the lateral stress is 40 MPa, rock burst area reduces to 60%, and the rock block ejection force decreases to 44.6%, compared to that at 10 MPa.

Influence of Axial Stress

Rock burst forms and rock block ejection force of the granites under different axial stress were shown in **Figure 12**. When the axial stress is 160 MPa, rock burst area is about 1700 mm^2, and the rock block ejection force is about 1.25 kN. When the axial stress is 200 MPa, rock burst area extends to 2.82 times, and rock block ejection force increases to 5.2 times, compared to that at 160 MPa. The rock burst area has one linear relation with axial stress, and the rock block ejection force has one power function relation with axial stress.

CONCLUSION

1) Unloading process of the granite can be divided into three stages: I- whole energy rapid release stage, II- side wall energy slow-release stage, and III- rock block ejection stage. The release and dissipation of strain energy decrease with the increase of distance from side wall, and the main energy-releasing body and ejection body are near the side wall.
2) The unloading velocity mainly affects the duration of the three stages of energy release, the energy release velocity and the dissipation velocity. It has little effect on the total amount of strain energy released and rock burst area. The strain energy release velocity and the energy dissipation velocity are positively correlated with the unloading velocity by one power function, and the rock block ejection force is also positively correlated with the unloading velocity by one power function.
3) Under the same axial stress, with the increase of lateral stress, the released energy amount, dissipation energy amount, and the energy dissipation ratio of unloading granite gradually decrease. Moreover, the strain energy release velocity and the energy dissipation velocity are negatively correlated with lateral stress in a power function, and the rock block ejection force and rock burst area are also negatively correlated with lateral stress in a power function.
4) Under the same lateral stress, with the increase of axial stress, the released energy amount, dissipation energy

amount, and the energy dissipation ratio of unloading granite gradually increase. Moreover, the strain energy release velocity and the energy dissipation velocity are positively correlated with the axial stress in a linear function. The rock burst area has one linear relation with axial stress, and the rock block ejection force has one power function relation with axial stress.

DATA AVAILABILITY STATEMENT

The original contributions presented in the study are included in the article/Supplementary Material; further inquiries can be directed to the corresponding author.

AUTHOR CONTRIBUTIONS

X-YW carried out numerical simulation tests. Y-CY wrote the manuscript. M-LX analyzed the simulation results. D-DZ proposed research ideas. YC and E-CW designed the simulation test schemes.

FUNDING

The study was financially supported by the Major Scientific and Technological Innovation Project of Shandong Provincial Key Research Development Program (2019SDZY02), National Natural Science Foundation of China (52074167), and China Postdoctoral Science Foundation-funded project (2019M660024).

REFERENCES

Bi, J., Zhou, X. P., and Qian, Q. H. (2016). The 3D Numerical Simulation for the Propagation Process of Multiple Pre-existing Flaws in Rock-like Materials Subjected to Biaxial Compressive Loads. *Rock Mech. Rock Eng.* 49 (5), 1611–1627. doi:10.1007/s00603-015-0867-y

Chen, S., Yue, Z. Q., and Tham, L. G. (2004). Digital Image-Based Numerical Modeling Method for Prediction of Inhomogeneous Rock Failure. *Int. J. Rock Mech. Min. Sci.* 41 (6), 939–957. doi:10.1016/j.ijrmms.2004.03.002

Chen, S., Yue, Z. Q., Tham, L. G., and Lee, P. K. K. (2003). Modeling of the Indirect Tensile Test for Inhomogeneous Granite Using a Digital Image-Based Numerical Method. *Int. J. Rock Mech. Min. Sci.* 41 (3), 447. doi:10.1016/j.ijrmms.2003.12.106

Feng, X., Chen, B., Li, S., Zhang, C., Xiao, Y., Feng, G., et al. (2012). Studies on the Evolution Process of Rockbursts in Deep Tunnels. *J. Rock Mech. Geotechnical Eng.* 4 (4), 289–295. doi:10.3724/sp.j.1235.2012.00289

Guo, W., Gu, Q., Tan, Y., and Hu, S. (2019). Case Studies of Rock Bursts in Tectonic Areas with Facies Change. *Energies* 12 (7), 1330. doi:10.3390/en12071330

He, M. C., Miao, J. L., and Feng, J. L. (2009). Rock Burst Process of Limestone and its Acoustic Emission Characteristics under True-Triaxial Unloading Conditions. *Int. J. Rock Mech. Min. Sci.* 47 (2), 286–298. doi:10.1016/j.ijrmms.2009.09.003

He, M., Ren, F., and Liu, D. (2018). Rockburst Mechanism Research and its Control. *Int. J. Min. Sci. Technol.* 28 (5), 829–837. doi:10.1016/j.ijmst.2018.09.002

He, M., Xia, H., Jia, X., Gong, W., Zhao, F., and Liang, K. (2012). Studies on Classification, Criteria and Control of Rockbursts. *J. Rock Mech. Geotechnical Eng.* 4 (2), 97–114. doi:10.3724/sp.j.1235.2012.00097

Huang, D., and Li, Y. (2014). Conversion of Strain Energy in Triaxial Unloading Tests on Marble. *Int. J. Rock Mech. Min. Sci.* 66, 160–168. doi:10.1016/j.ijrmms.2013.12.001

Jiang, Q., Feng, X.-T., Xiang, T.-B., and Su, G.-S. (2010). Rockburst Characteristics and Numerical Simulation Based on a New Energy Index: a Case Study of a Tunnel at 2,500 M Depth. *Bull. Eng. Geol. Environ.* 69 (3), 381–388. doi:10.1007/s10064-010-0275-1

Li, C. L. (2020). Principles and Methods of Rock Support for Rockburst Control. *J. Rock Mech. Geotechnical Eng.* 13 (01), 46–59. doi:10.1016/J.JRMGE.2020.11.001

Li, D., Zhao, F., and Zheng, M. (2014a). Fractal Characteristics of Cracks and Fragments Generated in Unloading Rockburst Tests. *Int. J. Min. Sci. Technol.* 24 (6), 819–823. doi:10.1016/j.ijmst.2014.10.014

Li, X., Cao, W., Zhou, Z., and Zou, Y. (2014b). Influence of Stress Path on Excavation Unloading Response. *Tunn. Undergr. Space Technol.* 42, 237–246. doi:10.1016/j.tust.2014.03.002

Li, Z.-H., Dou, L. M., Lu, C.P., Mu, Z. L., and Cao, A. Y. (2008). Study on Fault Induced Rock Bursts. *J. China Univ. Min. Technol.* 18 (3), 321–326. doi:10.1016/s1006-1266(08)60068-1

Meng, Q. X., Wang, H. L., Xu, W. Y., and Cai, M. (2018). A Numerical Homogenization Study of the Elastic Property of a Soil-Rock Mixture Using Random Mesostructure Generation. *Comput. Geotechnics* 98, 48–57. doi:10.1016/j.compgeo.2018.01.015

Peng, J., Wong, L. N. Y., Teh, C. I., and Li, Z. (2018). Modeling Micro-cracking Behavior of Bukit Timah Granite Using Grain-Based Model. *Rock Mech. Rock Eng.* 51 (1), 135–154. doi:10.1007/s00603-017-1316-x

Potyondy, D. O., and Cundall, P. A. (2004). A Bonded-Particle Model for Rock. *Int. J. Rock Mech. Min. Sci.* 41 (8), 1329–1364. doi:10.1016/j.ijrmms.2004.09.011

Si, X., and Gong, F. (2020). Strength-weakening Effect and Shear-Tension Failure Mode Transformation Mechanism of Rockburst for Fine-Grained Granite under Triaxial Unloading Compression. *Int. J. Rock Mech. Min. Sci.* 131, 104347. doi:10.1016/j.ijrmms.2020.104347

Sun, J. S., Zhu, Q. H., and Lu, W. B. (2007). Numerical Simulation of Rock Burst in Circular Tunnels under Unloading Conditions. *J. China Univ. Min. Technol.* 17 (4), 552–556. doi:10.1016/s1006-1266(07)60144-8

Tan, X., Konietzky, H., and Chen, W. (2016). Numerical Simulation of Heterogeneous Rock Using Discrete Element Model Based on Digital Image Processing. *Rock Mech. Rock Eng.* 49 (12), 4957–4964. doi:10.1007/s00603-016-1030-0

Wang, L., Lu, Z., and Gao, Q. (2012). A Numerical Study of Rock Burst Development and Strain Energy Release. *Int. J. Min. Sci. Technol.* 22 (5), 675–680. doi:10.1016/j.ijmst.2012.08.014

Wang, Y., Zhou, X., and Shou, Y. (2017). The Modeling of Crack Propagation and Coalescence in Rocks under Uniaxial Compression Using the Novel Conjugated Bond-Based Peridynamics. *Int. J. Mech. Sci.* 128-129, 614–643. doi:10.1016/j.ijmecsci.2017.05.019

Wang, Y., Zhou, X., Wang, Y., and Shou, Y. (2018). A 3-D Conjugated Bond-Pair-Based Peridynamic Formulation for Initiation and Propagation of Cracks in Brittle Solids. *Int. J. Solids Struct.* 134, 89–115. doi:10.1016/j.ijsolstr.2017.10.022

Wang, Y., Zhou, X., and Xu, X. (2016). Numerical Simulation of Propagation and Coalescence of Flaws in Rock Materials under Compressive Loads Using the Extended Non-ordinary State-Based Peridynamics. *Eng. Fract. Mech.* 163, 248–273. doi:10.1016/j.engfracmech.2016.06.013

Wu, F., Liu, T., Liu, J., and Tang, X. (2009). Excavation Unloading Destruction Phenomena in Rock Dam Foundations. *Bull. Eng. Geol. Environ.* 68 (2), 257–262. doi:10.1007/s10064-009-0202-5

Xiao, Y.-X., Feng, X.-T., Feng, G.-L., Liu, H.-J., Jiang, Q., and Qiu, S.-L. (2016). Mechanism of Evolution of Stress-Structure Controlled Collapse of Surrounding Rock in Caverns: A Case Study from the Baihetan Hydropower Station in China. *Tunn. Undergr. space Technol.* 51, 56–67. doi:10.1016/j.tust.2015.10.020

Yin, Y. C., Zhao, T. B., Zhang, Y. B., Tan, Y. L., Qiu, Y., Taheri, A., et al. (2019). An Innovative Method for Placement of Gangue Backfilling Material in Steep Underground Coal Mines. *Minerals* 9 (2), 107. doi:10.3390/min9020107

Yoon, J. (2007). Application of Experimental Design and Optimization to PFC Model Calibration in Uniaxial Compression Simulation. *Int. J. Rock Mech. Min. Sci.* 44 (6), 871–889. doi:10.1016/j.ijrmms.2007.01.004

Zhai, S., Su, G., Yin, S., Zhao, B., and Yan, L. (2020). Rockburst Characteristics of Several Hard Brittle Rocks: A True Triaxial Experimental Study. *J. Rock Mech. Geotechnical Eng.* 12 (2), 279–296. doi:10.1016/j.jrmge.2019.07.013

Zhang, Y., Zhao, T., Yin, Y., Tan, Y., and Qiu, Y. (2019). Numerical Research on Energy Evolution in Granite under Different Confining Pressures Using Otsu's Digital Image Processing and PFC2D. *Symmetry* 11 (2), 131. doi:10.3390/sym11020131

Zhao, G. Y., Dai, B., and Ma, C. (2012). Study of Effect of Microparameters on Macroproperties for Parallel Bonded Model. *Chin. J. Rock Mech. Eng.* 31 (7), 1491–1498. doi:10.1007/s11783-011-0280-z

Zhao, T. B., Guo, W. Y., Tan, Y. L., Yin, Y. C., Cai, L. S., and Pan, J. F. (2018). Case Studies of Rock Bursts under Complicated Geological Conditions during Multi-Seam Mining at a Depth of 800 M. *Rock Mech. Rock Eng.* 51 (5), 1539–1564. doi:10.1007/s00603-018-1411-7

Zhao, T., Yin, Y., Tan, Y., and Song, Y. (2015). Deformation Tests and Failure Process Analysis of an Anchorage Structure. *Int. J. Min. Sci. Technol.* 25 (2), 237–242. doi:10.1016/j.ijmst.2015.02.012

Zhou, X., Jia, Z., and Wang, L. (2021). A Field-Enriched Finite Element Method for Brittle Fracture in Rocks Subjected to Mixed Mode Loading. *Eng. Analysis Bound. Elem.* 129, 105–124. doi:10.1016/j.enganabound.2021.04.023

Zhou, X. P., Bi, J., and Qian, Q. H. (2015). Numerical Simulation of Crack Growth and Coalescence in Rock-like Materials Containing Multiple Pre-existing Flaws. *Rock Mech. Rock Eng.* 48 (3), 1097–1114. doi:10.1007/s00603-014-0627-4

Zhu, Z. D., Ni, X. H., Wang, W., Li, S. B., Zhao, J., and Wu, Y. Q. (2008). Dynamic Experimental Study on Rock Meso-Cracks Growth by Digital Image Processing Technique. *J. Central South Univ. Technol.* 15 (2), 114–120. doi:10.1007/s11771-008-0445-5

Conflict of Interest: D-DZ and YC were employed by Shandong Energy Group Co., Ltd.

The remaining authors declare that the research was conducted in the absence of any commercial or financial relationships that could be construed as a potential conflict of interest.

Publisher's Note: All claims expressed in this article are solely those of the authors and do not necessarily represent those of their affiliated organizations, or those of the publisher, the editors, and the reviewers. Any product that may be evaluated in this article, or claim that may be made by its manufacturer, is not guaranteed or endorsed by the publisher.

Copyright © 2022 Wang, Yin, Xing, Zhang, Chen and Wang. This is an open-access article distributed under the terms of the Creative Commons Attribution License (CC BY). The use, distribution or reproduction in other forums is permitted, provided the original author(s) and the copyright owner(s) are credited and that the original publication in this journal is cited, in accordance with accepted academic practice. No use, distribution or reproduction is permitted which does not comply with these terms.

frontiers | Frontiers in Earth Science

ORIGINAL RESEARCH
published: 01 July 2022
doi: 10.3389/feart.2022.909102

Experimental Analysis on Mechanical Characteristics of Foundation Soil in Rift Valley Area of Kenya Nairobi-Malaba Railway

Bing Hao[1], *Zhenghua Zhou*[1], *Yuandong Li*[1], *Xiaojun Li*[2]* and *Liguo Jin*[3]

[1]College of Transportation Engineering, Nanjing Tech University, Nanjing, China, [2]Key Laboratory of Urban Security and Disaster Engineering of China Ministry of Education, Beijing University of Technology, Beijing, China, [3]Institute of Geophysics, China Earthquake Administration, Beijing, China

The Rift Valley section of Kenya Nairobi-Malaba Railway locates in the Great Rift Valley of East Africa, with complex engineering geological conditions and well-developed geological structures. During the rainy season from March to May 2018, four large-scale ground fissures were formed in the first-stage project of the Nairobi-Malaba Railway of the valley floor section, accompanied by uneven surface settlement and trenches, seriously endangering the safety of the railway and its nearby projects. Through field investigation, it is preliminarily considered that the main reason induced ground fissures and surface settlement is the underlying soil layer being eroded by groundwater. The gully is further formed by surface water erosion on a base of uneven surface subsidence. The geological exploration trench at DK77 ground fissure revealed that the overlying soil layer is respectively grayish-yellow silty clay, cyan-gray volcanic ash, and brownish-yellow silty clay from top to bottom, and the underlying bedrock is volcanic tuff with wide cracks. The fluid flows out or into the bedrock through the cracks developing channels for groundwater up-down flowage. Under the erosion of groundwater to the underlying soil, this study proved the possibility of the occurrence of uneven settlement. When exposed to the groundwater, the underlying soil will exhibit special physical and mechanical properties which are conducive to the occurrence of ground cracks and subsidence. The conventional geotechnical tests are conducted for the three types of overlying soil, and the results reveal the causes of ground fissures and surface settlement from the physical and mechanical properties of the overlying soil and provide a basis for the further qualitative analysis of the mechanism of ground fissures and surface settlement.

Keywords: ground fissure, uneven settlement, collapsibility, subsurface erosion, clay content

OPEN ACCESS

Edited by:
Guang-Liang Feng,
Institute of Rock and Soil Mechanics (CAS), China

Reviewed by:
Liyuan Tong,
Southeast University, China
Wenjun Zheng,
Sun Yat-sen University, China
Meigen Zhang,
Institute of Geology and Geophysics (CAS), China

***Correspondence:**
Xiaojun Li
lixiaojun@bjut.edu.cn

Specialty section:
This article was submitted to Geohazards and Georisks, a section of the journal Frontiers in Earth Science

Received: *31 March 2022*
Accepted: *23 May 2022*
Published: *01 July 2022*

Citation:
Hao B, Zhou Z, Li Y, Li X and Jin L (2022) Experimental Analysis on Mechanical Characteristics of Foundation Soil in Rift Valley Area of Kenya Nairobi-Malaba Railway. Front. Earth Sci. 10:909102. doi: 10.3389/feart.2022.909102

1 INTRODUCTION

During the rainy season from March to May 2018, four large-scale ground fissures were generated in the East African Rift Valley section of the first phase of the Nairobi-Malaba Railway Project, accompanied by multiple uneven surface settlements, which seriously endangered the safety of the railway and its nearby projects. Considering that the safety of the Nairobi-Malaba Railway is related to the sustainability of the national, it is of great significance to deeply study these ground fissures to ensure the safe construction and operation of the Nairobi-Malaba Railway.

Ground fissure with a certain length and width on the ground is a macroscopic geological destruction phenomenon in which surface rock and soil crack under the action of natural or human factors (Youssef, 2013). As a geological disaster, ground fissures have caused serious harm to the natural environment and human engineering activities. Since Leonard (1929) devoted himself to the study the ground fissures in 1929 at first, subsequently a few scholars have studied the ground fissures, mainly focusing on the genetic mechanism, regularity of spatial distribution, and activity characteristics of ground fissures. The genetic mechanism involves geological tectonic activities (Ayalew, et al., 2004; Sarkar, 2004; Conway, 2015; Xu et al., 2016), underground mining (Budhu, 2011; Gabrielli et al., 2011; Youssef et al., 2014; Jin et al., 2016; Feng, et al., 2022), underground erosion of loess (Liu et al., 2015; Peng et al., 2020; Leng et al., 2021), and other factors (Fergason et al., 2015; Elahe et al., 2020; Jia et al., 2020). The regularity of spatial distribution shows that the overall trend of the ground fissures is approximately the same as that of the regional fault structures (Wang et al., 2020). The ground fissures with a large width in the ancient river course site, the artificial backfill soil site, and the low-lying and underwater mining settlement site have many branches (Nina et al., 2019). The activity characteristics show three-dimensional movement characteristics, that vertical movement, horizontal movement, and the movement rate of vertical movement are the largest while that of horizontal movement is relatively small (Timothy et al., 2016; Howard and Zhou, 2019; Liu et al., 2019). In recent years, with the massive construction of various infrastructure facilities under complex site conditions, the impact of ground fissures on the project has become increasingly prominent.

Among the four ground fissures formed in the Rift Valley area, DK76, DK77, and B3 road fissures are large in scale. Combined with previous studies on ground fissures, B3 road fissures have the characteristics of typical fault-type ground fissures, while the others show the phenomena of the discontinuous gullies, holes of different sizes in shallow soil, and uneven settlement of local surface, which are obviously different from fault-type ground fissures, and its genesis is difficult to be inferred. Our research aims to deeply study the genesis of ground fissures and surface subsidence in the rift zone, to provide a basis for the prevention and control of ground fissures and surface subsidence in railway projects and nearby constructions.

The research is divided into four stages: the first stage is to analyze the characteristics of undisturbed soil through basic physical properties experiments; the second stage is to analyze the influence of water content on the physical and mechanical properties of the soil, considering that ground fissures occur in the rainy season; next, put forward the hypothesis of ground fissure mechanism and the last, set up a series of simulation physical model experiments and give quantitative results to verify the hypothesis. This article presents the research results of the first three stages, and the results of the fourth part will be presented in the subsequent contents.

2 SUMMARY OF GROUND FISSURE AND SURFACE SUBSIDENCE IN RIFT VALLEY AREA

Since March 2018, four ground fissures have appeared successively in the Kenya Nairobi-Malaba Railway rift region (Geographical distribution is presented in **Figure 1**). Among them, the three large-scale ground fissures are respectively named B3 highway ground fissure, DK76 ground fissure, and DK77 ground fissure.

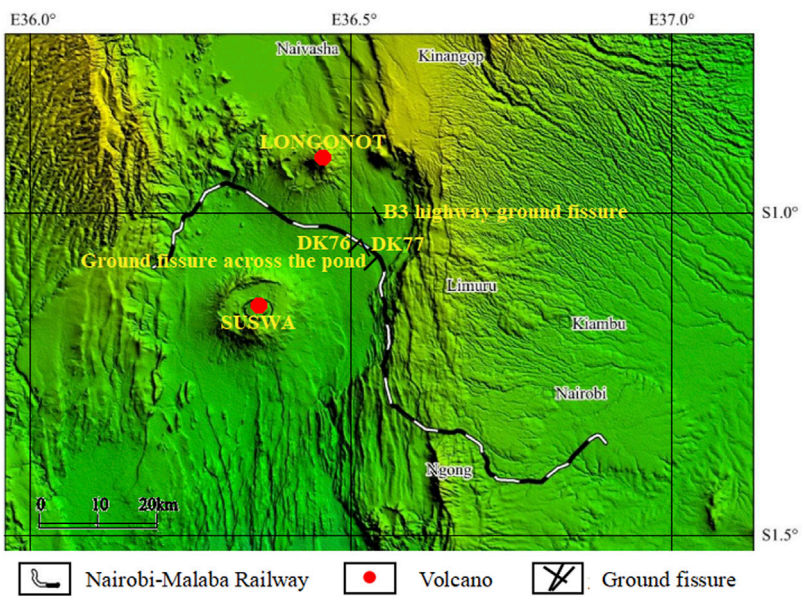


FIGURE 1 | Geographical distribution map of the fissures.



FIGURE 2 | Scene photos of ground fissures near the railway. **(A)** DK76; **(B)** B3 highway; **(C)** DK77; **(D)** ground fissure through a pond.

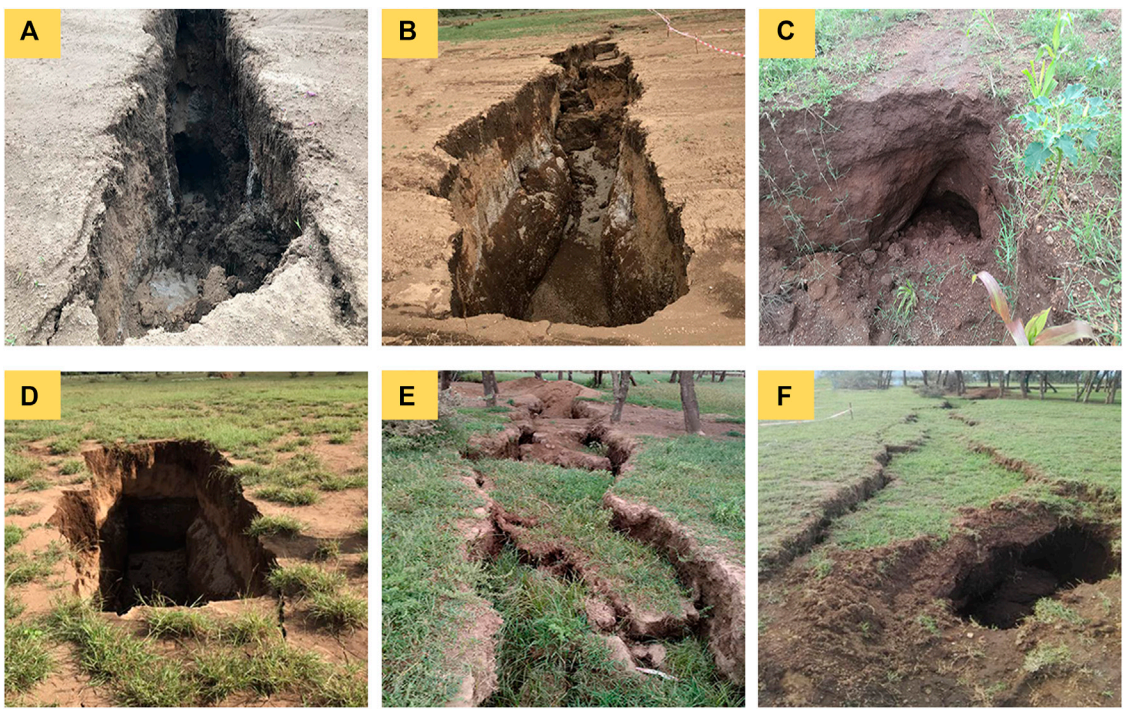


FIGURE 3 | Ground fissure morphology along the railway. **(A, B)** Discontinuous gullies; **(C, D)** holes of different sizes; **(E, F)** uneven settlement.

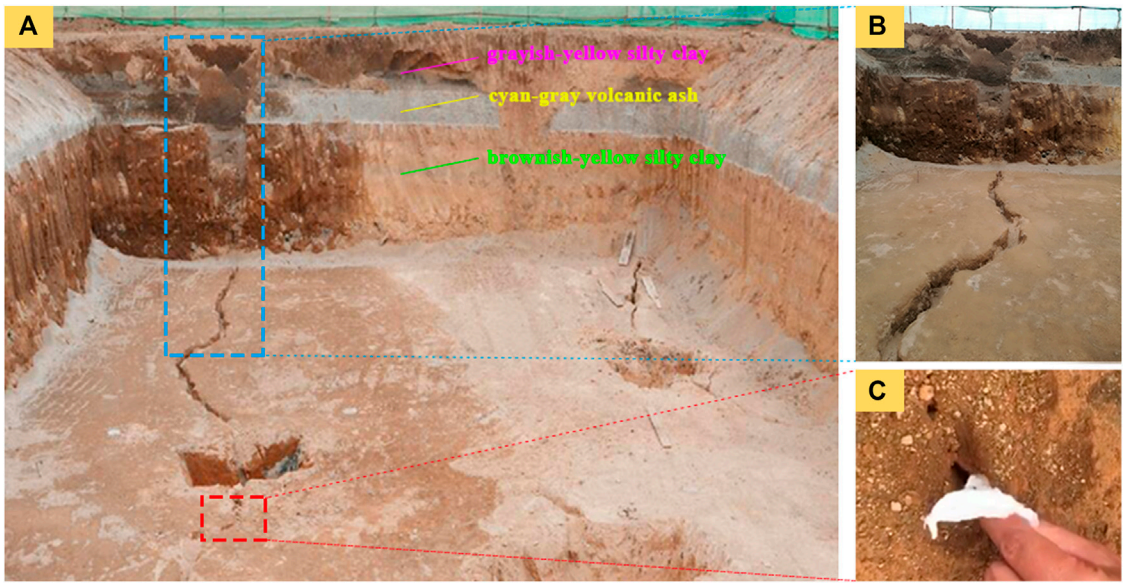


FIGURE 4 | Geological section and details of exploration trench. **(A)** The trench scene; **(B)** collapse and the crack facing it; **(C)** a small hole with air friction sound.

Due to consecutive rainfall, a ground crack and gully nearly orthogonal to the line appeared at DK76 + 798 of the Nairobi-Malaba Railway on 7 March 2018. the ground crack started at 50.0 m on the left side of the line, ran from north to south, gradually widened toward the right side of the line, and formed a gully, crossing the front channel, the gully was 3.4 m deep, 0.5–1.5 m wide and about 200.0 m long (as shown in **Figure 2A**). The ground fissure of the B3 highway is located near Nakuru in the Rift Valley region of East Africa, after several days of continuous rainfall, the ground fissure suddenly occurred and formed gullies on the evening of 13 March 2018, the ground fissure runs from north to south with a depth of 15 m, a width of 2–5 m, a length of several kilometers and cuts off B3 highway, according to the description of witnesses at the scene of the accident, the ground fissure occurred suddenly and developed rapidly (**Figure 2B**). The DK77 ground fissure is located at DK77 + 884 of the Nairobi-Malaba railway, 1 h after heavy rainfall on 4 May 2018, a crack with a north–south strike, a depth of 2–5 m, a width of 1–2 m, and a length of 300 m appeared (**Figure 2C**). The fourth ground fissure passes through a pond and intersects with the branch line of Nakuru-Kiambu Highway, which is approximately parallel to the south and north of the B3 Highway fissure, but with a smaller scale (**Figure 2D**).

According to geological mapping, the B3 highway ground fissure is a series of normal faults along the eastern boundary fault zone of the East African Great Rift Valley. Its strike is nearly the north–south direction, consistent with the strike of the fault, straight line, stretching for several kilometers, and continuous through, with a width of 2–5 m, which is a typical fault type ground fissure. While ground fissure of DK76, DK77, and the one through a pond is not only relatively short in length but also have discontinuous gullies (as shown in **Figures 3A**, **B**), holes of different sizes exist in shallow soil (**Figures 3C**, **D**), with uneven settlement occurs on the local surface (**Figures 3E**, **F**). The above characteristics of ground fissures indicate that the ground fissures and uneven surface settlement are not caused by earthquakes or surface rain erosion, but by the underlying soil layer being eroded by groundwater, while gullies are formed by surface water erosion based on uneven surface settlement. The existence of holes of different sizes in the shallow soil further supports this conjecture. At the same time, the surface vegetation at the uneven settlement of the surface is complete, which also indicates that the formation of ground fissures is related to the loss of the underlying soil mass.

To verify the above conjecture and investigate whether the underlying soil layer is disturbed and whether fissures are developed in the underlying bedrock, a geological trench survey was carried out at DK76 and DK77 (as shown in **Figure 4A**). The trench excavation shows that the left and right bedrock cracks are visible in the weathered layer of bedrock. The strike of the cracks on the right side of the trench is consistent with the surface cracks. The underground cracks are exposed to the overlying soil layer with settlement and collapse, and the discontinuity caused by collapse can be observed in the volcanic ash layer. The crack on the left side of the exploration trench is exposed to the new crack position, and there is an obvious collapse phenomenon at the overlying soil layer where the underground crack is facing directly (**Figure 4B**). The volcanic ash layer is interrupted due to the collapse of the soil layer; thus, it can be seen that the collapse of the soil layer is related to the underground bedrock crack. Meanwhile, fluid overflow was observed at the crack at the bottom of the trench, accompanied by a slight air friction sound, that is, there was the internal and external exchange of gas, which proved that there was a channel for fluid flow under the bedrock crack (**Figure 4C**).

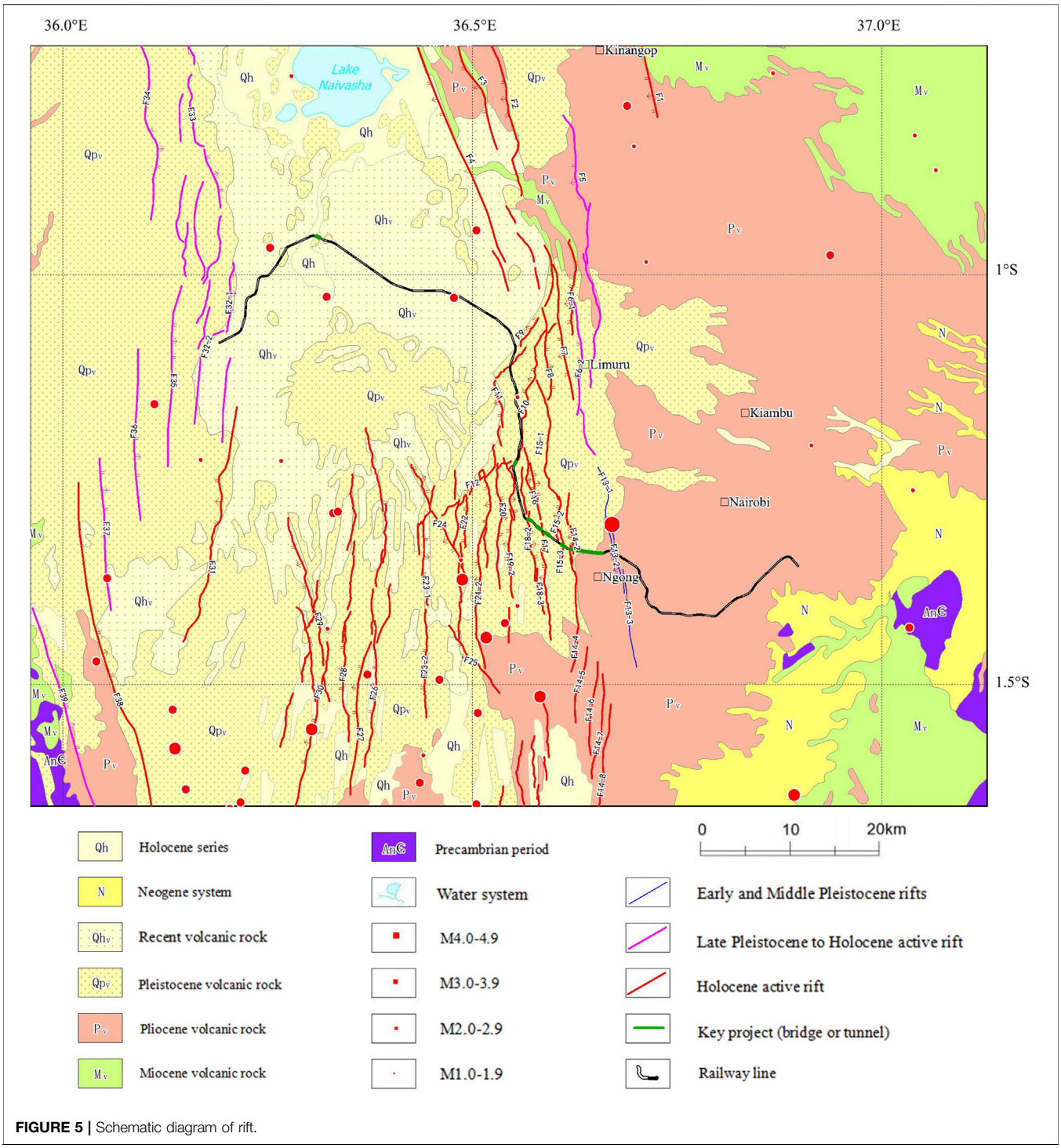


FIGURE 5 | Schematic diagram of rift.

Based on the results of the exploration trench, it is speculated that after continuous rainfall infiltration in the rainy season, a part of soil particles in the overburden migrate downward and lose along the bedrock cracks. At the same time, soil particles near the rock-soil interface are continuously lost along the bedrock cracks and gradually form holes under the action of underground water erosion. When the holes develop to a certain scale, it collapses unsteadily due to rainfall inducement, and the surface first appears one by one pit. With the continuous development and connection of the pits, the collapse forms ground fissures and uneven settlement of the surface, then scoured by surface rainwater to form gullies.

3 ENGINEERING GEOLOGICAL CONDITIONS OF SURFACE FISSURE SITE

3.1 Site Construction Environment

The first phase of the Nairobi-Malaba railway project in Kenya starts from Nairobi, Kenya's capital, and ends near Narok. The line passes through the floor area of the Great Rift Valley in East Africa. The valley floor area is about 40 km wide, with open and flat terrain, lava platforms, huge volcanic cones, and cliffs on both sides. The height difference between the valley floor and the top of the cliff is 450–2,000 m, and the ground elevation of the valley floor area is 1,650–1,820 m (Wang et al., 2019).

The valley floor area is a fault depression zone of the Great Rift Valley across North and South Africa, the geological structure is well developed, and most of the faults are Holocene active faults. The traces of these faults to the north are mostly covered by newer pyroclastic rocks and volcanic ash, with almost no outcrop on the surface. According to the comprehensive geophysical exploration results, there are 16 concealed rift fracture zones distributed under the overburden (**Figure 5**). In addition, a series of volcanoes are distributed in the Rift Valley area, mainly the SUSWA volcano on the south side of the line and the LONGONOT on the north side (Wadge et al., 2016), their distribution is shown in **Figure 1**. The floor area of the East African Rift Valley traversed by the line is characterized by active geological structure, frequent volcanoes, and geothermal anomalies, which provide basement structural conditions for the generation and development of underlying bedrock cracks.

3.2 Geotechnical Engineering Geological Characteristics

The overlying soil in the valley floor area is mainly Quaternary Holocene-Pleistocene strata. The overlying soil of pyroclastic accumulation and diluvium layer is stratified mainly composed of silty clay, volcanic ash, etc., with the characteristics of a large pore ratio, loose structure, poor gradation, and strong water permeability. The underlying bedrock is mainly volcanic tuff, covering the semi-diagenetic strata in the early Tertiary and Quaternary. The rock is hard and has concealed structural fractures, with tensile fractures and cavities distributed, which become channels for groundwater to flow up and down.

According to the engineering geological exploration report near the DK76 ground fissure, it can be seen that the engineering geological characteristics of the geotechnical layer exposed by the exploration trench are as follows: 1) silty clay: grayish-yellow, hard plastic, with high silty content and relatively uniform soil texture; 2) volcanic ash: cyan-gray, slightly wet, slightly dense, flaky particles, containing a small amount of gravel, accounting for 5%–10%, with poor gradation; 3) silty clay: brownish-yellow, hard plastic, mixed with fine sand, with high silty content; 4) tuff: brownish-gray, tuff structure, and blocky structure; drill core is 8–40 cm in a short column shape, locally broken blocky, with dumb hammering sound and easy to break. Under the geological background of the valley floor area where the line is located, combined with the above investigation and engineering geological investigation, it is qualitatively believed that the Rift Valley area has engineering geological and hydrogeological conditions for the development of ground fissures, and it is inferred that the ground fissures are the result of suffosion erosion effect of groundwater on the overlying soil layer through underlying bedrock cracks. The underlying bedrock crack is the prerequisite for the formation of the ground fissure, which determines the nature and spatial distribution characteristics of the ground fissure.

Considering that the main overlying soil layers may exhibit unique physical and mechanical properties when mixing with water, which are extremely vulnerable to groundwater erosion, causing structural damage or being washed away, thus resulting in ground fissures and surface settlement. Therefore, conventional geotechnical tests are carried out on the grayish-yellow silty clay, cyan-gray volcanic ash, and brownish-yellow silty clay samples obtained from drilling, to reveal the causes of ground fissures and surface settlement from the physical and mechanical properties, to provide a basis for their prevention and control.

4 TEST AND ANALYSIS OF SOIL MECHANICS AND PHYSICAL CHARACTERISTICS

4.1 Basic Physical Indexes of Soil and Analysis

According to the basic requirements of the geotechnical test, combined with the purpose of this test, dry density, specific gravity, water content, plastic limit, liquid limit, and porosity are selected as the basic physical indexes of the three types of soil to be measured. Specific gravity is measured by the pycnometer method, water content is measured by the drying method, plastic, and liquid limits are measured by plastic-liquid limit combined tester, and porosity is obtained by conversion of specific gravity, water content, and density according to the corresponding engineering geological exploration report which is based on Rules of Geotechnical Testing (GB/T50123-2019). The detailed experimental results are listed in **Table 1**.

According to the test results, the specific gravity and plastic and liquid limit indexes of the three types of soils are not significantly different from the similar soils of other regions. However, there were obvious differences in the state of the three types of soils after water immersion: after drying the grayish-yellow silty clay, the surface layer of the soil has a liquid-like touch (as shown in **Figure 6A**), which proves that it has a finer particle size. In addition, when it is sieved with 0.075 mm particle size, most of the particles will be sieved, but during the sieving process, a layer of soil film formed by interlinking fine particles tended to form on the surface layer of the sieve, which hinders the particles from passing through the sieve. This phenomenon indicates that this type of soil has a strong cementation effect at a lower water content, so it may have strong collapsibility. At 10% water content, the brown color deepens, and the fine particles form small balls, which crumble into powdered particles when lightly touched (**Figure 6B**). Under 20% water content, the brown color is deeper, the strength of the small balls formed with water

TABLE 1 | Basic physical indexes of three types of soils.

Types of soil	Dry density (g/cm^3)	Water content (%)	Specific gravity	Plastic limit (%)	Liquid limit (%)	Porosity
Grayish-yellow silty clay	1.31	17.82	2.71	15.31	34.29	0.58
Cyan-gray volcanic ash	1.42	10.07	2.68	19.57	38.71	0.52
Brownish-yellow silty clay	1.33	13.15	2.70	16.19	37.25	0.56

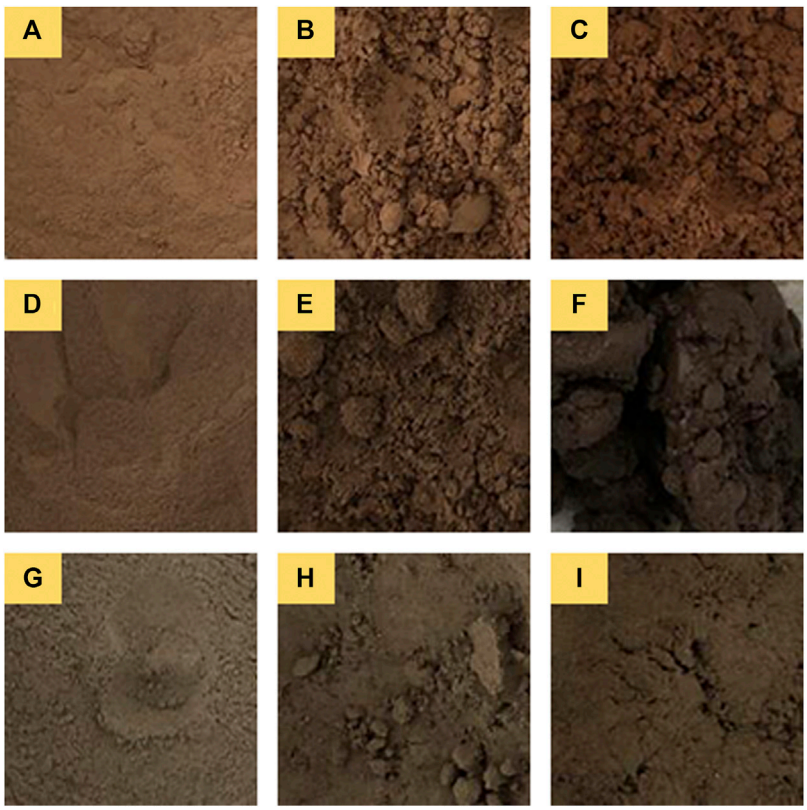


FIGURE 6 | Apparent phenomena of three kinds of experimental soils at different water contents. **(A)** Dried grayish-yellow silty clay; **(B)** 10% water content grayish-yellow silty clay; **(C)** 20% water content grayish-yellow silty clay; **(D)** Dried brownish-yellow silty clay; **(E)** 10% water content brownish-yellow silty clay; **(F)** 20% water content brownish-yellow silty clay; **(G)** Dried cyan-gray volcanic ash; **(H)** l0% water content cyan-gray volcanic ash; **(I)** 20% water content cyan-gray volcanic ash.

increases slightly, which crumble into powdered particles when lightly touched too (**Figure 6C**); the brownish-yellow silty clay is dry to the touch, and the connection between particles is weak, so there is no sieving conjunctive phenomenon (**Figure 6D**). At 10% water content, fine particles are combined into small balls with water, form smaller balls when pinched but do not crumble into powdered particles (**Figure 6E**), and at 20% water content, the brown color is darker, the small balls with water have higher strength, higher soil plasticity, not easy to be pinched, with high viscosity (**Figure 6F**). After drying, the cyan-gray volcanic ash is dry to the touch, with a weak connection between fine particles and no sieving conjunctive phenomenon (**Figure 6G**). Under 10% water content, the particles are knitted into larger clods, but the connection between particles is weak, and they are broken into multiple clods when lightly touched (**Figure 6H**); at 20% water content, the color deepens, the soil particles are connected to form larger clods, and the connection force between particles is still weak (**Figure 6I**).

Combined with the apparent phenomena of three kinds of soils with different water contents and the fact that ground fissures and uneven settlement occurred after several heavy rainfalls, it is inferred that the water content has an important influence on the mechanical properties of soil, and the clay content in the soil which is easy to be scoured by water may also be the cause of the occurrence of ground fissures. Therefore, the following experiments are carried out from three aspects, respectively, the direct shear experiment at different water contents to determine the effect of water content on the strength of the soil, the collapsibility test to determine the extent of collapsibility in a saturated state, and the clay content experiment to determine the proportion of clay particles in the fine particle soil. In the following, we first

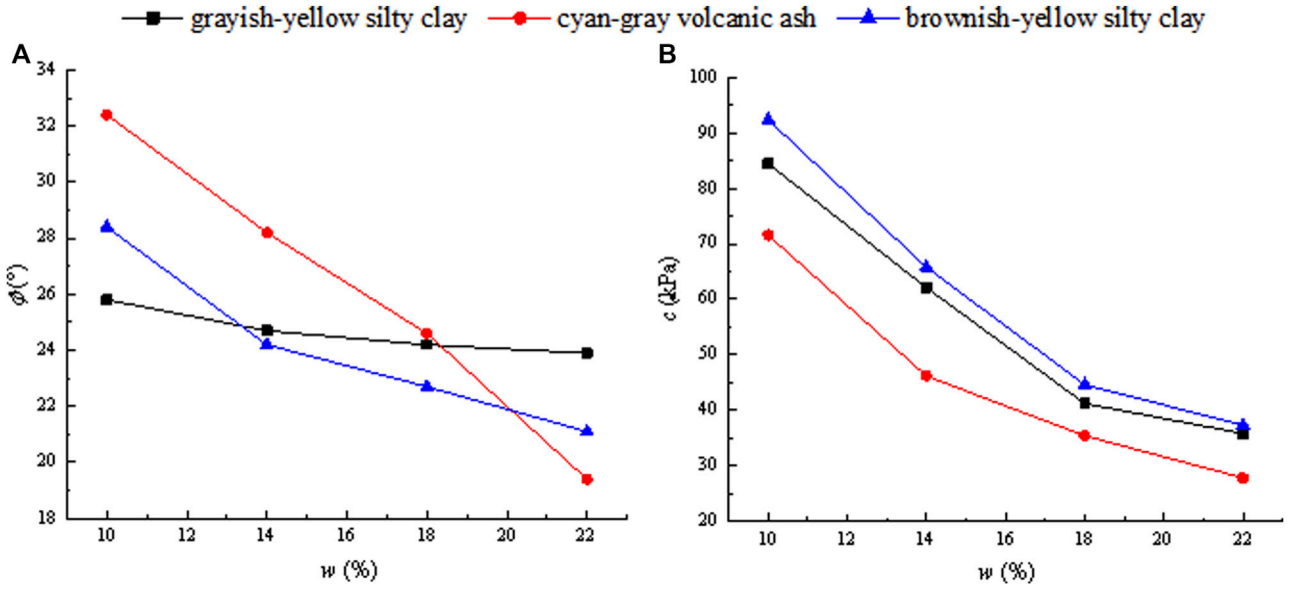


FIGURE 7 | Results of the direct shear test. **(A)** Relationship between cohesion and water content; **(B)** relationship between internal friction angle and water content.

analyze the variation characteristics of mechanical properties of the above three types of soils under the condition of different water contents.

4.2 Direct Shear Test

To study the influence of soil moisture content on its shear strength, three types of soil with water contents of 10%, 14%, 18%, and 22% were selected for direct shear tests, and the relationship between cohesion and internal friction angle with water content as represented in **Figure 7**. It can be observed that the cohesion and internal friction angle of the three types of soils decrease with the increase of water content. The cohesive force of brownish-yellow silty clay and grayish-yellow silty clay under different water contents are close to each other, and both are greater than that of cyan-gray volcanic ash, and the cohesive force decreases faster with the increase of water contents. The internal friction angle of the three types of soils shows obvious differences with the change in water content. The internal friction angle of the cyan-gray volcanic ash decreases rapidly with the increase of water content. The internal friction angle of the brownish-yellow silty clay decreases rapidly with the increase of water content at lower water content. When the water content is higher than 14%, the decreased speed of the internal friction angle becomes slower. The internal friction angle of grayish-yellow silty clay decreases slightly with the increase of water content.

4.3 Collapsibility Test

4.3.1 Test Preparation

From the above tests, it can be obtained that the moisture content has a significant impact on the shear strength of the three soils. Based on the different apparent characteristics of the three types of soil when meeting water in the sample preparation process, we will conduct collapsibility tests to quantitatively analyze the influence of the water immersion process on the mechanical properties of these soils. The main influencing factors of collapsibility include soil structure, overlying pressure, and water content,. Soil structure is affected by deposition conditions, mainly manifested by the degree of cementation between particles and the number of unstable macropores; overburden pressure is mainly controlled by the depth of the soil layer; water content is related to the strength of cementation before collapsibility, capillary pressure, matric suction, and soil permeability.

In the process of sampling, the three undisturbed soil samples in this test are all in a fragmented state after being taken out, which indicates that the soil structure generated by the natural deposition process is weak, and the soil structure loss is caused by remolding process is relatively small. For two soils with the same size and pore ratio, the bearing capacity of remolded soil will be larger than that of undisturbed soil; that is, remolded soil shows stronger collapsibility, so it is more conservative to calculate the settlement based on the results of remolded soil.

Based on the above factors, the collapsibility tests were conducted for three soils with axial pressure of 200 kPa, a porosity of 0.55, and water content of 5, 10, 13, 15, 17, and 20%, respectively.

4.3.2 Test Results and Analysis

The collapsibility test results of the three types of soil are shown in **Figure 8**. The collapsibility of the three types of soil will be analyzed based on the test results.

4.3.2.1 Grayish-Yellow Silty Clay

The collapsibility test results show that the collapsibility coefficient of grayish-yellow silty clay is very low, and its collapsibility gradually loses with the increase of water content. Combining the apparent phenomena in the sample preparation

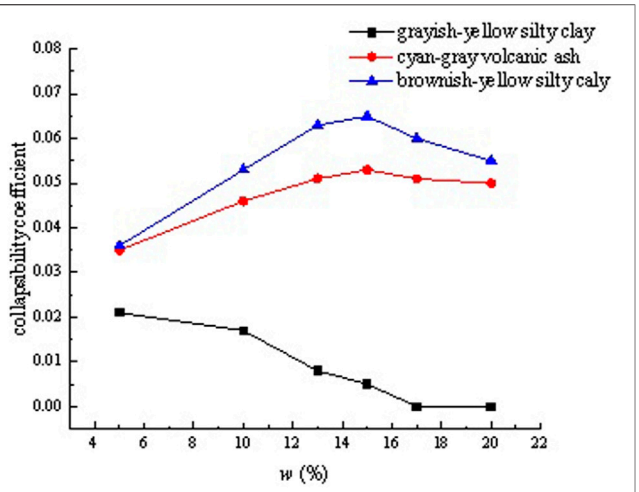


FIGURE 8 | Variation of collapsibility coefficient with water content.

process, the reasons for the variation of collapsibility coefficient under different water contents are analyzed: When the soil with lower water content starts to infiltrate, soil particles form small balls that are not easy to crush, and the combination between the particles becomes tight, soil structure gradually strengthens, and the macroscopic manifestation is that a small amount of settlement occurs in the soil. When water infiltrates to a certain extent, soil structure reaches the strongest, the formed particles are high in strength and viscosity, similar to plasticine, and will not be damaged due to further flooding, and the settlement will not increase in macroscopic.

For the soil with higher water content, the structure obtained by the preparation process is stronger than that with lower water content, and the settlement generated during infiltration is small; that is, collapsibility is small. When water content reaches 17%, the sample will no longer become compact due to immersion. At the same time, it will not cause structural damage due to the high strength and viscosity of the particles. Macroscopically, the settlement is zero, that is, there is no collapsibility.

4.3.2.2 Cyan-Gray Volcanic Ash

The test results show that the collapsibility coefficient of cyan-gray volcanic ash is relatively high, and the collapsibility increases to an extreme value first and then decreases slowly with the increase of water content, the test results are analyzed as follows: Volcanic ash particles have a poor affinity for water. Under low water content, the particles are arranged in a neat and tuff structure, which has strong structural properties. After encountering water, the tuff structure is partially destroyed, showing certain collapsibility. At higher water content, the surface of the sample shows a bleeding phenomenon, the arrangement of volcanic ash is scattered, and no tuff structure formed. The structure is obviously destroyed and collapsibility is significantly increased after mixing with water. When the water content continues to increase, the bleeding phenomenon on the surface of the sample is more obvious, and the structural property of volcanic ash is very weak, thus reducing the structural damage caused by collapsibility and reducing the collapsibility coefficient.

4.3.2.3 Brownish-Yellow Silty Clay

The test results show that brownish-yellow silty clay has the strongest collapsibility under each set of water content, which also has a process of first increasing and then decreasing with the increase of water content. In the screening process of sample preparation, it is found that brownish-yellow silty clay has an obvious "conjunctiva" phenomenon. Even when dry soil passes through a 0.075 mm sieve, fine particles that can be sieved will form a dense soil film on the surface of the sieve, which hinders the sieving of particles. When the sieve is knocked, the soil film is damaged and fine particles are sieved. It shows that the cohesive force of this kind of soil is strong under low water content. when the soil with low water content begins to soak, soil particles form small balls, the combination between the particles becomes tight, soil structure gradually increases, and the macroscopic manifestation is a small settlement. When the soil soaks to a certain extent, its structure will damage, and the settlement amount will further increase; when the soil with higher water content begins to infiltrate, the structure of the sample itself is stronger than that with lower water content, the structural damage and settlement are large; that is, collapsibility is strong. When the water content of the sample is very high, the structure of the soil becomes weak, the structural damage in the infiltration process is small, the settlement amount is small, and the collapsibility is weakened.

In addition, combining the exploration trench and drilling data, brownish-yellow silty clay is located on the underlying bedrock tuff, which is easily eroded by groundwater. Its properties are important factors that affect the ground settlement.

4.3.3 Analysis on Influencing Factors of Collapsibility

According to collapsibility theory, collapsibility is not only affected by soil structure and water content, but also by overlying pressure. In the following, the collapsibility tests on strong collapsibility soils of brownish-yellow silty clay and cyan-gray volcanic ash, with a porosity of 0.55 under different axial pressures are carried out to analyze the influence of overlying pressure.

Based on the test results demonstrated in **Figure 9**, the soil collapsibility is affected by both water content and axial pressure. The specific manifestation is that the soil collapsibility coefficient is larger under higher axial pressure. In the light of the curved shape, water content corresponding to the highest point of the collapsibility coefficient has an increasing trend with the increase of axial pressure, which is consistent with the changing trend of the optimal water content with axial pressure.

The difference in the apparent phenomena during sample preparation may be an important reason for the different collapsibility of soil. Based on the analysis of the brownish-yellow silty clay with the strongest collapsibility, it is easy to form larger spherical particles under a high water content, and the phenomenon of "conjunctiva" is accompanied with the sieving process. This indicates that the clay content in brownish-yellow silty clay is relatively high, so it is presumed that the clay content is also an important factor affecting collapsibility. The following will verify this presumption through fine particle analysis of three soils.

According to the densitometer method ($d < 0.075$ mm) in Rules of Geotechnical Testing (GB/T50123-2019), the fine particle analysis test was performed on three types of soils.

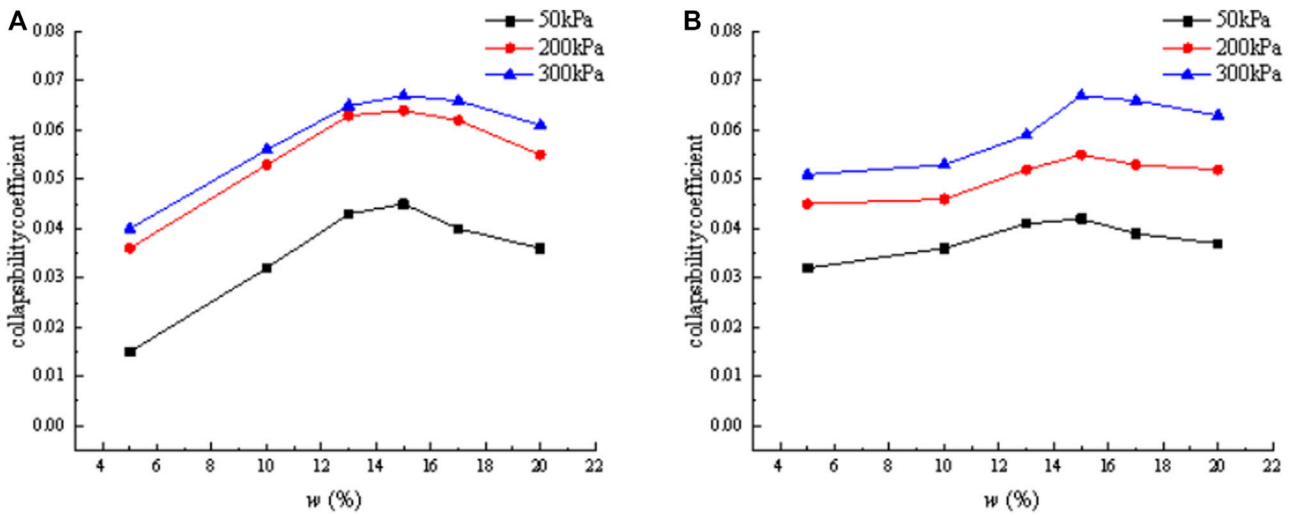


FIGURE 9 | Variation of collapsibility coefficient with water content under different axial pressures. **(A)** Brownish-yellow silty clay; **(B)** cyan-gray volcanic ash.

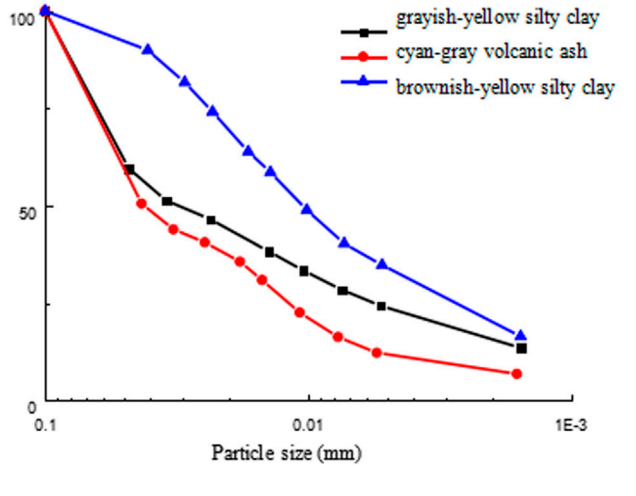


FIGURE 10 | Cumulative curve of finer particle gradation.

The results show that the clay content of grayish-yellow silty clay is 23.96%, and that of brownish-yellow silty clay is 34.81%, which is significantly higher than grayish-yellow silty clay (as represented in **Figure 10**), indicating that the higher the clay content, the stronger the soil collapsibility. But the content of cyan-gray volcanic ash clay is only 12.31%, and its collapsibility is stronger than grayish-yellow silty clay, which indicates that it is unreasonable to evaluate soil collapsibility only by considering the clay content. Combining the phenomena observed in sample preparation, soil collapsibility is analyzed as follows: The effect of clay content on the collapsibility increases with the increasing of clay content, and the clay around skeleton particles will gradually aggregate together. In this process, the fine particles, which were originally scattered in the pores between large particles, will gradually "agglomerate" under the influence of intermolecular attraction and gather towards the large particles. With the further increase of the clay particles' content, the large particles form the "grain chain," and the cohesion increases rapidly. Clay particles begin to play a major role in the macro-mechanical properties, while the "grain chain" completely wraps the large particles and becomes skeleton particles (Shao et al., 2014; Zhang et al., 2015). This phenomenon is especially obvious in soil with low water content and stronger bearing capacity. With the increase of water content, clay particles float, and original skeleton particles are destroyed, resulting in a more obvious settlement than in other similar soils. The soil with stronger binding water capacity forms skeleton particles with better water resistance, which will not be damaged due to the increase of water content and not further settle, that is, soil collapsibility is affected by both clay content and binding water capacity of soil particles (Zhou et al., 2020).

Comprehensive to the above tests and the apparent phenomenon of the cyan-gray volcanic ash after water, the mechanism of collapsibility of the soil can be summarized as follows: for the soil with low clay content, the main cause of collapsibility is the structural damage caused by soaking, such as when water infiltrating into the cyan-gray volcanic ash, its structure of tuff is damaged, and the settlement occurred. For the soil with high clay content, its collapsibility is affected by both clay content and the water-binding capacity of particles. When the binding water capacity of soil particles is strong, the soil will form skeleton particles with good water resistance, which increases the constitutive property of soil and will withhold structural damage due to further soaking. The collapsibility is lower under this state of cyan-gray volcanic ash and gradually decreases until disappears as the water content increases. When the water-binding capacity of soil particles is weak, the soil will form skeleton particles with poor water resistance, and exhibit a certain degree of collapsibility. With the further immersion of the ash, structural damage will occur, the settlement will increase, and exhibit strong collapsibility in general.

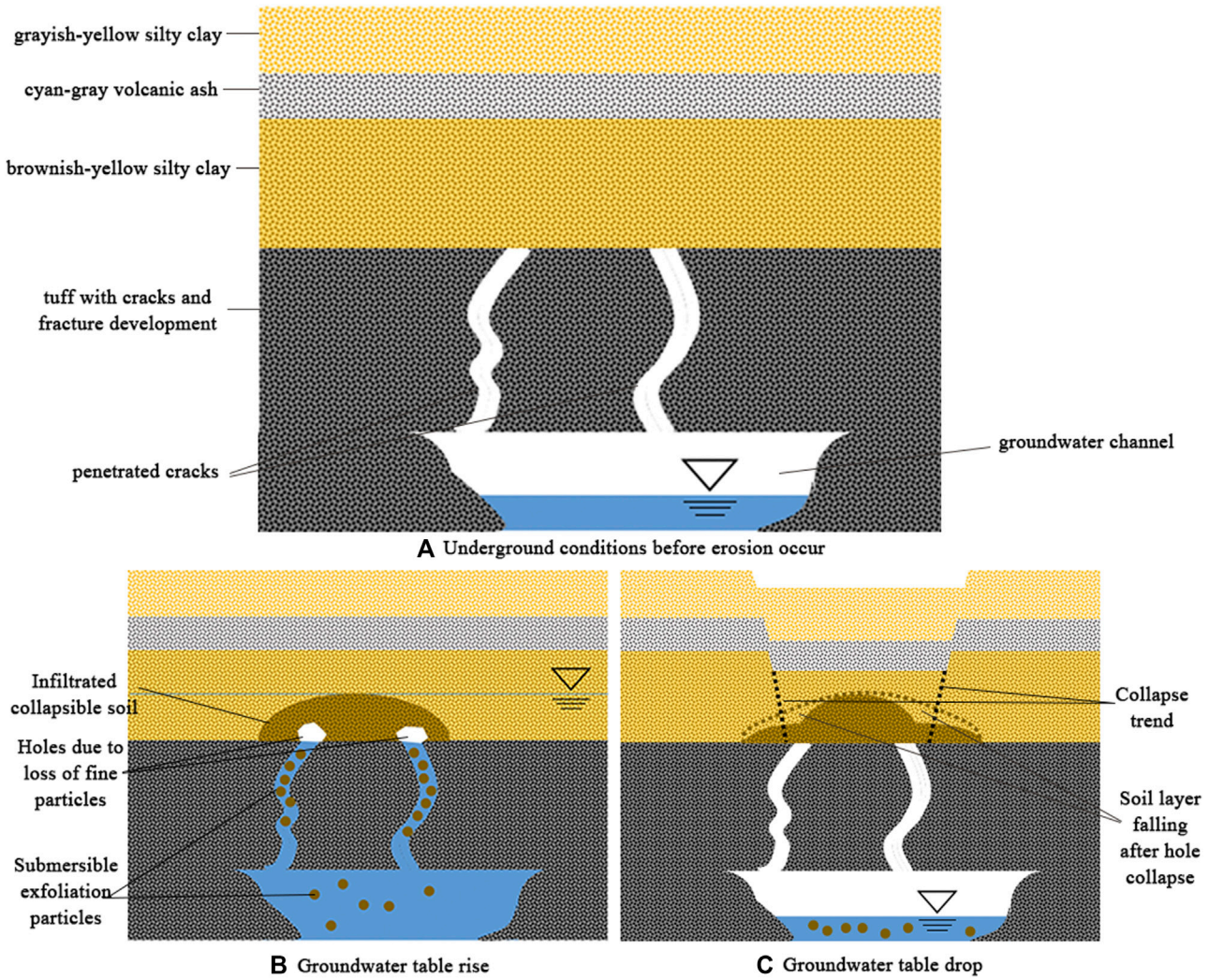


FIGURE 11 | Schematic diagram of the mechanism of surface uneven settlement. **(A)** Underground conditions before erosion occurs; **(B)** groundwater table rise; **(C)** groundwater table drop.

5 DISCUSSION

5.1 Mechanism Analysis of Settlement and Fissure Caused by Soil Collapsibility

Brownish-yellow silty clay with strong collapsibility overlay the bedrock (tuff) with a certain thickness and underlay cyan-gray volcanic ash and grayish-yellow silt clay. With such a soil layer structure, the surface settlement caused by surface water should be even, not localized or belted, whereas what is actually exhibited is the uneven settlement and local fissures. Therefore, it can be considered that the uneven settlement and fissures formed on the surface are not the collapsibility effect caused by surface water. Based on the exploratory trench DK76 results, the location of the surface uneven settlement is directly opposite to the hidden cracks of tuff (**Figure 4B**), which indicates that the uneven settlement is most likely caused by the erosion of groundwater into the overlying soil layer along the hidden cracks, its development process is speculated as follow: When groundwater level rises, water infiltrates into the brownish-yellow silty clay layer through hidden cracks in the bedrock, and the collapsibility causes the fine particles to be stripped from the soil structure and free in the soil layer. When the groundwater level falls, these fine particles are carried out along the bedrock cracks under the action of water flow, causing the soil to be partially lost and the structure of local soil damaged. With the alternating changes of groundwater level height, holes in soil form and gradually develop and penetrate, and the bearing capacity of the brownish-yellow silty clay layer gradually loses, hence ground fissures appear on the surface directly opposite to the hidden cracks, and the overlying soil sink under the further action of groundwater. When the bearing capacity is completely lost due to subsurface erosion, the holes collapse, showing local collapse and

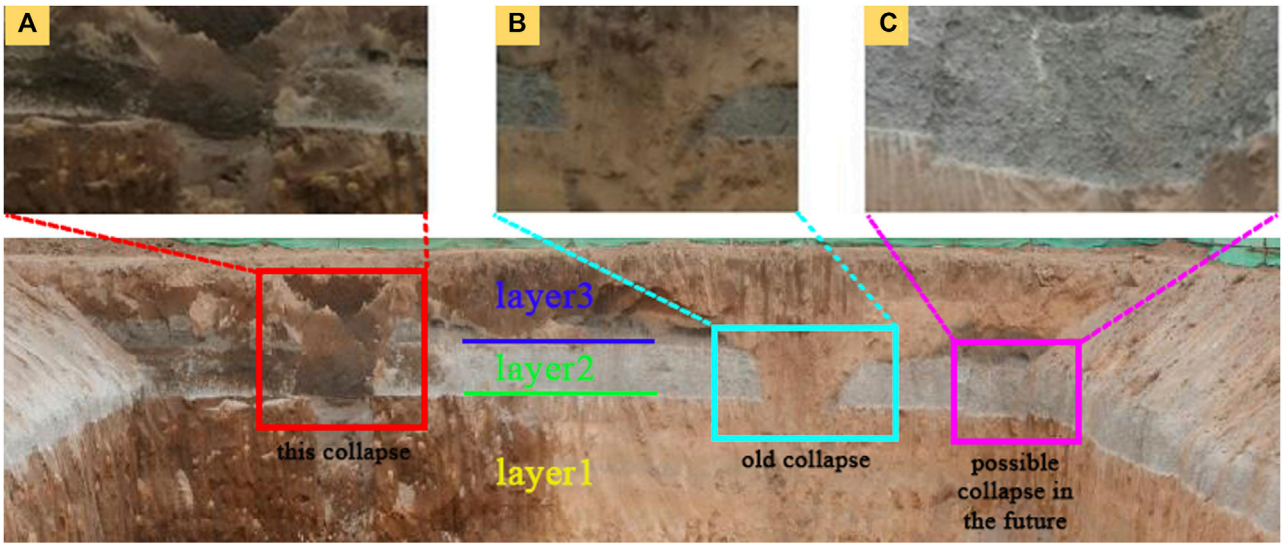


FIGURE 12 | Three collapse positions revealed by the DK76 trench. **(A)** Location of "this collapse"; **(B)** position of "old collapse"; **(C)** position of "possible collapse in the future".

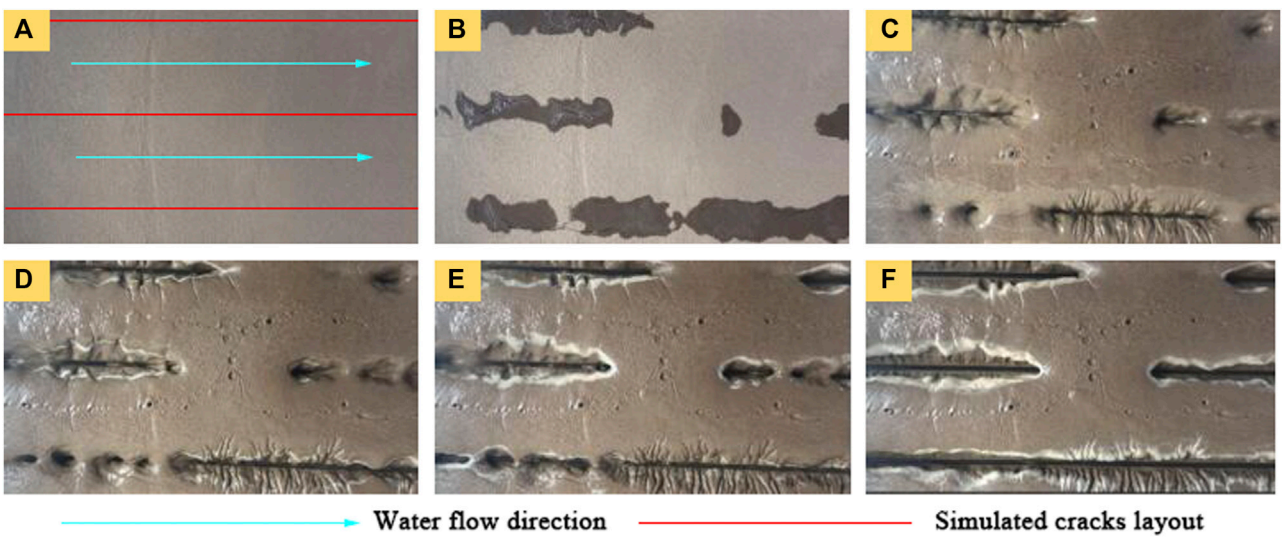


FIGURE 13 | Top view of soil surface collapse before and after soil erosion test. **(A)** After the first water reserve-discharge cycle, **(B)** after three water reserve-discharge cycles; **(C)** after five water reserve-discharge cycles; **(D)** after eight water reserve-discharge cycles; **(E)** after eleven water reserve-discharge cycles; and **(F)** after seventeen water reserve-discharge cycles.

uneven settlement on the surface (the geomorphological phenomenon exhibited in **Figure 2**). A schematic diagram of the mechanism of surface settlement is shown in **Figure 11**.

5.2 Deduce on Influencing Factors of Settlement Degree

As can be seen in **Figure 12**, the volcanic ash layer in the excavated DK76 trench has faults or dislocations at three locations. In "this collapse," it can be seen that the upper part of the volcanic ash layer has collapsed and slid down to the lower part. In "old collapse," we can see that the collapse has occurred before, the soil in the upper part has slipped down to the lower part in the previous collapse, and the collapse did not occur here in this rainfall, probably because the properties of the upper part soil are quite different from the lower part. When the soil adjacent to the bedrock crack is the lower volcanic ash layer, collapse can occur under certain rainfall conditions, while when the soil is in

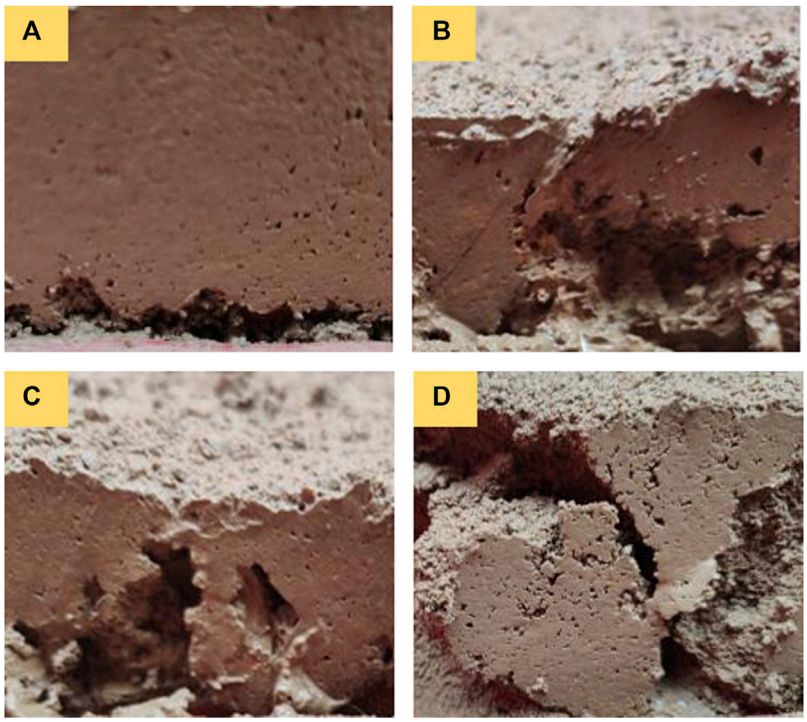


FIGURE 14 | Profile maps of subsurface erosion test. **(A)** Forming small holes; **(B)** the holes expand and penetrate; **(C)** the holes penetrate the soil surface; and **(D)** surface soil collapses.

the upper layer, the collapse will not occur under similar rainfall conditions. At "possible collapse in the future," the volcanic ash layer dislocated, indicating slight collapse has occurred, which may be due to the corresponding bedrock cracks directly below it being relatively narrow or their layouts are not conducive to groundwater erosion, thus leading to a small degree of collapse. In future geological activities or rainfall, the expansion of cracks or the enhancement of groundwater erosion may lead to a new collapse phenomenon at this location.

For the aforementioned inference, our team has set up a series of physical model experiments to verify its rationality. The experimental results show that subsurface erosion can cause the collapse of the overlying soil layer (as shown in **Figure 13**). During the repeated action of groundwater erosion, the change process of the surface soil layer is as follows: first, the soil at the surface layer directly opposite to the simulated cracks becomes wet (**Figure 13A**), next, the whole soil layer is infiltrated (**Figure 13B**), then local holes appear in the surface layer (**Figure 13C**), furthermore the holes penetrate along the simulated cracks (**Figure 13D**), finally the holes further develop and interconnect each other (**Figure 13E**), and a collapse along the simulated cracks is found and the trench is formed (**Figure 13F**). From **Figure 13**, it can qualitatively prove the rationality of the aforementioned inference in this article. The detailed quantitative research results will be published in a subsequent article.

In order to further explain the mechanism of ground fissures, the test profiles are drawn in **Figure 14**. It is seen that the collapse process of collapsibility soil in the subsurface erosion tests from **Figure 14**: under the action of groundwater, first, the collapsible soil layer is hollowed out, forming small holes (**Figure 14A**); next, the holes gradually expand and penetrate with each other under the further action of subsurface erosion (**Figure 14B**); then the holes continue to develop upward and penetrate the soil surface along simulated bedrock cracks (**Figure 14C**); eventually, the surface soil collapses (**Figure 14C**).

Sequential studies will further carry out physical model experiments on loess and silt with similar soil properties to the site soil of the Rift Valley area in Kenya, and quantitative indicators will be used to analyze the influence of collapsibility, hydraulic geology conditions, hidden cracks placement, and other aspects on surface uneven settlement. This article will not reiterate due to the space problem.

6 CONCLUSION

This study analyzes the characteristics and causes of ground fissures and surface uneven settlement in the Rift Valley section of Kenya Nairobi-Malaba Railway, and the main conclusions are as follows:

1) In the context of the regional geology of the Great Rift Valley in East Africa, combined with the field investigations of geological trenching, and drilling, it is found that the surface vegetation is relatively complete at settlement

locations, and holes of varying sizes exist under the surface. The trench excavation shows the left and right bedrock cracks are visible in the weathered layer. The strike of the cracks on the right side of the trench is consistent with surface cracks. The underground cracks are exposed to the overlying soil layer with settlement and collapse, and the discontinuity caused by collapse can be observed in the volcanic ash layer. The crack on the left side is exposed to the new crack position, there is an obvious collapse phenomenon at the overlying soil layer where the bedrock crack is facing directly. The volcanic ash layer is interrupted due to the collapse; thus, it is related to the bedrock crack.

2) Analysis of factors affecting collapsibility shows that the larger the axial pressure, the stronger the collapsibility of soil, and the higher the water content corresponding to the extreme value of collapsibility coefficient. In addition, taking into account the apparent phenomena during the sample preparation, the collapsibility mechanism of various types of soil is discussed from the perspectives of clay content and water-binding capacity of soil particles, for cyan-gray volcanic ash, the main cause of collapsibility is the structural damage caused by soil encountering water; for grayish-yellow silty clay, as its particles have the strong water-binding capacity and form skeleton particles with good water resistance after water, the soil collapsibility is weak after the soil is completely infiltrated; for brownish-yellow silty clay, the skeleton particles formed by water have poor water resistance due to their weak water binding capacity and exhibit strong collapsibility after the soil is fully saturated.
3) Soil collapsibility and groundwater erosion are the important causes of ground fissures and uneven surface settlement; this study infers that the causes of ground cracks in the Rift Valley are related to the settlement of overlying soil and the loss of soil particles. In the process of groundwater infiltration and outflow along bedrock cracks, the soil layer is affected by collapsibility and eroding at the same time, manifesting as a small amount of local settlement and loss of certain bearing capacity accompanied by structural damage. Meanwhile, soil particles are continuously lost along bedrock cracks, forming holes, further developing and penetrating. When the holes develop to a certain scale, the overlying soil loses its bearing capacity, and a hole first appears on the surface. As the holes continuously developed and penetrated, further instability and collapse form uneven settlement and ground fissures. During the rainy season, it is scoured by surface rainwater and then develops into gullies or ditches. Subsequently, the author will analyze the influence of groundwater erosion on ground fissures and uneven surface settlement through further experiments.

DATA AVAILABILITY STATEMENT

The original contributions presented in the study are included in the article/**Supplementary Material**, further inquiries can be directed to the corresponding author.

AUTHOR CONTRIBUTIONS

XL provided the background conditions for the research. ZZ contributed to the conception of the study and the materials needed for the experiments. designed and completed the series of experimental works. BH and YL processed and analyzed the results. BH wrote the first draft of the manuscript. YL enriched the manuscript and improved the quality of all the images. ZZ revised and embellished the language, and LJ revised the overall framework and format of the manuscript. All authors read and approved the submitted version.

ACKNOWLEDGMENTS

The author is grateful for the financial support for the study presented in this article from the National Natural Science Foundation of China (Grant Nos U1839202 and U2039208).

SUPPLEMENTARY MATERIAL

The Supplementary Material for this article can be found online at: https://www.frontiersin.org/articles/10.3389/feart.2022.909102/full#supplementary-material

REFERENCES

Ayalew, L., Yamagishi, H., and Reik, G. (2004). Ground Cracks in Ethiopian Rift Valley: Facts and Uncertainties. *Eng. Geol.* 75 (3–4), 309–324. doi:10.1016/j.enggeo.2004.06.018

Budhu, M. (2011). Earth Fissure Formation from the Mechanics of Groundwater Pumping. *Int. J. Geomech.* 11, 1–11. doi:10.1061/(asce)gm.1943-5622.0000060

Conway, B. D. (2015). Land Subsidence and Earth Fissures in South-Central and Southern Arizona, USA. *Hydrogeol. J.* 24 (3), 649–655. doi:10.1007/s10040-015-1329-z

Elahe, J., Philip, J., Vardon, S. C., and Steele, D. (2020). The Impact of Evaporation Induced Cracks and Precipitation on Temporal Slope Stability. *Comput. Geotechnics* 122, 103506. doi:10.1016/j.compgeo.2020.103506

Feng, D., Hou, E. K., Xie, X. S., and Che, X. Y. (2022). Prediction and Treatment of Water Leakage Risk Caused by the Dynamic Evolution of Ground Fissures in Gully Terrain. *Front. Earth Sci.* 3, 1–12. doi:10.3389/feart.2021.803721

Fergason, K. C., Rucker, M. L., and Panda, B. B. (2015). Methods for Monitoring Land Subsidence and Earth Fissures in the Western USA. *Proc. IAHS* 372, 361–366. doi:10.5194/piahs-372-361-2015

Gabrielli, C. P., Mcdonnell, J. J., and Jarvis, W. T. (2011). The Role of Bedrock Groundwater in Rainfall-Runoff Response at Hillslope and Catchment Scales. *J. Hydrol.* 450-451 (15), 117–133. doi:10.1016/j.jhydrol.2012.05.023

Howard, K. W. F., and Zhou, W. (2019). Overview of Ground Fissure Research in China. *Environ. Earth Sci.* 78 (3), 97. doi:10.1007/s12665-019-8114-6

Jia, Z., Lu, Q., Peng, J., Qiao, J., Wang, F., Wang, S., et al. (2020). Analysis and Comparison of Two Types of Ground Fissures in Dali County in the Weihe Basin, China. *Environ. Earth Sci.* 79 (1), 38. doi:10.1007/s12665-019-8783-1

Jin, W.-z., Luo, Z.-j., and Wu, X.-h. (2016). Sensitivity Analysis of Related Parameters in Simulation of Land Subsidence and Ground Fissures Caused

by Groundwater Exploitation. *Bull. Eng. Geol. Environ.* 75 (3), 1143–1156. doi:10.1007/s10064-016-0897-z

Leng, X. L., Wang, C., Zhang, J., Sheng, Q., Cao, S. L., and Chen, J. (2021). Deformation Development Mechanism in a Loess Slope with Seepage Fissures Subjected to Rainfall and Traffic Load. *Front. Earth Sci.* 9, 769257. doi:10.3389/feart.2021.769257

Leonard, R. J. (1929). An Earth Fissure in Southern Arizona. *J. Geol.* 37, 765–774. doi:10.1086/623676

Liu, H., Deng, K., Lei, S., and Bian, Z. (2015). Mechanism of Formation of Sliding Ground Fissure in Loess Hilly Areas Caused by Underground Mining. *Int. J. Min. Sci. Technol.* 25 (4), 553–558. doi:10.1016/j.ijmst.2015.05.006

Liu, N., Feng, X., Huang, Q., Fan, W., Peng, J., Lu, Q., et al. (2019). Dynamic Characteristics of a Ground Fissure Site. *Eng. Geol.* 248, 220–229. doi:10.1016/j.enggeo.2018.12.003

Nina, L., Xiao, F., Huang, Q. B., Wen, F., Peng, J. B., and Lu, Q. Z. (2019). Dynamic Characteristics of a Ground Fissure Site. *Eng. Geol.* 248, 220–229. doi:10.1016/j.enggeo.2018.12.003

Peng, J., Sun, X., Lu, Q., Meng, L., He, H., Qiao, J., et al. (2020). Characteristics and Mechanisms for Origin of Earth Fissures in Fenwei Basin, China. *Eng. Geol.* 266, 105445. doi:10.1016/j.enggeo.2019.105445

Sarkar, I. (2004). The Role of the 1999 Chamoli Earthquake in the Formation of Ground Cracks. *J. Asian Earth Sci.* 22 (5), 529–538. doi:10.1016/s1367-9120(03)00093-2

Shao, S. J., Wang, L. Q., Hu, T., and Wang, Q. (2014). Structural Index of Loess and its Relation with Granularity, Density and Humidity. *J. Geotechnical Eng.* 36 (8), 1387–1393. doi:10.11779/CJGE201408002

Timothy, G. C., Jung, H. K., George, P. M., Jae, K. K., Benedikt, H., and Apostolos, S. P. (2016). Effects of Tectonic Regime and Soil Conditions on the Pulse Period of Near-Fault Ground Motions. *Soil Dyn. Earthq. Eng.* 80, 102–118. doi:10.1016/j.soildyn.2015.09.011

Wadge, G., Biggs, J., Lloyd, R., and Kendall, J. M. (2016). Historical Volcanism and the State of Stress in the East African Rift System. *Front. Earth Sci.* 4, 86. doi:10.3389/feart.2016.00086

Wang, D. W., Liu, D., and Zhou, Z. G. (2019). Ground Fissure Characteristics of Great Rift Valley in Kenya and Railway Construction Countermeasure, China. *Subgr. Eng.* 4, 233–239. doi:10.13379/j.issn.1003-8825.2019.04.46

Wang, F., Peng, J., Chen, Z., Wang, Q., Meng, Z., Qiao, J., et al. (2020). Development Characteristics and Mechanisms of Damage-Causing Urban Ground Fissures in Datong City, China. *Eng. Geol.* 271, 105605. doi:10.1016/j.enggeo.2020.105605

Xu, L., Li, S., Cao, X., Somerville, I. D., Suo, Y., Liu, X., et al. (2016). Holocene Intracontinental Deformation of the Northern North China Plain: Evidence of Tectonic Ground Fissures. *J. Asian Earth Sci.* 119 (1), 49–64. doi:10.1016/j.jseaes.2016.01.003

Youssef, A. M. (2013). Overview of Some Geological Hazards in the Saudi Arabia. *Environ. Earth Sci.* 70 (31), 15–30. doi:10.1007/s12665-013-2373-4

Youssef, A. M., Sabtan, A. A., Maerz, N. H., and Zabramawi, Y. A. (2014). Earth Fissures in Wadi Najran, Kingdom of Saudi Arabia. *Nat. Hazards.* 71 (3), 2013–2027. doi:10.1007/s11069-013-0991-5

Zhang, J. R., Hu, Y., Yu, H. L., and Tao, G. L. (2015). Predicting Soil-Water Characteristic Curve from Multi-Fractal Particle-Size Distribution of Clay. *J. Hydraulic Eng.* 46 (6), 650–657. doi:10.13243/j.cnki.slxb.20141323

Zhou, X. X., Chi, S. C., Jia, Y. F., and Shao, X. Q. (2020). A New Wetting Deformation Simulation Method Based on Changes in Mechanical Properties. *Comput. Geotechnics* 117, 10326. doi:10.1016/j.compgeo.2019.103261

Conflict of Interest: The authors declare that the research was conducted in the absence of any commercial or financial relationships that could be construed as a potential conflict of interest.

Publisher's Note: All claims expressed in this article are solely those of the authors and do not necessarily represent those of their affiliated organizations, or those of the publisher, the editors, and the reviewers. Any product that may be evaluated in this article, or claim that may be made by its manufacturer, is not guaranteed or endorsed by the publisher.

Copyright © 2022 Hao, Zhou, Li, Li and Jin. This is an open-access article distributed under the terms of the Creative Commons Attribution License (CC BY). The use, distribution or reproduction in other forums is permitted, provided the original author(s) and the copyright owner(s) are credited and that the original publication in this journal is cited, in accordance with accepted academic practice. No use, distribution or reproduction is permitted which does not comply with these terms.

frontiers | Frontiers in Earth Science

ORIGINAL RESEARCH
published: 01 July 2022
doi: 10.3389/feart.2022.930130

A Comparative Study of Six Hybrid Prediction Models for Uniaxial Compressive Strength of Rock Based on Swarm Intelligence Optimization Algorithms

Yu Lei, Shengtao Zhou, Xuedong Luo, Shuaishuai Niu and Nan Jiang*

Faculty of Engineering, China University of Geosciences, Wuhan, China

Uniaxial compressive strength (UCS) is a significant parameter in mining engineering and rock engineering. The laboratory rock test is time-consuming and economically costly. Therefore, developing a reliable and accurate UCS prediction model through easily obtained rock parameters is a good way. In this paper, we set five input parameters and compare six hybrid models based on BP neural network and six swarm intelligence optimization algorithms–bird swarm algorithm (BSA), grey wolf optimization (GWO), whale optimization algorithm (WOA), seagull optimization algorithm (SOA), lion swarm optimization (LSO), firefly algorithm (FA) with the accuracy of two single models without optimization–BP neural network and random forest algorithm. Finally, the above eight models were evaluated and compared by root mean square error (RMSE), mean absolute percentage error (MAPE), coefficient of determination (R^2), and a10 index to obtain the most suitable prediction model. It is indicated that the best prediction model is the FA-BP model, with a RMSE value of 4.883, a MAPE value of 0.063, and a R^2 of 0.985, and an a10 index of 0.967. Furthermore, the normalized mutual information sensitivity analysis shows that point load strength is the most effective parameters on the UCS, respectively.

Keywords: uniaxial compressive strength, rock, BP neural network, swarm intelligence optimization algorithm, normalized mutual information

OPEN ACCESS

Edited by:
Guang-Liang Feng,
Institute of Rock and Soil Mechanics (CAS), China

Reviewed by:
Quan Jiang,
Institute of Rock and Soil Mechanics (CAS), China
Renguo Gu,
South China University of Technology, China
Yi Luo,
Wuhan University of Technology, China

****Correspondence:***
Xuedong Luo
cugluoxd@foxmail.com

Specialty section:
This article was submitted to Geohazards and Georisks, a section of the journal Frontiers in Earth Science

Received: *27 April 2022*
Accepted: *23 May 2022*
Published: *01 July 2022*

Citation:
Lei Y, Zhou S, Luo X, Niu S and Jiang N (2022) A Comparative Study of Six Hybrid Prediction Models for Uniaxial Compressive Strength of Rock Based on Swarm Intelligence Optimization Algorithms. Front. Earth Sci. 10:930130. doi: 10.3389/feart.2022.930130

INTRODUCTION

Uniaxial compressive strength is an important metric in rock mechanics and rock engineering, particularly in the evaluation of rock slope stability, tunneling design, and ore mining. On the other hand, the laboratory UCS test is time-consuming and costly. Many predict approaches have been offered to acquire the UCS quickly and cheaply.

The association between the physical and mechanical properties of rock samples and the UCS should be studied before the UCS can be predicted. Previous studies have found that a lot of rock parameters such as porosity, longitudinal wave velocity, point load strength, density, block impulse index (BPI), Young's modulus, Schmidt hammer rebound number were correlated with UCS (Bieniawski, 1978; Barton et al., 1980; Nicholson and Bieniawski, 1990; Mitri et al., 1994; Hoke and Brown, 1997; Barton, 2002; Tsiambaos and Sabatakakis, 2004; Hao et al., 2018; Shan and Lai, 2018; He et al., 2019). After determining the parameters that are closely related to UCS, scholars usually use the empirical equation prediction method and machine learning methods to predict the UCS by these parameters.

When using the empirical equation to predict the UCS, scholars selected one or more parameters of rock samples and fit the statistical relationship between them and UCS. Part of scholars choose a single parameter and make predictions through different types of empirical equations. Leite and Ferland (2001) took the porosity as the input variable, carried out the linear fitting between the porosity and UCS, and found that the porosity and UCS were negatively correlated. Lashkaripour (2002) investigated the relationship between the porosity and the UCS by the exponential function, a similar conclusion was obtained with Leite and Ferland. Yasar and Erdogan (2004) conducted linear fitting on the longitudinal wave velocity and UCS. Yılmaz and Sendır (2002) fitted the Schmidt hammer rebound number and UCS with a function combining logarithmic function and linear function and obtained a reliable UCS prediction equation. Broch and Franklin (1972) corrected the size of rock samples to obtain the point load strength, established a linear function between the point load strength and UCS, and found that these two parameters are closely related. Ulusay and Gokceglu. (1998) developed a block impulse index test device, using the BPI as a parameter to indirectly evaluate UCS, and fitting it with a power function. Yagiz (2011) found that the slake durability index could be selected as an input variable for predicting UCS. Moreover, some scholars choose a variety of rock parameters to conduct this work. Sachpazis (1990) tested the UCS, Young's modulus, and Schmidt hammer rebound number and established a regression equation between the three. Kayabasi et al. (2003) thought UCS was related to RQD value, Young's modulus, and weathering degree of rock samples, and fit these three parameters and UCS, and the established a regression equation could meet the requirement. On the whole, the fitting equation proposed with the traditional statistical methods could meet the needs of projects.

With the development of advanced artificial intelligence methods, various non-linear UCS prediction models have been established. In these models, several physical and mechanical parameters of rock samples are usually chosen at the same time as the input variables. Through tensile strength, point load strength, and Young's modulus, Armaghani et al. (2015) used the multiple regression analysis (MRA) and an adaptive neuro-fuzzy inference system (ANFIS) to obtain the UCS. Meulenkamp and Grima. (1999) used Young's modulus, porosity, and density to predict UCS by the artificial neural network, and accurate prediction results were obtained. By using longitudinal BPI, Schmidt hammer rebound number, and wave velocity, point load index, Mishra and Basu et al. (2013) predicted the UCS with the farthest candidate selection model. The results indicated that Schmidt hammer rebound number and point load strength are excellent input variables. However, in the UCS prediction of shale, the longitudinal wave velocity is not a suitable input parameter. Rezaei et al. (2012) selected three parameters of density, Schmidt hammer rebound number, and porosity as the input variables, then the UCS was predicted by the fuzzy inference system (FIS). As a result, the predicted values were quite close to the laboratory-measured values. Furthermore, in this study, the sensitivity analysis showed that the Schmidt hammer rebound number was the best input variable among them. Mahmoodzadeh et al. (2021) chose long short term memory, deep neural networks, K-nearest neighbor, decision tree, and support vector regression to predict the UCS, and these models all got good prediction results. Even if these single prediction models could effectively predict the UCS, combined optimization algorithms are gradually being applied. Majdi and Beiki. (2010) established a genetic algorithm-optimized artificial neural network model to predict the UCS with density, RQD value, and porosity. The predicted results showed that better results could be obtained by the optimized model. Although the selected input variables are different, Mohamad et al. (2015) and Momeni et al. (2015) both employed the artificial neural network (ANN) combined with the particle swarm optimization (PSO) for the UCS prediction, the predicted results show that the optimized artificial neural network could give better-predicted values than before. On the basis of BPI, point load strength, Schmidt hammer rebound number, and longitudinal wave velocity, Xue and Wei (2020) compare the predicted results of least-squares support vector machine (LSSVM) optimized by genetic algorithm, ANFIS, FIS, and ANN. The optimized models' accuracy is superior to the other three single models, according to the anticipated outcomes. Compared with the empirical equation prediction method, the prediction models established through different artificial intelligence algorithms have better performance in UCS prediction.

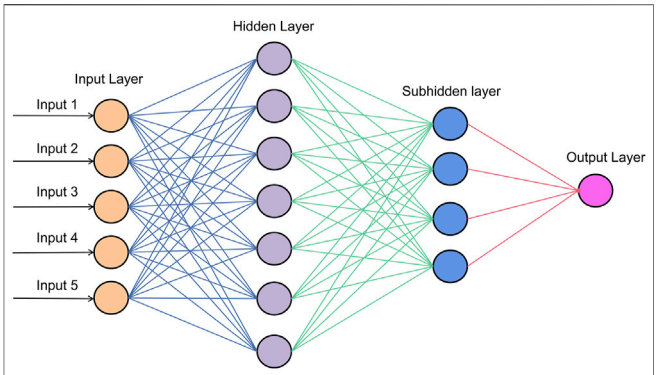


FIGURE 1 | Schematic representation of the topology of a BP neural network.

Although models built by artificial intelligence algorithms have found many applications in predicting UCS, its hybrid model building and the selection of input parameters still need to be refined. To find a suitable prediction algorithm and input parameters to predict UCS, in this paper, we selected five input parameters and used the six optimized BP neural networks with different swarm intelligence algorithms to predict the UCS, and evaluated the models through multiple evaluation indexes to find the optimal UCS prediction model. The findings of the study may be used as a reference to determine UCS quickly.

BASIC CONCEPTS AND ALGORITHMS OF PREDICT MODELS

BP Neural Network

The input layer, middle layers, and output layer make up a BP neural network, with all neurons in the input and middle layers and the output layer linked. It is worth noting that neurons in the

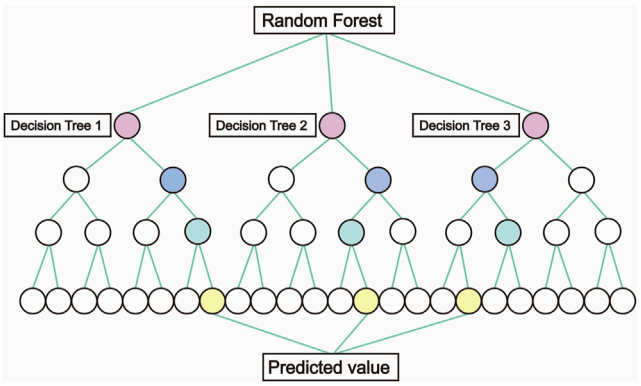


FIGURE 2 | Schematic diagram of the random forest structure.

same layer are not linked. (Yan and Zeng, 2013). The topology of a BP neural network is shown in **Figure 1**. Through learning the input data, BP neural networks could establish a mapping relationship between input and output data, which leads to this method being used in multivariate non-linear system analysis.

Random Forest Algorithm

Leo Breiman (2001) invented the Random Forest (RF) method, which is a classic machine learning approach, which integrates multiple decision trees through integration learning (Bureau et al., 2010). Decision tree is a tree-like structure **Figure 2** in which any internal node represents an attribute test. Each branch in decision tree represents an output result, and each leaf node represents a type. Within the integrated learning, multiple classifiers are generated, each classifier conducts learning and prediction without interfering and finally synthesizing a single prediction. The most widely used algorithms in integrated learning are the bagging algorithm and the boosting algorithm.

More explanations regarding the FA algorithm can be found in the literature (Yu et al., 2020a; Yu et al., 2020b; Yin et al., 2022).

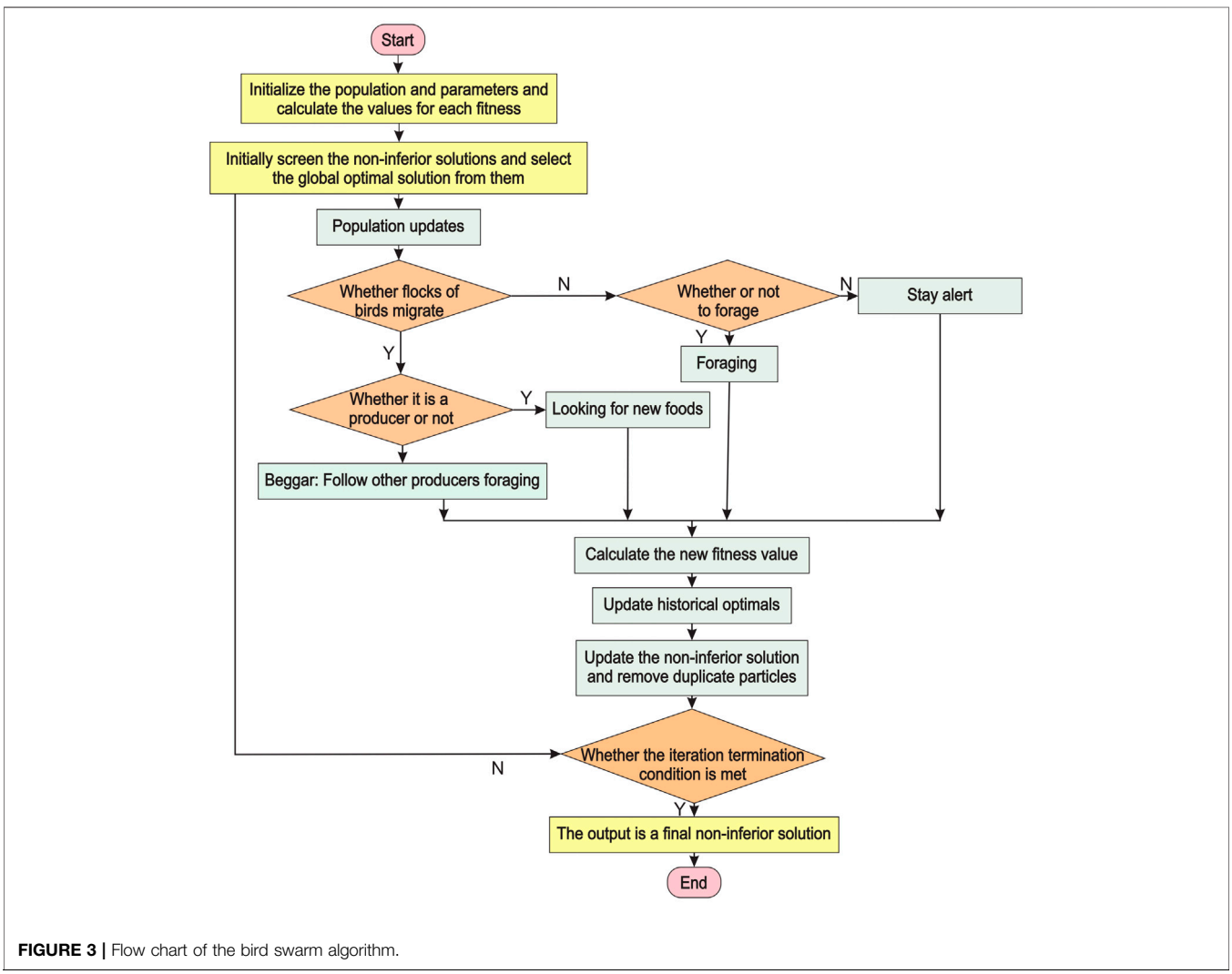


FIGURE 3 | Flow chart of the bird swarm algorithm.

Bird Swarm Algorithm

Bird is one of the flocking animals, and there are behaviors such as foraging, vigilance, and flight in their life (Meng et al., 2014). Bird swarm algorithm (BSA) is proposed inspired by these behaviors of birds. These community behaviors may be mimicked, and the swarm's state of foraging, vigilance, and flight could be changed using precise rules. The analogous equation while the swarm is foraging is as follows:

$$x_{i,j}^{t+1} = x_{i,j}^{t} + rand(0,1) \times C \times \left(p_{i,j} - x_{i,j}^{t}\right) + rand(0,1) \times S \times \left(g_j - x_{i,j}^{t}\right) \tag{1}$$

Where j is a positive integer between 1 and D, *rand* (0,1) is a uniformly distributed random number between 0 and 1, C is the cognitive acceleration factor, S is the social acceleration factor, and both C and S are positive integers, $P_{i,j}$ is the previous optimal position of the i_{th} bird, and g_j represents the previous optimal position in the swarm.

When the swarm is alert, each bird tries to get closer to the swarm's center. However, there is competition between every bird so that each bird does not move directly towards the swarm center. The flow chart of the BSA is shown in **Figure 3**. More explanations regarding the BSA algorithm can be found in the literature (Meng et al., 2015; Miramontes et al., 2018; Varol Altay and Alatas, 2019).

Grey Wolf Optimization

Grey wolf optimization (GWO) is a new meta-heuristic algorithm inspired by the grey wolf population's social structure. (Mirjalili and Lewis. 2016). There are four different types of grey wolves, α, β, Δ, and ω, in the social hierarchy. The α wolf has the highest status, followed by the β wolf, then the Δ wolf, and the lowest rank is the ω wolf. Moreover, Hunting behavior is divided into three steps–locking for prey, surrounding the prey, and attacking the prey (Kishor and Singh, 2016).

In the beginning, the wolves approach the prey by stalking and chasing. Then a group of grey wolves will surround the prey until the prey stops moving. Finally, they attack the prey. The behaviors of a wolf population could be defined as:

$$\vec{D}_G = \left|\vec{C}_G.\vec{X}_{PG}(t_G) - \vec{X}_G(t_G)\right| \tag{2}$$

$$\vec{X}_G(t+1) = \vec{X}_{PG}(t) - \vec{A}_G.\vec{D}_G \tag{3}$$

Where $\vec{D}_G$ is the distance between the wolf and the prey, $\vec{X}_{PG}$ is the prey position vector, $\vec{X}_G$ is the position vector of the grey wolf, t_{G} is the number of current iterations, $\vec{A}_G$ and $\vec{D}_G$ are the coefficient vectors. For a complete detail of the GWO algorithm, the readers can refer to the study conducted by Yu et al. (2019) and Yu et al. (2020c).

Whale Optimization Algorithm

Whales tend to hunt little fish at the surface of the ocean. Their feeding journey is a unique spiral upward path with many distinctive bubbles (Mirjalili and Lewis, 2016). There are three common behaviors in whales, searching for prey, surrounding prey, and hunting in the whale optimization algorithm (WOA).

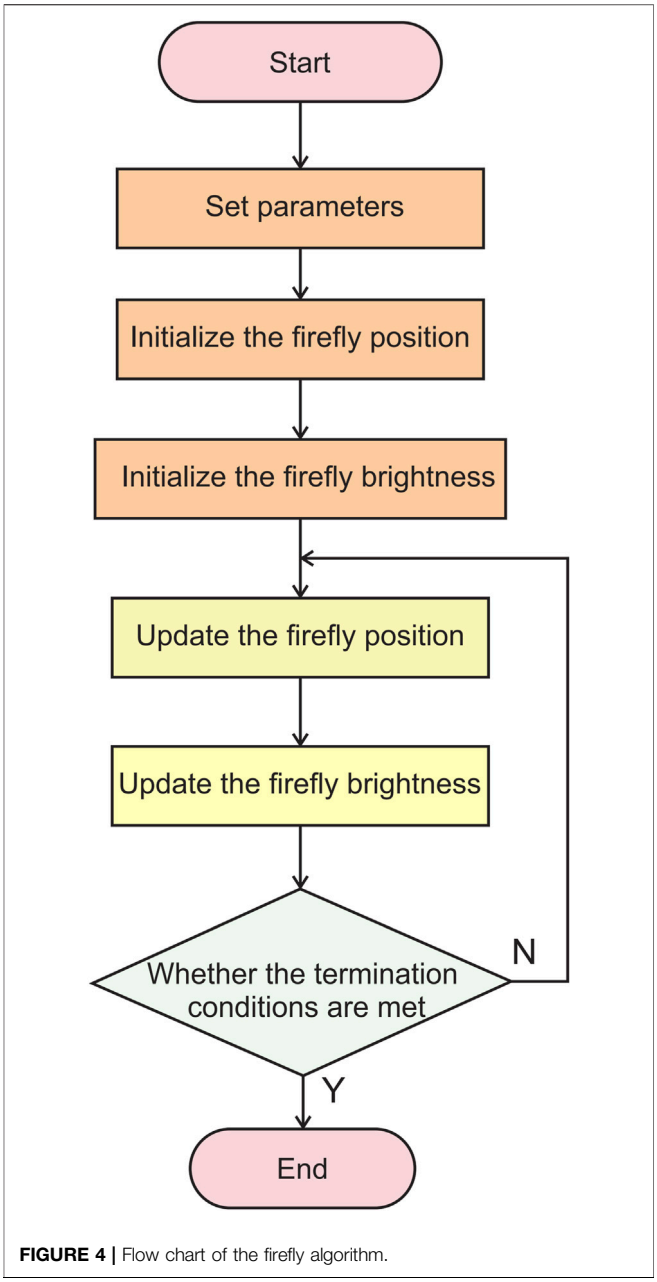


FIGURE 4 | Flow chart of the firefly algorithm.

Before hunting the prey, when $\vec{A}_W$ is greater than 1 or less than −1, the whale in the group randomly selects prey referring to each other's positions so that the global search ability would be improved, this behavior could be written as:

$$\vec{D}_W = \left|\vec{C}_W.\vec{X}_{\text{rand}}(t_W) - \vec{X}_W(t_W)\right| \tag{4}$$

$$\vec{X}_W(t_W+1) = \vec{X}_{\text{rand}}(t_W) - \vec{A}_W \cdot \vec{D}_W \tag{5}$$

Where $\vec{X}_{\text{rand}}$ is the randomly chosen location variable for the current whale population, $\vec{D}_W$ is the distance between the whale and the prey; $\vec{X}_W$ is the position vector of the optimal solution, t_{W} is the number of current iterations, $\vec{A}_W$ and $\vec{C}_W$ are both the

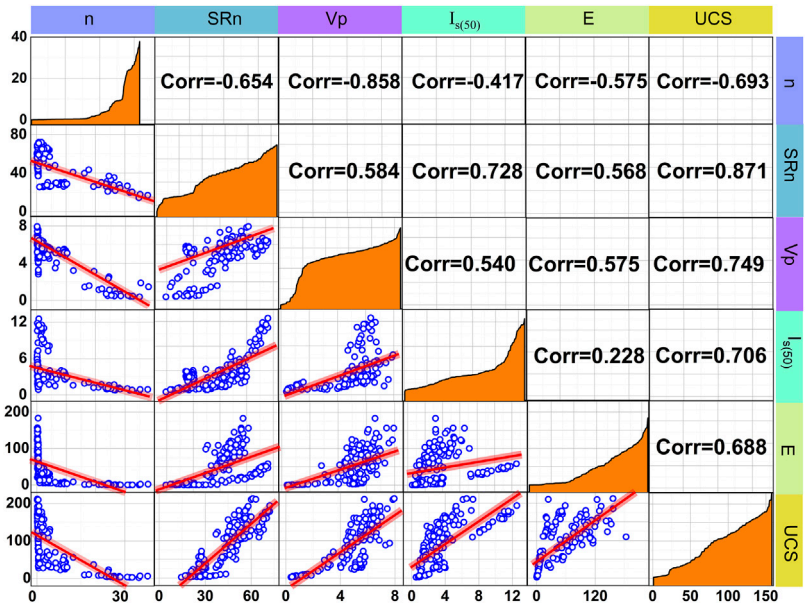


FIGURE 5 | Data matrix.

coefficient vectors. For more details, equations and implementation process of the WOA can be referred tothe published studies in literature (Aljarah et al., 2016; Mirjalili and Lewis, 2016; Mafarja and Mirjalili, 2017).

Seagull Optimization Algorithm

Migrating and feeding are the most essential characteristics of seagulls, and the seagull optimization method is based on these activities. To avoid colliding, each bird is at a distinct place. Seagulls may fly towards the direction of the best landing spot. Seagull groups maneuver in a spiral manner when hunting for prey. (Dhiman and Kumar, 2019).

To avoid colliding with other seagulls as they migrate, the new position of the seagull might be determined using the additional variable A as follows:

$$C_s(t_s) = A \times P_s(t_s) \tag{6}$$

Where C_s is a new position that is not in conflict with other seagulls, P_s is the seagull's present location, t_s is the current iteration. A reflects the seagull's movement behavior in the given search space, and it may be calculated as:

$$A = f_c - [t_s \times (f_c / MAX_{\text{iteration}})] \tag{7}$$

Where f_c is the frequency of the control variable A, with a value linearly decreasing from 2 to 0. To have a better understanding regarding the SOA optimization technique, other studies in literature can be considered (Dhiman and Kumar, 2019; Dhiman et al., 2020; Panagant et al., 2020).

Lion Swarm Optimization

Lion swarm optimization is a new intelligence optimization algorithm proposed to simulate lion hunting. There are three types of lions in the population: lion king, lioness, and young lion. The update of their position follows different rules. The algorithm initializes the lion pride positions. Similar to other swarm intelligence optimization algorithms, the parameters in LSO need to be initialized before optimization starts (Yazdani and Jolai, 2016).

The lion king travels in a small area around the best prey during hunting, and the corresponding position update equation is:

$$X_{\text{m}}^{t_L+1} = g^{t_L}\left(1 + \gamma\left(p_{\text{m}}^{t_L} - g^{t_L}\right)\right) \tag{8}$$

Where X_{m} is the update position of the lion king, γ is a random number that fits a normal distribution between N (0,1); g^{t_L} is the population optimal solution in the t_{Lth} iteration; and $p_{\text{m}}^{t_L}$ is the historical optimal solution for the m_{th} individual in the t_{Lth} iteration.

Through collaborative hunting, lionesses catch their prey, and this behavior can be described as:

$$X_i^{t_L+1} = \frac{P_i^{t_L} + P_c^{t_L}}{2}\left(1 + \alpha_f \gamma\right) \tag{9}$$

Where X is the position of the lioness moving, $P_c^{t_L}$ is the historical optimal solution for a randomly selected predation partner in the lioness' pride during the t_L iteration; α_f is the lioness' range perturbation factor, which mainly affects the lioness' range of movement so that the lioness can search for prey at a larger range and reduce the enclosure after finding prey. A complete version of the LSO optimization algorithm can be seen in previous work (Yazdani and Jolai, 2016).

Firefly Algorithm

Firefly algorithm (FA) is a group search-based stochastic optimization algorithm. There are a few parameters in FA. No

TABLE 1 | Rock sample data.

No.	Type	Location	Porosity (%)	SRn	V_P (km/s)	Is(50)(MP)	E (GPa)	UCS (MPa)
1	Granite	Malaysia	0.39	47	5.506	2.31	92.9	117.9
2	Granite	Malaysia	0.44	38	6.45	2.87	108.8	122.3
3	Granite	Malaysia	0.25	45	5.95	3.12	78.4	124.7
4	Travertine	Haji	3.35	27.42	5.66	3.00	11.45	63.68
5	Travertine	Haji	9.35	27.38	5.38	2.86	8.03	47.46
6	Travertine	Haji	8.14	30.13	5.09	3.63	6.15	37.89
7	Caliche	Adana area	28.12	28.00	0.68	1.13	0.55	5.63
8	Caliche	Adana area	28.44	25.00	0.49	0.97	0.19	3.37
9	Caliche	Adana area	21.00	28.00	1.15	1.25	0.88	7.85
.....	.....	.....	.....	.....	.....	.....	.....	.....
153	Sandstone	Southern Anatolia	2.32	52.00	4.75	3.30	18.10	122.00
154	Limestone	Southern Anatolia	0.66	59.00	5.84	2.20	15.90	112.00
155	Granite	Çatalca	0.20	67.00	6.37	10.58	45.09	165.79
156	Granite	Kapidağ	0.71	72.00	6.36	12.53	58.50	193.33
157	Granite	Kapidağ	0.21	69.00	6.69	11.83	51.20	175.49
158	Tonalite	Gönen	1.70	68.00	5.84	10.77	48.61	157.62

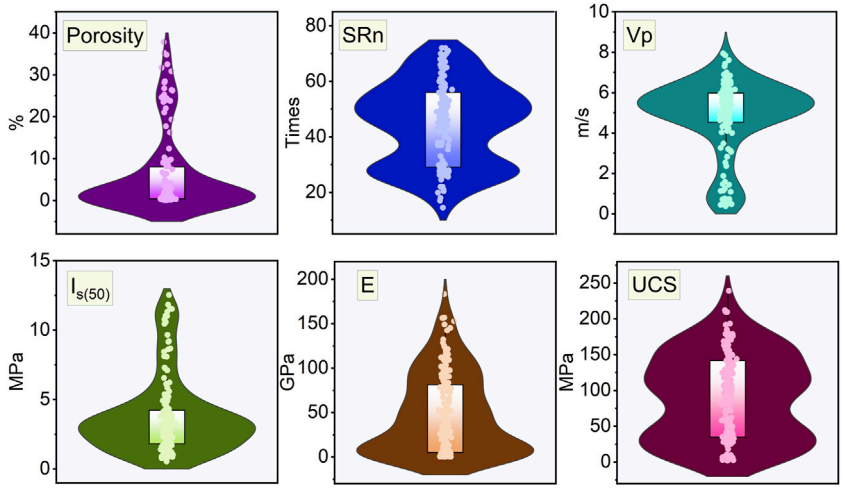


FIGURE 6 | Data violin plot.

complex operations such as variation and crossover, and the corresponding flow chart is shown in **Figure 4**.

There are two pivotal parameters in this method–light intensity and attractiveness (Gandomi et al., 2011).

The light intensity function can be described as:

$$I\left(r_{ij}\right) = I_0 e^{-\gamma r_{ij}^2} \tag{10}$$

Where I_0 is the initial light intensity of the firefly, r is the distance between two fireflies, γ is defined as the light intensity absorption coefficient, which could describe light lost in the propagation.

If two fireflies i and j are located at $\vec{X}_{iF}$ and $\vec{X}_{jF}$, respectively, the distance between them can be calculated through Euclidean distance as:

$$r_{ij} = \left\| \vec{X}_{iF} - \vec{X}_{jF} \right\| = \sqrt{\sum_{k=1}^{D} \left(X_{ik} - X_{jk} \right)^2} \tag{11}$$

Where D is the spatial dimension of the solution problem, X_{ik} is the coordinates of the i_{th} firefly in the k_{th} dimension.

The attractiveness of FA diminishes monotonically as the distance between them increases, and the attractiveness function $\beta(r)$ could be defined as.

$$\beta(r) = \beta_0 e^{-\gamma r^2} \tag{12}$$

Where β_0 is the attraction at the light source. A complete version of the FA optimization algorithm can be seen in previous works (Fister et al., 2013; Gandomi et al., 2013).

TABLE 2 | Initial parameters for hybrid model optimization.

Algorithm	Parameters	Value	Optimal parameters
BSA	a1	1	num_boosting_rounds = 2517
	a2	1	
	c	1	
	S	1	eta=0.0394
	FQ	5	
	N	20	
GWO	Convergence constant a	[2,0]	num_boosting_rounds = 2612 eta=0.0262
WOA	r	[0,1]	num_boosting_rounds = 2371
	a	[0,2]	eta=0.031
	b	1	
	l	[0,1]	
SOA	f_c	2	num_boosting_rounds = 795
	r_d	[0,1]	eta=0.031
LSO	γ	0.5	num_boosting_rounds = 2290
	α_f	0.4	eta=0.035
	α_c	0.4	
FA	γ	1	num_boosting_rounds = 262
	β_0	2	eta=0.021
	α	0.2	
	rand	0.98	

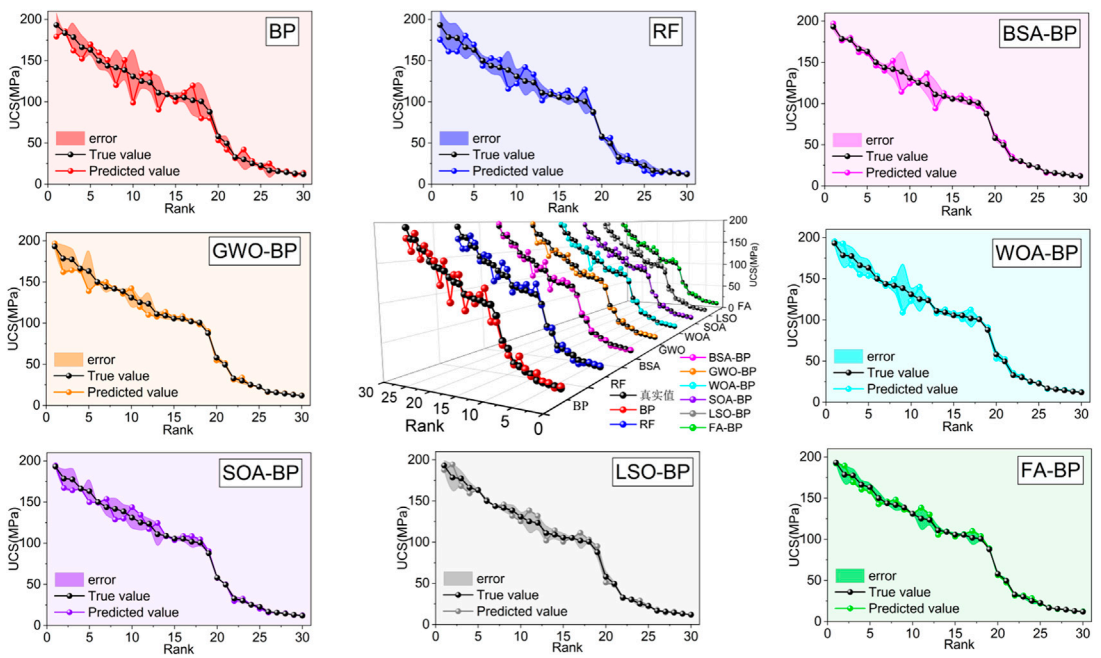


FIGURE 7 | Predicted vs. true values.

DATABASE AND DATA PRESENTATION

Selection of Input and Output Parameters

There are five input parameters–porosity, Schmidt hammer rebound number, longitudinal wave velocity, point load strength, Young's modulus, and one output parameter–the UCS in this paper. The first four input parameters could be obtained through non-destructive testing methods (Stroffek and Lesso, 2001; Liu et al., 2020). Moreover, the point load strength is easy to obtain in the field test. These five

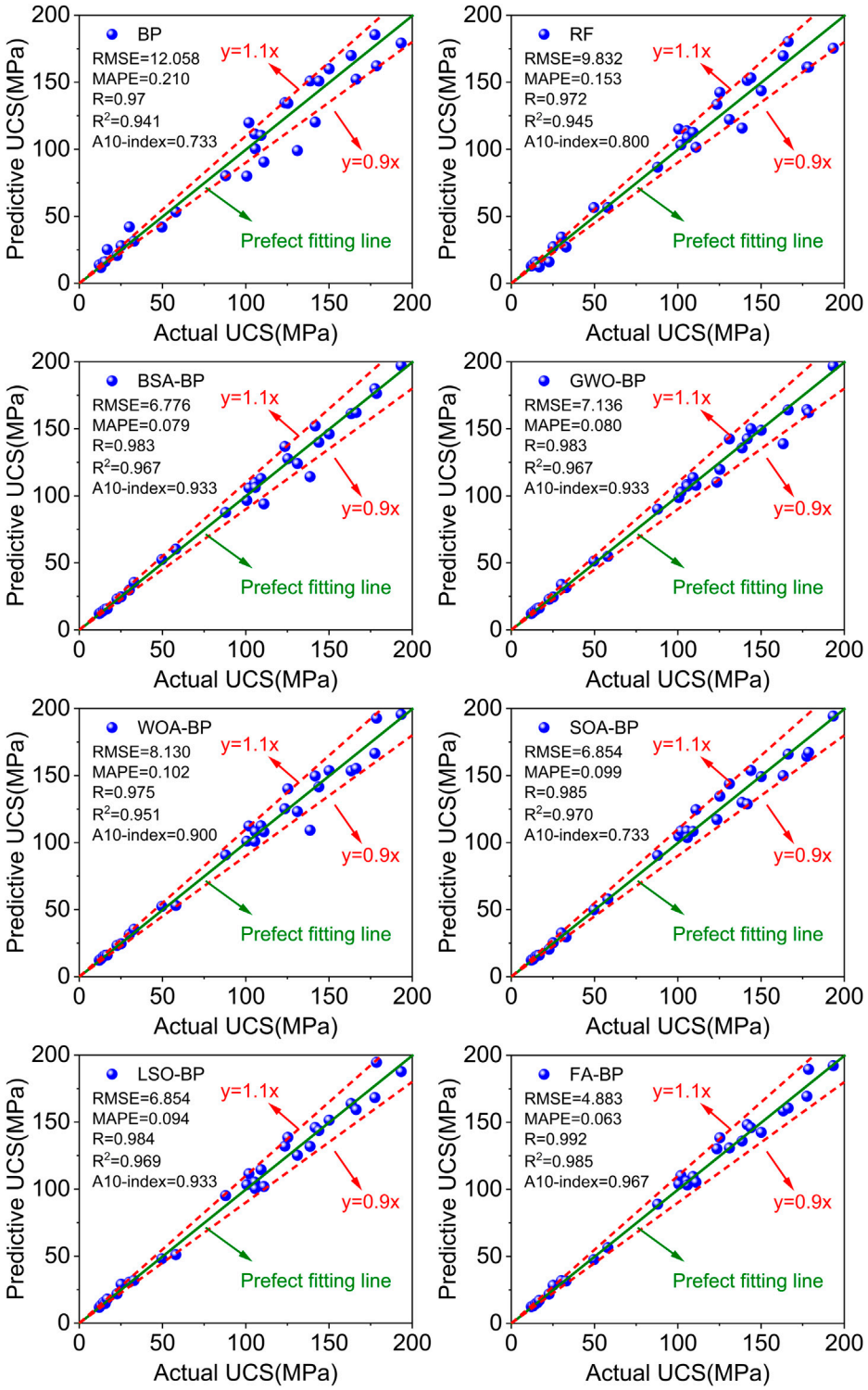


FIGURE 8 | Correlation analysis between predicted and actual values.

parameters have been used more often in many previous similar prediction models and are trustworthy parameters.

Database

The experimental data from the literature (Tugrul and Zarif, 1999; Dincer et al., 2008; Dehghan et al., 2010; Armaghani

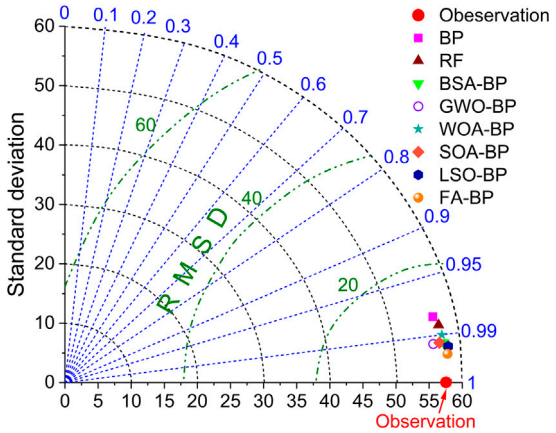


FIGURE 9 | Taylor diagrams for all prediction models.

et al., 2015) were collected to obtain the database in this paper, which includes a total of 158 test results, as shown in **Table 1**. Since the number of samples is too large, a matrix analysis plot is drawn to show the data (**Figure 5**), which examines the correlation between the input and output variables. It is indicated that there is a negative correlation between the porosity and the remaining four input variables. (The Corr in **Figure 5** means Pearson correlation coefficient). Moreover, longitudinal wave velocity, Schmidt hammer rebound number, point load strength, and Young's modulus are positively correlated with each other. To evaluate whether there are outliers in the data, a violin plot is drawn, as shown in **Figure 6**. The data we utilized in this study is evenly distributed. There are no obvious abnormal data in this database.

RESULT ANALYSIS

Parameters Initialization

Setting a proper ratio between the training samples and test samples in the dataset is significant. According to the Pareto principle, the training group number and the test group number should account for about 80% and 20% of the total samples (Forman and Peniwati, 1998; Yu et al., 2021). On the basis of this rule, in this study, the training group was set at 128 groups, accounting for 81%, and the test group was set at 30 groups, accounting for 19%. The initial parameters of the proposed six hybrid optimization models–SOA-BP, GWO-BP, WOA-BP, BSA-BP, LSO-BP and FA-BP are shown in **Table 2**.

Predicted Results

After using the eight models to predict the UCS values, the actual values and the predicted values are shown in **Figure 7**. It is found that there are some big errors in the BP and RF models. The predicted values related to these six hybrid models are closer to the actual values.

Evaluation Method of Prediction Models

To evaluate the predicted results of the mentioned eight models, four parameters–RMSE, MAPE, R^2, a10 index were introduced. RMSE is a machine learning metric that measures the difference between the predicted and real values. The prediction model's prediction effect improves as the RMSE decreases. (Barnston, 1992). RMSE could be calculated as:

$$RMSE = \sqrt{\sum_{i=1}^{N_0} (\hat{y}_i - y_i)^2 \Big/ N_0} \tag{13}$$

Where N_0 is the sample number in the test set, $\hat{y}_i$ is the predicted result and y_i is the actual value.

MAPE calculates the difference between the expected and actual value. MAPE has a range greater than or equal to 0. Once the MAPE is close to 0, it is indicated that the corresponding model has little errors. When MAPE is greater than 1, the model is called as inferior model (Bollen et al., 2011). MAPE could be calculated as follows:

$$MAPE = \frac{1}{N_0} \sum_{i=1}^{N_0} \left| \frac{\hat{y}_i - y_i}{y_i} \right| \times 100 \tag{14}$$

The coefficient of determination. When least squares are used for parameter estimation, R^2 is the ratio of explained sum of squares to sum of squares of deviations. And the larger the R^2 is, the more accurate the model is and the more significant the regression effect is. R^2 is a value between 0 and 1, where the closer it goes to 1, the better the model fits. It is generally considered that models with a R^2 over 0.8 are good. R^2 could be obtained as:

$$R^2 = 1 - \frac{\sum_{i=1}^{N_0} (y_i - \hat{y}_i)}{\sum_{i=1}^{N_0} (y_i - \bar{y}_i)} \tag{15}$$

Where $\bar{y}_i$ is the mean of predicted values.

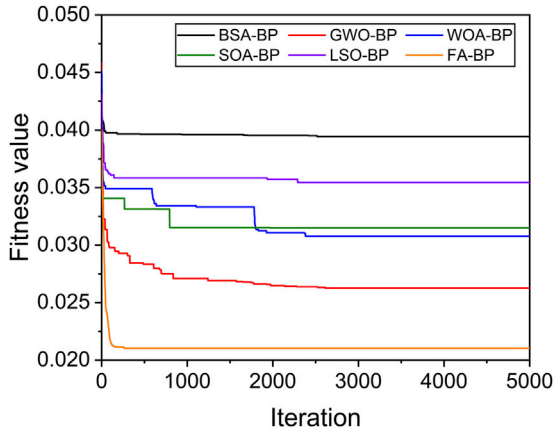


FIGURE 10 | Variations of fitness value with the number of iterations.

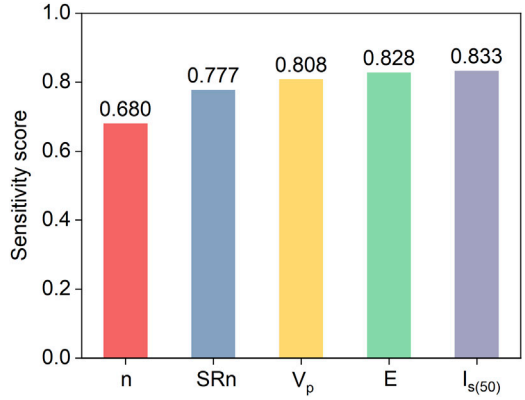


FIGURE 12 | Input volume sensitivity analysis diagram.

TABLE 3 | List of evaluation parameters.

	Model								
Training		RMSE	Score	MAPE	Score	R^2	Score	A10-index	Score
	BP	12.859	0.000	0.190	0.000	0.941	0.029	0.608	0.006
	RF	9.846	0.349	0.163	0.223	0.940	0.000	0.606	0.000
	BSA-BP	7.058	0.672	0.081	0.901	0.958	0.514	0.928	0.953
	GWO-BP	7.035	0.675	0.079	0.917	0.961	0.600	0.827	0.654
	WOA-BP	8.009	0.562	0.096	0.777	0.953	0.371	0.936	0.976
	SOA-BP	6.789	0.703	0.109	0.669	0.965	0.714	0.889	0.837
	LSO-BP	6.622	0.723	0.101	0.736	0.953	0.371	0.912	0.905
	FA-BP	4.228	1.000	0.069	1.000	0.975	1.000	0.944	1.000
Testing	BP	12.058	0.000	0.210	0.000	0.941	0.000	0.733	0.000
	RF	9.832	0.310	0.153	0.388	0.945	0.091	0.800	0.286
	BSA-BP	6.776	0.736	0.079	0.891	0.967	0.591	0.933	0.855
	GWO-BP	7.136	0.686	0.080	0.884	0.967	0.591	0.900	0.714
	WOA-BP	8.130	0.547	0.102	0.735	0.951	0.227	0.933	0.855
	SOA-BP	6.854	0.725	0.099	0.755	0.970	0.659	0.900	0.714
	LSO-BP	6.854	0.725	0.094	0.789	0.969	0.636	0.933	0.855
	FA-BP	4.883	1.000	0.063	1.000	0.985	1.000	0.967	1.000

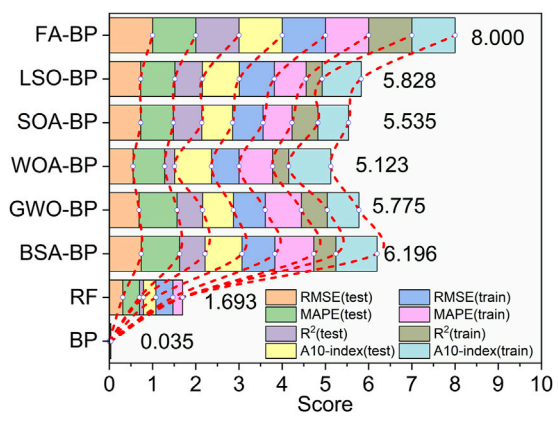


FIGURE 11 | Multiple model score graph.

a10 index is a novel index in statistics. It is the ratio of the number of scatter points falling between $\hat{y}_i = 0.9y_i$ and $\hat{y}_i = 1.1y_i$ to the total number of samples in the test set. a10 lies between 0 and 1. If the a10 is close to 1, the corresponding model is better. a10 can be calculated by the following equation (Cevik et al., 2011):

$$\text{a10} - \text{index} = \frac{m10}{M} \tag{16}$$

Where $m10$ is the number in test set falling between $\hat{y}_i = 0.9y_i$ and $\hat{y}_i = 1.1y_i$, M is the total number of samples in the test set.

Though the above four evaluate indexes, it is indicated that the FA-BP model is the best model in UCS prediction, with the RMSE of 4.883, a MAPE of 0.063, an R^2 of 0.985 and an a10 index of 0.967. The worst in the hybrid models was WOA-BP with the RMSE value of 8.130, the MAPE value of 0.102, the R^2 of 0.951, and the a10 index of 0.933. The other hybrid models all have an R^2 of 0.95

or higher, which shows that the hybrid models have better prediction results. On the contrary, the BP model had the RMSE value of 12.058, the MAPE value of 0.21, the R^2 of 0.941, and an a10 of 0.733. In the random forest, there are the RMSE value of 9.832, MAPE value of 0.153, R^2 of 0.945, and the a10 was 0.800. Their effects were all relatively poor. The relationship between the predicted and actual values was drawn in **Figure 8**. It could be seen in **Figure 8** that all points are distributed on both sides of the perfect fit line. The data points corresponding to the FA-BP model are closest to the perfect fit line, and the data points are the most discrete in the BP model.

To further evaluate the predict results of all prediction models, the Taylor diagrams were drawn to show the relevance of the standard deviation, root mean square error and correlation coefficient (Ciesielski et al., 2002), the relationship in these three parameters in Taylor diagrams could obtained by:

$$R = \frac{\frac{1}{Z}\sum_{1}^{Z}\left(l_n - \bar{l}\right)\left(m_n - \bar{m}\right)}{\sigma_l \sigma_m} \tag{17}$$

Where R is the correlation coefficient, Z is the number of discrete points, l_n and m_n is discrete variables, σ_1 and σ_m is the standard deviation of l and m, $\bar{l}$ and $\bar{m}$ are the means of σ_1 and σ_m, respectively.

All Taylor diagrams are listed in **Figure 9**, and all the fitness value curves with the increasing iterations were collected, as shown in **Figure 10**. It could be seen from **Figure 9** that the point corresponding to the FA-BP model is closest to the observation point in the 2D coordinates, indicating that this model has minimal prediction error. On the contrary, the point corresponding to the BP model is the furthest from the observation point, indicating that the prediction effect is poor. Moreover, the fitness curve corresponding to the FA-BP model decreases faster than that of other prediction models.

COMPREHENSIVE EVALUATION OF UCS PREDICTION MODELS

To further analyze and compare the prediction performance and algorithm stability of these six hybrid models and two single models, we scored and evaluated the evaluation metrics for each model training set and testing set. Within the widely used grading method, all evaluation indexes need to be ordered, and then graded (Yin et al., 2021). However, two similar values may be classified into different levels in this method. To avoid this condition, we only calculate the scores for each model. The same evaluation index of each model is normalized by the following equation (Rao et al., 2008):

$$y_i = \frac{x_i - \min_0}{\max_0 - \min_0} \tag{18}$$

Where y_i is the normalized value, x_i is one of the evaluation indexes, min_0 and max_0 are the minimum and maximum values of each evaluation index, respectively.

After the normalization, all normalized values are in the range of 0–1. Noting that the larger R^2 value and a10 index value represent better models. On the contrary, if RMSE and MAPE are smaller, the corresponding model is better. When calculating the evaluation score of these four evaluation indexes, the evaluation scores for RMSE and MAPE are the difference between 1 and their corresponding normalized values. For the R^2 value and a10 index value, the evaluation score is equal to their normalized values. By replacing the traditional simple grading method with this standardized evaluation index, the problem of excessive disparity between the scores of close evaluation parameters can be solved (Chen et al., 2013).

All the obtained evaluation scores according to the calculation procedures were listed in **Table 3** and **Figure 11**. As can be seen from **Table 3**, the scoring parameters of the training set and the testing set are relatively close in the same algorithm, which indicates that the algorithms are stable. Meanwhile, in order to better show the prediction effects of the eight algorithms, we accumulate the scores of the training and test sets of the algorithms to get the final scores of the algorithms, as shown in **Figure 11**. It is indicated from the evaluation results that the best prediction model is FA-BP, with a full score of 8. While the other five hybrid algorithms all scored between 5.123 and 6.196, the single model RF only scored 1.693 and the BP neural network scored 0.035. Noting that even if the other five hybrid models all have a worse effect than the FA-BP model, their predicted results are better than the unoptimized model–BP model and RF model.

SENSITIVITY ANALYSIS

It is evident from previous sections that the five input variables in this paper all have an obvious correlation with the UCS, but the significance level of each input variable is not yet known, and it needs to be further studied. Mutual information was often used by scholars in the information theory as a parameter to evaluate the correlation between two objects (Maes et al., 1997). Furthermore, normalized mutual information (NMI) can also be used to evaluate the relationships between each feature label. To make the overall predictive modeling scheme more convincing, the five input variables are evaluated by means of the Normalized Mutual Information (NMI) as a means of determining the importance of each variable parameter to the model. Mutual information I could be obtained as follows.

$$I(X;Y) = \sum_x \sum_y p(x,y)\log\frac{p(x,y)}{p(x)p(y)} \tag{19}$$

Where X and Y are two random variables, $p(x,y)$ is the joint distribution of these two random variables, and $p(x)$, $p(y)$ is the marginal distribution of x and y. Mutual information $I(X;Y)$ is the relative entropy of the joint distribution $p(x,y)$ and the product distributions $p(x)p(y)$. To compare the significance of all input variables, the mutual information should be normalized by the following equation:

$$NMI(X;Y) = \frac{2I(X;Y)}{H(X) + H(Y)} \tag{20}$$

Where $NMI(X;Y)$ is the normalized mutual information, and $H(X)$ and $H(Y)$ are the information entropy of the X and Y, respectively. On the basis of the values of the normalized

mutual information, the significance levels of these input variables using in UCS prediction can be obtained, as shown in **Figure 12**. The sensitivity scores of the four quantities–Schmidt hammer rebound number, rock longitudinal wave velocity, point load test strength, and Young's modulus are 0.777, 0.808, 0.828, and 0.833 respectively. Porosity has a low sensitivity score of 0.68. On the whole, the five parameters selected in this paper are in line with the requirements.

CONCLUSION

In this paper, to predict the UCS of rock samples with the collected database with the artificial intelligence algorithm, six hybrid models–BSA-BP, GWO-BP, WOA-BP, SOA-BP, LSO-BP, FA-BP, and two classic models–BP and RF were developed. The predicted results obtained from the developed eight models were compared through four evaluation indexes and comprehensive scores. The following conclusions could be drawn:

(1) When predicting the UCS, six hybrid models based on the swarm intelligence optimization algorithms in this study are all significantly more accurate and significantly better than the BP neural network model and random forest model.
(2) The prediction accuracy of the used eight models from high to low is the FA-BP model, BSA-BP model, GWO-BP model, LSO-BP model, SOA-BP model, WOA-BP model, RF model, BP model. Among them, the FA-BP hybrid model showed the best comprehensive performance in six hybrid models and two single models. When carrying out the UCS prediction, the FA-BP model should be considered first.
(3) In the sensitivity analysis, porosity, Schmidt hammer rebound number, longitudinal wave velocity, point load strength, and Young's modulus have the higher scores of 0.680, 0.777, 0.808, 0.828, and 0.833, respectively. They all could be utilized as input quantities when conducting the UCS prediction.

DATA AVAILABILITY STATEMENT

The original contributions presented in the study are included in the article/Supplementary Material, further inquiries can be directed to the corresponding author.

AUTHOR CONTRIBUTIONS

Investigation, YL and SZ; methodology, YL and SZ; writing-original draft preparation, YL and SZ; writing-review and editing, NJ and XL; supervision, XL; data curation, YL and SN; visualization, SN; funding acquisition, XL and NJ. All authors have read and agreed to the published version of the manuscript.

FUNDING

This project was supported by the National Natural Science Foundation of China (42072309, 41807265) and the Hubei Key Laboratory of Blasting Engineering Foundation (HKLBEF202002).

REFERENCES

Aljarah, I., Faris, H., and Mirjalili, S. (2016). Optimizing Connection Weights in Neural Networks Using the Whale Optimization Algorithm. *Soft Comput.* 22 (1), 1–15. doi:10.1007/s10462-019-09704-910.1007/s00500-016-2442-1

Armaghani, D. J., Tonnizam Mohamad, E., Momeni, E., Monjezi, M., and Sundaram Narayanasamy, M. (2015). Prediction of the Strength and Elasticity Modulus of Granite through an Expert Artificial Neural Network. *Arab. J. Geosci.* 9 (1), 48. doi:10.1007/s12517-015-2057-3

Barnston, A. G. (1992). Correspondence Among the Correlation, RMSE, and Heidke Forecast Verification Measures; Refinement of the Heidke Score. *Wea. Forecast.* 7 (4), 6992–7709. doi:10.1175/1520-0434(1992)007<0699:catcra>2.0.co;2

Barton, N. R., Løset, F., Lien, R., and Lunde, J. (1980). Application of the Q-System in Design Decisions Concerning Dimensions and Appropriate Support for Underground Installations. *In: Editor M. Bergmand, Subsurface space, New York: Pergamon,* 2, 553–561. doi:10.1016/B978-1-4832-8421-7.50080-6

Barton, N. (2002). Some New Q-Value Correlations to Assist in Site Characterisation and Tunnel Design. *Int. J. Rock Mech. Min. Sci.* 39 (2), 185–216. doi:10.1016/s1365-1609(02)00011-4

Bieniawski, Z. T. (1978). Determining Rock Mass Deformability: Experience from Case Histories. *Int. J. Rock Mech. Min. Sci. Geomechanics Abstr.* 15 (5), 237–247. doi:10.1016/0148-9062(78)90956-7

Bollen, J., Mao, H., and Zeng, X. (2011). Twitter Mood Predicts the Stock Market. *J. Comput. Sci.* 2 (1), 1–8. doi:10.1016/j.jocs.2010.12.007

Breiman, L. (2001). Random Forests. *Mach. Learn.* 45, 5–32. doi:10.1023/a:1010933404324

Broch, E., and Franklin, J. A. (1972). The Point-Load Strength Test. *Int. J. Rock Mech. Min. Sci. Geomechanics Abstr.* 9 (6), 669–676. doi:10.1016/0148-9062(72)90030-7

Bureau, A., Dupuis, J. e., Falls, K., Lunetta, K. L., Hayward, B., Keith, T. P., et al. (2005). Identifying SNPs Predictive of Phenotype Using Random Forests. *Genet. Epidemiol.* 28 (2), 171–182. doi:10.1002/gepi.20041

Cevik, A., Sezer, E. A., Cabalar, A. F., and Gokceoglu, C. (2011). Modeling of the Uniaxial Compressive Strength of Some Clay-Bearing Rocks Using Neural Network. *Appl. Soft Comput.* 11 (2), 2587–2594. doi:10.1016/j.asoc.2010.10.008

Chen, W., Yan, E. C., Cui, X. J., and Zhang, D. (2018). Variable Weight Interval Fuzzy Evaluation Method for Rock Mass Quality. *Yangtze River.* 49 (18), 72–74. doi:10.16232/j.cnki.1001-4179.2018.18.014

Ciesielski, M. J., Kalla, P., Zheng, Z., and Rouzeyre, B. (2002). "Taylor Expansion Diagrams: A Compact, Canonical Representation with Applications to Symbolic Verification," in Proceedings 2002 Design, Automation and Test in Europe Conference and Exhibition, Paris, France, 04-08 March 2002 (IEEE). doi:10.1109/DATE.2002.998286

Dehghan, S., Sattari, G., Chehreh Chelgani, S., and Aliabadi, M. (2010). Prediction of Uniaxial Compressive Strength and Modulus of Elasticity for Travertine Samples Using Regression and Artificial Neural Networks. *Min. Sci. Technol. (China)* 20 (1), 41–46. doi:10.1016/s1674-5264(09)60158-7

Dhiman, G., and Kumar, V. (2019). Seagull Optimization Algorithm: Theory and its Applications for Large-Scale Industrial Engineering Problems. *Knowledge-Based Syst.* 165, 169–196. doi:10.1016/j.knosys.2018.11.024

Dhiman, G., Singh, K. K., Slowik, A., Chang, V., Yildiz, A. R., Kaur, A., et al. (2020). EMoSOA: a New Evolutionary Multi-Objective Seagull Optimization

Algorithm for Global Optimization. *Int. J. Mach. Learn. Cyber.* 12 (2), 571–596. doi:10.1007/s13042-020-01189-1

Dinçer, İ., Acar, A., and Ural, S. (2008). Estimation of Strength and Deformation Properties of Quaternary Caliche Deposits. *Bull. Eng. Geol. Environ.* 67 (3), 353–366. doi:10.1007/s10064-008-0146-1

Emary, E., Zawbaa, H. M., and Hassanien, A. E. (2016). Binary Grey Wolf Optimization Approaches for Feature Selection. *Neurocomputing* 172, 371–381. doi:10.1016/j.neucom.2015.06.083

Fister, I., Fister, I., Yang, X., and Brest, J. (2013). A Comprehensive Review of Firefly Algorithms. *Swarm Evol. Comput.* 13, 34–36. doi:10.1016/j.swevo.2013.06.001

Forman, E., and Peniwati, K. (1998). Aggregating Individual Judgments and Priorities with the Analytic Hierarchy Process. *Eur. J. Operational Res.* 108 (1), 165–169. doi:10.1016/s0377-2217(97)00244-0

Gandomi, A. H., Yang, X.-S., and Alavi, A. H. (2011). Mixed Variable Structural Optimization Using Firefly Algorithm. *Comput. Struct.* 89 (23-24), 2325–2336. doi:10.1016/j.compstruc.2011.08.002

Gandomi, A. H., Yang, X.-S., Talatahari, S., and Alavi, A. H. (2013). Firefly Algorithm with Chaos. *Commun. Nonlinear Sci. Numer. Simul.* 18 (1), 89–98. doi:10.1016/j.cnsns.2012.06.009

Hao, X., Du, W., Jiang, Y., Tannant, D., Zhao, Y., and Guo, Y. (2018). Influence of Bedding and Cleats on the Mechanical Properties of a Hard Coal. *Arab. J. Geosci.* 11 (9), 1-17. doi:10.1007/s12517-018-3541-3

Hoek, E., and Brown, E. (1997). Practical Estimates of Rock Mass Strength. *Int. J. Rock Mech. Mining Sci.* 34 (8), 1165-1186. doi:10.1016/s1365-1609(97)80069-x

He, M., Zhang, Z., Ren, J., Huan, J., Li, G., Chen, Y., et al. (2019). Deep Convolutional Neural Network for Fast Determination of the Rock Strength Parameters Using Drilling Data. *Int. J. Rock Mech. Min. Sci.* 123, 104084. doi:10.1016/j.ijrmms.2019.104084

Kayabasi, A., Gokceoglu, C., and Ercanoglu, M. (2003). Estimating the Deformation Modulus of Rock Masses: a Comparative Study. *Int. J. Rock Mech. Min. Sci.* 40 (1), 55–63. doi:10.1016/s1365-1609(02)00112-0

Lashkaripour, G. R. (2002). Predicting Mechanical Properties of Mudrock from Index Parameters. *Bull. Eng. Geol. Environ.* 61 (1), 73–77. doi:10.1007/s100640100116

Leite, M., and Ferland, F. (2001). Determination of Unconfined Compressive Strength and Young's Modulus of Porous Materials by Indentation Tests. *Eng. Geol.* 59 (3-4), 267–280. doi:10.1016/s0013-7952(00)00081-8

Liu, Z., Yan, D., and Niu, X. (2020). Insights into Pore Structure and Fractal Characteristics of the Lower Cambrian Niutitang Formation Shale on the Yangtze Platform, South China. *J. Earth Sci.* 31 (1), 169–180. doi:10.1007/s12583-020-1259-0

Maes, F., Collignon, A., Vandermeulen, D., Marchal, G., and Suetens, P. (1997). Multimodality Image Registration by Maximization of Mutual Information. *IEEE Trans. Med. Imaging* 16 (2), 187–198. doi:10.1109/42.563664

Mafarja, M. M., and Mirjalili, S. (2017). Hybrid Whale Optimization Algorithm with Simulated Annealing for Feature Selection. *Neurocomputing* 260, 302–312. doi:10.1016/j.neucom.2017.04.053

Mahmoodzadeh, A., Mohammadi, M., Hashim Ibrahim, H., Nariman Abdulhamid, S., Ghafoor Salim, S., Farid Hama Ali, H., et al. (2021). Artificial Intelligence Forecasting Models of Uniaxial Compressive Strength. *Transp. Geotech.* 27, 100499. doi:10.1016/j.trgeo.2020.100499

Majdi, A., and Beiki, M. (2010). Evolving Neural Network Using a Genetic Algorithm for Predicting the Deformation Modulus of Rock Masses. *Int. J. Rock Mech. Min. Sci.* 47 (2), 246–253. doi:10.1016/j.ijrmms.2009.09.011

Meng, X.-B. X., Gao, X. Z., Lu, L., Liu, Y., and Zhang, H. (2015). A New Bio-Inspired Optimisation Algorithm: Bird Swarm Algorithm. *J. Exp. Theor. Artif. Intell.* 28 (4), 673–687. doi:10.1080/0952813x.2015.1042530

Meng, X., Yu, L., Gao, X., and Zhang, H. (2015). "A New Bio-Inspired Algorithm: Chicken Swarm Optimization," in International Conference in Swarm Intelligence (Advances in Swarm Intelligence), 8794, 89–94. doi:10.1007/978-3-319-11857-4_10

Meulenkamp, F., and Grima, M. A. (1999). Application of Neural Networks for the Prediction of the Unconfined Compressive Strength (UCS) from Equotip Hardness. *Int. J. Rock Mech. Min. Sci.* 36 (1), 29–39. doi:10.1016/s0148-9062(98)00173-9

Miramontes, I., Guzman, J., Melin, P., and Prado-Arechiga, G. (2018). Optimal Design of Interval Type-2 Fuzzy Heart Rate Level Classification Systems Using the Bird Swarm Algorithm. *Algorithms* 11 (12), 206. doi:10.3390/a11120206

Mirjalili, S., and Lewis, A. (2016). The Whale Optimization Algorithm. *Adv. Eng. Softw.* 95, 51–67. doi:10.1016/j.advengsoft.2016.01.008

Mirjalili, S., Mirjalili, S. M., and Lewis, A. (2014). Grey Wolf Optimizer. *Adv. Eng. Softw.* 69, 46–61. doi:10.1016/j.advengsoft.2013.12.007

Mishra, D. A., and Basu, A. (2013). Estimation of Uniaxial Compressive Strength of Rock Materials by Index Tests Using Regression Analysis and Fuzzy Inference System. *Eng. Geol.* 160, 54–68. doi:10.1016/j.enggeo.2013.04.004

Mitri, H. S., Edrissi, R., and Henning, J. G. (1994). *Finite Element Modelling of Cable-Bolted Stopes in Hard Rock Underground Mines*. Presented at the SME Annual Meeting, New Mexico, Albuquerque, 94–116.

Mohamad, E. T., Jahed Armaghani, D., Momeni, E., and Alavi Nezhad Khalil Abad, S. V. (2015). Prediction of the Unconfined Compressive Strength of Soft Rocks: a PSO-Based ANN Approach. *Bull. Eng. Geol. Environ.* 74 (3), 745–757. doi:10.1007/s10064-014-0638-0

Momeni, E., Jahed Armaghani, D., Hajihassani, M., and Mohd Amin, M. F. (2015). Prediction of Uniaxial Compressive Strength of Rock Samples Using Hybrid Particle Swarm Optimization-Based Artificial Neural Networks. *Measurement* 60, 50–63. doi:10.1016/j.measurement.2014.09.075

Nicholson, G. A., and Bieniawski, Z. T. (1990). A Nonlinear Deformation Modulus Based on Rock Mass Classification. *Int. J. Min. Geol. Eng.* 8 (3), 181–202. doi:10.1007/bf01554041

Panagant, N., Pholdee, N., Bureerat, S., Kaen, K., Yıldız, A. R., and Sait, S. M. (2020). Seagull Optimization Algorithm for Solving Real-World Design Optimization Problems. *Mater. Test.* 62 (6), 640–644. doi:10.3139/120.111529

Rao, Y., Lee, Y., Jarjoura, D., Ruppert, A., Liu, C., and Hsu, J. (2008). A Comparison of Normalization Techniques for MicroRNA Microarray Data. *Stat. Appl. Genet. Mol. Biol.* 7 (1). doi:10.2202/1544-6115.1287

Rezaei, M., Majdi, A., and Monjezi, M. (2012). An Intelligent Approach to Predict Unconfined Compressive Strength of Rock Surrounding Access Tunnels in Longwall Coal Mining. *Neural Comput. Applic* 24 (1), 233–241. doi:10.1007/s00521-012-1221-x

Sachpazis, C. I. (1990). Correlating Schmidt Hardness with Compressive Strength and Young's Modulus of Carbonate Rocks. *Bull. Int. Assoc. Eng. Geol.* 42 (1), 75–83. doi:10.1007/bf02592622

Shan, P. F., and Lai, X. P. (2018). Numerical Simulation of the Fluid-Solid Coupling Process during the Failure of a Fractured Coal-Rock Mass Based on the Regional Geostress. *Transp. Porous Med.* 124 (3), 1061–1079. doi:10.1007/s11242-018-1110-6

Kishor, A., and Singh, P.K. (2016). Empirical Study of Grey Wolf Optimizer. *In Proc. Fifth Int. Conf. Soft Computing for Problem Solving* 436, 1037–49. doi:10.1007/978-981-10-0448-3-87

Stroffek, E., and Lesso, I. (2001). Acoustic Method for Measurement of Young's Modulus of Steel Wire Ropes. *Metalurgija* 40 (4), 219–221.

Tsiambaos, G., and Sabatakakis, N. (2004). Considerations on Strength of Intact Sedimentary Rocks. *Eng. Geol.* 72 (3-4), 261–273. doi:10.1016/j.enggeo.2003.10.001

Tuğrul, A., and Zarif, I. (1999). Correlation of Mineralogical and Textural Characteristics with Engineering Properties of Selected Granitic Rocks from Turkey. *Eng. Geol.* 51 (4), 303–317. doi:10.1016/s0013-7952(98)00071-410.1016/s0013-7952(98)00071-4

Ulusay, R., and Gokceglu, C. (1998). An Experimental Study on the Size Effect in Block Punch Index Test and its General Usefulness. *Int. J. Rock Mech. Min. Sci.* 35 (4-5), 628–629. doi:10.1016/s0148-9062(98)00024-2

Varol Altay, E., and Alatas, B. (2019). Bird Swarm Algorithms with Chaotic Mapping. *Artif. Intell. Rev.* 53 (2), 1373–1414. doi:10.1007/s10462-019-09704-9

Xue, X., and Wei, Y. (2020). A Hybrid Modelling Approach for Prediction of UCS of Rock Materials. *Comptes Rendus. Mécanique* 348 (3), 235–243. doi:10.5802/crmeca.17

Yagiz, S. (2011). Correlation between Slake Durability and Rock Properties for Some Carbonate Rocks. *Bull. Eng. Geol. Environ.* 70 (3), 377–383. doi:10.1007/s10064-010-0317-8

Yan, Z., and Zeng, L. (2013). "The BP Neural Network with MATLAB," in 2013 International Conference on Electrical, Control and Automation Engineering (ECAE 2013), December 1-2, 2013 (Hong Kong: ECAE).

Yaşar, E., and Erdoğan, Y. (2004). Estimation of Rock Physicomechanical Properties Using Hardness Methods. *Eng. Geol.* 71 (3-4), 281–288. doi:10.1016/s0013-7952(03)00141-8

Yazdani, M., and Jolai, F. (2016). Lion Optimization Algorithm (LOA): A Nature-Inspired Metaheuristic Algorithm. *J. Comput. Des. Eng.* 3 (1), 24–36. doi:10.1016/j.jcde.2015.06.003

Yılmaz, I., and Sendır, H. (2002). Correlation of Schmidt Hardness with Unconfined Compressive Strength and Young's Modulus in Gypsum from Sivas (Turkey). *Eng. Geol.* 66 (3-4), 211–219. doi:10.1016/s0013-7952(02)00041-8

Yin, X., Liu, Q., Huang, X., and Pan, Y. (2022). Perception Model of Surrounding Rock Geological Conditions Based on TBM Operational Big Data and Combined Unsupervised-Supervised Learning. *Tunn. Undergr. Space Technol.* 120, 104285. doi:10.1016/J.TUST.2021.104285

Yin, X., Liu, Q., Pan, Y., Huang, X., Wu, J., and Wang, X. (2021). Strength of Stacking Technique of Ensemble Learning in Rockburst Prediction with Imbalanced Data: Comparison of Eight Single and Ensemble Models. *Nat. Resour. Res.* 30 (2), 1795–1815. doi:10.1007/s11053-020-09787-0

Yu, Z., Shi, X., Miao, X., Zhou, J., Khandelwal, M., Chen, X., et al. (2021). Intelligent Modeling of Blast-Induced Rock Movement Prediction Using Dimensional Analysis and Optimized Artificial Neural Network Technique. *Int. J. Rock Mech. Min. Sci.* 143, 104794. doi:10.1016/j.ijrmms.2021.104794

Yu, Z., Shi, X., Qiu, X., Zhou, J., Chen, X., and Gou, Y. (2020b). Optimization of Postblast Ore Boundary Determination Using a Novel Sine Cosine Algorithm-Based Random Forest Technique and Monte Carlo Simulation. *Eng. Optim.* 53 (9), 1467–1482. doi:10.1080/0305215x.2020.1801668

Yu, Z., Shi, X., Zhou, J., Chen, X., Miao, X., Teng, B., et al. (2019). Prediction of Blast-Induced Rock Movement during Bench Blasting: Use of Gray Wolf Optimizer and Support Vector Regression. *Nat. Resour. Res.* 29 (2), 843–865. doi:10.1007/s11053-019-09593-3

Yu, Z., Shi, X., Zhou, J., Chen, X., and Qiu, X. (2020a). Effective Assessment of Blast-Induced Ground Vibration Using an Optimized Random Forest Model Based on a Harris Hawks Optimization Algorithm. *Appl. Sci.* 10 (4), 1403. doi:10.3390/app10041403

Yu, Z., Shi, X., Zhou, J., Gou, Y., Huo, X., Zhang, J., et al. (2020c). A New Multikernel Relevance Vector Machine Based on the HPSOGWO Algorithm for Predicting and Controlling Blast-Induced Ground Vibration. *Eng. Comput.* 38 (2), 1905–1920. doi:10.1007/s00366-020-01136-2

Conflict of Interest: The authors declare that the research was conducted in the absence of any commercial or financial relationships that could be construed as a potential conflict of interest.

Publisher's Note: All claims expressed in this article are solely those of the authors and do not necessarily represent those of their affiliated organizations, or those of the publisher, the editors and the reviewers. Any product that may be evaluated in this article, or claim that may be made by its manufacturer, is not guaranteed or endorsed by the publisher.

Copyright © 2022 Lei, Zhou, Luo, Niu and Jiang. This is an open-access article distributed under the terms of the Creative Commons Attribution License (CC BY). The use, distribution or reproduction in other forums is permitted, provided the original author(s) and the copyright owner(s) are credited and that the original publication in this journal is cited, in accordance with accepted academic practice. No use, distribution or reproduction is permitted which does not comply with these terms.

frontiers | Frontiers in Earth Science

ORIGINAL RESEARCH
published: 05 July 2022
doi: 10.3389/feart.2022.904703

The Calculation of Inelastic Zone Width of Coal Pillar in Highwall Mining With Backfill

Juyu Jiang, Ye Lu, Lanzhu Cao, Dong Wang, Laigui Wang, Xinping Han, Huiwen Yang and Zhengzhao Jia*

College of Mines, Liaoning Technical University, Fuxin, China

Highwall mining with backfill technology will be one of the main techniques of raising the recovery rate of coal resources under the end-slope all over the world in the future, in which the coal pillar setting is the key to ensure the successful application of this technology, and the calculation of inelastic zone width of a coal pillar has important guiding significance for the coal pillar setting in highwall mining with backfill. However, at present, in order to accurately calculate the inelastic zone width of a coal pillar under the condition of highwall mining with backfill, a calculation model of the inelastic zone width of highwall mining with backfill independent of empirical parameters is established by using a limit equilibrium method, orthogonal experiment method, and non-linear fitting method. In order to verify the correctness and reliability of the model, this study takes the geological conditions of the Antaibao open-pit mine in Pingshuo, Shanxi Province, China, as the engineering background to verify the calculation accuracy of the model. The results show that the calculation model established in this study can accurately calculate the inelastic zone width of the coal pillar under highwall mining with backfill and can meet the engineering needs.

Keywords: highwall mining with backfill, inelastic zone width, coal pillar, complete filling, incomplete filling

OPEN ACCESS

Edited by:
Fengqiang Gong,
Southeast University, China

Reviewed by:
Haiqiang Jiang,
Northeastern University, China
Lijie Guo,
Beijing General Research Institute of Mining and Metallurgy, China
Peng Huang,
China University of Mining and Technology, China

****Correspondence:***
Ye Lu
luye_186@163.com

Specialty section:
This article was submitted to Geohazards and Georisks, a section of the journal Frontiers in Earth Science

Received: *25 March 2022*
Accepted: *30 May 2022*
Published: *05 July 2022*

Citation:
Jiang J, Lu Y, Cao L, Wang D, Wang L, Han X, Yang H and Jia Z (2022) The Calculation of Inelastic Zone Width of Coal Pillar in Highwall Mining With Backfill. Front. Earth Sci. 10:904703. doi: 10.3389/feart.2022.904703

1 INTRODUCTION

According to statistics, in the past 40 years, about two-thirds of the world's coal production came from open-pit mining (Matsui et al., 2004; Brent, 2011; Shimada et al., 2013; Dixit and Pradhan, 20142014; Kuznetsova and Anfyorov, 2019; Looney, 2021). However, in the process of open-pit mining, end-slope pressure coal occurs because of the change of coal seam inclination, the problem of mining boundary, the arrangement of the bucket truck production system required for open-pit mining, and the need of maintaining slope stability. It means that it will leave a large number of "stagnant" coal that requires special measures to mine under the end-slope at the end of mining (Matsui et al., 2001; Wang et al., 2019). If these "stagnant coals" are not mined, they will be buried again once the inner dumping is formed, eventually leading to a waste of resources (Chen et al., 2011; Chen et al., 2013). According to incomplete statistics, it is estimated that the amount of coal pressed by the end-slope in China has reached 20% of the mining reserves (Tao and Shuang-shuang, 2020), and more than 20 million tons of coal is pressed by the end-slope each year. In addition, the coal pressed by the end-slope will be buried at a rate greater than 300 m each year with the follow-up of the internal dumping, becoming a permanent "stagnant" resource (Shao-hui et al., 2014; Xiao-feng, 2015). Therefore, it is of great significance to carry out end-side mining, which not only brings huge economic benefits but also reduces potential safety hazards.

In the 1940s, the United States put forward the highwall mining technology to realize the mining of coal resources under the end-slope (Mo et al., 2016); by the 1970s, the technology was mature and formed the current highwall mining technology; by the 1980s, the technology was officially commercialized (Baotang, 2014). Highwall mining technology is a remote mining technology combined with open-pit and underground mining. It can realize the mining of coal resources under the end-slope without support by arranging continuous shearer or spiral shearer and other auxiliary production equipment under the end-slope and remotely controlling them (Porathur et al., 2014; Fan, 2015). Highwall mining technology has many advantages: short infrastructure time, low operating cost, relatively low labor cost, flexibility, easy operation, safety, and recovering small coal pieces. Therefore, major coal-producing countries such as Australia (Huang, 2015), India (Elmouttie and Karekal, 2017), Indonesia (Sasaoka et al., 2016), China (Wang and Zhang, 2019; Wang et al., 2021), and Thailand (Boeut, 2015) have successively introduced this technology from the United States and successfully applied it. At the same time, it has also become the primary method for countries to mine the coal resources pressed under the end-slope. In addition, it is reported that ADDCAR's continuous shearer-type highwall mining system has liberated 120 million tons of coal resources pressed under the end-slope from 1990 to 2019. Australia that introduced the technology earlier has successfully liberated more than 21 million tons of coal (Hartcher and Case, 2019).

Since highwall mining is almost under the condition of no support to mine the coal resources under the end-slope, it is necessary to ensure the stability of the mining hole, end-slope, and slope. In order to ensure the stability of the mining hole, end-slope, and slope, coal pillars shall be set between mining holes to support the overlying strata to achieve the purpose of the mining hole, end-slope, and slope stability. Studies have shown that when the supporting coal pillar setting is unreasonable, it will induce a catastrophic failure of the supporting coal pillar and the "domino" type chain instability of the supporting coal pillar group, which eventually leads to the collapse of the mining hole, instability of the sidewall and the large-scale landslide of the slope, and destruction of the highwall production system, resulting in economic losses and casualties (Zipf and Mark, 2005; Li et al., 2020). So, whether the coal pillar setting is reasonable or not directly determines the success of highwall mining. Therefore, the problem of the coal pillar setting in highwall mining has always been a research hotspot of experts and scholars all over the world. Through the continuous efforts of experts and scholars in the world, fruitful results have been achieved on this issue. These results include the empirical formula obtained by mathematical statistics analysis and fitting, the theoretical model obtained by mechanical theory derivation and analysis, and the laws obtained by numerical simulation. For example, Salamon (1967) obtained the Salamon–Munro coal pillar strength formula with far-reaching influence for the following Australian coal pillar strength formula [CSIRO coal pillar strength formula (Duncan Fama et al., 2001)] and Indian coal pillar strength formula [CIMFR coal pillar strength formula (Verma et al., 2014)] through statistical analysis of the geometric shapes of 96 stable coal pillars and 27 failure coal pillars in South African coal mines and an in-depth study of the strength of rectangular coal pillars; Wang et al. (2019) applied Hoek–brown and Mohr–Coulomb failure criteria to establish a mechanical model of the failure width of a collinearly supported coal pillar in order to study the failure of the supporting coal pillar caused by large deformation in open-pit mining in China, through which the instability mechanism and failure process of the supported coal pillar in highwall mining was revealed; in order to study the influence of highwall mining sequence on the stability of the supporting coal pillar, Huang (2015) studied it by using the FLAC^{3D} numerical simulation method. The results show that different mining sequence has a significant influence on the stability of the high slope. Skip mining can achieve better mining hole stability and a smaller coal pillar plastic area compared with sequential mining.

However, although the research on the stability of coal pillars in highwall mining has been conducted for decades and has achieved fruitful results, the research on the stability of coal pillars under the condition of highwall mining with backfill is scarce. The possible reason for this situation is that there is no highwall mining working face with backfill in the world at present. However, through numerical simulation research, experts and scholars around the world have shown that the highwall mining with backfill will further improve the supporting coal pillar stability and liberate more coal resources pressed under the end-slope while further reducing the size of the coal pillar set (Porathur et al., 2017). For example, Lier (2014) used numerical simulation to evaluate the feasibility of highwall mining with backfill in the West Bokaro mine in Jharkhand, India. Through numerical simulation, it was found that highwall mining with backfill can theoretically recover 36% more coal resources than traditional highwall mining methods; Mo et al. (2018) used numerical simulation to study the influence of backfill on the stability of coal pillars in highwall mining. Through the study, it was found that the performance of the coal pillar would change with the properties and backfill amount of backfill body and the high recovery rate of coal resources under the coal pillar with reasonable size can be realized under reasonable backfill strategy; Matsui et al. (2000) (2018) also found that implementing highwall mining with backfill can improve the stability of coal pillars, improve the recovery rate of coal resources, and avoid the occurrence of surface subsidence through a numerical simulation. However, a numerical simulation is based on some theories or assumptions, which is not real reality. If there are problems in the theoretical model itself or assumptions, as well as the calculation accuracy, it will affect the accuracy of the simulation results.

From the research of the aforementioned experts and scholars, it is not difficult to find that the coal pillar set is vital for highwall mining, supporting coal pillar stability of highwall mining, end-slope stability, and slope stability. The highwall mining with backfill can reduce the size of the coal pillar set, and further improve the stability of the supporting coal pillar and liberate more coal resources under the end-slope. Nevertheless, up to now, there are few reports on using mechanical theory to study the influence of highwall mining with backfill on coal pillars.

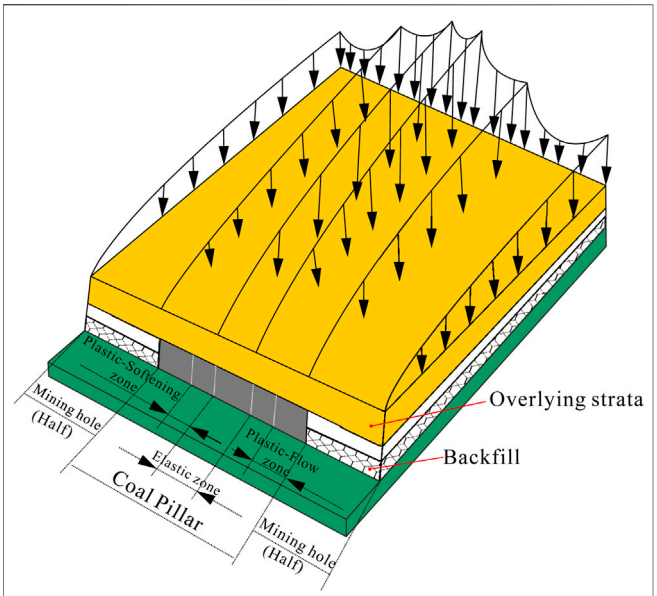


FIGURE 1 | Models of the elastic zone, plastic-softening zone, and plastic-flow zone of the coal pillar.

However, the theoretical model derived based on the mechanics theory has better applicability and generalization than the numerical simulation. In the study of the coal pillar setting, if the inelastic zone width can be calculated, it can be a good guide for the coal pillar setting and provide a numerical guarantee for the coal pillar setting. Therefore, this study uses the limit equilibrium method to construct the theoretical models of coal pillars under the conditions of incomplete filling and complete filling, respectively, and calculates the inelastic zone width of a coal pillar in highwall mining with backfill to provide numerical guarantee and ideas for the coal pillar setting in highwall mining with backfill.

Through the comparison between numerical simulation and engineering examples, the mechanical derivation results are verified, and the influence of filling body on the stability of the coal pillar in end-slope mining is studied to ensure the accuracy of the derivation results.

2 THE FULL STRESS AND STRAIN PROCESS OF COAL

Many experts and scholars in the world have shown that the failure of rock mass is a complex progressive failure process through theoretical analysis (Ti, 2021; Xu et al., 2021), laboratory experiments (Yumlu and Ozbay, 1995; Tiwari and Rao, 2006; Zhang et al., 2022), and outdoor experiments (Zhang et al., 2021). Furthermore, it will generally experience three deformation stages: elastic deformation stage, plastic-softening deformation stage, and plastic-flow deformation stage, as shown in **Figure 1**. Coal is also a particular rock, which exists underground and belongs to a part of the rock mass. Therefore, its failure will also experience the elastic deformation stage, plastic-softening deformation stage, and plastic-flow deformation stage. Medhurst and Brown (1998) carried out triaxial compression experiments on coal samples with different diameters and obtained the whole stress and strain curve. It can be seen that the failure of coal and rock also experienced the aforementioned three stages. These three stages will be reflected in the underground coal and rock mass in three zones: elastic zone, plastic-softening zone, and plastic-flow zone, in which the plastic-softening zone and plastic-flow zone are called inelastic zones. However, the inelastic zone is the danger zone in the critical failure state or already in the failure state. So, it is necessary to pay attention to the inelastic zone of the coal pillar, and for which this study also takes the calculation for the inelastic zone width as the research content.

3 MECHANICS MODEL BASED ON THE LIMIT EQUILIBRIUM METHOD

Through the study, we found that the strength of the coal pillar will change with the change of filling properties and filling amount. According to the Mohr–Coulomb criterion, the stress on the coal pillar is analyzed. It is assumed that before filling, the coal pillar is mainly subjected to the vertical stress generated by the self-weight of overlying strata and the corresponding lateral stress. By constructing the mechanical model of the coal pillar in highwall mining under different filling conditions, the effect of filling body on the coal pillar is analyzed.

3.1 Establishment of the Mechanical Model

According to the full stress and strain curve of coal obtained from the progressive failure process of rock mass studied by experts and scholars at home and abroad through a theoretical analysis and indoor and outdoor experiments, the stress at the upper interface of the coal pillar generally reaches a maximum peak ($k\gamma H$) at the interface between the elastic zone and the plastic-softening zone. At the same time, the stress value (γH) at the interface between the plastic-softening and plastic-flow zones is almost equal to the upper interface load. Filling mining is used because filling the backfill will provide lateral stress for the supporting coal pillar. The coal pillar will change from a biaxial stress state to a triaxial stress state, thereby inhibiting the expansion of the plastic zone of the coal pillar (Wang et al., 2011). Therefore, the backfill mainly provides lateral stress (P_x) to improve the stability of the coal pillar. Under the condition of incomplete filling, the coal pillar will expand and deform toward the mining hole under the action of overburden load. Since the mining hole has been filled, the expansion deformation will squeeze the backfill and make the backfill concave inward. It can be considered that the lateral stress provided by the backfill to the coal pillar at this time is the passive Earth pressure generated by the interaction between the backfill and the coal pillar. At the same time, due to incomplete filling, the upper interface of the filling body is not constrained, so the upper interface of the backfill will also expand and deform and move upward, resulting in downward friction force (T_y) at the interface between the backfill and the coal pillar. Under the condition of complete

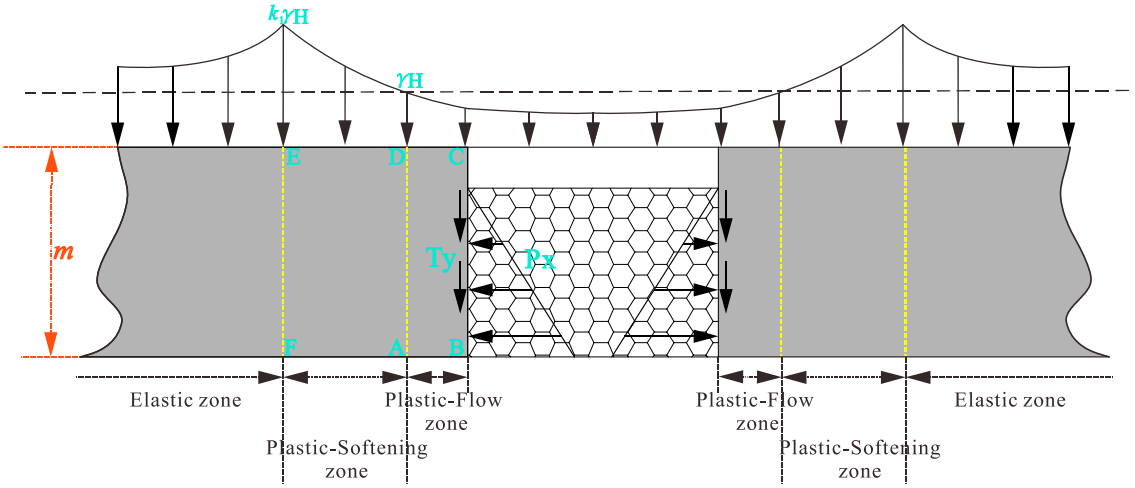


FIGURE 2 | Schematic diagram of the mechanical model without roof connection (single-side gob model).

filling, the backfill will cause downward depression compression in the longitudinal direction under the action of overburden load. Under this compression, the expansion deformation occurs in the horizontal direction simultaneously, thereby squeezing the coal pillar so that the coal pillar has the trend of depression compression inward and then inhibiting the expansion of the inelastic zone of the coal pillar. Therefore, it can be considered that the lateral stress provided by the backfill to the coal pillar is the active Earth pressure generated by the interaction between the backfill and the coal pillar. Due to the downward depression compression in the longitudinal direction, the backfill has downward movement, resulting in upward friction force (T_{y1}) at the interface between the backfill and the coal pillar. Based on these, the mechanical models are established as shown in schematic diagrams 2–3.

3.2 Calculation Model for the Inelastic Zone Width of Highwall Mining With Backfill Under the Incomplete Filling Condition

Because the principle of the limit equilibrium method is simple and has been very mature in the research and application of geotechnical engineering, the limit equilibrium method is used to calculate and study the inelastic zone width of the highwall mining with backfill under incomplete filling conditions. The research in the previous section shows that the coal pillar will form the elastic zone, plastic-softening zone, and plastic-flow zone under the action of overlying load. The plastic-softening zone and plastic-flow zone are collectively referred to as the inelastic zone. In order to simplify the research process, the plastic-flow zone and the plastic-softening zone are respectively taken as the separator for calculation and research and set the ABCD and ADEF in **Figure 2** as the plastic-flow zone and the plastic-softening zone, respectively. Their widths are x_0 and x_1, respectively. Finally, the calculation models for the inelastic zone width of highwall mining with backfill under incomplete filling conditions are established, as shown in **Figure 4**.

3.2.1 Calculation for Plastic-Flow Zone Width

Without considering the volume force, the interface stress in the limit equilibrium zone satisfies (Chen et al., 2020)

$$\begin{cases} \dfrac{\partial \sigma_x}{\partial x} + \dfrac{\partial \tau_{xy}}{\partial y} = 0, \\ \dfrac{\partial \tau_{xy}}{\partial x} + \dfrac{\partial \sigma_y}{\partial y} = 0, \\ \tau_{xy} = \sigma_y \tan \varphi_0 + C_0. \end{cases} \tag{1}$$

From **Eq. 1**, we can get

$$\frac{\partial \sigma_y}{\partial x} \tan \varphi_0 + \frac{\partial \sigma_y}{\partial y} = 0. \tag{2}$$

According to **Eq. 2**, it can be set as follows:

$$\sigma_y = f(x)g(y) + D_1. \tag{3}$$

Substituting **Eq. 3** into **Eq. 2**, we can get

$$f'(x)g(y)\tan \varphi_0 + f(x)g'(y) = 0. \tag{4}$$

After finishing, we can get

$$\frac{f'(x)\tan \varphi_0}{f(x)} = -\frac{g'(y)}{g(y)}. \tag{5}$$

Since the left and right sides of **Eq. 5** are functions about x and y, respectively, it can be set as follows:

$$\begin{cases} \dfrac{f'(x)\tan \varphi_0}{f(x)} = D, \\ -\dfrac{g'(y)}{g(y)} = D. \end{cases} \tag{6}$$

By solving the differential equations of **Eq. 6**, we can get

$$\begin{cases} f(x) = D_2 e^{\frac{Dx}{\tan\varphi_0}}, \\ g(y) = D_3 e^{-Dy}. \end{cases} \tag{7}$$

Substituting **Eq. 7** into **Eq. 3** and **Eq. 1**, we can get

$$\begin{cases} \sigma_y = D_2 D_3 e^{\frac{Dx}{\tan\varphi_0}} e^{-Dy} + D_1, \\ \tau_{xy} = \left(D_2 D_3 e^{\frac{Dx}{\tan\varphi_0}} e^{-Dy} + D_1 \right) \tan\varphi_0 + C_0 . \end{cases} \tag{8}$$

Because the upper boundary of the coal seam is $y = (\varpi\text{-}1)\ m$, it can be set as follows:

$$D_0 = D_2 D_3 e^{D(\varpi-1)m}. \tag{9}$$

Then the upper boundary stress of the coal seam can be obtained according to **Eq. 9** and **Eq. 8**, as follows:

$$\begin{cases} \sigma_y = D_0 e^{\frac{Dx}{\tan\varphi_0}} + D_1, \\ \tau_{xy} = \left(D_0 e^{\frac{Dx}{\tan\varphi_0}} + D_1 \right) \tan\varphi_0 + C_0 . \end{cases} \tag{10}$$

According to the mechanical model in **Figure 2**, the plastic-flow zone ABCD in the whole limit equilibrium zone is taken as the separator to obtain the model, as shown in **Figure 4**. Since the resultant force in the *x*-direction and the *y*-direction are both 0, we can get

$$\left.\begin{aligned} &\sum F_x = \int_0^{x_0} \tau'_{xy} dx + \int_0^{x_0} \tau_{xy} dx + P_x - mA\left[\sigma_y\right]_{x=x_0} = 0, \\ &\sum F_y = -\int_0^{x_0} \sigma'_y dx + T_y + \int_0^{x_0} \sigma_y dx = 0, \\ &\tau'_{xy} = \sigma'_y \tan\varphi_0 + C_0, \\ &T_y = f_1 P_x + C_0, \end{aligned}\right\}$$
$$\Rightarrow \sum F_x = \tan\varphi_0 \int_0^{x_0} \sigma_y dx + T_y \tan\varphi_0 + \int_0^{x_0} C_0 dx + \int_0^{x_0} \tau_{xy} dx + P_x - Am\left[\sigma_y\right]_{x=x_0} = 0. \tag{11}$$

As can be seen from **Eq. 11**, **Eq. 11** is an equilibrium equation about x_0, which can be derived from x_0:

$$\tan\varphi_0 \left[\sigma_y\right]_{x=x_0} + C_0 + \left[\tau_{xy}\right]_{x=x_0} - Am \frac{d\left[\sigma_y\right]_{x=x_0}}{dx_0} = 0, \tag{12}$$

i.e.,

$$2\tan\varphi_0 \left[\sigma_y\right]_{x=x_0} + 2C_0 - Am \frac{d\left[\sigma_y\right]_{x=x_0}}{dx_0} = 0. \tag{13}$$

Solving **Eq. 11**, we can get

$$\left[\sigma_y\right]_{x=x_0} = D' e^{\frac{2\tan\varphi_0 x_0}{Am}} - \frac{C_0}{\tan\varphi_0}. \tag{14}$$

Let $x = x_0$ in **Eq. 10** and compare it with **Eq. 13**, then we can get

$$\begin{cases} D = \dfrac{2\tan^2\varphi_0}{Am}, \\ D_0 = D', \\ D_1 = -\dfrac{C_0}{\tan\varphi_0}. \end{cases} \tag{15}$$

According to the assumption $[\sigma_y]_{x=x0}$ and **Eqs 11–14**, we can get

$$\begin{cases} \left[\sigma_y\right]_{x=x_0} = D_0 e^{\frac{2\tan\phi_0 x_0}{Am}} - \dfrac{C_0}{\tan\phi_0} = \gamma H, \\ \tan\phi_0 \displaystyle\int_0^{x_0} \sigma_y dx + T_y \tan\phi_0 + C_0 x_0 + \int_0^{x_0} \tau_{xy} dx + P_x - Am\gamma H = 0. \end{cases} \tag{16}$$

Since

$$\begin{cases} \displaystyle\int_0^{x_0} \tau_{xy} dx = \frac{A \cdot D_0 m}{2} \left[e^{\frac{2x_0\tan\varphi_0}{Am}} - 1 \right], \\ \displaystyle\int_0^{x_0} \sigma_y dx = \frac{A \cdot D_0 m}{2\tan\varphi_0} \left[e^{\frac{2x_0\tan\varphi_0}{Am}} - 1 \right] - \frac{C_0 x_0}{\tan\varphi_0}. \end{cases} \tag{17}$$

Eq. 16 becomes

$$A \cdot D_0 m \left[e^{\frac{2x_0\tan\varphi_0}{Am}} - 1 \right] + T_y \tan\varphi_0 + P_x - Am\gamma H = 0. \tag{18}$$

According to **Eq. 16** and **Eq. 18**, we can get

$$D_0 = \frac{C_0 Am + T_y \tan^2\varphi_0 + P_x \tan\varphi_0}{Am \tan\varphi_0}. \tag{19}$$

Substituting **Eq. 19** into **Eq. 16**, the plastic-flow zone width of the single side goaf in highwall mining with backfill under the incomplete filling condition can be obtained as follows:

$$x_0 = \frac{Am}{2\tan\varphi_0} \ln\left[\frac{Am\gamma H \tan\varphi_0 + AmC_0}{C_0 Am + T_y \tan^2\varphi_0 + P_x \tan\varphi_0} \right], \tag{20}$$

where A is lateral stress coefficient; m is the mining hole height, m; γ is the average volume force of overburden, N/m^3; H is the overlying rock mass height, m; φ_0 is the internal friction angle of coal, °; C_0 is the cohesion of coal, Pa; Px is the passive Earth pressure, Pa, P_x=0.5$\gamma_{backfill}$ $(\varpi m)^2 k_1{}^2$+2ϖmck_1; $\gamma_{backfill}$ is the bulk density of backfill, N/m^3; c is the cohesion of backfill, Pa; k_1 is the

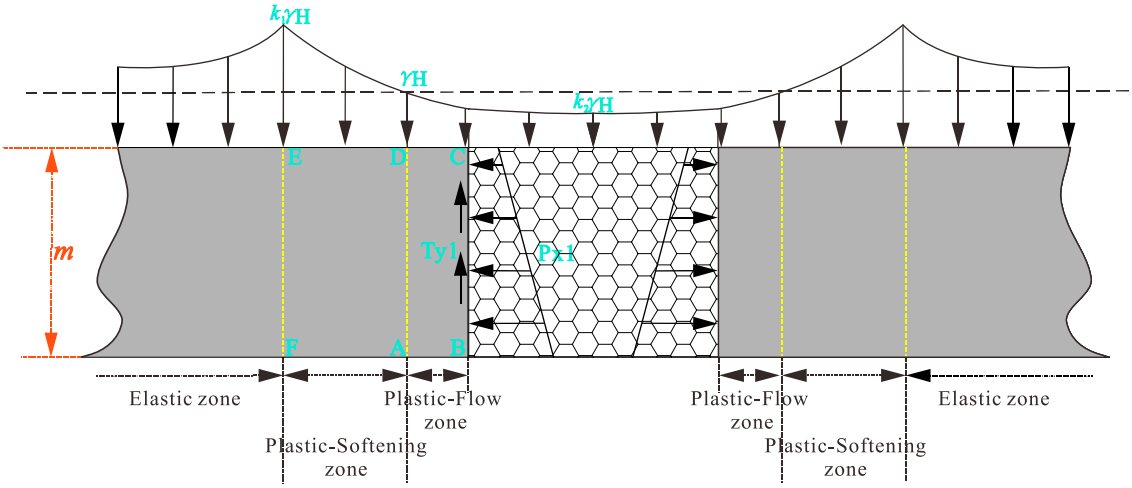


FIGURE 3 | Schematic diagram of the mechanical model during roof connection (single-side goaf model).

passive Earth pressure coefficient, k_1=tan(45°+φ/2); φ is the internal friction angle of backfill, °; and ϖ is the filling rate.

3.2.2 Calculation for Plastic-Softening Zone Width

According to the aforementioned **Eqs 1–10**, set and solve the equations in the same way, and combined with the mechanical model in **Figure 3**, take the plastic-softening zone ADEF in the whole limit equilibrium zone as the separator to obtain the model shown in **Figure 4**. From the natural balance in the *y*-direction, the resultant force in the *x*-direction is 0, and we can get

$$\sigma_{y_1} = D'_0 e^{\frac{\hat{D}x}{\tan\varphi_0}} + D'_1, \tag{21}$$

$$\tau_{xy_1} = \left(D'_0 e^{\frac{\hat{D}x}{\tan\varphi_0}} + D'_1 \right) \tan\varphi_0 + C_0, \tag{22}$$

$$\sum F_x = 2\int_0^{x_1} \tau_{xy1} dx + Am\left[\sigma_{y1}\right]_{x=0} - Am\left[\sigma_{y1}\right]_{x=x_1} = 0. \tag{23}$$

Similarly, it is known from **Eq. 23** that this is a balance equation about x1 so that it can be derived from x1 and solve the differential equation, and the following can be obtained:

$$\left[\sigma_{y1}\right]_{x=x_1} = D'' e^{\frac{2\tan\varphi_0 x_1}{Am}} - \frac{C_0}{\tan\varphi_0}. \tag{24}$$

Let $x = x_1$ in **Eq. 21** and compare it with **Eq. 24**, we can get

$$\begin{cases} \hat{D} = \dfrac{2\tan^2\varphi_0}{Am}, \\ D'_0 = D'', \\ D'_1 = -\dfrac{C_0}{\tan\varphi_0}. \end{cases} \tag{25}$$

According to the assumptions $[\sigma_{y1}]_{x=x1} = k\gamma H$ and $[\sigma_{y1}]_{x=x0} = \gamma H$ and **Eqs 21–25**, we can get

$$\begin{cases} \left[\sigma_y\right]_{x=x_1} = D'_0 e^{\frac{2\tan\varphi_0 x_1}{Am}} - \dfrac{C_0}{\tan\varphi_0} = k\gamma H, \\ 2\tan\varphi_0 \displaystyle\int_0^{x_1} \sigma_{y1} dx + 2C_0 x_1 + Am\gamma H - Amk\gamma H = 0. \end{cases} \tag{26}$$

Since

$$\int_0^{x_1} \sigma_{y1} dx = \frac{A \cdot D'_0 m}{2\tan\varphi_0}\left[e^{\frac{2x_1\tan\varphi_0}{Am}} - 1\right] - \frac{C_0 x_1}{\tan\varphi_0}, \tag{27}$$

Eq. 26 becomes

$$A \cdot D'_0 m\left[e^{\frac{2x_1\tan\varphi_0}{Am}} - 1\right] + A\gamma Hm - Ak\gamma Hm = 0. \tag{28}$$

According to **Eq. 28** and **Eq. 26**, we can get

$$D'_0 = \frac{C_0 Am + A\gamma Hm\tan\varphi_0}{Am\tan\varphi_0}. \tag{29}$$

Substituting **Eq. 29** into **Eq. 25**, the plastic-softening zone width of the single side goaf in highwall mining with backfill under the incomplete filling condition can be obtained as follows:

$$x_1 = \frac{Am}{2\tan\varphi_0}\ln\left(\frac{k\gamma H Am\tan\varphi_0 + C_0 Am}{Am\gamma H\tan\varphi_0 + C_0 Am}\right), \tag{30}$$

where A is the lateral stress coefficient; m is the mining hole height, m; γ is the average volume force of overburden, N/m^3; H is the overlying rock mass height, m; φ_0 is the internal friction angle of coal, °; C_0 is the cohesion of coal, Pa; and k is the vertical stress concentration factor.

In summary, the inelastic zone width of the single side goaf in highwall mining with backfill under the incomplete filling condition can be obtained as follows:

$$x = x_0 + x_1. \tag{31}$$

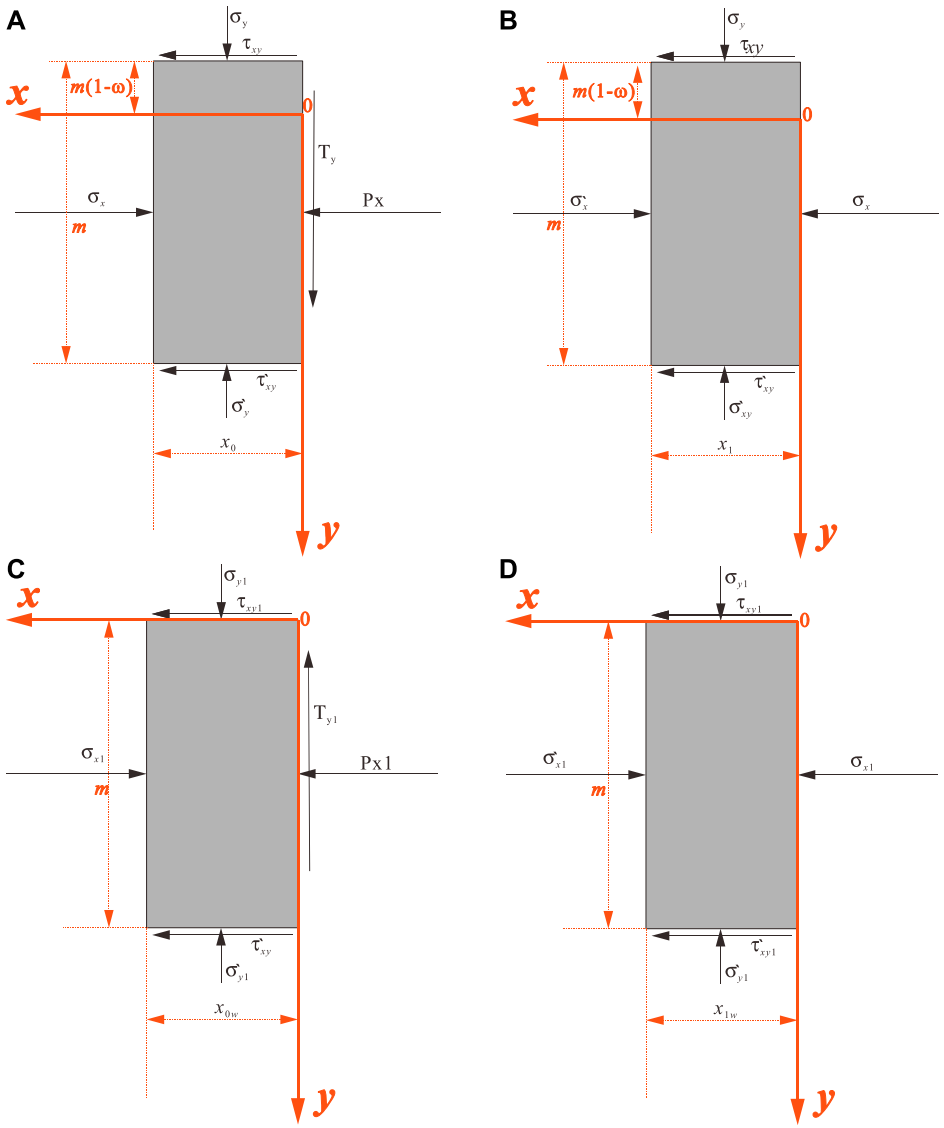


FIGURE 4 | Calculation model for highwall mining with backfill under the filling condition (single-side goaf model). **(A)** Calculation model for plastic-flow zone in highwall mining with backfill under the incomplete filling condition. **(B)** Calculation model for plastic-softening zone in highwall mining with backfill under the incomplete filling condition. **(C)** Calculation model for plastic-flow zone of highwall mining with backfill under the complete filling condition. **(D)** Calculation model for plastic-softening zone of highwall mining with backfill under the complete filling condition.

When both sides are mined out, there will be stress superposition. Therefore, under the condition of incomplete filling, the inelastic zone width x_s of the bilateral side goaf in highwall mining with backfill is twice that of the single side goaf, i.e.,

$$x_s = 2x. \tag{32}$$

3.3 Calculation Model for the Inelastic Zone Width of Highwall Mining With Backfill Under the Complete Filling Condition

The formula for the inelastic width of the highwall mining with backfill under the complete filling condition is derived according to the same derivation process as the previous section. In order to reduce unnecessary repetition, the calculation formulas for plastic-flow zone width x_{0w} and plastic-softening zone x_{1w} are derived by taking the plastic-flow zone ABCD and the plastic-softening zone ADEF (as shown in **Figure 4**) in the whole limit equilibrium zone in **Figure 3** as separators. The formulas obtained by derivation are shown in **Eq. 33** and **Eq. 34**:

$$x_{0w} = \frac{Am}{2\tan\varphi_0}\ln\left[\frac{AmyH\tan\varphi_0 + AmC_0}{P_{x1}\tan\varphi_0 + C_0Am - T_{y1}\tan^2\varphi_0}\right], \tag{33}$$

where A is the lateral stress coefficient; m is the mining hole height, m; γ the is average volume force of overburden, N/m^3; H is the overlying rock mass height, m; φ_0 is the internal friction angle

of coal, °; C_0 is the cohesion of coal, Pa; P_{x1} is the active Earth pressure, Pa, $P_{x1}=(0.5\gamma_{backfill}m^2+qm)k_3^2-2mck_3$; $\gamma_{backfill}$ is the bulk density of backfill, N/m^3; c is the cohesion of backfill, Pa; k_3 is the active Earth pressure coefficient, $k_3=\tan(45°-\varphi/2)$; φ is the internal friction angle of backfill, °; q is the load acting on backfill, $q=k_2\gamma H$; and k_2 is the stress coefficient.

$$x_{1w}=\frac{Aa}{2\tan\varphi_0}\ln\left(\frac{k\gamma HAm\tan\varphi_0+C_0Am}{Am\gamma H\tan\varphi_0+C_0Am}\right), \tag{34}$$

where A is the lateral stress coefficient; m is the mining hole height, m; γ is the average volume force of overburden, N/m^3; H is the overlying rock mass height, m; a is the height of backfill, m; φ_0 is the internal friction angle of coal, °; C_0 is the cohesion of coal, Pa; and k is the vertical stress concentration factor.

Finally, the inelastic zone width of highwall mining with backfill under complete filling condition is

$$x_w=x_{0w}+x_{1w}. \tag{35}$$

Similarly, when both sides are mined out, there will be stress superposition. Therefore, under the condition of complete filling, the inelastic zone width x_{sw} of the bilateral side goaf in highwall mining with backfill is twice that of the single side goaf, i.e.,:

$$x_{sw}=2x_w. \tag{36}$$

3.4 Model Correlation Coefficient Fitting

Through the mechanical derivation of **sections 3.1–3.3**, the mechanical models of **Eq. 20**, **Eq. 30**, **Eq. 33**, and **Eq. 34** are finally obtained. However, the lateral stress coefficient (A), vertical stress concentration coefficient (k), and stress coefficient (k_2) in the models are uncertain, which brings some obstacles to the model use. Suppose these coefficients become parameters related to mining design, such as mining hole width (D), mining hole height (G), filling rate (C), and overburden height (H). In that case, the applicability of the model will be significantly improved. According to experience, A, k, and k_2 will change with D, G, C, and H. Since the non-linear fitting method can study these relationships well, the non-linear fitting method is used to study the relationships between A, k, k_2 and D, G, C, and H, respectively.

In order to comprehensively study the relationship between A, k, and k_2, and D, G, C, and H with less experimental times, the orthogonal experimental method was adopted. Because the orthogonal experiment is based on the orthogonality from the comprehensive test to select some representative points with the "uniform dispersion, neat comparable" features for testing, it is a high efficiency, fast, and economical method for research multifactor multilevel experimental. Since A and k are related to D, G, C, and H, four factors affect A and k. In addition, it is hoped to obtain better experimental results with as few experiments as possible, so it is decided to set the experiment level to 4 (the level set as shown in **Table 1**), i.e., it is an orthogonal experiment with four factors and four levels. However, fitting k_2 is only for calculating the Earth pressure P_x with overlying load, but there is load above the backfill only when complete filling, so the filling rate

TABLE 1 | Four levels for research A and k.

	G/m	D/m	C	H/m
Level 1	2.5	3.0	0.65	155
Level 2	3.0	3.6	0.80	190
Level 3	3.5	4.0	0.95	225
Level 4	4.0	4.6	1.00	260

TABLE 2 | Four levels for research k_2.

	G/m	D/m	H/m
Level 1	2.5	3.0	155
Level 2	3.0	3.6	190
Level 3	3.5	4.0	225
Level 4	4.0	4.6	260

TABLE 3 | Orthogonal experiment table for researching A and k L16(4^4).

Experiment number	G/m	D/m	C	H/m
1	2.5	3.0	0.65	155
2	2.5	3.6	0.80	190
3	2.5	4.0	0.95	225
4	2.5	4.6	1.00	260
5	3.0	3.0	0.80	225
6	3.0	3.6	0.65	260
7	3.0	4.0	1.00	155
8	3.0	4.6	0.95	190
9	3.5	3.0	0.95	260
10	3.5	3.6	1.00	225
11	3.5	4.0	0.65	190
12	3.5	4.6	0.8	155
13	4.0	3.0	1.00	190
14	4.0	3.6	0.95	155
15	4.0	4.0	0.80	225
16	4.0	4.6	0.65	260

TABLE 4 | Orthogonal experiment table for researching k_2 L16(4^3).

Experiment number	G/m	D/m	H/m
1	2.5	3.0	155
2	2.5	3.6	190
3	2.5	4.0	225
4	2.5	4.6	260
5	3.0	3.0	190
6	3.0	3.6	155
7	3.0	4.0	260
8	3.0	4.6	225
9	3.5	3.0	225
10	3.5	3.6	260
11	3.5	4.0	155
12	3.5	4.6	190
13	4.0	3.0	260
14	4.0	3.6	225
15	4.0	4.0	190
16	4.0	4.6	155

TABLE 5 | Physical and mechanical parameters of the model in numerical simulation.

Lithology	Density (kg/m^3)	Tensile strength (MPa)	Cohesion (Mpa)	Internal friction angle (°)	Bulk modulus (GPa)	Shear modulus (GPa)
Mudstone (overburden)	2,500	1.5	2.00	30	1.19	1.26
Coal	1,500	0.3	1.50	25	0.09	0.08
Sand mudstone (floor)	2,700	1.7	2.30	32	2.90	2.27
Backfill	1,250	0.1	0.12	40	0.95	0.20

must be 1. Similarly, to obtain better experimental results, set the experiment level to 4 (each level setting is shown in **Table 2**). Finally, the experiment of k_2 is determined as an orthogonal experiment with three factors and four levels. After the number of influencing factors and experimental levels of the aforementioned experiments is determined, Minitab is used to generate the corresponding orthogonal experiment table automatically. The generated orthogonal experiment tables are shown in **Table 3** and **Table 4**.

However, the aforementioned experiments should be based on certain geological conditions, but this study is theoretical research. Therefore, to test the aforementioned experimental scheme quickly, effectively, and economically, the numerical simulation method is used. FLAC^{3D} numerical simulation software is now widely used in civil engineering, geotechnical engineering, hydraulic engineering, geological engineering, and other fields. Therefore, FLAC^{3D} numerical simulation software is used to simulate the experimental scheme in this study. In addition, also because this study is a theoretical research rather than a practical engineering application, the rock physical and mechanical parameters in the published studies can be used as the physical and mechanical parameters of the experimental research in this study. The study "*Simulation Research for the Influence of Mining Sequence on Coal Pillar Stability under Highwall Mining Method*" (Huang, 2015) studied the influence of mining sequence on coal pillar stability through numerical simulation. It belongs to the same field of highwall mining as this study. Therefore, some rock physical and mechanical parameters of the aforementioned study are used in this study. Moreover, the study "*The influence of roadway backfill on the coal pillar strength by numerical investigation*" (Wang et al., 2011) studied the influence of filling on coal pillar strength through numerical simulation. It involves the physical and mechanical parameters of the backfill. So, the physical and mechanical parameters of the backfill of the aforementioned study are used in this study. The physical and mechanical parameters of the numerical simulation model are shown in **Table 5**.

Since the calculation model studied in this study is mainly suitable for two-dimensional conditions, it is hoped that A and k at the elastic–plastic boundary of the upper interface in the coal seam and the k_2 at the upper interface in the backfill can be obtained through experiments. However, these are obtained through the calculation of vertical stress and horizontal stress. Therefore, according to the experimental plans, this study establishes the pseudo two-dimensional models with a thickness of 1 m, a width of 100 m, and a mining hole spacing of 7 m. Furthermore, it arranges a measuring line with 501 measuring points for monitoring vertical stress and horizontal stress on the upper interface of the coal seam in the model. The distance between the measuring points is 0.2 m. After simulating, the vertical and horizontal stress at the elastic–plastic interface is extracted and calculated by **Eq. 37** and **Eq. 38** for calculating A and k. Similarly, extract the vertical stress at the upper interface of the backfill, and calculate the stress coefficient k_2 with **Eq. 37**. After calculation and sorting, the experimental results of each group are shown in **Table 6**.

$$k = \frac{\sigma_{zm}}{\gamma H}, \tag{37}$$

$$A = \frac{\sigma_{xm}}{\sigma_{zm}}, \tag{38}$$

where k is the vertical stress concentration; A is the lateral horizontal stress coefficient; σ_{zm} is the vertical stress extracted from the model, Pa; σ_{xm} is the horizontal stress extracted from the model, Pa; γ is the average volume force of overburden, N/m^3; and H is the buried depth of unit body, m.

After sorting out the aforementioned experimental data, fit the relationship between k and A and G, D, C, and H, respectively, and the relationship between k_2 and G, D, and H. However, there is no prior model form before fitting these relations, so this study uses the "fast formula fitting search" function in the mathematical optimization software 1stOpt (Liu et al., 2020; Li et al., 2021a; Li et al., 2021b; Li et al., 2021c; Shen et al., 2021; Zhang et al., 2021) to fit the model. The relationship formula obtained by fitting is shown in **Eqs 39–41**, and the fitting curves are shown in **Figure 5**. RMSE, SSE, and R2 of fitting curves in each relationship formula show that RMSE and SSE are less than 0.05 and 0.03, respectively, and the R2 is greater than 0.87. Therefore (Li et al., 2021d; Kong et al., 2021; Shen et al., 2021; Kong et al., 2022; Niu et al., 2022), it can be explained that the fitted relationship formula has a high degree of fit with the experimental data and has a basis for use. Therefore, substituting **Eqs 39–41** into **Eq. 20**, **Eq. 30**, **Eq. 33**, and **Eq. 34** can obtain the final calculation model for the calculation of the inelastic zone width of the coal pillar in the highwall mining with backfill.

$$\begin{aligned} k = {} & 1.433G + 3.655C - 0.014H - 0.207G^2 - 0.114GD \\ & + 0.0729GC + 0.000874GH \\ & - 0.0363DC - 0.00244DH - 2.224C^2 - 0.00068CH \\ & + 5.55 \times 10^{-6}H^2 - 0.971, \end{aligned} \tag{39}$$

TABLE 6 | Orthogonal experimental results of A, k, and k_2.

Experiment number	k	A	k_2	Experiment number	k	A	k_2
1	1.319	0.456	0.535	9	1.175	0.426	0.483
2	1.321	0.547	0.535	10	1.243	0.485	0.477
3	1.363	0.568	0.545	11	1.295	0.495	0.492
4	1.482	0.582	0.568	12	1.341	0.552	0.515
5	1.280	0.437	0.497	13	1.172	0.635	0.475
6	1.301	0.445	0.517	14	1.179	0.456	0.471
7	1.359	0.557	0.529	15	1.211	0.309	0.515
8	1.468	0.583	0.550	16	1.316	0.223	0.502

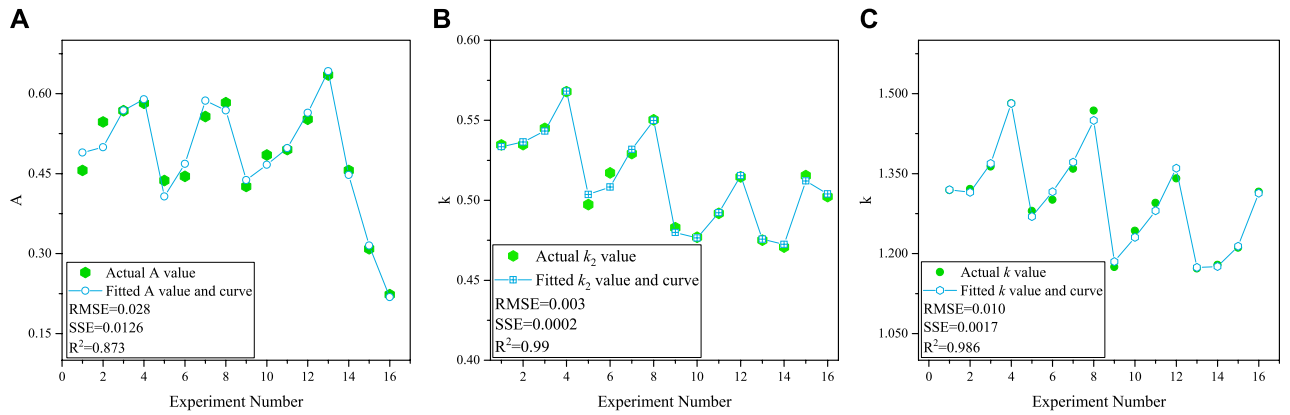


FIGURE 5 | Fitting curves of A, k, and k_2. **(A)** Fitting curve of A; **(B)** fitting curve of k_2; and **(C)** fitting curve of k.

$$A = 0.86G - 1.285C + 0.0069H - 0.142G^2 - 0.00141GD + 0.398GC - 0.00177GH - 0.244DC + 0.00118DH + 0.588C^2 + 0.00113CH - 0.000018H^2 - 0.969, \quad (40)$$

$$k_2 = \left[0.0373 + DH\tan(0.981GD)\sin(1.002GHD)e^{\frac{-16923.035G-71.423H+3148.368GD+1}{505+0.422GDH}}\right]G^2 + 0.0065GD - 0.298G + 0.994 + 1.89 \times 10^{-6}DH, \quad (41)$$

where G is the mining hole height, m; D is the mining hole width, m; C is the filling rate; and H is the overburden height, m.

4 NUMERICAL SIMULATION VERIFICATION BASED ON THE ANTAIBAO OPEN-PIT MINE

In the previous chapters, although the calculation model for the inelastic zone width of the coal pillar in the highwall mining with backfill is established after the mechanical derivation and the fitting of the correlation coefficients, the reliability and calculation accuracy of the calculation model needs to be tested. Therefore, in this chapter, the accuracy of the calculation model will be verified based on the geological conditions of the Antaibao open-pit mine in Pingshuo, Shanxi Province, China.

4.1 Overview of the Antaibao Open-Pit Mine in Pingshuo

The Antaibao open-pit mine belongs to China Coal Pingshuo Group Co., Ltd., located at the junction of Shuozhou city and Pinglu district, Shanxi Province, China. The mining boundary area is 18.53 km^2, and the recoverable reserves are 452.53 Mt. The Antaibao open-pit mine was completed and put into operation in 1987. The initial designed production capacity was 15.33 Mt/a. After continuous development, the Antaibao open-pit mine was re-approved for capacity adjustment in 2014, resulting in a final production capacity of 30.0 Mt/a. The geological structure of the Antaibao open-pit mine is simple and has no large faults. There are 11 coal seams in the minefield, of which the main ones are 4$^{\#}$ coal, 9$^{\#}$ coal, and 11$^{\#}$ coal. In addition, the coal seam within the minefield is relatively shallow, and the 11$^{\#}$ coal, which is the deepest buried, is only 228 m. The occurrence depth and physicomechanical parameters of each coal seam and stratum in the Antaibao open-pit mine are shown in **Figure 6** and **Table 7**.

4.2 Verifying the Calculation Model Accuracy Based on the Mining of 11$^{\#}$ Coal in the Antaibao Open-Pit Mine

The 11$^{\#}$ coal is the deepest buried in the minable coal seam of the Antaibao open-pit mine, and its average thickness is 3 m. It is

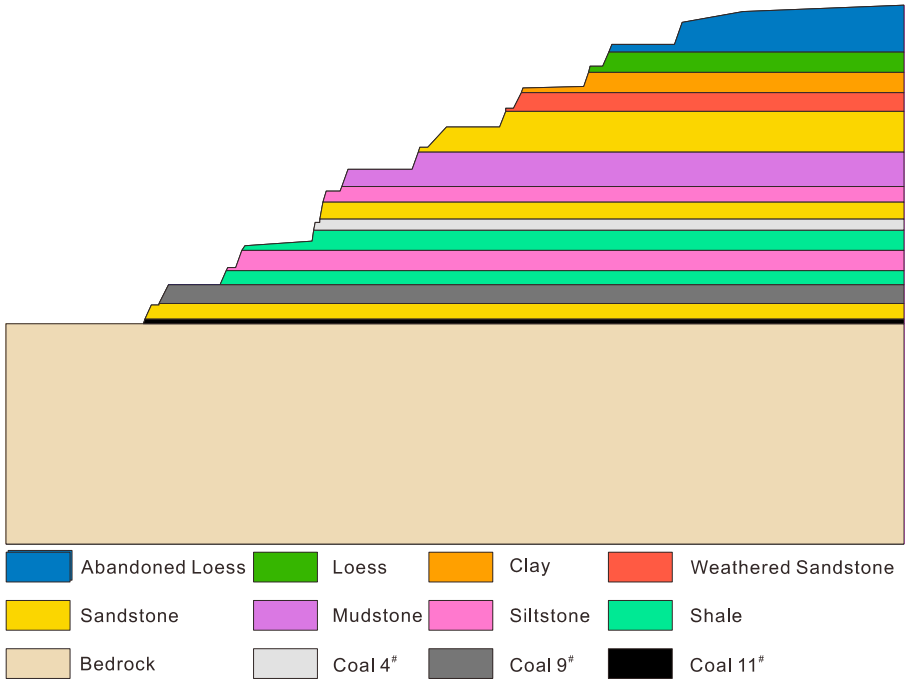


FIGURE 6 | Distribution map of rock strata in the Antaibao open-pit mine.

TABLE 7 | Buried depth, physical and mechanical parameters of coal seams, and strata in the Antaibao open-pit mine.

Strata	Buried depth (m)	Average thickness (m)	Density ($kg \cdot m^{-3}$)	Elastic modulus (GPa)	Poisson's ratio	Cohesion (MPa)	Internal friction angle (°)	Tensile strength (MPa)
Abandoned loess	0	34	1,760	0.015	0.42	0.04	25	0.006
Loess	34	15	1,960	0.015	0.42	0.085	28	0.013
Clay	49	14	1,980	0.011	0.36	0.131	20	0.18
Weathered sandstone	63	14	2,300	2.0	0.36	2.5	38	0.75
Sandstone	77	30	2,380	4.2	0.32	3.0	39	0.9
Mudstone	107	24	2,490	2.8	0.34	2.0	38	0.6
Siltstone	131	12	2,320	4.6	0.32	3.5	36	1.0
Sandstone	143	12	2,380	4.0	0.3	4.0	40	1.2
Coal $4^{\#}$	155	8	1,440	1.0	0.38	1.62	36	0.7
Shale	163	15	2,450	2.4	0.33	3.0	42	0.9
Siltstone	178	15	2,600	4.8	0.32	5.0	38	1.2
Shale	193	10	2,580	3.5	0.35	5.0	38	1.0
Coal $9^{\#}$	203	13	1,330	1.2	0.36	1.62	36	0.7
Sandstone	216	12	2,380	2.9	0.28	5.0	41	1.2
Coal $11^{\#}$	228	3	1,400	1.3	0.35	1.62	36	0.7
Bedrock	231	160	2,380	2.9	0.28	5.0	41	1.2

suitable for once mining full height. So, this study verifies the calculation model accuracy based on the mining of $11^{\#}$ coal in the Antaibao open-pit mine. In addition, the maximum mining width and depth of the current continuous shearer-type highwall wall mining system (Addcar) are 3.5 and 350 m, respectively, so set the width, height, and depth of the mining hole as 3.5, 3, and 350 m, respectively. Because it is only to verify the calculation model accuracy, the problem of slope stability is not considered here. Therefore, based on experience, this study sets coal pillars with a width of 3.5 m between mining holes and five mining holes to meet the calculation requirements. Then the three-dimensional model was established by usign Flac3D software according to the geological conditions of the Antaibao open-pit mine. After considering the factors affecting

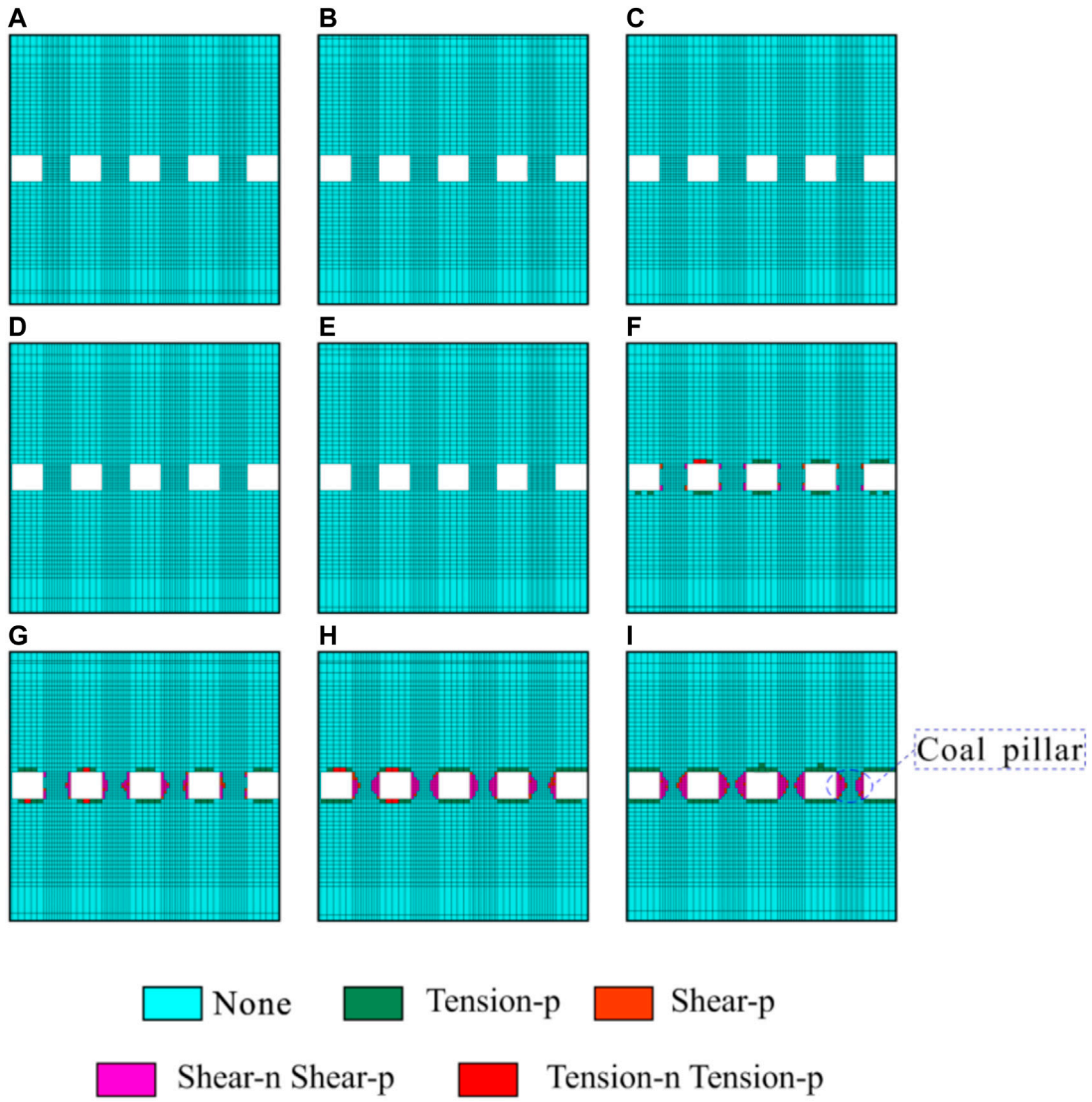


FIGURE 7 | Average width for the inelastic zone of the coal pillar in each section under the 0% filling rate condition. **(A)** 50 m; **(B)** 85 m; **(C)** 120 m; **(D)** 155 m; **(E)** 190 m; **(F)** 225 m; **(G)** 260 m; **(H)** 295 m; and **(I)** 330 m.

the accuracy of simulation results, such as the model boundary effect, a model with a total of 461,820 nodes, a length of 650 m, a width of 89.5 m, and a height of 391 m is established. The established model is shown in **Figure 7**. In order to fully verify the calculation accuracy and reliability of the model, this study calculates and verifies the inelastic zone width of the coal pillar under the conditions of 0%, 50%, and 100% filling rates. At the same time, nine points are taken equidistantly from 50 to 330 m away from the mining hole opening as the calculation points, i.e., the inelastic zone width of the coal pillars of nine sections at 50–330 m away from the mining hole opening is calculated. In order to be able to apply the physical and mechanical parameters and other related parameters of the Antaibao open-pit mine 11# coal to the model established in this study, this study performs the average calculation and related processing on the parameters. After average calculation and processing, the parameters are obtained, as shown in **Table 8**.

TABLE 8 | Physical and mechanical parameters of the Antaibao open-pit 11# coal obtained after average calculation and treatment.

G/m	*D*/m	γ/N·m^{-3}	φ_0/°	C_0/Pa	$\gamma_{backfill}$/N·m^{-3}	*c*/Pa	φ/°
3	3.5	21678.57	36	1620000	12500	120000	40

4.2.1 Filling Rate is 0%

Since the filling rate is 0%, i.e., incomplete filling, the parameters of physical and mechanical parameters and other relevant parameters of the Antaibao open-pit mine 11# coal obtained after average calculation are substituted into **Eq. 20** and **Eqs 30–32**, and each

TABLE 9 | Inelastic zone width for the coal pillar calculated by numerical calculation and numerical simulation under the 0% filling rate condition.

Distance from the calculation point to mining hole opening (m)	50	85	120	155	190	225	260	295	330
Numerical results (m)	0.00	0.00	0.01	0.37	0.37	0.89	1.45	2.12	2.92
Numerical simulation results (m)	0.00	0.00	00.00	0.00	0.00	0.60	1.40	1.90	3.20

TABLE 10 | Inelastic zone width of the coal pillar calculated by numerical calculation and numerical simulation under the 50% filling rate condition.

Distance from the calculation point to mining hole opening (m)	50	85	120	155	190	225	260	295	330
Numerical results (m)	0.00	0.00	0.00	0.19	0.19	0.72	1.26	1.80	2.84
Numerical simulation results (m)	0.00	0.00	0.00	0.00	0.00	0.60	1.20	2.20	2.80

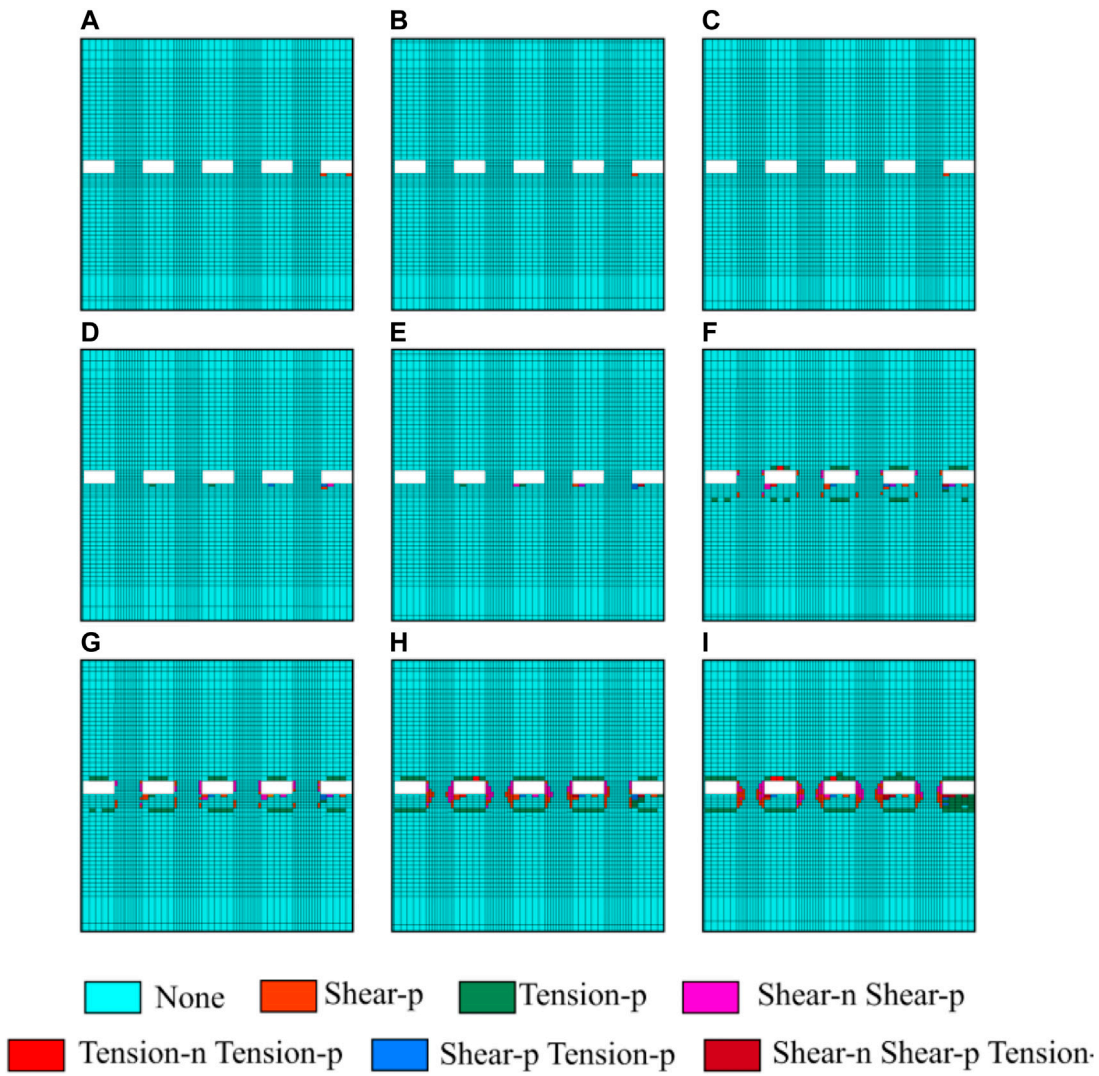


FIGURE 8 | Average width of the inelastic zone of the coal pillar in each section under the 50% filling rate condition. **(A)** 50 m; **(B)** 85 m; **(C)** 120 m; **(D)** 155 m; **(E)** 190 m; **(F)** 225 m; **(G)** 260 m; **(H)** 295 m; and **(I)** 330 m

TABLE 11 | Inelastic zone width of the coal pillar calculated by numerical calculation and numerical simulation under the 100% filling rate condition.

Distance from the calculation point to mining hole opening (m)	50	85	120	155	190	225	260	295	330
Numerical results (m)	0.00	0.03	0.04	0.22	0.30	0.35	0.55	1.68	2.62
Numerical simulation results (m)	0.00	0.00	0.00	0.00	0.00	0.35	0.50	1.40	2.50

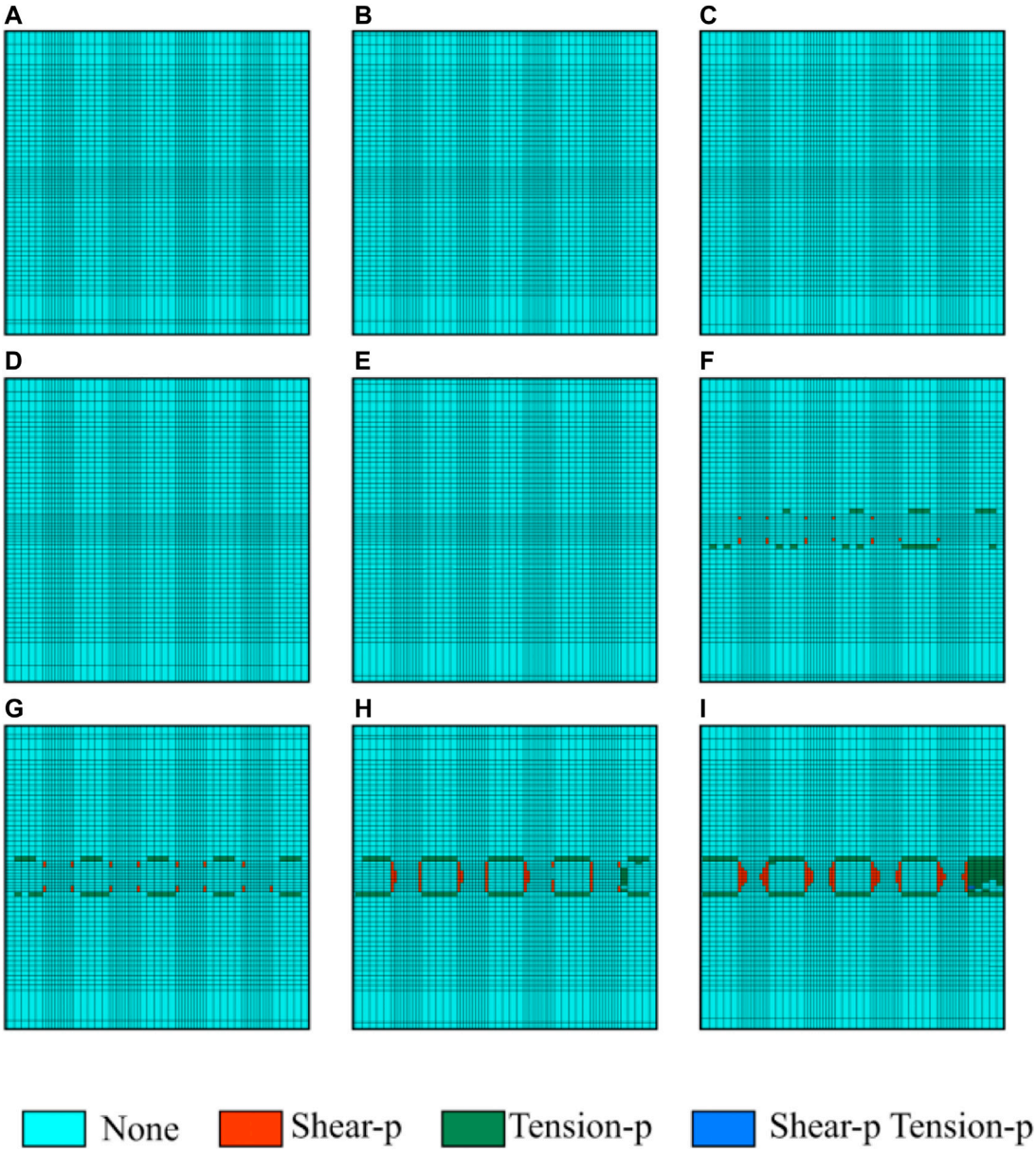


FIGURE 9 | Average width of the inelastic zone of the coal pillar in each section under the 100% filling rate condition. **(A)** 50 m; **(B)** 85 m; **(C)** 120 m; **(D)** 155 m; **(E)** 190 m; **(F)** 225 m; **(G)** 260 m; **(H)** 295 m; and **(I)** 330 m.

calculation point are calculated with MATLAB. After calculation, the inelastic zone width of the coal pillar at each calculation point is obtained, as shown in **Table 9**. At the same time, to compare the numerical calculation results with the numerical simulation results, take the section at the designated position of the numerical simulation model and count the average width of the inelastic zone of the coal pillar in each section. According to statistics, under the 0% filling rate condition, the average width for the inelastic zone of the coal pillar in each section is shown in **Table 9** and **Figure 7**.

4.2.2 Filling Rate is 50%

Similarly, since the filling rate is 50%, i.e., incomplete filling, the parameters of physical and mechanical parameters and other relevant parameters of the Antaibao open-pit mine 11$^{\#}$ coal obtained after average calculation are substituted into **Eq. 20** and **Eqs 30–32**, and each calculation point is calculated with MATLAB. After numerical calculation, the inelastic zone width for the coal pillar at each calculation point is obtained, as shown in **Table 10**. After numerical simulation calculation, the average width for the inelastic zone of the coal pillar in each section is shown in **Table 10**. The plastic failure of each section is shown in **Figure 8**.

4.2.3 Filling Rate is 100%

Since the filling rate is 100%, i.e., complete filling, the physical and mechanical parameters and other relevant parameters of the

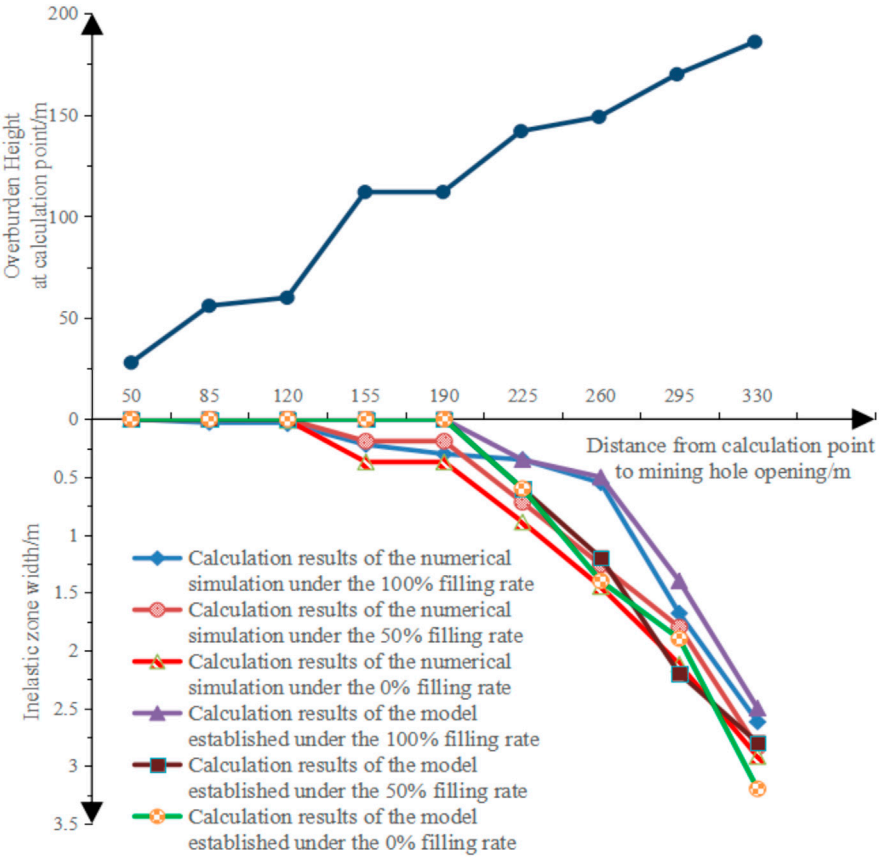


FIGURE 10 | Established model and numerical simulation results.

TABLE 12 | Buried depth, physical and mechanical parameters of coal seams, and strata in the West Bokaro open-pit mine.\

Strata	Buried depth (m)	Average thickness (m)	Density ($kg·m^{-3}$)	Elastic modulus (GPa)	Poisson's ratio	Cohesion (MPa)	Internal friction angle (°)	Tensile strength (MPa)
Overburden	0	140	2322.2	4.23	0.21	3.1	43.8	32.1
Coal $5^{\#}$	140	4.5	1550	3.47	0.2	1.21	40.2	25
Bedrock	144.5	100	2500	5.4	0.25	4.1	37	32.1

TABLE 13 | Physical and mechanical parameters of the West Bokaro open-pit mine $5^{\#}$ coal obtained after average calculation and treatment.

G/m	D/m	γ/N·m^{-3}	φ_0/°	C_0/Pa	$\gamma_{backfill}$/N·m^{-3}	c/Pa	φ/°
4.5	3.5	15,190	40.2	1210000	8959.16	117,000	29.6

Antaibao open-pit mine $11^{\#}$ coal are substituted into **Eqs 33–35** and Eq. 36. After numerical calculation, the inelastic zone width of the coal pillar at each calculation point is obtained, as shown in **Table 11**. After numerical simulation calculation, the average width of the inelastic zone of the coal pillar in each section is shown in **Table 11**, and the plastic failure of each section is shown in **Figure 9**.

It can be seen from **Tables 10–12** and **Figures 7–9** that the model established in this study can comparatively accurately calculate the inelastic zone width of the coal pillar. The inelastic zone width of the coal pillar calculated by the model established in this study is consistent with that calculated by numerical simulation. The maximum error is within 0.4 m. However, from **Tables 11**, **12** and **Figure 10**, it is not difficult to find that the results calculated by the model established in this study are generally larger than those calculated by numerical simulation. The reason why such a problem occurs is believed to be caused by two aspects. The first aspect may be that the model established in this study is based on the physical and mechanical parameters and other relevant parameters of the Antaibao open-pit mine $11^{\#}$ coal obtained after average calculation and relevant treatment, while the numerical simulation is calculated directly based on the original parameters, which leads to the result of the numerical calculation is larger than that of numerical simulation; another (He et al., 2022; Niu et al., 2022; Yang et al., 2022) aspect may be that the grid density limits the numerical simulation, making it impossible to calculate the inelastic zone with a width of less

TABLE 14 | Inelastic zone width for the coal pillar calculated by numerical calculation and numerical simulation under the 0% filling rate condition of the West Bokaro open-pit mine.

Distance from the calculation point to mining hole opening (m)	30	55	80	105	130	155	180	205	230
Numerical results (m)	0.62	0.97	1.59	1.64	1.78	1.89	2.01	2.12	2.21
Numerical simulation results (m)	0.50	0.89	1.43	1.57	1.74	1.93	2.05	2.14	2.35

TABLE 15 | Inelastic zone width of the coal pillar calculated by numerical calculation and numerical simulation under the 100% filling rate condition of the West Bokaro open-pit mine.

Distance from the calculation point to mining hole opening (m)	30	55	80	105	130	155	180	205	230
Numerical results (m)	0.40	0.72	1.13	1.20	1.32	1.51	1.67	1.81	1.92
Numerical simulation results (m)	0.30	0.67	1.04	1.13	1.40	1.62	1.78	1.90	2.06

than 0.35 m (in the numerical simulation, the grid width at the coal pillar is 0.35 m). Moreover (He et al., 2021; Wu et al., 2022), it also leads to the result of numerical calculation being larger than that of numerical simulation. However, in general, the accuracy of the calculation model for the inelastic zone width of the coal pillar in highwall mining with backfill established in this study can meet the actual production needs. Therefore, it also shows that the model established in this study is reliable and correct and has specific practical value.

5 NUMERICAL SIMULATION VERIFICATION BASED ON THE WEST BOKARO OPEN-PIT MINE

In the previous chapters, although the calculation model for the inelastic zone width of the coal pillar in the highwall mining with backfill is established after the mechanical derivation and the fitting of the correlation coefficients, the reliability and calculation accuracy of the calculation model needs to be tested. Therefore, in this chapter, the accuracy of the calculation model will be verified based on the geological conditions of the West Bokaro open-pit mine in Northeast India with the study of Lier (2014).

5.1 Verifying the Calculation Model Accuracy Based on the Mining of 5# Coal in the West Bokaro Open-Pit Mine

The occurrence depth and physicomechanical parameters of each coal seam and stratum in the study of Lier (2014) are shown in **Table 12**. In addition, the coal seam within the minefield is relatively shallow, and the 5# coal, which is the deepest buried, is only 140 m.

The 5# coal is the deepest buried in the minable coal seam of the West Bokaro open-pit mine, and its average thickness is 5.5 m. This study verifies the theoretical formula accuracy based on the mining of 5# coal in the West Bokaro open-pit mine. The study of Lier, 2014 set the width, height, and depth of the mining hole as 3.5, 4.5, and 250 m, respectively. In addition, the coal pillars with a width of 2.9 m between mining holes. In order to fully verify the calculation accuracy and reliability of the theoretical formula, this study calculates and verifies the inelastic zone width of the coal pillar under the conditions of 0% and 100% filling rates. At the same time, nine points are taken equidistantly from 30 to 230 m away from the mining hole opening as the calculation points, i.e., the inelastic zone width of the coal pillars of nine sections at 30–230 m away from the mining hole opening is calculated. The physical and mechanical parameters and other related parameters of the West Bokaro open-pit mine 5# coal is shown in **Table 13**.

5.2 Inelastic Zone Width Under the 0% Filling Rate Condition of the West Bokaro Open-Pit Mine

Since the filling rate is 0%, i.e., incomplete filling, the parameters of physical and mechanical parameters and other relevant parameters of the West Bokaro open-pit mine 5# coal obtained after average calculation are substituted into **Eq 20** and **Eqs 30–32**, and each calculation point are calculated with MATLAB. After calculation, the inelastic zone width of the coal pillar at each calculation point is obtained, as shown in **Table 9**. At the same time, to compare the numerical calculation results with the numerical simulation results, take the section at the designated position of the numerical simulation model and count the average width of the inelastic zone of the coal pillar in each section. According to statistics, under the 0% filling rate condition, the average width for the inelastic zone of the coal pillar in each section is shown in **Table 14**.

5.3 Inelastic Zone Width Under the 100% Filling Rate Condition of the West Bokaro Open-Pit Mine

Similarly, since the filling rate is 100%, i.e., incomplete filling, the parameters of physical and mechanical parameters and other relevant parameters of the Antaibao open-pit mine 5# coal obtained after average calculation are substituted into **Eqs 33–35** and Eq. 36, and each calculation point is calculated with MATLAB. After numerical calculation, the inelastic zone width for the coal pillar at each calculation point is obtained, as shown in **Table 15**.

It can be seen from **Tables 14**, **15** that the model established in this study can comparatively accurate calculate the inelastic zone width of the coal pillar. The inelastic zone width of the coal pillar calculated by the model established in this study is consistent with that calculated by numerical simulation. The maximum error is within 0.3 m. In general, the accuracy of the calculation model for the inelastic zone width of the coal pillar in highwall mining with backfill established in this study can meet the actual production needs. Therefore, it also shows that the model established in this study is reliable and correct and has a specific practical value.

6 CONCLUSION

(1) Based on the limit equilibrium method, this study establishes a calculation model for the inelastic zone width of the coal pillar in the highwall mining with backfill. At the same time, in order to improve the model's practicability, the relationship between model coefficient and geometric parameters such as mining hole width, mining hole height, filling rate, and overburden height is demonstrated. Thus, the calculation model for the inelastic zone width of the coal pillar in highwall mining with backfill without empirical parameters is established.

(2) In this study, the stress distribution of the coal pillar under complete filling and incomplete filling is analyzed and calculated, which shows that with the increase of mining depth, the influence of the filling rate on the width of the inelastic zone of the coal pillar becomes more and more obvious.

(3) In addition, in order to verify the correctness and reliability of the model, this study takes the Antaibao open-pit mine and the West Bokaro mine as the engineering background to carry out numerical simulation to verify the accuracy of the calculation model. Through verification and calculation, it is found that the width of the inelastic zone of the coal pillar calculated by the model established in this study is larger than that of numerical simulation. However, the maximum deviation between the two is less than 0.4 m, which meets the needs of the project.

(4) Therefore, it is fully proved that the calculation model of the inelastic zone width of the coal pillar in filling highwall mining established in this study is correct. The calculation results are more accurate and reliable. Through the research on the width of the plastic zone of the coal pillar under different filling rates, we can make better use of backfill highwall mining to reduce the size of the coal pillar group, further improve the stability of the supporting coal pillar, and liberate more coal resources under the end-slope. It lays a certain foundation for the practical application of highwall mining with backfill technology in the future.

DATA AVAILABILITY STATEMENT

The original contributions presented in the study are included in the article/Supplementary Material; further inquiries can be directed to the corresponding author.

AUTHOR CONTRIBUTIONS

Conceptualization: JJ and YL; methodology: JJ, LC, and DW; software: LW and YL; formal analysis: JJ, XH, and HY; data curation: JJ and ZJ; writing—original draft preparation: JJ and YL; writing—review and editing: JJ and YL; supervision: LC, DW, and LW; project administration: LC and DW; funding acquisition: LC. All authors have read and agreed to the published version of the manuscript.

REFERENCES

Baotang, S. (2014). *Highwall Mining Stability. 2014 2014-10-01*. Paris: Atlantis Press, 25–37.

Boeut, S. (2015). *Design of Auger Highwall Mining: A Case Study at Mae Tan Coal Mine*. Thailand: Chulalongkorn University.

Brent, G. F. (2011). Quantifying Eco-Efficiency within Life Cycle Management Using a Process Model of Strip Coal Mining. *Int. J. Min. Reclam. Environ.* 25, 258–273. doi:10.1080/17480930.2011.553476

Chen, L., Zhang, H., Kang, J., and Jia, G. (2020). Time and Space Evolution Law of Surrounding Rock Deformation under the Influence of Mining. *IOP Conf. Ser. Earth Environ. Sci.* 525, 12022. doi:10.1088/1755-1315/525/1/012022

Chen, Y. L., Cai, Q. X., Shang, T., and Che, Z. X. (2011). Mining System for Remaining Coal of Final Highwall. *J. Min. Sci.* 47, 771–777. doi:10.1134/s1062739147060098

Chen, Y., Shimada, H., Sasaoka, T., Hamanaka, A., and Matsui, K. (2013). Research on Exploiting Residual Coal Around Final End-Walls by Highwall Mining System in China. *Int. J. Min. Reclam. Environ.* 27, 166–179. doi:10.1080/17480930.2012.678768

Dixit, S. K., and Pradhan, M. (20142014). *Highwall Mining in India*. Cham: Springer International Publishing, 175–187. doi:10.1007/978-3-319-02678-7_18

Duncan Fama, M. E., Shen, B., and Maconochie, P. (2001). *Optimal Design and Monitoring of Layout Stability for Highwall Mining. ACARP Project C8033 Final Report*. Australia: CSIRO Exploration and Mining Report 887F.

Elmouttie, M., and Karekal, S. (2017). A Framework for Geotechnical Hazard Analysis in Highwall Mining Entries. *Procedia Eng.* 191, 1203–1210. doi:10.1016/j.proeng.2017.05.296

Fan, M. (2015). *Design Programs for Highwall Mining Operations. Master Thesis*. Morgantown (West Virginia): West Virginia University.

Hartcher, P., and Case, G. (2019). *The Experience of Addcar in Highwall Mining Operations*.

He, M., Zhang, Z., Zhu, J., and Ning, L. (2022). "Correlation between the Constant Mi of Hoek-Brown Criterion and Porosity of Intact Rock," in *Rock Mechanics and Rock Engineering*. Online Published November 2021.

He, M., Zhang, Z., Zhu, J., Li, N., Li, G., and Chen, Y. (2021). Correlation between the Rockburst Proneness and Friction Characteristics of Rock Materials and a New Method for Rockburst Proneness Prediction: Field Demonstration. *J. Petroleum Sci. Eng.* 205, 108997. doi:10.1016/j.petrol.2021.108997

Huang, J. (2015). Simulation Research for the Influence of Mining Sequence on Coal Pillar Stability under Highwall Mining Method. *Geofluids* 2021, 8864339.

Kong, X., He, D., Liu, X., Wang, E., Li, S., Liu, T., et al. (2022). Strain Characteristics and Energy Dissipation Laws of Gas-Bearing Coal during Impact Fracture Process. *Energy* 242, 123028. doi:10.1016/j.energy.2021.123028

Kong, X., Li, S., Wang, E., Wang, X., Zhou, Y., Ji, P., et al. (2021). Experimental and Numerical Investigations on Dynamic Mechanical Responses and Failure Process of Gas-Bearing Coal under Impact Load. *Soil Dyn. Earthq. Eng.* 142, 106579. doi:10.1016/j.soildyn.2021.106579

Kuznetsova, L. V., and Anfyorov, B. A. (2019). Combined Geotechnology Potentials in the Process of Coal Deposits Integrated Development. *IOP Conf. Ser. Earth Environ. Sci.* 377, 12003. doi:10.1088/1755-1315/377/1/012003

Li, X.-l., Chen, S.-j., Liu, S.-m., and Li, Z.-h. (2021). AE Waveform Characteristics of Rock Mass under Uniaxial Loading Based on Hilbert-Huang Transform. *J. Cent. South Univ.* 28 (6), 1843–1856. doi:10.1007/s11771-021-4734-6

Li, X., Cao, Z., and Xu, Y. (2020). *Characteristics and Trends of Coal Mine Safety Development, Energy Sources, Part A: Recovery, Utilization and Environmental Effects Philadelphia*, 1–19. doi:10.1080/15567036.2020.1852339Characteristics and Trends of Coal Mine Safety Development*Energy Sources, Part A Recovery, Util. Environ. Eff.*

Li, X. L., Chen, S. J., and Wang, S. (2021). Study on *In Situ* Stress Distribution Law of the Deep Mine Taking Linyi Mining Area as an Example. *Adv. Mater. Sci. Eng.* 9 (4), 5594181. doi:10.1155/2021/5594181

Li, X. L., Chen, S. J., Zhang, Q. M., Gao, X., and Feng, F. (2021). Research on Theory, Simulation and Measurement of Stress Behavior under Regenerated Roof Condition. *Geomechanics Eng.* 26 (1), 49–61.

Li, Z., Zhang, X., Wei, Y., and Ali, M. (2021). Experimental Study of Electric Potential Response Characteristics of Different Lithological Samples Subject to Uniaxial Loading. *Rock Mech. Rock Eng.* 54, 397–408. doi:10.1007/s00603-020-02276-z

Lier, J. S. (2014). *Backfill in Highwall Mining: An Assessment of the Possibilities in West Bokaro, India. Master Thesis*. Delft (Nederland): Delft University of Technology.

Liu, S., Li, X., Wang, D., and Zhang, D. (2020). *Investigations on the Mechanism of the Microstructural Evolution of Different Coal Ranks under Liquid Nitrogen Cold Soaking, Energy Sources, Part A: Recovery, Utilization*. and Environmental Effects Philadelphia, 1–17. doi:10.1080/15567036.2020.1841856

Looney, B. (2021). *Statistical Review of World Energy*.

Matsui, K., Shimada, H., Kramadibrata, S., and Rai, M. S. (2001). "Some Considerations of Highwall Mining Systems in Coal Mines," in *Proceedings of the 17 International Mining Congress and Exhibition in Turkey* (Ankara, 19–22.

Matsui, K., Shimada, H., Sasaoka, T., Furukawa, H., Ueda, T., Yabuki, A., et al. (2004). Highwall Stability Due to Punch Mining at Opencut Coal Mines. *Int. J. Surf. Min. Reclam. Environ.* 18, 185–204. doi:10.1080/13895260412331315544

Matsui, K., Shimada, H., Sasaoka, T., Ichinose, M., and Kubota, S. (20002018). *Highwall Mining System with Backfilling. Mine Planning and Equipment Selection*. London: Routledge, 333–338.

Medhurst, T. P., and Brown, E. T. (1998). A Study of the Mechanical Behaviour of Coal for Pillar Design. *Int. J. Rock Mech. Min. Sci.* 35, 1087–1105. doi:10.1016/s0148-9062(98)00168-5

Mo, S., Canbulat, I., Zhang, C., Oh, J., Shen, B., and Hagan, P. (2018). Numerical Investigation into the Effect of Backfilling on Coal Pillar Strength in Highwall Mining. *Int. J. Min. Sci. Technol.* 28, 281–286. doi:10.1016/j.ijmst.2017.07.003

Mo, S., Zhang, C., Canbulat, I., and Hagan, P. (2016). *A Review of Highwall Mining Experience and Practice*.

Niu, Y., Wang, E., and Li, Z. (2022). *Identification of Coal and Gas Outburst-Hazardous Zones by Electric Potential Inversion during Mining Process in Deep Coal Seam*. Paris: Rock Mech Rock Eng.

Porathur, J. L., Roy, P. P., Shen, B., and Karekal, S. (2017). *Highwall Mining: Applicability*. London: design & safety.

Porathur, J. L., Srikrishnan, S., Verma, C. P., Jhanwar, J. C., and Pal Roy, P. (2014). Slope Stability Assessment Approach for Multiple Seams Highwall Mining Extractions. *Int. J. Rock Mech. Min. Sci.* 70, 444–449. doi:10.1016/j.ijrmms.2014.04.023

Salamon, M. M. A. (1967). A Study of the Strength of Coal Pillars. *J. S. Afr. I. Min. Metall.* 68, 55–67.

Sasaoka, T., Karian, T., Hamanaka, A., Shimada, H., and Matsui, K. (2016). Application of Highwall Mining System in Weak Geological Condition. *Int. J. Coal Sci. Technol.* 3, 311–321. doi:10.1007/s40789-016-0121-6

Shao-hui, W., Qing-xiang, C., and Fu-ming, L. (2014). *Development Status and Suggestions of Open-Cut Mining Technology in China*. China: China Mining Magazine, 83–87.

Shen, W., Shi, G., Wang, Y., Bai, J., Zhang, R., and Wang, X. (2021). Tomography of the Dynamic Stress Coefficient for Stress Wave Prediction in Sedimentary Rock Layer under the Mining Additional Stress. *Int. J. Min. Sci. Technol.* 31, 653–663. doi:10.1016/j.ijmst.2021.04.003

Shimada, H., Chen, Y., Hamanaka, A., Sasaoka, T., Shimada, H., and Matsui, K. (2013). Application of Highwall Mining System to Recover Residual Coal in End-Walls. *Procedia Earth Planet. Sci.* 6, 311–318. doi:10.1016/j.proeps.2013.01.041

Tao, L. I., and Shuang-shuang, X. (2020). Design Method of Mining Parameters for End Slope Shearer in Surface Mine. *Coal Eng.* 52, 23–27.

Ti, Z. (2021). Fracture Mechanism in Overlying Strata during Longwall Mining. *Shock Vib.*, 4764732.

Tiwari, R. P., and Rao, K. S. (2006). Post Failure Behaviour of a Rock Mass under the Influence of Triaxial and True Triaxial Confinement. *Eng. Geol.* 84, 112–129. doi:10.1016/j.enggeo.2006.01.001

Verma, C. P., Porathur, J. L., Thote, N. R., Roy, P. P., and Karekal, S. (2014). Empirical Approaches for Design of Web Pillars in Highwall Mining: Review and Analysis. *Geotech. Geol. Eng.* 32, 587–599. doi:10.1007/s10706-013-9713-8

Wang, F., and Zhang, C. (2019). *Reasonable Coal Pillar Design and Remote Control Mining Technology for Highwall Residual Coal Resources*, 6. Royal Society open science SCImago (n.d.), 181–817. doi:10.1098/rsos.181817

Wang, H., Poulsen, B. A., Shen, B., Xue, S., and Jiang, Y. (2011). The Influence of Roadway Backfill on the Coal Pillar Strength by Numericalinvestigation. *Int. J. Rock Mech. Min. Sci.* 48, 443–450. doi:10.1016/j.ijrmms.2010.09.007

Wang, M., Tai, C., Zhang, Q., Yang, Z., Li, J., and Shen, K. (2021). Application of Improved and Optimized Fuzzy Neural Network in Classification Evaluation of Top Coal Cavability. *Sci. Rep.* 11, 19179. doi:10.1038/s41598-021-98630-4

Yan, S., Bai, S., Chang, Z., and Zhao, T. (2019). Theoretical Analysis of Damaged Width & Instability Mechanism of Rib Pillar in Open-Pit Highwall Mining. *Adv. Civ. Eng.*, 6328702.

Wu, H., Zhao, G., and Ma, S. (2022). Failure Behavior of Horseshoe-Shaped Tunnel in Hard Rock under High Stress: Phenomenon and Mechanisms. *Trans. Nonferrous Metals Soc. China* 32 (3), 639–656. doi:10.1016/s1003-6326(22)65822-9

Xiao-feng, Z. (2015). Study on End-Slope Mining Technology by Continuous Miner. *Coal Technol.* 34, 28–30.

Xu, G., Liu, H., Fu, B., and Yu, J. (2021). Research and Prospect of Post-peak Strain-Softening Characteristics of Rocks. *IOP Conf. Ser. Earth Environ. Sci.* 787, 12135. doi:10.1088/1755-1315/787/1/012135

Yang, B., He, M., Zhang, Z., Zhu, J., and Chen, Y. (2022). A New Criterion of Strain Rockburst in Consideration of the Plastic Zone of Tunnel Surrounding Rock. *Rock Mech. Rock Eng.* 55, 1777–1789. doi:10.1007/s00603-021-02725-3

Yumlu, M., and Ozbay, M. U. (1995). A Study of the Behaviour of Brittle Rocks under Plane Strain and Triaxial Loading Conditions. *Int. J. Rock Mech. Min. Sci. Geomechanics Abstr.* 32, 725–733. doi:10.1016/0148-9062(95)00025-c

Zhang, W., Cui, Y., Ding, X., Yin, Z., and Wang, Y. (2021). A Novel Tuning Method of Differential Forward Robust PID Controller for Integrating Systems Plus Time Delay Based on Direct Synthesis Method. *Int. J. Syst. Sci.* 52, 238–262. doi:10.1080/00207721.2020.1825871

Zhang, Y., Xie, Y., Yang, L., Liao, R., and Qiu, T. (2022). Intelligent Prediction of Coal Mine Water Inrush Based on Optimized SAPSO-ELM Model under the Influence of Multiple Factors. *Arabian J. Geosciences* 15 (430), 1–12. doi:10.1007/s12517-022-09756-2

Zipf, R. K., and Mark, C. (2005). Ground Control for Highwall Mining in the United States. *Int. J. Surf. Min. Reclam. Environ.* 19, 188–217. doi:10.1080/13895260500165353

Conflict of Interest: The authors declare that the research was conducted in the absence of any commercial or financial relationships that could be construed as a potential conflict of interest.

Publisher's Note: All claims expressed in this article are solely those of the authors and do not necessarily represent those of their affiliated organizations, or those of the publisher, the editors, and the reviewers. Any product that may be evaluated in this article, or claim that may be made by its manufacturer, is not guaranteed or endorsed by the publisher.

Copyright © 2022 Jiang, Lu, Cao, Wang, Wang, Han, Yang and Jia. This is an open-access article distributed under the terms of the Creative Commons Attribution License (CC BY). The use, distribution or reproduction in other forums is permitted, provided the original author(s) and the copyright owner(s) are credited and that the original publication in this journal is cited, in accordance with accepted academic practice. No use, distribution or reproduction is permitted which does not comply with these terms.

frontiers | Frontiers in Earth Science

ORIGINAL RESEARCH
published: 08 July 2022
doi: 10.3389/feart.2022.933284

An Effective Denoising Method Based on Cumulative Distribution Function Thresholding and its Application in the Microseismic Signal of a Metal Mine With High Sampling Rate (6 kHz)

Da Zhang[1,2,3], *Zhiyi Zeng*[4,5,6], *Yaqian Shi*[1,2,3], *Ying Chang*[1,2,3], *Rui Dai*[1,2,3], *Hu Ji*[1,2,3] *and Peng Han*[4,5,6]*

[1]*The Institute of Mining Engineering, BGRIMM Technology Group, Beijing, China,* [2]*China—South Africa Joint Research Center for Exploitation and Utilization of Mineral Resources, Beijing, China,* [3]*China—South Africa BRI Joint Laboratory for Sustainable Development and Utilization of Mineral Resources, Beijing, China,* [4]*Shenzhen Key Laboratory of Deep Offshore Oil and Gas Exploration Technology, Southern University of Science and Technology, Shenzhen, China,* [5]*Southern Marine Science and Engineering Guangdong Laboratory (Guangzhou), Guangzhou, China,* [6]*Department of Earth and Space Sciences, Southern University of Science and Technology, Shenzhen, China*

OPEN ACCESS

Edited by:
Fengqiang Gong,
Southeast University, China

Reviewed by:
Ren Tao,
Northeastern University, China
Bingxiang Huang,
China University of Mining and Technology, China

***Correspondence:**
Peng Han
hanp@sustech.edu.cn

Specialty section:
This article was submitted to Geohazards and Georisks, a section of the journal Frontiers in Earth Science

Received: *30 April 2022*
Accepted: *30 May 2022*
Published: *08 July 2022*

Citation:
Zhang D, Zeng Z, Shi Y, Chang Y, Dai R, Ji H and Han P (2022) An Effective Denoising Method Based on Cumulative Distribution Function Thresholding and its Application in the Microseismic Signal of a Metal Mine With High Sampling Rate (6 kHz). Front. Earth Sci. 10:933284. doi: 10.3389/feart.2022.933284

Microseismic events can be used to analyze the risk of tunnel collapse, rock burst, and other mine hazards in space and time. In practice, the artificial activities and other signals at the mining site can seriously interfere with the microseismic waveforms, reducing the signal-to-noise ratio. In this study, we propose a denoising method based on the threshold of the cumulative distribution function (CDF) of the wavelet coefficients in the wavelet domain using synchrosqueezed continuous wavelet transform (SS-CWT). First, the ratio of microseismic signal variance between two adjacent time windows is used to determine the range of background noise. Then, the microseismic signal is transformed into a wavelet domain using SS-CWT, and the threshold of wavelet coefficients at each scale is estimated based on the cumulative distribution function (CDF) of background noise. At last, a post-processing step is applied by utilizing an amplitude smoothing function, to further suppress the noise. The proposed denoising method is tested by both synthetic and filed microseismic data recorded in a metal mine. The results show that the method is effective in denoising and can improve the SNR of mine microseismic data with a high sampling rate.

Keywords: synchrosqueezed continuous wavelet transform (SS-CWT), wavelet coefficient thresholding, seismic denoising, microseismic detection, metal mine

INTRODUCTION

In order to monitor mine hazards, such as roof fall, collapse, and rockburst, passive microseismic monitoring technology was introduced in the mining industry (Young et al., 1992; Li et al., 2007; Hudyma and Potvin, 2010). By detecting and analyzing microseismograms, the location, magnitude, and source mechanism of microseismic events are calculated. Applying the seismological theories, the distribution of stress drops, displacements, and radiated energy can be obtained to provide basic data for the safety evaluation of surrounding environments during mining production (Yabe et al.,

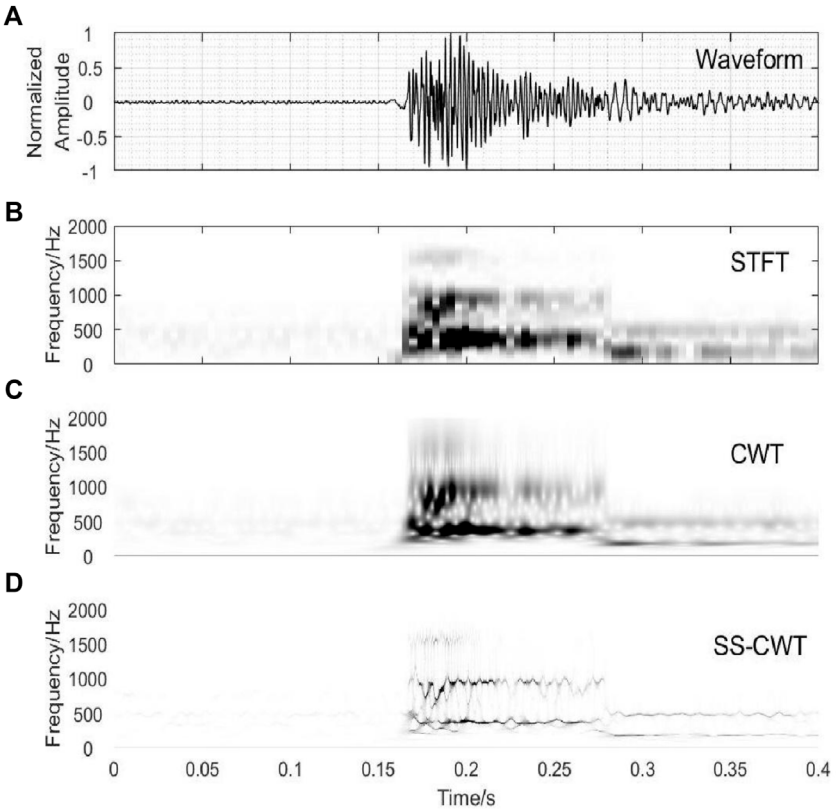


FIGURE 1 | Time-frequency Spectrum of a seismic record using STFT, CWT, and SSWT. **(A)** Field mine microseismic signal with high SNR, the sampling rate is 6000 Hz. **(B) (C)**, and **(D)** shows the STFT, CWT, and SS-CWT of the time series in **(A)**, respectively, where CWT and SS-CWT are both based on the Morlet wavelet.

2015). However, in many conventional seismic methods, the SNR of microseismic data strongly affects the reliability of data and the accuracy of waveform parameters' estimation, such as arrival time and polarity. As a result, the accuracy of microseismic location and other source parameters extracted from waveform is also influenced by the noise content. Especially for mine data, the high sampling rate and persistent human activities in the monitoring environment make complex noises being recorded and superimposed on the microseismic signal. Therefore, it is a challenging task to accurately separate microseismic signals from miscellaneous background noise. There is still a great need for developing suitable procedures that improve SNR allowing for robust seismic processing.

The noise in seismic data is divided into two categories: regular noise and random noise. Regular noise refers to the noise with a certain apparent velocity and frequency, such as surface wave, acoustic wave, secondary interference wave, multiple-wave, and 50 Hz alternating current interference. Spectral filtering is a common method for denoising noise with the specified frequency band, but it is not effective for removing noise with the same frequencies as the signal. Moreover, effective filter bands must be known in advance, and band-pass filtering inevitably distorts the signal and generates artifacts to influence the true onset time and polarity (Douglas, 1997; Scherbaum, 2001).

The microseismic data can also be denoised using multichannel methods, which are widely used in the active-source seismic community, such as predictive filtering methods (Liu et al., 2012; Liu and Chen 2013), singular spectrum analysis (Huang et al., 2015, 2016a; Zhang et al., 2016a; Zhang et al., 2016b; Zhang et al., 2016c), low-rank approximation based methods (Huang et al., 2016b; Xie et al., 2016; Chen et al., 2017; Zhou and Zhang 2017; Bai et al., 2018), dictionary learning-based methods (Chen 2017; Siahsar et al., 2017; Wu and Bai 2018a, b), and morphological filtering based method (Huang et al., 2017). The multichannel denoising methods rely on a fairly dense spatial sampling of the data. For most microseismic monitoring projects, where the number of spatial sensors is not large enough, the multichannel denoising methods are inapplicable or cannot give acceptable results. Especially, the sensors' number in one microseismic monitoring system is relatively small, and the spatial layout is irregular. Therefore, the denoising method based on multichannel information is not suitable for denoising of mining microseismic processing.

Many effective single-channel microseismic signal denoising methods based on time-frequency transformation have been developed, such as empirical mode decomposition (EMD) (Huang et al., 1998), short-time Fourier transform (STFT) (Mousavi and Langston, 2016a), continuous wavelet transform

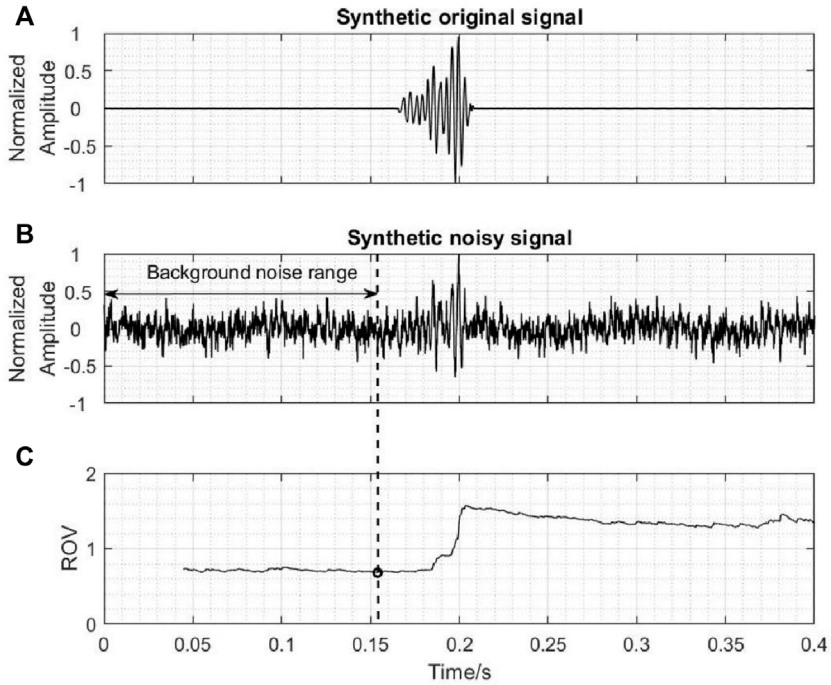


FIGURE 2 | The range of background noise estimation via ROV curve. **(A)** The waveform of the original seismic signal. **(B)** Synthetic seismic signal with noise. **(C)** ROV curve of the synthetic noisy signal, where a black circle indicates the minimum of ROV.

(CWT) (Goupillaud et al., 1984; Mousavi and Langston, 2016b), S transform (ST) (Stockwell et al., 1996; Askari and Siahkoohi, 2008; Wang et al., 2010), and general S transform (GST) (Wang et al., 2015). Recently, a new signal decomposition algorithm called synchrosqueezing transform (SST) was introduced by Daubechies et al. (2011) as an alternative to EMD. The SST can produce a sparse time-frequency representation for the modulated oscillation signal. More importantly, it has better mathematical support and more adaptive performance than EMD. Synchrosqueezed continuous wavelet transform (SS-CWT) combines wavelet analysis and SST to obtain time-frequency maps with significantly improved resolution. Mousavi et al. (2016c); Mousavi and Langston (2017) applied the SS-CWT to denoise single-channel microseismic data based on a custom thresholding strategy.

Donoho and Johnstone. (1997); Donoho and Johnstone (1995) showed that the universal threshold can be obtained for Gaussian noise in the time-frequency domain, which provides a reliable basis for subsequent denoising methods in the time-frequency domain. In this article, we introduce an effective denoising method based on cumulative distribution function (CDF) thresholding in the SS-CWT domain, including the range determination of pure background noise for noise level estimation, denoising noise based on CDF thresholding, and post-processing of weight suppression. Then, we use synthetic and field data examples to test and confirm the effectiveness of the proposed algorithm. Finally, we draw some key conclusions at the end of the article.

THEORETICAL BACKGROUND

Synchrosqueezed Continuous Wavelet Transform

Basically, the seismic data $s(t)$ recorded by geophones contains both microseismic signal and environmental noise, which can be expressed as

$$\boldsymbol{s}(\boldsymbol{t}) = \boldsymbol{s}_0(\boldsymbol{t}) + \boldsymbol{\eta}(\boldsymbol{t}), \tag{1}$$

where $s_0(t)$ is a microseismic signal, $\eta(t)$ is environmental noises.

The continuous wavelet transform (CWT) of $s(t)$ with a given mother wavelet ψ is (Daubechies, 1988; Heil and Walnut, 1989; Farge, 1992)

$$\boldsymbol{W}_s(\boldsymbol{a},\boldsymbol{\tau}) = \frac{\mathbf{1}}{\sqrt{\boldsymbol{a}}}\int_{-\infty}^{+\infty}\boldsymbol{s}(\boldsymbol{t})\boldsymbol{\psi}^*\left(\frac{\boldsymbol{t}-\boldsymbol{\tau}}{\boldsymbol{a}}\right)\boldsymbol{dt}, \tag{2}$$

where ψ^* represents the complex conjugate of a mother wavelet, a and τ are the scale variable and time shift, respectively.

With a flexible trade-off between time and frequency achieved by the variable length of the mother wavelet, the signal can be presented in the time-frequency domain. However, due to signal windowing and spectral leakage, the energy is spread out on a time-scale plane in the actual application, which leads to a blurred time-frequency spectrum. Hence, the synchrosqueezed transform is used here to squeeze the energy into the real instantaneous frequency of the signal, which improves the accuracy of wavelet-based transforms for frequency content estimation.

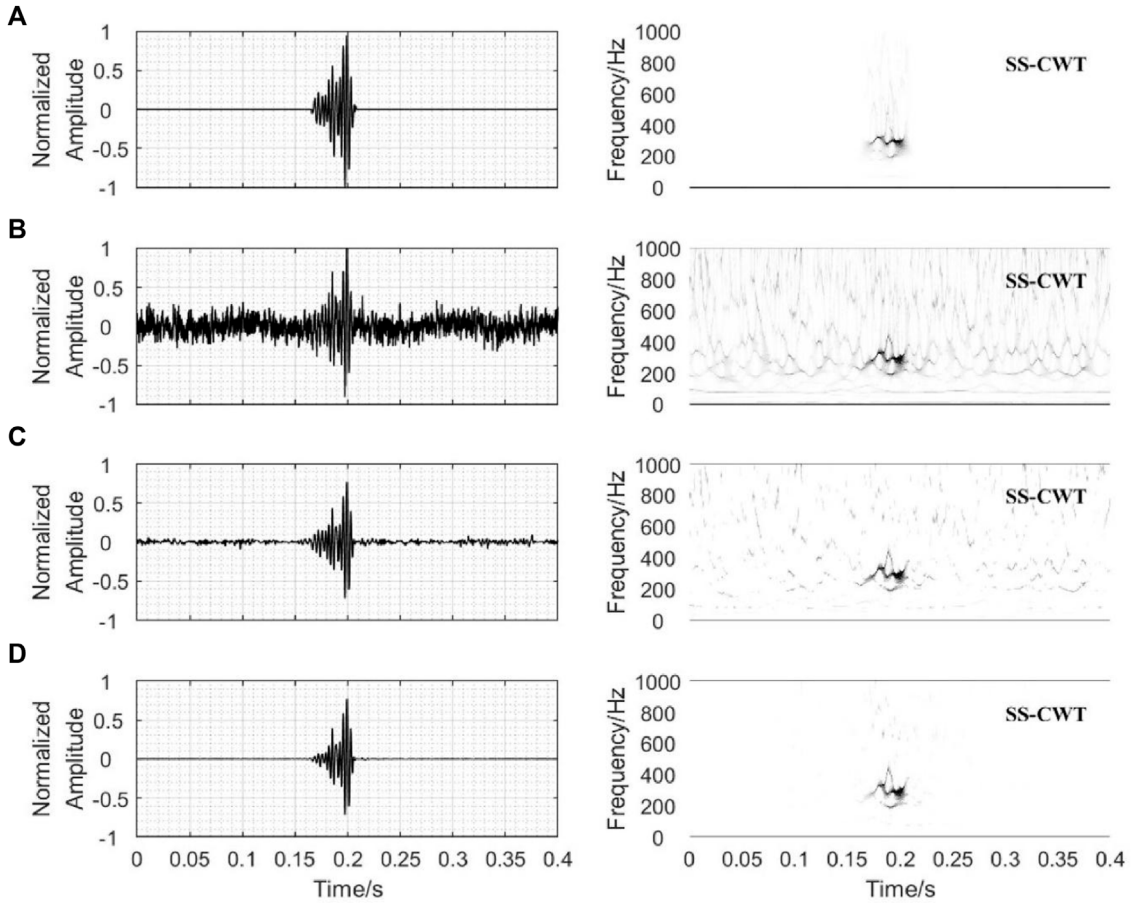


FIGURE 3 | Results of each step on denoising. **(A)** Synthetic original signal's waveform and SS-CWT spectrogram. **(B)** Synthetic noisy signal waveform and SSWT spectrogram. **(C)** Denoising waveform and SS-CWT spectrogram after CDF thresholding. **(D)** Denoising waveform and SS-CWT spectrogram after post-processing.

The instantaneous frequency can be estimated by the derivative of the wavelet coefficient (Auger et al., 2013):

$$\boldsymbol{\omega}(\boldsymbol{a},\boldsymbol{\tau}) = -\boldsymbol{i}\boldsymbol{W}_{\boldsymbol{s}}(\boldsymbol{a},\boldsymbol{\tau})^{-1}\frac{\partial \boldsymbol{W}_{\boldsymbol{s}}(\boldsymbol{a},\boldsymbol{\tau})}{2\pi\partial\boldsymbol{\tau}}, \textit{for } \boldsymbol{W}_{\boldsymbol{s}}(\boldsymbol{a},\boldsymbol{\tau}) \neq 0. \quad (3)$$

This allows us to convert the time-scale plane (a, τ) into the time-frequency plane ($w(a, \tau)$, τ). Also, the synchrosqueezed wavelet transform of $s(t)$ is (Daubechies et al., 2011)

$$\boldsymbol{T}_{\boldsymbol{s}}(\boldsymbol{\omega}_{\boldsymbol{l}},\boldsymbol{\tau}) = \frac{\mathbf{1}}{\Delta\boldsymbol{\omega}} \sum_{\boldsymbol{a}_{\boldsymbol{k}}:\ \left|\boldsymbol{w}(\boldsymbol{a}_{\boldsymbol{k}},\boldsymbol{\tau})-\boldsymbol{\omega}_{\boldsymbol{l}}\right| \le \frac{\Delta\boldsymbol{\omega}}{2}} \boldsymbol{W}_{\boldsymbol{s}}(\boldsymbol{a}_{\boldsymbol{k}},\boldsymbol{\tau})\boldsymbol{a}_{\boldsymbol{k}}^{\frac{-3}{2}}(\Delta\boldsymbol{a})_{\boldsymbol{k}}, \quad (4)$$

where ω_l is the lth discrete frequency and the center of the interval $[\omega_l - 1/2\Delta\omega, \omega_l + 1/2\Delta\omega]$. a_k is the kth scale, and $\Delta\omega = \omega_k - \omega_{k\text{-}1}$. The individual component s_k from the T_s can be reconstructed by integrating the coefficients over frequencies ω_l that corresponds to the kth component (Thakur et al., 2013).

The inverse transform of the SS-CWT is (Herrera et al., 2014)

$$\boldsymbol{s}(\boldsymbol{t}) = 2\boldsymbol{C}_{\boldsymbol{\psi}}^{-1}\boldsymbol{Re}\left(\sum_{\boldsymbol{l}} \boldsymbol{T}_{\boldsymbol{s}}(\boldsymbol{\omega}_{\boldsymbol{l}},\ \boldsymbol{t})\right), \quad (5)$$

where C_ψ is a constant, which is given in Thakur et al. (2013) depending on the mother wavelet. As an example, **Figure 1** shows the transform results of a field seismic signal using SS-CWT and other classic time-frequency analyses. Compared with STFT (**Figure 1B**) and CWT (**Figure 1C**), the SS-CWT (**Figure 1D**) exhibits higher energy concentration in the time-frequency plane, which brings advantages in threshold-based denoising.

METHODS

Estimation of Background Noise Range

The threshold function for denoising is determined based on the statistics of the noise. Therefore, it is important to estimate the pure background noise range accurately to obtain the threshold of each wavelet scale precisely. In the first step, the ratio of the microseismic signal variance between two adjacent time windows is proposed to determine the range of background noise. The core idea is from the conventional short-term-average (STA)/long-term-average (LTA) (Withers et al., 1998) algorithm for picking up arrival time, which utilizes the variance change of amplitude in

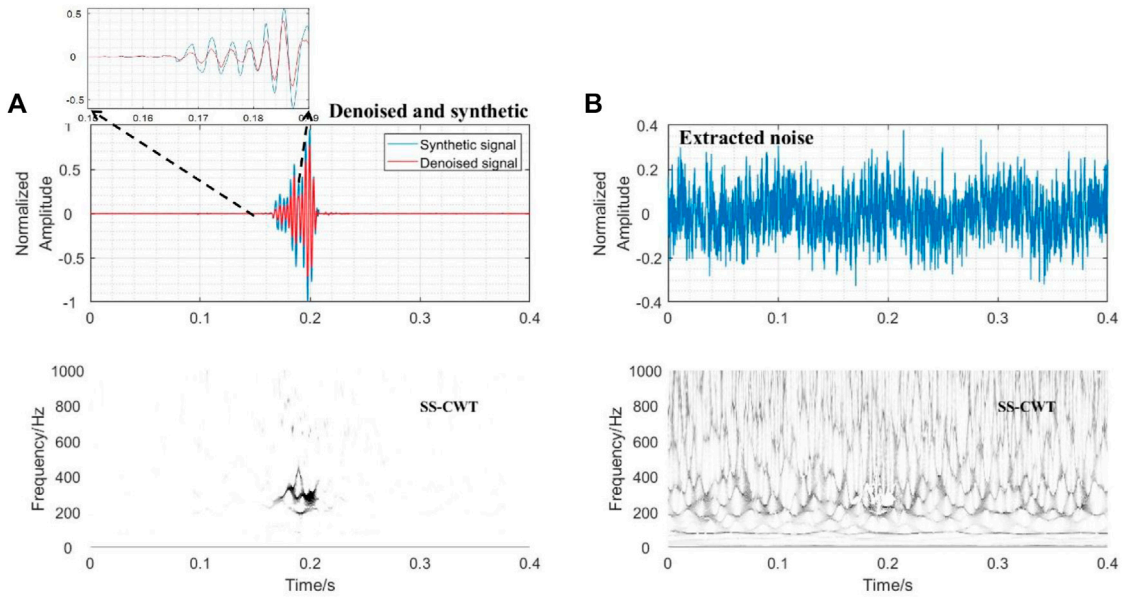


FIGURE 4 | (A) Denoised seismogram and its associated SS-CWT. **(B)** Extracted noise and its associated SS-CWT.

two windows to indicate whether the presence or absence of a signal. The ratio of variance (ROV) is defined by

$$\boldsymbol{ROV}\,(\boldsymbol{i}) = \frac{\boldsymbol{var}\left(\boldsymbol{s}_{0,i}\right)}{\boldsymbol{var}\left(\boldsymbol{s}_{i,N}\right)}, \tag{6}$$

where ROV(i) is the ratio of signal amplitude variance in two-time windows before and after the time i, $var(s_{0,\,i})$ and $var(s_{i,\,N})$ are the signal amplitude variance in two adjacent time windows, respectively. N is the length of the input data. The pure background noise range is determined according to the minimum point of ROV. **Figure 2** shows an example of background noise estimation using the ROV curve. The result suggests that the ROV method can provide reliable and real-time pure background noise data, which is essential to the accurate determination of wavelet threshold for denoising in the subsequent step.

Wavelet Threshold Determination Based on Cumulative Distribution Function

If the background noise obeys Gaussian distribution, the threshold function can be computed using the mean and standard deviation of the absolute value of the wavelet coefficients at each scale (Langston and Mousavi, 2019):

$$\boldsymbol{\beta}\,(\boldsymbol{a}) = \boldsymbol{mean}\,(|\boldsymbol{W}\,(\boldsymbol{a},\,\boldsymbol{\tau})|) + \boldsymbol{c} * \boldsymbol{st.dev.}\,(|\boldsymbol{W}\,(\boldsymbol{a},\,\boldsymbol{\tau})|), \tag{7}$$

where mean$(|W\,(a,\,\tau)|)$ and $st.dev.\,(|W\,(a,\,\tau)|)$ are the mean and standard deviation of wavelet coefficients at each scale a. Parameter c determines the value of wavelet coefficients threshold. It needs to be emphasized that $\beta(a)$ is computed using the pure background noise obtained in the previous step rather than the entire seismic data because the seismic signal would bias the statistic values in **Eq. 7**.

Donoho and Johnstone (1997) proposed a mild criterion to set the parameter c, and a widely used "universal threshold" is obtained:

$$\boldsymbol{c} = \sqrt{2\boldsymbol{log}_{10}\boldsymbol{N}}, \tag{8}$$

where parameter c is related to the number of noise samples N at each scale and its value is close to 3 from this relation if N has an order of 10^4. The threshold function will yield a confidence interval of about 99.7% for the number of noise samples N. Under such a threshold, most of the noise will be removed and about 0.3% of the noise is retained. To obtain the threshold more flexible, we take the approach of estimating the cumulative distribution function of Gaussian distribution for noise in the time window at each scale and calculating the confidence value for the distribution. The threshold function becomes

$$\boldsymbol{\beta}\,(\boldsymbol{a}) = \boldsymbol{CDF}^{-\boldsymbol{1}}_{\boldsymbol{Gauss}}\,(\boldsymbol{a})\ (\boldsymbol{P} = \boldsymbol{THRE}), \tag{9}$$

in which $CDF^{-1}_{Gauss}(a)$ is the inverse cumulative distribution function at the scale a using Gaussian distribution, and parameter THRE is the confidence value that needs to be set. Once the wavelet coefficient threshold $\beta(a)$ on each scale a is obtained, we can apply the hard thresholding method to remove noise in the time-frequency domain.

Hard thresholding is a nonlinear process. It keeps the wavelet coefficients if they are greater than a threshold criterion $\beta(a)$; otherwise, they are set to zero (Donoho and Johnstone, 1995). The denoising scheme can be expressed as follows:

$$\tilde{\boldsymbol{W}}\,(\boldsymbol{a},\boldsymbol{\tau}) = \begin{cases} \boldsymbol{W}\,(\boldsymbol{a},\boldsymbol{\tau}) & \boldsymbol{if}\ |\boldsymbol{W}\,(\boldsymbol{a},\boldsymbol{\tau})| \geq \boldsymbol{\beta}\,(\boldsymbol{a}) \\ 0 & \boldsymbol{otherwise} \end{cases}. \tag{10}$$

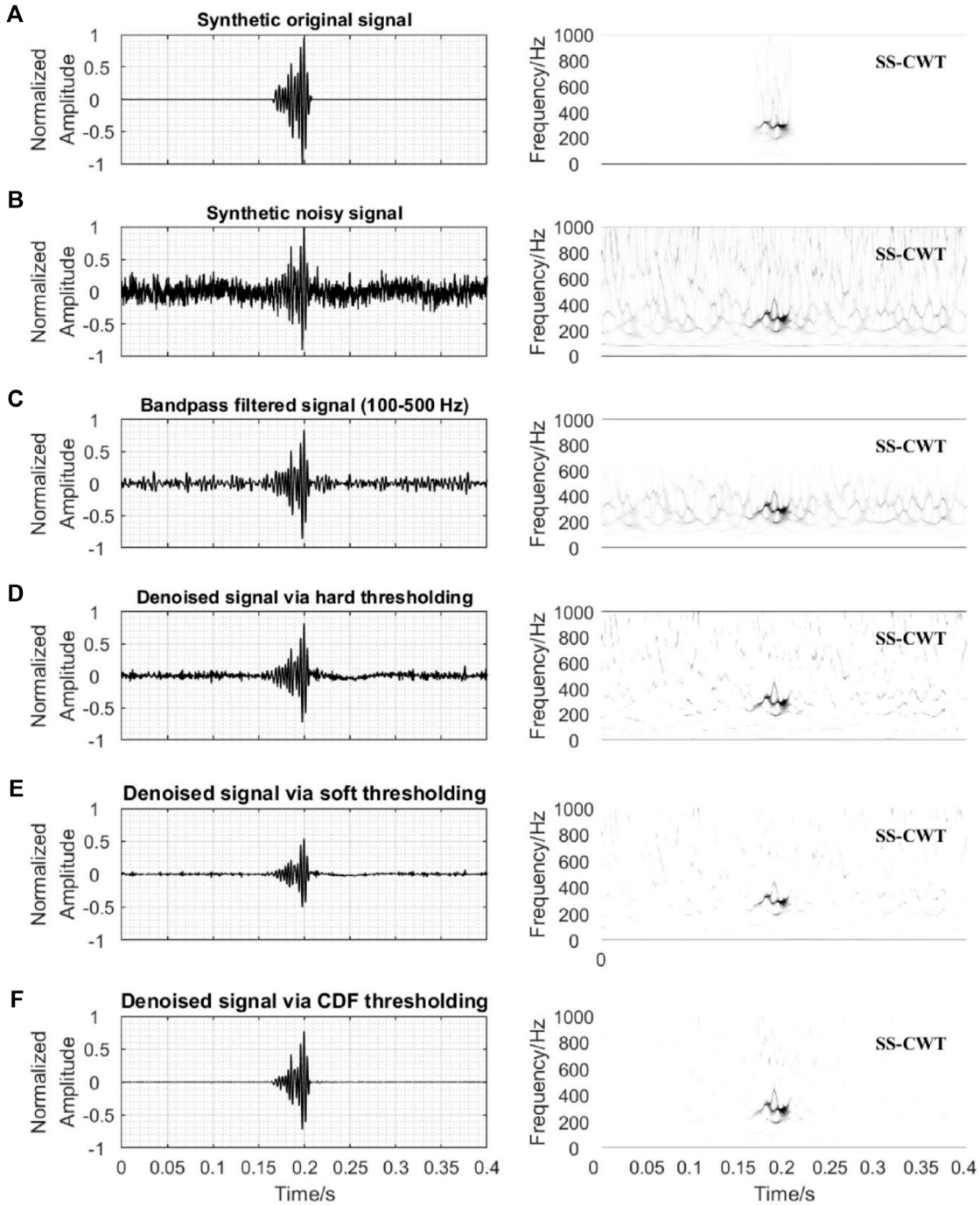


FIGURE 5 | (A) The original seismic data and its SS-CWT spectrogram. **(B)** The synthetic noisy data and its SS-CWT spectrogram. **(C)** Waveform and SS-CWT spectrogram of denoised data after band-pass filtering (100–500 Hz). **(D)** Waveform and SS-CWT spectrogram after hard thresholding. **(E)** Waveform and SS-CWT spectrogram of denoised data after soft thresholding. **(F)** Waveform and SS-CWT spectrogram after CDF thresholding and post-processing.

Hard thresholding is known to yield abrupt artifacts in the denoised signal (Chang et al., 2000). Therefore, many scholars have developed soft thresholding functions (Weaver et al., 1991; Yoon and Vaidyanathan., 2004; Shuchong and Xun, 2014). Soft thresholding produces smaller errors but often results in oversmoothing of the denoised signal. In the next step, we add a post-processing step to smooth residual noise and minimize damage to the amplitude of the microseismic signal as much as possible.

TABLE 1 | Comparison of RMS, SNR, CC, and time cost among different denoising approaches.

Method	RMS	SNR	CC	Time (s)	TFT
Noisy data	0.1076	2.9072	0.6277	——	——
Band-pass filtering	0.0593	4.7277	0.8336	0.03	——
Hard thresholding	0.0473	8.7472	0.8962	0.56	SS-CWT
Soft thresholding	0.0578	15.2117	0.9331	0.65	SS-CWT
CDF thresholding	0.0326	79.1576	0.9731	1.58	SS-CWT

Post-Processing

After hard thresholding in the previous step, most wavelet coefficients of noise are removed, while the wavelet coefficients of the seismic signal are almost retained. The energy of the seismic signal in the time-frequency domain exhibits higher connectivity and is numerically larger than the remaining noise. Therefore, to further suppress the noise, we construct a smoothing function, which comprehensively considers the continuity and intensity of wavelet coefficients on the time axis. To do this, the function DF is calculated by stacking the amplitude of wavelet coefficients using all scales:

$$\boldsymbol{DF}(\boldsymbol{\tau}) = \sum_{\boldsymbol{a}=1}^{\boldsymbol{n_a}} \left|\tilde{\boldsymbol{W}}(\boldsymbol{a},\boldsymbol{\tau})\right| \quad \textbf{for } \boldsymbol{\tau} = 1,\cdots,\boldsymbol{N}, \tag{11}$$

where n_a is the number of scales. Then, the smoothing function SF is calculated using DF:

$$\boldsymbol{SF}(\boldsymbol{\tau}) = \mathbf{1} - \left[\mathbf{1} - \boldsymbol{exp}\left(-\frac{\boldsymbol{\lambda}|\boldsymbol{\tau}-\boldsymbol{\tau_m}|}{\boldsymbol{N}}\right)\right]^{\boldsymbol{\alpha}\frac{\boldsymbol{DF}(\boldsymbol{\tau})}{\boldsymbol{DF_m}}}, \tag{12}$$

where DF_m is the maximum of the function DF, and τ_m is the time position of DF_m on the time series with length N. Parameters α and λ are nonnegative and used to adjust the importance of time distance $|\tau - \tau_m|$ and the ratio of the wavelet coefficient energy $DF(\tau)/DF_m$. If α is close to 0, the smoothing function mainly is dependent on the $|\tau - \tau_m|$ value; If λ is close to 0, the value $DF(\tau)/DF_m$ plays a dominant role in the smoothing function. The value of parameters α and λ should not be large so that the amplitude of the arrival waveform will be retained as much as possible. Notice that the smoothing function $SF(\tau)$ is only relative to time τ and independent of scale a. Therefore, the smoothing function is used to uniformly suppress the wavelet coefficients of the residual noise on all scales. An advantage of the proposed smoothing method is that the maximum amplitude of the microseismic event signal is not affected, which can improve the accuracy of mine local magnitude (M_L) calibration that utilizes the maximum amplitude information of the seismic signal.

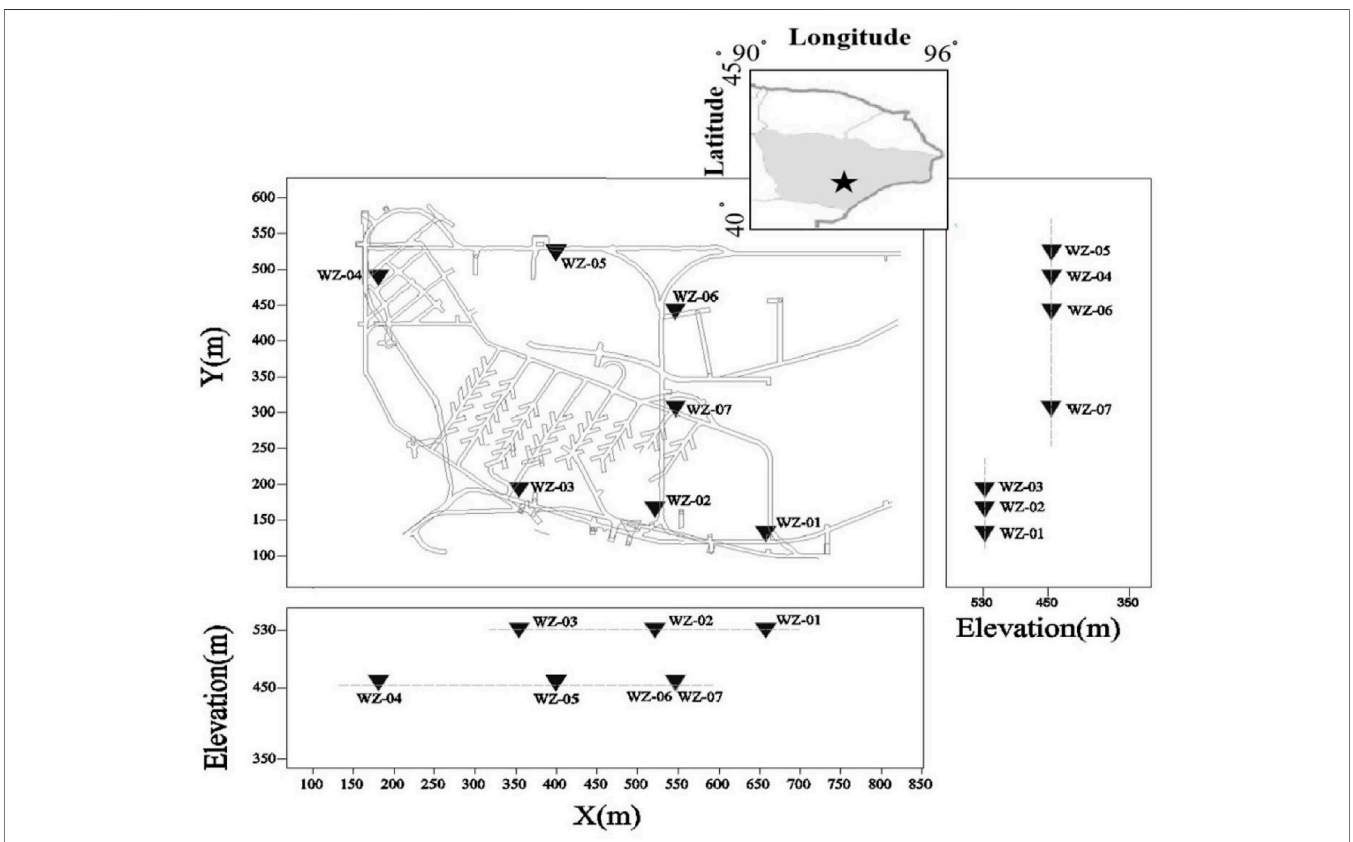


FIGURE 6 | A metal mine microseismic monitoring network in Xinjiang, China, shown in one horizontal (XY) and two vertical depth sections (XZ and ZY) views. Dark inverted triangles are triggered-based seismometers.

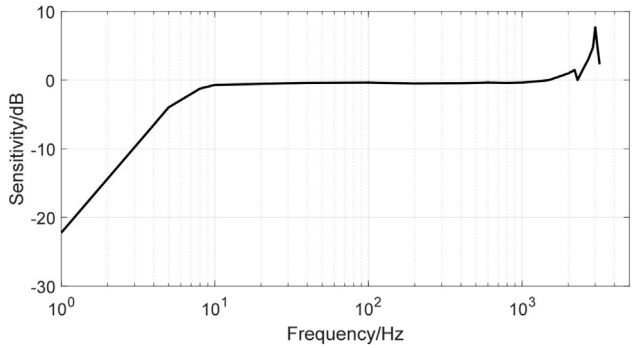


FIGURE 7 | Amplitude-frequency response curve of the seismometer utilized in the metal mine microseismic monitoring network in Xinjiang, China.

RESULTS

We first apply the method to synthetic data. In this way, the shape of the whole output signal can be compared with the theoretical signal. Then, the algorithm will be applied to observed microseismograms in a metal mine. In the synthetic data test, we will show the denoising performance of this method by comparing the information of phase-arrival shapes, root-mean-square error (RMS), SNR, and cross-correlation coefficients (CC) between the denoised and original signal. The SNR is measured as the ratio of the root-mean-square amplitude in a time window around the signal to that in the same length window of preceding noise. On the other hand, because the theoretical signal of the observed data in the mine is not known, we will compare the sensitivity of the onset pick-up threshold setting before and after signal denoising using a 2D microseismic event signal detector composed of STA/LTA and kurtosis algorithms. The lower the sensitivity of the microseismic event recognition threshold, the less likely it is to be misidentified.

Synthetic Data Test

The denoising algorithm is applied to a known synthetic signal and the original signal is from the field data with high SNR (**Figure 2A**). Then, the complex noise including the random and a fixed frequency of 50 Hz is added to the original signal to yield the resulting noisy signal with an SNR of 2.9072 (**Figure 2B**). According to the previous description of the denoising process, the pure background noise range should be estimated at first. **Figure 3B** shows that the ROV curve of the noisy signal and the range of pure background noise in a noisy signal is accurately obtained according to the minimum position of the curve, which indicates that the pure background noise estimation method we proposed is highly feasible. Then, the noisy signal is transformed into the time-frequency domain using SS-CWT and the wavelet coefficients at all scales are estimated using the hard thresholding rule of **Eq. 10**, scale-by-scale. In this step, the threshold function $\beta(a)$ is determined using **Eq. 9**, where the parameter THER is set to 99.9%, meaning the 99.9% confidence value for the distribution in the time window at each scale. The hard thresholding denoised result is shown in **Figure 3C**. Compared with the denoising result using the universal threshold of Donoho and Johnstone (1997) (**Figure 5D**), it can be seen that the wavelet coefficients of residual noise in the time-frequency spectrum of **Figure 3C** are less. Finally, the smoothing function of **Eq. 12** is applied to smooth the CDF thresholding signal to yield the final denoising signal as shown in **Figure 3D**. For the waveform after denoising, the SNR is significantly improved because the noise before and after the microseismic signal is effectively removed. In the denoising time-frequency spectrum, the isolated noisy coefficients remaining after the previous steps are cleaned up and the wavelet coefficients of the signal are retained completely.

The goal of the denoising algorithm is to observe the effects of the denoised process on the polarity, the onset time, and smoothing of very small emergent arrivals at the very beginning of the signal buried under the background noise and track the change in other parts more easily. We compare the denoised waveform with the original waveform as shown in **Figure 4A**. The denoised and synthetic signals match very well over the entire waveform, especially the onset and polarity are preserved very well. The arrival time that was buried under the noise became clear after denoising, which improves arrival time picking and further benefits the source location estimation. This is greatly significant to the mining microseismic monitoring which needs a high-precision location. Comparing SS-CWT spectrums in **Figures 4A,B**, the noise energy is completely extracted without destroying the signal energy, which can provide reliable noise information for background noise imaging research.

The superior performance of the CDF thresholding compared with other methods commonly used is clearly shown in **Figure 5**. A detailed observation of the useful information of the first arriving waveform (arrival time and polarity direction of the onset) illustrates the good performance of the proposed denoising method when compared with the band-pass filtering, hard and soft thresholding. Band-pass filtering removes noise with frequencies higher and lower than the signal's frequency range but noise within the frequency range of the signal is untouched (**Figure 5C**). Soft and hard thresholding preserve the structure of the signal, whereas they were much less effective in noise removal (**Figures 5D,E**).

The good performance of the CDF thresholding method can be further confirmed by quantitative comparative analysis of the RMS, SNR, and cross-correlation values between the denoised and original waveforms presented in **Table 1**. In this table, the CDF thresholding method has the smallest RMS (0.0326), the highest SNR (79.1576), and the maximal CC (0.9731) compared with the band-pass filtering and hard and soft thresholding. In terms of computational time, the CDF thresholding method takes more time to work, but it is acceptable.

Mine Microseismic Data

Complex background noise removal is a challenging task encountered in microseismic monitoring, especially in mine. The main reason is that the monitoring scope is small relative to the mine, so it's necessary to accurately identify and pick up the arrival time of the microseismic signal to get the accurate source

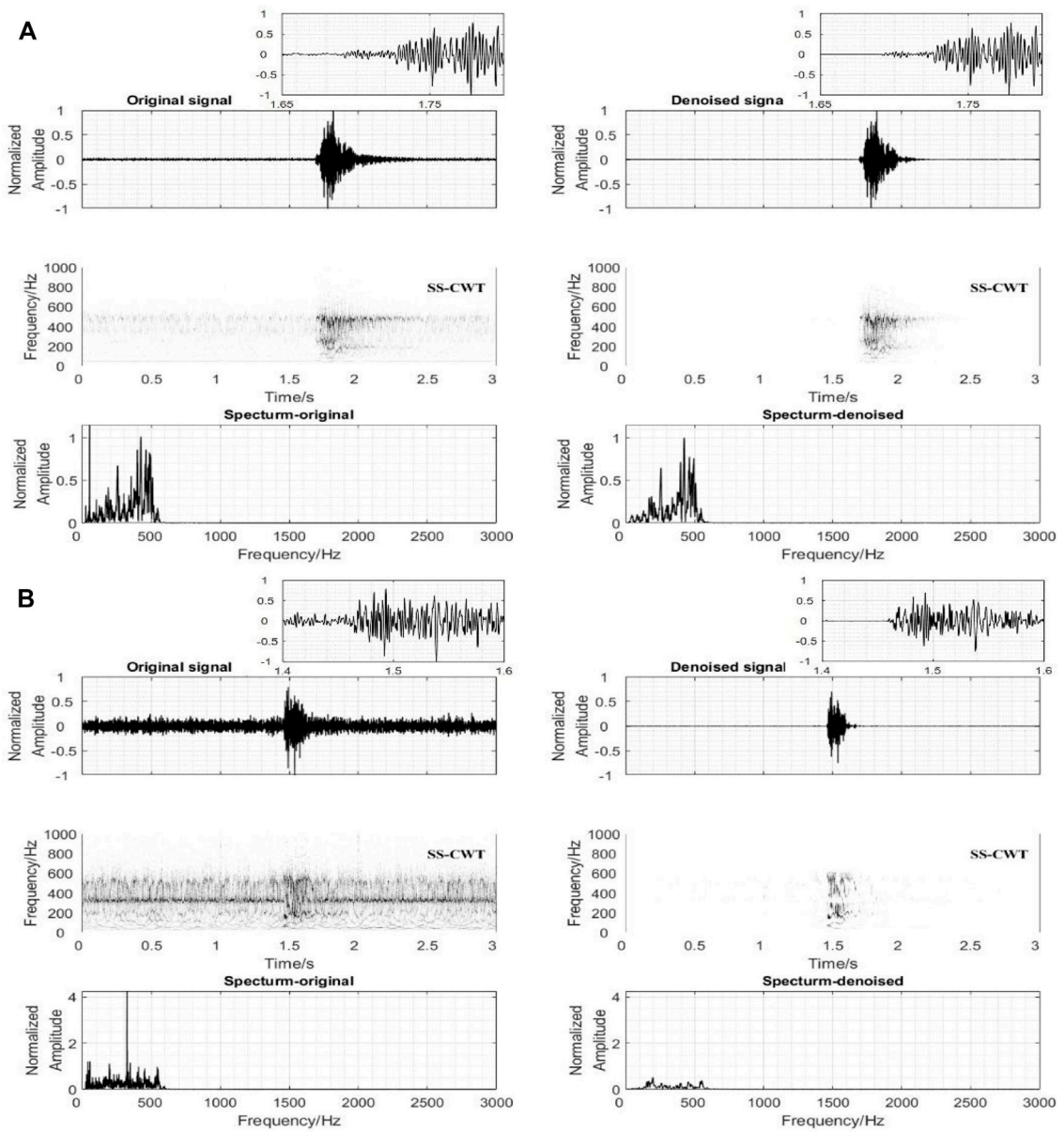


FIGURE 8 | Denoised results for mining-induced microseismic records of **(A)** high **(B)** moderate, and **(C)** low SNR using the proposed method.

location for seismicity analysis. Therefore, the sampling rate of the microseismic record needs to be high enough to capture the microseismicity. However, the high sampling rate simultaneously makes the microseismic event more susceptible to burry in diverse environmental noise. We apply the CDF thresholding to passively recorded, complex noise mine microseismic data with different SNR to test the performance of this method in denoising and automatic detection.

Field microseismic data was recorded by seismometers of high sampling rate (6 kHz) trigger-based network operation located at a metal mine in Xinjiang, China (**Figure 6**). The amplitude-frequency response curve of the seismometer is shown in **Figure 7**. The denoising frequency band is chosen as 10–1000 Hz because the amplitude-frequency response is stable in this frequency range.

The denoising results of microseismic signals with different SNRs using the CDF thresholding are shown in **Figure 8**. The comparison of microseismic signals before and after denoising are from time, time-frequency, and Fourier amplitude domains. For the waveform in the time domain, the SNR of the denoised microseismic signals has been significantly improved. This can facilitate the picking of the first arrival times and their polarity which has special importance for the source location and fracture imaging. Thus, denoising microearthquakes can help to improve the detection, location, and understanding of wave propagation, which are crucial steps in microseismic processing. Comparing

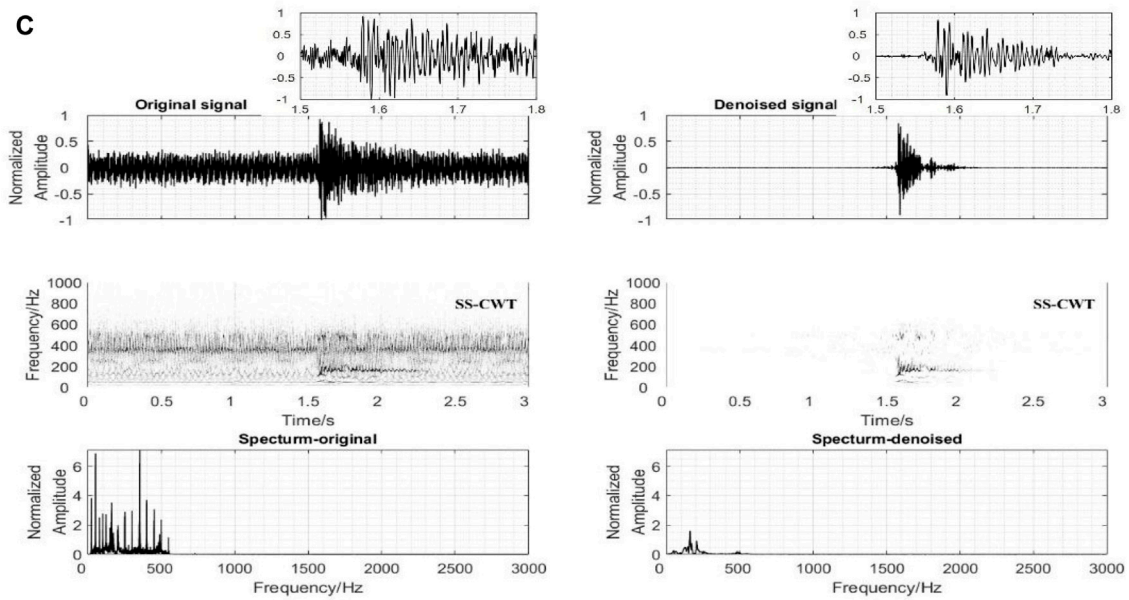


FIGURE 8 | (Continued).

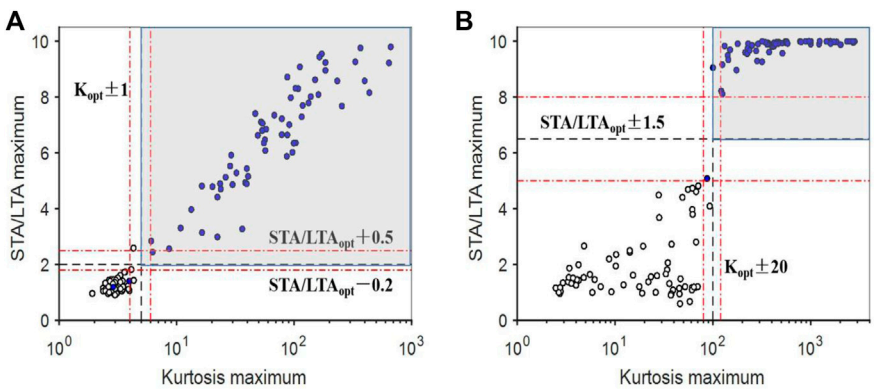


FIGURE 9 | Comparison of the robustness of automatic microseismic event detection before and after denoising. White dots indicate noise measurements, blue dots correspond to microseismic events. **(A)** Results of Original training data set, dark dashed lines indicate the selected optimal threshold level of maximum kurtosis (K_{opt}=5), and maximum STA/LTA (STA/LTA_{opt}=2), and red dashed lines indicate the selected optimal threshold level range of kurtosis (K_{opt} ± 1) and STA/LTA (STA/LTA_{opt} - 0.2 and STA/LTA_{opt} + 0.5). **(B)** Results of denoising data set, dark dashed lines indicate the selected optimal threshold level of maximum kurtosis (K_{opt}=100), and maximum STA/LTA (STA/LTA_{opt} = 6.5), red dashed lines indicate the selected optimal threshold level range of kurtosis (K_{opt} ± 20) and STA/LTA (STA/LTA_{opt} ± 1.5).

the signals before and after denoising in the time-frequency domain, the frequency band of the noise is almost consistent with the signal, which leads to the failure of the frequency band filtering method. The CDF thresholding method does not only cleanly remove the noise in the same frequency band as the signal, but also cleans the current interference noise of 50 Hz (**Figure 8A**) and the strong interference noise with multiples of 50 Hz (**Figures 8B,C**).

To further demonstrate the effectiveness of denoising, the performance of automatic detection is investigated. The STA/LTA (Withers et al., 1998) and kurtosis characterization function (Saragiotis et al., 2002) are combined, forming a 2D detector, which allows identifying time windows that potentially contain signals corresponding to microseismic events (Palgunadi et al., 2020). We used the training data set of 66 seismic events and 66 pure noise records to determine threshold values for this 2D detector. We recorded the maximum values of STA/LTA and kurtosis characterization functions in each event and each pure background noise time window, respectively. The result of the training data set before and after denoising is presented in **Figure 9**. The optimal threshold values of the original data set are around 2 and 5 for STA/LTA and kurtosis characterization function before denoising,

respectively. For the denoised data set, the optimal threshold values are around 6.5 and 100. In the automatic detection procedure, any time window with values of STA/LTA and kurtosis characterization function above the two thresholds is taken as containing a microseismic event (gray rectangle in **Figures 9A,B**). As shown in **Figure 9A**, the adjustable threshold range of the original data set is narrower, implying that the automatic detection results in **Figure 9A** are much more sensitive to the thresholds than that in **Figure 9B**. This suggests that the proposed denoising method could improve the robustness of the automatic detection of microseismic events.

DISCUSSION

The first step in the denoising process is to estimate the pure background noise range, which is extremely important to the entire denoising process, as the universal threshold is related to the statistical characteristics of the background noise. In practice, the noise and seismic signals mix up with each other, and it is very difficult to accurately tell when the seismic signal arrives before denoising. The proposed ROV method can be used to obtain the pure background noise closest to the microseismic signal, providing a real-time noise estimation. This theoretically enables a more precise threshold estimation of noise and increases the denoising efficiency in the following step.

The smoothing function in the post-processing step has two nonnegative parameters. Parameter λ adjusts the weights of time distance $|\tau - \tau_m|$ and parameter α modulates the decay rates according to the ratio of the wavelet coefficient energy $DF(\tau)/DF_m$. *SF* increases with λ and decreases with α. The two parameters are trained by a group of the synthetic data set, and their values are between 1 and 10. The denoising results are not sensitive to the values of the two parameters, suggesting the robustness of the proposed smoothing function. Our denoising method cannot preserve the amplitude of the entire seismic signal. However, the smoothing value is equal to 1 when $\tau = \tau_m$, where τ_m represents the position of the maximum amplitude of the microseismic signal. The smoothing function can preserve the maximum amplitude of the microseismic signal. Because local magnitude (M_L) calibration utilizes the maximum amplitude information of seismic signal, the preserved maximum amplitude after denoising benefits improves the accuracy of M_L. This is crucial for subsequent seismic risk assessment.

As shown in **Figure 4**, wavelet coefficients of the seismic signal can be accurately separated from the noisy data without changing the time-frequency structure of the background noise using the proposed method. This provides a useful way for extracting background noise, which is crucial to dispersion curve measurement and surface wave inversion from ambient noise (Bensen et al., 2007; Wang et al., 2019).

CONCLUSION

We propose a new denoising framework for complex noise removal based on CDF thresholding in the SS-CWT domain. The denoising method includes the estimation of pure background noise range, determination of thresholding function based on CDF, coefficient thresholding process for wavelet coefficient, and post-processing with smooth function. Performance on both synthetic and field data demonstrates the effectiveness of the denoising method. After denoising by the proposed method, the automatic seismic detection results become less sensitive to the detector threshold, suggesting the practical value of the denoising method in handling microseismic data with a high sampling rate.

DATA AVAILABILITY STATEMENT

The original contributions presented in the study are included in the article/Supplementary Material; further inquiries can be directed to the corresponding author.

AUTHOR CONTRIBUTIONS

Conceptualization: DZ, PH, and ZZ; methodology: ZZ and PH; software: ZZ; validation: DZ, ZZ, YS, YC, RD, HJ, and PH; formal analysis: ZZ; investigation: ZZ and PH; resources: DZ; data curation: DZ, ZZ, and PH; writing—original draft preparation: ZZ; writing—review and editing: ZZ, YC, DZ, and PH; visualization: ZZ; and supervision: DZ and PH. All authors have read and agreed to the published version of the manuscript.

FUNDING

This research was partly supported by the National Key Research & Development Program of China (2018YFE0121000 and 2020YFE0202800), Key Special Project for Introduced Talents Team of Southern Marine Science and Engineering Guangdong Laboratory (Guangzhou) (GML2019ZD0203), and Shenzhen Key Laboratory of Deep Offshore Oil and Gas Exploration Technology (Grant No. ZDSYS20190902093007855).

ACKNOWLEDGMENTS

The microseismic data are from the Institute of Mining Engineering, BGRIMM Technology Group, Beijing, China.

REFERENCES

Askari, R., and Siahkoohi, H. R. (2008). Ground Roll Attenuation Using the S and *X-F-K* Transforms. *Geophys. Prospect* 56, 105–114. doi:10.1111/j.1365-2478.2007.00659.x

Auger, F., Flandrin, P., Lin, Y.-T., McLaughlin, S., Meignen, S., Oberlin, T., et al. (2013). Time-frequency Reassignment and Synchrosqueezing: An Overview. *IEEE Signal Process. Mag.* 30, 32–41. doi:10.1109/MSP.2013.2265316

Bai, M., Wu, J., Xie, J., and Zhang, D. (2018). Least-squares Reverse Time Migration of Blended Data with Low-Rank Constraint along Structural Direction. *J. Seismic Explor.* 27 (1), 29–48.

Bensen, G. D., Ritzwoller, M. H., Barmin, M. P., Levshin, A. L., Lin, F., Moschetti, M. P., et al. (2007). Processing Seismic Ambient Noise Data to Obtain Reliable Broad-Band Surface Wave Dispersion Measurements. *Geophys. J. Int.* 169(3), 1239–1260.doi:10.1111/j.1365-246X.2007.03374.x

Chang, S. G., Bin YuYu, B., and Vetterli, M. (2000). Adaptive Wavelet Thresholding for Image Denoising and Compression. *IEEE Trans. Image Process.* 9, 1532–1546. doi:10.1109/83.862633

Chen, Y. (2017). Fast Dictionary Learning for Noise Attenuation of Multidimensional Seismic Data. *Geophys. J. Int.* 209, 21–31. doi:10.1093/gji/ggw492

Chen, Y., Zhou, Y., Chen, W., Zu, S., Huang, W., and Zhang, D. (2017). Empirical Low-Rank Approximation for Seismic Noise Attenuation. *IEEE Trans. Geosci. Remote Sens.* 55 (8), 4696–4711. doi:10.1109/TGRS.2017.2698342

Daubechies, I., Lu, J., and Wu, H.-T. (2011). Synchrosqueezed Wavelet Transforms: An Empirical Mode Decomposition-like Tool. *Appl. Comput. Harmon. Analysis* 30 (2), 243–261. doi:10.1016/j.acha.2010.08.002

Daubechies, I. (1998). Orthonormal Bases of Compactly Supported Wavelets. *Commun. Pure Appl. Math.* 41, 909–996. doi:10.1002/(ISSN)1097-0312

Donoho, D. L., and Johnstone, I. M. (1995). Adapting to Unknown Smoothness via Wavelet Shrinkage. *J. Am. Stat. Assoc.* 90 (432), 1200–1224. doi:10.1080/01621459.1995.10476626

Donoho, D. L., and Johnstone, I. M. (1994). Ideal Spatial Adaptation by Wavelet Shrinkage. *Biometrika* 81, 425–455. doi:10.1093/biomet/81.3.425

Douglas, A. (1997). Bandpass Filtering to Reduce Noise on Seismograms: Is There a Better Way? *Bull. Seismol. Soc. Am.* 87, 770–777. doi:10.1785/BSSA0870030770

Farge, M. (1992). Wavelet Transforms and Their Applications to Turbulence. *Annu. Rev. Fluid Mech.* 24, 395–458. doi:10.1146/annurev.fl.24.010192.002143

Goupillaud, P., Grossmann, A., and Morlet, J. (1984). Cycle-octave and Related Transforms in Seismic Signal Analysis. *Geoexploration* 23 (1), 85–102. doi:10.1016/0016-7142(84)90025-5

Heil, C. E., and Walnut, D. F. (1989). Continuous and Discrete Wavelet Transforms. *SIAM Rev.* 31, 628–666. doi:10.1137/1031129

Herrera, R. H., Han, J., and van der Baan, M. (2014). Applications of the Synchrosqueezing Transform in Seismic Time-Frequency Analysis. *Geophysics* 79 (3), V55–V64. doi:10.1190/geo2013-0204.1

Huang, N. E., Shen, Z., Long, S. R., Wuau, M. C., Shihau, H. H., Zhengau, Q., et al. (19981971). The Empirical Mode Decomposition and the Hilbert Spectrum for Nonlinear and Non-stationary Time Series Analysis. *Proc. R. Soc. Lond. A* 454, 903–995. doi:10.1098/rspa.1998.0193

Huang, W., Wang, R., Chen, X., Zhou, Y., Chen, Y., and You, J. (2017). "Lowfrequency Noise Attenuation of Seismic Data Using Mathematical Morphological Filtering," in 87th Annual International Meeting, SEG, Expanded Abstracts, Houston, Texas, September 28, 2017, 5011–5016. doi:10.1190/segam2017-17665921.1

Huang, W., Wang, R., Chen, Y., Yuan, Y., and Zhou, Y. (2016a). "Randomizedorder Multichannel Singular Spectrum Analysis for Simultaneously Attenuating Random and Coherent Noise," in 86th Annual International Meeting SEG Expanded Abstracts, Dallas, Texas, October 16–21, 2016, 4777–4781. doi:10.1190/segam2016-13859407.1

Huang, W., Wang, R., Zhang, M., Chen, Y., and Yu, J. (2015). "Random Noise Attenuation for 3D Seismic Data by Modified Multichannel Singular Spectrumanalysis." in 77th Annual International Conference and Exhibition, EAGE, Extended Abstracts. IFEMA Madrid, Spain, 1-4 June 2015.doi:10.3997/2214–4609.201412830

Huang, W., Wang, R., Zhou, Y., Chen, Y., and Yang, R. (2016b). "Improved Principal Component Analysis for 3D Seismic Data Simultaneous Reconstruction and Denoising," in 86th Annual International Meeting SEG Expanded Abstracts, Dallas, Texas, October 18, 2016, 4777–4781. doi:10.1190/segam2016-13858769.1

Hudyma, M., and Potvin, Y. H. (2010). An Engineering Approach to Seismic Risk Management in Hardrock Mines. *Rock Mech. Rock Eng.* 43 (6), 891–906. doi:10.1007/s00603-009-0070-0

Langston, C. A., and Mousavi, S. M. (2019). Separating Signal from Noise and from Other Signal Using Nonlinear Thresholding and Scale-Time Windowing of Continuous Wavelet Transforms. *Bull. Seismol. Soc. Am.* 109 (5), 1691–1700. doi:10.1785/0120190075

Li, T., Cai, M. F., and Cai, M. (2007). A Review of Mining-Induced Seismicity in China. *Int. J. Rock Mech. Min. Sci.* 44 (8), 1149–1171. doi:10.1016/j.ijrmms.2007.06.002

Liu, G., Chen, X., Du, J., and Wu, K. (2012). Random Noise Attenuation Using *F-X* Regularized Nonstationary Autoregression. *Geophysics* 77 (2), V61–V69. doi:10.1190/geo2011-0117.1

Liu, G., and Chen, X. (2013). Noncausal *F-X-Y* Regularized Nonstationary Prediction Filtering for Random Noise Attenuation on 3D Seismic Data. *J. Appl. Geophys.* 93, 60–66. doi:10.1016/j.jappgeo.2013.03.007

Mousavi, S. M., and Langston, C. A. (2016a). Adaptive Noise Estimation and Suppression for Improving Microseismic Event Detection. *J. Appl. Geophys.* 132, 116–124. doi:10.1016/j.jappgeo.2016.06.008

Mousavi, S. M., and Langston, C. A. (2017). Automatic Noise-Removal/signal-Removal Based on General Cross-Validation Thresholding in Synchrosqueezed Domain and its Application on Earthquake Data. *Geophysics* 82 (4), V211–V227. doi:10.1190/geo2016-0433.1

Mousavi, S. M., Langston, C. A., and Horton, S. P. (2016c). Automatic Microseismic Denoising and Onset Detection Using the Synchrosqueezed Continuous Wavelet Transform. *Geophysics* 81 (4), V341–V355. doi:10.1190/geo2015-0598.1

Mousavi, S. M., and Langston, C. A. (2016b). Hybrid Seismic Denoising Using Higher-Order Statistics and Improved Wavelet Block Thresholding. *Bull. Seismol. Soc. Am.* 106, 1380–1393. doi:10.1785/0120150345

Nazari SiahsarSiahsar, M. A., Gholtashi, S., Kahoo, A. R., Chen, W., and Chen, Y. (2017). Data-driven Multitask Sparse Dictionary Learning for Noise Attenuation of 3D Seismic Data. *Geophysics* 82 (6), V385–V396. doi:10.1190/geo2017–0084.110.1190/geo2017-0084.1

Palgunadi, K. H., Poiata, N., Kinscher, J., Bernard, P., De Santis, F., and Contrucci, I. (2020). Methodology for Full Waveform Near Real-Time Automatic Detection and Localization of Microseismic Events Using High (8 kHz) Sampling Rate Records in Mines: Application to the Garpenberg Mine (Sweden). *Seismol. Res. Lett.* 91 (1), 399–414. doi:10.1785/0220190074

Saragiotis, C. D., Hadjileontiadis, L. J., and Panas, S. M. (2002). PAI-S/K: A Robust Automatic Seismic P Phase Arrival Identification Scheme. *IEEE Trans. Geosci. Remote Sens.* 40 (6), 1395–1404. doi:10.1109/tgrs.2002.800438

Scherbaum, F. (2001). *Of Poles and Zeros Fundamentals of Digital Seismology*. 1st edn. Springer Dordrecht: Kluwer Academic Publishers.

Shuchong, L., and Xun, C. (2014). Seismic Signals Wavelet Packet De-noising Method Based on Improved Threshold Function and Adaptive Threshold. *Comput. Model. New Technol.* 18, 1291–1296.

Stockwell, R. G., Mansinha, L., and Lowe, R. P. (1996). Localization of the Complex Spectrum: the S Transform. *IEEE Trans. Signal Process.* 44 (4), 998–1001. doi:10.1109/78.492555

Thakur, G., Brevdo, E., FučkarFuckar, N. S., and Wu, H.-T. (2013). The Synchrosqueezing Algorithm for Time-Varying Spectral Analysis: Robustness Properties and New Paleoclimate Applications. *Signal Process.* 93, 1079–1094. doi:10.1016/j.sigpro.2012.11.029

Wang, D.-w., Li, Y.-j., Zhang, K., and Xu, H.-m. (2010). An Adaptive Time-Frequency Filtering Method for Nonstationary Signals Based on the Generalized S-Transform. *Optoelectron. Lett.* 6 (2), 133–136. doi:10.1007/s11801-010-9250-0

Wang, D., Wang, J., Liu, Y., and Xu, Z. (2015). "An Adaptive Time-Frequency Filtering Algorithm for Multi-Component LFM Signals Based on Generalized S-Transform," in 21st International Conference on Automation and Computing (ICAC), Glasgow, UK, 11-12 September 2015 (IEEE). doi:10.1109/iconac.2015.7314000

Wang, J., Wu, G., and Chen, X. (2019). Frequency-Bessel Transform Method for Effective Imaging of Higher-Mode Rayleigh Dispersion Curves From Ambient Seismic Noise Data. *J. Geophys. Res. Solid Earth* 124, 3708–3723. doi:10.1029/2018JB016595

Weaver, J. B., XuYansun, Y., Healy, D. M., and Cromwell, L. D. (1991). Filtering Noise from Images with Wavelet Transforms. *Magn. Reson. Med.* 21, 288–295. doi:10.1002/mrm.1910210213

Withers, M., Aster, R., Young, C., Beiriger, J., Harris, M., Moore, S., et al. (1998). A Comparison of Select Trigger Algorithms for Automated Global Seismic Phase and Event Detection. *Bull. Seismol. Soc. Am.* 88 (1), 95–106. doi:10.1785/BSSA0880010095

Wu, J., and Bai, M. (2018b). Attenuating Seismic Noise via Incoherent Dictionary Learning. *J. Geophys. Eng.* 15 (4), 1327–1338. doi:10.1093/jge/aaaf57

Wu, J., and Bai, M. (2018a). Incoherent Dictionary Learning for Reducing Crosstalk Noise in Least-Squares Reverse Time Migration. *Comput. Geosciences* 114, 11–21. doi:10.1016/j.cageo.2018.01.010

Xie, J., Di, B., Wei, J., Xie, Q., Zu, S., and Chen, Y. (2016). "Stacking Using Truncated Singular Value Decomposition and Local Similarity." in 78th Annual International Conference and Exhibition, EAGE, Extended Abstracts. Houten The Netherlands, May 2016 (European Association of Geoscientists & Engineers).doi:10.3997/2214–4609.201601325

Yabe, Y., Nakatani, M., Naoi, M., Philipp, J., Janssen, C., Watanabe, T., et al. (2015). Nucleation Process of an M2 Earthquake in a Deep Gold Mine in South Africa Inferred from On-Fault Foreshock Activity. *J. Geophys. Res. Solid Earth* 120, 5574–5594. doi:10.1002/2014JB011680

Yoon, B. J., and Vaidyanathan, P. P. (2004). "Wavelet-based Denoising by Customized Thresholding," in International Conference on Acoustic Speech Signal Process(ICASSP), Montreal, Québec, 17-21 May 2004 (IEEE).

Young, R. P., Maxwell, S. C., Urbancic, T. I., and Feignier, B. (1992). Mining-induced Microseismicity: Monitoring and Applications of Imaging and Source Mechanism Techniques. *Pageoph* 139, 697–719. doi:10.1007/BF00879959

Zhang, D., Chen, Y., and Gan, S. (2016a). "Iterative Reconstruction of 3D Seismic Data via Multiple Constraints," in 78th Annual International Conference and Exhibition, EAGE, Extended Abstracts, Houten The Netherlands, May 2016 (European Association of Geoscientists & Engineers). doi:10.3997/2214–4609.201601241

Zhang, D., Chen, Y., and Gan, S. (2016b). "Multi-Dimensional Seismic Data Reconstruction With Multiple Constraints," in 86th Annual International Meeting, SEG, Expanded Abstracts, Houston Texas UN, October 19, 2016 (Society of Exploration Geophysicists), 4801–4806. doi:10.1190/segam2016-13763335.1

Zhang, D., Chen, Y., Huang, W., and Gan, S. (2016c). "Multi-step Reconstruction of 3D Seismic Data via an Improved MSSA Algorithm," in 2016 International Geophysical Conference & Exposition, SEG, Expanded Abstracts, CPS/SEG Beijing, 745–749.

Zhou, Y., and Zhang, S. (2017). Robust Noise Attenuation Based on Nuclear Norm Minimization and a Trace Prediction Strategy. *J. Appl. Geophys.* 147, 52–67. doi:10.1016/j.jappgeo.2017.09.005

Conflict of Interest: The authors declare that the research was conducted in the absence of any commercial or financial relationships that could be construed as a potential conflict of interest.

Publisher's Note: All claims expressed in this article are solely those of the authors and do not necessarily represent those of their affiliated organizations, or those of the publisher, the editors, and the reviewers. Any product that may be evaluated in this article, or claim that may be made by its manufacturer, is not guaranteed or endorsed by the publisher.

Copyright © 2022 Zhang, Zeng, Shi, Chang, Dai, Ji and Han. This is an open-access article distributed under the terms of the Creative Commons Attribution License (CC BY). The use, distribution or reproduction in other forums is permitted, provided the original author(s) and the copyright owner(s) are credited and that the original publication in this journal is cited, in accordance with accepted academic practice. No use, distribution or reproduction is permitted which does not comply with these terms.

frontiers | Frontiers in Earth Science

ORIGINAL RESEARCH
published: 13 July 2022
doi: 10.3389/feart.2022.889545

Triggering and Relationship Between Mine Earthquake Activities and Stress of Earth Tides During Deep Mining

Yuezheng Zhang[1,2]*, *Hongguang Ji*[1,2] *and Haoyuan Wu*[1,2]

[1]University of Science and Technology Beijing, Beijing, China, [2]Beijing Key Laboratory of Urban Underground Space Engineering, Beijing, China

In the process of deep mining, the prevention and control of rock bursts, mine earthquakes, and other disasters are common problems. The stress of earth tides and its periodic actions should trigger mine earthquakes when the rock masses are in a critical state of rupture. In this study, the Yanbei coal mine was taken as the research background to explore the triggering effect of solid tides on mine earthquakes occurring in the floor. The relationship between the diurnal tidal stress phase and mine earthquakes was studied by statistically analyzing the mine earthquake frequency, and the triggering mechanism was also preliminarily discussed. It was found that the solid tide plays a significant role of trigger action in the occurrence of rock burst of the floor type. For different levels of mine earthquakes, the tidal stress triggering effect is different, but the overall trend is close. Compared with the components of tidal stress, vertical stress, north-south stress, and shear stress, rock burst occurred more at the stage close to 0° and ±180°. For different types of mine earthquakes, the triggered mechanics function of tidal stress is different. Mine earthquakes on the floor mainly include two kinds (the gravity control type and horizontal stress control type). The former easily occurs during the tidal stress vertical component of the maximum, while the latter easily occurs when the two horizontal components of the maximum are combined. The frequency of the former is larger than that of the latter. The results show that the floor seismic activity is correlated with the solid tidal activity of the earth's crust, which provides a new idea for understanding the mechanism and trigger conditions of mine earthquakes.

Keywords: coal mine, mine earthquake, tidal stress, floor, trigger mechanism

OPEN ACCESS

Edited by:
Guang-Liang Feng,
Institute of Rock and Soil Mechanics (CAS), China

Reviewed by:
Wuwei Mao,
Tongji University, China
Anye Cao,
China University of Mining and Technology, China

***Correspondence:**
Yuezheng Zhang
zhangyuezheng@ustb.edu.cn

Specialty section:
This article was submitted to Geohazards and Georisks, a section of the journal Frontiers in Earth Science

Received: *04 March 2022*
Accepted: *23 May 2022*
Published: *13 July 2022*

Citation:
Zhang Y, Ji H and Wu H (2022) Triggering and Relationship Between Mine Earthquake Activities and Stress of Earth Tides During Deep Mining. Front. Earth Sci. 10:889545. doi: 10.3389/feart.2022.889545

INTRODUCTION

Mine earthquakes occur under the combined effects of the geological structure environment, the geostress field, and other occurrence environments and mining disturbances. When the engineering rock mass reaches a critical state, a small disturbance will have an important impact on it, thereby promoting the occurrence of rock mass destruction (Feng et al., 2015; Xie et al., 2015; Zhang et al., 2016a). For example, in the local earth tidal activity, the action of tidal forces will form an additional stress field in the geostress field (Pan et al., 2020; Yuan, 2021). Luo et al. (2015) studied the effect of tidal force on coal and gas outbursts and found that there is a certain correlation between coal and gas outbursts and the tidal force of celestial bodies. The tidal force has a certain driving effect on the occurrence of outbursts. Li et al. (2011) also found that the occurrence of mine earthquakes was concentrated in local time periods when the statistics of the frequency distribution of mine earthquakes occurred. When analyzing the time of occurrence of rock bursts and the correlation between regions and changes in tidal force, Guo and Yang, (2021) found that the probability

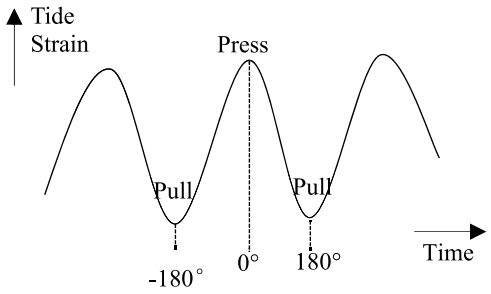


FIGURE 1 | Phase Angle of the tide.

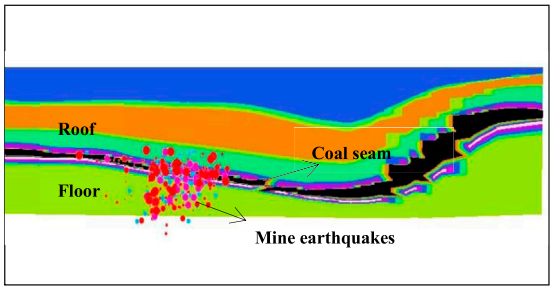


FIGURE 2 | Mine earthquake activity distribution characteristics.

and frequency of rock bursts occur more frequently in the period of extreme tidal generating force. It is found that there is a certain relationship between the area where mine earthquakes occur and the latitude and longitude. Seismic research has also confirmed that it has a certain triggering effect on earthquakes, which is mainly reflected in that when the tectonic stress in the source system rock reaches or is in a critical state; external factors such as earth tide modulation may cause system mutation and earthquakes under certain conditions (Glasby and Kasahara, 2001; Chen et al., 2006; Metivier et al., 2009; Li et al., 2014; Wu et al., 2020). According to Zhang et al. (2016b) statistics on roof-type mine earthquakes, it is found that solid tidal stress has a significant triggering effect on the occurrence of mine earthquakes. In recent years, with the development and application of technologies (such as roof control, roadway surrounding rock support, and pressure relief), floor impact dynamic disasters have become more prevalent. The impact damage to the floor directly causes serious damage and threat to the equipment and personnel lanes, and the impact on production safety is even more serious. As a critical phenomenon of multi-field evolution and coupling, floor-type mine earthquakes are induced during their transition from incubation to induction. The effect and mechanism of tidal stress on floor-type mine earthquakes need to be further explored.

In order to quantitatively analyze the correlation between earth tide action and induced floor-type mine earthquakes, the correlation of vertical, east-west, north-south, and north-south diurnal variation was studied by monitoring the earthquake in Yanbei coal mine in Gansu province. The magnitude and type of horizontal shear stress, local solid tidal stress, and floor type mine earthquake are analyzed. The inducing effect and mechanical mechanism of the earth's tide factors on the floor-type mine earthquakes are preliminarily discussed.

CHARACTERISTICS OF REGIONAL TECTONIC STRESS AND SOLID TIDAL STRESS

The Yanbei mining area in Gansu province is located at the eastern foot of the Liupan mountain and the southwestern edge of the Ordos block. It is at the intersection of the Liupanshan western marginal fault, the western marginal thrust belt of the Ordos Basin, and the Qingtongxia-Guyuan fault. The geological environment in this area is complex, and the tectonic stress is concentrated. The coalfield area has been subjected to structural compression from southwest to northeast and east to west for a long time, forming a spinning compound asymmetric synclinal structure of the "southeast structure, slow in the east and steep in the west, wide and slow in the middle, and converging in the north and south sections".

Under the action of the tide, the tidal force generated by the tidal force at different times and locations is different. The stress field in the formation will change periodically with a certain regularity, that is, the tidal additional stress field. The tidal force level calculation is shown in **Eqs 1–3** (Zahran et al., 2005; Kano and Yanagidani, 2006; Chen et al., 2012):

$$W = W_m + W_s, \tag{1}$$

$$W_m = D_m\left(\frac{r}{R}\right)^2\left[2\left(\frac{c_m}{r_m}\right)^3\left(\cos^3 z_m - \frac{1}{3}\right) + \frac{2}{3}\frac{r}{c_m}\left(\frac{c_m}{r_m}\right)^4\left(5\cos^3 z_m - 3\cos z_m\right)\right], \tag{2}$$

$$W_s = D_s\left(\frac{r}{R}\right)^2\left[2\left(\frac{c_s}{r_s}\right)^3\left(\cos^3 z_m - \frac{1}{3}\right)\right]. \tag{3}$$

W is the tidal force position; W_m and W_s are the moon and solar tidal force; D_m and D_s are Moon and Sun Dudson's constant; c_m and c_s are the average distance from the moon; r_m and r_s are the distance from the Sun to the center of the earth; z_m and z_s are the distance from the moon and that from the Sun to the center of the earth; R is the average radius of the earth.

The variable component of the solid tide is also related to the Love-Shida's number, and its calculation formula is as follows:

$$\begin{cases} e_{rr} = \sum_n \left(R\frac{\partial h_n}{\partial r} + nh_n\right)\frac{w_n}{Rg_0}, \\ e_{\phi\phi} = \sum_n \left(\frac{l_n}{Rg_0}\frac{\partial^2 W_n}{\partial \phi^2} + h_n\frac{w_n}{Rg_0}\right), \\ e_{\lambda\lambda} = \sum_n \left[\frac{l_n}{Rg_0\cos\phi}\left(\frac{\partial^2 W_n}{\cos\phi\partial\lambda^2} - \sin\phi\frac{\partial W_n}{\partial\phi}\right) + h_n\frac{w_n}{Rg_0}\right], \\ e_{\phi\lambda} = \sum_n \left[\frac{-2l_n}{Rg_0\cos\phi}\left(\frac{\partial^2 W_n}{\partial\phi\partial\lambda} + \tan\phi\frac{\partial W_n}{\partial\lambda}\right)\right]. \end{cases} \tag{4}$$

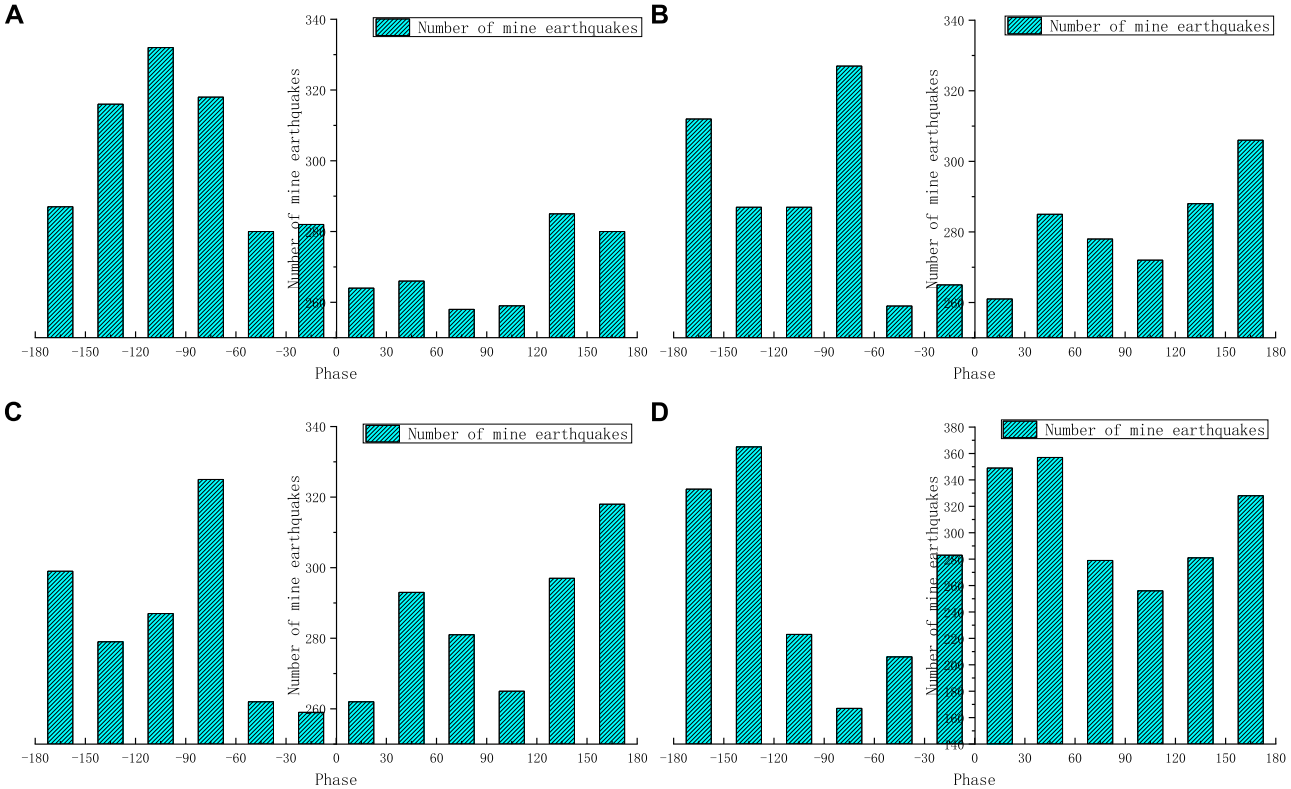


FIGURE 3 | Statistical histogram of the mine earthquake frequency.

e_{rr}, $e_{\phi\phi}$, $e_{\lambda\lambda}$, and $e_{\phi\lambda}$ are the vertical, north-south, east-west, and horizontal shear stress components of the solid tidal strain; l_n and h_n are the Love-Shida's number; ϕ latitude; λ longitude.

According to the relationship between stress and strain, the components of the corresponding solid tidal stress can be further obtained (Zhou et al., 2013; Xiong et al., 2015):

$$\sigma_{ij} = \lambda' \vartheta \delta_{ij} + 2\mu e_{ij}. \tag{5}$$

λ', μ, is the Lame constant at r, ϑ is the strained volume expansion, and δ_{ij} is the Kronecker symbol.

SCHUSTER TEST METHOD

Through calculation, the local tidal stress time history curve can be obtained. The triggering effect of the earth tide on the mine earthquake can be quantitatively analyzed by the change of P in the Schuster test method (Sun et al., 2014; Bucholc and Steacy, 2016; Zhu et al., 2021). P rejects the significance level of the null hypothesis (mine earthquakes occur randomly and have nothing to do with the tidal phase angle); the value range is 0–1. The smaller the value, the greater is the possibility of rejecting the null hypothesis. Taking $p < 0.05$ as the threshold for judging that the tide can trigger an earthquake, the calculation process is as follows.

The phase angle at the time of the earthquake is assigned according to the time-history of tidal stress, and the stress peak closest to the time of the earthquake is selected. The phase angle is 0°, and the phase angles in front of the tank and behind the tank are −180° and 180° respectively. Then, the angular distance is divided between the peaks and valleys linearly, as shown in **Figure 1**.

After determining the tidal phase angles of all earthquakes, the dominant phase angles of all seismic data are calculated, as shown in **Eq. 6**:

$$L = \sqrt{A^2 + B^2}, \tag{6}$$

$$A = \sum_{i=1}^{N} \cos\theta_i, \; B = \sum_{i=1}^{N} \sin\theta_i, \tag{7}$$

where θ_i represents the tidal phase angle of the first earthquake, N is the total number of earthquakes, and the value of P is calculated according to **Eq. 8**:

$$P = \exp\left(-\frac{L^2}{N}\right). \tag{8}$$

CORRELATION ANALYSIS BETWEEN THE SOLID TIDAL ACTION AND MINE EARTHQUAKE ACTIVITY

Figure 2 shows the source location results of some mine earthquakes (which induced rock burst events) in the

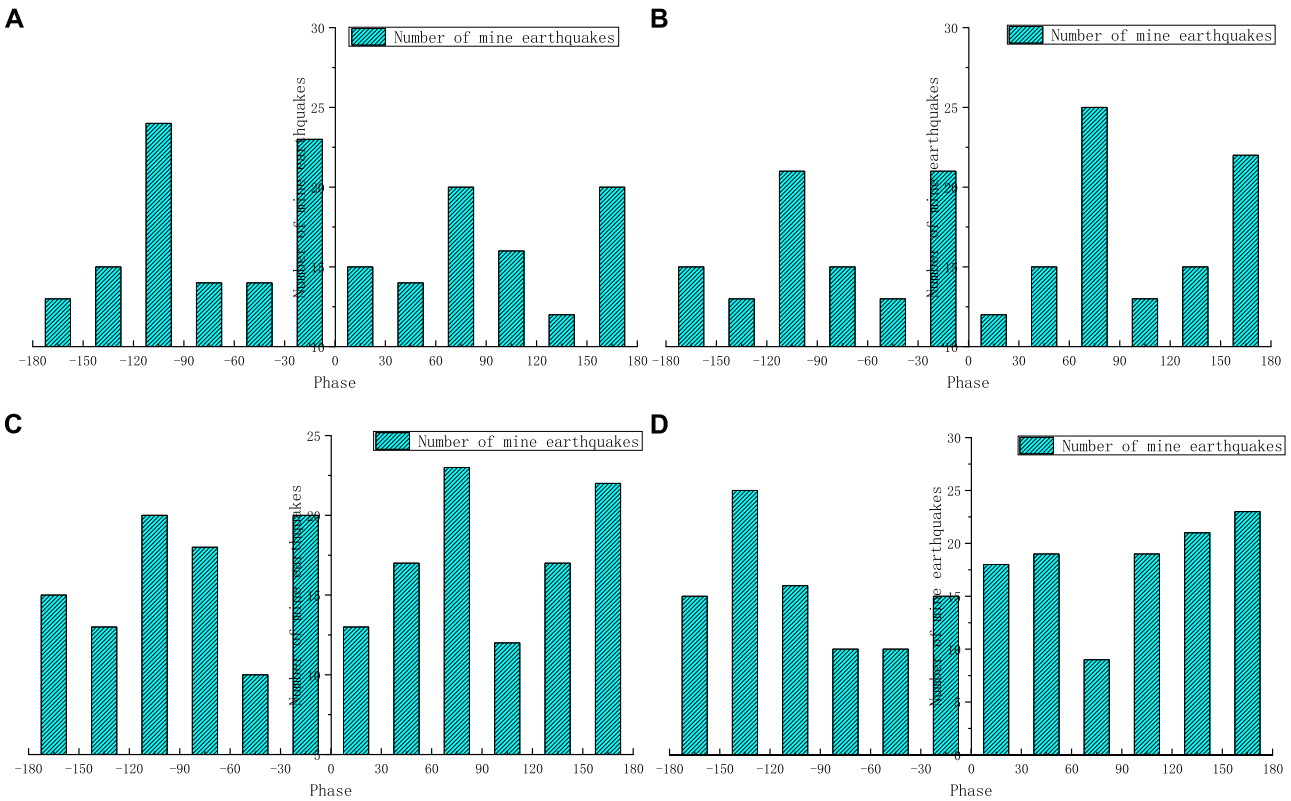


FIGURE 4 | Statistical histogram of the mine earthquake M_L<0 frequency.

stratigraphic section perpendicular to the syncline axis. It can be seen that mine earthquakes are distributed in the rock layers above and below the coal seam. Different types of mine earthquakes have different formation mechanisms, and their triggering factors are also different. Compared with the mining face location, mine earthquakes can be divided into the roof type and floor type (Li et al., 2006). According to the damage records caused by rock bursts, mine shocks that occur in the floor often cause more serious damage. Therefore, in order to analyze the correlation between mine earthquakes and tidal stress, more than 30,000 floor-type mine earthquakes that occurred in this area are mainly selected as the analysis objects.

Triggering Effect of Different Components of Tidal Stress on Mine Earthquakes

The study is based on the local strain solid tidal stress of the Yanbei coal mine, while selecting the vertical component, east-west component, north-south component, and horizontal shear stress component of the solid tidal stress as the tidal curve, respectively, to calculate the phase angle between the mine earthquakes in the Yanbei coal field and the tidal component. According to the interval of 30°, statistics of the mine earthquake data between −180° and +180° are carried out on a histogram. The statistical results are shown in **Figure 3**. Among them, (a), (b), (c), and (d) are the statistical results relative to the vertical, east–west, north–south, and horizontal shear stress components, respectively.

It can be seen from **Figure 3** that in different components of tidal stress, there is a clear correlation between the frequency and phase angle of mine earthquakes in the floor. Compared with the vertical component, mine earthquake events are more distributed in the phase range near −100°, followed by the frequency near +150° phase and less frequently near 0°–90° phase. Compared with the north-south and east-west horizontal components, mine earthquake events are more distributed near the −75°phase; fewer events occur near the ±180° phase, and the least occur near the 0°phase. Compared with the horizontal shear component, there are more events near the 0° phase and ±180° phase and fewer events near the −70° phase. At the same time, compared to the Schuster test for the four tidal curves, the p values obtained are 1.32E−04, 0.0281, 0.0595, and 2.91E−07, respectively, and since the p values of each component are all lower than the threshold value of 0.05 for tidal-triggered earthquakes but north–south, it can be considered that the floor-type mine earthquakes in this area are triggered by tides.

Analysis of the Triggering Effect of Tidal Stress on Mine Earthquakes of Different Magnitudes

In earthquake research, it is found that solid tides have more obvious inducing effects on small-scale earthquakes than natural

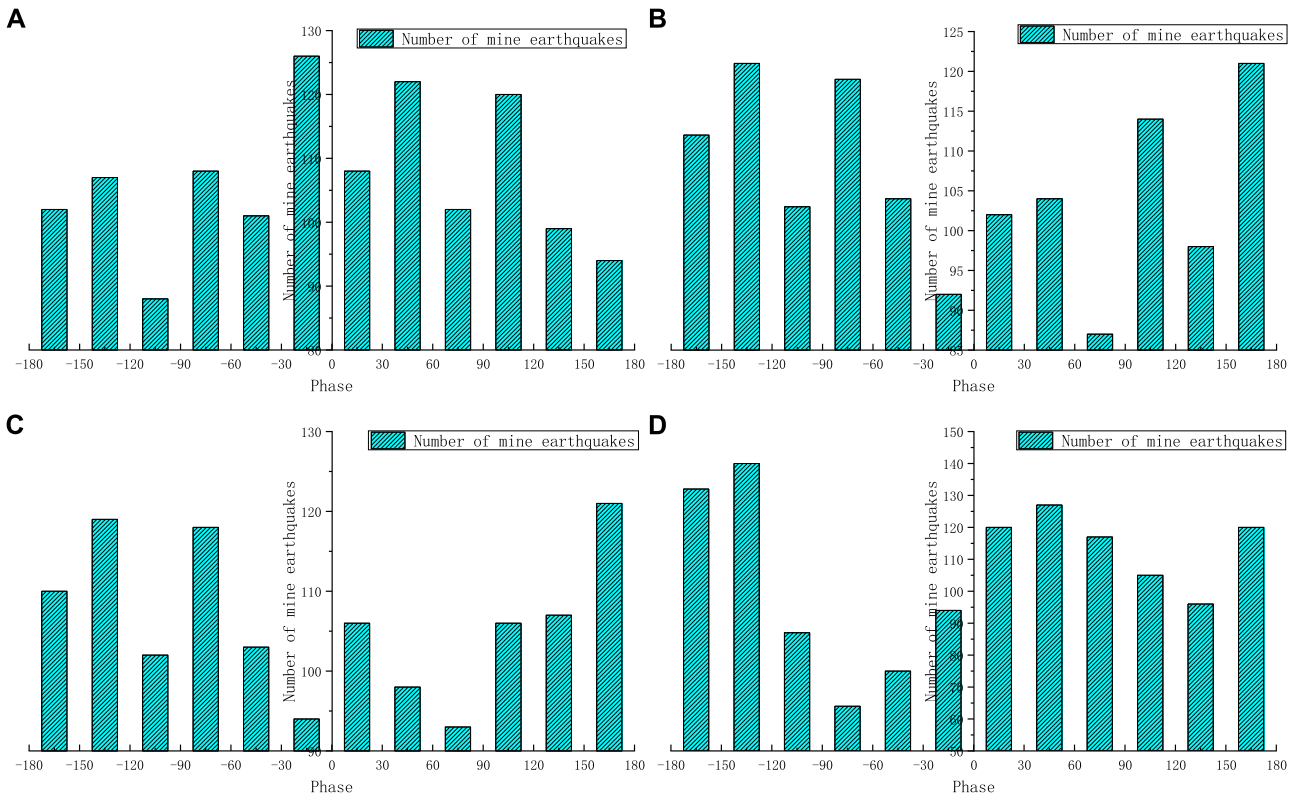


FIGURE 5 | Statistical histogram of the mine earthquake $0 \leq M_L<0.5$ frequency.

large earthquakes. For mine earthquakes, although the magnitude is low, the causes and triggering mechanisms of mine earthquakes of different scales are also different. In order to analyze the triggering effect and the difference in the earth's tide in the process of different scales of mine earthquakes, the mine earthquake events are divided into "<0, 0–0.5, 0.5–1.0, 1.0–1.5, and >1.5", according to the magnitude (M_L). **Figure 4** to **Figure 8**, respectively, show the corresponding relationship between the frequency of occurrence of different levels of mine earthquake events and the tidal phase. Among them, (a), (b), (c), (d) are the statistical results relative to the vertical, east-west, north-south, and horizontal shear stress components, respectively.

It can be seen from **Figure 4** that for the vertical component, mine earthquake events are more distributed in the phase range near 0° and ±90°, and few occur near the −180° phase. For the north–south and east–west horizontal components, mine earthquake events are more distributed near the 0° and ±90° phases, and few occur near the −60° and 100° phases. For the horizontal shear component, the events near the ±150° phase are the most, followed by the phase distribution near 30°, and the least events near the phases of −90°~ −30° and 60°–90°.

It can be seen from **Figure 5** that for the vertical component, mine earthquake events are more distributed in the phase range near 0°, and less occur near the ±180° phase. For the north–south and east–west horizontal components, mine earthquake events are more distributed near the ±180° phases, and less occur near the 0° phases. For the horizontal shear component, the law is obvious. It is more distributed near 30°–60° and ±180°, and the events near −90°~−60° phase are the least.

It can be seen from **Figure 6** that for the vertical component, mine earthquake events are more distributed in the phase range around 0° and ±120°, and few occur near the phase of ±180°. For the north-south and east–west horizontal components, mine earthquake events are more distributed near the ±60° and ±180° phases, and few occur near the 0° phase. For the horizontal shear component, there are more events around the phases of 0° and ±180°, and the least phase events are around ±90°.

It can be seen from **Figure 7** that for the vertical component, mine earthquake events are more distributed in the phase range around −0° and +100°, but at near ±180°, +60° phases there is less occurrence. For the two horizontal components, north-south and east-west, there are more ore earthquake events near the phases of ±90°. For the horizontal shear component, there are more events around the phases of 0°–60°, and ±180°.

It can be seen from **Figure 8** that for the vertical component, mine earthquake events are more distributed in the phase range near the ±90° phase, and few occur near the ±60° phase. For the north–south and east–west horizontal components, mine earthquake events are more distributed near the ±90° phase, followed by near ±180°, and few occur near the ±120° phase. For the horizontal shear component, there are more events around the 0° phase, followed by the phase around +180°, and the least phase events around ±90°.

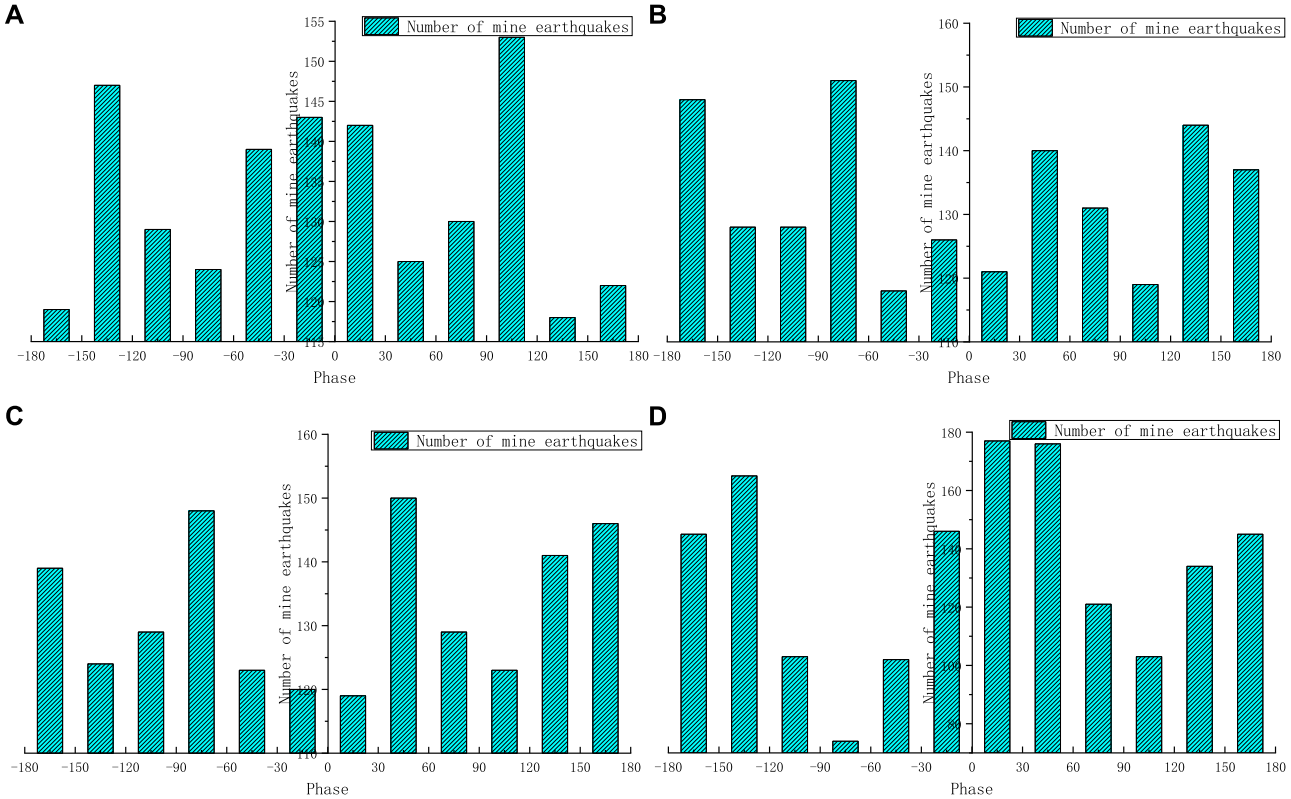


FIGURE 6 | Statistical histogram of the mine earthquake $0.5 \leq M_L < 1.0$ frequency.

From the statistical results of the above-mentioned magnitude files, it is apparent there are differences in the triggering effects of solid tides on different levels of mine earthquakes. This level is the closest to the overall distribution trend in **Figure 4**, where the level of $M_L<0$ is the discrete maximum, and the other levels are close to the general trend. Observing the *p* value result in **Figure 9** also shows this law. The statistical *p* value of the horizontal shear component of the mine earthquake is closer to 0.05, and the triggering effect is obvious. The vertical, east–west, and north–south components of mine earthquakes with $M_L<0$ have *p* values close to 1. The corresponding statistical results of phase distribution are also very discrete, indicating that the occurrence of such a large-scale mine earthquake is not triggered by the earth's tide. Although the *p* value of other grades is greater than 0.05, the frequency distribution of the corresponding phase still maintains a more obvious regularity. In the corresponding statistical study of earthquakes, $p < 0.05$ is not the only criterion for the triggering of earth tides, and the distribution of earthquakes in the tidal phase is more important.

Although there are differences in the distribution of the phases of the various components of the earth's tides for mine earthquakes of different magnitudes, the overall law tends to be the same: relative to the vertical component, mine earthquakes mostly occur near the 0° and ±90° phases, and the distribution is closer to the 0° phase. For the east-west and north-south horizontal components, mine earthquakes occur more frequently near the phases of 0° and ±180° and are more widely distributed near the phases of ±180°. For the horizontal shear stress component, mine earthquakes occur frequently near the phases of 0° and ±180°, and with the change in magnitude, this stress component maintains a significant correlation with the triggering of mine earthquakes.

DISCUSSION OF THE TRIGGERING EFFECT OF TIDAL STRESS ON FLOOR-TYPE MINE EARTHQUAKES

Affected by the dynamic disturbance process of mining, the roof and floor of the coal seam have been undergoing dynamic evolution and adjustment. The development and evolution of the "three belts" in the roof; the periodic breakage of the roof and the appearance of periodic pressure; the bottom heave and protrusions in the floor; and impact, deformation, and destruction of the two gangs are all external manifestations of this dynamic evolution process. Regardless of whether it is the top floor or the two banks of surrounding rocks, the failure and instability processes are all based on the original stress state in the formation as the starting point. Under the effect of mining disturbance, the surrounding rock structure and its evolution process gradually approach or reach their "critical state" and then cause local damage or large-scale instability (Cui et al., 2022; Feng

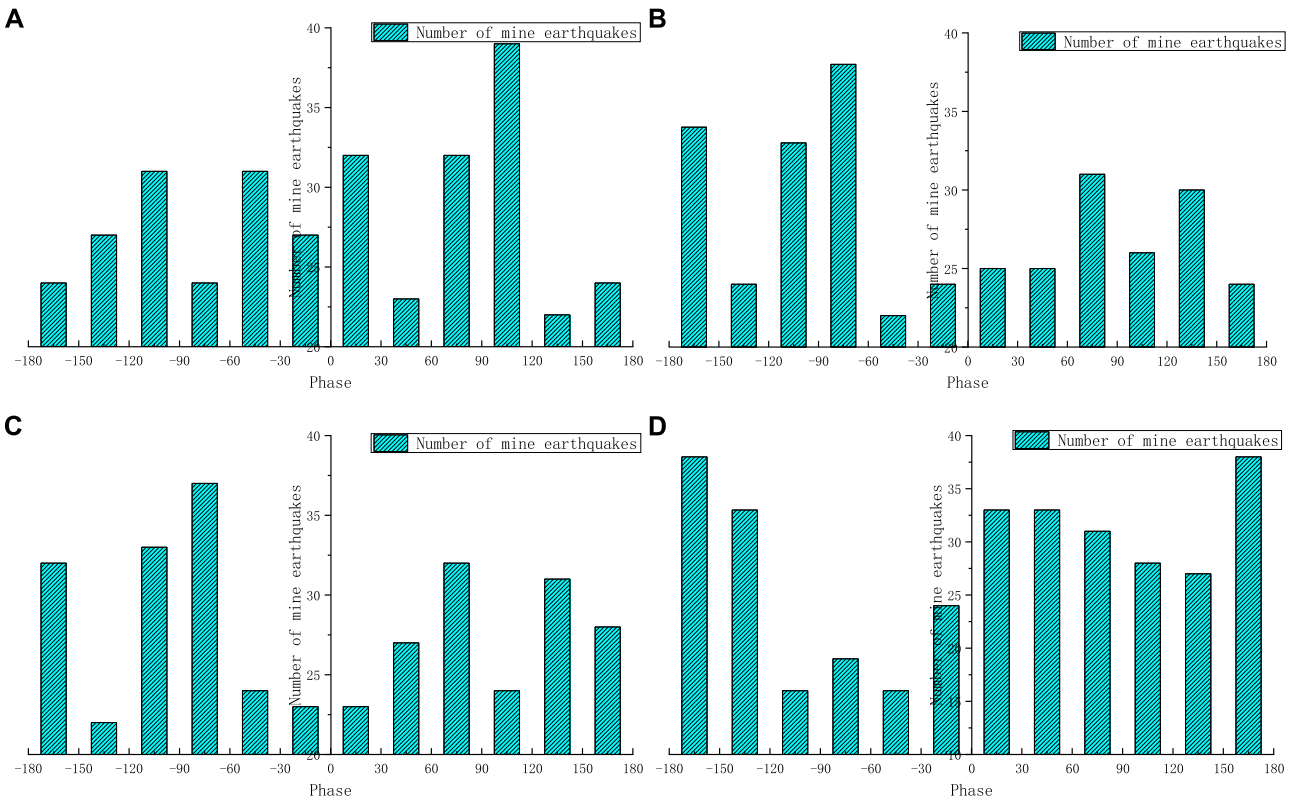


FIGURE 7 | Statistical histogram of the mine earthquake 1.0 ≤ M_L<1.5 frequency.

et al., 2022). Therefore, the emergence and evolution of "critical fracture zones" in roofs, floors, or roadways reflects the comprehensive action of multiple factors such as the overburden rock structure, original stress field, and mining disturbance. In particular, on the roof and floor, its incubation, expansion, and evolution processes intensively reflect multiple physical and mechanical fields and synergistic mechanisms and state evolution processes on multiple spatial scales.

In the mining process, affected by mining disturbance, the surrounding rock of the stope has been in a process of dynamic change. Among them, in the surrounding rock of the roof and floor, the stress state of certain areas will break due to reaching their critical conditions, which will cause a large number of microseismic events. The spatial distribution characteristics and dynamic evolution process of microseismic sources in the roof and floor also well reflect the temporal and spatial evolution process and law of the "critical fracture zone" in the surrounding rock of the roof and floor. In the mining process, the stress state and failure mode of the roof and floor of the coal seam are very different. Therefore, although the top plate and the top plate rupture, both show a common microseismic activity. However, the microseisms that occur on the top and bottom plates are very different in both the incubation environment, the induced mechanism, and the regional dynamic response. This difference also caused the obvious difference in the triggering effect of the solid tidal stress on the roof and floor (Wu et al., 1999).

The spatial distribution characteristics and dynamic evolution process of microseismic sources in the roof and floor also better reflect the temporal and spatial evolution process and law of the "critical fracture zone" in the surrounding rock of the roof and floor. In the mining process, the stress state and failure mode of the roof and floor of the coal seam are very different. Therefore, although the top plate and the top plate rupture, both show a common microseismic activity. However, the microseisms that occur on the top and bottom plates are very different in both the incubation environment, the induced mechanism, and the regional dynamic response. This difference also caused the obvious difference in the triggering effect of the solid tidal stress on the roof and floor (Gao et al., 2021). According to the value of *p* in **Figure 9** and the literature (Zhang et al., 2016b), compared with roof-type mine earthquakes, the triggering effect of solid tide stress on floor-type mine earthquakes is smaller, which is also caused by the difference in the occurrence mechanism between the two.

Comparing the statistical results of the actual occurrence of mine earthquakes, it is found that the distribution characteristics of the phases of the tidal stress components of the mine earthquakes of different scales on the floor are consistent with the above-mentioned trigger mechanism. The occurrence of floor-type mine earthquakes is controlled by

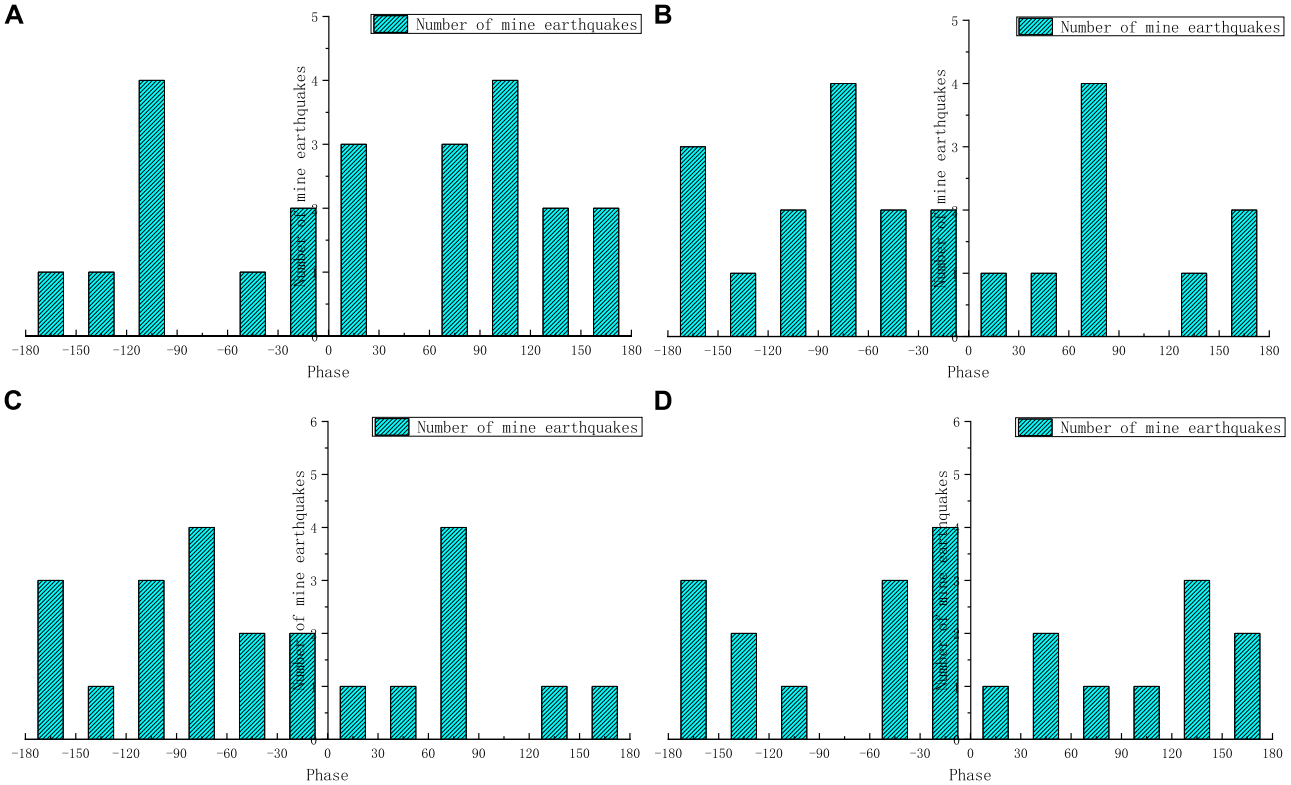


FIGURE 8 | Statistical histogram of the mine earthquake M_L>1.5 frequency.

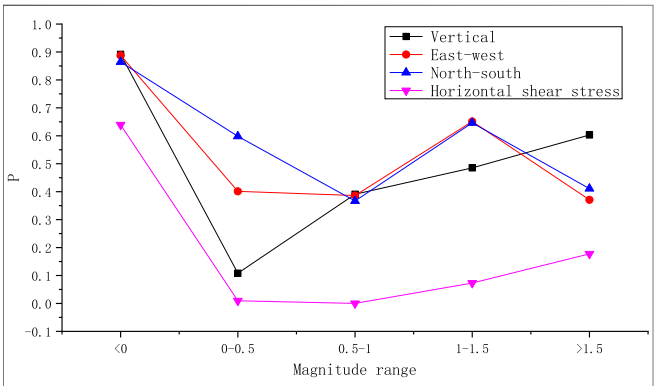


FIGURE 9 | *p*-values of different tidal stress components at different magnitude levels.

both the gravity field and the horizontal tectonic stress field. Taking the vertical component of tidal stress as a reference, mine earthquakes are most distributed near the 0° phase, and this type of mine earthquake is controlled by gravity; the frequency of mine earthquakes occurring near the ±180° phase is the second, and this type of mine earthquake is controlled by horizontal tectonic stress. This difference in quantity also shows that the gravity-controlled type of mine earthquakes that occurred on the coal seam floor of the Yanbei mining area accounted for the majority. At the same time, the cause of the dual control of gravity and tectonic movement due to mining is also an important difference between it and the natural earthquake induced by the fault tectonic activity, so there are differences in response to the triggering action of solid tides (Xu et al., 2010; Yu et al., 2022).

The advance warning of a mine earthquake or rock burst has always been a difficult problem in coal mine safety mining. As an additional disturbance stress, solid tidal stress can only be triggered when the surrounding rock is in a critical state. Therefore, in engineering practice, the accuracy of prediction can be improved by combining monitoring technologies such as microearthquake, ground sound, and electromagnetic radiation. For example, when it is judged that the surrounding rock enters the critical state according to this monitoring information, the early warning parameters can be optimized according to the time-phase characteristics of solid tidal stress, which is also the focus of application research in the next step (Zhang et al., 2013).

CONCLUSION

1) As a "hidden" periodic change factor that occurs in the interior of the earth, solid tides have a significant triggering effect on the occurrence of floor-type mining earthquakes.
2) The triggering effects of tidal stress on different magnitudes of floor-type mine earthquakes are different, but the overall

trend is similar. In terms of phase distribution, most mine earthquakes occur near 0° and ±180° phases in vertical, east–west, north–south, and horizontal shear stress components of tidal stress.

3) The triggering mechanical effects of tidal stress on different types of mine earthquakes are different. There are mainly two types of gravity control: vertical type and horizontal stress control type in the floor. The former is prone to occur when the vertical component of tidal stress is the largest, and the latter is prone to occur when the east–west and north–south horizontal components are the largest. In the frequency of occurrence, the former is more common than the latter.
4) The statistical analysis of floor-type mine earthquakes shows that there is a correlation between the periodic micro-dynamic effects of solid tides in the crust and mine earthquake activities. This provides new ideas for revealing the incubation and triggering conditions of mine earthquakes. In the follow-up study, on the basis of the existing coal mine dynamic disaster early warning technology, the triggering effect of the earth's tide factor can be considered to improve the effectiveness of disaster early warning.

DATA AVAILABILITY STATEMENT

The original contributions presented in the study are included in the article/supplementary material; further inquiries can be directed to the corresponding author.

AUTHOR CONTRIBUTIONS

YZ and HJ conceived and designed the methods, provided the guide of theoretical research for the study, completed the data analysis, and economically supported the project. HW completed the data collection.

FUNDING

This work is supported by the National Key Research and Development Program of China under the Grant No. 2017YFC1503100 and the major scientific and technological innovation projects in Shandong Province under the Grant No. 2019SDZY02.

REFERENCES

Bucholc, M., and Steacy, S. (2016). Tidal Stress Triggering of Earthquakes in Southern California. *Geophys. J. Int.* 205 (2), 681–693. doi:10.1093/gji/ggw045

Chen, L., Chen, J. G., and Xu, Q. H. (2012). Correlations between Solid Tides and Worldwide Earthquakes <i>M</i>_S ≥ 7.0 since 1900. *Nat. Hazards Earth Syst. Sci.* 12 (3), 587–590. doi:10.5194/nhess-12-587-2012

Chen, X. H., Li, W. Q., and Song, W. H. (2006). Analysis of Celestial Body's Activity on Crustal Stress and Rock Burst. *J. Liaoning Tech. Univ.* 25 (05), 652–654. doi:10.3969/j.issn.1008-0562.2006.05.004

Cui, G. D., Wang, W. X., Dou, B., and Li, Y. (2022). Geothermal Energy Exploitation and Power Generation via a Single Vertical Well Combined with Hydraulic Fracturing. *J. Energy Eng.* 148 (1). doi:10.1061/(ASCE)EY.1943-7897.0000809

Feng, G. L., Chen, B. R., Xiao, Y. X., Jiang, Q., Li, P-X., Zheng, H., et al. (2022). Microseismic Characteristics of Rockburst Development in Deep TBM Tunnels with Alternating Soft–Hard Strata and Application to Rockburst Warning: A Case Study of the Neelum–Jhelum Hydropower Project. *Tunn. Undergr. Space Technol.* 122, AR 104398. doi:10.1016/j.tust.2022.104398

Feng, G.-L., Feng, X.-T., Chen, B.-r., Xiao, Y.-X., and Yu, Y. (2015). A Microseismic Method for Dynamic Warning of Rockburst Development Processes in Tunnels. *Rock Mech. Rock Eng.* 48 (5), 2061–2076. doi:10.1007/s00603-014-0689-3

Gao, M. Z., Xie, J., Gao, Y. N., Wang, W., Li, C., Yang, B., et al. (2021). Mechanical Behavior of Coal under Different Mining Rates: A Case Study from Laboratory Experiments to Field Testing. *Int. J. Min. Sci. Technol.* 31 (5), 825–841. doi:10.1016/j.ijmst.2021.06.007

Glasby, G. P., and Kasahara, J. (2001). Influence of Tidal Effects on the Periodicity of Earthquake Activity in Diverse Geological Settings with Particular Emphasis on Submarine Hydrothermal Systems. *Earth-Science Rev.* 52 (04), 261–297. doi:10.1016/s0012-8252(00)00031-3

Guo, G. C., and Yang, Y. K. (2021). Study on the Mechanism of Rockburst Induced by Tidal Force. *J. Taiyuan Univ. Technol.* 52 (04), 534–541. doi:10.16355/j.cnki.issn1007-9432tyut.2021.04.004

Kano, Y., and Yanagidani, T. (2006). Broadband Hydroseismograms Observed by Closed Borehole Wells in the Kamioka Mine, Central Japan: Response of Pore Pressure to Seismic Waves from 0.05 to 2 Hz. *J. Geophys. research-solid earth* 111 (B3). doi:10.1029/2005jb003656

Li, J., Jiang, H. K., Huang, Y., Qu, J-h., and Gao, C-j. (2014). Statistical Analysis on Tidal Triggering of Recent Earthquakes in the Tianshan Seismic Zone. *Earthquake* 34 (02), 35–44. doi:10.3969/j.issn.1000-3274.2014.02.004

Li, T., Cai, M. F., and Cai, M. (2006). A Discussion on Classification of Mining-Induced Seismicity. *Chin. J. Rock Mech. Eng.* 25 (s2), 3679–3686. doi:10.3321/j.issn:1000-6915.2006.z2.054

Li, T., Zhang, J. W., Lv, Y. G., Zhou, P., Qiao, Z-D., and Chen, S. H. (2011). Relationship between Mining and Mining-Induced Seismicity. *J. China Coal Soc.* 36 (12), 2127–2132. doi:10.13225/j.cnki.jccs.2011.12.031

Luo, Y., Tao, W. B., Ma, H. F., Tao, J., and Hou, J. L. (2015). Mechanism of the Astro-Tidal-Triggering to Coal and Gas Outburst. *Chin. J. Rock Mech. Eng.* 34 (s1), 3005–3011. doi:10.13722/j.cnki.jrme.2014.0826

Metivier, L., De Viron, O., Conrad, C. P., Renault, S., Diament, M., and Patau, G. (2009). Evidence of Earthquake Triggering by the Solid Earth Tides. *Earth Planet. Sci. Lett.* 278 (3-4), 370–375. doi:10.1016/j.epsl.2008.12.024

Pan, J. F., Qi, Q. X., Liu, S. H., Wang, S. W., Ma, W. T., and Kang, X. C. (2020). Characteristics, Types and Prevention and Control Technology of Rock Burst in Deep Coal Mining in China. *J. China Coal Soc.* 45 (1), 111–121. doi:10.13722/j.cnki.jrme.2014.0826

Sun, C. Q., Yan, C. H., Wu, X. P., and Xu, Y-j. (2014). The Effect of Tidal Triggering on Seismic Fault in Eastern Tibetan Plateau and its Neighboring Areas. *Chin. J. Geophys.* 57 (02), 2054–2064. doi:10.6038/cjg20140703

Wu, K., Ji, C., Luo, L., and Wang, X. (2020). Simulation Study of Moon-Based InSAR Observation for Solid Earth Tides. *Remote Sens.* 12 (1). doi:10.3390/rs12010123

Wu, X. P., Mao, W., Huang, Y., and Jiang, J. (1999). Statistical Analysis of Tidal Stress Effect on Seismic Faults. *Chin. J. Geophys.* 42 (s1), 65–74.

Xie, H. P., Gao, F., and Ju, Y. (2015). Research Review of the State Key Research Development Program of China: Deep Rock Mechanics and Mining Theory. *Chin. J. Rock Mech. Eng.* 34 (11), 2161–2178. doi:10.13722/j.cnki.jrme.2015.1369

Xiong, Z. Y., Xie, Z. Z., Lei, X. L., Fu, H., and Ma, Q. B. (2015). Triggering Relationship between Seismic Activity and Tidal Stress in Dayao-Yaoan and its Adjacent Area of Yunnan Province. *J. Seismol. Res.* 38 (01), 66–74. doi:10.3969/j.issn.1000-0666.2015.01.009

Xu, X. F., Dou, L. M., Liu, J., Cui, X-h., Zhang, Y-l., and Yao, X-y. (2010). Research of Reasons and Controlling for Floor Burst in Coal Mine Roadway. *Rock Soil Mech.* 31 (6), 1977–1982. doi:10.16285/j.rsm.2010.06.001

Yu, Y., Zhao, D. C., Feng, G. L., Geng, D-X., and Guo, H-S. (2022). Energy Evolution and Acoustic Emission Characteristics of Uniaxial Compression

Failure of Anchored Layered Sandstone. *Front. Earth Sci.* 10, AR 841598. doi:10.3389/feart.2022.841598

Yuan, L. (2021). Research Progress of Mining Response and Disaster Prevention and Control in Deep Coal Mines. *J. China Coal Soc.* 46 (3), 716–725. doi:10.13225/j.cnki.jccs.YT21.0158

Zahran, K. H., Jentzsch, G., and Seeber, G. (2005). World-wide Synthetic Tide Parameters for Gravity and Vertical and Horizontal Displacements. *J. Geodesy* 79 (6-7), 293–299. doi:10.1007/s00190-005-0460-3

Zhang, R., Jiang, Z. Q., Li, X. H., Chao, H. D., and Sun, J. (2013). Study on the Failure Depth of Thick Seam Floor in Deep Mining. *J. China Coal Soc.* 38 (01), 67–62. doi:10.13225/j.cnki.jccs.2013.01.024

Zhang, Y. Z., Ji, H. G., Cai, M. F., Li, T., and Xiang, P. (2016b). Triggered Effect of Solid Tidal Stress on Rockburst and its Mechanism. *J. Min. Saf. Eng.* 33 (03), 535–543. doi:10.13545/j.cnki.jmse.2016.03.024

Zhang, Y. Z., Ji, H. G., Peng, H., and Xiang, P. (2016a). Correlation between Rockburst and Regional Tectonic Stress Environment and its Strain Response Characteristics. *J. China Coal Soc.* 41 (S2), 311–318. doi:10.13225/j.cnki.jccs.2015.1473

Zhou, J. C., Sun, H. P., Xu, J. Q., and Chen, X-D. (2013). Tidal Strain and Tidal Stress in the Earth's Interor. *Chin. J. Geophys.* 56 (11), 3779–3787. doi:10.6038/cjg20131119

Zhu, C., He, M. C., Zhang, X. H., Tao, Z. G., Yin, Q., and Li, L. F. (2021). Nonlinear Mechanical Model of Constant Resistance and Large Deformation Bolt and Influence Parameters Analysis of Constant Resistance Behavior. *Rock Soil Mech.* 42 (07), 1911–1924. doi:10.16285/j.rsm.2020.1764

Conflict of Interest: The authors declare that the research was conducted in the absence of any commercial or financial relationships that could be construed as a potential conflict of interest.

Publisher's Note: All claims expressed in this article are solely those of the authors and do not necessarily represent those of their affiliated organizations, or those of the publisher, the editors, and the reviewers. Any product that may be evaluated in this article, or claim that may be made by its manufacturer, is not guaranteed or endorsed by the publisher.

Copyright © 2022 Zhang, Ji and Wu. This is an open-access article distributed under the terms of the Creative Commons Attribution License (CC BY). The use, distribution or reproduction in other forums is permitted, provided the original author(s) and the copyright owner(s) are credited and that the original publication in this journal is cited, in accordance with accepted academic practice. No use, distribution or reproduction is permitted which does not comply with these terms.

frontiers | Frontiers in Earth Science

ORIGINAL RESEARCH
published: 25 July 2022
doi: 10.3389/feart.2022.872040

Numerical Method for the Deformation Calculation of the Shallow Buried Tunnel Caused by the Excavation of Overlying Soil Based on Soil Rebounding Characteristics

Jian Li[1], Shichang Li[1,2], Yu Zhang[3], Shanxiong Chen[1], Fei Yu[1], Zhangjun Dai[1] and Chaoxiong Li[1]*

[1]State Key Laboratory of Geomechanics and Geotechnical Engineering, Institute of Rock and Soil Mechanics (CAS), Wuhan, China, [2]University of Chinese Academy of Sciences, Beijing, China, [3]Sichuan Water Develeopment Group Co., Ltd., Chengdu, China

OPEN ACCESS

Edited by:
Shibing Huang,
Wuhan University of Science and Technology, China

Reviewed by:
Fei Wang,
Tarleton State University, United States
Zecheng Chi,
China University of Geosciences Wuhan, China
Hhuazhe Jiao,
Henan Polytechnic University, China

***Correspondence:**
Yu Zhang
jordanzhy@163.com

Specialty section:
This article was submitted to Geohazards and Georisks, a section of the journal Frontiers in Earth Science

Received: 09 February 2022
Accepted: 30 May 2022
Published: 25 July 2022

Citation:
Li J, Li S, Zhang Y, Chen S, Yu F, Dai Z and Li C (2022) Numerical Method for the Deformation Calculation of the Shallow Buried Tunnel Caused by the Excavation of Overlying Soil Based on Soil Rebounding Characteristics. Front. Earth Sci. 10:872040. doi: 10.3389/feart.2022.872040

In view of strict deformation control standards, it is important to calculate the shallow tunnel deformation caused by the unloading of overburdened soil for analyzing tunnel structure safety. Due to the obvious nonlinear characteristics and the significantly smaller rebound deformation of soil under unloading conditions, previous numerical calculation methods need to be improved and adapted to the soil deformation characteristics under unloading. Based on the above background, cyclic loading and unloading tests were carried out to study the deformation characteristics of soil under different loading levels, stress history, and unloading levels. Secondly, a unified modulus calculation model was established, especially for the unloading modulus, which considers the unloading stress history and current unloading stress level, and can provide the value of soil modulus in different states. The relationship between the unloading rebound modulus E_{sc} and the rebound modulus E_{c0} used in the numerical simulation was studied. Finally, a set of numerical calculation and analysis methods for shallow tunnel deformation caused by overlying soil excavation based on its rebounding characteristics is proposed. The rationality of the method is verified by two examples, and is applied to a practical project.

Keywords: soil rebounding characteristics, soil unloaded construction, shallow buried tunnel, numerical simulation method, deformation calculation

1 INTRODUCTION

With the development of urbanization, there are increasing instances of cross-geotechnical engineering. As this new engineering is close to the existing engineering, it is necessary to carry out calculations and analyses of the influence of new engineering on the existing engineering (Zhang et al., 2018a; Zhang et al., 2018b; Jiang et al., 2020). Civil structure constructions adjacent to subway tunnels are the most common cross-geotechnical engineering in the city (Chang et al., 2001; Sharma et al., 2001; Hu et al., 2003; Chen and Zhang, 2004; Wang and Yu, 2004). As subway tunnels undertake a large number of urban public transport functions, urban management needs to ensure the safe operation of these tunnels. For the problem of shallow tunnel deformation caused by adjacent engineering, many scholars have carried out relevant research and solved academic problems to a

certain extent. At present, the calculation of shallow tunnel deformation caused by adjacent engineering can be divided into two categories: one is theoretical calculation methods (Wang et al., 2006; Devriendt et al., 2010; Liu et al., 2010; Huang et al., 2013; Shi and Ng, 2015; Liang et al., 2017); the other is numerical calculations (Chen and Li, 2005; Zhang et al., 2013a; Zhang et al., 2013b; Zh ang et al., 2015; Liang et al., 2017; Qiu et al., 2021). These two kinds of methods have characteristics and advantages.

The characteristics of the theoretical calculation method are to treat the tunnel as a discretized beam structure. By assuming that the discrete elements meet certain mechanical balance conditions, the mechanical balance equations of the tunnel are established, and the deformation of the tunnel is calculated by solving the balance equations. The advantage of the theoretical method is that it is easy for engineers to calculate the deformation of the tunnel in real engineering when the calculation formula and solution method are derived. The advantage of numerical calculation is that the complete stress-strain relationship and interaction between the adjacent engineering can be considered with the establishment of a complete numerical model, which can provide reliable and comprehensive results for analysis. Although the theoretical calculation method is convenient for engineering applications, it is not adequate for analyzing the interaction between the adjacent engineering and the subway tunnels, and a numerical calculation method could completely overcome the limitations of the theoretical calculation method.

The numerical calculation method is a mainstream way of shallow tunnel deformation calculation and analysis, but the application of the numerical calculation method in shallow tunnel deformation calculation still needs to be improved. The reason for this is that, for special shallow buried tunnels, the safety control standards for deformation are strict. China's relevant regulations (Urban and rural areas of the People's Republic of China, 2011; Urban and rural areas of the People's Republic of China, 2013) stipulate that the deformation of subway tunnels should not exceed 5 mm and the ellipticity should not exceed 5%. Facing such strict control standards, the most important question of how to improve the accuracy and reliability of the calculation results for the numerical calculation method remains.

According to previous research experience and results, the calculated tunnel deformation due to soil unloading is usually larger than the actual situation under conventional calculation modes. The main reasons are as follows: 1) the unloading deformation of the soil itself is a nonlinear process, and the rebound modulus is several times the compression modulus, and its correlation varies greatly with different soil properties. 2) The actual unloading deformation of each layer is related to its stress history, unloading stress level, and unloading stress path. It can not be analyzed according to the mechanical parameters of the complete unloading state (conventional laboratory test). It is also necessary to carry out a large amount of demonstration work to realize the millimeter-level deformation calculation because of the discreteness, variability, and the complexity of physical and mechanical characteristics of the soil.

According to the analysis above, it is known that the soil nonlinear deformation is mainly affected by the variety of the mechanical parameters under different stress states, especially the change of the deformation modulus and it must be considered during the whole calculation process. On this basis, the deformation characteristics of the soil under repeated loading and unloading conditions are studied at first. And then a deformation calculation and analysis method for the shallow buried tunnel is proposed, which can reflect the actual state of the engineering. The rationality of the proposed method is validated through several examples. Finally, the method is applied to real engineering to illustrate its applicability and guidance for engineering.

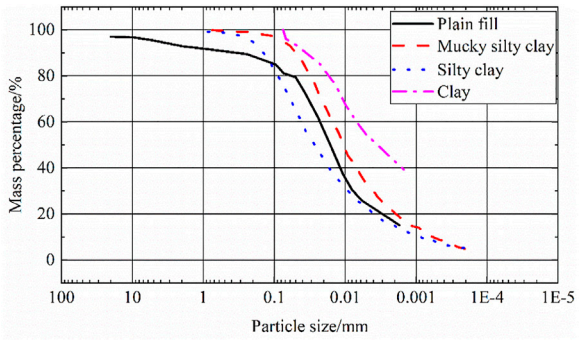


FIGURE 1 | Cumulative curve of soil particle size grading.

2 ANALYSIS OF CYCLIC COMPRESSION-REBOUND CHARACTERISTICS OF SOIL

For numerical calculation, the parameters must be reasonable to get the rational calculation results. The rebounding parameter of soil determines the rationality of shallow tunnel deformation calculation. We discuss the compression-rebound characteristics of soil under different load levels and get the value of the rebounding modulus of soil under rebound conditions at first. Then, we substitute the test value into the numerical calculation model to reasonably calculate the deformation of the shallow buried tunnel.

The particle size distribution of the typical soil is shown in **Figure 1**. The basic physical parameters of the typical soil are respectively: 1) fill: water content 28.4%, liquid limit 35.6% and plastic limit 21.4%; 2) mucky silty clay: water content 31.7%%, liquid limit 34.7% and plastic limit 21.3%; 3) silty clay: water content 29.9%, liquid limit 37.3% and plastic limit 21.5%; 4) clay: water content 27%, liquid limit 38.8% and plastic limit 22.3%. Note that the water content listed above was obtained by the field investigation, which is the natural moisture content of the original soil. For different types of soil, the natural water content is different and is not the saturated water content. Indeed, the water content influences the deformation of soil. According to the general law, with the increase of water content, the deformation resisting ability of soil decreases.

2.1 Compression-Rebound Test Conditions for Soil

The compression-rebound test of soil is carried out with a standard consolidation instrument (as shown in **Figure 1**). The size of the soil

TABLE 1 | Soil compression-rebound test conditions.

Soil Property	Loading Classification/kPa	Unloading/Reloading Classification/kPa
Plain fill	Load point1:25	
	Load point2:50	1. 25-12.5-0-12.5-25
	Load point3:100	2. 50-25-0-25-50
	Load point4:200	3. 100-50-25-0-25-50-100
Mucky silty clay	Load point1:25	4. 200-150-100-50-0-50-100-150-200
	Load point2:50	5. 400-300-150-50-0-50-150-300-400
	Load point3:100	6. 600-400-200-100-0-100-200-400-600
	Load point4:200	7. 800-600-400-200-0-200-400-600-800
	Load point5:400	
Silty clay	Load point1:25	
	Load point2:50	
	Load point3:100	
	Load point4:200	
	Load point5:400	
Clay	Load point1:100	
	Load point2:200	
	Load point3:400	
	Load point4:600	
	Load point5:800;	

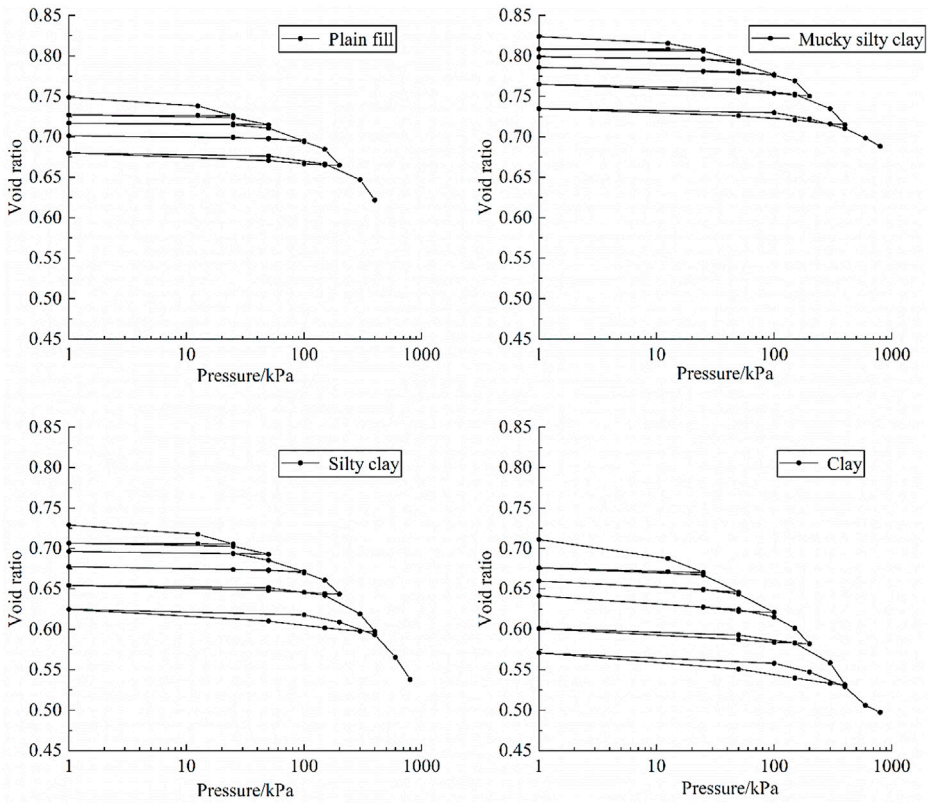


FIGURE 2 | Compression-rebound test curve of typical soil.

sample is φ61.8 mm in diameter and 20 mm in height. The test condition is to limit the deformation of soil laterally, and then apply the vertical load on the top of the sample. After the vertical load is loaded to a certain stress level, it is unloaded in stages. Each loading or unloading step needs to wait until the soil sample is stabilized in deformation, and the height of the soil sample is recorded to calculate the change of pore ratio and compression or rebound modulus of the soil sample. Specific test conditions are shown in **Table 1**.

2.2 Compression-Rebound Characteristics of Soil

Both elastic deformation and plastic deformation will occur during the compression process, and the deformation curve of soil appeared to have hysteretic characteristics during the rebound and re-compression process. This feature needs to be taken into account in the calculation to make it more realistic. **Figure 2** shows typical compression-rebound test curves of different soils.

As can be seen from **Figure 2**, no matter whether it is soft soil or hard soil, the soil pore ratio could not return to the initial pore ratio when unloading under different overlaying loads, which indicates that both elastic deformation and plastic deformation occurred in the soil during compression, and the plastic deformation is relatively large.

It can also be seen that in the process of soil rebound, the load-pore ratio curve of soil is not a straight line (the rebound curve appears to be a straight line under the condition of low load unloading, it is a curve, but the bending is not obvious, which will be reflected in the fitting model later). This indicates that during the process of soil rebound, the stress-strain relationship of soil is elastic-plastic, and the deformation modulus of soil changes can not be used by the unified elastic modulus.

In addition, the hysteretic characteristics of soil rebound-recompression deformation are different under high pressure and low pressure. When soil is unloaded and reloaded under a low compression load (less than 100 kPa), the load-pore ratio curve of soil overlaps and there are no hysteretic characteristics. When the soil is unloaded and reloaded under a high compression load, the load-pore ratio curve shows obvious hysteretic characteristics. At the initial stage of unloading under a high compression load, the load-pore ratio curve of soil is relatively smooth and the rebound deformation is small, which indicates that the rebound modulus is large at the initial stage of unloading. When unloading to a certain extent, the load-pore ratio curve begins to bend and the rebound deformation occurs rapidly. The hysteresis characteristics of soil under high compression load are consistent with the existing results (Li and Teng, 2018; Wang et al., 2020), but that under low compression load is rarely reported. What should be emphasized is that the excavation on the ground will usually cause the deformation of the shallow soil layer. Therefore, the unloading rebound characteristics of soil under low compression load are more significant for shallowly buried tunnel engineering.

2.3 Method for Calculating Rebound Modulus E_{sc} of Soil in Different Construction Stages

For numerical calculation, the most commonly used and most convenient constitutive model is the Mole Coulomb model. The parameters used in the mole Coulomb model are elastic modulus E_0, Poisson's ratio ν, cohesion c, and friction Angle φ, among which, the impact of the elastic modulus on deformation is the largest. But for engineering investigation, the compression test is used to determine the modulus of soil mass. To avoid confusion, here we use E_s and E_{sc} to represent the compression modulus and rebound modulus determined by the compression-rebound test and use E_0 and E_{c0} to represent the elastic modulus and rebound modulus before and after the excavation construction in the numerical simulation. The problem of shallow buried tunnel deformation caused by soil excavation does not involve soil re-compression, therefore, the estimation of soil re-compression modulus is not included in this research.

The compression curve of soil is shown in **Figure 3(1)** , and the rebound curve of soil is shown in **Figure 3(2)**. In terms of morphology, the compression curve and the rebound curve have similar morphology, so they can be fitted by one equation. After a comprehensive comparison, we choose the power function of three parameters as the fitting function of E_s and E_{sc}. The specific equation is as follows:

$$e = a(1 + p/b)^c \tag{1}$$

Where: a,b,c are model parameters; e is porosity ratio; p is the current pressure value/kPa.

1) Comparison of test data and formula fitting data in the soil compression test
2) Comparison of test data and formula fitting data in soil rebound test

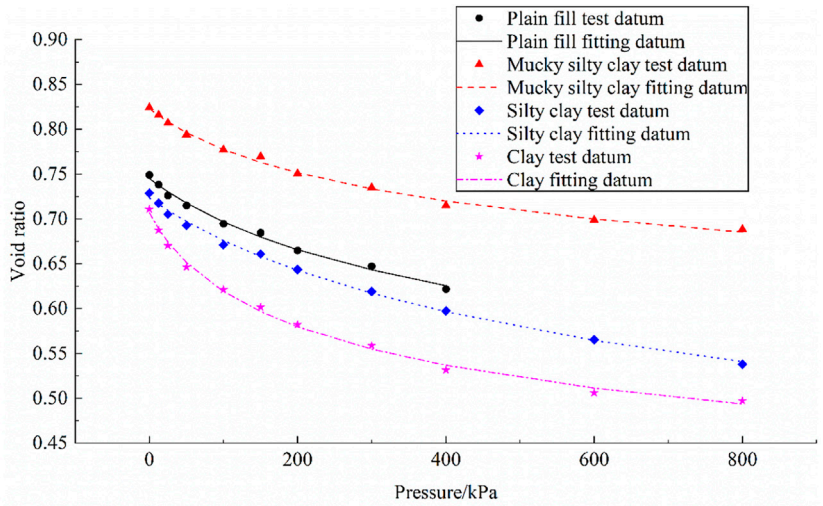
As shown in **Figure 3**, the fitting effect of the soil compression curve and rebound curve is good, and the fitting model can accurately reflect the compression and rebound characteristics of different soils. For the convenience of application, the fitting parameters of the compression curve are listed in **Table 2**. For rebound conditions, there are different fitting parameters for the rebound curve under different pressure values. The function relationship between the three fitting parameters and the pressure values can be further established to facilitate the application of numerical calculation in the later period. The fitting functions of different soil rebound parameters are also listed in **Table 2** below.

For excavation construction, the soil should be unloaded at different load levels, so the rebound modulus E_{sc} of soil should be calculated according to the excavation depth and the unloading level. It is worth noting that the above model and calculation parameters are used to calculate the current pore ratio of soil, which need to be converted to modulus if the modulus is wanted.

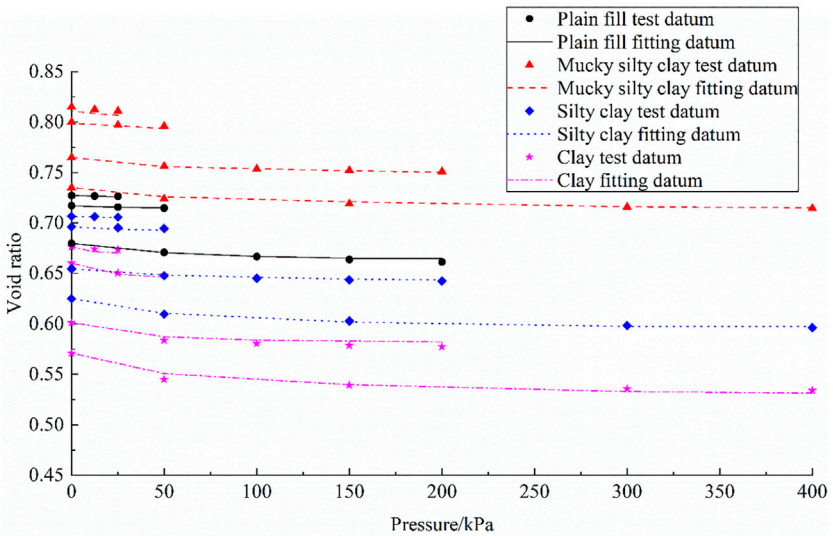
2.4 Determination of Soil Rebound Modulus E_{c0} in Different Construction Stages

Some scholars have discussed the relationship between soil compression modulus E_s and elastic modulus E_0 under compression, and the conclusion is that there is a certain proportional relationship between E_s and E_0 (Jia et al., 2008; Yu, 2014). However, there is no literature report on the relationship between E_{sc} and E_{c0}, used in numerical calculation. Therefore, it is necessary to determine the relationship between them to provide reliable parameters for the subsequent calculation of shallow buried tunnel deformation.

Figure 4(1) shows the comparison between the numerical simulation and the test conditions of different soil compression-rebound tests. It can be seen that the conditions of the



(1) Comparison of test data and formula fitting data in the soil compression test



(2) Comparison of test data and formula fitting data in soil rebound test

FIGURE 3 | Comparison of test data and formula fitting data in soil compression-rebound test.

compression rebound test and the numerical simulation are the same: the numerical model has a diameter of 6.18 cm and a height of 2 cm, the horizontal deformation is constrained around the soil sample, displacement is completely constrained at the bottom of the soil sample, and only axial load is applied or reduced at the upper part of the numerical model. The loading step is also the same as the real test which is that after the consolidation under a certain load level is completed, the next load will be added to the surface of the model.

Figure 4(2) shows the datum comparison of the compression-rebound test and the numerical simulation of different soil samples under different rebound conditions. Here, the rebound modulus E_{sc} obtained by the compression-rebound test is constantly adjusted, and the multiple relationships between E_{c0} used in numerical simulation and E_{sc} obtained by the test are determined, that is, $E_{c0} = 4.0E_{sc}$. It can be seen from the figure that the soil rebound curve obtained by numerical simulation is in good agreement with the test curve, which can well reflect the deformation of soil under the rebound conditions. Therefore, in the subsequent deformation calculation of shallow buried tunnel, E_{c0} will be set whose value is 4 times E_{sc} according to the different compression state and unloading level.

3 CALCULATION METHOD OF SHALLOW BURIED TUNNEL DEFORMATION

According to the results of the soil compression rebound test, the E_s or E_{sc} of soil has the following characteristics:

TABLE 2 | Fitting parameters of the compression and rebound curve.

Fitting parameter		Soil			
		Plain fill	Mucky silty clay	Silty clay	Clay
Compression fitting parameter	a	7.45E-01	7.23E-01	7.07E-01	8.23E-01
	b	1.67E+02	2.56E+02	5.91E+01	1.03E+02
	c	-1.43E-01	-2.05E-01	-1.34E-01	-8.45E-02

Fitting parameter		Soil											
		Plain fill			Mucky silty clay			Silty clay			Clay		
Rebounding fitting parameter	a	$A(1 + p/B)C$	A	7.36E-01	$A(1 + p/B)C$	A	8.21E-01	$A(1 + p/B)C$	A	7.16E-01	$A(1 + p/B)C$	A	6.98E-01
			B	2.27E+02		B	1.09E+02		B	1.12E+02		B	8.20E+01
			C	-1.40E-01		C	-8.47E-02		C	-9.47E-02		C	-9.68E-02
	b	$A(1 + p/B)C$	A	5.09E+02	$A(1 + p/B)C$	A	1.17E+02	$A(1 + p/B)C$	A	2.00E+02	$A(1 + p/B)C$	A	1.89E+01
			B	4.57E+01		B	3.38E-02		B	2.23E+01		B	4.65E-01
			C	-1.64E+00		C	-3.90E-01		C	-1.25E+00		C	-3.87E-01
	c	$Aexp(B/p)$	A	-1.41E-02	$A(1 + p/B)C$	A	1.00E+02	$A(1 + p/B)C$	A	-2.23E-03	$A + pB + p/C2$	A	-5.60E-03
			B	-8.56E+00		B	-1.00E+02		B	5.89E+01		B	-8.36E-06
						C	1.44E+00		C	8.87E-01		C	2.25E+00

1) Whether in compression or rebound state, the compression moduus E_s or the rebound modulus E_{sc} of soil varies with the overlaying pressure. This means that in the numerical calculation, the modulus of soil should be adjusted according to the overlaying pressure.
2) Especially for the rebound state, the rebound modulus E_{sc} is not only related to the initial unloading pressure but also related to the unloading state, that is, different initial unloading pressure and different soil rebound modulus. Under the same initial unloading pressure, the rebound modulus of soil is different with different unloading levels.

Therefore, for small deformation of shallow buried tunnel deformation calculation, the value of E_{c0} rebound modulus of soil under the rebound condition is critical, which should be reasonably determined to make the results more in line with engineering practices and more convincing.

Based on the above research results, this method proposed for shallow tunnel deformation can be summarized in the following steps:

1) Initial ground stress calculation: according to the basic physical and mechanical parameters of soil, estimate the dead weight load of different soil layers in advance, transform the compression modulus E_s into E_0, which is assigned to the soil model along with the parameters of Poisson's ratio ν, cohesion c, and internal friction Angle φ, and then calculate to balance.
2) Calculation of shallow buried tunnel construction: simulate tunnel excavation and calculation, monitor the change of soil pressure in real time, dynamically adjust the elastic modulus of soil E_0, calculate to the model balance, and record the pressure information of soil.
3) Calculation of shallow tunnel deformation: simulation soil excavation upon the shallow tunnel, determine the initial unloading pressure according to the pressure information of soil elements, monitor the pressure variation of the soil elements in time and dynamically, calculate the rebound modulus E_{sc} according to the initial unloading pressure and current pressure, and transfer it into E_{c0}, then continually adjust the E_{c0} during the calculation process to make tunnel deformation results more reasonable.

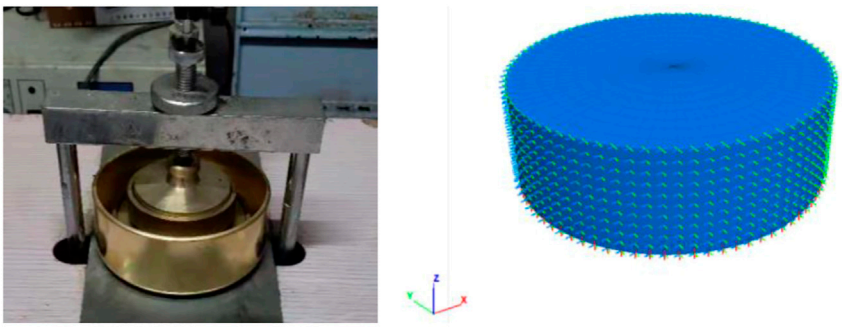
In order to more clearly show the calculation method and process of shallow buried tunnel calculations proposed in this paper, the specific process is given in the form of a flow chart in **Figure 5**.

4 VERIFICATION OF CALCULATION METHOD

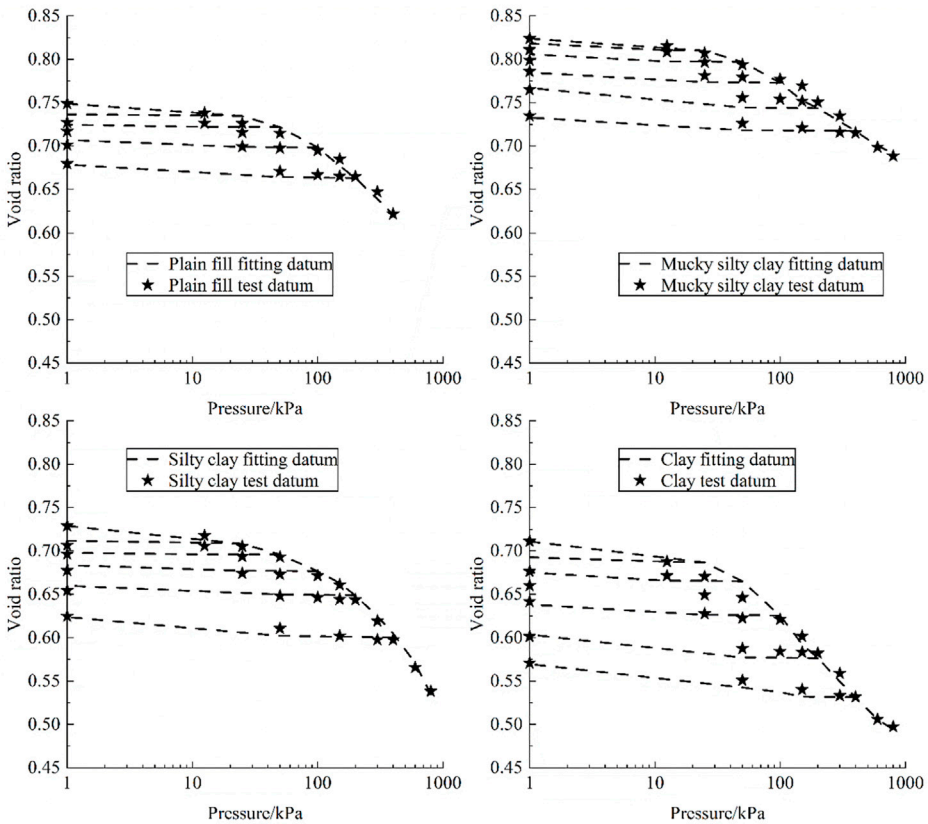
4.1 Case I: Influence of Shanghai Daning Commercial Center Foundation Excavation to Shanghai Metro Line One

A previous study by Wang et al. (2006) reported on the influence of the Shanghai Daning Commercial Center foundation excavation on its nearby metro tunnel. Another study (Liang et al., 2017) reported a simplified analytical method to evaluate the effects of the excavation of the tunnel. In this literature, the deformation datum by the analytical calculation and in-site measuring are compared. This datum is used as the base datum to verify the calculated metro tunnel deformation obtained by the method proposed in this paper.

The layout of the foundation pit and its position in relation to the metro tunnel are shown in **Figure 6**. The length and width of



(1) Numerical simulation model extraction



(2) Comparison of test data and simulation data in soil compression-rebound test

FIGURE 4 | Numerical simulation model extraction and comparison of test data and simulation data.

the foundation pit are 240 m × 230 m, and the distance between the supported pile and the tunnel is only 5.4 m. In the adjacent area, there are four layers of soil, which respectively are: 1 fill; 2 silty clay; 4 muddy clay; 5_1clay. The external diameter of the metro tunnel is 6.2 and its liner thickness is 0.3 m. The numerical model is modeled according to the project and is shown in **Figure 6**.

The basic parameters of the soil and supported structure are the same as that used in other literature (Wang et al., 2006), which are 1 fill: Poisson ratio 0.32, cohesion 1 kPa, friction 22°; 2 silty clay: Poisson ratio 0.35, cohesion 18 kPa, friction 18°; 4 muddy clay: Poisson ratio 0.4, cohesion 12 kPa, friction 10°; 5_1clay: Poisson ratio 0.35, cohesion 20 kPa, friction 16°. In a contrasting situation considering the type of the surrounding

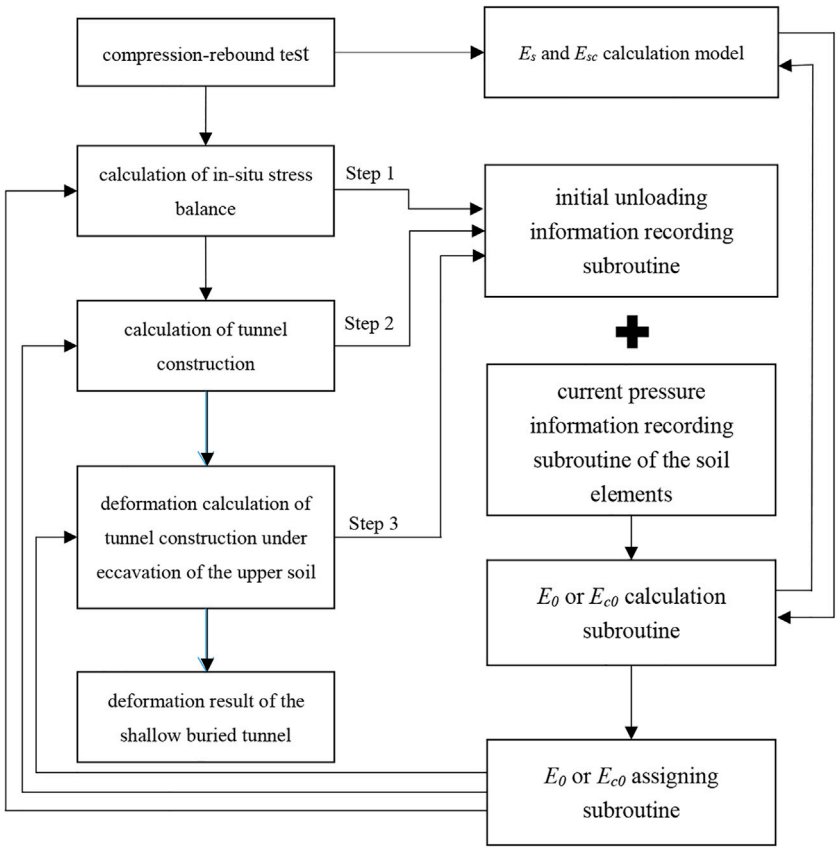


FIGURE 5 | Calculation process of the proposed method.

soil, the resilience parameters are determined referred to the test results in this paper.

As the downline tunnel is closer to the foundation pit than the upline tunnel, the deformation of this tunnel is considered and contrasted to verify the rationality of the method proposed in this paper. The calculated deformation datum obtained from wider literature (Wang et al., 2006; Liang et al., 2017) and the proposed method are compared with the measured results. As shown in **Figure 7**, although the calculated datum obtained by the three methods all reflect the deformation of the metro tunnel, the datum calculated by the method in this paper is closer to the measured datum and better reflects the tunnel deformation trend.

4.2 Case II: Influence of the Shanghai Bund Underground Passage Construction on the Existing Tunnel

To better verify the rationality of the proposed method, another project case is introduced below. In this case, the Bund Underground Passage in Shanghai was constructed on the metro tunnel. The layout of the underground passage and its position in relation to the metro tunnel is shown below in **Figure 8(1)**.

The underground passage was constructed using the open-cut method. The foundation pit was supported by several retaining walls, as shown in **Figure 8**. In this case, four conditions with different Dz (Plan I: Dz = 11 m; Plan II: Dz = 16.5; Plan III: Dz = 22 m; Plan IV: Dz = 27.5) were calculated, and the results are compared with those in the literature (Huang et al., 2013).

The numerical model is shown in **Figure 8(2)**. The engineering geological condition is that there are three soil layers: 1. Clay layer; 2. Silty clay layer; 3. Sandy silty clay layer. The mechanical parameters of the soil are the same as that used in the literature (Huang et al., 2013)which are ①clay: Poisson ratio 0.32, cohesion 8 kPa, friction 23°; ②silty clay: Poisson ratio 0.31, cohesion 13 kPa, friction 27°; ③sandy silty clay: Poisson ratio 0.3, cohesion 3 kPa, friction 30°. As with Case I, in this case, the resilience parameters are also referred to in the test results in this paper.

Figure 9 compares the results of this study and the wider literature (Huang et al., 2013). It can be seen that the tunnel deformation results calculated by the two methods can all reflect the law that with the increase of the burial depth of the tunnel, the deformation of the tunnel decreases, and the maximum deformations obtained by the two methods are almost the same. However, from the axial deformation variation law, the results of the two methods have certain differences. This could be caused by setting the different parameters of the supported structure. According to experience, we believe that under the supported structure with enough strength, the influence range

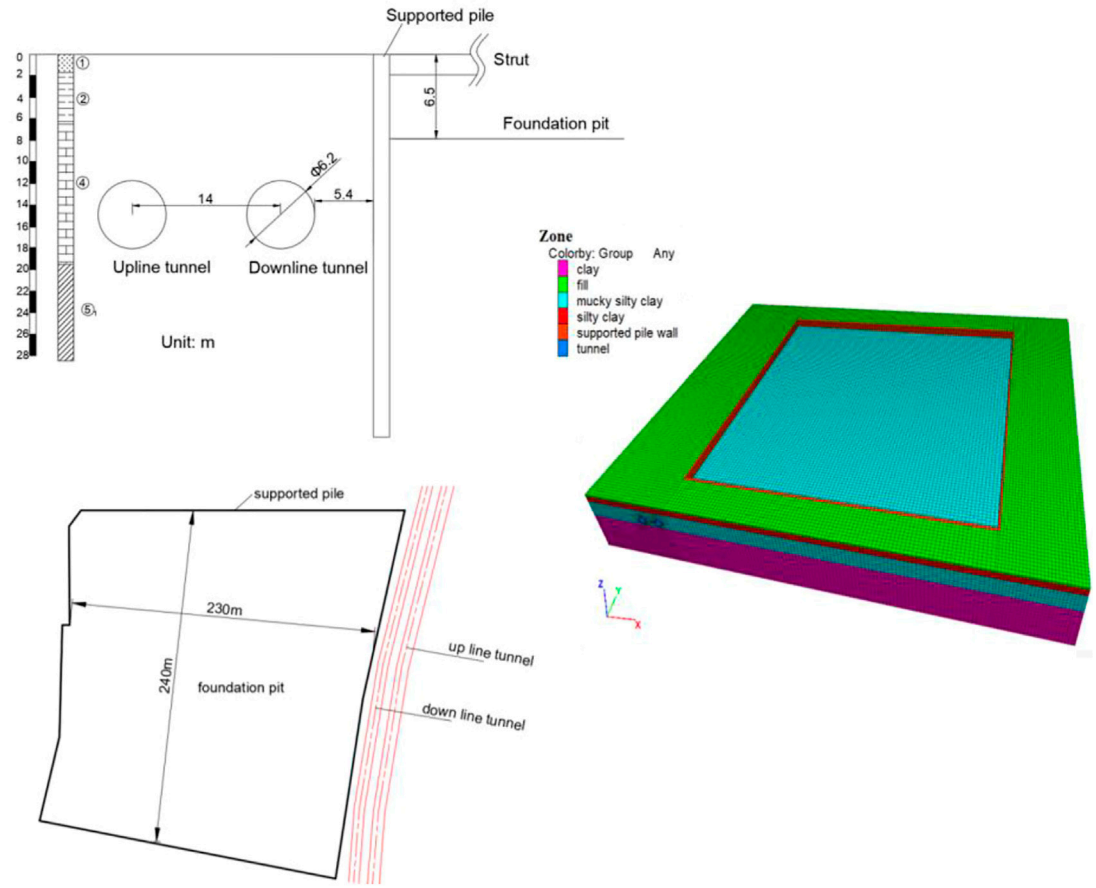


FIGURE 6 | The numerical model according to the project layout in Case I.

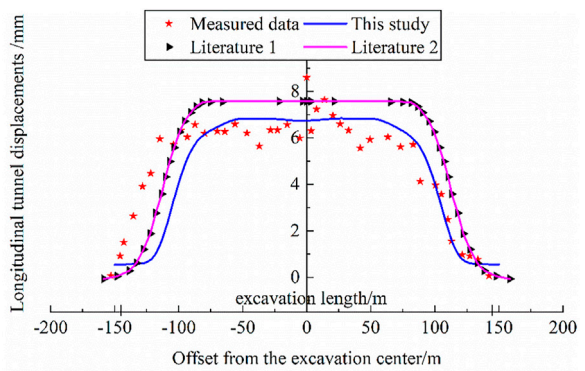


FIGURE 7 | Results comparison between this method and two studies in Case I.

should be limited in the cutting construction area. Because the supporting structure can effectively block the deformation surrounding the foundation pit wall. This understanding is also confirmed by Case I, in which the deformed range of the metro tunnel is consistent with that of the cutting construction (see **Figure 8**).

5 PROJECT APPLICATION—INFLUENCE OF SOIL UNLOADING ON WUHAN METRO LINE FOUR

Before the project construction, the influence on the nearby existing engineering structure must be first assessed. Here an application of the influence of soil unloading on Wuhan metro line four using the proposed method in this paper is introduced. The deformation law of the metro tunnel caused by soil unloading on the ground surface is calculated. The deformation of the tunnel is used to judge whether the deformation standards specified in the relevant codes are exceeded. Then the calculated tunnel deformation is compared with the in-site measured results. The proposed method is therefore validated and checked.

5.1 Project Background

A real estate project was constructed above the Wuhan metro line 4, and before its construction, an influence assessment was done to ensure the engineering can be conducted.

The range of the soil unloading and its position in relation to the Wuhan metro line four is shown in **Figure 10(1)**. As seen in the figure, the unloading soil lay directly on the metro tunnel. The

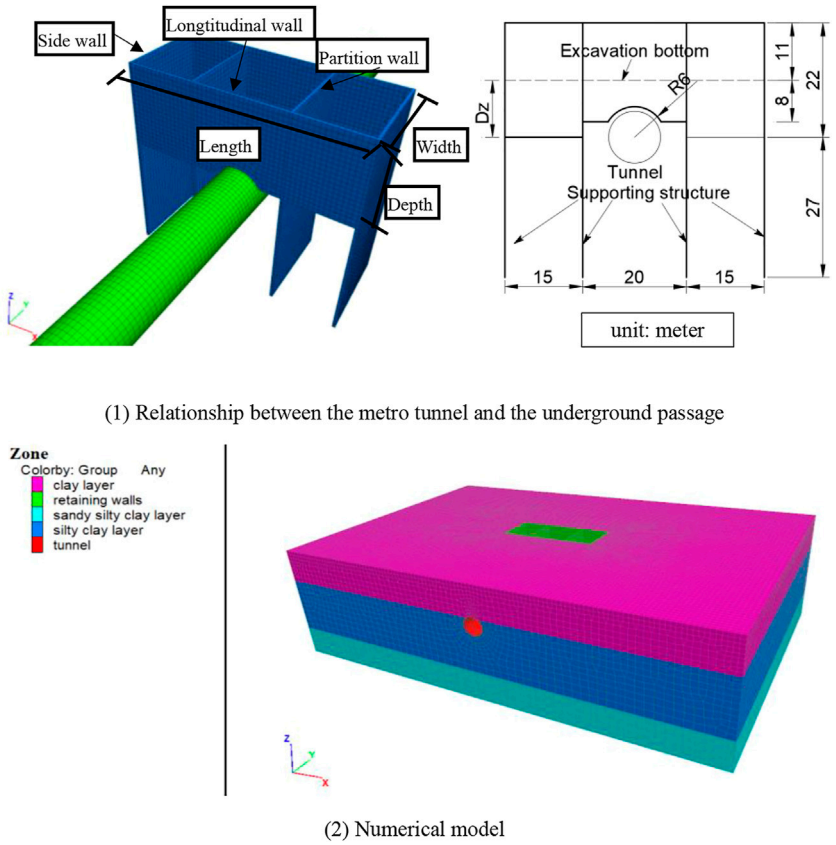


FIGURE 8 | Numerical model of the intersection engineering of Case**II**.

whole unloading area is divided into two parts: 1) part I: the north of the red line and 2) part II: the south of the red line. The elevation of part I after soil unloading is 23.5 m, the unloading thickness is 8–12 m and the tunnel buried depth is 10.9–13.8 m. The elevation of part II after soil unloading is 22 m, the unloading thickness is 4.2–7.8 m and the tunnel buried depth is 13.8–19.6 m. Based on engineering experience, the influence of unloading construction in part I should be greater than that in part II due to the larger buried depth of the tunnel and unloading thickness. Therefore, the tunnel deformation calculation in part I was under heavy consideration in the assessment.

5.2 Numerical Model, Parameters, and Simulation Procedure

For establishing the numerical model, we selected two typical sections of part I, which can be seen in **Figure 10(2)**. The distance between the two sections is about 50 m and the 3D numerical model is obtained by extrusion operation from sections A_1A_2 to A_3A_4. The 3D numerical model can be seen in **Figure 10(3)**. The length and height of the model are respectively 220 m and 50 m. The diameter of the metro tunnel is 5.5 m and the thickness of the concrete supporting structure is 0.35 m.

The engineering geological condition is also shown in **Figure 10(3)**. It can be seen that the soil layers under the unloading soil are respectively 1) fill; 2) clay; 3) silty clay; 4) clay; 5) highly weathered mud sandstone; and 6) medium weathered mud sandstone.

The initial parameters of the model are listed in **Table 3** and the parameter adjustment in the calculation process is achieved by the method in **Section 2.3**. What needs illustration is that the initial parameters are necessary before the calculation and along with the calculation, the parameters would be periodically and continually adjusted according to the indoor test results.

As mentioned in **Section 3**, the whole calculation procedure is divided into three stages: I. initial stress balance stage; II. tunnel construction stage; and III soil unloading on the ground stage. In stage I, the whole model consists of soil, while in stage II, the tunnel construction is simulated. In this stage, the deformation of the tunnel is resisted by the concrete supporting structure. Finally, in stage III, all the deformation in stage II is eliminated, and the deformation caused by soil unloading is studied.

5.3 Influence Assessment According to the Calculation Result

5.3.1 Deformation on the Ground Surface and Tunnel Crown

Figure 11(1) is the heaving deformation contours after the ground soil unloading. **Figure 11(2)** shows the heaving

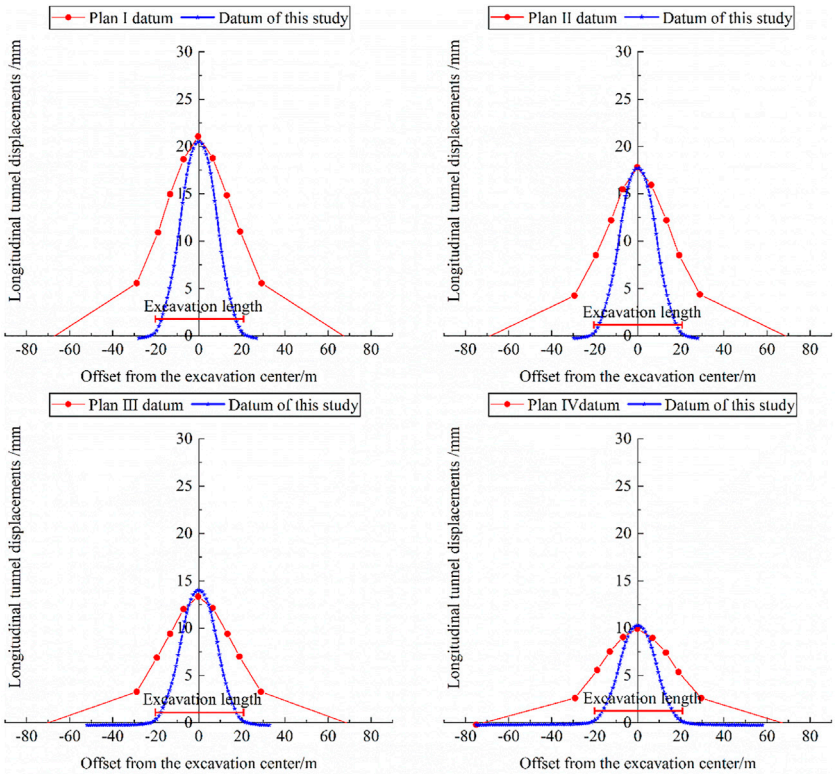


FIGURE 9 | Results comparison between this method and studies in CaseII.

deformation of the soil and **Figure 11(3)** shows the heaving deformation of the tunnel.

From the figures, we can see that due to the large area of soil unloading construction, the ground surface has a large heaving deformation. The biggest heaving deformation occurs at the position with the biggest soil unloading thickness, whose value is about 19.6 mm.

After the soil was unloaded, along with the rebounding deformation of the surrounding soil, heaving deformation also occurs on the metro tunnel. But because of the greater stiffness of the tunnel supporting liner, the heaving deformation is smaller than that of the soil.

According to the position relationship, the metro tunnel is located in the down right of the unloading soil, therefore, the deformation is upward to the upper left direction. In addition, the right line is closer to the unloading soil, so its deformation is bigger than that of the left line. From the value of the tunnel heaving deformation, the maximum heaving deformation on the right line is about 2.1 mm and that of the left line is about 1.7 mm. The maximum horizontal deformation of the two lines are 0.65 mm and 0.50 mm, respectively.

5.4 Deformation Law of the Metro Tunnel

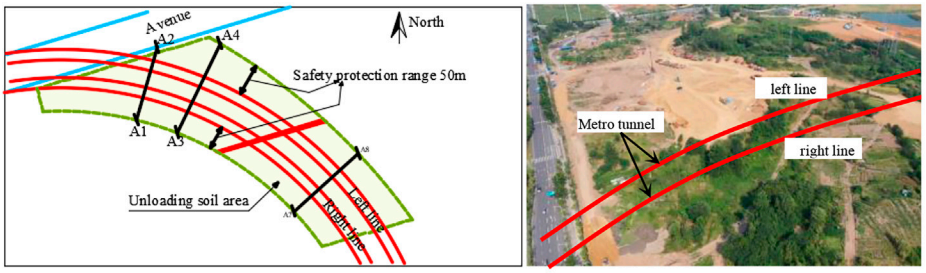
5.4.1 The Deformed Shape Analysis of Metro Tunnel Structure

Figure 12 shows the deformed shape of the metro tunnel structure in the typical section. It is known that after the cutting soil was unloaded, the tunnel structure shape was changed from a circle to an approximate ellipse. After deformation, the upper curvature of the tunnel structure was small and the curvature of the lower part was large. This phenomenon further shows that the deformation at the crown of the tunnel was greater than that of the bottom.

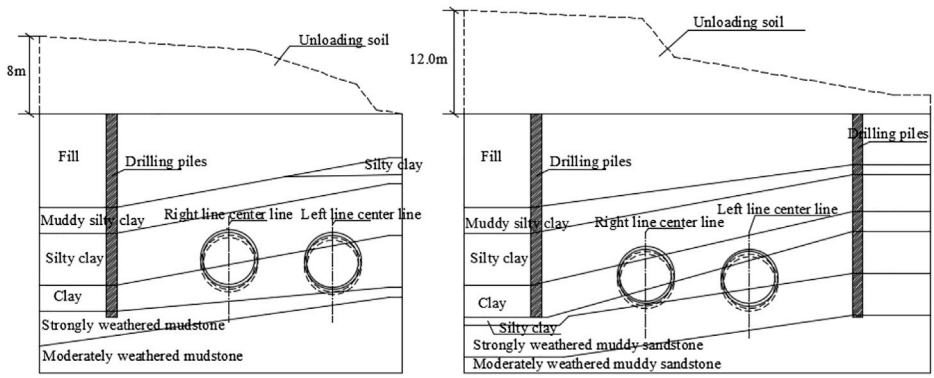
From the deformation direction at the crown of the tunnel, its direction pointed to the thickest part of the unloaded soil, therefore, the long axis of the elliptical shape of the deformed tunnel rotated to left. Due to the different horizontal distance between the left and right tunnels to the thickest part of the unloaded soil, the rotating angle of the long axis of the ellipse of the left tunnel was smaller than that of the right tunnel.

5.4.2 Law of the Maximum Deformation of the Tunnel Structure Under Different Unloaded Thickness

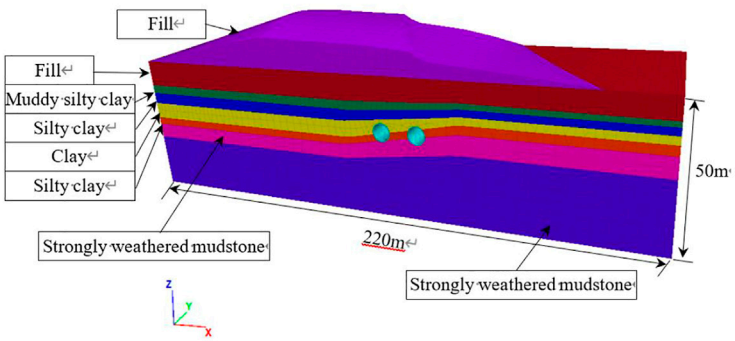
Figure 13 gives the maximum deformation of the tunnel under different unloading thicknesses. For the maximum heaving deformation, the value increased along with the increase of the unloaded soil thickness, whose relationship belonged to a straight line. This showed that the heaving deformation of the tunnel was directly related to the thickness of the unloaded soil. On the other hand, as for the maximum horizontal deformation, when the unloaded thickness was smaller than 8 m, the deformation value increased linearly with the increase in unloaded thickness. However, when the unloaded thickness



(1) Relationship between the soil excavation area and the metro tunnel



(2) Typical section of part I

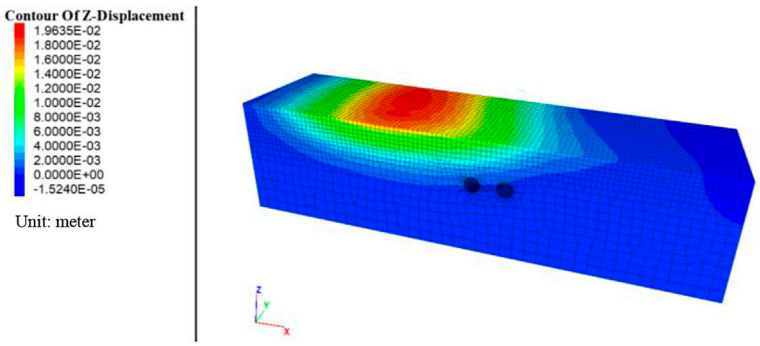


(3) 3D numerical model

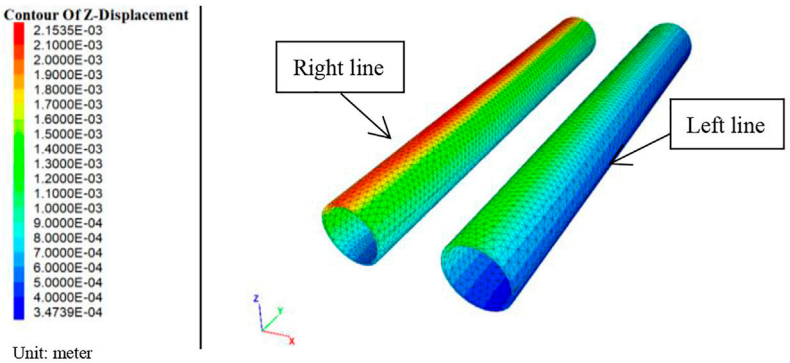
FIGURE 10 | Numerical modeling process.

TABLE 3 | Calculation parameters.

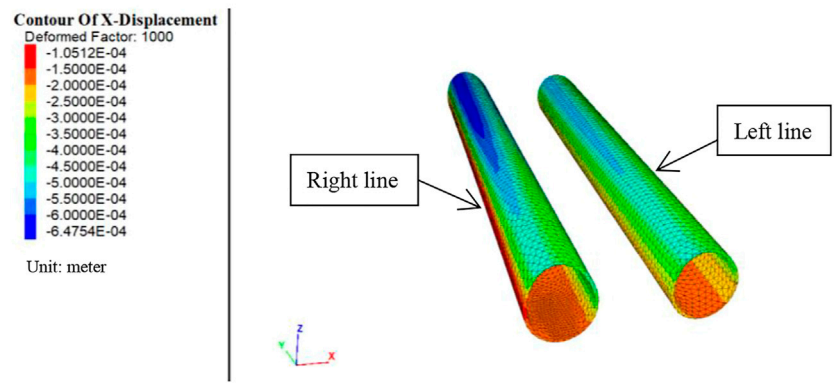
No.	Soil layer	Initial young modulus (MPa)	Density (kN/m^3)	Cohesion (kPa)	Friction angle (°)<	*v*
1	Fill	20	1,770	8	15	0.26
2	Muddy silty clay	12	1,650	11	4	0.28
3	Clay	22	1,810	21	12	0.27
4	Silty clay 1	32	1,860	28	15	0.26
5	Silty clay 2	56	1,920	36	16	0.25
6	Strongly weathered muddy sandstone	150	1,980	80	34	0.23
7	Moderately weathered muddy sandstone	200	2,250	150	42	0.22



(1) heaving deformation contour of the whole model



(2) heaving deformation contour of the tunnel



(3) Horizontal deformation of the tunnel

FIGURE 11 | Deformation contour of the two metro tunnels (heaving and horizontal deformation).

was bigger than 8 m, the influence of the unloaded thickness on horizontal deformation weakened quickly.

5.5 Contrast Between the Calculation Result and the in Site Measured Datum

To verify the calculation results, the contrast between the measured datum and the simulation result is shown in the following section. In the *in situ* deformation measure, the absolute deformation on the tunnel crown and bottom was conducted. The deformation of the whole tunnel in the soil unloading range was measured during the construction, and the simulation section was in the measuring range. The interval length between the measuring section was about 5.5 m.

1) Heaving deformation on the tunnel CRown

Figures 14(1)a,(2)a show the contrast of the heaving deformation on the tunnel crown between the calculation result and the in site measured datum.

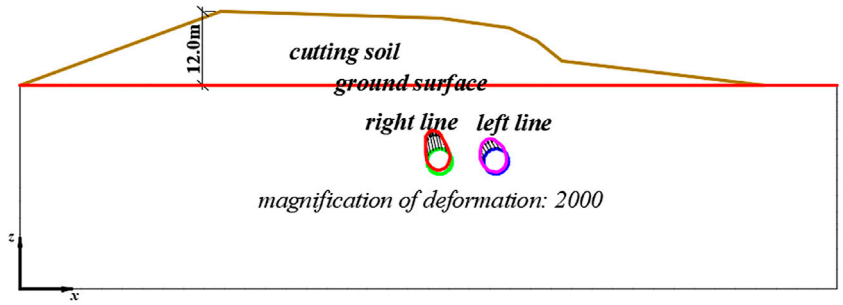


FIGURE 12 | The shape of the deformed metro tunnel structure after unloading the cutting soil (the deformation is magnified 2000 times).

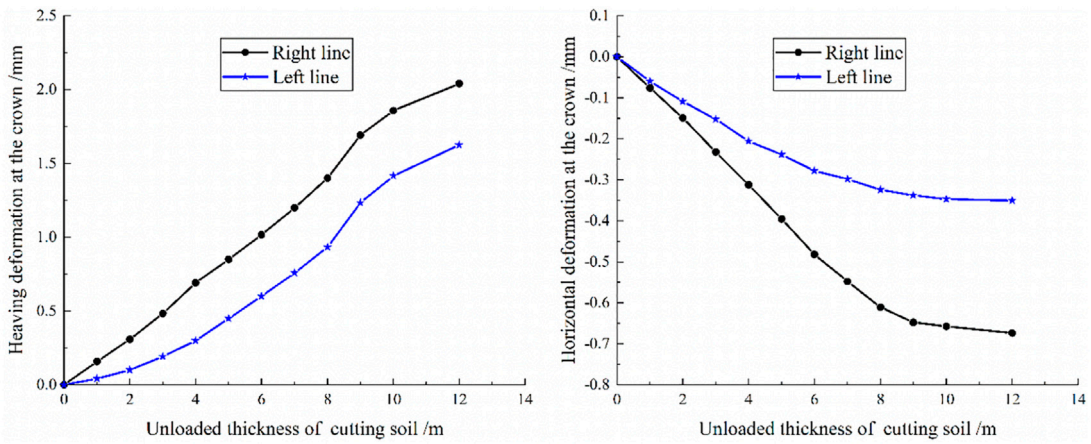


FIGURE 13 | The maximum deformation of the tunnel under different unloaded thickness.

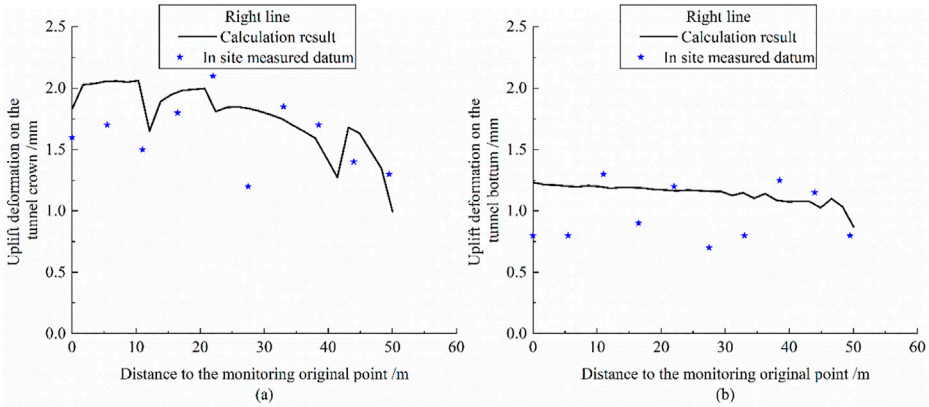
From the figures, it can be seen that after the soil excavation construction, deformation occurs on the tunnel crown, which is in agreement with the *in situ* measured data. The resulting agreement can be reflected in three aspects. First, on one hand, given the heaving deformation of the tunnel crown, the calculated maximum deformation is 2.1 mm and the measured maximum deformation is 2.2 mm, which indicates that they are consistent. Secondly, on the other hand, from the perspective of longitudinal tunnel deformation, due to the different thickness of the unloading soil, the heaving deformation values of the tunnel crown at different positions should be different, and the numerical simulation results accord with the distribution trend of the measured deformation of the tunnel. Finally, because the right line of the subway tunnel is closer to the maximum thickness of the unloading soil, the value of the heaving deformation of the right line tunnel should be larger than that of the left line tunnel, and the numerical simulation results are consistent with the measured data.

2) Heaving deformation on the tunnel bottom

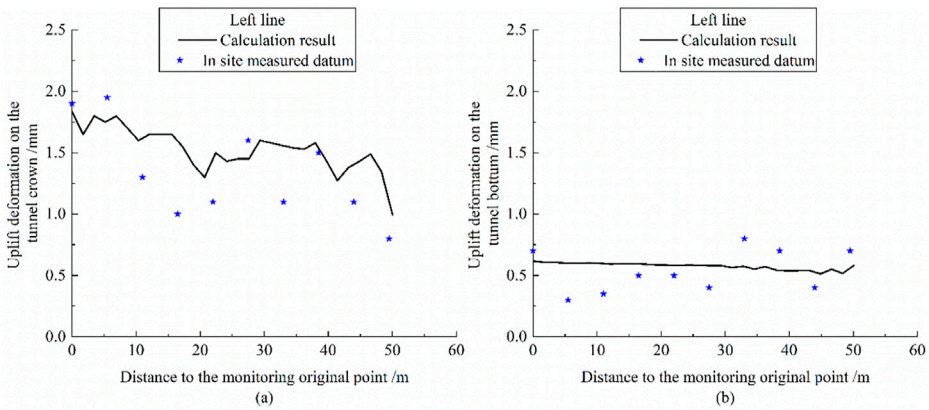
Figures 14(1)b,(2)b show the contrast of the heaving deformation on the tunnel bottom between the calculation result and the in site measured datum.

From the Figures, it can be seen that:

1) Due to the soil unloading construction on the ground, the rebound deformation of the foundation soil caused the heaving deformation of the subway tunnel. Due to the relatively deep depth at the bottom of the tunnel and the large rigidity of the tunnel lining structure, the heaving deformation at the bottom of the tunnel was significantly smaller than that at the top of the tunnel.
2) According to the value of the heaving deformation at the bottom of the tunnel, the deformation on the right line is larger than that on the left because the tunnel on the right line is closer to the position of the deepest soil unloading. This shows consistency between the numerical simulation results and measured data. The maximum deformation at the bottom of the right line tunnel is about 1.3 mm, and the measured data is about 1.4 mm.
3) The numerical simulation results are consistent with the measured data of the heaving deformation at the bottom of the tunnel, which reflects the heaving deformation trend at different longitudinal positions of the tunnel. However, influenced by the buried depth, structural stiffness and so on, the heaving deformation at the bottom of the tunnel is small, so the deformation difference is not obvious.



(1) Heaving deformation of the right line



(2) Heaving deformation of the left line

FIGURE 14 | Heaving deformation contrast on the tunnel between the calculation result and the in site measured datum.

3) Convergence deformation of the tunnel in the vertical direction

Figure 15 shows the vertical clearance convergence deformation of the subway tunnel in the longitudinal direction. The positive and negative values of vertical clearance convergence deformation of the tunnel are defined as: the positive value of deformation represents the stretching of the tunnel section, and the negative value represents the contraction of the tunnel section.

These figures indicate that:

1) Due to the soil unloading construction on the ground, the heaving deformation occurs on the soil and the tunnel. Although there is heaving deformation at the tip and bottom of the tunnel, the heaving deformation on the crown of the tunnel is larger than that the bottom. Therefore, the vertical section of the tunnel is stretched and its shape tends to become elliptical.
2) After the tunnel deformation, the elliptic long axis points to the position with the largest unloading thickness, indicating that the greater the unloading thickness is, the greater the surface rebound deformation is, and causing the tunnel upward arched deformation to this position.
3) The numerical simulation results are consistent with the measured datum, reflecting the distribution law of vertical clearance convergence deformation of the tunnel. The calculated deformation magnitude is also consistent with the measured data. The maximum vertical clearance convergence deformation of the tunnel on the right side is about 0.9 mm, and the measured data is about 1.05 mm.

5.6 Assessment of the Influence of the Soil Unloading to the Metro Tunnel

According to the 'Technical code for safety protection of urban rail transit structures (CJJ/t202-2013' of China, the metro tunnel deformation must be limited to 5 mm and the ellipticity ratio (calculated by the **formula (2)**) of the tunnel must be limited within 5‰.

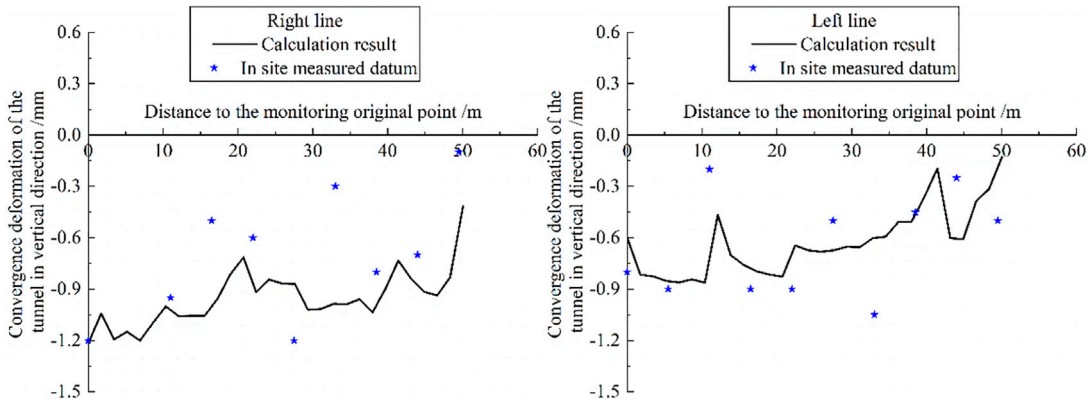


FIGURE 15 | Vertical clearance convergence deformation contrast between the calculation result and the in site measured data.

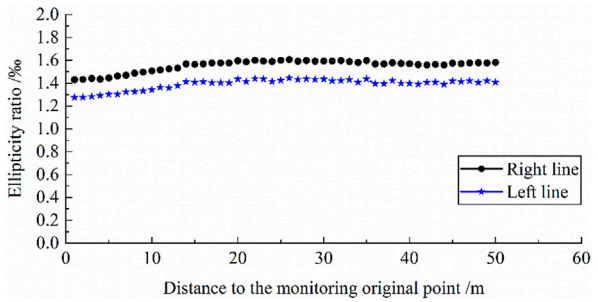


FIGURE 16 | The ellipticity ratio of the tunnel in the longitudinal direction.

$$Ellipticity Ratio = (D_{\max} - D_{\min}) / D_{design} \quad (2)$$

Where, $D_{\max}$ and $D_{\min}$ are respectively the maximum and minimum diameters of the deformed tunnel and D_{design} is the designed diameter of the tunnel.

Figure 16 shows the ellipticity ratio of the two metro tunnels of the soil unloading construction. It can be seen that the ellipticity ratio of the two metro lines is all smaller than the mandatory standard. The maximum ellipticity ratios of the two tunnels are respectively 1.6‰ and 1.42‰. From the deformation aspect, the values of the horizontal and vertical deformation of the two tunnels are all within the demand of the code. Therefore, although the soil unloading construction would have a certain influence on the metro tunnels, the tunnels are still in accordance with the relevant regulations, meaning the tunnels can be deemed safe.

6 CONCLUSION

This paper summarized the research status of tunnel deformation caused by overlaying soil excavation, the deformation characteristics of soil under rebound conditions were first studied and the rebound deformation law and calculation model were obtained. Then, the transferring relationship of the E_{sc} and E_{c0} were researched through numerical inversion. Finally, based on the summary of the defamation law under the rebound condition, a set of numerical simulation calculations and analysis methods considering different stress histories and stress levels was presented. The main conclusions are as follows:

1) The soil rebound curve under unloading conditions shows nonlinear characteristics, especially under high pressure conditions, the nonlinear characteristics are more obvious. Therefore, the variation of the used rebound modulus according to the different stress states should be considered.
2) The hysteretic characteristics of the rebound curve of soil under high pressure and low pressure are different. When the soil is unloaded and reloaded under a low compression load (less than 100 kPa), the load-pore ratio curve of the soil overlaps. There are no hysteretic characteristics. When the soil is unloaded and reloaded under a high compression load, the load-pore ratio curve shows obvious hysteretic characteristics. It also further shows that the modulus parameters of soil are different under different stress states, and should be taken into consideration when evaluating the modulus.
3) Based on our experimental study, the deformation calculation and analysis method for shallow buried tunnels considering different stress history and stress states were put forward. In the calculation process, this proposed method can monitor the stress state and unloading stress history of different soil elements in real-time, and dynamically adjust the modulus parameters of soil according to this information and the results of indoor tests. The deformation law of shallow buried tunnels characterized by small deformation can be obtained, which makes the calculation results more in line with the engineering practice and provides a reliable reference for engineering construction.
4) The engineering example verification and engineering application results show that the deformation calculation method for the shallow buried tunnel considering different stress history and stress states proposed in this paper can

better obtain the small deformation characteristics of the shallow buried tunnel under unloading conditions, which is in good agreement with the actual monitoring results and verifies the rationality of the method proposed in this paper.

DATA AVAILABILITY STATEMENT

The original contributions presented in the study are included in the article/Supplementary Material, further inquiries can be directed to the corresponding authors.

AUTHOR CONTRIBUTIONS

JL: Methodology, Calculation, Writing and Revising; SC: Data analysis; FY: Data analysis; ZD: Modelling; SL: Parameter validation; YZ: Modelling; CL: Language Reviewing and Editing.

FUNDING

This research was funded by the National Natural Science Foundation of China (No. 42172308) and the Youth Innovation Promotion Association CAS (No. 2022331).

REFERENCES

Chang, C. T., Sun, C. W., Duann, S. W., and Hwang, R. N. (2001). Response of a Taipei rapid transit system (TRTS) tunnel to adjacent excavation. *Tunn. Undergr. Space Technol.* 16 (3), 151–158. doi:10.1016/s0886-7798(01)00049-9

Chen, Y., and Li, Y. S. (2005). Calculation of tunnel heavingdue to unloading of pit excavation. *Chin. J. Undergr. space Eng.* 1 (1), 91–94. (in chinese).

Chen, Y., and Zhang, D. M. (2004). Analysis of monitoring data on tunnel heavingdue to unloading of foundation pit excavation. *Undergr. Space* 24 (5), 748–751. (in Chinese).

Devriendt, M., Doughty, L., Morrison, P., and Pillai, A. (2010). Displacement of tunnels from a basement excavation in London. *Proc. Institution Civ. Eng. - Geotechnical Eng.* 163 (3), 131–145. doi:10.1680/geng.2010.163.3.131

Hu, Z. F., Yue, Z. Q., Zhou, J., and Tham, L. G. (2003). Design and construction of a deep excavation in soft soils adjacent to the Shanghai Metro tunnels. *Can. Geotech. J.* 40 (5), 933–948. doi:10.1139/t03-041

Huang, X., Schweiger, H. F., and Huang, H. W. (2013). Influence of deep excavations on nearby existing tunnels. *Int. J. Geomech.* 13 (2), 170–180. doi:10.1061/(asce)gm.1943-5622.0000188

Jia, D., Shi, F., and Zheng, G. (2008). Elastic modulus of soil used in numerical simulation of deep foundation pits. *Chin. J. Geotechnical Eng.* 30 (s1), 154–158. (in chinese).

Jiang, N., Zhu, B., He, X., Zhou, C., Luo, X., and Wu, T. (2020). Safety assessment of buried pressurized gas pipelines subject to blasting vibrations induced by metro foundation pit excavation. *Tunn. Undergr. Space Technol.* 102, 103448. doi:10.1016/j.tust.2020.103448

Li, J. M., and Teng, Y. J. (2018). Regularity and calculation method of rebound deformation and recompression deformation of soil based on bearing test. *Roc Soil Mech.* 39 (s1), 113–121. (in chinese).

Liang, R. Z., Xia, T. D., Huang, M. S., and Lin, C. (2017). Simplified analytical method for evaluating the effects of adjacent excavation on shield tunnel considering the shearing effect. *Comput. Geotechnics* 81, 167–187. doi:10.1016/j.compgeo.2016.08.017

Liu, H. L., Li, P., and Liu, J. (2010). Numerical investigation of underlying tunnel heave during a new tunnel construction. *Tunn. Undergr. Space Technol.* 26 (2), 276–283. doi:10.1016/j.tust.2010.10.002

Qiu, J. T., Jiang, J., and Zhou, X. J. (2021). *Analytical solution for evaluating deformation response of existing metro tunnel due to excavation of adjacent foundation pit*. English edition. Journal of Central South University, 25.

Sharma, J. S., Hefny, A. M., Zhao, J., and Chan, C. (2001). Effect of large excavation on deformation of adjacent MRT tunnels. *Tunn. Undergr. Space Technol.* 16 (2), 93–98. doi:10.1016/s0886-7798(01)00033-5

Shi, J., and Ng, C. W. W. (2015). Three-dimensional numerical parametric study of the influence of basement excavation on existing tunnel. *Comput. Geotechnics* 63, 146–158. doi:10.1016/j.compgeo.2014.09.002

Urban and rural areas of the People's Republic of China (2011). *Code for risk management of urban rail transit underground engineering construction*. GB50652-2011)(in chinese).

Urban and rural areas of the People's Republic of China (2013). *Technical code for protetion structures of urban rail transit*. CJJ/T202-2013)(in chinese).

Wang, R. L., and Yu, B. (2004). Protecting of the metro tunnel during construction of Dongfang Rd underpass. *Undergr. Eng. Tunnels* 4, 33–39. (in Chinese).

Wang, S. G., Li, Q. R., and Li, J. M. (2020). Discussion on some issures of resilient deformation calculation. *China Civ. Eng. J.* 53 (8), 108–115. (in chinese).

Wang, W. D., Shen, J., and Weng, Q. P. (2006). Analysis and countermeasures of influence of excavation on adjacent tunnels. *Chin. J. Geotechnical Eng.* 28 (S1), 1340–1345.

Yu, L. P. (2014). Analysis of soil's elastic modulus values based on FLAC3D simulation. *J. Water Resour. Archit. Eng.* 12 (2), 162–166. (in chinese).

Zhang, Z., Zhang, M., and Zhao, Q. (2015). A simplified analysis for deformation behavior of buried pipelines considering disturbance effects of underground excavation in soft clays. *Arab. J. Geosci.* 8 (10), 7771–7785. doi:10.1007/s12517-014-1773-4

Zhang, J. F., Chen, J. J., Wang, J. H., and Zhu, Y. F. (2013). Prediction of tunnel displacement induced by adjacent excavation in soft soil. *Tunn. Undergr. Space Technol.* 36, 24–33. doi:10.1016/j.tust.2013.01.011

Zhang, J., Xie, R., and Zhang, H. (2018). Mechanical response analysis of the buried pipeline due to adjacent foundation pit excavation. *Tunn. Undergr. Space Technol.* 78, 135–145. doi:10.1016/j.tust.2018.04.026

Zhang, X. M., Yang, J. S., Zhang, Y. X., and Gao, Y. (2018). Cause investigation of damages in existing building adjacent to foundation pit in construction. *Eng. Fail. Anal.* 83, 117–124. doi:10.1016/j.engfailanal.2017.09.016

Zhang, Z., Huang, M., and Wang, W. (2013). Evaluation of deformation response for adjacent tunnels due to soil unloading in excavation engineering. *Tunn. Undergr. Space Technol.* 38 (3), 244–253. doi:10.1016/j.tust.2013.07.002

Conflict of Interest: Author YZ is employed by Sichuan Water Develeopment Group CO.,LTD.

The remaining authors declare that the research was conducted in the absence of any commercial or financial relationships that could be construed as a potential conflict of interest.

Publisher's Note: All claims expressed in this article are solely those of the authors and do not necessarily represent those of their affiliated organizations, or those of the publisher, the editors and the reviewers. Any product that may be evaluated in this article, or claim that may be made by its manufacturer, is not guaranteed or endorsed by the publisher.

Copyright © 2022 Li, Li, Zhang, Chen, Yu, Dai and Li. This is an open-access article distributed under the terms of the Creative Commons Attribution License (CC BY). The use, distribution or reproduction in other forums is permitted, provided the original author(s) and the copyright owner(s) are credited and that the original publication in this journal is cited, in accordance with accepted academic practice. No use, distribution or reproduction is permitted which does not comply with these terms.

frontiers | Frontiers in Earth Science

TYPE Original Research
PUBLISHED 04 August 2022
DOI 10.3389/feart.2022.967328

Check for updates

OPEN ACCESS

EDITED BY
Guang-Liang Feng,
Institute of Rock and Soil Mechanics (CAS), China

REVIEWED BY
Tao Zhou,
Shenzhen University, China
Lishuai Jiang,
Shandong University of Science and Technology, China

*CORRESPONDENCE
Shuangli Zhu,
195512078@csu.edu.cn
Chao Chen,
csuchenchao@csu.edu.cn,
chao_chen_best@hotmail.com

SPECIALTY SECTION
This article was submitted to Geohazards and Georisks, a section of the journal Frontiers in Earth Science

RECEIVED 12 June 2022
ACCEPTED 05 July 2022
PUBLISHED 04 August 2022

CITATION
Wei C, Zhu S, Chen C and Zhou J (2022), Developing an evaluation model based on unascertained measurement for evaluation of tunnel squeezing. *Front. Earth Sci.* 10:967328. doi: 10.3389/feart.2022.967328

COPYRIGHT
© 2022 Wei, Zhu, Chen and Zhou. This is an open-access article distributed under the terms of the Creative Commons Attribution License (CC BY). The use, distribution or reproduction in other forums is permitted, provided the original author(s) and the copyright owner(s) are credited and that the original publication in this journal is cited, in accordance with accepted academic practice. No use, distribution or reproduction is permitted which does not comply with these terms.

Developing an evaluation model based on unascertained measurement for evaluation of tunnel squeezing

Cong Wei[1], Shuangli Zhu[1]*, Chao Chen[1,2]* and Jian Zhou[1]

[1]School of Resources and Safety Engineering, Central South University, Changsha, China, [2]Department of Mechanical and Industrial Engineering, Norwegian University of Science and Technology, Trondheim, Norway

Tunnel squeezing brought great difficulties to the construction and severely threatened the safety of on-site operators. The researches regarding large deformation evaluation have been widely developed, but actual conditions of tunnels are considerably complex, producing a large variety of uncertainty information existing in the evaluation process. Therefore, we constructed an unascertained measurement model incorporating four membership functions for evaluation of tunnel squeezing based on the collected datasets. Simultaneously, information entropy was introduced to objectively calculate the index importance for each index. For the first group data (GPI), the accuracy associated with four membership functions are 100%, 83.33%, 50%, and 83.33%, respectively, while the accuracy of GPII are 70%、77.5%、67.5%, and 70%, respectively. Linear function and parabolic function show better performance on uncertainty information interpretation according to the classification results. The results revealed that the uncertainty model constructed in this study can enrich the available uncertainty evaluation system.

KEYWORDS

Squeezing, Unascertained measurement, Information entropy, Classification, Risk evaluation

Introduction

Various technologies related to tunnel engineering have been greatly developed, such as ventilation technology, support technology, excavation technology, operation management, rock characteristics (Wang et al., 2021b; Du et al., 2022; Wang et al., 2022; Yu et al., 2022), prediction and prevention of geological disasters (Feng et al., 2015; Wang et al., 2021a; Feng et al., 2022; Zhou et al., 2021a; Zhou et al., 2021b), among which geological disasters are the main risk factors in engineering. In recent years, with the excavation of various tunnels in underground at great depth, the hazards regarding large deformation of surrounding rock frequently occurred. Currently, the scientific community gradually focused on the large deformation of excavated tunnels (Zhang et al., 2003; Singh et al., 2007; Chen, 2008; Lai et al., 2018; Sharma et al., 2020). Large deformation of surrounding rock can be divided into extrusion and expansion (Wood,

1972; Barton et al., 1974; Jethwa et al., 1984; Barla, 1995; Barla, 2001; He et al., 2002). The former occurs in soft rocks with high geostress, while the latter mainly occurs in rock mass with strong expansion properties. The stress redistribution caused by excavation exceeds the ultimate shear stress, resulting in a large-scale plastic failure zone in the surrounding rock of the tunnel (Gioda and Cividini, 1996; Panet, 1996; Barla, 2001; Singh et al., 2007; Dwivedi et al., 2013). Most of the large deformation of surrounding rock occurs in deep and long soft rock tunnels, e.g., in China, Zhegushan Highway Tunnel, Guanjiao Tunnel, Jiazhuqing Tunnel, Dazhailing Tunnel, the China-Laos railway tunnel, etc. The above-mentioned tunnels all suffered from large deformation to some extent, which brought great difficulties to the construction. In addition, the weak surrounding rock is more prone to squeeze and occur large deformation under the action of high *in-situ* stress. At this time, the surrounding rock ruptures and squeezes out of the tunnel boundary and further damages the supporting structure, which will seriously lead to tunnel collapse even cause damage to construction workers (Liu, 2004; Chen, 2008; Liu et al., 2008; Yu, 2020; Ren et al., 2021). The large deformation of surrounding rock is gradually accelerated with the development of time (Bhasin and Grimstad, 1996; Barla, 2001; Singh et al., 2007; Azizi et al., 2019). Therefore, the evaluation of tunnel squeezing is of great significance for improving the construction efficiency, reducing the cost, and ensuring the safety of the construction personnel (Aydan et al., 1993; Aydan et al., 1996; Hoek, 2001; Ghiasi et al., 2012; Panthi, 2013; Azizi et al., 2019).

The tunnel squeezing is a major engineering problem that needs to be solved urgently in this field. Many scholars tried to use different methods to evaluate the severity of large extrusion deformation (Dube et al., 1986; Jiang et al., 2004; Fatemi Aghda et al., 2016; Azizi et al., 2019; Liao et al., 2020). For example, Singh et al. (2007) evaluated the tunnel squeezing based on burial depth (H) and rock quality index (Q). Then, Goel et al. (1995) introduced the rock mass number N (the Q value of SRF = 1) into the fitting curve equation. Additionally, Liu et al. (2019) proposed an improved cloud model for the prediction of large deformation of surrounding rock in Mila Mountain Tunnel in Tibet based on the uncertainty and randomness of tunnel squeezing prediction. Although various methods associated with tunnel squeezing evaluation has been widely explored, the mechanism of this geological hazard is considerably complex, leading to a large variety of uncertainty exists in the evaluation of tunnel squeezing. (ISRM, 1995; Steiner, 1996; Malan and Basson, 1998; Palmstrom and Broch, 2006; Williams, 2010; Dwivedi et al., 2014; Farhadian and Nikvar-Hassani, 2020; Zhang et al., 2020).

In view of the wide application and robust uncertainty information interpretation of unascertained measurement theory in this field, e,g., stability evaluation, scheme optimization, risk assessment, and performance evaluation. This study aims to develop a hybrid model based on information entropy and unascertained measurement incorporating four membership functions to evaluate the tunnel squeezing, which is able to enrich the available risk evaluation methods for underground excavation projects.

Method description

There are n samples in the evaluation object space $Y = \{y_1, y_2, ..., y_i, ..., y_n\}$, $(i = 1, 2, 3, ..., n)$, and each sample contains m predictors. $X = \{x_1, x_2, ..., x_j, ..., x_m\}$, $(j = 1, 2, 3, ..., m)$ was used to represent the predictor space. There, $y_i = \{x_{i1}, x_{i2}, x_{i3}, ..., x_{ij}, ..., x_{im}\}$, $(y_i \in Y)$, where, $x_{ij}\,(i = 1, 2, 3, ..., n;\ j = 1, 2, 3, ..., m)$ represents the j^{th} predictor variable of the i^{th} sample. Assuming that there are K evaluation levels for the degrees of deformation, therefore, the grade set can be shown as $\Omega = \{L_1, L_2, L_3, ..., L_k, ..., L_K\}$, $(k = 1, 2, 3, ..., K)$. It is worth noting that the evaluation space is an ordered segmentation category (Jing and Hua, 2008; Tu et al., 2008; Wang, 2019), that is, $L_{k+1} > L_K$.

Single-index measurement matrix

According to the above $y_i \in Y$, $(i = 1, 2, 3, ..., n)$ is the i^{th} research sample in the evaluation system, and the predictor $x_j \in X$, $(j = 1, 2, 3, ..., m)$ reflects the characteristic of the research object. In this paper, y_{ij}, $(i = 1, 2, 3, ..., n;\ j = 1, 2, 3, ..., m)$ was defined as the measure-valued of y_i under the index x_j. It is assumed that there are K evaluation levels for each measure-valued (y_{ij}), and the grade set is $\Omega = \{L_1, L_2, L_3, ..., L_k, ..., L_K\}$, $(k = 1, 2, 3, ..., K)$. Afterwards, we defined a possibility measure $a_{ij}^k = a(y_{ij} \in L_k)$, it is known as the unascertained measure. It indicates the degree to which the measured value y_{ij} belongs to the k^{th} evaluation level and satisfies the following three requirements at the same time: non-negativity, normalization equation and additivity, as shown in Eqs 1–3 respectively.

$$0 \le a\left(y_{ij} \in L_k\right) \le 1 \tag{1}$$

$$a\left(y_{ij} \in \Omega\right) = 1 \tag{2}$$

$$a\left[y_{ij} \in \bigcup_{k=1}^{K} L_k\right] = \sum_{k=1}^{K} y_{ij} \in L_k\,(k = 1, 2, \cdots, K) \tag{3}$$

$$\left(a_{ij}^k\right)_{m\times K} = \begin{bmatrix} a_{i1}^1 & a_{i1}^2 & \cdots & a_{i1}^K \\ a_{i2}^1 & a_{i2}^2 & \cdots & a_{i2}^K \\ \vdots & \vdots & \ddots & \vdots \\ a_{im}^1 & a_{im}^2 & \cdots & a_{im}^K \end{bmatrix} \tag{4}$$

The above Eq. 4 $(a_{ij}^k)_{m\times K}$, $(i = 1, 2, ..., n;\ j = 1, 2, ..., m;\ k = 1, 2, ..., K)$ is the single-index measurement matrix of i^{th} sample.

The single index measurement judgment matrix is calculated by the membership function. In this paper, we will use four types

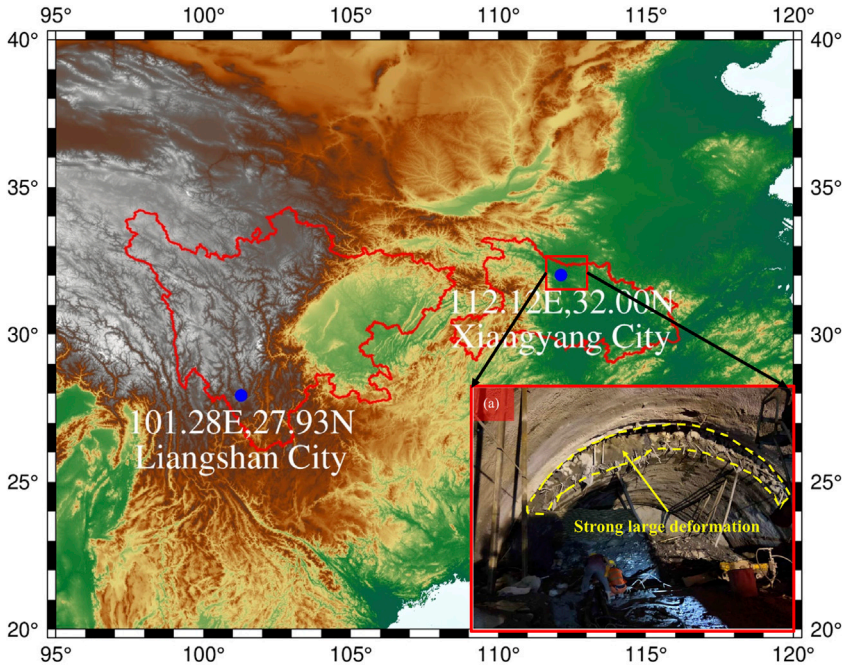


FIGURE 1
Spatial location of engineering cases used in this study.

membership functions (Zhou et al., 2020b; Zhou et al., 2021a): linear, parabolic, exponential and sine functions, as shown in Eqs 5–8 respectively.

$$\begin{cases} a_r(x) = \begin{cases} \dfrac{-x}{b_{r+1}-b_r} + \dfrac{b_{r+1}}{b_{r+1}-b_r} & (b_r < x \le b_{r+1}) \\ 0 & (x > b_{r+1}) \end{cases} \\ a_{r+1}(x) = \begin{cases} 0 & (x \le b_r) \\ \dfrac{x}{b_{r+1}-b_r} - \dfrac{b_r}{b_{r+1}-b_r} & (b_r < x \le b_{r+1}) \end{cases} \end{cases} \tag{5}$$

$$\begin{cases} a_r(x) = \begin{cases} 1 - \left(\dfrac{x-b_r}{b_{r+1}-b_r}\right)^2 & (b_r < x \le b_{r+1}) \\ 0 & (x > b_{r+1}) \end{cases} \\ a_{r+1}(x) = \begin{cases} 0 & (x \le b_r) \\ \left(\dfrac{x-b_r}{b_{r+1}-b_r}\right)^2 & (b_r < x \le b_{r+1}) \end{cases} \end{cases} \tag{6}$$

$$\begin{cases} a_r(x) = \begin{cases} 1 - \dfrac{1-e^{x-b_r}}{1-e^{b_{r+1}-b_r}} & \\ 0 & (x > b_{r+1}) \end{cases} \\ a_{r+1}(x) = \begin{cases} 0 & (x \le b_r) \\ \dfrac{1-e^{x-b_r}}{1-e^{b_{r+1}-b_r}} & (b_r < x \le b_{r+1}) \end{cases} \end{cases} \tag{7}$$

$$\begin{cases} a_r(x) = \begin{cases} \dfrac{1}{2} - \dfrac{1}{2}\sin\dfrac{\pi}{b_{r+1}-b_r}\left(x - \dfrac{b_{r+1}-b_r}{2}\right) & (b_r < x \le b_{r+1}) \\ 0 & (x > b_{r+1}) \end{cases} \\ a_{r+1}(x) = \begin{cases} 0 & (x \le b_r) \\ \dfrac{1}{2} + \dfrac{1}{2}\sin\dfrac{\pi}{b_{r+1}-b_r}\left(x - \dfrac{b_{r+1}-b_r}{2}\right) & (b_r < x \le b_{r+1}) \end{cases} \end{cases} \tag{8}$$

Where, $a_r(x)$ and $a_{r+1}(x)$ are the membership corresponding to grade L_k and L_{k+1}, respectively. b_r and b_{r+1} are the left and right endpoints, respectively.

Information entropy theory

Based on the above single-index measurement matrix (Eq. 4), a more objective method is applied to determine the index weight in this paper, i.e., information entropy (Ruan et al., 2021). W_{ij} represents the weight of jth index under ith sample, which can be calculated through Eq. 9.

$$W_{ij} = \frac{\xi_{ij}}{\sum_{j=1}^{m} \xi_{ij}}, \ (i = 1, 2, \ldots, n; \ j = 1, 2, \ldots, m) \tag{9}$$

Where, $0 \le W_{ij} \le 1, and \sum_{j=1}^{m} W_{ij} = 1.$ ξ_{ij} $(0 \le \xi_{ij} \le 1)$ represents the value of entropy, which can be

TABLE 1 Engineering cases used for tunnel squeezing evaluation.

Indicators cases	1	2	3	4	5	6	
C1	P1(m)	15	14.9	13.12	13.42	15.86	14.12
	P2(m)	9.88	9.78	8.66	8.94	9.24	9.08
	P3	0.5	0.25	0.5	0.75	0.5	0.5
	P4(d)	12	24	11	10	106	100
	P5	0.25	0.5	0.25	0.25	0.75	0.75
	P6(m)	4	2	3	3.2	0.6	0.6
C2	P7(m)	176	131	62	159	63	65.5
	P8	0.25	0.5	0.25	0.25	1	0.75
	P9	4	3	2	2	7	5
	P10	0.5	1	0.5	0.5	0.75	0.75
C3	P11 (MPa)	20	4.5	10	15	2	5
	P12 (MPa)	20,000	10,000	15,000	17,000	8,000	10,000
	P13 (%)	0.44	2.62	1.09	0.77	2.91	2.66
	P14	1.33	0.38	0.71	1	0.08	0.22
Actual grade		1	2	1	1	4	3

TABLE 2 The classification standards of tunnel squeezing.

Indicator	Risk predictive grades for large deformation				
		L_1	L_2	L_3	L_4
C1	P1	<5	10 (0.5)	15 (0.75)	>20 (1)
	P2	<4 (0.25)	8 (0.5)	12 (0.75)	>16 (1)
	P3	Reasonable (0.25)	Basically reasonable (0.5)	Unreasonable (0.75)	Extremely unreasonable (1)
	P4	<15 (0.17)	30 (0.33)	60 (0.67)	>90 (1)
	P5	Reasonable (0.25)	Basically reasonable (0.5	Unreasonable (0.75)	Extremely unreasonable (1)
	P6	>4 (1)	3 (0.75)	2 (0.5)	<1 (0.25)
C2	P7	<50 (0.25)	100 (0.5)	150 (0.75)	>200 (1)
	P8	Dry (0.25)	Wet (0.5)	Dripping (0.75)	Gushing (1)
	P9	<2 (0.4)	3 (0.6)	4 (0.8)	>5 (1)
	P10	Weak weathering (0.25)	Medium weathering (0.5)	Strong weathering (0.75)	Complete weathering (1)
C3	P11	>40 (1)	22.5 (0.563)	10 (0.25)	>2.5 (0.063)
	P12	>2000 (1)	1750 (0.875)	1,250 (0.625)	<1,000 (0.5)
	P13	<2 (0.33)	3 (0.5)	5 (0.83)	>6 (1)
	P14	>0.75 (1)	0.375 (0.5)	0.2 (0.27)	<0.15 (0.2)

calculated via the single index measurement vectors a_{ij}^k, referring to Eq. 10.

$$\xi_{ij} = 1 + \frac{1}{\ln K}\left(\sum_{k=1}^{K} a_{ij}^k \ln a_{ij}^k\right) \tag{10}$$

Then, the index weight vector of the i^{th} sample can be expressed as: $W_{ij} = (W_{i1}, W_{i2}, \ldots, W_{ij}, \ldots, W_{im})$.

Comprehensive measurement matrix

The multi-index comprehensive measurement matrix is calculated as follows (Jia et al., 2019; Ma et al., 2021).

$$A_i^k = \sum_{j=1}^{m} W_{ij} a_{ij}^k, \ (i = 1, 2, \ldots, n; k = 1, 2, \ldots, K) \tag{11}$$

Where, $A_i^k = A(y_i \in L_k)$ is the multi-index comprehensive measurement vector. It represents the degree to which the

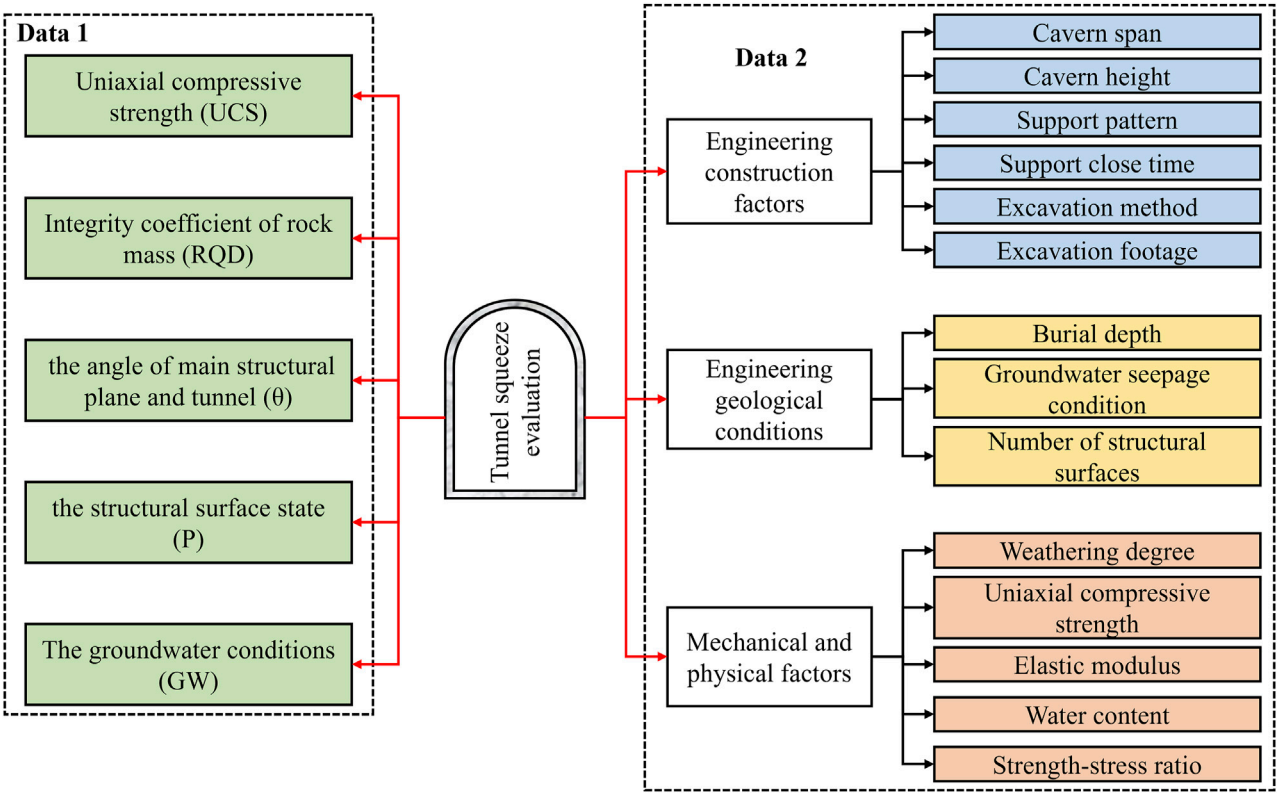


FIGURE 2
Index system of squeeze evaluation.

evaluation sample y_i belongs to the grade k. In addition, $0 \le A_i^k \le 1, and \sum_{k=1}^{K} A_i^k = \sum_{k=1}^{K}\sum_{j=1}^{m} W_{ij} a_{ij}^k = \sum_{j=1}^{m} (\sum_{k=1}^{K} a_{ij}^k) \cdot W_{ij} = 1.$

$$\left(A_i^k\right)_{n\times K} = \begin{bmatrix} A_1^1 & A_1^2 & \cdots & A_1^K \\ A_2^1 & A_2^2 & \cdots & A_2^K \\ \vdots & \vdots & \ddots & \vdots \\ A_n^1 & A_n^2 & \cdots & A_n^K \end{bmatrix} \tag{12}$$

Where, $(A_i^k)_{n\times K}, (i = 1, 2, \ldots, n; k = 1, 2, \ldots, K)$ is the multi-index comprehensive measurement matrix. Then the multi-index comprehensive measurement vector of the i^{th} sample can be expressed as: $A_i = (A_i^1, A_i^2, \ldots, A_i^k, \ldots, A_i^K)$.

Credible identification principle

In order to determine the grade of individual sample, the credible identification principle was utilized. The grade of samples can be calculated through Eq. 13 based on the above-mentioned comprehensive multi-index measurement vectors (Shi et al., 2010).

$$L_{ik} = \min\left(\sum_{k=1}^{K} A_i^k \ge \lambda, k = 1, 2, \ldots, K\right) \tag{13}$$

Where, L_{ik} is the grade of sample i^{th}, and $L_{ik} \in \Omega$, $(\Omega = \{L_1, L_2, L_3, \ldots, L_k, \ldots, L_K\}$. $\lambda (\lambda \ge 0.5)$, normally, $\lambda = 0.6$ or $\lambda = 0.7$ (Zhou et al., 2020a; Zhou et al., 2020b; Zhou et al., 2021b; Chen et al., 2021).

Sample score

Although the risk level of samples is judged through credible identification principle, it is difficult to further distinguish the severity of the tunnel deformation, that is, the large deformation cannot be quantitatively analyzed. There, each sample can be scored by the following equation.

$$SC_i = \sum_{k=1}^{K} Num_k A_{ik}, (1 \le k \le K; 1 \le i \le n) \tag{14}$$

where, SC_i is the score of sample i^{th}, Num_k is the value assigned to grades $\{GR_1, GR_2, GR_3, GR_4\}$.

TABLE 3 Engineering cases of tunnel squeezing.

Samples	Rc	RQD/Mpa	GW/10 L/(min·m)	θ	P	Deformation grade
1	45	0.46	18	26	0.58	3
2	51	0.53	19	38	0.51	3
3	26	0.42	22	42	0.61	3
4	51	0.51	19	66	0.31	4
5	55	0.52	17	39	0.62	3
6	18	0.38	18	28	0.31	5
7	15	0.37	55	62	0.28	5
8	26	0.25	57	55	0.45	4
9	31	0.45	62	58	0.26	4
10	29	0.47	79	63	0.33	4
11	12	0.31	113	56	0.28	5
12	59	0.43	99	67	0.31	4
13	56	0.41	75	71	0.45	4
14	37	0.46	62	69	0.32	4
15	29	0.44	78	22	0.33	4
16	35	0.42	99	26	0.41	4
17	42	0.41	76	58	0.55	4
18	36	0.43	55	60	0.61	5
19	49	0.44	67	62	0.31	4
20	31	0.42	74	61	0.58	4
21	22	0.35	72	66	0.21	4
22	26	0.55	81	63	0.36	4
23	13	0.58	94	22	0.55	5
24	29	0.47	39	57	0.62	5
25	21	0.41	63	27	0.52	4
26	37	0.44	74	29	0.41	4
27	32	0.49	91	59	0.41	4
28	56	0.28	92	58	0.55	4
29	11	0.22	96	61	0.43	4
30	49	0.51	110	63	0.33	3
31	55	0.45	16	16	0.5	3
32	58	0.5	26	22	0.5	3
33	29	0.22	55	26	0.6	4
34	49	0.75	19	31	0.3	3
35	31	0.39	37	15	0.6	4
36	53	0.45	12	19	0.3	3
37	46	0.59	10	19	0.2	3
38	56	0.61	66	21	0.4	3
39	26	0.35	23	29	0.2	4
40	31	0.28	71	21	0.3	4

Squeezing evaluation using unascertained measurement

The influencing factors of tunnel squeezing are divided into objective and subjective factors, the former includes geological conditions, such as rock mass conditions, engineering geological conditions, and geo-hydrologic conditions; the latter refers to construction technology, survey and design. Studies shown that poor geological conditions are the main factors for tunnel squeezing, such as the strength of surrounding rock, *in-situ* stress, and groundwater. This study employed two sets of data collected from the literature to evaluate tunnel squeezing. For the first group of data, the construction of index system

TABLE 4 Classification standard for tunnel squeezing.

Grade	Rc/Mpa	RQD/%	GW/10 L/(min·m)	θ	P
L_1	80–120	80–100	0–5	0–18	0–0.2
L_2	60–80	60–80	5–10	18–36	0.2–0.4
L_3	40–60	40–60	10–25	36–54	0.4–0.6
L_4	20–40	20–40	25–125	54–72	0.6–0.8
L_5	0–20	0–20	125–250	72–90	0.8–1

considers geological factors and construction technology, while only geological factors are taken into consideration for the second one. Simultaneously, we use GP_I to represent the first set of data, and the second group data is described by GP_{II}. The spatial location of datasets used in this study was shown in Figure 1.

The first group data is composed of six research samples, simultaneously, the evaluation results are categorized into four grades $\Omega(GP_I) = \{L_1, L_2, L_3, L_4\}$, namely, no large deformation, slight large deformation, medium large deformation and strong large deformation. The initial data (Bai et al., 2021) of these six samples are listed in Tables 1, 2 is the classification standard corresponding to individual index. The first set of data includes 14 evaluation indicators, which can be generally divided into three categories: tunnel design and engineering construction factor (C1), the engineering geological condition (C2), the mechanical and physical properties of rock (C3). There are six second-level indicators in C1, four in C2 and four in C3, as shown in Figure 2.

The second group was obtained from the Telmo Tunnel in the Chengdu-Kunming Railway double track (Wang, 2019), which is a deep-buried tunnel with poor surrounding rock conditions. Combine the current railway tunnel deformation classification standard and previous tunnel deformation research, five factors, i.e., the rock uniaxial compressive strength (Rc), the integrity coefficient of rock mass (RQD), the groundwater condition (GW), the angle between the main structural plane and the axis of the tunnel (θ), and the structural surface state (P) are considered as the evaluation indexes, as shown in Figure 2. The evaluation set $\Omega(GP_{II}) = \{L_1, L_2, L_3, L_4, L_5\}$ is denoted as no large deformation, slight large deformation, medium large deformation, strong large deformation and severe large deformation. The related samples and classification standards (Wang, 2019) are presented in Tables 3, 4, respectively.

Single index measurement of samples

Firstly, based on the four different membership functions shown in Eqs 5–8, the index measurement matrix calculated by different membership functions are obtained. In Figures 3A,B, different membership functions, corresponding to profit and cost index, respectively, are displayed, which can easily calculate the index membership

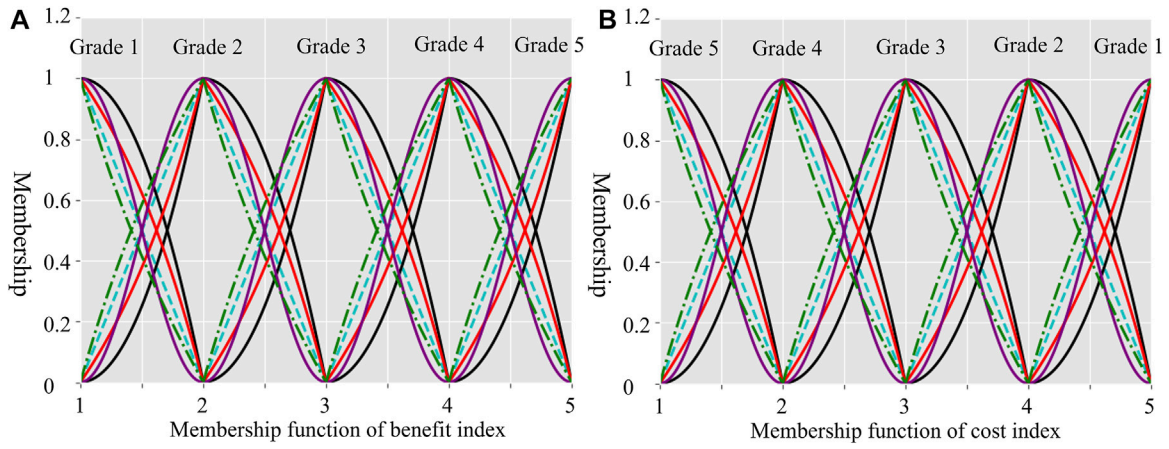


FIGURE 3
Membership function for different indexes. **(A)** Membership function of benefit index, and **(B)** Membership function of cost index.

incorporating Eqs 5–8. The single-index measurement matrix of the first and second group data can be represented by GP_I: $(a_{ij}^k)_{m\times K}$, $(i = 1, 2, \ldots, n, n = 6; j = 1, 2, \ldots, m, m = 14; k = 1, 2, \ldots, K, K = 4)$ and GP_{II}: $(a_{ij}^k)_{m\times K}$, $(i = 1, 2, \ldots, n, n = 40; j = 1, 2, \ldots, m, m = 5; k = 1, 2, \ldots, K, K = 5)$ respectively.

Finally, taking sample 1 (GP_I: y_1) of the first set of data as an example, the single index measurement matrix of sample1 is listed in Eqs 14–17.

$$GP_I: \left(a_{1j}^K\right)_{14\times 4}^{linear} = \begin{bmatrix} 0 & 0 & 1 & 0 \\ 0 & 0.53 & 0.47 & 0 \\ 0 & 1 & 0 & 0 \\ 1 & 0 & 0 & 0 \\ 1 & 0 & 0 & 0 \\ 1 & 0 & 0 & 0 \\ 0 & 0 & 0.48 & 0.52 \\ 1 & 0 & 0 & 0 \\ 0 & 0 & 1 & 0 \\ 0 & 1 & 0 & 0 \\ 0 & 0.8 & 0.2 & 0 \\ 1 & 0 & 0 & 0 \\ 1 & 0 & 0 & 0 \\ 1 & 0 & 0 & 0 \end{bmatrix} \tag{14a}$$

$$GP_I: \left(a_{1j}^k\right)_{14\times 4}^{parabolic} = \begin{bmatrix} 0 & 0 & 1 & 0 \\ 0 & 0.779 & 0.221 & 0 \\ 0 & 1 & 0 & 0 \\ 1 & 0 & 0 & 0 \\ 1 & 0 & 0 & 0 \\ 1 & 0 & 0 & 0 \\ 0 & 0 & 0.730 & 0.270 \\ 1 & 0 & 0 & 0 \\ 0 & 0 & 1 & 0 \\ 0 & 1 & 0 & 0 \\ 0 & 0.96 & 0.04 & 0 \\ 1 & 0 & 0 & 0 \\ 1 & 0 & 0 & 0 \\ 1 & 0 & 0 & 0 \end{bmatrix} \tag{15}$$

$$GP_I: \left(a_{1j}^k\right)_{14\times 4}^{exponential} = \begin{bmatrix} 0 & 0 & 1 & 0 \\ 0 & 0.896 & 0.164 & 0 \\ 0 & 1 & 0 & 0 \\ 1 & 0 & 0 & 0 \\ 1 & 0 & 0 & 0 \\ 1 & 0 & 0 & 0 \\ 0 & 0 & 1 & 0 \\ 1 & 0 & 0 & 0 \\ 0 & 0 & 1 & 0 \\ 0 & 1 & 0 & 0 \\ 0 & 0.082 & 0.918 & 0 \\ 1 & 0 & 0 & 0 \\ 1 & 0 & 0 & 0 \\ 1 & 0 & 0 & 0 \end{bmatrix} \tag{16}$$

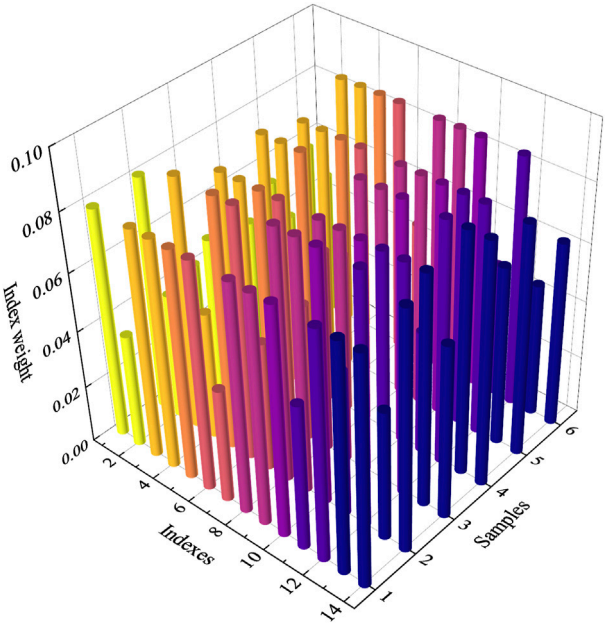


FIGURE 4
Index weights calculated through linear membership function.

$$GP_I\left(a_{1j}^k\right)_{14\times 4}^{sine} = \begin{bmatrix} 0 & 0 & 1 & 0 \\ 0 & 0.547 & 0.453 & 0 \\ 0 & 1 & 0 & 0 \\ 1 & 0 & 0 & 0 \\ 1 & 0 & 0 & 0 \\ 1 & 0 & 0 & 0 \\ 0 & 0 & 0.469 & 0.531 \\ 1 & 0 & 0 & 0 \\ 0 & 0 & 1 & 0 \\ 0 & 1 & 0 & 0 \\ 0 & 0.905 & 0.095 & 0 \\ 1 & 0 & 0 & 0 \\ 1 & 0 & 0 & 0 \\ 1 & 0 & 0 & 0 \end{bmatrix} \tag{17}$$

Index weight of squeezing evaluation

In this study, information entropy is introduced to calculate the index weight coefficients of each sample referring to Eqs 9, 10. There, only the weights calculated by linear function are visualized, as shown in Figure 4.

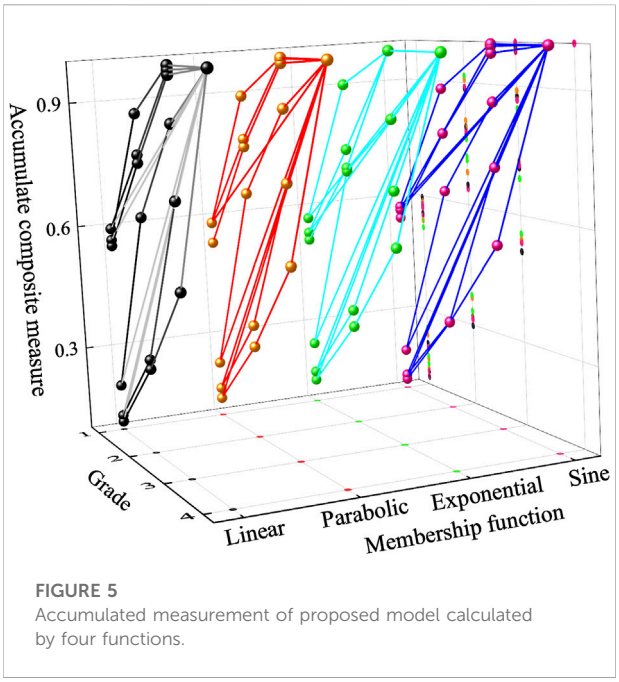


FIGURE 5
Accumulated measurement of proposed model calculated by four functions.

Determination of squeezing grade

For the first sample of first group, the multi-index comprehensive measurement vectors calculated through the linear function are listed GP_I: $A_1^k = (A_1^1, A_1^2, \ldots, A_1^k, \ldots, A_1^K) = (A_1^1, A_1^2, \ldots, A_1^4) = (0.5538, 0.2197, 0.2060, 0.0206)$. Similarly, the multi-index comprehensive evaluation vectors of sample one calculated by the remaining three measurement functions (i.e., parabolic, exponential and sine function) are shown in Table 5. In this paper, the classification standard of the first group is set as 0.55, that is $\lambda_I = 0.55$, and $\lambda_{II} = 0.6$ for second one. Therefore, according to the comprehensive measurement vector in Table 5, the deformation grade of sample one can be identified through Eq. 13. For instance, incorporating the calculation results of the linear function into Eq. 13: $A_1^1 + A_1^2 = 0.5538 > 0.55$, it can be clear that the risk level of sample one is L_1. The grade of sample one is calculated as L_2 while using parabolic function, exponential function and sine function, as shown in Table 5. According to the above criteria, the remaining samples are evaluated, and the results are listed in Figure 5; Table 6. Similarly, the squeezing level of dataset two also can be calculated as shown in Figure 6. Both sets of data show that the evaluation performance of exponential function is not ideal, and both are lower than the other three membership functions.

Sample score for tunnel squeezing

For most comprehensive evaluation models, risk level judgment of samples can be high-efficiently calculated, however, few models are able to quantify the samples simultaneously. Sample score can easily distinguish the risk

TABLE 5 Comprehensive unascertained measure based on linear function.

Sample	Comprehensive unascertained measure				Grade	
	L_1	L_2	L_3	L_4	Actual	Predictive
1	0.5538	0.2197	0.2060	0.0206	1	1 (Linear)
	0.5353	0.2543	0.1984	0.0120	1	2 (parabolic)
	0.5164	0.2026	0.2810	2.785×10^{-12}	1	2 (exponential)
	0.5478	0.2328	0.1985	0.0209	1	2 (sine)

TABLE 6 Evaluation results of unascertained measurement (GP_I).

Samples	Actual grade	Unascertained measure theory ($\lambda_I = 0.55$)			
		Linear	Parabolic	Exponential	Sine
1	1	1	2	2	2
2	2	2	2	2	2
3	1	1	1	1	1
4	1	1	1	2	1
5	4	4	4	3	4
6	3	3	3	3	3
Accuracy		100%	83.33%	50%	83.33%

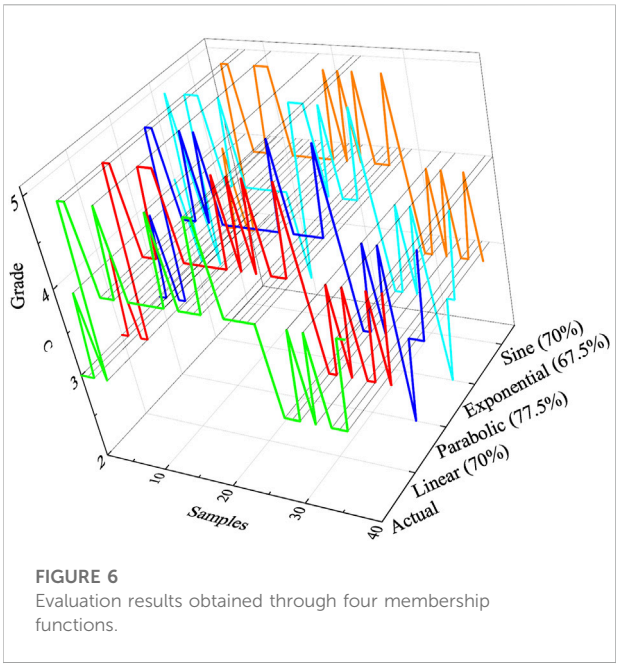


FIGURE 6
Evaluation results obtained through four membership functions.

state of samples at the same grade, which is beneficial to take more accurate measures to prevent geological hazards for on-site engineering issues. There, the scores of samples existing in

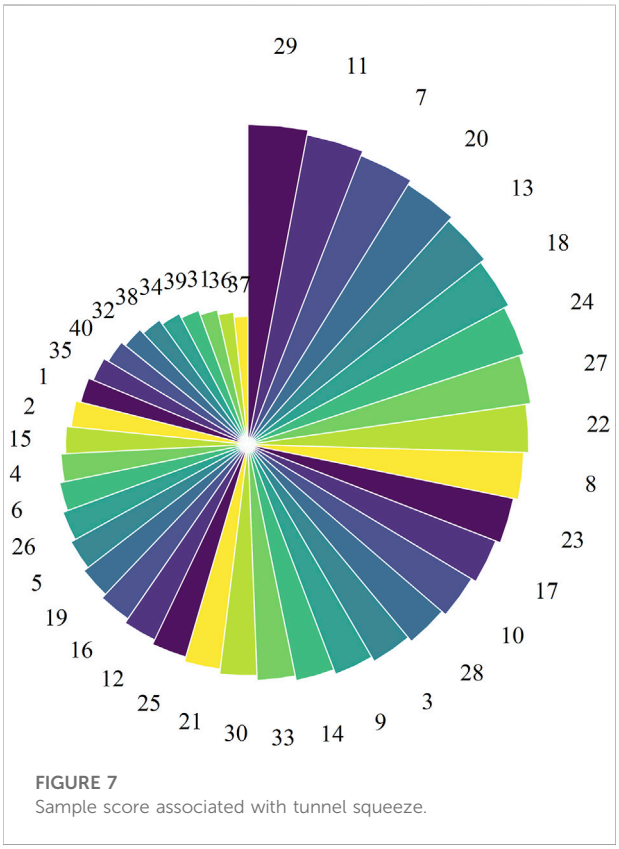


FIGURE 7
Sample score associated with tunnel squeeze.

TABLE 7 Quantitative scoring of individual sample about tunnel squeezing (GP_i).

Samples	Membership function type			
	Linear	Parabolic	Exponential	Sine
1	1.69	1.69	1.76	1.69
2	2.26	2.20	2.19	2.29
3	1.55	1.51	1.51	1.53
4	1.62	1.61	1.70	1.66
5	3.07	3.00	2.95	3.03
6	2.83	2.74	2.76	2.83

the two groups data are shown in Table 7; Figure 7, making it possible to identify the most dangerous sample in the dataset. In Figure 7, the score of sample 29 is highest in comparison with other samples, that is, this sample is more likely to occur large deformation.

Conclusion

In this paper, two sets of data with different evaluation index system are collected, and the unascertained measurement theory is used to comprehensively evaluate the tunnel squeezing. The calculation of this hybrid model includes single-index measurement matrix, index weight coefficient and comprehensive measurement matrix. Ultimately, credible identification principle is used to evaluate the risk level. The main conclusions are listed as following:

(1) Four membership functions are used in this paper: linear, parabolic, exponential, and sine function. The accuracy of the first datasets are: 100%, 83.33%, 50%, and 83.33%, respectively, while the accuracy of second dataset are: 70%, 77.5%, 67.5%, and 70%, respectively.
(2) Two groups of data evaluate the tunnel squeezing through constructing different dataset. For the first dataset, sample five is the most dangerous sample while sample 29 is the most dangerous one for the other dataset.
(3) The factors affecting the large deformation of surrounding rock are complex, not only related to the mechanical properties of rock and engineering geological factors, but also related to the construction conditions. There is high uncertainty in the evaluation of large deformation of surrounding rock, more models should be explored to remove various uncertainty existing in the evaluation process in the next research.

Data availability statement

The original contributions presented in the study are included in the article/supplementary material, further inquiries can be directed to the corresponding authors.

Author contributions

Writing—original draft preparation, CW, JZ, CC, and SZ; Modelling, CC and CW; Writing—review and editing, CW, JZ, and CC. All authors have read and agreed to the published version of the manuscript.

Funding

This research was funded by the National Science Foundation of China (42177164 and 41807259) the Distinguished Youth Science Foundation of Hunan Province of China (2022JJ10073) and the Innovation-Driven Project of Central South University (No. 2020CX040). The authors gratefully acknowledge financial support from the China Scholarship Council (Grant No. 202206370030).

Conflict of interest

The authors declare that the research was conducted in the absence of any commercial or financial relationships that could be construed as a potential conflict of interest.

Publisher's note

All claims expressed in this article are solely those of the authors and do not necessarily represent those of their affiliated organizations, or those of the publisher, the editors and the reviewers. Any product that may be evaluated in this article, or claim that may be made by its manufacturer, is not guaranteed or endorsed by the publisher.

References

Aydan, Ö., Akagi, T., and Kawamoto, T. (1996). The squeezing potential of rock around tunnels: theory and prediction with examples taken from Japan. *Rock Mech. Rock Eng.* 29 (3), 125–143. doi:10.1007/bf01032650

Aydan, Ö., Akagi, T., and Kawamoto, T. (1993). The squeezing potential of rocks around tunnels; theory and prediction. *Rock Mech. Rock Eng.* 26 (2), 137–163. doi:10.1007/bf01023620

Azizi, F., Koopialipoor, M., and Khoshrou, H. (2019). Estimation of rock mass squeezing potential in tunnel route (case study: Kerman water conveyance tunnel). *Geotech. Geol. Eng. (Dordr).* 37 (3), 1671–1685. doi:10.1007/s10706-018-0714-5

Bai, C., Xue, Y., Qiu, D., Yang, W., Su, M., Ma, X., et al. (2021). Real-time updated risk assessment model for the large deformation of the soft rock tunnel. *Int. J. Geomech.* 21 (1), 04020234. doi:10.1061/(asce)gm.1943-5622.0001887

Barla, G. (1995). Squeezing rocks in tunnels. *Int. Soc. Rock Mech. New J.* 2 (3/4), 44–49. [J].

ISRM (1995). Editor G. Barla (Tokyo: Proc.Workshop 8th ICRM). [A].*Commission on squeezing rocks in tunnels tunneling in difficult ground*

Barla, G. (2001). *Tunnelling under squeezing rock conditions*. Innsbruck: Eurosummer-school in tunnel mechanics, 169–268.

Barton, N., Lien, R., and Lunde, J. (1974). Engineering classification of rock masses for the design of tunnel support. *Rock Mech.* 6 (4), 189–236. doi:10.1007/bf01239496

Bhasin, R., and Grimstad, E. (1996). The use of stress-strength relationships in the assessment of tunnel stability. *Tunn. Undergr. Space Technol.* 11 (1), 93–98. doi:10.1016/0886-7798(95)00047-x

Chen, C., Zhou, J., Zhou, T., and Yong, W. (2021). Evaluation of vertical shaft stability in underground mines: comparison of three weight methods with uncertainty theory. *Nat. Hazards (Dordr).* 109 (2), 1457–1479. doi:10.1007/s11069-021-04885-5

Chen, Yu. (2008). *Study on large deformation mechanism and prevention technique of the wall rock in Gong He tunnel*. Chongqing, China: Chongqing University. [D].

Du, K., Li, X., Su, R., Tao, M., Lv, S., Luo, J., et al. (2022). Shape ratio effects on the mechanical characteristics of rectangular prism rocks and isolated pillars under uniaxial compression. *Int. J. Min. Sci. Technol.* 32 (2), 347–362.

Dube, A. K., Singh, B., and Singh, B. (1986). Study of squeezing pressure phenomenon in a tunnell—II. *Tunn. Undergr. space Technol.* 1 (1), 41–48. doi:10.1016/0886-7798(86)90126-4

Dwivedi, R. D., Singh, M., Viladkar, M. N., and Goel, R. K. (2014). Estimation of support pressure during tunnelling through squeezing grounds. *Eng. Geol.* 168, 9–22. doi:10.1016/j.enggeo.2013.10.020

Dwivedi, R. D., Singh, M., Viladkar, M. N., and Goel, R. K. (2013). Prediction of tunnel deformation in squeezing grounds. *Eng. Geol.* 161, 55–64. doi:10.1016/j.enggeo.2013.04.005

Farhadian, H., and Nikvar-Hassani, A. (2020). Development of a new empirical method for tunnel squeezing classification (TSC). *Q. J. Eng. Geol. Hydrogeology* 53 (4), 655–660. doi:10.1144/qjegh2019-108

Fatemi Aghda, S. M., Ganjalipour, K., and Esmaeil Zadeh, M. (2016). Comparison of squeezing prediction methods: a case study on nowsoud tunnel. *Geotech. Geol. Eng. (Dordr).* 34 (5), 1487–1512. doi:10.1007/s10706-016-0056-0

Feng, G. L., Chen, B. R., Xiao, Y. X., Jiang, Q., Li, P. X., Zheng, H., et al. (2022). Microseismic characteristics of rockburst development in deep tbm tunnels with alternating soft–hard strata and application to rockburst warning: A case study of the neelum–jhelum hydropower project. *Tunn. Undergr. Space Technol.* 122, 104398. doi:10.1016/j.tust.2022.104398

Feng, G. L., Feng, X. T., Chen, B. R., Xiao, Y. X., and Yu, Y. (2015). A microseismic method for dynamic warning of rockburst development processes in tunnels. *Rock Mech. Rock Eng.* 48 (5), 2061–2076. doi:10.1007/s00603-014-0689-3

Ghiasi, V., Ghiasi, S., and Prasad, A. (2012). Evaluation of tunnels under squeezing rock condition. *J. Eng. Des. Technol.* 10, 168–179. doi:10.1108/17260531211241167

Gioda, G., and Cividini, A. (1996). Numerical methods for the analysis of tunnel performance in squeezing rocks. *Rock Mech. Rock Eng.* 29 (4), 171–193. doi:10.1007/bf01042531

Goel, R. K., Jethwa, J. L., and Paithankar, A. G. (1995). Tunnelling through the young himalayas—a case history of the maneri-uttarkashi power tunnel. *Eng. Geol.* 39 (1-2), 31–44. doi:10.1016/0013-7952(94)00002-j

He, M. C., Jing, H., and Sun, X. (2002). *Soft rock engineering Mechanics*. Beijin: Science Press. [M].

Hoek, E. (2001). Big tunnels in bad rock. *J. Geotech. Geoenviron. Eng.* 127 (9), 726–740. doi:10.1061/(asce)1090-0241(2001)127:9(726)

Jethwa, J. L., Singh, B., and Singh, B. (1984). "28 estimation of ultimate rock pressure for tunnel linings under squeezing rock conditions—a new approach," in Design and Performance of Underground Excavations: ISRM Symposium, Cambridge UK, 3–6 September 1984 (Thomas Telford Publishing), 231–238.

Jia, Q., Wu, L., Li, B., Chen, C., and Peng, Y. (2019). The comprehensive prediction model of rockburst tendency in tunnel based on optimized unascertained measure theory. *Geotech. Geol. Eng. (Dordr).* 37 (4), 3399–3411. doi:10.1007/s10706-019-00854-9

Jiang, Y., Li, Y., Li, T., and Wang, L. (2004). Study of the classified system of types and mechanism of great distortion in tunnel and underground engineering. *J. Geol. Hazards Environ. Preserv.* 15 (4), 46–51.

Jing, Y., and Hua, J. (2008). "Study on the evaluation of community informatization level based on unascertained measure model," in *2008 international workshop on modelling, simulation and optimization* (New York, US: IEEE), 69–73.

Lai, J., Wang, X., Qiu, J., Chen, J., Hu, Z., Wang, H., et al. (2018). Extreme deformation characteristics and countermeasures for a tunnel in difficult grounds in southern Shaanxi, China. *Environ. Earth Sci.* 77 (19), 706. doi:10.1007/s12665-018-7888-2

Liao, Y., Guo, D., Liu, Z., and Chen, D. (2020). Application of peripheral strain and squeezing factor methods in the prediction of large deformation of tunnel surrounding rocks. *Mod. Tunn. Technol.* 57 (04), 20–26. doi:10.13807/j.cnki.mtt.2020.04.003

Liu, Q. S. (2004). *The study of control technique for great deformation tunnels in soft surrounding rock of press*. Chengdu, China: Southwest Jiaotong University. [D].

Liu, Z., Xie, Q., Xu, S., and Yang, W. (2019). Improved cloud model for evaluation of large deformation of tunnel surrounding rock and its application[J]. *Water Resour. Hydropower Eng.* 50 (09), 108–113.

Liu, Z. C., Zhu, Y. Q., Li, W. J., and Liu, P. X. (2008). Mechanism and classification criterion for large deformation of squeezing ground tunnels. *Chin. J. Geotechnical Eng.* 30 (5), 690–697.

Ma, H., Zhou, Y., Rao, B., Ma, Q., and Chen, S. (2021). Optimization of qualified lump size of ore based on undetermined measure theory. *Min. Technol.* 21 (06), 176–179. doi:10.13828/j.cnki.ckjs.2021.06.046

Malan, D. F., and Basson, F. R. P. (1998). Ultra-deep mining: the increased potential for squeezing conditions. *J. South. Afr. Inst. Min. Metallurgy* 98 (7), 353–363.

Palmstrom, A., and Broch, E. (2006). Use and misuse of rock mass classification systems with particular reference to the Q-system. *Tunn. Undergr. space Technol.* 21 (6), 575–593. doi:10.1016/j.tust.2005.10.005

Panet, M. (1996). Two case histories of tunnels through squeezing rocks. *Rock Mech. Rock Eng.* 29 (3), 155–164. doi:10.1007/bf01032652

Panthi, K. K. (2013). Predicting tunnel squeezing: a discussion based on two tunnel projects. *Hydro Nepal.* 12, 20–25. doi:10.3126/hn.v12i0.9027

Ren, H., Zhang, B., Bian, P., Wang, S., and Wang, L. (2021). Case analysis and technical countermeasures of tunnelling in squeezing surrounding rocks. *Mod. tunneling Technol.* 58 (S2), 165–171. doi:10.13807/j.cnki.mtt.2021.S2.025

Ruan, C., Zhang, Y., Li, H., Hou, W., Dong, D., and Tian, H. (2021). Construction risk assessment of urban wastewater deep-buried tunnel under passing existing railway based on the improved entropy weight unascertained measurement model. *Saf. Environ. Eng.* 28 (06), 84–90. doi:10.13578/j.cnki.issn.1671-1556.20201160

Sharma, S., Muthreja, I. L., and Yerpude, R. R. (2020). Application and comparison of squeezing estimation methods for Himalayan tunnels. *Bull. Eng. Geol. Environ.* 79 (1), 205–223. doi:10.1007/s10064-019-01530-1

Shi, X., Zhou, J., Dong, L., Hu, H., Wang, H., and Chen, S. (2010). Application of unascertained measurement model to prediction of classifiation of rockburst intensity. *Chin. J. Mech. Eng.* 29 (S1), 2720–2726.

Singh, M., Singh, B., and Choudhari, J. (2007). Critical strain and squeezing of rock mass in tunnels. *Tunn. Undergr. space Technol.* 22 (3), 343–350. doi:10.1016/j.tust.2006.06.005

Steiner, W. (1996). Tunnelling in squeezing rocks: case histories. *Rock Mech. Rock Eng.* 29 (4), 211–246. doi:10.1007/bf01042534

Tu, S. W., Guo, X. C., and He, J. M. (2008). "Safety evaluation for first class Highway design based on unascertained measure model," in *2008 workshop on power electronics and intelligent transportation system* (New York, US: IEEE), 511–514.

Wang, L. (2019). *Research on nonlinear prediction of large deformation drade of mountain railway tunnel and supporting measures*. Jinan, China: Shan Dong University.

Wang, S. M., Zhou, J., Li, C. Q., Armaghani, D. J., Li, X. B., and Mitri, H. S. (2021a). Rockburst prediction in hard rock mines developing bagging and boosting tree-based ensemble techniques. *J. Cent. South Univ.* 28 (2), 527–542.

Wang, S. F., Yu, T. A. N. G., Li, X. B., and Kun, D. U. (2021b). Analyses and predictions of rock cuttabilities under different confining stresses and rock properties based on rock indentation tests by conical pick. *Trans. Nonferrous Metals Soc. China* 31 (6), 1766–1783. doi:10.1016/s1003-6326(21)65615-7

Wang, S., Sun, L., Li, X., Zhou, J., Du, K., Wang, S., et al. (2022). Experimental investigation and theoretical analysis of indentations on cuboid hard rock using a conical pick under uniaxial lateral stress. *Geomech. Geophys. Geo. Energy. Ge. Resour.* 8 (1), 34. doi:10.1007/s40948-022-00345-x

Williams, A. S. (2010). "Estimating the squeeze potential for long, deep tunnels beneath the santa mountains of southern California," in 44th US Rock Mechanics Symposium and 5th US-Canada Rock Mechanics Symposium, Salt Lake City, Utah, June 27–30, 2010. OnePetro.

Wood, A. M. M. (1972). Tunnels for roads and motorways. *Q. J. Eng. Geol. Hydrogeology* 5 (1-2), 111–126. doi:10.1144/gsl.qjeg.1972.005.01.12

Yu, X., and Zhang, W. (2020). Study on control technique for large deformation of soft rocks in huifulai tunnel of China-Laos raiway[J]. *Int. J. Equity Health* 11 (03), 12. doi:10.1186/s12939-020-1128-6

Yu, Y., Zhao, D. C., Feng, G. L., Geng, D. X., and Guo, H. S. (2022). Energy evolution and acoustic emission characteristics of uniaxial compression failure of anchored layered sandstone. *Front. Earth Sci. (Lausanne).* 10, 841598. doi:10.3389/feart.2022.841598

Zhang, J., Li, D., and Wang, Y. (2020). Predicting tunnel squeezing using a hybrid classifier ensemble with incomplete data. *Bull. Eng. Geol. Environ.* 79 (6), 3245–3256. doi:10.1007/s10064-020-01747-5

Zhang, Z. (2003). Discussion and study on large deformation of tunnel in squeezing ground. *Mod. Tunn. Technol.* (2), 5–12+40. doi:10.13807/j.cnki.mtt.2003.02.002

Zhou, J., Chen, C., Armaghani, D. J., and Ma, S. (2020a). Developing a hybrid model of information entropy and unascertained measurement theory for evaluation of the excavatability in rock mass. *Eng. Comput.* 38, 247–270. doi:10.1007/s00366-020-01053-4

Zhou, J., Chen, C., Du, K., Jahed Armaghani, D., and Li, C. (2020b). A new hybrid model of information entropy and unascertained measurement with different membership functions for evaluating destressability in burst-prone underground mines. *Eng. Comput.* 38, 381–399. doi:10.1007/s00366-020-01151-3

Zhou, J., Chen, C., Khandelwal, M., Tao, M., and Li, C. (2021a). Novel approach to evaluate rock mass fragmentation in block caving using unascertained measurement model and information entropy with flexible credible identification criterion. *Eng. Comput.*, 1–21. doi:10.1007/s00366-020-01230-5

Zhou, J., Chen, C., Wang, M., and Khandelwal, M. (2021b). Proposing a novel comprehensive evaluation model for the coal burst liability in underground coal mines considering uncertainty factors. *Int. J. Min. Sci. Technol.* 31 (5), 799–812. doi:10.1016/j.ijmst.2021.07.011

Zhou, J., Chen, C., Wei, C., and Du, K. (2022a). An improved connection cloud model of an updated database: A multicriteria uncertainty model for coal burst liability evaluation. *Nat. Resour. Res.* 31 (3), 1687–1704.

Zhou, J., Zhu, S., Qiu, Y., Armaghani, D. J., Zhou, A., and Yong, W. (2022b). Predicting tunnel squeezing using support vector machine optimized by whale optimization algorithm. *Acta Geotech.* 17 (4), 1343–1366.

frontiers | Frontiers in Earth Science

TYPE Original Research
PUBLISHED 04 August 2022
DOI 10.3389/feart.2022.954547

Check for updates

OPEN ACCESS

EDITED BY
Guang-Liang Feng,
Institute of Rock and Soil Mechanics (CAS), China

REVIEWED BY
Liu Liu,
Institute of Rock and Soil Mechanics (CAS), China
Qiu Enxi,
Southwest Petroleum University, China

*CORRESPONDENCE
Zhang Jun,
zhangjun07@tyut.edu.cn

SPECIALTY SECTION
This article was submitted to Geohazards and Georisks, a section of the journal Frontiers in Earth Science

RECEIVED 27 May 2022
ACCEPTED 27 June 2022
PUBLISHED 04 August 2022

CITATION
Jun Z, Yiliang W, Liming C, Ning W, Yuepin B and Chaofan W (2022), Workspace analysis and motion control strategy of robotic mine anchor drilling truck manipulator based on the WOA-FOPID algorithm.
Front. Earth Sci. 10:954547.
doi: 10.3389/feart.2022.954547

COPYRIGHT
© 2022 Jun, Yiliang, Liming, Ning, Yuepin and Chaofan. This is an open-access article distributed under the terms of the Creative Commons Attribution License (CC BY). The use, distribution or reproduction in other forums is permitted, provided the original author(s) and the copyright owner(s) are credited and that the original publication in this journal is cited, in accordance with accepted academic practice. No use, distribution or reproduction is permitted which does not comply with these terms.

Workspace analysis and motion control strategy of robotic mine anchor drilling truck manipulator based on the WOA-FOPID algorithm

Zhang Jun[1,2,3]*, Wang Yiliang[1], Che Liming[2,4], Wang Ning[5], Bai Yuepin[5] and Wang Chaofan[1]

[1]School of Mechanical and Transportation Engineering, Taiyuan University of Technology, Taiyuan, China, [2]China Coal Science and Industry Group Co., Ltd., Beijing, China, [3]Ningxia Tiandi Benniu Industrial Group Co, Ltd., Shizuishan, China, [4]Taiyuan Research Institute of China Coal Science and Industry Group, Taiyuan, China, [5]Shanghai Research Institute of China Coal Science and Industry Group, Shanghai, China

The manipulator is the key component of the anchor drilling robot to automatically complete the anchoring operation underground. Due to the complexity of its motion equation and the limitations of its control strategy, the real-time pose and the positioning accuracy of the manipulator are inferior, which seriously restricts the safety, efficiency, and speed of roadway excavation. In order to improve the positioning accuracy and realize the optimal efficiency of the manipulator, this article designs a manipulator structure with four degrees of freedom. With the help of the D-H method and the intelligent parameter setting method, this article carries out the basic theoretical research on the kinematics and the fractional order FOPID control algorithm of the manipulator of the mining roof bolter, and formulates a manipulator motion control strategy. At the same time, combined with numerical simulations and field experiments, we explore the robustness and control efficiency of the hydraulic system of the manipulator under the working conditions of a harsh environment and limited space, and reveal that the intelligent optimization algorithm can control the motion state of the manipulator more accurately and stably after the parameters of the fractional order FOPID controller are positively determined. This study effectively solved the dynamic model uncertainty caused by time-varying internal parameters and external loads of the hydraulic servo system, optimized and reconstructed the structure and motion coefficient parameters of the manipulator, and revealed the control mechanism of a precise spatial positioning and online trajectory planning of the hydraulic servo system of the manipulator. Compared with the traditional PID control algorithm, this algorithm has a faster response speed and better expected track tracking ability. This research lays a theoretical foundation for the precise positioning and automatic support of the manipulator, and also provides a reference for the design of similar motion control algorithms.

KEYWORDS
manipulator, fractional FOPID, whale algorithm, motion control, anchor drilling robot

1 Introduction

The intellectualization of coal mines is the core technical support for the high-quality development of China's coal industry (Wang et al., 2019; Liu et al., 2021). Intelligent equipment and support technology of mining are key factors for coal intellectualization, and the roadway support theory and technology have always been the core of the coal mine strata control (Kang, 2007; Wang et al., 2018; Wang et al., 2020; Yang et al., 2022). In the "Catalog of Key Research and Development of Coal Mine Robots" (Author Anonymous, 2019; Li et al., 2019; Ge and Hu, 2020), it clearly points out the need to vigorously advance the research and development of coal mining, tunneling, transportation, safety control and rescue, and 38 kinds of coal mine robots, which is an important way to achieve the coal mines' intellectualization. It is a key method to solve the problems of roadway excavation, support imbalance and high labor intensity to use the manipulator of anchor drilling robot on accurate location, and the completion of the automatic anchoring work, replacing the traditional manual completion of automatic positioning and support work of the drilling frame (Zhang et al., 2019; Zhang and Li, 2019).

Compared with developed countries, the ineffective bolt support in some coal mines in China has led to many roof falling accidents. While the main reason is that the existing support operations still rely on manual demolition, with the installation of drill pipes or bolts, bolt fastening, and other processes, with a great danger. The Guiding Opinions on Accelerating the Intelligent Development of Coal Mines clearly points out that the development of an anchor drilling support robot is an effective way to solve the key problems of slow speed and high labor intensity of roadway excavation.

Based on the guidance of the support theory, the bottleneck problem to be solved is to complete the automatic anchoring work with the use of an anchor drilling manipulator for precise positioning, replacing the traditional manual to complete of the drilling frame space positioning, and automatic support work. Since presently, the drivage speed and coal quantity have increases, so new requirements have been put forward for the way of the operation, process time, and the safety of the anchor drilling manipulator. Especially in harsh or limited spaces, manipulator ends need to accurately find the 22 mm diameter hole in the roof, effectively avoid the grid reinforced at the same time, and ensure that the drilling time does not exceed 3 min. However, in the process of drilling and anchoring by a manipulator-replacing manual operation, due to limitations in the formulation of control strategy, the real-time pose and positioning accuracy of the manipulator are inferior, essentially because the research studies are not sufficient in the fields of structural design, motion law, and control mechanism of the anchor drilling manipulator.

In recent years, the way to control the motion of the manipulator is a research hotspot with great significance. Because of its uncertainties in parameter uptake and external interference, the manipulator is a complex research object featuring high non-linearity, multi-variability, and high coupling. In order to make the manipulator in a specific action, it is necessary to control the hydraulic cylinder and hydraulic motor at each joint of the manipulator to cooperate with each other to complete the corresponding rotation angle of each joint. Presently, the manipulator structure has become increasingly complex, and the *PID* control method, with characteristics of independence on the system model, simple and flexible, is unable to meet the motion control of the current manipulator's complex structure. In view of this practical need, many experts and scholars put forward some new methods based on the idea of control. For example, Chen Wei et al. (Chen et al., 2013) adopted the control method and designed the control algorithm of active and passive joints respectively, realized the underactuated manipulator with passive joints and flexible bars in a piecewise control, and the active and passive joints could effectively complete the operation tasks of the manipulator through the control method. Li et al. (Li and Xing, 2007) studied the skid situation of the left and right tracks of the underwater robot under the complex damping coupling action, and established a *PID* control model for automatic tracking of the predetermined mining path with ADAMS/Hydraulics and MATLAB/Simulink, which confirmed that the maximum skid rate of the underwater robot in China was 15%. Jing Xuedong et al. (Jing and Pan, 2018) adopted the switch structure control method with acceleration feedback to improve the positioning accuracy of the manipulator. Compared with the traditional *PID* control method, the fuzzy *PID* control system has more advantages in overshoot and reaction speed. Zhang Tiemin (Zhang et al., 2002) et al. used the switch structure control method with acceleration feedback to reduce the vibration amplitude to 1/10 of the *PID* control method and shorten the vibration attenuation time. Luo Yanlei (Luo et al., 2021) et al. established a model on the basis of MATLAB and the AMEsim software and designed a system method of fuzzy *PID* controller, adopted fuzzy *PID* controller strategy, which has increased the accuracy and working speed of the hydraulic blanking machine, and has advantages of a strong tracking ability and good robustness. However, in some special conditions, to quickly achieve the goal of spatial positioning and trajectory tracking with the manipulator, the effect of a traditional *PID* control is not ideal, as the expected control goal is still not achieved even if the parameters are reset. Since the defects of integer order *PID* control technology cannot be overcome in essence, it is difficult

to thoroughly develop the control principle of a fast and accurate spatial positioning and trajectory planning of the manipulator control system. To sum up, in the process of realizing the control of the multi-degree of the freedom electro-hydraulic servo manipulator, a series of problems of complicated mechanisms, motion characteristics, hydraulic servo drive non-linear, feedback control characteristics, and energy characteristics, are critical points to fulfill the precision, stability, and efficiency of the motion control of the anchor drilling manipulator.

With the gradual development of artificial intelligence technology and its wide application in the industrial field, a large number of efficient optimization algorithms have emerged, such as the genetic algorithm (Zhang et al., 2002; Yin et al., 2014a; Luo et al., 2021), particle swarm optimization algorithm (Feng et al., 2015; Al-Saggaf et al., 2020; Feng et al., 2022), search algorithm (Wu and Huang, 2021), and whale algorithm (Li et al., 2021). Applying the intelligent optimization algorithm to controller parameter tuning can greatly improve the control effect. Whale algorithm is a kind of meta-heuristic optimization algorithm, which has the characteristics of strong robustness, simple structure, and few control parameters. Most scholars (Dalir and Bigdeli, 2020; Bushnaq et al., 2021; Nguyen et al., 2021) have applied the whale algorithm and achieved successful examples in the field of continuous domain problem optimization.

To sum up, many experts have conducted in-depth research studies on the method of the intelligent control PID parameter adjustment and achieved a lot of results, but the control method of the drilling and anchor manipulator completing automatic support operation underground needs further research. This is mainly due to some particularity of the drilling and anchoring manipulator working underground: 1) limited space and a complex environment; 2) The end of the anchor drilling mechanical arm is mainly connected with the automatic drill frame. Due to the dead weight of the end and the drilling force of about 20,000 n, the arm end will vibrate greatly, making it difficult to achieve accurate control; 3) Underground electrical parts need explosion-prevention treatment, especially sensors. Compared with sensors on the ground, many performance indicators are difficult to achieve, so it will affect the accurate positioning of the drilling and anchoring manipulator in the roadway space. It seriously restricts the application of intelligent control technology in an underground coal mine robot.

In order to realize the goal of rapid spatial positioning and trajectory tracking of the manipulator, the intelligent control technology of the drilling anchor manipulator is studied. According to the spinor theory, the joint coordinate system and coordinate transformation matrix expression of the manipulator are established by using the D–H method, and the point cloud diagram of the manipulator workspace is solved by using the Monte Carlo algorithm. Based on the independent joint control theory, the single input single output system model of the hydraulic motor/cylinder at the joint of the manipulator is designed by using the MATLAB Simulink software and fractional order FOPID control technology. This article analyzes four intelligent optimization algorithms based on the genetic algorithm (GA), particle swarm optimization (PSO), whale algorithm (WOA), and search algorithm (GPS), evaluates the three dynamic indexes of standard deviation, overshoot, and stability time, and analyzes the effect of step influence under different control combination strategies of the hydraulic motor/oil cylinder. The simulation results show that the optimization ability of the *WOA* algorithm is obvious. For the fractional order controlled object, it can be stable in 0.19 s, and the overshoot is 3.49%, which shows that the controlled system has better stability and fully reflects the advantages of the *FOPID* fractional order controller. Finally, the design and experiment are carried out combined with the manipulator control system of the anchor drilling robot.

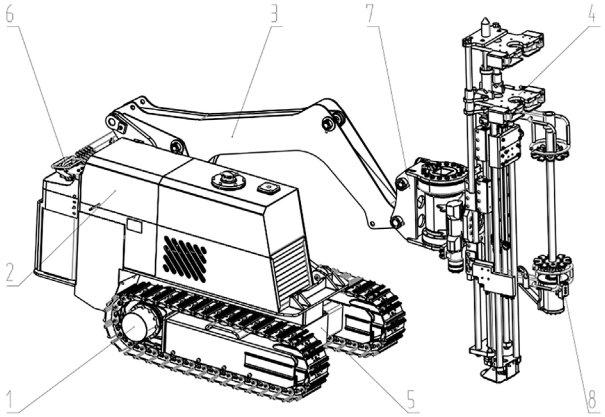


FIGURE 1
Structural diagram of the mine anchor drill frame.

2 Structural design and working principle of the manipulator

Mining roof bolter is suitable for automatic support of the top and side walls of the mine tunnel in an underground coal mine, and can realize accurate identification and positioning technology of the manipulator hole location through binocular stereo vision. The structure of the machine is shown in Figure 1. The manipulator connected the frame with the translation pair and the rotation pair realizes the support work of the automatic drilling frame, and ensures the support work of the top and side walls of the roadway with different heights and widths in the mine environment.

1-Variable frequency speed-regulating traveling mechanism, 2-Electrical control system, 3-Connecting rod, 4-Automatic drill

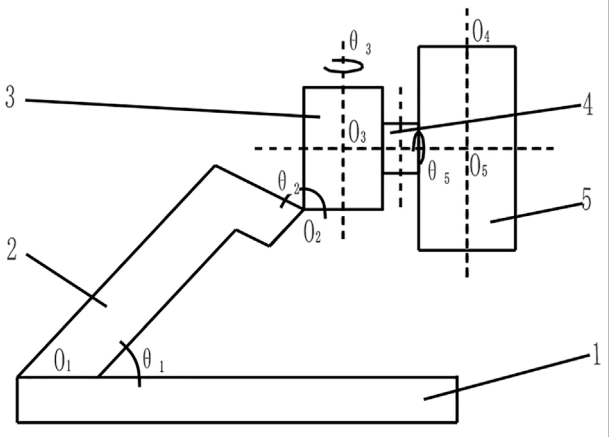


FIGURE 2
Structure diagram of the manipulator.

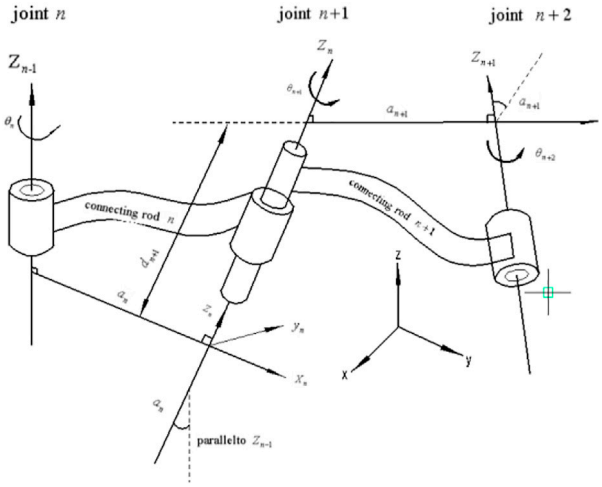


FIGURE 3
Schematic diagram of the *D* – *H* model.

frame, 5-Frame, 6-Driving operation and monitoring mechanism, 7-Rotary reducer, 8-Anchor rod silo.

During mining roof bolter into the mine roadway, firstly, it is driven to the work scheduled area, after being stable, the manipulator controlled by the hydraulic system to automatically drill stands up to the right height through the rotary gear reducer to adjust the automatic drill's stand posture. Then, the automatic drill starts to work on the working surface, and finally completes the mine roadway support work.

3 Kinematic workspace analysis of the manipulator

The manipulator is the main working structure of the equipment to realize the automatic support of the top and side walls of the roadway. The positioning system of the manipulator is the important factor to ensure that mining roof bolter can meets the working requirements and work quality. It is required that the displacement working accuracy offset of the manipulator shall not be more than 5 mm, and the displacement working accuracy offset of the manipulator end shall not be more than 10 mm. In addition, as the bad environment in the mine roadway, frequent vibration, and changeable load, a manipulator structure with five degrees of freedom is specially designed to meet the actual requirements of the aforementioned working process. The manipulator is mainly composed of a connecting rod, rotary reducer, coupling, automatic drilling frame, and so on. Its structural diagram is shown in Figure 2.

1 - Frame; 2 - Connecting rod; 3 - Rotary reducer; 4 - Connection shaft; 5-Automatic drilling rig.

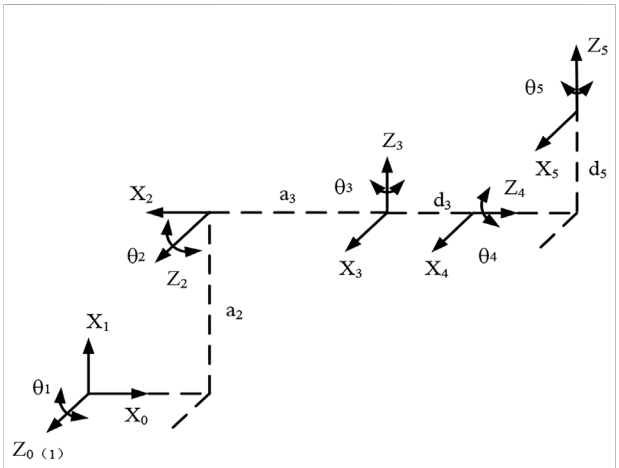


FIGURE 4
Establishment of a joint coordinate system of the manipulator by using the *D* – *H* method.

The frame is set at the lower end of the whole manipulator as the main body supporting the whole manipulator; the connecting rod is connected through the shaft, and the hydraulic cylinder provides power which can rotate θ_1 around O_1 in the vertical direction; the rotary reducer is located at the top of the other end of the connecting rod. Through the shaft connection, the hydraulic cylinder provides power and can rotate θ_2 around O_2 in the vertical direction. The connecting shaft is located in the middle of the rotary reducer and can rotate θ_3 around O_3 in the horizontal direction; the automatic drilling frame is placed on one

TABLE 1 $D-H$ parameters.

Rod order	Length of connecting rod a/mm	Distance between joints d/mm	Connecting rod rotation angle $a/(°)$	Joint rotation angle $\theta/(°)$	Variable range
1	0	0	90	θ_1	(0–45)
2	2054.86	0	0	θ_2	(−45–45)
3	314.48	0	90	θ_3	(0–180)
4	0	160	90	θ_4	(−90–90)
5	0	786.6	90		0

side of the connecting shaft, which can rotate θ_5, contrary to the position of the rotary reducer.

3.1 Kinematics model based on screw theory

In accordance with the principles and parameters of the $D-H$ connecting rod coordinate system of the manipulator, the homogeneous transformation relationship between the joints of the manipulator can also be expressed by the rotation matrix and the translation vector, so the homogeneous transformation moments of the front and rear joints of the manipulator are shown in Figure 3.

The homogeneous transformation matrix is expressed as T, the rotation matrix as R and translation matrix as P, then the homogeneous transformation matrix from joint $n-1$ to joint n can be expressed as ${}^{n-1}T_n$, as shown in Eq. (1). Establishment of a joint coordinate system of the manipulator by using the $D-H$ method, as shown in Figure 4.

$$ {}^{n-1}T_n = \begin{bmatrix} \cos\theta_n & -\sin\theta_n\cos\theta_n & \sin\theta_n\sin\theta_n & \alpha_n\cos\theta_n \\ \sin\theta_n & \cos\theta_n\cos\theta_n & -\cos\theta_n\cos\theta_n & \alpha_n\sin\theta_n \\ 0 & \sin\theta_n & \cos\theta_n & d_n \\ 0 & 0 & 0 & 1 \end{bmatrix} \quad (1) $$

Based on Table 1, the transformation relation matrix T_1 from coordinate system X_0-Y_0 to coordinate system X_1-Y_1 is firstly established according to the $D-H$ principle, as shown in Eq. (2). Using the same method, the subsequent transformation relation matrices between the two adjacent coordinate systems are T_2, T_3, T_4, and T_5, respectively. The expressions of the five coordinate-change matrices are shown in Eqs 3-6:

$$ T_1 = \begin{bmatrix} \cos\theta_1 & 0 & \sin\theta_1 & \alpha_1\cos\theta_1 \\ \sin\theta_1 & 0 & 0 & \alpha_1\sin\theta_1 \\ 0 & 1 & 0 & d_1 \\ 0 & 0 & 0 & 1 \end{bmatrix} \quad (2) $$

$$ T_2 = \begin{bmatrix} \cos\theta_2 & -\sin\theta_1 & 0 & \alpha_2\cos\theta_2 \\ \sin\theta_2 & \cos\theta_2 & -\cos\theta_2 & \alpha_2\sin\theta_2 \\ 0 & 0 & 1 & d_2 \\ 0 & 0 & 0 & 1 \end{bmatrix} \quad (3) $$

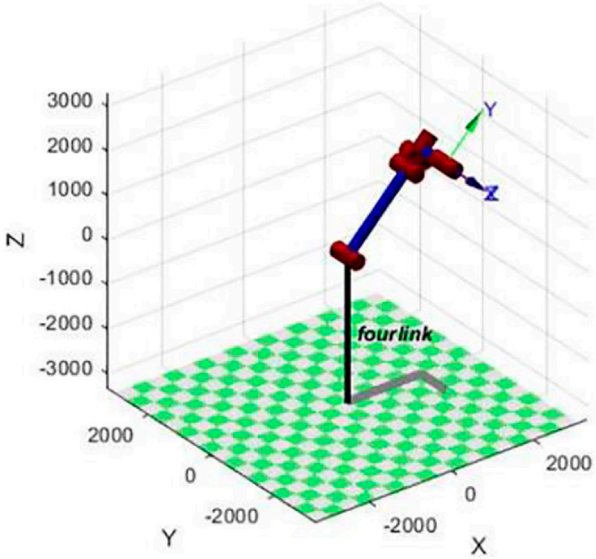


FIGURE 5
Five degrees of freedom manipulator.

$$ T_3 = \begin{bmatrix} \cos\theta_3 & 0 & \sin\theta_3 & \alpha_3\cos\theta_3 \\ \sin\theta_3 & 0 & 0 & \alpha_3\sin\theta_3 \\ 0 & 1 & 0 & d_3 \\ 0 & 0 & 0 & 1 \end{bmatrix} \quad (4) $$

$$ T_4 = \begin{bmatrix} \cos\theta_4 & 0 & \sin\theta_4 & \alpha_4\cos\theta_4 \\ \sin\theta_4 & 0 & 0 & \alpha_4\sin\theta_4 \\ 0 & 1 & 0 & d_4 \\ 0 & 0 & 0 & 1 \end{bmatrix} \quad (5) $$

$$ T_5 = \begin{bmatrix} \cos\theta_5 & 0 & \sin\theta_5 & \alpha_5\cos\theta_5 \\ \sin\theta_5 & 0 & 0 & \alpha_5\sin\theta_5 \\ 0 & 1 & 0 & d_5 \\ 0 & 0 & 0 & 1 \end{bmatrix} \quad (6) $$

All revolute joints of the manipulator in this article are represented by the $D-H$ parameters related to position and pose. The motion of the manipulator in this article is chain motion. By multiplying the homogeneous transformation matrix T_i of each joint according to the subscript number, the total

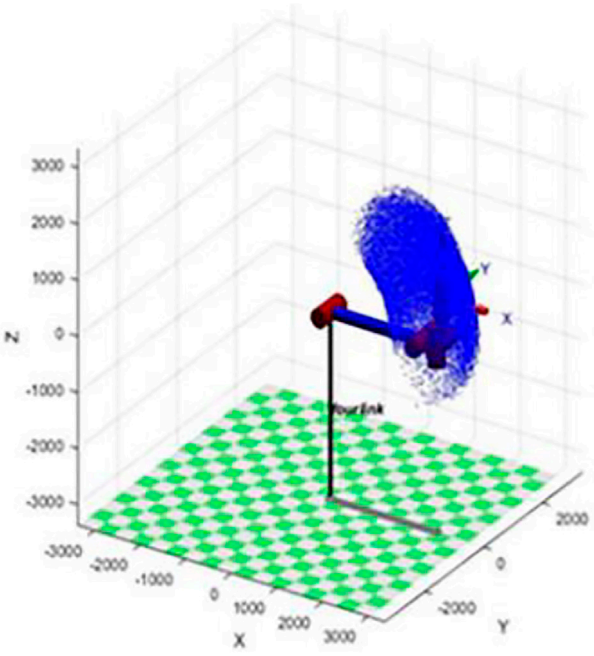


FIGURE 6
Cloud diagram of the manipulator movement space.

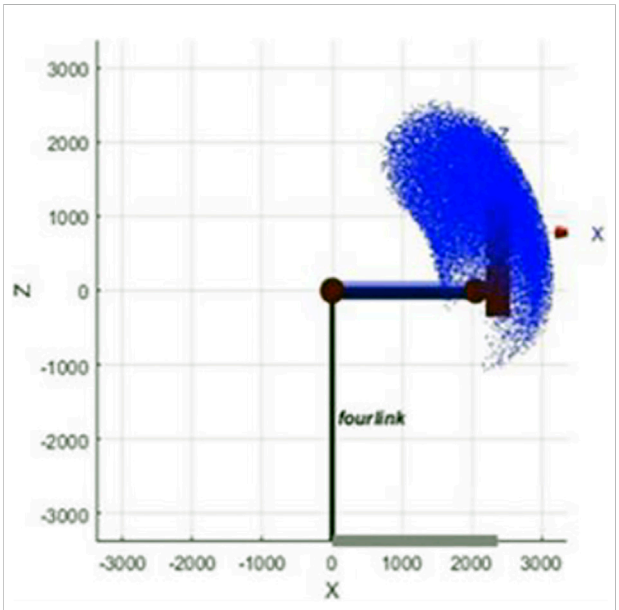


FIGURE 7
Spatial cloud diagram of the ZOX surface motion.

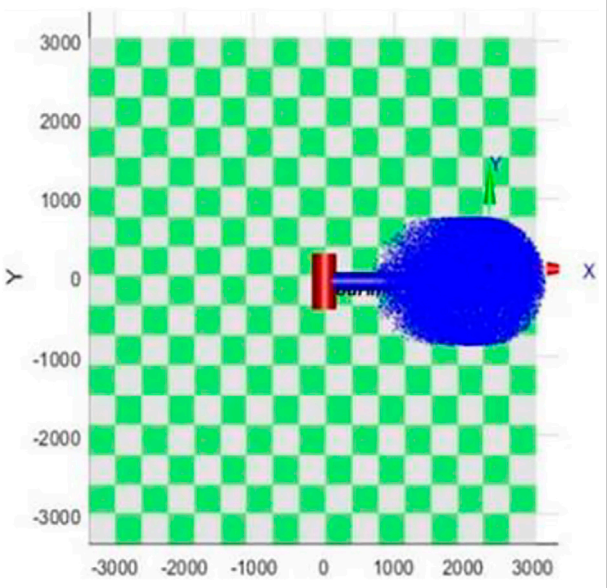


FIGURE 8
Spatial cloud diagram of the YOX surface motion.

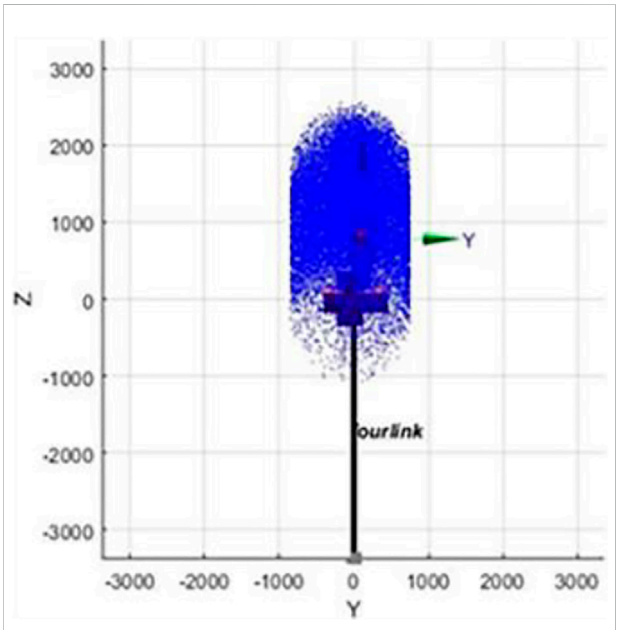


FIGURE 9
Cloud diagram of the ZOY plane motion space.

transformation matrix of the manipulator from the cloud platform to the end effector can be obtained, as shown in Eq. (7).

$$^{1}T_5 = T_1T_2T_3T_4T_5 \tag{7}$$

3.2 Motion space analysis of the manipulator

The simplified model of the manipulator of the mining roof bolter is shown in Figure 5. When the angle θ of each joint is

known, the end position X, Y, Z can be obtained; on the contrary, when the end position X, Y, Z is known, the angle of each joint can be obtained, so the inverse solution of the manipulator of the mining roof bolter can be obtained.

To describe the working space of the manipulator of the mining roof bolter, the root of the manipulator is set as $(0, 0, 0)$, and according to the forward kinematics solution of the manipulator, (x, y, z) can be obtained. The random number is obtained by using the *Rand* function in *MATLAB* in accordance with the limit of each joint, and the random value is put into the forward kinematics equation to obtain the vector of the corresponding position. The working cloud diagram of the manipulator of the mining roof bolter is obtained, as shown in Figures 6–9.

From Figures 7–9, it can be seen that the working range of the manipulator of mining roof bolter is $X \in [500, 3200]$, $Y \in [-900, +900]$, $Z \in [-1100, 2500]$; the working space of the manipulator of the mining roof bolter is approximately a part of the ellipse, and the simulated working space is compacted in the structure. Each joint of the simulated moving space is in line with the actual moving space, which can truly describe the working space of the manipulator.

4 Fractional order FOPID motion control algorithm based on WOA-FOPID parameter tuning

4.1 Fractional order control theory and the parameter tuning optimization process

4.1.1 Fractional order control theory

As a branch of the control field, fractional order control has been widely used in the design of different types of controllers (Yin et al., 2014b; Al-Saggaf et al., 2020; Sheng et al., 2021) for its advantages such as flexibility and precise parameter adjustment, increasing system stability margin and enhancing system robustness, etc. Fractional order $PI^{\lambda}D^{\mu}$ control was first proposed and demonstrated its superiority over the traditional *PID* control by Igor Podlubny through the response analysis (Podlubny, 1999; Semmari et al., 2017; Cuong et al., 2020; Dalir and Bigdeli, 2020; Bushnaq et al., 2021; Musarrat and Fekih, 2021; Nguyen et al., 2021; Wu and Huang, 2021; Huang et al., 2022). The order parameters λ, μ of the fractional order $PI^{\lambda}D^{\mu}$ controller can be taken as any real number. In the $P-I-D$ plane, values can be taken according to different controller parameters. The specific expression and range of values are shown in Figure 10.

$$C(s) = \frac{U(s)}{R(s)} = K_p + \frac{K_i}{s^{\lambda}} + K_d s^{\mu} \tag{8}$$

K_p is the proportional gain; K_i is the integral gain; $\vec{r}$ is the differential gain; $\vec{r}$ and $\vec{r}$ are the fractional, differential, and integral order, respectively.

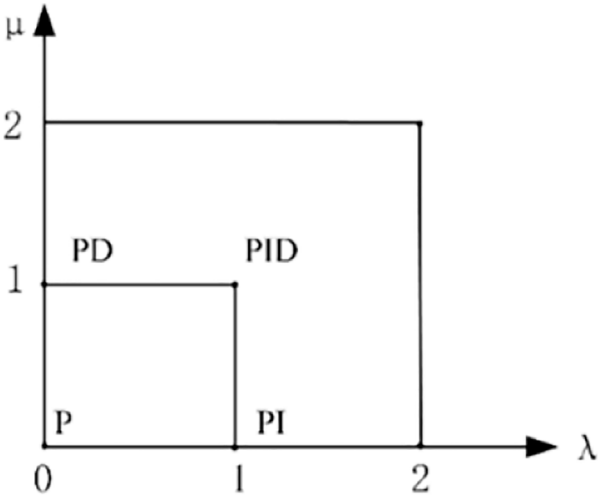


FIGURE 10
Order value range of the FOPID controller. The mathematical expression of FOPID is given.

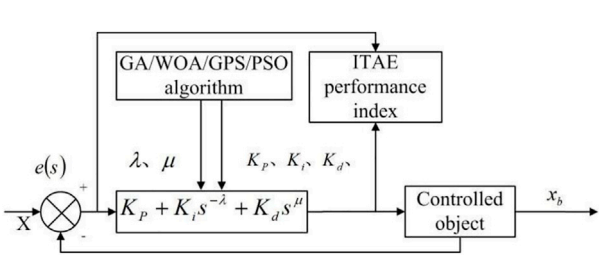


FIGURE 11
Parameter setting principle of the intelligent optimization algorithm.

Compared with the traditional *PID* control, fractional order $PI^{\lambda}D^{\mu}$ control can better subtly reflect the transition process from proportional control to integral control and differential control, so as to achieve more precision, better stability, and stronger anti-interference control effect. Therefore, the author considers designing a fractional order $PI^{\lambda}D^{\mu}$ control (FOPID) for the electronic control system of the raise boring machine in this article.

4.1.2 Parameter tuning and the optimization process

There are many kinds of parameter tuning methods. With the development of intelligent and control technology, according to the regulation characteristics of the algorithm itself, it is mainly divided into a traditional method tuning and an intelligent optimization algorithm tuning, and the latter one is widely used for its adaptability. The four intelligent optimization

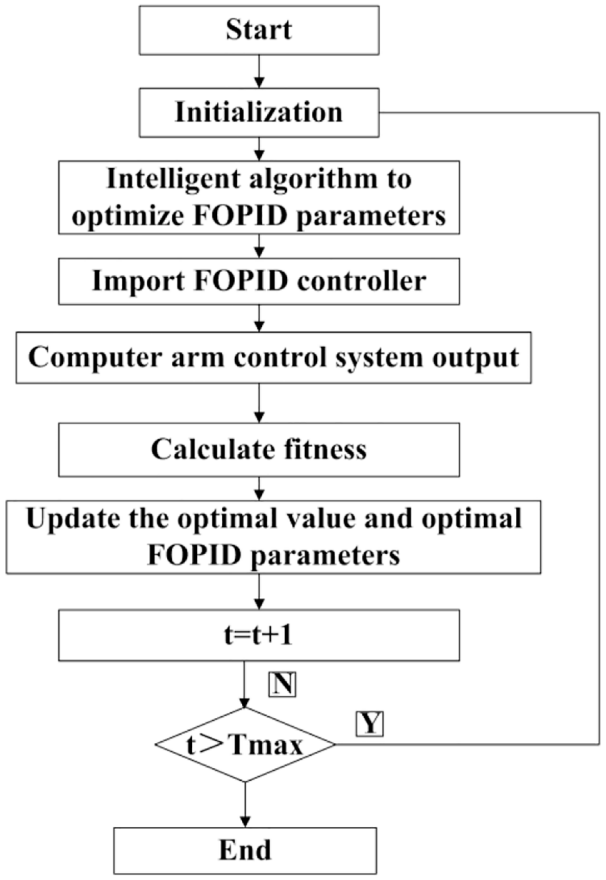


FIGURE 12
Flow chart of the intelligent optimization algorithm for tuning.

algorithms, genetic algorithm (GA), particle swarm optimization (PSO), whale algorithm (WOA), and search algorithm (GPS), have been used for real-time parameter tuning to obtain the optimal value. The parameter tuning principle of the four intelligent optimization algorithms is shown in Figure 11, and the flow chart of the intelligent optimization algorithm for tuning the FOPID parameters is shown in Figure 12. The specific mathematical theories and related expressions of the four intelligent optimization algorithms such as the whale algorithm will not be repeated.

4.2 Mathematical modeling and simulation test of the hydraulic cylinder/hydraulic motor at the joint of the manipulator

In this article, genetic algorithm (GA), particle swarm optimization algorithm (PSO), whale algorithm (WOA), and search algorithm (GPS) are combined with PID and $FOPID$, respectively, Through different combined control strategies, the control effect of the valve-controlled hydraulic cylinder is further analyzed and compared.

For the optimization algorithms used in different control strategies, an objective function is usually set to select the optimal value. The common error performance indicators include ISE (square deviation integral), ITSE (time square deviation integral), IAE (absolute deviation integral), ITAE (time absolute deviation integral), etc. In servo control, the ITAE (time absolute deviation integral) performance index weights the error, so that the error signal converges to zero as soon as possible. Therefore, this article takes the ITAE performance index as the objective function for parameter tuning (Semmari et al., 2017) as shown in Figure 11.

Here, the specific parameters of each algorithm are set as follows: PSO parameter settings: $Max_iter = 200$, $N = 20$, $C_1 = C_2 = 1.49$; the GA parameters are set as: $N = 50$, $Max_iter = 200$ and the variation parameter is 0.8, and the variation probability is 0.75; The $WOA - FOPID$ parameter is set to: dim = 5, $Max_iter = 50$, $SearchAgents_no = 100$; $WOA - PID$ is set to: dim = 3, $Max_iter = 50$, $SearchAgents_no = 100$, the simulation time is second (s). The comparison of different combination strategies and control indexes is shown in Tables 2, 3. Figure 11 shows the comparison of the dynamic response curves of each combination strategy of the regulating system, a is the step-response diagram of each algorithm and PID combination strategy, and b is the step-response diagram of each algorithm and $FOPID$ combination strategy. The comparison of the WOA algorithm-based PID and $FOPID$ combined control strategies is shown in Figure 11. The numerical iteration curve of the$WOA - FOPID$ fitness function is shown in Figure 11.

(1) $WE9 - 62T - HRWR160 - U - REV.D$ mathematical modeling and simulation test of the hydraulic motor

$WE9 - 62T - HRWR160 - U - REV.D$ integer order mathematical model (Dasgupta et al., 1996; Maiti et al., 2008; Long et al., 2018; Caponetto et al., 2019; Wachholz et al., 2019; Do et al., 2020):

$$G(s) = \frac{\varpi_m(s)}{U(s)} = K_\alpha \frac{K_i}{ms^2 + cs + K_s + K_y} \frac{\frac{K_q}{D_m}}{\left(\frac{s^2}{\varpi_h^2} + \frac{2\xi_h}{\omega_h} + 1\right)} = \frac{1}{2.1393 \times 10^{-7}s^4 + 4.66 \times 10^{-5}s^3 + 2.79 \times 10^{-3}s^2 + 1.42 \times 10^{-2}s + 0.61} \quad (9)$$

$WE9 - 62T - HRWR160 - U - REV.D$ fractional mathematical model of the hydraulic motor (Dimeas et al., 2017; Do et al., 2020; Ma; Higazy, 2020):

TABLE 2 Mathematical modeling parameter table of the fractional integer order of the hydraulic motor.

Symbol	Parameter meaning	Parameter value	Parameter unit
K_α	Gain of proportional amplifier	0.2	A/V
ω_n	Natural frequency of valve core	15.1	——
m	Quality of valve core armature assembly	0.5	kg
ξ	Damping ratio of valve core	0.046	——
K_s	Spring stiffness	50	N/m
c	Damping coefficient of valve core armature assembly	0.7	N/m/s
K_i	Current force gain of proportional electromagnet	3	N/A
K_y	Total spring stiffness	64	N/m
K_c	Flow pressure coefficient	1.2×10^{-11}	$m^5/(N\bullet s)$
K_q	Flow gain	2.42	m2/s
K_d	Dynamic head coefficient	0.61	——
C_{tm}	Total leakage coefficient of hydraulic motor	2.65×10^{-12}	$m^5/(N\bullet s)$
D_m	Motor displacement	1.19×10^{-4}	m^3/rad
ω_d	Hydraulic natural frequency	51	Rad/s
ζ_d	Hydraulic damping ratio	0.46	——
β_e	Effective bulk modulus of elasticity	6.9×10^8	N/m^2
V_t	Total volume of hydraulic motor and connecting pipeline	3×10^{-4}	m^3
B_m	Viscous damping coefficient of hydraulic motor and load	200	$N\bullet m\bullet s/rad$
B_e	Viscous damping coefficient of reducer	3.48	$N\bullet m\bullet s/rad$
B_d	Viscous damping coefficient of power head	983.5	$N\bullet m\bullet s/rad$
J_1	Equivalent inertia of motor shaft	15	$kg\bullet m^2$
J_e	Equivalent inertia of reducer	0.476	$kg\bullet m^2$
J_d	Equivalent inertia of power head	74	$kg\bullet m^2$
C_d	Flow coefficient of solenoid proportional directional valve	0.6	——
ρ	Hydraulic oil density	860	kg/m^3
i	Transmission ratio of reducer	4.9	——

$$G(s) = \frac{\varpi_m(s)}{U(s)} = K_\alpha \frac{K_i}{ms^2 + cs + K_s + K_y} \frac{\frac{K_q}{D_m}}{\left(\frac{s^2}{\omega_h^2} + \frac{2\xi_h}{\omega_h}s + 1\right)} = \frac{1}{2.14 \times 10^{-7}s^{3.99} + 4.66 \times 10^{-5}s^{3.0042} + 0.0028s^{1.998} + 0.0143s^1 + 0.61} \tag{10}$$

Fractional order *FOPID* controller is expressed as: (Elkhazali, 2013; Maâmar and Rachid, 2014; Tolba et al., 2018):

$$G_c = 0.487 + 5.4042s^{-0.023} + 5.4837s^{1.2908} \tag{11}$$

Integer order *PID* controller expression is: (Zamani et al., 2009; Ding et al., 2017; Ren et al., 2019).

$$G_c = 30 + 1.6952s^{-2} + 24.5197s \tag{12}$$

Respectively, four types of the intelligent control algorithm are used for parameter tuning of the *FOPID* controller—integer order parameter, the *FOPID* controller—fractional order controlled object, the *PID* controller—fractional integer order controlled object, and the *FOPID* controller—fractional integer order controlled object. From Table 3 and Figure 13, according to the results of the simulation experiments, the *PID* control is not dominant in a complex system compared to FOPID, overshoot amount at about 30%, and settling time floating around 0.7 s; According to the results of the data based on *WOA* algorithm parameters tuning of the system has a certain advantage, settling time reduced to 0.3 s.

On the whole, the *FOPID* controller has shown a better control effect on the fractional order-controlled object, and the overshoot has been reduced. According to the data results, the optimization ability of the *WOA* algorithm is obvious, which makes the controlled system have better stability. For the fractional controlled object, the stability can be achieved in 0.19s, and the overshoot is 3.49%. This fully reflects the superiority of the fractional order *FOPID* controller, as shown in Figure 13.

In response speed, adjustment time, and steady-state accuracy, the fractional order *WOA – FOPID* controller has a

TABLE 3 Hydraulic motor's parameter table.

Combinations	Dynamic indicators		
	Standard deviation	Overshoot (%)	Settling time/s
GA – FOPID -Integer order	0.05865	39	0.29
PSO – FOPID -Integer order	0.05853	38.72	0.28
GPS – FOPID -Integer order	0.0444	23.45	0.41
Optimal-*FOPID* -Integer order	0.05869	38.819	0.28
WOA – FOPID -Integer order	0.03653	15.18	0.09
GA – FOPID -Fractional order	0.03944	27.91	0.59
PSO – FOPID -Fractional order	0.0475	25.52	0.52
GPS – FOPID -Fractional order	0.04547	26.12	0.39
Optimal-*FOPID* -Fractional order	0.05803	37.67	0.28
WOA – FOPID -FrActional order	0.05529	3.49	0.19
GA – PID -Integer order	0.04421	29.59	0.7
PSO – PID -Integer order	0.04421	29.6	0.7
GPS – PID -Integer order	0.04421	29.6	0.7
Optimal-*PID* -Integer order	0.07034	53.57	0.27
WOA – PID -Integer order	0.04092	27.03	0.34
GA – PID -Fractional order	0.0448	30.7	0.67
PSO – PID -Fractional order	0.0448	30.7	0.67
GPS – PID -Fractional order	0.0448	30.7	0.67
Optimal-*PID* -Fractional order	0.07027	53.3	0.27
WOA – PID -Fractional order	0.4019	26.27	0.31

better control effect than the fractional order *GPS – FOPID* controller, integer order *GPS – PID* controller, fractional order *GA – FOPID* controller, integer order *GA – PID* controller, fractional order *PSO – FOPID* controller, integer order *PSO – PID* controller, and integer order *WOA – FD* controller. In this study, the intelligent optimized whale algorithm *WOA* is directly applied to the systematic controllers of the oil cylinder *DOA*090470 – 1 (1) and *DOA*090260 – 1 in the manipulator for parameter tuning, and the control strategies of different combinations are compared and analyzed (Table 4).

(2) Mathematical modeling and simulation test of the hydraulic cylinder *DOA*090470 – 1 (1)

The integer order mathematical model of the hydraulic cylinder *DOA*090470 – 1 (1) (Zhan et al., 2015; Dingyu, 2020):

$$G(s) = \frac{X_P}{U} = \frac{\frac{K_q}{A_p}K_i k_x}{s\left(\frac{s^2}{\omega_h^2} + \frac{2\xi_h}{\omega_h}s + 1\right)} = \frac{48.625}{s\left(3.6 \times 10^{-3}s^2 + 0.727s + 1\right)} \tag{13}$$

$$G(s) = \frac{X_P}{U} = \frac{\frac{K_q}{A_p}K_i k_x}{s\left(\frac{s^2}{\omega_h^2} + \frac{2\xi_h}{\omega_h}s + 1\right)} = \frac{48.625}{s\left(7.38 \times 10^{-4}s^{2.0214} + 1.48 \times 10^{-3}s^{0.9731} + 1.99 \times 10^{-2}\right)} \tag{14}$$

Integer order *PID* controller expression (Elkhazali, 2013; Maâmar and Rachid, 2014; Tolba et al., 2018):

$$G_c = 18.4022 + 30s^{-1} \tag{15}$$

Fractional order *FOPID* controller expression (Zamani et al., 2009; Ding et al., 2017; Ren et al., 2019):

$$G_c = 29.9442 + 29.9660s^{-0.0308} + 13.1634s^{1.104} \tag{16}$$

Figure 14 and Table 5 show that the *PID* controller is not fit in complex systems, and the results show that it fails to fulfill fine-tuning, especially as the controlled object gradually stabilizes after 6.06s when the *PID* fractional order acts. In the complex system, the *FOPID* controller has a better control effect on the fractional order controlled object, and the overshoot is 8.672%, which can be settled in 0.02s. The*DOA*090470 – 1 (1) hydraulic cylinder parameter is shown in Table 6.

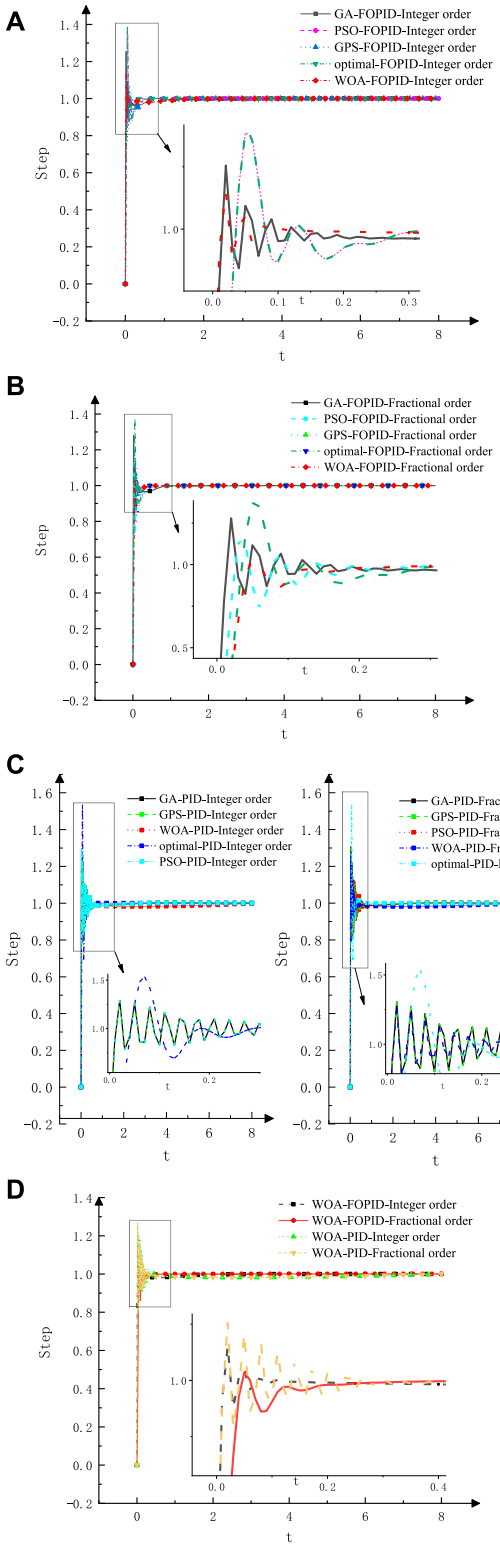


FIGURE 13
Control effect and step response of different combination strategies of the hydraulic motor. **(A)** The intelligent control

(*Continued*)

FIGURE 13 | algorithm for FOPID controller - integer order parameter setting diagram of controlled objects; **(B)** Parameter tuning diagram of FOPID controller-fractional controlled object by intelligent control algorithm; **(C)** Intelligent control algorithm PID controller - fractional integer order controlled object parameter setting diagram; **(D)** The intelligent control algorithm for FOPID controller - fractional integer order parameter setting graph of controlled objects.

(3) Mathematical modeling and simulation test of the hydraulic cylinder *DOA*090260 − 1

Integer order mathematical model of the hydraulic cylinder *DOA*090260 − 1 (Zhan et al., 2015; Dingyu, 2020):

$$G(s) = \frac{X_P}{U} = \frac{\frac{K_q}{A_p}K_i k_x}{s\left(\frac{s^2}{\omega_h^2} + \frac{2\xi_h}{\omega_h}s + 1\right)} = \frac{48.625}{s(2 \times 10^{-3}s^2 + 0.0726s + 1)} \tag{17}$$

$$G(s) = \frac{X_P}{U} = \frac{\frac{K_q}{A_p}K_i k_x}{s\left(\frac{s^2}{\omega_h^2} + \frac{2\xi_h}{\omega_h}s + 1\right)} = \frac{48.625}{s(4.11 \times 10^{-5}s^{1.9946} + 0.0015s^{0.9989} + 0.02)} \tag{18}$$

Expression of the integer order PID controller [41–43]:

$$G_c = 11.2292 + 30s^{-2} + 1.35 \times 10^{-8}s \tag{19}$$

Expression of the fractional order *FOPID* controller (Zamani et al., 2009; Ding et al., 2017; Ren et al., 2019):

$$G_c = 0.4758 + 27.2283s^{-2.5323} + 29.9673s^{1.0212} \tag{20}$$

Figure 15 and Table 7 show that the *FOPID* controller has a better control effect for fractional controlled objects, and the overshoot can reach 6.84% in 0.5s. On the whole, the *FOPID* controller is more stable than the *PID* controller, and the *PID* control strategy shows almost the same control effect, which is about 20%. In the actual support work of the manipulator, if there is an overshoot in the oil cylinder displacement control system, it will lead to the inaccurate positioning in the drilling hole, which will take more time, and even influence the effectiveness of electronic components in the manipulator. If 16 bolts need to be installed in a roadway section, the mechanical arm takes one more minute for installation of each bolt due to the overshoot, and takes another 16 min in total to complete the support work of a section. Cost function vs. iterations is plotted for the mathematical modeling and simulation tests of the hydraulic cylinder, as shown in Figure 16.

TABLE 4 Doa090470-1 (1) hydraulic cylinder parameter table.

No.	Symbol	Parameter meaning	Parameter value	Parameter units
1	X_p	Piston displacement of hydraulic cylinder	--	--
2	ω_h	Hydraulic natural frequency	16.77	*rad/s*
3	M	Total load quality	--	*Kg*
4	ξ_h	Hydraulic damping ratio	0.61	--
5	B_p	Viscous damping coefficient of load	--	--
6	k_x	Gain of Electro - hydraulic Proportional Valve	7.78×10^{-4}	--
7	K_i	Gain of proportional amplifier	0.2	---
8	K_q	Flow Gain of Hydraulic Cylinder	300	--
9	U	Potential signal	--	--
10	A_p	Effective area of piston	9.6×10^{-4}	m^3

Fractional order mathematical model of hydraulic cylinder *DOA*090470 – 1(1).

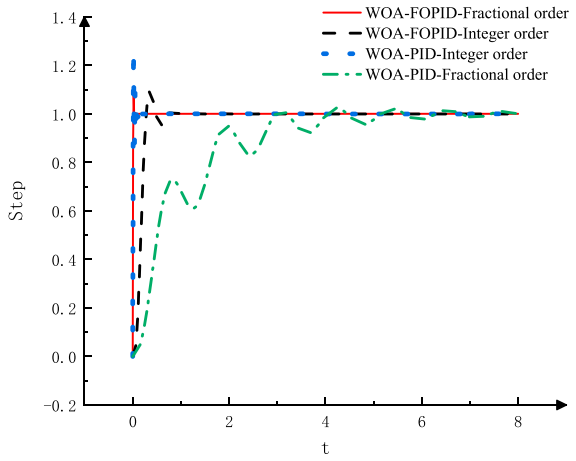


FIGURE 14
*DOA*090470 – 1(1) step response diagram of the control effect of different combination strategies of the hydraulic cylinder.

5 Experiment

In order to verify the correctness and effectiveness of the control strategy in the manipulator control system of the mining roof bolter, the ground training and industrial tests were carried out in the underground roadway, as shown in Figure 17 and Figure 18. The test platform is the underground roadway, with a section height of 2.8–4 m, a width of 3.8–5.6 m, a maximum inclination of 20°, and a maximum drilling depth of 8.3 m. All of them are in a gas-free working environment. The test lasted a total of 9 days. In the first test, there were 14 anchor cable holes of 8.3 m, with a total of 116 m; 46.3 m anchor cable holes, 25 m in total; 124 m anchor cable holes, 48 m in total. In the second test, there were 6 anchor cable holes of 4 m, with a total of 24 m; 6.3 m anchor cable holes, totaling 37 m; 122.5 m anchor cable holes, 30 m in total.

5.1 Composition of the control system

The plan of an electric–control system is shown in Figure 19. The control system adopts a modular design, and each functional module runs independently without interference, so as to avoid whole equipment paralysis due to a single failure. The electric control system can be divided into five modules: main circuit unit, power unit, protection unit, signal conditioning isolation unit, and logic control unit. The block diagram of the control system module is shown in Figure 20.

TABLE 5 Comparison of different combination strategies and control indexes of the *DOA*090470 – 1(1) hydraulic cylinder.

Combination	Dynamic indicators		
	Standard deviation	Overshoot (%)	Settling time/s
WOA – FOPID -Integer order	0.1307	9.5	0.68
WOA – FOPID -Fractional order	0.03571	8.672	0.02
WOA – PID -Integer order	0.03753	25.78	0.09s
WOA – PID -Fractional order	0.2206	2.5	6.06s

TABLE 6 *DOA*090470 – 1(1) hydraulic cylinder parameter table.

No	Symbol	Parameter meaning	Parameter value	Parameter units
1	ω_h	Hydraulic natural frequency	22.6	
2	ς_h	Hydraulic damping ratio	0.82	
3	A_p	Effective area of piston	9.6×10^{-4}	m^3
4	V_t		2.5×10^{-4}	
5	K_x	Gain of electro-hydraulic proportional valve	300	
6	K_q	Flow Gain of Hydraulic Cylinder	7.78	
7	K_i	Gain of proportional amplifier	0.2	
8	M	Total load quality	2×10^4	kg

Fractional order mathematical model of hydraulic cylinder *DOA*090260 – 1 .

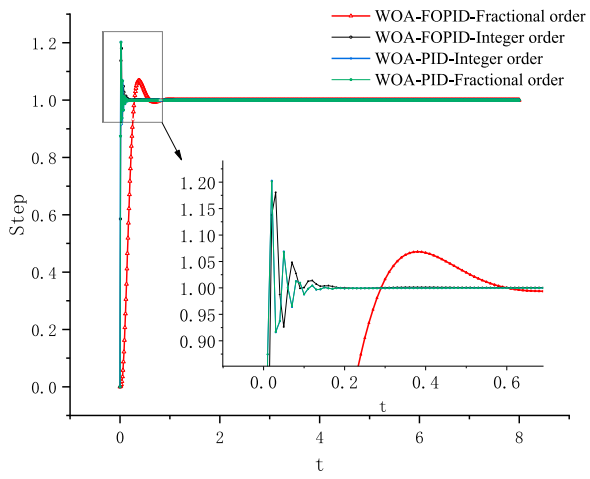


FIGURE 15
WOA-FOPID–fractional transfer function unit step diagram.

The main circuit module defines the main structure of the system, and the isolation switch is applied as the switch of the main circuit power supply of the electrical control box to control the oil pump circuit. In terms of control, a vacuum contactor is used in the oil pump circuit, and installed the resistance and capacitance absorption device, to absorb the high voltage generated by the motor in the vacuum contactor disconnection. There are three current transmitters on the cables of each circuit to complete the acquisition of analog quantity.

The power module is mainly composed of a main transformer and four air circuit breakers. The main transformer has three voltage ranges of the input tap: 1,250, 1,140, and 1,025 V. When the voltage is unstable in the coal mine, the transformer tap can be adjusted with the voltage change to ensure the stability of the output voltage, and then ensure the reliability of the control loop. A 24 V tap provides power for the lamp, 220 V for the contactor coil and power modules, and 127 V for the intrinsic safe power supply.

The short-circuit protection of the main circuit and the transformer circuit is realized by a circuit breaker. The motor over-current, overload, and phase break of each driving mechanism are prevented by the *PLC* controller. Leakage locking, leakage monitoring, and overheating are prevented by using an integrated protector. Signal acquisition of the main circuit and the control circuit by a current transmitter and protection unit on each branch cable is processed and judged by an electronic circuit and controller program.

The signal isolation module and the signal conversion module together constitute the signal conditioning isolation module. The isolation module realizes the conversion of (non) intrinsic safety signal, the input and output of various controllers and peripheral devices in the control system. The logic control

TABLE 7 Comparison of different combination strategies and control indicators.

Combination	Dynamic indicators		
	Standard deviation	Overshoot (%)	Settling time/s
WOA – FOPID-Integer order	0.03923	18.04	0.09
WOA – FOPID-Fractional order	0.1247	6.84	0.5
WOA – PID-Integer order	0.03663	20.3	0.09
WOA – PID- Fractional order	0.0366	20.12	0.09

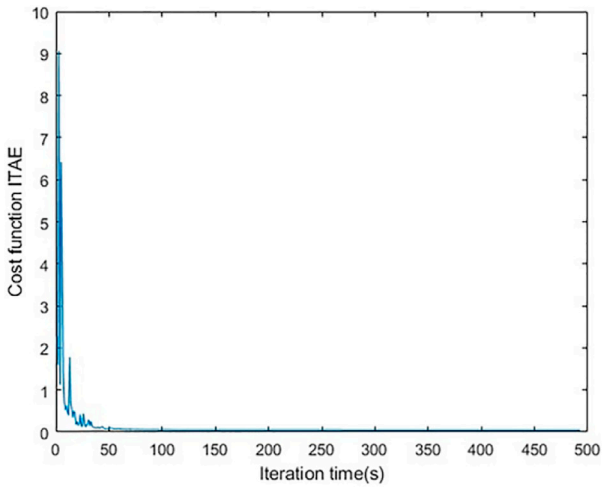


FIGURE 16
Cost function vs. iterations.



FIGURE 17
Ground experiment.

unit is the core part of the entire electrical system, which can complete various protection functions and communication functions of the motor, and also realize the corresponding

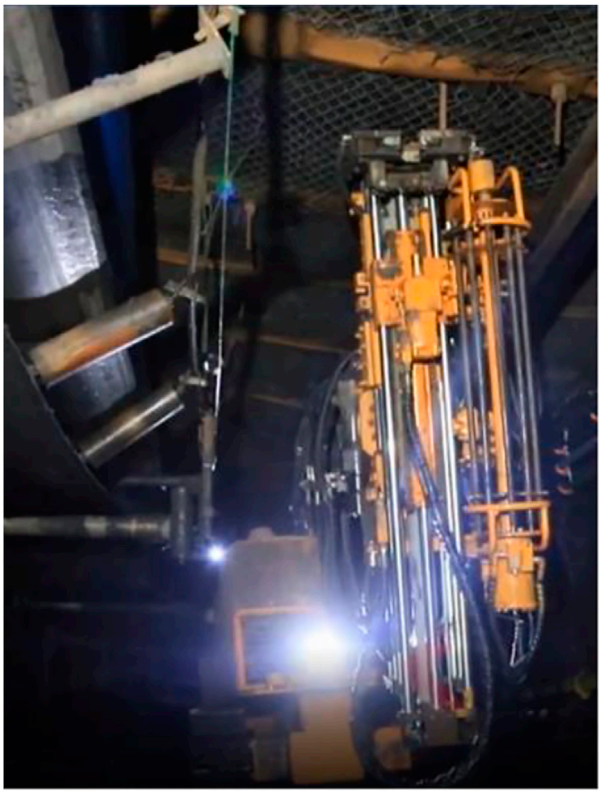


FIGURE 18
Downhole experiment.

control functions: the actual running state of each motor is judged through the calculation and processing of the collection parameters of the system; if a fault occurs, appropriate trip instructions are issued according to the type of fault.

5.2 Hardware structural design of the control system

The control cabinet consists of a PLC controller module, HMI module, and a receiver module. Each working condition monitoring unit and input/output driving unit cooperate with each other to ensure the stable operation of each control function of the system. The hardware structure block diagram of the control system is shown in Figure 19. Digital input drive unit, analog input drive unit, and the antenna are the control center of the main input module, in which the knob and switch sensor units input information to the digital input drive unit; the handle potentiometer and analog sensor input information to the analog input drive unit; the remote transmitter inputs information to the receiver module through the antenna. The digital output drive unit comprises of a light, an indicator light, and a switching electro-magnetic valve; the analog output drive unit

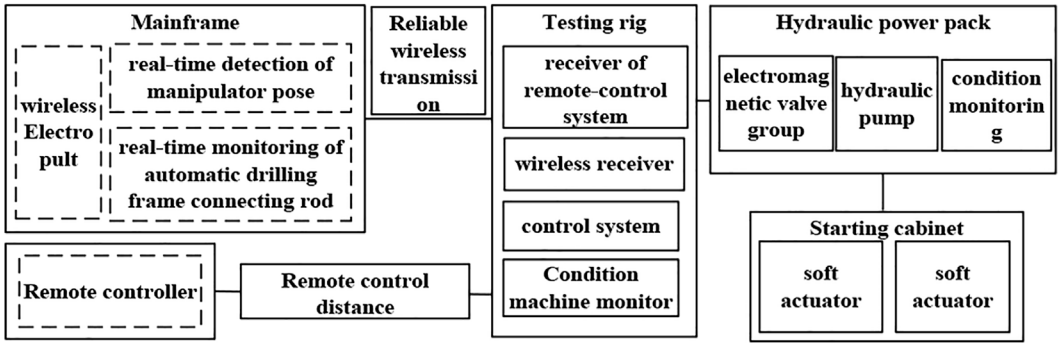


FIGURE 19
General scheme of an electric control system for the mining roof bolter.

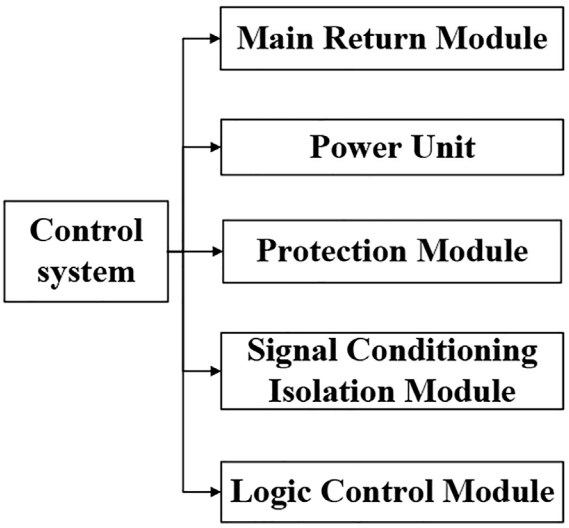


FIGURE 20
Composition of a control system module.

includes a variable pump and a proportional electro-magnetic valve. The hardware structural block diagram is shown in Figure 21. In addition, this study carried out the design of the power circuit and selection of the main components.

5.3 Control system software composition

The software system is composed of an operation signal processor, video signal processor, fault information alarm software, equipment parameter setting software, data display and analysis software, data storage and analysis software, and signal output control software. Its structural block diagram is shown in Figure 22.

5.4 Control principle

The electronic control system adopts the Siemens 200 series *PLC* host and its corresponding expansion module (analog output/input), and communicates with the remote control receiving unit through the *PLC* host's own *RS*485 communication interface (*Modbus* · *RTU*) , so as to precisely conduct motions, such as pump motor start and stop, large manipulator movements, expansion of the front and rear top tightening cylinders, forward and reverse rotations of the rotary motor, cylinder's forward and backward, horizontal rotary positively and negatively, vertical rotary positively and negatively, adjustment of the oil cylinder, cylinder of gripper opening and closing, upper rod of manipulator sending, opening and closing of manipulator, drilling rod storeroom forward and reversing rotary, pin hydraulic cylinder opening and closing, water valve opening and closing, detection and protection of the hydraulic system through the acquisition of oil tank temperature and hydraulic system pressure sensor signals, and the display on the remote transmitter screen through *RS*485 communication. A position sensor is installed to detect the position of the mainframe and the drilling rod store to ensure the precision control of automatic drilling/un-drilling. Motor intelligent integrated protector can display the real-time voltage and current of the system, with protection functions avoiding over voltage, under voltage, overload, short circuit, circuit break, phase break, leakage, display, and store alarm fault in real time. A proportional electro-hydraulic valve can adjust the hydraulic valve opening and pressure value through the *PWM* output signal of the *PLC* analog expansion module and proportional amplifier. Manual/automatic control of a locomotive can be realized by an internal ladder diagram program operation. Automatic control adopts the one-button operation, where the equipment can automatically complete the drilling/un-drilling process and have the suspension function and the one-button emergency stop function for the operator to deal with the emergency situation in the process of an automatic operation.

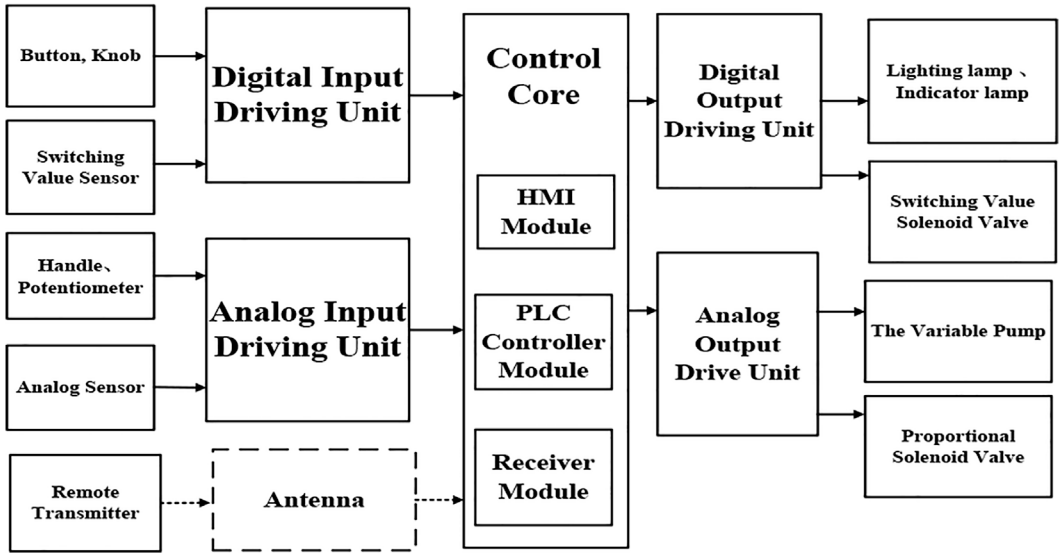


FIGURE 21
Hardware structure block diagram of the control system.

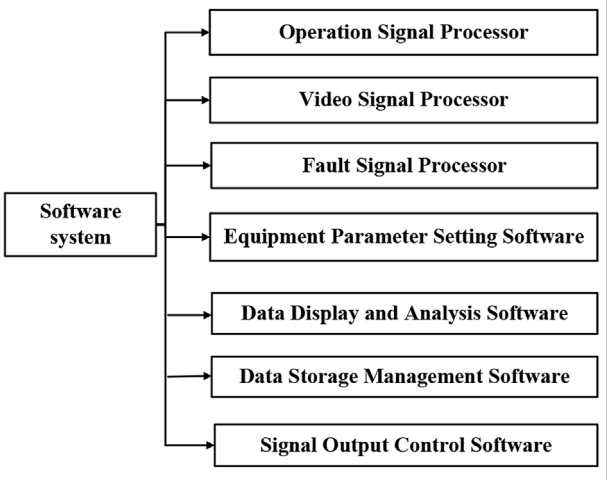


FIGURE 22
Control software and hardware structures' block diagrams.

5.5 Implementation plan

A hydraulic anchor rod drill truck was carried out to the ground training drill from August 22 to August 23,2019, arrived to the coal mine on August 24, on August 25, in 11,505W, the transport lane carried out an industrial test, on August 26 implemented fire debugging, operation, and on August 28 began an advanced supporting anchor cable test behind the excavator. The periodic summary is as follows:

As of September 9, 38 holes were drilled, among which 35 were anchored, 3 holes were drilled during the test, respectively 3.0, 5.0, and 5.5 m, without anchoring.

With a 6.3 m grouting anchor, it takes about 4 min on average to move forward to adjust the position of the drill truck, 14 min on average to drill, 8 min on average to withdraw the drill, 4 min on average to install the anchor cable, and 30 min on average in total. Fourteen representative boreholes in the early experimental period were selected for analysis, as follows in Table 8.

According to the experimental conclusions:

(1) After the control system design is completed, it is debugged and applied on the roof bolter. The control system realizes the remote pump station start–stop control, hydraulic cylinder position control, and meets the requirements of the process operation. The experiment proves that the $WOA-FOPID$ control strategy in an electro-hydraulic drive control system of effectiveness. The control strategy can make the electric hydraulic drive control in good real-time performance, accuracy, and rapidity. The manipulator can achieve high precision control in the underground roadway and can be used as a new control method for roof bolter.
(2) The automatic support system of the manipulator of the mining roof bolter breaks through the technology of automatic transportation of anchoring agents and the technology of transportation bolts and cables, and realizes a real automatic support working line without man-made

TABLE 8 Test record of the anchor rod drill truck.

Times	Drilling time	Undrilling time	Anchor installation	Truck moving	Total minutes
1	10:25–10:42	10:42–10:55	10:55–11:01	11:01–11:06	41
2	9:35–10:05	10:05–9:43	9:43–9:48	9:48–9:52	37
3	9:15–9:31	9:31–9:43	9:43–9:48	9:48–9:52	37
4	12:22–12:39	12:39–12:49	12:51–12:56	12:58–13:04	38
5	9:32–9:46	9:46–9:54	9:54–9:58	9:59–10:03	30
6	10:31–10:48	10:48–11:03	11:03–11:06	11:07–11:50	39
7	11:18–11:31	11:31–11:39	11:39–11:43	11:44–11:50	31
8	11:57–12:10	12:10–12:18	12:18–12:23	12:23–12:28	31
9	12:47–13:00	13:00–13:14	13:17–13:20	13:20–13:24	34
10	13:44–1:59	13:50–14:08	14:08–14:12	Stop	28
11	10:50–11:08	11:08–11:15	13:34–13:38	11:18–11:20	30
12	11:21–12:56	12:56–13:05	13:05–13:09	12:38–12:42	81
13	12:42–12:56	12:56–13:05	13:05–13:09	13:15–13:20	32
14	13:25–13:40	13:40–13:52	13:52–13:54	Stop	29

interference. The manipulator can automatically drill bolt holes, cable holes, cut top holes, coal powder detection holes, water injection holes, and 360° all-round drilling. In the later stage, the automatic support working line can be combined with the automatic tunneling cutting, and the unmanned driving face can be built.

6 Conclusion

To find whether the mining roof bolter can realize precise hole positioning, in a complex environment, this article uses *FOPID* control fine-tuning features in a non-linear control object, proposes a method based on the whale algorithm (*WOA*) for *FOPID* parameter tuning. Through establishing the electro-hydraulic coupling model of the hydraulic motor and hydraulic cylinder at four joints of the manipulator of the mining roof bolter and the simulation analysis in *Matlab/Simulink* , the following conclusions can be obtained:

(1) From the model built from *Matlab/Simulink* and the objective function *WOA* numerical iteration process, it can be found that the *WOA* has good optimization ability and convergence performance, which verifies the excellent performance of *WOA* in the control parameter tuning. The *WOA – FOPID* control strategy has a certain anti-interference performance, and can be timely corrected when the electro-hydraulic coupling model of the manipulator is disturbed, so that all parameters can fluctuate in a small range, which has a good engineering application prospect.

(2) The effectiveness of the *WOA – FOPID* control strategy in the electro-hydraulic drive control system can be verified by the industrial test on the mining roof bolter. The control strategy can make the electro-hydraulic drive control in good real-time performance, accuracy, and rapidity.

Data availability statement

The original contributions presented in the study are included in the article/supplementary material; further inquiries can be directed to the corresponding author.

Author contributions

Writing the original draft, ZJ; Funding acquisition, ZJ; Data curation, WY, CL, WN, BY, and WC. All authors have read and agreed to the published version of the manuscript.

Funding

The author wishes to thank the Youth fund of National Natural Science Foundation of China (No. 52104165), Free exploration general fund of Shanxi Provincial Department of science and technology (No: 20210302123123), State Key Laboratory of robotics and systems (No.SKLRS-2021-KF-16).

Conflict of interest

ZJ was employed by China Coal Science and Industry Group Co., Ltd. and Ningxia Tiandi Benniu Industrial Group Co., Ltd. CL, WN, and BY were employed by China Coal Science and Industry Group Co., Ltd. The remaining authors declare that the research was conducted in the absence of any commercial or financial relationships that could be construed as a potential conflict of interest.

Publisher's note

All claims expressed in this article are solely those of the authors and do not necessarily represent those of their affiliated organizations, or those of the publisher, the editors, and the reviewers. Any product that may be evaluated in this article, or claim that may be made by its manufacturer, is not guaranteed or endorsed by the publisher.

References

Al-Saggaf, U., Mansouri, R., Bettayeb, M., Mehedi, I. M., and Munawar, K. (2020). Robustness improvement of the fractional order LADRC scheme for integer high order system, IEEE Transactions on Industrial Electronics (ISSN:0278-0046), 99. IEEE, 1. doi:10.1109/TIE.2020.3016258

Author Anonymous State Administration of coal mine safety Key R & D catalogue of coal mine robot [Z] Announcement No. 1, 2019.

Bushnaq, S., Saeed, T., Torres, D. F. M., and Zeb, A. (2021). Control of COVID-19 dynamics through a fractional-order model. *Alexandria Eng. J.*, 3587–4359. (ISSN.1110-0168). doi:10.1016/j.aej.2021.02.022

Caponetto, R., Machado, J. T., Murgano, E., and Xibilia, M. G. (2019). Model order reduction: A comparison between integer and non-integer order systems approaches. *Entropy* 9, 876. (ISSN:1099-4300) 21. doi:10.3390/e21090876

Chen, Wei, Yu, Y, and Zhao, X (2013). Position control strategy and experimental research of 2R underactuated planar flexible manipulators. *J. Mech. Eng.* 49 (23), 80. (ISSN:1823-5514). doi:10.3901/jme.2013.23.080

Cuong, H. M., Quoc Dong, H., Trieu, P. V., and Tuan, L. A. (2020). Adaptive fractional-order terminal sliding mode control of rubber-tired gantry cranes with uncertainties and unknown disturbances. *Mech. Syst. Signal Process.* 154, 107601. (ISSN:0888-3270). doi:10.1016/j.ymssp.2020.107601

Dalir, M., and Bigdeli, N. (2020). The design of a new hybrid controller for fractional-order uncertain chaotic systems with unknown time-varying delays. *Appl. Soft Comput.* 87, 106000. doi:10.1016/j.asoc.2019.106000

Dasgupta, K., Mukherjee, A., and Maiti, R. (1996). Modeling and dynamics of epitrochoid generated orbital rotary piston lsht hydraulic motor: A bondgraph approach. *J. Manuf. Sci. Eng.* 118, 415–421. doi:10.1115/1.2831046

Dimeas, I., Petras, I., and Psychalinos, C. (2017). New analog implementation technique for fractional-order controller: A dc motor control. *AEU - Int. J. Electron. Commun.* 78, 192–200. doi:10.1016/j.aeue.2017.03.010

Ding, Y., Xu, J., Cao, J., and Zhang, D. (2017). Mathematical modeling about nonlinear delayed hydraulic cylinder system and its analysis on dynamical behaviors. *Discrete Cont. Dyn. S* 10 (5), 943–958. doi:10.3934/dcdss.2017049

Dingyu, P. X. (2020). *Lecture hall Volume 4 MATLAB optimization calculation [M*. Beijing: Tsinghua University Press.

Do, T. C., Trần, T. D., Dinh, T. Q., Ahn, K. K., et al. (2020). Tracking control for an electro-hydraulic rotary actuator using fractional order fuzzy PID controller. *Electronics*, 926. (ISSN:2079-9292) 9.6. doi:10.3390/electronics9060926

Elkhazali, R. (2013). *Fractional-order PI λD controller design[M]*. Pergamon Press.

Feng, G.-L., Chen, B.-R., Xiao, Y.-X., Jiang, Q., Li, P.-X., Zheng, H., et al. (2022). Microseismic characteristics of rockburst development in deep tbm tunnels with alternating soft-hard strata and application to rockburst warning: A case study of the neelum-jhelum hydropower project. *Tunn. Undergr. Space Technol.* 122, 104398. doi:10.1016/j.tust.2022.104398

Feng, G.-L., Feng, X.-T., Chen, B.-r., Xiao, Y.-X., and Yu, Y. (2015). A microseismic method for dynamic warning of rockburst development processes in tunnels. *Rock Mech. Rock Eng.* 48 (5), 2061–2076. doi:10.1007/s00603-014-0689-3

Ge, S., and Hu, P. W (2020). Coal mine robot system and key technology. *J. coal* 45 (01), 455–463. (ISSN: 0166-5162).

Higazy, M. (2020). Novel fractional order SIDARTHE mathematical model of COVID-19 pandemic. *Chaos, Solit. Fractals* 138, 110007. ISSN:0960-0779. doi:10.1016/j.chaos.2020.110007

Huang, S., Wang, J., Huang, C., Zhou, L., Xiong, L., Liu, J., et al. (2022). A fixed-time fractional-order sliding mode control strategy for power quality enhancement of PMSG wind turbine. *Int. J. Electr. Power & Energy Syst.* 134, 107354. (ISSN:0142-0615). doi:10.1016/j.ijepes.2021.107354

Jing, X, and pan, X. W (2018). Fuzzy PID *attitude* control of pesticide spraying four axis aircraft. *J. drainage irrigation Mech. Eng.* 36 (5), 7. doi:10.3969/j.issn.1674.8530.17.0187

Kang, H. P. (2007). *Wang Jinhua Roadway bolt support theory and complete set of technology [M]*. Beijing: Coal Industry Press.

Li, F., Hu, J., and Zhang, D. R. (2019). Development and application status and trend of coal mine robot. *China coal.*. 045 (007), 28–32. doi:10.19880/j.cnki.ccm.2019.07.005

Li, R., Cao, J., Xue, C., and Manivannan, R. (2021). Quasi-stability and quasi-synchronization control of quaternion-valued fractional-order discrete-time memristive neural networks. *Appl. Math. Comput.* 395, 125851. (ISSN:0096-3003). doi:10.1016/j.amc.2020.125851

Li, Z, and Xing, l (2007). Submarine robot automatic tracking scheduled mining path control. *J. Mech. Eng.* 43 (1), 6. doi:10.3321/j.issn:0577-6686.2007.01.025

Liu, F., Cao, W., and Zhang, J. (2021). Scientific and technological innovation progress of China's coal industry and the development direction of the 14th five year plan. *J. coal* 46 (1), 1–15. doi:10.13225/j.cnki.jccs.2021.0042

Long, Z-M., Guan, B-J., Chen, S-Y., Chen, G-J., and Guo, S-Q. (2018). "Modeling and simulation of hydraulic motor tracking servo motor driving load," in ICSGEA, 118–121. doi:10.1109/icsgea.2018.00037

Luo, Y, Du, L, Zhou, S, and Luo, K (2021). Simulation *research* on electro-hydraulic proportional position control system of blanking based on fuzzy PID. *Mach. tool hydraulic*. doi:10.3969/j.issn.1001-3881.2021.22.030

Ma, F. *Research on Modeling and control of single-phase PWM rectifier based on fractional order*. Zhengzhou: Henan University of technology.

Maâmar, B., and Rachid, M. (2014). IMC-PID-fractional-order-filter controllers design for integer order systems. *ISA Trans.* 53, 1620–1628. 0019-0578*)* 53. doi:10.1016/j.isatra.2014.05.007

Maiti, D., Biswas, S., and Konar, A. (2008). Design of a fractional order PID controller using particle swarm optimization technique. *Int. J. Adv. Manuf. Technol.*, 521–531. *ISSN:0268-3768)* 58.5-8.

Musarrat, M. N., and Fekih, A. (2021). A fractional order sliding mode control-based topology to improve the transient stability of wind energy systems. *Int. J. Electr. Power & Energy Syst.* 133, 107306. (ISSN:0142-0615). doi:10.1016/j.ijepes.2021.107306

Nguyen, D., Bao, D. L., and Choi, S-B. (2021). Smart dampers-based vibration control–Part 2: Fractional-order sliding control for vehicle suspension system. *Mech. Syst. Signal Process.* 148, 107145. (ISSN:0888-3270). doi:10.1016/j.ymssp.2020.107145

Podlubny, I. (1999). Fractional-order systems and PI/sup/spl lambda//D/sup/spl mu//-controllers. *IEEE Trans. Autom. Contr.* 44, 208–214. doi:10.1109/9.739144

Ren, H. P., Fan, J. T., and Kaynak, O. (2019). "Optimal design of a fractional-order proportional-integer-differential controller for a pneumatic position servo system," in IEEE Transactions on Industrial Electronics (IEEE). (ISSN:0278-0046). doi:10.1109/TIE.2018.2870412

Semmari, H., Mauran, S., and Stitou, D. (2017). Experimental validation of an analytical model of hydraulic motor operating under variable electrical loads and pressure heads. *Appl. Energy* 206, 1309–1320. (ISSN:0306-2619). doi:10.1016/j.apenergy.2017.10.010

Sheng, Y., Bai, W., and Xie, Y. (2021). Fractional-order $$PI{\\lambda D$$ sliding mode control for hypersonic vehicles with neural network disturbance compensator. *Nonlinear Dyn.* 103 (3). (ISSN:0924-090X). doi:10.1007/s11071-020-06046-y

Tolba, M. F., AboAlNaga, B. D. M., Said, L. A., Madian, A. H., and Radwan, A. G. (2018). Fractional order integrator/differentiator: FPGA implementation and

FOPID controller application. *AEU - Int. J. Electron. Commun.* 98, 220–229. doi:10.1016/j.aeue.2018.10.007

Wachholz, L. C., Valdiero, A. C., and Rasia, L. A. . "Mathematical modeling of a hydraulic motor operated and controlled by proportional valve." COB2019 2019. doi:10.26678/ABCM.COBEM2019.COB2019-2272

Wang, G., Liu, F., Pang, Y., Ren, H., and Ma, Y. (2019). Coal mine intelligence -- the core technical support for the high-quality development of coal industry. *J. coal* 44 (02), 349–357. (ISSN: 0166-5162).

Wang, G., Wang, H., and Ren, H. (2018). Scenario objectives and development path of smart coal mine 2025. *J. coal* 43 (02), 295–305. doi:10.13225/j.cnki.jccs.2018.0152

Wang, H., Wang, J., and Zhang, X. (2020). Theory and technology of integrated and efficient excavation with excavation and anchor. *J. coal* 45 (6), 2021–2030. (ISSN: 0166-5162).

Wu, X., and Huang, Y. (2021). Adaptive fractional-order *non*-singular terminal sliding mode control based on fuzzy wavelet neural networks for omnidirectional mobile robot manipulator - ScienceDirect. *ISA Trans.* 121, 258–267. doi:10.1016/j.isatra.2021.03.035

Yang, Y., Zhao, D-C., Feng, G-L., Geng, D-X., and Guo, H-S. (2022). Energy evolution and acoustic emission characteristics of uniaxial compression failure of anchored layered sandstone. *Front. Earth Sci.* 10, 841598. doi:10.3389/feart.2022.841598

Yin, C., Chen, Y. Q., and Zhong, S. M. (2014). Fractional-order sliding mode based extremum seeking control of a class of nonlinear systems. *Automatica* 50 (3), 3173–3181. doi:10.1016/j.automatica.2014.10.027

Yin, C., Chen, Y. Q., and Zhong, S. M. (2014). Fractional-order sliding mode based extremum seeking control of a class of nonlinear systems. *Automatica* 50 (12), 3173–3181. (ISSN:0005-1098). doi:10.1016/j.automatica.2014.10.027

Zamani, M., Karimi-Ghartemani, M., Sadati, N., and Parniani, M. (2009). Design of a fractional order PID controller for an AVR using particle swarm optimization. *Control Eng. Pract.* 17 (12), 1380–1387. (ISSN:0967-0661). doi:10.1016/j.conengprac.2009.07.005

Zhan, C, Deng, J, and Chen, K (2015). Research on low friction high frequency response variable clearance sealed hydraulic cylinder. *J. Mech. Eng.* 51 (24), 7–5. doi:10.3901/JME.2015.24.161

Zhang, J, and Li, Y (2019). Kinematic error analysis of mechanical arm of roof bolter with uncertain parameters. *J. coal* 44 (10), 3223–3232. (ISSN: 0166-5162).

Zhang, J, Zhang, Q. G., and Zhifu, U (2019). Dynamic uncertainty analysis of mechanical arm of mine roof bolter. *J. coal* 44 (S1), 351–360. (ISSN: 0166-5162).

Zhang, T, Li, G, and Liang, L (2002). Switching variable structure *control* of flexible manipulator with acceleration feedback. *J. Mech. Eng.* 38 (3), 4. doi:10.3321/j.issn:0577-6686.2002.03.009

frontiers | Frontiers in Earth Science

TYPE Original Research
PUBLISHED 12 August 2022
DOI 10.3389/feart.2022.933286

Check for updates

OPEN ACCESS

EDITED BY
Fengqiang Gong,
Southeast University, China

REVIEWED BY
Wenzheng Yue,
China University of Petroleum, China
Ahmed Reda,
Curtin University, Australia

*CORRESPONDENCE
Jinchao Wang,
jcwang@whrsm.ac.cn

SPECIALTY SECTION
This article was submitted to Geohazards and Georisks, a section of the journal Frontiers in Earth Science

RECEIVED 30 April 2022
ACCEPTED 27 June 2022
PUBLISHED 12 August 2022

CITATION
Wang J, Wang C, Huang J, Han Z, Zeng W and Wang Y (2022), In situ stress measurement method of deep borehole based on multi-array ultrasonic scanning technology. *Front. Earth Sci.* 10:933286. doi: 10.3389/feart.2022.933286

COPYRIGHT
© 2022 Wang, Wang, Huang, Han, Zeng and Wang. This is an open-access article distributed under the terms of the Creative Commons Attribution License (CC BY). The use, distribution or reproduction in other forums is permitted, provided the original author(s) and the copyright owner(s) are credited and that the original publication in this journal is cited, in accordance with accepted academic practice. No use, distribution or reproduction is permitted which does not comply with these terms.

In situ stress measurement method of deep borehole based on multi-array ultrasonic scanning technology

Jinchao Wang[1]*, Chuanying Wang[1], Junfeng Huang[2], Zengqiang Han[1], Wenhao Zeng[2] and Yiteng Wang[1]

[1]State Key Laboratory of Geomechanics and Geotechnical Engineering, Institute of Rock and Soil Mechanics, Chinese Academy of Sciences, Wuhan, China, [2]Emergency Surveying and Mapping Support Center, Hubei Provincial Department of Natural Resources, Wuhan, China

In order to improve the accuracy and efficiency of deep *in-situ* stress measurement, based on the wall collapse in deep borehole, a deep borehole *in-situ* stress measurement method based on multi-array ultrasonic scanning technology is proposed in this paper. The solution idea of using the combination of multiple elements for borehole contour scanning is put forward, and a multi-array ultrasonic scanning technology suitable for fine horizontal section scanning of deep geological borehole contour is formed. Through the analysis of the calculation principle of hole wall caving method and the derivation of multi-array element ultrasonic scanning solution algorithm, a multi-array ultrasonic scanning device is developed by using the effective fusion of multi-array ultrasonic full waveform scanning signals and the reconstruction of horizontal section contour. The measurement method of *in-situ* stress in deep borehole combined with hole wall caving method is studied. Finally, the feasibility and accuracy of this method are verified by physical experiments. The results show that: the effective fusion of multi-array ultrasonic full waveform scanning signals and horizontal section contour reconstruction can break through the limitations of conventional in borehole probe placement and in borehole medium sound velocity calibration, and improve the fine reconstruction and accurate measurement of 360° wall shape. The multi-array ultrasonic scanning technology can obtain the borehole shape data at any borehole depth, and then obtain the three-dimensional shape measurement of borehole wall, which can provide a new technical means for the three-dimensional detection of borehole wall and *in-situ* stress measurement.

KEYWORDS

deep *in-situ* stress, multi-element ultrasound, hole wall profile, borehole survey, ultrasonic scanning

Introduction

With the increasing scale and depth of rock engineering, the problems of rock mechanics are diversified and complex, which puts forward higher requirements for the discipline of rock mechanics. It is necessary to further carry out basic theoretical research, improve and develop theoretical methods and test means, so as to better solve the problems of rock engineering. *In situ* stress is the natural stress that exists in the Earth's crust and is not disturbed by engineering. It is also known as the initial stress, absolute stress or original rock stress of rock mass. In a broad sense, it also refers to the stress in the Earth's body. It includes stresses caused by geothermal, gravity, changes in the Earth's rotation speed and other factors. Initial *in-situ* stress, absolute stress or original rock stress are important factors affecting the stability of rock mass surrounding rock. They are not only the main controlling factors affecting the mechanical behavior of rock mass, but also one of the main force sources causing rock mass deformation and failure. The reasons for the formation of *in-situ* stress are complex and diverse. It is generally believed that it is the result of the self weight of rock mass and the development of previous tectonic movements of the Earth plate. At the same time, it is also affected by the environment in which it occurs, such as lithology, topography, faults and fractures. *In situ* stress is an important basic data for the stability design of mining, power station, tunnel and other projects, and it is also one of the most important factors to consider in the excavation design and stability analysis of underground space. Therefore, *in situ* stress parameters have become very important in the excavation of deep underground projects (Bai et al., 2018; Ji 2009; Sun et al., 2020; Wang and Wang 2017).

With the deepening of seismic exploration and mining engineering research, the Ministry of oil and gas exploration and scientific research will continue to point to more and more important targets. At present, deep *in-situ* stress measurement mainly adopts hydraulic fracturing, hole wall caving method and differential strain method based on core measurement. Various methods have advantages and disadvantages (Han et al., 2018). Among them, borehole wall caving method is to analyze the magnitude and direction of *in-situ* stress according to the caving characteristics of borehole wall rock. Borehole caving analysis, as a part of comprehensive stress estimation, has become a routine work of continental deep drilling plan (Amadei and Stephansson, 1986; Zoback et al., 1985). In 1964, R. Leeman found the phenomenon of hole wall breakage in the drilling of gold mine at a depth of 2000 m in South Africa, and had the trend of collapse in the dominant direction. He pointed out that this collapse was the result of compressive stress, which opened the precedent of *in-situ* stress measurement by hole wall caving method (Leeman, 1964). D. I. Gough and J. S. bell studied the mechanical mechanism of hole wall collapse, pointed out that this is the result of rock shear fracture caused by stress concentration around the hole wall, and elaborated the principle of *in-situ* stress measurement of hole wall collapse method (Gough and Bell 1982). Therefore, the key of hole wall caving method is how to correctly observe the parameters of hole wall caving, such as orientation, shape, width and depth, and then infer the magnitude and direction of horizontal principal stress.

Ultrasonic borehole television is one of the commonly used hole wall caving measurement methods. It uses the principle of ultrasonic scanning imaging to reconstruct the hole wall image. By analyzing the image, it can roughly judge the shape, orientation, width and other parameters of the caving position. Through these parameters, the direction of horizontal principal stress can be calculated, but this method still belongs to hole wall plane imaging, and there is a certain error in judging the hole wall caving phenomenon, Moreover, the depth of hole wall collapse cannot be measured (Deng et al., 2011; Schuette et al., 2010; Uhlmann and Sammler 2010). At the same time, the probe in the hole usually swings, resulting in the probe not centered, which affects the ultrasonic imaging effect. In view of the above problems, this paper proposes a multi-array element ultrasonic scanning technology, which makes full use of the scanning data of the borehole wall obtained by multiple ultrasonic transducer arrays, weakens the signal interference caused by the non centering of the probe, provides the imaging quality of the horizontal section contour of the borehole wall, and realizes the high-precision measurement of the borehole contour. Multi-array ultrasonic scanning technology can not only measure the orientation and width of hole wall collapse, but also measure the depth and borehole shape of hole wall collapse. The measurement results can be used for *in-situ* stress calculation of hole wall collapse method. Theoretically, the rock mass stress measurement method proposed in this paper will not be limited by the measurement depth. It will provide a new method and way for *in-situ* stress measurement, especially deep *in-situ* stress measurement, and can fully meet the needs of *in-situ* stress measurement of deep rock mass in Continental Scientific Drilling Program.

Multi-array ultrasonic scanning technology

Multi-array ultrasonic scanning system

According to the hardware structure of multi-array element ultrasonic scanning system, it mainly includes probe, transmission cable, depth encoder, cable winch, orifice support, integrated control box, communication cable, computer, etc. The probe is used to acquire the contour information of the hole wall in the borehole, and the transmission cable is used to realize the data communication between the ground and underground in real time. The probe is vertically suspended in the borehole through the transmission cable, and the depth encoder is placed at the borehole orifice and

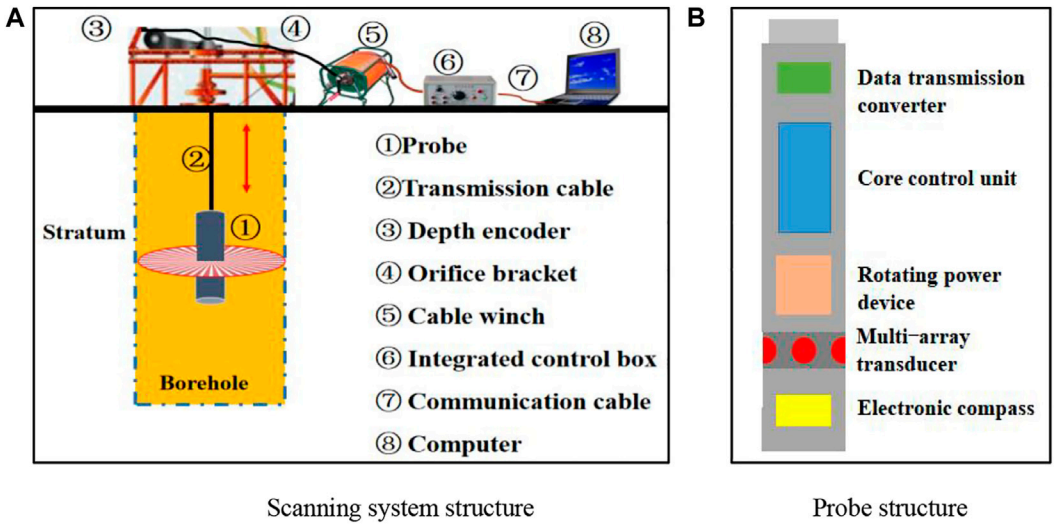


FIGURE 1
System structure.

fixed on the orifice support. The encoder is used to record the detection depth in real time. The transmission cable passes through the depth encoder and is connected with the cable winch to realize the lifting or lowering of the optical fiber cable through the cable winch. The transmission cable is connected to the integrated control box to complete the coding and interpretation of the signal. The signal is transmitted through the communication cable and enters the computer to realize the real-time processing, display and storage of data. The structural diagram of the scanning system is shown in Figure 1A. The probe is the core component of the whole system. The probe is mainly composed of data transmission converter, core control unit, rotating power unit, multi-array transducer and electronic compass. The structural composition diagram of the probe is shown in Figure 1B.

Multi-array ultrasonic scanning technology realizes the high-precision measurement of borehole contour by making full use of the borehole wall scanning data obtained by multiple ultrasonic transducers. The basic working principle of this technology: Firstly, the multi-array element ultrasonic probe is lowered to a certain height in the borehole. Driven by the transmitting device, the multi-array element ultrasonic probe transmits ultrasonic waves to the rock wall of the borehole along the direction of various probes, and the multi-channel ultrasonic signals propagate in the fluid medium in the borehole. When the ultrasonic signal is transmitted to the borehole wall, acoustic reflection will occur at the borehole wall due to the obvious difference in the acoustic impedance of the medium inside and outside the rock wall. The receiving device of the multi-array ultrasonic probe obtains the ultrasonic reflection signal received in the corresponding direction. Then, the acoustic electric signal conversion device inside the probe converts the received acoustic signal into an electrical signal and uploads it to the ground data processing and storage device. The data processing and storage device forms the acoustic image corresponding to the borehole wall according to the characteristics of the ultrasonic wave. The rotating device drives the multi-array ultrasonic probe to rotate a certain angle in a step-by-step way to realize the horizontal circumferential rotation. Through 360° step, the full section contour scanning of the borehole at the same height can be realized. At the same time, with the cooperation of the up and down movement of the cable, the full hole acoustic scanning of the drilling hole can be carried out. Finally, the ultrasonic scanning data on different borehole walls can be synthesized and processed by different azimuth transducers, and finally the ultrasonic related data on the whole borehole wall can be processed. Based on the 3D borehole scanning data, a series of parameters of hole wall contour features can be extracted. The schematic diagram of multi-array element ultrasonic vertical section scanning is shown in Figure 2A, and the schematic diagram of multi-array element ultrasonic horizontal section scanning is shown in Figure 2B.

Scanning model of borehole horizontal profile

The up and down movement of the multi-array ultrasonic scanning probe in the borehole is a free fall movement, and the borehole has the possibility of vertical inclination. The position of the probe in the borehole is usually in the position of the non borehole central axis. Therefore, it is necessary to establish a horizontal section scanning model according to the scanning data of the multi-array acoustic probe to determine the position

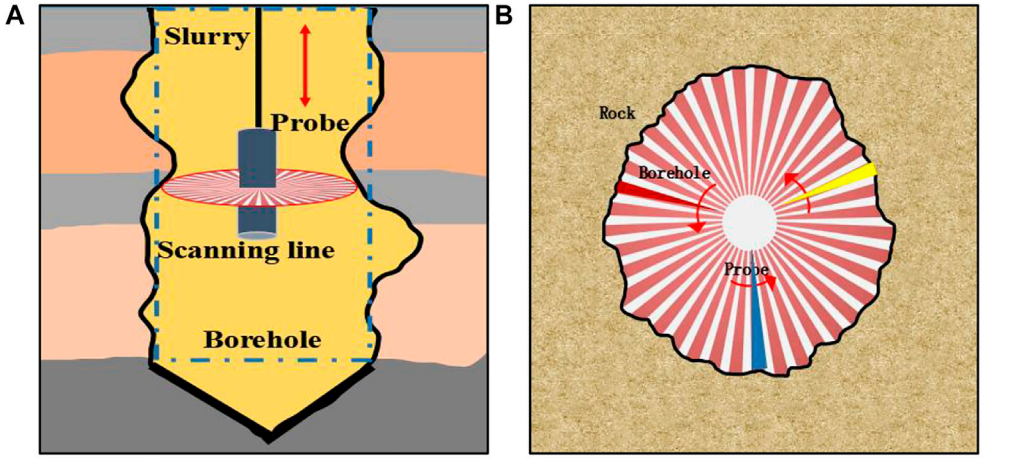


FIGURE 2
Schematic diagram of multi-array ultrasonic scanning principle.

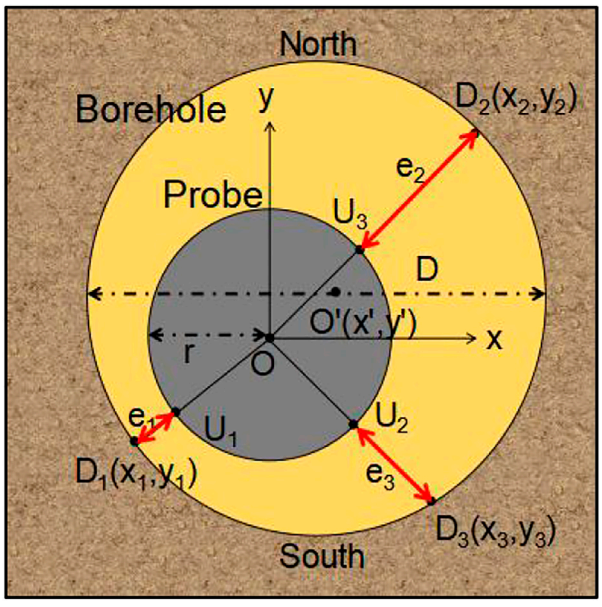


FIGURE 3
Schematic diagram of horizontal section scanning.

relationship between the probe central position and the borehole. As shown in Figure 3, it is assumed that the borehole is an ideal standard circle before being affected by *in-situ* stress. Taking the central position of the multi-array ultrasonic scanning probe as the coordinate axis dot o, a plane coordinate system is established. The geographical east direction is taken as the positive direction of the *x*-axis and the geographical North direction is taken as the positive direction of the *y*-axis. The ideal drilling diameter of the cast-in-place pile is D, and the distance from the center of the transmitting surface of the probe to the central point of the circular ring is r. In the rectangular coordinate system, the central point of the borehole is o ', and its coordinates are expressed in (x', y'), the point closest to the vertical distance of the probe from the borehole is D_1 (x_1, y_1), the corresponding ultrasonic array element on the probe is U_1, and the distance between U_1 and D_1 is e_1. The point with the farthest vertical distance from the probe to the borehole is D_2 (x_2, y_2), the corresponding ultrasonic array element on the probe is U_2, and the distance between U_2 and D_2 is e_2. The point with moderate vertical distance from the probe to the borehole is D_3 (x_3, y_3), the corresponding ultrasonic array element on the probe is U_3, and the distance between U_3 and D_3 is e_3.

The corresponding relationship between the multi-array ultrasonic scanning probe and the borehole is as follows:

$$\begin{cases} e_1 = \sqrt{x_1^2 + y_1^2} - r \\ e_2 = \sqrt{x_2^2 + y_2^2} - r \\ e_3 = \sqrt{x_3^2 + y_3^2} - r \end{cases} \quad (1)$$

Since the multi-array ultrasonic scanning probe can effectively calculate the values of e_1, e_2 and e_3 , according to the Pythagorean theorem of triangle, the relationship 1) can be deformed and solved:

$$\begin{cases} x_i = (e_i + r) * \cos(\alpha_i - \pi/2) \\ y_i = (e_i + r) * \sin(\alpha_i - \pi/2) \end{cases} \quad (2)$$

Where, i = 1, 2, 3. α_1 represents the geographic azimuth corresponding to the ultrasonic array element U_1, α_2

represents the geographic azimuth corresponding to the ultrasonic array element U_2, and α_3 represents the geographic azimuth corresponding to the ultrasonic array element U_3. The geographic azimuth is the included angle between the location of the ultrasonic array element and the geographic north pole. Points D_1, D_2 and D_3 are all located on the circumference of the borehole. According to the circular equation, it can be concluded that:

$$\begin{cases} (x_1 - x')^2 + (y_1 - y')^2 = (D/2)^2 \\ (x_2 - x')^2 + (y_2 - y')^2 = (D/2)^2 \\ (x_3 - x')^2 + (y_3 - y')^2 = (D/2)^2 \end{cases} \tag{3}$$

Through simultaneous Eqs 2, 3, the center coordinates (x ', y') of the borehole and the distance |O '| of the probe from the borehole center can be solved. The expression is:

$$\begin{cases} x' = v - (u - v) * k_2 / (k_1 - k_2) \\ y' = (u - v) / (k_1 - k_2) \\ |OO'| = \sqrt{x'^2 + y'^2} \end{cases} \tag{4}$$

The corresponding variable expression is:

$$\begin{cases} u = (x_1^2 - x_2^2 + y_1^2 - y_2^2) / (2x_1 - 2x_2) \\ v = (x_1^2 - x_3^2 + y_1^2 - y_3^2) / (2x_1 - 2x_3) \\ k_1 = (y_1 - y_2) / (x_1 - x_2) \\ k_2 = (y_1 - y_3) / (x_1 - x_3) \end{cases} \tag{5}$$

The assumption of the horizontal profile scanning model is that the borehole is a standard circle, while the actual borehole wall is not a cylindrical surface in the strict sense, accompanied by local defects, such as borehole necking, local hole collapse, local hole expansion, local skew and so on. Therefore, during data analysis, it is necessary to search the standard circle of the data or tabulate the standard area, and the casing remaining in the borehole can be used as the calibration circle of the horizontal profile scanning model. Thus, the position of multi-array ultrasonic scanning probe in the borehole can be effectively determined, and the transmission SPPED of sound wave in the borehole can also be obtained. Its expression is:

$$SPEED = \frac{2(D_s - 2r)}{t_1 + t_2} \tag{6}$$

Where D_S is the diameter of the calibration circle, t_1 is the arrival time of the first wave of the echo received by the ultrasonic array element U_1, t_2 is the arrival time of the first wave of the echo received by the ultrasonic array element U_2, and R is the radius of the multi-array element ultrasonic scanning probe.

Reconstruction of horizontal profile of borehole

The contour reconstruction of the borehole can be realized independently through n multivariate scanning data $H(n)|_{h,i,j}$. However, since the multi-array ultrasonic scanning probe is easy to deviate from the central position of the borehole in the borehole, or the borehole is subject to necking, local hole collapse, local hole expansion, local skew and other phenomena, at least some multivariate scanning data $H(n)|_{h,i,j}$ are invalid or have large errors. In order to reduce the interference of the data and improve the contour reconstruction accuracy of the borehole, It is necessary to make full use of multivariate scanning data $H(n)|_{h,i,j}$ to realize the fusion and reconstruction of multivariate scanning data. Assuming that the multi-element scanning fusion data of horizontal section at depth h is $R_{h,i,j}$, its expression is:

$$R_{h,i,j} = \sum_{n=1}^{N} \lambda_{n,h,j} * H(n)|_{h,i,j} \qquad \left(\sum_{n=1}^{N} \lambda_{n,h,j} = 1 \right) \tag{7}$$

Where, $\lambda_{n,h,j}$ is the composite weighting factor of the *j*th sampling data of the *n*th array element ultrasonic probe at depth h, $\lambda_{n,h,j}$ is a non negative number, the maximum value of $\lambda_{n,h,j}$ is 1, and the minimum value of $\lambda_{n,h,j}$ is 0. The value of $\lambda_{n,h,j}$ depends on the actual situation. Generally, the value of $\lambda_{n,h,j}$ is 1/N. When the data obtained by the array element ultrasonic probe is abnormal, the smaller the corresponding $\lambda_{n,h,j}$ value is, and when the data signal obtained by the array element ultrasonic probe is strong, the larger the corresponding $\lambda_{n,h,j}$ value is.

Multivariate data fusion map combines the acoustic scanning data of multi-array probe. It is necessary to normalize the multivariate data fusion map to obtain the maximum value $MAX|R_{h,i,j}|$ and minimum value $MIN|R_{h,i,j}|$ of each row and column of the horizontal section, so that the value of multivariate reconstructed data $\hat{R}_{h,i,j}$ is within the range [$MIN|R_{h,i,j}|$, $MAX|R_{h,i,j}|$]. The multi-element reconstructed data $\hat{R}_{h,i,j}$ is processed in gray, and the bright region is used to represent the contour region of the horizontal scanning section, and the dark region is used to represent the propagation medium region. After completing the reconstruction of each horizontal section contour of the borehole, the whole hole stereo contour image of the borehole can be formed by interpolating and fitting the connected horizontal section data, and the mapping of multi-array ultrasonic scanning data can be completed. The horizontal profile reconstruction of a certain depth borehole is realized, which provides a basic number for the *in-situ* stress measurement method described in this paper.

In situ stress measurement method of deep borehole

Based on the multi-array ultrasonic scanning technology, this paper combines the fine profile of the horizontal section of the deep borehole with the hole wall caving method to realize the *in-situ* stress measurement of the deep borehole and effectively improve the accuracy and efficiency of the *in-situ* stress measurement.

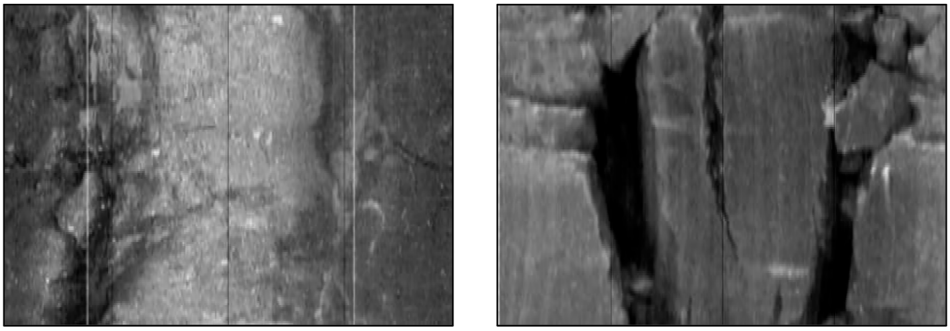


FIGURE 4
Borehole imaging of deep borehole wall collapse.

Basic principle of borehole *in-situ* stress measurement

Because the deep rock mass structure usually has high *in-situ* stress, and the depth of deep drilling is usually more than 1,000 m, the hole wall collapse is easy to occur in the deep part of drilling due to the action of high ground stress (Liu et al., 2010; Liu and Sun 2016; Wu et al., 2016). Borehole collapse refers to the phenomenon that the rock on the hole wall breaks and falls off under the action of high stress, as shown in Figure 4. Initially, only the maximum principal stress direction on the cross section of the borehole can be obtained. With the help of geophysical logging, deformation and failure mechanism of deep rock mass and laboratory test results, the stress can be estimated according to the collapse shape elements and the cohesion and internal friction angle of rock. The maximum horizontal principal stress direction of hole wall caving method is more accurate, but the calculation accuracy of stress value needs to be further improved. When there is no collapse in the borehole, the relevant *in-situ* stress information cannot be obtained. If the anisotropy or heterogeneity of rock is prominent, it will also bring great errors to the determination of ground stress value and orientation.

Because the multi-element ultrasonic scanning technology can not only measure the direction and width of borehole wall collapse, but also measure the borehole wall collapse depth and borehole shape, which can effectively reflect the collapse width and depth of borehole collapse area. Therefore, in order to obtain the width and depth of the borehole collapse area as shown in Figure 4, this paper first uses the multi-element ultrasonic scanning technology to scan the borehole horizontal section profile in the collapse area to form the horizontal section profile at a certain depth of the borehole, as shown in Figure 5A. Then, by scanning multiple horizontal sections of the borehole, the contour reconstruction of a specific area of the borehole can be realized, as shown in Figure 5B. Finally, through the extraction of contour feature points, the width and depth of the collapse area are calculated as shown in Figure 5C, providing data parameters for the methods described later. The specific borehole contour acquisition is the content of Chapter 2. Contour feature point extraction and data processing are analyzed and stated in detail in this chapter.

The mechanism of hole wall collapse is the rock compression shear failure caused by the stress concentration near the hole wall. This phenomenon occurs at the position with the maximum tangential stress, and the collapse direction is consistent with the direction of the minimum horizontal principal stress. Before drilling, the stress is in equilibrium. After drilling, the original rock stress balance around the borehole is destroyed. In order to maintain the balance, the stress on the borehole wall is redistributed. For a circular hole in an infinite, uniform and isotropic elastic thin plate, when it receives the maximum and minimum horizontal principal stress, the stress distribution near the hole wall can be solved according to Kirsch equation, and its expression is:

$$\begin{cases} \sigma_\theta = \dfrac{\sigma_1+\sigma_2}{2}\left(1+\dfrac{a^2}{r^2}\right) - \dfrac{\sigma_1-\sigma_2}{2}\left(1+\dfrac{3a^4}{r^4}\right)\cos(2\theta) - \Delta p\dfrac{a^2}{r^2} \\ \sigma_r = \dfrac{\sigma_1+\sigma_2}{2}\left(1-\dfrac{a^2}{r^2}\right) + \dfrac{\sigma_1-\sigma_2}{2}\left(1-\dfrac{4a^2}{r^2}+\dfrac{3a^4}{r^4}\right)\cos(2\theta) + -\Delta p\dfrac{a^2}{r^2} \\ \sigma_z = \sigma_3 - 2\nu(\sigma_1-\sigma_2)\cos(2\theta) \\ \tau_{r\theta} = \dfrac{\sigma_1-\sigma_2}{2}\left(1+\dfrac{2a^2}{r^2}-\dfrac{3a^4}{r^4}\right)\sin(2\theta) \end{cases} \tag{8}$$

Where: σ_θ, σ_r, σ_z, $\tau_{r\theta}$ are the tangential, radial normal stress, vertical stress and shear stress of the failure point respectively. σ_1 , σ_2 is the highest and lowest level principal stress of original rock respectively. σ_3 is the vertical stress of original rock. σ_3 is the radius of circular hole. R is the radial distance to the central axis. ν is the Poisson's ratio of rock; ΔP is the excess borehole fluid pressure exceeding the rock pore pressure. θ is the included angle in the initial σ_1 counterclockwise direction. It can be seen from the relation (8) that the maximum stress is the tangential stress, and σ_θ acts in the directions of $\theta = 90^\circ$ and $\theta = 270^\circ$ along the

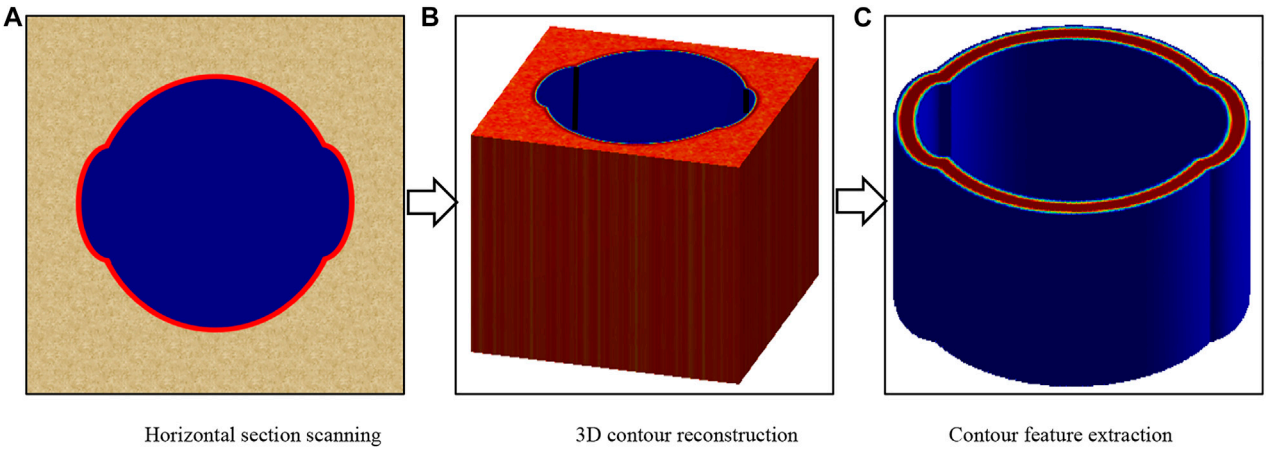


FIGURE 5
Schematic diagram for obtaining width and depth of borehole wall collapse area.

arch line. When r = a, it is the stress state of the hole wall. According to the relationship (8), the shear stress on the hole wall is 0, which can be ignored. σ_θ is a function of σ_z angle θ. When $\theta = 90^\circ$ or $\theta = 270^\circ$, σ_θ and σ_z take the maximum value, then the relationship (8) becomes:

$$\begin{cases} \sigma_r = \Delta p \\ \sigma_\theta = 3\sigma_1 - \sigma_2 - \Delta p \\ \sigma_z = \sigma_3 - 2\nu(\sigma_1 - \sigma_2) \end{cases} \tag{9}$$

If ΔP becomes smaller, σ_r becomes smaller and σ_θ becomes larger. If σ_θ exceeds the compressive stress of rock, the rock will undergo shear failure, that is, hole wall collapse. Since the rock failure of hole wall is generally shear failure, which obeys Mohr strength criterion, the stress state of failure point meets the following equation:

$$c_0 = (1+\mu^2)^{\frac{1}{2}}\left[\left(\frac{\sigma_\theta - \sigma_r}{2}\right)^2 + \tau_{r\theta}^2\right]^{\frac{1}{2}} - \mu\left(\frac{\sigma_\theta + \sigma_r}{2}\right) \tag{10}$$

Where: c_0,μ is the bonding force and internal friction coefficient of rock respectively. Therefore, as long as the borehole wall collapse width θ_b and the borehole wall collapse depth r_b is measured, and determine the rock expressions of σ_θ , σ_r, $\tau_{r\theta}$ into Eq 8, then the values of σ_1 and σ_2 can be solved. The schematic diagram of borehole collapse is shown in Figure 6. Borehole wall collapse width θ_b corresponds to the opening angle of borehole collapse. When the borehole collapse reaches the critical value M point, θ_b the corresponding formula is:

$$\theta = \frac{\pi - \theta_b}{2} \tag{11}$$

Where: θ corresponds to the specific angle of point M. If the borehole wall collapse width θ_b is known, θ corresponds to the specific angle of point M can be solved according to Eq. 11. At this time, the tangential stress σ_θ at the critical point of compressive stress concentration failure (the junction of borehole collapse area and non collapse area) can be obtained.

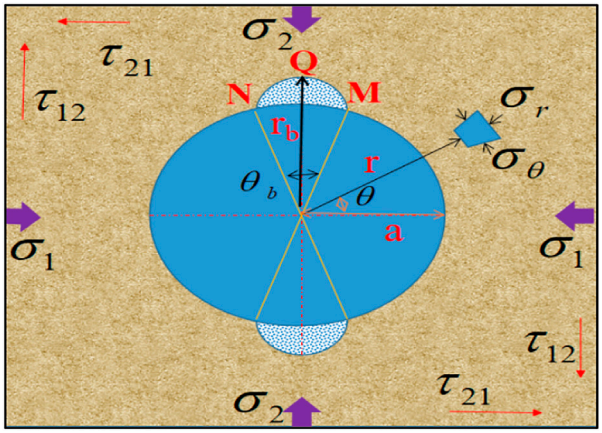


FIGURE 6
Schematic diagram of circumferential stress state of borehole cross section.

Experimental test and data processing

In order to verify the accuracy of multi-array ultrasonic scanning technology to obtain the width and depth of hole wall collapse, indoor physical simulation experiments were carried out for data processing and analysis. The equipment used in the physical simulation test experiment is the multi-

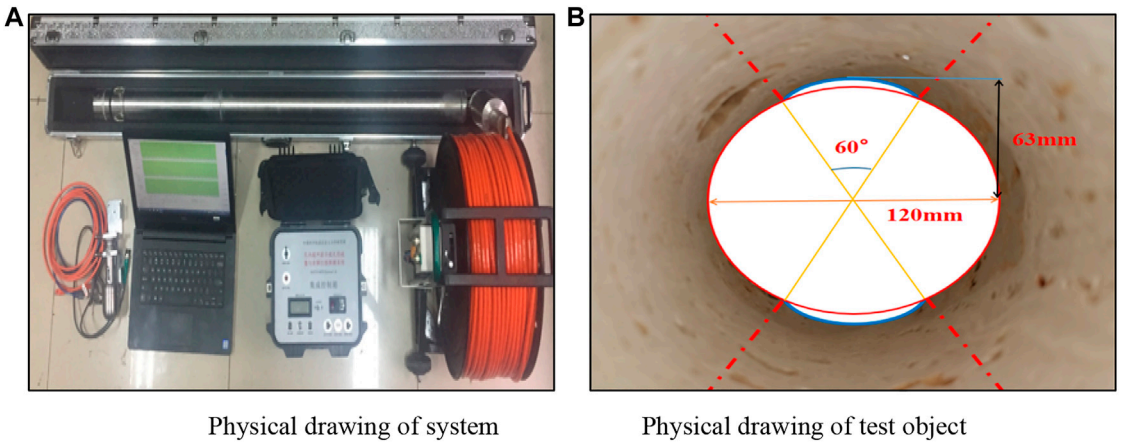


FIGURE 7
Indoor physical test.

element ultrasonic scanning equipment independently developed by Institute of Rock and Soil Mechanics, Chinese Academy of Sciences. The physical diagram of the equipment is shown in Figure 7A. The equipment has three ultrasonic array element transducers, and the frequency of the ultrasonic transducer is 1 MHz. The physical test object is the calibrated borehole after rock processing. Two symmetrical circular grooves are made in the standard circular borehole to simulate the deformation state of the borehole under external force. The diameter of the round hole of the test model is 120mm, the depth r_b is 63mm, and the collapse width of the hole wall θb is 60°, rock bonding force c_0= 8MPa, internal friction coefficient μ = 0.5. The model image is shown in Figure 7B.

The specific working steps of indoor physical test are as follows: fill the borehole with purified water, lower the probe into the borehole, and after the probe is lowered to the depth a in the borehole, the integrated control box will supply power and command control for the probe. The multi-array ultrasonic probe starts to scan the borehole horizontally. After receiving the rotation command from the control system, multiple ultrasonic transducers rotate in a step-by-step manner from the set orientation and rotate horizontally in a clockwise direction at every fixed angle. After each rotation to a fixed angle, multiple ultrasonic transmitting transducers transmit pulse signals to the rock wall surface for ultrasonic scanning of multiple rock wall scanning points. Multiple ultrasonic receiving transducers receive the reflected echo signal corresponding to the direction, and the parameters such as multiple transmission signals, echo signals, azimuth signals and control signals are transmitted to the ground system through the transmission cable. Then, the multi-element ultrasonic probe mechanically rotates a step angle and continues the above process until the 360° scanning of the whole horizontal section profile at the coverage depth A. After completing the horizontal profile scanning of the drilling profile at depth a, change the length of the transmission cable, and the transmission cable moves the probe upward to the depth of the test section B to realize the horizontal profile scanning at drilling depth B. Then, complete the full horizontal section contour scanning of the borehole at the borehole depth C. Finally, through computer data analysis and data processing, the contour fine reconstruction of multiple depth horizontal sections of borehole is realized. The schematic diagram of the test process is shown in Figure 8A, and the borehole contour scanning diagram of the horizontal section at depth B is shown in Figure 8B.

According to the borehole horizontal profile scanning model constructed in this paper, the data obtained by three ultrasonic array elements are synthesized, and the three scanned images of the same section are fused. The results are shown in Figure 9A. On the circumferential scanning image synthesized by multiple array elements, take the position of the probe determined by the multiple array metadata as the central origin, establish a plane rectangular coordinate system, and add several sound beam search scanning lines, as shown in Figure 9B, in which the number is N and the included angle between the sound beam search scanning lines is two Π/N. At depth B, the first wave detection distance of ultrasonic sound beam corresponding to the I sound beam search scanning line is $L_{h,i}$. In calculating the acoustic wave transmission time corresponding to $L_{h,i}$, the arrival time of the first wave is calculated according to the characteristics of relatively large energy of the first wave beam. In order to minimize the time of

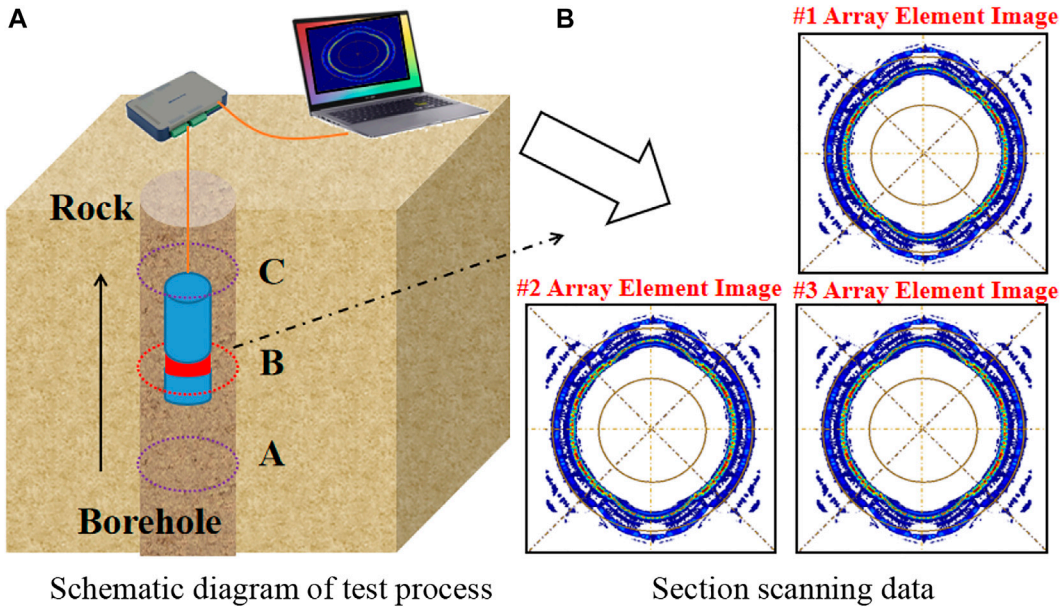


FIGURE 8
Test process and scanned image.

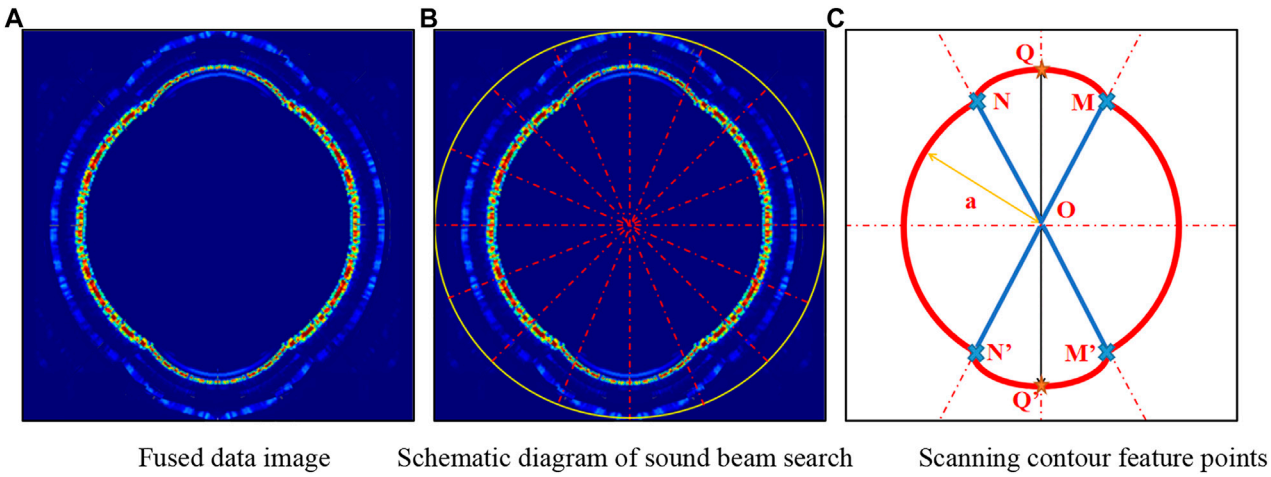


FIGURE 9
Scanned data image.

real-time operation of searching the maximum energy interval, the energy center convergence method is adopted. Firstly, at depth B, the ultrasonic beam w corresponding to the i beam search scan line is divided into four sub windows, the energy of each sub window is calculated, and then two are added and combined into three new sub windows. The sub window corresponding to the one with the largest energy in the new sub window is W ′, repeat the above iterative steps, and after the iteration is terminated, further move the sub window on the time axis to find a more accurate area with the largest energy value. According to the principle of energy center, the arrival time T of the first wave is:

$$T = \frac{\sum_{i=1}^{N} A_i t_i}{\sum_{i=1}^{N} A_i} \tag{12}$$

In the above formula, A_i is the amplitude at time t_i in the region with the maximum energy corresponding to the sound beam search scan line. At the depth h, assuming that the optimal scanning line is in the plane image coordinate system, the number of pixels in the x-axis direction is MH and the number of pixels in the y-axis direction is N_h, then according to the corresponding relationship between the contour size calibration value and the image scanning line, it can be calculated that at the depth B, the length represented by the horizontal distance of a pixel in the horizontal section scanning image of the borehole is ξ_h and the length represented by the longitudinal distance is ζ_h, The following relationship exists:

$$\begin{cases} \xi_h = v_h T_{h,i} \cos\alpha / M_h \\ \zeta_h = v_h T_{h,i} \sin\alpha / N_h \end{cases} \tag{13}$$

In the above formula, α represents the angle between the image scanning line and the x-axis direction, and v_h represents the propagation speed of sound in the medium. After the contour dimension calibration of the optimal scanning line is completed, the contour dimension on the circumferential scanning image of the borehole scanning section can be calculated back according to the length value represented by the pixel points. The maximum distance between the scanned image contour and the central O point is Q, and the contour mutation points are m and N respectively. The three feature points corresponding to the other side of the image are Q′, M′, N′, as shown in Figure 9C. Through calculation, a = 60.00mm, $|\overline{OQ}|$= 62.99mm, $|\overline{OQ'}|$= 62.98mm, $\angle MON$= 60.00°, $\angle M'ON'$= 60.00°, $\angle MOQ$= 30.00°, $\angle M'OQ'$= 60.00°.

Calculation results and analysis

The stress σ_1 and σ_2 corresponding to the physical test object are 12.944 and 6.665 MPa respectively. According to the hole wall collapse width and depth obtained by multi-array ultrasonic scanning technology, combined with Eqs, 8–10. Calculate the stress of point m and point Q respectively, and the stress of point M is calculated as follows:

$$\begin{cases} \sigma_{\theta 1} = \frac{\sigma_1+\sigma_2}{2}\left(1+\frac{60^2}{60^2}\right) - \frac{\sigma_1-\sigma_2}{2}\left(1+3\times\frac{60^4}{60^4}\right)\cos(2\times 60.00^\circ) = 2\sigma_1 \\ \sigma_{r1} = \frac{\sigma_1+\sigma_2}{2}\left(1-\frac{60^2}{60^2}\right) + \frac{\sigma_1-\sigma_2}{2}\left(1-4\times\frac{60^2}{60^2}+3\times\frac{60^4}{60^4}\right)\cos(2\times 60.00^\circ) = 0 \\ \tau_{r\theta 1} = \frac{\sigma_1-\sigma_2}{2}\left(1+2\times\frac{60^2}{60^2}-3\times\frac{60^4}{60^4}\right)\sin(2\times 60.00^\circ) = 0 \\ c_0 = (1+\mu^2)^{\frac{1}{2}}\left[\left(\frac{\sigma_{\theta 1}-\sigma_{r1}}{2}\right)^2+\tau_{r\theta 1}^2\right]^{\frac{1}{2}} - \mu\left(\frac{\sigma_{\theta 1}+\sigma_{r1}}{2}\right) \end{cases} \tag{14}$$

The solution is, σ_1= 12.944 MPa. Similarly, the stress at point Q is calculated as follows:

$$\begin{cases} \sigma_{\theta 2} = \frac{\sigma_1+\sigma_2}{2}\left(1+\frac{60^2}{62.99^2}\right) - \frac{\sigma_1-\sigma_2}{2}\left(1+3\times\frac{60^4}{62.99^4}\right)\cos(2\times 90.00^\circ) = 2.688\sigma_1 - 0.781\sigma_2 \\ \sigma_{r2} = \frac{\sigma_1+\sigma_2}{2}\left(1-\frac{60^2}{62.99^2}\right) + \frac{\sigma_1-\sigma_2}{2}\left(1-4\times\frac{60^2}{62.99^2}+3\times\frac{60^4}{62.99^4}\right)\cos(2\times 90.00^\circ) = 0.126\sigma_1 - 0.033\sigma_2 \\ \tau_{r\theta 2} = \frac{\sigma_1-\sigma_2}{2}\left(1+2\times\frac{60^2}{62.99^2}-3\times\frac{60^4}{62.99^4}\right)\sin(2\times 90.00^\circ) = 0 \\ c_0 = (1+\mu^2)^{\frac{1}{2}}\left[\left(\frac{\sigma_{\theta 2}-\sigma_{r2}}{2}\right)^2+\tau_{r\theta 1}^2\right]^{\frac{1}{2}} - \mu\left(\frac{\sigma_{\theta 2}+\sigma_{r2}}{2}\right) \end{cases} \tag{15}$$

The solution is, σ_2= 6.665 MPa. Through comparison, it can be seen that the results obtained by multi-element ultrasonic scanning technology are basically consistent with the results of *in-situ* stress calculation. This is mainly because the parameters obtained by multi-element ultrasonic scanning technology are close to the size of the physical model, and the size error is 0.01 mm, which has little impact on the results of *in-situ* stress calculation. The calculation process of hole wall caving method is simple, and the core parameters are the width and depth of hole wall rock mass caving, that is, the real contour of the borehole. The scanned contour images at depths A, B and C obtained by this technology are reconstructed and extracted respectively. The results are shown in Figure 10. It can be seen from Figure 10 that the scanning contour images at depths A, B and C are basically consistent. At the same time, comparing the scanning contour images at depths A, B and C obtained by this technology with the real physical model, it also has good consistency, which shows that the method described in this paper can effectively obtain the characteristics of hole wall collapse caused by high stress in depth.

In terms of quantitative analysis, the collapse width and depth of hole wall rock mass obtained at depths A, B and C are compared with the physical model. The comparison results of collapse width are shown in Figure 11A, and the comparison results of collapse depth are shown in Figure 11B. As can be seen from Figure 11A, the collapse width of boreholes at depths A, B and C is basically the same as that of the physical model. This is mainly because the equipment adopts high-resolution electronic azimuth compass, combined with multivariate data correction, and has high directional scanning characteristics, so that the starting and ending positions of collapse width can be accurately reflected. The consistency of multiple measurement results also verifies the repeatability reliability of this technology. It can be seen from Figure 11B that the borehole caving depth at depths A, B and C is basically the same, and is consistent with the size of the physical model, with occasional small deviation. This is mainly due to the accidental error in the process of acoustic signal acquisition. Combined with the multivariate data correction of this technology, the measurement accuracy of caving depth can be significantly improved, with an error of about 0.02%, which has little impact on *in-situ* stress measurement. The multiple measurement results of borehole collapse depth also verify the correctness and repeatability of this method.

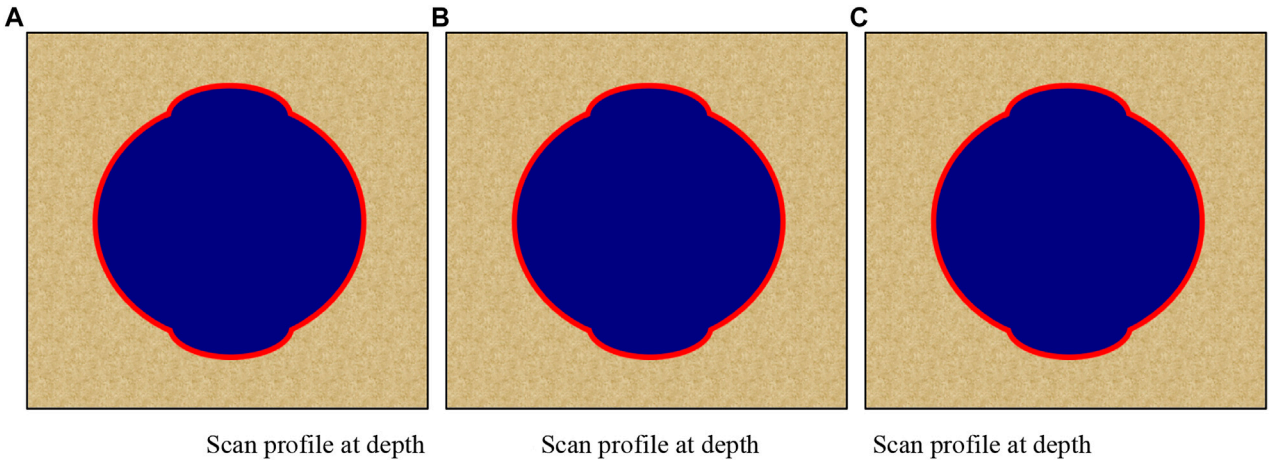


FIGURE 10
Scanning contour at different depths. **(A)** Scan profile at depth A. **(B)** Scan profile at depth B. **(C)** Scan profile at depth C.

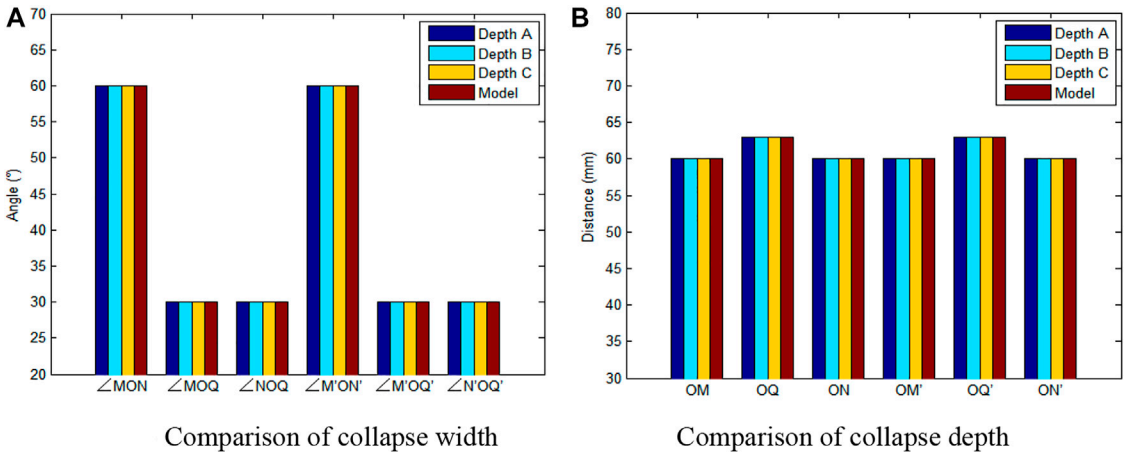


FIGURE 11
Comparison of collapse.

The horizontal section contours at depths A, B and C are interpolated and fitted to form a three-dimensional morphology image of the model, as shown in Figure 12A. From the Figure 12A, it can be seen that the characteristics of the model are consistent with the actual physical model. In order to verify the superiority of this method, the results of multi-array element processing in this paper are compared with the results of single array metadata. The results of single array metadata formation are shown in Figure 12B. From Figure 12B, it can be seen that the single array element scanning diagram can reflect certain scanning area features, but the influence of multiple echoes and interference waves is more prominent, so it is difficult to extract effective echo signals, resulting in low accuracy of each horizontal contour feature curve extracted, It can not realize the fine reconstruction of contour features, which verifies the superiority of multi-array ultrasonic scanning technology and method in this paper.

In order to improve the accuracy and efficiency of deep *in-situ* stress measurement, based on multiple full waveform scanning signals obtained by multi-array element ultrasonic scanning equipment, a deep borehole *in-situ* stress measurement method based on multi-array element ultrasonic scanning technology is proposed. The advantage of multi-element ultrasonic scanning technology lies in the fine

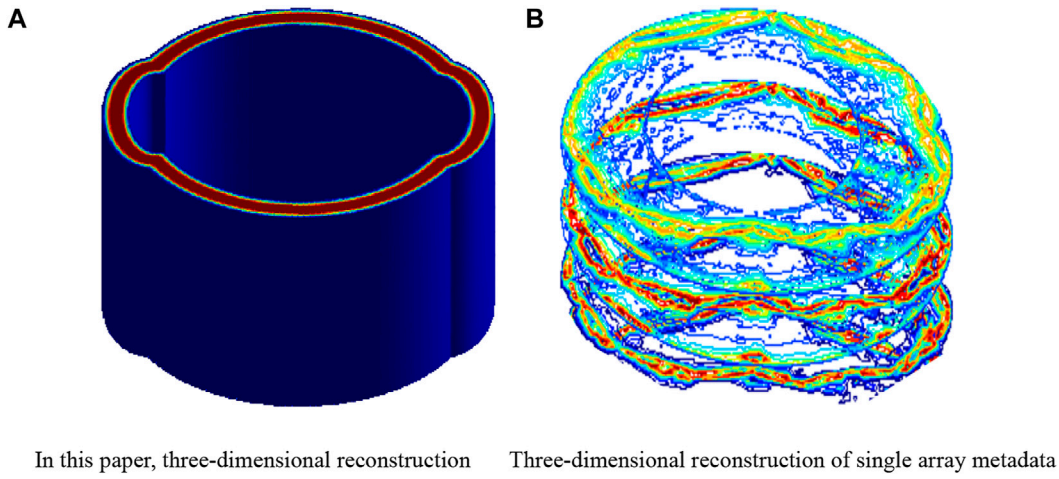


FIGURE 12
Comparison of three-dimensional reconstruction between this method and single array element method. **(A)** Three-dimensional morphology image. **(B)** Single array metadata formation.

reconstruction of the horizontal section contour of the hole wall, which can realize the accurate measurement of the collapse width and depth of the hole wall, so that the method is feasible and accurate in theory. This technology also has some limitations. If there is no fluid medium in the borehole, the attenuation of ultrasonic signal in the air is very fast, and the ultrasonic transducer is difficult to effectively collect the reflected echo signal of the borehole wall. In addition, if the fluid medium in the borehole is uneven, the acoustic propagation characteristics of ultrasonic will also change, and the technical results of this method may have deviation. However, due to the use of multi-array signal, the number of ultrasonic array elements can be appropriately increased or data correction can be used to improve the accuracy of measurement results. In general, in the deep *in-situ* stress measurement, this technology uses geological drilling to scan the contour of the hole wall at different depths, effectively identify the collapse area of the hole wall, and estimate the *in-situ* stress size and direction at different positions of the deep formation in combination with the calculation method in this paper. Because this method can quickly calculate the horizontal *in-situ* stress of borehole rock mass at different depths, through the contour scanning of different depths, it can efficiently present the *in-situ* stress distribution of the whole borehole, realize the three-dimensional visualization of the *in-situ* stress distribution of the whole borehole, provide effective data support for deep underground engineering, and have a broad development space.

In addition, the key basis of this study is to assume that the collapse width and depth are related to stress, which requires accurate measurement of borehole deformation under pressure. In fact, the borehole shape is usually irregular, often accompanied by cracks, grains and other phenomena. Therefore, it is necessary to identify and distinguish the characteristics of borehole wall collapse caused by *in-situ* stress, so as to determine whether the borehole deformation is caused by stress. According to the mechanical mechanism analysis of borehole collapse ellipse formation, we summarize the characteristics of the collapse ellipse as follows: 1) The cross section of the borehole has an obvious long axis direction. The contour diameter of a small part of the area is obviously larger than the borehole diameter, while the contour diameter of most areas is close to or equal to the borehole diameter. 2) The elliptical borehole section has a certain length in depth. At different depths of the same borehole, the caving hole section is sometimes short, several meters or tens of meters, sometimes quite long, up to tens of meters or even hundreds of meters, but its long axis direction is basically unchanged. 3) For elliptical borehole sections formed by fault fracture zones and high angle natural fractures, because they are similar in shape on the well diameter curve, it is difficult to distinguish the true from the false. It is necessary to analyze them with the help of other technical means to divide the hole sections and eliminate them. In order to improve and solve this problem, relevant research will be further carried out in the follow-up research work to realize the collapse feature recognition under the complex geological borehole environment.

Conclusion

The main conclusions are as follows: 1) This technology can effectively overcome the influence of the transparency of

the propagation medium in the borehole on the visualization of the borehole wall compared with the conventional technology. The horizontal profile scanning model of borehole can quantitatively calculate and analyze the collapse area caused by local *in-situ* stress; 2) The effective fusion of multi-array ultrasonic full waveform scanning signals and the reconstruction of horizontal section contour are adopted, which can break through the limitations of the conventional in hole probe that needs to be placed in the middle and the sound velocity calibration of the medium in the borehole, and improve the fine reconstruction and accurate measurement of 360° wall shape; 3) The multi-array element ultrasonic scanning technology can obtain the borehole shape data at any depth, which can realize the measurement of borehole wall three-dimensional shape. It has the feasibility of theory, method and technology in the borehole wall caving *in-situ* stress measurement, which can provide a new technical means for the three-dimensional detection of the borehole wall and *in-situ* stress measurement.

Data availability statement

The original contributions presented in the study are included in the article/supplementary material further inquiries can be directed to the corresponding author.

Author contributions

JW: Methodology, writing—review and editing. CW: Supervision. JH: Review. ZH, WZ, and YW: Investigation.

Funding

This work was supported by the National Natural Science Foundation for the Youth of China (Grant No.41902294); the Science and Technology Project of Hubei Provincial Department of Natural Resources (Grant No. ZRZY2022KJ08); the Systematic Project of Guangxi Key Laboratory of Disaster Prevention and Engineering Safety (Grant No.2019ZDK053).

Acknowledgments

The authors would like to express deep gratitude to the editors and reviewers for their valuable comments and suggestions that greatly improved this paper.

Conflict of interest

The authors declare that the research was conducted in the absence of any commercial or financial relationships that could be construed as a potential conflict of interest.

Publisher's note

All claims expressed in this article are solely those of the authors and do not necessarily represent those of their affiliated organizations, or those of the publisher, the editors and the reviewers. Any product that may be evaluated in this article, or claim that may be made by its manufacturer, is not guaranteed or endorsed by the publisher.

References

Amadei, B., and Stephansson, O. (1986). *Rock stress and its measurement*, 1. London: Centek Publishers, 95–116. [S.l.].

Bai, X., Zhang, D.-m., Wang, H., Li, S.-j., and Rao, Z. (2018). A novel *in situ* stress measurement method based on acoustic emission kaiser effect: A theoretical and experimental study. *R. Soc. open Sci.* 5 (10), 181263. doi:10.1098/rsos.181263

Deng, Z., Yao, C., and Jia, Y. (2011). Application of ultrasonic detection to quality testing of super-deep foundation concrete cutoff wall. *Water Resour. Hydropower Eng.* 11 (42), 69–73. doi:10.13928/j.cnki.wrahe.2011.11.021

Gough, D. I., and Bell, J. S. (1982). Stress orientations from borehole wall fractures with examples from Colorado, east Texas, and northern Canada,east Texas,and northern Canada. *Can. J. Earth Sci.* 19 (7), 1358–1370. doi:10.1139/e82-118

Han, Z., Wang, C., and Zou, X. (2018). Application of borehole stereo pair imaging technology in borehole wall caving *in-situ* stress measurement. *J. rock Mech. Eng.* 37 (A02), 4177–4183. doi:10.13722/j.cnki.jrme.2017.1192

Ji, Z. (2009). Study on *in-situ* stress measurement method and engineering application. *Mod. Min.* 487 (11), 67–69. doi:10.13207/j.cnki.jnwafu.2011.06.007

Leeman, E. (1964). The measurement of stress in rock. *J. South. Afr. Inst. Min. Metallurgy* 65 (12), 656–664.

Liu, J., and Sun, J. (2016). Borehole wall collapse and control in shale gas well drilling. *Drill. Fluid & Complet. Fluid* 33 (3), 25–29. doi:10.1016/j.jngse.2016.06.017

Liu, X., Zheng, X., and Wang, Z. (2010). Study of the silicate fluid for prevention of borehole-wall collapse and its application to drilling in carbonaceous mudstone. *Geol. Explor.* 46 (5), 967–971. doi:10.1145/1836845.1836984

Schuette, W. H., Shawker, T. H., and Whitehouse, W. C. (2010). Television synchronization of a real time ultrasonic sector scanner. *J. Clin. Ultrasound* 6 (1), 16–18. doi:10.1002/jcu.1870060106

Sun, D., Chen, Q., Li, A.-w., and Yang, Y. (2020). Anelastic strain recovery *in situ* stress measurement method and its application prospect in underground mines. *IOP Conf. Ser. Earth Environ. Sci.* 570, 042021. doi:10.1088/1755-1315/570/4/042021

Uhlmann, E., and Sammler, C. (2010). Influence of coolant conditions in ultrasonic assisted grinding of high performance ceramics. *Prod. Eng. Res. Devel.* 4 (6), 581–587. doi:10.1007/s11740-010-0265-y

Wang, X., and Wang, J . (2017). 3D hydraulic fracturing *in-situ* stress measurement method in single borehole and its application. *Bull. Inst. Crustal Dyn.* 1, 170–177.

Wu, M., Mouyang, Q., and Gao, J. (2016). Discussion on the mud loss and borehole wall collapse prevention in horizontal drilling in Sulige gas field. *Drill. Fluid & Complet. Fluid* 33 (3), 46–50. doi:10.3696/j.issn.1001-5620.2016.03.009

Zoback, M. D., Moos, D., Mastin, L., and Anderson, R. N. (1985). Well bore breakouts and *in situ* stress. *J. Geophys. Res.90* 90, 5523–5530. doi:10.1029/jb090ib07p05523

frontiers | Frontiers in Earth Science

ORIGINAL RESEARCH
published: 15 August 2022
doi: 10.3389/feart.2022.911823

Deformation and Failure Characteristics of Loading and Unloading Rock Based on Volume Crack Strain

Xiaohui Liu[1,2,3]*, *Yu Zheng*[1,3,4], *Jinyun Guo*[5], *Qijun Hao*[2] and *Yang Xue*[1,3]

[1]Key Laboratory of Fluid and Power Machinery, Ministry of Education, Xihua University, Chengdu, China, [2]Key Laboratory of Deep Earth Science and Engineering, Ministry of Education, Sichuan University, Chengdu, China, [3]School of Energy and Power Engineering, Xihua University, Chengdu, China, [4]Southwest Municipal Engineering Design & Research Institute of China, Chengdu, China, [5]Research Center for Social Development and Social Risk Control of Sichuan Province, Key Research Base of Philosophy and Social Science, Sichuan University, Chengdu, China

In order to study the laws of crack evolution in rock and explain its fracture instability mechanism, a series of laboratory tests were carried out with Jinping Marbles. The test results show that the failure degree of marbles under unloading conditions is more severe than that under loading conditions. Based on volume crack strain, five progressive failure stages of crack evolution under different conditions are divided, and the corresponding characteristic stresses are determined. The pre-peak volume crack propagation strain without considering the initial damage is used to evaluate the pre-peak crack growth propagation degree of rock, and it is found that the lower the confining pressure, the higher the strain rate and unloading rate, the less the cracks generated before the peak, and the more the rock is prone to brittle failure after the peak. The starting point of the sharp increase of volume crack strain rate is proposed as the failure precursor point, and stress levels of failure precursor of marbles are in 70%–100%, which decrease as confining pressure, strain rate, and unloading rate rise. Under unloading conditions, failure precursor points appear later and are close to the unloading point, and unloading rocks are more prone to sudden brittle failure.

Keywords: Jinping marble, loading and unloading, progressive failure, volume crack strain, failure precursor

OPEN ACCESS

Edited by:
Guang-Liang Feng,
Institute of Rock and Soil Mechanics (CAS), China

Reviewed by:
Jianping Zuo,
China University of Mining and Technology-Beijing, China
Longjun Dong,
Central South University, China

***Correspondence:**
Xiaohui Liu
liuxh@mail.xhu.edu.cn

Specialty section:
This article was submitted to Geohazards and Georisks, a section of the journal Frontiers in Earth Science

Received: *03 April 2022*
Accepted: *02 June 2022*
Published: *15 August 2022*

Citation:
Liu X, Zheng Y, Guo J, Hao Q and Xue Y (2022) Deformation and Failure Characteristics of Loading and Unloading Rock Based on Volume Crack Strain. Front. Earth Sci. 10:911823. doi: 10.3389/feart.2022.911823

1 INTRODUCTION

There are many defects in rock, such as joints, cracks, and pores in natural rock materials due to complex geological tectonic movement. These inherent discontinuities seriously weaken the mechanical properties and the stability of the internal structure of rock (Li et al., 2018; Li et al., 2020; Yan et al., 2021). Especially under the condition of high ground stress, a large amount of energy is accumulated in deep rock mass, and the energy stored in rock mass is rapidly released under the action of excavation and unloading, causing dynamic disasters such as rock burst and impact instability, which brings great challenges to the safety of construction workers and equipment (Cai and Kaiser, 2005; Zhou et al., 2015; Dong et al., 2020; Feng et al., 2022). Therefore, this study investigates the deformation and failure mechanisms of rock under different excavation disturbance conditions, and predicts the failure precursors of rock, which is of great significance to the stability of surrounding rock and early warning of rock dynamic disasters.

Deformation and failure of rock are the result of internal micro-cracks evolution, which leads to the deterioration of rock mechanical properties and the instability of its internal structure. In order to interpret crack evolution laws of rocks under different conditions, scholars usually analyze from macroscopic and microscopic aspects. From the perspective of macroscopic mechanical properties, deformation and failure characteristics of rock can be reflected by stress-strain curve, strength deformation parameters, and macroscopic damage characteristics. From the microscopic point of view, the acoustic emission method can be used to monitor the engineering rock mass in real-time, and directly judge the structure of abnormal areas in rock mass to predict the occurrence of dynamic disasters (Dong et al., 2021a). However, in laboratory tests, the root cause of rock instability and failure can be better explored based on the non-linear evolution law of micro-cracks inside rock (Chen et al., 2016; Jin et al., 2017; Zuo et al., 2017; Chen and Guo, 2020). Based on lots of rock mechanics tests, Bieniawski analyzed rock fracture characteristics using fracture mechanics theory, and found that the crack evolution process can be divided into stable and unstable stages (Bieniawski, 1967). To clarify the deformation and failure stages of rock, Martin firstly proposed to use the crack strain variable to analyze (Martin, 1993). Through compression tests of granites, Martin and Chandler further expounded the progressive failure process and fracture mechanism of rock in detail (Martin and Chandler, 1994). On this basis, Cai et al. (2004) found that characteristic stress thresholds can be obtained according to evolution characteristics of crack strain, which is still an important method to determine characteristic stresses of rock. In addition, to ensure the safety and stability of the project, it is necessary to identify rock failure precursors and predict rock failure. From a macro perspective, the turning point where tensile cracks extend and merge with shear cracks can be regarded as a failure precursor point, but it is difficult to be captured in laboratory tests (Hoek and Martin, 2014). From a micro perspective, rock failure precursor also can be determined by Acoustic emission (AE) (Yu et al., 2022), infrared thermography, and other auxiliary monitoring methods. Dong et al. (2021b, 2021c) predicted the precursors of rock instability and failure based on the unstable evolution trend of the AE event rate in the plastic stage. However, there are still some limitations, such as failure precursors with infrared thermography that usually appear later and are not prioritised in time, and that AE is greatly influenced by lithology, loading and unloading conditions, and is difficult to satisfy the conditions for determining failure precursors (Cong et al., 2016; Chen et al., 2021). Since instability of the rock medium was directly caused by microcrack propagation, crack propagation velocity variation reflects the change of rock damage degree. Based on this, how to propose a more accurate and universal prediction method of rock failure precursor is worth in-depth consideration. Considering different excavation disturbance conditions, to determine more accurate failure precursor based on evolution law of volume crack strain rate, is significant to earlier warning and prevention of rock dynamic disaster and ensure the long-term stability of surrounding rock.

However, the crack propagation characteristics of rock are different when under different stress states. Zuo et al. (2019) studied the crack evolution laws of rock during the progressive failure process under the influence of confining pressure, and pointed out that confining pressure can restrain crack propagation in rock (Chen et al., 2020). Xing et al. (2018) found that the stress level of crack initiation is higher under quasi-static strain rate than that under dynamic strain rate, indicating that rock fracture is more rapid in dynamic conditions. At present, relevant studies based on conventional loading tests have obtained abundant achievements, but there are few reports on the crack evolution laws of unloading rock. Before the excavation of underground geotechnical engineering, rock is in a three-dimensional pressure state, and conventional compression tests are sufficient to study the general mechanical behavior of rock. While in actual projects (such as underground chamber and tunnel excavation), rock mass is disturbed differently with different excavation rates, which affects rock cracking behavior to some extent (Zhou et al., 2018; Zhao et al., 2019), and the non-linear mechanical properties of rock cannot be fully interpreted through conventional loading tests at this time. Therefore, considering confining pressure, strain rate, and unloading rate conditions, loading and unloading rock mechanical tests were carried out to study the crack evolution law of rocks under different conditions to obtain progressive failure characteristics and predict failure precursor, which is beneficial to explain rock deformation mechanism under complex stress, and to provide technical support for design, construction, and risk control of underground tunnel and surrounding rock.

2 LOADING AND UNLOADING TESTS OF MARBLE

2.1 Test Specimen and Equipment

Rock samples in the tests are marbles taken from Jinping II hydropower station, with a burial depth of +2400m. According to the recommended standard of the International Society for Rock Mechanics, i.e., ISRM (Ulusay, 2014), rock cores were cut and polished into standard cylindrical samples, with a diameter of 50 mm and a height of 100 mm, some of the marble samples can be seen in **Figure 1A**. It is requested that the diameter should be controlled at 50^{+6}_{-2} mm, the height to diameter ratio is 2 ± 0.2, the non-parallelism of both ends of the specimen is no more than 0.05 mm, and both ends are perpendicular to the specimen axis and the maximum deviation is ±0.25°. In this test, 30 standard cylindrical marble samples were made, and 15 rock samples were respectively used in loading and unloading tests.

Both loading and unloading tests were carried out on the MTS815 Flex Test GT rock mechanics test system of the Key Laboratory of Deep Earth Science and Engineering Ministry of Education of Sichuan University, which was shown in **Figure 1B**, and the MTS test system is mainly composed of power system, hydraulic power system, servo threshold system, and host system. This system can be used to carry out uniaxial tests and triaxial

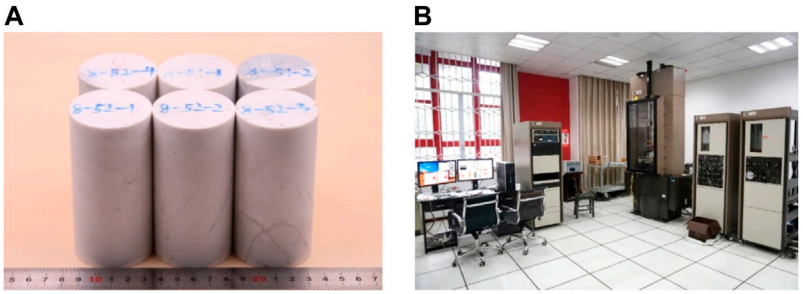


FIGURE 1 | Test specimen and equipment: **(A)** Marble specimens; **(B)** MTS815 rock mechanics test system.

TABLE 1 | Discrete analysis of marble samples.

Test type	Physical quantity	Average value	Standard deviation	Variation coefficient/%
Loading test	p	2.805	0.012	0.418
	ρ/ρ_{max}	0.994	0.004	0.413
	V_p	3,890.733	155.132	3.987
	$V_p/V_{p\ max}$	0.875	0.03987	3.980
Unloading test	p	2.808	0.017	0.596
	ρ/ρ_{max}	0.982	0.006	0.601
	V_p	3,772.333	180.252	4.778
	$V_p/V_{p\ max}$	0.913	0.044	4.792

loading and unloading tests under dynamic or static conditions, and it is loaded by stress or strain control.

2.2 Discrete Analysis

Affected by the geological tectonic movement, there exist some primary defects inside marble, which means that the rock samples taken from the same environment have a certain discreteness. In order to reduce the influence of rock sample discreteness on test results, rock samples with similar physical parameters, such as density and p-wave velocity, were selected and tested in the same group. The higher the density and p-wave velocity, the denser the internal structure of rock, and the stronger its mechanical strength, and the two parameters can indirectly reflect differences in rock internal structure. The dispersion degree of rock samples can be analyzed by dispersion indexes, such as mean value, standard deviation, and variation coefficient, and the analysis results were listed in **Table 1**. It can be seen from the table that the standard deviation of ρ, ρ/ρ_{max}, $V_p/V_{p\ max}$ under loading and unloading tests is much less than 1, and their variation coefficient is within 10%, which indicates that the dispersion degree of rock samples meets the requirements of the test specification.

2.3 Test Plan

In order to study crack evolution law in rock under different excavation conditions and explain its deformation and failure mechanism, taking Jinping marble as an example to carry out indoor tests under different loading and unloading conditions. In this paper, quasi-static triaxial compression test, constant confining pressure loading test, and unloading test under different initial confining pressure and unloading rate were designed, and there are three rock samples in each group of parallel tests. The detailed test plans were listed in **Table 2**.

The stress path diagram of the triaxial loading and unloading test was shown in **Figure 2**, and the detailed test methods are as follows:

(1) In the quasi-static loading test, first respectively load confining pressure and axial pressure to 50 MPa at 0.06 mm/min and 3 MPa/min loading rate, and then continue to load axial pressure at $10^{-5}s^{-1}$, $10^{-4}s^{-1}$, and $10^{-3}s^{-1}$ strain rates respectively by strain control. In this test, strain control loading is realized by the Linear Variable Differential Transformer, i.e., LVDT, and the loading rates corresponding to $10^{-5}s^{-1}$, $10^{-4}s^{-1}$, and $10^{-3}s^{-1}$ strain rate are 0.06 mm/min, 0.6 mm/min, and 6 mm/min respectively.

(2) In the constant confining pressure loading test, the strain rate maintains at $10^{-5}s^{-1}$, and the application of confining pressure is controlled by stress. The test procedure of the constant confining pressure loading test is consistent with the quasi-static loading test, but in the initial stage, confining pressure is respectively imposed to 25, 50, and 80 MPa at 3 MPa/min loading rate.

(3) In the triaxial unloading test, after being loaded to hydrostatic pressure state, continue loading to preset axial pressure at 0.06 mm/min loading rate, then start to unload the confining pressure until rock sample damages, and the stress level at the unloading point is 80% of the triaxial compressive strength in this test. In the unloading

TABLE 2 | Test plan.

Simulated condition	Test type	Test condition		Sample quantity
Different excavation disturbance	Quasi-static strain rate triaxial loading test	σ_3 = 50 MPa	$\dot{\varepsilon}$= $10^{-5}s^{-1}$ $\dot{\varepsilon}$= $10^{-4}s^{-1}$ $\dot{\varepsilon}$= $10^{-3}s^{-1}$	3 × 3
Different depths	Constant confining pressure loading test	$\dot{\varepsilon}$= $10^{-5}s^{-1}$	σ_3 = 25 MPa σ_3 = 50 MPa σ_3 = 80 MPa	3 × 3
Different depth unloading	Unloading test under different initial confining pressure	$\Delta\sigma_3$ = 0.01 MPa/s	σ_3 = 25 MPa σ_3 = 50 MPa σ_3 = 80 MPa	3 × 3
Different excavation rates	Unloading test with different unloading rate	σ_3 = 50 MPa	$\Delta\sigma_3$ = 0.01 MPa/s $\Delta\sigma_3$ = 0.1 MPa/s $\Delta\sigma_3$ = 1 MPa/s	3 × 3

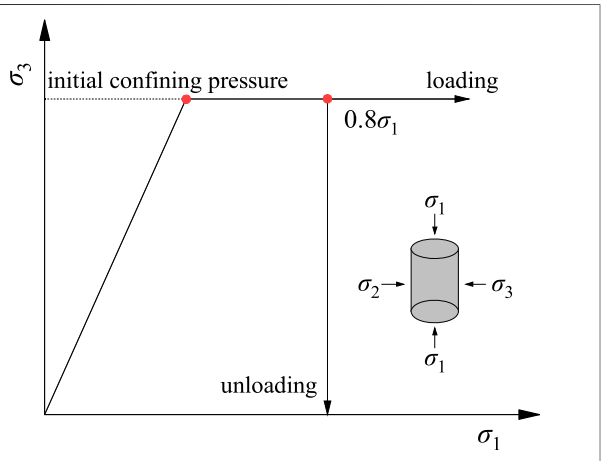


FIGURE 2 | Stress path of loading and unloading tests.

test, when considering the influence of initial confining pressure, unload at 0.01 MPa/s unloading rate under conditions of 25, 50, and 80 MPa confining pressure respectively; While considering the influence of unloading rate, the initial confining pressure is 50 MPa, then unload at 0.01, 0.1, and 1 MPa/s unloading rate respectively.

3 ANALYSIS OF TEST RESULTS

3.1 Stress-Strain Curve

Stress-strain curves of marbles under different loading and unloading conditions were plotted in **Figure 3**, they all show a trend of changing from linear growth to non-linear growth. Taking the marble sample under 25 MPa confining pressure as an example, the stress-strain curves of marbles can be simply divided into four stages, that is linear stage A, non-linear stage B, stress plateau stage C, and post-peak failure stage D. It can be seen that in the linear stage before the peak, stress-strain curves are basically consistent under different conditions, and rock is in an elastic state with little difference in elastic modulus at this stage. As stress increases further, the rock enters the plastic stage, and the strain increases faster than stress. Meanwhile, the external input energy is mainly used for the micro crack evolution, and the micro-cracks begin to expand and extend rapidly, leading to the plastic deformation of marble. With initial confining pressure rising, the plastic characteristics of marble enhance, but strain rate and unloading rate have no significant effect on it. At peak stress, there is no immediate stress drop under confining pressure conditions, but there is a stress flat, where the stress distribution inside the rock reaches a steady state.

In the post-peak failure stage, stress drop occurs but the stress drop degree in the unloading state is obviously higher

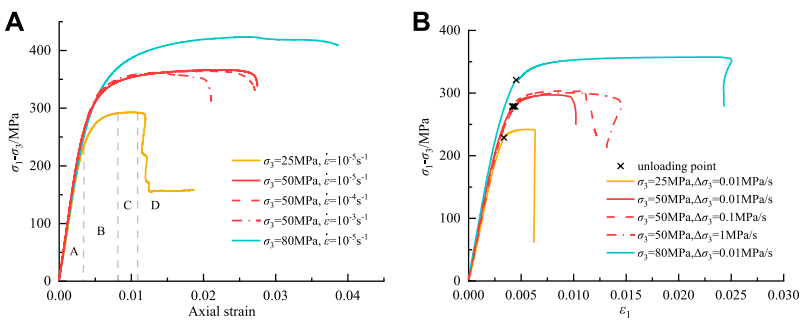


FIGURE 3 | Deviatoric stress-axial strain curves of marble samples: **(A)** loading condition; **(B)** unloading condition.

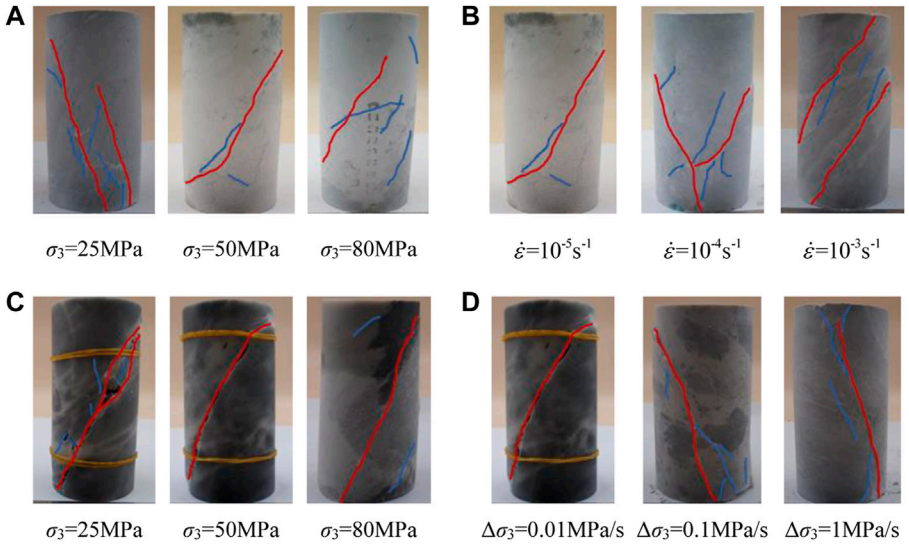


FIGURE 4 | Macroscopic failure modes of marble samples: **(A)** constant confining pressure condition ($\dot{\varepsilon}$= $10^{-5}s^{-1}$); **(B)** strain rate condition (σ_3 = 50 MPa); **(C)** unloading confining pressure condition ($\Delta\sigma_3$ = 0.01 MPa/s); **(D)** unloading rate condition (σ_3 = 50 MPa).

than the loading state, showing that unloading marble is more prone to severe brittle failure. With an increase of initial confining pressure, the stress drop rate gradually decreases, and the failure of marble transitions from brittle to plastic. Under 80 MPa confining pressure, there is even no obvious stress drop, and the rock shows an approximately ideal plastic state. The influence of strain rate and unloading rate on the stress-strain curve is more obvious in post-peak. As strain rate and unloading rate increase, stress drop rate increases slightly, and brittle failure characteristics of marble enhance. It can be seen that marbles have different mechanical responses under the action of confining pressure, strain rate, and unloading rate, and the effect of confining pressure on mechanical behavior is more significant.

Under the quasi-static strain rate, the peak stress of triaxial marble fluctuates around 350 MPa. For loading and unloading tests under different confining pressures, the peak stress under both stress paths increases with the increase of confining pressure, but the peak stress of unloaded marble is lower than that of loading under the same initial confining pressure, which indicates that unloading weakens rock ability to resist deformation and failure. When unloading under the initial confining pressure of 50 MPa, the peak stress increases slightly as the unloading rate increases. In the loading and unloading test, linear stages of stress-strain curves under different strain rates and unloading rates basically coincide, and the elastic modulus of marble has little difference. With confining pressure increasing, the slope of the linear phase of the stress-strain curve gradually increases, and the elastic modulus of marble also increases. The larger the elastic modulus, the stronger the rock stiffness and the ability to resist deformation and damage, which also shows that confining pressure can restrain rock deformation.

3.2 Macroscopic Failure Characteristics

Macroscopic failure modes of marbles under loading and unloading were seen in **Figure 4**, the red line in the figure represents the main crack and the blue line represents the secondary crack. As shown in **Figure 4A**, rock sample under 25 MPa confining pressure occurs double-shear failure, and tensile fissures highly develop between two parallel main shear cracks. At 50 MPa confining pressure, the sample shows single-shear failure, and there are few secondary shear cracks around the main shear crack. At 80 MPa confining pressure, microcracks fully developed under the action of axial stress, main shear crack without penetration, and dilatancy appears. As confining pressure rises, variation of failure modes of marble specimens shows that confining pressure limits the circumferential deformation of rock. As shown in **Figure 4B**, the sample under $10^{-4}s^{-1}$ strain rate occurs shear failure in "V" shape, and secondary shear cracks are distributed near the main cracks. At $10^{-3}s^{-1}$ strain rate, two parallel shear cracks penetrate surface the rock surface, and secondary cracks are distributed between them. As the strain rate increases, marble specimens change from single-shear failure to double-shear failure, and the failure degree gradually intensifies.

Under unloading conditions, as shown in **Figure 4C**, under 25 MPa initial confining pressure, a shear zone with large width is formed on the rock surface, and there are many fragments distributed in the zone, which is caused by friction and extrusion between fracture surfaces. Under 50 MPa initial confining pressure, the shear zone gets narrowed, and at higher confining pressure only one thin shear crack penetrates the rock surface. Therefore, with the increase of initial confining pressure, unloading marbles transition from tensile-shear composite failure to shear failure. As shown in **Figure 4D**, under 0.1 MPa/s unloading rate, a shear zone with small width penetrates the rock sample, and secondary cracks appear near it. Under 1 MPa/s unloading rate, the sample undergoes tensile shear

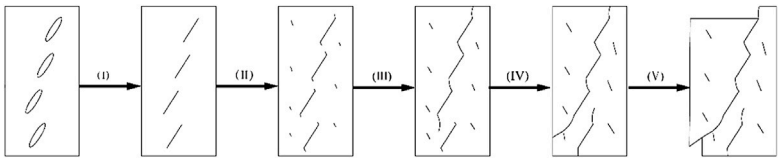


FIGURE 5 | General progressive failure process of rock.

failure, the fracture surface is steep, and shows brittle failure is obvious. Therefore, as the unloading rate increases, marble failure modes transition from shear failure to tensile shear failure. Compared with the loading path, the macroscopic failure degree of marble under unloading condition is more serious, and micro-cracks develop more fully, which is unfavorable for engineering.

3.3 Progressive Failure Process Based on Crack Strain

As is known, micro-crack evolution is a direct cause of rock failure. As shown in **Figure 5**, rock instability and failure are mainly caused by microcrack closure, initiation, expansion, and coalescence, which is a progressive failure process. As can be seen from **Section 3.1**, the stress-strain curve of marble tends to change in stages, but each stage cannot be defined accurately from the curve, which has certain subjectivity. In order to study the deformation and failure mechanism of rock during progressive failure stages, and quantitatively analyze crack evolution law in rock during the loading and unloading process, the crack strain variable can be used to describe crack propagation characteristics in rock. Crack strain refers to the axial and circumferential deformation caused by initiation, propagation, and coalescence of original cracks and initiation of new cracks under the action of external loads (Martin, 1993). Its physical significance is the difference between the true strain and elastic strain of rock under small deformation conditions. In this paper, in order to directly reflect the amount of rock deformation, volume crack strain was used to reflect the deformation caused by both axial and circumferential crack propagation. Based on this, the calculation method of volume crack strain can be described as:

$$\varepsilon_v^c = \varepsilon_v - \varepsilon_v^e \tag{1}$$

where, ε_v , ε_v^e , ε_v^c are volume strain, volume elastic strain, and volume crack strain respectively; And ε_v can be calculated as **Eq. 2**, in which axial strain ε_1 and lateral strain ε_3 can be directly obtained by axial and circumferential extensometer respectively.

$$\varepsilon_v = \varepsilon_1 + 2\varepsilon_3 \tag{2}$$

According to Hooke's law,

$$\begin{cases} \varepsilon_1^e = \dfrac{1}{E}\left[\left(\sigma_1 - \mu(\sigma_2 + \sigma_3)\right)\right] \\ \varepsilon_3^e = \dfrac{1}{E}\left[\left(\sigma_2 - \mu(\sigma_1 + \sigma_3)\right)\right] \end{cases} \tag{3}$$

where, ε_1^e, ε_3^e are axial elastic strain and lateral elastic strain respectively; σ_1 is axial stress; σ_2, σ_3 are lateral stress, when in conventional triaxial test, $\sigma_2 = \sigma_3$; E、 μ are the elastic modulus and Poisson ratio of rock respectively.

Therefore, crack strain can be calculated as (Zuo et al., 2019):

$$\varepsilon_v^c = \varepsilon_v - \frac{1-2\mu}{E}(\sigma_1 + 2\sigma_3) \tag{4}$$

According to **Eq. 4**, the volume crack strain of rock samples under different stress conditions can be calculated, and then taking the volume crack strain and volume strain as the main analysis variables. Through the evolution characteristics of deviatoric stress-axial strain, volume strain-axial strain, and volume crack strain-axial strain curves of marble (seen in **Figure 6**), its progressive failure process under loading and unloading conditions can be divided into five stages. In the crack closure stage (Stage I), volume crack strain first increases in a positive direction and then tends to be stable, this is because original fissures in rock gradually closure under external loads. When primary cracks reach a completely closuring state, volume crack strain is close to 0, and the corresponding stress at point A is the closure stress σ_{cc}. In the linear elastic stage (Stage II), the volume crack strain is almost constant, indicating that the rock sample is in a linear elastic state. If unloading at this stage, the sample can be restored to its original state. In the crack stable growth stage (stage III), volume crack strain increases in a negative direction as loading continues, and the corresponding stress at the initial increasing point (point B) is the initiation stress σ_{ci}. At this time, original cracks gradually propagate and tension cracks initiate, causing irreversible damage to the rock. In the crack rapid growth stage (stage IV), volume strain gradually decreases from the positive maximum value, showing that the rock sample turns from compression to expansion, and the stress at the maximum point C of volume strain is the damage stress σ_{cd}. And during this process, tension cracks rapidly expand and then conflate to form shear cracks, which leads to macrocracks appearing in the specimen surface. In the post-peak failure stage (Stage V), after peak stress (point D), macrocracks penetrate the rock sample, dislocation slip occurs at the fracture surface, and the rock sample eventually fractures.

Different stages of crack evolution correspond to different stress levels, and characteristic stress is an important index to characterize the progressive failure process of rock, it can be defined as the closure stress σ_{cc}, initiation stress $\sigma_{ci,}$ and damage stress σ_{cd}. Meanwhile, characteristic stress is also an important index to evaluate the damage degree of rock mass

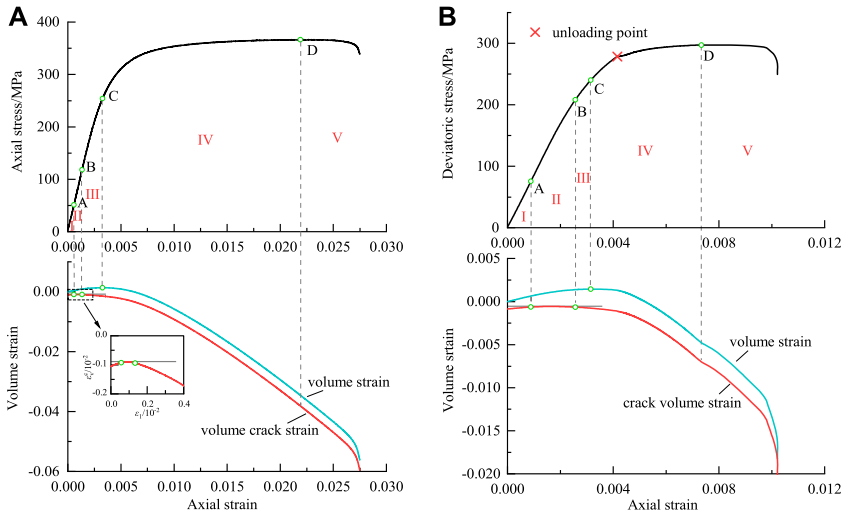


FIGURE 6 | Progressive failure process of marble samples: **(A)** loading condition [(σ_3 = 50MPa, $\dot{\varepsilon}$= $10^{-5}s^{-1}$)]; **(B)** unloading conditionσ_3 = 50MPa, $\Delta\sigma_3$ = 0.01MPa/s.

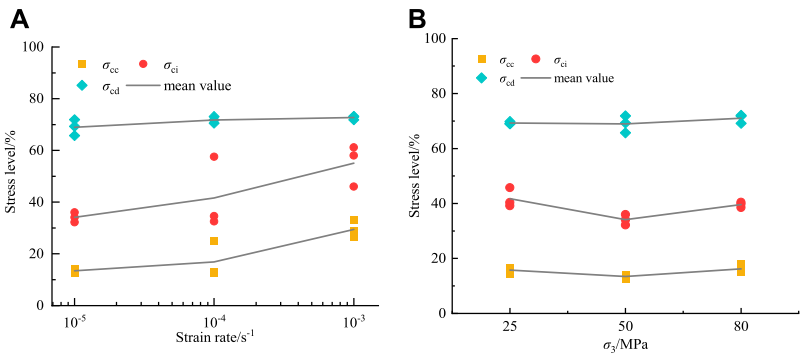


FIGURE 7 | Characteristic stress thresholds of marbles: **(A)** strain rate condition; **(B)** confining pressure condition.

caused by excavation disturbance in engineering rock mass excavation, which is significant to the design and long-term stability of geotechnical engineering (Martin and Chandler, 1994). As mentioned above, taking volume crack strain and volume strain as analysis variables, the progressive failure process of marble is divided and the corresponding characteristic stress thresholds are determined. Since unloading conditions only weaken rock peak stress, the influence of strain rate and confining pressure on characteristic stresses of marble was discussed in this paper. As shown in **Figure 7**, in order to eliminate the effect of differences in marble samples on characteristic stresses, they were normalized to be analyzed. It can be found from **Figure 7A** that as the strain rate rises from $10^{-5}s^{-1}$ to $10^{-3}s^{-1}$, stress levels of σ_{cc}, $\sigma_{ci,}$ and σ_{cd} respectively increase from 0.135,0.341, and 0.690 to 0.295,0.551, and 0.727. With confining pressure increasing from 25 to 80 MPa, stress levels of σ_{cc} and σ_{cd} respectively increase from 0.158 and 0.693 to 0.162 and 0.710, and σ_{ci} first decrease from 0.418 to 0.341 and then increase to 0.396. In general, the higher the strain rate and confining pressure, the higher the stress level of characteristic stress, this is because the increase in confining pressure and strain rate enhances rock bearing capacity, and crack propagation in rock needs to reach a higher stress level.

3.4 Progressive Evolution Law of Deformation Parameters

To interpret progressive failure mechanisms of marble under loading and unloading conditions, the deformation modulus E and generalized Poisson's ratio μ were introduced to further analyze. Deformation modulus refers to the ratio of stress increment to strain increment, and Poisson's ratio is the ratio of lateral strain to axial strain. The calculation method of deformation modulus and Poisson's ratio under triaxial conditions is as follows (Zhu et al., 2020):

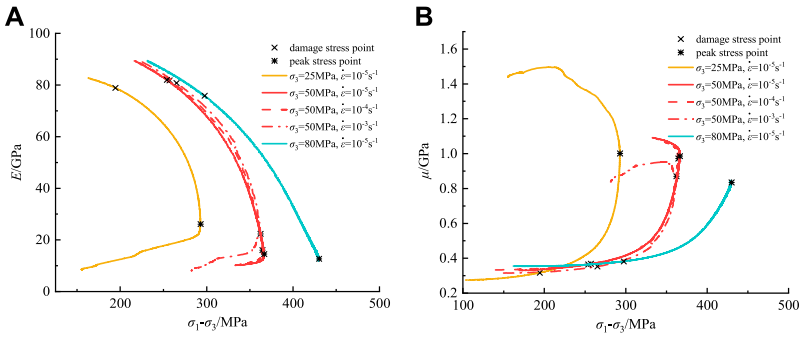


FIGURE 8 | Deformation parameters under loading conditions: **(A)** deformation modulus; **(B)** Poisson's ratio.

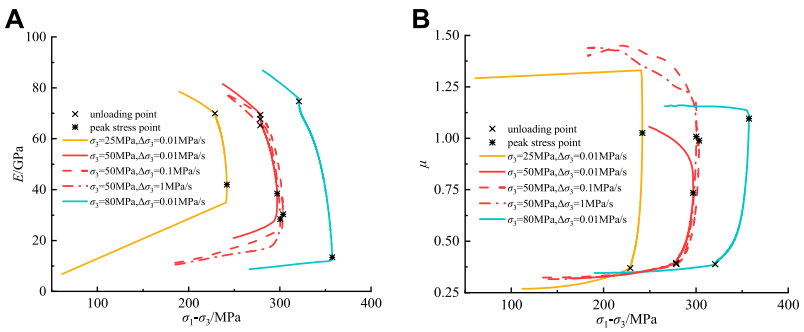


FIGURE 9 | Deformation parameters under unloading conditions: **(A)** deformation modulus; **(B)** Poisson's ratio.

$$E = \frac{\sigma_1 - 2\mu\sigma_3}{\varepsilon_1} \tag{5}$$

$$\mu = \frac{\sigma_1\varepsilon_3 - \sigma_3\varepsilon_1}{\sigma_3(2\varepsilon_3 - \varepsilon_1) - \sigma_1\varepsilon_1} \tag{6}$$

Deformation modulus and Poisson ratio of marbles under loading and unloading tests were calculated by **Eqs. 5**, **6**, and evolution curves of deformation parameters under two conditions were respectively plotted in **Figures 8**, **9**. In the loading state, as shown in **Figure 8A**, with confining pressure rising from 25 to 80 MPa, initial deformation modulus increases from about 81 to 90 GPa, but strain rate has no obvious effect on initial deformation modulus of marble. After reaching damage stress, deformation modulus all show a continuously declining trend, and its decreasing rate becomes faster when stress is closer to the peak value, which is due to the continuous increase of plastic deformation caused by rapid propagation of internal cracks in marble. During this period, the lower the confining pressure and the higher the strain rate, the faster the decreasing rate of deformation modulus, indicating that amount of rock deformation is larger under low confining pressure and high strain rate. After peak stress, rock fracture leads its bearing capacity to weaken and deformation modulus to decrease, and the decreasing rate is obviously lower than that of the pre-peak stage. As shown in **Figure 8B**, the Poisson ratio before the damage stress is basically stable which can be considered as an elastic constant, since marble is approximately in an elastic state and only generates little circumferential deformation at this time. After damage stress, circumferential deformation increases rapidly due to crack propagation and conflation, and the Poisson ratio correspondingly increases to more than 0.5. At this time, Poisson's ratio includes both volume deformation and crack propagation deformation, so it is called generalized Poisson's ratio and cannot be regarded as an elastic constant (Martino and Chandler, 2004; Xing et al., 2018). With the increase of confining pressure, the increasing rate of Poisson's ratio decreases gradually, and the Poisson's ratio at peak stress also decreases, but its variation trend under different strain rates is almost similar. After peak stress, the increasing rate of Poisson's ratio slows down and then gradually stabilizes.

In the unloading state, as shown in **Figure 9A**, With initial confining pressure rising from 25 to 80 MPa, the initial deformation modulus increases from about 79 to 89 GPa. After the unloading point, the deformation modulus drops suddenly, since unloading the confining pressure makes the tension cracks fully propagate, axial deformation greatly increases, and decreasing rate of deformation modulus is faster than that of the loading state. With an increase of initial confining pressure and unloading rate, the decreasing rate of deformation modulus in this stage decreases slightly. When peak stress is reached, the deformation modulus decreases slowly. As shown in **Figure 9B**, the Poisson ratio can also be regarded as an elastic constant before the unloading point, but after the unloading point due to the decrease of confining pressure, a large amount of

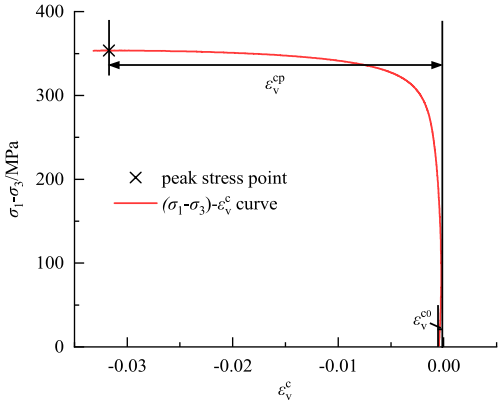


FIGURE 10 | Typical deviatoric stress-crack volumetric strain curves of marble.

circumferential deformation rapidly occurs resulting in a sharp increase in Poisson's ratio, and its increasing rate is significantly higher than that of loading state. Under unloading conditions, the Poisson ratio at peak stress point is almost greater than 1, which indicates that unloading marbles generate more deformation amount. With initial confining pressure increasing and unloading rate decreasing, the increasing rate of Poisson's ratio decreases slightly. After peak stress, the Poisson ratio continues to increase due to the complete failure of the rock.

4 DISCUSSION

4.1 Characteristic Volume Crack Strain

Typical deviatoric stress-crack volumetric strain curves of marble was plotted in **Figure 10**, from which its crack propagation characteristic can be analyzed. Under the action of external loads, as deviator stress increases volume crack strain shows a trend of first increasing, then remaining constant, and finally decreasing. The larger the volume crack strain, the smaller its absolute value, reversely, the smaller the volume crack strain, the larger its absolute value, which indicates that more microcracks are generated in the rock.

Defining the variable quantity of volume crack strain in the crack closure stage as the initial volume crack closure strain ε_v^{c0}, which is caused by the closure of the primary crack and can be used to reflect the initial damage degree of rock (Ji et al., 2016), the larger the absolute value of ε_v^{c0}, the greater the crack closure degree, and the greater the initial damage of rock. The volume crack propagation strain ε_v^{cp}, which represents crack propagation ability before rock failure, was defined as the variable quantity of volume crack strain in the crack stable growth stage and rapid growth stage (Chen et al., 2020). The larger the absolute value of ε_v^{cp}, the more sufficient the crack propagation degree, the more cracks are generated before rock failure. As shown in **Eq. 7**, defining the absolute value of the difference between volume crack propagation strain and initial volume crack closure strain as the pre-peak volume crack propagation strain without considering initial damage of rock, i.e., $\Delta\varepsilon_v^c$, to avoid influence of original structure in rock on crack propagation during loading and unloading process.

$$\Delta\varepsilon_v^c = \left|\varepsilon_v^{cp} - \varepsilon_v^{c0}\right| \tag{7}$$

The pre-peak volume crack propagation strain without considering initial damage under different loading and unloading conditions was shown in **Figure 11**. In the loading state, as the strain rate rises from $10^{-5}s^{-1}$ to $10^{-3}s^{-1}$, the mean value of $\Delta\varepsilon_v^c$ decreases from 0.029 to 0.019, while as confining pressure rises from 25 to 80 MPa, mean value of $\Delta\varepsilon_v^c$ increases from 0.013 to 0.028. $\Delta\varepsilon_v^c$ value in the unloading state is generally smaller than that in the loading state, and with the unloading rate rising from 0.01 MPa/s to 1 MPa/s, the mean value of $\Delta\varepsilon_v^c$ decreases from 0.016 to 0.013, and with initial confining pressure rising from 25 to 80 MPa, mean value of $\Delta\varepsilon_v^c$ increases from 0.011 to 0.033. The results show that $\Delta\varepsilon_v^c$ value under loading and unloading conditions all exhibit a growth trend as initial confining pressure rises, indicating that pre-peak crack propagation degree is higher and more microcracks are generated in rock under higher confining pressure. Reversely, the $\Delta\varepsilon_v^c$ value decreases with strain rate and unloading rate rising, indicating that pre-peak crack propagation degree is lower and fewer microcracks are generated in rock under higher strain rate and unloading rate. If cracks propagate more fully in pre-peak, tensile cracks will propagate and merge to form shear cracks, and rock mainly suffers plastic shear failure after the peak. If crack propagation degree is relatively low pre-peak, since

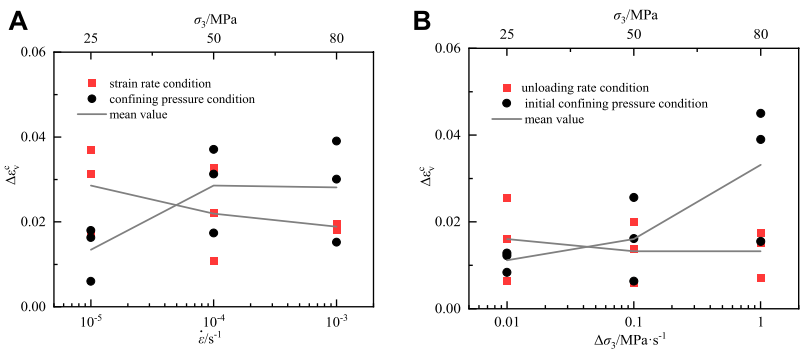


FIGURE 11 | Volume crack propagation characteristic of marble samples: **(A)** loading condition; **(B)** unloading condition.

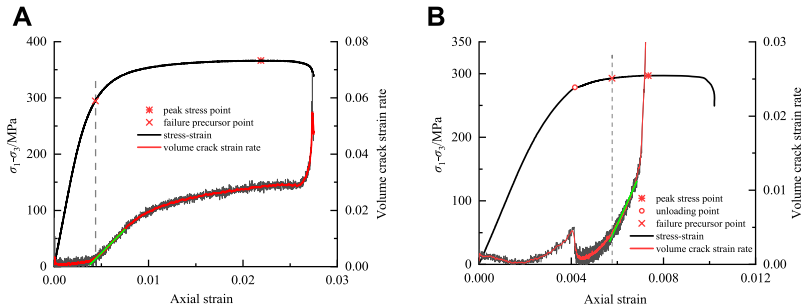


FIGURE 12 | Crack strain rate curves of marble samples: **(A)** loading condition (σ_3 = 50MPa, $\dot{\varepsilon}$= $10^{-5}s^{-1}$); **(B)** unloading condition (σ_3 = 50MPa, $\Delta\sigma_3$ = 0.01MPa/s).

the tensile crack is unable to fully extend and conflate, the rock will undergo tensile-shear composite failure. Therefore, the increase of strain rate and unloading rate easily causes insufficient expansion of internal cracks before surrounding rock failure, resulting in sudden brittle failure of rock mass and serious dynamic disasters such as rock burst.

4.2 Evolution Characteristics of Volume Crack Strain Rate

Under the action of external loads, crack propagation velocity plays a decisive role in failure process of rock (Alneasan et al., 2019). In laboratory tests, it is difficult to directly and effectively obtain the crack propagation velocity of rock. Since the variation rate of volume crack strain in each progressive failure stage is obviously different, it also can reflect crack propagation degree in rock in different failure stages. In this paper, volume crack strain rate, which is the derivative of volume crack strain to time, was introduced to quantitatively analyze the progressive failure process of marble, and its calculation method is as follows.

$$V_v^c = \frac{d\varepsilon_v^c}{dt} \tag{8}$$

where t is the loading and unloading time, s; V_v^c is the volume crack strain rate, s^{-1}。

Volume crack strain rate of marble under different loading and unloading conditions was shown in **Figure 12**. Marble samples with $10^{-5}s^{-1}$ strain rate and 0.01 Mpa/s unloading rate under the initial confining pressure of 50 MPa were respectively taken as examples. Due to the discreteness of test data, the calculated volume crack strain rate fluctuates, a smooth volume crack strain rate curve can be obtained by the moving average method. It can be seen from **Figure 12A** that the volume crack strain rate curve of marble increases non-linearly with axial strain increasing. In the crack closure stage and linear elastic stage, the volume crack strain rate is relatively low, and the rock is almost in a stable state. After entering the crack stable growth stage, the volume crack strain rate increases slowly, but its growth rate increases at the crack rapid growth stage. In the peak stress flat stage, the growth rate of volume crack strain rate first slows down as marble reaches a new stable state, and then suddenly increases in post-peak. As shown in **Figure 12B**, in the unloading state, the variation trend of volume crack strain rate before the unloading point is similar to that under loading conditions. It can be found that the volume crack strain rate drops suddenly at the unloading point and then continues to rise until rock failure, the reason why is that there was a brief pause in the test caused by the change from axial compression to confining pressure unloading at unloading point. After the unloading point, although confining pressure continues to decrease, the deviator stress still increases slowly under the condition of constant axial pressure, and after the short stress re-adjustment, lateral restraint on the rock is gradually weakened due to the influence of unloading confining pressure. Meanwhile, microcracks extend rapidly and the crack strain rate sharply increases accordingly, so the steady increase state of crack strain rate in this stage does not occur in the unloading state.

4.3 Identification of Failure Precursor Based on Volume Crack Strain Rate

Impact instability, rock burst, and other dynamic disasters caused by excavation disturbance are results of unstable deformation of rock mass mechanical system. Instability of any rock medium will cause disturbance of rock mass mechanical system, thus studying rock deformation mechanism and failure precursor information is of great significance to the prediction and prevention of engineering disasters. It can be seen from **Section 4.2** that the evolution curve of volume crack strain rate shows various characteristics in different deformation and failure stages. Volume crack strain rate changing from stable growth to sharp growth indicates that cracks inside rock propagate rapidly, and then penetrate specimen surface to generate macrocracks, at this time, the turning point can be regarded as a failure precursor point of rock. Identifying precursory information of rock failure based on crack strain is closer to the realistic process of rock failure, and determining failure precursory point through volume crack strain rate is a direct and effective method, which can be used to identify failure precursory information of rock under different stress paths.

On this basis, stress levels corresponding to failure precursor points of marbles under different loading and unloading conditions was plotted in **Figure 13**. In the loading state, with strain rate increasing from $10^{-5}s^{-1}$ to $10^{-3}s^{-1}$ and confining pressure rising from 25 to 80 MPa, stress levels of failure precursor respectively decrease from 0.822 to 0.742 and 0.883 to 0.772. In the unloading state, as the unloading rate increases from 0.01 MPa/s to 1 MPa/s and initial confining pressure rises from 25 to 80 MPa, the stress levels of failure precursors respectively

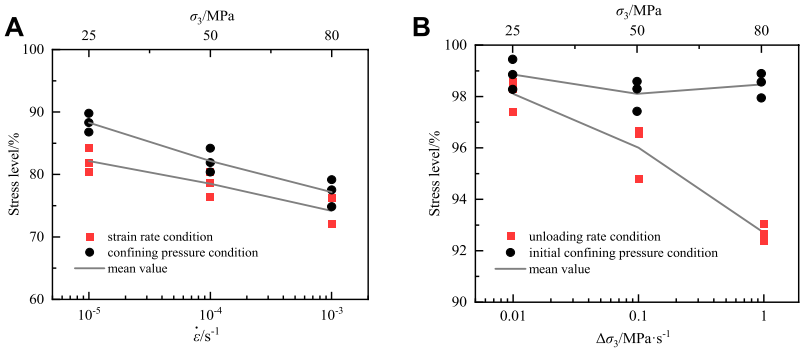


FIGURE 13 | Failure precursor stress levels of marbles based on crack strain rate: **(A)** loading test; **(B)** unloading test.

drop from 0.981 to 0.927 and 0.989 to 0.985. Under the four conditions, failure precursor stress level generally shows a decreasing trend, the lower the stress level, the earlier the failure precursor point appears. The stress levels of failure precursor are between 70% and 90% when loading, which is lower than the stress levels between 90% and 100% under unloading conditions, the peak stress of rock decreases under the action of unloading, leading to an increase in the failure precursor stress level of the unloading rock. Failure precursor point of unloading marble is close to the unloading point, indicating that unloading marble is more prone to sudden fracture or even rock burst disaster. Since the failure precursor in this paper was determined by the turning point that volume crack strain rate changes from steady growth to rapid growth, actually microcracks are about to or have already begun to extend rapidly after the unloading point, thus the sudden brittle failure usually occurs soon after unloading.

5 CONCLUSION

(1) Under different conditions, stress-strain curves of marbles are similar in the linear stage, but they are significantly affected by initial confining pressure, strain rate, and unloading rate in non-linear and post-peak stages. Under different stress paths, triaxial marble mainly suffers shear failure, and the failure degree under the unloading state is more serious than the loading state. In the loading state, as confining pressure increases and strain rate decreases, the brittle failure degree of marble decreases. In the unloading state, marble is less prone to brittle failure when unloading at a lower unloading rate.

(2) The progressive failure process of marble can be divided into crack closure, linear elastic, crack stable growth, crack rapid growth, and post-peak failure stages based on volume crack strain, correspondingly the characteristic stress thresholds are determined. The higher the strain rate and confining pressure, the higher the stress level of characteristic stress, while the unloading conditions only weakens the peak stress. As stress level rises, deformation modulus decreases, the Poisson ratio increases, and their changing rate in unloading conditions is faster than in loading conditions, indicating that more deformation is generated in marble under unloading conditions, especially under higher unloading rate and lower initial confining pressure.

(3) Introducing the pre-peak volume crack propagation strain without considering initial damage to quantitatively analyze the crack propagation degree of marble before the peak. The lower the confining pressure, the higher the strain rate and unloading rate, and the fewer the cracks generated before the peak. The turning point of volume crack strain rate from stable growth to rapid growth is defined as the failure precursor point of rock. Stress levels of marble failure precursors in loading and unloading conditions are between 70% and 100%, and decrease as the strain rate increases, confining the pressure and unloading rate. In the unloading state, the failure precursor point appears later and is close to the unloading point, showing that unloading rock is more prone to sudden fracture.

DATA AVAILABILITY STATEMENT

The original contributions presented in the study are included in the article/supplementary material, further inquiries can be directed to the corresponding author.

AUTHOR CONTRIBUTIONS

XL contributed to the conception of the study; YZ, QH, and YX performed the experiment; XL and YZ contributed significantly to the analysis and manuscript preparation; YZ performed the data analyses and wrote the manuscript; JG helped perform the analysis with constructive discussions.

FUNDING

This research was funded by the Opening Fund of Key Laboratory of Deep Earth Science and Engineering, Ministry of Education, Sichuan University (No. DESE202003), the Key Scientific Research Fund of Xihua University (No. Z17113), and the Research Center for Social Development and Social Risk Control of Sichuan Province, Key Research Base of Philosophy and Social Sciences, Sichuan University (No. SR21A04).

REFERENCES

Alneasan, M., Behnia, M., and Bagherpour, R. (2019). Analytical and numerical investigations of dynamic crack propagation in brittle rocks under mixed mode loading. *Constr. Build. Mat.* 222, 544–555. doi:10.1016/j.conbuildmat.2019.06.163

Bieniawski, Z. T. (1967). Mechanism of brittle fracture of rock: Part I-theory of the fracture process. *Int. J. Rock Mech. Min. Sci. Geomechanics Abstr.* 4 (4), 395–404. doi:10.1016/0148-9062(67)90030-7

Cai, M., and Kaiser, P. K. (2005). Assessment of excavation damaged zone using a micromechanics model. *Tunn. Undergr. Space Technol.* 20 (4), 301–310. doi:10.1016/j.tust.2004.12.002

Cai, M., Kaiser, P. K., Tasaka, Y., Maejima, T., Morioka, H., Minami, M., et al. (2004). Generalized crack initiation and crack damage stress thresholds of brittle rock masses near underground excavations. *Int. J. Rock Mech. Min. Sci. (1997).* 41 (5), 833–847. doi:10.1016/j.ijrmms.2004.02.001

Chen, G. Q., Zhang, Y., Li, Y., Pan, Y. G., and Jin, C. Y. (2021). Thermal-acoustic precursor information chain of rock failure under true triaxial loading. *Chin. J. Rock Mech. Eng.* 40 (9), 1764–1776. doi:10.13722/j.cnki.jrme.2020.0984

Chen, Y. F., Wei, K., Liu, W., Hu, S. H., Hu, R., Zhou, C. B., et al. (2016). Experimental characterization and micromechanical modelling of anisotropic slates. *Rock Mech. Rock Eng.* 49 (9), 3541–3557. doi:10.1007/s00603-016-1009-x

Chen, Y., and Guo, B. (2020). Crack closure effect and energy dissipation model for rocks under uniaxial compression. *Geotech. Geol. Eng. (Dordr).* 38 (6), 621–629. doi:10.1007/s10706-019-01051-4

Chen, Y., Zuo, J. P., Li, Z. H., and Dou, R. (2020). Experimental investigation on the crack propagation behaviors of sandstone under different loading and unloading conditions. *Int. J. Rock Mech. Min. Sci. (1997).* 130, 104310. doi:10.1016/j.ijrmms.2020.104310

Cong, Y., Feng, X. T., Zheng, Y. R., Wang, Z. Q., and Qiu, S. L. (2016). Study on effects of unloading rate on macro-meso failure mechanism of brittle rock. *Chin. J. Rock Mech. Eng.* 35 (S2), 3696–3705. doi:10.13722/j.cnki.jrme.2015.1159

Dong, L. J., Chen, Y. C., Sun, D. Y., and Zhang, Y. H. (2021c). Implications for rock instability precursors and principal stress direction from rock acoustic experiments. *Int. J. Min. Sci. Technol.* 31 (5), 789–798. doi:10.1016/j.ijmst.2021.06.006

Dong, L. J., Hu, Q. C., Tong, X. J., and Liu, Y. F. (2020). Velocity-Free MS/AE source location method for three-dimensional hole-containing structures. *Engineering* 6 (7), 827–834. doi:10.1016/j.eng.2019.12.016

Dong, L. J., Tong, X. J., Hu, Q. C., and Tao, Q. (2021b). Empty region identification method and experimental verification for the two-dimensional complex structure. *Int. J. Rock Mech. Min. Sci. (1997).* 147, 104885. doi:10.1016/j.ijrmms.2021.104885

Dong, L. J., Tong, X. J., and Ma, J. (2021a). Quantitative investigation of tomographic effects in abnormal regions of complex structures. *Engineering* 7 (7), 1011–1022. doi:10.1016/j.eng.2020.06.021

Feng, G. L., Chen, B. R., Xiao, Y. X., Jiang, Q., Li, P. X., Zheng, H., et al. (2022). Microseismic characteristics of rockburst development in deep tbm tunnels with alternating soft-hard strata and application to rockburst warning: A case study of the neelum-jhelum hydropower project. *Tunn. Undergr. Space Technol.* 122, 104398. doi:10.1016/j.tust.2022.104398

Hoek, E., and Martin, C. D. (2014). Fracture initiation and propagation in intact rock - a review. *J. Rock Mech. Geotechnical Eng.* 6 (4), 287–300. doi:10.1016/j.jrmge.2014.06.001

Ji, W. W., Pan, P. Z., Su, F. S., and Du, M. P. (2016). Failure mechanism of deep-buried marble under loading-unloading conditions based on crack volumetric strain. *Rock Soil Mech.* 37 (11), 3079–3088. doi:10.16285/j.rsm.2016.11.006

Jin, P. J., Wang, E. Y., and Song, D. Z. (2017). Study on correlation of acoustic emission and plastic strain based on coal-rock damage theory. *Geomech. Eng.* 12 (4), 627–637. doi:10.12989/gae.2017.12.4.627

Li, A., Liu, Y., Dai, F., Liu, K., and Wei, M. D. (2020). Continuum analysis of the structurally controlled displacements for large- scale underground caverns in bedded rock masses. *Tunn. Undergr. Space Technol.* 97, 103288. doi:10.1016/j.tust.2020.103288

Li, X. Z., Qi, C. Z., Shao, Z. S., and Ma, C. (2018). Evaluation of strength and failure of brittle rock containing initial cracks under lithospheric conditions. *Acta Geophys.* 66 (2), 141–152. doi:10.1007/s11600-018-0123-4

Martin, C. D., and Chandler, N. A. (1994). The progressive fracture of Lac Du Bonnet granite. *Int. J. Rock Mech. Min. Sci. Geomechanics Abstr.* 31 (6), 643–659. doi:10.1016/0148-9062(94)90005-1

Martin, C. D. (1993). *The strength of massive lac du bonnet granite around underground openings*. Canada: University of Manitoba.

Martino, J. B., and Chandler, N. A. (2004). Excavation-induced damage studies at the underground research laboratory. *Int. J. Rock Mech. Min. Sci. (1997).* 41 (8), 1413–1426. doi:10.1016/j.ijrmms.2004.09.010

Ulusay, R. (2014). *The ISRM suggested methods for rock characterization testing and monitoring 2007-2014*. Berlin: Springer.

Xing, H. A., Zhang, Q. B., and Zhao, J. (2018). Stress thresholds of crack development and Poisson ' s ratio of rock material at high strain rate. *Rock Mech. Rock Eng.* 51 (3), 945–951. doi:10.1007/s00603-017-1377-x

Yan, Z. L., Dai, F., Zhu, J. B., and Xu, Y. (2021). Dynamic cracking behaviors and energy evolution of multi-flawed rocks under static pre-compression. *Rock Mech. Rock Eng.* 54 (9), 5117–5139. doi:10.1007/s00603-021-02564-2

Yu, Y., Zhao, D. C., Feng, G. L., Geng, D. X., and Guo, H. S. (2022). Energy evolution and acoustic emission characteristics of uniaxial compression failure of anchored layered sandstone. *Front. Earth Sci. (Lausanne).* 10, 841598. doi:10.3389/feart.2022.841598

Zhao, P. X., Li, S. G., Ho, C. H., Lin, H. F., and Zhuo, R. S. (2019). Crack propagation and material characteristics of rocklike specimens subject to different loading rates. *J. Mat. Civ. Eng.* 31 (7), 04019113. doi:10.1061/(ASCE)MT.1943-5533.0002768

Zhou, L., Zhu, Z. M., Qiu, H., Zhang, X. S., and Lang, L. (2018). Study of the effect of loading rates on crack propagation velocity and rock fracture toughness using cracked tunnel specimens. *Int. J. Rock Mech. Min. Sci. (1997).* 112, 25–34. doi:10.1016/j.ijrmms.2018.10.011

Zhou, X. P., Bi, J., and Qian, Q. H. (2015). Numerical simulation of crack growth and coalescence in rock-Like materials containing multiple pre-existing flaws. *Rock Mech. Rock Eng.* 48 (3), 1097–1114. doi:10.1007/s00603-014-0627-4

Zhu, Z. H., Yu, L. Y., Li, J. L., Meng, Q. B., Sui, B., and Zhang, Z. Q. (2020). Deformation evolution and dissipated energy characteristicsof marble under pre-peak unloading conditions. *J. China Coal Soc* 45 (S1), 181–190. doi:10.13225/j.cnki.jccs.SJ20.0122

Zuo, J. P., Chen, Y., and Liu, X. L. (2019). Crack evolution behavior of rocks under confining pressures and its propagation model before peak stress. *J. Cent. South Univ.* 26 (11), 3045–3056. doi:10.1007/s11771-019-4235-z

Zuo, J. P., Chen, Y., Song, H. Q., and Wei, X. (2017). Evolution of pre-peak axial crack strain and nonlinear model for coal-rock combined body. *Chin. J. Geotech. Eng.* 39 (9), 1609–1615. doi:10.11779/CJGE201709008

Conflict of Interest: The authors declare that the research was conducted in the absence of any commercial or financial relationships that could be construed as a potential conflict of interest.

Publisher's Note: All claims expressed in this article are solely those of the authors and do not necessarily represent those of their affiliated organizations, or those of the publisher, the editors and the reviewers. Any product that may be evaluated in this article, or claim that may be made by its manufacturer, is not guaranteed or endorsed by the publisher.

Copyright © 2022 Liu, Zheng, Guo, Hao and Xue. This is an open-access article distributed under the terms of the Creative Commons Attribution License (CC BY). The use, distribution or reproduction in other forums is permitted, provided the original author(s) and the copyright owner(s) are credited and that the original publication in this journal is cited, in accordance with accepted academic practice. No use, distribution or reproduction is permitted which does not comply with these terms.

frontiers | Frontiers in Earth Science

TYPE Original Research
PUBLISHED 22 August 2022
DOI 10.3389/feart.2022.966222

Check for updates

OPEN ACCESS

EDITED BY
Fengqiang Gong,
Southeast University, China

REVIEWED BY
Quan Jiang,
Institute of Rock and Soil Mechanics (CAS), China
Annan Jiang,
Dalian Maritime University, China
Chang'An Qin,
Beijing University of Civil Engineering and Architecture, China

*CORRESPONDENCE
Liang Zhang,
zhangliang@hncu.edu.cn

SPECIALTY SECTION
This article was submitted to Geohazards and Georisks, a section of the journal Frontiers in Earth Science

RECEIVED 10 June 2022
ACCEPTED 06 July 2022
PUBLISHED 22 August 2022

CITATION
Zhang L, Zhang S, Ling T and Deng Z (2022), Frequency spectrum and energy refinement characteristics of blasting vibration signals in raw water pipeline tunnel excavation.
Front. Earth Sci. 10:966222.
doi: 10.3389/feart.2022.966222

COPYRIGHT
© 2022 Zhang, Zhang, Ling and Deng. This is an open-access article distributed under the terms of the Creative Commons Attribution License (CC BY). The use, distribution or reproduction in other forums is permitted, provided the original author(s) and the copyright owner(s) are credited and that the original publication in this journal is cited, in accordance with accepted academic practice. No use, distribution or reproduction is permitted which does not comply with these terms.

Frequency spectrum and energy refinement characteristics of blasting vibration signals in raw water pipeline tunnel excavation

Liang Zhang[1]*, Sheng Zhang[1], Tonghua Ling[2] and Zongwei Deng[1]

[1]College of Civil Engineering, Hunan City University, Yiyang, China, [2]School of Civil Engineering, Changsha University of Science and Technology, Changsha, China

The analysis of time-frequency variation and energy refinement characteristics of blasting vibration signals has contributed to understanding the propagation law of blasting vibration wave and reducing the possible losses. Combined with the measured data of tunnel blasting excavation and based on the newly constructed wavelet function, the spectrum distribution and energy refinement characteristics of tunnel blasting vibration signals are deeply explored and studied. The results demonstrated that compared to the Fourier spectrum, the innovative method of scale energy spectrum can not only acquire the dominant frequency of the blasting vibration signals, but also the obtained spectrum curve is smoother and can clearly reflect the change trend of the signal spectrum. The newly constructed biorthogonal wavelet has the characteristics of high vanishing moment, high regularity and matching with the waveform variation of the measured blasting vibration signals, and can describe the subtle variation characteristics of blasting vibration signal frequency. The continuous wavelet transform energy spectrum can reflect the three-dimensional energy distribution of blasting vibration signal in the time-scale domain, and the occurrence time of frequency, the frequency duration interval and time range of blasting vibration signal can also be acquired. Wavelet packet algorithm can precisely calculate the energy distribution of each frequency component in the signal, the tunnel blasting vibration signals (YBJ1, YBJ2) generated near the power tower presents low frequency, while the signals (YBF3,YBF4) far away from the power tower presents relatively high frequency. Measures should be taken to control the vibration and resonance of power tower caused by tunnel blasting. This research is of great significance for recognizing the propagation law of vibration waves, reducing the impact of blasting on surrounding buildings, and ensuring the safety of tunnel construction and surrounding buildings.

KEYWORDS

blasting vibration, continuous wavelet transform, wavelet packet, spectrum distribution, energy refinement characteristics

Introduction

Drilling and blasting method is the main tunneling method in tunnel construction, which is especially suitable for the excavation of solid rock and sub-solid rock mountain tunnels (Koopialipoor et al., 2019; Sharafat et al., 2021; Li, et al., 2022; Ma et al., 2022). Drilling and blasting will not only cause damage and disturbance to the surrounding rock of the tunnel, but also the seismic wave effect caused by blasting will affect the stability and safety of the buildings around the tunnel (Singh et al., 2020; Kan et al., 2022). Energy and frequency are the main parameter indexes to measure the performance of blasting vibration signal. Among them, energy is the most direct quantity reflecting the strength of blasting vibration signal, and the harm to the tunnel is more intuitive, while the impact of blasting vibration signal frequency on structures is more subtle, but it is also the main factor threatening and damaging the stability of buildings (Chen et al., 2022; Mehboob et al., 2022; Wang et al., 2022; Wu et al., 2022). The principle of the effect of the frequency characteristics of the blasting vibration wave on the structure is that when the blasting vibration wave groups with different periods are transmitted from the blasting source to the structure, the structure will amplify some frequency wave groups consistent with or close to the natural period of the structure and act on the structure, while some frequency waves that are inconsistent with the natural period of the structure are reduced or filtered. It is precisely because of the amplification of the frequency close to the structure that the blasting vibration frequency is more harmful to the structure.

For a long time, confined to the development of theory, the Fourier transform method is often used to process the blasting vibration signal. The Fast Fourier transform (FFT) technology is quite effective for the analysis of periodic stationary signals and can obtain high accuracy and good results. However, Fourier theory is a global transformation theory, which can only determine the overall nature of the singularity of a function, lacking the positioning function of time and frequency (Robustelli and Pugliano, 2018; Tyrtaiou and Elenas, 2020; Zhang et al., 2022), so as that it has great limitations in analyzing blasting vibration signals. As an improvement of FFT method, short-time Fourier transform (STFT) can perform time localization analysis to a certain extent, but it cannot take into account the needs of frequency and time resolution, that means high time resolution and frequency resolution cannot be achieved simultaneously (Jing et al., 2018; Khodja et al., 2019). Wavelet analysis is a research method developed and evolved from the traditional Fourier transform theory. Due to the constant Q property and multiresolution analysis, it can meet the requirements of time subdivision at high frequency and frequency subdivision at low frequency (Quaye-Ballard et al., 2020; Babouri et al., 2021). It has great advantages in the processing of complex, nonlinear and nonstationary signals. Wavelet (packet) analysis has the property of spatial localization and has dual analysis characteristics of



FIGURE 1
Plane location map of the raw water pipeline tunnel.

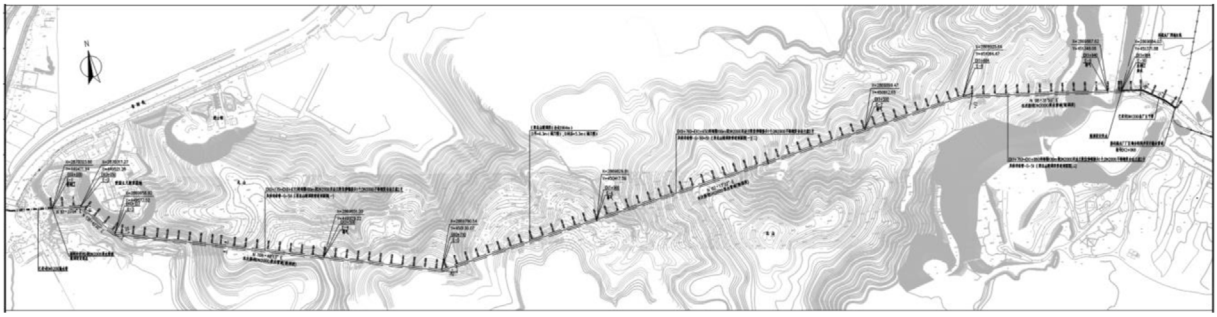


FIGURE 2
Geological plan of tunnel area.

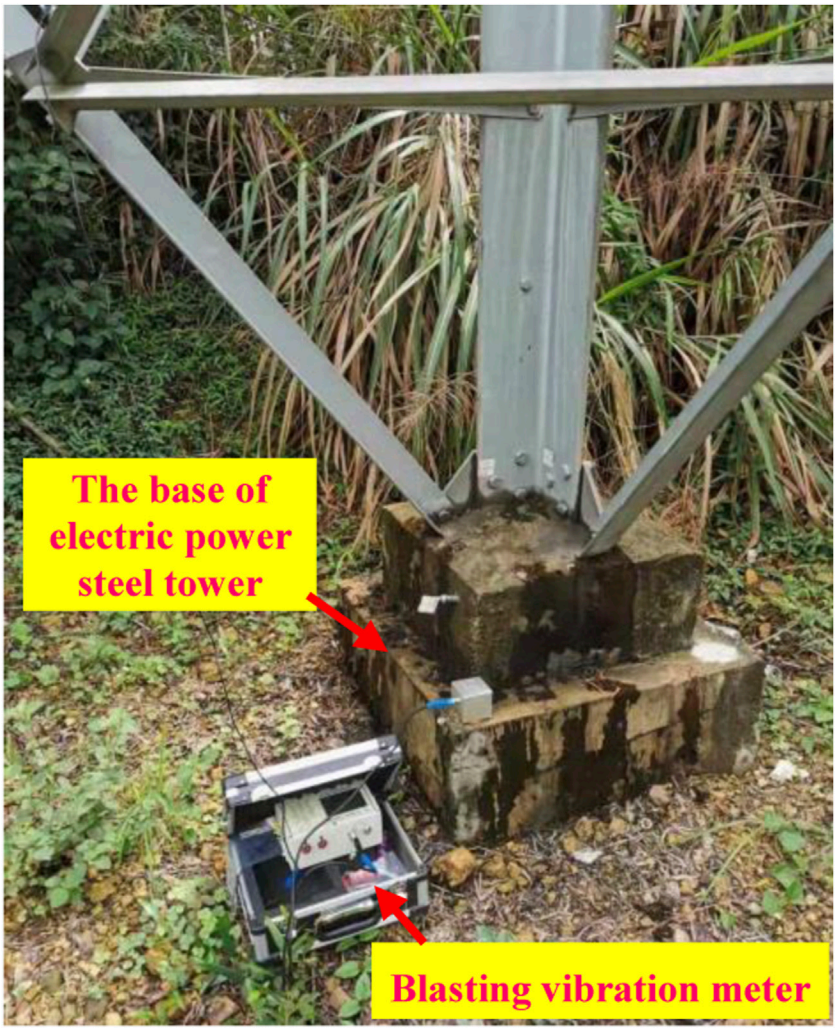


FIGURE 3
Electric power tower base and blasting vibration meter.



FIGURE 4
Panorama of tunnel entrance section.

frequency and time, which can reveal and reflect the propagation law of signal frequency and energy over time (Hamid et al., 2019; Shahryari et al., 2019; Tian et al., 2019).

The key lies in the selection or construction of the optimal wavelet basis when performing wavelet analysis on blasting vibration signals (Hafiz et al., 2018; Graf et al., 2019; Zhang S. et al., 2021). Usually a general basic wavelet is selected from MATLAB wavelet library for engineering signal analysis. The construction of an existing general wavelet basis often only starts from the basic conditions and mathematical theorems satisfied by the wavelet function, and not consider the problem of matching with the structural characteristics of specific engineering signals. Therefore, the existing general wavelet basis is generally not targeted and matched when analyzing specific engineering signals. The wavelet basis function should not only meet the basic requirements of tight support and attenuation, but also consider the problem of matching with specific engineering signals. In this study, the continuous wavelet transform and wavelet packet theories are applied to concretely analyze the time-frequency localization property, frequency spectrum characteristics, frequency band energy refinement characteristics of the blasting vibration signals generated from different excavation positions of tunnel on the basis of constructing the biorthogonal wavelet function for blasting vibration signal analysis, to accurately obtain the frequency spectrum information and propagation law of blasting vibration wave, evaluate the safety impact of blasting vibration on the power tower around the tunnel, and provide references and guidelines for the research on the impact of related drilling and blasting excavation on the surrounding buildings.

Engineering situation

This project is the construction of DN2000 raw water pipeline from Yanshan Pumping Station to Yuanhang Waterworks. The raw water management project is

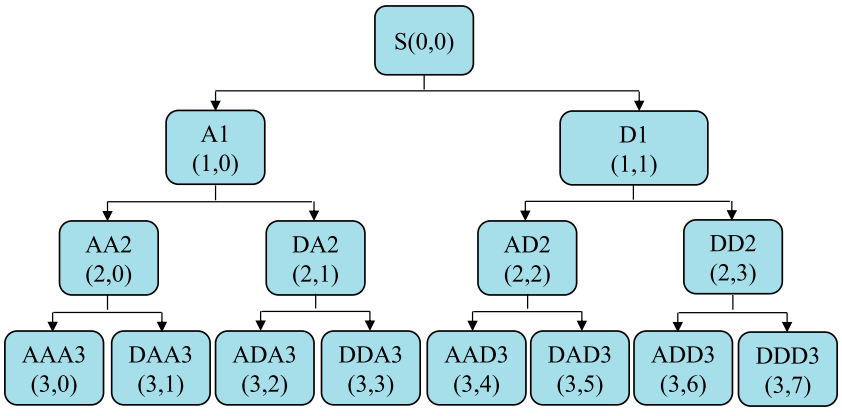


FIGURE 5
Tree structure of three-layer wavelet packet decomposition.

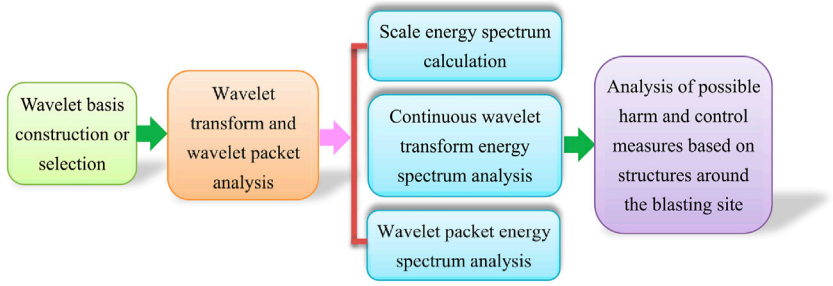


FIGURE 6
Flow chart of time-frequency characteristic analysis of blasting vibration signals.

constructed to meet the water consumption of residents and enterprises in Changle City. The raw water pipeline in this design starts from Yanshan Water Pumping Station and ends at Changle Yuanhang water plant. The design scope of this project is divided into five sections, in which the starting and ending pile numbers of the tunnel are EK0+000~EK1+964.

The diameter of the raw water pipeline is DN 2000, and the length of the whole pipeline is nearly 9.0 km, of which the length of the raw water pipeline in the tunnel is 2.1 km. The tunnel area is mainly composed of tuff of Jurassic Upper Nanyuan Formation (J_{3n}), with simple lithology and geological structural conditions, and poor groundwater development. There are no other adverse geological phenomena except for the possible collapse of the local tunnel section due to the development of fault structures. Most of the surrounding rocks in the tunnel site are grades II~III. The tunnel location of the project is shown in Figure 1. The green line in the figure indicates the tunnel excavation route and an electric power tower is close to the tunnel site. The tunnel excavation method is drilling and blasting. The geological plan of the study area is shown in Figure 2. The blasting vibration meter is placed under the power tower, and the sensor of the blasting vibration meter is put on the concrete base of the power tower, and is closely connected with the base surface (see Figure 3). Each time the tunnel is blasted, the sensor receives the vibration wave data

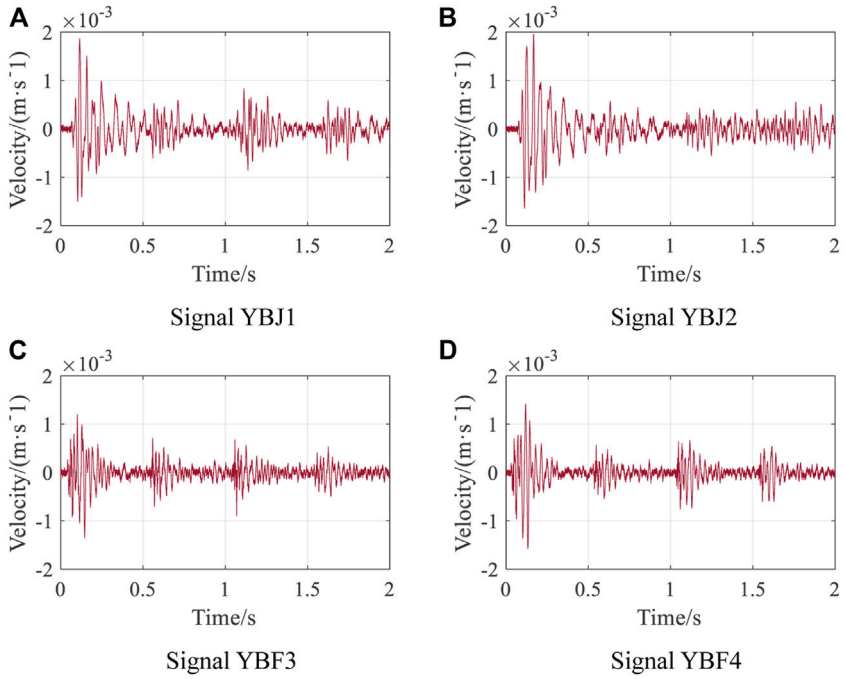


FIGURE 7
Waveforms of original blasting vibration signals generated by different excavation positions of the tunnel.

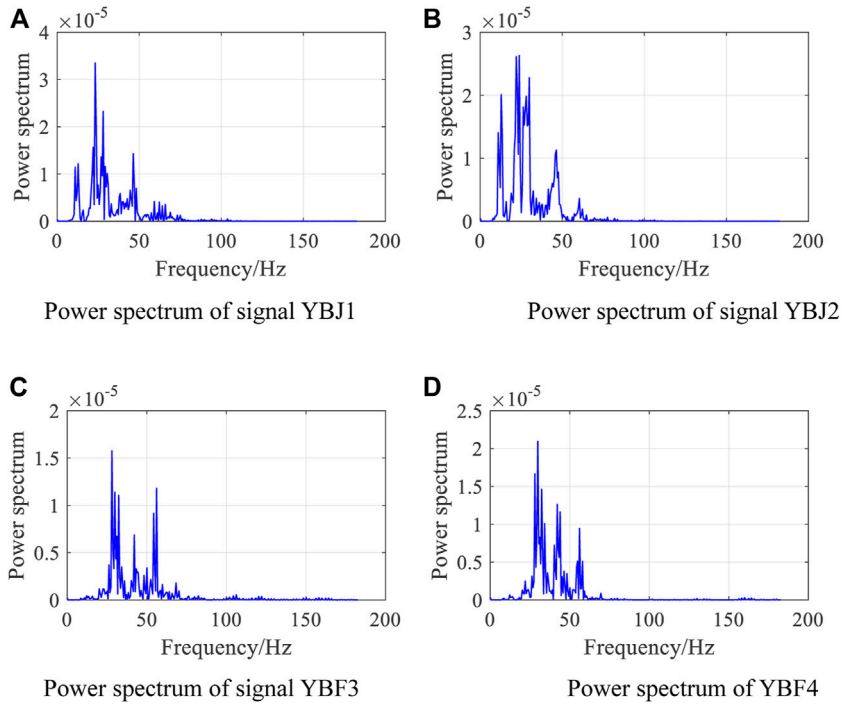


FIGURE 8
Spectrum analysis of different original blasting vibration signals.

of the power tower and records it into the memory of the blasting vibration meter. The panorama near the entrance of the tunnel is shown in Figure 4.

Biorthogonal wavelet construction based on second generation lifting method

The blasting vibration signal has nonlinear and nonstationary characteristics. The effective method to analyze the blasting vibration signal is wavelet analysis. Selecting or constructing the wavelet basis function corresponding to the structural characteristics of the analyzed blasting signal is of great significance to improve the effect of wavelet analysis and accurately extract the characteristic information of the target signal (Zhang L. et al., 2021). The biorthogonal wavelet basis matching the structural characteristics of the blasting vibration signal is constructed by using the second generation lifting scheme wavelet theory and particle swarm optimization algorithm (Daubechies and Sweldens, 1998; Tomiyama and Kawamura, 2016). Let $\{\tilde{h}_0, \tilde{g}_0, h_0, g_0\}$ denote a set of initial biorthogonal wavelet filters. Among them, $\tilde{h}_0$ and $\tilde{g}_0$ are a set of analytical filters, representing low-pass and high-pass filters at the decomposition end, respectively, and h_0 and g_0 are a set of synthetic filters, constituting low-pass and high-pass filters at the reconstruction end and assume that the initial dual wavelet filter ($\tilde{g}_0$) and the initial wavelet filter (g_0) have vanishing moment of $\tilde{N}_0$ and N_0 respectively. Let the new set of biorthogonal wavelet filters after one step of dual lifting and original lifting be $\{\tilde{h}_{update}, \tilde{g}_{update}, h_{update}, g_{update}\}$, and the construction expression of the new filter bank is as follows (Li et al., 2001; Ling et al., 2019):

$$\left.\begin{aligned} g_{update}(z) &= g_0(z) + h_0(z)s(z^2) \\ \tilde{h}_{update}(z) &= \tilde{h}_0(z) - \tilde{g}_0(z)s(z^{-2}) \end{aligned}\right\} \tag{1}$$

$$\left.\begin{aligned} h_{\text{update}}(z) &= h_0(z) - g_0(z)\tilde{s}(z^{-2}) \\ \tilde{g}_{update}(z) &= \tilde{g}_0(z) + \tilde{h}_0(z)\tilde{s}(z^2) \end{aligned}\right\} \tag{2}$$

where $s(z)$ represents the lifting operator and $\tilde{s}(z)$ represents the dual lifting operator, both of them are Laurent polynomials.

Assuming that the initial wavelet is a lazy wavelet, the vanishing moments of the dual wavelet and the main wavelet after one-step alternating lifting are 2 and 4, respectively. Firstly, the dual lifting is performed on the initial filter bank with dual lifting operator $\tilde{s}(z) = (z-1)^{\tilde{N}_0}\tilde{U}(z)$. The dual lifting objective is to raise the vanishing moment of $\tilde{g}_0$ from $\tilde{N}_0 = 0$ to $\tilde{N} = 2$, so it exists

$$\tilde{P}(z) = \tilde{q}_0(z) + \tilde{h}_0(z)(z+1)^{\tilde{N}_0}\tilde{U}(z^2), \frac{d^{\tilde{k}}\tilde{P}(z)}{dz^{\tilde{k}}}\Big|_{z=1} = 0, \tilde{k} = 0, 1$$

where $\tilde{q}_0(z) = z^{-1}$.

TABLE 1 Signal reconstruction error and center frequency of different wavelet basis.

Wavelet functions	Maximum reconstruction error of signal	Average reconstruction error	Wavelet center frequency
Db3	1.4402×10^{-14}	1.4648×10^{-15}	0.8000
Db4	2.7187×10^{-15}	2.6920×10^{-16}	0.7143
Db5	5.1315×10^{-15}	4.8111×10^{-16}	0.6667
Db6	3.1388×10^{-15}	3.1474×10^{-16}	0.7273
Db7	2.7365×10^{-15}	2.5907×10^{-16}	0.6923
Db8	7.9667×10^{-15}	7.4318×10^{-16}	0.6667
Db9	1.9853×10^{-14}	2.4248×10^{-15}	0.7059
Db10	4.0458×10^{-15}	4.5968×10^{-16}	0.6842
Bior1.3	1.9516×10^{-18}	1.0869×10^{-19}	0.8006
bior1.5	2.1684×10^{-18}	1.0865×10^{-19}	0.7781
Bior2.2	1.7347×10^{-18}	1.3705×10^{-19}	1.0008
Bior2.4	1.3010×10^{-18}	6.5516×10^{-20}	0.8893
Bior2.6	2.1684×10^{-18}	6.8718×10^{-20}	0.9234
Bior2.8	1.7347×10^{-18}	1.0104×10^{-19}	0.8826
bior3.1	2.3852×10^{-18}	1.9167×10^{-19}	1.0013
bior3.3	2.1684×10^{-18}	1.0913×10^{-19}	1.0006
bior3.5	1.7347×10^{-18}	1.1262×10^{-19}	1.0004
Bior3.7	1.7347×10^{-18}	1.2854×10^{-19}	0.9336
Bior3.9	1.7347×10^{-18}	1.2947×10^{-19}	0.9476
Blas2.4	1.0842×10^{-18}	4.6991×10^{-20}	0.8464

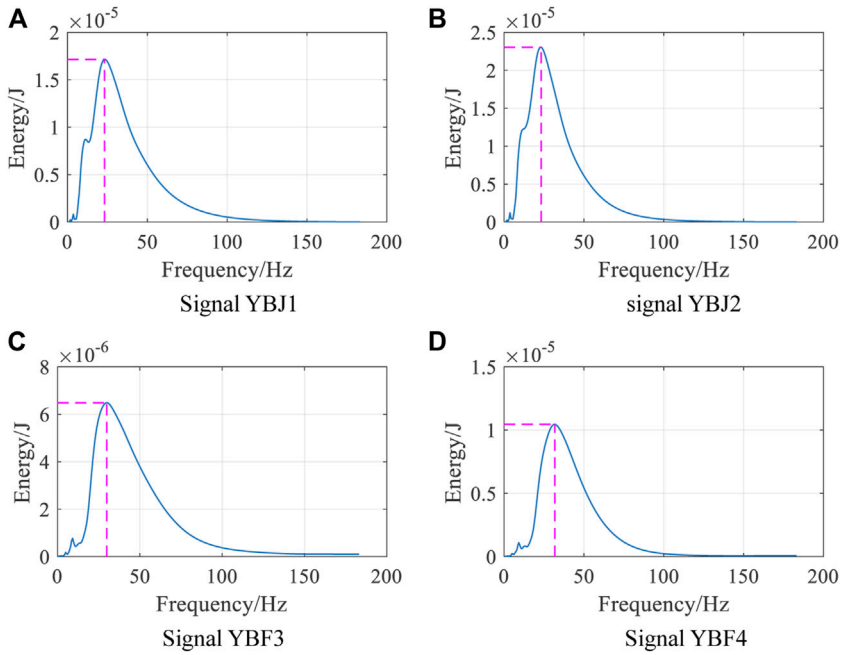


FIGURE 9
Scale energy spectrum of blasting vibration signals based on Blas2.4 wavelet.

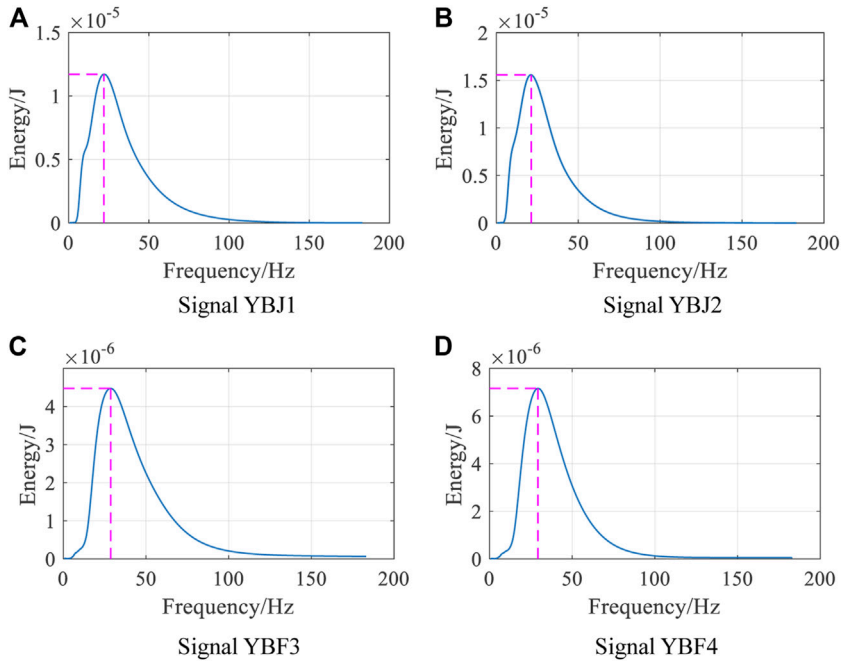


FIGURE 10
Scale energy spectrum of blasting vibration signals based on Db5 general wavelet.

The new filter bank is transformed into $\{\tilde{h}_0, \tilde{g}_{update}, h_{update}, g_0\}$ after dual lifting, and then the original liftings of $\tilde{h}_0$ and g_0 are performed, and there exists an lifting operator $s(z) = (z-1)^{N_0}U(z)$, the original lifting target is to raise the vanishing moment of filter g_0 from $N_0 = 0$ to $N = 4$. The initial filter $g_0(z)$ can be represented as $g_0(z) = (z-1)^{N_0}q_0(z)$, and the filter $h_0(z)$ has been converted to be h_{update} due to a dual lifting. According to the above Eq. 1, there exists

$$\begin{aligned} g_{update}(z) &= g_0(z) + h_0(z)s(z^2) \\ &= (z-1)^{N_0}q_0(z) + h_{update}(z)s(z^2) \\ &= (z-1)^{N}Q(z) \end{aligned}$$

i.e.

$$\frac{(z-1)^{N_0}q_0(z) + h_{update}(z)s(z^2)}{(z-1)^{N}} = Q(z) \tag{3}$$

where $q_0(z) = z^{-1}$, and $Q(z)$ is a Laurent polynomial.

Through simplification, it can be obtained as

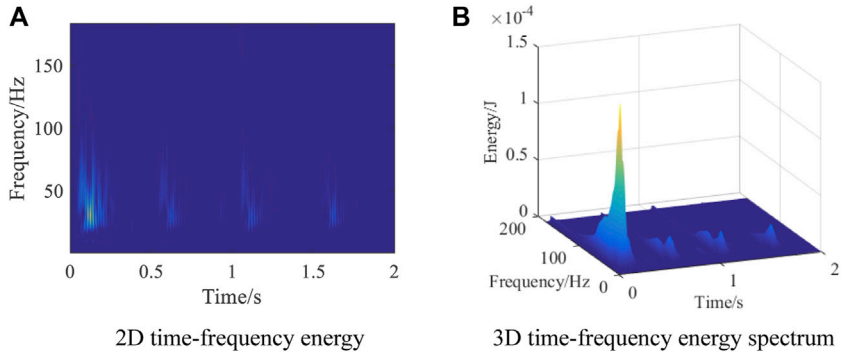


FIGURE 11
Time frequency energy diagram of continuous wavelet transform for blasting vibration signal.

$$P(z) = q_0(z) + h_{\text{update}}(z)(z+1)^{N_0}U(z^2), \frac{d^k P(z)}{dz^k}|_{z=1} = 0, \quad k = 0, 1, 2, 3$$

The new filter bank can be transformed as $\{\tilde{h}_{update}, \tilde{g}_{update}, h_{update}, g_{update}\}$ after the dual lifting and original lifting. Combined with the structural characteristics of the field measured blasting vibration signal and by searching and calculating, the coefficients of the newly constructed biorthogonal wavelet filter are as follows

$$\begin{cases} \left\{\tilde{h}_{update}\right\} = \left\{\begin{array}{l} 0, -0.0031, 0, 0.0555, -0.0341, -0.1737, 0.3876, 0.9497, 0.3876, \\ -0.1737, -0.0341, 0.0555, 0, -0.0031 \end{array}\right\} \\ \left\{\tilde{g}_{update}\right\} = \{0, 0, 0, -0.0645, 0, 0.4180, -0.7071, 0.4180, 0, -0.0645, 0, 0, 0, 0\} \\ \left\{h_{update}\right\} = \{0, 0, 0, -0.0645, 0, 0.4180, 0.7071, 0.4180, 0, -0.0645, 0, 0, 0, 0\} \\ \left\{g_{update}\right\} = \left\{\begin{array}{l} 0, 0.0031, 0, -0.0555, -0.0341, 0.1737, 0.3876, -0.9497, 0.3876, \\ 0.1737, -0.0341, -0.0555, 0, 0.0031 \end{array}\right\} \end{cases}$$

The biorthogonal wavelet function (Blas2.4 wavelet), which matches the structural characteristics of blasting vibration signals, can be achieved by iterative operation.

Algorithm and principles

Continuous wavelet transform

Wavelet transform is the development and extension of Fourier analysis. Continuous wavelet transform breaks through the limitation of Fourier transform base, which uses the translation and expansion of a function as the base to study the spectrum of the function (signals). For any square integrable function $\psi(x)$ in Hilbert space, if $\psi(x) \in L^2(R)$ and there is an admissible condition (Shah and Tantary, 2018; Kulak and Aydin, 2020):

$$C_\psi = \int_R \frac{|\hat{\psi}(\omega)|^2}{\omega} d\omega < +\infty \tag{4}$$

where $\hat{\psi}(\omega)$ is the Fourier transform of $\psi(x)$, $\psi(x)$ is called the mother wavelet. A set of functions that can be generated by the mother wavelet through translation and expansion

$$\psi_{a,b}(x) = \frac{1}{\sqrt{a}}\psi\left(\frac{x-b}{a}\right) \tag{5}$$

This can be called a wavelet basis function. where a is the scale parameter (dilation factor), b is the translation factor, with a, $b \in R$, and $a \neq 0$.

Let $f(x) \in L^2(R)$ and $\psi(x)$ be the mother wavelet, and define the formula (Lee et al., 2017; Rhif et al., 2019)

$$\begin{aligned} W_f(a,b) &= \langle f, \psi(a,b) \rangle \\ &= \int_R f(x)|a|^{-1/2}\overline{\psi\left(\frac{x-b}{a}\right)}dx \end{aligned} \tag{6}$$

Which is a continuous wavelet transform on the basis wavelet ψ. Where $\bar{X}$ denotes the conjugate operation of X.

Formula of inverse continuous wavelet transform can be exhibited as

$$f(x) = \frac{1}{C_\psi}\int_{-\infty}^{+\infty}\int_{-\infty}^{+\infty} W_f(a,b)\psi_{a,b}(x)\frac{da}{a^2}db \tag{7}$$

TABLE 2 Percentage of energy distribution in different frequency bands.

No.	Frequency intervals/Hz	Signals				No.	Frequency intervals/Hz	Signals			
		YBJ1/%	YBJ2/%	YBF3/%	YBF4%			YBJ1/%	YBJ2/%	YBF3/%	YBF4%
1	0~2.44	0.10	0.10	0.08	0.06	16	36.62~39.06	3.05	0.51	2.20	3.25
2	2.44~4.88	0.25	0.37	0.05	0.13	17	39.06~41.50	0.62	1.31	1.22	2.47
3	4.88~7.32	0.54	1.94	0.17	0.34	18	41.50~43.95	4.26	8.05	2.15	6.97
4	7.32~9.77	3.65	1.17	0.23	0.57	19	43.95~46.39	1.00	3.19	4.91	6.13
5	9.77~12.21	5.30	6.44	0.80	1.19	20	46.39~48.83	3.02	3.86	3.49	1.01
6	12.21~14.65	5.06	5.61	1.17	1.39	21	48.83~51.27	1.48	0.80	3.02	1.18
7	14.65~17.09	4.46	7.38	0.55	0.34	22	51.27~53.71	0.78	0.27	4.12	2.92
8	17.09~19.53	4.58	5.38	0.63	0.21	23	53.71~56.15	0.84	0.41	4.78	1.82
9	19.53~21.97	5.58	3.54	0.55	0.30	24	56.15~58.59	1.57	1.45	5.33	3.55
10	21.97~24.41	15.41	14.39	2.38	1.39	25	58.59~61.04	0.56	0.32	1.38	1.84
11	24.41~26.86	4.12	2.42	2.77	1.75	26	61.04~63.48	0.46	0.40	1.23	1.75
12	26.86~29.30	7.46	8.75	6.22	4.77	27	63.48~65.92	0.31	0.20	0.83	0.23
13	29.30~31.74	7.28	11.88	13.01	18.91	28	65.92~68.36	0.88	0.18	0.41	0.23
14	31.74~34.18	4.72	5.17	7.58	12.78	29	68.36~70.80	0.19	0.19	1.10	0.19
15	34.18~36.62	7.44	1.30	13.76	15.84	30	70.80~f_s/2	5.05	3.03	13.85	6.49

Continuous wavelet transform maps the original one-dimensional time-domain function to the two-dimensional "time-scale" domain to analyze the time-frequency characteristics of the signal. Wavelets with different time-frequency widths can be obtained to match any position of the original signal by adjusting the expansion factor *a* and the translation factor *b*, to achieve the purpose of the signal's time-frequency localization analysis.

Scale energy spectrum and time-scale energy spectrum of blasting vibration signals

The amplitude square of the continuous wavelet transform coefficient of blasting vibration signal $f(x)$ with the scale parameter a and translation factor b is called time-scale energy spectrum, i.e.

$$E_{W_{fx}(a,b)} = \left|W_{fx}(a,b)\right|^2 \tag{8}$$

The total energy of the signal $f(x)$ in the time-scale domain is as follows

$$E_{W_f all} = \int_0^{+\infty} \int_{-\infty}^{+\infty} E_{W_{fx}(a,b)} dadb \tag{9}$$

If the energy spectrum density on the time-scale two-dimensional plane is integrated with the translation factor b, the wavelet energy spectrum on the scale axis can be obtained

$$E_{W_f all(a)} = \int_{-\infty}^{+\infty} E_{W_{fx}(a,b)} db \tag{10}$$

The integration of time-frequency energy spectrum of blasting vibration signal with the time factor is the scale energy spectrum, which reflects the energy distribution of blasting vibration signal on different scales. Since the scale factor corresponds to the frequency of the signal in a certain sense, the scale energy spectrum can be used to characterize and research the energy variation of blasting vibration signals in different frequency intervals.

Wavelet packet analysis

Wavelet packet analysis, which can divide the signal frequency band into multiple levels and further decompose the high-frequency components that are not subdivided in wavelet analysis, is a more refined signal processing method. In multiresolution analysis, for the scale subspace V_j and wavelet subspace W_j, there exists an orthogonal decomposition $V_{j+1}=V_j+W_j$. If a unified subspace U_j^n is used to represent, and let $U_j^0 = V_j$, $U_j^1 = W_j$, then there is

$$U_{j+1}^0 = U_j^0 \oplus U_j^1, j \in Z \tag{11}$$

Define subspace U_j^n as the closure space of the function $u_n(t)$ and U_j^{2n} as the closure space of the function $u_{2n}(t)$. The following two-scale equations hold

$$\begin{cases} u_{2n}(x) = \sum_{k\in Z} h_k u_n(2x-k) \\ u_{2n+1}(x) = \sum_{k\in Z} g_k u_n(2x-k) \end{cases} \tag{12}$$

where the two coefficients g_k and h_k have an orthogonal relationship, that is, $g_k = (-1)^k h_{1-k}$. The following spatial decomposition can be obtained by using Eq. 12.

$$U_{j+1}^n = U_j^{2n} \oplus U_j^{2n+1}, j \in Z; n \in Z_+ \tag{13}$$

A three-layer wavelet packet decomposition tree structure is shown in Figure 5.

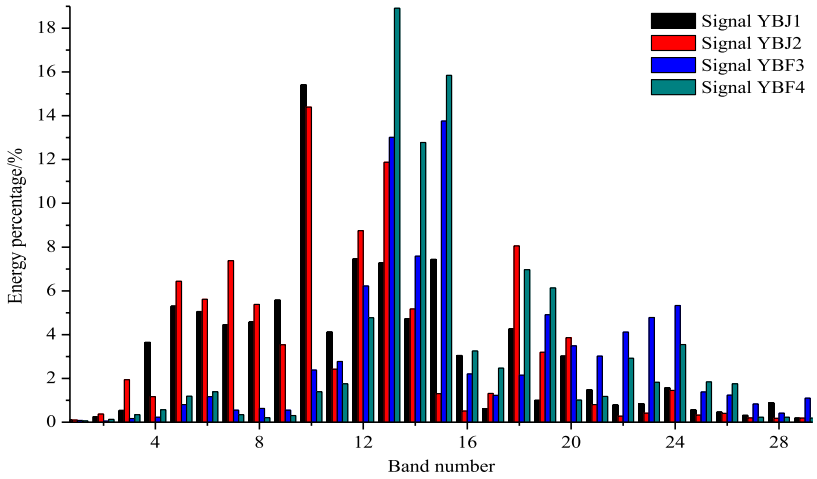


FIGURE 12
The percentage of energy distribution in each frequency band of blasting vibration signals.

Assuming that the wavelet packet algorithm is used to decompose the blasting vibration signal in layer i, the original signal can be expressed as

$$s(x) = \sum_{j=0}^{2^i-1} s_{i,j} = s_{i,0} + s_{i,1} + \cdots + s_{i,2^i-1} \tag{14}$$

where $s_{i,j}$ represents the wavelet packet decomposition subsignal. The energy of the subsignal $s_{i,j}$ can be expressed as

$$E_{i,j} = \int |s_{i,j}(t)|^2 dt = \sum_{n=1}^{n} |f_{j,k}|^2 \tag{15}$$

where $f_{j,k}$ represents the amplitude of the discrete points of the reconstructed subsignal $s_{i,j}$ $(j = 0, 1, 2, \cdots, 2^i - 1; k = 1, 2, \cdots, m$, m represents the number of sampling points of the reconstructed subsignal).

Then the total energy of blasting vibration signal is

$$E_a = \sum_{j=0}^{2^i-1} E_{i,j} \tag{16}$$

The percentage of energy in each frequency band to the total energy of blasting vibration signal can be expressed as

$$P_j = \frac{E_{i,j}}{E_a} \times 100\% \tag{17}$$

Analysis process of time-frequency characteristics of blasting vibration signals

The continuous wavelet transform and wavelet packet methods are proposed to analyze the blasting vibration signals from the perspective of time-frequency and energy refinement characteristics. First, select and determine the optimal basis wavelet used in the continuous wavelet transform and wavelet packet decomposition according to the reconstruction error of Db orthogonal wavelets, Bior series biorthogonal wavelet and blas2.4 new wavelet on the measured blasting vibration signals, and calculate the center frequency of the optimal wavelet basis. Second, the scale energy spectrum and wavelet packet energy spectrum of the original vibration signals at different excavation positions are analyzed, and moreover, the possible safety impact of blasting is explored in combination with the actual situation of buildings around the tunnel excavation site. The analysis flow is shown in Figure 6.

Spectrum analysis of blasting vibration signals

To analyze the propagation law of blasting vibration signals and the impact of blasting vibration on buildings around the city, especially the power tower, a blasting vibration meter is fixed at the power tower to test and record the blasting vibration signals under the tunnel construction at different positions. A total of four complete blasting vibration signals monitored were extracted for analysis, and the signal numbers were YBJ1, YBJ2, YBF3, and YBF4, respectively. Signals of YBJ1, YBJ2 are the seismic signals monitored by the blasting excavation of the tunnel close to the power tower, the corresponding tunnel excavation mileages are EK0+060 and EK0+100, and the plane distances from the blasting site to the power tower are approximately 32m and 72 m respectively; the tunnel excavation mileages corresponding the signals of YBF3, YBF4 are EK1+450 and EK1+570, the distances from the power tower are approximately 1,350 and 1480 m respectively. The tunnel excavation position corresponding to YBJ1 signal is closest to the power tower. The millisecond blasting technology is used for tunnel excavation. The four blasting charges were all 72 kg. The waveforms of the original blasting vibration signals are illustrated in Figure 7 and the power spectrum calculation results are shown in Figure 8 based on the fast Fourier transform theory.

From the power spectrum, the frequency range of each signal is below 200Hz, and the spectrum distribution is relatively dispersed, showing multiple local peaks of the spectrum. The dominating vibration frequency of blasting vibration signals can be determined from the figures, which are 23.19 Hz, 23.80 Hz, 28.08 Hz, and 29.91 Hz, respectively. Among them, the subdominant frequencies of YBJ2 and YBF3 signals are also prominent. The subdominant frequency of YBJ2 signal is 21.97 Hz, and that of YBF3 signal is 56.15 Hz. The dominant frequency of YBJ1 and YBJ2 signals generated by blasting excavation near the power tower is lower than that of YBF3 and YBF4 signals. The spectrum distribution of blasting vibration signal shows a sharp peak, and Fourier transform can only provide the result of signal spectrum distribution, but cannot provide the detailed information of signal time-frequency distribution and energy distribution.

Time-frequency characteristics analysis for blasting vibration signals

Selection of wavelet basis for blasting vibration signal analysis

Wavelet analysis is an applied mathematical method with fixed window size but variable shape (time window and frequency window are variable), which has multiresolution analysis characteristics and automatically adapts to the requirements of time-frequency signal and it is suitable for nonstationary signal processing of blasting vibration. The wavelet functions used in wavelet transform are nonuniqueness and diverse. An important task in wavelet

analysis is to select the optimal wavelet basis according to the characteristics of the blasting vibration signal. Daubechies series wavelets have orthogonality and compact support and Bior series wavelets have symmetry and high vanishing distance (Dai and Cao, 2017; Zhao et al., 2018). They are commonly used to process the measured blasting vibration signals. The center frequency of Daubechies wavelet series, Bior biorthogonal wavelet series, and the constructed Blas2.4 wavelet and the reconstruction error of the measured blasting vibration signals have been calculated and analyzed respectively to select the best wavelet basis suitable for the analysis of blasting vibration signals. In Daubechies wavelet basis, the smoothness of Db1 and Db2 wavelets is too poor to be used for blasting vibration signal processing, Db5 and Db8 wavelets have a small center frequency, which are suitable for wavelet decomposition and reconstruction of blasting vibration signals, and Db5 wavelet has a lower signal reconstruction error as seen in Table 1, so the Db5 wavelet is selected in Daubechies series to analyze the blasting vibration signals. The newly constructed Blas2.4 wavelet among the biorthogonal wavelets has the highest reconstruction accuracy and smaller central frequency value. Therefore, Blas2.4 wavelet and db5 wavelet are preliminarily selected to analyze the measured blasting vibration signals.

Scale energy spectrum of blasting vibration signals

Scale is a parameter applied to represent the expansion of the basic wavelet and it corresponds to the frequency of the signal in the time-frequency analysis. The scale energy spectrum characterizes the energy of the signal on different scales. By calculating the center frequency of the wavelet function and converting the scale parameters to the actual frequency, the scale energy spectrum can be applied to measure and master the frequency variation law of the blasting vibration signals from the perspective of wavelet transform. Based on Eqs. 6, 8, 10, the obtained signal scale energy spectrum is shown in Figure 9 by taking the constructed Blas2.4 as the basic wavelet.

The signal spectrogram obtained by the Fourier method is in the shapes of local spike. When the dominant frequency is almost the same as the subdominant frequency value, it is difficult to judge the dominant frequency of the signal directly from the spectrogram. The scale factor in the scale energy spectrum corresponds to the actual frequency of the signal through the length of the scale sequence and the center frequency of the wavelet function used. Different from the sawtooth waveform of the Fourier operation, the scale energy spectrum has smoothness and transition and can reflect the frequency variation of the blasting vibration signals concretely and continuously. Since the basis function used in the scale energy spectrum is compatible with the waveform change of the specific engineering signal, the dominant frequency of the signal can be accurately extracted and obtained. It can be seen from the above figures that the frequencies corresponding to the maximum energy of the four blasting signals YBJ1, YBJ2, YBF3, and YBF4 are 23.19 Hz, 23.80 Hz, 29.91 Hz, and 31.74 Hz respectively, which are basically consistent with the dominant vibration frequencies (23.19 Hz, 23.8 Hz, 28.08 Hz, and 29.91 Hz) obtained by Fourier spectrum. The sum of the relative error between the signal dominant frequency calculated by Blas2.4 wavelet and the Fourier spectrum results is only 11.89%, by accurate calculation, it can be seen that the scale energy spectrum can accurately represent the signal dominant frequency. And compared with the Fourier spectrum, the shape of the scale energy spectrum distribution curve is smoother, which can better reflect the spectrum change law and the trend of blasting vibration signal.

Taking the Db5 orthogonal wavelet, which is commonly used to analyze blasting vibration signals, as the basic wavelet, the calculated scale energy spectra of the blasting vibration signals are showed in Figure 10.

From the figure that the scale energy spectrum method based on db5 general wavelet can also obtain the dominant frequency of the signal, and the obtained scale energy spectrum curve is relatively smooth. The dominant frequency is 21.97 Hz, 21.36 Hz, 28.69 Hz, and 29.29 Hz, respectively, and the total relative error is 19.75% compared with the frequency values of Fourier spectrum. The calculated results show a large inconsistency with the Fourier spectrum relative to the frequency results of Blas2.4 new wavelet. And the scale energy spectrum curves of the blasting vibration signals acquired by db5 general wavelet are basically the same in shape, which cannot reflect the difference of signal spectrum distribution. That is, due to the lack of matching with the blasting vibration signals, the traditional general wavelet cannot accurately analyze and characterize the measured blasting vibration signals, nor can distinguish the difference between the signals, and the spectral calculation results are relatively low accuracy.

Continuous wavelet transform energy spectrum and wavelet packet energy analysis

According to the principles of Eqs. 6, 8, the continuous wavelet transform energy spectrum, which represents the change law of blasting vibration signal energy with time and frequency of signal can be calculated. The essence of wavelet transform is to represent any function $f(t)$ in $\mathbf{L}^2(\mathbf{R})$ space as the superposition of its projection on the wavelet function $\psi_{a,b}(t)$ with different scaling factors a and translation factors b. Therefore, the continuous wavelet transform can map one-dimensional time domain function to two-dimensional "time-scale" domain to achieve the purpose of time-frequency localization analysis of signals. Through the continuous wavelet transform energy spectrum, the occurrence time corresponding to the signal frequency can be obtained. In wavelet analysis, the selection of wavelet basis plays an important

role in obtaining accurate analysis results. From the previous section that the newly constructed blas2.4 wavelet can better highlight and characterize the details and characteristic information of blasting vibration signals, and is more suitable for analyzing blasting signals in this project. Therefore, the newly constructed blas2.4 wavelet is used as the basic wavelet, and taking the signal YBF3 as an example, the continuous wavelet transform energy spectrum of blasting vibration signal is shown in Figures 11A,B are the two-dimensional and three-dimensional time-frequency energy spectra, respectively. There are clearly four local energy peaks in the figure, which are consistent with the number of local speed peaks in the original signal. The first peak energy accounts for the majority. The frequency distribution range of the whole signal is mainly 5–70 Hz, and the time range is 0.05~1.70 s. The frequency distribution range is consistent with the Fourier frequency range corresponding to the signal in Figure 7C. The occurrence times corresponding to the local energy peaks are approximately 0.1300, 0.6255, 1.1260, and 1.6250 s, which is basically consistent with the time corresponding to the local peak of velocity in the vibration velocity diagram.

The wavelet packet theory is applied to analyze the energy refinement characteristics of blasting vibration and to explore the energy ratio of each frequency band in the signal. According to Shannon's sampling theorem, the sampling frequency of the signal is f_s=5,000 Hz, so the Nyquist analysis frequency is $f_s/2$=2,500 Hz, the signal can be decomposed into 10 layers, with a total of 2^{10}=1,024 wavelet packets, so the original blasting vibration signal in the frequency domain can be divided into 1,024 frequency bands, each sub-band width is 2.44 Hz, the minimum sub-band range is 0~2.44 Hz. In wavelet packet decomposition, the new constructed Blas2.4 wavelet is used as the wavelet basis, and the calculation program is compiled according to the formulas. The energy percentage of the reconstructed subsignals in each frequency band is shown in Table 2, and the energy percentage distribution of each frequency band is illustrated in Figure 12. Since the blasting vibration signal frequency is mainly in the range of 0~70 Hz, the energy distribution of the first 70 Hz sub-band signals is mainly calculated and analyzed.

Table 2 shows that the dominant frequencies of YBJ1 and YBJ2 are concentrated in frequency band 10, and the corresponding frequency range is 21.97~24.41 Hz, while the dominant frequencies of YBF3 and YBF4 signals far from the power tower are located in frequency bands 15 and 13, respectively, and the corresponding frequency ranges are 34.18~36.62 Hz and 29.30~31.74 Hz. From the Figure that before the frequency band 11 (24.41~26.86 Hz), the energy proportion of signals YBJ1 and YBJ2 is much larger than that of YBF3 and YBF4. The closer to the power tower, the lower the main vibration frequency of the blasting vibration signal, and the farther away from the power tower, the higher the main vibration frequency of the signal. The energy proportion of each signal in the low frequency band (0~12.21 Hz) is 9.84%, 10.01%, 1.33%, and 2.30%, respectively, the energy proportion in the medium frequency band (12.21~51.27 Hz) is 79.51%, 83.54%, 65.63% and 78.69% respectively, and the energy proportion in the high frequency band (51.27~2500 Hz) is 10.65%, 6.45%, 33.04% and 19.01% respectively. Since the natural vibration frequency of engineering structures is generally low (about 0~10Hz), the YBJ1 and YBJ2 signals generated by excavation near the power tower contain more low-frequency signals. Therefore, from the perspective of dynamic response analysis, it should take note of the resonance effect of tunnel blasting on the power tower when the excavation is close to that.

Conclusion

Analyzing and acquiring the time-frequency characteristics and energy distribution law of blasting vibration signal are of great importance in judging the harm caused by blasting vibration, formulating preventive and control measures, and ensuring the safety of blasting construction. On the basis of the constructed high-performance blas2.4 biorthogonal wavelet, the spectrum distribution and energy characteristics of the measured blasting vibration signals are deeply explored and compared from the aspects of continuous wavelet and wavelet packet transform, and the impact of blasting vibration on the buildings around the city, especially the power tower, is analyzed. The main conclusions are drawn as follows:

(1) An biorthogonal wavelet basis (namely Blas2.4 wavelet) with high vanishing moment, high regularity and matching with the waveform characteristics of the measured blasting vibration signals by using the improved second-generation lifting scheme wavelet theory and optimization algorithm were constructed. The wavelet basis has excellent tight support, smoothness and symmetry, and has high precision in the decomposition and reconstruction of blasting vibration signals, which can provide a solid theoretical basis for the subsequent continuous wavelet transform and wavelet packet analysis of blasting vibration signals.
(2) The method of scale energy spectrum was creatively proposed to study the spectrum characteristics of measured blasting vibration signals on the basis of wavelet analysis. The dominant frequency of the blasting vibration signals can be obtained by the scale energy spectrum method, and the obtained spectrum curve is smoother, which can clearly reflect the change trend of the signal spectrum.
(3) The energy distribution of blasting vibration signals in the two-dimensional "time-scale" domain can be obtained by using the continuous wavelet transform method, and the frequency duration interval and the main time range of blasting vibration signal can be acquired, also the occurrence time corresponding to the frequency can be determined. The energy refinement characteristics of the blasting vibration signals were calculated by using wavelet

packet theory. The blasting vibration signal generated by tunnel excavation near the power tower has more low-frequency components, while the signal far away from the power tower contains more medium and high-frequency components.

(4) The measures such as pre-splitting blasting, controlling one-time excavation footage of the tunnel, limiting the amount of primary explosive, uncoupled charging and interval charging are suggested to optimize the blasting design and reduce the impact of blasting vibration on nearby electric power steel tower. The next step is to study the active control of blasting vibration to achieve the ideal vibration reduction effect. By changing the millisecond delay time, controlling the maximum charge per delay and the total charge, explore the relationship between the millisecond delay time, charge amount and the peak velocity, dominant frequency of the blasting vibration signals.

Data availability statement

The original contributions presented in the study are included in the article/supplementary material, further inquiries can be directed to the corresponding author.

Author contributions

Conceptualization, LZ; methodology, LZ and SZ; software, LZ and SZ.; validation, LZ and TL; formal analysis, SZ and ZD; investigation, LZ; resources, SZ, LZ, and TL; data curation, LZ and ZD; writing—original draft preparation, LZ and SZ; writing—review and editing, LZ and SZ; visualization, LZ; supervision, TL; project administration, LZ, SZ, and TL; funding acquisition, LZ, SZ, and TL. All authors have read and agreed to the published version of the manuscript.

Funding

The research described in this paper was financially supported by the National Natural Science Foundation of China (Nos. 51878074 and 52078061), the Natural Science Foundation of Hunan Province in China (Nos. 2018JJ3022 and 2020JJ5588) and the Outstanding Youth Project of Hunan Provincial Department of Education (21B0725).

Conflict of interest

The authors declare that the research was conducted in the absence of any commercial or financial relationships that could be construed as a potential conflict of interest.

Publisher's note

All claims expressed in this article are solely those of the authors and do not necessarily represent those of their affiliated organizations, or those of the publisher, the editors and the reviewers. Any product that may be evaluated in this article, or claim that may be made by its manufacturer, is not guaranteed or endorsed by the publisher.

Reference

Babouri, M. K., Ouelaa, N., Kebabsa, T., and Djebala, A. (2021). Diagnosis of mechanical defects using a hybrid method based on complete ensemble empirical mode decomposition with adaptive noise (CEEMDAN) and optimized wavelet multi-resolution analysis (OWMRA): Experimental study. *Int. J. Adv. Manuf. Technol.* 112, 2657–2681. doi:10.1007/s00170-020-06496-z

Chen, H., Qiu, X., Shi, X., Zhang, J., Huo, X., and Li, D. (2022). Experimental study on fracturing characteristics of double-hole blasting under static stresses. *Front. Earth Sci.* 9, 829258. doi:10.3389/feart.2021.829258

Dai, H., and Cao, Z. (2017). A wavelet support vector machine-based neural network metamodel for structural reliability assessment. *Computer-Aided Civ. Infrastructure Eng.* 32 (4), 344–357. doi:10.1111/mice.12257

Daubechies, I., and Sweldens, W. (1998). Factoring wavelet transforms into lifting steps. *J. Fourier Anal. Appl.* 4 (3), 247–269. doi:10.1007/BF02476026

Graf, R., Zhu, S., and Sivakumar, B. (2019). Forecasting river water temperature time series using a wavelet–neural network hybrid modelling approach. *J. Hydrol. X.* 578 (11), 124115. doi:10.1016/j.jhydrol.2019.124115

Hafiz, F., Swain, A., Naik, C., Abecrombie, S., and Eaton, A. (2018). Identification of power quality events: Selection of optimum base wavelet and machine learning algorithm. *IET Sci. Meas. &. Technol.* 13 (2), 260–271. doi:10.1049/iet-smt.2018.5044

Hamid, M., Usman, M., Haq, R. U., Khan, Z. H., and Wang, W. (2019). Wavelet analysis of stagnation point flow of non-Newtonian nanofluid. *Appl. Math. Mech.* 40 (8), 1211–1226. doi:10.1007/s10483-019-2508-6

Jing, F., Zhang, C., Si, W., Wang, Y., and Jiao, S. (2018). Polynomial phase estimation based on adaptive short-time fourier transform. *Sensors* 18 (2), 568. doi:10.3390/s18020568

Kan, J., Dou, L., Li, J., Li, X., Bai, J., and Wang, M. (2022). Characteristics of microseismic waveforms induced by underground destress blasting: Comparison with those induced by ground blasting and coal mining. *Front. Earth Sci.* 10, 797358. doi:10.3389/feart.2022.797358

Khodja, M. E. A., Aimer, A. F., Boudinar, A. H., Benouzza, N., and Bendiabdellah, A. (2019). Bearing fault diagnosis of a PWM inverter fed-induction motor using an improved short time Fourier transform. *J. Electr. Eng. Technol.* 14 (3), 1201–1210. doi:10.1007/s42835-019-00096-y

Koopialipoor, M., Armaghani, D. J., Haghighi, M., and Ghaleini, E. N. (2019). A neuro-genetic predictive model to approximate overbreak induced by drilling and blasting operation in tunnels. *Bull. Eng. Geol. Environ.* 78 (2), 981–990. doi:10.1007/s10064-017-1116-2

Kulak, Ö., and Aydin, İ. (2020). Inverse continuous wavelet transform in weighted variable exponent amalgam spaces. *Commun. Fac. Sci. Univ.* 69 (2), 177–189. doi:10.31801/cfsuasmas.710208

Lee, W. K., Ratnam, M. M., and Ahmad, Z. A. (2017). Detection of chipping in ceramic cutting inserts from workpiece profile during turning using fast Fourier transform (FFT) and continuous wavelet transform (CWT). *Precis. Eng.* 47, 406–423. doi:10.1016/j.precisioneng.2016.09.014

Li, H., Wang, Q., and Wu, L. (2001). A novel design of lifting scheme from general wavelet. *IEEE Trans. Signal Process.* 49 (8), 1714–1717. doi:10.1109/78.934141

Li, S., Zhang, Y., Cao, M., and Wang, Z. (2022). Study on excavation sequence of pilot tunnels for a rectangular tunnel using numerical simulation and field monitoring method. *Rock Mech. Rock Eng.* 55, 3507–3523. doi:10.1007/s00603-022-02814-x

Ling, T., Zhang, L., Liu, H., Huang, F., Gu, D., and Yu, B. (2019). Quantitative identification and analysis of tunnel lining defect based on the wavelet lifting scheme theory. *China J. Highw. Transp.* 32 (12), 197–204. doi:10.19721/j.cnki.1001-7372.2019.12.020

Ma, L., Lin, F., Liu, R., Liu, P., Xia, G., and Chen, L. (2022). Disturbance and control of national strategic gas storage induced by adjacent tunnel blasting. *Front. Earth Sci.* 9, 807073. doi:10.3389/feart.2021.807073

Mehboob, S., Khan, Q. U. Z., Ahmad, S., and Anwar, S. M. (2022). Health assessment of RC building subjected to ambient excitation: Strategy and application. *Earthq. Struct.* 22 (2), 185–201. doi:10.12989/eas.2022.22.2.185

Quaye-Ballard, J. A., Okrah, T. M., Andam-Akorful, S. A., Awotwi, A., Osei-Wusu, W., Antwi, T., et al. (2020). Assessment of vegetation dynamics in Upper East Region of Ghana based on wavelet multi-resolution analysis. *Model. Earth Syst. Environ.* 6 (3), 1783–1793. doi:10.1007/s40808-020-00789-8

Rhif, M., Ben Abbes, A., Farah, I. R., Martínez, B., and Sang, Y. (2019). Wavelet transform application for/in non-stationary time-series analysis: A review. *Appl. Sci. (Basel).* 9 (7), 1345. doi:10.3390/app9071345

Robustelli, U., and Pugliano, G. (2018). GNSS code multipath short-time fourier transform analysis. *J. Inst. Navig.* 65 (3), 353–362. doi:10.1002/navi.247

Shah, F. A., and Tantary, A. Y. (2018). Polar wavelet transform and the associated uncertainty principles. *Int. J. Theor. Phys.* 57 (6), 1774–1786. doi:10.1007/s10773-018-3703-9

Shahryari, H., Karami, M. R., and Chiniforush, A. A. (2019). Summarized IDA curves by the wavelet transform and bees optimization algorithm. *Earthq. Struct.* 16 (2), 165–175. doi:10.12989/eas.2019.16.2.165

Sharafat, A., Khan, M. S., Latif, K., and Seo, J. (2021). BIM-based tunnel information modeling framework for visualization, management, and simulation of drill-and-blast tunneling projects. *J. Comput. Civ. Eng.* 35 (2), 04020068. doi:10.1061/(ASCE)CP.1943-5487.0000955

Singh, C. P., Agrawal, H., and Mishra, A. K. (2020). A study on influence of blast-induced ground vibration in dragline bench blasting using signature hole analysis. *Arab. J. Geosci.* 13 (13), 522–529. doi:10.1007/s12517-020-05562-w

Tian, L., Dong, X., Pan, H., and He, X. (2019). The critical angle of seismic incidence of transmission tower-line system based on wavelet energy method. *Earthq. Struct.* 17 (4), 387–398. doi:10.12989/eas.2019.17.4.387

Tomiyama, K., and Kawamura, A. (2016). Application of lifting wavelet transform for pavement surface monitoring by use of a mobile profilometer. *Int. J. Pavement Res. Technol.* 9 (5), 345–353. doi:10.1016/j.ijprt.2016.08.007

Tyrtaiou, M., and Elenas, A. (2020). Seismic damage potential described by intensity parameters based on Hilbert-Huang Transform analysis and fundamental frequency of structures. *Earthq. Struct.* 18 (4), 507–517. doi:10.12989/eas.2020.18.4.507

Wang, X., Li, J., Zhao, X., and Liang, Y. (2022). Propagation characteristics and prediction of blast-induced vibration on closely spaced rock tunnels. *Tunn. Undergr. Space Technol.* 123, 104416. doi:10.1016/j.tust.2022.104416

Wu, H., Zhao, G., and Ma, S. (2022). Failure behavior of horseshoe-shaped tunnel in hard rock under high stress: Phenomenon and mechanisms. *Trans. Nonferrous Metals Soc. China* 32 (2), 639–656. doi:10.1016/S1003-6326(22)65822-9

Zhang, L., Ling, T. H., Yu, B., Huang, F., and Zhang, S. (2021). Intensive interferences processing for GPR signal based on the wavelet transform and F-K filtering. *J. Appl. Geophy.* 186, 104273. doi:10.1016/j.jappgeo.2021.104273

Zhang, S., Zhang, L., He, W., Ling, T., Deng, Z., and Fu, G. (2022). Three-dimensional quantitative recognition of filler materials ahead of a tunnel face via time–energy density analysis of wavelet transforms. *Minerals* 12 (2), 234. doi:10.3390/min12020234

Zhang, S., Zhang, L., Ling, T., Fu, G., and Guo, Y. (2021). Experimental research on evaluation of soil water content using ground penetrating radar and wavelet packet-based energy analysis. *Remote Sens.* 13 (24), 5047. doi:10.3390/rs13245047

Zhao, M., Kang, M., Tang, B., and Pecht, M. (2018). Multiple wavelet coefficients fusion in deep residual networks for fault diagnosis. *IEEE Trans. Ind. Electron.* 66 (6), 4696–4706. doi:10.1109/TIE.2018.2866050

frontiers | Frontiers in Earth Science

TYPE Original Research
PUBLISHED 23 August 2022
DOI 10.3389/feart.2022.931071

Check for updates

OPEN ACCESS

EDITED BY
Shibing Huang,
Wuhan University of Science and Technology, China

REVIEWED BY
Jianxin Yu,
Henan Polytechnic University, China
Yong Fan,
China Three Gorges University, China

*CORRESPONDENCE
Junpeng Zou,
zoujunpeng@cug.edu.cn

SPECIALTY SECTION
This article was submitted to Geohazards and Georisks, a section of the journal Frontiers in Earth Science

RECEIVED 28 April 2022
ACCEPTED 04 July 2022
PUBLISHED 23 August 2022

CITATION
Li C, Zou J, He W, Ding X, Zheng G, Zhuang Y and Wang M (2022), Study on anti-collision behavior of new precast concrete curb components in a highway tunnel.
Front. Earth Sci. 10:931071.
doi: 10.3389/feart.2022.931071

COPYRIGHT
© 2022 Li, Zou, He, Ding, Zheng, Zhuang and Wang. This is an open-access article distributed under the terms of the Creative Commons Attribution License (CC BY). The use, distribution or reproduction in other forums is permitted, provided the original author(s) and the copyright owner(s) are credited and that the original publication in this journal is cited, in accordance with accepted academic practice. No use, distribution or reproduction is permitted which does not comply with these terms.

Study on anti-collision behavior of new precast concrete curb components in a highway tunnel

Changjun Li[1], Junpeng Zou[2]*, Wenbin He[3], Xianying Ding[4], Guoping Zheng[3], Yizhou Zhuang[3] and Man Wang[5]

[1]Zhejiang Institute of Communication Co., Ltd., Hangzhou, China, [2]Faculty of Engineering, China University of Geosciences, Wuhan, China, [3]School of Civil Engineering, Zhejiang University of Technology, Hangzhou, China, [4]Shaoxing Keqiao Transportation Investment and Construction Co., Ltd., Shaoxing, China, [5]School of Information Engineering, Wuhan Business University, Wuhan, China

In order to improve the prefabrication level of highway mountain tunnels, improve the quality of the project, and shorten the construction period, a new type of prefabricated concrete curb member was developed based on an actual project. The production process, construction technical points, and on-site assembly technology are discussed. In addition, a method to calculate the anti-collision performance of the curb components is proposed, that is, the collision force of 850 kN was calculated by the pseudo-static method, and then finite element simulation analysis was used to obtain the stress of the concrete structure and reinforcement. The results show that the reinforcement will not fail, which will ensure the curb component will not undergo brittle fracture. This study provides a reference to improve the prefabrication level of highway tunnels.

KEYWORDS

highway tunnel, curb component, crashworthiness, pseudo static method, finite element method

Introduction

In recent years, prefabricated structures have been widely used after the promotion of the Chinese government related to the conservation of resources, reduction of construction pollution, and improved labor safety. This might enhance the deep integration of the construction industry with information technology and industrialization, foster new industries and new driving forces, as well as dissolve excessing capacity. In the field of tunnel and underground engineering, prefabrication technology has been widely used for shield tunneling. It has been applied in cut-over highway tunnels (Jiang, 2018), municipal facility tunnels (Kuang et al., 2022), cable culverts (Tao, 2018), and other fields. However, the range of prefabricated components used in drill-blast road tunnels is low. The main and auxiliary structures of prefabricated components are still primarily cast-in-place, including curb components. The structure size is generally fine and the wall thickness is mostly between 10 and 15 cm. It is difficult to ensure the construction quality of site erection formwork pouring, which frequently leads to a rough surface on the side groove, poor drainage, debris deposition, cracking and

missing angles (Wang et al., 2018), and an uneven road surface (see Figure 1). Moreover, the site erection template has poor construction efficiency and requires a long construction period.

However, curb components are the most easily damaged parts in a tunnel because vehicles deviate from the lane and collide with them. Accident severity is generally high (Bassan, 2016) and there is a risk of fire, although the frequency of collisions in a tunnel is lower than on roads outside the tunnel. Pervez and Caliendo et al. conducted statistical and predictive research on the collision frequency in tunnels (Caliendo et al., 2013, 2016, 2019; Pervez et al., 2020, 2021; Tang et al., 2022). This problem needs to be studied to improve the durability of tunnel structures and avoid traffic interruptions due to damaged curb components. However, there is still a gap in the anti-collision performance requirements and checking calculation methods of curbs in China's code for highway tunnel design. In light of the above, it is essential to investigate vehicle-bridge collisions based on the existing achievements. Cao et al. (2019) and Heng et al. (2021) studied the collision of heavy trucks against the bridge caps and piers of cross-line bridges. High-fidelity finite element analysis by Oppong et al. (2021)was used to assess the impact of ultra-tall vehicles on the main girder. Thilakarathna et al. (2010) used a nonlinear numerical analysis model to research the impact of vehicles on piers and columns, and obtained analysis results of the impact force time-history curve, structural displacement, and reaction force. Based on refined nonlinear finite element analysis, Xu et al. (2012) studied the damage mechanism of a bridge superstructure and reported a time history of impact force when over-height vehicles collided with curb components.

In this paper, a new type of precast concrete curb component for highway tunnel was proposed to improve the precast level of highway tunnel structures by drilling and blasting. A pseudo-static method and finite element modeling were used to calculate the impact load and check its anti-collision performance. Finally, the key technologies and engineering applications of its construction are introduced to provide a reference for improving the prefabrication level of highway tunnels.

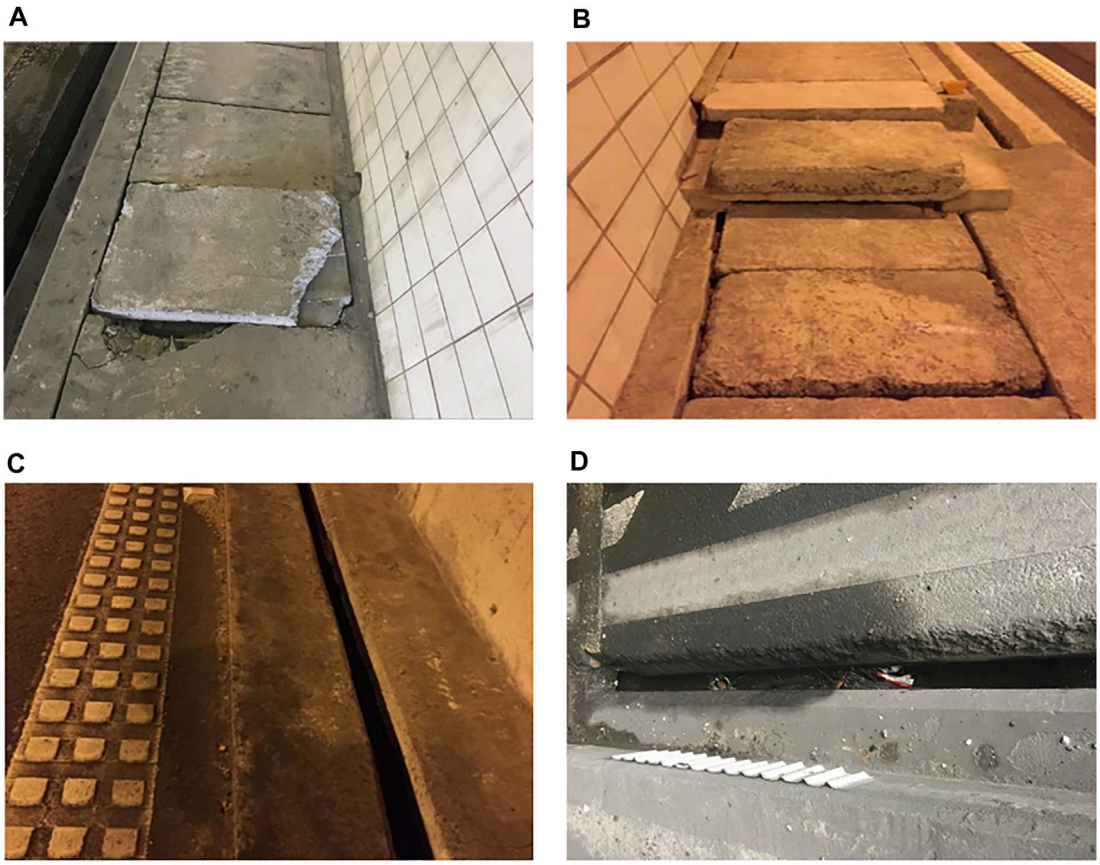


FIGURE 1
Photos of damaged traditional curb components: **(A)** cover plate missing corners, **(B)** flatness of cover plate is poor, **(C)** slotted ditch above the road surface, and **(D)** debris clogged up in a slotted ditch.

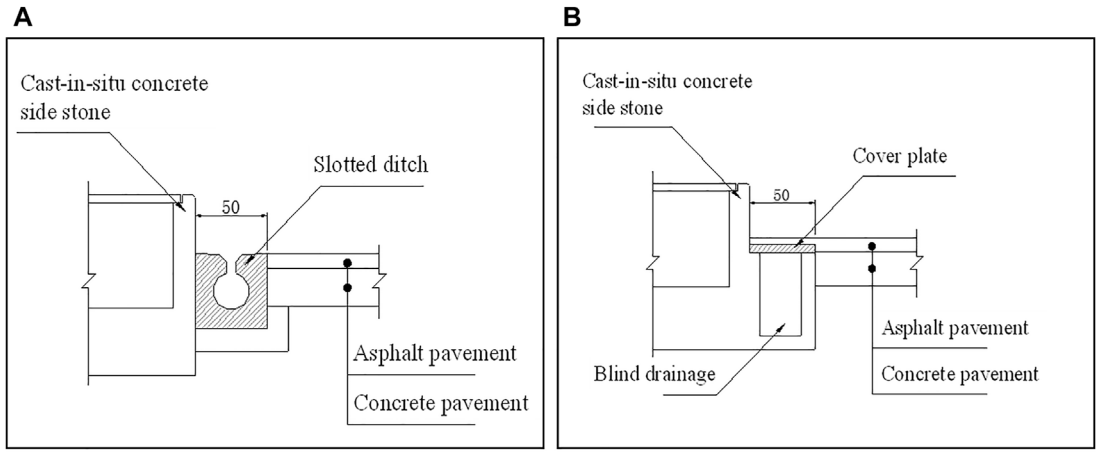


FIGURE 2
The tunnel curb components: **(A)** slotted ditch, **(B)** blind drainage.

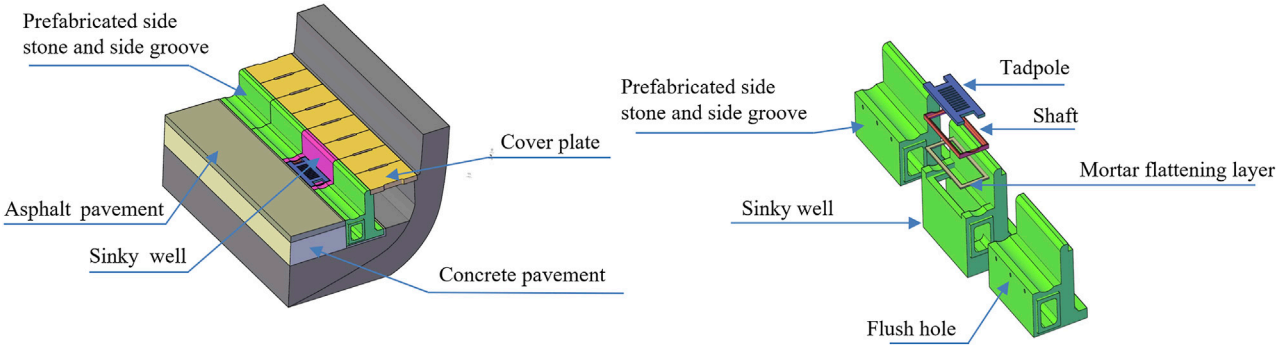


FIGURE 3
Three-dimensional structural drawing of the integral curb components.

Design of tunnel curb components

Curb components usually include a side ditch, side stone, cable trench, and cover plate. Cover plates are usually prefabricated components. Among these components, the side ditch and side stone need to be considered for construction technology.

As shown in Figure 2, there are two common kinds of roadside ditches, the slotted ditch and blind drainage, each with its own characteristics: the slotted ditch is easy to install and does not require bottom and slurry processes. However, the construction of blind drainage is more difficult, including paving of the asphalt pavement at the edge, resulting in an uneven pavement surface, which is prone to water accumulation.

In contrast, a slotted ditch is superior and is more commonly used on highways in Zhejiang province. However, the following problems remain:

1) It is difficult to clean the slotted ditch, which increases the maintenance difficulty of the highway operating unit;
2) Due to the infiltration of groundwater into the asphalt and concrete pavement in the tunnel, it is difficult for the slotted ditch to drain the interlayer water under the asphalt surface;
3) Because the width of the slotted ditch is 50 cm, it can invade the carriageway pavement.

Figures 3, 4 show a three-dimensional structural drawing of the integral curb components (i.e., a slotted ditch component that prefabricates the side stones and side ditch together), with a size

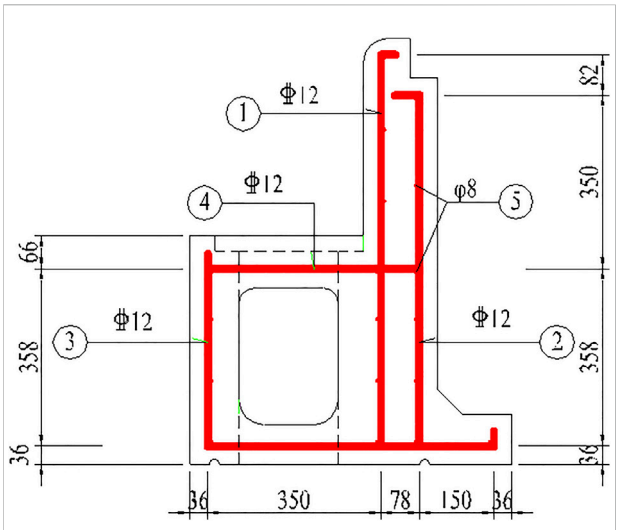


FIGURE 4
Design of the side stone and side ditch, and detailed drawing of the reinforcement.

of 65 × 86 × 100 cm, a segment length of 1 m, and mass for each segment of 612.25 kg.

To improve the shear resistance between segments, they are connected by tension, which is better and smoother than the current cast-in-situ concrete curb components. The width of the ditch is 35 cm, which effectively ensures the road surface of the driveway. Compared with the previous curb components, the maintenance cost of prefabricated curb components is lower, that is, the ditch top of the prefabricated curb components is equipped with a drainage ditch (that quickly drains the tunnel pavement water) and a flushing hole (that effectively dredges debris blocking the ditch). The grate on the sand sediment trap in the middle of the side ditch collects debris and three drainage holes arranged symmetrically on the ditch side of the prefabricated curb components allow seepage to discharge to the asphalt layer. According to the actual engineering situation, the arrangement of the drainage holes can also effectively prevent groundwater from infiltrating into the asphalt and concrete pavement layers.

Calculation of anti-collision performance

Common check calculation methods

The impact process is a transient dynamic action, and engineering often converts the dynamic action into a static load for design. Commonly used equivalent static calculation methods include: the global average method, local average method, and equivalent displacement method. According to previous studies, when a vehicle's speed is 80 km/h, the displacement method has the greatest accuracy to calculate the equivalent static force. The equivalent impact force is determined by:

$$P_d = \frac{d_2}{d_1} \tag{1}$$

where d_1 is the displacement at the action point where a unit is applied to the action point, and d_2 is the corresponding displacement obtained after applying the impact force and bending moment time history at the action point.

China's "General Specifications for Design of Highway Bridges and Culverts" (JTG D60-2015) stipulates that the state of vehicle impact should be calculated for bridge piers subjected to vehicle impact without anti-collision measures. The impact force along the vehicle direction should be 1000 kN, the impact force perpendicular to the driving direction of the vehicle should be 500 kN, and the two equivalent forces should be considered at different times.

The "Design Specifications for Highway Safety Facilities" (JTGD 81–2017) adopts the pseudo-static method to solve the collision force of a car on the guardrail. The pseudo-static method adopts the assumptions of average speed, rigid car and guardrail, and average acceleration.

The lateral displacement of the car can be expressed as:

$$\Delta S_L = C\sin\theta - b(1-\cos\theta) + D \tag{2}$$

where C is the distance between the gravitational center of the car and the front bumper; θ is the collision angle; b is half the width of the vehicle; and$D$ is the lateral displacement of the guardrail (usually 0).

The lateral average speed is determined by:

$$\bar{v}_L = \frac{v_1\sin\theta}{2} \tag{3}$$

where v_1 is the driving speed before the impact.

The time required for lateral displacement is determined by:

$$\Delta_t = \frac{\Delta S_L}{\bar{v}_L} = \frac{C\sin\theta - b(1-\cos\theta) + D}{v_1\sin\theta/2} \tag{4}$$

The lateral acceleration of the car is determined by:

$$a_L = \frac{(\Delta v)_L}{\Delta_t} = \frac{v_1\sin\theta}{\Delta_t} = \frac{v_1^2\sin^2\theta}{2[C\sin\theta - b(1-\cos\theta) + D]} \tag{5}$$

Then, the lateral collision force can be obtained as:

$$F_L = ma_L = \frac{m(v_1\sin\theta)^2}{2[C\sin\theta - b(1-\cos\theta) + D]} \tag{6}$$

Assuming that the stiffness of the car and the guardrail is a linear spring, the relationship between the collision force and time is a sine curve, and the maximum lateral acceleration of the car is determined by:

TABLE 1 Material parameters of concrete.

Density (tonne/mm^3)	Young modulus (MPa)	Poisson ratio
2.4e-09	31500	0.2

TABLE 2 Material parameters of reinforcement.

Reinforcement	Density (tonne/mm^3)	Young modulus (MPa)	Poisson ratio	Yield stress
Q235	7.85e-09	200000	0.3	235
HRB400	7.85e-09	210000	0.3	400

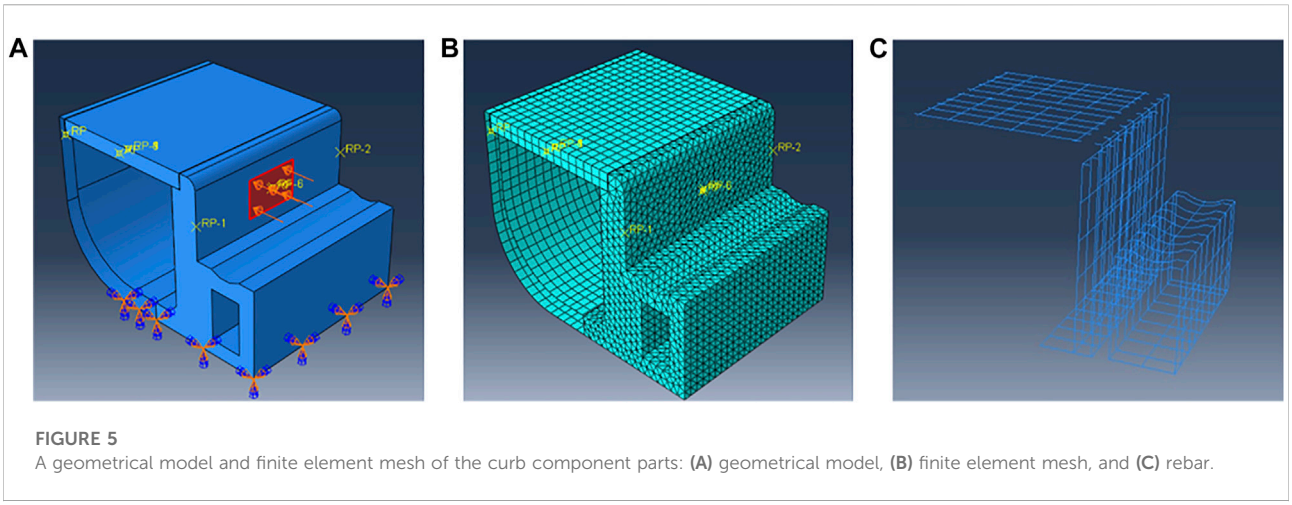


FIGURE 5
A geometrical model and finite element mesh of the curb component parts: **(A)** geometrical model, **(B)** finite element mesh, and **(C)** rebar.

$$(a_L)max = \frac{\pi}{2} a_L \tag{7}$$

Then, the maximum lateral collision force is determined by:

$$(F_L)\max = \frac{\pi}{2} \cdot \frac{m(v_1 \sin\theta)^2}{2[C\sin\theta - b(1-\cos\theta) + D]} \tag{8}$$

Adding the dynamic correction coefficient to the above formula, the calculation formula of the lateral collision force can be obtained as follows:

$$F_1 = \xi \cdot \frac{\pi}{2} \cdot \frac{m(v_1 \sin\theta)^2}{2[C\sin\theta - b(1-\cos\theta) + D]} \tag{9}$$

This calculation method for the collision force takes into account factors including vehicle size and collision angle, and is more suitable for calculating the collision force from different vehicles; however, it ignores the deformation of vehicles and piers. In actual situations, the car in the collision process often undergoes deformation. Therefore, the calculation results may be different from the actual value.

Finite element modeling

In this study, we used the instantaneous impact force, equivalent static force, and pseudo-static force to calculate the anti-collision energy of curb component side stone structures. The simulation setting speed was 80 km/h, the oblique impact angle was 20°, and the body weight was 8 t. Formula (9) shows that the lateral impact force obtained using the pseudo-static method was 850 kN, which is greater than the 500 kN recommended by The General Code for Highway Bridge design (JTG D60-2015); therefore, the former value was used as a conservative estimate.

For specific materials related to the concrete and reinforced materials, see Tables 1, 2.

Figure 5 shows the geometrical model and the finite element mesh of the parts of the curb components. The force of the friction and the friction formula are Lagrange multipliers, and the model's plat and integral curb component side stones and side ditches adopt physical units, the top of which adopts the "hard contact". There is a 5 mm reserved space at the lap joint of the

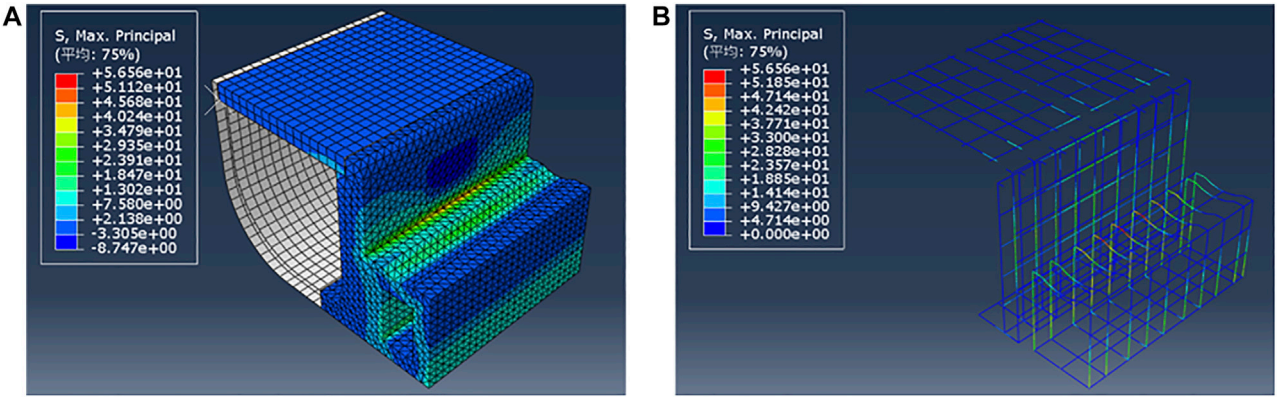


FIGURE 6
Results of finite element analysis: **(A)** maximum principal stress of concrete structure (MPa), **(B)** reinforcement stress (MPa).

cover plate. In order to reduce integral and hourglass control, the grid cell of the integral curb component side stones and side ditches contains a ten-node quadratic tetrahedral element (C3D10), whereas the cover plate and segment components contain an eight-node linear hexahedral element (C3D8R). Standard model test piece concrete contains C35. The main reinforcement type is φ12 mm HRB400, whereas the distributional reinforcement was φ8 mm HPB235. The steel bar uses a line element, and the mesh element type is a two-node linear three-dimension truss element (T3D2). The interaction of the "built-in zone" means the reinforcement and concrete are completely fixed regardless of the slip between the reinforcement and concrete.

Boundary conditions and loadings

According to the installation method of the curb components, the bottom of the side stone and side ditch of the curb component is the fixed end (i.e., the displacement is 0). According to the wheel load area distribution table in the "General Specification for Highway Bridges and Culverts Design" (JTG D60-2015), a rectangular area of 0.3 m × 0.2 m is used, to which a uniform force of 14.2 MPa is applied, as shown in Figure 5.

Results

Figure 6 is a sketch map of the calculation results of maximum principal stress and reinforcement stress of the concrete structure.

The joint of the side stone and side ditch is a right-angle structure that has large tensile stress after bearing the force of an impact. When the axial tensile strength of C35 concrete exceeds 2.20 MPa the concrete will crack. However, the maximum tensile stress of the steel bar is about 56 MPa (i.e., the steel bar will not be damaged); therefore, a brittle fracture of the curb components will not occur.

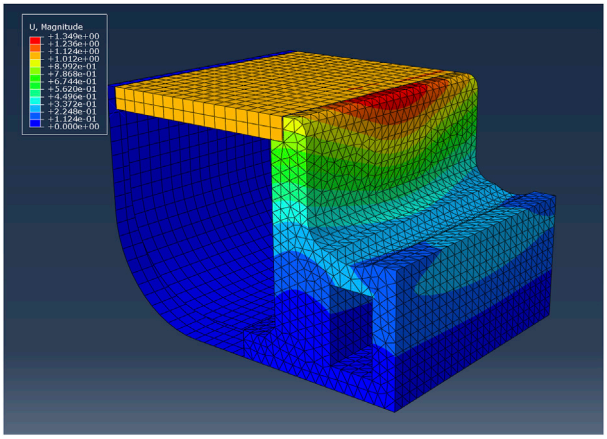


FIGURE 7
Displacement cloud map (MPa).

The maximum displacement of the member (i.e., the displacement of the top of the side stone) was 1.34 mm, and the displacement generated by the collision position was 7.8–8.5 mm. The specific displacement after a collision with the components is shown in Figure 7.

Construction of prefabricated curb components

The construction process of prefabricated road edge components is shown in Figure 8. The concrete design

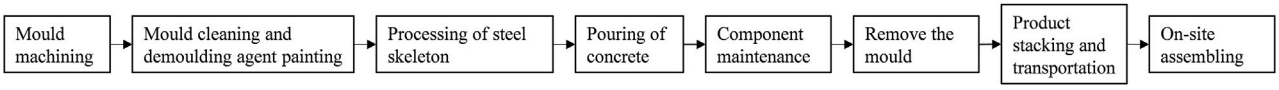


FIGURE 8
Construction process of the prefabricated curb components.



FIGURE 9
Molds for prefabricated curb components.

strength was C35, the segmental length was 1 m, the recommended mix ratio was cement:sand:gravel:fly ash: water:admixture = 270:850:1000:90:160:1.8, and the slump should be controlled at 5–7 cm. The precast concrete drainage ditch forming process used an attached vibration platform. The concrete pouring height of each layer should not exceed 300 mm.

In general, the first vibration time was 60—80 s, the second vibration time was 30—40 s, and the interval time between the two vibrations was 60—90 s. After finishing the plastering process, a non-woven geotextile was sprayed with water cover. After the surface concrete was finally solidified, spray maintenance was performed. Under a high temperature, the spray was performed every 30 min in the daytime for 5 min, and every 1 h at night for 5 min. The spray maintenance was performed for 5 d, and the cover maintenance was performed for 7 d. Demoulding was performed when the concrete strength reached 75% or more of the design strength (see Figure 9).

The assembly process was performed and hoisted by small machinery. The installation position was laid out and flatted, and mortar was used for the secondary level before installation. In order to ensure the assembly accuracy of the components, site lofting was performed before the assembly.

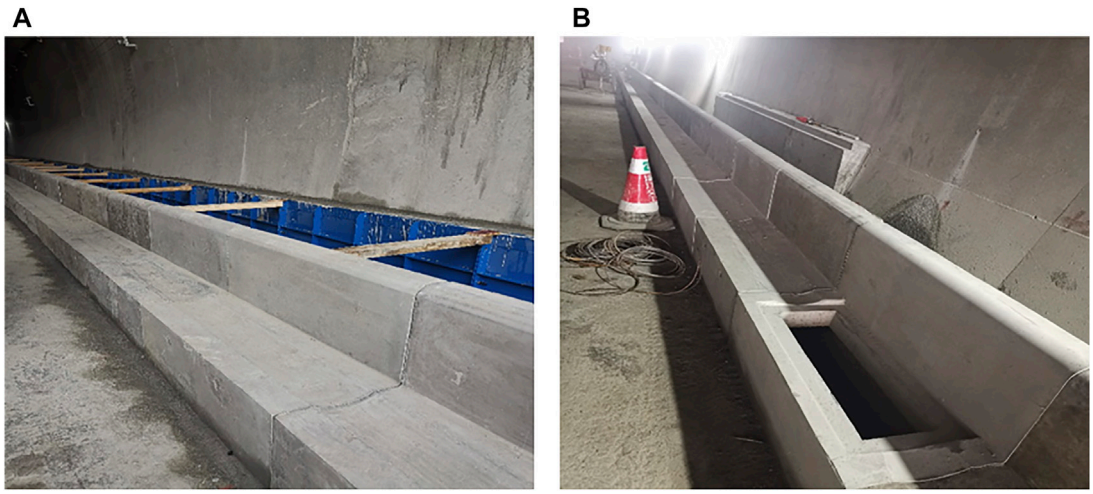


FIGURE 10
Pictures of prefabricated curb components at a construction site: **(A)** side ditches and side stones, **(B)** sand sediment trap.

Engineering application

Through careful design and construction, this new type of prefabricated road component has been successfully used in the mountain tunnels of many highways in Zhejiang Province. The cumulative length exceeds 10 km. Compared with the original pouring road edge component, this new prefabricated road component is a big improvement (Figure 10).

Conclusions

This study developed new prefabricated curb components for highway mountain tunnels, which have the advantages of centralized prefabrication, component standardization, and commercialization. The prefabricated construction method allows the factory prefabrication of structural components ahead of or parallel to the excavation time of the corresponding parts in the tunnel, saving the implementation time of the linear construction process in the tunnel. Prefabricated curb components overcome the disadvantages related to the quality of the traditional slotted ditch, which is difficult to control, and improve the accuracy of field construction.

In addition, this study presents a method of calculating the collision-proof energy of the prefabricated curb components. The impact force of vehicle side rock in operation, which was 850 kN, was calculated using a pseudo-static method. The stress on the concrete structure and steel bar obtained by finite element simulation was analyzed, and the results showed that no brittle fracture would occur in prefabricated curb components after a collision.

Data availability statement

The original contributions presented in this study are included in the article/Supplementary material, and further inquiries can be directed to the corresponding author.

Author contributions

Investigation, CL and JZ; methodology, WH and XD; writing-original draft preparation, CL and GZ; writing-review and editing, YZ and MW. All authors have read and agreed to the published version of the manuscript.

Funding

This work was supported by the China National Natural Science Foundation (Nos. 42177152 and 41902293), the Guiding Project of the Scientific Research Plan of the Hubei Provincial Department of Education (No. B2021272), and Doctoral Fund of Wuhan Business University (No. 201908214).

Conflict of interest

CL is employed by Zhejiang Institute of Communication Co., Ltd. and XD is employed by Shaoxing Keqiao Transportation Investment and Construction Co., Ltd.

The remaining authors declare that the research was conducted in the absence of any commercial or financial relationships that could be construed as a potential conflict of interest.

Publisher's note

All claims expressed in this article are solely those of the authors and do not necessarily represent those of their affiliated organizations, or those of the publisher, the editors, and the reviewers. Any product that may be evaluated in this article, or claim that may be made by its manufacturer, is not guaranteed, or endorsed by the publisher.

References

Bassan, S. (2016). Overview of traffic safety aspects and design in road tunnels. *IATSS Res.* 40 (1), 35–46. doi:10.1016/j.iatssr.2016.02.002

Caliendo, C., De, G., and Guida, M. (2013). A crash-prediction model for road tunnels. *Accid. Analysis Prev.* 55, 107–115. doi:10.1016/j.aap.2013.02.024

Caliendo, C., De, G., and Guida, M. (2016). Comparison and analysis of road tunnel traffic accident frequencies and rates using random-parameter models. *J. Transp. Saf. Secur.* 8 (2), 177–195. doi:10.1080/19439962.2015.1013167

Caliendo, C., De, G., and Russo, I. (2019). Analysis of crash frequency in motorway tunnels based on a correlated random-parameters approach. *Tunn. Undergr. Space Technol.* 85, 243–251. doi:10.1016/j.tust.2018.12.012

Cao, R., Agrawal, A., El-tawil, S., Xu, X., and Wong, W. (2019). Heavy truck collision with bridge piers: Computational simulation study. *J. Bridge Eng.* 24 (6), 04019052. doi:10.1061/(asce)be.1943-5592.0001398

Heng, K., Li, R., Li, Z., and Wu, H. (2021). Dynamic responses of highway bridge subjected to heavy truck impact. *Eng. Struct.* 232, 111828. doi:10.1016/j.engstruct.2020.111828

Jiang, H. (2018). "A summary of precast technology application in tunneling," in *Proceedings of the proceedings of GeoShanghai 2018 international conference: Tunnelling and underground construction* (Singapore: Springer Singapore).

Kuang, Y., Peng, Z., Yang, J., Zhou, M., He, C., Liu, Y., et al. (2022). Physical and numerical simulations on mechanical properties of a prefabricated underground utility tunnel. *Materials* 15 (6), 2276. doi:10.3390/ma15062276

Oppong, K., Saini, D., and Shafei, B. (2021). Characterization of impact-induced forces and damage to bridge superstructures due to over-height collision. *Eng. Struct.* 236, 112014. doi:10.1016/j.engstruct.2021.112014

Pervez, A., Huang, H., Han, C., Wang, J., and Li, Y. (2020). Revisiting freeway single tunnel crash characteristics analysis: A six-zone analytic approach. *Accid. Analysis Prev.* 142, 105542. doi:10.1016/j.aap.2020.105542

Pervez, A., Huang, H., Lee, J., Han, C., Wang, J., and Zhang, X. (2021). Crash analysis of expressway long tunnels using a seven-zone analytic approach. *J. Transp. Saf. Secur.* 13 (1), 108–122. doi:10.1080/19439962.2019.1605642

Tang, Z., Wu, Z., and Zou, J. (2022). Appraisal of the number of asperity peaks, their radii and heights for three-dimensional rock fracture. *Int. J. rock Mech. Min. Sci.* 153, 105080. doi:10.1016/j.ijrmms.2022.105080

Tao, L. (2018). Research and analysis on construction technology of precast square culvert component in cable tunnel. *Build. Technol. Dev.* 45 (6), 49–50.

Thilakarathna, H., Thambiratnam, D., Dhanasekar, M., and Perera, N. (2010). Numerical simulation of axially loaded concrete columns under transverse impact and vulnerability assessment. *Int. J. Impact Eng.* 37 (11), 1100–1112. doi:10.1016/j.ijimpeng.2010.06.003

Wang, Y., Zhou, X., Wang, Y., and Shou, Y. (2018). A 3-D conjugated bond-pair-based peridynamic formulation for initiation and propagation of cracks in brittle solids. *Int. J. Solids Struct.* 134, 89–115. doi:10.1016/j.ijsolstr.2017.10.022

Xu, L., Lu, X., Smith, S., and He, S. (2012). Scaled model test for collision between over-height truck and bridge superstructure. *Int. J. Impact Eng.* 49, 31–42. doi:10.1016/j.ijimpeng.2012.05.003

frontiers | Frontiers in Earth Science

TYPE Original Research
PUBLISHED 19 September 2022
DOI 10.3389/feart.2022.1011291

Check for updates

OPEN ACCESS

EDITED BY
Guang-Liang Feng,
Institute of Rock and Soil Mechanics (CAS), China

REVIEWED BY
Hao-sen Guo,
East China Jiaotong University, China
Gang Liu,
Heilongjiang University of Science and Technology, China

*CORRESPONDENCE
Bowen Zhao,
seawolf_zbw@163.com

SPECIALTY SECTION
This article was submitted to Geohazards and Georisks, a section of the journal Frontiers in Earth Science

RECEIVED 04 August 2022
ACCEPTED 02 September 2022
PUBLISHED 19 September 2022

CITATION
Zhang D, Zhao B and Zhu K (2022), Mechanical characteristics analysis of horizontal lifting of subsea pipeline with different burial depths.
Front. Earth Sci. 10:1011291.
doi: 10.3389/feart.2022.1011291

COPYRIGHT
© 2022 Zhang, Zhao and Zhu. This is an open-access article distributed under the terms of the Creative Commons Attribution License (CC BY). The use, distribution or reproduction in other forums is permitted, provided the original author(s) and the copyright owner(s) are credited and that the original publication in this journal is cited, in accordance with accepted academic practice. No use, distribution or reproduction is permitted which does not comply with these terms.

Mechanical characteristics analysis of horizontal lifting of subsea pipeline with different burial depths

Dapeng Zhang[1], Bowen Zhao[2]* and Keqiang Zhu[3]

[1]Ship and Maritime College, Guangdong Ocean University, Zhanjiang, China, [2]Ocean College, Zhejiang University, Hangzhou, China, [3]Faculty of Maritime and Transportation, Ningbo University, Ningbo, China

Different burial depths have different effects on the mechanical characteristics of the horizontal lifting of subsea pipelines. With the consideration of the soil resistance to subsea pipelines, combined with the specific sea condition parameters of a certain sea area, and based on the lumped mass method, the subsea pipeline is discretized into a lumped mass model, the dynamic analysis model of the three-point horizontal lifting of subsea pipelines with different burial depths is established. The stress and bending of the pipelines with different burial depths are analyzed. The calculation results with different burial depths are compared. The variation of mechanical characteristics of the process of lifting horizontal pipelines with different buried depths is obtained. The results show that the change of burial depth has a significant influence on the effective tension of the pipeline. With the increase of the burial depth, the maximum degree of stretching of the pipeline first decreases and then increases. Within a certain depth range, burying the pipeline in the seabed can reduce both the effective tension and the intensity of the fluctuation of the effective tension when the pipeline is lifted. The change of burial depths for the shear action is mainly reflected in the numerical values of the shear force. There is no significant impact on the degree and variation fluctuation of the shear force. The conclusions can provide a certain theoretical reference for the design of the process of horizontal pipeline lifting.

KEYWORDS

lumped mass model, three-point horizontal lifting, subsea pipelines, burial depth, dynamic characteristics

Introduction

Subsea pipelines refer to pipelines that act as the media transportation between offshore facilities and terrestrial terminals. Subsea pipelines play an irreplaceable role in the development of offshore oil and gas. Subsea pipelines are widely used in the underwater production equipment and subsea production system operations for providing power, signal transmission, and other reagents for the underwater oil exploration equipment.

A lot of research has been carried out on the uses and mechanisms of various types of subsea pipelines. The methods for the design analysis of pipelines, flexible pipes, and umbilicals were summarized by Sævik and Ye. An in-depth understanding of the structural behavior of flexible pipelines was shown and the methods used to perform global and local strength analysis with a focus on analytical as well as finite element methods were given, which can serve as a reference for ocean engineering (Sævik and Ye, 2015). An optimized design methodology for pipelines/fishing gear interaction was presented by Amdal et al., in which the response of pipelines due to trawling pull-over loads was investigated (Amdal et al., 2011). Naess and Leira summarized the law of stochastic dynamics of marine structures, which is a text for students and a reference for professionals on the basic theory and methods used for stochastic modeling and analysis of marine structures subjected to environmental loads (Næss and Moan, 2013). Sævik made some theoretical and experimental studies of stress in flexible pipes, in which one model for predicting stresses with axisymmetric effects was given (Saevik, 2011). The nonlinear formulation for the axisymmetric response of umbilical cables and flexible pipes was derived by Custodio A and Vaz (Custodio and Vaz, 2002). An experimental study was made by De Sousa et al., in which the effect of axial compression on the mechanical response of flexible pipes was given (De Sousa et al., 2012). A penalty-based contact element for pipelines and the 3D rigid body interaction was developed by Longva and Sævik (Longva and Sævik, 2013). Gao et al. made a damage assessment for submarine photoelectric composite cable under anchor impact, in which the material nonlinearity and component interaction were considered (Gao et al., 2018). A nonlinear model for deep-water steel lazy-wave riser configuration with ocean current and internal flow was established by Wang and Duan (Wang and Duan, 2015; Wang et al., 2015). The configurations and dynamic behavior of deep-water J-lay systems were studied by Gong et al., in which the numerical simulation and the stiffened catenary theory were used (Gong et al., 2011; Gong and Xu, 2016; Gong et al., 2020). The dynamic analysis of pipelines was made by Bai and Zhang, from which the lumped mass method was derived (Bai et al., 2018). The research on subsea pipelines involves all aspects, including structural analysis (Knapp and Shimabukuro, 2007), dynamic response analysis (Williams and Paton, 2002; Ajayi and Aribike, 2015), renewable energy (Martinelli et al., 2010), vortex-induced vibration (Liu et al., 2022), and installation process (Gao et al., 2014; Gong et al., 2014).

Subsea pipeline laying and maintenance has naturally become a very important research subject. The maintenance of the submarine pipeline is a very complex and difficult project. Because its construction design needs to be changed according to different sea conditions, construction ships, pipelines, and other conditions (Bruschi et al., 2015). The repair and maintenance of the underwater pipeline need to cut off the damaged or broken pipeline at specific points, then the damaged part of the pipeline is repaired by lifting the pipeline above the water surface with the lifting device of the construction ship. After completing the above work, the pipeline is put back to the bottom of the sea, then the repair work is completed. Research work has been done on the horizontal lifting of subsea pipelines. For example, a two-points lifting model of the submarine pipeline was established by Qu et al. (Qu et al., 2012). The interaction between the pipeline and the seabed was considered emphatically. With the utilization of commercial software, a finite element analysis program for the lifting of single and double-layer pipelines on the elastic and rigid seabed was developed by Qiao et al. (Qiao, 2010). Cui analyzed the stress of the single-point lifting and the two-points lifting of the pipeline and established the mechanical models (Cui, 2007).

As can be seen from the brief review of the most advanced research, the current research on subsea pipelines mainly focuses on the overall dynamic characteristics of pipelines during in-place operation and the mechanical characteristics. The horizontal lifting process is very common. However, little research has been done on the dynamic characteristics of the horizontal lifting process during marine pipeline maintenance, especially when considering the interaction between the pipeline and the seabed sediment. Some properties of seabed soil have an important impact on the process of pipe lifting (Guo et al., 2022a; Guo et al., 2022b). Therefore, it is of great importance to study the mechanical characteristics of the horizontal lifting of subsea pipelines. In this paper, with the consideration of the effect of soil resistance, combined with the specific conditions of the horizontal lifting of subsea pipelines, the mechanical characteristics of the horizontal lifting of subsea pipelines at different burial depths are explored in order to get some valuable conclusions, which will play a certain guiding role in specific engineering practice.

Computational theory

In addition to withstanding the wind, waves, and current loads, since the pipeline is buried in the subsea soil, it will inevitably be subject to three different kinds of resistance during lifting (Morison et al., 1950): the weight of the pipeline itself, the passive resistance caused by the static weight of soil and the pipeline, the active shear resistance moving along the edge of the vertical sliding surface.

When the pipeline is buried in cohesive soil, the soil resistance R of the pipeline during lifting can be expressed as the following:

$$R = \gamma' \cdot H \cdot D + \gamma' \cdot D^2 \cdot \left(\frac{1}{2} - \frac{\pi}{8}\right) + 2 \cdot S_M\left(H + \frac{D}{2}\right) \quad (1)$$

Where: γ' is the unit weight of the soil in the seabed, H is the burial depth; S_M is the saturated undrained shear strength of the soil; D is the diameter of the pipeline.

When the pipeline is buried in non-cohesive soil, the soil resistance R of the pipeline during the lifting process is:

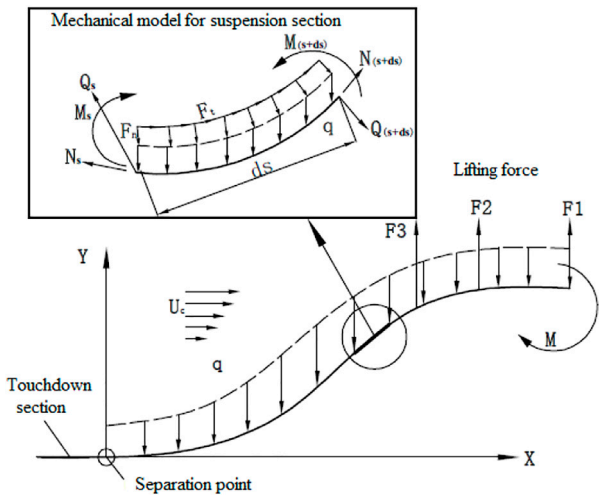


FIGURE 1
Schematic diagram of mechanical analysis of horizontal lifting of subsea pipeline.

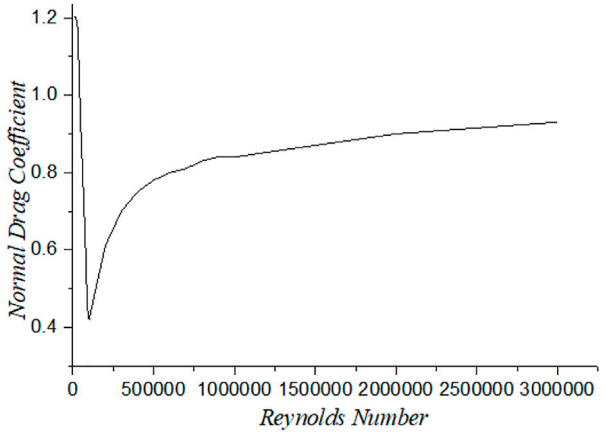


FIGURE 2
Normal drag coefficient of the pipeline versus Reynolds Number.

$$R = \gamma' \cdot H \cdot D + \gamma' \cdot D^2 \cdot \left(\frac{1}{2} - \frac{\pi}{8}\right) + f \cdot \gamma' \left(H + \frac{D}{2}\right)^2 \quad (2)$$

Where f is the lift coefficient.

Through the above formulas, the soil resistance of the pipeline during lifting can be obtained.

Since the suspension section of the pipeline is the most easily accidental position after lifting, it is necessary to make a corresponding mechanical analysis for it. Since the length of the pipeline laid on the seabed is long enough, the position of the separation point of the pipeline on the seabed can be taken as the fixed end of the model.

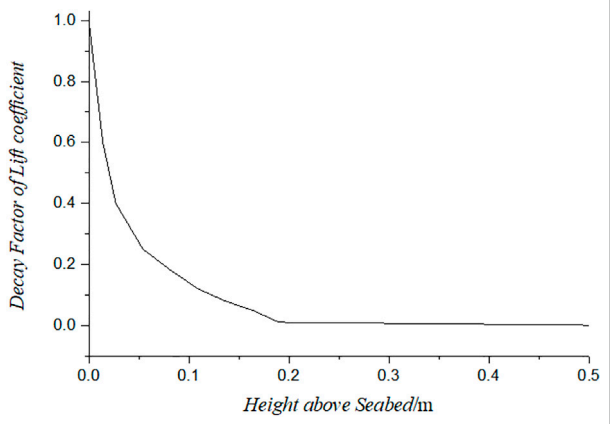


FIGURE 3
Lift coefficient of the pipeline versus height above seabed.

Then the equilibrium differential equation of the suspended span section during the pipeline lifting is established according to the deformation theory of large deflection beam. The stress model is shown in Figure 1. The pipeline lifting can be divided into two types: J-type lifting and S-type lifting. In general, the J-type lifting is applied to the welding of riser and subsea horizontal pipelines. The S-type lifting is widely used for repairing and recovering submarine pipelines. To facilitate the connection between two sections of the pipeline and reduce the initial stress caused by welding, the free end of the pipeline must be kept close parallel to the horizontal plane when the pipeline is out of water. In this paper, the damage to submarine pipelines caused by anchorage is taken as an example, the numerical simulation of the horizontal lifting of subsea pipelines is carried out, and the S-type lifting mechanical model is adopted.

According to the mechanical model shown in Figure 1, the equilibrium differential equation of the submarine pipeline can be written as:

$$\begin{aligned} -qds\sin\theta + F_t ds + dN + Qd\theta &= 0 \\ -qds\cos\theta - F_n ds - dQ + Nd\theta &= 0 \\ dM - Qds &= 0 \end{aligned} \quad (3)$$

Where: q is the weight per unit length of the pipeline in seawater; ds is the arc length of the selected micro-segment; F_t is the tangential wave and current force uniformly distributed along the pipeline axis; F_n is the normal wave and current force uniformly distributed perpendicular to the pipeline axis; N is the axial tension of the pipeline; Q is the shear force at the pipeline end; θ is the included angle between pipeline axis and horizontal plane; M is the bending moment at the end of the pipeline. The wave and current forces on the submarine pipeline can be calculated by the Morrison equations.

The normal component of current force:

$$F_{nc} = \frac{1}{2} C_n \rho D v_n^2 \quad (4)$$

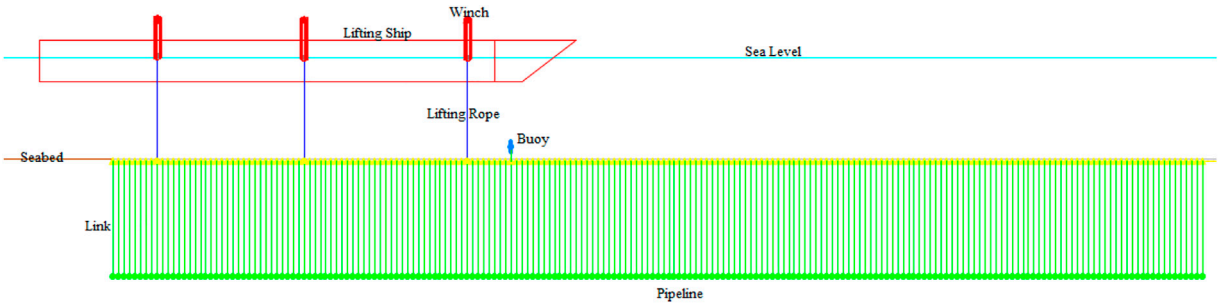


FIGURE 4
Multi-point horizontal lifting model.

The tangential component of current force:

$$F_{tc} = \frac{1}{2} C_t \rho D v_n^2 \tag{5}$$

The normal component of wave force:

$$F_{nw} = \frac{1}{2} C_n \rho D u_n^2 + C_m \rho \frac{\pi D^2}{4} \frac{\partial u}{\partial t} \tag{6}$$

The tangential component of wave force:

$$F_{tw} = \frac{1}{2} C_t \rho D u_t^2 \tag{7}$$

Where: C_n is the normal drag coefficient, C_t is the tangential drag coefficient, the numerical value of the drag coefficient changes with Reynolds number; C_m is the inertia force coefficient, the numerical value is 2; U_c is the resultant velocity of the current velocity v and the wave velocity u; v_n=v·sin, v_t=v·cos, they are the normal velocity and tangential velocity of the current, respectively; u_n=u·sin, u_t=u·cos, they are the normal velocity and tangential velocity of the wave, respectively.

Since the lifting of the submarine pipeline belongs to the problem of large length-diameter ratio and large bending deformation, the axial deformation and the shear deformation of the pipeline can be ignored, and only the bending deformation of the pipeline can be considered, then the following relationships can be obtained:

$$EI \frac{d\theta}{ds} = M(s) \tag{8}$$

$$\sin\theta = \frac{dy}{ds} \cos\theta = \frac{du}{ds} + 1 \tag{9}$$

Where: EI is the bending stiffness of the submarine pipeline; b is the length of the suspension section; y(s) and u(s) are the deflections and horizontal displacement at any point of the pipeline, respectively.

The boundary conditions of the S-type lifting can be simplified as follows: at the separation point, s=0, y (0)=0, θ(0)=0, u (0)=0, N (0)=0, M(0)=0; at the free end, s=b, $N(b)$·$\sin(b)$-$Q(b)$·$\cos(b)$=F, $M(b)$=M. The dimensionless parameter s/b is introduced into Eq. 1 to change the solution interval from (0, b) to (0,1). Other

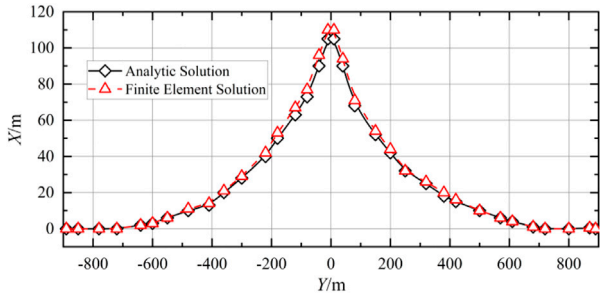


FIGURE 5
Verification of the modeling method.

parameters such as deflection, bending moment, and shear force are also dimensionless simplified, just as shown in Eq. 10:

$$y_n(\xi) = \frac{y(s)}{a}, u_n(\xi) = \frac{u(s)}{a}, N_n(\xi) = \frac{N(s)}{qa}, Q_n(\xi) = \frac{Q(s)}{qa}, M_n(\xi) = \frac{M(s)}{qa^2} \tag{10}$$

Substitute Eqs 7–9 into Eq. 3, then the following equation can be obtained:

$$\begin{aligned} &-\sin\theta + \frac{F_{tc} + F_{tw}}{q} + \frac{dN_n}{d\xi} + Q_n \frac{d\theta}{d\xi} = 0 \\ &-\cos\theta - \frac{F_{nc} + F_{nw}}{q} - \frac{dQ}{d\xi} + N_n \frac{d\theta}{d\xi} = 0 \\ &\frac{dM_n}{d\xi} - Q_n = 0 \\ &\frac{d\theta}{d\xi} = M_n k \\ &\sin\theta = \frac{dy_n}{d\xi} \\ &\cos\theta = \frac{du_n}{d\xi} + 1 \end{aligned} \tag{11}$$

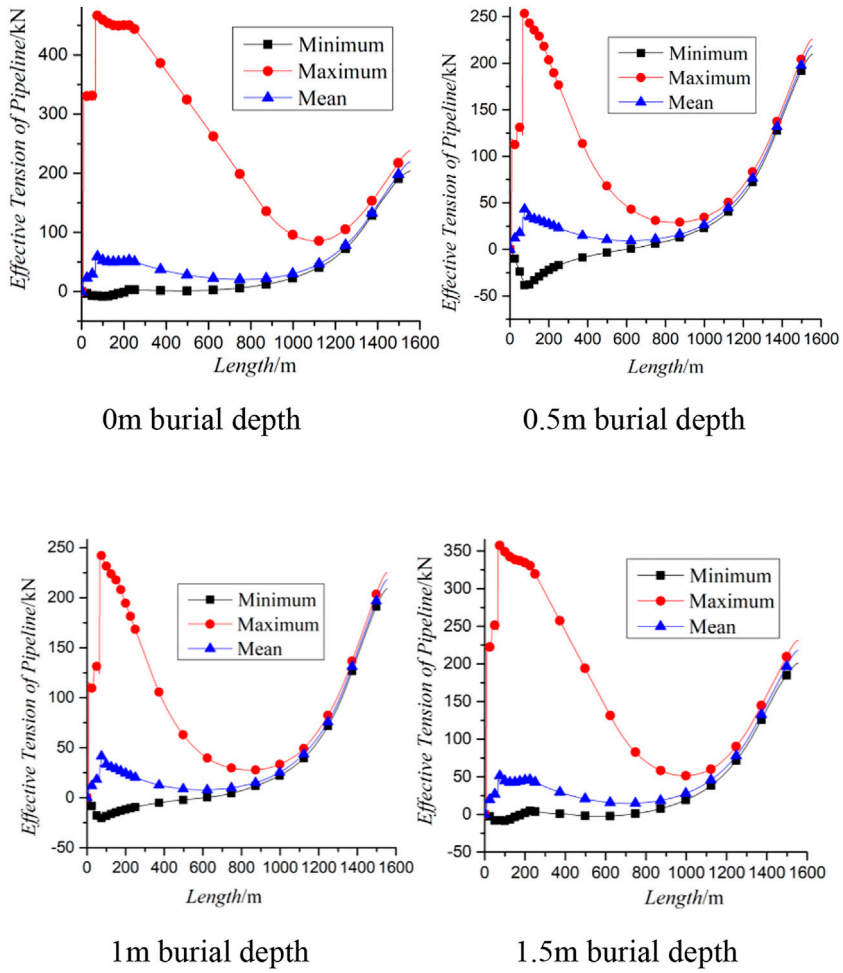


FIGURE 6
Effective tension of the pipeline in the length direction with different burial depths.

Finally, the boundary problem of the suspension section can be solved by the above equations.

Establishment of dynamic simulation model

Environmental and pipeline parameters

The water depth is 18.7 m, the current direction is 180°, the current is 1 m/s, The type of wave spectrum is the Jonswap spectrum, the wave direction is 90°, The significant wave height H_s is 1m, and the mean zero-crossing period T_z is 11.35s.

The length of the pipeline is 1555 m, the outer diameter is 0.2191 m, the inner diameter is 0.194 m and Young's modulus is 2.07×10^5 MPa, Poisson ratio is 0.3, the density is 7.85 t/m^3, the normal additional mass coefficient of the pipeline is 1, the axial additional mass coefficient of the pipeline is 0, the axial drag coefficient of the pipeline is 0.008, the normal drag coefficient of the pipeline is shown in Figure 2., and the lift coefficient of the pipeline is shown in Figure 3. The normal and axial friction coefficients between the pipeline and the seabed are both 0.5.

The influence of the shape, slope, and stiffness of the seabed on the lifting of submarine pipelines cannot be neglected. However, for the convenience of modeling, the seabed is simplified as a flat seabed with a vertical stiffness coefficient of 1.866 kN/m^3 and a shear stiffness coefficient of 100 kN/m^3. Soil resistance cannot be directly applied to the pipeline in OrcaFlex. There, to simulate the effect of the soil suction on the subsea pipeline, the Link unit is used in this paper to simulate the vertical soil resistance. Since the soil resistance of the pipeline Section 250 m away from the free end of the pipeline has little influence on the lifting operation, to simulate the normal resistance of the seabed within the range of 0–200 m near the

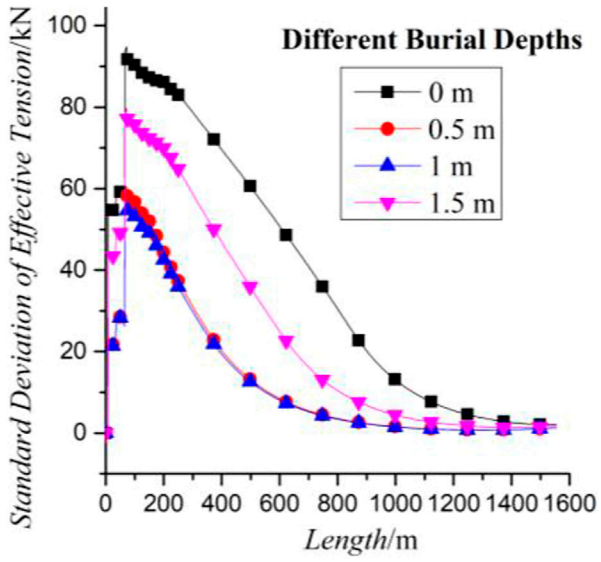


FIGURE 7
Standard deviation of the effective tension of the pipeline in the length direction with different burial depths.

lifting ship, a total of 200 Link units are arranged, and every 1 m is a Link unit. This will make the numerical model more compatible with the actual lifting operation and make the data more reliable.

Establishment of dynamic simulation model

The pipeline part of 0–250 m near the operation area of the lifting ship is the area with obvious pipeline deformation, so the segment length of this part is 1m, and it is divided into 250 units in total. The unit length of the remaining 1305 m pipeline is 5 m, and it is divided into 261 units in total. Therefore, the entire pipeline is divided into 511 segmented units. A Link unit is connected to a circular buoy with a mass of 0.005t and a volume of 5 m^3 at the length direction of 73 m. The function of the buoy is mainly used to provide a certain buoyancy for the lifting operation.

Since the length of the lifting rope varies throughout the dynamic lifting process, the Winch unit with variable length is used to simulate the lifting rope. One end of the Winch unit is connected to the subsea pipeline and the other end is connected to the lifting ship. Three Winch units are arranged at the pipeline length direction of 8, 35, and 65 m, respectively. The coordinates of these three Winch units on the lifting vessel are (-27 m, -16.5 m, 6.78 m), (0 m, -12 m, 7 m), (30 m, -12 m, 7 m).

The position of the lifting ship remains unchanged, and the whole lifting process is mainly controlled by the length of the lifting rope. The length of the prolongation and contraction of the lifting rope at each stage needs to be determined according to the parameters of the winch and other equipment on the ship. In the simulation, to make the model converge more easily, the contraction process of the lifting rope will be realized through 24 analysis steps. Because submarine pipelines are generally buried under the seabed, the non-linear pipe-soil interaction will inevitably occur during the process of pipeline lifting, which can be simplified as vertical soil resistance, just as shown in Figure 4.

Accuracy verification of the modeling method

To verify the accuracy of the modeling method, according to the actual situation of submarine pipeline laying and lowering under a certain working condition, the modeling method proposed in this paper is used for modeling, and the simulation modeling results are compared with the theoretical calculation results, just as shown in Figure 5.

It can be seen from Figure 5 that the configuration of the curve obtained during the lifting process of the submarine cable by the finite element solution in OrcaFlex is very similar to that of the analytical solution. The curves obtained by the two methods are convex from the middle and nearly symmetrical on both sides. By further observing the graph and comparing the data, it is found that the error between the two is less than 10%, which verifies the correctness of the modeling method proposed in this paper.

Calculation results

Effective tension of the pipeline

With the observation of the distribution of the effective tension in the length direction with different burial depths in Figure 6, it is found that the change of burial depth has a significant influence on the effective tension of the pipeline.

By comparing and observing the distribution curves of the maximum effective tension in the length direction with different burial depths, it can be seen that the change of the burial depth does not change the position where the maximum tension occurs. The maximum effective tension of the pipeline reflects the maximum degree of stretching that the pipeline is subjected to.

Further comparative observation shows that the maximum degree of stretching of the pipeline does not increase with the increase in burial depth of the pipeline. With the increase of the burial depth of the pipeline, when the burial depth of the pipeline increases to 0.5 m, compared with the burial depth of 0m, the maximum stretching degree decreases significantly. When the burial depth of the pipeline continues to increase to 1m, the

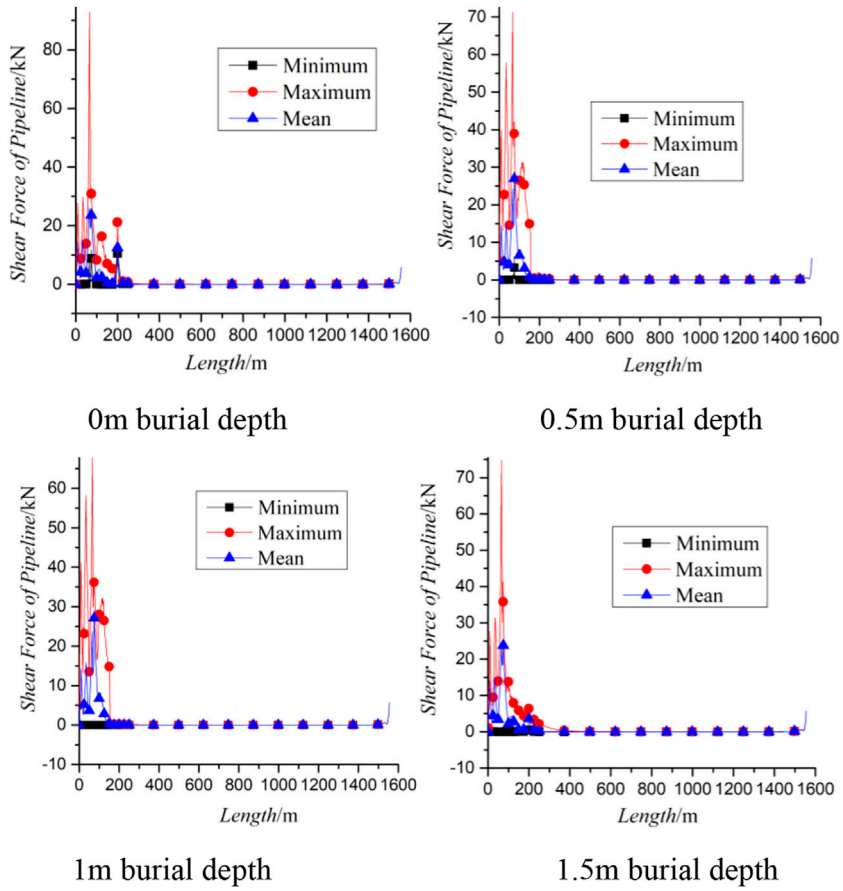


FIGURE 8
Shear force of the pipeline in the length direction with different burial depths.

maximum stretching degree decreases slightly. However, when the burial depth of the pipeline continues to increase to 1.5 m, the maximum effective tension of the pipeline at the point where the maximum stretching degree occurs increases again.

Further observation can be found that in the length range of 1,100m–1555 m, the curves of the maximum, minimum, and mean effective tension of the pipeline in the length direction are highly coincident, which indicates that the stretching effect of the lifting operation on the pipeline in this length range is almost constant in the time domain without much fluctuation.

With the observation of the distribution curves of the standard deviation of the effective tension in the length direction with different burial depths in Figure 7., it can be seen that the standard deviation of effective tension of the pipeline shows a tendency of repeated changes with the increase of the burial depth. When the burial depth of the pipeline is 0m, the standard deviation of the effective tension of the pipeline is the largest. When the burial depths are 0.5 and 1 m, the standard deviation curves of the effective tension of the pipeline are highly overlapped. When the burial depth is 1.5 m, the standard deviation of the effective tension of the pipeline is smaller than that with 0 m burial depth but larger than that with 0.5 m burial depth. Combined with the calculation results, it can be seen that a certain degree of burial depth during the lifting process may be helpful to reduce the degree of axial tension and the intensity of axial tension fluctuation, which may be helpful to reduce the fatigue damage of the pipeline during the lifting process.

Shear force of the pipeline

With the observation of the distribution of the shear force in the length direction with different burial depths in Figure 8., it can be seen that a small shear force will be generated at the end of the pipeline at 1555 m with different burial depths. It means that in the lifting process, as the pipeline is gradually lifted, the end of the pipeline near the seabed will be supported by the seabed, and this concentrated support increases with the increase of the lifting

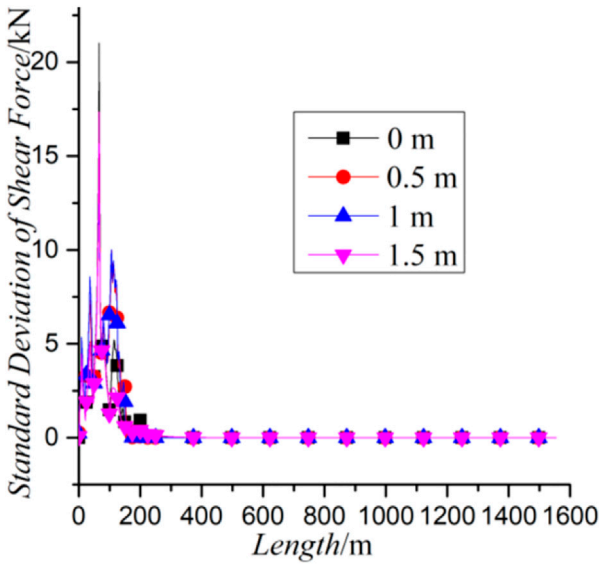


FIGURE 9
Standard deviation of the shear force of the pipeline in the length direction with different burial depths.

length of the pipeline, which is the reason for the small increase in shear force at the end of the pipeline.

Further observation shows that with the increase of the burial depth, the location of the maximum shear force in the length direction does not change significantly, but the magnitude of maximum shear force at the location of the maximum shearing action decreases first and then increases with the increase of the burial depth. Combined with the calculation results, it can be seen that in the lifting process, the pipeline will be subjected to both axial stretching and shearing effects, and both the shearing action and the axial stretching action are smaller when the burial depth is 1 m. This provides a possible choice for optimizing the burial depth of the pipeline, the lifting operation at this burial depth can reduce both the tensile force and the shear force of the pipeline.

With the observation of the distribution of the standard deviation of the shear force in the length direction with different burial depths in Figure 9., it can be seen that the degree of the shear force fluctuation of the pipeline is the same with different burial depths, which indicates that the change of the burial depth is the main reason for the numerical value of the shear force.

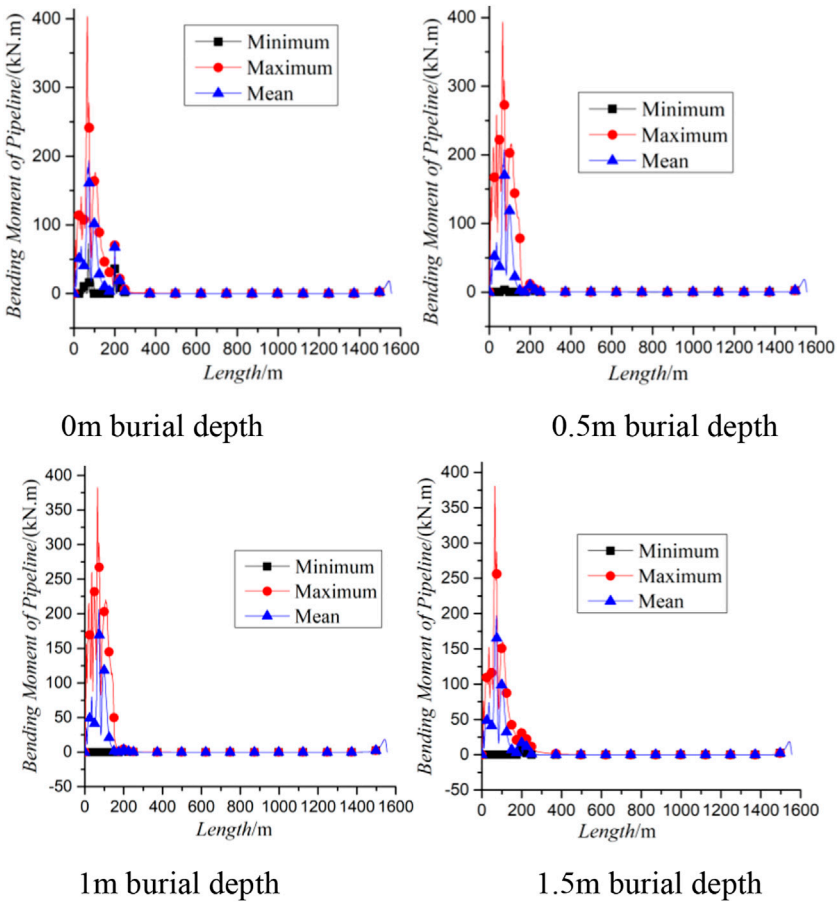


FIGURE 10
Bending moment of the pipeline in the length direction with different burial depths.

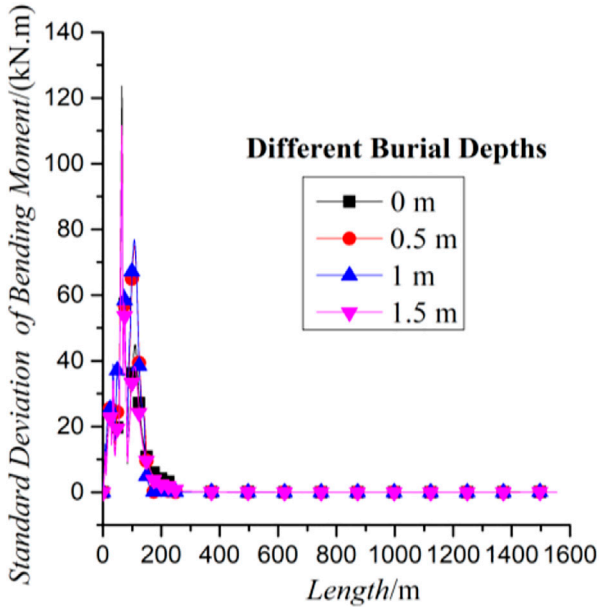


FIGURE 11
Standard deviation of the bending moment of the pipeline in the length with different burial depths.

It means that the change of burial depth for the change of shear action is mainly reflected in the change of the numerical value of the shear force, and has no significant impact on the degree and variation fluctuation of the shear force.

Bending moment of the pipeline

By observing the distribution of the bending moment in the length direction with different burial depths in Figure 10., it can be seen that there is no significant difference in the distribution of the bending moment in the length direction of the pipeline with the increase of the burial depth, which shows that the increase of burial depth does not bring about an obvious increase of the bending moment. In a sense, it means that within a certain range, the change of the burial depth will not lead to a significant increase in the bending moment of the pipeline during the lifting process.

With the observation of the distribution of the standard deviation of the bending moment in length direction with different burial depths in Figure 11., it can be seen that the bending intensity of the pipeline does not increase with the increase of the burial depth, and the area where the pipeline

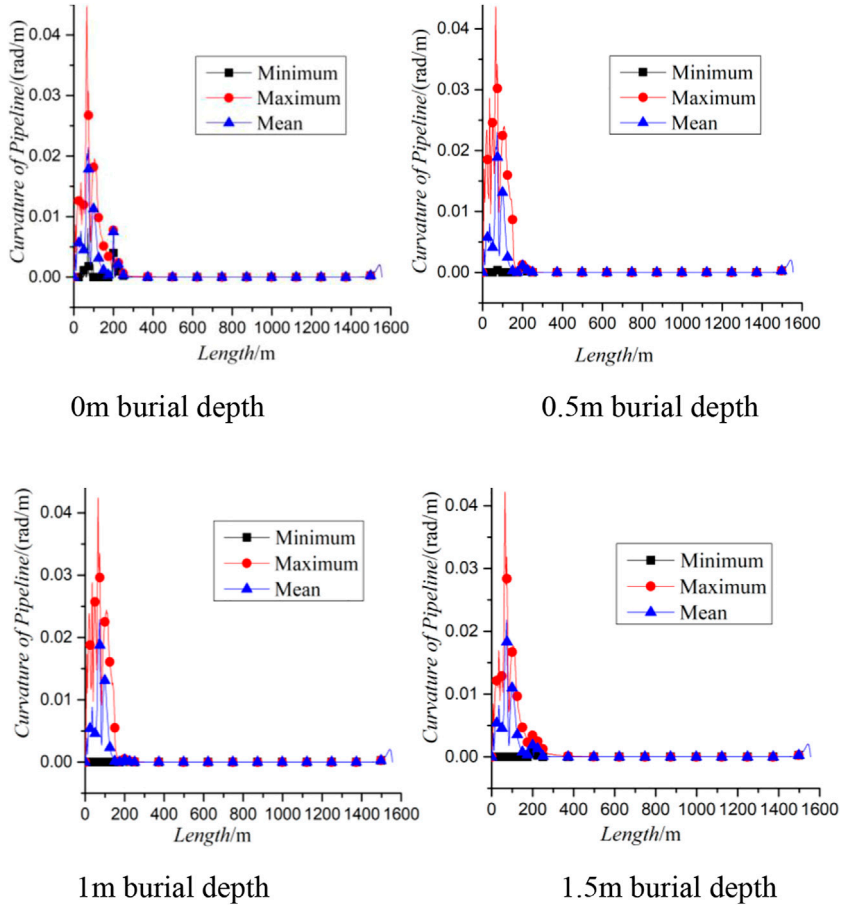


FIGURE 12
Curvature of the pipeline in the length direction with different burial depths.

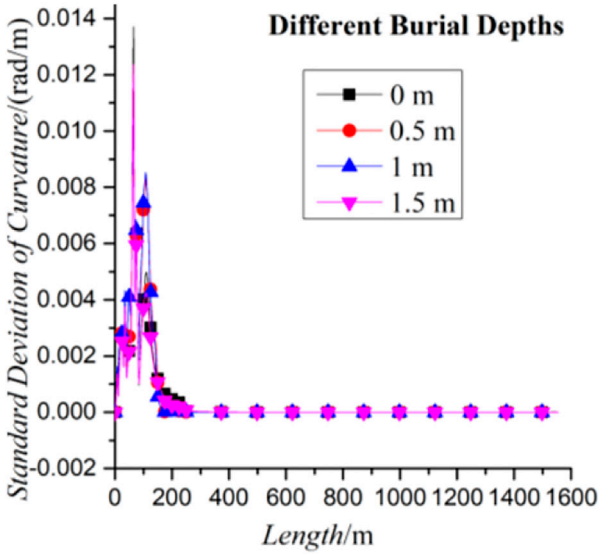


FIGURE 13
Standard deviation of the curvature of the pipeline in the length direction with different burial depths.

bends more intensely is also the area where pipeline bears larger bending moment. This indicates that the location where the bending transfer of the pipeline is discrete in the time domain is the location where the maximum bending moment of the pipeline is likely to occur.

Curvature of the pipeline

With the comparison and observation of the curve distribution configurations of the bending moment and curvature in the length direction with different burial depths in Figure 12., it can be found that the distribution configurations of the bending moment curve and the curve of the curvature in the length direction are highly similar at the same burial depth. It means that the bending moment and curvature change synchronously, and there is no hysteresis in the bending deformation of the pipeline during the lifting process.

By comparing and observing the curve distribution configurations of the standard deviation of the bending moment and the standard deviation of the curvature of the

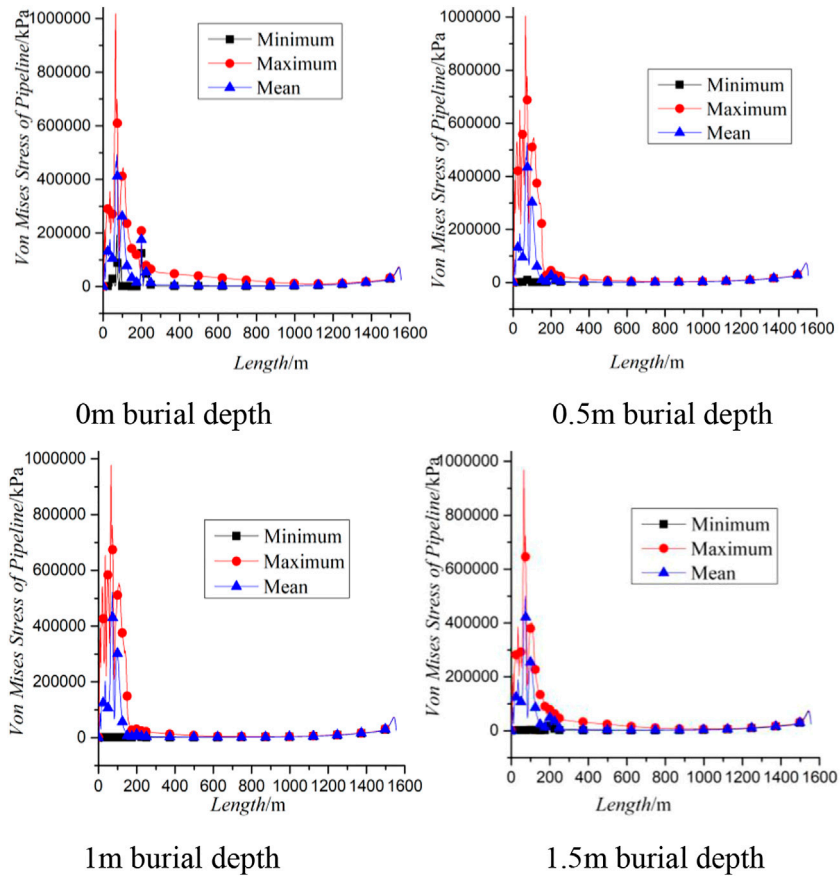


FIGURE 14
Von Mises stresses the pipeline in the length direction with different burial depths.

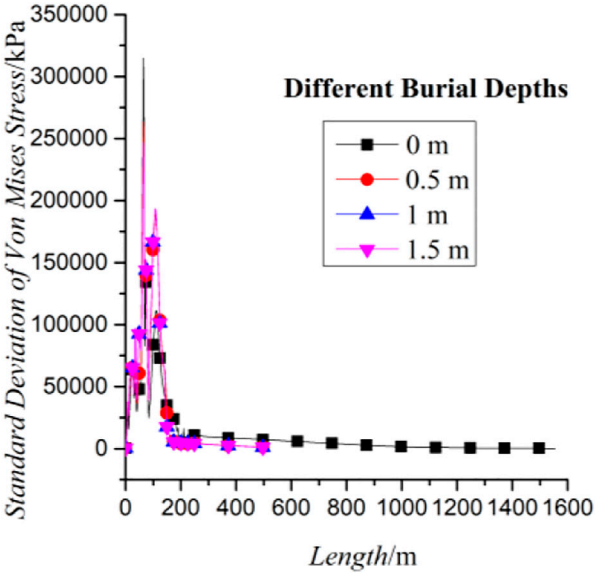


FIGURE 15
Standard deviation of Von Mises of the pipeline in the length direction with different burial depths.

pipeline in the length direction with different burial depths in Figure 13., it can be found that the distribution configurations of the standard deviation curve of the bending moment and the standard deviation curve of the curvature of the pipeline in the length direction at the same burial depth are highly similar, which again shows the high consistency of the change of the bending moment and the change of the curvature caused by the bending action in the time domain. It also shows that the parts with sharp bending changes have large bending moments and curvature.

Von Mises stress of the pipeline

With the observation of the distribution of von Mises stresses in the length direction with different burial depths in Figure 14., it can be seen that the change of the burial depth has little effect on von Mises stresses, and von Mises stresses are almost zero in the length range of 200–800 m, which again verifies the correctness of the calculation. The bending moment and the shear force of the pipeline are also 0 in the length range of 200–800 m, which is the reason for the phenomenon that von Mises stress is 0 in this length range.

However, it can be found that the distributions of von Mises stress in the length range of 0–200 m with different burial depths have some differences. It means that von Mises' stresses show a complex trend in this length range. The generation of von Mises stress is inseparable from the combined loads such as tensile, bending, and shearing of the pipeline. Therefore, the part with high von Mises stress is also the part where the pipeline is subjected to large bending, tensile and shearing loads during the lifting process.

By observing the distribution of von Mises stress standard deviation in the length direction with different burial depths in Figure 15., it can be seen that the standard deviation of von Mises stress tends to zero in the range of 200–1555 m, which indicates that von Mises stress is not only small in this range of length but also the intensity of von Mises stress fluctuation is also very small, the reason for this phenomenon is that section in the range of 200–1555 m is far from the operation area.

Conclusion

1) The change of burial depth has a significant influence on the effective tension of the pipeline. The maximum effective tension of the pipeline reflects the maximum degree of stretching that the pipeline is subjected to. With the increase of the burial depth of the pipeline, the maximum degree of stretching of the pipeline first decreases and then increases. A certain degree of burial depth during the lifting process may be helpful to reduce the degree of axial tension and the intensity of axial tension fluctuation, which may be helpful to reduce the fatigue damage of the pipeline during the lifting process.
2) As the pipeline is gradually lifted, the end of the pipeline near the seabed will be supported by the seabed, and this concentrated support increases with the increase of the lifting length of the pipeline. This is the reason for the small increase in shear force at the end of the pipeline. In the lifting process, the shearing action and the axial stretching action are smaller when the burial depth is 1 m. This provides a possible choice for optimizing the burial depth of the pipeline. The change of burial depth for the change of shear action is mainly reflected in the change of the numerical value of the shear force.
3) Within a certain range, the influence of the bending factors on the pipeline does not need to be considered too much during the lifting process. And the part with high von Mises stress is also the part where the pipeline is subjected to large bending, tensile and shearing loads during the lifting process.

Data availability statement

The original contributions presented in the study are included in the article/supplementary material, further inquiries can be directed to the corresponding author.

Author contributions

Investigation, DZ and BZ; methodology, DZ and BZ; writing original draft preparation, DZ and KZ; writing review and editing, BZ. All authors have read and agreed to the published version of the manuscript.

Funding

This work was supported by the Program for Scientific Research Start-up Funds of Guangdong Ocean University under Grant 060302072101; Comparative Study and Optimization of Horizontal Lifting of Subsea Pipeline under Grant 2021E05011.

Conflict of interest

The authors declare that the research was conducted in the absence of any commercial or financial relationships that could be construed as a potential conflict of interest.

Publisher's note

All claims expressed in this article are solely those of the authors and do not necessarily represent those of their affiliated organizations, or those of the publisher, the editors and the reviewers. Any product that may be evaluated in this article, or claim that may be made by its manufacturer, is not guaranteed or endorsed by the publisher.

References

Ajayi, O. O., and Aribike, O. O. (2015). Modelling and simulation of subsea umbilical dynamics: A numerical approach. *Int. J. Comput. Thechniques* 2 (1), 12.

Amdal, L. W., Rneid, S., and Etterdal, B. (2011). "Optimised design of pipelines exposed to trawl pull-over," in ISOPE-2011 Maui;International offshore and polar engineering conference.

Bai, Y., Zhang, D., Zhu, K., and Zhang, T. (2018). Dynamic analysis of umbilical cable under interference with riser. *Ships Offshore Struct.* 13 (8), 1–13. doi:10.1080/17445302.2018.1460082

Bruschi, R., Vitali, L., Marchionni, L., Parrella, A., and Mancini, A. (2015). Pipe technology and installation equipment for frontier deepwater projects. *Ocean. Eng.* 108, 369–392. doi:10.1016/j.oceaneng.2015.08.008

Cui, Y. (2007). Lifting analysis and program development of pipelines in beach and sea area, Master Thesis. Tianjin: Tianjin University.

Custodio, A., and Vaz, M. (2002). A nonlinear formulation for the axisymmetric response of umbilical cables and flexible pipes. *Appl. Ocean Res.* 24, 21–29. doi:10.1016/s0141-1187(02)00007-x

De Sousa, J., Viero, P., Magluta, C., and Roitman, N. (2012). An experimental and numerical study on the axial compression response of flexible pipes. *J. Offshore Mech. Arct. Eng.* 134 (3), 031703. doi:10.1115/1.4005181

Gao, Q., Duan, M., Liu, X., Wang, Y., Jia, X., An, C., et al. (2018). Damage assessment for submarine photoelectric composite cable under anchor impact. *Appl. Ocean Res.* 73, 42–58. doi:10.1016/j.apor.2018.01.006

Gao, Y., Wei, H., Jiang, Y., Wang, Y., et al. (2014). Current technology and development trend of process facilities in deep water subsea production system. *China Offshore Oil Gas* 26 (4), 84–90.

Gong, S., Chen, K., Chen, Y., Jin, W., Li, Z., and Zhao, D. (2011). Configuration analysis of deepwater S-lay pipeline. *China Ocean. Eng.* 25 (3), 519–530. doi:10.1007/s13344-011-0042-5

Gong, S., Xu, P., Bao, S., Zhong, W., He, N., and Yan, H. (2014). Numerical modelling on dynamic behaviour of deepwater S-lay pipeline. *Ocean. Eng.* 88, 393–408. doi:10.1016/j.oceaneng.2014.07.016

Gong, S., and Xu, P. (2016). The influence of sea state on dynamic behaviour of offshore pipelines for deepwater S-lay. *Ocean. Eng.* 111, 398–413. doi:10.1016/j.oceaneng.2015.11.013

Gong, S., Zhang, T., Wang, X., and Liu, C. (2020). Numerical simulation on dynamic behaviour of deepwater J-lay systems. *Ocean. Eng.* 196 (15), 106771. doi:10.1016/j.oceaneng.2019.106771

Guo, X., Nian, T., Wang, D., and Gu, Z. d. (2022). Evaluation of undrained shear strength of surficial marine clays using ball penetration-based CFD modelling. *Acta Geotech.* 17 (5), 1627–1643. doi:10.1007/s11440-021-01347-x

Guo, X., Nian, T., Zhao, W., Gu, Z., Liu, C., Liu, X., et al. (2022). Centrifuge experiment on the penetration test for evaluating undrained strength of deep-sea surface soils. *Int. J. Min. Sci. Technol.* 32 (2), 363–373. doi:10.1016/j.ijmst.2021.12.005

Knapp, R. H., and Shimabukuro, T. S. (2007). "Structural analysis of composite umbilical cables," in The Seventeenth International Offshore and Polar Engineering Conference.

Liu, Z., Guo, H., Li, P., Li, F., Gu, H., An, W., et al. (2022). Experimental investigation on the vortex-induced vibration (VIV) suppression of the umbilical cable attached with helical strakes. *Nav. Eng. J.* 134 (1), 117–132.

Longva, V., and Sævik, S. (2013). A penalty-based contact element for pipe and 3D rigid body interaction. *Eng. Struct.* 56, 1580–1592. doi:10.1016/j.engstruct.2013.07.025

Martinelli, L., Lamberti, A., Ruol, P., Ricci, P., Kirrane, P., Fenton, C., et al. (2010). "Power umbilical for ocean renewable energy systems-feasibility and dynamic response analysis," in Proc. Int Conf Ocean Energy.

Morison, J. R., Johnson, J. W., Schaaf, S. A., et al. (1950). The force exerted by surface waves on piles. *J. Petroleum Technol.* 2 (5), 149–154. doi:10.2118/950149-g

Næss, A., and Moan, T. (2013). *Stochastic dynamics of marine structures*. Cambridge: Cambridge University Press.

Qiao, F. (2010). Development for the strength analysis program of submarine pipeline lifting, Master Thesis. Tianjin: Tianjin University.

Qu, Y., Liu, X., Yi, P., et al. (2012). A finite element analysis of the multi-point hoist of offshore pipeline. *China Pet. Mach.* (3), 53–56.

Saevik, S. (2011). Theoretical and experimental studies of stresses in flexible pipes. *Comput. Struct.* 89 (2324), 2273–2291. doi:10.1016/j.compstruc.2011.08.008

Sævik, S., and Ye, N. (2015). *Aspects of design and analysis of offshore pipelines and flexibles*. Chengdu: Southwest Jiaotong University Press.

Wang, J., and Duan, M. (2015). A nonlinear model for deepwater steel lazy-wave riser configuration with ocean current and internal flow. *Ocean. Eng.* 94, 155–162. doi:10.1016/j.oceaneng.2014.11.025

Wang, J., Duan, M., Wang, Y., Li, X., and Luo, J. (2015). A non-linear mechanical model for deepwater steel lazy-wave riser transfer process during installation. *Appl. Ocean Res.* 50, 217–226. doi:10.1016/j.apor.2015.02.004

Williams, V. T., and Paton, K. M. (2002). "Malampaya deep water gas-to-power project: Subsea umbilical challenge," in Offshore Technology Conference.

frontiers | Frontiers in Earth Science

TYPE Original Research
PUBLISHED 20 September 2022
DOI 10.3389/feart.2022.1016605

Check for updates

OPEN ACCESS

EDITED BY
Guang-Liang Feng,
Chinese Academy of Sciences (CAS), China

REVIEWED BY
Guozhu Zhang,
Southeast University, China
Qiang Feng,
Shandong University of Science and Technology, China

*CORRESPONDENCE
Faming Huang,
faminghuang@ncu.edu.cn

SPECIALTY SECTION
This article was submitted to Geohazards and Georisks, a section of the journal Frontiers in Earth Science

RECEIVED 11 August 2022
ACCEPTED 25 August 2022
PUBLISHED 20 September 2022

CITATION
Lv Z, Wu M, Huang F and Cai Y (2022), Analytical solution of mechanical response in cold region tunnels under transversely isotropic freeze–thaw circle induced by unidirectional freeze–thaw damage.
Front. Earth Sci. 10:1016605.
doi: 10.3389/feart.2022.1016605

COPYRIGHT
© 2022 Lv, Wu, Huang and Cai. This is an open-access article distributed under the terms of the Creative Commons Attribution License (CC BY). The use, distribution or reproduction in other forums is permitted, provided the original author(s) and the copyright owner(s) are credited and that the original publication in this journal is cited, in accordance with accepted academic practice. No use, distribution or reproduction is permitted which does not comply with these terms.

Analytical solution of mechanical response in cold region tunnels under transversely isotropic freeze–thaw circle induced by unidirectional freeze–thaw damage

Zhitao Lv, Mingchao Wu, Faming Huang* and Yi Cai

School of Infrastructure Engineering, Nanchang University, Nanchang, China

During the operation stage of cold region tunnels, the isotropic surrounding rock in a freeze–thaw circle suffers long-term unidirectional freeze–thaw cycles and gradually transforms into transversely isotropic material, which induces the variation of stress and displacement distribution of cold region tunnels. Aimed at this phenomenon, an analytical solution of mechanical response in cold region tunnels under transversely isotropic freeze–thaw circles induced by unidirectional freeze–thaw damage is proposed. The analytical solution is derived under two different states of the freeze–thaw circle: *1*) transversely isotropic and unfrozen state (state TU) and *2*) transversely isotropic and frozen state (state TF). In addition, the stress distribution in the lining and surrounding rock with a transversely isotropic freeze–thaw circle is analyzed. The transformation of the surrounding rock in a freeze–thaw circle from isotropic material into transversely isotropic material leads to the increase of stress in the lining, especially for a significant increase under state TF. Finally, the influence of the deterioration coefficient and the degree of anisotropy on the stress distribution in the lining is analyzed. The stress in the lining increases linearly as the deterioration coefficient decreases, while it increases nonlinearly as the degree of anisotropy decreases. The smaller the degree of anisotropy is, the greater the increase rate of the stress is. Moreover, the increase of stress with deterioration coefficient and degree of anisotropy under state TF is much greater than that under state TU. Both deterioration coefficient and degree of anisotropy decrease from 1.0 with increasing unidirectional freeze–thaw cycles suffered by surrounding rock, and, thus, induce the increase of stresses in the lining. In addition, the deterioration coefficient has a greater influence than the degree of anisotropy on the stress in the lining.

KEYWORDS

stress distribution, cold region tunnels, transversely isotropic freeze–thaw circle, mechanical response, unidirectional freeze–thaw

Introduction

With the economic growth and increasing traffic demand, more and more cold region tunnels are constructed in cold areas such as Alaska, north Japan, Russia, and Norway, especially in Tibet Plateau and north China. However, most cold region tunnels suffer destructive and troublesome frost damage induced by special climate and geological environment, which even leads to stability and safety problems (Huang et al., 2020, 2022).

The temperature field of cold region tunnels varies significantly above and below the freezing point every year due to the peculiar climate of tunnel sites (Li et al., 2015; Yu et al., 2018), resulting in the freezing and thawing of surrounding rock and groundwater, and, thus, induces various kinds of frost damages. As the temperature field is a basis for frost resisting, plenty of model experiments were performed to investigate the temperature evolution of cold region tunnels and the influence of factors such as airflow temperature (Zeng et al., 2017), inlet wind velocity (Liu L. et al., 2018), and construction disturbance (Zhang et al., 2018). Moreover, numerical models coupled the heat convection and heat conduction between airflow and surrounding rock were proposed to forecast the temperature evolution of cold region tunnels (Lai et al., 2005; Tan et al., 2014). Numerical models involving the influence of train-induced ventilation on temperature evolution were also established (Zhou et al., 2016).

Freeze proofing is a type of measure to resist frost damage, and the thermal insulation layer has currently been the most popular and effective method in freeze proofing. An optimization method to design a thermal insulation layer has been found by Li et al. (2017) based on a coupled heat-water numerical model. Feng et al. (2016) conducted physical modelling experiments in the Yuximolegai tunnel and investigated the reliability of the thermal insulation layer design. Li et al. (2020) analyzed the capacity degradation of thermal insulation materials after moisture absorption and complete freezing in cold region tunnels. There are also applications of other freeze-proofing methods, such as the ground heat exchanger system utilizing heat in deeper surrounding rock (Zhang et al., 2016, 2017; Chang et al., 2022).

Furthermore, the stress distribution and stability of cold region tunnels are significantly influenced by the temperature evolution and freezing of surrounding rock and groundwater. At present, stability analysis on cold region tunnels is mostly based on the freeze–thaw circle frost heave model first proposed by Lai et al. (2000). This model holds that frost heaving force is induced by the frost heave of the freeze–thaw circle, and solutions based on this model can be categorized into three kinds according to their assumptions. The first kind assumes the frost heave displacement mode of the freeze–thaw circle. For example, Gao et al. (2012) derived a solution assuming that displacement does not occur at the center line of the freeze–thaw circle when frost heave generates. The second kind of solution assumes isotropic frost heave in the freeze–thaw circle. According to this assumption, a visco-elastic stress solution (Lai et al., 2000) and an elasto-plastic stress solution (Feng et al., 2014) on cold region tunnels when the surrounding rock freezes have been developed. In addition, an elastic stress solution under non-axisymmetric stress has been derived by Feng et al. (2017), assuming isotropic frost heave in cold region tunnels. The third kind of solution assumes that the frost heave of the freeze–thaw circle is anisotropic. For example, Xia et al. (2018) proved the transversely isotropic frost heave of the freeze–thaw circle through frost heave experiments on rock and then established an elastic stress solution which considered this specific frost heaving property of surrounding rock in cold region tunnels. On the basis of the experimental study and elastic solution of Xia et al., Lv et al. (2019) further derived an elasto-plastic solution of stress with the same assumption of transversely isotropic frost heave in cold region tunnels and found a remarkable influence of transversely isotropic frost heave on stress distribution. Feng et al. (2019) established a similar elasto-plastic solution with a different yield criterion. Moreover, Liu W. et al. (2018) built an elasto-plastic solution of stress on cold region tunnels taking the coupling influence of anisotropic frost heaving property of surrounding rock, support strength, and support time into consideration.

However, most current stress solutions of cold region tunnels regard the mechanical properties of surrounding rock as invariant. In fact, surrounding rock suffers freeze–thaw cycles and deteriorates during the operation stage of cold region tunnels. Ding et al. (2020) investigated the deterioration in mechanical properties with freeze–thaw cycles in a tight sandstone and studied changes to its pore structure using nuclear magnetic resonance technology. Huang et al. (2022a, b) studied the pore structure change of red sandstone under freeze–thaw cycles by mercury intrusion porosimetry and found that both the uniaxial compressive strength and the triaxial compressive strength decrease due to the growth of macropores. Liu et al. (2020) investigated the effect of water saturation on the physico-mechanical properties of clay-bearing rock under freeze–thaw by testing the uniaxial compressive strength and P-wave velocity. Moreover, the damage model and damage constitutive model of rock to describe its deterioration under freeze–thaw action were built (Huang et al., 2021; Meng et al., 2021; Feng et al., 2022). Hence, the mechanical properties of rock in freeze–thaw circles evolve continuously as the suffered freeze–thaw cycles increase. Liu et al. (2019) developed a frost heaving force solution concerning the combined influence of decreasing elastic modulus and increasing void ratio of rock in a freeze–thaw circle resulting from the freeze–thaw action. In addition to the reducing mechanical parameters, experiments show that isotropic rocks transform into transversely isotropic materials under long-term unidirectional freeze–thaw action (Nakamura et al., 2009, 2012; Murton et al., 2016; Xia et al., 2018). When cold air in winter or hot air in summer flows into cold region tunnels, heat mainly transfers along the radial direction with the main temperature

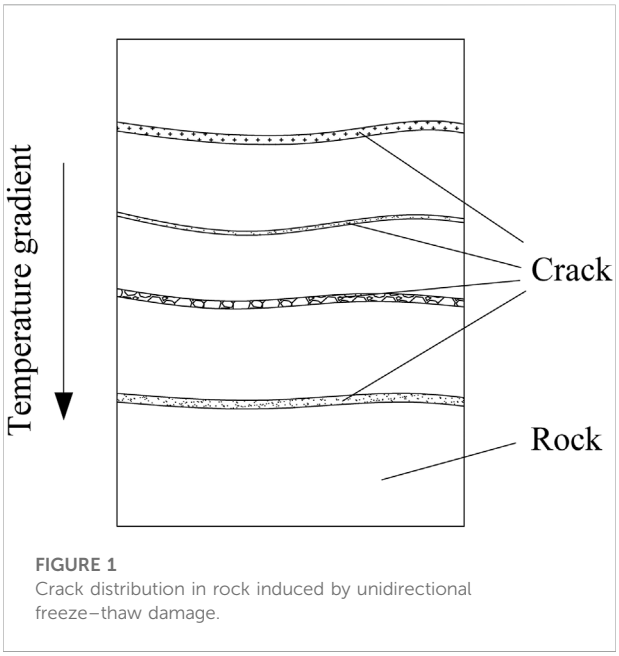


FIGURE 1
Crack distribution in rock induced by unidirectional freeze–thaw damage.

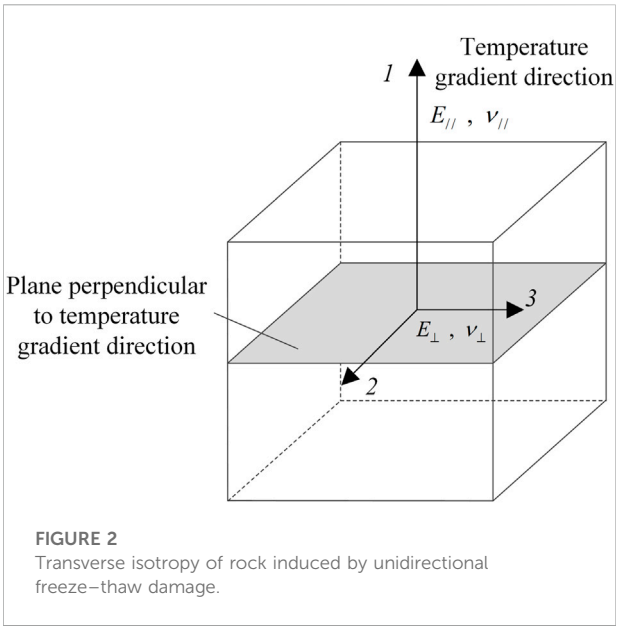


FIGURE 2
Transverse isotropy of rock induced by unidirectional freeze–thaw damage.

gradient in the radial direction, and the surrounding rock in the freeze–thaw circle suffers unidirectional freeze–thaw action. Consequently, the isotropic rock in the freeze–thaw circle gradually transforms into transversely isotropic material as the result of long-term unidirectional freeze–thaw action, and the aforementioned solutions are inapplicable for transversely isotropic surrounding rock.

Therefore, in this study, an analytical solution of the mechanical response of cold region tunnels with a transversely isotropic freeze–thaw circle induced by unidirectional freeze–thaw damage is established. The analytical solution is derived under two different states of the freeze–thaw circle: *1*) transversely isotropic and unfrozen state and *2*) transversely isotropic and frozen state. Furthermore, based on the solutions, the stress field in the lining and surrounding rock with a transversely isotropic freeze–thaw circle is analyzed, and the influence of the deterioration coefficient and the degree of anisotropy on the mechanical response of cold region tunnels is analyzed.

Mechanical model of cold region tunnels under a transversely isotropic freeze–thaw circle

Transversely isotropic freeze–thaw circle induced by unidirectional freeze–thaw damage

Lots of experiments show that layered cracks perpendicular to the temperature gradient direction will generate in a rock under long-term unidirectional freeze–thaw action (Nakamura et al., 2009, 2012; Murton et al., 2016; Xia et al., 2018), as shown in Figure 1. When the rock with layered cracks is considered a continuous medium, it is similar to the stratified rock in macro-mechanical properties and can be regarded as transversely isotropic material. As illustrated in Figure 2, any plane perpendicular to the temperature gradient direction is the plane of isotropy, and any line parallel to the temperature gradient direction is the axis of transverse isotropy. Therefore, isotropic rocks will gradually transform into transversely isotropic materials under unidirectional freeze–thaw conditions.

As illustrated in Figure 3, when the cold air in winter or the hot air in summer flows into cold region tunnels, heat mainly transfers along the radial direction with a prime temperature gradient in the radial direction, and the temperature gradient along the circumferential or axial direction is negligible (Lai et al., 2002; Zhang et al., 2002). Hence, the surrounding rock in freeze–thaw circles suffers unidirectional freeze–thaw action every year. Thus, the mechanical properties of rock in freeze–thaw circles gradually transform into transverse isotropy. As shown in Figure 4, the radial direction, namely, the temperature gradient direction, is the axis of transverse isotropy, and the cylindrical surface composed of the axial direction and circumferential direction, which is perpendicular to the radial direction, is the plane of isotropy.

Mechanical model of cold region tunnels

Figure 5 illustrates the mechanical model of the stress and deformation response of cold region tunnels with transversely isotropic rock in freeze–thaw circles induced by unidirectional

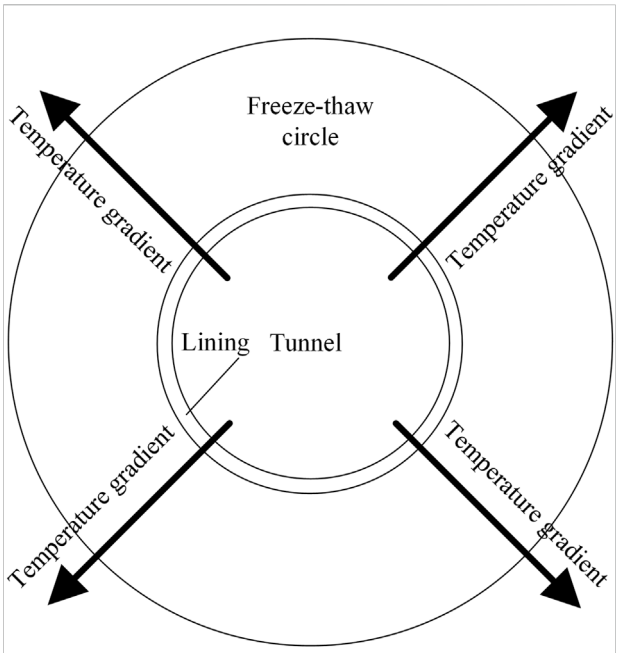


FIGURE 3
Temperature gradient in cold region tunnels.

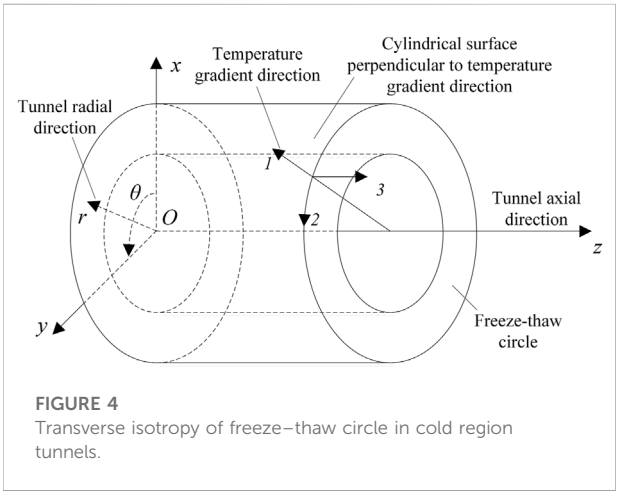


FIGURE 4
Transverse isotropy of freeze–thaw circle in cold region tunnels.

freeze–thaw damage. As displayed in Figure 5, in the initial state, when the construction of the tunnel completes, the surrounding rock is isotropic; after entering the cold season, the surrounding rock in the freeze–thaw circle freezes gradually, and, thus, the freeze–thaw circle is isotropic and frozen, which can be referred to as state F. During the operation of the tunnel, the surrounding rock in the freeze–thaw circle gradually transform into transversely isotropic material due to the unidirectional freeze–thaw damage. The stress and displacement in cold region tunnels will significantly change with the transformation of the freeze–thaw circle from isotropic material to transversely isotropic material. In the warm season, the freeze–thaw circle is transversely isotropic and unfrozen, which can be referred to as state TU; in the cold season, the freeze–thaw circle is transversely isotropic and frozen, which can be referred to as state TF, as shown in Figure 5. In Figure 5, zone I is the lining, and zone V is isotropic and unfrozen surrounding rock. Zone II is the isotropic and frozen surrounding rock in state F; zone III is the transversely isotropic and unfrozen surrounding rock in state TU; and zone IV is the transversely isotropic and frozen surrounding rock in state TF.

Moreover, in Figure 5, r_0 and r_1 represent the internal and external radius of lining, respectively; r_f represents the external radius of the freeze–thaw circle; R_0 extends somewhere far away. P_l is the radial stress act on the lining, and P_f represents the radial stress act on the interface between freeze–thaw circle and zone V. P_0 represent the initial ground stress.

The compressive stress, strain, and displacement are regarded as positive. To obtain the analytical solution of mechanical response under a transversely isotropic freeze–thaw circle, assumptions are introduced as follows:

(1) The cross-section of cold region tunnels is approximated as a circle.
(2) The plane strain condition is introduced.
(3) The surrounding rock and lining are considered as continuous, homogeneous, and elastic materials in each zone.
(4) The lining and the surrounding rock in zones II and V are isotropic material, whereas the surrounding rock in zones III and IV are transversely isotropic material induced by the unidirectional freeze–thaw damage.

Solution of mechanical response in cold region tunnels with a transversely isotropic freeze–thaw circle

Solution of mechanical response in cold region tunnels under state TU

Stress and displacement in a transversely isotropic and unfrozen freeze–thaw circle (zone III)

The constitutive relations of a transversely isotropic freeze–thaw circle in zone III can be written as (Lekhnitskii, 1981) follows:

$$\begin{cases} \varepsilon_r = a_{11}\sigma_r + a_{12}\sigma_\theta + a_{13}\sigma_z \\ \varepsilon_\theta = a_{12}\sigma_r + a_{22}\sigma_\theta + a_{23}\sigma_z \\ \varepsilon_z = a_{13}\sigma_r + a_{23}\sigma_\theta + a_{33}\sigma_z, \end{cases} \tag{1}$$

where ε and σ are the strain and stress, respectively; the subscript r, θ, and z refer to the radial, circumferential, and axial direction; $a_{11} = \frac{1}{E_r}$, $a_{12} = a_{13} = -\frac{\mu_{\theta r}}{E_r}$, $a_{22} = a_{33} = \frac{1}{E_\theta}$, and $a_{23} = -\frac{\mu_{\theta z}}{E_\theta}$; E_r is Young's modulus along the radial direction; E_θ is Young's

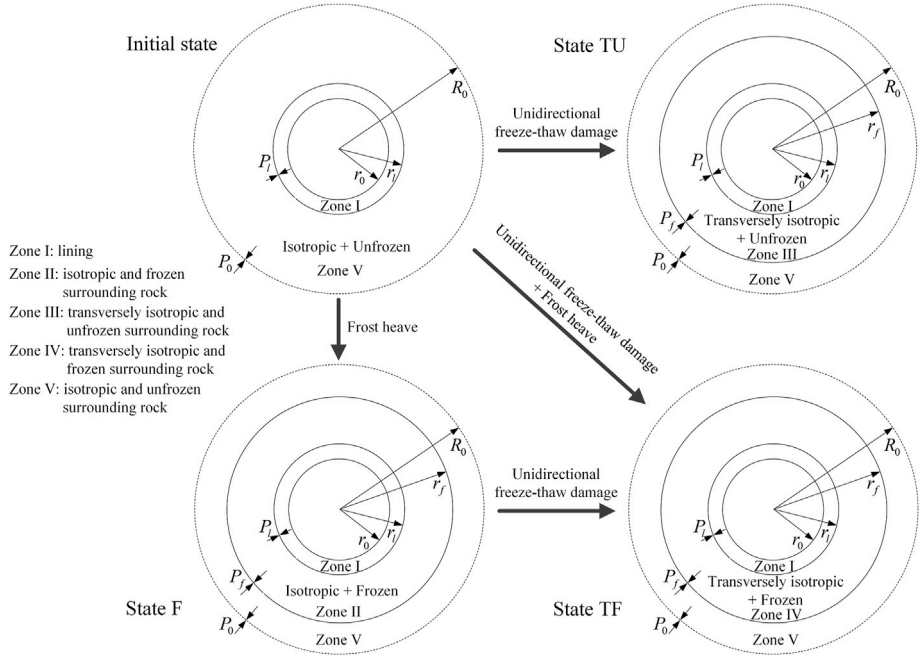


FIGURE 5
Mechanical model of cold region tunnels.

modulus in the isotropic cylindrical surface; $\mu_{\theta r}$ is the Poisson's ratio defining strain induced in the isotropic surface by stress applied in the radial direction; and $\mu_{\theta z}$ is the Poisson's ratio defining strain induced in the isotropic surface by stress applied in the surface.

Under the plane strain condition, $\varepsilon_z = 0$. Hence, σ_z can be acquired from Eq. 1:

$$\sigma_z = -\frac{1}{a_{33}}(a_{13}\sigma_r + a_{23}\sigma_\theta). \tag{2}$$

Substituting Eq. 2 into Eq. 1, ε_r and ε_θ can be obtained as follows:

$$\begin{cases} \varepsilon_r = \beta_{11}\sigma_r + \beta_{12}\sigma_\theta \\ \varepsilon_\theta = \beta_{12}\sigma_r + \beta_{22}\sigma_\theta, \end{cases} \tag{3}$$

where $\beta_{ij} = a_{ij} - \frac{a_{i3}}{a_{33}}a_{j3}$, (i, j= 1, 2).

According to the elasticity, the geometric equations and the compatibility condition of the axisymmetric problem are as follows:

$$\varepsilon_r = \frac{\mathrm{d}u_r}{\mathrm{d}r},\ \varepsilon_\theta = \frac{u_r}{r}, \tag{4a}$$

$$\varepsilon_r = \frac{d}{dr}(r\varepsilon_\theta), \tag{4b}$$

where u_r represents the displacement in the radial direction.

Moreover, the equilibrium equation of the axisymmetric problem is

$$r\frac{d\sigma_r}{dr} + \sigma_r - \sigma_\theta = 0. \tag{5}$$

Combining Eqs 3, 4b, and 5, the following equation can be acquired:

$$r^2\frac{d^2\sigma_r}{dr^2} + 3r\frac{d\sigma_r}{dr} - \left(\frac{\beta_{11}}{\beta_{22}} - 1\right)\sigma_r = 0. \tag{6}$$

The general solution of Eq. 6 is

$$\sigma_r = A_1 r^{n-1} + B_1 r^{-(n+1)}, \tag{7}$$

where A_1 and B_1 are undetermined integral constants, and $n = \sqrt{\frac{\beta_{11}}{\beta_{22}}}$.

The stress boundary conditions of zone III are:

$$\begin{cases} \sigma_r^{\mathrm{III}} = P_l\,(r = r_l) \\ \sigma_r^{\mathrm{III}} = P_f\left(r = r_f\right), \end{cases} \tag{8}$$

where the superscript III represents zone III. In addition, the following superscripts I, II, IV, and V represent zones I, II, IV, and V, respectively.

Considering Eqs 7 and 8, A_1 and B_1 can be obtained:

$$\begin{cases} A_1 = \dfrac{P_l r_l^{n+1} - P_f r_f^{n+1}}{r_l^{2n} - r_f^{2n}} \\ B_1 = \dfrac{P_f r_f^{n+1} r_l^{2n} - P_l r_l^{n+1} r_f^{2n}}{r_l^{2n} - r_f^{2n}}. \end{cases} \tag{9}$$

Combining Eqs 9, 7, and 5, σ_r and σ_θ in zone III can be acquired:

$$\begin{cases} \sigma_r^{\mathrm{III}} = \dfrac{P_l r_l^{n+1} - P_f r_f^{n+1}}{r_l^{2n} - r_f^{2n}} r^{n-1} + \dfrac{P_f r_f^{n+1} r_l^{2n} - P_l r_l^{n+1} r_f^{2n}}{r_l^{2n} - r_f^{2n}} r^{-(n+1)} \\ \sigma_\theta^{\mathrm{III}} = n\dfrac{P_l r_l^{n+1} - P_f r_f^{n+1}}{r_l^{2n} - r_f^{2n}} r^{n-1} - n\dfrac{P_f r_f^{n+1} r_l^{2n} - P_l r_l^{n+1} r_f^{2n}}{r_l^{2n} - r_f^{2n}} r^{-(n+1)}. \end{cases} \tag{10}$$

Plugging Eqs 1–3, ε_θ of zone III is acquired:

$$\begin{aligned} \varepsilon_\theta^{\mathrm{III}} = {} & (\beta_{12} + n\beta_{22}) \frac{P_l r_l^{n+1} - P_f r_f^{n+1}}{r_l^{2n} - r_f^{2n}} r^{n-1} \\ & + (\beta_{12} - n\beta_{22}) \frac{P_f r_f^{n+1} r_l^{2n} - P_l r_l^{n+1} r_f^{2n}}{r_l^{2n} - r_f^{2n}} r^{-(n+1)}. \end{aligned} \tag{11}$$

Plugging Eq. 11 to Eq. 4a, u_r of zone III is acquired:

$$\begin{aligned} u_r^{\mathrm{III}} = {} & (\beta_{12} + n\beta_{22}) \frac{P_l r_l^{n+1} - P_f r_f^{n+1}}{r_l^{2n} - r_f^{2n}} r^{n} \\ & + (\beta_{12} - n\beta_{22}) \frac{P_f r_f^{n+1} r_l^{2n} - P_l r_l^{n+1} r_f^{2n}}{r_l^{2n} - r_f^{2n}} r^{-n}. \end{aligned} \tag{12}$$

Stress and displacement in isotropic and unfrozen zone V and lining

According to the solution upon axisymmetric problem (Yu, 2000), the displacement and stress in isotropic and unfrozen zone V under the action of P_f at $r = r_f$ and P_0 at $r = R_0$ are as follows:

$$u_r^{\mathrm{V}} = \frac{1+\mu_u}{E_u} \frac{r_f^2}{r} \left(P_0 - P_f\right), \tag{13}$$

$$\begin{cases} \sigma_r^V = P_0 \left(1 - \dfrac{r_f^2}{r^2}\right) + P_f \dfrac{r_f^2}{r^2} \\ \sigma_\theta^V = P_0 \left(1 - \dfrac{r_f^2}{r^2}\right) - P_f \dfrac{r_f^2}{r^2}, \end{cases} \tag{14}$$

where E_u and μ_u refer to Young's modulus and Poisson's ratio of the isotropic and unfrozen zone V, respectively.

In addition, according to the solution upon axisymmetric problem (Yu, 2000), the displacement and stress in lining (zone I) under the action of P_l at $r = r_l$ are as follows:

$$u_r^{\mathrm{I}} = \frac{1+\mu_l}{E_l} \frac{(1-2\mu_l) r_l^2 r^2 + r_l^2 r_0^2}{r\left(r_l^2 - r_0^2\right)} P_l, \tag{15}$$

$$\begin{cases} \sigma_r^{\mathrm{I}} = \dfrac{r_l^2 \left(r^2 - r_0^2\right)}{\left(r_l^2 - r_0^2\right) r^2} P_l \\ \sigma_\theta^{\mathrm{I}} = \dfrac{r_l^2 \left(r_0^2 + r^2\right)}{\left(r_l^2 - r_0^2\right) r^2} P_l, \end{cases} \tag{16}$$

where E_l and μ_l refer to Young's modulus and Poisson's ratio of lining, respectively.

Continuity conditions and mechanical response solution

The continuity conditions of displacement at interfaces $r = r_l$ and $r = r_f$ are as follows:

$$u_r^{\mathrm{I}} = u_r^{\mathrm{III}} \left(r = r_l\right), \tag{17a}$$

$$u_r^{\mathrm{III}} = u_r^{\mathrm{V}} \left(r = r_f\right). \tag{17b}$$

The undetermined quantities are P_l and P_f, and they can be obtained by substituting Eqs 12, 13, and 15 to Eq. 17 as follows:

$$P_l = \frac{C_2 \frac{1+\mu_u}{E_u} P_0}{C_2 C_3 + \left[\beta_{12} - C_1 + \frac{1+\mu_u}{E_u}\right]\left[\beta_{12} + C_1 - \frac{1+\mu_l}{E_l} \frac{\left(1-2\mu_l\right) r_l^2 + r_0^2}{\left(r_l^2 - r_0^2\right)}\right]}, \tag{18a}$$

$$P_f = \frac{\frac{1+\mu_u}{E_u} P_0 \left[\beta_{12} + C_1 - \frac{1+\mu_l}{E_l} \frac{\left(1-2\mu_l\right) r_l^2 + r_0^2}{\left(r_l^2 - r_0^2\right)}\right]}{C_2 C_3 + \left[\beta_{12} - C_1 + \frac{1+\mu_u}{E_u}\right]\left[\beta_{12} + C_1 - \frac{1+\mu_l}{E_l} \frac{\left(1-2\mu_l\right) r_l^2 + r_0^2}{\left(r_l^2 - r_0^2\right)}\right]}, \tag{18b}$$

where $C_1 = \frac{n\beta_{22}\left(r_l^{2n} + r_f^{2n}\right)}{r_l^{2n} - r_f^{2n}}$, $C_2 = \frac{2n\beta_{22} r_f^{n+1} r_l^{n-1}}{r_l^{2n} - r_f^{2n}}$, and $C_3 = \frac{2n\beta_{22} r_l^{n+1} r_f^{n-1}}{r_l^{2n} - r_f^{2n}}$.

Finally, substituting the value of P_l and P_f into Eqs 15 and 16, the stress and displacement response in the lining under state TU can be acquired. Similarly, substituting P_l and P_f into Eqs 13 and 14, the stress and displacement response in the freeze–thaw circle under state TU can also be acquired.

Solution of the mechanical response in cold region tunnels under state TF

Stress and displacement in a transversely isotropic and frozen freeze–thaw circle (zone IV)

In the frozen zone IV, the total strain of surrounding rock consists of the strain resulting from local stress and the frost heaving strain. Therefore, the constitutive relations of the transversely isotropic and frozen rock in the freeze–thaw circle in zone IV are as follows:

$$\begin{cases} \varepsilon_r = a_{11}\sigma_r + a_{12}\sigma_\theta + a_{13}\sigma_z - \varepsilon_r^f \\ \varepsilon_\theta = a_{12}\sigma_r + a_{22}\sigma_\theta + a_{23}\sigma_z - \varepsilon_\theta^f \\ \varepsilon_z = a_{13}\sigma_r + a_{23}\sigma_\theta + a_{33}\sigma_z - \varepsilon_z^f, \end{cases} \tag{19}$$

where ε_r^f, ε_θ^f, and ε_z^f represent the frost heaving strains along the radial, circumferential, and axial directions, respectively; the meanings of the other symbols are the same as those in section 3.1, whereas the related parameters should take the values under the frozen state. Moreover, ε_r^f, ε_θ^f, and ε_z^f can be expressed by volumetric frost heaving strain $\varepsilon_{\mathrm{v}}^f$ (Xia et al., 2018; Lv et al., 2019):

$$\begin{cases} \varepsilon_r^f = \dfrac{k}{k+2} \varepsilon_{\mathrm{v}}^f \\ \varepsilon_\theta^f = \varepsilon_z^f = \dfrac{1}{k+2} \varepsilon_{\mathrm{v}}^f, \end{cases} \tag{20}$$

where ϵ_r^f, and k is the anisotropic frost heave coefficient defined as the ratio of ϵ_r^f to ϵ_θ^f.

Under the plane strain condition, $\varepsilon_z = 0$. Hence, σ_z can be acquired from Eq. 19:

$$\sigma_z = -\frac{1}{a_{33}}\left(a_{13}\sigma_r + a_{23}\sigma_\theta - \varepsilon_\theta^f\right). \tag{21}$$

Substituting Eq. 21 into Eq. 19, ε_r and ε_θ can be obtained:

$$\begin{cases} \varepsilon_r = \beta_{11}\sigma_r + \beta_{12}\sigma_\theta + \beta_1\varepsilon_\theta^f \\ \varepsilon_\theta = \beta_{12}\sigma_r + \beta_{22}\sigma_\theta + \beta_2\varepsilon_\theta^f, \end{cases} \tag{22}$$

where $\beta_{ij} = a_{ij} - \frac{a_{i3}}{a_{33}}a_{j3}$, (i, j= 1, 2); $\beta_1 = \frac{a_{13}}{a_{33}} - k$, and $\beta_2 = \frac{a_{23}}{a_{33}} - 1$.

Combining Eqs 22, 4b, and 5, the following equation can be acquired:

$$r^2\frac{d^2\sigma_r}{dr^2} + 3r\frac{d\sigma_r}{dr} - \left(\frac{\beta_{11}}{\beta_{22}} - 1\right)\sigma_r = \frac{\beta_1 - \beta_2}{\beta_{22}}\varepsilon_\theta^f. \tag{23}$$

The general solution of Eq. 23 can be obtained as follows:

$$\sigma_r = A_2 r^{n-1} + B_2 r^{-(n+1)} - \frac{\beta_1 - \beta_2}{\beta_{11} - \beta_{22}}\varepsilon_\theta^f, \tag{24}$$

where A_2 and B_2 are undetermined integral constants, and $n = \sqrt{\frac{\beta_{11}}{\beta_{22}}}$.

The stress boundary conditions of zone IV are

$$\begin{cases} \sigma_r^{\mathrm{IV}} = P_l\,(r = r_l) \\ \sigma_r^{\mathrm{IV}} = P_f\left(r = r_f\right). \end{cases} \tag{25}$$

Plugging Eq. 24 into Eq. 25, A_2 and B_2 are acquired:

$$\begin{cases} A_2 = \dfrac{P_l r_l^{n+1} - P_f r_f^{n+1} + \dfrac{\beta_1 - \beta_2}{\beta_{11} - \beta_{22}}\varepsilon_\theta^f\left(r_l^{n+1} - r_f^{n+1}\right)}{r_l^{2n} - r_f^{2n}} \\ B_2 = \dfrac{P_f r_f^{n+1} r_l^{2n} - P_l r_l^{n+1} r_f^{2n} + \dfrac{\beta_1 - \beta_2}{\beta_{11} - \beta_{22}}\varepsilon_\theta^f\left(r_l^{2n} r_f^{n+1} - r_l^{n+1} r_f^{2n}\right)}{r_l^{2n} - r_f^{2n}} \end{cases}. \tag{26}$$

Combining Eqs 26, 24, and 5, σ_θ in zone IV can be obtained:

$$\sigma_\theta^{\mathrm{IV}} = nA_2 r^{n-1} - nB_2 r^{-(n+1)} - \frac{\beta_1 - \beta_2}{\beta_{11} - \beta_{22}}\varepsilon_\theta^f. \tag{27}$$

Substituting Eqs 27 and 24 into Eq. 22, ε_θ in zone IV can be obtained. Then, substituting ε_θ into Eq. 4a, u_r in zone IV can be obtained:

$$\begin{aligned} u_r^{\mathrm{IV}} = {} & (\beta_{12} + n\beta_{22})A_2 r^n + (\beta_{12} - n\beta_{22})B_2 r^{-n} \\ & - \frac{\beta_1 - \beta_2}{\beta_{11} - \beta_{22}}\varepsilon_\theta^f(\beta_{12} + \beta_{22})r + \beta_2\varepsilon_\theta^f r. \end{aligned} \tag{28}$$

Continuity conditions and mechanical response solution

The continuity conditions of displacement at interfaces $r = r_1$, $r = r_f$ are as follows:

$$u_r^{\mathrm{I}} = u_r^{\mathrm{IV}}\,(r = r_l), \tag{29a}$$

$$u_r^{\mathrm{IV}} = u_r^{\mathrm{V}}\left(r = r_f\right), \tag{29b}$$

The stress and displacement in isotropic and unfrozen zone V and lining (zone I) under state TF are the same as those given in Eqs 13–16, except that P_l and P_f should take the values under state TF. The undetermined quantities are P_l and P_f, and they can be obtained through plugging Eqs 13, 15, and 28 into Eq. 29:

$$P_l = \frac{\frac{1+\mu_u}{E_u}C_2 P_0 - \frac{\beta_1-\beta_2}{\beta_{11}-\beta_{22}}\varepsilon_\theta^f\left[(C_1 - C_2 - \beta_{22})\left(\beta_{12} - C_1 + \frac{1+\mu_u}{E_u}\right) + C_2(C_3 - C_1 - \beta_{22})\right] - \beta_2\varepsilon_\theta^f\left[C_2 + \left(\beta_{12} - C_1 + \frac{1+\mu_u}{E_u}\right)\right]}{\left[C_2 C_3 + \left(\beta_{12} + C_1 - \frac{1+\mu_l}{E_l}\frac{(1-2\mu_l)r_l^2 + r_0^2}{(r_l^2 - r_0^2)}\right)\left(\beta_{12} - C_1 + \frac{1+\mu_u}{E_u}\right)\right]}, \tag{30a}$$

$$\begin{aligned} P_f = {} & \frac{\left(\beta_{12} + C_1 - \frac{1+\mu_l}{E_l}\frac{(1-2\mu_l)r_l^2 + r_0^2}{(r_l^2 - r_0^2)}\right)}{C_2}P_l \\ & + \frac{\frac{\beta_1-\beta_2}{\beta_{11}-\beta_{22}}\varepsilon_\theta^f(C_1 - C_2 - \beta_{22}) + \beta_2\varepsilon_\theta^f}{C_2}, \end{aligned} \tag{30b}$$

where C_1, C_2, and C_3 are the same as those in section 3.1 except that the related parameters should take the values under the frozen state.

Finally, substituting the value of P_l and P_f into the corresponding formulas, the stress and displacement in the lining and freeze–thaw circle under state TF can be acquired.

Solution of stress and displacement in cold region tunnels under initial state and state F

To analyze the effect of transversely isotropic rock in freeze–thaw circles on the mechanical response of cold region tunnels, comparisons among the initial state, state F, state TU, and state TF are necessary. Hence, the solutions of stress and displacement in cold region tunnels under initial state and state F are also provided here.

The stress and displacement in the lining (zone I) under the initial state are the same as those given in Eqs 15 and 16, except that P_l should take the value under the initial state. In addition, according to the solution to the axisymmetric problem (Yu, 2000), the radial displacement and stress in isotropic and unfrozen zone V under the action of P_l at $r = r_l$ and P_0 at $r = R_0$ are acquired:

$$u_r^{\mathrm{V}} = \frac{1 + \mu_u}{E_u}\frac{r_l^2}{r}(P_0 - P_l), \tag{31}$$

TABLE 1 Parameters of the section K105+785 in the cold region tunnel.

Parameter	r_0(m)	r_l(m)	r_f(m)	E_l(MPa)	μ_l	P_0(MPa)
Value	4.55	5.45	6.85	28,300	0.18	3.0
Parameter	E_u(MPa)	μ_u	E_f(MPa)	μ_f	ϵ_V^f	k
Value	25,000	0.37	27,500	0.37	0.45%	1.5

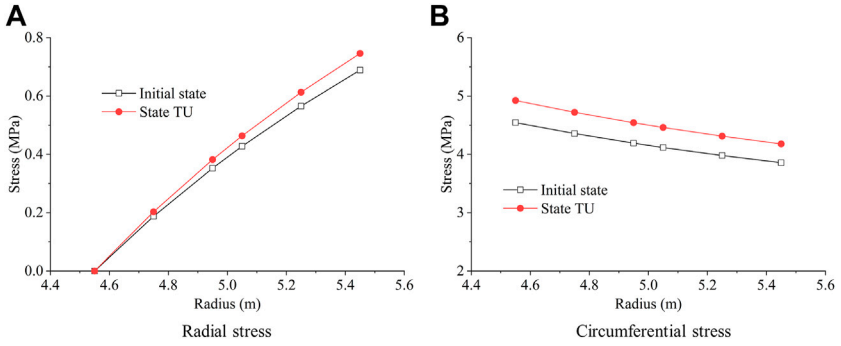


FIGURE 6
Stress of lining under initial state and state TU.

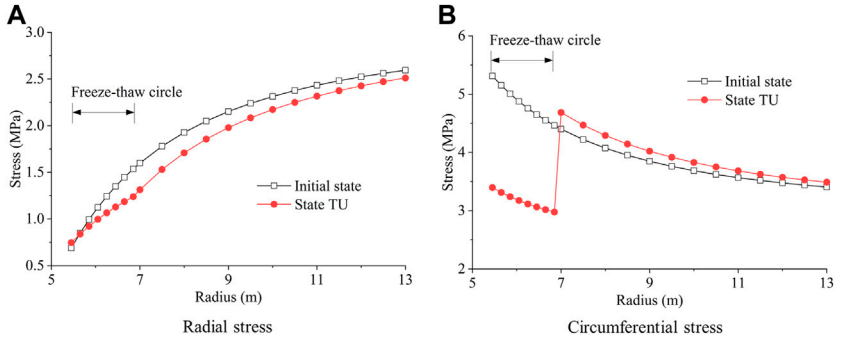


FIGURE 7
Stress of surrounding rock under initial state and state TU.

$$\begin{cases} \sigma_r^{\mathrm{V}} = P_0\left(1 - \dfrac{r_1^2}{r^2}\right) + P_l\dfrac{r_l^2}{r^2} \\ \sigma_\theta^{\mathrm{V}} = P_0\left(1 + \dfrac{r_l^2}{r^2}\right) - P_l\dfrac{r_l^2}{r^2} \end{cases}. \tag{32}$$

The displacement continuity conditions at interface $r = r_l$ is

$$u_r^{\mathrm{I}} = u_r^{\mathrm{V}}\,(r = r_l). \tag{33}$$

The undetermined quantity is P_l, and it is obtained through plugging Eqs 15 and 31 into Eq. 33 as follows:

$$P_l = \frac{\frac{1+\mu_u}{E_u}P_0}{\frac{1+\mu_l}{E_l}\frac{(1-2\mu_l)r_l^2+r_0^2}{r_l^2-r_0^2} + \frac{1+\mu_u}{E_u}}, \tag{34}$$

Finally, substituting the value of P_l into the corresponding formulas, the stress and displacement of lining and surrounding rock under the initial state can be acquired.

Furthermore, the stress and displacement of isotropic and unfrozen zone V and lining (zone I) under state F are the same as those given in Eqs 13–16, except that P_l and P_f should take the values under state F. The solutions of P_l and P_f under state F

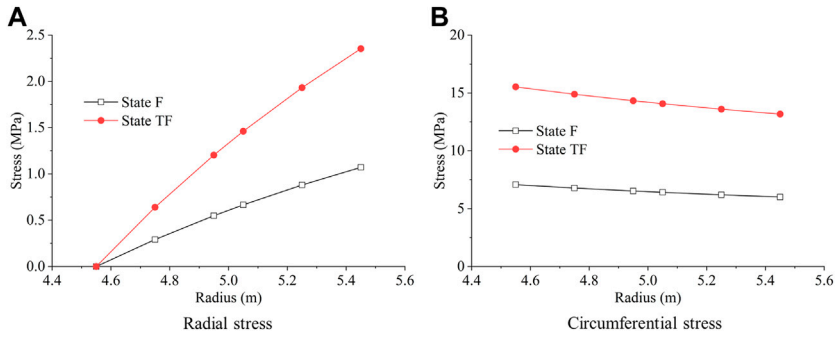


FIGURE 8
Stress of lining under state F and state TF.

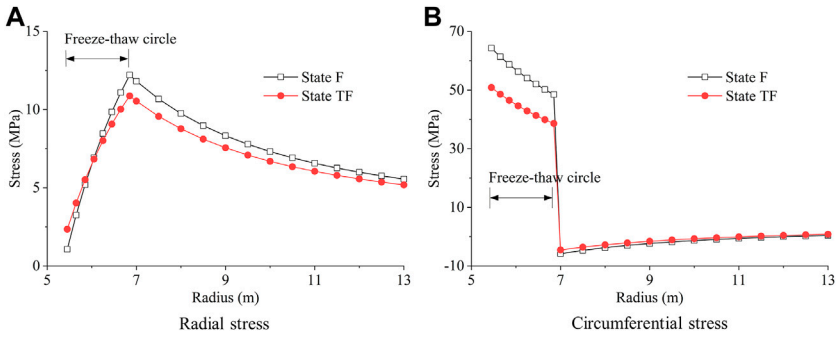


FIGURE 9
Stress of surrounding rock under state F and state TF.

have been proposed by Lv et al. (2019), namely, Eq. 38 or Eq. 39 in the study by Lv et al. (2019). In addition, the solutions of stress and displacement in the isotropic and frozen zone II under state F have also been proposed by Lv et al. (2019), namely, Eqs 34 and 35 in the study by Lv et al. (2019).

Case study

Stress distribution in the lining and surrounding rock

The proposed analytical solutions of stress and displacement under states TU and TF are extensions of the stress analysis on cold region tunnels involving transversely isotropic rock in freeze–thaw circle induced by unidirectional freeze–thaw damage. The engineering case in the study by Lv et al. (2019) can be referred to analyze the effect of a transversely isotropic freeze–thaw circles on the mechanical response of cold region tunnels. The related parameters are presented in Table 1, and E_f and μ_f in Table 1 are Young's modulus and Poisson's ratio of the isotropic and frozen surrounding rock (zone II).

During the operation stage of the cold region tunnel, the surrounding rock in the freeze–thaw circle gradually transforms to the transversely isotropic material resulting from unidirectional freeze–thaw damage, and E_r and E_θ also gradually decreases as the deterioration. To describe the deterioration effect of freeze–thaw damage on surrounding rock, the deterioration coefficient k_d is defined as E_θ/E_u under state TU or E_θ/E_f under state TF. Moreover, the degree of anisotropy k_a is defined as E_r/E_θ to describe the evolution of the transverse isotropy. Both k_d and k_a decrease from 1.0 with the increasing freeze–thaw cycles. In addition, the variation of Poisson's ratio is not considered.

Under the initial state, the radial stress act on the lining P_l calculated by the solution under the initial state is 0.69 MPa. Furthermore, under state TU, if $E_r = E_\theta = E_u$ and $\mu_{\theta r} = \mu_{\theta z} = \mu_u$ are assumed, namely, $k_d = 1.0$ and $k_a = 1.0$, state TU transforms to the initial state. In this special case, P_l calculated by the

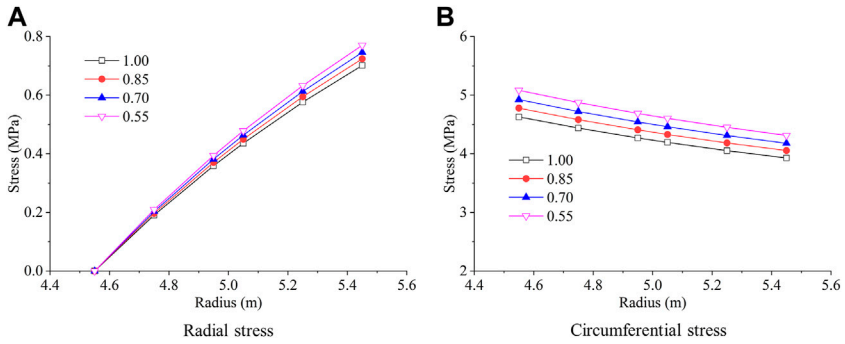


FIGURE 10
Influence of deterioration coefficient k_d under state TU.

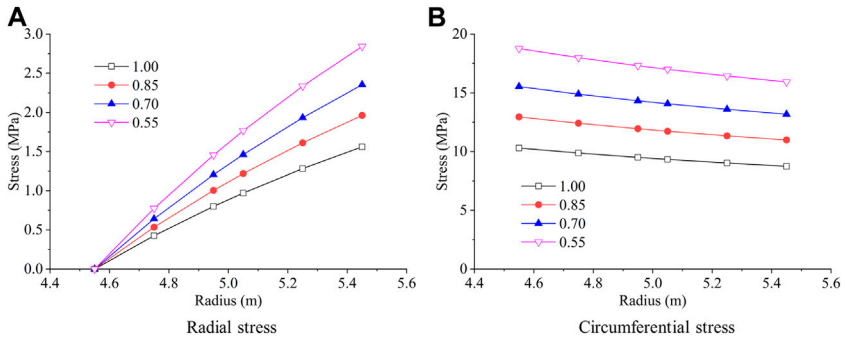


FIGURE 11
Influence of deterioration coefficient k_d under state TF.

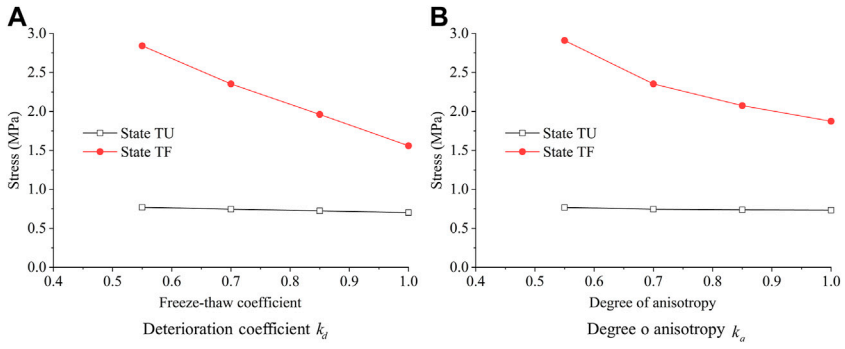


FIGURE 12
Influence of deterioration coefficient k_d and degree of anisotropy k_a on P_l.

solution under state TU is 0.69 MPa. The special case that $E_r = E_\theta = E_u$ and $\mu_{\theta r} = \mu_{\theta z} = \mu_u$ under state TU is identical to the initial state, and the results of P_l calculated by the two abovementioned different solutions are the same, thus, the correctness of the derivation processes of the solution under state TU can be verified.

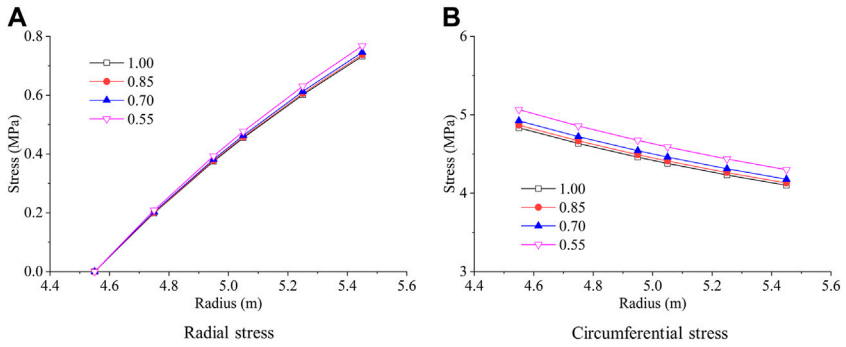


FIGURE 13
Influence of degree of anisotropy k_a under state TU.

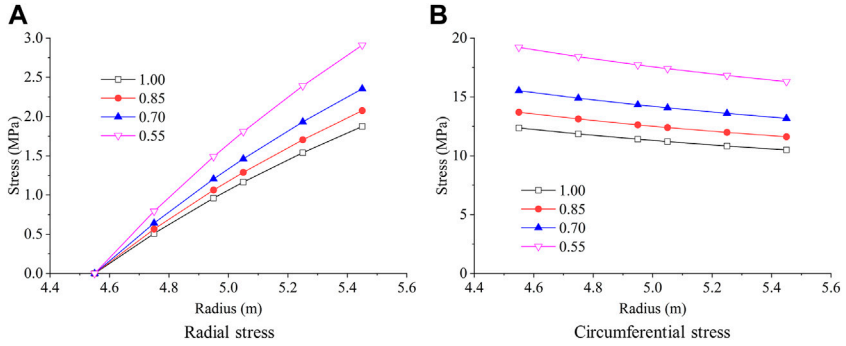


FIGURE 14
Influence of degree of anisotropy k_a under state TF.

Under state F, P_l calculated by the solution under state F is 1.07 MPa. Moreover, under state TF, if $E_r = E_\theta = E_f$ and $\mu_{\theta r} = \mu_{\theta z} = \mu_f$ are assumed, namely, $k_d = 1.0$ and $k_a = 1.0$, state TF transforms to state F. In this special case, P_l calculated by the solution under state TF is 1.08 MPa. The special case that $E_r = E_\theta = E_f$ and $\mu_{\theta r} = \mu_{\theta z} = \mu_f$ under state TF is identical to state F, and the results of P_l calculated by the solutions under state F and state TF are the same, which verifies the correctness of the derivation processes of the solution under state TF.

To study the mechanical response of cold region tunnels under a transversely isotropic freeze–thaw circle, the stress distribution in lining and surrounding rock in the case that $k_d = 0.7$ and $k_a = 0.7$ under states TU and TF are shown in Figures 6–9. Under state TF, $E_\theta = k_d E_f$, $E_r = k_a E_\theta$, and $\mu_{\theta r} = \mu_{\theta z} = \mu_f$. The other parameters are included in Table 1. To demonstrate the influence of the transverse isotropy of the freeze–thaw circle, the stress distribution under the initial state and state F are also exhibited in Figures 6–9.

The surrounding rock is unfrozen under the initial state and state TU. The stress distribution in the lining is similar under these two states, whereas the radial and circumferential stress in the lining increase by about 8% when the surrounding rock in the freeze–thaw circle transforms from isotropic material into transversely isotropic material, as displayed in Figure 6. In addition, the radial stress in surrounding rock under state TU is gently less than that under the initial state, and the greatest difference occurs at the outer interface of the freeze–thaw circle, as displayed in Figure 7. Phenomenon of discontinuity generates in the circumferential stress of surrounding rock under state TU, and the circumferential stress in the freeze–thaw circle under state TU is significantly less than that under the initial state.

The surrounding rock in the freeze–thaw circle is frozen under states F and TF. The stress in the lining under state TF significantly increases to be greater than two times of that under state F when the surrounding rock in the freeze–thaw circle transforms from isotropic material into transversely isotropic

material, as illustrated in Figure 8. For example, the radial stress at the outer interface of the lining is 1.07 MPa under state F, while it increases to 2.35 MPa under state TF. Moreover, the difference of radial stress in surrounding rock under states F and TF is slight, and the circumferential stress in the freeze–thaw circle under state TF is less than that under state F, as illustrated in Figure 9.

Therefore, the transformation of surrounding rock in the freeze–thaw circle from isotropic material into transversely isotropic material adversely affects the stress distribution in the lining, especially for state TF, under which the stress in the lining increases significantly. Hence, the influence of the transversely isotropic freeze–thaw circle should be considered to maintain the long-term stability of cold region tunnels.

Analysis of influencing factors

The abovementioned engineering case can be considered to research the effect of the deterioration coefficient k_d and the degree of anisotropy k_a on the mechanical response of cold region tunnels. In the base condition, values of k_d = 0.7 and k_a = 0.7 are taken, and values of other parameters are listed in Table 1. Change the value of k_d or k_a in the base condition to study their influences.

Figures 10 and 11 show the influence of the deterioration coefficient k_d on the stress in the lining under states TU and TF, respectively. The stress in the lining increases uniformly for both states TU and TF as the decrease of k_d, whereas the increase of stress under state TF is much greater. For example, as k_d decreases from 1.0 to 0.55, the radial stress at outer interface of the lining increases by 10% under state TU, while it increases by 80% under state TF.

Moreover, Figure 12 shows the variation of the pressure act on the lining P_l with k_d and k_a. As k_d decreases from 1.0 to 0.55, P_l linearly increases from 1.56 to 2.84 MPa under state TF and it increases from 0.70 to 0.77 MPa under state TU. k_d has greater influence on P_l under state TF. k_d decreases from 1.0 as unidirectional freeze–thaw cycles suffered by surrounding rock increases, and, thus, induces the increase of the radial and circumferential stresses in the lining. Furthermore, k_a has much greater influence on P_l under state TF than that under state TU. As k_a decreases from 1.0 to 0.55, the radial stress at outer interface of the lining increases by 5% under state TU, while it increases by 55% under state TF. k_a decreases from 1.0 as unidirectional freeze–thaw cycles suffered by surrounding rock increases, and thus induces the increase of the radial and circumferential stresses in the lining.

Figures 13 and 14 show the influence of the degree of anisotropy k_a on the stress in the lining under states TU and TF, respectively. The stress in the lining increases nonlinearly for both states TU and TF as the decrease of k_a. The smaller the k_a is, the greater the increase rate of the stress is. For example, under state TF, the circumferential stress at inner surface of the lining increases from 10.50 to 11.62 MPa, as k_a decreases from 1.0 to 0.85, whereas it increases from 13.18 to 16.30 MPa, as k_a decreases from 0.70 to 0.55. Moreover, the increase of stress with k_a under state TF is much greater that under state TU. Comparing Figures 10–12 with Figures 13 and 14, k_d has greater influence than k_a on the stress in the lining.

Conclusion

In cold region tunnels, surrounding rock in a freeze–thaw circle suffers unidirectional freeze–thaw cycles during the operation process, and, thus, isotropic surrounding rocks gradually transform into transversely isotropic materials. Based on this phenomenon, an analytical solution to the mechanical response of cold region tunnels with a transversely isotropic freeze–thaw circle induced by unidirectional freeze–thaw damage is proposed. The analytical solution is derived under two different states of the freeze–thaw circle: *1*) transversely isotropic and unfrozen state and *2*) transversely isotropic and frozen state.

Additionally, the stress distribution in the lining and surrounding rock with a transversely isotropic freeze–thaw circle is analyzed. The transformation of the surrounding rock in a freeze–thaw circle from isotropic material into transversely isotropic material adversely affects the stress distribution in the lining, especially in the transversely isotropic and frozen state, under which the stress in the lining increases significantly.

Finally, the influence of the deterioration coefficient k_d and the degree of anisotropy k_a on the mechanical response in cold region tunnels is analyzed. The stress in the lining increases linearly with the decrease of k_d, whereas the increase of stress under the transversely isotropic and frozen state is much greater. The stress in the lining increases nonlinearly with the decrease of k_a. The smaller the k_a is, the greater the increase rate of the stress is. Moreover, the increase of stress with k_a under the transversely isotropic and frozen state is much greater than that under the transversely isotropic and unfrozen state. Both k_d and k_a decrease from 1.0 as unidirectional freeze–thaw cycles suffered by surrounding rock increase, and, thus, induce the increase of stresses in the lining. In addition, k_d has a greater influence than k_a on the stress in the lining.

Data availability statement

The raw data supporting the conclusions of this article will be made available by the authors, without undue reservation.

Author contributions

ZL: funding acquisition, writing—original draft, and methodology. MW: data curation and validation. FH: conceptualization, writing—review and editing. YC: formal analysis and investigation.

Funding

This research was supported by the National Natural Science Foundation of China (No. 52108370) and Jiangxi Provincial Natural Science Foundation (No. 20212BAB214062).

Conflict of interest

The authors declare that the research was conducted in the absence of any commercial or financial relationships that could be construed as a potential conflict of interest.

Publisher's note

All claims expressed in this article are solely those of the authors and do not necessarily represent those of their affiliated organizations, or those of the publisher, the editors, and the reviewers. Any product that may be evaluated in this article, or claim that may be made by its manufacturer, is not guaranteed or endorsed by the publisher.

References

Chang, Z., Catani, F., Huang, F., Liu, G., Meena, S., Huang, J., et al. (2022). Landslide susceptibility prediction using slope unit-based machine learning models considering the heterogeneity of conditioning factors. *J. Rock Mech. Geotechnical Eng.* doi:10.1016/j.jrmge.2022.07.009

Ding, S., Jia, H., Zi, F., Dong, Y., and Yao, Y. (2020). Frost damage in tight sandstone: Experimental evaluation and interpretation of damage mechanisms. *Materials* 13, 4617. doi:10.3390/ma13204617

Feng, Q., Fu, S., Wang, C., Liu, W., Wang, Y., and Qiao, W. (2019). Analytical elasto-plastic solution for frost force of cold-region tunnels considering anisotropic frost heave in the surrounding rock. *KSCE J. Civ. Eng.* 23, 3831–3842. doi:10.1007/s12205-019-1446-7

Feng, Q., Jiang, B.-S., Zhang, Q., and Wang, G. (2016). Reliability research on the 5-cm-thick insulation layer used in the Yuximolegai tunnel based on a physical model test. *Cold Regions Sci. Technol.* 124, 54–66. doi:10.1016/j.coldregions.2016.01.001

Feng, Q., Jiang, B.-S., Zhang, Q., and Wang, L. (2014). Analytical elasto-plastic solution for stress and deformation of surrounding rock in cold region tunnels. *Cold Regions Sci. Technol.* 108, 59–68. doi:10.1016/j.coldregions.2014.08.001

Feng, Q., Jin, J., Zhang, S., Liu, W., Yang, X., and Li, W. (2022). Study on a damage model and uniaxial compression simulation method of frozen-thawed rock. *Rock Mech. Rock Eng.* 55, 187–211. doi:10.1007/s00603-021-02645-2

Feng, Q., Liu, W., and Jiang, B.-S. (2017). Analytical solution for the stress and deformation of rock surrounding a cold-regional tunnel under unequal compression. *Cold Regions Sci. Technol.* 139, 1–10. doi:10.1016/j.coldregions.2017.04.003

Gao, G. Y., Chen, Q. S., Zhang, Q. S., and Chen, G. Q. (2012). Analytical elasto-plastic solution for stress and plastic zone of surrounding rock in cold region tunnels. *Cold Regions Sci. Technol.* 72, 50–57. doi:10.1016/j.coldregions.2011.11.007

Huang, F., Cao, Z., Jiang, S., Zhou, C., Huang, Z., and Guo, Z. (2020). Landslide susceptibility prediction based on a semi-supervised multiple-layer perceptron model. *Landslides* 17, 2919–2930. doi:10.1007/s10346-020-01473-9

Huang, F., Chen, J., Liu, W., Huang, J., Hong, H., and Chen, W. (2022). Regional rainfall-induced landslide hazard warning based on landslide susceptibility mapping and a critical rainfall threshold. *Geomorphology* 408, 108236. doi:10.1016/j.geomorph.2022.108236

Huang, F., Tao, S., Chang, Z., Huang, J., Fan, S., Jiang, L., et al. (2021). Efficient and automatic extraction of slope units based on multi-scale segmentation method for landslide assessments. *Landslides* 18, 3715–3731. doi:10.1007/s10346-021-01756-9

Huang, S., He, Y., Yu, S., and Cai, C. (2022a). Experimental investigation and prediction model for UCS loss of unsaturated sandstones under freeze-thaw action. *Int. J. Min. Sci. Technol.* 32, 41–49. doi:10.1016/j.ijmst.2021.10.012

Huang, S., Yu, S., Ye, Y., Ye, Z., and Cheng, A. (2022b). Pore structure change and physico-mechanical properties deterioration of sandstone suffering freeze-thaw actions. *Constr. Build. Mater.* 330, 127200. doi:10.1016/j.conbuildmat.2022.127200

Lai, Y., Hui, H., Ziwang, Z., Songyu, S., and Xuejun, X. (2000). Analytical viscoelastic solution for frost force in cold-region tunnels. *Cold Regions Sci. Technol.* 31, 227–234. doi:10.1016/S0165-232X(00)00017-3

Lai, Y., Liu, S., Wu, Z., and Yu, W. (2002). Approximate analytical solution for temperature fields in cold regions circular tunnels. *Cold Regions Sci. Technol.* 34, 43–49. doi:10.1016/S0165-232X(01)00050-7

Lekhnitskii, S. G. (1981). *Theory of elasticity of an anisotropic body*. Moscow: Mir Publishers.

Li, S., Niu, F., Lai, Y., Pei, W., and Yu, W. (2017). Optimal design of thermal insulation layer of a tunnel in permafrost regions based on coupled heat-water simulation. *Appl. Therm. Eng.* 110, 1264–1273. doi:10.1016/j.applthermaleng.2016.09.033

Li, W., Wu, Y., Fu, H., and Zhang, J. (2015). Long-term continuous *in-situ* monitoring of tunnel lining surface temperature in cold region and its application. *Ijht* 33, 39–44. doi:10.18280/ijht.330206

Li, Y., Sun, Y., Qiu, J., Liu, T., Yang, L., and She, H. (2020). Moisture absorption characteristics and thermal insulation performance of thermal insulation materials for cold region tunnels. *Constr. Build. Mater.* 237, 117765. doi:10.1016/j.conbuildmat.2019.117765

Liu, H., Yuan, X., and Xie, T. (2019). A damage model for frost heaving pressure in circular rock tunnel under freezing-thawing cycles. *Tunn. Undergr. Space Technol.* 83, 401–408. doi:10.1016/j.tust.2018.10.012

Liu, L., Li, Z., Liu, X., and Li, Y. (2018a). Frost front research of a cold-region tunnel considering ventilation based on a physical model test. *Tunn. Undergr. Space Technol.* 77, 261–279. doi:10.1016/j.tust.2018.04.011

Liu, W., Feng, Q., Fu, S., and Wang, C. (2018b). Elasto-plastic solution for cold-regional tunnels considering the compound effect of non-uniform frost heave, supporting strength and supporting time. *Tunn. Undergr. Space Technol.* 82, 293–302. doi:10.1016/j.tust.2018.08.054

Liu, Y., Cai, Y., Huang, S., Guo, Y., and Liu, G. (2020). Effect of water saturation on uniaxial compressive strength and damage degree of clay-bearing sandstone under freeze-thaw. *Bull. Eng. Geol. Environ.* 79, 2021–2036. doi:10.1007/s10064-019-01686-w

Lv, Z., Xia, C., Wang, Y., and Luo, J. (2019). Analytical elasto-plastic solution of frost heaving force in cold region tunnels considering transversely isotropic frost heave of surrounding rock. *Cold Regions Sci. Technol.* 163, 87–97. doi:10.1016/j.coldregions.2019.04.008

Meng, X., Zhang, H., and Liu, X. (2021). Rock damage constitutive model based on the modified logistic equation under freeze–thaw and load conditions. *J. Cold Reg. Eng.* 35, 04021016. doi:10.1061/(ASCE)CR.1943-5495.0000268

Murton, J. B., Ozouf, J.-C., and Peterson, R. (2016). Heave, settlement and fracture of chalk during physical modelling experiments with temperature cycling above and below 0°C. *Geomorphology* 270, 71–87. doi:10.1016/j.geomorph.2016.07.016

Nakamura, D., Goto, T., Ito, Y., Suzuki, T., and Yamashita, S. (2009). "A basic study on frost susceptibility of rock: Differences between frost susceptibility of rock and soil," in *Proceeding of 14th conference on cold regions engineering* (Duluth, Minnesota: ASCE), doi:10.1061/41072(359)11

Nakamura, D., Goto, T., Suzuki, T., Ito, Y., Yamashita, S., Kawaguchi, T., et al. (2012). "Basic study on the frost heave pressure of rocks: Dependence of the location of frost heave on the strength of the rock," in *Cold regions engineering 2012:*

Sustainable infrastructure development in a changing cold environment (Quebec City, Canada: American Society of Civil Engineers), 124–133. doi:10.1061/9780784412473.013

Tan, X., Chen, W., Yang, D., Dai, Y., Wu, G., Yang, J., et al. (2014). Study on the influence of airflow on the temperature of the surrounding rock in a cold region tunnel and its application to insulation layer design. *Appl. Therm. Eng.* 67, 320–334. doi:10.1016/j.applthermaleng.2014.03.016

Xia, C., Lv, Z., Li, Q., Huang, J., and Bai, X. (2018). Transversely isotropic frost heave of saturated rock under unidirectional freezing condition and induced frost heaving force in cold region tunnels. *Cold Regions Sci. Technol.* 152, 48–58. doi:10.1016/j.coldregions.2018.04.011

Yu, H. (2000). *Cavity expansion methods in geomechanics.* Berlin, Heidelberg: Springer Science+Business Media.

Yu, W., Lu, Y., Han, F., Liu, Y., and Zhang, X. (2018). Dynamic process of the thermal regime of a permafrost tunnel on Tibetan Plateau. *Tunn. Undergr. Space Technol.* 71, 159–165. doi:10.1016/j.tust.2017.08.021

Yuanming, Y., Xuefu, X., Wenbing, W., Shujuan, S., Zhiqiang, Z., and Jianzhang, J. (2005). Three-dimensional nonlinear analysis for the coupled problem of the heat transfer of the surrounding rock and the heat convection between the air and the surrounding rock in cold-region tunnel. *Tunn. Undergr. Space Technol.* 20, 323–332. doi:10.1016/j.tust.2004.12.004

Zeng, Y., Liu, K., Zhou, X., and Fan, L. (2017). Tunnel temperature fields analysis under the couple effect of convection-conduction in cold regions. *Appl. Therm. Eng.* 120, 378–392. doi:10.1016/j.applthermaleng.2017.03.143

Zhang, G., Liu, S., Zhao, X., Ye, M., Chen, R., Zhang, H., et al. (2017). The coupling effect of ventilation and groundwater flow on the thermal performance of tunnel lining GHEs. *Appl. Therm. Eng.* 112, 595–605. doi:10.1016/j.applthermaleng.2016.10.120

Zhang, G., Xia, C., Zhao, X., and Zhou, S. (2016). Effect of ventilation on the thermal performance of tunnel lining GHEs. *Appl. Therm. Eng.* 93, 416–424. doi:10.1016/j.applthermaleng.2015.10.008

Zhang, X., Lai, Y., Yu, W., and Zhang, S. (2002). Non-linear analysis for the freezing-thawing situation of the rock surrounding the tunnel in cold regions under the conditions of different construction seasons, initial temperatures and insulations. *Tunn. Undergr. Space Technol.* 17, 315–325. doi:10.1016/S0886-7798(02)00030-5

Zhang, X., Zhou, Z., Li, J., Zhou, Y., and Han, F. (2018). A physical model experiment for investigating into temperature redistribution in surrounding rock of permafrost tunnel. *Cold Regions Sci. Technol.* 151, 47–52. doi:10.1016/j.coldregions.2018.03.007

Zhou, X., Zeng, Y., and Fan, L. (2016). Temperature field analysis of a cold-region railway tunnel considering mechanical and train-induced ventilation effects. *Appl. Therm. Eng.* 100, 114–124. doi:10.1016/j.applthermaleng.2016.01.070

frontiers | Frontiers in Earth Science

TYPE Original Research
PUBLISHED 05 January 2023
DOI 10.3389/feart.2022.1056695

Check for updates

OPEN ACCESS

EDITED BY
Shibing Huang,
Wuhan University of Science and Technology, China

REVIEWED BY
Li Wang,
China Three Gorges University, China
Fei Guo,
China Three Gorges University, China

*CORRESPONDENCE
Mingwei Guo,
mwguo@whrsm.ac.cn

SPECIALTY SECTION
This article was submitted to Geohazards and Georisks, a section of the journal Frontiers in Earth Science

RECEIVED 29 September 2022
ACCEPTED 05 December 2022
PUBLISHED 05 January 2023

CITATION
Guo M, Dong X and Yang Z (2023), Settlement analysis of the giant open caisson during the construction of the Changtai Yangtze River Bridge. *Front. Earth Sci.* 10:1056695. doi: 10.3389/feart.2022.1056695

COPYRIGHT
© 2023 Guo, Dong and Yang. This is an open-access article distributed under the terms of the Creative Commons Attribution License (CC BY). The use, distribution or reproduction in other forums is permitted, provided the original author(s) and the copyright owner(s) are credited and that the original publication in this journal is cited, in accordance with accepted academic practice. No use, distribution or reproduction is permitted which does not comply with these terms.

Settlement analysis of the giant open caisson during the construction of the Changtai Yangtze River Bridge

Mingwei Guo[1,2]*, Xuechao Dong[1,2] and Zhi Yang[1,3]

[1]State Key Laboratory of Geomechanics and Geotechnical Engineering, Institute of Rock and Soil Mechanics, Chinese Academy of Sciences, Wuhan, China, [2]University of Chinese Academy of Sciences, Beijing, China, [3]School of Civil Engineering and Architecture, Anhui University of Science and Technology, Huainan, China

With the increasing size of open caissons in large-span bridge projects, the overall settlement of giant open caissons is vital to the safe construction of bridge superstructures. Taking the engineering case of the Changtai Yangtze River Bridge, the overall deformation of an open caisson was studied during the construction stage of the bridge's superstructures. First, the theoretical layer-wise summation method was utilized to analyze the settlement of the open caisson. Then, a 3-D finite element model was established to simulate the installation stage of the bridge superstructure. Finally, a large centrifuge model test was performed to obtain the deformation of the open caisson at each step of bridge's construction. The results of these approaches demonstrated that final settlements were quite consistent—approximately 225 mm when the bridge superstructure was completely installed—and the settlement deformation curve could be divided into three stages: slowly increasing, rapid, and stabilizing. This study can provide significant guidance for the construction of the Changtai Yangtze River Bridge and be a reference for similar open caisson engineering projects.

KEYWORDS

open caisson, layer-wise summation method, 3-D finite element analysis, large centrifuge model test, Changtai Yangtze River Bridge

1 Introduction

Open caissons are used for the foundations of the deep piers of bridges or other heavy structures when their bearing beds are deep under the soil surface or below water (Nonveiller, 1987). Open caissons have the advantage of good integrity, high structural stiffness, high bearing capacity, small deformation, and full utilization of internal space (Mu et al., 2015; Li et al., 2020). In recent years, they have been widely applied in deep foundations and underground structural engineering projects; they have become one of the main types of foundation in long-span bridge engineering projects (Allenby et al., 2009; Jiang et al., 2019).

TABLE 1 Statistical table of the main open caissons around the world.

Year	Country	Name	Plane size (m)	Sinking depth (m)
1936	America	Anchorage caisson foundation of the San Francisco–Oakland Bridge	43.5 × 28	73.28
1938	Canada	North tower anchorage caisson of the Lion Gate bridge	36.57 × 20.68	12.7
1938	America	Anchorage caissons in the new Greenville Bridge	36 × 24	58 (62)
1995	China	North anchorage caisson of the Jiangyin Bridge	69 × 51	58
1998	Japan	No.1 anchorage caisson of the Akashi Kaikyo Bridge	∅ 80	65
2003	China	Main pier caisson of the Hankou Century Bridge	29.8 × 18.6	40.6
2007	China	Middle tower caisson of the Taizhou Yangtze River Bridge	58.4 × 44.4	76
2007	China	North anchorage caisson of the Taizhou Yangtze River Bridge	67.9 × 52	57
2007	China	South anchorage caisson of the Taizhou Yangtze River Bridge	67.9 × 52	41
2008	China	North anchorage caisson of the fourth Nanjing Yangtze River Bridge	69 × 58	52.8
2010	China	North anchorage caisson of the Maanshan Yangtze River Bridge	60.2 × 55.4	51
2011	China	North anchorage caisson of the Yingwuzhou Yangtze River Bridge	∅ 66.4	43
2014	China	Main pier caisson of the Hutong Yangtze River Bridge	86.9 × 58.7	115
2019	China	Middle tower caisson of the Oujiang Beikou Bridge	66 × 56	50
2020	China	Main pier caisson of the Changtai Yangtze River Bridge	95 × 57.8	47.0

Table 1 shows the statistics of the principal open caisson projects around the world and shows that many open caissons have been used in long-span bridges in China since 2000 and for many major bridge projects. It can be anticipated that many more giant open caissons will appear one after another with the development of future long-span bridges. As a result, the overall settlement of open caissons has become a key issue in bridge construction and is of great significance for the reasonable assessment of the settlement deformation of caisson foundations to ensure the safe installation of bridge superstructures.

Research into open caissons has mainly been twofold. One aspect has focused on the sinking process of the open caisson, and the other, on the deformation behavior of the open caisson after sinking to the desired depth. The sinking process of open caissons has been studied by theoretical analysis, laboratory tests, numerical analysis, and the analysis of field monitoring data to determine the mechanical responses and deformation characteristics of the surrounding soil that are induced by the installation of open caissons (Yan and Shi, 2013; Jiang, et al., 2019; Zhou et al., 2019; Royston et al., 2020; Guo et al., 2021; Templeman et al., 2021). Due to this focus on settlement deformation after sinking to the desired depth, studies on the sinking process of open caissons are not described in detail in this paper.

The bearing capacity of the foundation soil and the deformation behavior of an open caisson after sinking to the desired depth during the installation of a bridge superstructure have been comprehensively studied. Alampalli and Peddibotla (1997) conducted experiments on the settlement and deflection behavior of open-ended caissons in sandy soil. Solov'ev (2008) studied the bearing capacity of the foundation soil beneath the cutting edge of an open caisson using limit equilibrium theory, and Chavda et al. (2019) carried out a series of model tests to study the vertical bearing capacity and the soil flow mechanism around the cutting edge of an open caisson. Moreover, for offshore caisson foundations, the bearing capacity under combined V–H–M (vertical–horizontal–moment) loads was studied in clay (Zhang et al., 2011; Hung and Kim, 2014; Fu et al., 2018; Skau et al., 2018), sand (Cheng and Cassidy, 2016; Park et al., 2016; Jin et al., 2019), in sand over clay (Qiu and Henke, 2011; Park and Park, 2017; Zou et al., 2018), and in stiff over soft clay (Xia, et al., 2021). Some studies have also investigated the dynamic response of large embedded foundations (caisson foundations and anchorage open caissons) under horizontal and vertical vibrations (Apsel and Luco, 1987; Latini and Zania, 2017; Chen et al., 2007; Senjuntichai et al., 2006; Bilotta et al., 2015; Chen et al., 2019). To date, few studies have investigated the settlement deformation of caisson foundations after sinking to the desired depth during the installation of bridge superstructures (Chuanbao, 2021). However, it is vitally important to the safe installation of bridge superstructures to determine the overall settlement of open caissons.

The aim of this study is to investigate the deformation characteristics of open caissons during the installation of large-span bridge superstructures. The Changtai Yangtze

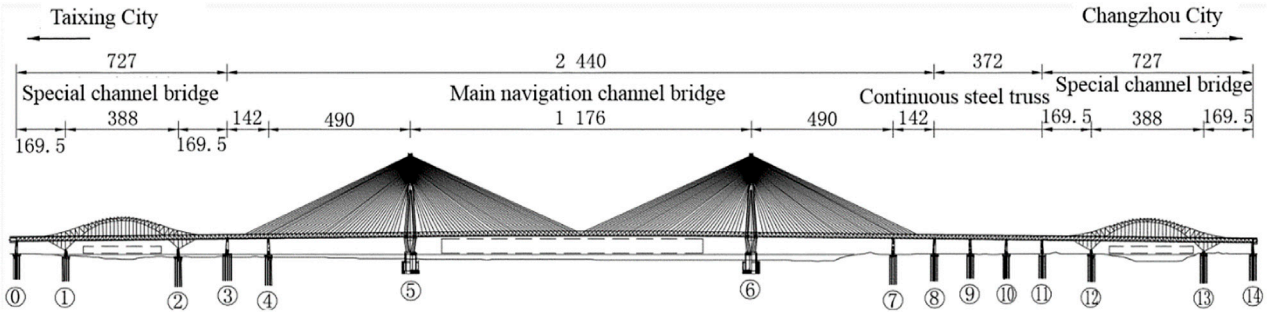


FIGURE 1
Main sections of the Changtai Yangtze River Bridge (units: m).

River Bridge is presently under construction. It is a cable-stayed bridge with the longest span in the world, and giant open caissons were used under the main piers of this bridge (Figure 1). To reasonably assess the deformation characteristics of the open caissons during the installation of a large-span bridge superstructure, theoretical layer-wise summation was first used, and then, the 3D finite element technique was employed. Finally, a large centrifuge model test was performed to validate the results by theoretical methods and numerical analysis. More importantly, it played an important role in the installation of bridge superstructures by determining settlement deformations of the open caisson studied in this paper, and it also has importance as a significant reference for similar open caisson projects.

2 Changtai Yangtze River Bridge

2.1 General description

Figure 1 shows the overall layout of the Changtai Yangtze River Bridge that connects Changzhou City and Taixing City. It is a rail-cum-road cable-stayed bridge with an asymmetric layout of double towers and double cable planes. The lower layer of the bridge contains an intercity railway and an ordinary two-way four-lane road; its upper layer contains a two-way six-lane expressway. At present, it is the largest cable-stayed bridge in the world, with a span of 1,176 m. In Figure 1, the sections numbered ⑤ and ⑥ are the open caissons under the main piers of this bridge.

The main pier of the bridge is located on typically deep and sedimentary soil. To satisfy the action of the huge load of the bridge structure and meet the strict requirements of bridge alignment, an open caisson was proposed for use under the main pier through comprehensive technical and economic considerations (Qin et al., 2020).

2.2 Geological conditions

The Yangtze River at the bridge site has an irregular semi-diurnal shallow-sea tidal pattern. The tide rises and falls twice a day, with a maximum tidal level of +5.28 m, minimum level of −1.14 m, and average level of +1.69 m.

The Quaternary overburden soil layer is widely distributed in the engineering field. Due to several past sea transgressions, the soil layers have changed in an orderly but complex manner. The main soils are alluvial clayish soil and sandy soil, and the underlying bedrock is mainly Neogene siltstone. At the bridge site, the thickness of the Quaternary loose sediment is more than 160 m, with strata of interbedded clay and sand. The upper part has a hard plastic silty clay layer with a thickness of 4 m ~ 6 m; loose silty sand, silt, and soft plastic silty clay are distributed in its middle. Its lower layers are dense fine-medium sand that can be used as the bearing layer of an open caisson. The typical geological stratification is shown in Table 2.

From this stratigraphic distribution, it is evident that, above −40 m elevation, there are interlayers of silty clay with soft ~ hard plastic characteristics and silty-fine sand with slightly~ medium dense features. At the elevation between −40 m and −55 m is medium dense fine sand with continuous and uniform distribution features, and at an elevation between −55 m and −65 m is soft plastic silty clay with layered continuous distribution features. The medium, fine, and coarse sands are followed by dense and thin features. It should be noted that soft plastic silty clay of 12 m thickness was continuously distributed between −72 m and −84 m elevation. This silty clay had a particular structure: its water content and void ratio were high. Thus, the physical and mechanical properties of its soil needed to be thoroughly studied because of its significant influence on the deformation of the open caisson. At −84 m elevation, the soils are almost dense with medium sand of high strength and low compressibility; this has little influence on the overall deformation of the open caisson foundation.

TABLE 2 Stratigraphic distribution.

Stratum	Top altitude/m	Bottom altitude/m	Weight/ (kN/m^3)	Stratum	Top altitude/m	Bottom altitude/m	Weight/ (kN/m^3)
Silty clay	−18.1	−22.7	19.4	Silty clay	−56.3	−64.9	19.0
Loose silt	−22.7	−28.2	20.6	Dense fine sand	−64.9	−72.2	19.8
Hard plastic silty clay	−28.2	−31.3	20.0	Silty clay	−72.2	−84.1	20.1
Slightly dense silt	−31.3	−33.2	20.6	Dense fine sand	−84.1	−87.6	19.1
Soft plastic silty clay	−33.2	−39.7	19.0	Silty clay	−87.6	−91.3	20.3
Medium dense silt	−39.7	−48.2	20.6	Dense fine sand	−91.3	−96.7	20.5
Dense fine sand	−48.2	−53.9	19.8	Dense mealy sand	−96.7	−108.5	21.7
Dense medium sand	−53.9	−56.3	20.0	Medium sand	−108.5	−128.5	21.0

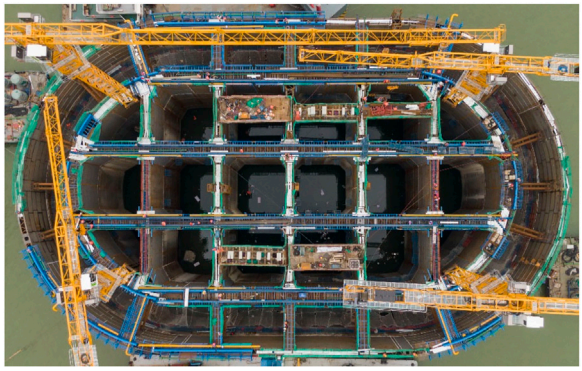


FIGURE 2
Open caisson at the field site.

According to the strata distributions under the main pier of the bridge and its load superstructure, it was suggested that the open caisson be sunk at −65 m elevation for the deformation requirement of the open caisson to be met. Therefore, the soft plastic silty clay with 12 m thickness between −72 m and −84 m elevation became the focus of the design of the open caisson foundation, which affected the caisson's investment and construction period. It thus became necessary to reasonably evaluate the settlement deformation of open caissons to provide strong technical support for the bridge's construction.

2.3 Stepped open caisson foundation

A round-end plane shape for the open caisson was adopted for the Changtai Yangtze River Bridge. The stepped caisson foundation was first designed with a small top and a large base; its bottom surface is 95 m long across the bridge and 57.8 m wide along the bridge, and the radii of the circular ends are 28.9 m. The top surface is 77 m long and 39.8 m wide, and the radii of the circular ends are 19.9 m. The total height of the caisson foundation is 72 m, of which the lower step is 43 m and the upper step is 29 m. Steel shell concrete was used for the caisson foundation from top to bottom—currently the largest underwater steel caisson foundation in the world. It contains 36 compartments, including 18 inner shafts and 18 outer shafts (Figure 2).

3 Layer-wise summation method

The layer-wise summation method divides the soil into several layers based on its stratigraphic distribution and stress state within the influence depth of the foundation settlement. This method calculates the settlement of each layer separately and sums all settlements as the final settlement of the foundation. This method, which was written in the specific code for the design of building foundations in China (GB50007-2011), was applied and verified to be rational for practical foundation engineering.

The calculation formula of this method is shown as Eq. 1.

$$S = m_s \sum_{i=1}^{n} \Delta S_i = m_s \sum_{i=1}^{n} \frac{\sigma_{z(0)}}{E_{si}} (z_i C_i - z_{i-1} C_{i-1}), \quad (1)$$

$$\sigma_{z(0)} = \frac{P + F}{A} - \sigma_0, \quad (2)$$

where S is the final settlement of the foundation (mm), m_s is the empirical coefficient of the settlement calculation, n is the number of soil layers divided within the influence depth of foundation settlement, ΔS_i is the settlement of the i^{th} layer of soil, $\sigma_{z(0)}$ is the additional compressive stress at the bottom of the

TABLE 3 Compression modulus.

Name of the soil layer	Depth (m)	$E_{s0.1-0.2}$ (MPa)	E_s (MPa)
Dense sand	7.30	12.63	25.76
Silty clay	11.9	7.08	17.83
Dense fine sand	3.50	13.83	32.50
Silty clay	3.70	7.08	17.83
Dense sand	5.40	14.14	34.50
Dense mealy sand	11.8	10.84	42.86
Medium sand	12.0	12.13	44.26

foundation (kPa), which can be obtained by Eq. 2, P is the additional force applied on the top of the foundation, F is the effective gravity of the foundation, A is the basal area of the foundation, σ_0 is the gravity stress at the bottom of the foundation, E_{si} is the compressive modulus of the ith layer of soil (MPa), z_i is the distance from the bottom of the foundation to the bottom of the i^{th} soil layer (m), and C_i is the coefficient of average additional stress within the range of the foundation bottom to the bottom of the i^{th} soil layer. The influence depth of the foundation settlement can be determined by the condition $\Delta S_n \le 0.025\sum_{i=1}^{n}\Delta S_i$.

It can be seen from Eq. 1that the soil compressive modulus E_S is the key parameter in the layered sum method. E_S is defined as the ratio of the vertical stress increase to the vertical strain increase under the condition of complete lateral confinement corresponding to a certain stress range based on the soil compression curve (e-p curve) (Eqs 3, 4).

$$E_s = \frac{\Delta p}{\Delta \varepsilon_z} = \frac{p_{i+1} - p_i}{s_{i+1} - s_i} = \frac{(1 + e_0)}{a}, \tag{3}$$

$$a = -\frac{\Delta e}{\Delta p} = -\frac{e_i - e_{i+1}}{p_{i+1} - p_i} = -\frac{(1 + e_0)(s_{i+1} - s_i)}{p_{i+1} - p_i}, \tag{4}$$

where e_0 is the natural void ratio of the soil, a is the compression coefficient, and s_i is the settlement under the pressure p_i. Additionally, the negative sign indicates that the void ratio e decreases with increasing compressive stress.

According to the actual strata distributions in the area of the open caisson, the compressive modulus of each layer of soil was obtained based on uniaxial compression tests of the soil, which were calculated by Eq. 3 and are shown in Table 3. In Table 3, $E_{s0.1-0.2}$ corresponds to the compressive modulus under pressures of 100 kPa to 200 kPa—widely used in shallow foundation engineering—and E_s corresponds to the pressure from the gravity stress of the soil to the actual stress under engineering loads. The empirical coefficient of settlement m_s is generally determined by regional subsidence observation data and engineering experience; if there is no engineering experience, it can be obtained based on the equivalent value of the compression modulus, which is calculated by Eq. 5. With respect to the actual strata distributions of this open caisson, the equivalent values of the compression moduli were greater than 20.0 MPa, and the corresponding empirical coefficients were 0.2, based on the specific code for the design of building foundations in China (GB50007-2011).

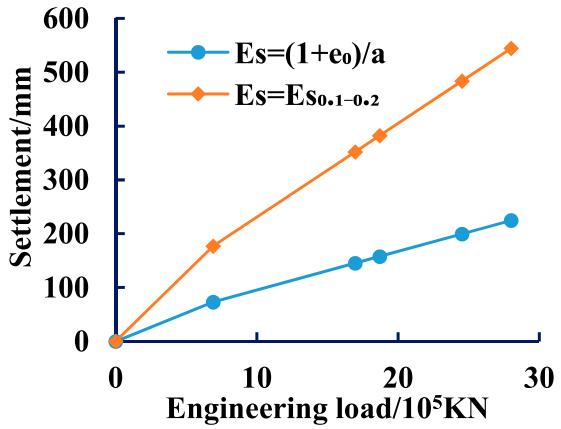


FIGURE 3
Load vs. settlement using different modulus values.

$$\overline{E_S} = \frac{\sum A_i}{\sum A_i / E_{si}}, \tag{5}$$

where A_i is the area of the additional compressive stress profile in the ith layer of soil, and E_{si} is the compression modulus of the ith layer of soil.

It is known that the compressive modulus E_s generally increases with increasing compressive pressure. Table 3 shows that the actual compressive modulus E_s of each soil layer was greater than the conventional compressive modulus $E_{s0.1-0.2}$ because the vertical stress values of each soil layer under engineering load were greater than 200 kPa.

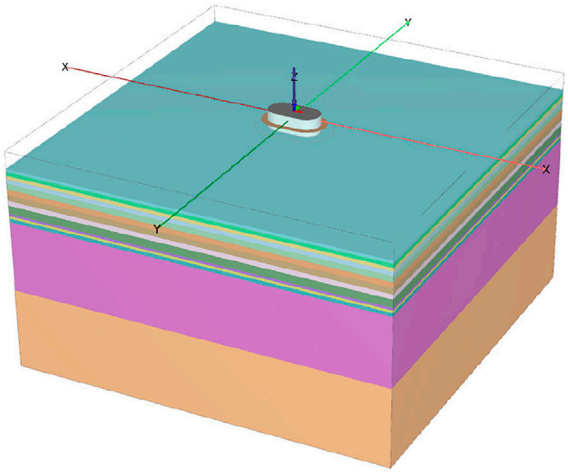


FIGURE 4
3-D calculating solid model of a large stepped open caisson.

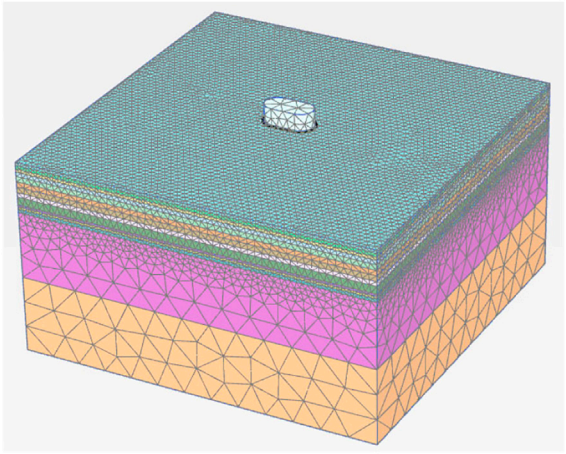


FIGURE 5
3-D finite element mesh model.

Accordingly, for the open caisson under the main pier of the Changtai Yangtze River Bridge, the settlement of the open caisson was calculated by layer-wise summation at the installation stage of the bridge superstructure. The influence depth of the foundation settlement was 62 m, based on the actual strata distributions, and the empirical coefficient m_s was 0.2. Figure 3 shows that the settlement using the two compressive moduli gradually increases with an increasing engineering load, and the overall settlement is 544.47 mm calculated by $Es_{0.1\text{-}0.2}$ when the bridge is completely constructed—2.42 times the settlement using the actual compressive modulus (224.65 mm).

4 3-D finite element numerical analysis

A 3-D finite element numerical method was also used to assess the deformation characteristics of the open caisson during the installation stage of the bridge superstructure in the Changtai Yangtze River Bridge project.

4.1 3-D finite element numerical model

The size of the foundation is as follows: the bottom is 95 m long across the bridge, 57.8 m wide along the bridge, and the radii of the circular ends are 28.9 m. The top surface is 77 m long and 39.8 m wide, and the radii of the circular ends are 19.9 m. The total height is 72 m, of which the lower step is 43 m, the upper step is 29 m, and the target sinking elevation is −65 m.

Due to the focus on the deformation characteristics of open caissons during the installation stage of the bridge superstructure, the open caisson was simplified to be a solid structure based on equivalent bulk density. Considering the actual size of this foundation and the boundary effect of finite element analysis, a 3-D calculation model was established (Figure 4), the size of which is 560 m×560 m×300 m—length×width×height. PLAXIS 3D software was used to numerically analyze the deformation of the open caisson under the bridge loads. Figure 5 shows the finite element mesh model, and 10-node tetrahedral elements were utilized in the calculation model.

4.2 Computing conditions

For constitutive models of soils, the ideal elastic–plastic constitutive model based on the Mohr–Coulomb strength failure criterion is popularly applied in geotechnical engineering, although it does not consider the effects of the stress path and strain hardening on the mechanical properties of the soil. However, in practical engineering, there are strain hardening phenomena in the process of soil deformation under external loads. The hardening constitutive model of small strain soil (HSS), which is different from the Mohr–Coulomb model, was developed on the basis of the hardening soil model (HS) first proposed by Benz (2006). The HSS model has the advantages of reflecting the compression characteristics and dilatancy of soil, distinguishing the loading and unloading stiffness, and considering the shear hardening and compression hardening at the same time—these can effectively reflect the mechanical properties of soil in triaxial and consolidation tests, especially the dependence of soil stiffness on the stress path. Furthermore, the HSS model has been verified to be rational, and

TABLE 4 Soil parameters.

Name	Top elevation (m)	Density (kN/m^3)	Cohesion (kPa)	Friction angle (°)	E_{oed}^{ref} (MPa)	E_{50}^{ref} (MPa)	E_{ur}^{ref} (MPa)
Dense sand	-65	19.8	5.2	36.9	34.11	34.11	170.55
Silty clay	-72.2	20.1	27.08	18.3	17.09	17.09	85.45
Dense fine sand	-84.1	19.1	5.2	36.9	22.30	22.3	111.5
Silty clay	-87.6	20.3	27.08	18.3	17.09	17.09	85.45
Dense fine sand	-91.3	20.5	5.2	36.9	34.50	34.5	172.5
Dense mealy sand	-96.7	21.7	4.7	38.3	42.86	42.86	214.3
Medium sand	-108.5	21.0	4.2	38.7	41.84	41.84	209.2

the results were consistent with the practical deformation in foundation engineering (Mu and Huang, 2016; Fan and Zhai, 2019). To reasonably simulate the mechanical behavior of the bottom soil of an open caisson during the construction stage of long-span bridge engineering, the hardening constitutive model of small strain soil (HSS) was used to analyze the deformation of the caisson foundation.

The HSS model inherits all the characteristics of the HS model and accounts for the increase in soil stiffness in the small strain stage. The HSS model has some advantages over other models in soil shear hardening, compression hardening, loading and unloading, and small strain deformation. In recent years, practical engineering cases have demonstrated that the HSS model is more suitable for simulating the mechanical behavior of the soil in deep foundation engineering.

There are 13 soil parameters needed in the HSS model; except for the two small strain parameters of the HSS model, 11 of these are the same as those of the HS model. Based on field investigation, indoor tests of the soil, and existing research on the determination of soil parameters in the HSS model, the soil parameters are listed in Table 4. According to a previous study (Wang et al., 2012; Lian-xiang et al., 2019), the loading and unloading tangent modulus E_{ur}^{ref} was determined to be five times the value of the consolidation test E_{oed}^{ref} or five times the value of the triaxial consolidation drained shear test E_{50}^{ref}. Based on Benz (2006), the power exponent m related to the modulus stress level was determined to be 0.8 for clay soils and 0.5 for the sandy soils. For the two small strain parameters, the initial shear modulus in the small strain deformation stage G_0^{ref} was suggested as being between one and two times the E_{ur}^{ref} value by Benz (2006); for the shear strain $\gamma_{0.7}$ reflecting the stress level, it is in the range of (0.6–3.0)×10^{-4} under a pressure of 100 kPa for sandy soils, based again on Benz (2006). In this paper, G_0^{ref} was set to be equal to E_{ur}^{ref}, and $\gamma_{0.7}$ was determined to be 2.0×10^{-4} for use in the non-linear finite element analysis.

For the boundary conditions of the calculating model, the bottom is completely restricted, and the rest are normal constraints. To reasonably assess the mechanical interactions between the soil and the open caisson, the contact between them was considered, and, in PLAXIS 3D software, the strength reduction factor R_{inter} was set on the interface between the soil and the open caisson. The strength on the interface depends on the strength of the soil, and it was set to be R_{inter} times the strength of the corresponding soil. Due to the difficulty in determining the factor R_{inter} through field tests, it is suggested to be two-thirds of this value in numerical analysis based on the recommendation in this software. In addition, for the calculated working conditions, the initial stress state was obtained for when the caisson had sunk to the desired depth. The superstructure installation containing five steps is listed in Table 5, and the deformation characteristics can be simulated based on the construction schedule of the main navigation channel bridge.

TABLE 5 Construction schedule of the main navigation channel bridge.

Step	Structure	Time (month)	Load (KN)
1	Lower pylon column	7	691,385
2	Middle tower column	8	1,696,699
3	Upper pylon	10	1,870,007
4	Girder structure	8	2,452,937
5	Accessory structure	3	2,801,186

4.3 Result analysis

During the construction of the main navigation channel bridge, the settlement deformation was simulated by gradually applying vertical loads on the top surface of the open caisson. Figure 6 shows the vertical deformation at the different installation steps of the bridge superstructure. It can be seen in these figures that the vertical displacement is symmetrical because of the symmetry of the bridge structure and engineering

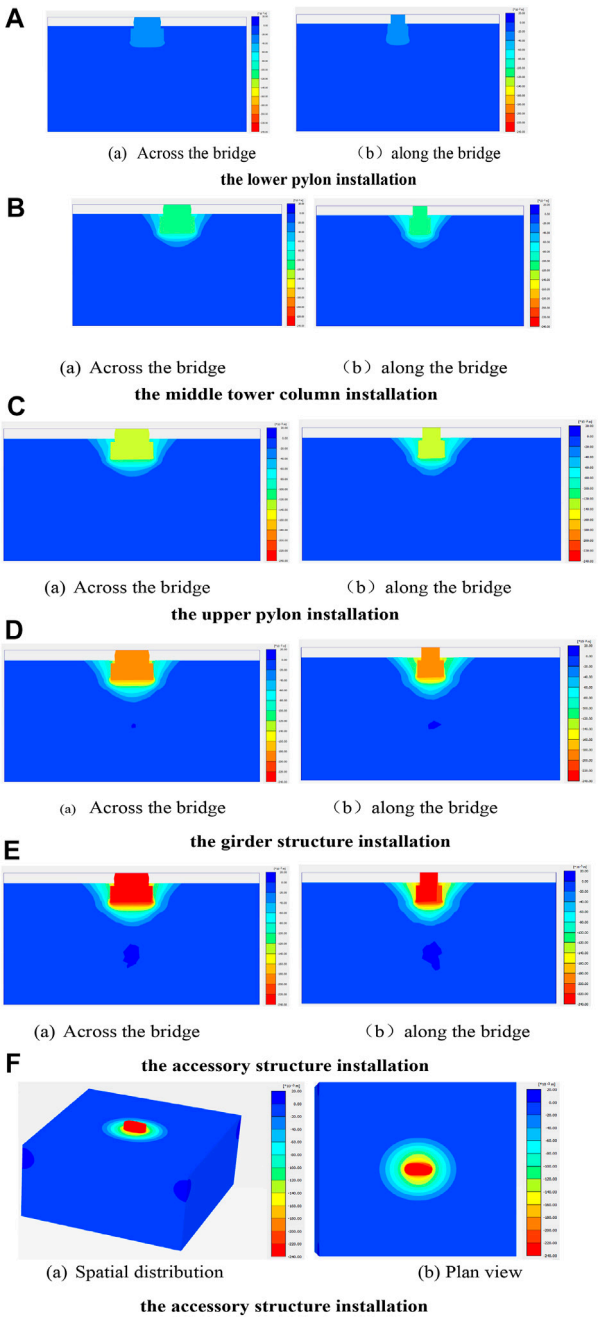


FIGURE 6
Isochromatic map of the vertical displacement distribution of the open caisson: **(A)** lower pylon installation; **(B)** middle tower column installation; **(C)** upper pylon installation; **(D)** girder structure installation; **(E)** accessory structure installation; **(F)** accessory structure installation.

loads; furthermore, the settlement of the open caisson gradually increased with the installation of the bridge superstructure. The final settlement of the open caisson foundation was 225.7 mm after finishing the main navigation channel bridge construction.

The maximum settlement amounts of the open caisson during the installation of the bridge superstructure are listed in Table 6. To compare the settlement amounts by finite element analysis with those by the layer-wise summation method, the settlement comparison is presented in Figure 7. Figure 7 shows that the settlement amounts determined by the layer-wise summation method were larger than those determined by numerical analysis with the installation of the bridge superstructure; however, when the main navigation channel bridge was completed, the final settlement amounts determined by numerical analysis agreed well with those determined by finite element analysis. Moreover, the relative errors between the settlements by both methods gradually decreased, and the relative error of the final settlement was only approximately 0.5%.

5 Large centrifuge model test

To rationally evaluate the settlement deformation of the open caisson during the installation of the bridge superstructure, a large centrifuge model test was especially designed and conducted based on its actual size and engineering geological conditions. Figure 8 shows the large geotechnical centrifuge equipment (TK-C500). The maximum acceleration was 250 g. Here, g is gravity acceleration, the maximum effective load is 50 kN, the maximum radius of rotation is 5 m, and the maximum size of the model box is 1.2 m×1.0 m×1.2 m (length×width×height). The total weight of the open caisson used in this bridge is approximately 0.5 million tons, and the construction period was approximately 21 months. The total weight of the bridge superstructure is approximately 0.28 million tons, and the installation period was approximately 38 months.

5.1 Test model

5.1.1 Open caisson model

The size of the open caisson is 95 m×57.8 m×72 m (length×width×height), and the size of the model box is 1.2 m×1.0 m×1.2 m (l×w×h). Taking the influence of the boundary effect into account, half of the symmetrical open caisson was modeled in the centrifuge test; based on the sizes of the open caisson and model box of the centrifuge equipment, the similarity ratio was comprehensively selected as 150, that is, the acceleration of the centrifuge was 150 g when the equipment was running steadily in the test process.

Figure 9 shows the solid model of the open caisson based on the design of the open caisson. Given the similarity ratio and the actual size of the open caisson, the size of the model is 317 mm×385 mm ×480 mm (l×w×h) made with 6,061 aluminum alloy material.

TABLE 6 Settlement amounts corresponding to different installation steps.

Step	Vertical load (10^5 kN)	Maximum settlement (mm)
Lower pylon column	6.9	30.5
Middle tower column	17.0	115.5
Upper pylon	18.7	131.1
Girder structure	24.5	188.6
Accessory structure	28.1	225.7

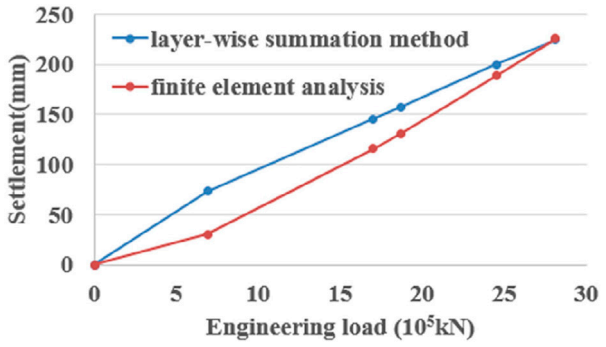


FIGURE 7
Settlement comparison of both methods.

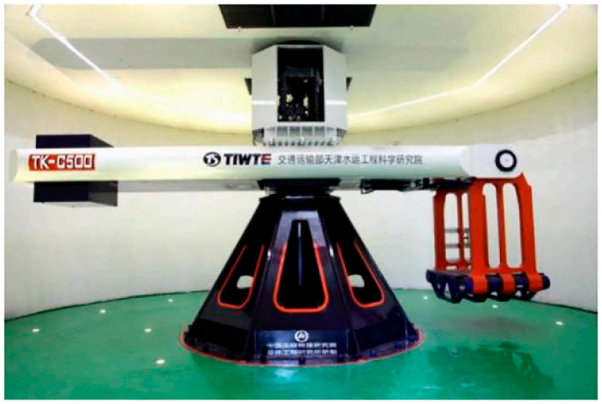


FIGURE 8
TK-C500 geotechnical centrifuge equipment.

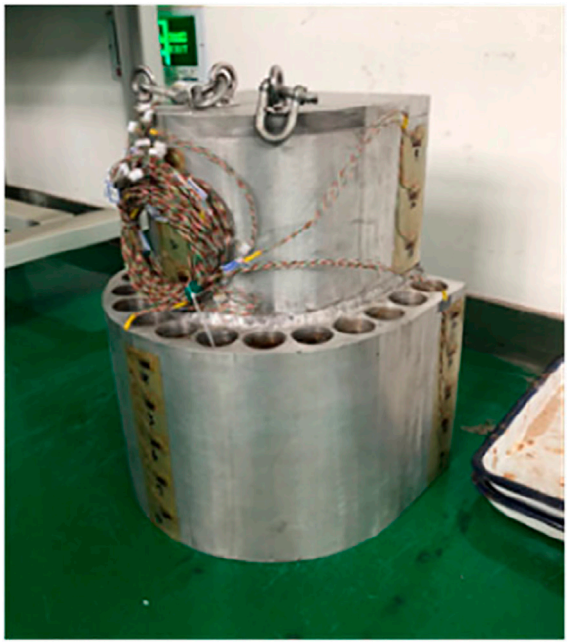


FIGURE 9
Solid model of the open caisson.

5.1.2 Foundation model

The physical and mechanical parameters of the soils were determined by indoor geotechnical tests after field drilling and sampling, and the clay and sand used in the model test were based on the corresponding physical and mechanical parameters of the soils. Before making the foundation model, drainage equipment was placed at the bottom of the model box to ensure saturation after completing the model. To reduce the influence of the boundary effect on the test model, Vaseline was applied to the inner wall of the model box to simulate a semi-infinite field (Figure 10).

For the foundation soils placed in the test model, a conventional sand-pouring method was used to produce the sand layer, and the vibration compaction method was used for the silty clay layer.

(1) Conventional sand pouring method for sand

The sand in the model box was placed by using the sand pouring method, which is related to the compactness and failing



FIGURE 10
Vaseline applied to the wall of the model box.

distance of the sand. To ensure the uniformity of the sand samples, the falling distance was calibrated in advance before placing the sand in the model box, and compaction was carried out to control the relative compactness of the sand. The preprepared sand samples were then loaded into the sand box, which was lifted to the specified initial height, and the circular sand-drop sieve mouth was used to place the sand. Later, the height of the sand rainier was gradually adjusted to maintain the falling distance of the sand. The process of placing the sand is shown in Figure 11.

(2) Compaction method for silty clay

For the silty clay, the vibration compaction method was used to prepare the soil samples in the model. The soil in this method needs to be compacted layer by layer, with the dry density at the site used as the controlling parameter of the soil. To keep the parameters of the soil consistent, it was necessary to ensure that the compaction times were the same in the different parts of the same layer of soil (Figure 12A). After the preparation of one layer of silty clay, the surface of the soil needed to be scraped to increase the biting degree of the soil (Figure 12B).

After the soil compartments were completely filled, water was slowly injected from the bottom of the model box upward to avoid disturbing the sand layer or creating bubbles in it. Sufficient water was injected to guarantee that the water surface was 1 cm higher than the top surface of the soil; thence, the water injection was stopped, and the soil model was soaked for 24 h. Before commencing the centrifuge model test, to ensure that the soil model was fully saturated, the water was again injected through the water pipe at the bottom of the model box until the water surface was 1 cm higher than the top surface of the soil model. Finally, the centrifugal testing machine was operated for 30 min under 150 g conditions to fully saturate the soil model. Figure 13 shows the solid model after completing the open caisson and soil model.

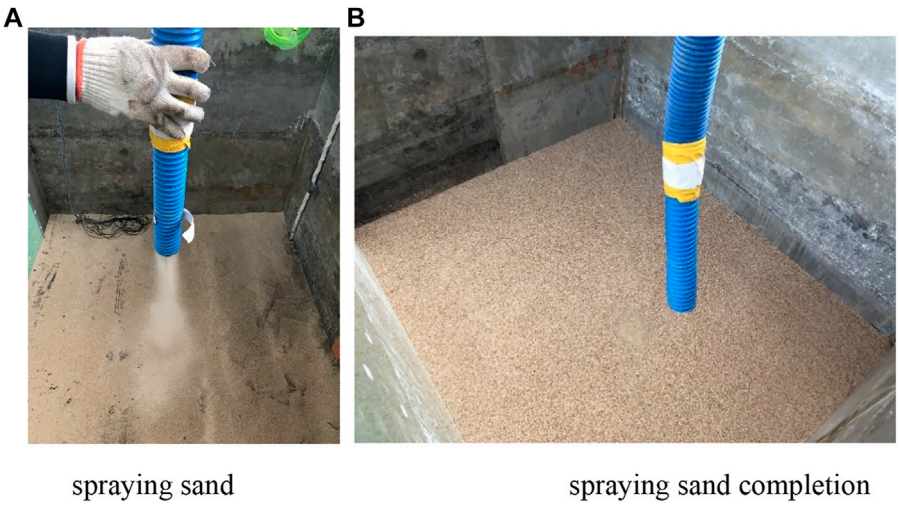


FIGURE 11
Sand placement process: **(A)** spraying sand; **(B)** spraying sand completion.

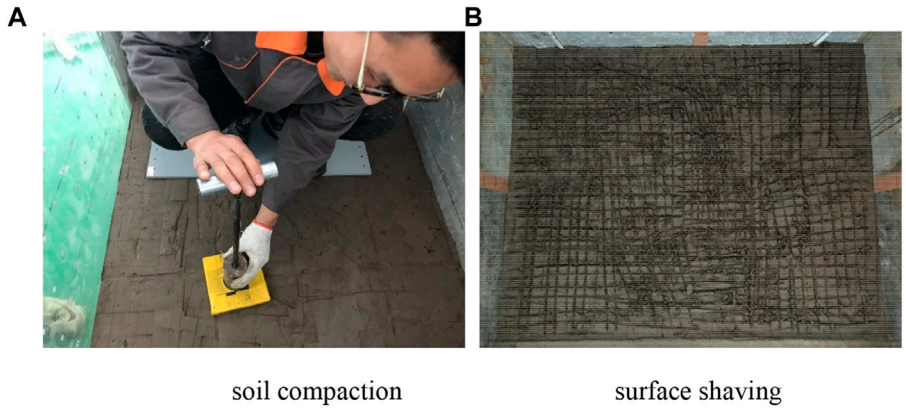


FIGURE 12
Silty clay placement process: **(A)** soil compaction; **(B)** surface shaving.

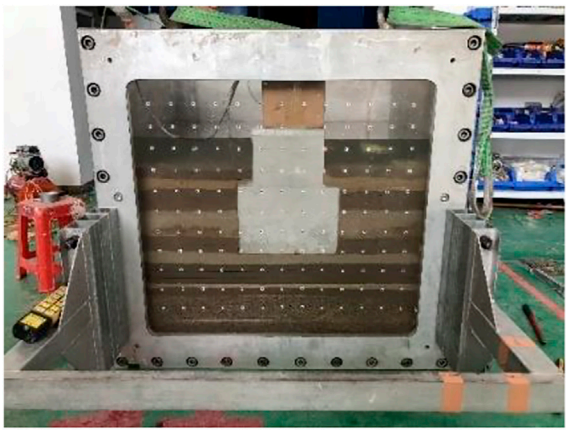


FIGURE 13
Completion of the model test.

5.2 Layout of monitoring points

During the centrifuge model test, a laser displacement sensor was used to monitor the settlement of the open caisson, and the earth pressure sensor was used to monitor the earth pressure in the silty clay under the open caisson.

Figure 14A shows the locations of four laser displacement sensors on the upper surface of the open caisson in the model test. The sensors were HG-C1200 laser sensors with a range of 200 ± 80 mm. Under the open caisson is a layer of silty clay approximately 12 m thick, which was a primary concern for this model test. Therefore, six mini earth-pressure sensors with a measuring range of 2 MPa were arranged on the surface and in the middle of the silty clay in this test (Figure 14B).

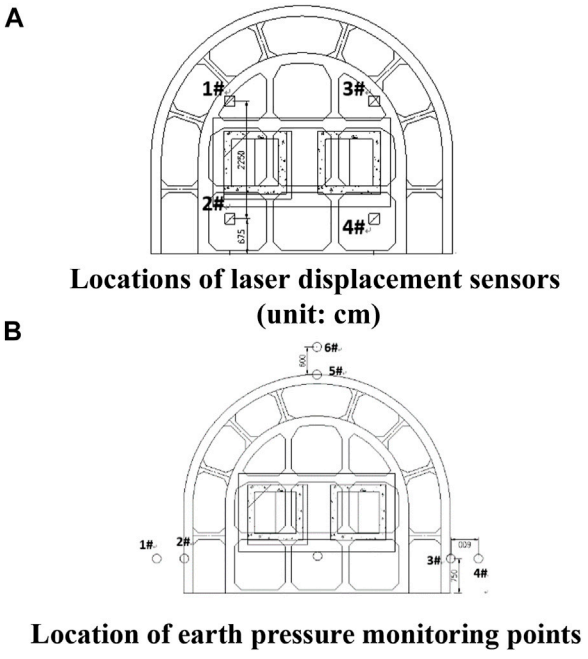


FIGURE 14
Locations of monitoring points (units:cm): **(A)** laser displacement sensor; **(B)** earth pressure sensor.

5.3 Loading process

The loading system of the centrifuge model test was mainly composed of the frame above the model box, the loading beam, the loading equipment placed on the beam, and the controller. When the soil model was assembled, the hydraulic loading system was installed and simultaneously tested. This loading

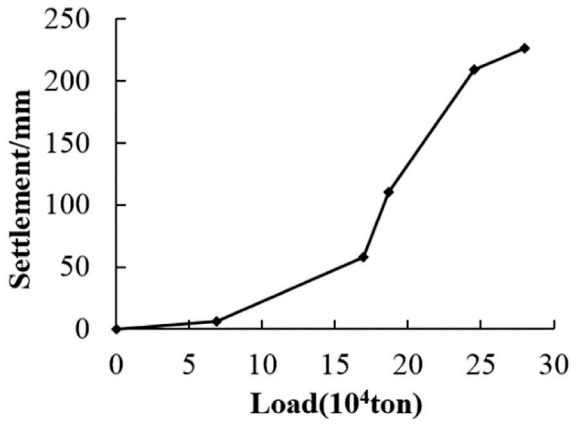


FIGURE 15
Settlement of the open caisson determined by the centrifuge model test.

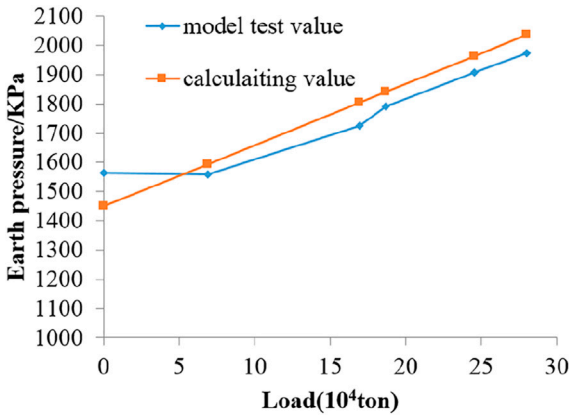


FIGURE 16
Earth pressure results determined by calculation and model test.

system was controlled by the feedback signals from the force and displacement sensors. Furthermore, based on the actual installation of the bridge superstructure (Table 3), a hierarchical loading stage sequence can be set in the loading system, and automatic loading can be realized under a high centrifugal environment. According to the installation schedule of the bridge superstructure, the loading parameters can be obtained on the basis of the similarity ratio, and segment loading was carried out during the model test. After the first stage load was applied, the settlement and the earth pressure were observed until they stabilized; the next level of load was then applied until all the loads were completely applied in the test.

The whole centrifuge model test comprised four steps:

1) After the test model was completely assembled, the model box was lifted into the centrifuge basket and properly placed. Then, the loading system was installed, and the initial values of the sensors were reset to 0 before starting the test.
2) For loading during the centrifuge test, 20 g intervals were used. The load was gradually applied until it reached 150 g. The centrifugal machine test required only 10 min to correspond to the 156 days that the original model, under gravity, required to restore the natural stress state of the actual foundation. The loading test was carried out after the monitoring values of the sensors stabilized.
3) The loading test was conducted based on the actual installation (Table 3), and the loading parameters were imported into the loading system software. Photographs and videos could be taken at any time during the test.
4) The results of the centrifuge test were saved once the test was completely finished; the model box was then lifted out of the centrifugal basket.

5.4 Result analysis

Figure 15 shows the settlement results of the open caisson obtained by the centrifuge model test. Due to the few differences among the four settlement locations in the test (Figure 15), the average value of settlement locations was used as the overall settlement of the open caisson.

From Table 3 and Figure 15, the bridge superstructure installation was divided into five steps. The first step is the installation of the lower pylon column. The engineering load was approximately 0.69 million tons, and the corresponding settlement of the caisson foundation was 6.38 mm, which belongs to the slow subsidence stage. The second step was the installation of the middle tower column with a total load of 1.16 million tons and a corresponding settlement of 58.26 mm. The third stage was the installation of the upper pylon with a total load of 1.87 million tons and a corresponding settlement of 110.75 mm. In this stage, the settlement speed of the open caisson increases sharply, which is the fastest stage of subsidence during the entire installation of the bridge superstructure. In the fourth stage of girder installation, the total load reached 2.45 million tons, and the settlement was 209.46 mm, the speed of which was slower than that of upper pylon installation. The last stage was accessory structure installation, in which the load reached the maximum value of 2.80 million tons, the settlement of the open caisson tended to be gentle, and the corresponding settlement was 226.25 mm. The overall settlement of the open caisson gradually increased with increasing load during the bridge superstructure installation. The deformation curve of the open caisson can be roughly divided into three stages of deformation: slowly increasing, rapid, and tending to become stable. From the lower pylon column to middle tower column stage, the deformation was in the slowly increasing stage, while it is in the sharp deformation stage from middle tower installation to girder structure installation; the settlement then tended to become

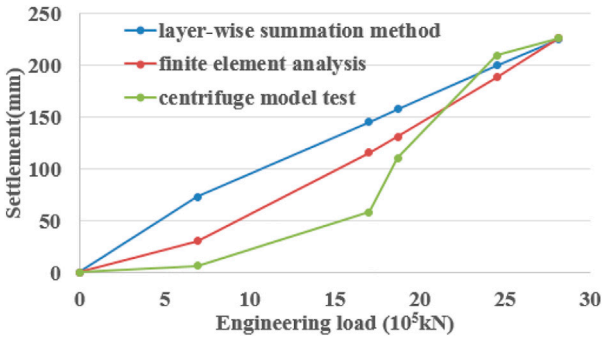


FIGURE 17
Settlements determined by the different approaches during bridge superstructure installation

stable from girder structure installation to accessory structure installation.

Figure 16 shows the earth pressure results from the centrifuge model test and the calculation. In Figure 16, the test value is the earth pressure monitored in the middle of the silty clay soil, and the calculation results are computed based on the actual stratum and depth of the silty clay. The comprehensive bulk density of the open caisson was set to 20 kN/m^3, and the calculated earth pressure does not consider the influence of stress diffusion from the bottom of the foundation to the silty clay layer. During the superstructure installation period, the soil pressure measured in the middle of the silty clay increased with the increasing load of the bridge superstructure installation. The calculated values generally increased linearly with increasing engineering loads, and the calculated values of the earth pressure were slightly larger than those of the model test, which may be due to stress diffusion not considered in the calculations.

6 Comparison analysis

Figure 17 shows the settlement curves of the open caisson with the installation of the bridge superstructure calculated by the theoretical layer-wise summation method, the 3D finite element method, and the centrifuge model test. The final settlement was approximately 225 mm when the installation of the bridge superstructure was completed. For the layer-wise summation and finite element methods, the settlements increased linearly with the installation of the bridge superstructure. However, the settlement obtained by the centrifugal model test could be divided into three deformation stages: slowly increasing, rapid, and tending to become stable—these were mainly related to the shear failure characteristics of the soil under the open caisson. By comparing the settlement curves determined by the three methods mentioned previously, it can be seen that the finite element method could simulate the soil characteristics better than layer-wise summation because the former considers the strain hardening characteristics under the vertical load. Furthermore, although there are differences in the settlement of the open caisson during the installation of bridge superstructures, the final settlement values determined by the three methods were consistent.

For the sand layer, the existing studies showed that, with the increase in deviatoric stress, the loose sand gradually becomes dense, and strain hardening occurs, while the dense sand undergoes strain softening after the deviatoric stress reaches its peak value. Whether in loose or dense sand, shear shrinkage occurs under high confining pressure. Strain softening is an unstable process of rearranging and balancing the position of sand particles. In essence, the occlusions between the sand particles are damaged due to the increased stress. The friction strength is more complex in clay soil than in sandy soil. In addition to the sliding and occlusion of the soil particles, the cohesive force of clay has a great influence on its friction strength, which is not only related to the strength of the cementing material but also because it will be strengthened over time. Remolded rather than undisturbed soils were used in the centrifugal model test. Therefore, the shear strength of remolded soil was usually slightly different than undisturbed soil; the older the sedimentary age, the greater is the strength of the undisturbed soil than that of the remolded soil.

According to the actual strata of the caisson foundation in this bridge project, it is sandy soil with a thickness of 7 m under the open caisson, followed by silty clay with a thickness of 12 m. From the settlement curve of the open caisson from the centrifuge test, the deformation characteristics of the soil under the foundation can be described as follows. Before the complete installation of the middle tower column, the soil under the open caisson is further compacted and gradually reaches its peak strength due to the application of the engineering load, which naturally causes the overall settlement to gradually increase with the installation of the middle tower column. During the installation of the middle tower column to the girder structure, the deformation of the soil is characterized by strain softening with increasing deviatoric stress, so the settlement of the caisson foundation presents rapidly increasing characteristics. However, during the installation of the accessory structures, the local soil with shear failure reached a new equilibrium state, and the overall settlement of the caisson foundation tended to become stable under a total engineering load of 0.28 million tons.

7 Conclusion

1) The settlement deformation of a giant open caisson under the main pier was comprehensively analyzed by a theoretical layer-wise summation method, numerical analysis method, and large centrifuge model test during the construction of the Changtai Yangtze River Bridge. The results demonstrate that the final settlements obtained by three methods were

consistent: approximately 225 mm when the bridge superstructure was completely installed.

2) For the theoretical layer-wise summation method, the settlement (544.5 mm) using conventional compression modulus was 2.42 times that of using the compression modulus under actual stress; it is suggested that the compression modulus under the actual stress state of the soil should be utilized rather than under the stress range of 100 kPa ~ 200 kPa.
3) The results of the 3D finite element analysis showed that the settlement of the open caisson linearly increased during the installation of the bridge superstructure, and the final settlement was completely consistent with the results of the centrifuge model test. This verified that the HSS constitutive model can reflect the mechanical behavior of the soil in the installation of bridge superstructures.
4) The results of the centrifuge model test demonstrate that the settlement curve of the open caisson can be roughly divided into three deformation stages: slowly increasing, rapid, and tending to become stable. From the lower pylon column to middle tower column stage, the deformation belongs to the slowly increasing stage; it is in the rapid deformation stage from middle tower installation to girder structure installation; the settlement tended to become stable from girder structure installation to accessory structure installation.

Data availability statement

The raw data supporting the conclusions of this article will be made available by the authors, without undue reservation.

Author contributions

MG wrote the draft of the manuscript, XD completed the simulation analysis section, and ZY made some contribution to the theoretical analysis.

Funding

The authors gratefully acknowledge the financial support of the National Natural Science Foundation of China under Grant No. 51674239.

Conflict of interest

The authors declare that the research was conducted in the absence of any commercial or financial relationships that could be construed as a potential conflict of interest.

Publisher's note

All claims expressed in this article are solely those of the authors and do not necessarily represent those of their affiliated organizations, or those of the publisher, the editors, and the reviewers. Any product that may be evaluated in this article, or claim that may be made by its manufacturer, is not guaranteed or endorsed by the publisher.

References

Allenby, D., Waley, G., and Kilburn, D. (2009). Examples of open caisson sinking in Scotland. *Proc. Inst. Civ. Eng. Geotech. Eng.* 162 (1), 59–70. doi:10.1680/geng.2009.162.1.59

Apsel, R. J., and Luco, J. E. (1987). Impedance functions for foundations embedded in a layered medium: an integral equation approach. *Earthq. Eng. Struct. Dyn.* 15, 213–231. doi:10.1002/eqe.4290150205

Benz, T. (2006). *Small strain stiffness of soils and its numerical consequences [D]*. Stuttgart: University of Stuttgart.

Bilotta, E., De Sanctis, L., Di Laora, R., D'Onofrio, A., and Silvesti, F. (2015). Importance of seismic site response and soil–structure interaction in dynamic behaviour of a tall building. *Géotechnique* 65, 391–400. doi:10.1680/geot.sip.15.p.016

Chavda, J. T., Mishra, S., and Dodagoudar, G. R. (2019). Experimental evaluation of ultimate bearing capacity of the cutting edge of an open caisson. *Int. J. Phys. Model. Geotechnics* 20 (5), 281–294. doi:10.1680/jphmg.18.00052

Chen, S. L., Chen, L. Z., and Pan, E. (2007). Three-dimensional time-harmonic Green's functions of saturated soil under buried loading. *Soil Dyn. Earthq. Eng.* 27, 448–462. doi:10.1016/j.soildyn.2006.09.006

Chen, Y., Wen, Z., Jia, P., Han, J., and Guan, Y. (2019). Dynamic behavior of an embedded foundation under horizontal vibration in a poroelastic half-space. *Appl. sciences-basel* 9, 740. doi:10.3390/app9040740

Cheng, N., and Cassidy, M. J. (2016). Development of a force–resultant model for spudcan footings on loose sand under combined loads. *Can. Geotech. J.* 53 (12), 2014–2029. doi:10.1139/cgj-2015-0597

Chuanbao, F. (2021). Caisson foundation deformation analysis for north anchorage of Wufengshan Yangtze river bridge. *Bridge Constr.* 51 (1), 74–81. (in Chinese).

Fan, P. C., and Zhai, C. (2019). HSS ans M-C model analysis of deformation characteristics of subway. *Subgr. Eng.* 202 (1), 180–183. in Chinese.

Fu, D., Gaudin, C., Bienen, B., Tian, Y., and Cassidy, M. J. (2018). Combined load capacity of a preloaded skirted circular foundation in clay. *J. Geotech. Geoenviron. Eng.* 144 (11), 4018084. doi:10.1061/(asce)gt.1943-5606.0001960

Guo, M., Dong, X., and Li, J. (2021). Study on the earth pressure during sinking stage of super large caisson foundation. *Appl. Sci.* 11 (21), 10488. doi:10.3390/app112110488

Hung, L. C., and Kim, S. R. (2014). Evaluation of undrained bearing capacities of bucket foundations under combined loads. *Mar. Georesour. Geotechnol.* 32 (1), 76–92. doi:10.1080/1064119x.2012.735346

Jiang, B. N., Wang, M. T., Chen, T., Zhang, L. L., and Ma, J. L. (2019). Experimental study on the migration regularity of sand outside a large, deep-water, open caisson during sinking. *Ocean. Eng.* 193, 106601. doi:10.1016/j.oceaneng.2019.106601

Jin, Z., Yin, Z., Kotronis, P., and Li, Z. (2019). Advanced numerical modelling of caisson foundations in sand to investigate the failure envelope in the H-M-V space. *Ocean. Eng.* 190, 106394. doi:10.1016/j.oceaneng.2019.106394

Latini, C., and Zania, V. (2017). Dynamic lateral response of suction caissons. *Soil Dyn. Earthq. Eng.* 100, 59–71. doi:10.1016/j.soildyn.2017.05.020

Li, J. T., Qin, S. Q., and Zhang, R. X. (2020). Developments and prospects of deep-water foundations for bridge. *Bridge Constr.* 50 (03), 17–24. (in Chinese).

Lian-xiang, L., Jia-dian, L., and Li, K-J. (2019). Study on selection method and applicability of HSS parameters of typical stratum in Jinan[J]. *Rock Soil Mech.* 40 (10), 4021–4029. (in Chinese).

Mu, B. G., Zhu, J. M., and Gong, W. M. (2015). *Design, construction and monitoring of large open caisson*. CN: Beijing: China Architecture & Building Press. (in Chinese).

Mu, L., and Huang, M. (2016). Small strain based method for predicting three-dimensional soil displacements induced by braced excavation. *Tunn. Undergr. Space Technol.* 52 (2), 12–22. doi:10.1016/j.tust.2015.11.001

Nonveiller, E. (1987). Open caissons for deep foundations. *J. geotechnical Eng.* 113 (5), 424–439. doi:10.1061/(asce)0733-9410(1987)113:5(424)

Park, J., and Park, D. (2017). Vertical bearing capacity of bucket foundation in sand overlying clay. *Ocean. Eng.* 134, 62–76. doi:10.1016/j.oceaneng.2017.02.015

Park, J., Park, D., and Yoo, J. (2016). Vertical bearing capacity of bucket foundations in sand. *Ocean. Eng.* 121, 453–461. doi:10.1016/j.oceaneng.2016.05.056

Qin, S. Q., Xu, W., Lu, Q. F., Zheng, Q. G., Fu, Z. G., Yuan, R. A., et al. (2020). Overall design and concept development for main navigational channel bridge of Changtai Changjiang River Bridge. *Bridge Constr.* 50 (03), 1–10.

Qiu, G., and Henke, S. (2011). Controlled installation of spudcan foundations on loose sand overlying weak clay. *Mar. Struct.* 24 (4), 528–550. doi:10.1016/j.marstruc.2011.06.005

Royston, R., Sheil, B. B., and Byrne, B. W. (2020). Monitoring the construction of a large-diameter caisson in sand. *P. I. Civ. Eng.-Geotec* 175 (3), 323–339. doi:10.1680/jgeen.19.00266

Senjuntichai, T., Mani, S., and Rajapakse, R. K. N. D. (2006). Vertical vibration of an embedded rigid foundation in a poroelastic soil. *Soil Dyn. Earthq. Eng.* 26, 626–636. doi:10.1016/j.soildyn.2006.01.013

Skau, K. S., Chen, Y., and Jostad, H. P. (2018). A numerical study of capacity and stiffness of circular skirted foundations in clay subjected to combined static and cyclic general loading. *Geotechnique* 68 (3), 205–220. doi:10.1680/jgeot.16.p.092

Templeman, J. O., Phillips, B. M., and Sheil, B. B. (2021). Cutting shoe design for open caissons in sand: influence on vertical bearing capacity. *ICE Proc. Geotec. Eng.*, 1–16. doi:10.1680/jgeen.20.00218

Wang, W-D., Wang, H-R., and Xu, Z-H. (2012). Experimental study of parameters of hardening soil model for numerical analysis of excavations of foundation pits[J]. *Rock Soil Mech.* 33 (8), 2283–2290. doi:10.16285/j.rsm.2012.08.006

Xia, H., Zhou, X., Zhou, M., Niu, F., and Zhang, X. (2021). Capacity of caissons in stiff-over-soft clay under combined V–H-M loadings. *Ocean. Eng.* 229 (1), 109007. doi:10.1016/j.oceaneng.2021.109007

Yan, F. Y., and Shi, G. (2013). Analysis of limiting soil resistance beneath cutting curb during sinking of open caisson. *Rock Soil Mech.* 34 (S1), 80–87. doi:10.16285/j.rsm.2013.s1.063

Zhang, Y., Bienen, B., Cassidy, M. J., and Gourvenec, S. (2011). The undrained bearing capacity of a spudcan foundation under combined loading in soft clay. *Mar. Struct.* 24 (4), 459–477. doi:10.1016/j.marstruc.2011.06.002

Zhou, H. X., Ma, J. L., Zhang, K., Luo, C. Y., and Yang, B. (2019). Study of sinking resistance of large and deep caisson based on centrifugal model test. *Rock Soil Mech.* 40 (10), 3969–3976. doi:10.16285/j.rsm.2018.0360

Zou, X., Hu, Y., Hossain, M. S., and Zhou, M. (2018). Capacity of skirted foundations in sandover-clay under combined V-H-M loading. *Ocean. Eng.* 159, 201–218. doi:10.1016/j.oceaneng.2018.04.007

frontiers | Frontiers in Earth Science

TYPE Original Research
PUBLISHED 10 January 2023
DOI 10.3389/feart.2022.1006642

Check for updates

OPEN ACCESS

EDITED BY
Fengqiang Gong,
Southeast University, China

REVIEWED BY
Yanlin Zhao,
Hunan University of Science and Technology, China
Quan Jiang,
Institute of Rock and Soil Mechanics (CAS), China
Annan Jiang,
Dalian Maritime University, China
Chang'An Qin,
Beijing University of Civil Engineering and Architecture, China
Liu Liu,
Institute of Rock and Soil Mechanics (CAS), China

*CORRESPONDENCE
Xiaoli Liu,
xiaoli.liu@tsinghua.edu.cn
Xinlei Zhang,
472120638@stu.lntu.edu.cn

SPECIALTY SECTION
This article was submitted to Geohazards and Georisks, a section of the journal Frontiers in Earth Science

RECEIVED 29 July 2022
ACCEPTED 30 September 2022
PUBLISHED 10 January 2023

CITATION
Jin J, Zhang X, Liu X, Li Y and Li S (2023), Study on critical slowdown characteristics and early warning model of damage evolution of sandstone under freeze–thaw cycles.
Front. Earth Sci. 10:1006642.
doi: 10.3389/feart.2022.1006642

COPYRIGHT
© 2023 Jin, Zhang, Liu, Li and Li. This is an open-access article distributed under the terms of the Creative Commons Attribution License (CC BY). The use, distribution or reproduction in other forums is permitted, provided the original author(s) and the copyright owner(s) are credited and that the original publication in this journal is cited, in accordance with accepted academic practice. No use, distribution or reproduction is permitted which does not comply with these terms.

Study on critical slowdown characteristics and early warning model of damage evolution of sandstone under freeze–thaw cycles

Jiaxu Jin[1,2], Xinlei Zhang[1]*, Xiaoli Liu[3]*, Yahao Li[1] and Shaohua Li[4]

[1]School of Civil Engineering, Liaoning Technical University, Fuxin, China, [2]Liaoning Key Laboratory of Mine Subsidence Disaster Prevention and Control, Fuxin, China, [3]State Key Laboratory of Hydroscience and Engineering, Tsinghua University, Beijing, China, [4]Department of the Built Environment, Eindhoven University of Technology, Eindhoven, Netherlands

Freeze–thaw damage of rock mass poses a great threat to the safety of rock engineering, ground buildings, and low-temperature storage of liquefied natural gas (LNG) in cold regions. By collecting acoustic emission (AE) signals of sandstone during uniaxial compression failures, this paper analyzed the critical slowdown phenomenon of different types of sandstone during the freeze–thaw failure. According to the auto-correlation coefficients and the variance of AE signals under different windows and steps, the precursors were determined and a warning model of rock engineering failure precursors based on the critical slowdown principle was proposed. Then the Grey Wolf Optimizer (GWO) algorithm was used to optimize the initial weights and thresholds of the back propagation (BP) neural network, and the influence factors of rock engineering failure under different working conditions were input as training sets to train the network. The results showed that the correlation coefficients between the predicted value and real value of the GWO-BP neural network reached 99.90% and 98.81% respectively, indicating that the accuracy of the BP neural network prediction was improved. This study provides a new method for rock engineering failure early warning, and has great theoretical and guiding significance for enriching and improving the rock mass AE monitoring technology.

KEYWORDS

freeze-thaw cycle, acoustic emission, critical slowdown, precursors, GWO-BP neural network

1 Introduction

Globally, more than 25% of the land area is covered by permafrost, while the distribution of cold regions is more extensive. Under the condition of freezing and thawing, the corresponding damage of rocks in cold regions will lead to a series of engineering problems, such as the frost heaving, cracking of oil pipelines and tunnel surrounding rocks, instability and failure of the supporting structure, erosion and weathering of slope engineering, instability of the high-risk rock mass, storage of liquid resources, and weathering of rock cultural relics (Liu et al., 2018). The freeze–thaw damage of rocks is mainly caused by the volume expansion of 9% frozen water in pores (pores or cracks) and the thermal stress at low temperature conditions (B et al., 2018, Girard et al., 2013). Under such conditions, the frost heaving force in the saturated pores caused by water/ice phase transition can cause cracks and defects, further leading to the destruction of rock engineering in cold regions (Kock et al., 2015; Park et al., 2015; Tan et al., 2018; Kong et al., 2020). Zhao et al. studied the creep failure mechanism of rock cracks under hydraulic pressure and derived the compression-shear fracture criterion of rock under hydro-mechanical coupling (Liu et al., 2022; Zhao et al., 2019). Therefore, to develop an early warning model of rock engineering failure is of great significance for engineering safety evaluation.

The energy theory research shows that the fundamental roles of rock deformation and failure are the dissipation and release of energy. The instability and failure of rocks are the result of the sudden release of internal energy, the main forms of which are the kinetic energy and acoustic emission (Zhao et al., 2019). Therefore, the theory based on the view of energy can well describe the deformation and failure of rocks. AE is a non-destructive monitoring method which can identify the crack propagation and the failure mechanism of materials and structures, and it is widely used in civil engineering due to its high sensitivity and accurate evaluation. AE parameters as another characterization of waveform are widely used in the study of the critical slowdown phenomenon. When the complex dynamic system approaches the critical point before mutation, there is a phenomenon called critical slowdown, which is manifested by the increase of precursor variance and auto-correlation coefficients (Leemput et al., 2013; Maturana et al., 2020). Critical slowdown phenomenon has great potential in revealing whether complex dynamic systems are prone to catastrophic mutations. Lei et al. (2004) pointed out that AE signals of the sandstone failure have obvious stage characteristics, the cumulative AE count has a good correspondence with the sandstone damage, and the sudden large-scale increase of self-correlation coefficients and the variance of AE count can be employed as precursors of the sandstone engineering failure. When the rock is close to collapse, there will be a series of key deceleration characteristics, including the significant increase of the AE count and density value per unit time (Lei et al., 2004; Huang et al., 2016), indicating that the AE signals generated in the process of rock failure make a critical change (Xia et al., 2022), Kong et al. (2015) believed that under the triaxial compression conditions of different confining and pore pressures, the AE characteristics of coal and rock samples underwent a critical deceleration process. The variance and auto-correlation coefficients of AE count and time series increased before the failure of coal and rock. Therefore, the variance and auto-correlation coefficients could be used as the precursors of coal failure. Compared with the AE cumulative signals as the mutation points of precursors, the time delay between precursors and mutation points was shortened within a reasonable range, accounting for 2%–10% of the total loading time (Kong et al., 2015).

With the development of digital signal technology, the neural network as an intelligent algorithm has excellent nonlinear adaptive characteristics and is suitable for parallel processing and hardware implementation (Rumelhart et al., 1986). Due to the improper parameter selection into local minimum in some cases, the algorithm converges to the mean square error gradient descent direction, meanwhile its convergence speed is slow, thus the back propagation (BP) neural network is very sensitive to the initial weight threshold. Chai et al. optimized the BP neural network through the wavelet analysis, removed the noise of the initial data by the wavelet function, and employed the BP neural network and the gradient descent method to train and adjust the neural network parameters. Although the accuracy of the prediction results has been improved, the convergence speed has been reduced (Chai et al., 2016). Xie et al. proposed a new damage constitutive model related to Weibull distribution and statistical damage theory. (Xie et al., 2020). The finite element method of seepage-damage coupling was carried out in FORTRAN in Zhao Yanlin's study (Zhao et al., 2021). Grey Wolf Optimizer (GWO) algorithm was proposed by Mirjalili et al. (2014) by simulating the social class and predatory strategy of Grey Wolf. Since this algorithm has the characteristics of strong global search ability, fast convergence speed, and simple implementation, it can make up for the deficiency of BP neural network algorithm and has been widely used (Zhang and Zhou, 2015).

In summary, previous studies on the critical slowing of rock failure have made a lot of achievements, but there are few reports on establishing an early warning model of rock failure in cold regions based on neural networks through the critical slowing characteristics of rock failure. Therefore, this paper intends to carry out uniaxial compression experiments of sandstone with different saturations, and explore the critical slowing down phenomenon of acoustic emission signals in the process of rock uniaxial compression experiments. According to the critical slowing down phenomenon of sandstone compression failure, a precursory signal model for rock engineering failure is proposed based on GWO-BP algorithm.

2 Uniaxial compression experiment of sandstone under freeze–thaw conditions

The equipment used in the uniaxial compression test is the WDW-300E microcomputer controlled electronic universal testing machine made in China. The maximum test force is 300 kN, the effective measurement range is 0.4%–100% of the maximum test force, and the measurement accuracy is less than or equal to ±1%. The axial range of deformation is 0–5 mm, the radial range is 0–3 mm, and the measurement accuracy is less than or equal to ±1%. The DS5-8B AE instrument used in the AE signal acquisition test in the uniaxial compression process has two to eight channels. The continuous data pass rate of DS5-8B acoustic emission instrument is 65.5 MB/S, the pass rate of waveform data is 48 MB/S, interface form is USB3.0, data acquisition method is multi-channel synchronous acquisition, software operating environment for win7/8/10 operating system, the storage method is full waveform acquisition, and all channels can continuously store waveform data for several hours to ensure that no doubtful data is lost during acquisition, the sampling rate is 10 M per channel when using 2 channels, 5 M or 6 M per channel when using 4 channels, and 3 M or 2.5 M per channel when using 8 channels. External parameter sampling frequency is 30 KHz and 25 KHz, external parameter conversion accuracy is 16bit, external parameter input range is±5 V or ±10 V. The loading device and data acquisition system are shown in Figure 1.

All the test rock blocks were taken from the fresh sandstone of a rock slope in the transition section between Sichuan Basin and Qinghai Tibet Plateau of the Sichuan-Tibet railway. The surface water and rivers in the study area have obvious erosion and cutting effects on the mountain and subgrade. Both groundwater and water-bearing rocks receive atmospheric precipitation in summer, and supplied by melting ice in winter, The annual average temperature is 7.1°C, the extreme maximum temperature is 23.4°C, and the extreme minimum temperature is −19.1°C, The external forces are mainly hydraulic erosion and freezing and thawing, which are typical plateau landforms. All test samples were derived from the same non-jointed rock core. The rock samples had high homogeneity, small discreteness and relatively large porosity, so they can ensure different gradient water content (Zhang et al., 2019). According to the International Society for Rock Mechanics (ISRM) test procedure, the experimental rock samples were processed, and the size of the specimens was specified as Φ50 mm×100 mm. The accuracy of the rock sample processing meets that the non-parallelism error of the two ends shall not be greater than 0.05 mm, and the end surface roughness error is not greater than 0.02 mm. Then, the ultrasonic detector was used to test the sound velocity of the specimens with uniform texture and complete appearance. After the test, the rock samples with large dispersion were removed, then the rock samples with similar quality were selected as the test rock sample. The initial dry density of the rock sample is 2.33 g/cm^3 , the saturated density is 2.52 g/cm^3 , and the porosity is 9.32%. Firstly, the specimens were dried at 105°C for 48 h to a constant weight (the mass change was not more than 0.1% within 12 h), and then the mass of each rock sample was weighed and recorded. Rock samples with different saturations (0%, 30%, 60%, 75%, 85%, 95%, and 100%) were prepared by using chemical thermodynamic methods. When the humidity was close to that of the saturated salt solution, the humidity environment was basically stable. When the mass change of rock samples before and after the measurement was not more than 0.1%, it was considered that the system reached equilibrium and the rock sample lost water to the target saturation. The changes of pore structure in sandstone with different saturations were observed by JSM-7500F scanning electron microscope. 1) In the dry state, the internal structure integrity of the sample is good, the particles are arranged closely, the cracks are angular, the grain lines are clear, the particle surface is smooth, and there is no softening damage phenomenon and no obvious debris. 2) When the saturation is between 30% and 85%, the internal structure of sandstone is gradually destroyed, the structure is obviously loose, the surface texture is deepened, the particles begin to soften and decompose, the softening and crushing degree of sandstone particles are intensified, and the pores between particles and within particles are gradually developed. 3) When the saturation reaches 85%–100%, the edges and corners of the crack boundary tend to be smooth, the local damage of the internal structure is intensified, the integrity is poor, and the cementation of the connecting parts between particles is weakened. With the increase of saturation, there are obvious brittle cracks between mineral particles, and the original internal voids begin to expand and gradually connect. Different saturation samples were put into freeze–thaw box for experimenting. The freezing and melting temperatures were set to −20°C and 20°C respectively. The cooling and freezing time lasted for 2 h and 10 h respectively. The time period of the raising and constant melting temperatures was 1 h and 11 h respectively. Each freeze–thaw cycle lasted for 24 h and was performed 5 times. The WDW-300E microcomputer controlled electronic universal testing machine was used for the uniaxial compression test of specimens after the freeze–thaw treatment. The displacement loading method was used in the loading process with the loading rate of 0.12 mm/min. During the experiment, the DS5 full information AE measurement system and 8-channel transient recorder were used to study the mechanical properties and damage evolution of the specimen. Each sample was arranged with 8 acoustic emission probes, which were symmetrically arranged on the sample. The acoustic emission signal threshold was set to 40 dB and the sampling frequency was 5 MHz.

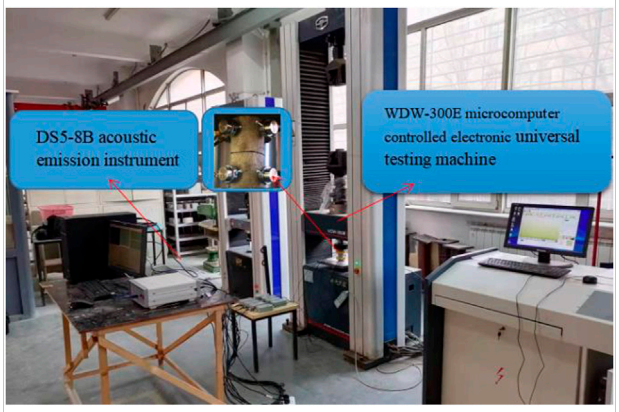


FIGURE 1
The loading device and data acquisition system.

3 Critical slowdown of sandstone failure under freeze–thaw cycles

3.1 AE signals of sandstone during the uniaxial compression

Crack initiation and propagation of rock materials are often accompanied by the release of elastic waves, which can be recorded as AE signals through the AE monitoring system (Dai et al., 2019). Kong et al. (2017) divided the failure stage into the quiet, linear increase, rapid increase, and saturation stages according to the AE cumulative count curve (Kong et al., 2017). Yang et al. (2018) divided the failure stage of sandstone into three stages according to the AE signals: initial compaction, slow growth, and rapid growth stages. Based on the previous studies and the change of ringing count in the process of rock failure, the rock failure stage can be divided into four stages: initial compaction (OA stage), slow growth (AB stage), rapid growth (BC stage) and failure (CE stage). Figure 2 describes the load–displacement curves and the ringing counts of seven rocks with different saturations.

As a kind of porous medium material, sandstone contains many primary cracks and fissures. In the initial compaction stage (OA), the unclosed cracks and pores in the original interior of the rock sample were closed due to compression, the force on the rock sample failed to form a linear relationship with the displacement, and the load-displacement curve tended to be concave. At this time, the ringing count generally had a short-term mutation. This is because during the initial contact process, due to the inertia effect, the instantaneous stress would be too large, resulting in a sudden increase in the ringing count at the initial stage. With the increase of saturation, the OA stage obviously prolonged under a certain axial pressure, that is, (g) in Figure 2 corresponded to the longest OA stage. This is due to the increase of water molecular content, a part of hydraulic pressure offset the axial pressure, which prolonged the closure time of initial microcracks and pores.

With the progress of loading, the initial pores and cracks of the rock samples had been closed. This stage was the slow growth stage (AB). The load increased linearly with the displacement. The rock samples showed elastic deformation under uniaxial pressure. The acoustic emission events were relatively few, and the acoustic emission activity remained basically in a stable state during the whole process.

During the rapid growth stage (BC), the load-displacement curve of this stage showed a convex trend, which was an obvious nonlinear growth stage. Cracks began to form inside the rock sample and developed cumulatively. The propagation of cracks continuously demanded for energy. Externally, the AE activity was relatively quiet, and the ringing count fluctuation was small. However, there were many sudden changes during this stage as polymerization appeared in the rock sample in the loading process of microcracks, resulting in large fluctuations of the ringing count. Therefore, in the monitoring and early warning of rock mass engineering in cold regions, it was necessary to pay attention to these fluctuations to avoid misjudgment in monitoring and early warning.

With the increase of axial pressure, the internal energy of the rock sample continued to accumulate. When the internal structure of the rock sample reached the bearing limit, the penetrating cracks appeared and the sample was destroyed. At this time, the acoustic emission activity became extremely active. The rock sample entered the failure stage (CE), and the ringing count suddenly increased obviously. After the peak stress, the microcracks and pores in the sandstone continued to expand. Even at a small stress level, the acoustic emission count was still at a high level.

3.2 Critical slowdown principle

Critical slowdown refers to the dispersion and fluctuation phenomenon conducive to the formation of new phases in the dynamic system near the critical point before it changes from one phase state to another (Scheffer, 2009). During the failure process of rock samples, the change of crack motion form during the initiation and propagation of cracks to the failure process of crack instability can be regarded as the transformation process from one phase to another, which is accompanied by the surge of ringing count. This change trend is not only manifested as an increase of the signal amplitude, but also accompanied by a slow recovery rate and the weakening ability to recover to the old phase (Nes and Scheffer, 2007; Scheffer et al., 2009).

According to the critical moderation principle, the variance is a characteristic quantity that describes the extent to which the data in the sample deviates from the mean $\bar{x}$, denoted as s^2:

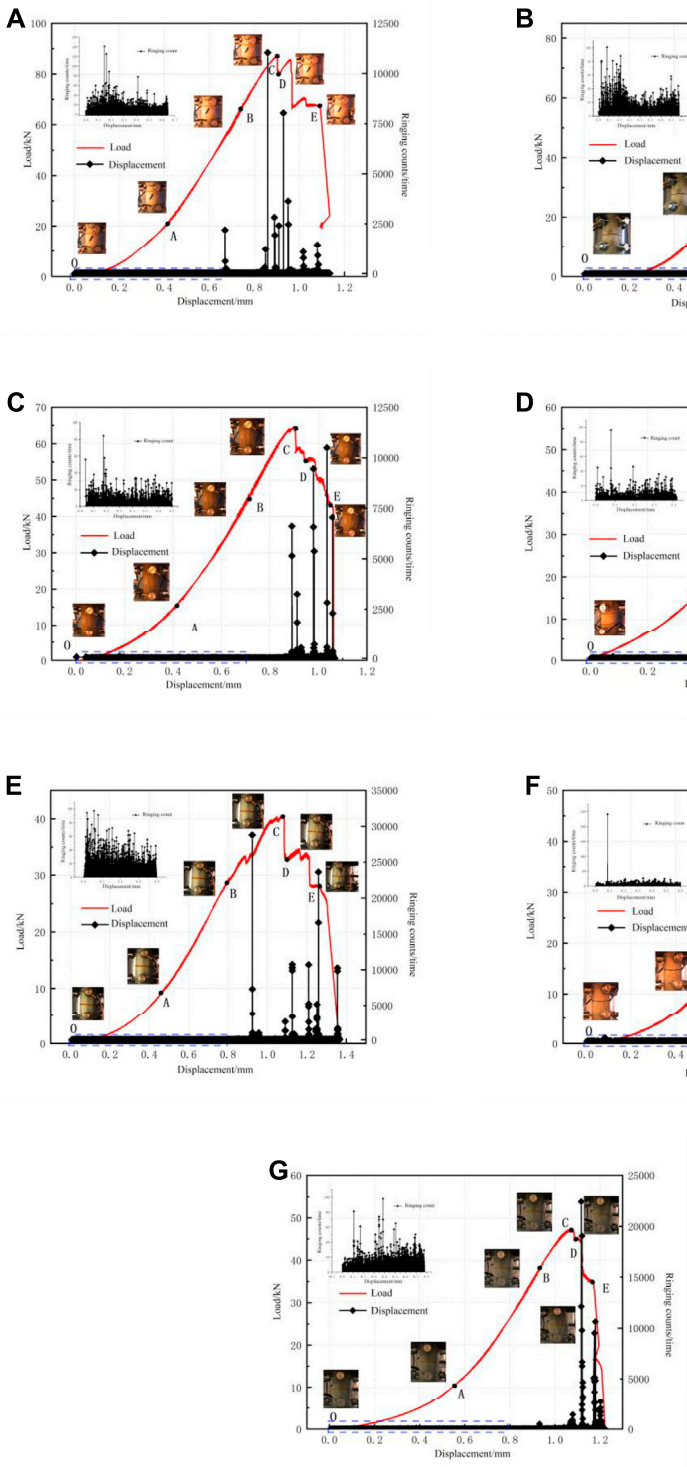


FIGURE 2
The acoustic emission (AE) signal of loading process: **(A)** 0%, **(B)** 30%, **(C)** 60%, **(D)** 75%, **(E)** 85%, **(F)** 95%, **(G)** 100%.

$$s^2 = \frac{1}{n}\sum_{i=1}^{n}\left(x_i - \bar{x}\right)^2 \quad (1)$$

where x_i represents the ith data, and n is the number of data in the sample.

The auto-correlation coefficient is a statistic that describes the correlation between different moments of the same variable. The auto-correlation coefficient of the variable x with a lag length of j is denoted by $\alpha(j)$:

$$\alpha(j) = \sum_{i=1}^{n-j}\left(\frac{x_i - \bar{x}}{s}\right)\left(\frac{x_{i+j} - \bar{x}}{s}\right) \quad (2)$$

Assume that the stage variable has a forced disturbance with the period Δt, in the process of disturbance, the equilibrium regression is in an approximate exponential relationship with the recovery speed λ. The model can be expressed as:

$$x_{n+1} = e^{\lambda\Delta t}x_n + s\epsilon_n \quad (3)$$

where x_n is the deviation from the system stage variable to the equilibrium stage, ϵ_n is a random quantity with normal distribution, s is the mean square error, if λ and Δt do not depend on x_n , Eq. 3 can be simplified as:

$$x_{n+1} = \alpha x_n + s\epsilon_n \quad (4)$$

where $\alpha = e^{\lambda\Delta t}$ is the auto-correlation coefficient.

Equation 4 is analyzed by the variance:

$$Var(x_{n+1}) = E(x_n^2) + \left(E(x_n^2)\right)^2 = \frac{s^2}{1-\alpha^2} \quad (5)$$

When the dynamic system approaches the critical point, the recovery rate of small amplitude disturbance will be slower and slower, and the recovery rate λ, the auto-correlation coefficient α, and the variance will be close to 0, 1, and infinity respectively. Therefore, the increase of auto-correlation coefficient and variance can be used as precursors for the system to approach the critical point.

3.3 Effects of different windows and lag steps

The AE signals collected by sandstone in the process of uniaxial compression were used to investigate the variation law of the critical slowdown in different windows and lag steps. Due to the similar law obtained by different saturations, the critical slowdown in the process of sandstone compression under saturation is listed here.

In the process of studying the auto-correlation coefficient and variance of critical slowdown characteristics in dynamic systems, there were advantages and disadvantages in parameter data (Dakos et al., 2012). Firstly, the meanings of the window length and lag step length were defined. Here the window length referred to the basic unit for sequence calculation, the lag step length to the lag sequence length from the sequence of the selected window length to another new sequence, the variance to that of the new sequence obtained by the selected window length and the lag fixed step length, and the auto-correlation coefficient to the correlation between the sequence of selected window length and the new sequence obtained by the lag fixed step length. The parameter amount of the data representing system was particularly important: the larger the amount of data selected was, the more reliable the early warning signal in the system was (Carpenter et al., 2011). At the same time, as a non-destructive monitoring technology, the AE technology has been widely used in geotechnical engineering monitoring. Therefore, the AE signal was selected to study the influence of different window lengths and lag steps on the critical slowdown phenomenon.

By using the AE signals collected in the uniaxial compression process of sandstone, the changing rule of critical slowdown with different window and lag step lengths was found. Different window lengths and lag steps have an impact on the stability of the auto-correlation coefficient and variance. According to Figure 3, the influence of different window lengths on variance and auto-correlation coefficient was studied when the window lengths were 1,000, 1,500 and 2000 with the same lag step. According to Figure 4, the influence of different lag steps on variance and auto-correlation coefficient was studied when the lag steps were 100, 200 and 300 with the same window length.

From Figures 3A,B,E, it can be seen that when the lag step is constant, the auto-correlation coefficient curves corresponding to the window lengths of 1,000, 1,500 and 2000 are almost coincident, and the fluctuation trend is consistent. With the increase of window length, the fluctuation shows a gradually stable trend. With the increase of lag step, the fluctuation range of auto-correlation coefficient curve also increases. For the variance curve, the variances under the same lag step and different window lengths are no longer coincident, and the variation ranges are slightly different. The fluctuation range decreases with the increase of the window length, but the mutation point is slightly advanced with the increase of the window length. The variance curves of different lag steps are basically coincident under the same window length—The variance curve does not change with the lag step length. It can be seen from Figure 4 that under the same window length, the auto-correlation coefficient curves corresponding to different lag steps are chaotic and do not show certain rules, but most of the variance curves corresponding to different lag steps overlap. When the lag step is 100, the variance of the precursor signal is the largest. When the lag step is 200 and 300, the variance of the precursor signal decreases in turn. And with the increase of lag step, the variance curve mutation point corresponding to the smaller displacement. Comparing Figures 4B,D,F, with the increase of the window length, the amplification of the inflection point of the variance

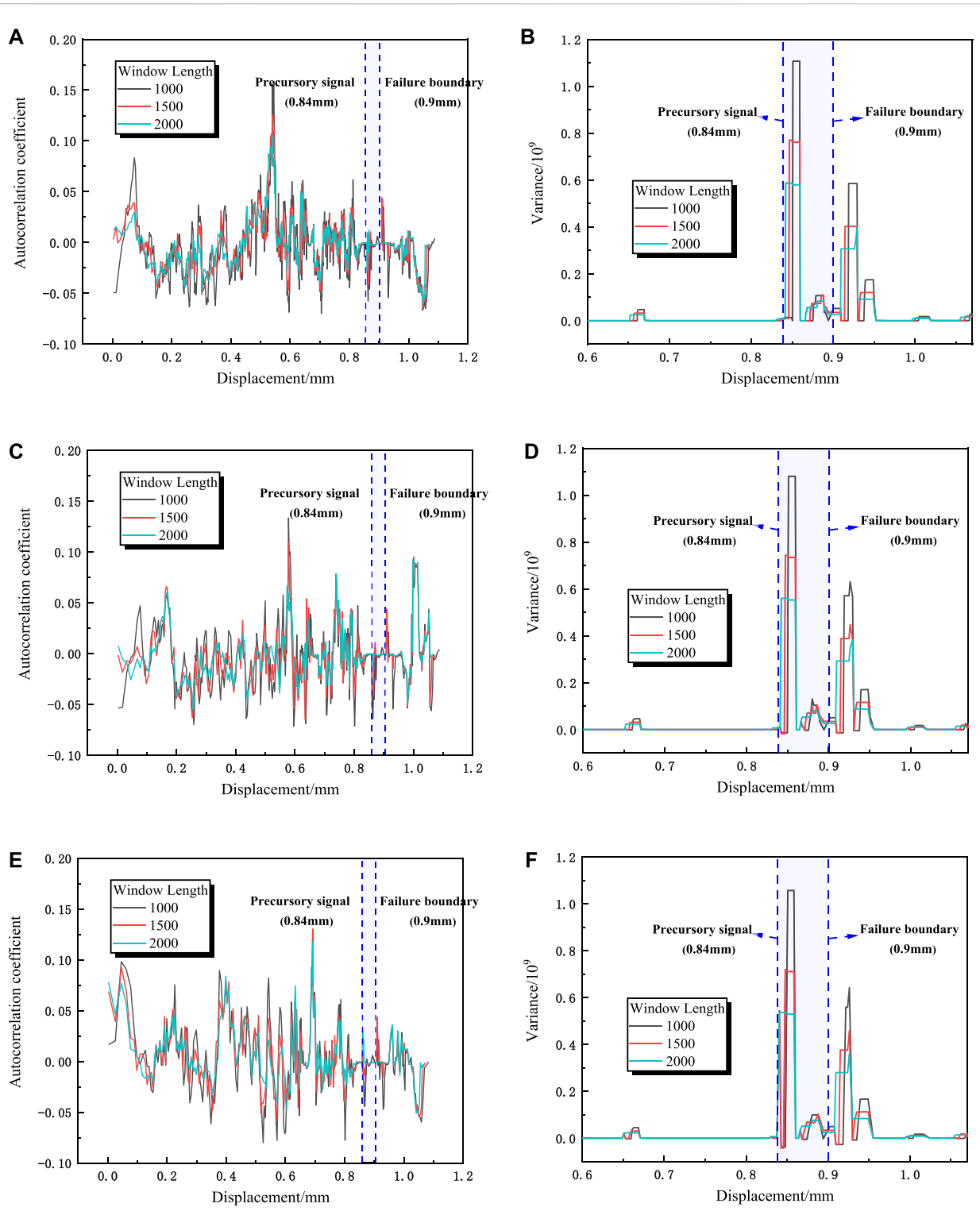


FIGURE 3
The self-correlation coefficient and variance variation characteristics of different window lengths **(A,B)**:lag step length 100, **(C,D)**:lag step length 200, **(E,F)**:lag step length 300).

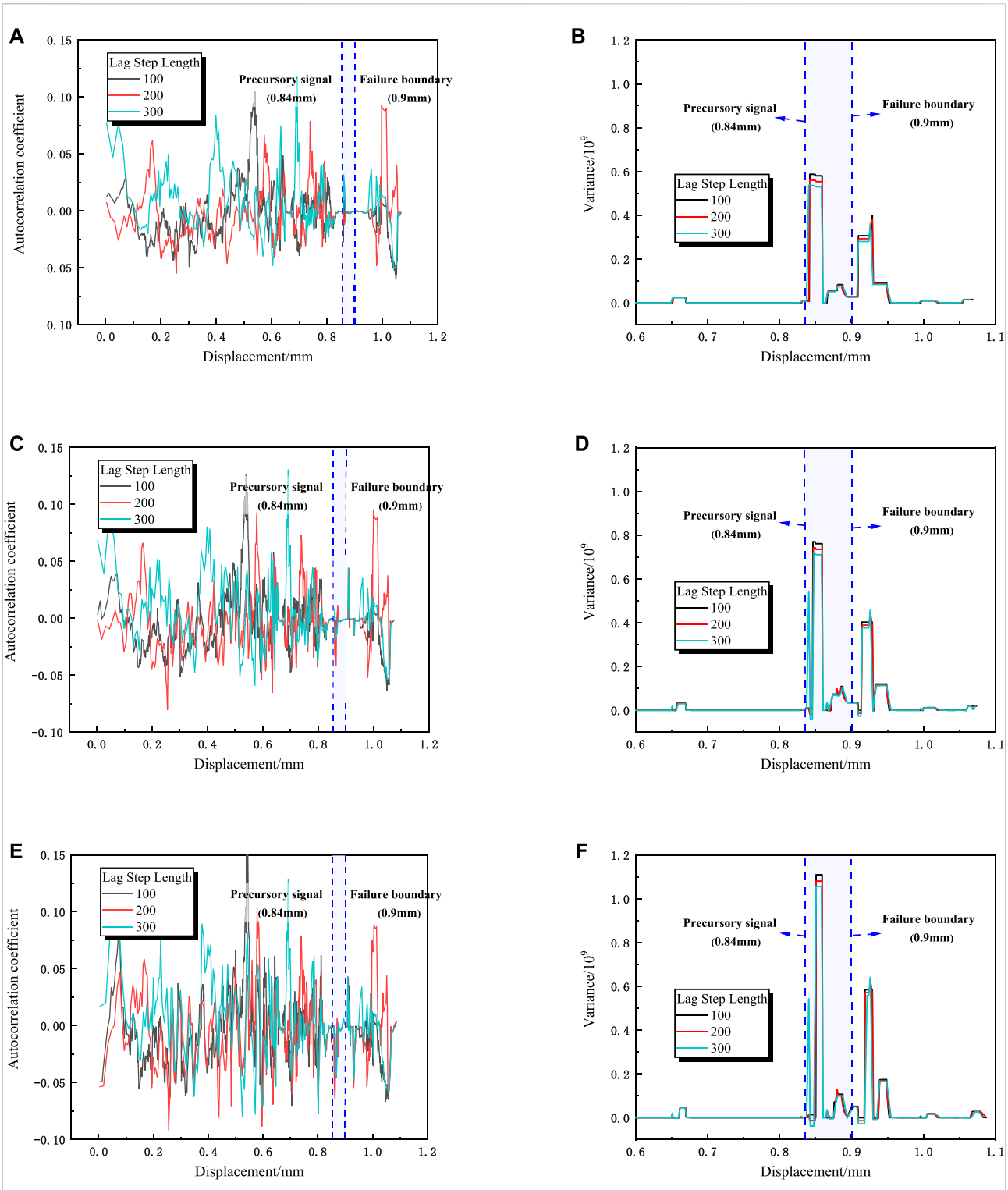


FIGURE 4
The self-correlation coefficient and variance variation characteristics of different lag steps **(A,B)**:window length 2000, **(C,D)**:window length 1,500, **(E,F)**:window length 1,000).

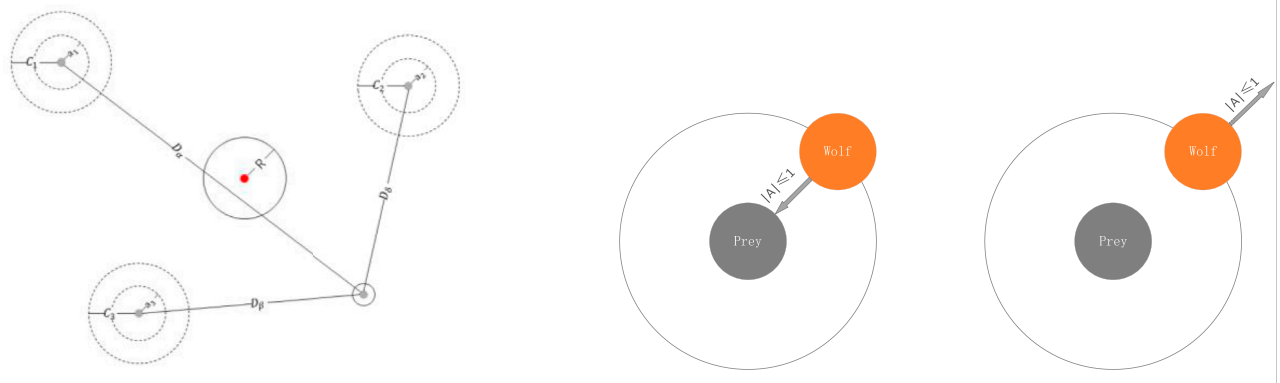


FIGURE 5
Chart of grey wolf searching and attacking prey.

curve corresponding to the same lag step decreases, consistent with the conclusion of Li et al. (2021), Wei et al. (2018).

Through the comparison between Figure 3 and Figure 4, it can be found that the precursor points located by the auto-correlation coefficient and variance are about 0.84 mm, and the failure position is 0.9 mm, reaching 90% of the sandstone strength, which can better characterize the sample entering the dangerous fracture stage. By comparing the auto-correlation coefficient curve and the variance curve, it is found that the auto-correlation coefficient curve has more peaks, that is, more spurious signals are generated in the auto-correlation coefficient curve. Compared with the auto-correlation coefficient, the variance trend is more intuitive, the mutation point (precursor point) is easier to be identified, and is less affected by the lag length selection. Therefore, in terms of monitoring and early warning, the variance trend is more suitable as a precursor for the failure of sandstone samples.

4 A GWO-BP neural network based early warning model for rock failure in cold regions

4.1 GWO-BP neural network

The BP neural network algorithm is a widely used neural network, which is essentially a gradient descent method. The objective function to be optimized is very complex, which leads to the slow convergence of the BP neural network algorithm. The selection of BP neural network structure lacks a unified and complete theoretical guidance, instead it generally depends on experience. Therefore, how to select an appropriate network structure for application is an important issue. Aiming at overcoming the shortcomings of BP neural network, the GWO algorithm is employed.

GWO is a new swarm intelligence optimization algorithm proposed by Mirjailili et al. (2014). Its core is to optimize the dynamic process of parameters by simulating the hunting process of grey wolves in searching, enclosing, and attacking prey. In order to mathematically model the social hierarchy of wolves when designing GWO, the optimal scheme is defined as α, and the second and third best schemes are β and δ respectively. The GWO algorithm is the process of expelling and surrounding the optimization target by ω under the guidance of α, β, and δ wolves (Gupta and Deep, 2019). The diagram is shown in Figure 5.

The first step is to lock the target and surround it. The following equations are proposed:

$$\vec{D} = \left|\vec{C} \cdot \overrightarrow{X_p}(t) - \vec{X}(t)\right| \tag{6}$$

$$\vec{X}(t+1) = \overrightarrow{X_p}(t) - \vec{D} \cdot A \tag{7}$$

where t denotes the current iteration, $\vec{A}$ and $\vec{C}$ are coefficient vectors, $\overrightarrow{X_p}$ is the position vector of prey, $\vec{X}$ is the position vector of the grey wolf. The calculation formulas of $\vec{A}$ and $\vec{C}$ are as follows:

$$\vec{A} = 2\vec{a} \cdot \overrightarrow{r_1} - \vec{a} \tag{8}$$

$$\vec{C} = 2 \cdot \overrightarrow{r_2} \tag{9}$$

where $\vec{a}$ is the convergence factor, and as the number of iterations decreases linearly from 2 to 0, the modulus between $\overrightarrow{r_1}$ and $\overrightarrow{r_2}$ is [0, 1].

$$a = 2 - 2 \cdot \frac{t}{t_{max}} \tag{10}$$

$\overrightarrow{D_\alpha}$, $\overrightarrow{D_\beta}$, and $\overrightarrow{D_\delta}$ corresponds to the distance between α, β, δ and other individuals, $\overrightarrow{X_\alpha}$, $\overrightarrow{X_\beta}$, and $\overrightarrow{X_\delta}$ represent the current positions of α, β, and δ, respectively, $\overrightarrow{C_1}$, $\overrightarrow{C_2}$, and $\overrightarrow{C_3}$ are the random vector, and $\vec{X}$ is the position of the current grey wolf.

The last step is attacking, which is to obtain the optimal solution. The solution is mainly obtained by reducing the value of

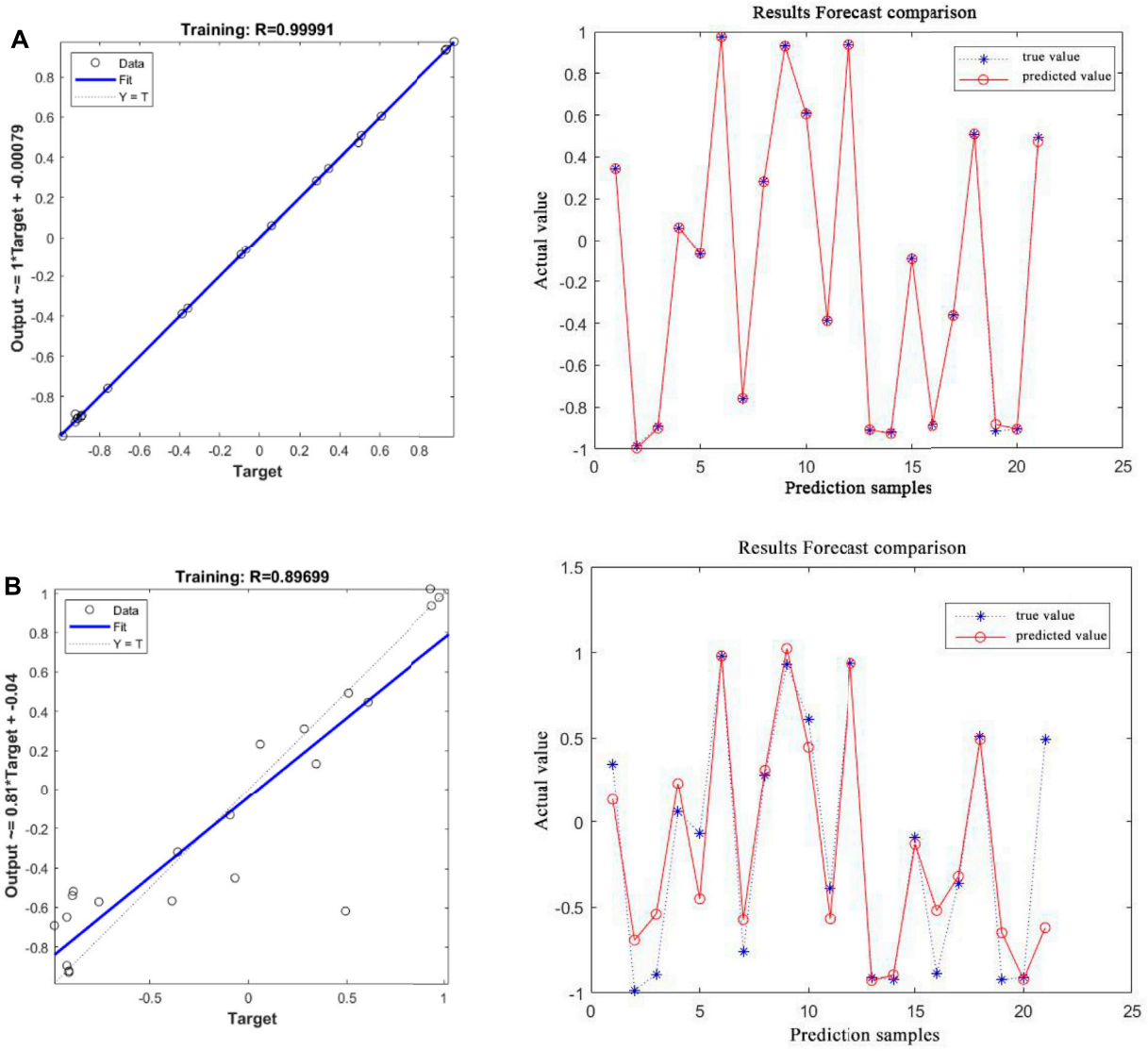


FIGURE 6
Comparison of the prediction results of precursors: **(A)** GWO-BP, **(B)** BP.

$\vec{a}$, and $\vec{A}$ varies within the interval $[-2\vec{a}, 2\vec{a}]$. When the value of A is within the interval and $|a| \leq 1$, the wolf can attack the prey.

$$\begin{cases} \overrightarrow{X_1} = \left|\overrightarrow{X_\alpha} - A_1 \cdot \overrightarrow{D_\alpha}\right| \\ \overrightarrow{X_2} = \left|\overrightarrow{X_\beta} - A_2 \cdot \overrightarrow{D_\beta}\right| \\ \overrightarrow{X_3} = \left|\overrightarrow{X_\delta} - A_3 \cdot \overrightarrow{D_\delta}\right| \end{cases} \tag{11}$$

$$\vec{X}(t+1) = \frac{\overrightarrow{X_1} + \overrightarrow{X_2} + \overrightarrow{X_3}}{3} \tag{12}$$

Equation 6 defines the step length and the direction of ω individuals in the wolves towards α, β, and δ, and Eq. 7 defines the final position of ω.

Based on the divergence of mathematical modeling, the global search of the GWO algorithm is realized by adjusting the value of $\vec{A}$. When $|\vec{A}| > 1$, the grey wolf of the global search is separated from the target, and the global search continues to find more suitable prey. The GWO algorithm also has another component $\vec{C}$ to help find new solutions, Eq. 9 shows that $\vec{C}$ is a random value within [0, 2], C represents the random weight of the impact of the location of the wolf on the prey, $\overrightarrow{C} > 1$ indicates that the impact weight is significant, and *vice versa*. This helps the GWO algorithm to perform more randomly and support exploration, while avoiding falling into local optimum in the optimization process. In addition, $\vec{C}$ is non-linearly reduced, thus from the initial iteration to the final

TABLE 1 Selection of neural network parameters.

Input layer neurons	5
Hidden layer	1
Implicit layer neurons	10
Output layer neurons	1
Training function	Trainlm
Algorithm	Levenberg–Marquardt BP algorithm
Maximum training times	15,000
Training error	0.01

iteration, it provides global search in decision space. When the algorithm falls into local optimum and is not easy to jump out, the randomness of $\vec{C}$ plays a very important role in avoiding local optimum, especially in the iteration which calls for a global optimal solution.

BP model randomly allocates the weight matrix and threshold of the hidden layer neurons between the input layer and hidden layer, containing many variable parameters that are difficult to control, and the results are unstable. The GWO-BP algorithm can effectively extract the optimal matrix connecting weights and thresholds, and can dynamically optimize the penalty factor and kernel parameters of the BP neural network, so as to achieve the relatively stable prediction results. The core of the GWO-BP algorithm is to take the weights and thresholds of the BP neural network as the position information $X(t)$ of the grey wolf, and the updated position is equal to the weights and thresholds of the BP neural network, so as to find out the global optimal value. The specific steps are as follows:

1) Extract the feature vectors and normalize these data.
2) Initialize the deviations and weights, and set the minimum error, maximum number of iterations, and learning rate.
3) Initialize the GWO algorithm, set the number of wolves and the maximum number of iterations, use the initial deviations and weights as the initial solutions to find the optimal solution.
4) For the training of BP neural network, use the output of each layer to calculate the training errors and adjust the deviations and weights of each layer, repeat this operation until the maximum number of iterations or error is less than the threshold.
5) Test the BP neural network by using the test data to determine whether the accuracy meets the requirements.

4.2 A GWO-BP based early warning model of rock failure in cold regions

Freeze–thaw damage of rock mass poses a great threat to the safety of rock engineering, stone buildings, and low-temperature storage of liquefied natural gas (LNG) in cold regions. How to prevent and manage freeze–thaw disasters is what this paper considered, and what is more suitable than managing freeze–thaw disasters is for preventing disasters. At present, with the improvement of monitoring means, plenty of real-time monitoring data of rock engineering can be extracted, therefore, in this paper, the AE equipment is used as the monitoring method to analyze the critical slowdown in the process of rock failure, and the precursors of rock failure is obtained, a warning model of rock failure in cold regions is proposed through the GWO-BP neural network. The specific steps are as follows:

1) The failure process of engineering rock samples in cold regions under different environments was selected for AE monitoring.
2) The critical slowdown of rock samples under various working conditions was analyzed to obtain the failure precursors.
3) The GWO-BP neural network was constructed, and the effective influencing factors were selected to predict the precursors and strength. In this paper, 105 groups of experiments under 21 working conditions of sandstone in cold regions were carried out to establish and test the network.
4) The AE signal of rock engineering was monitored, and the GWO-BP neural network was imported to obtain the strength value at this time. Compared with the precursor points, the early warning was carried out.

4.3 Verification of early warning model

BP neural network is usually composed of input layer, hidden layer and output layer. The number of input and output neurons is determined by the parameters needed for modeling, while the number of nodes and layers in hidden layer is not fixed, which will have a certain impact on the performance of BP neural network. In the present study, as listed in Table 1, The input layer consisted of five neurons, one for each independent variable, which typically influenced the sandstone failure process, these variables included saturation, density, longitudinal wave velocity, freeze-thaw times and porosity. The output layer consisted of only one neuron,i.e. precursory signal. Generally speaking, too few neurons in the hidden layer will lead to a decrease in the prediction accuracy of the network, and there will be under-fitting. Increasing the number of neurons can improve the accuracy of the model, but if the number of nodes is too large, it may make the model over-fitting. Therefore, in the construction of this model, the hidden layer selected one layer since one hidden layer was considered sufficient for developing a sound neural network, and the number of neurons in the hidden layer was determined to be 10 by using the method of minimizing network error, which had the highest accuracy. The training algorithm used the Levenberg-Marquardt back propagation method to minimize the mean squared error (MSE) (Low

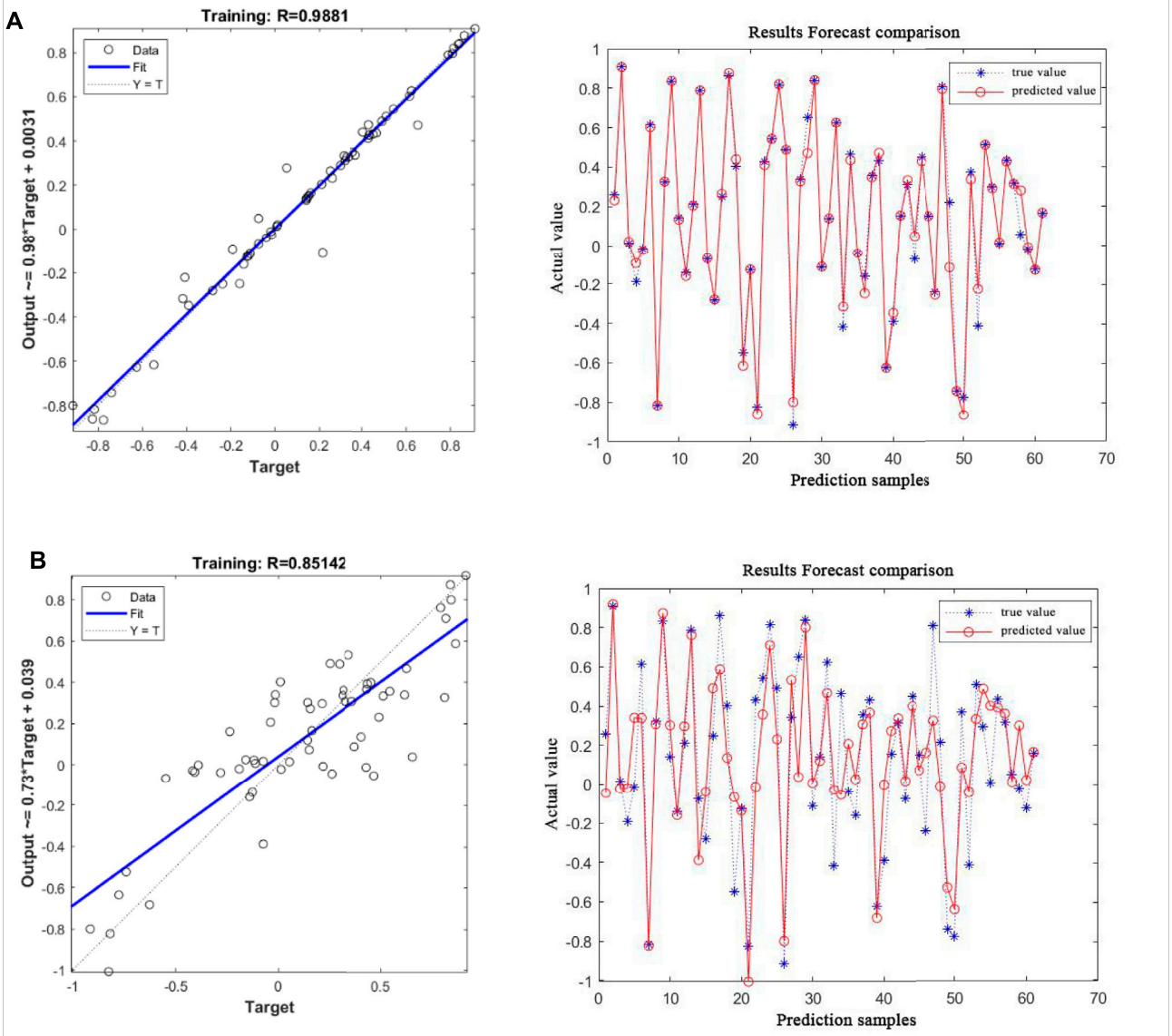


FIGURE 7
Comparison of the strength prediction results: **(A)** GWO-BP, **(B)** BP.

MSE indicates good performance of neural network). With the increase of training error, the influence of the output error of the model on the parameters will increase, and the speed of parameter updating will be faster, but the parameters will be disturbed by a large number of abnormal data at the same time, and it is very easy to diverge. In this paper, the training error was set to 0.01 of the default. The maximum number of training times was selected to be 15,000. In the GWO model, the population was 20 and the maximum number of iterations was 15.

Firstly, the precursors were predicted according to the uniaxial tests of 105 frozen–thawed sandstones. 4 groups of parallel tests (84 in total) under each working condition are selected for network training. One is selected for each working condition to predict the precursor signals, and the correlation between the predicted value and the real value was used to determine the pros and cons of the prediction.

Then, according to the intensity prediction of AE signals, the number of AE ringing, energy, duration, and impact number were extracted as characteristic parameters. A total of 84,760 groups of data were selected, and 84,700 groups of data were randomly selected for network training. The

remaining 60 groups of data were used to test the accuracy of the network.

By comparing the results of the precursors and intensity in GWO-BP and BP predictions (Figures 6, 7), it is found that the correlation between the BP neural network prediction value and the real value is 0.8514. The correlation coefficient between the predicted value and the real value of BP neural network optimized by GWO reaches 0.9990 and 0.9881 respectively, which greatly improves the prediction accuracy. The predicted value of the GWO-BP neural network is credible. The precursor warning model provides a new guarantee for the safety of rock engineering in cold regions.

5 Conclusion

In this paper, TAW is used to load the freeze-thaw sandstone with different saturations, and the loading process is recorded by acoustic emission. The critical slowing down theory is used to analyze the acoustic emission signal during the loading process of sandstone. Based on GWO-BP algorithm, the precursor signal warning model of rock failure in cold region is constructed. The conclusions are as follows.

1) During the whole loading process, the acoustic emission ringing count corresponds well with the damage and failure process of sandstone, showing obvious stages. Therefore, according to the change of ringing count in the failure process of rock samples, the damage and failure process of sandstone is divided into initial compaction stage, slow growth stage, rapid growth stage and failure stage. There are many mutations in the ringing count in the rapid growth stage, so the on-site monitoring and early warning need to eliminate these false signals through improved algorithms to improve prediction accuracy.
2) The window length and lag step length have little effect on the occurrence time of the precursory characteristics of the variance, but have a great influence on the stability of the auto-correlation coefficient. Compared with the auto-correlation coefficient, the variance trend is more intuitive and the precursory points are easier to identify. Therefore, in terms of monitoring and early warning, the variance trend is more suitable as a precursory point for sandstone sample failure prediction.
3) The grey wolf algorithm is introduced to optimize the penalty factor and kernel parameters of BP neural network. An early signal warning model is constructed based on GWO-BP algorithm to warn the failure of rock failure. After data comparison, the correlation coefficient between the predicted value obtained by this model and the real value reaches 0.999 and 0.9881, and the prediction effect is excellent. Precursory signal warning model provides a new guarantee for the safety of rock engineering in cold regions.

Data availability statement

The original contributions presented in the study are included in the article/supplementary material, further inquiries can be directed to the corresponding authors.

Author contributions

JJ provided the research direction and research plan of the manuscript, XZ was responsible for obtaining experimental data and writing the first draft of the article, XL was responsible for revising the first draft, YL was responsible for analyzing experimental data and drawing, and SL was responsible for developing the GWO-BP neural network.

Funding

This work was supported by the National Key Research and Development Program of China (Grant No. 2018YFC1504801), National Natural Science Foundation of China (Grant No.52079068, Grant No.52274206), and State Key Laboratory of Hydroscience and Hydraulic Engineering (Grant No. 2021-KY-04).

Conflict of interest

The authors declare that the research was conducted in the absence of any commercial or financial relationships that could be construed as a potential conflict of interest.

Publisher's note

All claims expressed in this article are solely those of the authors and do not necessarily represent those of their affiliated organizations, or those of the publisher, the editors and the reviewers. Any product that may be evaluated in this article, or claim that may be made by its manufacturer, is not guaranteed or endorsed by the publisher.

References

Carpenter, S. R., Cole, J. J., Pace, M. L., Batt, R., Brock, W. A., Cline, T., et al. (2011). Early warnings of regime shifts: A whole-ecosystem experiment. *Science* 332 (6033), 1079–1082. doi:10.1126/science.1203672

Chai, Y., Huang, D., and Ling, Z. (2016). "A short-term traffic flow prediction method based on wavelet analysis and neural network," in Control & Decision Conference, Yinchuan, China, 28-30 May 2016.

Dai, S., Liu, X., and Nawnit, K. (2019). Experimental study on the fracture process zone characteristics in concrete utilizing DIC and AE methods. *Appl. Sci.* 9 (7), 1346. doi:10.3390/app9071346

Dakos, V., Nes, E., D'Odorico, P., and Scheffer, M. (2012). Robustness of variance and autocorrelation as indicators of critical slowing down. *Ecology* 93 (2), 264–271. doi:10.1890/11-0889.1

Girard, L., Gruber, S., Weber, S., and Beutel, J. (2013). Environmental controls of frost cracking revealed through *in situ* acoustic emission measurements in steep bedrock. *Geophys. Res. Lett.* 40 (9), 1748–1753. doi:10.1002/grl.50384

Gupta, S., and Deep, K. (2019). "Hybrid grey wolf optimizer with mutation operator: SocProS 2017, volume 2," in *Soft computing for problem solving*. Editors J. C. Bansal, K. N. Das, A. Nagar, K. Deep, and A. K. Ojha (Berlin, Germany: Springer).

Huang, Y.-H., Yang, S.-Q., Tian, W.-L., Zeng, W., and Yu, L.-Y. (2016). An experimental study on fracture mechanical behavior of rock-like materials containing two unparallel fissures under uniaxial compression. *Acta Mech. Sin.* 32 (03), 442–455. doi:10.1007/s10409-015-0489-3

Kock, T. D., Boone, M. A., Schryver, T. D., Stappen, J. V., Derluyn, H., Masschaele, B., et al. (2015). A pore-scale study of fracture dynamics in rock using X-ray micro-CT under ambient freeze-thaw cycling. *Environ. Sci. Technol.* 49 (5), 2867–2874. doi:10.1021/es505738d

Kong, L., Wang, Y., Sun, W., and Qi, J. (2020). Influence of plasticity on unfrozen water content of frozen soils as determined by nuclear magnetic resonance. *Cold Regions Sci. Technol.* 172, 102993. doi:10.1016/j.coldregions.2020.102993

Kong, X., Wang, E., He, X., Li, D., and Liu, Q. (2017). Time-varying multifractal of acoustic emission about coal samples subjected to uniaxial compression. *Chaos Solit. Fractals* 103, 571–577. doi:10.1016/j.chaos.2017.07.015

Kong, X., Wang, E., Hu, S., Li, Z., Zhan, T., Fang, B., et al. (2015). Critical slowing down on acoustic emission characteristics of coal containing methane. *J. Nat. Gas Sci. Eng.* 24, 156–165. doi:10.1016/j.jngse.2015.03.020

Leemput, I. A. V. D., Wichers, M., Cramer, A. O. J., Borsboom, D., Tuerlinckx, F., Kuppens, P., et al. (2013). Critical slowing down as early warning for the onset and termination of depression. *Proc. Natl. Acad. Sci. U. S. A.* 111, 87–92. doi:10.1073/pnas.1312114110

Lei, X., Masuda, K., Nishizawa, O., Jouniaux, L., Kusunose, K., Ma, W., et al. (2004). Detailed analysis of acoustic emission activity during catastrophic fracture of faults in rock. *J. Struct. Geol.* 26 (2), 247–258. doi:10.1016/s0191-8141(03)00095-6

Li, H., Shen, R., and Qiao, Y. (2021). Acoustic emission signal characteristics and its critical slowing down phenomenon during the loading process of water-bearing sandstone. *J. Appl. Geophys.* 194, 104458.

Liu, Q., Zhao, Y., Tang, L., Liao, J., Wang, X., Tan, T., et al. (2022). Mechanical characteristics of single cracked limestone in compression-shear fracture under hydro-mechanical coupling. *Theor. Appl. Fract. Mech.* 119, 103371. doi:10.1016/j.tafmec.2022.103371

Liu, X., Han, G., Wang, E., Wang, S., and Nawnit, K. (2018). Multiscale hierarchical analysis of rock mass and prediction of its mechanical and hydraulic properties. *J. Rock Mech. Geotechnical Eng.* 10, 694–702. doi:10.1016/j.jrmge.2018.04.003

Maturana, M. I., Meisel, C., Dell, K., Karoly, P. J., Freestone, D. R., Grayden, D. B., et al. (2020). Critical slowing down as a biomarker for seizure susceptibility. *Nat. Commun.* 11 (1), 2172. doi:10.1038/s41467-020-15908-3

Mirjalili, S., Mirjalili, S. M., and Lewis, A. (2014). Grey wolf optimizer. *Adv. Eng. Soft.* 69, 46–61.

Nes, E., and Scheffer, M. (2007). Slow recovery from perturbations as a generic indicator of a nearby catastrophic shift. *Am. Nat.* 169 (6), 738–747. doi:10.1086/516845

Park, J., Hyun, C. U., and Park, H. D. (2015). Changes in microstructure and physical properties of rocks caused by artificial freeze–thaw action. *Bull. Eng. Geol. Environ.* 74 (2), 555–565. doi:10.1007/s10064-014-0630-8

Rumelhart, D. E., Hinton, G. E., and Williams, R. J. (1986). Learning representations by back-propagating errors. *Nature* 323, 533–536. doi:10.1038/323533a0

Scheffer, M., Bascompte, J., Brock, W. A., Brovkin, V., Carpenter, S. R., Dakos, V., et al. (2009). Early-warning signals for critical transitions. *Nature* 461 (7260), 53–59. doi:10.1038/nature08227

Scheffer, M. (2009). *Critical transitions in nature and society*. New Jersey, United States: Princeton University Press.

Tan, X., Chen, W., Liu, H., Wang, L., Ma, W., and Chan, A. (2018). A unified model for frost heave pressure in the rock with a penny-shaped fracture during freezing. *Cold Regions Sci. Technol.* 153, 1–9. doi:10.1016/j.coldregions.2018.04.016

Wei, Y., Li, Z., and Kong, X. (2018). The precursory information of acoustic emission during sandstone loading based on critical slowing down theory. *J. Geophys. Eng.* 15 (5), 2150–2158.

Xia, Y., Liu, B., Zhang, C., Liu, N., Zhou, H., Chen, J., et al. (2022). Investigations of mechanical and failure properties of 3D printed columnar jointed rock mass under true triaxial compression with one free face. *Geomech. Geophys. Geo. Energy. Ge. Resour.* 8 (1), 26–24. doi:10.1007/s40948-021-00331-9

Xie, S., Lin, H., Wang, Y., Chen, Y., Xiong, W., Zhao, Y., et al. (2020). A statistical damage constitutive model considering whole joint shear deformation. *Int. J. Damage Mech.* 29 (6), 988–1008. doi:10.1177/1056789519900778

Zhang, J., Deng, H., Taheri, A., Ke, B., and Liu, C. (2019). Deterioration and strain energy development of sandstones under quasi-static and dynamic loading after freeze-thaw cycles. *Cold Regions Sci. Technol.* 160, 252–264. doi:10.1016/j.coldregions.2019.01.007

Zhang, S., and Zhou, Y. (2015). Grey wolf optimizer based on powell local optimization method for clustering analysis. *Discrete Dyn. Nat. Soc.* 2015, 1–17. doi:10.1155/2015/481360

Zhao, Y., Liu, Q., Zhang, C., Liao, J., Lin, H., and Wang, Y. (2021). Coupled seepage-damage effect in fractured rock masses: Model development and a case study. *Int. J. Rock Mech. Min. Sci.* 144, 104822. doi:10.1016/j.ijrmms.2021.104822

Zhao, Y., Wang, Y., Wang, W., Tang, L., Liu, Q., and Cheng, G. (2019). Modeling of rheological fracture behavior of rock cracks subjected to hydraulic pressure and far field stresses. *Theor. Appl. Fract. Mech.* 101, 59–66. doi:10.1016/j.tafmec.2019.01.026

frontiers | Frontiers in Earth Science

TYPE Original Research
PUBLISHED 16 January 2023
DOI 10.3389/feart.2022.1031665

Check for updates

OPEN ACCESS

EDITED BY
Guang-Liang Feng,
Institute of Rock and Soil Mechanics (CAS), China

REVIEWED BY
Wenjing Niu,
Guangxi University, China
Subodh Chandra Pal,
University of Burdwan, India

*CORRESPONDENCE
Wenyuan Wu,
wuwy@hznu.edu.cn

SPECIALTY SECTION
This article was submitted to Geohazards and Georisks, a section of the journal Frontiers in Earth Science

RECEIVED 30 August 2022
ACCEPTED 09 November 2022
PUBLISHED 16 January 2023

CITATION
Xu L, Wu W, Qian J, Huang S, Xie B, Hu T, Lang X, He B and Hu C (2023), Analysis of geothermal potential in Hangjiahu area based on remote sensing and geographic information system. *Front. Earth Sci.* 10:1031665. doi: 10.3389/feart.2022.1031665

COPYRIGHT
© 2023 Xu, Wu, Qian, Huang, Xie, Hu, Lang, He and Hu. This is an open-access article distributed under the terms of the Creative Commons Attribution License (CC BY). The use, distribution or reproduction in other forums is permitted, provided the original author(s) and the copyright owner(s) are credited and that the original publication in this journal is cited, in accordance with accepted academic practice. No use, distribution or reproduction is permitted which does not comply with these terms.

Analysis of geothermal potential in Hangjiahu area based on remote sensing and geographic information system

Linxia Xu[1], Wenyuan Wu[1,2]*, Junfeng Qian[3,4], Shujia Huang[1], Bin Xie[1,2], Tangao Hu[1,2], Xiayi Lang[1], Bowen He[1] and Chenghao Hu[1]

[1]School of Information Science and Technology, Hangzhou Normal University, Hangzhou, China, [2]Zhejiang Provincial Key Laboratory of Urban Wetlands and Regional Change, Hangzhou Normal University, Hangzhou, China, [3]Zhejiang Bureau of Coal Geology, China National Administration of Coal Geology, Hangzhou, China, [4]Zhejiang Institute of Geology and Mineral Resources, Hangzhou, China

Geothermal resources are one of the most valuable renewable energy sources because of their stability, reliability, cleanliness, safety and abundant reserves. Efficient and economical remote sensing and GIS (Geographic Information System) technology has high practical value in geothermal resources exploration. However, different study areas have different geothermal formation mechanisms. In the process of establishing the model, which factors are used for modeling and how to quantify the factors reasonably are still problems to be analyzed and studied. Taking Hangjiahu Plain of Zhejiang Province as an example, based on geothermal exploration and remote sensing interpretation data, the correlation between the existing geothermal hot spots and geothermal related factors was evaluated in this paper, such as lithology, fault zone distance, surface water system and its distance, seismic point distance, magmatic rock and volcanic rock distance, surface water, farmland, woodland temperature and so on. The relationship between geothermal potential and distribution characteristics of surface thermal environment, fault activity, surface water system and other factors was explored. AHP (Analytic Hierarchy Process) and BP (Back Propagation) neural network were used for establishing geothermal potential target evaluation models. The potential geothermal areas of Hangjiahu Plain were divided into five grades using geothermal exploration model, and most geothermal drilling sites were distributed in extremely high potential areas and high potential areas. The results show that it is feasible to analyze geothermal potential targets using remote sensing interpretation data and geographic information system analysis databased on analytic hierarchy process analytic hierarchy process and back propagation neural network, and the distribution characteristics of surface thermal environment, fault activity, surface water system and other related factors are also related to geothermal distribution. The prediction results of the model coincide with the existing geothermal drilling sites, which provides a new idea for geothermal exploration.

KEYWORDS

geothermal resource, land surface temperature, analytic hierarchy process, back propagation neural network, geographic information system technology

1 Introduction

Geothermal resource is one of the most valuable renewable energy because of its stable, reliable, clean, safe and abundant reserves (Zhang et al., 2015; Zhou et al., 2015; Zhang et al., 2020). As one of the five non-carbon-based energy sources, geothermal energy has been included in the study of carbon neutral framework roadmap of China to control the total consumption of fossil energy, deepen the reform of the power system, and the geothermal energy industry will usher in new opportunities for development. The overall planning of mineral resources in Zhejiang Province (2021–2025) clearly points out that the development and utilization intensity of clean energy, such as geothermal and shallow low-temperature energy should be increased to form a mineral resources development pattern dominated by geothermal and other minerals. Traditional geothermal exploration is characterized by great difficulty, high economic cost and low success rate. Geothermal geological mapping and geophysical exploration are restricted by many factors, such as river system, residential buildings and multiple solutions of geophysical exploration (Zhang et al., 2016).

Remote sensing and GIS technology with high efficiency and economy have high practical value in geothermal resources exploration. On the one hand, the tone of thermal infrared remote sensing image can reflect the thermal radiation energy of ground objects, and geothermal anomaly information can be directly obtained from thermal infrared remote sensing images in areas with shallow geothermal or hot springs (Liu et al., 2004; Chen et al., 2006; Zhang and Zhang, 2006). On the other hand, based on the principles of geology and geophysics, scholars at home and abroad have established various mathematical models for geothermal resource exploration, and have obtained good results on the distribution characteristics and potential of geothermal water (Noorollahi et al., 2008; Yousefi et al., 2010; Moghaddam et al., 2014; Sadeghi and Khalajmasoumi, 2014; Trumpy et al., 2015; Meng et al., 2021). However, there are still some problems in these works, such as mainly driven by expert prior knowledge, simple model design, low accuracy and universality of the model.

In recent years, many new models have been introduced into the establishment of various geological models. Analytic Hierarchy Process (AHP), Fuzzy Comprehension Evaluation Method (FCEM) and Back Propagation Neural Network (BPNN) have been applied to geological environment exploration and geological prospecting effectively (Yu et al., 2017; Chakrabortty et al., 2018; Pal et al., 2019; Ahmad et al., 2020; Das and Pal, 2020a; Das and Pal, 2020b; Liang et al., 2020; Pang et al., 2020; Shao et al., 2020; Wang and Song, 2021; Pal et al., 2022; Ruidas et al., 2022). AHP and GIS technique have been applied in modeling and mapping of groundwater potentiality zones by factors, such as geology, slope gradient, LULC (land use land cover), soil texture, rainfall, lineament density, drainage density, groundwater fluctuation and so on (Chakrabortty et al., 2018), and also applied in modeling and mapping of potential landslide vulnerability zonation by factors, such as rock type, geomorphology, slope, aspect, drainage density, soil type and land use and land cover (Pal et al., 2019). MCDA, AHP, fuzzy logic and ensemble method in a GIS environment have been used in assessing the vulnerability of groundwater by factors, such as groundwater recharge, geology, ground, elevation, the groundwater level in the pre-monsoon season, soil texture, and LULC (Das and Pal, 2020a; Das and Pal, 2020b). The weight of each factor is calculated by the AHP model, and the geothermal potential target area model is established by BP neural network, which can reduce the dependence of the model on expert prior knowledge and make the delimitation of geothermal target area more intelligent and scientific.

However, different study areas have different geothermal formation mechanisms. In the process of establishing the model, which factors are used for modelling and how to quantify the factors reasonably are still problems to be further analyzed and studied. Many studies have shown that the distribution of geothermal activity is closely related to seismic activity, fault activity, fault fold distribution, igneous rocks and other factors, and the correlation between geothermal potential and various factors has also been evaluated (Johnson, 2014; Mcguire et al., 2015; Li and Zhang, 2017). In recent years, many studies have also shown that geothermal distribution is related to remote sensing surface thermal environment, and surface thermal environment is also related to topography and fault activity to a certain extent (Li and Zhang, 2017; Wu et al., 2019; Peng et al., 2020; Wu et al., 2012a; Wu et al., 2012b), so it can be seen that the distribution characteristics of surface thermal environment, fault activity and topographic characteristics should also be added to the factor quantification. At the same time, it is also found in the survey practice that the surface water system is related to the regional geothermal distribution, which requires the actual factor quantitative analysis and evaluation.

Therefore, in order to use the actual factor quantitative analysis and evaluation to study the correlation between geothermal distribution and remote sensing of surface thermal environment, topography, fault activity and surface water system, and to avoid the problems in previous work, the geothermal exploration area of Hangjiahu Plain in the north of Zhejiang Province was taken as an example in this paper based on remote sensing images and GIS analysis, the spatial distribution correlation characteristics between known

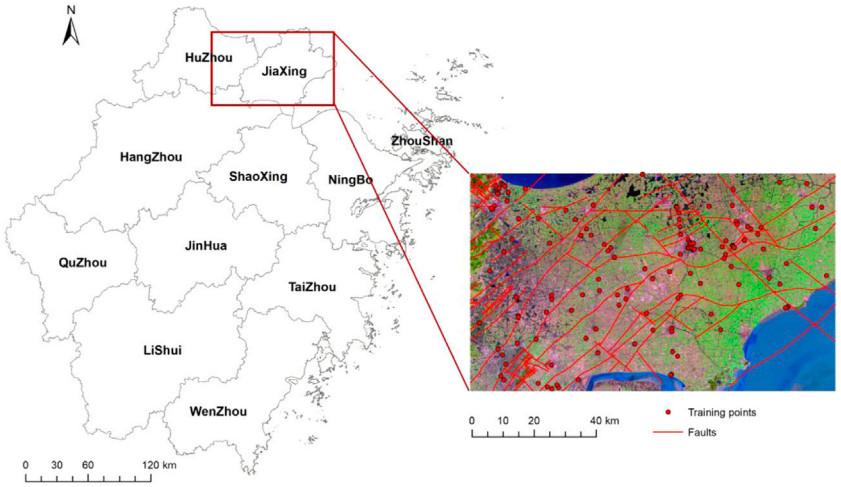


FIGURE 1
Location of study area.

geothermal hot spots and related geothermal factors, such as lithology, fault zone distance, surface water system and its distance, seismic point distance, magmatic rock and volcanic rock distance, surface water, farmland and woodland temperature were studied. In this paper, the AHP and BP neural network was used for establishing the evaluation model of geothermal potential target areas, and the potential areas of geothermal resources in Hangjiahu Plain were divided, providingdecision-making basis and direction for the establishment of geothermal exploration model in Hangjiahu Plain, and providing data and method supports for the construction of ecological and low-carbon Zhejiang.

2 Study area and data

2.1 Overview of the study area

The Study Area is located in the Hangzhou-Jiaxing-Huzhou Plain in the northern part of Zhejiang Province, as shown in Figure 1, which roughly includes the vast area south of Taihu Lake, north of Qiantang River and Hangzhou Bay, east of Tianmu Mountain and west of the East China Sea. Its geographical range is 120° 00′ –121° 15′ E, 30° 20′ –31° 00′ N, and its administrative divisions include Hangzhou, Jiaxing and Huzhou. The area has a subtropical monsoon climate with a dense water network.

Geothermal heat in the Study Area is in the framework of regional faults in NE and EW directions, with Huzhou-Jiashan active fault in the north, Huzhou-Linan active fault in the west and Xiaoshan-Qiuchuan active faults in the east. In addition, the Changxing-Fenghua fault zone and Majin-Wuzhen fault zone cross the region. The intersection of multiple fault zones and the active neotectonic movement have increased the water-bearing space of rocks. In addition, the heat source in the region is mainly deep conduction heat flow balance, and the fault zone is also a good conduction channel, which makes the Hangjiahu plain one of the areas with abundant geothermal resources in Zhejiang Province (Hu et al., 2011).

There are 134 geothermal drilling points in the Study Area, including four geothermal gradient >5°C/100 m anomalies and 19 geothermal gradient >4°C/100 m anomalies. Among them, the water temperature of Huimin Point, Wangdian Point and Jiaxing Cement Plant is 26°C–28°C, which is obviously higher than the normal water temperature calculated according to the average geothermal gradient of Hangjiahu Plain, and belongs to low temperature hot water. Tongxiang No.3 well and Jiashan No.6 well are sudden geothermal hot spots, and the water temperature is kept at 40.95°C and 58 C respectively. These geothermal anomalies indicate that there are more abundant underground hot water resources in the depth of the Study Area due to the shallow depth of exploration boreholes. Geothermal drilling sites, such as geothermal exploration data, can be used for analyzing the spatial correlation between geothermal drilling sites and geothermal factors and verifying the scientificity and rationality of the prediction model results.

2.2 Data source and data preprocessing

Two Landsat 5 TM multi-spectral and thermal infrared images on February 20 and 21, 2002 were used in this study.

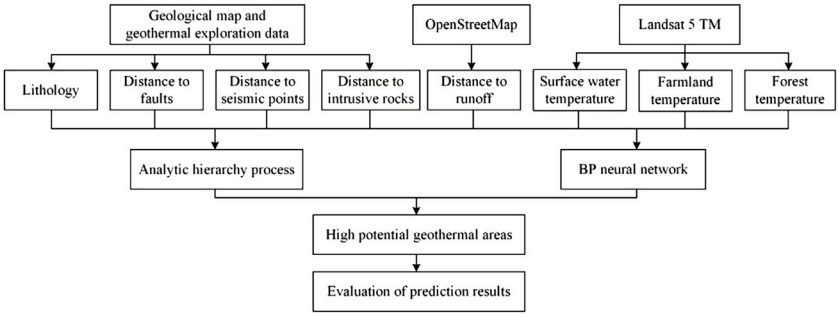


FIGURE 2
Flowchart of the analysis.

The data set was provided by Geospatial Data Cloud, Computer Network Information Center, Chinese Academy of Sciences (http://www.gscloud.cn). Six multi-spectral bands (with a resolution of 30 m) were used for extracting land cover types, and one thermal infrared band (with a resolution of 120 m) was used for retrieving land surface temperature. Selecting historical images can weaken the influence of urban land surface, and selecting winter images can reduce the influence of solar radiation on land surface temperature to some extent. The preprocessing mainly includes radiometric calibration and atmospheric correction to eliminate the radiation errors caused by atmospheric scattering and absorption.

Based on the geological map and geothermal exploration data provided by Zhejiang Coal Geology Bureau of China Coal Geology General Administration, the ArcGIS software was used for vectorization to obtain the geothermal factor data of the Study Area, including stratigraphic lithology, magmatic rock distribution, seismic point distribution, fault zone distribution and so on The vector data of surface water system was obtained by OpenStreetMap (https://www.openstreetmap.org/). These auxiliary data can be used for quantitative analysis of geothermal factors.

3 Research methods

3.1 Geothermal factor quantification

In order to better establish the geothermal potential target area evaluation model, quantitative research on the related geothermal factor data was conducted in this paper, such as stratigraphic lithology, fault zone distribution, surface water system, seismic point distribution, magmatic rock and volcanic rock distribution, surface water temperature, surface farmland temperature and surface forest temperature. The research method is shown in Figure 2.

3.1.1 Formation lithology

Rock porosity, faults and fractures in different lithological distribution areas have different development characteristics, which are important factors affecting geothermal (Sang et al., 2017). Geothermal resources may exist in various geological environments composed of limestone, volcanic rock and granite (Moghaddam et al., 2014). Thermal reservoir is the key to store geothermal fluid and form enough geothermal fluid productivity, which provides a good space for the occurrence of hot water (Guan and Fang, 2021). Therefore, the thermal reservoir is the key to the quantification of formation lithology factors.

The regional exploration research shows that the Hangjiahu Plain is mainly divided into three sets of thermal reservoirs and caprocks. The first caprock is about 144 m thick Carboniferous Gaolishan Formation C1g, and the corresponding underlying thermal reservoirs are about 200 m thick Devonian Wutong Formation D3w and about 1,500 m thick Silurian Maoshan Formation S3m; the second set is shallower, with the Permian Longtan Formation P2l with a thickness of about 350 m and the Yanqiao Formation P1y (Gufeng Formation P1g) with a thickness of about 200 m as the caprock, and the underlying thermal reservoirs are the Permian Qixia Formation P1q with a depth of about 159m, the Carboniferous Chuanshan Formation C2c with a depth of about 42.8 m and the Huanglong Formation C2h with a width of about 90m; the third set of the uppermost caprock is the Cretaceous Qifangcun Formation K1q, which is more than 800 m thick, and the Jurassic Jiande Group J3, which is about 900 m thick; the underlying thermal reservoir is the Triassic Qinglong Group T1-2 Q, which is about 583 m thick, and the Permian Changxing Formation P2c, about 169 m thick. Magmatic activities in the area mainly occurred in the late Yanshanian-Cretaceous, with magmatic intrusions in the Yanshanian and volcanic eruptions in the Jurassic and Cretaceous. Magmatic rocks are widely distributed in the area, mainly K-feldspar granite, granite porphyry, and quartz diorite, *etc.*, while volcanic rocks are mainly volcanic lava and pyroclastic

TABLE 1 Numerical table of stratigraphic lithology.

Depth/m	Formation lithology	
2,743.8	Magmatic and volcanic rocks	
	Tertiary	Changhe Formation
	Cretaceous	Tongxiang Formation, Quxian Formation, Jinhua Formation and Zhongdai Formation
	Jurassic	Huangjian Formation and Laocun Formation
1,991.8	Permian	Longtan Formation and Qixia Formation
1,832.8	Carboniferous	Chuanshan Formation
1,790	Carboniferous	Huanglong Formation
1,700	Carboniferous	Yejiatang Formation
	Devonian	Zhuzangwu Formation and Xihu Formation
1,500	Silurian	Tangjiawu Formation, Kangshan Formation, Helixi Formation and Xiaxiang Formation
0	Ordovician	Wenchang Formation and Changwu Formation
	Cambrian	Chaofeng Formation, Yangliugang Formation, Dachenling Formation and Hetang Formation
	Sinian	Piyuancun Formation, Banqiaoshan Formation and Dengying Formation
		Jinshan Group

rocks. The water permeability and water abundance of the strata are poor, and they are relatively aquicludes and geothermal insulation layers.

The vector stratigraphic lithology data obtained by digitizing the bedrock geological map are shown in Table 1. The thermal reservoir with a certain buried depth and a tight cap at the top is regarded as a high-quality reservoir. The greater the thickness of the thermal reservoir in the underlying strata of the bedrock, the greater the geothermal resource potential at that point. Taking the Tertiary, Cretaceous and Jurassic strata as an example, the thickness of the underlying Triassic Qinglong Group T1-2q, Permian Changxing Formation P2c and Qixia Formation P1q, Carboniferous Chuanshan Formation C3c and Huanglong Formation C2h, Devonian Wutong Formation D3w and Silurian Maoshan Formation S3m was added up to 2,743.8 as the value of the corresponding formation in the vector formation lithology data. Similarly, the Permian strata were assigned the thickness of the underlying thermal reservoir and 1,991.8 m. See Table 1 for the values of Carboniferous, Devonian, Silurian and other strata. Due to the strong correlation between magmatic rocks and volcanic rocks and geothermal hot spots, the magmatic rocks and volcanic rocks are also set at 2,743.8 m, which is consistent with the Tertiary, Cretaceous and Jurassic.

Through statistical analysis, among the 134 geothermal drilling points in the area, 53 (39.6% of the total) are located in Huangjian Formation and Laocun Formation of Jurassic System, 43 (32.1% of the total) are located in Zhongdai Formation, Jinhua Formation and Tongxiang Formation of Cretaceous System, and 15 (11.2%) are in Changhe Formation of Tertiary System. That is to say, 111 geothermal drilling points (accounting for 82.8% of the total) are distributed in the Tertiary, Cretaceous and Jurassic strata with thick underlying thermal reservoirs, indicating that there is a certain correlation between the thickness of underlying thermal reservoirs and geothermal resources.

3.1.2 Distance of fault zone

In addition to hot dry rock-type geothermal systems, natural circulation of meteoric water in faults and fractures plays a dominant role in geothermal systems (Wu et al., 2012b). Faults and fractures, as water circulation channels, are one of the main controlling elements of geothermal systems, in which hot water flows or directly becomes geothermal reservoirs (Guan and Fang, 2021).

Large scale NE, EW and NW fault zones are developed in the basement of Hangjiahu area, which are mainly controlled by NE and EW fault zones, and on this basis, secondary fault structures are developed, which have obvious influence on geothermal anomalies and geothermal gradient anomalies (Feng, 2005).

In Figure 3A, most of the geothermal drilling points are distributed along the fault zone, and there is a certain negative correlation between the geothermal resources and the distance of the fault zone, that is, disconnection. The closer the rift zone is, the hotter spots there are. In order to quantify the impact factors of the fault zone on geothermal resources, the Euclidean distance tool of ArcGIS was used for processing the vector fault zone data into a fault zone distance map to analyze its spatial relationship with geothermal drilling sites. The value of each pixel in Figure 3B represents the vertical distance from the pixel to the nearest fracture zone. After statistical analysis, 126 geothermal drilling sites (94% of the total) are located within 4 km from the nearest fault zone, as shown in Table 2.

3.1.3 Surface water system and its distance

Water is an ideal medium for heat exchange, and the existence of water is a necessary condition for the development of geothermal

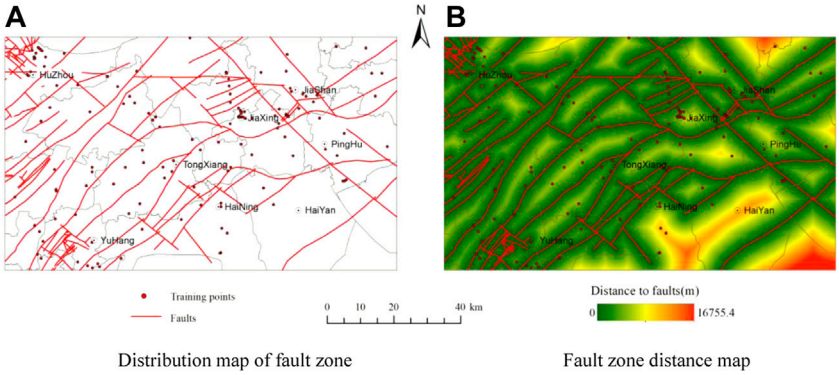


FIGURE 3
Distribution and distance map of faults in Study Area. **(A)** Distribution map of fault zone **(B)** Fault zone distance map.

TABLE 2 Distance to the faults intervals and statistical results.

Number	Fracture zone distance departure interval/km	Geothermal drilling points number	Interval proportion/%	Cumulative proportion/%
1	0–1	44	32.84	32.84
2	1–2	38	28.36	61.19
3	2–3	21	15.67	76.87
4	3–4	23	17.16	94.03
5	4–9	8	5.97	100.00
6	>9	0	0.00	100.00

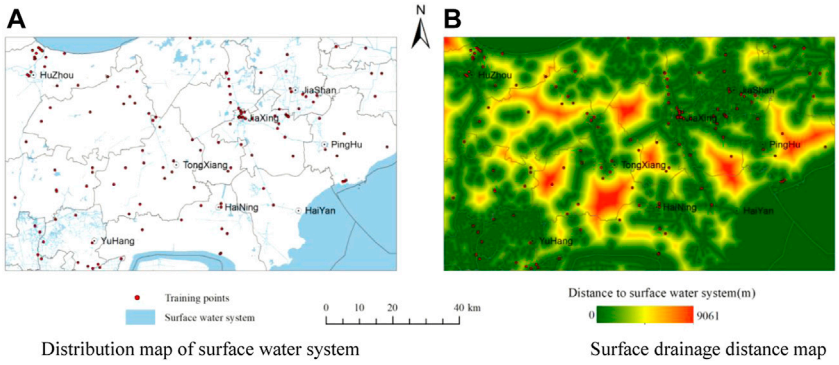


FIGURE 4
Distribution and distance map of surface water system in Study Area. **(A)** Distribution map of surface water system **(B)** Surface drainage distance map.

fields and hot springs (Sang et al., 2017). The field survey shows that the surface water system can provide sufficient water for hydrothermal activities, which should be regarded as an important factor in geothermal resources exploration.

Most of the geothermal drilling points in the Study Area are distributed near the surface water system, as shown in Figure 4A. The distance between geothermal resources and surface water system shows a certain negative correlation, that is, the closer to

TABLE 3 Distance to the surface water system intervals and statistical results.

Number	Surface water system distance interval/km	Geothermal drilling points number	Interval proportion/%	Cumulative proportion/%
1	0–1	78	58.21	58.21
2	1–2	29	21.64	79.85
3	2–3	14	10.45	90.30
4	3–4	7	5.22	95.52
5	4–5	4	2.99	98.51
6	>5	2	1.49	100.00

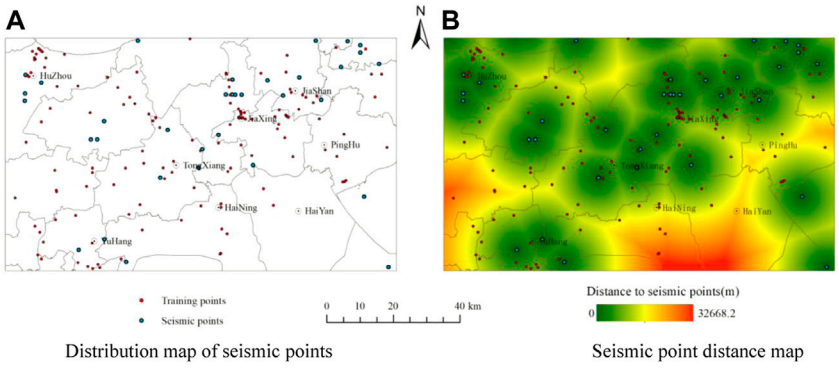


FIGURE 5
Distribution and distance map of seismic points in Study Area. **(A)** Distribution map of seismic points **(B)** Seismic point distance map.

the surface water system, the more geothermal hot spots. In order to evaluate the impact of surface water system on geothermal resources, the Euclidean distance tool of ArcGIS was used to process the vector surface water system data into a surface water distance map to analyze its spatial relationship with geothermal drilling sites, and the vertical distance from each pixel to the nearest surface water system was obtained, as shown in Figure 4B. Statistical analysis shows that 128 geothermal drilling sites (95.5% of the total) are located within 4 km of the nearest surface water system, as shown in Table 3.

3.1.4 Distance of seismic point

Fault activity is usually related to seismicity (Yao, 2008). Because the hot water in the active fault zone has high permeability and convection, geothermal resources are commonly found in the fault zone where earthquakes occur (Tufekci et al., 2010).

Earthquake records from 1971 to 2019 in the Area was used in the study, and the epicenter location was used as the geographic location of seismicity. There is a certain correlation between the distribution of geothermal drilling points and seismic points in Figure 5A, and there are many geothermal drilling points near the seismic points. In order to evaluate the correlation between seismic points and geothermal points, the Euclidean distance tool of ArcGIS was used for obtaining the distance map from each pixel of the full map to the nearest seismic point, as shown in Figure 5B. Statistical analysis shows that 126 geothermal drilling sites (94% of the total) are located within 15 km from the nearest seismic site, as shown in Table 4.

3.1.5 Magmatic and volcanic rock distances

Magmatic rocks and volcanic rocks have the function of water insulation and heat preservation with a certain correlation with the fault zone. At the same time, the higher geothermal gradient is related to the subduction friction of magmatic rocks, magma replacement, eruption and the influence of the bottom of magma. In many areas, young intrusive bodies are the source of heat for geothermal systems. The potential for geothermal resources is higher when young intrusions are located at shallow depths and close to areas where intrusions have been identified (Yousefi et al., 2010). Mesozoic basalts in Hangjiahu Plain are relatively good bedrock aquifers and favorable heat storage layers due to their deep burial depth, developed joints, fissures and pores, and impermeable roof and floor.

TABLE 4 Distance to the seismic points intervals and statistical results.

Number	Seismic point distance interval/km	Geothermal drilling points number	Interval proportion/%	Cumulative proportion/%
1	0–5	36	26.87	26.87
2	5–10	58	43.28	70.15
3	10–15	32	23.88	94.03
4	15–20	4	2.99	97.01
5	20–25	2	1.49	98.51
6	25–30	2	1.49	100.00
7	>30	0	0.00	100.00

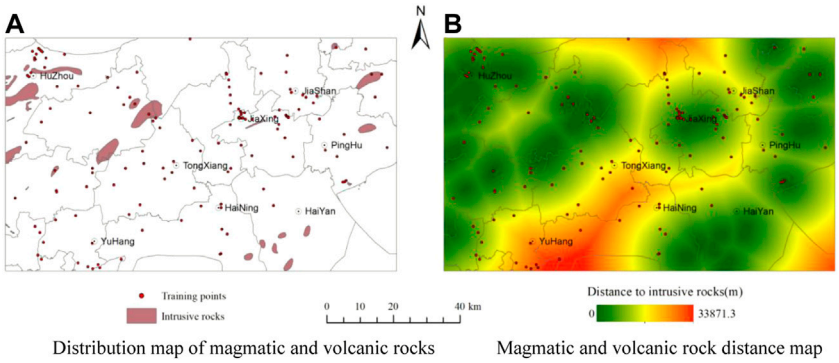


FIGURE 6
Distribution and distance map of intrusive rocks in Study Area. **(A)** Distribution map of magmatic and volcanic rocks **(B)** Magmatic and volcanic rock distance map.

TABLE 5 Distance to the intrusive rock intervals and statistical results.

Number	Magmatic and volcanic rock distance map/km	Geothermal drilling points number	Interval proportion%	Cumulative proportion/%
1	0–5	50	37.31	37.31
2	5–10	36	26.87	64.18
3	10–15	25	18.66	82.84
4	15–20	12	8.96	91.79
5	20–25	7	5.22	97.01
6	25–30	4	2.99	100.00
7	>30	0	0.00	100.00

Magmatic and volcanic rocks cover a total area of 207.48 km^2 in the Study Area, accounting for about 2.52% of the total area. In Figure 6A, and there are certain geothermal drilling points near the magmatic rocks and volcanic rocks, indicating that the closer to the magmatic rocks and volcanic rocks, the more abundant the geothermal resources are. Using the Euclidean distance tool of ArcGIS, the vector magmatic and volcanic rock data were processed into a vertical distance map of each pixel of the full map to the nearest magmatic and volcanic rock, as shown in Figure 6B, for analyzing its spatial relationship with geothermal

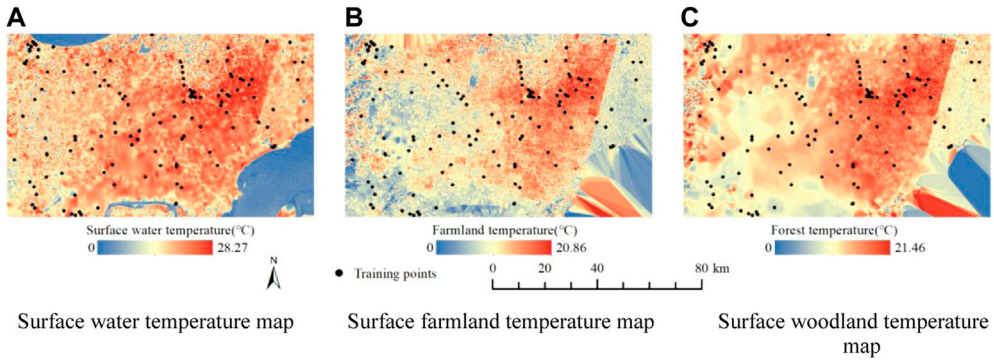


FIGURE 7
Temperature map of surface water, farmland and forest in Study Area. **(A)** Surface water temperature map **(B)** Surface farmland temperature map **(C)** Surface woodland temperature map.

drilling sites. Statistical analysis shows that 111 geothermal drilling sites (82.8% of the total) are located within 15 km of the nearest magmatic and volcanic rocks, as shown in Table 5.

3.1.6 Surface water temperature of farmland and forest land

The surface thermal environment is related to geothermal to some extent, and the surface temperature can reflect a certain surface thermal environment (Li and Zhang, 2017). In the work, based on the thermal infrared band of Landsat 5 TM, the radiative transfer equation method was used for finding the abnormal area of surface thermal environment and analyzing the correlation between the geothermal hot spot and the abnormal area of surface thermal environment (Tu, 2006; Yang, 2015).

The land surface temperature was discussed in a separate surface feature type after removing the influence of various surface features. Therefore, the land surface temperature data of the Study Area was obtained through the inversion of the above steps on combination of the land use types obtained by supervised classification, the land surface temperatures of water bodies, farmlands and woodlands were masked and extracted. The surface temperature point data of water, farmland and woodland were obtained by using the raster turning point tool of ArcGIS. The Kriging interpolation method was used for drawing the surface temperature trend map corresponding to the water body, farmland and woodland in the Study Area, as shown in Figure 7, and the relationship between the surface thermal environment of different land types, such as water body, farmland and woodland and geothermal spots was counted. After statistical analysis, it is found that most of the hot spots are concentrated in the areas with higher temperature, and the trend map of water surface temperature is more obvious, followed by farmland and woodland.

TABLE 6 Weight assignment criteria for the thematic map.

Number	Geothermal factor	Weight value
1	Formation lithology	8
2	Fault zone distance	7
3	Surface water system and its distance	6
4	Seismic point distance	5
5	Magmatic and volcanic rock distances	4
6	Surface water temperature	3
7	Surface farmland temperature	2
8	Surface woodland temperature	1

3.2 Analytic hierarchy process (AHP)

Analytic Hierarchy Process (AHP) is a combination of qualitative and quantitative decision analysis method, which is often used for solving multi-objective, multi-criteria, multi-factor, multi-level and unstructured complex decision-making problems, focusing on clarifying the factors involved in the problem and analyzing their internal relations. AHP is widely used in the fields of groundwater, shallow geothermal energy and geothermy (Chakrabortty et al., 2018; Xu et al., 2018; Lv et al., 2019; Pal et al., 2019; Das and Pal, 2020a; Das and Pal, 2020b; Shao et al., 2020; Pal et al., 2022; Ruidas et al., 2022).

Based on prior knowledge and expert analysis and evaluation, eight geothermal potential factors, including stratigraphic lithology, fault zone distance, surface water system and its distance, seismic point distance, magmatic rock and volcanic rock distance, and surface water, farmland and woodland temperature, are compared in pairs according to their importance in geothermal exploration and their correlation with geothermal resources. Eigenvalues and eigenvectors are calculated and passed the consistency check. The higher the

TABLE 7 Assigned and normalized weights of the factors for eight thematic maps.

Geothermal factor	Actual numerical partition	Weights	Specific gravity	Geothermal factor	Actual numerical partition	Weights	Specific gravity
Formation lithology	2,743.8	9	0.321	Surface water temperature	11.48–25.39°C	9	0.36
	1991.8	6	0.214		10.19–11.48°C	7	0.28
	1832.8	5	0.179		8.32–10.19°C	5	0.2
	1700,1790	4	0.143		5.06–8.32°C	3	0.12
	1,500	3	0.107		0.33–5.06°C	1	0.04
	0	1	0.036				
Surface farmland temperature	12.49–19.14°C	9	0.36	Surface woodland temperature	12.59–16.44°C	9	0.36
	11.68–12.49°C	7	0.28		11.86–12.59°C	7	0.28
	10.86–11.68°C	5	0.2		11.17–11.86°C	5	0.2
	9.82–10.86°C	3	0.12		9.96–11.17°C	3	0.12
	0.37–9.82°C	1	0.04		3.06–9.96°C	1	0.04
Fault zone distance	0–1 km	9	0.273	Surface water system and its distance	0–1 km	9	0.273
	1–2 km	8	0.242		1–2 km	8	0.242
	2–3 km	7	0.212		2–3 km	7	0.212
	3–4 km	6	0.182		3–4 km	6	0.182
	4–9 km	2	0.061		4–5 km	2	0.061
	>9 km	1	0.03		>5 km	1	0.03
Seismic point distance	0–5 km	9	0.268	Magmatic and volcanic rock distances	0–5 km	9	0.268
	5–10 km	8	0.238		5–10 km	8	0.238
	10–15 km	7	0.196		10–15 km	7	0.196
	15–20 km	4	0.119		15–20 km	4	0.119
	20–25 km	3	0.089		20–25 km	3	0.089
	25–30 km	2	0.06		25–30 km	2	0.06
	>30 km	1	0.03		>30 km	1	0.03

weight value of the geothermal factor is, the more important the geothermal factor is and the more relevant it is to the potential geothermal target area.

In order to obtain the potential target area zoning map of the AHP method, firstly the weight difference between the geothermal factors was evaluated, and the geothermal factor assignment table was obtained, as shown in Table 6. Due to the important influence of formation lithology on geothermal resources, it is assumed that the formation lithology is absolutely more important, and its weight is determined to be 8. Similarly, as the channel of heat transfer mechanism, the distribution of fault zones is more important than the surface water system, and the weights are determined to be 7 and 6, respectively. The distribution of seismic points can indirectly reflect the activity of the fault zone, and its weight is determined to be 5. The outcropping magmatic rocks and volcanic rocks are less distributed in the Study Area and have less spatial association with the known geothermal drilling sites, and their weights are determined to be 4. In the study, the temperatures of surface water, farmland and woodland obtained by Kriging interpolation method were innovatively used as geothermal potential factors, and their impacts on geothermal resources reduced successively, with weights of 3, 2 and 1 in turn.

In combination with the correlation between each geothermal factor and geothermal hot spot, the hierarchical analysis method is used for obtaining the classification and standardization weights of eight geothermal factors, as shown in Table 7. Taking the formation lithology as an example, the lithology is divided into six categories. The greater the thickness of the underlying thermal reservoir, the more geothermal resources it may contain. The greater the value set, the higher the weight given. The fault zone and the surface water system are used as the channel and medium for heat exchange, respectively, and are divided into six categories according to the distance to the nearest fault zone and surface water system; the distance to the nearest seismic point,

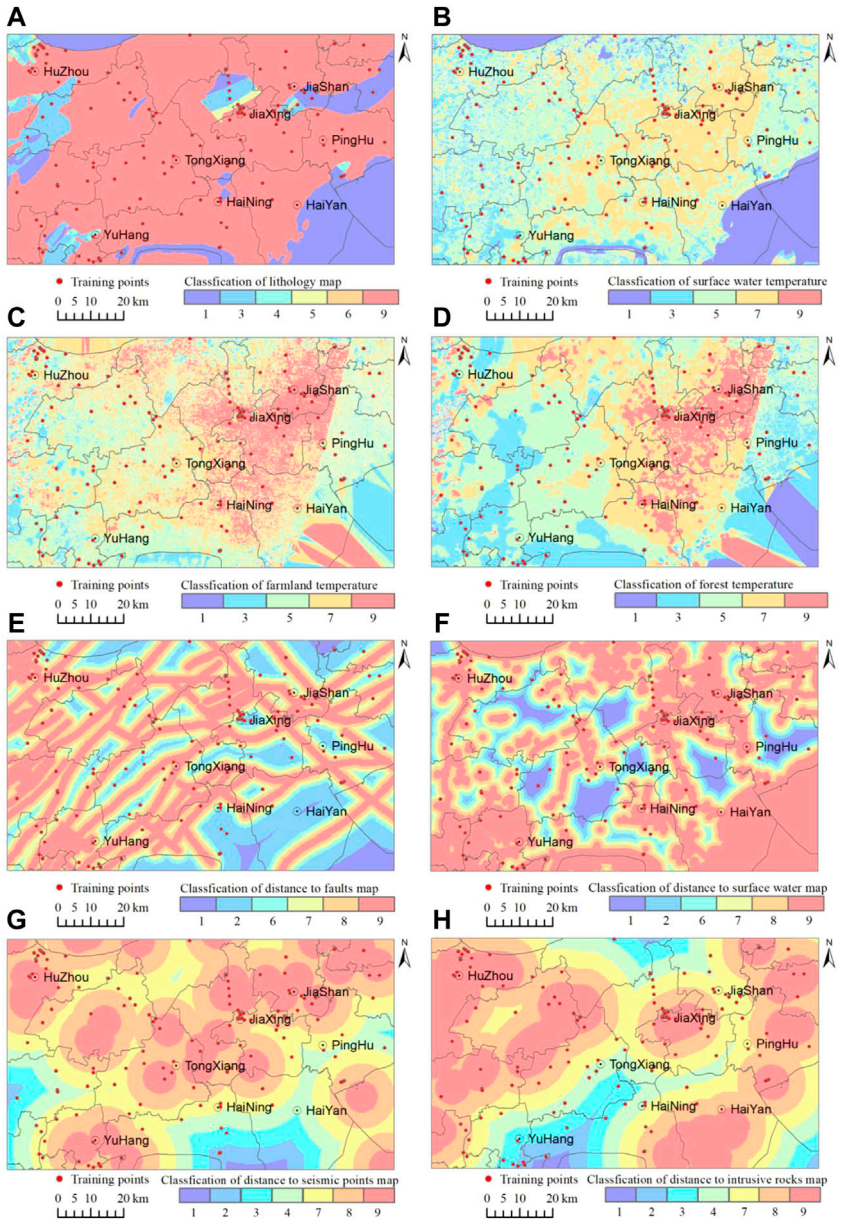


FIGURE 8
Geothermal factor weight map based on AHP. **(A)** Classification of lithology map; **(B)** Classification of surface water temperature; **(C)** Classification of farmland temperature; **(D)** Classification of forest temperature; **(E)** Classification of distance to faults map; **(F)** Classification of distance to surface water map; **(G)** Classification of distance to seismic points map; **(H)** Classification of distance to intrusive rocks map.

magmatic rock and volcanic rock, which have less correlation, are also divided into seven categories according to the distances to the nearest seismic point, magmatic rock and volcanic rock; the closer the distance is, the higher the weight is set. The temperatures trend charts of water body, farmland and woodland obtained by Kriging interpolation were divided into five categories by natural breakpoint method, and the higher the temperature was, the higher the weight was.

According to the classification threshold in Table 7, the eight geothermal factors are re-classified, and the weight map of regional geothermal factors based on AHP is shown in Figure 8. The coincidence degree of geothermal hot spots and high-value parts is high, reflecting the accuracy of the weighting of geothermal factors in AHP to a certain extent. The geothermal factors were used for calculating the AHP geothermal potential target zoning map. In the AHP geothermal potential target zoning map, geothermal potential target zone was categorized

as five levels by using the equal interval classification method: extremely high potential region, high potential region, medium potential region, low potential region and potential region.

3.3 Neural network

BP neural network is a kind of multilayer feedforward neural network which is trained according to the error back propagation algorithm. It is composed of input layer, hidden layer and output layer. It has the advantages of rigorous derivation, high algorithm accuracy and good versatility, and can obtain suitable connection weights by learning a large number of samples, and can reflect the nonlinear relationship of multi-factor interaction. The results obtained by BP neural network are accurate and simple in hydrologic analysis, water quality evaluation and prediction (Liu et al., 2008).

The eight geothermal factor zones in the Study Area are shown in Figure 8. The Study Area was divided into a regular 30 m × 30 m grid, and each pixel in the sampled raster data was a sample group containing eight geothermal factors. Taking the overall data set as an example, the training intensity accounts for 70% of the data volume in the entire data set, the verification intensity accounts for 20% of the data volume in the entire data set, and the final test intensity accounts for 10% of the total data volume. In order to avoid the gradient explosion phenomenon in the subsequent model calculation process and the fitting failure caused by the fact that some factor values are far greater than other values, the input data are normalized. Set the sum of the layers of the input layer and the hidden layer to 15, the number of nodes to 1,024, and the number of nodes of the output layer to 5.

The activation function aims at helping the network learn the complex patterns in the data. In this study, the ReLU function is used as the action function of the hidden layer and the output layer, and its expression is

$$\mathrm{Re}LU(x) = \max(x, 0) \tag{1}$$

The advantage of ReLU function is that it saves the amount of calculation, has a faster actual convergence speed, avoids the gradient disappearance, reduces the interdependence of parameters, alleviates the occurrence of over-fitting problems, and is more in line with the biological neural activation mechanism.

The training uses the SparseCategoricalCrossEntropy sparse cross-entropy loss function and the Adam optimization algorithm, and the optimal learning rate is considered to be 0.001.

And in the BP Neural Network Target Zoning Map, geothermal potential target zone is divided into five levels: extremely high potential area, high potential area, medium potential area, low potential area and potential area.

4 Analysis of results

4.1 Geothermal potential target area zoning map of analytic hierarchy process

Based on the Regional Geothermal Factor Weight Map, the AHP Geothermal Potential Target Zoning Map is obtained by calculation. In order to highlight the spatial distribution of geothermal resource potential in Hangjiahu Plain, the Groundwater Potential Map calculated by AHP is divided into five levels by using the equal interval classification method: extremely high potential region, high potential region, medium potential region, low potential region and potential region as shown in Figure 9.

The extremely high potential areas are mainly located near Huzhou City in the northwest, Jiashan County and Jiaxing City in the northeast, and Tongxiang City in the central part of the Study Area, covering an area of about 1,766.39 km^2 (21.46%). The high potential area is mainly in the form of northeast-trending strips, accounting for 42.25% (3,477.50 km^2) of the total area. The area of medium potential area is about 1,864.90 km^2 (22.66%), which is mainly distributed in the land part of the whole Study Area.

In order to verify the accuracy of the AHP model, the results of the model were compared with the existing 134 geothermal drilling locations. Sixty geothermal drilling sites (44.78% of the total) are located in very high potential areas, and 54 geothermal drilling sites (40.30% of the total) are located in high potential areas. That is to say, 114 geothermal drilling points (accounting for 85.07% of the total) are distributed in extremely high potential areas and high potential areas, which shows that the comprehensive analysis model of geothermal water exploration established by AHP is more accurate and effective.

4.2 Back propagation Neural Network Geothermal Potential Target Zoning Map

In order to analyze the spatial distribution of geothermal resource potential in Hangjiahu Plain, the BP neural network model is used for calculating and obtaining the BP Neural Network Geothermal Potential Target Zoning Map. As shown in Figure 10, the geothermal potential target area is divided into five levels: extremely high potential area, high potential area, medium potential area, low potential area and potential area.

The extremely high potential areas are relatively scattered, mainly concentrated near Huzhou City in the northwest, Jiashan County and Jiaxing City in the northeast of the Study Area, covering an area of about 814.75 km^2 (9.90%). The high potential area mainly surrounds the very high potential area and accounts for 10.24% (843.22 km^2) of the total area. The area of medium potential area is about 1,006.86 km^2 (12.23%), which is mainly accompanied by extremely high and high potential areas.

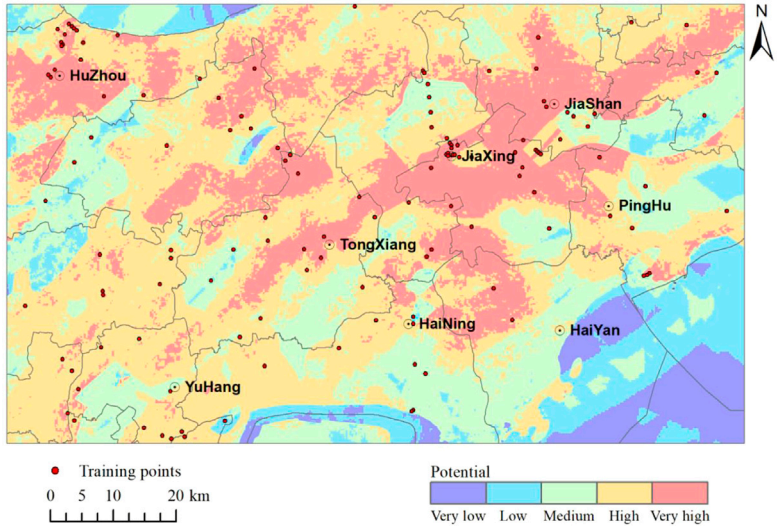


FIGURE 9
Possibility class maps for the AHP model.

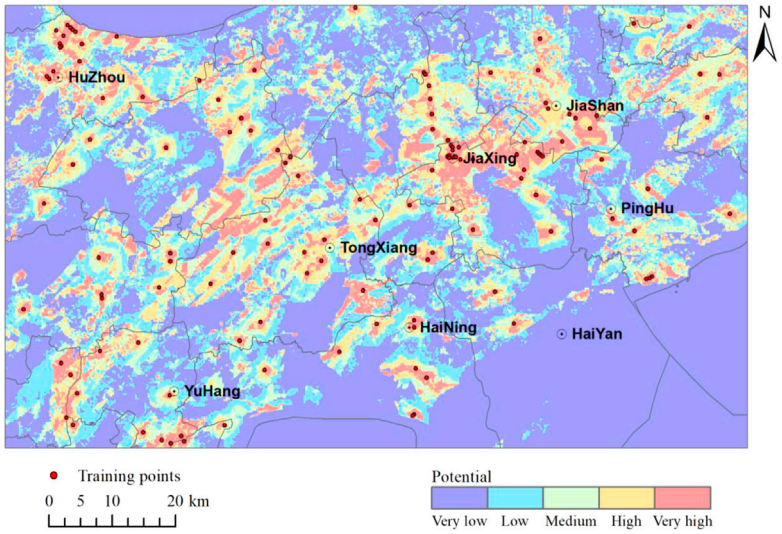


FIGURE 10
Possibility class maps for the Back Propagation Neural Network model.

In order to verify the accuracy of the BP neural network model, the results of the model are compared with the existing 134 geothermal drilling sites. 123 geothermal drilling points (accounting for 91.79% of the total) are located in the extremely high potential areas, which shows that the comprehensive analysis model of geothermal water exploration established by BP neural network is more accurate and has high coincidence. At the same time, the precision of BP neural network model is evaluated, and the Kappa coefficient of the model is 0.785, which shows that the precision is high.

The possibility class maps obtained by AHP model and BP neural network model in the study are similar to the existing geothermal targets in this region (Feng, 2005; Hu et al., 2011). However, the result this time is more accurate than the

previous target location, and the classification is more suitable for future exploration.

5 Conclusion

Taking Hangjiahu Plain as an example, based on the inversion of land surface temperature from Landsat TM data, the geothermal factors are spatially analyzed and quantified, and the geothermal exploration model is established by using AHP and BP neural network to analyze the potential geothermal target areas.

(1) Based on geological maps, geothermal exploration data and remote sensing images, factor data affecting the distribution of geothermal resources are obtained. In the selection of geothermal factors, the influence of surface thermal environment and surface water system is innovatively considered. Quantitative analysises are carried out one by one, which are classified according to their spatial association with known hot spots.
(2) The weight of each geothermal factor is calculated by AHP, and the geothermal potential target area model is established by BP neural network, which can reduce the dependence of the model on expert prior knowledge and make the delimitation of geothermal resource potential area more intelligent and scientific.
(3) The results show that, the known hot spots and high potential areas have a good coincidence degree, and the model accuracy meets the requirements.
(4) The results also show that using remote sensing interpretation data and GIS analysis data, it is feasible to analyze geothermal potential targets based on AHP analytic hierarchy process and BP neural network, and the distribution characteristics of surface thermal environment, fault activity, surface water system and other related factors are also related to geothermal distribution. The prediction results of the model coincide with the existing geothermal drilling sites, which provides a new idea for geothermal exploration.

Data availability statement

The original contributions presented in the study are included in the article/Supplementary Material, further inquiries can be directed to the corresponding author.

Author contributions

XL and WW: Conceptualization, Data Curation, and Writing—original draft; WW and QJ: Writing—review and editing; HS and XB: Resources and Data processing; HT: Research Conceptualization; LX, HB, and HC: Validation, Investigation. All authors have read and agreed to the published version of the manuscript.

Funding

This paper was supported by Zhejiang Provincial Natural Science Foundation of China (NO: GF19D020002); Science and technology project of China National Administration of Coal Geology (NO: ZMKJ-2020-J11-2); National Natural Science Foundation of China (NO: 41402304); Zhejiang Provincial Natural Science Foundation of China (NO: LQ13D020002).

Conflict of interest

The authors declare that the research was conducted in the absence of any commercial or financial relationships that could be construed as a potential conflict of interest.

Publisher's note

All claims expressed in this article are solely those of the authors and do not necessarily represent those of their affiliated organizations, or those of the publisher, the editors and the reviewers. Any product that may be evaluated in this article, or claim that may be made by its manufacturer, is not guaranteed or endorsed by the publisher.

References

Ahmad, I., Dar, M. A., Tekaa, H., Teshome, M., Andualem, T. G., Teshome, A., et al. (2020). GIS and fuzzy logic techniques-based demarcation of groundwater potential zones: A case study from jemma river basin, Ethiopia. *J. Afr. Earth Sci.* 169, 103860. doi:10.1016/j.jafrearsci.2020.103860

Chakrabortty, R., Pal, S. C., Malik, S., and Das, B. (2018). Modeling and mapping of groundwater potentiality zones using AHP and GIS technique: a case study of Raniganj block, Paschim bardhaman, West Bengal. *Model. Earth Syst. Environ.* 4, 1085–1110. doi:10.1007/s40808-018-0471-8

Chen, S. Y., Liu, P. X., Liu, L. Q., Ma, J., and Chen, G. Q. (2006). Wavelet analysis of thermal infrared radiation of land surface and its implication in the study of current tectonic activities. *Chin. J. Geophys.* 49 (3), 717–723. in Chinese. doi:10.1002/cjg2.886

Das, B., and Pal, S. C. (2020). Assessment of groundwater vulnerability to over-exploitation using MCDA, AHP, fuzzy logic and novel ensemble models: a case study of Goghat-I and II blocks of West Bengal, India. *Environ. Earth Sci.* 79, 104. doi:10.1007/s12665-020-8843-6

Das, B., and Pal, S. C. (2020). Irrigation practices causing vulnerability of groundwater resources in water scarce Goghat-I and II Blocks of Hugli District using MCDA, AHP, Fuzzy logic and novel ensemble models. *Adv. Space Res.* 65 (12), 2733–2748. doi:10.1016/j.asr.2020.03.027

Feng, Y. W. (2005). Geological analysis of geothermal water in Hangjiahu area. *Zhejiang Land Resour.* 6, 40–43. (in Chinese). doi:10.3969/j.issn.1672-6960.2005.06.017

Guan, J., and Fang, S. (2021). Concept and heat transfer mechanism of geothermal system: A review. *Geol. Resour.* 30 (2), 207–213+206. (in Chinese). doi:10.13686/j.cnki.dzyzy.2021.02.013

Hu, N., Zhang, L. H., Gao, H. F., and Han, F. (2011). Target delineation and drilling verification of geothermal resources exploration in Hangjiahu plain of Zhejiang Province. *Geol. China* 38 (1), 138–144. (in Chinese). doi:10.3969/j.issn.1000-3657.2011.01.015

Johnson, L. R. (2014). Source mechanisms of induced earthquakes at the geysers geothermal reservoir. *Pure Appl. Geophys.* 171 (8), 1641–1668. doi:10.1007/s00024-014-0795-x

Li, J. M., and Zhang, Y. J. (2017). GIS-supported certainty factor (CF) models for assessment of geothermal potential: A case study of tengchong county, southwest China. *Energy* 140, 552–565. doi:10.1016/j.energy.2017.09.012

Liang, Q. Z., Wang, L. Q., Liu, D., and Li, G. X. (2020). PSO-ELM prediction model of regional groundwater depth based on EEMD. *Water Resour. Hydropower Eng.* 51 (9), 45–51. (in Chinese). doi:10.13928/j.cnki.wrahe.2020.09.005

Liu, P. X., Liu, L. Q., and Chen, S. Y. (2004). Heat Penetrability Index (HPI) method for distilling subsurface thermal information from satellite infrared images. *Seismol. Geol.* 26 (3), 519–527. in Chinese. doi:10.3969/j.issn.0253-4967.2004.03.016

Liu, R. T., Fu, Q., Feng, Y., Gai, Z. M., Li, G. L., and Li, W. Y. (2008). Grey BP neural networks model based on RAGA and its application in groundwater dynamic prediction of the Sanjiang plain. *Syst. Eng.-Theory Pract.* 28 (5), 171–176. (in Chinese). doi:10.3321/j.issn:1000-6788.2008.05.023

Lv, Z. M., Ding, J. P., Chu, X. W., Zhang, X. M., and Linghu, X. Y. (2019). Application of grey relational analysis based on fuzzy analytic hierarchy process in groundwater quality evaluation. *J. Guizhou Univ. Sci. Ed.* 36 (1), 118–124. (in Chinese). doi:10.15958/j.cnki.gdxbzrb.2019.01.22

Mcguire, J. J., Lohman, R. B., Catchings, R. D., Rymer, M. J., and Goldman, M. R. (2015). Relationships among seismic velocity, metamorphism, and seismic and aseismic fault slip in the Salton Sea Geothermal Field region. *J. Geophys. Res. Solid Earth* 120 (4), 2600–2615. doi:10.1002/2014JB011579

Meng, F. A., Liang, X. J., Xiao, C. L., and Wang, G. (2021). Geothermal resource potential assessment utilizing GIS - based multi criteria decision analysis method. *Geothermics* 89 (8), 101969. doi:10.1016/j.geothermics.2020.101969

Moghaddam, M. K., Samadzadegan, F., Noorollah, i. Y., Sharifi, M. A., and Itoi, R. (2014). Spatial analysis and multi-criteria decision making for regional-scale geothermal favorability map. *Geothermics* 50 (2), 189–201. doi:10.1016/j.geothermics.2013.09.004

Noorollahi, Y., Itor, R., Fujii, H., and Tanaka, T. (2008). GIS integration model for geothermal exploration and well siting. *Geothermics* 37 (2), 107–131. doi:10.1016/j.geothermics.2007.12.001

Pal, S. C., Das, B., and Malik, S. (2019). Potential landslide vulnerability zonation using integrated analytic hierarchy process and GIS technique of upper Rangit catchment area, west Sikkim, India. *J. Indian Soc. Remote Sens.* 47, 1643–1655. doi:10.1007/s12524-019-01009-2

Pal, S. C., Ruidas, D., Saha, A., Islam, A. R. M. T., and Chowdhuri, I. (2022). Application of novel data-mining technique based nitrate concentration susceptibility prediction approach for coastal aquifers in India. *J. Clean. Prod.* 346, 131205. doi:10.1016/j.jclepro.2022.131205

Pang, Z. H., Luo, J., Cheng, Y. Z., Duan, Z. F., Tian, J., Kong, Y. L., et al. (2020). Evaluation of geological conditions for the development of deep geothermal energy in China. *Earth Sci. Front.* 27 (1), 134–151. (in Chinese). doi:10.13745/j.esf.2020.1.15

Peng, X. X., Wu, W. Y., Zheng, Y. Y., Sun, J., Hu, T., and Wang, P. (2020). Correlation analysis of land surface temperature and topographic elements in Hangzhou, China. *Sci. Rep.* 10 (1), 10451. doi:10.1038/s41598-020-67423-6

Ruidas, D., Pal, S. C., Saha, A., Chowdhuri, I., and Shit, M. (2022). Hydrogeochemical characterization based water resources vulnerability assessment in India's first Ramsar site of Chilka lake. *Mar. Pollut. Bull.* 184, 114107. doi:10.1016/j.marpolbul.2022.114107

Sadeghi, B., and Khalajmasoumi, M. (2014). A futuristic review for evaluation of geothermal potentials using fuzzy logic and binary index overlay in GIS environment. *Renew. Sustain. Energy Rev.* 43, 818–831. doi:10.1016/j.rser.2014.11.079

Sang, X. J., Xue, L. F., Liu, J. W., and Zhan, L. (2017). A novel workflow for geothermal prospectively mapping weights-of-evidence in liaoning province, northeast China. *Energies* 10 (7), 1069. doi:10.3390/en10071069

Shao, Z. F., Huq, M. E., Cai, B. W., Altan, O., and Li, Y. (2020). Integrated remote sensing and GIS approach using Fuzzy-AHP to delineate and identify groundwater potential zones in semi-arid Shanxi Province, China. *Environ. Model. Softw.* 134, 104868. doi:10.1016/j.envsoft.2020.104868

Trumpy, E., Donato, A., Gianellli, G., Gola, G., Minissale, A., Montanari, D., et al. (2015). Data integration and favourability maps for exploring geothermal systems in Sicily, southern Italy. *Geothermics* 56, 1–16. doi:10.1016/j.geothermics.2015.03.004

Tu, L. P. (2006). *Land surface temperature (LST) retrieval and land surface emissivity (LSE) estimation from Landsat TM data*. Hangzhou: Zhejiang University, 33–35. (in Chinese).

Tufekci, N., Suzen, M. L., and Gulec, N. (2010). GIS based geothermal potential assessment: A case study from western anatolia, Turkey. *Energy* 35 (1), 246–261. doi:10.1016/j.energy.2009.09.016

Wang, S. S., and Song, B. L. (2021). Application of fuzzy analytic hierarchy process in sandstone aquifer water yield property evaluation. *Environ. Technol. Innovation* 22, 101488. doi:10.1016/j.eti.2021.101488

Wu, W. Y., Zou, L. J., Shen, X. H., Lu, S., Su, N., Kong, F., et al. (2012). Thermal infrared remote-sensing detection of thermal information associated with faults: A case study in western sichuan basin, China. *J. Asian Earth Sci.* 43 (1), 110–117. doi:10.1016/j.jseaes.2011.08.015

Wu, W. Y., Zou, L. J., Shen, X. H., Lu, S., Su, N., and Kong, F. (2012). Thermal anomalies associated with faults: a case study of the jinhua-quzhou basin of Zhejiang province, China. *Int. J. Remote Sens.* 33 (6), 1850–1867. doi:10.1080/01431161.2011.602992

Wu, W. Y., Jin, C., Pang, Y. W., Zhao, L. J., Song, Y., Hu, T. G., et al. (2019). Distribution characteristics of surface thermal environment in Zhejiang province based on thermal infrared remote sensing. *J. Remote Sens.* 23 (4), 796–808. (in Chinese). doi:10.11834/jrs.20197339

Xu, X. W., Ma, K. H., and Zou, S. (2018). Application research of AHP fuzzy comprehensive evaluation model in groundwater vulnerability assessment. *Ground Water* 40 (5), 1–4. (in Chinese). doi:10.3969/j.issn.1004-1184.2018.05.001

Yang, X. S. (2015). *Research on the single-channel algorithm for land surface temperature retrieval from Landsat8 data*. Beijing: China University of Geosciences, 26–29. (in Chinese).

Yao, Q. (2008). *Neotectonics of NW-SE trending faults in Hangzhou Bay, China*. Hangzhou: Zhejiang University, 10–13. (in Chinese).

Yousefi, H., Noorollahi, Y., Ehara, S., Itoi, R., Yousefi, A., Fujimitsu, Y., et al. (2010). Developing the geothermal resources map of Iran. *Geothermics* 39 (2), 140–151. doi:10.1016/j.geothermics.2009.11.001

Yu, L. M., Yan, W. G., Gong, D. Z., Li, Y., Feng, Y., and Jiang, D. (2017). Temporal and spatial distribution prediction of shallow groundwater level based on ELM model. *Trans. Chin. Soc. Agric. Mach.* 48 (2), 215–223. (in Chinese). doi:10.6041/j.issn.1000-1298.2017.02.029

Zhang, P. M., and Zhang, J. L. (2006). Identification of remote sensing information in geothermal abnormal area. *Remote Sens. Inf.* (2), 42–45+81. in Chinese. doi:10.3969/j.issn.1000-3177.2006.02.013

Zhang, Y. J., Guo, L. L., Li, Z. W., Yu, Z. W., Xu, T. F., and Lan, C. Y. (2015). Electricity generation and heating potential from enhanced geothermal system in Songliao Basin, China: Different reservoir stimulation strategies for tight rock and naturally fractured formations. *Energy* 93 (2), 1860–1885. doi:10.1016/j.energy.2015.10.059

Zhang, Y. J., Xie, Y. Y., Zhang, T., Liu, T., and Zhang, C. (2016). 2m survey method and its improved device application in Dongshan geothermal field in Xiamen in China. *Environ. Earth Sci.* 75 (18), 1290. doi:10.1007/s12665-016-6048-9

Zhang, Y., Zhang, Y. J., Yu, H., Li, J., Xie, Y., and Lei, Z. (2020). Geothermal resource potential assessment of Fujian Province, China, based on geographic information system (GIS) -supported models. *Renew. Energy* 153, 564–579. doi:10.1016/j.renene.2020.02.044

Zhou, Z. Y., Liu, S. L., and Liu, J. X. (2015). Study on the characteristics and development strategies of geothermal resources in China. *J. Nat. Resour.* 30 (7), 1210–1221. in Chinese. doi:10.11849/zrzyxb.2015.07.013

frontiers | Frontiers in Earth Science

TYPE Original Research
PUBLISHED 16 January 2023
DOI 10.3389/feart.2022.1033441

Check for updates

OPEN ACCESS

EDITED BY
Guang-Liang Feng,
Institute of Rock and Soil Mechanics (CAS), China

REVIEWED BY
Yan Zhang,
Chengdu University of Technology, China
Pongsakorn Suppakittpaisarn,
Chiang Mai University, Thailand

*CORRESPONDENCE
Na Chen,
chenna825@hnu.edu.cn

SPECIALTY SECTION
This article was submitted to Geohazards and Georisks, a section of the journal Frontiers in Earth Science

RECEIVED 31 August 2022
ACCEPTED 24 October 2022
PUBLISHED 16 January 2023

CITATION
Chen N, Guo H and Xiang H (2023), Evaluation of urban resilience level and analysis of obstacle factors: A case study of Hunan Province, China.
Front. Earth Sci. 10:1033441.
doi: 10.3389/feart.2022.1033441

COPYRIGHT
© 2023 Chen, Guo and Xiang. This is an open-access article distributed under the terms of the Creative Commons Attribution License (CC BY). The use, distribution or reproduction in other forums is permitted, provided the original author(s) and the copyright owner(s) are credited and that the original publication in this journal is cited, in accordance with accepted academic practice. No use, distribution or reproduction is permitted which does not comply with these terms.

Evaluation of urban resilience level and analysis of obstacle factors: A case study of Hunan Province, China

Na Chen[1,2]*, Hongxia Guo[1] and Hui Xiang[1,2]

[1]School of Architecture, Hunan University, Changsha, China, [2]Hunan Key Laboratory of Sciences of Urban and Rural Human Settlements in Hills Areas, Hunan University, Changsha, China

Resilient city is an ideal goal and model of urban development proposed in response to today's complex and dynamic environmental changes. In this study, a resilient city evaluation framework of "social resilience-economic resilience-urban infrastructure and service-urban governance" was built upon the multi-dimensionality of the urban system; the entropy weight method was used to measure the level of urban resilience in Hunan Province while an obstacle degree model was used to identify any obstacle factor restricting to the development of resilience. The results show that the level of urban resilience in Hunan Province has grown slowly over the past 10 years, and there is an obvious regional difference in it. There are more and more highly resilient cities, but medium/low-resilience cities still dominate the province, forming a spatial process of evolution from "medium/high-level dispersion" to "medium/high-level aggregation" in the Changsha-Zhuzhou-Xiangtan Urban Agglomeration. The level of urban resilience is predominantly hindered by the social and economic systems; at the index layer, most obstacle factors are moving from the economic system to the social-economic-urban infrastructure and service system.

KEYWORDS

resilient city, sustainable development, entropy method, spatial-temporal evolution, obstacle factors

1 Introduction

At present, a profound change is taking place in science and technology, industry, energy, and finance worldwide, resulting in increasingly prominent conflicts between populations, resources and the environment. Accordingly, the world is becoming increasingly complex and unpredictable, requiring cities to keep more resilient and smarter in response to various challenges and crises. On the one hand, cities need to cope with long-term risks, but more importantly, they shall enhance their ability to tackle unknown and sudden risks, such as droughts and floods caused by extreme weather; urban damage caused by major natural disasters; intensified social conflicts caused by economic crises; social instability caused by terrorist attacks; serious impact of public health events on the urban medical system and urban governance,

etc. All the resultant dynamic changes and uncertainties in urban development are universal problems faced by every city.

In today's world, where there are all kinds of crises and uncertainties, the international community is gradually abandoning the traditional development model that mainly relies on resource degradation and environmental disruption. The concept of sustainable development is widely accepted and used to guide the practice of urban development. However, 93 environment-related indexes in the SDGs were already assessed in *The Global Environment Outlook 6 (GEO-6)*, showing that only 20 indexes had undergone significant improvements over the past 15 years (UNEP, 2019). The environment remains under increasing pressure from growing population, economic activities and global consumption and production.

For cities, a pressing issue that needs to be solved is how to cope with various changes and crises to maintain their vitality and sustainable development. Since the beginning of the 21st century, the concept of resilience has become an important complement to sustainable development. Sustainability and resilience are closely linked (Zhang and Li, 2018). Resilience is the preferred method (Levin et al., 1998) and a necessary condition (Lebel et al., 2006) for the sustainable development of natural and social systems, bringing new impetus for understanding and recognizing the inherent complexity and uncertainty of cities.

Resilient city helps to implement the concept of sustainable development in a specific space—the "city." Essentially, it is designed to promote the coordinated development of social-economic-natural subsystems, as well as the urban system and surrounding areas. As urbanization deepens, the complex, huge urban system is achieving optimal development to finally improve people's wellbeing and quality of life (Cui et al., 2010). As a multi-objective and multi-dimensional development framework, sustainable urbanization focuses on the long process of development (Kanuri et al., 2016). During this process, a series of prerequisites for safe urban development should be ensured, and events such as crises and disasters should be avoided as much as possible. If avoidance is not possible, resilience must be built to resist the negative impact of these events, so that the city can maintain its daily functions (Gebre-Egziabher, 2004). Compared with sustainable cities, resilient cities are more capable of coping with specific risks. On the one hand, they have the ability to defend and create buffers against disasters, crises and uncertainties, as well as high self-recovery capacity after destruction; on the other hand, the internal development vitality of the urban system is emphasized, so that cities can find opportunities in challenges and effectively convert them into resources. Therefore, the concept of resilient city not only is compatible with several important goals that contemporary cities need to achieve, such as sustainable development, but also serves as a strong complement and extension of sustainable urbanization. It therefore provides a new idea for coping with the crisis, uncertainty and complexity of future urbanization.

2 Literature review

2.1 Resilience and resilient city

The concept of "resilience" was first proposed by the American ecologist Holling. It is the ability of an ecosystem to quickly restore back its original state and maintain its structure and function in the face of external shocks (Holling, 1973). Later, resilience achieved further deepening and development in the research areas of sociology (Dovers and Handmer, 1992; Adger, 2000; Brakman et al., 2015) and economics (Polèse, 2010; Hudec et al., 2018; Wilson and Jonas, 2018), used to describe the ability of communities or residents to cope with social, political, and economic changes. For these concepts, there is a significant difference in the scope and connotation of research, but they all agree that the most basic meaning of resilience is the ability of a system to resolve external shocks and maintain its main functions during a crisis. Moreover, by absorbing and adapting to the external shocks, restoring to its original state and learning from experience, the system can adjust itself to a new context and enter the next equilibrium state (Hudec et al., 2018).

Since the 1990s, the resilience theory has increasingly spilled over into the urban system. At first, it was used to test the vulnerability of the urban system to natural disasters, especially those caused by climate change (Colten et al., 2008). Later, it was further applied to other city systems, such as the urban social system (Waley, 2005), economic system (Pike et al., 2010), and safety system in response to growing terrorist threats (Coaffee, 2016). It was also applied to the spatial system (Cumming, 2011) and urban governance model (Klein et al., 2017), Thus began an improvement in its practical applicability, developing up a new vision of urban planning research (Davoudi et al., 2012).

2.2 Urban resilience assessment

Gunderson and Holling argue that resilience can be quantified (Holling and Gunderson, 2002) in terms of the degree of disturbance, provided that the system is able absorb disturbance and remain unchanged. The quantification, evaluation and empirical research of resilient city started after 2000. Presently, the research is in the process of exploration from theory to practice. Due to the complexity

of the urban system and the universal goal of building resilient cities, the academic community has conducted continuous and diverse explorations on intrinsic dimensions and construction methods. As the Bonn Conference was held in Germany in 2010, many countries, including the United States, the United Kingdom, Australia, and Switzerland, formulated urban development strategies and policies based on resilience theory (Pestel, 2010; ARUP, 2014). Subsequently, more and more evaluation activities were held by international non-profit organizations and government agencies.

Chinese academic researchers turned their attention to resilient city in the early 21st century. At the Liberal Forum on "Risk Society and Resilient City" held during the China Urban Conference on Urban Planning in 2015, they proposed that cities should develop a comprehensive and systematic understanding of the importance of the urban resilience assessment by assessing, predicting and pre-evaluating different environment risks. Some scholars began to conduct research on resilient city assessment for China. The studies can be roughly classified into three categories: First urban resilience was measured based on different research scales, covering the whole country, urban agglomerations, cities, communities, etc (Li and Zhai 2017; Xiu et al., 2018; Zhang and Feng, 2019; Shen et al., 2021). Second, an urban resilience evaluation framework was developed from different perspectives, such as disaster management, sponge city, and geography (Zheng et al., 2018; Li et al., 2019; Li et al., 2022).Third, a discussion was made on the relationship between urban resilience and other urban characteristics, including urban space, city scale, etc (Wei and Pan, 2021; Fang et al., 2022).

Although academics have recognized the importance of urban resilience research, how to systematically and dynamically understand urban resilience remains difficult point in academic discussions. As a comprehensive and dynamically evolutionary system, urban resilience differs significantly from city to city because of regional developmental background in the presence of uncertain disturbing factors. Moreover, the dominating factors are different. Therefore, a multi-dimensional resilient city evaluation framework of "social resilience-economic resilience-urban infrastructure and service-urban governance" was built in this paper based on a comprehensive urban system; then, the entropy weight method was used to measure the level of urban resilience in Hunan Province, while an obstacle degree model was used to identify any obstacle factors to the development of resilience. Meanwhile, the dynamic changing process of the system was put under observation in an attempt to put forward relevant recommendations on enhancing urban resilience and promoting the sustainable coordinated development of intraregional cities.

3 Study area, index system construction and research methodology

3.1 Study area

According to the present status of social and economic development, China is divided into four economic regions, including East China, Central China, West China, and Northeast China. As the transition area between East China and West China, Central China comprises of six provinces including Shanxi, Henan, Anhui, Jiangxi, Hubei and Hunan. Located in the core inland area, Central China plays an important role in linking other parts of the country together. In this study, Hunan Province, part of Central China, was selected as the research object. By reference to the Statistical Yearbook of Hunan Province, the statistical yearbooks of the cities and prefectures under its jurisdiction, the Statistical Communiqué of the People's Republic of China on the 2021 National Economy and Social Development, etc., the years 2010, 2015, and 2020 were selected for evaluation research on the urban resilience of Hunan Province and for identification of obstacle factors.

3.2 Index system construction and research methodology

3.2.1 Index system framework

Resilient city evaluation indexes provide a conceptual representation of the causes of urban resilience. Each index is designed to identify the basic elements related to resilience and explore the internal relation between resilience drivers from different perspectives. Compared with other relevant urban evaluation indexes, a resilient city should be problem-oriented and risk-targeted, and focus more on how to enhance the urban system's resistance to multiple pressures as well as its diverse absorptive capacity. All the major constituents of the resilient city system, including the society, economy, environment, population health, policy management, and infrastructure, should be reflected in the index system, and multiple indexes should be used to form an organic whole. The index system should not only reflect the connotation of resilient city, but also comprehensively consider social economic characteristics; be not only conducive to leadership decision-making, but also highly understandable for the public.

In this study, the classification framework of the resilient city index system is defined as follows: 1) A classic classification framework widely recognized by the academic community is adopted for the index system; 2) The index system comprehensively reflects various aspects of resilient city development. Based on the above literature research and data availability, expert opinions and correlative analysis, a resilient city evaluation framework of "social resilience-economic resilience-urban infrastructure and service-urban governance"

TABLE 1 Comprehensive weight table of urban resilience evaluation indexes.

Target layer	Criterion layer	Weight	Domain layer	Weight	Index layer	Unit	Weight
Urban resilience evaluation index system (A)	Social resilience (A1)	0.329	Education (B1)	0.104	Teacher-student ratio (C1)	%	0.015
					Ratio of education expenditure to local government expenditure (C2)	%	0.050
					Number of school places per 10,000 people (C3)	people/ 10,000 people	0.039
			Health (B2)	0.112	Average life expectancy of population (C4)	Year	0.031
					Number of doctors per 10,000 people (C5)	people/ 10,000 people	0.045
					Number of hospital beds per 10,000 people (C6)	PCS/ 10,000 people	0.036
			Social security (B3)	0.067	Basic pension insurance coverage (C7)	%	0.028
					Ratio of fiscal expenditure for social security to total fiscal expenditure (C8)	%	0.039
			Social equity (B4)	0.046	Affordable housing coverage (C9)	%	0.014
					Housing price-to-income ratio (C10)		0.032
	Economic resilience (A2)	0.261	Economic prosperity (B5)	0.062	Per capita disposable income of urban residents (C11)	yuan	0.033
					Registered urban unemployment rate (C12)	%	0.015
					Ratio of local fiscal revenue to GDP (C13)	%	0.014
			Structural improvement (B6)	0.109	Ratio of the added value of the tertiary industry to GDP (C14)	%	0.060
					Ratio of the added value of high-tech industries to industrial added value (C15)	%	0.049
			Innovation potential (B7)	0.090	Ratio of expenditure for research and experimental development to fiscal expenditure (C16)	%	0.061
					Number of effective invention patents per 10,000 people (C17)	PCS/ 10,000 people	0.029
	Urban infrastructure and service resilience (A3)	0.255	Ecological environment management (B8)	0.144	Urban air quality compliance rate (C18)	%	0.027
					Comprehensive utilization rate of industrial solid waste (C19)	%	0.015
					Park land per capita (C20)	m2	0.065
					GDP energy consumption for every ten thousand yuan (C21)	TCE/ 10,000 yuan	0.037
			Critical infrastructure (B9)	0.111	Public traffic network density (C22)	km/km2	0.043
					Natural gas penetration rate in urban areas (C23)	%	0.025
					Internet penetration rate (C24)	Household/ 100 people	0.043
	Urban governance resilience (A4)	0.155	Social integration (B10)	0.052	Proportion of community-based health service centers (C25)	%	0.034
					Ratio of personnel engaged in public administration, social security and social organizations (C26)	%	0.018
			Emergency management (B11)	0.103	Per-capita shelter area (C27)	sqm/person	0.058
					Number of large-scale urban public facilities eligible for emergency renovation (C28)	sqm/person	0.045

was selected. Different topics were set under each category, and 28 indexes were placed under the topics to represent the status of each topic. Finally, an evaluation index framework system was built for resilient city (Table 1).

3.2.2 Research methodology

All index data underwent dimensionless preprocessing, so as to have the same character; then, Pearson correlation analysis was conducted to remove a small number of indexes highly correlated with one another. The rationality of index weight has direct influence on the correctness of comprehensive evaluation, so the weight of each index should reflect its importance to resilient city development. In this study, the entropy weight method (Shannon, 1948) was used to scientifically determine the weight of each index. Also, an urban resilience evaluation model was built and used to measure the urban resilience of Hunan Province. Furthermore, an obstacle degree model was used to identify the obstacle factors to resilience.

(i) Data source and preprocessing

Most of the data adopted in this study came from the Statistical Yearbook of Hunan Province, the statistical yearbooks of the cities and prefectures under its jurisdiction, the Statistical Communiqué of the People's Republic of China on the 2021 National Economy and Social Development, and the official website of each prefectural bureau of statistics. Some other data was obtained by basic information calculation.

The evaluation indexes underwent dimensionless processing in order to eliminate the difference between the indexes and make the data comparable. The calculation formula is as follows:

Let there be n years and m evaluation indexes selected for the study, So, Vij is the jth index value of Hunan Province for the ith year, where n=i (i=1.2.3. . . . . .n);m=j (1.2.3. . . . . .m).

If the index is a positive index, the following formula can be used:

$$V_{ij} = \frac{v_{ij} - m_j}{M_j - m_j} \tag{1}$$

If the index is a negative index, the following formula can be used:

$$V_{ij} = \frac{M_j - v_{ij}}{M_j - m_j} \tag{2}$$

where M_j is the maximum value of v_{ij}; m_j is the minimum value of v_{ij}.

(ii) Entropy weight method

The discreteness of data matter much if the entropy weight method is adopted for weight determination. According to the amount of information provided by indexes, the degree of dispersion between indexes can be analyzed to objectively determine index weight, thus avoiding the impact of experts' subjective thinking to a certain extent (Toumi et al., 2017). The higher the index weight, the greater its impact on comprehensive evaluation. The calculation steps are as follows:

The p-value obtained index normalization is as follows:

$$P_{ij} = \frac{V_{ij}}{\sum_{i=1}^{n} V_{ij}} \tag{3}$$

The entropy was calculated. The entropy E_j of the jth index is as follows:

$$E_j = \frac{-1}{\ln n \sum_{i=1}^{n} P_{ij} \ln P_{ij}} \tag{4}$$

The G value of difference coefficient was calculated:

$$G_j = 1 - E_j \tag{5}$$

The weight W_j of each index was calculated, obtaining a comprehensive weight table of resilient city evaluation indexes (Table 1):

$$W_j = \frac{G_j}{\sum_{j=1}^{m} G_j} \tag{6}$$

The comprehensive score of urban resilience was calculated. Then, the index weight was multiplied by P_{ij}:

$$S = \sum_{j=1}^{m} W_j P_{ij} \tag{7}$$

(iii) Obstacle degree model

The obstacle degree model, which can be used to objectively and scientifically find out any obstacle factors to a certain evaluation object (Xu J., 2002), is a mathematical method used to identify the factors restricting the development of things based on index deviation and explain the varying degree that each index hinders the evaluation system.

$$D_{ij} = \left(1 - V_{ij}\right) W_{ij} \Big/ \sum_{i=1}^{n} \left(1 - V_{ij}\right) W_{ij} \tag{8}$$

4 Research results and analysis

4.1 Spatial-temporal evolution characteristics of urban resilience of Hunan Province

4.1.1 Temporal evolution characteristics

By the above calculation steps, the resilience level of 14 cities in Hunan Province could be calculated for the years 2010, 2015,

TABLE 2 Score of urban resilience of each administrative region in Hunan Province.

	Changsha city	Zhuzhou city	Xiangtan city	Hengyang city	Shaoyang city	Yueyang city	Changde city
2010	0.4273	0.3253	0.3224	0.2635	0.3507	0.3858	0.4158
2015	0.5342	0.3677	0.4206	0.3823	0.3033	0.3509	0.3576
2020	0.5950	0.4288	0.4257	0.4042	0.3412	0.4019	0.3707
	Zhangjiajie city	Yiyang city	Chenzhou city	Yongzhou city	Huaihua city	Loudi city	Xiangxi prefecture
2010	0.4107	0.3413	0.3662	0.3888	0.3944	0.3829	0.3731
2015	0.3091	0.3232	0.3104	0.3642	0.3251	0.3174	0.3196
2020	0.4237	0.3406	0.3485	0.3972	0.3943	0.3911	0.3014

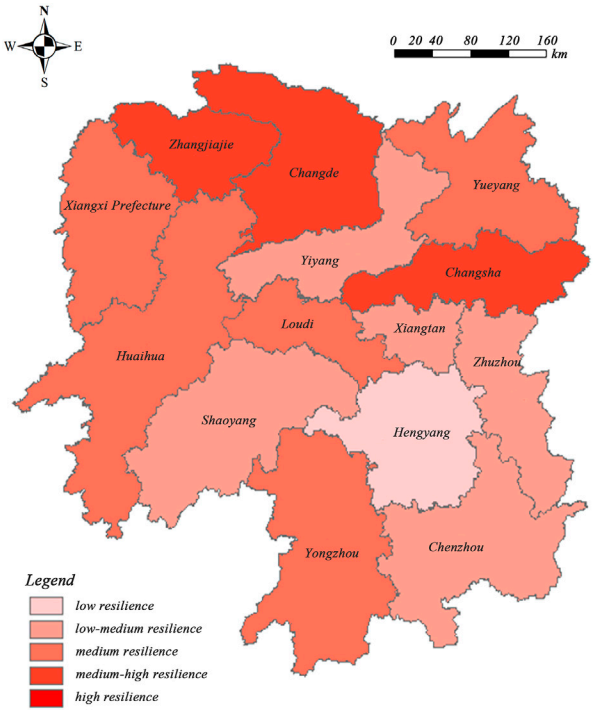


FIGURE 1
Urban resilience level of Hunan Province in 2010.

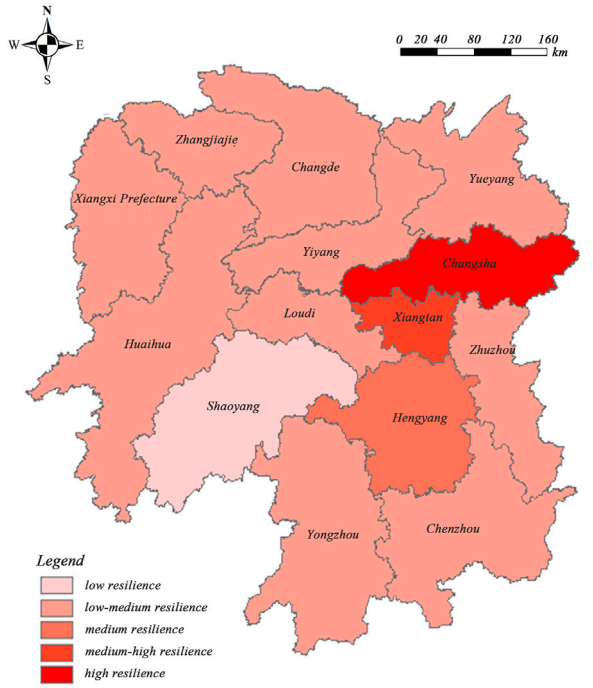


FIGURE 2
Urban resilience level of Hunan Province in 2015.

and 2020 (Table 2). The higher the score, the higher the urban resilience level and *vice versa*.

As can be seen from Table 2, the urban resilience level of each administrative region in Hunan fluctuates over time, with the majority of the cities showing a slow growth trend. Changsha had the highest resilience level, and ranked first in the 3 years. It received the highest score, 0.5950, in 2020; the city that received the lowest scores vary across the three time sections. Hengyang received a score of 0.2635 only in 2010, the lowest in 3 years, with a difference of 0.3325 from the highest value. It can be seen that the development of resilience levels in various cities is uneven and there are large differences.

Urban resilience levels can be classified into the following three evolutionary states: The first evolutionary state is that the resilience level keeps rising over time. Such cities include Changsha, Zhuzhou, Xiangtan and Hengyang, accounting for 29% of the total. The second evolutionary state is that the resilience level rebounds after a decline, showing undulating changes. Such cities account for the highest proportion, at 64%, including Shaoyang, Yueyang, Changde, Zhangjiajie, Yiyang, Chenzhou, Yongzhou, Huaihua, and Loudi, a total of

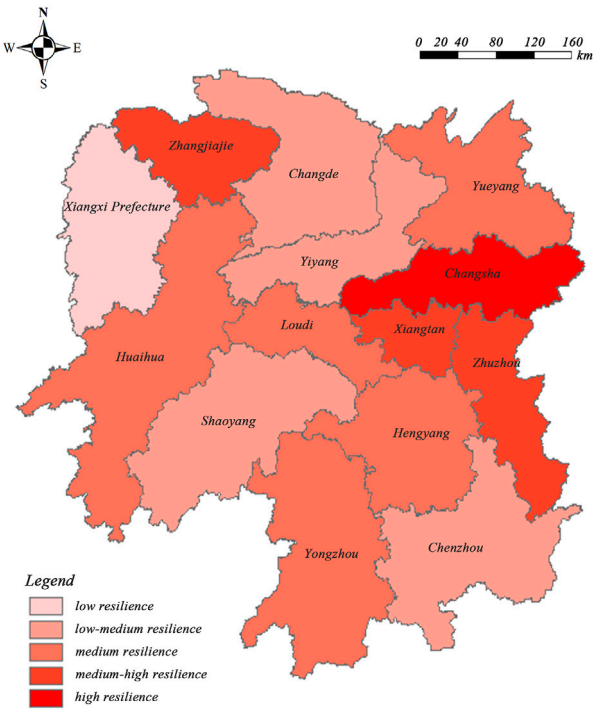


FIGURE 3
Urban resilience level of Hunan Province in 2020.

nine cities. Finally, as the only weakened city, Xiangxi Autonomous Prefecture has been in a state of decline for the past 10 years.

4.1.2 Spatial-temporal evolution characteristics

In Gis software, the natural breaks classification method (Jenks, 1967) was used to divide Hunan Province into cities with low (low, low-medium), medium and high (high, medium-high) resilience (Figure 1, Figure 2, Figure 3). For the cities with high resilience, their score is 0.4042; the score of those with medium resilience is 0.3707–0.4042; the score of those with low resilience is below 0.3707.

As can be seen, there is a significant spatial difference in urban resilience, and high-resilience cities have a space radiation effect with the provincial capital Changsha as the core. Other cities are medium/low-resilience regions, but have changed in the three time sections. For example, the medium and medium/low-resilience regions in North Hunan were reduced to medium/low-resilience regions, and their score began to rise again in 2020. A continuous change takes place in the cities with low resilience, primarily including Hengyang, Shaoyang, and Xiangxi.

As can be seen from the 2010–2020 development trend, the number of cities with medium/low-resilience gradually decreased, while the number of those with high resilience increased, score increasing faster than it decreased. Therefore, the comprehensive urban resilience level of Hunan Province was on the rise. The cities with medium/high resilience were located closer to the provincial capital Changsha. This was similar to Hunan Province's urban structure, in which "Changsha, Zhuzhou and Xiangtan," the core cities in Hunan Province, developed together with other cities. In other words, eastern Hunan was in the lead, with its predominance gradually spreading from east to west, forming a space pattern with Xiangxi as a low-resilience region.

4.2 Identification of major obstacle factors for urban resilience of Hunan Province

A targeted urban resilience optimization strategy was put forward in order to further identify the weaknesses of urban resilience development to help city managers prioritize the construction and development of various urban systems in accordance with urban needs. The obstacle degree of all 2010–2020 obstacle factors was calculated. Due to limited space, the top 6 obstacle factors were selected and arranged in order. See (Table 3) for details.

4.2.1 Obstacle type recognition on criterion layer

As can be seen from the 3D diagnostic results of obstacle factors on the criterion layer (Figure 4), urban resilience is primarily hindered by the social and economic systems. The two systems of urban infrastructure and services and urban governance are weak obstacles. In 2010, the economic system brought about the greatest obstacle, 35.72%. From 2010 to 2020, with the continuous development of the economy, the obstacle degree of the economic system showed a downward trend, while that of the social system and infrastructure system rose in a wave-like manner, and that of the urban governance system gradually increased. Thus it can be seen that rapid urbanization enhanced economic resilience, leading to a decline in the obstacle degree of the economic resilience system. However, the construction of the society, infrastructure and service and urban governance lagged behind, with the obstacle degree undulating, becoming an important factor affecting the urban resilience of Hunan Province. Although the obstacles degree of the economic system tends to gradually reduced compared with other systems, due to the original poor foundation and the low overall level of the urban economy in Hunan Province, its expenditure on education, medical care and social security is limited. Therefore, the social and economic systems would play a leading role in dominating the urban resilience level for a long time.

4.2.2 Obstacle type recognition on index layer

Judging from the diagnostic results of obstacle factors on the index layer, from 2010 to 2015, the top three obstacle factors affecting the urban resilience of Hunan Province

TABLE 3 Rank order list of major obstacle factors to the development of urban resilience in Hunan Province Unit: %.

Year	2010			2015			2020		
Rank	Obstacle factors		Obstacle degree	Obstacle factors		Obstacle degree	Obstacle factors		Obstacle degree
1	Ratio of expenditure for research and experimental development to fiscal expenditure	C16	8.29	Ratio of expenditure for research and experimental development to fiscal expenditure	C16	7.96	Park land per capita	C20	10.42
2	Ratio of the added value of the tertiary industry to GDP	C14	8.21	Ratio of the added value of the tertiary industry to GDP	C14	7.49	Per-capita shelter area	C27	7.75
3	Ratio of the added value of high-tech industries to industrial added value	C15	7.59	Ratio of the added value of high-tech industries to industrial added value	C15	7.31	Ratio of education expenditure to local government expenditure	C2	7.69
4	Per-capita shelter area	C27	6.49	Per-capita shelter area	C27	7.2	Ratio of the added value of high-tech industries to industrial added value	C15	7.5
5	Ratio of education expenditure to local government expenditure	C2	6.44	Number of doctors per 10,000 people	C5	6.07	Ratio of expenditure for research and experimental development to fiscal expenditure	C16	6.98
6	Number of large-scale urban public facilities eligible for emergency renovation	C28	6.24	Number of school places per 10,000 people	C3	5.61	Number of school places per 10,000 people	C3	5.92

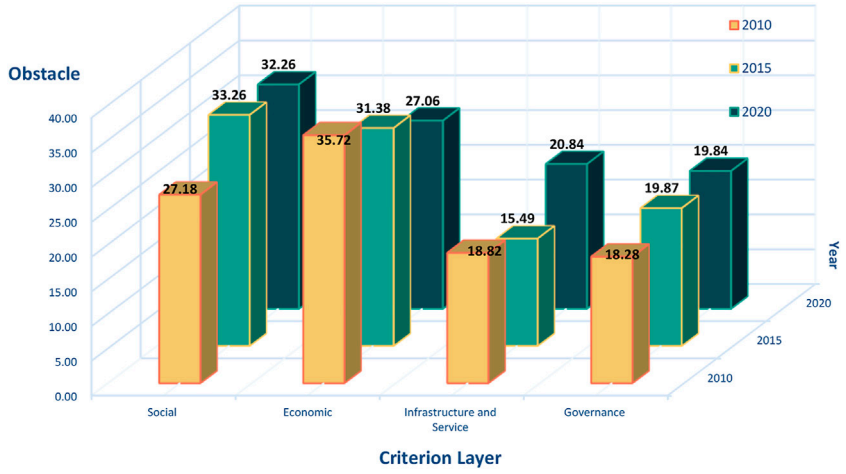


FIGURE 4
Obstacle on criterion layer level of Hunan Province.

were the ratio of expenditure for research and experimental development to fiscal expenditure (C16), the ratio of the added value of the tertiary industry to GDP (C14), and the ratio of the added value of high-tech industries to industrial added value (C15), suggesting that Hunan Province should focus on optimizing its economic structure and tap economic innovation potential in order to enhance its urban resilience.

In 2020, the park land per capita (C20) appeared among major obstacle factors, and became a first obstacle factor restricting the development of urban resilience. The ratio of expenditure for research and experimental development to fiscal expenditure (C16), which had its obstacle degree lowered to a small extent, ranked behind. The per-capita shelter area (C27) and ratio of education expenditure to local government expenditure (C2) obstacle degree

increased to some extent, mainly due to the fact that infrastructure construction failed to keep pace with the fast development of urban economy in Hunan Province. In general, the obstacle factors to the development of urban resilience from 2010 to 2020 transitioned from the economic system to the social-economic-urban infrastructure and service systems.

5 Conclusions and suggestions

5.1 Conclusions

(1) In terms of time, the urban resilience level of Hunan Province has increased at a slow pace over the past 10 years; the overall level is not high, and there are differences from city to city; the provincial capital city Changsha has obvious development advantages and ranks first in terms of resilience level. Zhuzhou and Xiangtan have had their resilience level significantly improved with the construction of a new urban system centered on the Changsha-Zhuzhou-Xiangtan Urban Agglomeration. Other cities, especially non-regional central cities, generally have a low resilience level. In terms of space, there have been more and more cities with high resilience over the past 10 years, but the cities with low or medium-resilience still occupy a dominant position, forming a spatial process of evolution from "medium/high-level dispersion" to "medium/high-level aggregation" in the Changsha-Zhuzhou-Xiangtan Urban Agglomeration.

(2) Over the past 10 years, the level of urban resilience in Hunan Province has mainly been hindered by the social and economic systems, but the degree of economic system obstacles has improved with the development of the economy, while the other three system obstacles have shown a fluctuating increase. From the perspective of obstacle factors on the index layer, from 2010 to 2015, the major obstacle factors were the ratio of expenditure for research and experimental development to fiscal expenditure, the ratio of the added value of the tertiary industry to GDP, and the ratio of the added value of high-tech industries to industrial added value, which are part of the economic system. In 2020, the above major obstacle factors were replaced by those in the social-economic-urban infrastructure and service system, including the per-capita shelter area and ratio of education expenditure to local government expenditure.

5.2 Suggestions

Considering the evaluation results of Hunan Province's urban resilience and the diagnostic results of obstacle factors, the following suggestions are put forward in order to improve the urban resilience and sustainable coordinated development of cities in Hunan Province:

(1) Support non-central cities and stabilize the development of the cities with medium/high resilience. On 24 February 2022, the Changsha-Zhuzhu-Xiangtan Metropolitan Area Development Plan was officially approved, meaning that Changsha, Zhuzhu and Xiangtan can achieve further regional integration. In the long run, it is necessary to actively exploit the surrounding cities with medium/low resilience, such as Hengyang, Yueyang, Changde, Yiyang, Loudi, etc., to build a greater metropolitan area "with Changsha, Zhuzhu and Xiangtan as the core to drive the integrated development of Northeast Hunan," so as to greatly improve the urban resilience level of Hunan Province and the city agglomerations in the middle reaches of the Yangtze River. Non-central remote cities, such as Chenzhou, Huaihua, and Zhangjiajie, can build themselves into a second echelon of resilient cities in Hunan Province with the aid of their unique resource advantages and location characteristics. As a low-resilience city, the Xiangxi Prefecture should make full use of its local features to keep promoting rural revitalization. The opening of the Zhangjiajie-Jishou-Huaihua High-speed Railway at the end of 2021 will also significantly promote the economic vitality of the northwest region.

(2) Reduce the obstacle degree of the major economic and social systems. Regarding the economic system, it is necessary to focus on optimizing the economic structure and tapping economic innovation potential. On the one hand, Hunan Province should strengthen reasonable supply and guarantees in the industrial space to build an important national highland of advanced manufacturing, so as to establish a modern industrial development pattern with core leadership, rational division of labor and high agglomeration efficiency. On the other hand, it is necessary to insist on innovation, place an emphasis on human resources, carry on the supply-side reform with technological innovation, and promote the optimization of industrial structure and the transformation of economic development to achieve a balance between supply and demand, so as to realize high-quality economic development. As for high-tech industries, it should give prominence to industries and key projects, establish high-tech industrial advantages, promote industrial restructuring and increase the industrial scale, strengthen industry-university-research integration, etc. On this basis, it is necessary to steadily improve the social system, enhance the fair and reasonable allocation of public resources such as education and medical care,

ameliorate the active social policy system, and carry out a policy reform in social security, pension service, employment support, etc.

(3) Strengthen infrastructure and service construction to enhance the efficiency of urban governance. Public traffic networks, Internet communication projects, public parks, etc., which are closely related to the public, provide vitality for urban development, and are of great significance to the improvement of urban resilience. The advent of a risk society has put forward new demands and requirements for urban governance, while the emergence of major public health emergencies, such as COVID-19 pandemic, has constituted a direct tests on the level of urban governance. Through more intensive and efficient institutional arrangements, as well as IT-based urban public management and services, economic resilience, social resilience and facility resilience can be combined together organically by urban governance under the construction of resilient cities, so that the cities can obtain resilient forces that enable them to renew, recovery and develop themselves.

The significance of the evaluation of urban resilience level lies in a more scientific and comprehensive assessment of a city's adaptability to external changes and self-regulation capabilities. This study has certain limitations. This is first manifested in dependency on the accumulation and accuracy of basic statistical data on population, socioeconomic status, environment, infrastructure, etc. However, in the current period of rapid urbanization, Chinese cities all have difficulties in collecting data or lack existing data. Therefore, when selecting indexes, we tried to consider choosing those included in the scope of government monitoring. Second, owing to a large gap in urbanization among different regions in China, it is hard to use a unified standard to evaluate cities that differ greatly. In this index system, there are many indicators that are common in the current index systems of international organizations. Although every city agrees with a set of basic indexes during the evaluation, each city also needs to screen or expand the indicator system according to the characteristics and policy preferences of the specific city, so as to better serve the development and construction of resilient city.

Data availability statement

The datasets presented in this study can be found in online repositories. The names of the repository/repositories and accession number(s) can be found below: HUNAN STATISTICAL YEARBOOK 2020: http://tjj.hunan.gov.cn/hntj/tjsj/tjnj/202011/t20201130_13972011.html HUNAN STATISTICAL YEARBOOK 2015: http://tjj.hunan.gov.cn/hntj/tjsj/tjnj/201605/t20160506_3818593.html HUNAN STATISTICAL YEARBOOK 2010: http://tjj.hunan.gov.cn/hntj/tjsj/tjnj/201103/t20110315_5295798.html.

Author contributions

NC: Proposed research propositions, designed experiments, drafted papers, and revised key academic contents; HG: Collect experimental data, conduct experiments and analyze the results; HX: Finalizing and proofreading the article.

Funding

This work was supported partially by the National Natural Science Foundation of China (No. 51908202). All opinions are the responsibility of the authors alone.

Conflict of interest

The authors declare that the research was conducted in the absence of any commercial or financial relationships that could be construed as a potential conflict of interest.

Publisher's note

All claims expressed in this article are solely those of the authors and do not necessarily represent those of their affiliated organizations, or those of the publisher, the editors and the reviewers. Any product that may be evaluated in this article, or claim that may be made by its manufacturer, is not guaranteed or endorsed by the publisher.

Supplementary material

The Supplementary Material for this article can be found online at: https://www.frontiersin.org/articles/10.3389/feart.2022.1033441/full#supplementary-material

References

Adger, W. N. (2000). Social and ecological resilience: Are they related? *Prog. Hum. Geogr.* 24 (3), 347–364. doi:10.1191/030913200701540465

ARUP (2014). *City resilience framework*. New York, NY: The Rockefeller Foundation.

Brakman, S., Garretsen, H., and van Marrewijk, C. (2015). Regional resilience across Europe: On urbanisation and the initial impact of the Great Recession. *Camb. J. Regions, Econ. Soc.* 8 (2), 225–240. doi:10.1093/cjres/rsv005

Coaffee, J. (2016). *Terrorism, risk and the global city: Towards urban resilience*. Routledge. Oxfordshire, England, UK.

Colten, C. E., Kates, R. W., and Laska, S. B. (2008). Three years after Katrina: Lessons for community resilience. *Environ. Sci. Policy Sustain. Dev.* 50 (5), 36–47. doi:10.3200/envt.50.5.36-47

Cui, S. H., Li, F. Y., Yu, Y. X., and Lin, J. (2010). Theoretical thinking on urbanization and sustainable urbanization. *Urban Stud.* 3, 19. doi:10.3969/j.issn.1006-3862.2010.03.004

Cumming, G. S. (2011). Spatial resilience: Integrating landscape ecology, resilience, and sustainability. *Landsc. Ecol.* 26 (7), 899–909. doi:10.1007/s10980-011-9623-1

Davoudi, S., Shaw, K., Haider, J., Quinlan, A., Peterson, G., Wilkinson, C., et al. (2012). Resilience: A bridging concept or a dead end? *Planing Theory & Pract.* 13, 299–333. doi:10.1080/14649357.2012.677124

Dovers, S. R., and Handmer, J. W. (1992). Uncertainty, sustainability and change. *Glob. Environ. Change* 2 (4), 262–276. doi:10.1016/0959-3780(92)90044-8

Fang, Y. L., Su, X. Q., Huang, Z. F., and Guo, B. B. (2022). Structural characteristics and resilience evaluation of tourism flow networksin five major urban agglomerations in coastal China: From the perspective of evolutionary resilience. *Econ. Geograrphy* 42 (02), 203–211. doi:10.15957/j.cnki.jjdl.2022.02.022

Gebre-Egziabher, A. (2004). Sustainable cities programme: A joint UN-habitat-UNep facility on the urban environment with participation of the Dutch government. *Ann. N. Y. Acad. Sci.* 1023 (1), 62–79. doi:10.1196/annals.1319.016

Holling, C. S., and Gunderson, L. H. (2002). *Panarchy: Understanding transformations in human and natural systems*. Washington, DC: Island Press.

Holling, C. S. (1973). Resilience and stability of ecological systems. *Annu. Rev. Ecol. Syst.*, 25 1–23. doi:10.1146/annurev.es.04.110173.000245

Hudec, O., Reggiani, A., and Šiserová, M. (2018). Resilience capacity and vulnerability: A joint analysis with reference to Slovak urban districts. *Cities* 73, 24–35. doi:10.1016/j.cities.2017.10.004

Jenks, G. F. (1967). The data model concept in statistical mapping. *Int. Yearb. Cartogr.* 7, 186–190.

Kanuri, C., Revi, A., Espey, J., and Kuhle, H. (2016). *Getting started with the SDGs in cities: A guide for stakeholders*. JSTOR.

Klein, B., Koenig, R., and Schmitt, G. (2017). Managing urban resilience. *Informatik-Spektrum* 40 (1), 35–45. doi:10.1007/s00287-016-1005-2

Lebel, L., Anderies, J. M., Campbell, B., Folke, C., Hatfield-Dodds, S., Hughes, T. P., et al. (2006). Governance and the capacity to manage resilience in regional social-ecological systems. *Ecol. Soc.* 11 (1). doi:10.5751/es-01606-110119

Levin, S. A., Barrett, S., Aniyar, S., Baumol, W., Bliss, C., Bolin, B., et al. (1998). Resilience in natural and socioeconomic systems. *Environ. Dev. Econ.* 3 (2), 221–262. doi:10.1017/s1355770x98240125

Li, Y., Chen, W., and Sun, Y. (2019). New reflections on the analysis of regional resilience in geographical sciences from a relational-dynamic perspective. *Geogr. Res.* 38 (7), 1694–1704. doi:10.11821/dlyj020180256

Li, Z. Z., Fu, D. F., Wang, J. X., Min, K. D., and Zhang, J. Y. (2022). Urban resilience assessment model for waterlogging disasters and its application. *J. Tsinghua Univ. Sci. Technol.* 62 (2), 266–276. doi:10.16511/j.cnki.qhdxxb.2021.22.037

Li, Y., and Zhai, G. F. (2017). China's urban disaster resilience evaluation and promotion. *Planners* 33 (8), 5–11. doi:10.3969/j.issn.1006-0022.2017.08.001

Pestel Institut (2010). *Regionale krisenfestigkeit: Eine indikatorengestützte bestandsaufnahme auf der ebene der kreise und kreisfreien städte*. Hannover: Selbstverlag.

Pike, A., Dawley, S., and Tomaney, J. (2010). Resilience, adaptation and adaptability. *Camb. J. regions, Econ. Soc.* 3 (1), 59–70. doi:10.1093/cjres/rsq001

Polèse, M. (2010). *The resilient city: On the determinants of successful urban economies*. London: Forthcoming Press.

Shannon, C. E. (1948). A mathematical theory of communication. *Bell Syst. Tech. J.* 27 (3), 379–423. doi:10.1002/j.1538-7305.1948.tb01338.x

Shen, L. N., Tian, Y. P., and Du, Y. X. (2021). Resilience reconstruction of old communities based on resilience system. *Urban Probl.* 8, 45–54. doi:10.13239/j.bjsshkxy.cswt.210805

Toumi, O., Le Gallo, J., and Rejeb, J. B. (2017). Assessment of Latin American sustainability. *Renew. Sustain. Energy Rev.* 78, 878–885. doi:10.1016/j.rser.2017.05.013

Unep (2019). *Environment outlook GEO-6*. United Kingdom: Cambridge University Press.

Waley, P. (2005). The vulnerability of cities: Natural disasters and social resilience. *Geogr. J.* 171, 190. doi:10.4324/9781849773379

Wei, S. M., and Pan, J. H. (2021). Network structure resilience of cities at the prefecture level and above in China. *Acta Geogr. Sin.* 76 (6), 1394–1407.doi:10.11821/dlxb202106006

Wilson, D., and Jonas, A. E. (2018). Urban resilience: An urban political movement. *Urban Geogr.* 39 (8), 1265–1267. doi:10.1080/02723638.2018.1452873

Xiu, C. L., Wei, Y., and Wang, Q. (2018). Evaluation of urban resilience of Dalian city based on the perspective of "Size-Density-Morphology. *Acta Geogr. Sin.* 73 (12), 2315–2328. doi:10.11821/dlxb201812004

Xu, J. H. (2002). *Mathematical methods in contemporary geography*. 3rd Ed. Beijing: Higher Education Press.

Zhang, M. D., and Feng, X. Q. (2019). A comparative study of urban resilience and economic development level of cities in Yangtze river delta urban agglomeration. *Urban Dev. Stud.* 26 (1), 82–91. doi:10.3969/j.issn.1006-3862.2019.01.017

Zhang, X., and Li, H. (2018). Urban resilience and urban sustainability: What we know and what do not know? *Cities* 72, 141–148. doi:10.1016/j.cities.2017.08.009

Zheng, Y., Zhai, J. Q., Wu, Z. Y., Li, Y. N., and Shi, W. (2018). A typology analysis on resilient cities based on adaptive cycle —Taking cases of Chinese sponge cities and climate resilient cites pilot projects. *China Population,Resources Environ.* 28 (3), 31–38. doi:10.12062/cpre.20171109

frontiers | Frontiers in Earth Science

TYPE Original Research
PUBLISHED 17 January 2023
DOI 10.3389/feart.2022.1010134

Check for updates

OPEN ACCESS

EDITED BY
Guang-Liang Feng,
Institute of Rock and Soil Mechanics (CAS), China

REVIEWED BY
Qiu Enxi,
Southwest Petroleum University, China
Hong Xu,
Changsha University of Science and Technology, China

*CORRESPONDENCE
Yulong Dong,
stxfdyl1122@yeah.net

SPECIALTY SECTION
This article was submitted to Geohazards and Georisks, a section of the journal Frontiers in Earth Science

RECEIVED 02 August 2022
ACCEPTED 29 November 2022
PUBLISHED 17 January 2023

CITATION
Yang P, Dong Y, Zhang Y, Wu G and Yao Y (2023), Research on prevention and control methods of land subsidence induced by groundwater overexploitation based on three-dimensional fluid solid coupling model—a case study of Guangrao County.
Front. Earth Sci. 10:1010134.
doi: 10.3389/feart.2022.1010134

COPYRIGHT
© 2023 Yang, Dong, Zhang, Wu and Yao. This is an open-access article distributed under the terms of the Creative Commons Attribution License (CC BY). The use, distribution or reproduction in other forums is permitted, provided the original author(s) and the copyright owner(s) are credited and that the original publication in this journal is cited, in accordance with accepted academic practice. No use, distribution or reproduction is permitted which does not comply with these terms.

Research on prevention and control methods of land subsidence induced by groundwater overexploitation based on three-dimensional fluid solid coupling model—a case study of Guangrao County

Peijie Yang[1,2], Yulong Dong[1,2]*, Yongwei Zhang[1,2], Guangwei Wu[1,2] and Yue Yao[3]

[1]Shandong Provincial Territorial Spatial Ecological Restoration Center, Jinan, China, [2]Yellow River Delta Land Use Security Field Scientific Observation and Research Station, Ministry of Natural Resources, Binzhou, China, [3]Institute of Marine Science and Technology, Shandong University, Qingdao, Shandong, China

Land subsidence is an environmental geological phenomenon with slowly decreasing ground elevation, The North China Plain is one of the areas with the most serious land subsidence in China, and Guangrao County is one of the subsidence centers. This paper is based on the hydrogeological and engineering geological data of Guangrao County, the groundwater monitoring data for many years and the land subsidence monitoring data, systematically analyzes the dynamic characteristics of groundwater, the distribution and evolution of land subsidence, and the correlation between groundwater exploitation and land subsidence development in different layers of this area. Based on Biot porous medium consolidation theory, establishes a three-dimensional fluid solid coupling numerical model of land subsidence in Guangrao County, restores the development process of land subsidence, predicts and analyzes the subsidence evolution law under different groundwater exploitation schemes, and proposes targeted prevention and control measures. The research results show that: the shallow groundwater forms a cone of depression with Guangbei Salt Field as the center, and the deep groundwater forms an elliptical regional cone of depression with the urban area as the center. The ground is gradually formed two small settlement areas with the urban area of Guangrao County and Guangbei Salt Field as the settlement center, and there is a trend of interrelated expansion. The three-dimensional fluid solid coupling model of land subsidence accurately restored the development process of land subsidence in the study area, predicted that under the current groundwater exploitation conditions, by 2040, the settlement of Guangrao urban settlement center will increase to 1,350 mm, forming a large regional funnel centered around the urban area, and gradually developing and expanding around. Prohibition of groundwater exploitation in

the main funnel area is a more reasonable and effective exploitation plan to prevent the development of land subsidence.

KEYWORDS

land subsidence, groundwater overexploitation, three-dimensional, fluid-solid coupling numerical model, evolution trend

1 Introduction

Land subsidence is an environmental geological phenomenon that the regional ground elevation decreases slowly due to the consolidation and compression of the surface soil of the crust caused by natural or human factors. It has the characteristics of slow growth, long duration, expansive influence, complex genesis mechanism, and difficult prevention and control (Xue et al., 2003), (Xue et al., 2006), (Ora et al., 2019). The main causes of land subsidence are the development and utilization of underground fluid resources (groundwater, oil, natural gas, etc.), geological structure subsidence, solid mineral exploitation and engineering environmental effects, and overexploitation of groundwater is widely considered to be the most important cause of land subsidence (Liu, 2001), (Galloway and Burbey, 2011). The impact of land subsidence is mainly reflected in four aspects: 1) damage to infrastructure such as pipelines, buildings and dams (Sarah et al., 1779); 2) causing the deformation of pavement and railway foundation, and affect the service capacity of highway and railway; 3) increasing the risk of flooding (Du et al., 2018); 4) a potential channel for ground pollution sources to penetrate into the underground, causing groundwater pollution (Hussain and Abed, 2019).

Since the first discovery of land subsidence in Mexico City in 1891 (Ortega-Guerrero et al., 1999), land subsidence has been found in Ravenna and Venice in Italy (Antonellini et al., 2019), Tokyo and Osaka in Japan (Inaba et al., 1970), San Joaquin Vally and Santa Clara in the United States (Tolma and Poland, 1940), (Jeanne et al., 2019), Bangkok in Thailand (Phien-Wej et al., 2006), Jakarta in Indonesia (Abidin et al., 2011), Saudi Arabia (Othman and Abotalib, 2019), Kathmandu Watershed in Nepal and other regions (Shrestha et al., 2017), and has carried out relevant exploration and research. In China, the earliest record of land subsidence disaster was in Shanghai in 1923 (Zhang and Wei, 2002). Subsequently, land subsidence was found and became increasingly serious in whole the country. The Yangtze River Delta represented by Shanghai and Suzhou Wuxi Changzhou (Li and Wang, 2006), the North China Plain represented by Beijing, Tianjin, Hebei and Shandong (Zhang, 2014), and the Fenwei Basin represented by Xi'an (Wang et al., 2014) are the regions most affected by land subsidence in China, They have invested in a lot of research and achieved many research results.

The North China Plain is among the area with the most serious overexploitation of groundwater in the world, and also the area with the largest land subsidence funnel and the largest subsidence coverage area (He et al., 2006). As an important part of the land subsidence funnel in the North China Plain, the land subsidence in northern Shandong Province is particularly serious. The land subsidence phenomenon in Shandong mainly occurs in Dongying, Dezhou, Binzhou and Weifang, relevant scholars have carried out some research work in Dezhou, Binzhou and other regions (Jia et al., 2015). At present, no scholar has systematically analyzed and studied the land subsidence in Guangrao, Dongying. According to the relevant data of the Dongying land subsidence monitoring network established in 2002, the deep groundwater level in Guangrao County has continued to decline for many years, and the land subsidence rate has not slowed down.

At present, the research on land subsidence mainly focuses on the following aspects: 1) study the settlement mechanism of land subsidence and analyze its related influencing factors (Ji et al., 2019); 2) Investigate on land subsidence disasters, and expand to the secondary disasters caused by land subsidence, such as ground fissures, land collapse, urban waterlogging and water logging (Qin et al., 2018), (Jia et al., 2019); 3) Carry out research on the simulation and prediction of land subsidence, from simple qualitative prediction of single factor to quantitative prediction of multiple models with comprehensive effect of multiple factors (Luo et al., 2018); 4) In terms of land subsidence monitoring technology, make the subsidence monitoring results more accurate and intuitive by expanding from a single leveling method to a variety of monitoring means such as InSAR and GPS using satellite remote sensing technology (Xue et al., 2021); 5) In terms of the prevention and control measures of land subsidence, change the previous mode of discovering disasters—managing them to predicting—controlling disasters (Li et al., 2021).

For the calculation of land subsidence caused by pumping, the current research focuses more on the study of soil constitutive relationship or fluid solid coupling effect with characteristics such as soil creep and parameter time variation, so as to propose the characteristics and laws of soil deformation under different hydraulic conditions. However, for regional land subsidence, due to the existence of a large number of pumping wells, the pumping horizon and pumping volume are different. When conventional numerical analysis methods are used to deal with the boundary conditions of the pumping wells, the grid division is too dense, which will lead to a huge amount of calculation. However, the simplified processing also affects the calculation accuracy, and cannot reasonably and accurately reflect the development characteristics of regional land subsidence based on different pumping information of pumping wells, and predict its development trend.

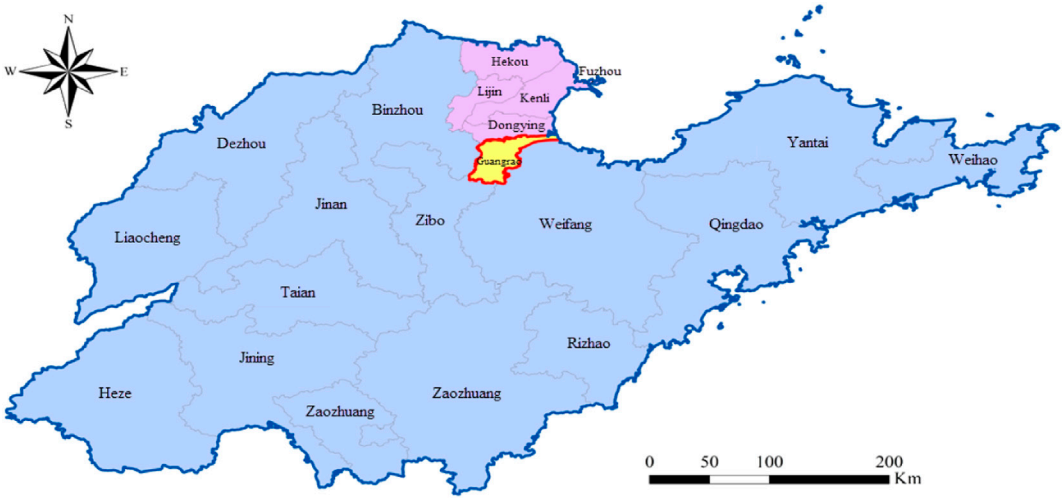


FIGURE 1
Geographical location of the study area.

Therefore, this paper takes Guangrao County, Dongying City, North China Plain as the study area, fully learns from and absorb the research achievements of land subsidence at home and abroad, widely collects the hydrogeology and engineering geology of Guangrao County, the monitoring data of groundwater for many years and the monitoring data of land subsidence over the years, uses the effective stress theory, deeply analyzes the formation mechanism of land subsidence in Guangrao County. Using Biot consolidation fluid solid coupling theory, establishes a three-dimensional porous medium fluid solid coupling numerical model for land subsidence in Guangrao County. Using the line source mass flux method, simulates the production volume of each pumping well, accurately depicts the hydraulic boundary conditions of hundreds of pumping wells with different production horizons and different production volumes in the area. Through numerical analysis, accurately restores the evolution law of land subsidence caused by groundwater exploitation in this area. At the same time, through the design of different groundwater exploitation schemes, predicts the development of land subsidence and proposes effective prevention and control measures. It provides theoretical basis and data support for land subsidence prevention in this area.

2 Overview of the study area

2.1 Physical geography overview

Guangrao County is located in the north of the central part of Shandong Province (Figure 1). The geographical coordinates are 118°17′~118°57′ east longitude and 36°56′~37°21′ north latitude, with a gross area of 1,166 square kilometers. The northeast of the study area is adjacent to Laizhou Bay of Bohai Sea, with a coastline of 12.35 km. The county is located in the overlapping zone of Mount Tai Yi northern foot piedmont alluvial plain and the Yellow River flood plain. The area terrain gradually inclines from southwest to northeast. The highest elevation in the southwest is 28 m, and the lowest elevation in the northeast is 2 m. The natural slope is 1/1,000~1/2000. The study area has a monsoon climate, and there is no significant difference in the climate within the territory. The annual average precipitation is about 587 mm, mainly from June to September.

2.2 Dynamic distribution characteristics of groundwater

According to the hydrogeological and engineering geological survey data of the study area, the groundwater system in the area is composed of shallow phreatic water micro confined water system (buried depth 0~60 m), medium and deep confined water system (buried depth 60~250 m), and deep confined water system (buried depth >250 m). The buried depth of shallow groundwater level varies greatly, and its distribution characteristics are roughly bounded by Xiaoqing River. The south of Xiaoqing River is mostly well irrigation area, the buried depth of the water level is large, and the main supply source is atmospheric precipitation, followed by river leakage supply, irrigation infiltration supply and runoff supply, and the discharge way is mainly manual pumping. Generally, The year presents the dynamic characteristics of “two peaks and one valley”. From March to April, the spring irrigation starts, and the groundwater is recharged by irrigation infiltration. The water

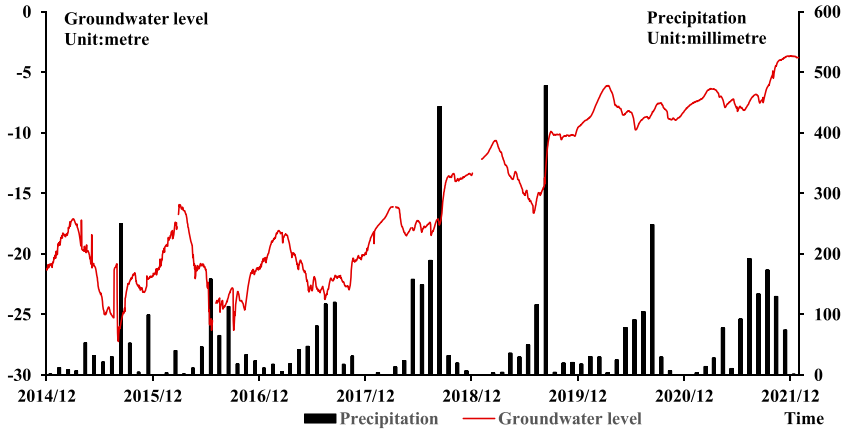


FIGURE 2
Relationship between shallow groundwater dynamics and precipitation in the south of Xiaoqing River.

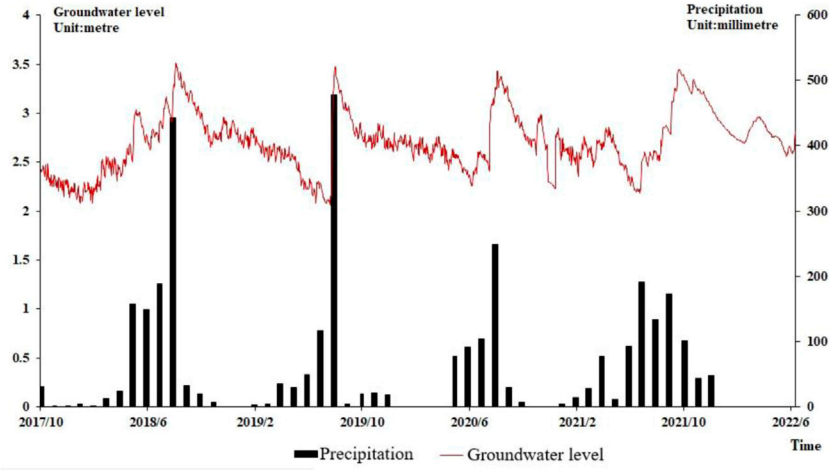


FIGURE 3
Relationship between shallow groundwater dynamics and precipitation in the north of Xiaoqing River.

level has its first peak in the year. Later, the water level drops due to continuous pumping, the lowest water level in the year occurs in June. In July, with the arrival of the rainy season, the groundwater is recharged by precipitation infiltration, and the water level has its second peak in the year. Due to the large buried depth of water level and the insufficient intensity of single precipitation, it is difficult for precipitation to effectively recharge groundwater. Therefore, the second peak of water level in the rainy season of 2015–2017 is not obvious. The annual variation of water level affected by artificial exploitation is large, generally more than 10 m. In recent years, the water level continues to return due to the policy of reducing groundwater exploitation (Figure 2). The buried depth of water level in the north of Xiaoqing River is small, the upper soil permeability is good, and it is greatly affected by precipitation and evaporation intensity. The phreatic water is mainly in vertical movement, which is mainly supplied by precipitation infiltration, followed by the Yellow River lateral infiltration and irrigation infiltration; It has the characteristics of direct infiltration replenish, direct excretion, intermittent replenish and continuous excretion; Generally, the lowest water level in the year is reached before the rainy season, and the highest water level in the year is reached in the rainy season. The annual variation is generally less than 2 m (Figure 3). The water level of middle and deep groundwater is very weakly affected by the atmosphere, but mainly affected by artificial exploitation;

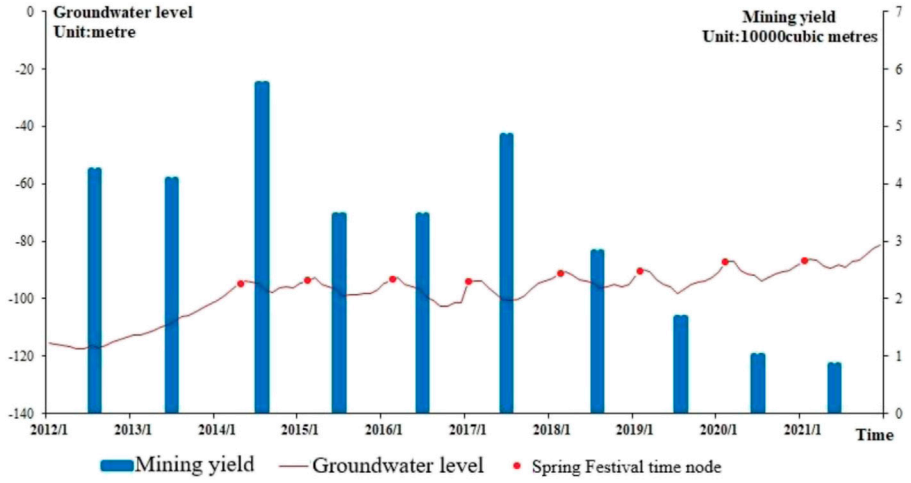


FIGURE 4
Relationship between deep groundwater dynamics and annual exploitation.

Generally, the lowest water level occurs during the peak period of water use in summer, and the highest water level occurs during the Spring Festival holiday (Figure 4). In addition, there are 12 rivers in the study area, they belong to the two major water systems of Xiaoqing River and Zhimai River respectively, mainly including Xiaoqing River, Zihe River, Zhimai River, Zhinv River, Yang River, spillway river and preparatory river.

The hydrogeological conditions and water system distribution in Guangrao County are different from north to south, and the spatial distribution of water resources is also different. The shallow and deep groundwater in the southern well irrigation area is relatively abundant, with good water quality, convenient water intake and stable water supply. However, overexploitation of groundwater for many years has led to a continuous and substantial decline in the groundwater level, causing geological environmental problems such as salt water intrusion and ground fissures. The shallow groundwater in the northern region is brackish water and saline water. Only the deep confined fresh water can be used. The amount of resources is, however, limited, and it is difficult to replenish. The fluorine content of water quality generally exceeds the standard of drinking water, and the development potential is limited. In the north, there are Xiaoqing River, Zhimai River and Yellow River. The surface water is relatively abundant, and the diversion of the Yellow River is relatively convenient.

2.3 Development characteristics of land subsidence

The first land subsidence leveling survey was carried out in Dongying City in 2002. According to the monitoring data of land subsidence for many years, there is widespread land subsidence in Dongying City, of which Guangrao urban area is one of the subsidence centers, and the cumulative subsidence of the subsidence center is more than 1.5 m (Figure 5), from 2017 to 2021, the area with accumulated subsidence more than 300 mm is 647.81-square-kilometres.On the whole, the development trend of land subsidence in the main urban area and coastal areas of Guangrao County is the most obvious, with an average annual settlement rate of 135.1 mm. The amount of land subsidence in Guangrao County is increasing year by year and developing rapidly. The Development Zone in the north of the city and the coastal area in the East have formed a relatively obvious subsidence funnel. The land subsidence funnel is constantly expanding and connecting with other small funnels, and there is a trend to form a large regional land subsidence funnel, It has had a significant impact on local urban planning and construction, social and economic development and people's lives (Yang, 2014), (Zhang et al., 2018), (Liu et al., 2014).

3 Correlation analysis of groundwater and land subsidence in different layers

Both groundwater funnel and land subsidence are caused by the reduction of water level in the pumping area due to excessive exploitation of groundwater, and the occurrence time of funnel is synchronized with the occurrence of land subsidence, so it is closely related to the occurrence of land subsidence. The contour lines of groundwater funnel level and land subsidence in different aquifers are drawn by GIS software, and they are superimposed for analysis.

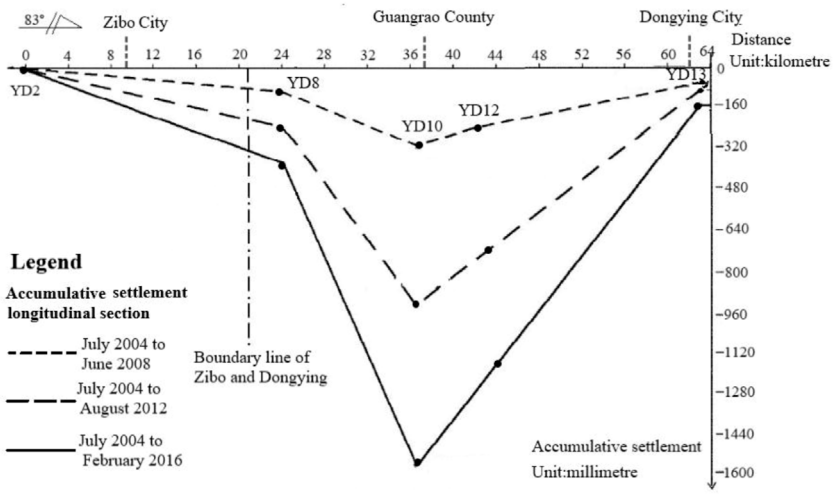


FIGURE 5
Land subsidence accumulative settlement of longitudinal section of Guangrao.

The center of shallow groundwater funnel is located in Dawang Town-Xiliuqiao Village- Damatou Town and Guangbei salt field. The buried depth of the central water level is 50~56 m, The funnel area with -30 m constant water level coil closed is about 393.32 square kilometers, There are also the serious land subsidence area in the above areas, and the points with the largest subsidence rate are located in the funnel range, the average settlement rate for many years is 102mm/a. This shows that the land subsidence in these areas is closely related to the exploitation of shallow groundwater (Figure 6). The development and utilization of groundwater in the middle layer is low, and there is no groundwater funnel, so it has little correlation with land subsidence (Figure 7). The center of deep groundwater funnel is located in Guangrao urban area, and the buried depth of the central water level is 118~121 m, The funnel area with −70 m constant water level coil closed is about 428.65 square kilometers, At the same time, there is also a Serious Land Subsidence Area in this area. The point with the largest subsidence rate is located in the funnel range, and the average settlement rate for many years is 131.5 mm/a. The deep groundwater funnel in this area basically coincides with most settlement funnel areas (Figure 8); The analysis shows that the land subsidence here is mainly induced by the exploitation of deep groundwater. Pumping reduces the pore water pressure and increases the effective stress, which leads to land subsidence.

According to the field survey of Guangrao County, combined with the flow field of shallow, middle and deep groundwater and the distribution of land subsidence, the influencing factors of land subsidence in each funnel area are shown in Table 1.

4 Three dimensional fluid solid coupling model of land subsidence

The consolidation settlement of soil mass due to water loss is a typical fluid-solid coupling process in porous media, which is microscopically described as the coupling of seepage field and stress field (Jia et al., 2019). Based on groundwater seepage theory and soil consolidation theory, a three-dimensional fluid-solid coupling numerical model of land subsidence is established to predict the evolution trend of land subsidence induced by groundwater exploitation in the study area (Luo et al., 2018) (Xue et al., 2021).

4.1 Theoretical method

In the coupling model of groundwater flow and porous media, by considering the coupling relationship between pore water pressure dissipation and skeleton deformation in the process of water loss consolidation of soil, derives the three-dimensional consolidation equation of soil with time varying average total stress, gives the stress-strain constitutive relationship in the form of tensor:

$$\sigma = C.\varepsilon - \alpha_B p_f I, \tag{1}$$

where, σ is the stress tensor, ε is the strain tensor, the symbol ":" represents the second order tensor product, α_B is Biot-Willis coefficient, p_f is the fluid pore pressure, C is the fourth order elastic tensor obtained by measuring the stress-strain relationship of soil under constant pore water pressure, I is the unit matrix.

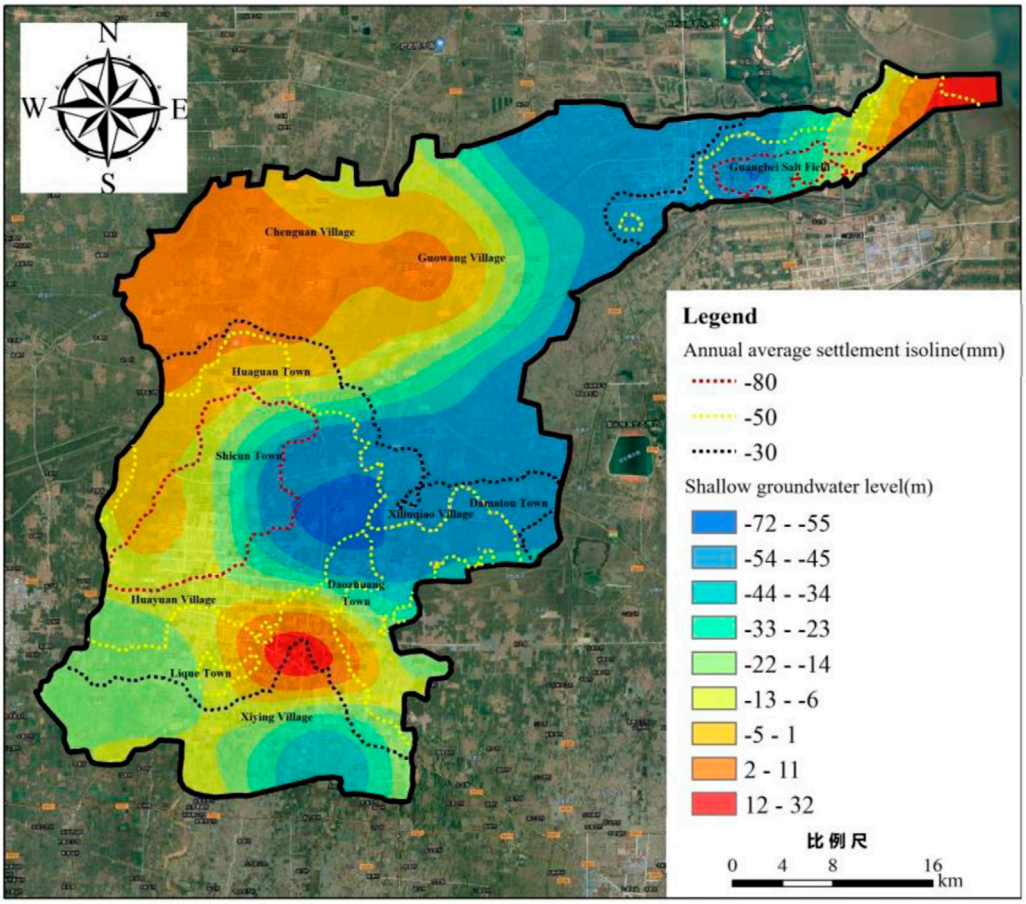


FIGURE 6
Superimposed chart of land subsidence and shallow groundwater funnel development.

The equilibrium equation of porous media under self weight load is:

$$-\nabla \cdot \sigma = \rho_{av} g = \left(\rho_f \varepsilon_p + \rho_d\right)\mathrm{g}, \tag{2}$$

where, σ is the total stress tensor in Eq. 1, ρ_{av}, ρ_f and ρ_d represents average density, fluid density and dry density, respectively, ε_p is porosity.

Geometric equation of deformation of porous media material through its total strain tensor ε and displacement tensor u give:

$$\varepsilon = \frac{1}{2}\left[\nabla u + 2ig\left(\nabla u^T\right)\right]. \tag{3}$$

For fluid motion, the flow field equation in the porous medium model can be established by combining Darcy's law and the fluid mass conservation equation:

$$\rho_f S \frac{\partial p_f}{\partial t} + \nabla \cdot \rho_f \left[-\frac{k}{\mu}\nabla p_f + \rho_f g \nabla \mathrm{D} \right] = -\rho_f \alpha_B \frac{\partial}{\partial t}\varepsilon_{\omega l}, \tag{4}$$

$$\mathrm{S} = \frac{\varepsilon_P}{K_f} + \left(\alpha_B - \varepsilon_P\right)\frac{1-\alpha_B}{K_d}, \tag{5}$$

Where, $\partial\varepsilon_{\omega l}/\partial t$ is the volumetric strain rate of the porous matrix, ρ_f is the fluid density, α_B is Biot-Willis coefficient, the storage term S is calculated by Eq. 5, the first term on the right of the equal sign can be understood as the expansion rate of the pore space.

In the model, for the simulation of pumping wells, the method of one-time application of water level boundary conditions can be used to directly apply the water level change or water pressure change after pumping to the boundary of the pumping well model, or the pumping rate can be applied to the wall model of the corresponding pumping horizon in the model. This method is only applicable to the non-point source pumping wells, and the boundary conditions are:

$$\text{Water Head boundary condition}: H = H(t) \tag{6}$$

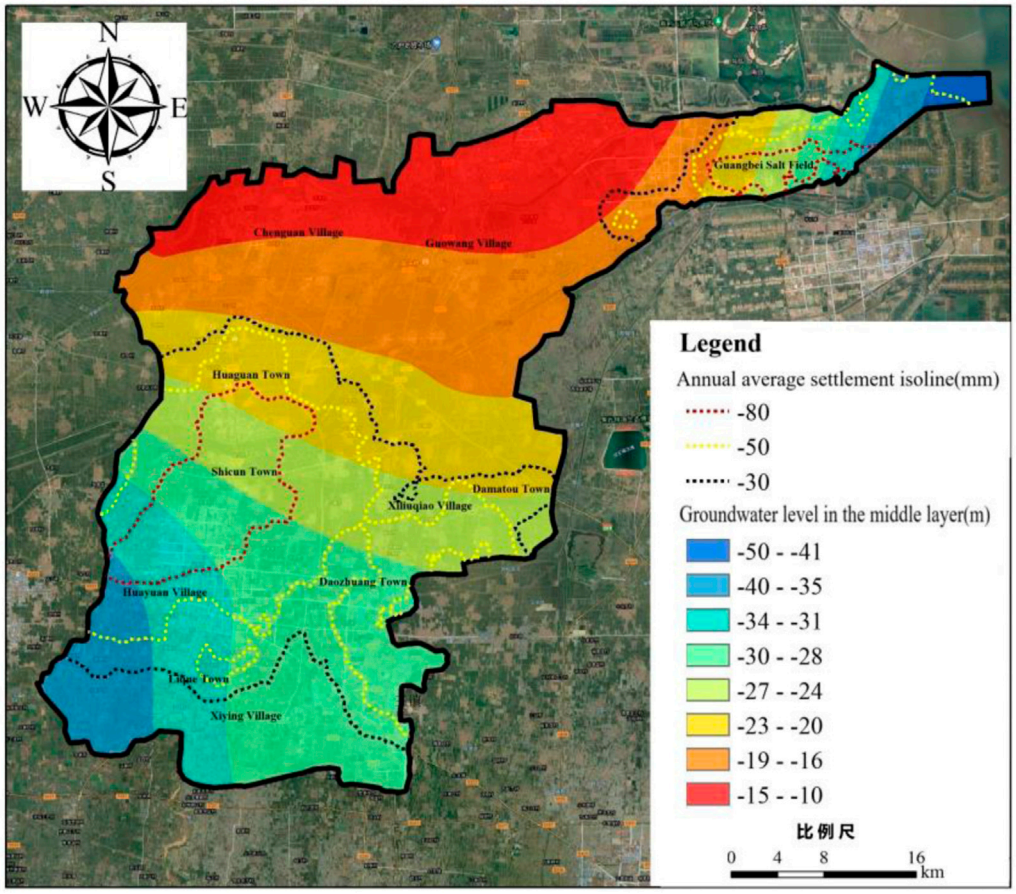


FIGURE 7
Superimposed chart of land subsidence and middle layer groundwater funnel development.

$$\text{Water Velocity boundary condition}: V = V(t) \quad (7)$$

The third method is to use the mass flux method to directly apply the pumping volume to the edge of the model of the production well, including the model of the non-point source production well and the line source production well, and its effect is equivalent to the pumping rate. The boundary conditions are:

$$\text{Boundary conditions of line source pumping}: \quad N = Nt = V(t)\rho_f\,(kg/m \cdot s). \quad (8)$$

$$\text{Boundary conditions of non} - \text{point source pumping}: \quad N = Nt = V(t)\rho_f\,(kg/m^2 \cdot s) \quad (9)$$

4.2 Model establishment

In this study, according to the formation conditions, groundwater data, drilling data and relevant data of pumping well location in the study area, the strata are divided into 4 aquitards and 3 aquifers (Figure 9). The soil parameters of each layer are obtained according to the relevant engineering geological survey reports in the study area and combined with the empirical data on Soil in the [Engineering Geology Manual (Fifth Edition)] (Hua and Zheng, 2017) (Table 2).

The boundary conditions are defined as follows: the flow boundary is used around the study area, and the hydraulic change conditions are obtained by analyzing and calculating the dynamic evolution of groundwater flow field, while limiting the horizontal movement and vertical free sliding; The surface is a zero flow boundary and a free moving boundary; The bottom is a zero flow boundary with fixed displacement in horizontal and vertical directions; The pumping well adopts the flow boundary condition, which converts the actual production into the unit mass flux to limit the horizontal displacement and the vertical free movement. The model boundary is composed of multiple line segments connected with each other, which is equivalent to the actual boundary. Mesh division adopts free subdivision tetrahedral mesh. The numerical model of land subsidence in Guangrao County, Dongying City is divided into 117,538 domain

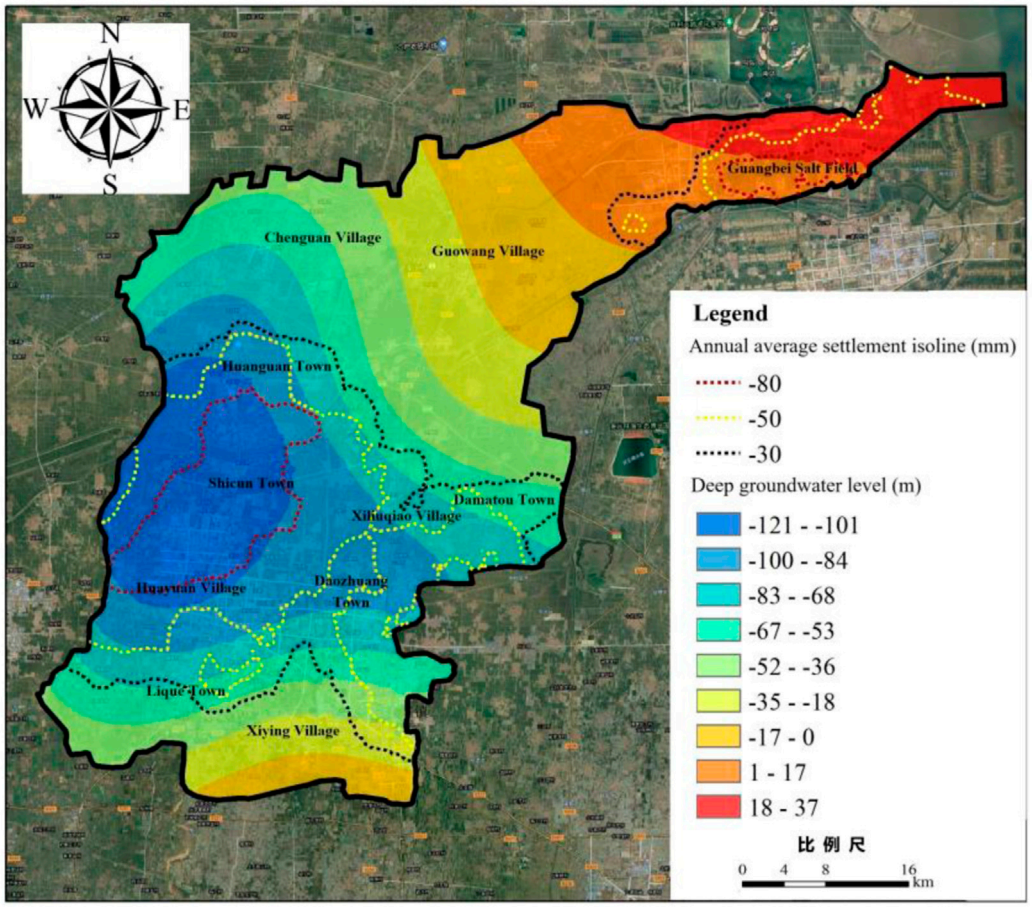


FIGURE 8
Superimposed chart of land subsidence and deep layer groundwater funnel development.

TABLE 1 Correlation between ground subsidence and groundwater in each aquifer in Guangrao County.

Serial number	Funnel position	Area (km^2)	Influence factor
1	Main urban area of Guangrao County, Shicun Town, Huayuan Village	73.82	The middle and west sides of the urban area are mainly affected by the exploitation of deep groundwater; The east side is jointly affected by shallow and deep groundwater
2	Huaguan Town	116.75	There are many factories with large water consumption, so the land subsidence is mainly affected by the exploitation of deep groundwater
3	Daozhuang Town, Xiliuqiao Village, Damatou Town	105.42	It is mainly affected by shallow groundwater exploitation, followed by deep groundwater
4	Lique Town	28.35	This area is a water source exploitation area and there are industrial parks, which are mainly affected by the exploitation of deep groundwater, followed by shallow groundwater
5	Dawang Town	47.04	This is a fully diluted groundwater area, which is jointly affected by shallow, medium and deep layers
6	Coastal area of Guangrao County	62.99	A large number of salt fields are distributed here, which are mainly affected by the exploitation of shallow groundwater; At the same time, the industrial and agricultural exploitation of medium and deep groundwater also affects the settlement of this area

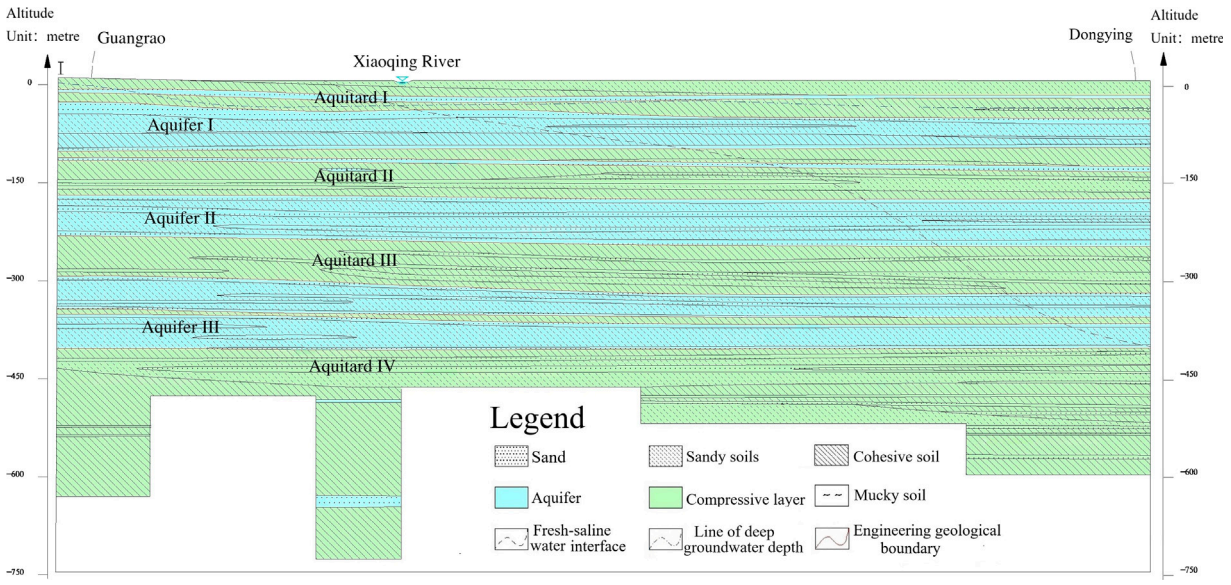


FIGURE 9
Guangrao County division of engineering geological characteristic layers.

TABLE 2 Physical and mechanical parametres of each layer (range).

Engineering geological layer	Buried depth of bottom plate (m)	Modulus of elasticity (MPa)	Poisson's ratio (1)	Density (kg/m^3)	Porosity (1)	Compressibility coefficient (MPa^{-1})
Aquitard I	45~50	37.49	0.37~0.42	1977~1983	0.657~0.790	0.18~0.32
Aquifer I	105~110	43.01	0.32~0.35	1989~1997	0.659~0.758	—
Aquitard II	173~176	55.66	0.30~0.40	2032~2049	0.547~0.690	0.11~0.17
Aquifer II	245~250	36.34	0.21~0.27	2053~2059	0.567~0.721	—
Aquitard III	321~325	46.23	0.25~0.35	2065~2073	0.561~0.672	0.09~0.15
Aquifer III	407~411	68.31	0.27~0.32	2067~2077	0.587~0.701	—
Aquitard IV	597~600	49.68	0.23~0.29	2070~2020	0.355~0.365	0.025~0.027

elements, 49,989 boundary elements and 3,994 boundary elements. The numerical model and mesh division are shown in Figure 10.

4.3 Model establishment

4.3.1 Validation using InSAR data

Based on the existing InSAR settlement data and GIS spatial analysis technology, the distribution chart of cumulative land subsidence in Guangrao County, Dongying City, Shandong Province from 2017 to 2021 was obtained (Figure 11). Taking 2017 to 2021 as the model validation period, the land subsidence of Guangrao County during this period was simulated by using a three-dimensional numerical model (Figure 12). Through comparative analysis:

1) The spatial ranges of the land subsidence area obtained by the two methods are highly coincident. The model calculates that the area of the settlement area with the accumulated settlement >300 mm is 606-square-kilometres, which differs with the InSAR interpretation area by 6.9%. The settlement range includes the south of Huaguan Town, Shicun town and Huayuan Village, and there is also a certain settlement funnel in the Northeast coastal area.

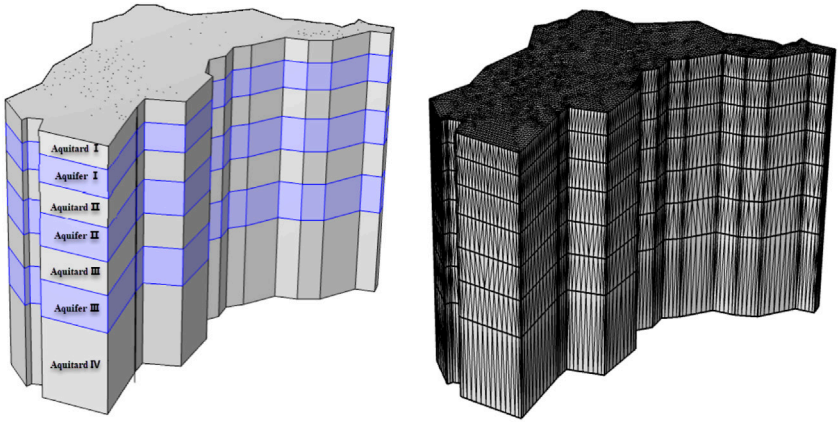


FIGURE 10
Three dimensional fluid solid coupling numerical model of land subsidence in Guangrao County.

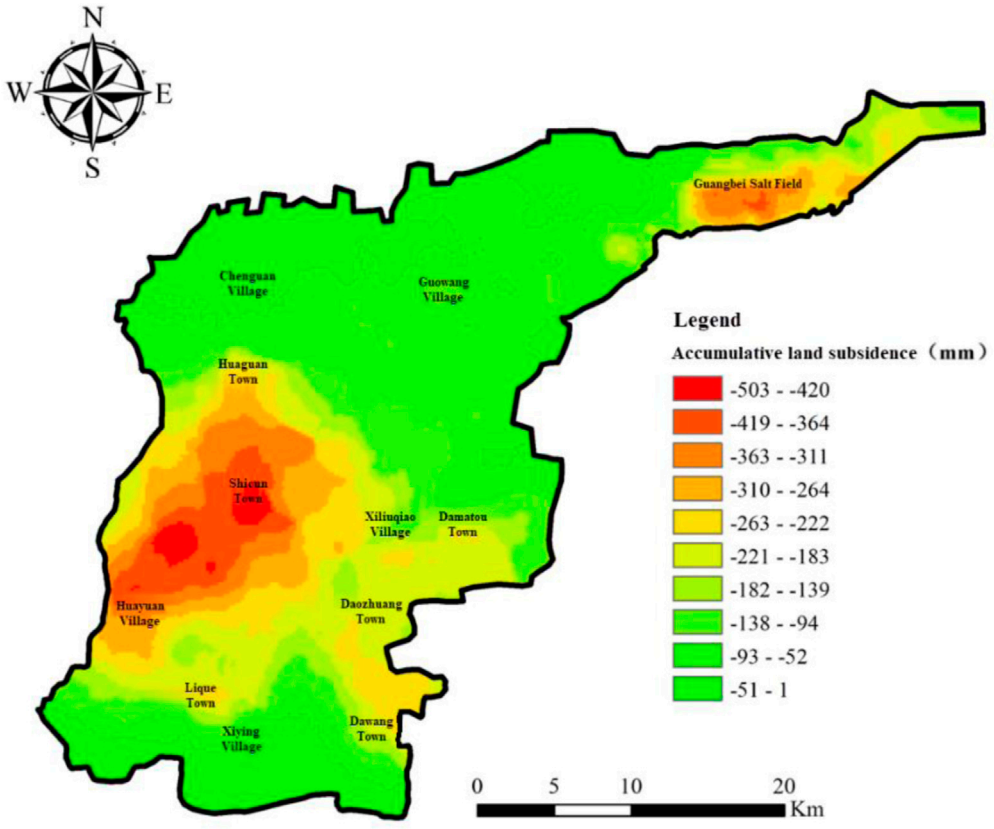


FIGURE 11
distribution chart of land subsidence in Guangrao County, Dongying City (2017–2021).

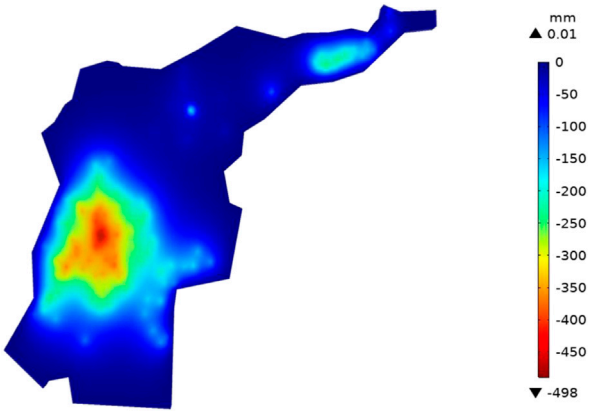


FIGURE 12
| Numerical simulation of land subsidence in Guangrao County, Dongying City (2017–2021).

2) The funnel centers obtained by the two methods is the same. In the region, Regionally Guangrao city is the funnel center, and the small settlement funnel in the Northeast coastal area is the Guangbei salt field.
3) The settlement rates obtained by the two methods are similar. The simulated accumulated settlement of the land subsidence center in 48 months is 498 mm, and the average annual settlement rate for many years is 124.5 mm; According to InSAR interpretation, the accumulated settlement in 48 months is 526 mm, and the average annual settlement rate is 131.5 mm, thus the difference between them is 5.6%

From the comparison of numerical simulation results with InSAR Data, it can be concluded that the simulation effect of land subsidence in this period is relatively ideal, which can reflect the actual settlement trend of the region during this period.

4.3.2 Verification with leveling results

At present, there are 11 monitoring points in Guangrao County, Dongying City, and the monitoring data are the four-year cumulative settlement from 2017 to 2021. Among them, The actual effective monitoring data are 20, 55, 63 and 68 points, which are distributed in Lique Town, Shicun town and Daozhuang town (Figure 13). The actual settlement of each effective monitoring control point is statistically compared with the three-dimensional fluid solid coupling numerical simulation results. The results are shown in Table 3.

Comparing the actual measured values of each monitoring point with the simulated values from three-dimensional fluid-solid coupling numerical model, it can be found that the simulated values are in good agreement with the measured values. The minimum absolute simulation error is 2.44%, and the maximum absolute simulation error is 12.14%. The results of the two coincide well, which shows that the numerical model of land subsidence can reflect reliably the development and evolution trend and law of land subsidence in this area.

4.4 Analysis on the development process of land subsidence in Guangrao

Based on the calibrated three-dimensional fluid solid coupling numerical model of Guangrao land subsidence, taking the land subsidence of Guangrao County in 2017 as the initial state, restores the evolution process and development law of land subsidence in the region during 2017~2020, Figures 14A–C show the land subsidence development of Guangrao County in 2017–2018, 2018–2019 and 2019–2020 respectively. It can be seen from the analysis in the figure that the land subsidence in Guangrao County will decrease first and then increase during 2017–2020, the land subsidence from 2017 to 2018 is a stage of rapid development, the development rate from 2018 to 2019 has slightly decreased, but it still maintains a rapid development. After 2019, the land subsidence develops rapidly. On the whole, the development trend of land subsidence in the urban area and coastal area of Guangrao County is the most obvious, with the average annual subsidence rate of 135.1 mm/a and 102 mm/a, respectively. The Open Economic Zone and Guangbei salt field have formed obvious subsidence funnels. The land subsidence funnels are expanding and connecting other small funnels, forming a large regional land subsidence funnels.

By restoring the development process of land subsidence in Guangrao, and combining the statistical information such as distribution of mining wells, mining horizon, and mining volume in the study area, and dynamic distribution characteristics of groundwater. It is found that the main exploitation horizon of groundwater in the urban area of Guangrao County is the fourth and fifth deep groundwater aquifers, which is consistent with the deep groundwater funnel of Guangrao County. Therefore, it is believed that the land subsidence in the urban area of Guangrao County is mainly related to the exploitation of deep groundwater in the fourth and fifth aquifers. Guangbei Salt Field has a large number of brine exploitation wells, The main mining horizon is the second and third aquifers, and the distribution of land subsidence coincides with the distribution of shallow brine funnels. Therefore, it is considered that the land subsidence in Guangbei Salt Field area is relatively related to the mining of shallow brine.

5 Prediction of evolution trend of Guangrao land subsidence and its prevention and control measures

Based on the established three-dimensional fluid-structure coupling numerical model of land subsidence in Guangrao

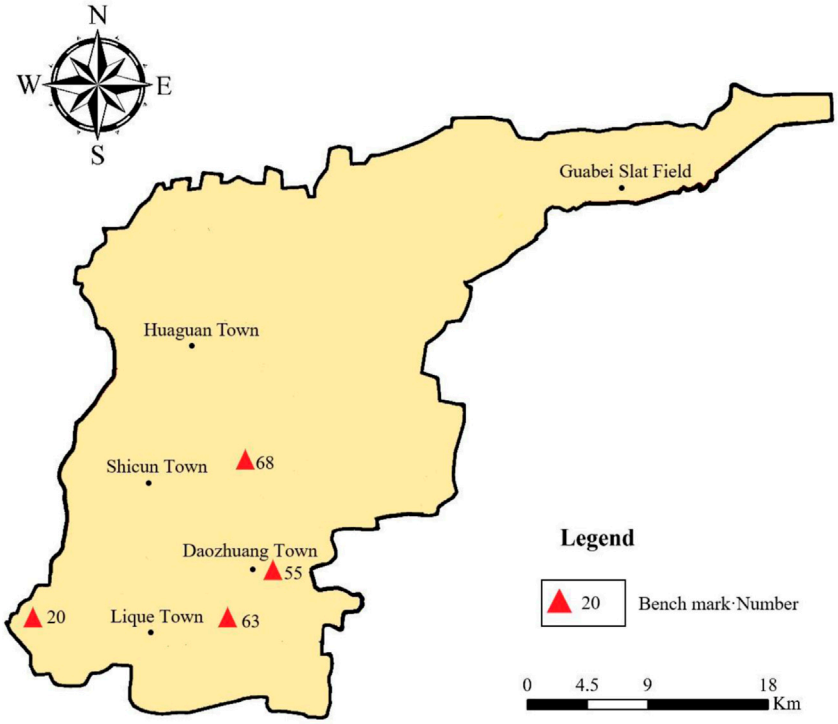


FIGURE 13
Distribution of effective monitoring points.

TABLE 3 Comparison between actual monitoring values and numerical simulation results of some settlement monitoring points in Guangrao County, Dongying City.

Monitoring point	Source of value	2017~2018		2018~2019		2019~2020		2020~2021	
		Settlement (mm)	Error (%)	Settlement (mm)	Error (%)	Settlement (mm)	Error (%)	Settlement (mm)	Error (%)
20	Measured value	−43	4.07	−15	9.00	−44	12.14	−35	9.86
	Analog value	−41.25		−16.35		−38.64		−31.55	
55	Measured value	−41	9.19	−18	2.44	−38	5.66	−28	11.07
	Analog value	−37.23		−17.56		−40.15		−24.9	
63	Measured value	−22	7.91	−9	11.78	−23	5.04	−17	10.35
	Analog value	−23.74		−10.06		−21.84		−15.24	
68	Measured value	−53	10.66	−38	9.16	−55	6.87	−46	9.72
	Analog value	−47.35		−34.52		−51.22		−41.53	

County, the land subsidence trend and rule in Guangrao County in the next 20 years were simulated, calculated and predicted under the condition of maintaining the current pumping conditions and reducing groundwater extraction, and targeted groundwater prevention and control schemes and measures were proposed.

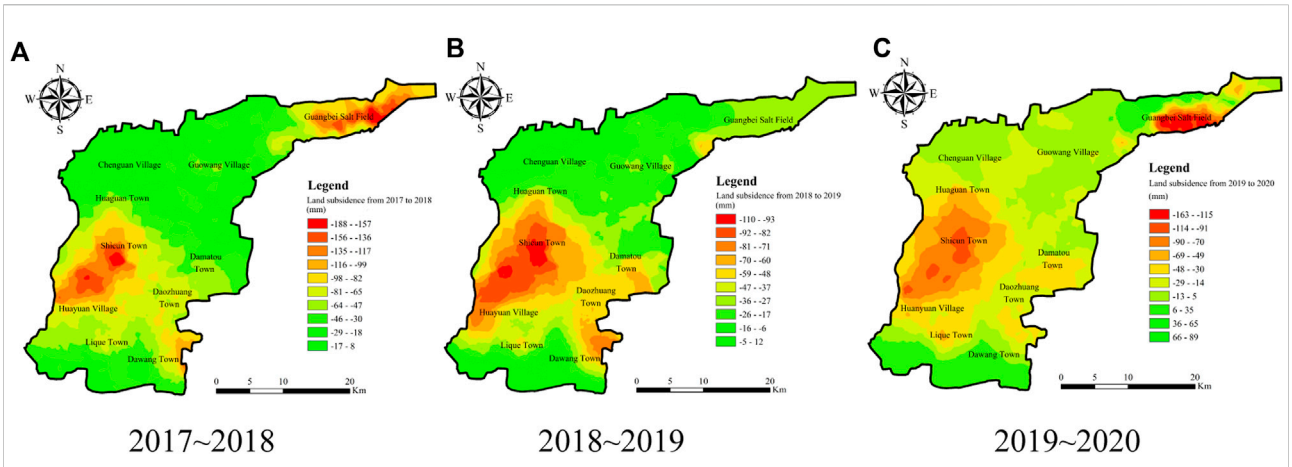


FIGURE 14
Evolution trend of land subsidence in Guangrao County.

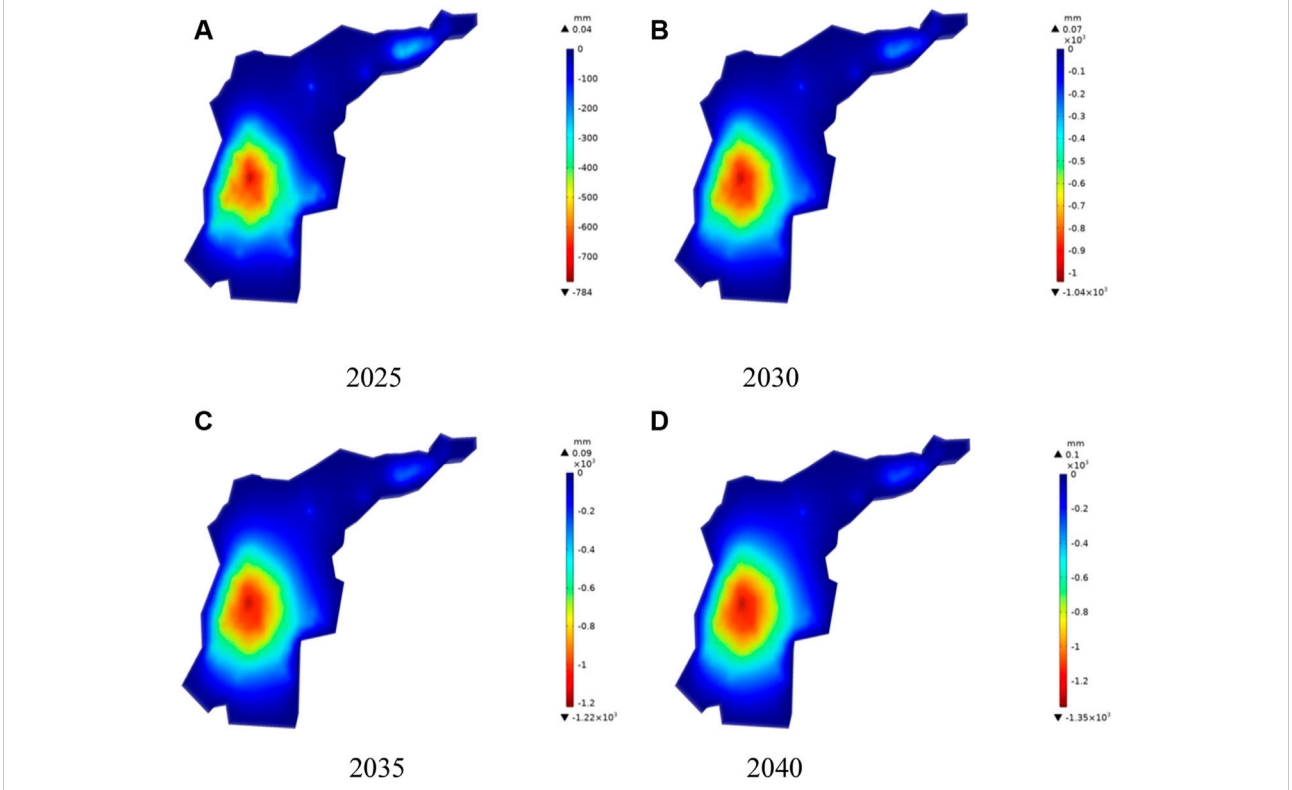


FIGURE 15
The evolution trend of land subsidence in different periods.

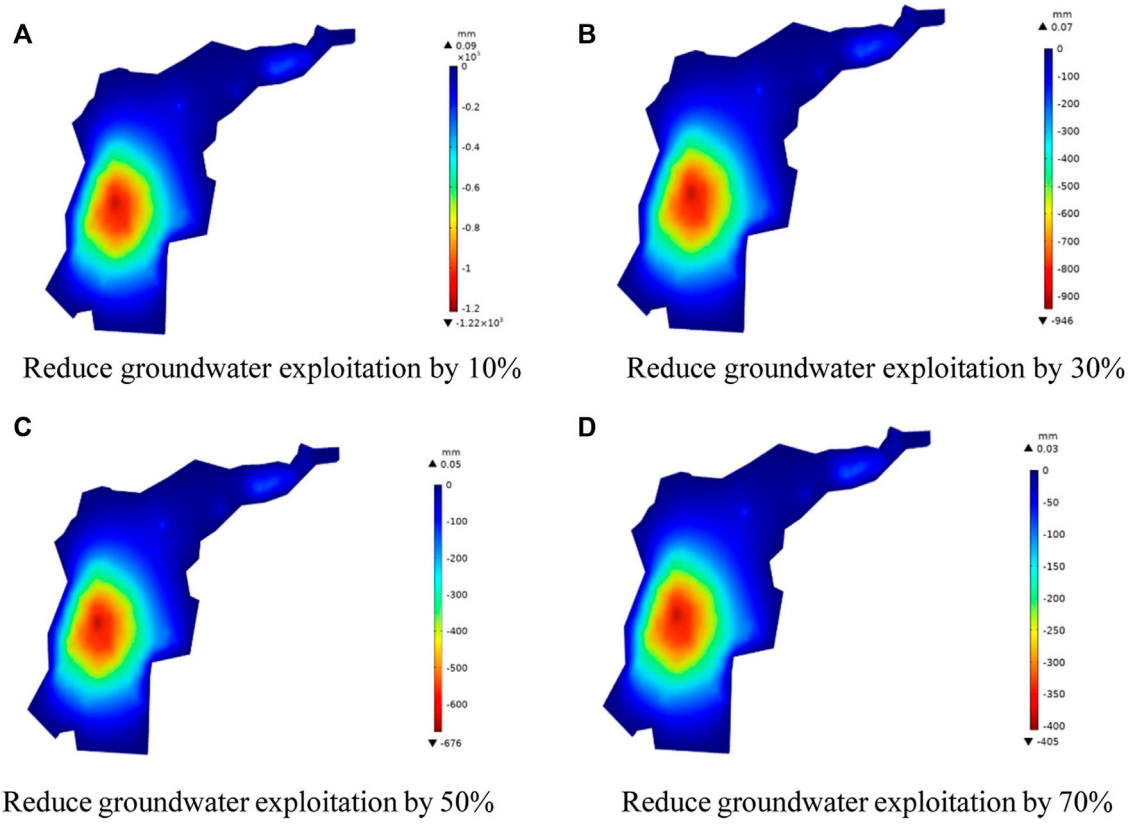


FIGURE 16
Development trends of land subsidence under different groundwater reduction plans in 2040. **(A)** Reduce groundwater exploitation by 10% **(B)** Reduce groundwater exploitation by 30%. **(C)** Reduce groundwater exploitation by 50% **(D)** Reduce groundwater exploitation by 70%.

5.1 Prediction of land subsidence evolution trend in Guangrao

5.1.1 Prediction of land subsidence trend under current mining conditions

Using the established three-dimensional fluid-solid coupling numerical model of land subsidence in Guangrao area, assuming that the current groundwater exploitation conditions remain unchanged, the land subsidence and groundwater exploitation in 2021 are taken as the initial state to predict the change trend and regulation of land subsidence in the study area in the next 20 years. Our analysis shows that if the current pumping state is maintained, the land subsidence in Guangrao area will continue and increase much more in the next 20 years, by 2025, the maximum settlement of funnel center in Guangrao city will be 784 mm (a), by 2030, the maximum settlement will increase to 1040 mm(b), by 2035, the maximum settlement will be 1220 mm(c), By 2040, the maximum accumulated land subsidence in the study area will reach 1,350 mm, more than three times the maximum accumulated land subsidence in 2021(d). However, the ground subsidence funnel centered on Guangbei Salt Field will gradually recover in the future due to less brine exploitation in recent years. The results are shown in Figure 15.

Maintain the current groundwater exploitation, and by 2040, the land subsidence funnel in Guangrao County will become a large funnel, and gradually develop and expand around. According to the distribution of local groundwater extraction wells, even if there is no strong pumping source or underground engineering excavation and other factors in the connecting belt areas such as Ligue Town, Dawang Town and Xiliuqiao Town, the phenomenon of land subsidence will also form and develop gradually due to the influence of the nearby land subsidence center. Therefore, when formulating the prevention and control plans or measures for land subsidence, we should consider the phenomenon of “passive subsidence” formed in the middle connecting belt due to the correlation and influence of the centers of multiple land subsidence funnels. We should pay attention to strengthening the investigation and analysis in this aspect, especially when it involves the construction of important engineering buildings or high-precision projects where this phenomenon is often ignored.

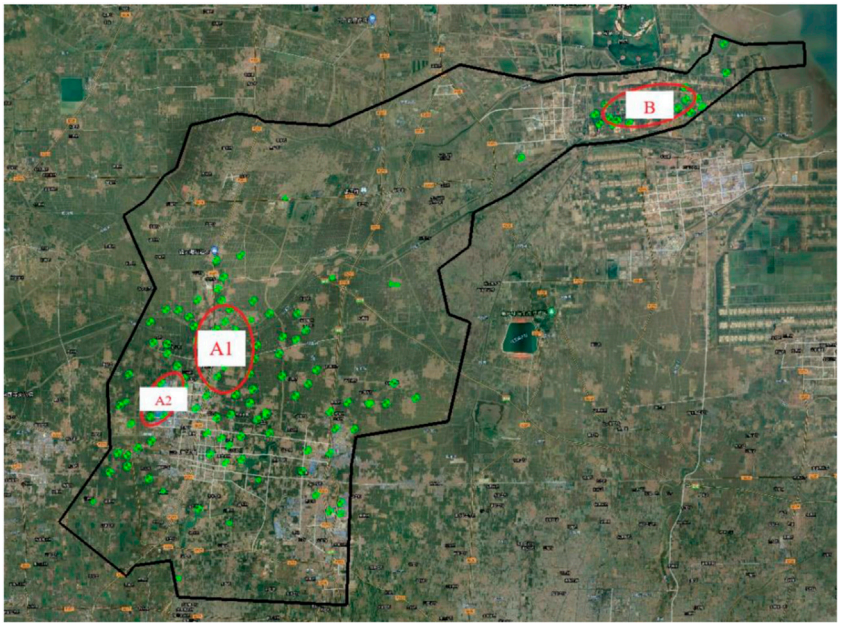


FIGURE 17
Sketch chart of demarcation of prohibited pumping area.

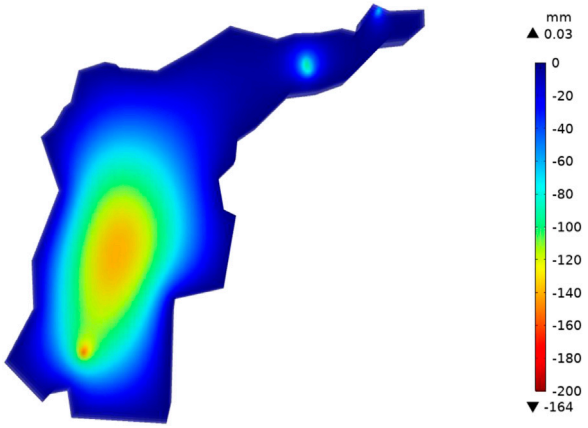


FIGURE 18
Forecast chart of land subsidence in Guangrao County in 2040.

5.1.2 Land subsidence prediction under reduced groundwater extraction

Based on the groundwater extraction of each pumping well in 2021, four groundwater reduction schemes, namely 10% reduction, 30% reduction, 50% reduction and 70% reduction, were respectively adopted. The land subsidence distribution chart of the study area in 2040 was obtained through the simulation calculation of the land subsidence fluid-solid coupling model in Guangrao area. The influence law of different groundwater recovery control on land subsidence was analyzed.

Figures 16A–D show the evolvement cloud chart of land subsidence distribution in Guangrao area in 2040 under the condition that the groundwater extraction in 2020 decreases by 10%, 30%, 50% and 70%.

It can be seen that with the decrease of groundwater extraction, although the location of the land subsidence funnel is not changed, its development trend will be obviously curbed, especially the land subsidence phenomenon at the center of the land subsidence funnel is significantly slowed down. The maximum cumulative land subsidence in Guangrao County in 2040 is extracted, and the values under the condition of 10%, 30%, 50% and 70% reduction are 1,220 mm, 946 mm, 676 mm and 405 mm respectively. Compared with the maximum cumulative land subsidence under the current groundwater mining condition (1,350 mm), The declines reached 7.63%, 26.93%, 52.93% and 78.00% respectively. The results show that reducing groundwater extraction is one of the simplest and most effective measures to prevent land subsidence.

5.1.3 Land subsidence prediction under restricted groundwater exploitation

According to the planning scheme of Dongying Municipal government for partial groundwater exploitation in Guangrao County and the current exploitation amount of each pumping well in the study area, the two areas with the most serious land

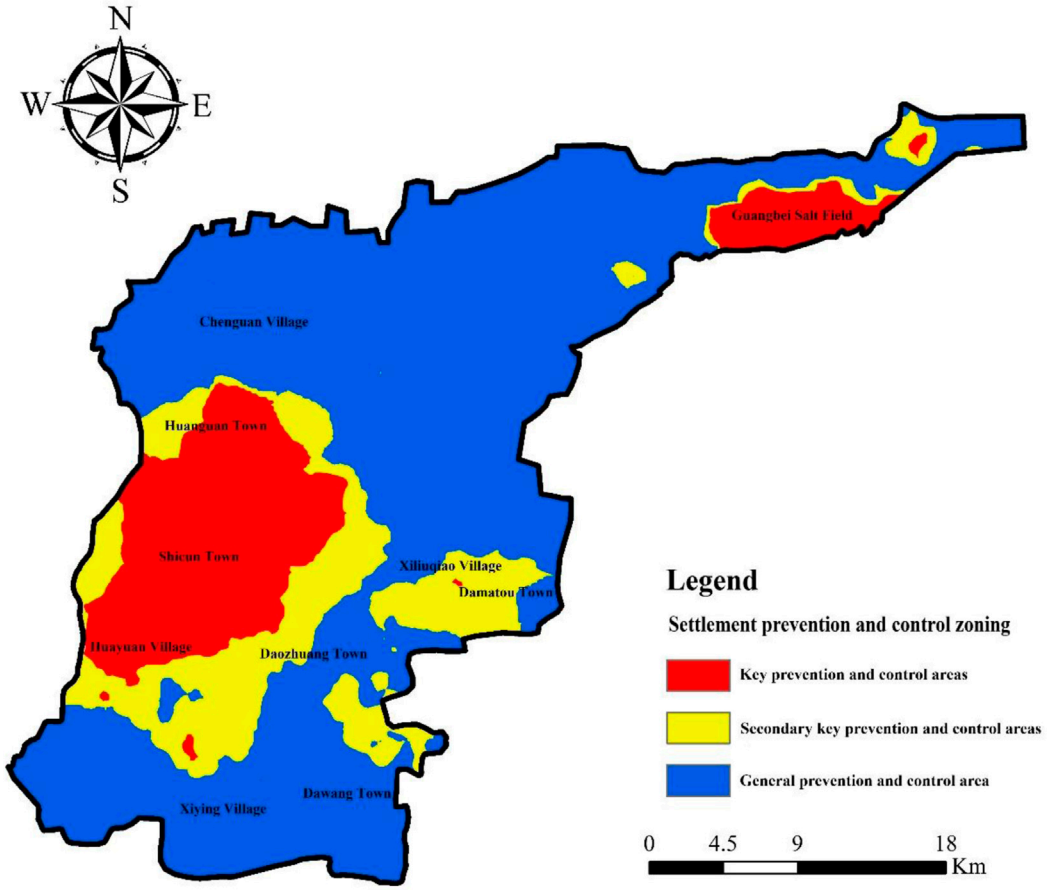


FIGURE 19
Zoning chart of land subsidence prevention and control in Guangrao County.

TABLE 4 Zoning table of land subsidence prevention and control in Guangrao County.

Partition name	Distribution location	Area (Square kilometres)	Prevention and control measures
Key prevention and control areas	Main urban area and coastal area of Guangrao County	201.847	Limit the exploitation of shallow and medium deep groundwater, adjust the structure of water use, and strengthen monitoring
Secondary key prevention and control area	Huagua Town, Xiliuqiao Village, Daozhuang Town, Lique Town, Dawang town,etc	189.619	It mainly restricts the exploitation of deep groundwater, reduces the exploitation of shallow groundwater, adjusts the structure of water use, and strengthens monitoring
General prevention and control area	Chenguan Village, Xiying Village, etc.	760.268	Adjust water use structure and strengthen monitoring

subsidence in the study area are selected as the no-pumping areas (A and B) in this study, and the requirement that all pumping Wells in the area be shut down is strictly followed. The restricted mining area is shown in Figure 17.

The fluid-solid coupling model was used to simulate the land subsidence in Guangrao area, and the land subsidence distribution chart (Figure 18) in 2040 when the mining prohibition measures were adopted was calculated, and the influence of the groundwater extraction prohibition on the land subsidence in the study area was analyzed.

It can be seen that the subsidence trend will change greatly after effective mining prohibition in the main subsidence area. In

addition, the maximum land subsidence in the study area in 2040 under the mining prohibition condition is also reduced compared with the current mining condition, from 1,350 mm to 164.00 mm. Moreover, it can be seen that if the mining prohibition measures are implemented in a certain area, not only the land subsidence trend of the area will be slowed down, but also the land subsidence trend of the nearby area will be slowed down. It shows that it is feasible and effective to adopt a scientific mining prohibition scheme for the area with serious land subsidence.

5.2 Zoning and suggestions for prevention and control of land subsidence

In view of the development characteristics, current situation and development trend of land subsidence in Guangrao County, effective prevention and control of land subsidence in Guangrao County must be carried out. In order to better control the land subsidence within an acceptable range, it is necessary to carry out the prevention and control of land subsidence from the perspective of the whole region. Therefore, it is necessary to divide the prevention and control areas of land subsidence.

It is divided according to the characteristics, current situation and development trend of land subsidence, and the following principles are followed: the objectivity of land subsidence, the difference of land subsidence prevention and control, and the consistency between the prevention and control scope and the prevention and control subject. Taking into account in a comprehensive way the development status, evolution characteristics, cause analysis of land subsidence and the dynamic characteristics of shallow and deep groundwater, the whole area is divided into three areas: Key prevention and control area, Secondary key prevention and control area and General prevention and control area (Figure 19). Based on the analysis and research of land subsidence monitoring results, groundwater dynamic monitoring data and numerical simulation prediction results, and referring to the «Technical code for land subsidence monitor and control», the prevention and control measures for each region are proposed, as shown in Table 4.

6 Discussion

1) The numerical simulation calculation in this paper is based on the stratigraphic structure and physical and mechanical parameters in Guangrao area. It is assumed that the soil is continuously homogeneous and the aquifers are all one hydrogeological unit. The completely connected and boundary are continuous replenishment conditions with fixed head, which can form a stable groundwater flow. However, the actual groundwater storage environment and recharge conditions are complex, so it is difficult to have completely continuous aquifer or aquifer in practice, almost all of them are discontinuous and heterogeneous, and there is often hydraulic connection between aquifers. Therefore, there may be some deviation in the deformation and settlement characteristics of stratum in actual engineering.
2) The main purpose of this study is to analyze, restore and predict the regional characteristics and spatio-temporal evolution of land subsidence in the study area, and the accurate simulation of land deformation is not within the scope of this study. In order to improve the calculation efficiency, the porous elastic fluid-solid coupling calculation model does not consider the time effect of land subsidence lag caused by clay creep, etc., so the simulation results may have some errors, but it has no impact on the overall regional distribution characteristics and evolution trend prediction of land subsidence.

7 Conclusion

1) The land subsidence in Guangrao County has obvious regional characteristics, and gradually formed two subsidence funnels centered on the urban area and the Guangbei Salt Field. The average annual subsidence rate of the urban subsidence center is 131.5 mm/a, and the regional subsidence range includes the south of Huaguan Town, Shicun Town and Huayuan Town, which has a good spatial correlation with the deep groundwater descending funnel, which is mainly caused by excessive exploitation of deep groundwater in the fourth and fifth aquifers, The buried depth of the central water level of the funnel is 118–121 m. The average annual subsidence rate of the subsidence center of the Guangbei Salt Field is 102 mm/a, which has a good spatial correlation with the shallow groundwater descending funnel, which is mainly caused by excessive exploitation of the second and third aquifers, and the buried depth of the central water level of the funnel is 50–56 m.
2) A three-dimensional fluid-solid coupling numerical model of land subsidence in Guangrao County was established to restore the development process of land subsidence in Guangrao County from 2017 to 2020. It is predicted that under the current groundwater exploitation plan, the land subsidence in Guangrao County will continue to develop at a large rate in the next 20 years. By 2040, the land subsidence in Guangrao County will form a large regional subsidence funnel, and the maximum accumulated land subsidence in the urban area will reach 1,350 mm. Attention should be paid to the possible “passive subsidence” phenomenon in the connecting belt such as Lique Town, Dawang Town and Xiliuqiao Town.
3) This paper analyzes and predicts the evolution law of ground subsidence under the reduced and restricted groundwater exploitation schemes. Reducing or restricting groundwater exploitation can significantly slow down the development rate of ground subsidence. In order to curb the rapid development

of ground subsidence, it is suggested to strictly control the exploitation of groundwater resources in the main urban area of Guangrao and around the Guangbei Salt Field, adjust the exploitation layout, and strengthen the introduction of foreign water resources. Xiliuqiao Town, Daozhuang Town, Lique Town, Guowang Village and other places can take control of mining, adjust the mining layout, strengthen the exploitation and utilization of shallow groundwater and other measures; The groundwater exploitation in Changuan Village, Xiying Village and other areas is basically in a balanced state.

Data availability statement

The original contributions presented in the study are included in the article/Supplementary Material, further inquiries can be directed to the corresponding author.

Author contributions

PY: Conceptualization, Investigation, formal analysis, Writing—original draft; YD: Resources, Methodology, Writing—original draft; GW: Investigation, formal analysis, Writing—review and editing; BH: Investigation, Writing—review and editing; YY: Resources, Supervision. All authors have read and agreed to the published version of the manuscript.

Funding

The authors would like to show the gratitude to the financial supports from special financial projects of Shandong Province, Investigation, monitoring and prevention of land subsidence in Shandong Province (No. 3700202100001-14).

Conflict of interest

The authors declare that the research was conducted in the absence of any commercial or financial relationships that could be construed as a potential conflict of interest.

Publisher's note

All claims expressed in this article are solely those of the authors and do not necessarily represent those of their affiliated organizations, or those of the publisher, the editors and the reviewers. Any product that may be evaluated in this article, or claim that may be made by its manufacturer, is not guaranteed or endorsed by the publisher.

References

Abidin, H, Z., Andreas, H., Gumilar, I., Fukuda, Y., Pohan, Y, E., and Deguchi, T. (2011). Land subsidence of Jakarta (Indonesia) and its relation with urban development. *Nat. Hazards (Dordr).* 59 (3), 1753–1771. doi:10.1007/s11069-011-9866-9

Antonellini, M., Giambastiani, B, M, S., Greggio, N., Bonzi, L., Calabrese, L., Luciani, P., et al. (2019). Processes governing natural land subsidence in the shallow coastal aquifer of the Ravenna coast, Italy. *Catena (Amst)* 172, 76–86. doi:10.1016/j.catena.2018.08.019

Du, Z., Ge, L., Ng, H. M., Zhu, Q., and Yang, X. (2018). Correlating the subsidence pattern and land use in Bandung, Indonesia with both Sentinel-1/2 and ALOS-2 satellite images. *Int. J. Appl. Earth Obs. Geoinf.* 67, 54–68. doi:10.1016/j.jag.2018.01.001

Galloway, D. L., and Burbey, T. J. (2011). Review: Regional land subsidence accompanying groundwater extraction. *Hydrogeol. J.* 19 (8), 1459–1486. doi:10.1007/s10040-011-0775-5

He, Q. C., Liu, W. b., and Li, Z. M. (2006). Land subsidence survey and monitoring in the North China Plain. *Geol. J. China Univ.* 12 (2), 195–209. doi:10.3969/j.issn.1006-7493.2006.02.006

Hua, J.-X., and Zheng, J. G. (2017). *Engineering geology manual*. Fifth Edition. Xicheng, China: M. China Architecture & Building Press, 212–216.

Hussain, M. R., and Abed, B. S. (2019). Simulation and assessment of groundwater for domestic and irrigation uses. *Civ. Eng. J.* 5 (9), 1877–1892. doi:10.28991/cej-2019-03091379

Inaba, Y., Abe, I., Iwasaki, S., Aoki, S., Endo, T., and Kaido, R. (1970). Reviews of land subsidence researches in Tokyo.Land subsidence. *Proc. Tokyo Symposium* 1, 87–96.

Jeanne, P., Farr, T., Rutqvist, J., and Vasco, D. (2019). Role of agricultural activity on land subsidence in the san Joaquin valley, California. *J. Hydrology* 569, 462–469. doi:10.1016/j.jhydrol.2018.11.077

Ji, H. L., Yang, Y. B., Zhang, Y. W., Liu, S. Z., and Zhu, Z. Y. (2019). Quaternary sedimentary characteristics and land subsidence model in North Shandong Plain. *Acta Geol. Sin.* 93 (1), 241–250.

Jia, C., Zhang, G. R., Wang, J. B., and Zhang, Y. W. (2015). Study on land subsidence induced by groundwater extraction and its engineering application: taking Dezhou area of Shandong as an example. *J. Earth Sci. Rnvironment* 37 (04), 102–110. doi:10.3969/j.issn.1672-6561.2015.04.015

Jia, S. M., Tian, F., and Qi, G. (2019). Urban "chronic disease" - causes of land subsidence and comprehensive prevention and Control Countermeasures. *Prev. control Geol. disaster* 25 (1), 22–27.

Li, Q, F., and Wang, H. M. (2006). A study on land subsidence in Shanghai. *Geol. J. China Univ.* 12 (02), 169–178. doi:10.3969/j.issn.1006-7493.2006.02.003

Li, W. P., Wang, L. F., Guo, H. P., Wang, H. G., Wang, Y. L., Zhu, J. Y., et al. (2021). Effectiveness and countermeasures of land subsidence control in China. *China Water Resour.* 7, 32–35. doi:10.3969/j.issn.1000-1123.2021.07.015

Liu, Y. (2001). New progress and problems in land subsidence research. *Earth Sci. Front.* 2001 (2), 273–278. doi:10.3321/j.issn:1005-2321.2001.02.009

Liu, Y., Huang, H. J., and Li, P. Y. (2014). Characteristics of land subsidence caused by deep groundwater funnel in the Yellow River Delta. *J. Basic Sci. Eng.* 22 (05), 896–908. doi:10.1007/s11069-013-0648-4

Luo, Y., Ye, S. J., Wu, J. C., Zhang, Y. H., Jiao, X., and Wang, H. M. (2018). Global sensitivity analysis of parameters in land subsidence model. *J. Zhejiang Univ. Eng. Sci.* 52 (10), 2007–2013. doi:10.3785/j.issn.1008-973X.2018.10.021

Ora, B., Ag, C., Tb, D., Keesstra, S., Mohammadi, F., and Daliakopoulos, I. N. (2019). Land subsidence hazard modeling: Machine learning to identify predictors and the role of human activities. *J. Environ. Manag.* 236, 466–480. doi:10.1016/j.jenvman.2019.02.020

Ortega-Guerrero, A., Rudolph, D, L., and Cherry, J, A. (1999). Analysis of long-term land subsidence near Mexico City;field investigations and predictive modeling. *Water Resour. Res.* 35 (11), 3327–3341. doi:10.1029/1999wr900148

Othman, A., and Abotalib, A, Z. (2019). Land subsidence triggered by groundwater withdrawal under hyper-arid conditions:case study from Central Saudi Arabia. *Environ. Earth Sci.* 78 (7), 243–248. doi:10.1007/s12665-019-8254-8

Phien-Wej, N., Giao, P, H., and Nutalaya, P. (2006). Land subsidence in Bangkok, Thailand. *Eng. Geol.* 82 (4), 187–201. doi:10.1016/j.enggeo.2005.10.004

Qin, T. C., Cheng, G. M., and Wang, H. G. (2018). The latest progress of research on land subsidence abroad and its inspiration to China. *Geo Log. Bull. China* 37 (2/3), 503–509. doi:10.3969/j.issn.1671-2552.2018.02.028

Sarah, D., Soebowo, E., and Satriyo, N. A. Review of the land subsidence hazard in pekalongan delta.central java: Insights from the subsurface. *Sch. J.* 36 (4), 163–176. doi:10.17794/rgn.2021.4.13

Shrestha, P, K., Shakya, N, M., Pandey, V, P., Bikinshaw, S, J., and Shrestha, S. (2017). Model-based estimation of land subsidence in Kathmandu Valley, Nepal. *Geomatics, Nat. Hazards Risk* 8 (2), 974–996. doi:10.1080/19475705.2017.1289985

Tolma, C. F., and Poland, J. F. (1940). *Ground-water,salt-water infiltration, and ground-surface recession in Santa Clara Valley,Santa Clara county, California*. California, CA, USA: American Geophysical Union. doi:10.1029/Tr021i001p00023

Wang, Q. Y., Peng, J. B., Jiang, Z. W., and Teng, H. Q. (2014). Numerical simulation and layerwise mark monitoring of land subsidence and ground fissures of typical section in Xi'an. *Rock Soil Mech.* 35 (11), 3298–3302.

Xue, Y. Q., Zhang, Y., Ye, S. J., and Li, Q. F. (2003). Land subsidence in China and several problems to be solved. *Quat. Res.* 2003 (06), 585–593. doi:10.3321/j.issn:1001-7410.2003.06.001

Xue, Y. Q., Zhang, Y., Ye, S. J., Wu, J. C., Wei, Z. X., Li, Q. F., et al. (2006). Study on some problems of land subsidence in China. *Geol. J. Coll. Univ.* 12 (02), 153–160. doi:10.3969/j.issn.1006-7493.2006.02.001

Xue, T. X., Shen, C. Y., and Chen, R. Z. (2021). Monitoring methods and control measures of land subsidence. *Constr. Des. Proj.* 11 (2), 20–22. doi:10.13616/j.cnki.gcjsysj.2021.11.206

Yang, J. S. (2014). Research progress of land subsidence prevention and control in Shandong Province and analysis of land subsidence law in typical areas. *China Popul. Resour. Environ.* 24 (S3), 194–198.

Zhang, A., and Wei, Z, X. (2002). Past, present and future research on land subsidence in Shanghai City. *Hydrogeology&Engineering Geol.* 2002 (05), 72–75. doi:10.3969/j.issn.1000-3665.2002.05.023

Zhang, Y. W. (2014). Formation mechanism,monitoring and warning,controlling research of subsidence of Dezhou in North China Plain. Ph.D thesis (Jinan: Shandong University). doi:10.7666/d.Y2595854

Zhang, Y. W., Shao, M., and Xiao, M. (2018). Progress of land subsidence monitoring and prevention in Shandong Province. *Shandong land Resour.* 34 (08), 62–66.

frontiers | Frontiers in Earth Science

TYPE Original Research
PUBLISHED 19 January 2023
DOI 10.3389/feart.2022.1046135

Check for updates

OPEN ACCESS

EDITED BY
Shibing Huang,
Wuhan University of Science and Technology, China

REVIEWED BY
Youjun Ning,
Southwest Petroleum University, China
Izzet Sakalli,
Eastern Mediterranean University, Turkey

*CORRESPONDENCE
Zhi Tang,
tangzhi0127@163.com

SPECIALTY SECTION
This article was submitted to Geohazards and Georisks, a section of the journal Frontiers in Earth Science

RECEIVED 16 September 2022
ACCEPTED 28 November 2022
PUBLISHED 19 January 2023

CITATION
Tang Z, Wu H, Lv J and Chang D (2023), Effects of deflection angle on the mechanical properties of constant-resistance, energy-absorbing, and anti-scouring bolts.
Front. Earth Sci. 10:1046135.
doi: 10.3389/feart.2022.1046135

COPYRIGHT
© 2023 Tang, Wu, Lv and Chang. This is an open-access article distributed under the terms of the Creative Commons Attribution License (CC BY). The use, distribution or reproduction in other forums is permitted, provided the original author(s) and the copyright owner(s) are credited and that the original publication in this journal is cited, in accordance with accepted academic practice. No use, distribution or reproduction is permitted which does not comply with these terms.

Effects of deflection angle on the mechanical properties of constant-resistance, energy-absorbing, and anti-scouring bolts

Zhi Tang*, Hao Wu, Jinguo Lv and Dezhi Chang

School of Mechanics and Engineering, Liaoning Technical University, Fuxin, China

In practice, constant-resistance, energy-absorbing, and anti-scouring bolts inevitably deflect at an angle from the coal wall and other bearing surfaces, eventually giving way and losing their energy-absorbing function. The aim of this study was to determine the applicable range of deflection angles for constant-resistance, energy-absorbing, and anti-scouring bolts and to provide a reference design for bolt construction. The principle of application of bolts under various deflection angles was proposed, and the numerical simulation of use of constant-resistance, energy-absorbing, and anti-scouring bolts was carried out using ABAQUS finite element software. The effects of deflection angle, impact energy, and impact velocity on the deformation performance, load-bearing performance, and energy absorption performance of the bolts were investigated. The deformation process of the bolt based on deflection angle was found to change from axial stretching to "stretching and bending". As the deflection angle increased, the load bearing capacity of the anti-punching device increased, and the bolt's breaking force increased after decreasing, and then decreased again while absorption energy decreased non-linearly. The bolt yield distance decreased while the displacement of bolts remained essentially the same and the deflection distance of the anti-punching device decreased. The stroke efficiency of bolts decreased and, based on the design principles of constant-resistance, energy-absorbing, and anti-scouring bolts, it was determined that the bolt was still applicable within a deflection angle of 0–17°. The impact energy had a minor effect on the bolt indicators of yield force, breaking force, and energy absorption, and the bolt's impact resistance time decreased non-linearly with increasing impact energy. Impact velocity had less effect on bolt yield force and breaking force. Both yielding time and anti-punching load capacity of the bolt decreased with increased impact velocity. As the impact velocity increased, yield distance, anti-punching deflection distance, and stroke efficiency all increased. The absorption energy increased linearly with increasing impact velocity. The results of this study provide a reference for similar anchor angle studies and a guide for the design of field construction.

KEYWORDS

deflection angle, energy-absorbing anti-scour anchor, numerical analysis, impact energy, impact velocity

Introduction

Rock burst is one of the most serious natural disasters in coal mining (Pan, 2018; Jiang et al., 2014; Dou et al., 2022). With increases in mining depth, rock burst in coal mines is becoming more and more serious. The core problem of roadway envelope deformation control in the coal mining process is in coordinating the support of the roadway envelope. In recent years, energy-absorbing supports and constant-resistance, energy-absorbing, and anti-scouring bolts have been shown to effectively control deformation of the roadway envelope (Zheng et al., 2020; Dong et al., 2022; Zhang et al., 2019).

Scholars at home and abroad have conducted a substantial amount of research on energy-absorbing bolts and have developed bolts with many advantages, such as high strength, elongation, and yielding distance, as well as high energy-absorbing and prestress characteristics (Wang et al., 2017; Zhang et al., 2016; Zhu et al., 2021; Gong et al., 2018). He et al. (2016) developed a new type of high constant-resistance large deformation anchor (NPR anchor), consisting of a piston-like cone, rod, casing, tray, and fastening nut, which has a negative Poisson's ratio effect and excellent performance in terms of impact resistance, shear resistance, and energy absorption. Kang et al. (2007) developed high prestressing and powerful support systems, such as ultra-high strength heat treatment anchors (Wu et al., 2015) and powerful anchors that can effectively control the deformation and damage of the surrounding rock. Wang Q et al. (2022) developed a constant-resistance large deformation bolt which consists of a constant-resistance device, anchor rod body, connection sleeve, tray, and nut, and a new NPR material was used to develop a constant-resistance energy-absorbing bolt. The comparison test between static tension and dynamic impact showed that the constant-resistance, energy-absorbing bolt has good impact resistance and overall deformation capacity. Wang et al. (2017) et al. designed a new type of energy-absorbing bolt (ropes) comprising an energy-absorbing connecting sleeve, a threaded steel anchor rod with an extruded round table and a friction cylinder at the end, a steel strand anchor cable, and an energy-absorbing device at the end. The new energy-absorbing bolts (cable) have good self-protection and impact adaptability compared with ordinary anchor rods, as shown in the combination static and impact tensile tests. Tang et al. (2021) designed a constant-resistance, energy-absorbing, and anti-scouring bolt consisting of a rod body, a tray, an anti-punching device, and a profiled nut. It was concluded that, under static and impact loads, the indices of the constant-resistance, energy-absorbing, and anti-scouring bolts, including yield distance, anti-scour time, and energy absorption, were significantly better than those of the conventional bolts.

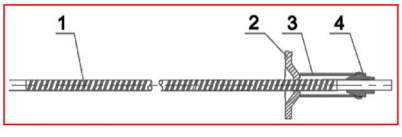
In actual engineering, the design requirements of the roadway support, the unevenness of the rock or coal wall, the axial direction of the rod, and the normal direction of the bearing surface produce a certain angle (deflection angle) (Liu et al., 2021; Guo et al., 2021; Hao et al., 2017). The mechanical properties of the constant-resistance, energy-absorbing, and anti-impact bolts are affected by the deflection angle and, depending on the angle, may not work properly. Therefore, this study used numerical simulation to assess the influence of deflection angle on the yield distance, energy absorption, load capacity, and deformation distance of constant-resistance, energy-absorbing, and anti-scouring bolts to determine the range of angles within which the bolts function properly to provide a reference for practical construction design.

Definition of deflection angle and principle of application of constant-resistance, energy-absorbing, and anti-scouring bolts

Parameter design and definition of deflection angle

The constant-resistance, energy-absorbing, and anti-scouring properties of bolts are determined by a bolt's body, a tray, an anti-punching device, and a shaped nut. For our study the bolt's body was 2560 mm long and 20 mm in diameter, the pallet was 150*150*10 mm, with a central hole of Φ25 mm. The anti-punching device had an inner diameter of 40 mm, a wall thickness of 3 mm, and a height of 150 mm. The profile nut had a height of 38 mm, a diameter of 28 mm at the thin end and 48 mm at the thick end, and a taper angle of 26.5° at the ends, as shown in Figure 1.

The deflection angle is defined as the angle between the axial direction of the bolt and the normal direction of the bearing surface;



1) Bolt's body 2)Tray 3)Anti-punching device 4)Shaped nut

FIGURE 1
Structure of the constant-resistance, energy-absorbing, and anti-scouring bolt.

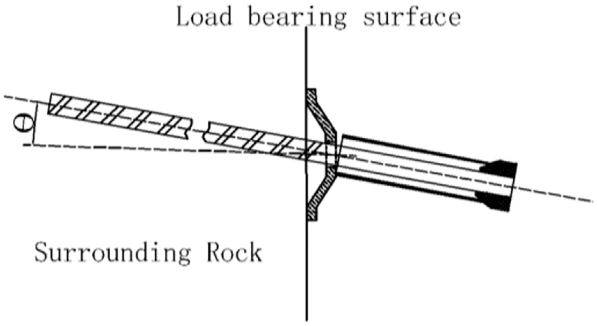


FIGURE 2
Diagram of the deflection angle θ of a constant-resistance, energy-absorbing, and anti-scouring bolt.

ideally, the anchor should be driven vertically into the surrounding rock or coal wall, at which point the deflection angle is 0°. However, in actual engineering, the bolt produces an angle between the anchor rod and the surface of the surrounding rock of the roadway due to construction errors (errors in drilling bolt holes), design requirements for roadway support, unevenness around the surrounding rock (e.g., flake bubbles in the coal rock body), etc. The angle between the axial direction of the bolt and the normal direction of the bearing surface of the surrounding rock is the deflection angle θ, as shown in the schematic diagram in Figure 2.

In practice, bolts are constructed in the following sequence: hole drilling, anchor bolt insertion, insertion of the tray and anti-punching device and, finally, tightening of the nut to apply preload. As the centre hole diameter of the pallet is slightly larger than the diameter of the rod, the rod can be deflected at a certain angle, defining the maximum angle at which the centre hole allows the bolt to be deflected, i.e., the maximum deflection angle. When the deflection angle is less than the maximum, the pallet can be tightened against the load bearing surface, but the impact protector is not sufficiently tightened against the pallet (see Figure 2). When the deflection angle is greater than the maximum, the pallet does not fit tightly against the load bearing surface; therefore, under the action of preload, the pallet bends or shears the rod, which is not conducive to maintenance of the bolt's tensile performance.

To determine conditions that allow full use of the tensile properties of the rod, a theoretical analysis of the maximum deflection angle was carried out. The positioning of the bolt and the pallets was simplified, as shown in Figure 3, and the geometric relationship was obtained from:

$$\frac{20}{\cos\theta} + 10 * \tan\theta = 25 \quad (1)$$

Solution: θ_1 = 20.2° and θ_2 = -63.8° (rounded off).

From the results, it can be seen that the maximum deflection angle that can be generated between the bolt and the pallet is 20.2° (Figure 3A).When the deflection angle is less than 20.2°, the pallet only acts in the axial direction of the rod; when the deflection angle is greater than 20.2°, the pallet cannot be tightened against the load-bearing surface (Figure 3B), and under the action of the preload or external load, the wall of the central hole of the pallet will exert a lateral force on the bolt, which results in bending or shear deformation of the rod.

Principles of application of constant-resistance, energy-absorbing, and anti-scouring bolts in the presence of a deflection angle

Bolts have a much larger dimension in the lengthwise direction than the other two directions, providing mainly tensile and shear resistance, with very little bending and compression resistance (Wu 2009). Based on the theory of yielding scour protection support and the principles of ideal energy-absorbing device design (Pan et al., 2014a; Pan et al., 2014b; Tang et al., 2022), it is proposed that constant-resistance, energy-absorbing, and anti-scouring bolts in the presence of deflection angles should have the following basic characteristics: 1) Reasonable deformation load threshold. The load carrying capacity of the anti-puncher in the force-

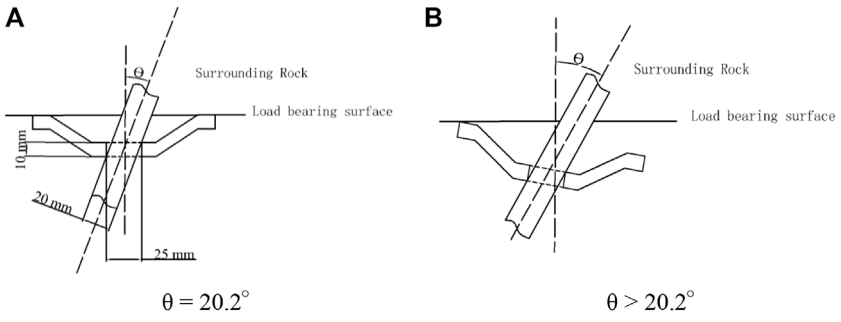


FIGURE 3
Position relation of the pallet and the bolt. **(A)** θ = 20.2° and **(B)** θ > 20.2°.

10.3389/feart.2022.1046135

TABLE 1 Comparison of mechanical properties of bolts with different deflection angles.

Deflection angle	0°	3°	5°	7°	10°	13°	15°	17°	20°	23°	25°	27°	30°	33°	35°
Yield distance/mm	365.3	362.8	349.2	353.6	346.0	310.6	308.9	293.4	266.8	269.4	270.6	262.9	205.6	190.1	164.8
Yield distance of anti-punching device/mm	142.0	140.2	138.0	136.1	136.4	134.2	131.3	132.4	130.0	130.0	122.1	108.2	42.4	30.1	26.1
Stroke efficiency/%	94.7	93.3	92.0	90.7	90.7	89.3	87.3	88.1	86.7	86.7	81.3	72.0	28.0	20.0	17.3
Breaking force/kN	171.2	168.1	163.0	162.4	159.2	154.2	151.3	151.2	134.3	138.8	140.4	138.1	143.1	147.0	131.8
Load capacity of the anti-punching device/kN	120.1	120.1	121.1	122.6	124.8	129.0	130.7	132.3	131.4	130.7	133.8	133.1	137.7	135.2	127.8
Yield force/kN	122.9	123.2	123.2	122.8	123.2	123.1	123.0	122.9	123.0	122.8	123.2	122.8	122.6	124.9	124.0
Energy absorption/kJ	46.2	46.0	43.7	44.8	43.4	38.2	38.3	36.0	32.0	32.5	33.0	31.9	24.6	22.1	18.7

displacement curve of the anchor rod is the deformation load threshold of the anchor rod, which is set at 90–110% of the yielding force of the rod to ensure that the anti-punching device is playing a role near the yielding stage of the rod. 2) High stroke efficiency. The performance of the bolt giving way depends largely on the adequacy of the deformation of the anti-punching device, which can be considered adequate when the stroke efficiency is 85–99%. 3) Constant reaction force. The reaction force of the anti-punching device should be kept as constant as possible during the deformation of the surrounding rock, which ensures that it protects the bolt. 4) A stable and repeatable deformation damage pattern to ensure the reliability of the anti-punching device in complex situations. 5) High load-bearing capacity. Anchor rods with a deflection angle should have a breaking force that is not less than 85% of the breaking force under axial tension to be considered as having a high support resistance to the surrounding rock. 6) Good energy absorption performance. The energy absorption of the bolt should be higher than 75% of its energy absorption in axial tension to allow good energy absorption performance. 7) Good deflection capacity. The yield distance of the bolt should be higher than 80% of its yield distance in the tensile test, which indicates good deflection capacity.

Influence of deflection angle on mechanical properties of an anchor bolt under static load

Using ABAQUS software, the finite element models of the rod, pallet, energy absorber, and profile nut were built according to the dimensions described above, and explicit dynamic analysis was performed. The material parameters for the bolt's body, pallets, anti-punching device, and shaped nuts were set in the properties module. The settings included density of 7850 kg/m^3, modulus of elasticity of 210 GPa, and Poisson's ratio of 0.3. The plasticity parameters were taken from laboratory tensile tests of the bolt and converted to yield strength of 400 MPa and tensile strength of 588 MPa. The rods were set for flexible damage in ductile metal damage. The anti-punching device used self-contact, other surface contact methods were set to surface-to-surface contact, the contact method was the penalty contact method, and the coefficient of friction was taken as 0.3. The boundary conditions of the model were set: the left end of the bar was completely fixed and only axial displacement was allowed at 10 mm from the pallet. The model was assembled in the relative positions shown in Figure 1. A rigid plate with a diameter greater than that of the bolt's body was displaced 450 mm to the right from the left side of the pallet, treating the plate as a load bearing surface with an angle of the bolt. Mesh settings: C3D8R cells were used for each part, the mesh shape was hexahedral, the mesh size of the pallet and bolt were set to 5, the size of the anti-punching device was set to 2, the bolt's cell

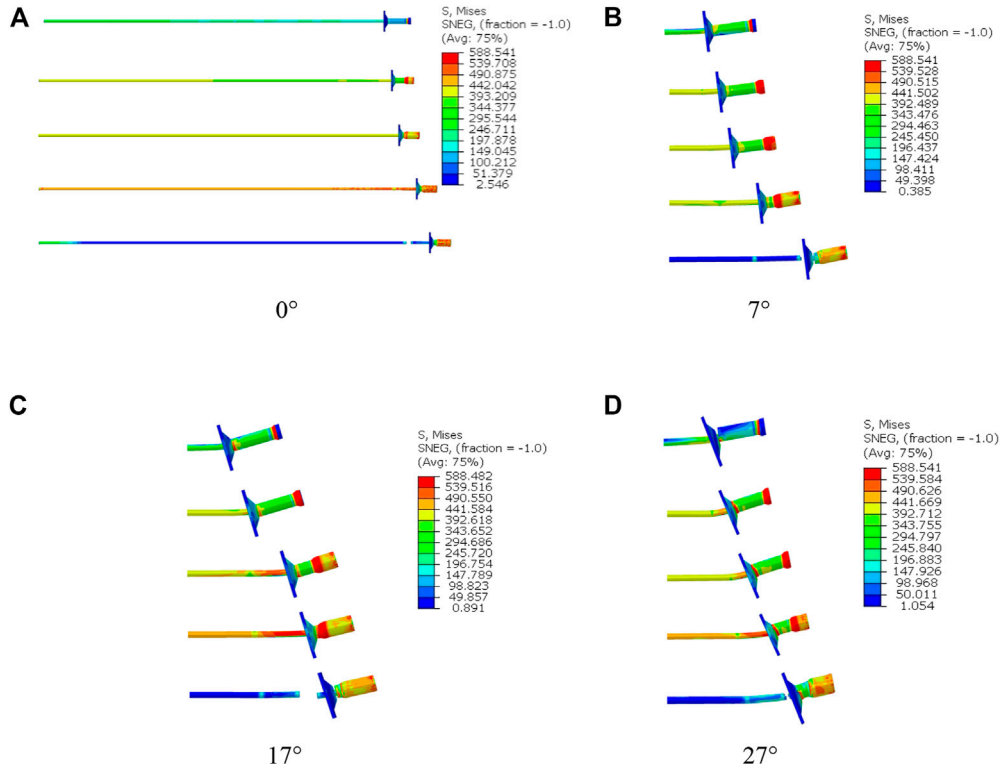


FIGURE 4
Deformation of bolt and anti-punching device at partial deflection angles.

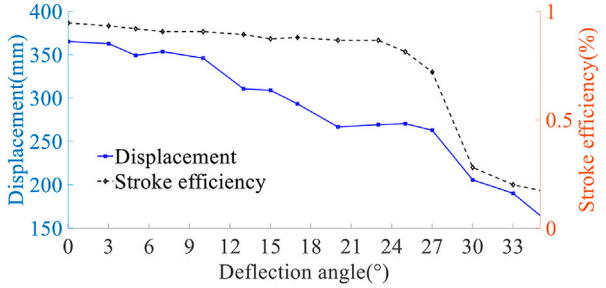


FIGURE 5
Displacement of the bolt/stroke efficiency of the anti-punching device—deflection angle curve.

type was set to hourglass control for stiffness, and the cell delete was set.

To determine the influence of the deflection angle on the mechanical properties of the constant-resistance, energy-absorbing, and anti-scouring bolts under static load, simulations of the tensile process of the bolts were carried out at deflection angles of 0, 3, 5, 7, 10, 13, 15, 17, 20, 23, 25, 27, 30, 33, and 35°. The mechanical properties of the bolts at different angles are shown in Table 1.

Effect of deflection angle on deformation performance

The deformation process of the bolt at partial deflection angles is shown in Figure 4. The displacement of the bolt/stroke efficiency of the anti-punching device—deflection angle curve is shown in Figure 5. Figures 4, 5 and Table 1 indicate that:

1) With a deflection angle of 0° (Figure 4A), the bolt as a whole underwent only axial tension and no bending deformation. In the deflection angle range of 3–35° (Figures 4B–D), the pallet-nut section of the bolt was deformed in "stretching + bending". At a deflection angle of 27°, the pallet did not fit sufficiently with the anti-punching device due to the angle, and the stress was concentrated on the side of the anti-punching device, which was the first to reach its strength limit and show damage. These data demonstrate that the deflection angle

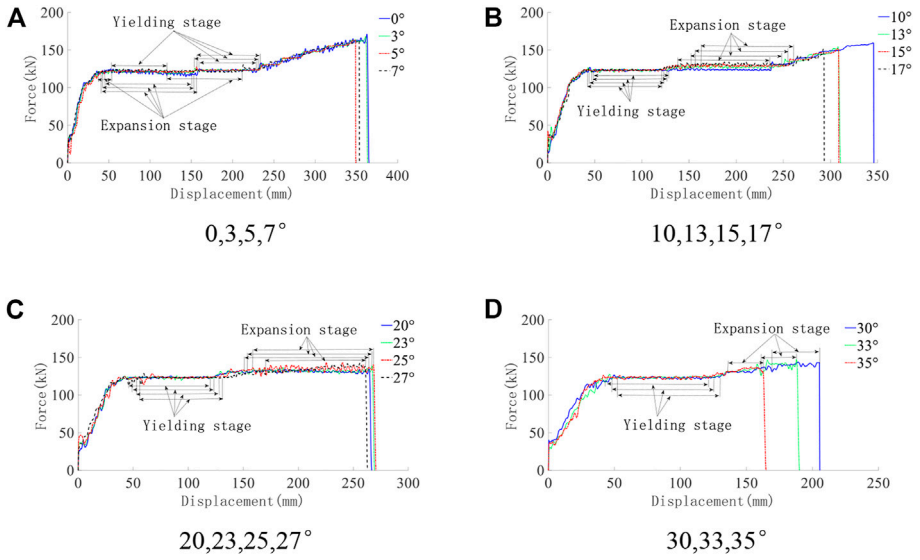


FIGURE 6
Force-displacement curves for bolt with different deflection angles. **(A)** 0, 3, 5, and 7°, **(B)** 10, 13, 15, and 17°, **(C)** 20, 23, 25, and 27°, and **(D)** 30, 33, and 35°.

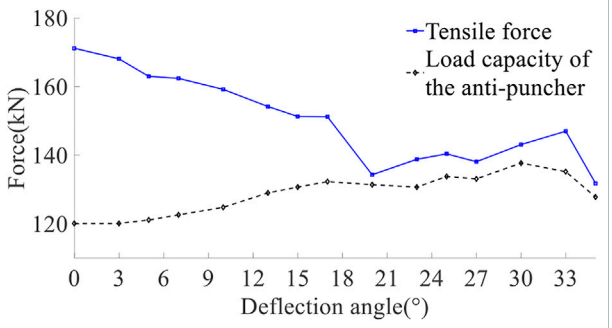


FIGURE 7
Breaking force of bolt/load bearing force of anti-punching device—deflection angle curve.

changes the deformation of the bolt from axial tension to a combination of "stretching + bending".

2) The let-off distance of the bolt is the sum of the displacement of the bolt's body and the deformation distance of the anti-puncher. With a deflection angle in the range of 0–20°, the nut was first in contact with the side of the anti-puncher, the compressive stress increased, and the bolt was curved by the eccentric load. The angle of deflection increased and the degree of pole bending increased. The locations of the stress concentration in the anti-puncher and the bending of the pole took the lead in plastic deformation and damage, with a reduction in both pole displacement and anti-puncher deformation distance. The anchor deflection distance decreased from 365.3 mm to 266.8 mm, with an average decrease of 4.93 mm/°. In the range of 20–27°, the pallet contacted the anti-puncher first on one side, and stresses were concentrated and the pallet acted laterally on the bolt's body. The direction of action of the anti-puncher on the nut was opposite to the direction of force on the rod and the deformation of the bolt was reduced. There was a small variation in the deflection distance in the range of 270.6 mm–262.9 mm. In the range of 27–35°, the stress concentration of the pallet on the anti-puncher increased and the local plastic deformation of the anti-puncher was too large. The bending of the rod was large and the expansion of the anti-puncher was hindered. The yield distance dropped from 262.9 mm to 164.8 mm, with an average drop of 12.26 mm/°. These data indicate that the yield distance decreases overall with increasing deflection angle. The yielding distance decreased to a lesser extent before 20°; it remained almost constant from 20 to 27° and decreased to a greater extent after 27°.

3) Stroke efficiency is the ratio of the deformation distance to its own length. During the "stretching and bending" deformation of the bolt, the side of the anti-puncher was first in contact with the nut, resulting in stress concentration and plastic deformation. The increase in angle increased the degree of deformation and decreased the distance of deformation. For deflection angles in the range of 0–23°, the yield distance of the anti-punching device reduced

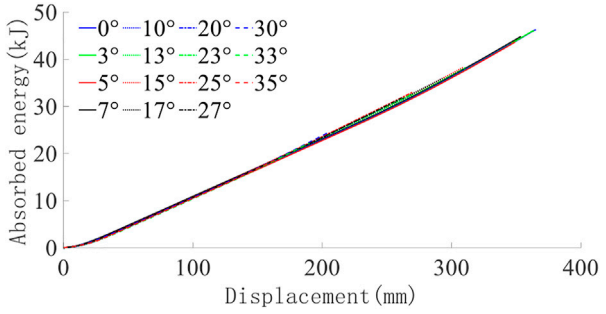


FIGURE 8
Energy absorption-displacement curves for bolts at different angles.

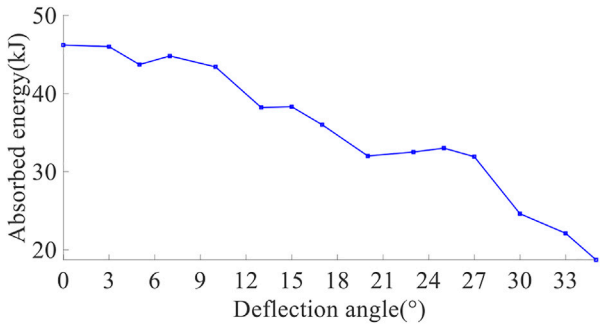


FIGURE 9
Energy absorption—deflection angle curve.

from 142.0 mm to 130.0 mm and the stroke efficiency reduced from 94.7% to 86.7%. In the range of 23–35°, the deformation distance was reduced from 130.0 mm to 26.1 mm and the stroke efficiency dropped rapidly from 86.7% to 17.3%. These data indicate that the larger the deflection angle, the smaller the deflection distance and the lower the stroke efficiency. Before 23°, the deformation distance and stroke efficiency of the anti-puncher device were less influenced by the deflection angle; after 23°, they were greatly influenced by the deflection angle.

Influence of deflection angle on load bearing performance

The anchor rod force-displacement curves for different deflection angles are shown in Figure 6. The breaking force of bolt/load bearing force of the anti-punching device deflection angle curve is shown in Figure 7. The load bearing force of the anti-punching device was defined as the value of the anti-punching reaction force during the expansion stage. Figure 6, Figure 7, and Table 1 indicate that:

1) When the deflection angle was in the range of 0–20°, there was still a gap between the centre hole of the pallet and the rod body. The pallet had no force on the pole, but there was a certain angle between the anti-puncher and the pallet, which made them unevenly stressed. The pole was bent and deformed. The bolt breaking force decreased gradually in the range of 171.1–134.3 kN. In the range of 20–33°, the pole was affected by the composite lateral action of the pallet and the nut, and resulted in less deformation of the pole and a small increase in load capacity. The breaking force rose gradually in the range of 134.3–147.0 kN. The bending of the bolt was greater at 35° and the load capacity was greatly reduced. The breaking force was 131.8 kN. These data indicate that the breaking force of the anchor is not linearly related to the angle of deflection, but rather tends to fall, then rise slightly and then continue to fall.
2) After the bending and deformation of the rod, the anti-puncher was squeezed by the pallet, in addition to the frictional and pressure effects with the nut. Plastic damage occurred at the contact position. As the angle increased, the deformation of the anti-puncher increased. The force state changed from friction to friction and plastic deformation, and the anti-puncher reaction force increased significantly. The load carrying capacity of the anti-puncher increased from 120.0 kN to 137.7 kN over the range of 0–30° of deflection. The rate of increase was 0.57 kN/° over the range of 0–20° and 0.63 kN/° over the range of 20–30°. These data indicate that the load-bearing capacity of the anti-punching device increases with increase of deflection angle.
3) The force-displacement curve of a constant-resistance, energy-absorbing, and anti-scouring bolt consists of five parts: "linear elastic stage", "expansion stage", "yielding stage", "strengthening stage", and "breaking stage" (Tang et al., 2022). The change in position of the expansion stage reflects the strength between load-bearing properties of the anti-punching device and bolt. The anchor pull-off force decreased as the angle increased, while the load-bearing capacity of the anti-puncher increased as the angle increased. In the deflection angle range of 0–5°, the expansion stage occurred after the linear elastic stage and before the yielding stage. At a deflection angle of 7°, the expansion phase occurred partly after the inline elastic stage, partly after the yielding stage, and before the strengthening stage. In the range of 10–17°, the expansion phase occurred after the yielding phase and before the strengthening stage; in the range of 20–35°, the expansion stage occurred simultaneously with the strengthening stage. The curve of the expansion stage is smoother at all deflection angles, indicating that the bolt had a constant reaction force. The position of the spreading stage in the curve varied for different deflection angles.

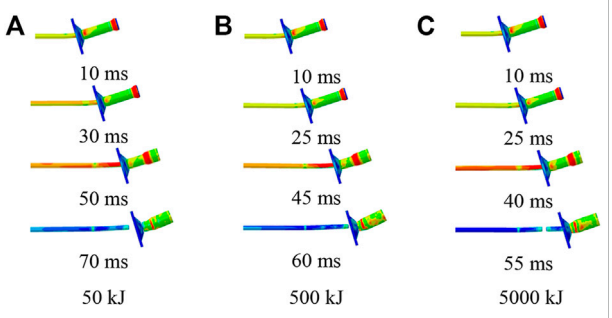


FIGURE 10
Deformation of bolt with time at different impact energies.

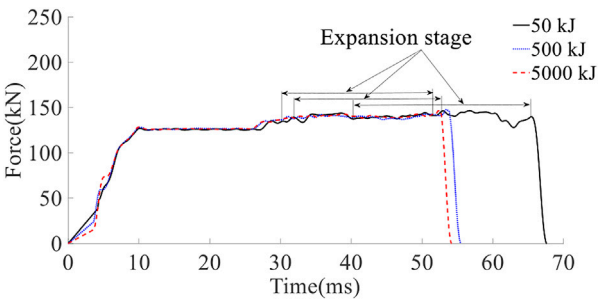


FIGURE 11
Anchor force-time curve.

Effect of deflection angle on energy absorption performance

The absorption energy-displacement curves for different deflection angles are shown in Figure 8 and the absorption energy-deflection angle curves are shown in Figure 9. Figure 8, Figure 9, and Table 1 indicate that:

1) The area enclosed by the force-displacement curve reflects the amount of energy absorbed by the anchor. The bearing capacity and yield distance of the bolt decreased as the deflection angle increased, so the amount of energy absorbed should also decrease as the deflection angle increases. In the deflection angle range of 0–20°, the energy absorbed by the anchor dropped from 46.2 kJ to 32.0 kJ. In the range of 20–27°, the energy absorption fluctuated slightly within 31.9–33.0 kJ; in the range of 27–35°, it decreased from 31.9 kJ to 18.7 kJ. These data demonstrate that energy absorption decreases non-linearly with increase of the deflection angle.
2) In the range of 0–20°, the reduction rate of the energy absorption of the bolt was 0.71 kJ/°; in the range of 27–35°, the absorbed energy decreased from 31.9 kJ to 18.7 kJ, with an average reduction rate of 1.65 kJ/° (> 0.71 kJ/°). These data indicate that the bolt had good energy absorption performance before 20°, but performance was severely reduced in the range of 27–35°.
3) The ratio of energy absorption to displacement (energy absorption per unit of displacement) is the slope of the energy absorption-displacement curve, and the energy absorption per displacement of the bolt at each deflection angle is 7.88 kJ/mm, 7.88 kJ/mm, 7.88 kJ/mm, 7.89 kJ/mm, 7.97 kJ/mm, 7.99 kJ/mm, 7.99 kJ/mm, 7.99 kJ/mm, 8.19 kJ/mm, 8.19 kJ/mm, 8.18 kJ/mm, 8.19 kJ/mm, 8.39 kJ/mm, 8.39 kJ/mm, 8.39 kJ/mm, and 8.39 kJ/mm, respectively. These data demonstrate that the amount of energy absorbed by the anchor rod increases linearly with displacement for different deflection angles. The effect of deflection angle on the energy absorption per displacement of bolt was minor.

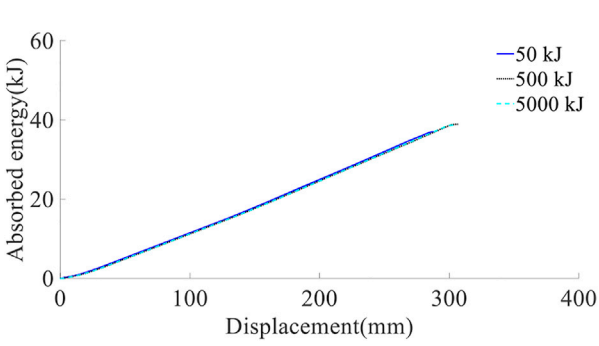


FIGURE 12
Anchor energy absorption-displacement curve.

Determination of the scope of application of constant-resistance, energy-absorbing, and anti-scouring bolts

Through the above analysis and based on the design principles, the indicators corresponding to different deflection angles have been collated and analysed, and the percentage of each indicator is shown in Table 2.

We studied the reasonable range of deflection angles based on the applicable principles presented earlier in this article. The deformation process of the bolt includes the “elastic stage”, “yielding stage”, “expansion deformation stage”, “strengthening stage”, and “breaking stage”, indicating that the bolts have a repeatable deformation mode. The deformation stage of the anti-punching device is the expansion stage. The force-displacement curve of the bolt at each angle has a constant reaction force with a small floating range of reaction force in the

10.3389/feart.2022.1046135

TABLE 2 Percentage of each indicator for bolts with different deflection angles.

Deflection angle	0°	3°	5°	7°	10°	13°	15°	17°	20°	23°	25°	27°	30°	33°	35°
Deformation threshold/% (90–110)	97.7	97.5	98.3	99.8	101.3	104.8	106.3	107.6	106.8	106.4	108.6	108.4	112.3	108.2	103.1
Stroke efficiency/% (85–99)	94.7	93.3	92.0	90.7	90.7	89.3	87.3	85.3	86.7	86.7	81.3	72.0	28.0	20.0	17.3
Breaking force/% (85)	100.0	98.2	95.2	94.9	93.0	90.1	88.4	88.3	78.4	81.1	82.0	80.7	83.6	85.9	77.0
Energy absorption/% (75)	100.0	99.6	94.6	97.0	93.9	82.7	82.9	77.9	69.3	70.3	71.4	69.0	53.2	47.8	40.5
Displacement/% (80)	100.0	99.3	95.6	96.8	94.7	85.0	84.6	80.3	73.0	73.7	74.1	72.0	56.3	52.0	45.1

expansion stage. All angles in the deformation threshold indicator, except 30°, are in accordance with the design principles. The stroke efficiency indicators are in accordance with the design principles for all angles except 25, 27, 30, 33, and 35°. At 0–17° and 33°, the breaking force percentage indicators are in accordance with the design principles. At 0–17° the energy absorption ratio indicator is in accordance with the design principles. As the bolt should all satisfy the above design principles when there is a deflection angle, our analysis demonstrates that the deflection angle of the anchor bolts in the range of 0–17° is still considered applicable.

Analysis of mechanical properties of bolts under impact loading

In this study, we investigated the mechanical properties of constant-resistance, energy-absorbing, and anti-scouring bolts under impact loading in the presence of deflection angle. Combined with the results of static analysis, we chose to use ABAQUS finite element software to simulate the impact loading of the bolt with a deflection angle of 17°. Due to the large amount of impact energy released by the impact ground pressure working at the pallets of the bolts, a rigid body with mass and velocity was used to simulate the impact energy of the surrounding rock and to study the mechanical properties of the bolts under the action of different impact energies and impact velocities. The parameters were set in the same way as for static loads, with an angle of 17° between the rigid plate and the pallet.

Effect of impact energy on mechanical properties of bolts

The impact velocity was 6 m/s and the impact energy was 50, 500, and 5000 kJ. Separate impact loading simulations were carried out on constant-resistance, energy-absorbing, and anti-scouring bolts with a deflection angle of 17°. The deformation of the bolts is shown in Figure 10, the force-time curve of the bolts is shown in Figure 11, the energy absorption-displacement is shown in Figure 12, and the mechanical properties are shown in Table 3. From Figures 10–12 and Table 3, it can be seen that:

1) At different impact energies, the deformation process of the bolt underwent the “elastic stage”, the “yielding stage”, the “reinforcement stage + anti-punching device expansion deformation stage”, the “breaking stage”, and the “breakage stage”. These data indicate that the bolt has a repeatable deformation pattern.

TABLE 3 Mechanical properties of anchor bolts at different impact energies.

Impact energy/kJ	Yield force/kN	Breaking force/kN	Resistance time/ms	Energy absorption/kJ	Yield distance/mm	Load capacity of the anti-punching device/kN	Deformation distance/mm	Stroke efficiency/%
50	125.8	139.7	67.6	36.9	293.5	140.3	127.4	84.9
500	126.7	146.5	55.4	38.9	306.8	139.6	141.1	94.1
5000	126.4	146.2	54.1	38.6	305.8	140.1	140.3	93.5

2) As the impact energy increased, the load-bearing capacity of the anti-punching device remained between 139.6 and 140.3 kN, which indicates that the anti-punching device has a relatively constant reaction force.
3) Under the impact energy of 50, 500, and 5000 kJ, the deflection distances of the bolt (equal to the bolt's body displacement plus the deformation distance of the anti-punching device) were 293.5, 306.8, and 305.8, mm respectively, and the deformation distances of the anti-punching device were 127.4, 141.1, and 140.3 mm, respectively. Stroke efficiency was 84.9, 94.1, and 93.5% respectively. The displacement of the bolt's body was 166.1, 165.7, and 165.5 mm, respectively. These data indicate that the impact energy has a minor effect on the deformation distance and stroke efficiency of the bolt and on yield distance of the anti-puncher.
4) At 50, 500, and 5000 kJ impact energy, the yield force of the bolt was 125.8, 126.7, and 126.4 kN, respectively, and the breaking force was 139.7, 146.5, and 146.2 kN, respectively. The impact energy had a small effect on the yield force, breaking force, and load bearing capacity of the anchor.
5) Under the action of 50, 500, and 5000 kJ impact energy, the energy absorption of anchor rods was 36.9, 38.9, and 38.6 kJ respectively, indicating that the impact energy has a small effect on the energy absorption index of anchor rods.
6) The impact resistance times were 67.6, 55.4, and 54.1 ms at 50, 500, and 5000 kJ impact energy, respectively, indicating that the impact resistance time decreases with increasing impact energy.

Effect of impact velocity on mechanical properties of bolts

The impact energy was chosen as 50 kJ and the impact velocities were 2, 4, 6, and 8 m/s, respectively. The impact loading simulations were carried out for a constant-resistance, energy-absorbing, and anti-scouring bolt with a deflection angle of 17°. The bolt's deformation is shown in Figure 13, the force-time curve of the bolt is shown in Figure 14, the energy absorption-displacement is shown in Figure 15, and the mechanical properties of the anchor rod are shown in Table 4. From Figures 13–18 and Table 4, it can be seen that:

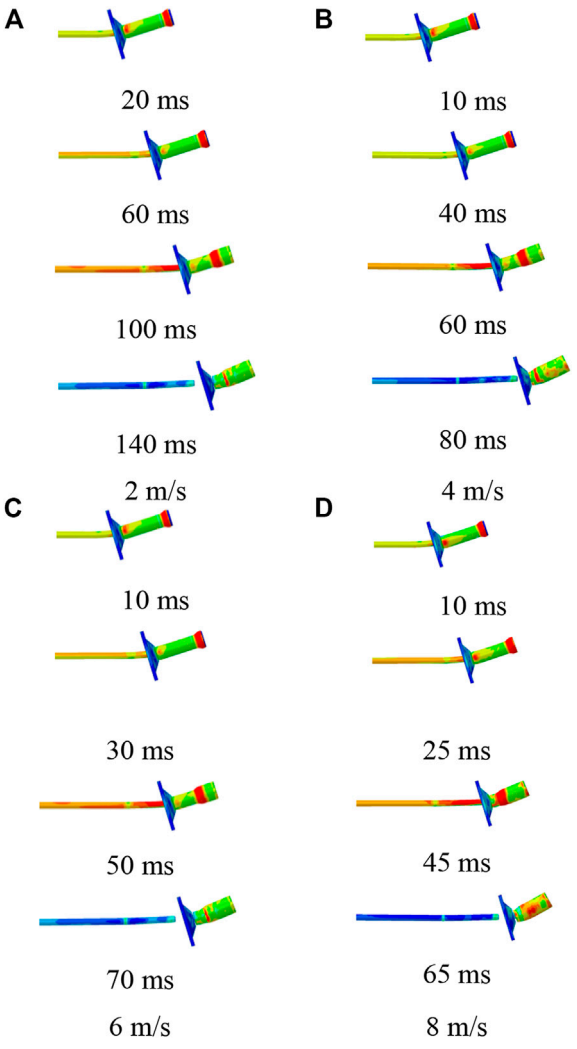


FIGURE 13
Deformation of bolt with time at different impact velocities.

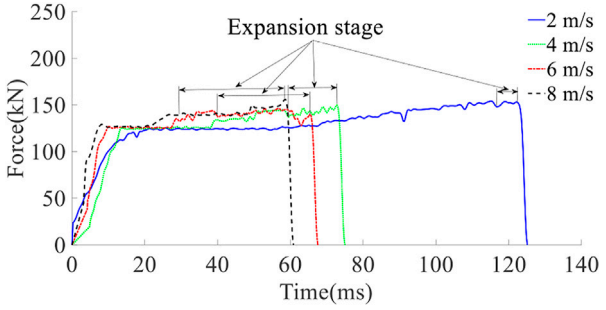


FIGURE 14
Anchor force-time curve.

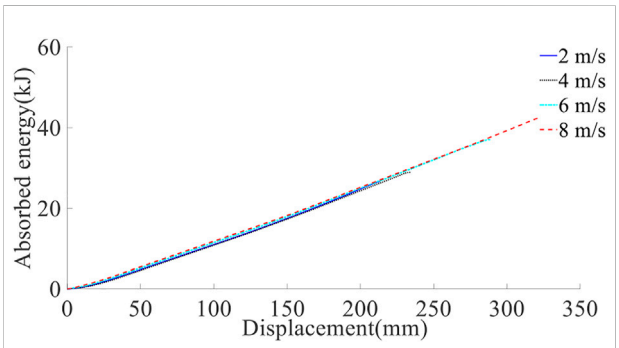


FIGURE 15
Anchor energy absorption-displacement curve.

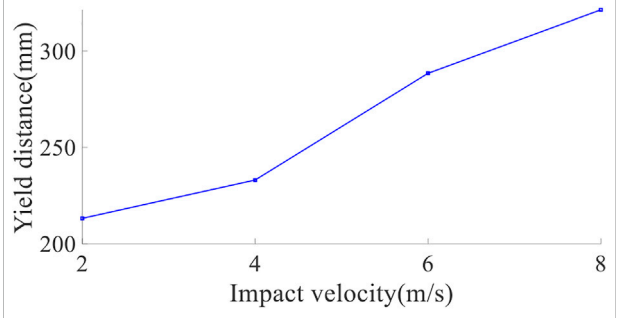


FIGURE 16
Anchor give way distance at different impact velocities.

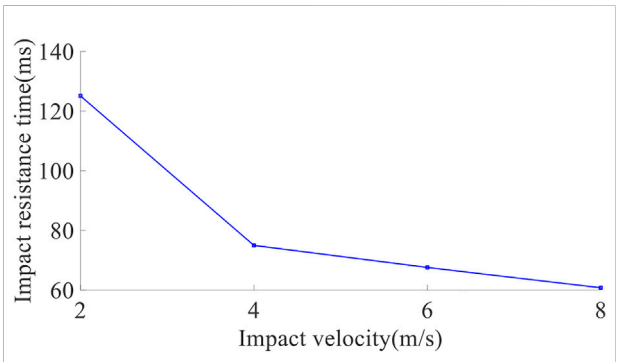


FIGURE 17
Anchor impact resistance time for different impact velocities.

TABLE 4 Mechanical properties of anchor bolts at different impact velocities.

Impact energy/kJ	Yield force/kN	Breaking force/kN	Resistance time/ms	Energy absorption/kJ	Yield distance/mm	Load capacity of the anti-punching device/kN	Deformation distance/mm	Stroke efficiency/%
2	124.1	152.7	125.1	26.5	213.2	151.5	41.7	27.8
4	124.7	149.6	75.0	28.9	233.1	142.6	63.2	42.1
6	125.8	139.7	67.6	36.9	293.5	140.3	127.4	84.9
8	126.1	155.7	60.8	42.3	321.4	141.5	144.1	96.1

1) At impact speeds of 2, 4, 6, and 8 m/s, the deformation process of the bolt experienced the "elastic stage", the "yielding stage", and the "reinforcement + expansion deformation stage", indicating that the bolt has a repeatable deformation mode at different impact speeds.
2) As the impact velocity increased, the load-bearing force of the anti-punching device remained between 140.3 and 151.5 kN, indicating that the anti-punching device has a relatively constant reaction force.
3) At impact velocities of 2, 4, 6, and 8 m/s, the bolt yield distances were 213.2, 233.1, 293.5, and 321.4 mm, respectively. The deformation distances of the anti-punching device were 41.7, 63.2, 127.4, and 144.1 mm, and the stroke efficiencies were 27.8, 42.1, 84.9, and 96.1%, respectively. The displacements of bolt's

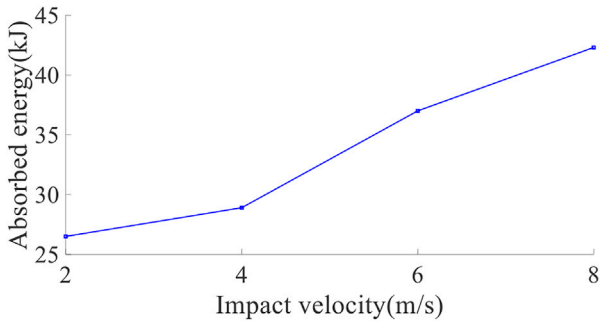


FIGURE 18
Absorption energy of anchor bolt at different impact velocities.

body were 171.5, 170.0, 166.1, and 177.3 mm, respectively. These data indicate that the impact velocity has a small effect on the displacement of the bolt. The yielding distance of the bolts, and the deformation distance and stroke efficiency of the anti-punching device increased with the increase of the impact velocity.

4) At impact speeds of 2, 4, 6, and 8 m/s, the yield forces of the bolt were 124.1, 124.7, 125.8, and 126.1 kN respectively; the tensile forces were 152.7, 149.6, 139.7, and 155.7 kN, respectively, and the load bearing force of the anti-punching device was 151.5, 142.6, 140.3, and 141.5 kN, respectively. These data indicate that impact velocity has a minor effect on the yield force and breaking force of the bolt. The load breaking force of the anti-punching device remained essentially the same with the increase of impact velocity.
5) The energy absorption of the bolt was 26.5, 28.9, 37.0, and 42.3 kJ, respectively, for impact velocities of 2, 4, 6, and 8 m/s, indicating that energy absorption increases approximately linearly with impact velocity.
6) The impact velocities of the bolts were 125.1, 75.0, 67.6, and 60.8 ms for impact velocities of 2, 4, 6, and 8 m/s, respectively, indicating that impact resistance time decreases with increasing impact velocity.

Conclusion

Constant-resistance, energy-absorbing, and anti-scouring bolts were simulated by static loading at different deflection angles and by impact loading of the anchors at a deflection angle of 17°. The main conclusions of this study are:

1) Design principles for constant-resistance, energy-absorbing, and anti-scouring bolts at deflection angles are proposed.
2) At the angle of deflection, the deformation process of the bolt changes from an axially stretching form to a "stretching and bending" form. The bolt has a repeatable deformation mode and a relatively constant reaction force.
3) As the deflection angle increases, the load bearing force of the anti-punching device increases, the breaking force of the bolt increases after decreasing and then decreases again, the energy absorption decreases non-linearly, the yield distance of the bolt decreases (the displacement of the bolt remains basically the same and the deformation distance of the anti-punching device decreases), and the stroke efficiency decreases. According to the principles of constant-resistance, energy-absorption, and anti-scouring bolt design, it was determined that the bolt is still applicable within a deflection angle of 0–17°.
4) Impact energy has a minor effect on the indices of yield force, breaking force, and energy absorption of the bolt. The impact resistance time decreases non-linearly with increase in impact energy.
5) Impact velocity has a minor effect on the yield force and breaking force of the bolt. The impact resistance time and the load bearing force of the anti-puncher device both decrease with increasing impact velocity. The yield distance of the bolt, and the deformation distance and stroke efficiency of the anti-punching device all increase with increasing impact velocity. Absorption energy increases linearly with increasing impact velocity.

Data availability statement

The original contributions presented in the study are included in the article/Supplementary material; further inquiries can be directed to the corresponding author.

Author contributions

Conceptualization, ZT; methodology, ZT; software, ZT and HW; validation, JL; investigation, HW; resources, ZT; data curation, HW; writing—original draft preparation, HW; writing-review and editing, ZT; visualization, HW; supervision, DC; project administration, ZT; funding acquisition, ZT.

Funding

This study was funded by the National Natural Science Foundation of China (51804152, 52174116), Liaoning Revitalization Talents Program (XLYC1907168), and Natural Science Foundation of Liaoning Province (2019-MS-163, 2021-MS-337).

Conflict of interest

The authors declare that the research was conducted in the absence of any commercial or financial relationships that could be construed as a potential conflict of interest.

Publisher's note

All claims expressed in this article are solely those of the authors and do not necessarily represent those of their affiliated organizations, or those of the publisher, the editors, and the reviewers. Any product that may be evaluated in this article, or claim that may be made by its manufacturer, is not guaranteed or endorsed by the publisher.

References

Dong, J. J., Zheng, G. Y., and Yang, D. (2022). FBG bolts used for bolt support for safety monitoring of mining roadways. *J. Min. Saf. Eng.* 39 (02), 328–334. doi:10.13545/j.cnki.jmse.2021.0224

Dou, L. M., Tian, X. Y., Cao, A. Y., Gong, S. Y., He, H., He, J., et al. (2022). Present situation and problems of coal mine rock burst prevention and control in China. *J. China Coal Soc.* 47 (01), 152–171. doi:10.13225/j.cnki.jccs.yg21.1873

Gong, W. L., Sun, Y. X., Gao, X., He, M. C., and Qi, P. (2018). Dynamic characteristics of constant-resistance-large-deformation bolts based on weight-dropping tests. *Chin. J. Rock Mech. Eng.* 37 (11), 2498–2509. doi:10.13722/j.cnki.jrme.2018.0674

Guo, J. G., Li, Y. H., He, F. L., Chen, J. H., Zhao, G. M., and Zhang, J. W. (2021). Pullout simulation on fully grouted rock bolts based on residual shear strength. *Rock Soil Mech.* 42 (11), 2953–2960. doi:10.16285/j.rsm.2021.0544

Hao, C. S., Shang, D., Sun, M., Zhang, P., and Chen, Z. (2017). Supporting parameters impact on pretensioned distribution of roadway. *Coal Technol.* 36 (03), 17–21. doi:10.13301/j.cnki.ct.2017.03.007

He, M. C., Li, C., Gong, W. L., Wang, J., and Tao, Z. G. (2016). Support principles of NPR bolts/cables and control techniques of large deformation. *Chin. J. Rock Mech. Eng.* 35 (08), 1513–1529. doi:10.13722/j.cnki.jrme.2015.1246

Jiang, Y. D., Pan, Y. S., Jiang, F. X., Dou, L. M., and Ju, Y. (2014). State of the art review on mechanism and prevention of coal bumps in China. *J. China Coal Soc.* 39 (02), 205–213. doi:10.13225/j.cnki.jccs.2013.0024

Kang, H. P., Wang, J. H., and Lin, J. (2007). High pretensioned stress and intensive bolting system and its application in deep roadways. *J. China Coal Soc.* (12), 1233–1238. doi:10.13225/j.cnki.jccs.2007.12.003

Liu, H. Y., Zuo, J. P., Liu, D. J., Li, C. Y., Xu, F., and Lei, B. (2021). Optimization of roadway bolt support based on orthogonal matrix analysis. *J. Min. Saf. Eng.* 38 (01), 84–93. doi:10.13545/j.cnki.jmse.2019.0420

Pan, Y. S. (2018). Instability theory of coal mine impact ground pressure disturbance response and application. *J. Coal* 43 (08), 2091–2098. doi:10.13225/j.cnki.jccs.2018.0604

Pan, Y. S., Ma, X., Xiao, Y. H., and Li, Z. H. (2014b). Numerical analysis and experimental study of a coal mine anti-impact and energy-absorption supporting component. *J. Exp. Mech.* 29 (02), 231–238. doi:10.7520/1001-4888-13-089

Pan, Y. S., Xiao, Y. H., Li, Z. H., and Wang, K. X. (2014a). Study of tunnel support theory of rockburst in coal mine and its application. *J. China Coal Soc.* 39 (02), 222–228. doi:10.13225/j.cnki.jccs.2013.2015

Tang, Z., Wu, H., Liu, Y., Pan, Y., Lv, J., and Chang, D. (2022). Numerical analysis of mechanical characteristics of constant-resistance, energy-absorbing and anti-scour bolts. *Materials* 15 (10), 3464–3510. doi:10.3390/ma15103464

Tang, Z., Wu, H., Lv, J., Xin, Z., and Zuo, W. (2021). Study on mechanical characteristics of energy-absorbing and anti-scour bolts. *Complexity* 2021, 1–9. doi:10.1155/2021/8876517

Wang, A. W., Fan, D. W., Pan, Y. S., Zhao, B. Y., and Dai, L. P. (2022). Expansion-friction energy-absorption anti-impact cable and its mechanical characteristics. *J. China Coal Soc.* 47 (02), 695–710. doi:10.13225/j.cnki.jccs.xr21.1728

Wang, A. W., Pan, Y. S., Zhao, B. Y., and Sheng, J. Q. (2017). Static and dynamic mechanical properties of energy absorption bolts (cable) and field tests. *Chin. J. Geotechnical Eng.* 39 (07), 1292–1301. doi:10.11779/CJGE201707016

Wang, Q., He, M. C., Xu, S., Xin, Z. X., Jiang, B., and Wei, H. Y. (2022). Mechanical properties and engineering application of constant resistance energy absorbing bolt. *J. China Coal Soc.* 47 (04), 1490–1500. doi:10.13225/j.cnki.jccs.2021.0383

Wu, Y. Z., Kang, H. P., Ding, J., Wu, J. X., and Wang, Q. (2015). Development and application of ultrahigh-heat processed rock bolts. *J. China Coal Soc.* 40 (02), 308–313. doi:10.13225/j.cnki.jccs.2014.0283

Wu, Y. Z. (2009). *Study on stress and supporting effects of bolt body*". China Coal Research Institute.

Zhang, B., Zhang, Z. Q., Wang, B., and Zhou, L. (2016). Experimental study of application of yielding bolt to large deformation tunnel. *Rock Soil Mech.* 37 (07), 2047–2055. doi:10.16285/j.rsm.2016.07.028

Zhang, H. J., Li, H. Y., Zhang, T. P., Wang, Q., Wang, W., Wang, X., et al. (2019). Research and engineering application of high pre-stressed resistance enhancement large deformation bolt in deep soft rock roadway. *J. China Coal Soc.* 44 (02), 409–418. doi:10.13225/j.cnki.jccs.2018.0495

Zheng, G., Lei, Y. W., Cheng, X. S., Li, X. Y., and Wang, R. Z. (2020). Influences and mechanisms of anchor failure on anchored pile retaining system of deep excavations. *Chin. J. Geotechnical Eng.* 42 (03), 421–429. doi:10.16285/j.rsm.2021.1715

Zhu, C., He, M. C., Zhang, X. H., Tao, Z. G., Yin, Q., and Li, L. F. (2021). Nonlinear mechanical model of constant resistance and large deformation bolt and influence parameters analysis of constant resistance behavior. *Rock Soil Mech.* 42 (07), 1911–1924. doi:10.16285/j.rsm.2020.1764

Frontiers in Earth Science

Investigates the processes operating within the major spheres of our planet

Advances our understanding across the earth sciences, providing a theoretical background for better use of our planet's resources and equipping us to face major environmental challenges.

Discover the latest Research Topics

See more →



Frontiers

Avenue du Tribunal-Fédéral 34
1005 Lausanne, Switzerland
frontiersin.org

Contact us

+41 (0)21 510 17 00
frontiersin.org/about/contact